

ASTRONOMY AND ASTROPHYSICS LIBRARY

C. Aerts  
J. Christensen-Dalsgaard  
D.W. Kurtz

# Asteroseismology



Springer



# ASTRONOMY AND ASTROPHYSICS LIBRARY

---

**Series Editors:**

- G. Börner, Garching, Germany  
A. Burkert, München, Germany  
W. B. Burton, Charlottesville, VA, USA and  
Leiden, The Netherlands  
M. A. Dopita, Canberra, Australia  
A. Eckart, Köln, Germany  
E. K. Grebel, Heidelberg, Germany  
B. Leibundgut, Garching, Germany  
A. Maeder, Sauverny, Switzerland  
V. Trimble, College Park, MD, and Irvine, CA, USA

For further volumes:  
<http://www.springer.com/series/848>

C. Aerts • J. Christensen-Dalsgaard • D.W. Kurtz

# Asteroseismology



Springer

Conny Aerts  
K.U. Leuven  
Instituut voor Sterrenkunde  
Celestijnenlaan 200D  
3001 Leuven  
Belgium  
conny@ster.kuleuven.be  
and  
Radboud Universiteit Nijmegen  
Department of Astrophysics (IMAPP)  
Heyendaalseweg 135  
6525 AJ Nijmegen  
The Netherlands

Jørgen Christensen-Dalsgaard  
Aarhus University  
Department of Physics and Astronomy  
Building 1520, Ny Munkegade  
8000 Aarhus C  
Denmark  
jcd@phys.au.dk

Donald W. Kurtz  
University of Central Lancashire  
Centre for Astrophysics  
Preston PR1 2HE  
United Kingdom  
dwkurtz@uclan.ac.uk

ISSN 0941-7834  
ISBN 978-1-4020-5178-4 e-ISBN 978-1-4020-5803-5  
DOI 10.1007/978-1-4020-5803-5  
Springer Dordrecht Heidelberg London New York

Library of Congress Control Number: 2009942128

© Springer Science+Business Media B.V. 2010

No part of this work may be reproduced, stored in a retrieval system, or transmitted in any form or by any means, electronic, mechanical, photocopying, microfilming, recording or otherwise, without written permission from the Publisher, with the exception of any material supplied specifically for the purpose of being entered and executed on a computer system, for exclusive use by the purchaser of the work.

*Cover design:* eStudio Calamar S.L.

Printed on acid-free paper

Springer is part of Springer Science+Business Media ([www.springer.com](http://www.springer.com))

---

## Dedication

*To Geert, An, and Jasper (CA)*

*To Birte, Karen, Signe, Clara, and Anna (JCD)*

*To June (DWK)*

---

## Preface

Understanding the stars is the bedrock of modern astrophysics. Stars are the source of life. The chemical enrichment of our Milky Way and of the Universe with all elements heavier than lithium originates in the interiors of stars. Stars are the tracers of the dynamics of the Universe, gravitationally implying much more than meets the eye. Stars ionize the interstellar medium and re-ionized the early intergalactic medium. Understanding stellar structure and evolution is fundamental.

While stellar structure and evolution are understood in general terms, we lack important physical ingredients, despite extensive research during recent decades. Classical spectroscopy, photometry, astrometry and interferometry of stars have traditionally been used as observational constraints to deduce the internal stellar physics. Unfortunately, these types of observations only allow the tuning of the basic common physics laws under stellar conditions with relatively poor precision. The situation is even more worrisome for unknown aspects of the physics and dynamics in stars. These are usually dealt with by using parameterised descriptions of, *e.g.*, the treatments of convection, rotation, angular momentum transport, the equation of state, atomic diffusion and settling of elements, magneto-hydrodynamical processes, and more. There is a dearth of observational constraints on these processes, thus solar values are often assigned to them. Yet it is hard to imagine that one set of parameters is appropriate for the vast range of stars.

Helioseismology led to a large step forward in the precision of the internal structural model of the Sun. Asteroseismology aims to obtain similar improvements for different types of stars by means of their oscillations. Stellar oscillations indeed offer a unique opportunity to probe the internal properties and processes, because these affect the observable frequencies. Moreover, stellar rotation and magnetic fields also modify the frequencies of a star's modes of oscillation. The confrontation between the measured oscillation frequencies and those predicted by models improves the input physics of models to a precision that cannot be reached by any other method, as we have learned from helioseismology.

## VIII Preface

Stellar oscillations are the only diagnostic known that allows us to improve the stellar structure and evolution models by at least an order of magnitude. This book, the first dedicated to this research field, explains how this can be achieved. As such, it encompasses all aspects of the field: we treat raw data gathering and reduction (Chapter 4), oscillation frequency determination through time series analysis (Chapter 5), techniques for the identification of the spherical wavenumbers of the oscillation modes from data (Chapter 6), as well as the theory of stellar oscillations with specific emphasis on the aspects of the physics that can be improved by asteroseismology (Chapter 3). The book begins with an intuitive descriptive introduction into the topic for the non-expert by comparing stellar oscillations with musical sound waves (Chapter 1), then provides an overview of all the various classes of stars in which oscillations have been discovered (Chapter 2). Having introduced all the methodology, Chapter 7 is dedicated to some selected case studies of successful applications of asteroseismology, including a brief overview of helioseismology.

Up to now, the best applications of asteroseismology, *i.e.*, those that have led to improved values of the input physics, have relied dominantly on ground-based data sets. This will change dramatically when the results of the presently operational CoRoT and Kepler missions and other future space missions become available, while ground-based spectroscopic measurements will remain a requirement for a full asteroseismic analysis. We look into the future of this booming research field in Chapter 8 where we emphasize the immense progress that is being made in the quality and quantity of asteroseismic data from ongoing and future space missions, as well as from ground-based instrumentation.

---

## Acknowledgements

It is a pleasure to thank all the scientists and students whose paths we have crossed during conferences, meetings, schools, observing trips, scientific visits, etc., for the interesting discussions and debates and for the education we received. This book could not have been accomplished without considerable help and advice from many colleagues.

We are very grateful to the numerous scientists who gave us permission to use figures from their original publications and for providing us with the electronic files to reproduce them in this monograph. We have included the reference to the original source for each reproduced figure. We acknowledge the copyright holders: Acta Astronomica, Astronomy and Astrophysics, Astronomy and Astrophysics Review, Cambridge University Press, Monthly Notices of the Royal Astronomical Society published by Wiley-Blackwell, Cambridge University Press, Memorie della Societa Astronomica Italiana, and The Astronomical Journal and The Astrophysical journal published by the American Astronomical Society, for granting us the kind permission to reprint the figures from their publications. We thank the BiSON and GOLF teams for the use of figures from their project website and the American Association of Variable Star Observers (AAVSO) for the production of several figures for us.

The preparation of this book has been a memorable period of fruitful and enjoyable collaboration for us.

31 March 2009

Conny Aerts  
K.U.Leuven, Belgium  
Radboud University Nijmegen, the Netherlands

Jørgen Christensen-Dalsgaard  
Aarhus University, Denmark

Donald W. Kurtz  
University of Central Lancashire, United Kingdom

---

# Contents

<b>1</b>	<b>Introducing Asteroseismology</b>	<b>1</b>
1.1	Introduction	1
1.1.1	The Music of the Spheres	1
1.1.2	Seeing with Sound	2
1.1.3	Can we “Hear” the Stars?	6
1.1.4	Pressure Modes and Gravity Modes	7
1.2	1-D Oscillations	7
1.2.1	1-D Oscillations on a String	7
1.2.2	1-D Oscillations in an Organ Pipe	8
1.3	2-D Oscillations in a Drum Head	8
1.4	3-D Oscillations in Stars	10
1.4.1	Radial Modes	11
1.4.2	Nonradial Modes	12
1.4.3	The Effect of Rotation	15
1.4.4	So how does Asteroseismology Work?	17
1.4.5	p Modes and g Modes	17
1.5	An Asteroseismic HR Diagram for p-Mode Pulsators	21
1.6	A Pulsation HR Diagram	23
1.6.1	How do Stars Pulsate: The Relevant Time Scales	23
1.6.2	Why do Stars Pulsate: Driving Mechanisms	26
1.6.3	What Selects the Modes of Pulsation in Stars?	28
<b>2</b>	<b>Stellar Oscillations across the Hertzsprung-Russell Diagram</b>	<b>31</b>
2.1	Stellar Evolution in a Nutshell	33
2.2	Variability Studies from Large-Scale Surveys	38
2.2.1	Hipparcos	38
2.2.2	Ground-Based Surveys	39
2.3	Oscillations Near the Main Sequence	42
2.3.1	Solar-Like Oscillations in Solar-Like Stars	42
2.3.2	$\gamma$ Dor Stars	45
2.3.3	$\delta$ Sct Stars	49

2.3.4	SX Phe Stars . . . . .	53
2.3.5	Rapidly Oscillating Ap Stars . . . . .	56
2.3.6	Slowly Pulsating B Stars . . . . .	60
2.3.7	$\beta$ Cep Stars . . . . .	65
2.3.8	Pulsating Be Stars . . . . .	68
2.4	Oscillations in Pre-Main-Sequence Stars . . . . .	72
2.5	Pulsations in Evolved Stars with $M \leq 9 M_{\odot}$ . . . . .	75
2.5.1	RR Lyrae Stars . . . . .	75
2.5.2	Cepheids . . . . .	80
2.5.3	RV Tauri Stars . . . . .	86
2.5.4	Mira and Semi-Regular Variables . . . . .	88
2.5.5	Solar-Like Oscillations in Red Giants . . . . .	92
2.6	Pulsations in Evolved Stars with $M \geq 9 M_{\odot}$ . . . . .	95
2.6.1	Periodically Variable B and A Supergiants . . . . .	96
2.6.2	Wolf-Rayet Stars . . . . .	101
2.6.3	The Role of Core g Modes in Supernova Explosions . . . . .	103
2.7	Compact Oscillators . . . . .	104
2.7.1	Variable Subdwarf B Stars . . . . .	105
2.7.2	White Dwarf Stars . . . . .	110
2.7.3	Neutron Stars . . . . .	124
2.8	Pulsations in Binaries . . . . .	126
2.8.1	Tidal Perturbations of Free Oscillations . . . . .	127
2.8.2	Tidally Induced Oscillations . . . . .	128
2.8.3	Are the SX Phe Stars all Blue Stragglers? . . . . .	129
2.8.4	Are all Dusty RV Tauri Stars Binaries? . . . . .	131
2.8.5	Hydrogen-Deficient Carbon Stars and Extreme Helium Stars . . . . .	131
2.8.6	Pulsating sdB Primaries . . . . .	133
2.8.7	Pulsating Cataclysmic Variables . . . . .	134
2.8.8	X-Ray Burst Oscillations . . . . .	136
2.9	Conclusions . . . . .	136
3	<b>Theory of Stellar Oscillations</b> . . . . .	137
3.1	General Hydrodynamics . . . . .	137
3.1.1	Equations of Hydrodynamics . . . . .	137
3.1.2	The Adiabatic Approximation . . . . .	142
3.1.3	Equilibrium States and Perturbation Analysis . . . . .	143
3.1.4	Simple Waves . . . . .	147
3.2	Equilibrium Stellar Structure . . . . .	154
3.2.1	Basic Properties of Stellar Evolution . . . . .	154
3.2.2	Microphysics of Stellar Interiors . . . . .	161
3.2.3	Standard Stellar Evolution . . . . .	167
3.2.4	Complications . . . . .	179
3.3	Equations of Linear Stellar Oscillations . . . . .	188
3.3.1	The Oscillation Equations . . . . .	188

3.3.2	Linear, Adiabatic Oscillations . . . . .	195
3.3.3	The Dependence of the Frequencies on the Equilibrium Structure . . . . .	199
3.4	Asymptotic Theory of Stellar Oscillations . . . . .	202
3.4.1	The Cowling Approximation . . . . .	203
3.4.2	Trapping of p and g Modes . . . . .	203
3.4.3	Asymptotic Properties of Frequencies and Eigenfunctions . . . . .	212
3.5	Computed Properties of Modes of Oscillation . . . . .	222
3.5.1	Results for the Present Sun . . . . .	222
3.5.2	The Classification of Modes . . . . .	229
3.5.3	Results for the Models with Convective Cores . . . . .	231
3.6	Variational Properties of Stellar Adiabatic Oscillations . . . . .	234
3.6.1	The Oscillation Equations as Linear Eigenvalue Problems in a Hilbert Space . . . . .	235
3.6.2	Effects on Frequencies of a Change in the Model . . . . .	238
3.7	Driving Mechanisms . . . . .	240
3.7.1	The Work Integral . . . . .	241
3.7.2	The Condition for Instability . . . . .	246
3.7.3	Effects of Convection on Stellar Stability . . . . .	253
3.7.4	Excitation of High-Order g Modes . . . . .	256
3.7.5	Stochastic Excitation of Oscillations . . . . .	258
3.8	Effects of Rotation . . . . .	265
3.8.1	A Simplified Description of the Effect of Rotation . . . . .	265
3.8.2	The Effect of Large-Scale Velocities on the Oscillation Frequencies . . . . .	266
3.8.3	The Effect of Pure Rotation . . . . .	269
3.8.4	Properties of Rotational Splitting . . . . .	272
3.8.5	Effects of Rotation on Low-Frequency Modes . . . . .	276
3.8.6	Higher-Order Rotational Effects . . . . .	284
3.8.7	Effect of Rotation on the Excitation of Oscillations . . . . .	290
4	<b>Observational Techniques . . . . .</b>	295
4.1	Duty Cycle . . . . .	297
4.2	Time . . . . .	298
4.3	Photometry . . . . .	301
4.3.1	Sources of Error in Photometry . . . . .	302
4.3.2	Differential Photometry . . . . .	309
4.3.3	High-Speed Photometry (Non-differential Photometry) . . . . .	311
4.3.4	Filters . . . . .	313
4.4	Spectroscopy . . . . .	315
4.4.1	Wavelength Stability and Low Frequency Noise in Spectroscopy . . . . .	318
4.4.2	High-Resolution Spectroscopy and Line Profile Variations . . . . .	319
4.4.3	Requirements of Spectroscopy for Asteroseismology . . . . .	322

4.4.4	Observational Line Diagnostics . . . . .	325
4.4.5	Increasing the Signal-to-Noise Ratio of the Line Profile Variations . . . . .	328
4.4.6	Increasing the Radial Velocity Precision in the Context of Exoplanet Finding and Solar-Like Oscillations . . . . .	331
4.4.7	Disentangling Spectra to Interpret the Oscillations of Double-Lined Binaries . . . . .	333
<b>5</b>	<b>Frequency Analysis . . . . .</b>	<b>337</b>
5.1	Harmonic Analysis by Least Squares . . . . .	338
5.1.1	Searching for a Single Frequency . . . . .	338
5.1.2	Searching for Multiple Frequencies . . . . .	341
5.2	Non-parametric Frequency Analysis Methods . . . . .	342
5.2.1	String Length Methods . . . . .	342
5.2.2	Phase Dispersion Minimization . . . . .	348
5.3	Parametric Frequency Analysis Methods . . . . .	350
5.3.1	The Continuous Fourier Transform of an Infinite Time Series . . . . .	351
5.3.2	The Continuous Fourier Transform of a Finite Time Series . . . . .	352
5.3.3	Real Life: The Discrete Fourier Transform . . . . .	354
5.3.4	The Classical Periodogram . . . . .	360
5.3.5	The Lomb-Scargle Periodogram . . . . .	361
5.4	Significance Criteria . . . . .	363
5.5	Error Estimation of the Derived Frequencies . . . . .	366
5.5.1	Data without Alias Problems . . . . .	366
5.5.2	Data suffering from Aliasing . . . . .	368
5.6	The use of Weights in Merging different Data Sets for Frequency Analysis . . . . .	369
5.7	Damped Oscillations . . . . .	372
5.8	Eliminating Aliases . . . . .	374
5.9	Conclusions . . . . .	375
<b>6</b>	<b>Mode Identification . . . . .</b>	<b>377</b>
6.1	Mode Identification from Multicolour Photometry . . . . .	379
6.1.1	General Considerations . . . . .	380
6.1.2	Detailed Description . . . . .	383
6.1.3	Mode Identification Schemes . . . . .	393
6.2	Mode Identification from High-Resolution Spectroscopy . . . . .	405
6.2.1	Calculation of Theoretical Line-Profile Variations . . . . .	406
6.2.2	Line Profile Fitting . . . . .	414
6.2.3	The Moment Method . . . . .	415
6.2.4	The Pixel-by-Pixel Method . . . . .	434
6.3	Mode Identification from Combined Photometry and Spectroscopy . . . . .	440

6.4	Towards Mode Identification from Combined Interferometry and Spectroscopy? . . . . .	442
6.5	Towards Mode Identification from Eclipse Mapping? . . . . .	445
<b>7</b>	<b>Applications of Asteroseismology . . . . .</b>	<b>447</b>
7.1	Helioseismology . . . . .	447
7.1.1	Introduction . . . . .	447
7.1.2	Analysis of Solar-Oscillation Observations . . . . .	456
7.1.3	Observational Results on Solar Oscillations . . . . .	461
7.1.4	Properties of Solar Oscillations . . . . .	470
7.1.5	Principles of Inverse Analysis . . . . .	488
7.1.6	Inversion for Solar Structure . . . . .	500
7.1.7	Results on Solar Structure . . . . .	505
7.1.8	Results for Solar Rotation . . . . .	522
7.1.9	Temporal Variations of the Solar Interior . . . . .	529
7.2	Solar-Like Pulsators . . . . .	535
7.2.1	Observational Aspects . . . . .	535
7.2.2	Asteroseismic Diagnostics . . . . .	539
7.2.3	The Binary $\alpha$ Centauri A and B . . . . .	558
7.2.4	The Subgiant $\eta$ Bootis . . . . .	576
7.2.5	The Red Giant $\varepsilon$ Ophiuchi . . . . .	591
7.3	Heat Driven Main Sequence Stars . . . . .	603
7.3.1	The $\beta$ Cep Star V836 Centauri . . . . .	603
7.3.2	The $\beta$ Cep Star $\nu$ Eridani . . . . .	614
7.3.3	The $\beta$ Cep Binary $\theta$ Ophiuchi . . . . .	625
7.3.4	HR 1217 among the roAp Stars . . . . .	634
7.4	Compact Pulsators . . . . .	646
7.4.1	The GW Vir Star PG 1159–035, GW Vir itself . . . . .	646
7.4.2	The DB White Dwarf GD 358, V777 Her . . . . .	651
7.4.3	The Subdwarf B Star PG 0014+067 . . . . .	656
7.4.4	The Subdwarf B Eclipsing Binary PG 1336–018, NY Vir . . . . .	661
<b>8</b>	<b>The Future . . . . .</b>	<b>669</b>
8.1	Space Missions . . . . .	670
8.1.1	CoRoT . . . . .	671
8.1.2	The Kepler Mission . . . . .	672
8.1.3	BRITE . . . . .	673
8.1.4	PLATO . . . . .	673
8.1.5	Solar Missions . . . . .	674
8.2	Ground-Based Networks and Antarctica . . . . .	675
8.2.1	SONG: A Ground-Based Radial Velocity Network . . . . .	675
8.2.2	Antarctic Asteroseismology . . . . .	676
<b>A</b>	<b>Summary of the Different Classes of Stellar Pulsators . . . . .</b>	<b>679</b>

<b>B Properties of Legendre Functions and Spherical Harmonics</b> .....	683
B.1 Properties of Legendre Functions .....	683
B.2 Properties of Spherical Harmonics .....	685
<b>C Mathematical Preliminaries</b> .....	689
C.1 Formulation of Oscillation Equations in Complex Form .....	689
C.2 Vector Operators in Spherical Polar Coordinates .....	690
<b>D Adiabatic Oscillations in an Isothermal Atmosphere</b> .....	693
D.1 Equilibrium Structure .....	693
D.2 Oscillation Properties .....	694
D.3 Boundary Conditions in a Stellar Atmosphere .....	696
<b>E Asymptotic Theory of Stellar Oscillations</b> .....	699
E.1 A General Asymptotic Expression .....	699
E.2 JWKB Analysis .....	701
E.3 The Duvall Law for p-Mode Frequencies .....	705
E.3.1 Frequencies in Polytropic Envelopes .....	707
E.3.2 Frequencies of Low-Degree Modes .....	709
E.4 Asymptotic Properties of Eigenfunctions .....	710
E.4.1 Asymptotic Properties of the p-Mode Eigenfunctions ..	712
E.4.2 Asymptotic Properties of the g-Mode Eigenfunctions ..	715
<b>Bibliography</b> .....	717
<b>Subject Index</b> .....	845
<b>Object Index</b> .....	861
<b>Acronym Definition Index</b> .....	865

# 1

---

## Introducing Asteroseismology<sup>1</sup>

### 1.1 Introduction

#### 1.1.1 The Music of the Spheres

Pythagoras of Samos (c. 569–475 BC) is best-known now for the Pythagorean Theorem relating the sides of a right triangle:  $a^2 + b^2 = c^2$ , but his accomplishments go far beyond this. When Pythagoras was a young man (c. 530 BC) he emigrated to Kroton in southern Italy where he founded the Pythagorean Brotherhood who soon held secular power over not just Kroton, but more extended parts of Magna Grecia. He and his followers were natural philosophers (they invented the term “philosophy”) trying to understand the world around them; in the modern sense we would call them scientists. They believed that there was a natural harmony to everything, that music, mathematics and what we now call physics were intimately related. In particular, they believed that the motions of the Sun, moon, planets and stars generated musical sounds. They imagined that the Earth is a free-floating sphere and that the daily motion of the stars and the movement through the stars of the Sun, moon and planets were the result of the spinning of crystalline spheres or wheels that carried these objects around the sky. The gods, and those who were more-than-human (such as Pythagoras), could hear the hum of the spinning crystalline spheres: they could hear the *Music of the Spheres* (see Koestler 1959).

The idea of the Music of the Spheres seems to resonate in the human mind; the expression is alive and current today, 2500 years later. A century after Pythagoras, Plato (c. 427–347 BC) said that “a siren sits on each planet, who carols a most sweet song, agreeing to the motion of her own particular planet, but harmonizing with all the others” (see Brewer 1894). Two millennia

---

<sup>1</sup> Text partly reproduced from Kurtz, D.W., 2006, Stellar Pulsation: an Overview, ASP, Volume 349, 101, Astrophysics of Variable Stars, Eds C. Sterken & C. Aerts, with permission from the Astronomical Society of the Pacific.

after Plato, Johannes Kepler (1571 – 1630) so believed in the Music of the Spheres that he spent years trying to understand the motions of the planets in terms of musical harmonies. He did admit that “no sounds are given forth,” but still held “that the movements of the planets are modulated according to harmonic proportions.” It was only after Herculean efforts failed that Kepler gave up on what he wanted to be true, the Music of the Spheres, started over and discovered his famous third law for the planets,<sup>2</sup>  $P^2 = a^3$ . It was this willingness to discard a cherished belief, an ancient and venerable idea, and begin again that made Kepler a truly modern scientist.

William Shakespeare (1564 – 1616) was a contemporary of Kepler, and of course you can find the Music of the Spheres in Shakespeare (*Merchant of Venice*, v. 1):

There's not the smallest orb which thou beholdest  
but in his motion like an angel sings  
Still quiring to the young-eyed cherubim

The Music of the Spheres never left artistic thought or disappeared from the language, but as a “scientific” idea it faded from view with Kepler’s Laws of motion of the planets. And so it languished until the 1970s when astronomers discovered that there is resonant sound inside stars, that stars “ring” like giant bells, that there is a real Music of the Spheres.

### 1.1.2 Seeing with Sound

In the opening paragraph of his now-classic book, *The Internal Constitution of the Stars* (Eddington 1926), Sir Arthur Stanley Eddington lamented:

At first sight it would seem that the deep interior of the Sun and stars is less accessible to scientific investigation than any other region of the universe. Our telescopes may probe farther and farther into the depths of space; but how can we ever obtain certain knowledge of that which is hidden behind substantial barriers? What appliance can pierce through the outer layers of a star and test the conditions within?

Eddington considered theory to be the proper answer to that question: From our knowledge of the basic laws of physics, and from the observable boundary conditions at the surface of a star, we can *calculate* its interior structure, and we can do so with confidence.

While we humans shower honours, fame and fortune on those who can run 100 m in less than 10 s, leap over a 2-m bar, or lift 250 kg over their heads, cheetahs, dolphins and elephants (if they could understand our enthusiasm for such competitions) would have a good laugh at us for those pitiful efforts. We are no competition for them in physical abilities. But *we* can calculate

---

<sup>2</sup> Relating period  $P$  and semi-major axis  $a$  of the orbit of the planet.

the inside of a star! That is at the zenith of human achievement. No other creature on planet Earth can aspire to this most amazing feat.

Some humility is called for, however. In *The Internal Constitution of the Stars* Eddington reminds us on page 1: “We should be unwise to trust scientific inference very far when it becomes divorced from opportunity for observational test.” Indeed! Therefore he would have been amazed and delighted to know that there is now a way to see inside the stars – not just calculate their interiors – but literally *see*. We have invented Eddington’s “appliance” to pierce the outer layers of a star: It is asteroseismology, the probing of stellar interiors through the study of their surface pulsations.

Stars are not quiet places. They are noisy; they have sound waves in them. Those sounds cannot get out of a star, of course; sound does not travel in a vacuum. But for many kinds of stars – the pulsating stars – the sound waves make the star periodically swell and contract, get hotter and cooler. With our telescopes we can see the effects of this: the periodic changes in the star’s brightness; the periodic motion of its surface moving up-and-down, back-and-forth. Thus we can detect the natural oscillations of the star and “hear” the sounds inside them.

Close your eyes and imagine that you are in a concert hall listening to an orchestra tuning up: The first violinist walks over to the piano and plunks middle-A which oscillates at 440 Hz. All the instruments of the orchestra then tune to that frequency. And yet, listen! You can hear the violin. You can hear the bassoon. You can hear the French horn. You can hear the cello, the flute, the clarinet and the trumpet. Out of the cacophony you can hear each and every instrument separately and identify them, even though they are all playing exactly the same frequency. How *do* you do that?

Each instrument in the orchestra is shaped to put power into some of its natural harmonics and to damp others. The shape of the instrument determines its natural oscillation modes, so determines which harmonics are driven and which are damped. It is the combination of the frequencies, amplitudes and phases of the harmonics that defines the character of the sound emanated, that gives the timbre of the instrument, that gives it its unique sound. It is the combination of the harmonics that defines the rate of change of pressure with time emanating from the instrument – that defines the sound waves it creates.

A sound wave is a pressure wave. In a gas this is a rarefaction and compression of the gas that propagates at the speed of sound. The high pressure pushes, compresses and propagates. Ultimately, this is done at the molecular level; the information that the high pressure is coming is transmitted by individual molecular collisions. In the adiabatic case, the speed of sound is  $c = \sqrt{\Gamma_1 p / \rho}$ , where  $\Gamma_1$  is one of the adiabatic exponents (see Eqs(3.18) in Chapter 3 for a definition),  $p$  is pressure and  $\rho$  is density. Of course, for an ideal gas  $p = \rho k_B T / \mu m_u$ , where  $k_B$  is Boltzmann’s constant,  $\mu$  is mean molecular weight, and  $m_u$  is the atomic mass unit; thus  $c = \sqrt{\Gamma_1 k_B T / \mu m_u}$ . The changes in pressure are therefore accompanied by changes in density and

temperature. Principally, as we can see from the last relationship, in this case the speed of sound depends on the temperature and chemical composition of the gas.<sup>3</sup> Thus, if the temperature is higher, and the molecules are moving more quickly, they collide more often and the sound speed is higher. And at a given temperature in thermal equilibrium, lighter gases move more quickly, collide more often, and the sound speed is higher than for heavier gases.

This last effect is the cause of a well-known party trick. Untie a helium balloon, breathe in a lung-full of helium, and you will sound like Donald Duck when you talk! The speed of sound in helium at standard temperature and pressure is  $970\text{ m s}^{-1}$ , compared to  $330\text{ m s}^{-1}$  in air (78% molecular nitrogen, 21% molecular oxygen and 1% argon). With the nearly three times higher sound speed in helium the frequency of your voice goes up by that factor of three, hence the high-pitched hilarity. (As an aside: breathing helium is safe, so long you do not do it for too long, *i.e.*, so long as it is not the only thing you are breathing. It is inert and will not react chemically. Deep-sea divers breathe heliox, a mixture of helium and oxygen, to reduce decompression time compared to breathing an air mixture, since helium comes out of solution in the blood more quickly than does molecular nitrogen.)

Thus, if you can measure the speed of sound in a gas, you have information about the pressure and density of that gas, and, from the equation of state, you may constrain the temperature and chemical composition. Stars are made of gas, and they are like giant musical instruments. They have natural overtones (not the harmonics of musical instruments, so the sounds of the stars are dissonant to our ears when we play them at audible frequencies), and just as you can hear what instrument makes the sounds of an orchestra, *i.e.*, you can “hear” the shape of the instrument, we can use the frequencies, amplitudes and phases of the sound waves that we detect in the stars to “see” their interiors – to see their internal “shapes”. A goal of asteroseismology is to measure the sound speed throughout a star so that we can know those fundamental parameters of the stellar structure.

We humans are incredibly *visual* creatures; for us, sight is a dominant sense. We think “seeing is believing”. Yet other animals perceive the world in other ways. Take a dog for a walk. The dog dedicates 60 times more brain to its sense of smell than you do. Dogs can see, but for them “smelling is believing”. If a dog sees an object that it does not understand and does not trust, it will approach cautiously (sometimes with its hackles up) until the suspicious object can be smelled, and *then* the situation will be clarified and the dog will “know” the object. For them “smelling is believing.”

What happens to you when you “see”? Does your brain detect the light? Is there a real image in your head? Of course not. Your eye forms an image on your retina, the photons are absorbed, an electro-chemical signal passes

---

<sup>3</sup> On the other hand, for a gas dominated by the pressure of degenerate electrons, the thermodynamic properties, and hence the sound speed, depend little on temperature.

down your optic nerve to the part of your brain that interprets the incoming visual signal, and you have the impression that there is a 3-D theatre in your head. You “see” an image of the world.

So what then happens to you when you “hear”? Does your brain hear the sound? Are the sound waves in your head? Again, of course not. Your eardrum oscillates in and out with the increasing and decreasing pressure of the sound wave. Through the bones in your ears and through sensitive hairs the sound is transmitted, then transformed into an electro-chemical signal that passes to the part of your brain that interprets the incoming aural signal, and you have the impression that there is a 3-D sound system in your head. You “hear” the world.

While our perceptions of sight and sound are very different experiences, they are physiologically similar, and they are both providing us with information about the world around us. So it is possible to “see” with sound? Yes. Of course it is. Bats do it with echo-locating. They emit sounds and the returning echoes tell the bat where everything in its environment is, down to the small insects that they catch for food (and also provide velocity information from the Doppler shift). Those sounds are converted to electro-chemical signals in the bat’s brain, and the bat has a picture of the world around it. That is “seeing” with sound. A colony of a million bats leaving a narrow cave mouth in the dark has few collisions; the bats can “see” each other. It is not possible to get inside the mind of another creature. We cannot even do it with a fellow human; we cannot know if another person has the same experience that we have, *e.g.*, of colour, of tone, of taste. We assume that they do, and get along well with that assumption, so similarly we may assume that bats “see” the world through sound. Their sense of hearing powers the 3-D theatre in their minds, just as our sense of sight does for us. We may surmise that the experiences of seeing with light or sound are similar.

Similarly, asteroseismology uses astronomical observations – photometric and spectroscopic ones – to extract the frequencies, amplitudes and phases of the sounds at a star’s surface. Then we use basic physics and mathematical models to infer the sound speed and density inside a star, throughout its interior, and thence the pressure. With reasonable assumptions about chemical composition and knowledge of appropriate equations of state, the temperature can then be derived. These are, in a real sense, all the equivalent of the electro-chemical signals in our brains. We build up a picture in the 3-D theatre in our minds of what the inside of a star looks like. We see inside the star. The sounds tell us what the interior structure of the star *has* to be.

Who has not been amazed to see a picture of the face of a foetus in the womb, imaged using ultrasound waves? Do you question the reality of that? No. That is a real picture of the baby before it is born. Identically, using infrasound from the stars, the pictures of their insides that we see using asteroseismology have this same reality.

We have answered Eddington's question, "What appliance can pierce through the outer layers of a star and test the conditions within?" The answer is: **Asteroseismology, the real Music of the Spheres.**

### 1.1.3 Can we "Hear" the Stars?

So you have been persuaded that there are sounds in stars and we can use those to "see" inside them. But can we actually hear them? Is there really a Music of the Spheres? Amazingly, the answer to that is also yes.

What we consider to be musical is mostly the relationships among the frequencies, amplitudes and phases of sounds, not their absolute pitch. A few humans have perfect pitch, and serious musicians and music-lovers do care about the key that a piece of music is played in – for the sound, and sometimes for the ease of playing it. But for most people a change of key does not change the character of the music – a melody is still recognizable in another key – because the *relationships* among the frequencies are not changed.

Now think about this: We have sound recording equipment that can detect the ultrasound of bats. We record the frequencies, amplitudes and phases of those sounds. Then, we simply shift the frequencies down into the audible range while keeping the frequency ratios the same, while keeping the amplitude and phase relationships; *i.e.*, we come down some octaves and perform a change of key. Played through a speaker we can then hear what bats sound like. It is a legitimate experience and may even be close to what it would be like to have ultrasound hearing and actually hear the bats directly with our own ears. (Fortunately, we cannot hear the bats, for they are loud and they are noisy; we probably would not like it.)

Similarly, with the right equipment we may record the infrasounds of whales, shift them up in frequency into the audible, and experience the haunting "songs" of the whales. This, too, is really hearing the sounds of the whales. (Unfortunately, the whales can hear the infrasounds of our many ships, so their environment has become vastly noisier over the last two centuries.)

Therefore, it is fair to say that when we observe the frequencies, amplitudes and phases of a pulsating star that are caused by sounds in the star, and we shift those by many octaves (usually with a key change) up into the audible and play them through a speaker, we are experiencing the real Music of the Spheres. Pythagoras and Kepler would have been amazed.

While it is possible to use our observations of pulsating stars to generate sound files for the stars, and listen to them, we do not do science that way. Asteroseismology uses the frequencies, amplitudes and phases from observations of pulsating stars directly to model and probe the stellar interiors. But the sounds are intellectually intriguing, and they are even aesthetically pleasing.

The first musical composition based on the sounds of the stars is called *Stellar Music No 1*, by Jenő Keuler and Zoltán Kolláth of Konkoly Observa-

tory. Discussion of the music, a sound file and a score can be found on Zoltán Kolláth's website<sup>4</sup>.

### 1.1.4 Pressure Modes and Gravity Modes

When an idea is being discussed in Belgium, the response often begins, "Well, it's not as simple as that!" This expression, much loved by Belgian astronomers, is often useful to the rest of us, too. Therefore, given all that has been said so far: It is not as simple as that.

There is more to stellar pulsation than acoustic waves – sound waves – in stars. Those acoustic waves are known as “pressure” modes, or p modes. There are equally important “gravity” modes, or g modes, where the restoring force of the pulsation is not pressure, but buoyancy. Much of the picture of stellar pulsation that we have been painting is a valid view of gravity modes, too; they also probe the interiors of stars, and let us see below their surfaces. But gravity modes are not acoustic – they are not caused by sounds in the stars. We shall discuss these two kinds of pulsation in parallel as our view of stellar pulsation grows clearer.

Now we need to build in our minds a picture of what the 3-D pulsations of stars look like.

## 1.2 1-D Oscillations

### 1.2.1 1-D Oscillations on a String

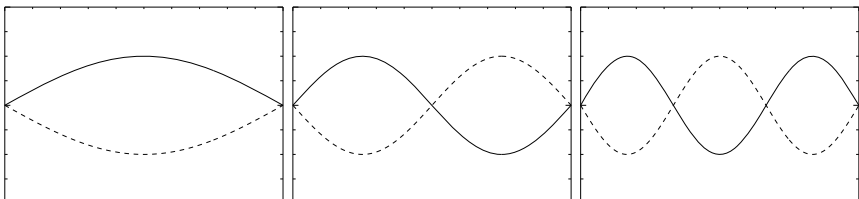


**Fig. 1.1.** The first three oscillation modes for a string that is fixed at both ends, such as a violin string or a guitar string. On the left is the fundamental mode; in the centre is the first overtone which has a single node; and on the right is the second overtone which has two nodes. Note that the nodes are uniformly spaced.

Figure 1.1 shows the fundamental mode and the first and second overtone modes for a vibrating string such as those on violins, guitars or any musical string instrument. The frequencies of these modes depend on the length of

---

<sup>4</sup> <https://www.konkoly.hu/staff/kollath/stellarmusic/>.

the string, the tension and the material the string is made of. Importantly, the tension and composition of the string are uniform along its length. Under those conditions the first overtone mode has twice the frequency of the fundamental mode, the second overtone mode has a frequency three times that of the fundamental mode, and so on. We therefore refer to these overtones as “harmonics”, since they have small integer ratios. To our ears the frequencies with small integer ratios, such as 2:1, 3:2, 4:3, are harmonious. But note that here we distinguish the words “overtone” and “harmonic”; while they are the same for modes on a uniform string, they are not the same for stars, as we shall see.

### 1.2.2 1-D Oscillations in an Organ Pipe

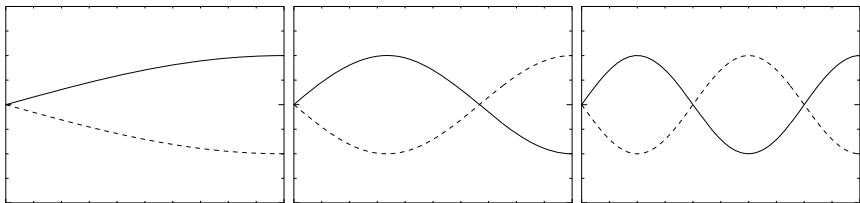


**Fig. 1.2.** The first three oscillation modes for an organ pipe with one end (on the left) closed, and one end (on the right) open. On the left is the fundamental mode; in the centre is the first overtone which has a single node; and on the right is the second overtone which has two nodes. Note that the open end is an anti-node in the displacement of the air, and that the nodes are uniformly spaced.

If instead of a string we think of the oscillations of the air in an organ pipe, or any wind instrument with one closed end, then there is a displacement node at the closed end of the pipe, and the other, open end has a displacement antinode. Figure 1.2 shows this schematically. As for the string in the previous section, note that the overtones are harmonic with small integer ratios – in the cases in Fig. 1.2 these are 3:1 and 5:1 – since the air temperature and chemical composition are uniform within the pipe, so the sound speed is constant along the pipe. While the organ pipe is in some ways a simple analogue of a radially pulsating star, the uniform temperature is far from true for stars, as we shall see, and therein lies a big difference.

### 1.3 2-D Oscillations in a Drum Head

To imagine the oscillations of a 2-D membrane, a drum head is easy to visualize, as can be seen in Fig. 1.3. Because the drum head is two-dimensional,

there are nodes in two orthogonal directions. One set of modes has nodes that are concentric circles on the drum head, and those modes are called *radial* modes. For a drum head the rim is always a node, so the fundamental radial mode simply has the drum head move up and down with circular symmetry with maximum amplitude at the centre, which is an antinode. The first radial overtone has a node that is a circle on the drum head with the centre and outside annulus moving in antiphase; the second radial overtone has two concentric circles as nodes, and so on. (These radial modes are rapidly damped in an actual drum head, so contribute only to the initial sound of the drum being struck, and not much to the ringing oscillations that follow.)

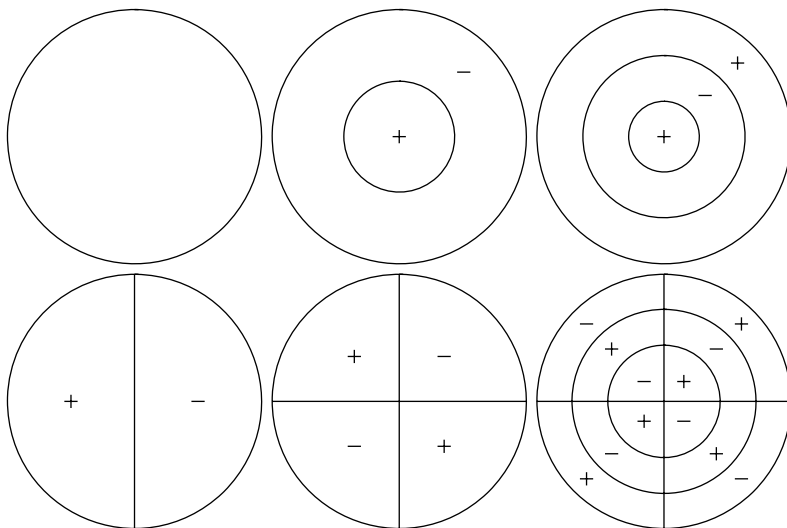


**Fig. 1.3.** Representations of some oscillation modes in a drum head. The rim of the drum is fixed, so is forced to be a node in all cases. The top left circle represents the fundamental radial mode for the drum: the rim is a node and the centre of the drum is an anti-node. The middle top figure represents the first *radial* overtone, with one node which is a concentric circle. The plus and minus signs indicate that the outer annulus moves outwards while the inner circle moves inwards, and vice versa. The top right figure represents the second radial overtone. The bottom left figure shows the simplest *nonradial* mode for a drum, the dipole mode, where a line across the middle of the drum is a node and one side moves up, while the other moves down, then vice versa. The middle bottom panel represents the quadrupole nonradial mode, and the bottom right figure shows the second overtone quadrupole mode. The modes are characterized by quantum numbers, one for the number of radial nodes, and one for the number of nonradial nodes. So reading from left-to-right, top-to-bottom, the modes are numbered (0,0), (1,0), (2,0), (0,1), (0,2) and (2,2). A similar notation in 3-D exists for stellar pulsation modes, as we shall see.

The second direction of nodes in a drum head gives rise to the *nonradial* modes. The first nonradial mode is the dipole mode which has a node that is a line across the drum head dividing it in two, so that the two halves oscillate in antiphase. The second nonradial overtone has two crossing nodes dividing the drum into four equal sections. Of course, there are modes that have both radial and nonradial nodes. The important point about the drum head is that these modes do *not* have frequencies with small integer ratios, so the drum is not harmonic; it does not ring with a musical sound<sup>5</sup>. For a uniform density and tension drum head, the solutions to the oscillation equations are Bessel functions, as illustrated by the radial nodes in Fig. 1.3. To visualize drum head oscillations better, excellent graphical movies can be found on the web site of Dan Russell<sup>6</sup>.

## 1.4 3-D Oscillations in Stars

Stars are three-dimensional, so their natural oscillation modes have nodes in three orthogonal directions. These are described by the distance  $r$  to the centre, co-latitude  $\theta$  and longitude  $\phi$ ; here  $\theta$  is measured from the pulsation pole, the axis of symmetry (hence is co-latitude, since latitude is measured from the equator). The nodes are concentric shells at constant  $r$ , cones of constant  $\theta$  and planes of constant  $\phi$ . For a spherically symmetric star the solutions to the equations of motion have displacements in the  $(r, \theta, \phi)$  directions and are given by<sup>7</sup>

$$\xi_r(r, \theta, \phi, t) = a(r) Y_l^m(\theta, \phi) \exp(-i 2\pi\nu t), \quad (1.1)$$

$$\xi_\theta(r, \theta, \phi, t) = b(r) \frac{\partial Y_l^m(\theta, \phi)}{\partial \theta} \exp(-i 2\pi\nu t), \quad (1.2)$$

$$\xi_\phi(r, \theta, \phi, t) = \frac{b(r)}{\sin \theta} \frac{\partial Y_l^m(\theta, \phi)}{\partial \phi} \exp(-i 2\pi\nu t), \quad (1.3)$$

where  $\xi_r$ ,  $\xi_\theta$  and  $\xi_\phi$  are the displacements,  $a(r)$  and  $b(r)$  are amplitudes,  $\nu$  is the oscillation frequency<sup>8</sup> and  $Y_l^m(\theta, \phi)$  are spherical harmonics given by

<sup>5</sup> Tympani do have a musical tone. This is the result of careful design where the air pressure in the drum damps some modes, and allows those that are close to harmonic to oscillate, thus giving a recognizable note.

<sup>6</sup> <http://www.kettering.edu/~drussell/Demos/MembraneCircle/Circle.html>.

<sup>7</sup> Here the displacements are written in complex form which is a mathematical convenience; the physically meaningful quantities are obtained by taking the real parts. See also Section C.1.

<sup>8</sup> more precisely, the *cyclic* frequency; later we also introduce the *angular* frequency  $\omega = 2\pi\nu$ .

$$Y_l^m(\theta, \phi) = (-1)^m \sqrt{\frac{2l+1}{4\pi} \frac{(l-m)!}{(l+m)!}} P_l^m(\cos \theta) \exp(im\phi) \quad (1.4)$$

and  $P_l^m(\cos \theta)$  are Legendre polynomials (see also Appendix B) given by

$$P_l^m(\cos \theta) = \frac{1}{2^l l!} (1 - \cos^2 \theta)^{m/2} \frac{d^{l+m}}{d \cos^{l+m} \theta} (\cos^2 \theta - 1)^l. \quad (1.5)$$

Note that the spherical harmonics are usually defined such that the integral of  $|Y_l^m|^2$  over the unit sphere equals 1, as secured by the normalization constant

$$c_{lm} \equiv \sqrt{\frac{2l+1}{4\pi} \frac{(l-m)!}{(l+m)!}} \quad (1.6)$$

(cf. Eq. (1.4)).

In most pulsating stars the pulsation axis coincides with the rotation axis. The main exceptions are the rapidly oscillating Ap stars where the axis of pulsational symmetry is the magnetic axis which is inclined to the rotational axis (see Section 2.3.5 in Chapter 2).

As with the drum heads, where there were two quantum numbers to specify the modes, for 3-D stars there are three quantum numbers to specify these modes:  $n$  is related to the number of radial nodes and is called the *overtone* of the mode<sup>9</sup>;  $l$  is the *degree* of the mode and specifies the number of surface nodes that are present;  $m$  is the *azimuthal order* of the mode, where  $|m|$  specifies how many of the surface nodes are lines of longitude. It follows therefore that the number of surface nodes that are lines of co-latitude is equal to  $l - |m|$ . The values of  $m$  range from  $-l$  to  $+l$ , so there are  $2l + 1$  modes for each degree  $l$ .

What do these modes in stars look like?

### 1.4.1 Radial Modes

The simplest modes are the *radial* modes with  $l = 0$ , and the simplest of those is the fundamental radial mode. In this mode the star swells and contracts, heats and cools, spherically symmetrically with the core as a node and the surface as a displacement antinode. It is the 3-D analogy to the organ pipe in its fundamental mode shown in the left-hand panel of Fig. 1.2. This is the usual mode of pulsation for Cepheid variables and for RR Lyrae stars, amongst others.

The first overtone radial mode has one radial node that is a concentric shell within the star. As we are thinking in terms of the radial displacement, that shell is a node that does not move; the motions above and below the node

---

<sup>9</sup> A rigorous definition of  $n$  will be given in Chapter 3. Sometimes  $k$  is preferred to represent this quantum number, particularly amongst those working on pulsating white dwarf stars.

move in antiphase. As an example, in the roAp stars (which are nonradial pulsators) radial nodes can be directly observed in their atmospheres with just this kind of motion in antiphase above and below the radial node (Kurtz *et al.* 2005b). The surface of the star is again an antinode.

There are Cepheid variables, RR Lyrae stars and  $\delta$  Sct stars (see Chapter 2 for a definition) that pulsate simultaneously in the fundamental and first overtone radial modes. In the cases of the Cepheids and RR Lyrae stars they are known as double-mode Cepheids and RRd stars, respectively. For the Cepheids the ratio of the first overtone period to the fundamental period is 0.71; for the  $\delta$  Sct stars it is 0.77. This is in obvious contrast with the 0.33 ratio found in organ pipes and the 0.5 ratio found on strings (see Figs 1.1 and 1.2).

This difference is profound and it is our first use of asteroseismology. If the star were of uniform temperature and chemical composition (so that the sound speed were constant), then the ratio would be similar to that in the organ pipe.<sup>10</sup> The larger ratios in the Cepheids and  $\delta$  Sct stars are a direct consequence of the sound speed gradient in them, hence of the temperature and (in some places) of chemical composition gradients. The small, but significant differences between the Cepheid and  $\delta$  Sct ratios are a consequence of the Cepheid giant star being more centrally condensed than the hydrogen core-burning  $\delta$  Sct star. Thus, just by observing two pulsation frequencies we have had our first look into the interiors of some stars.

#### 1.4.2 Nonradial Modes

The simplest of the nonradial modes is the axisymmetric *dipole* mode with  $l = 1, m = 0$ . For this mode the equator is a node; the northern hemisphere swells up while the southern hemisphere contracts, then vice versa; one hemisphere heats while the other cools, and vice versa – all with the simple cosine dependence of  $P_1^0(\cos \theta) = \cos \theta$ , where  $\theta$  is the co-latitude. There is no change to the circular cross-section of the star, so from the observer’s point of view, the star seems to oscillate up and down in space.

That is disturbing to contemplate. What about Newton’s laws? How can a star “bounce” up and down in free space without an external driving force? The answer is that an incompressible sphere cannot do this; it cannot pulsate in a dipole mode. After a large earthquake the Earth oscillates in modes such as those we are describing. But it does not oscillate in the dipole mode and bounce up and down in space. It cannot. There was a time when it was thought that stars could not do this either (Pekeris 1938), but first Smeyers (1966) in the adiabatic case, then Christensen-Dalsgaard (1976) more generally showed that the centre-of-mass of a star is not displaced during dipole oscillations, so stars can pulsate in such modes.

---

<sup>10</sup> For an isothermal sphere in hydrostatic equilibrium the ratio is around 0.5 (Taff & Van Horn 1974).

Nonradial modes only occur for  $n \geq 1$ , so in the case of the  $l = 1$  dipole mode, there is at least one radial node within the star. While the outer shell is displaced upwards from the point of view of the observer, the inner shell is displaced downwards and the centre of mass stays fixed. Dipole modes are the dominant modes observed in the rapidly oscillating Ap stars, and are also seen in many other kinds of pulsating variables.

Modes with two surface nodes ( $l = 2$ ) are known as quadrupole modes. For the  $l = 2, m = 0$  mode the nodes lie at latitudes  $\pm 35^\circ$ , since  $P_2^0(\cos \theta) = (3\cos^2 \theta - 1)/2$  (see also Appendix B for the position of the nodal lines of different modes). The poles of an  $l = 2, m = 0$  mode swell up (and heat up, although not usually in phase with the swelling) while the equator contracts (and cools), and vice versa. Figure 1.4 represents and explains a set of *octupole* modes with  $l = 3$ , giving a mental picture of what the modes look like on the stellar surface which is generally inclined with respect to the line-of-sight.

Unfortunately, we are not yet at the stage where we can resolve stellar surfaces and detect the nodal lines directly from intensity or Doppler maps such as the ones shown in Fig. 1.4. This can only be done for the Sun so far. As a consequence, for other stars we have to deal with observations representing integrated quantities over the stellar surface, such as the surface-averaged brightness or radial velocity. It is then intuitively clear that, for a fixed value of the amplitude of the oscillation, and for a particular value of the inclination of the symmetry axis of pulsation with respect to the line-of-sight, such observed quantities must be smaller for higher degree  $l$  modes than for lower degree modes. Indeed, the higher  $l$ , the more sectors and/or zones will divide the stellar surface, with neighbouring regions having opposite sign in intensity or velocity. Their influence on the integrated quantity therefore partially tends to cancel out. This so-called *partial cancellation* is a simple consequence of the total number of nodal lines on the stellar surface.

We will derive rigorous mathematical expressions for the partial cancellation in Chapter 6 for the various integrated quantities defined in Chapters 4 and 6. To get a feel for the consequences of this effect, let us assume here the simplest case, which is the surface-integrated intensity of an axisymmetric mode over a stellar disc that does not suffer from limb darkening. In that simplest case, the partial cancellation is described well by an integral of the intensity eigenfunction over the visible stellar disc, *i.e.*, it is proportional to

$$c_{l0} \int_0^{\pi/2} P_l(\cos \theta) \sin \theta \cos \theta d\theta, \quad (1.7)$$

where  $c_{l0}$  is defined in Eq. (1.6). This factor is shown for all axisymmetric modes with  $l = 0, \dots, 10$  in Fig. 1.5.

The radial mode does not suffer from partial cancellation and thus reaches value unity, which is about twice as high as a dipole  $l = 2$  mode. It is very important to be aware that axisymmetric  $l = 3$  modes are almost invisible in intensity measurements due to the partial cancelling. The same holds true

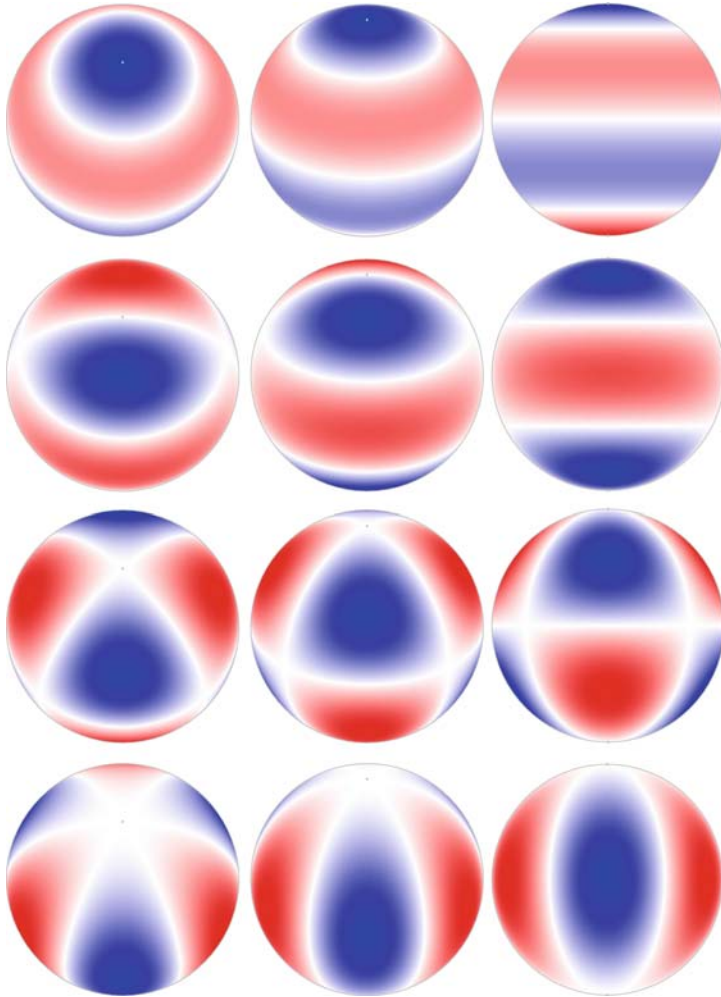


**Fig. 1.4.** Snapshot of the radial component of the  $l = 3$  octupole modes. The columns show the modes from different viewing angles; the left column is for an inclination of the pulsation pole of  $30^\circ$ , the middle column is for  $60^\circ$ , and the right column is for  $90^\circ$ . The white bands represent the positions of the surface nodes; red and blue represent sections of the star that are moving in (out) and/or heating (cooling) at any given time, then vice versa. The top row shows the axisymmetric octupole mode ( $l = 3, m = 0$ ) where the nodes lie at latitudes  $\pm 51^\circ$  and  $0^\circ$ . The second row shows the *tesseral* (meaning  $0 < |m| < l$ )  $l = 3, m = \pm 1$  mode with two nodes that are lines of latitude and one that is a line of longitude. The third row is the tesseral  $l = 3, m = \pm 2$  mode, and the bottom row shows the *sectoral* mode (meaning  $l = |m|$ ) with  $l = 3, m = \pm 3$ . Importantly, rotation distinguishes the sign of  $m$ , as discussed in the Section 1.4.3.

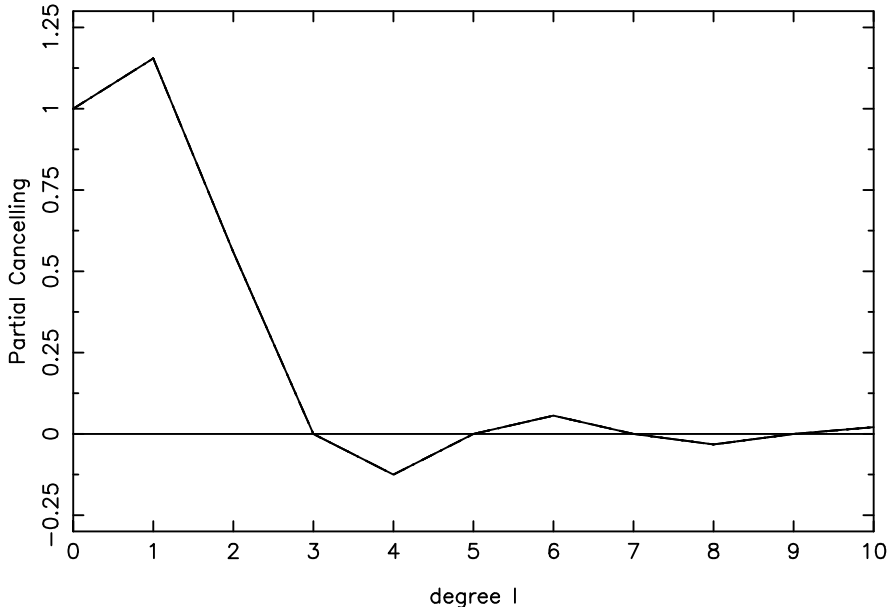


**Fig. 1.5.** The partial cancelling factor for the surface-integrated intensity in the case of axisymmetric modes for  $l = 0, \dots, 10$ , when ignoring the darkening at the limb of the stellar surface.

for all the higher-degree odd axisymmetric modes. Partial cancellation for the  $l = 4$  mode is a factor 10 greater than that of the dipole mode, and this factor increases as  $l$  increases. While the inclusion of rotation and limb darkening complicates this simplistic description, and the effects are more complicated for velocity quantities than for the intensity (as will be explained in detail in Chapter 6), Fig. 1.5 explains why even modes are much easier to detect in the data than odd modes, except for the special case of the dipole mode. Moreover, the modes become more difficult to detect as their degree increases. This will become obvious when we discuss observations of modes in the following chapters.

#### 1.4.3 The Effect of Rotation

In Eqs (1.1) and (1.4) it can be seen that for modes with  $m \neq 0$  the exponentials in the two equations combine to give a time dependence that goes as  $\exp[-i(2\pi\nu t - m\phi)]$ . This phase factor in the time dependence means that the  $m \neq 0$  modes are travelling waves, where our sign convention is that modes with positive  $m$  are travelling in the direction of rotation (*prograde* modes), and modes with negative  $m$  are travelling against the direction of rotation (*retrograde* modes).

For a spherically symmetric star the frequencies of all  $2l + 1$  members of a multiplet (such as the octupole septuplet  $l = 3, m = -3, -2, -1, 0, +1, +2, +3$ ) are the same. But deviations from spherical symmetry can lift this frequency degeneracy, and the most important physical cause of a star's departure from spherical symmetry is rotation. For example, in a rotating star the Coriolis force causes pulsational variations that would have been up-and-down to become circular with the direction of the Coriolis force being against the direction of rotation. Because of this effect and others that will be explained in Chapter 3, the prograde modes travelling in the direction of rotation have frequencies slightly lower than the  $m = 0$  axisymmetric mode, and the retrograde modes going against the rotation have slightly higher frequencies, *in the co-rotating reference frame* of the star, thus the degeneracy of the frequencies of the multiplet is lifted.

This was discussed by Ledoux (1951) in a study of the  $\beta$  Cep star  $\beta$  CMa (see Chapter 2 for a definition of this class of stars). In the *observer's frame of reference* the Ledoux rotational splitting relation for a uniformly rotating star is

$$\nu_{nlm} = \nu_{nl0} + m(1 - C_{nl})\Omega/2\pi , \quad (1.8)$$

where  $\nu_{nlm}$  is the observed frequency,  $\nu_{nl0}$  is the unperturbed central frequency of the multiplet (for which  $m = 0$ ) which is unaffected by the rotation,  $C_{nl}$  is a mode-dependent and model-dependent quantity with value below 1 that will be defined in Chapter 3, and  $\Omega$  is the angular velocity, corresponding to a rotation frequency of  $\Omega/2\pi$ . If we rewrite Eq. (1.8) as

$$\nu_{nlm} = \nu_{nl0} - mC_{nl}\Omega/2\pi + m\Omega/2\pi , \quad (1.9)$$

then it is easy to see that the Coriolis force reduces the frequency of the prograde modes with positive  $m$  slightly in the co-rotating rest frame, but then the rotation frequency is added to that since the mode is going in the direction of rotation. Likewise the retrograde modes with negative  $m$  are travelling against the rotation so have their frequency in the observer's frame reduced by the rotation frequency.

In this way we end up with a multiplet with  $2l + 1$  components all separated by *the rotational splitting*  $(1 - C_{nl})\Omega/2\pi$ . In a real star rotation is not expected to be uniform and hence the rotational splitting would depend on the properties of the modes in a more complicated manner; also, the various components of the multiplet may be excited to different amplitudes, and some may not have any observable amplitude, so all members of the multiplet may not be present. The importance for asteroseismology is that where such rotationally-split multiplets are observed, the  $l$  and  $m$  for the modes may be identified and the splitting used to measure the rotation rate of the star. Where multiplets of modes of different degree or different overtone are observed, it is possible to gain knowledge of the *interior* rotation rate of the star – something that is not knowable by any other means.

In the case of the Sun, helioseismology has spectacularly measured the differential rotation rate of the Sun down to about half way to the core. Below the convection zone at  $r/R_\odot \sim 0.7$  the Sun rotates approximately rigidly with a period close to the 27-d period seen at latitudes of about  $35^\circ$  on the surface (see Thompson *et al.* 2003). Within the convection zone the rotation is not simply dependent on distance from the solar rotation axis, as had been expected in the absence of any direct observation. It is a remarkable triumph of helioseismology that we can know the internal rotation behaviour of the Sun – thanks to rotational multiplets!

#### 1.4.4 So how does Asteroseismology Work?

Since p modes are acoustic waves, for modes that are not directed at the centre of the star (*i.e.*, the nonradial modes) the lower part of the wave is in a higher temperature environment than the upper part of the wave, thus in a region of higher sound speed. As a consequence the wave is refracted back to the surface, where it is then reflected, since the acoustic energy is trapped in the star, as can be seen in Fig. 1.7. While the number of reflection points is not equal to the degree of the mode, higher  $l$  modes have more reflection points. This means that high degree modes penetrate only to a shallow depth, while lower degree modes penetrate more deeply. The frequency of the mode observed at the surface depends on the sound travel time along its ray path, hence on the integral of the sound speed within its “acoustic cavity”. Clearly, if many modes that penetrate to all possible depths can be observed on the surface, then it is possible to “invert” the observations to make a map of the sound speed throughout the star, and from that deduce the temperature profile, with reasonable assumptions about the chemical composition. In the Sun the sound speed is now known to a few parts per thousand over 90% of its radius. To do the same for other stars is an ultimate goal of asteroseismology.

Thus asteroseismology lets us literally see the insides of stars because different modes penetrate to different depths in the star. But as was noted in Section 1.1.4, stellar oscillations are not so simple as just p modes. We can also see inside the stars with g modes. In fact, for some stars, and for parts of others, we can only see with g modes.

#### 1.4.5 p Modes and g Modes

There are two main sets of solutions to the equation of motion for a pulsating star, and these lead to two types of pulsation modes: p modes and g modes. For the p modes, or pressure modes, pressure is the primary restoring force for a star perturbed from equilibrium. These p modes are acoustic waves and have gas motions that are primarily vertical. For the g modes, or gravity modes, buoyancy is the restoring force and the gas motions are primarily horizontal. There is also an f mode situated between the p mode of radial order 1 and the g mode of radial order 1 for all  $l \geq 2$ .

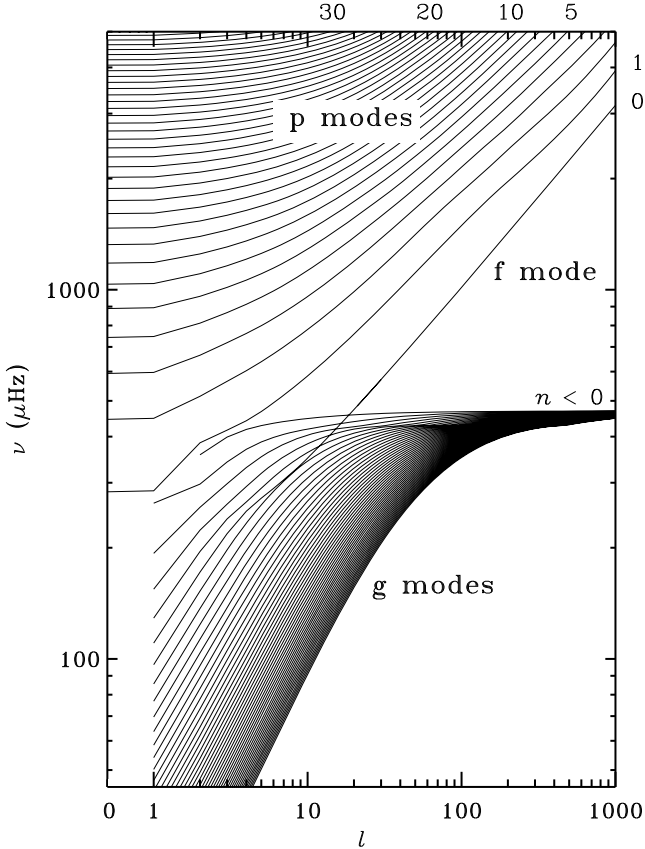


**Fig. 1.6.** The frequency of modes versus their degree  $l$  for a solar model. The figure clearly illustrates the general property of p modes that frequency increases with overtone  $n$  and degree  $l$ . For g modes frequency decreases with higher overtone, but increases with  $n$  if we use the convention that  $n$  is negative for g modes. Frequency still increases with degree  $l$  for g modes, just as it does for p modes. Some values of the overtone  $n$  are given for the p modes lines in the upper right of the figure. Note that while continuous lines are shown for clarity, the individual modes are discrete points, corresponding to integer  $l$ , which are not shown here.

Both p and g modes of high order can be described in terms of the propagation of rays (see also Gough 1993). This provides illuminating graphical representations of their properties; examples are shown in Figs 1.7 and 1.8. Also, as discussed extensively in Chapter 3, this representation forms the basis for powerful asymptotic descriptions of the modes.

There are three other important properties of p modes and g modes: 1) as the number of radial nodes increases the frequencies of the p modes increase,

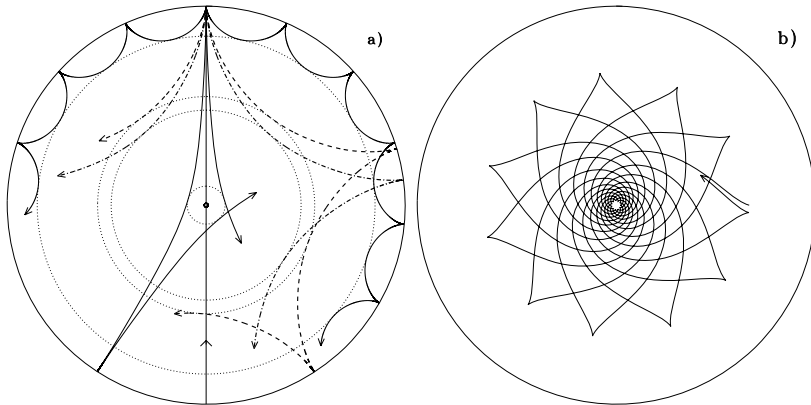


**Fig. 1.7.** Propagation of rays of sound or gravity waves in a cross-section of a Sun-like star. The acoustic ray paths (panel a) are bent by the increase in sound speed with depth until they reach the inner turning point (indicated by the dotted circles) where they undergo total internal refraction. At the surface the acoustic waves are reflected by the rapid decrease in density. Shown are rays corresponding to modes of frequency  $3000 \mu\text{Hz}$  and degrees (in order of increasing penetration depth)  $l = 75, 25, 20$  and  $2$ ; the line passing through the centre schematically illustrates the behaviour of a radial mode. The g-mode ray path (panel b) corresponds to a mode of frequency  $190 \mu\text{Hz}$  and degree  $5$  and is trapped in the interior. In this example, it does not propagate in the convective outer part. As we shall see in Chapter 2, g modes are observed at the surface of other types of pulsators. This figure illustrates that the g modes are sensitive to the conditions in the very core of the star, an important property. From Cunha *et al.* (2007).

but the frequencies of the g modes decrease, as is shown in Fig. 1.6; 2) the p modes are most sensitive to conditions in the outer part of the star, whereas g modes are most sensitive to conditions in the deep interior of the star,<sup>11</sup> as is shown in Fig. 1.7; 3) for  $n \gg l$  there is an asymptotic relation for p modes saying that they are approximately equally spaced in frequency, and there is another asymptotic relation for g modes pointing out that they are approximately equally spaced in period.

As illustrated in Fig. 1.7, g modes in solar-like stars are trapped beneath the convective envelope, when viewed as rays. In reality the modes have finite amplitudes also in the outer parts of the star and hence, at least in principle, can be observed on the surface; this is in fact the case in the  $\gamma$ Dor stars which have convective envelopes. In more massive main-sequence stars, such as illustrated in Fig. 1.8, the g-mode rays are confined outside the convective core.

<sup>11</sup> except in white dwarfs where the g modes are sensitive mainly to conditions in the stellar envelope; see Section 3.4.2.

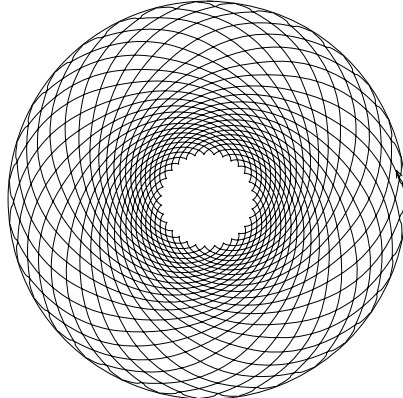


**Fig. 1.8.** Propagation of rays of gravity waves in a cross-section of an  $8 M_{\odot}$  ZAMS star. The ray path corresponds to a mode of frequency  $50 \mu\text{Hz}$  and degree 5. It is trapped outside the convective core of the star.

The asymptotic relations are very important in many pulsating stars. From Tassoul (1980, 1990) they show that for the p modes, the frequencies are approximately given by

$$\nu_{nl} = \Delta\nu \left( n + \frac{l}{2} + \tilde{\alpha} \right) + \epsilon_{nl}, \quad (1.10)$$

where  $n$  and  $l$  are the overtone and degree of the mode,  $\tilde{\alpha}$  is a constant of order unity, and  $\epsilon_{nl}$  is a small correction.  $\Delta\nu$  is known as the *large separation* and is the inverse of the sound travel time for a sound wave from the surface of the star to the core and back again, given by

$$\Delta\nu = \left( 2 \int_0^R \frac{dr}{c(r)} \right)^{-1}, \quad (1.11)$$

where  $c(r)$  is the sound speed. The large separation is obviously sensitive to the radius of the star, hence near the main sequence it is a good measure of the mass of the star. The term  $\epsilon_{nl}$  gives rise to the *small separation*  $\delta\nu$ ; this is sensitive to the core condensation, hence age of the star.

The periods of g modes, asymptotically given by

$$\Pi_{nl} = \frac{\Pi_0}{\sqrt{l(l+1)}} (n + \epsilon), \quad (1.12)$$

are nearly uniformly spaced; here  $n$  and  $l$  are again the overtone and degree of the mode,  $\epsilon$  is a small constant, and  $\Pi_0$  is given by

$$\Pi_0 = 2\pi^2 \left( \int \frac{N}{r} dr \right)^{-1}, \quad (1.13)$$

where  $N$  is the Brunt-Väisälä frequency and the integral is over the cavity in which the g mode propagates (as in panel b of Fig. 1.7). Deviations of the period spacing for g modes are used to diagnose stratification in stars, since strong mean molecular weight gradients trap modes and cause deviations from the simple asymptotic relation given in Eq. (1.12). This technique has been particularly successful in measuring the stratification in white dwarf atmospheres with carbon-oxygen cores and layers of helium and hydrogen above (see Section 7.4 in Chapter 7).

## 1.5 An Asteroseismic HR Diagram for p-Mode Pulsators

Figure 1.9 shows a power spectrum of the radial velocity variations observed over a time span of 9.5 years for the Sun by BiSON, the **B**irmingham **S**olar **O**scillation **N**etwork<sup>12</sup>. This shows the “comb” of frequencies expected from Eq. (1.10) for high overtone, low degree ( $n \gg l$ ) p modes. The noise level is so stunningly low in this diagram that it is essentially invisible at this scale. It is equivalent to an amplitude of only  $0.5 \text{ mm s}^{-1}$ , precise enough to detect a mode with a total displacement over the whole pulsation cycle of only 10s of cm! It is noteworthy that the comb of frequencies consists of alternating even and odd  $l$ -modes, as expected from Eq. (1.10), where it can be seen that (to first order) modes of  $(n, l)$  and  $(n - 1, l + 2)$  have the same frequency. It is the small separation,  $\delta\nu$ , that lifts this degeneracy.

That may be seen in Fig. 1.10 which is a portion of an amplitude spectrum of the radial velocity variations of the Sun seen as a star made by the GOLF (Global Oscillation at Low Frequencies<sup>13</sup>) experiment on SOHO (SOlar and Heliospheric Observatory<sup>14</sup>) orbiting at the Earth-Sun L<sub>1</sub> Lagrangian point. Here it can be seen that the large separations for even and odd  $l$ -modes (*cf.*  $\Delta\nu_0$ ,  $\Delta\nu_1$ ) are very similar, that the small separation lifts the degeneracy between modes of  $(n, l)$  and  $(n - 1, l + 2)$ , and that there is a substantial difference between the small separations for even and odd  $l$ -modes (*cf.*  $\delta\nu_0$ ,  $\delta\nu_1$ ).<sup>15</sup>

Ultimately, it is the goal of asteroseismology for any star to detect enough frequencies over ranges in  $n$ ,  $l$  and  $m$  that the interior sound speed may be mapped with precision, so that deductions can be made about interior temperature, pressure, density, chemical composition and rotation, *i.e.*, it is the goal to “see”, and to see clearly, inside the star. A step along the way is to resolve sufficient frequencies in a star, and to identify the modes associated

<sup>12</sup> <http://bison.ph.bham.ac.uk/>.

<sup>13</sup> <http://golfwww.medoc-ias.u-psud.fr/>.

<sup>14</sup> <http://sohowww.nascom.nasa.gov/>.

<sup>15</sup> As shown in Chapter 3,  $\delta\nu_1 \simeq 5/3 \delta\nu_0$ .

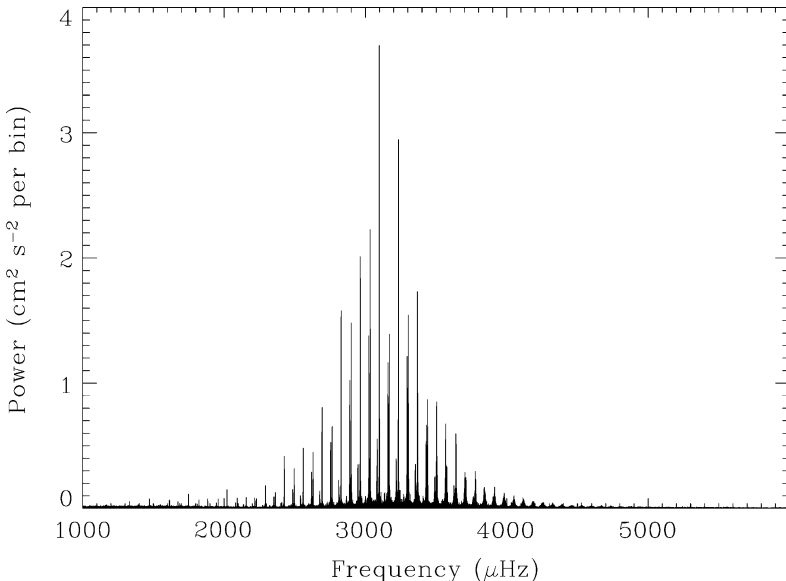


**Fig. 1.9.** A power spectrum of radial velocity variations in the Sun seen as a star for 9.5 years of data taken with the Birmingham Solar Oscillation Network (BiSON) telescopes. The equivalent amplitude noise level in this diagram is  $0.5 \text{ mm s}^{-1}$ . Figure courtesy of the BiSON team.

with them unambiguously such that the large and small separations may be deduced with confidence. That step alone leads to determinations of the fundamental parameters of mass and age for some kinds of stars.

Figure 1.11 shows an “asteroseismic HR Diagram” (Christensen-Dalsgaard 1993a) where the large separation clearly is a measure of mass (largely because of the relationship between mass and radius), and the small separation is most sensitive to the central mass fraction of hydrogen, hence age. Now that many solar-type oscillators have been found, it is possible to begin to model them using the large and small separations (see Section 7.2 for case studies). The pattern of high overtone even and odd  $l$  modes is also observed in some roAp stars, although their interpretation for those stars is more complex because of the strong effects of their global magnetic fields on the frequency separations (see Section 7.3.4).

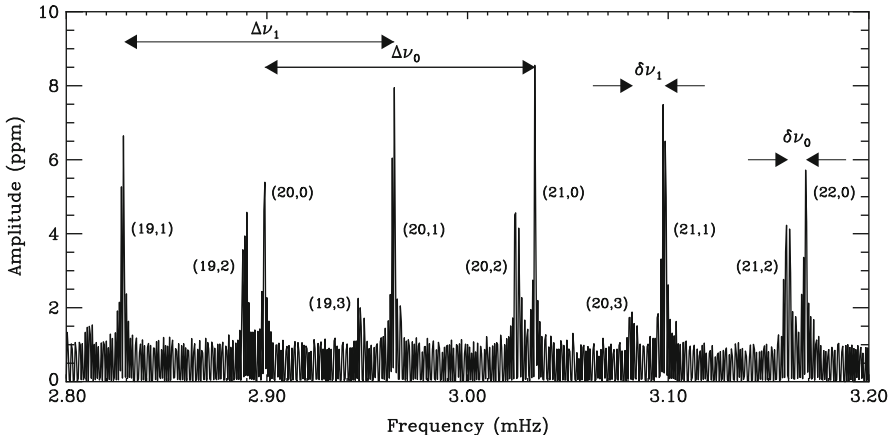


**Fig. 1.10.** This amplitude spectrum of radial velocity variations observed with the GOLF instrument on SOHO clearly shows the large and small separations in the p modes of the Sun. Courtesy of the GOLF science team.

## 1.6 A Pulsation HR Diagram

Figure 1.12 shows a black-and-white version of the “pulsation HR Diagram”. The much more colourful version of this diagram is frequently presented at stellar pulsation meetings to put particular classes of stars into perspective. As an example, in Section 1.4.5 it was pointed out that the g modes are particularly sensitive to the core conditions in the star (see Fig. 1.7). It is that sensitivity that has made the discovery of g modes in the Sun such a long-sought goal – so much so that the discovery of g modes in the Sun has been claimed repeatedly, but general acceptance of those claims is still lacking. On the other hand, g-mode pulsators are common amongst other types of stars – even some, the  $\gamma$  Dor stars, that are not very much hotter than the Sun and are overlapping with the solar-like oscillators, keeping hope alive that g modes may eventually be detected with confidence in the Sun. There are three places in Fig. 1.12 where there are p-mode and g-mode pulsators of similar stellar structure: for the  $\beta$  Cep (p-mode) and Slowly Pulsating B (SPB; g-mode) stars on the upper main sequence; for the  $\delta$  Sct (p-mode) and  $\gamma$  Dor (g-mode) stars of the middle main sequence; and for the EC 14026 subdwarf B variables (p-mode) and the PG 1716+426 stars (g-mode). Stars pulsating in both p modes and g modes promise particularly rich asteroseismic views of their interiors.

### 1.6.1 How do Stars Pulsate: The Relevant Time Scales

To understand the properties of the oscillations discussed for the various pulsators in Chapter 2, it is instructive to consider the relevant time scales of stars. These are deduced from time-dependent differential equations that each

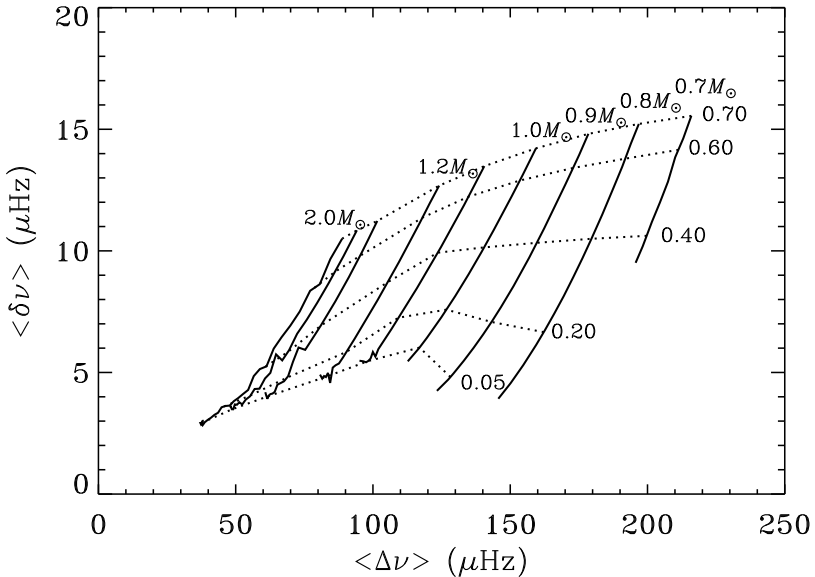


**Fig. 1.11.** An asteroseismic HR Diagram in which the large separation  $\Delta\nu$  is most sensitive to mass, and the small separation  $\delta\nu$  is most sensitive to age. The solid, nearly vertical lines are lines of constant mass, and the nearly horizontal dashed lines are isopleths of constant hydrogen mass fraction in the core, at the values indicated in the figure.

deal with structural changes, the details of which are presented in Chapter 3. Each of these changes has its own characteristic time scale, which is the ratio of the quantity that is changed and its rate of change. Relevant quantities are: the radius, the internal energy and the nuclear energy of the star.

The longest relevant time scale is the *nuclear time scale*,

$$\tau_{\text{nuc}} \equiv \frac{\epsilon q M c^2}{L}, \quad (1.14)$$

where  $q$  is the small fraction (typically below 10%) of the stellar mass that can take part in the nuclear burning and  $\epsilon$  is the fraction of that mass which is converted into energy in the nuclear reactions (around 0.7% for hydrogen fusion); thus the numerator of this expression is the nuclear energy reservoir of the star. This time scale essentially expresses how long the star can shine with nuclear fusion as its energy source, given its luminosity. The nuclear time scale ranges from less than a million years to trillions of years for the highest to the lowest mass stars, respectively. In the solar case, the nuclear time scale is around 10 billion years.

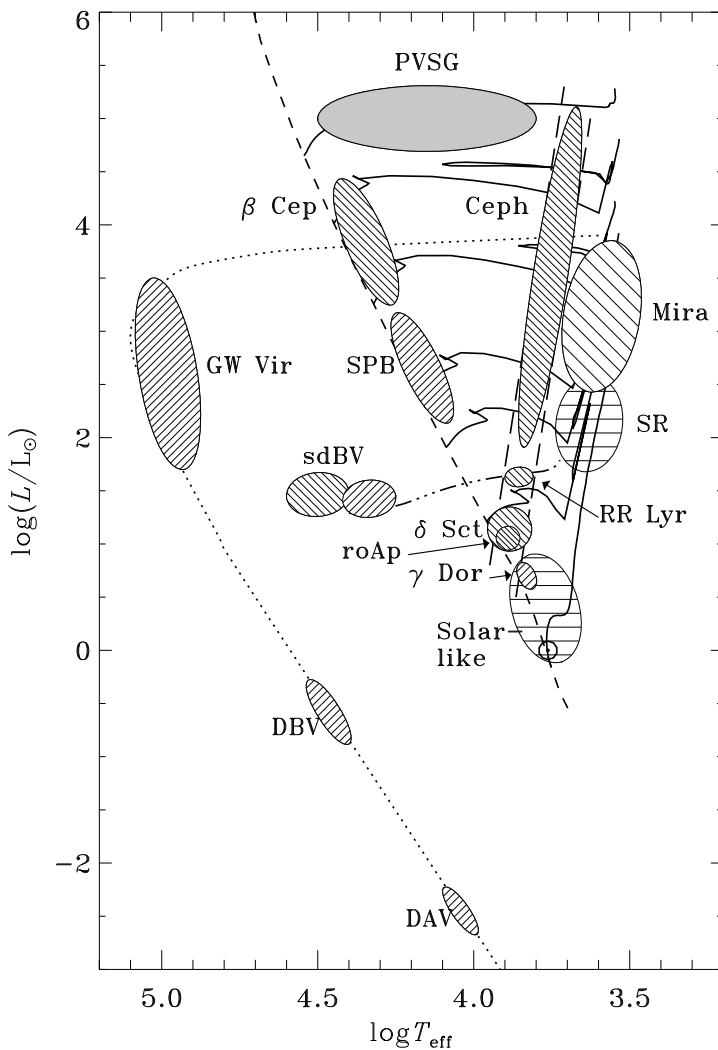


**Fig. 1.12.** A pulsation HR Diagram showing many classes of pulsating stars for which asteroseismology is possible.

On the other hand, the shortest relevant time scale is the *dynamical time scale*,

$$\tau_{\text{dyn}} \simeq \sqrt{\frac{R^3}{GM}} \simeq \sqrt{\frac{1}{G \bar{\rho}}}, \quad (1.15)$$

where  $\bar{\rho}$  stands for the average stellar density. It expresses the time the star needs to recover its equilibrium whenever the balance between the pressure and gravitational forces is disturbed by some dynamical process. For a star close to such *hydrostatic equilibrium*, this time scale is equivalent to the time it takes a sound wave to travel from the stellar centre to the surface, as well as to the free-fall time scale of the star. For the Sun,  $\tau_{\text{dyn}} \simeq 20$  min while for a white dwarf it is typically less than a few tens of seconds. Pressure modes are dynamical processes that disturb the pressure equilibrium and thus their oscillation periods are expected to be shorter than  $\tau_{\text{dyn}}$ . Equation (1.15) explains why these periods allow us to estimate the mean density of the star. This has also, particularly in older publications, been used to characterize the periods  $\Pi$  of pulsating stars by their *pulsation constant*

$$Q = \Pi \left( \frac{M}{M_{\odot}} \right)^{1/2} \left( \frac{R}{R_{\odot}} \right)^{-3/2}. \quad (1.16)$$

Finally, we introduce the *thermal time scale*,

$$\tau_{\text{th}} \simeq \frac{GM^2}{RL}, \quad (1.17)$$

also termed the *Kelvin-Helmholtz time scale*. This expresses the time a star can shine with gravitational potential energy as its only energy source, *i.e.*, without a nuclear source. The gravitational potential energy of a star is connected with its internal energy, and thus the thermal time scale may also be expressed as

$$\tau_{\text{th}} \simeq \frac{\langle c_p T \rangle M}{L}, \quad (1.18)$$

where  $c_p$  is the heat capacity of the gas at constant pressure, and  $\langle \dots \rangle$  denotes a suitable average over the star. The thermal time scale of the Sun amounts to several tens of million years.

### 1.6.2 Why do Stars Pulsate: Driving Mechanisms

We have looked in some detail now at *how* stars pulsate. But *why* do they pulsate? Firstly, not all stars do. It is an interesting question as to whether all stars would be observed to pulsate at some level, if only we had the precision to detect those pulsations. For now, at the level of the precision of our observations of  $\mu\text{mag}$  in photometry and  $\text{cm s}^{-1}$  in radial velocity, we can say that some stars do *not* pulsate.

The ones that do are pulsating in their natural modes of oscillation, which have been described in the previous sections. In the longest known case of a pulsating star, that of *o Ceti* (Mira), we usually attribute the discovery of its variability to Fabricius in 1596. So this star has been pulsating for hundreds of years, at least. In many other cases we have good light curves going back over a century, so we know that stellar pulsation is a relatively stable phenomenon

in many stars. That means that energy must be fed into the pulsation via what are known as *driving mechanisms*.

As a star pulsates, it swells and contracts, heats and cools as described in the previous sections. For most of the interior of the star, energy is lost in each pulsation cycle, *i.e.*, most of the volume of the star *damps* the pulsation. The observed pulsation can only continue, therefore, if there is some part of the interior of the star where not only is energy fed into the pulsation, but as much energy is fed in as is damped throughout the rest of the bulk of the star.

A region in the star, usually a radial layer, that gains heat during the compression part of the pulsation cycle drives the pulsation. All other layers that lose heat on compression damp the pulsation. If this region succeeds in driving the oscillation, the star functions as a heat engine, converting thermal energy into mechanical energy; thus we refer to this type of driving as a *heat-engine mechanism*. For Cepheid variables, RR Lyrae stars,  $\delta$  Sct stars,  $\beta$  Cep stars – for most of the pulsating variables seen in Fig. 1.12 – the driving mechanism is connected with the opacity, thus it is known as the  $\kappa$  *mechanism*. For the  $\kappa$  mechanism to work there must be plenty of opacity, so major drivers of pulsation are, not at all surprisingly, hydrogen and helium.

Simplistically, in the ionization layers for H and He opacity blocks radiation, the gas heats and the pressure increases causing the star to swell past its equilibrium point. But the ionization of the gas reduces the opacity, radiation flows through, the gas cools and can no longer support the weight of the overlying layers, so the star contracts. On contraction the H or He recombines and flux is once more absorbed, hence the condition for a heat engine is present: the layer gains heat on compression.

Of course, since the layers doing the driving are ionization zones, some of the energy is being deposited in electrostatic potential energy as electrons are stripped from their nuclei, and that changes the adiabatic exponent  $\Gamma_1$ . That causes the adiabatic temperature gradient to be small, so these zones are convection zones, too, and variations in  $\Gamma_1$  can make small contributions to the driving in some cases (see Chapter 3 for a thorough explanation). Note that when the driving takes place in convective regions the perturbations to the convective flux must also be taken into account, introducing major uncertainties in the calculation of stellar stability.

For decades the pulsation driving mechanism for  $\beta$  Cep stars was not understood. Only since 1992 has it been found that the  $\kappa$  mechanism – operating on Fe-group elements, not H or He – can drive the pulsation in these stars. Similarly, pulsation in p-mode and g-mode sdBV pulsators in Fig. 1.12 – as explained in Chapter 2 – is driven by the  $\kappa$  mechanism operating on Fe.

The other major driving mechanism that operates in the Sun and solar-like oscillators, as well as some pulsating red giant stars, is *stochastic* driving. In this case the heat-engine mechanism is not able to drive the oscillations and the modes are intrinsically stable. However, there is sufficient acoustic energy in the outer convection zone in the star that the star resonates in some of its

natural oscillation frequencies where some of the stochastic noise is transferred to energy of global oscillation. In a similar way, in a very noisy environment, musical string instruments can be heard to sound faintly in resonance with the noise that has the right frequency.

The third major theoretical driving mechanism is the  $\epsilon$  mechanism, where in this case that is the epsilon that is commonly used to refer to the energy generation rate in the core of the star. Potentially, variations in  $\epsilon$  could drive global pulsations. This has been discussed as a possible driving mechanism in some cases of evolved very massive stars, but there is no known class of pulsating stars at present that are thought to be driven by the  $\epsilon$  mechanism alone.

### 1.6.3 What Selects the Modes of Pulsation in Stars?

So a star is driven to pulsate by one of the driving mechanisms described above. What decides *which* mode or modes it pulsates in? Why do most Cepheids pulsate in the fundamental radial mode, but some pulsate also in the first overtone radial mode, and rarely a few pulsate only in overtone modes? Why do the Sun, solar-like oscillators and roAp stars pulsate in high overtone p modes? Why do white dwarfs pulsate in high overtone g modes? What is the mode selection mechanism in these stars?

These are complex questions for which answers are not always known. The fundamental mode is most strongly excited for many stars, as it is for musical instruments, but not for all. The position of the driving zone as well as the shape of the mode eigenfunctions determine which modes are excited, just as where a musical instrument is excited will determine which harmonics are played, and with what amplitude. For example, if a guitar is plucked at its twelfth fret (right in the centre of the string), then the first harmonic (which has a node there) will not be excited. You cannot drive a mode by putting energy in a node where that mode does not oscillate. So if the driving zone for a star lies near the node of some modes, those modes are unlikely to be excited. Any physical property of an oscillator that forces a node will select against some modes, and/or perturb the frequencies and eigenfunctions of the modes.

For example, in roAp stars the strong, mostly-dipolar magnetic field almost certainly determines that dipole pulsation modes are favoured. In stratified white dwarf stars, the steep gradient of mean molecular weight between layers of H, He and C/O modifies the character of some modes and may select modes. Thus the shape of the mode eigenfunction needs to be suitable, *i.e.*, not change too rapidly with depth in the potential driving zone for the mode to be excited. This is, however, not a sufficient condition. Some modes fulfil this requirement, but still are not excited because they are subjected to strong damping effects activated by layers outside of the driving zone that overwhelm the driving. As already mentioned, the overall net balance between driving and damping needs to be optimal throughout the star for the mode to be excited globally.

Another requirement for modes to be excited by the  $\kappa$  mechanism concerns their periods of oscillation and is closely related to the discussion of time scales in Section 1.6.1. Equations (1.14), (1.15), (1.18) are approximate averages over the entire star. The great difference between the dynamical and thermal time scales shows that globally the heat loss during a pulsation period is very small; in other words, globally the oscillation is very nearly adiabatic. However, to investigate the excitation of the oscillations we need to work with local time scales in the driving zones that may have vastly different values than those listed above. Of particular relevance is the local thermal time scale of the driving zone, defined as

$$\tau_{\text{th}} \equiv \int_r^R \frac{c_p T dm}{L} \quad (1.19)$$

(Pamyatnykh 1999).<sup>16</sup> This introduces another condition that must be fulfilled in order to have driving by the  $\kappa$  mechanism: the period of the oscillation must be similar to the thermal time scale in the driving zone. If the oscillation period is much longer than  $\tau_{\text{th}}$ , then the driving layer will remain in thermal equilibrium and not be able to excite the mode. Typical values for  $\tau_{\text{th}}$  in the driving zones of  $\beta$ Cep, SPB and  $\delta$ Sct stars amount to 0.3 d, 3 d, and 0.1 d, respectively. Note how different these values are compared to the global thermal time scales of such stars, illustrating that the driving zones are very close to the stellar surface where heat can easily escape. In the stochastically driven pulsators the modes excited are those that have natural frequencies near to the characteristic time scale for the vigorous convective motions in the near-surface layers of a star with a convective envelope.

Even if all the above requirements are fulfilled, it is still not clear why some modes predicted to be excited actually are not observed, *i.e.*, there are obviously additional mode selection criteria at work. Moreover, as already mentioned, some stars that seemingly fulfil the requirements for pulsation are not observed to oscillate. Clearly, our understand of mode selection is incomplete. As already mentioned, any physical property of an oscillator that forces a node will select against some modes, and/or perturb the frequencies and eigenfunctions of the modes, as in the examples given above of the effects of the magnetic field in roAp stars and of the mean molecular weight stratification in white dwarf stars. Thus, there is some understanding of mode selection, but in many stars the precise reason why certain modes are excited, and others not, is not known, or is incompletely understood. A related issue which is even more uncertain is the mechanisms which determine the limiting amplitudes of modes excited by the  $\kappa$  mechanism; this, too, affects whether the modes are likely to be observed.

Some physical characteristic of the star is selecting the modes that are excited, or not damped, as the case may be, and a determination of that

---

<sup>16</sup> Note that here and the following we use  $m$  to denote the mass inside a given point in the star, in addition to the azimuthal order of a mode. With attention to context, this should not cause confusion.

selection mechanism will allow us a clearer, more detailed look at the interior of the star. And that, of course, is the goal of asteroseismology.

## Observations of Stellar Oscillations across the Hertzsprung-Russell Diagram

This chapter is a journey through the Hertzsprung-Russell (HR) Diagram with stops at all the ellipses shown in Fig. 1.12. We discuss briefly each of the currently known classes of pulsating stars, outlining their most important properties, such as their fundamental stellar parameters and the general character of their oscillations, but skipping many of the details due to page constraints. For each class, we provide a recent overview paper and/or book to which we refer for additional information and deeper discussion. We provide one prototypical time series of a class member and sometimes its Fourier transform to give the reader a first impression of the frequency range and the behaviour of the oscillations. We further restrict ourselves to a description of the basic properties of the stars. A summary of the properties is provided in Appendix A. Detailed asteroseismic applications of some selected stars are presented in Chapter 7. A concise overview of stellar variability, including a description of extrinsic variables such as binaries and of spotted stars, is available in Eyer & Mowlawi (2008).

Observations of stellar oscillations cannot stand alone but must be supplemented by other observations of stellar properties. Such “classical observations” include photometry and spectroscopy, to determine atmospheric properties of the star such as surface gravity, effective temperature and composition. The latter is in many cases described just in terms of the abundance of elements heavier than helium, collectively known as “metals”, and hence the abundance is referred to as the *metallicity*. If a reliable parallax is available, the luminosity of the star can in addition be determined. Well-observed binary stars are particularly valuable in providing information about stellar masses and, for eclipsing binaries, stellar radii. Accurate determinations of such global parameters greatly increase the power of asteroseismic data in providing information about the properties of stellar interiors.

An evident conclusion from Fig. 1.12 is that stellar oscillations occur in almost all phases of stellar evolution. However, there clearly exists a particular region in the HR Diagram in which the density of pulsating stars is greater than elsewhere. This region is situated between the two slanted dashed lines

in Fig. 1.12 and is called the *classical instability strip*. The oscillations in the stars situated in this strip are caused by the heat mechanism (see Chapter 3 for an explanation of the physics) primarily acting in the second partial ionization zone of helium, *i.e.*, the zone in which both He II and He III occur. The Cepheids, RR Lyrae stars,  $\delta$  Scuti stars and rapidly oscillating Ap stars are all situated in this strip, along with pre-main-sequence pulsators. On the other hand, the first partial ionization zones of hydrogen and helium, combined with strong and efficient convection, are responsible for the heat-driven oscillations in cool red giants and supergiants, such as the Mira stars and semiregular variables; hence they are situated along the cool, that is, red, side of the classical instability strip. Finally, opacity features associated with the iron-group elements are responsible for oscillations in the hottest stars, such as  $\beta$  Cep stars, slowly pulsating B stars, B supergiants, and also in the evolved subdwarf B stars. Stochastically excited oscillations are expected in all stars with an outer convective envelope, *i.e.*, along the main sequence up to masses of about  $1.5 M_{\odot}$  and anywhere from the end of the main sequence up to the giant and asymptotic giant branch. The hottest pulsators among the compact stars are grouped together in a class termed GW Vir stars. They are dominantly driven by the heat mechanism acting in the partial ionization zones of carbon and oxygen at their surface. It was only recently realized that there is a common cause of the oscillations for stars in this part of the HR Diagram, which includes the DOV and DBV stars, as well as the central stars of planetary nebulae and Wolf-Rayet stars (Quirion *et al.* 2006). The cooler DAV stars, on the other hand, are compact pulsators driven by a phenomenon termed convective driving by Brickhill (1991a). A convection-related mechanism, convective blocking, also operates in the  $\gamma$  Dor stars along the main sequence.

Adopting a philosophy similar to the one in the review by Gautschy & Saio (1996), we organize the journey with five main stopping areas to discuss pulsations near the main sequence, in pre-main-sequence stars, in evolved stars of low mass, in evolved stars of high mass and in compact objects. With the exception of the B1Ib supergiant HD 163899 (Saio *et al.* 2006), evolved stars of high mass are currently not yet the subject of seismic inference because the observational establishment of their oscillation frequencies is much harder than for the stars in all other categories, due to occurrence of several kinds of instabilities in their atmospheres. Moreover, our theoretical understanding of their oscillations is far less detailed than for lower-mass stars for which radiation-driven mass loss can be ignored. For this reason we are at present unable to make a detailed comparison between their overall observed variability and in-depth stellar structure and oscillation computations; hence we do not come back to these stars after this chapter. The same holds true for the pre-main-sequence pulsators. While oscillations have clearly been found in several of these, we lack good knowledge of their frequency spectra and mode identification for the moment. Gravitational-wave asteroseismology through nonradial oscillations of interacting white-dwarf binary stars, neutron stars

and black holes is also a field still under development lacking strong observational constraints. We discuss it briefly in this chapter. Finally, the classical large-amplitude monoperiodic radial pulsators, such as RR Lyrae stars, Cepheids, RV Tauri stars, Mira stars and semi-regular variables, are not suitable for seismic modelling of interior physics. We discuss their pulsational characteristics in this chapter, including the seismic potential of double- and triple-mode classical pulsators, in the section on Cepheids and do not return to them further on in the book.

Before beginning our journey into asteroseismology, we first give a brief overview of stellar evolution and of the impact of large-scale surveys on pulsating star research.

## 2.1 Stellar Evolution in a Nutshell

Excellent books on stellar structure and evolution are available already and we do not repeat their contents here. Rather we merely want to set the scene of stellar evolution before starting our journey towards the pulsating stars in the HR Diagram. We highly recommend the book by Kippenhahn & Weigert (1990) as a standard work. Together with Hansen *et al.*'s (2004) detailed description of stellar interiors, it provides an excellent in-depth overview of stellar structure and evolution. A somewhat less heavy and mathematically easier textbook, ideally suited for undergraduate students, was written by Pringle (2000). An extensive recent monograph on the physics, formation, and evolution of rotating stars, containing both introductory and specialized chapters, is available in Maeder (2009). Here, we limit to a brief discussion only<sup>1</sup>.

Stars are born in groups, called clusters, when dense interstellar molecular clouds collapse under the effect of gravity. Any perturbation within the cloud, due to whatever origin, will result in a collapse whenever the mass of the cloud is above a certain threshold:  $M > M_J \propto T^{3/2} \rho^{-1/2} \mu^{-3/2}$ , with  $T$  the temperature of the cloud,  $\rho$  its mean density and  $\mu$  its mean molecular weight. This condition for free-fall collapse is known as the *Jeans criterion*. The process will continue as long as the collapse happens isothermally. As soon as the free-fall time becomes similar to the thermal relaxation time, however, an adiabatic contraction takes over, and the process comes to a natural end, leaving behind protostellar fragments with masses of the order of stellar masses. Owing to their rather low internal temperature and consequent high opacity, the entities that result from the process, called *protostars*, are initially fully convective and hence are located on the *Hayashi track*.

After the rapid dynamical contraction, the protostar reaches hydrostatic equilibrium and is said to have entered its *pre-main-sequence phase*. The fur-

---

<sup>1</sup> The authors benefited greatly from private discussions with Anja Andersen, Arlette Noels, Hans Van Winckel, and Lee Anne Willson for the brief descriptions of stellar evolution in this chapter and in Chapter 3.

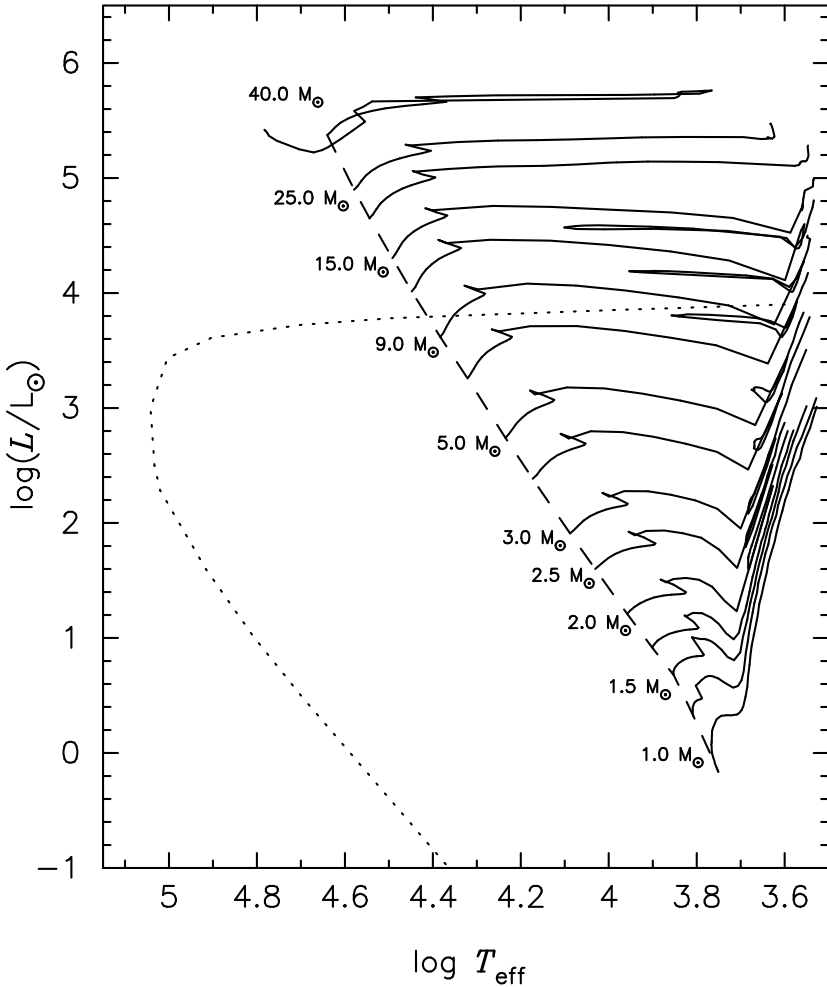


**Fig. 2.1.** HR Diagram showing the evolutionary tracks of stars with masses between  $1 M_{\odot}$  and  $40 M_{\odot}$  (full lines, Schaller *et al.* 1992). The dashed line is the zero-age main sequence and the dotted line symbolizes the transition phase from the Asymptotic Giant Branch to the white-dwarf cooling track.

ther contraction of the star implies that the star descends the Hayashi track, keeping essentially the same effective temperature and decreasing in luminosity. As the internal temperature gradually increases, the opacity decreases and the convective zone starts to recede from the center of the star. This implies that the star leaves its Hayashi track and starts radiative contraction along its *Henyey track*. As contraction proceeds in a more and more transparent matter, the star reverses its downward luminosity trend into a rising one.

The increasing core temperature initiates the proton-proton reaction, which converts H into  $^2\text{H}$ , and this fresh deuterium is immediately burnt into  $^3\text{He}$ . The less massive the pre-main-sequence star, the closer to the Hayashi track occurs this first nuclear burning. The full *proton-proton (PP) chain* cannot be completed yet since  $^3\text{He}$  is still too scarce for hydrogen burning to happen in full equilibrium. As a consequence, the temperature sensitivity of the nuclear reactions is high (about three times the sensitivity of the proton-proton chain operating at equilibrium) and this leads to the development of a convective core. In stars less massive than about  $1.1 \text{ M}_\odot$ , this convective core will disappear as soon as the PP chain has all its intermediate chemical species at equilibrium. More massive stars, on the contrary, rapidly switch to hydrogen burning through the *CNO cycle*, which is far more temperature sensitive than the PP chain at equilibrium, and they keep their convective core during the whole central hydrogen burning phase.

The accretion continues during most of the pre-main-sequence phase, on a thermal (or Kelvin-Helmholtz) time scale. Consequently, protostars with masses above about  $9 \text{ M}_\odot$  move so fast from their Hayashi track to the main sequence that they are unobservable in their pre-main-sequence phase as they remain embedded in a thick circumstellar shell of infalling material. Pre-main-sequence stars with masses between  $\sim 1.6$  and  $9 \text{ M}_\odot$  end their accretion phase before they reach the main sequence. Such pre-main-sequence stars are termed *Herbig Ae/Be stars*. In pre-main-sequence stars with masses between some  $0.8$  and  $1.6 \text{ M}_\odot$ , as soon as the accretion process stops, the star lights up in the HR Diagram as an optically bright source called a *T Tauri star*. Observations of both Herbig Ae/Be stars and T Tauri stars suggest that they undergo active surface phenomena such as a stellar wind and differential rotation.

Once the hydrogen is burning in full equilibrium and completely dominates the energy production, the star reaches a state of thermal equilibrium and is said to be born on the *zero-age main sequence* (ZAMS). The circumstellar remnant material vanishes within a thermal time scale and the star forgets its formation history. Protostars with a mass below some  $0.08 \text{ M}_\odot$  never reach the ZAMS because they become degenerate before having reached a high enough central temperature to burn hydrogen in equilibrium. Such objects are called *brown dwarfs*. Since oscillations have not yet been found in brown dwarfs we will not discuss them further.

The stars spend about 90% of their life on the main sequence, burning H into He on a nuclear time scale. Depending on their mass, the interior structure in terms of radiative, convective, diffusive and rotational energy transport is very different. The initial chemical composition is also a determining factor in the details of the evolution. Once the central hydrogen is exhausted, the star has reached the *terminal-age main sequence* (TAMS). At that time the hydrogen shell burning takes over as the energy source; the helium core starts contracting, while the outer parts of the star expand greatly, causing the star to move back to and up the Hayashi track as a red giant. The further evolution

of the star is now again largely dependent on its mass. Evolutionary tracks for different masses are indicated in Fig. 2.1 and are briefly discussed below.

The gas in the cores of stars with  $M \geq 9 M_{\odot}$  does not become degenerate before carbon burning, so these objects follow subsequent central burning and shell burning cycles, producing all elements up to iron and nickel. At that stage, the star encounters a major problem because  $^{56}\text{Fe}$  and  $^{62}\text{Ni}$  are the most tightly bound nuclei. Their fusion into heavier elements would result in less tightly bound nuclei and thus would require an input of energy. The inescapable core contraction leads to temperatures of billions of Kelvin accompanied by photodissociation of heavy nuclei, transforming them into He nuclei and neutrons, with a catastrophic loss of thermal energy and pressure causing the core to collapse. The stupendous release of gravitational potential energy implies that the rest of the star explodes as a supernova, blowing away a huge fraction of its processed material which thus enriches the interstellar medium in the surroundings, and leaving a neutron star or a black hole as a remnant. Rapid neutron capture operates for a brief period during supernova explosions, producing a substantial fraction of the heavy elements beyond iron. The internal mixing processes acting in these stars while they evolve from the TAMS to the supernova stage are very uncertain, as are the details of their mass loss, which implies we are not able to make accurate predictions of the properties of the star just before the supernova explosion. Stars of such initial masses have typical lifetimes less than a few tens of million years.

Stars with masses above some  $25 M_{\odot}$  are subject to very strong radiatively-driven winds while on the main sequence; such stars lose a huge amount of mass because of that, dramatically affecting their evolution. The radiation pressure is so strong that they are not very stable, resulting in complex phenomena such as instabilities and outbursts. Such stars are termed *luminous blue variables* and, after a large fraction of their hydrogen envelope has been blown away, *Wolf-Rayet stars*. They live less than a few million years, also finishing their lives in supernovae explosions, and are likely progenitors of stellar black holes.

At the other end of the mass range, stars with masses below about  $0.5 M_{\odot}$  have not yet had time to evolve off the main sequence, but when they do their core temperatures will not become high enough to initiate helium burning, so they will finish their lives as He white dwarfs. Stars with an initial mass in the range  $0.5 \leq M \leq 2.3 M_{\odot}$ , the precise cut-off depending on the metallicity, have a degenerate helium core after the main sequence. They reach the TAMS after a few to several gigayears, depending on the birth mass. The shell burning after the TAMS accompanies a shrinkage of the core until the latter reaches the temperature at which helium burning through the triple- $\alpha$  reaction starts. Since this happens in degenerate matter, a thermal runaway occurs and the star is said to undergo a *helium flash*. The helium flash lifts the degeneracy in the helium core, and the star settles down on the *horizontal branch* burning helium in its core and hydrogen in a shell. In cases where the metal abundance is less than about 10% that of the Sun, the horizontal branch is very extended,

depending on the mass and the extent of the hydrogen-rich envelope (*e.g.*, Chapter 8 of Prialnik 2000). Stars with higher metallicity are redder because their opacity is higher, and they cluster near the red-giant branch in the *red clump*.

At that stage of evolution, the low-mass central helium burning objects join the stars with initial birth mass  $2.3 M_{\odot} \leq M \leq 9 M_{\odot}$ , which started helium burning calmly as their core at the end of the TAMS did not reach degeneracy. After the central helium exhaustion, the stars are forced to shine by helium- and hydrogen-shell burning. They are said to ascend the *Asymptotic Giant Branch* (AGB). In this phase nuclear burning involves *thermal pulses* due to the extinction and re-ignition of the helium shell burning. This implies a large amount of internal mixing, leading to complex nuclear reactions. The slow-neutron capture process becomes active and leads to nuclear yields beyond the iron-peak elements. These products are dredged up for stars with  $M \geq 4 M_{\odot}$ . Stars with initial masses above some  $6 M_{\odot}$  and below some  $9 M_{\odot}$  may experience some stages of carbon burning, leading in the end to an O, Ne, Mg white dwarf. The lower limit mentioned of  $6 M_{\odot}$  in birth mass for which this occurs is rather uncertain and depends heavily on the mass loss and rotational mixing since the TAMS. It may be that only the heaviest stars in this mass range effectively ignite carbon. Stars on the AGB lose a significant amount of their mass through a dust-driven wind in combination with large-amplitude pulsations. The outer layers are so loosely bound due to the envelope expansion accompanying the shell burning that they are easily removed by the radiation acting on dust particles. The dust-driven mass loss stops as soon as the hydrogen-burning shell is largely extinguished and the star enters its *post-Asymptotic Giant Branch* (post-AGB) phase. The remaining envelope is rapidly lost and the resulting circumstellar material shines for a few thousand years as a *planetary nebula*. This exposes the degenerate core as a *white dwarf*, which subsequently evolves down along the *white-dwarf cooling track* over a time scale of billions of years. The coolest, and hence oldest, white dwarfs in the solar neighbourhood have the same age as the Galaxy, around 10 Gyr.

Most of the post-AGB stars start cooling off directly as a white dwarf, *i.e.*, do not return to the AGB once they left it. About 25% of the post-AGB stars, however, undergo a so-called *born-again* episode. Such episodes are due to a late thermal pulse, re-igniting helium near the hot white-dwarf core, either when the hydrogen shell burning is still active or else shortly after the hydrogen burning has essentially stopped. In both cases, the star returns rapidly to the AGB and becomes a hydrogen-deficient helium-burning object, consisting of a CO core surrounded by surface layers rich in helium, carbon and oxygen (Werner & Herwig 2006). They traverse once more the HR Diagram towards the white-dwarf phase in less than 200 years. Depending on the core mass and on the effective temperature, a strong or a weak radiation-driven wind occurs in that stage. The star thus shows up as a hydrogen-deficient compact central star of a planetary nebula. These stars are almost indistinguishable from the

Wolf-Rayet central stars of planetary nebulae, usually denoted as [WCE], in the sense that their position in the HR Diagram is the same. Their spectra look different, though, because the Wolf-Rayet stars have emission lines in their spectra due to a strong wind, while the luminosity of the post-AGB central stars of planetary nebulae is such that they have only a weak line-driven wind and thus absorption lines.

## 2.2 Variability Studies from Large-Scale Surveys

### 2.2.1 Hipparcos

One of the most important large surveys of variable stars was carried out by the satellite Hipparcos of the European Space Agency. The mission's name stands for **H**igh **P**recision **P**ARallax **C**ollecting **S**atellite. It was launched in 1989 and has measured the parallax of some 120 000 bright stars in the solar neighbourhood. The satellite's name is not only an acronym but also refers to the Greek astronomer Hipparchus of Nicea, who was the first to compose a stellar catalogue with the position and brightness of many stars, based upon personal naked-eye observations. Therefore, Hipparchus is considered to be the father of astrometry.

The prime goal of the Hipparcos mission was to measure the distances of stars with unprecedented precision of 2 milli-arc-seconds (mas) for the parallax. The proper motions of the stars were measured with an accuracy of 2 mas per year. This was achieved by measuring each star on average 100 times during the 3.3-year lifetime of the mission. The Hipparcos filter was a broad-band white-light filter sensitive to wavelengths between 4 000 Å and 8 000 Å. The Hipparcos data were further complemented with those of the Tycho experiment, which determined the parallax and proper motion of a million fainter stars with an accuracy of 30 mas (per year).

A very important by-product of the Hipparcos mission was that it provided us for the first time with an unbiased view of variable stars with periods longer than approximately one hour in the solar neighbourhood. Indeed, for each star a unique time series was measured, with, on average, 100 time points that were quasi-randomly chosen during the 3.3 years. These are time series that are very different from those obtained with ground-based instruments. The input catalogue was completely unbiased in the sense that the pre-selection of the target stars did not take into account any knowledge of variability.

The Hipparcos mission led to the discovery of a few thousand new periodically variable stars and yet another few thousand variables without a clear dominant periodicity. These were made publicly available by means of two catalogues: the “Catalogue of Periodic Variables” and the “Catalogue of Unsolved Variables”. The latter contains stars that are clearly variable but for which no obvious periodicity could be unravelled from the data for different types of reasons (long-term trends, very long uncovered periods, too low amplitude variability, *etc.*).

One of the more striking results derived from the mission was the discovery of numerous new variables with periods of the order of days. Such variables are indeed very hard to find from (single-site) ground-based data, which suffer from strong one-day aliasing (see Chapter 5 for a definition of this phenomenon). The Hipparcos mission particularly had a large impact on the study of slowly pulsating B stars and  $\gamma$  Dor stars. The number of such non-radial g-mode pulsators known was increased by a factor more than ten in both cases (Waelkens *et al.* 1998; Handler 1999a), leading to about one hundred candidate class members for each of these two classes. As a result, extensive follow-up long-term ground-based photometric and spectroscopic campaigns were organized to study the pulsational behaviour of the brightest such class members (Aerts *et al.* 1999; Mathias *et al.* 2001; De Cat & Aerts 2002; and De Cat *et al.* 2007 for the slowly pulsating B stars and Eyer & Aerts 2000; Handler & Shobbrook 2002; Henry & Fekel 2005, Henry *et al.* 2005; Mathias *et al.* 2004; De Cat *et al.* 2006 and Cuypers *et al.* 2009 for the  $\gamma$  Dor stars). These campaigns led to the general properties of the stars discussed further on in this chapter.

It is also worth noting that the number of known eclipsing binaries was about doubled from Hipparcos, with the discovery of 343 new ones (*e.g.*, Söderjhelm 2000).

Surveys of variable stars from space will come from the high time-resolution missions CoRoT<sup>2</sup> (Convection, Rotation and planetary Transits, launched on 27 December 2006) and Kepler<sup>3</sup> (launched on 7 March 2009), as well as from Gaia<sup>4</sup> (scheduled for launch near the end of 2011), and, hopefully, PLATO<sup>5</sup> (to be launched in 2017 if approved for implementation by ESA in 2011). The numbers of new variables to be discovered from these missions will be outrageously large (certainly in the millions), requiring fully automated variability classification tools based on Artificial Intelligence methodology (Debosscher *et al.* 2007; Sarro *et al.* 2009).

### 2.2.2 Ground-Based Surveys

Significant progress on the group properties of large-amplitude oscillators, such as Cepheids, RR Lyrae stars, and red-giant and supergiant pulsators, was made by several large surveys that were initiated in the early nineties. These surveys were set up with the goal to search for **M**ASSive Compact **H**alo **O**bjects or MACHOs. The idea was that such MACHOs, if discovered, could perhaps help explain some of the missing dark matter in the Universe. The primary aim of the surveys was therefore to test the hypothesis that a significant fraction of the dark matter in the halo of the Milky Way is made up of objects such as brown dwarfs and planets.

<sup>2</sup> <http://corot.oamp.fr/>.

<sup>3</sup> <http://www.kepler.arc.nasa.gov/>.

<sup>4</sup> <http://www.rssd.esa.int/SA-general/Projects/GAIA/>.

<sup>5</sup> <http://lesia.obspm.fr/cosmicvision/plato/>.

It was Paczyński (1986) who suggested that dark matter could be discovered from a microlensing effect. The idea is that, when a dark compact massive body (the lens) passes in between us and a background light source, the latter's apparent luminosity increases because the dark body acts as a gravitational lens, concentrating the light rays of the source in the line of sight due to light bending according to general relativity. This implies a magnification of the source luminosity, which is independent of wavelength. One can therefore use this phenomenon to discover dark compact bodies within our galactic halo, *e.g.*, using the stars of the Magellanic Clouds or of the Galactic Bulge as light sources. The duration of the magnification depends on the speed, the position and the mass of the deflector and ranges from half an hour to about two months for dark masses ranging from a lunar mass to a solar mass. The magnification can reach values from a few to a thousand. The phenomenon is rare and non-repetitive, as it requires a good alignment of light source, lensing dark body and observer while the lens and observer move with respect to each other. Microlensing can also be used to discover exoplanets orbiting around the lens. In that case, the effect of the planet on the lensing gravitational field causes a brief increase in the magnification.

The detection of microlensing events thus requires long-term monitoring of a vast number of light sources with high precision photometry, since the events are rare. Several large observational initiatives to discover MACHOs were set up more than two decades ago and additional ones were started after 1995 to search for exoplanets. Important by-products of such surveys are huge inventories of accurate light curves of stars, among them Cepheids and RR Lyrae stars and long-period red variables, but also many other periodic variables.

The best known surveys are MACHO<sup>6</sup> itself and OGLE<sup>7</sup> which stands for Optical Gravitational Lensing Experiment. EROS<sup>8</sup> is another survey whose acronym stands for Expérience pour la Recherche d'Objets Sombres while MOA<sup>9</sup>, which denotes Microlensing Observations in Astrophysics, started somewhat later than the previous three surveys.

These surveys, and others that can be found through links on the web pages mentioned, several of which specifically designed for exoplanet detection, have resulted in millions of stars in the Galactic Bulge and Magellanic Clouds being monitored and led to thousands of lensing events. Besides these events, tens of thousands of variable stars were discovered in the Galactic Bulge and Magellanic Clouds, among which are hundreds of Cepheids, RR Lyrae stars, eclipsing binaries and ellipsoidal variables, as well as nonradial pulsators (Sarro *et al.* 2008).

---

<sup>6</sup> <http://wwwmacho.mcmaster.ca/>.

<sup>7</sup> <http://bulge.princeton.edu/~ogle/>.

<sup>8</sup> <http://eros.in2p3.fr/>.

<sup>9</sup> <http://www3.vuw.ac.nz/scps/moa/>.

In addition to the microlensing surveys, there are also all-sky surveys specifically designed to find variable stars. They have been carried out with small wide-field cameras since the mid-1990s. The best known and largest of these surveys is ASAS<sup>10</sup>, the **All-Sky Automated Survey** (Pojmański 1997). A summary of the variables found by ASAS is provided in Pojmański & Maciejewski (2004, 2005 and references therein). The **2 Micron All Sky Survey**<sup>11</sup> (2MASS, Beichmann *et al.* 1998), on the other hand, is a catalogue of over 100 000 000 individual objects, the vast majority of which are stars of spectral type K and later. Its monitoring was carried out in three wavebands,  $J$  ( $1.25\text{ }\mu\text{m}$ ),  $H$  ( $1.65\text{ }\mu\text{m}$ ), and  $K$  ( $2.2\text{ }\mu\text{m}$ ), with limiting sensitivity ( $10\sigma$  detection) of point sources with  $K$  less than 14. The all-sky coverage was selected primarily to support studies of the large scale structure of the Milky Way and the Local Universe. Nevertheless, the catalogue is of much value for variable star research, particularly when combined with the microlensing surveys discussed above, *e.g.*, Fraser *et al.*'s (2005) study of long period variables to which we will return later in this chapter.

The **Sloan Digital Sky Survey**<sup>12</sup> (SDSS, Stoughton *et al.* 2002) is an imaging survey that covers one quarter of the celestial sphere while collecting also spectra of hundreds of thousands of targets. The imaging data are collected in five bandpasses ( $u$ ,  $g$ ,  $r$ ,  $i$ , and  $z$ ) and are complete to magnitudes 22.0, 22.2, 22.2, 21.3, and 20.5, respectively. The SDSS turned out to be a very important survey for faint (compact) objects that had been missed in previous surveys with brighter limits, such as Cataclysmic Variables (CVs, Szkody *et al.* 2004), cool dwarfs (Hawley *et al.* 2002), white dwarfs (Harris *et al.* 2003; Eisenstein *et al.* 2006a), and spectroscopic binaries (Pourbaix *et al.* 2005), and of course the pulsating ones among all these categories. Another important, more recent survey, specifically designed to find emission line objects, is IPHAS, which stands for the **I**saac **N**ewton **T**elescope **P**hotometric **H**-**A**lpha **S**urvey<sup>13</sup> of the Northern Galactic Plane (Witham *et al.* 2008). It spans the latitude range  $-5^\circ < b < +5^\circ$  and reaches down to  $r' = 19.5$ . It contains photometry on about 80 million objects, making it a major source for the study of stellar populations in the disc of the Milky Way. Presently, thousands of point sources have been found to exhibit strong photometric evidence for H $\alpha$  emission, representing a wide range of objects, such as early-type emission-line stars, active late-type stars, interacting binaries, young stellar objects and compact nebulae. The Radial Velocity Experiment<sup>14</sup> (RAVE, Zwitter *et al.* 2008) is a spectroscopic survey to measure radial velocities and stellar atmosphere parameters of up to one million stars. It will operate in the time frame 2003 to 2010 and uses the multi-object spectrograph on the 1.2 m

<sup>10</sup> <http://archive.princeton.edu/~asas/>.

<sup>11</sup> <http://www.ipac.caltech.edu/2mass/>.

<sup>12</sup> <http://www.sdss.org/>.

<sup>13</sup> <http://astro.ic.ac.uk/Research/Halpha/North/index.shtml>.

<sup>14</sup> <http://www.rave-survey.org/>.

UK Schmidt Telescope of the Anglo-Australian Observatory. Presently, some 50,000 radial velocities as well as stellar parameters for some 20,000 stars have been published and made available to the community, mainly to study galactic kinematics.

The impact of large scale surveys on pulsating star research was summarized after about ten years of microlensing monitoring in Szabados & Kurtz (2000). We refer to the web pages of the consortia mentioned above for more up-to-date achievements and recent papers on variable star research, as well as on detected lenses and their interpretation. While the surveys mainly led to the discovery of new large amplitude pulsators, some nonradial pulsators such as  $\beta$  Cep stars and  $\delta$  Sct stars were also found (see, *e.g.*, Pigulski & Kołaczkowski 2002; Pigulski *et al.* 2003; Pigulski 2005), as well as numerous new compact pulsators (see below). As the surveys mainly observe faint members of the classes, and as they do not provide multicolour photometry of mmag level precision nor high resolution, high signal-to-noise spectroscopy (see Chapter 4 for definitions of such type of data), these discoveries have not yet led to mode identification; hence asteroseismic modelling of the individual targets has so far not been possible. Massive follow-up projects are thus required specifically dedicated to this task.

## 2.3 Oscillations Near the Main Sequence

Our journey along the main sequence starts at the low-mass end and finishes with the highest mass pulsators.

### 2.3.1 Solar-Like Oscillations in Solar-Like Stars

The best case of a solar-like star with the clearest solar-like oscillations is of course the Sun. Its oscillation frequency spectrum has already been shown in Fig. 1.9 and reveals hundreds of peaks centred on 3 mHz with corresponding periods between 3 and 15 min. The brightness variations have amplitudes near 8 ppm for the strongest modes and down to the detection threshold of about 1 ppm. These variations correspond to velocity amplitudes of a few to tens of  $\text{cm s}^{-1}$ .

As the oscillations of the Sun are caused by turbulent convective motions near its surface, we expect such oscillations to be excited in all stars with outer convection zones. Solar-like oscillations are indeed predicted for the lowest mass main sequence stars up to objects near the cool edge of the classical instability strip with masses near some  $1.6 M_{\odot}$  (*e.g.*, Christensen-Dalsgaard 1982a; Christensen-Dalsgaard & Frandsen 1983a; Houdek *et al.* 1999) as well as in red giants (Dziembowski *et al.* 2001a). Such stochastically excited oscillations have very tiny amplitudes, which makes them hard to detect, particularly for the low mass stars. The velocity amplitudes were predicted to scale roughly as  $L/M$  before the first firm discoveries of such oscillations in stars

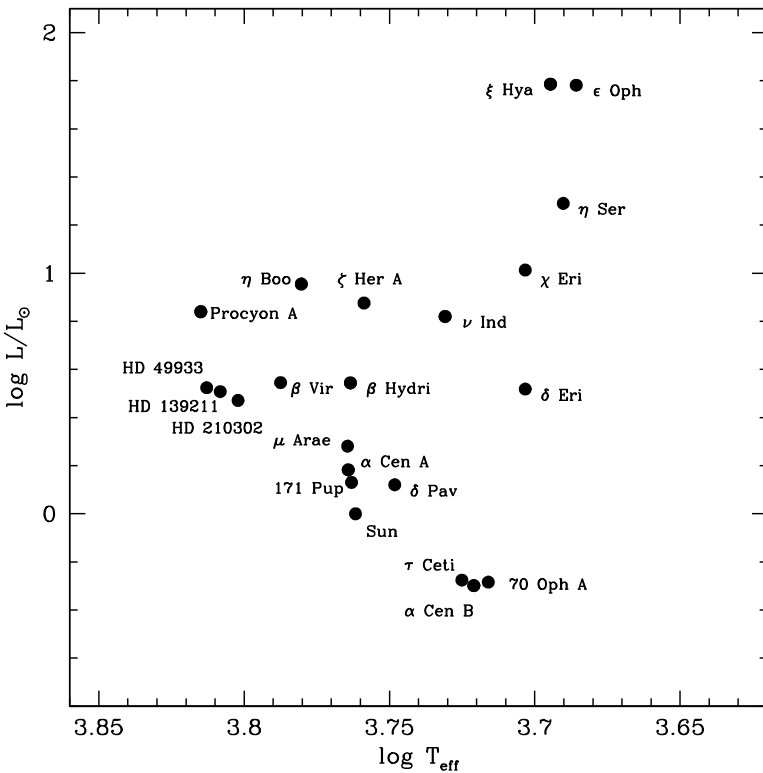


**Fig. 2.2.** HR Diagram showing the stars in which solar-like oscillations have been detected (with HD 49933 = HR 2530). The discoveries for 171 Pup, HD 139211 (HR 5803) and HD 210302 ( $\tau$  PsA) are unpublished (Carrier *et al.*, in preparation). Figure courtesy of Fabien Carrier.

other than the Sun (Kjeldsen & Bedding 1995). This scaling law was later modified to  $(L/M)^{0.8}$  from excitation predictions based on 3D computations of the outer atmosphere of the stars (Samadi *et al.* 2005), resulting in lower amplitudes compared with those found for 1D models.

The search for solar-like oscillations in stars in the solar neighbourhood has been ongoing since the early 1980s. The first indication of stellar power with a frequency dependence similar to that of the Sun was obtained by Brown *et al.* (1991) in  $\alpha$  CMi (Procyon, F5IV). The first detection of individual frequencies of solar-like oscillation was achieved from high precision time-resolved spectroscopic measurements only in 1995 for the G5IV star  $\eta$  Boo (Kjeldsen *et al.* 1995); Brown *et al.* (1997) could not establish a confirmation of this detection from independent measurements, but it was subsequently

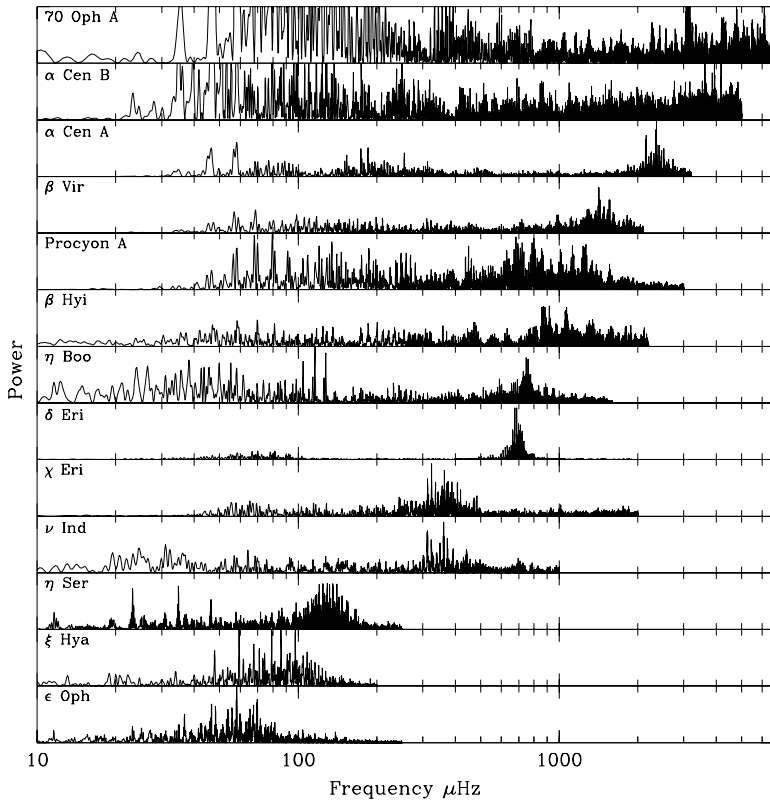


**Fig. 2.3.** Frequency spectra of a sample of solar-like oscillators covering the entire range in spectral type. Figure courtesy of Fabien Carrier.

confirmed by Kjeldsen *et al.* (2003) and Carrier *et al.* (2005). It took another four years before solar-like oscillations were definitely established in Procyon (Martić *et al.* 1999). Subsequently, such oscillations were found in two more stars: the G2IV star  $\beta$  Hyi (Bedding *et al.* 2001) and the solar twin  $\alpha$  Cen A (Bouchy & Carrier 2001). These important discoveries opened the floodgates which led to several more discoveries, summaries of which were provided by Bedding & Kjeldsen (2003, 2007). Meanwhile, solar-like oscillations have been firmly established in numerous stars. Their position in the HR Diagram is displayed in Fig. 2.2. Frequency spectra of a selected sample, covering the whole range in spectral type, are shown in Fig. 2.3. The detected frequencies and frequency separations for all stars behave as expected from theoretical predictions and scaling relations based on extrapolations from helioseismology.

Detailed seismic studies of stars with stochastically excited modes are currently still in their infancy compared with helioseismology (see Chapter 7). However, given the recent detections and the continuing efforts to improve them, we expect a real breakthrough in the seismic interpretation of the targets in the coming years. We refer to Chapter 7 for in-depth seismic modelling attempts for a few selected stars.

The quest for solar-like oscillations in metal poor stars considerably less massive than the Sun is an important goal of asteroseismic space missions. This is particularly so because asteroseismology has proven to be a very successful technique to probe interior stellar structure and derive a high precision age estimate (Christensen-Dalsgaard 2002; see also Chapter 7). Indeed, such low mass stars are among the oldest in our Galaxy (and hence in the Universe) and accurate age estimates of such objects, which can in principle be achieved from measuring their large and small separations as in the Sun (see Chapter 1), can provide a good age determination of the Universe which would be completely independent of any method currently in use.

### 2.3.2 $\gamma$ Dor Stars

In 1995, a new group of Population I nonradially oscillating stars was established near the intersection of the red edge of the classical instability strip and the main sequence. This followed from the discovery of multiperiodic variability with amplitude near 0.1 mag in the F0V star 9 Aur and the realization that the three stars  $\gamma$  Doradus (F4III), HD 96008 (F0V), and HD 164515 (F2IV-V) have similar behaviour (Krisciunas *et al.* 1993). These stars have early-F spectral types and are called after the prototype, the star  $\gamma$  Doradus whose variability was first discovered by Cousins *et al.* (1989; Cousins 1992) and extensively studied by Balona *et al.* (1996).

As already mentioned in Section 2.2.1, the Hipparcos mission was very important for the discovery of new class members in view of the intrinsic periodicities near one day and the difficulty to study such variations from the ground. Some 50 confirmed members are established by now, while more than 100 additional candidates are being studied observationally (*e.g.*, Mathias *et al.* 2004; Henry *et al.* 2005; De Cat *et al.* 2006; Cuypers *et al.* 2009, and references therein), most of them originally found from mining the Hipparcos database. The stars have multiperiodic behaviour with individual periods between about 0.5 and 3 d, which is an order of magnitude longer than acoustic modes would have for such stars. Their variability is therefore interpreted in terms of multiperiodic high order nonradial g modes.

Long term multicolour and/or high resolution spectroscopic datasets are meanwhile available for several  $\gamma$  Dor stars (*e.g.*, Poretti *et al.* 2002; Aerts *et al.* 2004; Cuypers *et al.* 2009). The particular case of g modes with long periods of the order of a day implies that the data sets of such oscillators consist of only a few points per night, and makes it difficult to illustrate the periodicity in the time domain. One therefore usually uses phase diagrams

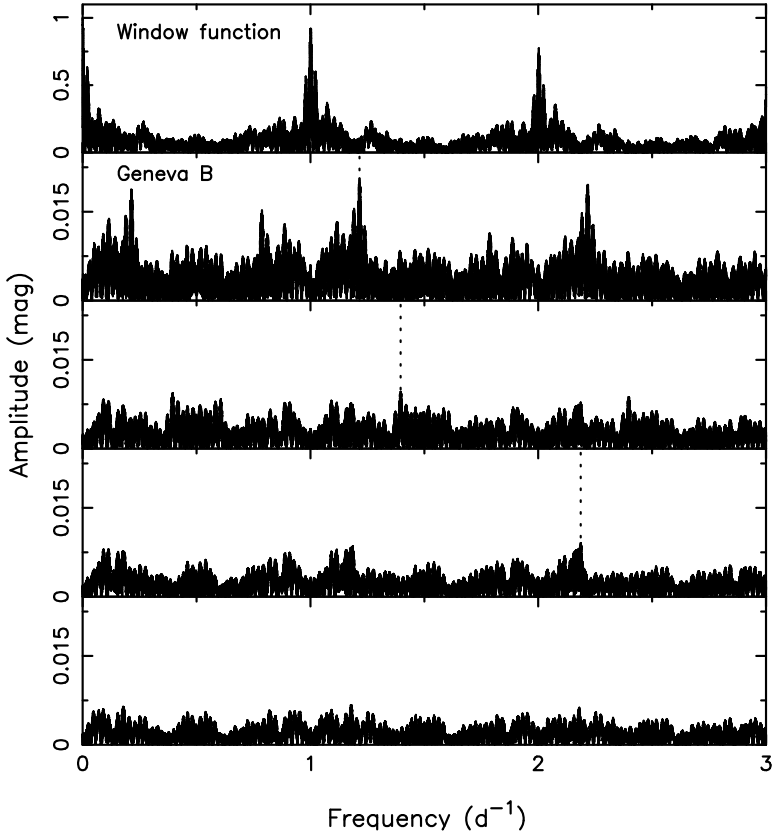


**Fig. 2.4.** Spectral window (top) and frequency spectra after subsequent stages of prewhitening (see Chapter 5 for a definition of this procedure; second to fifth panel) for single site ground based Geneva *B* data of the  $\gamma$  Dor star HD 12901. The three detected frequencies that were derived from independent data sets are indicated as dotted lines. From Aerts *et al.* (2004a).

(see Chapter 6 for a formal definition). The periodograms of the ground based Geneva data of HD 12901 (F2V) are shown as a representative example for the whole class in Fig. 2.4. Figure 2.5 shows the phase diagrams after identification of the frequencies. It can be seen from Fig. 2.5 that the variations have low amplitudes. The three frequencies indicated are trustworthy only because they occur in independent datasets (Hipparcos and multicolour ground photometry, and sometimes radial velocity data in addition), a situation often encountered in frequency analysis as will be explained in Chapter 5. All existing data are in agreement with the interpretation in terms of multiperiodic g modes.

The observational properties of  $\gamma$  Dor stars were summarized by Kaye *et al.* (1999). The class members have masses between  $1.5$  and  $1.8 M_{\odot}$ . Handler

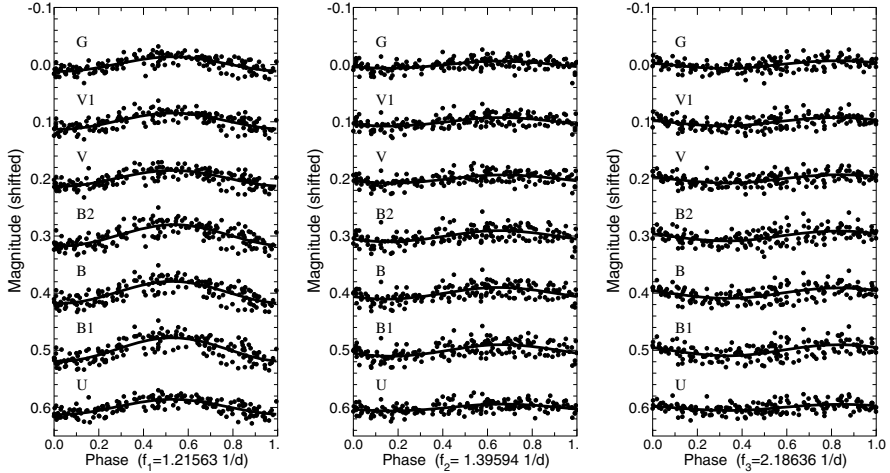


**Fig. 2.5.** Phase diagrams of the  $\gamma$  Dor star HD 12901 for the three frequencies indicated as dotted lines in Fig. 2.4. From Aerts *et al.* (2004a).

& Shobbrook (2002) made a careful observational study to understand the relationship between  $\delta$  Sct oscillations (see below) and the behaviour of the  $\gamma$  Dor stars. They found a very clear separation in oscillatory behaviour between the two classes, except for the hybrid star HD 209295 which has both p and g modes, but this object is a member of a very close eccentric binary and its g modes seem to be tidally driven (Handler *et al.* 2002, see Section 2.8.2).

The earliest proposals for an excitation mechanism came from Guzik *et al.* (2000), who proposed driving by convective flux blocking at the base of the convective envelope. This mechanism was treated in the frozen convection approximation, in which the perturbation to the convective flux is ignored. The resulting instability strip was studied by Warner *et al.* (2003). However, as noted by Löffler (2000) and Dupret *et al.* (2005a), these instability calculations did not appropriately take into account that these stars have well-developed outer convection zones interacting with the pulsation. This was achieved by Dupret *et al.* (2005a) by means of a time dependent treatment of the convection. It allowed them to interpret and predict the g-mode instabilities observed in the  $\gamma$  Dor stars and to quantify an appropriate value of the mixing length parameter between 1.8 and 2.2 local pressure scale heights for  $\gamma$  Dor stars. Their instability strip is shown in Fig. 2.6. Interestingly, they found that convective blocking was in fact the dominant instability mechanism. Moreover, Dupret *et al.* (2005b) applied their theory to interpret successfully the multicolour behaviour of the five best studied  $\gamma$  Dor stars. A warning is needed, however, since these theoretical computations ignore the effects of the Coriolis and centrifugal forces, while most of the  $\gamma$  Dor stars are relatively fast rotators, in the sense that their oscillation periods are of similar magnitude

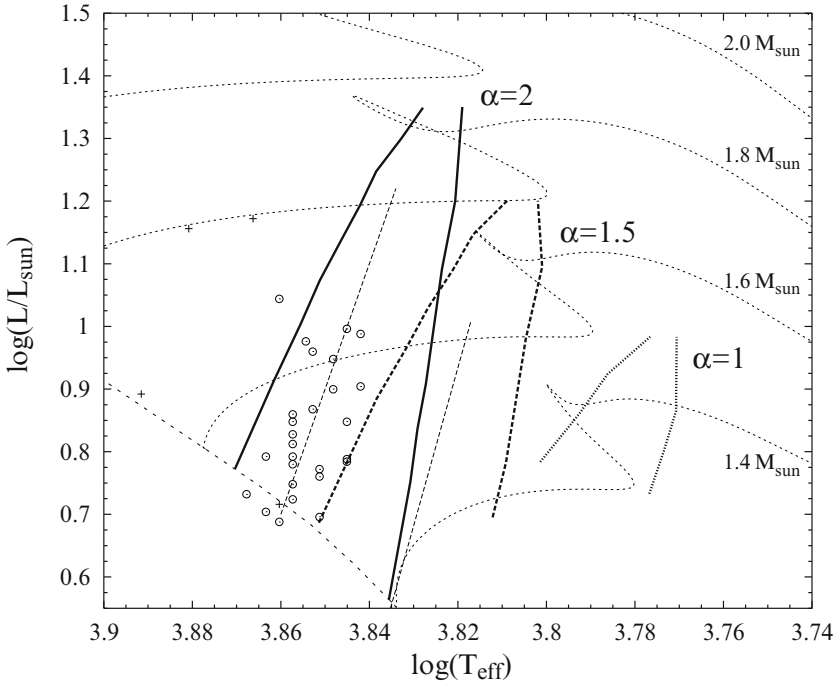


**Fig. 2.6.** The instability strip for  $l = 1$  modes of the  $\gamma$  Dor stars for three different values of the mixing length parameter  $\ell_{\text{ML}} = \alpha_{\text{ML}} H_p$  (see Chapter 3 for a definition) based on the convective blocking mechanism for a time dependent treatment of the convection (Dupret *et al.* 2005a). The results for the frozen convection approximation with mixing length parameter  $\ell_{\text{ML}} = 1.87 H_p$  obtained by Warner *et al.* (2003) are shown as thin dashed lines for comparison. The open circles are all of the bona fide  $\gamma$  Dor stars known up to 2005. The squares are binary  $\gamma$  Dor stars. The evolution tracks are for the masses indicated and were computed assuming overshoot from the convective core of  $\alpha_{\text{ov}} = 0.2$ . From Dupret *et al.* (2005a).

to their rotation period. The urgently required investigation of the rotational effects on current theoretical predictions remains to be carried out.

At present, very large observing efforts are being undertaken by several research teams, including long term multicolour photometric monitoring and/or high resolution spectroscopic campaigns (*e.g.*, De Cat *et al.* 2006; Arentoft *et al.* 2007; Uytterhoeven *et al.* 2008; Bruntt *et al.* 2008, and references therein). The  $\gamma$  Dor stars are very challenging objects in this respect, because beat periods up to years occur. Nevertheless, it seems worthwhile to undertake such endeavours, because these pulsators have the potential to undergo at the same time g modes and solar-like p modes. Indeed, they are situated at the high mass end where solar-like oscillations are predicted (Fig. 1.12). The firm establishment of the occurrence of both these types of oscillations, which probe

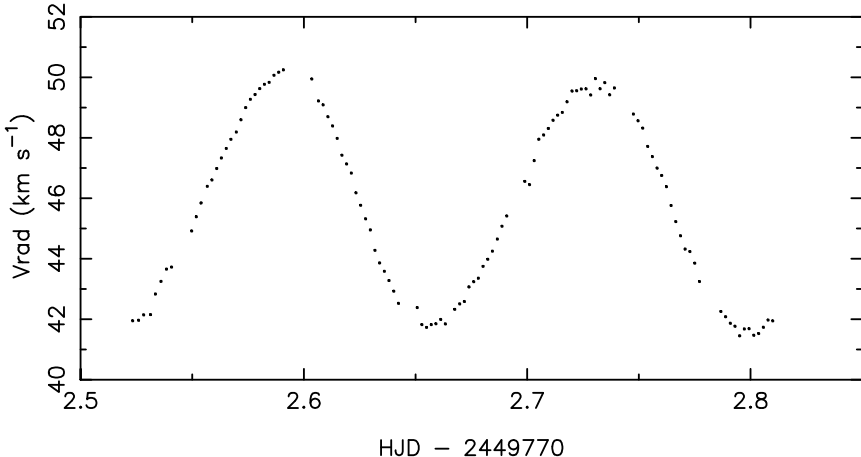


**Fig. 2.7.** Radial velocity curve of the high amplitude  $\delta$  Scuti star  $\rho$  Pup derived from high quality spectra of which some are shown in Fig. 6.15. Note the slight deviation from symmetry in this observed curve. Data taken from Mathias *et al.* (1997).

very different inner stellar regions, holds great potential for high precision seismic inference of their interior structure (*e.g.*, Miglio *et al.* 2008). For this reason,  $\gamma$  Dor stars are among the prime targets of the CoRoT space mission.

### 2.3.3 $\delta$ Sct Stars

The  $\delta$  Sct stars form a well established group of Population I pulsating stars with masses in the range  $1.5 - 2.5 M_{\odot}$ . They are situated at the position where the classical instability strip crosses the main sequence (see Fig. 1.12) and so are in a stage of central hydrogen or shell hydrogen burning. The oscillations are driven by the heat mechanism active in the second partial ionization zone of helium.

Both radial and nonradial oscillations occur in  $\delta$  Sct stars. Those are generally low order p modes with periods in the range 18 min to 8 hr. The observed amplitudes have a large range, from mmag up to tenths of a magnitude. The highest amplitude  $\delta$  Sct stars (also called HADS, meaning high amplitude  $\delta$  Sct stars) are claimed to be monoperiodic radial fundamental mode oscillators and so, at first sight, of less interest for asteroseismology. Nevertheless, Mathias *et al.* (1997) have shown convincingly that the very precise radial velocity curve they obtained for the HADS  $\rho$  Pup (Fig. 2.7) yielded the detection of low amplitude nonradial modes besides the dominant radial one. Moreover, Poretti (2003) found nonradial modes in the light curves of some HADS. It may very well be that this is a property of all HADS. In several lower amplitude  $\delta$  Sct stars, many nonradial oscillations have been detected. The most

up-to-date catalogue of  $\delta$  Sct stars was provided by Rodríguez *et al.* (2000). It contains a summary of all the observational characteristics of more than 600 class members that had been studied up until 2000. A comprehensive analysis of the properties of all these class members was made by Rodríguez & Breger (2001). Montgomery & Breger (2000) and Zverko *et al.* (2004) present the proceedings of two international meetings on, respectively,  $\delta$  Sct and related stars, and A stars in general, containing a wealth of information.

A few  $\delta$  Sct stars have been observed from space, *e.g.*,  $\theta^2$  Tau and Altair with the star tracker on the WIRE<sup>15</sup> (Wide-field InfraRed Explorer) satellite (Poretti *et al.* 2002; Buzasi *et al.* 2005, respectively), and HD 263551 with the MOST (Microvariability and Oscillations of STars)<sup>16</sup> satellite.

Within the class of  $\delta$  Sct stars one sometimes considers the subclasses of the pulsating  $\lambda$  Boo stars, and pulsating classical and evolved metallic line A (Am) stars known as  $\delta$  Del or  $\rho$  Pup stars; (Kurtz *et al.* 1995). These types of stars have been defined in general (*i.e.*, irrespective of their pulsational nature) as specific classes with anomalous spectra that are interpreted to be caused by anomalous surface abundances. The latter affect the oscillations and, therefore, these subclasses have slightly different behaviour compared to the  $\delta$  Sct stars with normal abundances (Rodríguez & Breger 2001). Keeping this in mind, the pulsations of the  $\lambda$  Boo and Am stars are fully compatible with those of normal  $\delta$  Sct pulsators and we do not consider them as separate classes of pulsators (hence they are not explicitly indicated on Fig. 1.12).

Numerous radial and nonradial modes have been detected in some selected  $\delta$  Sct stars, such as FG Vir (79 frequencies; Breger *et al.* 2005, see Figs 2.8 and 2.9), 4 CVn (34 frequencies; Breger 2000, see Fig. 2.10) and XX Pyx (30 frequencies; Handler *et al.* 1998, 2000). These results were all obtained by the Delta Scuti Network<sup>17</sup> (DSN), consisting of several telescopes around the globe and led by Michel Breger and his research team at Vienna University in Austria. The frequency spectra of these few, selected, well-studied stars show that the  $\delta$  Sct stars have complex oscillation patterns, with variable amplitudes from season to season and non-linear resonant mode coupling (*e.g.*, the case of 4 CVn: Breger *et al.* 1999a and Fig. 2.10; V1162 Ori: Arentoft *et al.* 2001b; FG Vir: Breger & Pamyatnykh 2006). This complexity turns out to lead to a problem in identifying the modes and hence hampers in-depth seismic interpretation, despite the large number of detected oscillations. An additional problem in identifying the modes is that mixed modes occur, particularly in the more evolved class members. These are modes that have a mixed character, *i.e.*, a g-mode character in the interior and a p-mode character in the outer layers of the star. Mixed modes occur in general in stars that have evolved off the main sequence and are undergoing hydrogen shell burning.

<sup>15</sup> <http://www.ipac.caltech.edu/wire/>.

<sup>16</sup> <http://www.astro.ubc.ca/MOST/index.html>.

<sup>17</sup> <http://www.astro.univie.ac.at/~dsn/index.html>.

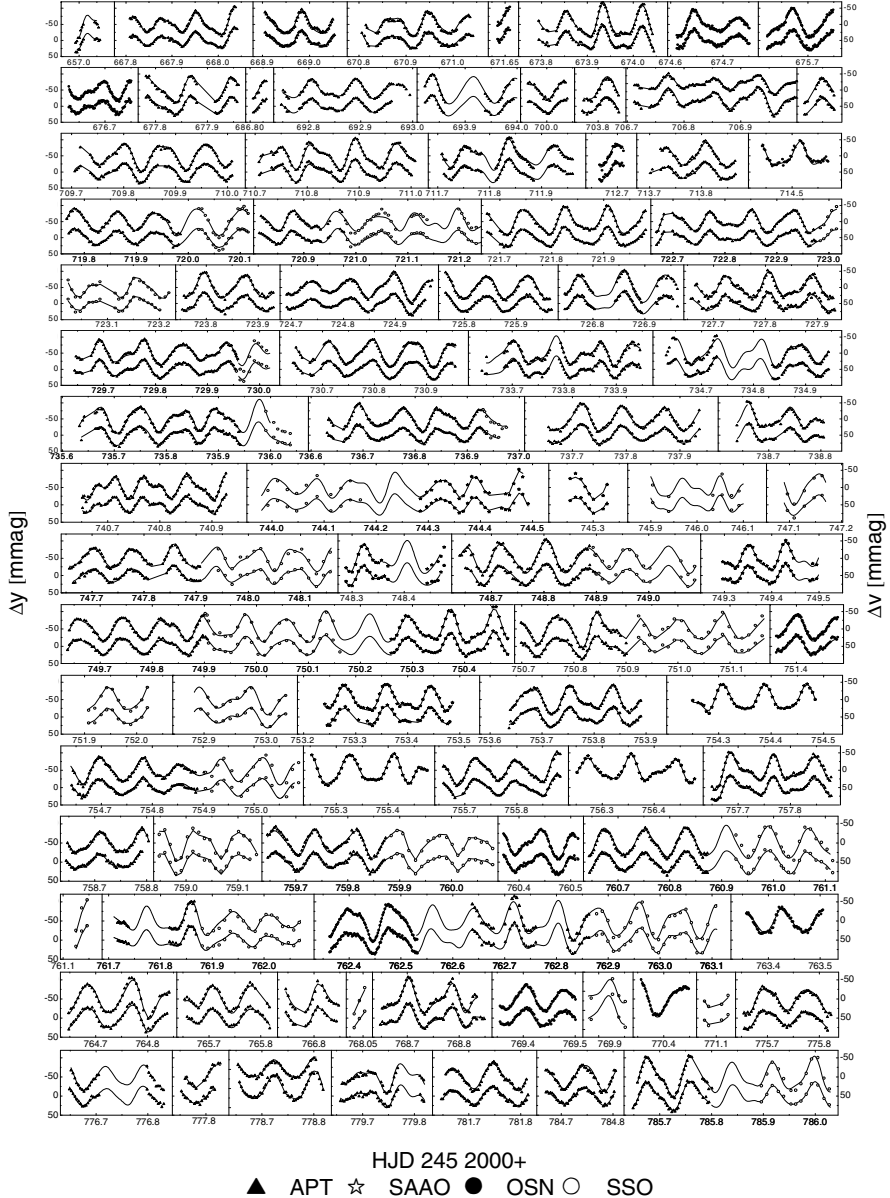


**Fig. 2.8.** Some observed light curves for FG Vir obtained by the DSN (dots) and a fit including 79 significant frequencies (full line). From Breger *et al.* (2005).

Pamyatnykh (1999) provided an extensive overview of the history of instability computations in the upper HR Diagram and presented his own computations based on improvements in opacity determinations by Iglesias & Rogers

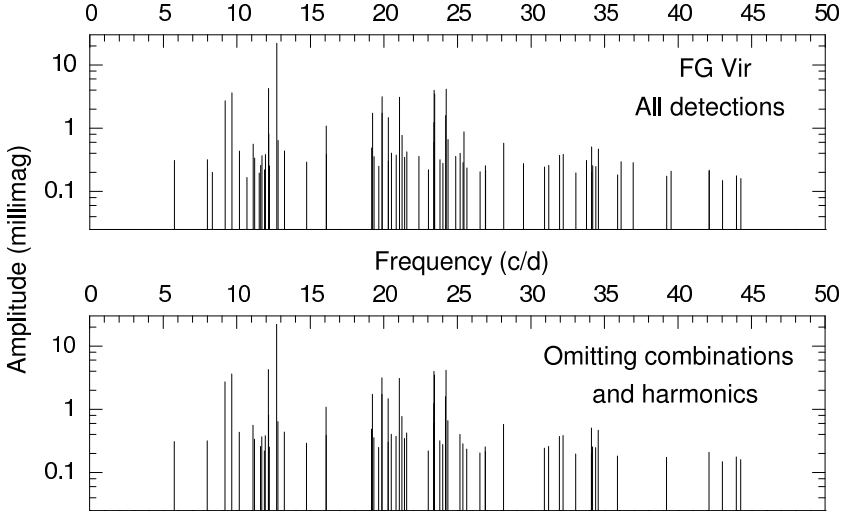


**Fig. 2.9.** Schematic frequency diagram of the  $\delta$  Sct star FG Vir deduced from DSN data, some of which is shown in Fig. 2.8. From Breger *et al.* (2005).

(1996) and Seaton (1996). His work included the determination of the blue edge of the classical instability strip, which is mainly determined by the helium opacity bump. The unstable modes in the hottest  $\delta$  Sct ZAMS models are found near  $\log L / L_{\odot} \approx 2$ , while instability in the radial fundamental mode occurs all the way up to  $\log L / L_{\odot} = 5$  for evolved stellar models. In practice, the  $\delta$  Sct stars are found on the main sequence and near the TAMS, with luminosities ranging from  $\log L / L_{\odot} \approx 0.6$  up to  $\log L / L_{\odot} \approx 2$  (Rodríguez & Breger 2001). The heat mechanism is no longer effective for the coolest  $\delta$  Sct star models. The red edge could therefore not be determined by Pamyatnykh (1999). For such cool stars, the damping and excitation are strongly affected by convection (see Section 3.7.3). Houdek (2000) included the time dependent heat and momentum fluxes following the formulation by Gough (1977a) in calculations of  $\delta$  Sct models and found a return to stability at approximately the correct location of the red edge. The red edge of the instability strip was also computed by Dupret *et al.* (2005a, see Fig. 2.11), who included a time dependent convection treatment for  $\delta$  Sct star models with different values of the mixing length parameter. They compared the results obtained from their time dependent convection treatment with those resulting from a frozen convection treatment and found much better agreement with observations. Both Houdek's and Dupret *et al.*'s treatments approximate the red edge in a satisfactory way (Fig. 2.11).

Main sequence stars near  $2 M_{\odot}$  are transition objects as far as the occurrence of a convective ( $M < 2 M_{\odot}$ ) versus radiative ( $M > 2 M_{\odot}$ ) outer zone is concerned. On the other hand, stars develop a convective core between  $1 M_{\odot}$

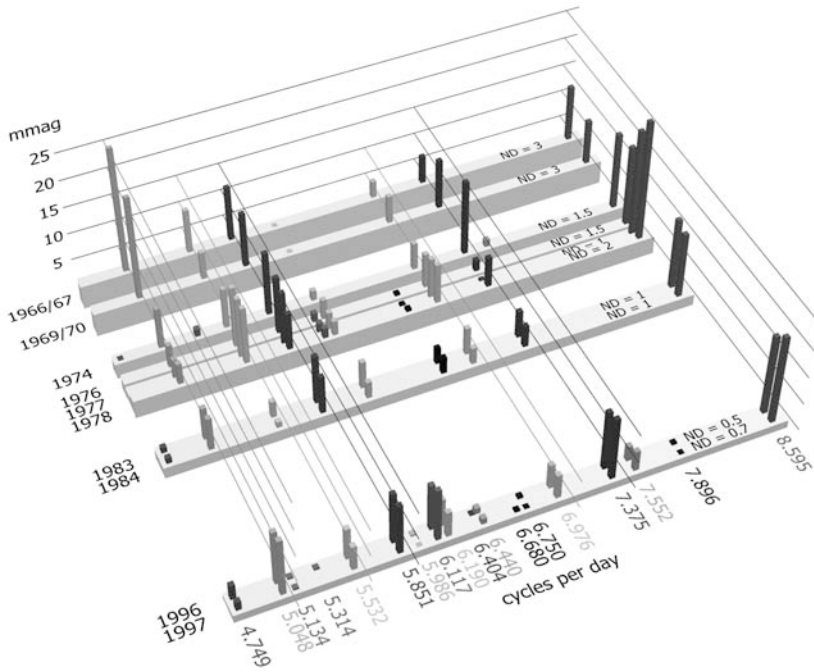


**Fig. 2.10.** Amplitude variability found from season to season in DSN data of the  $\delta$  Sct star 4 CVn. From Breger (2000).

and  $2 M_{\odot}$ . The class of  $\delta$  Sct stars encompasses such transition objects and asteroseismology could in principle fine-tune our knowledge of the detailed physics of these transitions from convective to radiative energy transport and mixing. Dziembowski & Pamyatnykh (1991) pointed out that the sensitivity of particular nonradial oscillation modes to the size of the mixed stellar core could provide a very valuable asteroseismic test of core overshooting in A- and B-type oscillators. At present, this stage is not yet reached for  $\delta$  Sct stars, however. Another outlook for the future is the simultaneous detection of heat driven and stochastically excited acoustic modes. Indeed, Samadi *et al.* (2002) predicted the occurrence of the latter type of oscillations in this area of the HR Diagram. For all these reasons,  $\delta$  Sct stars are the prime targets for CoRoT.

### 2.3.4 SX Phe Stars

The SX Phe stars have variability behaviour which is very similar to the large amplitude  $\delta$  Sct stars known as HADS (see the previous section), but the SX Phe stars are old Population II stars, while the HADS are younger Population I stars. For this reason, the SX Phe stars were proposed as a separate

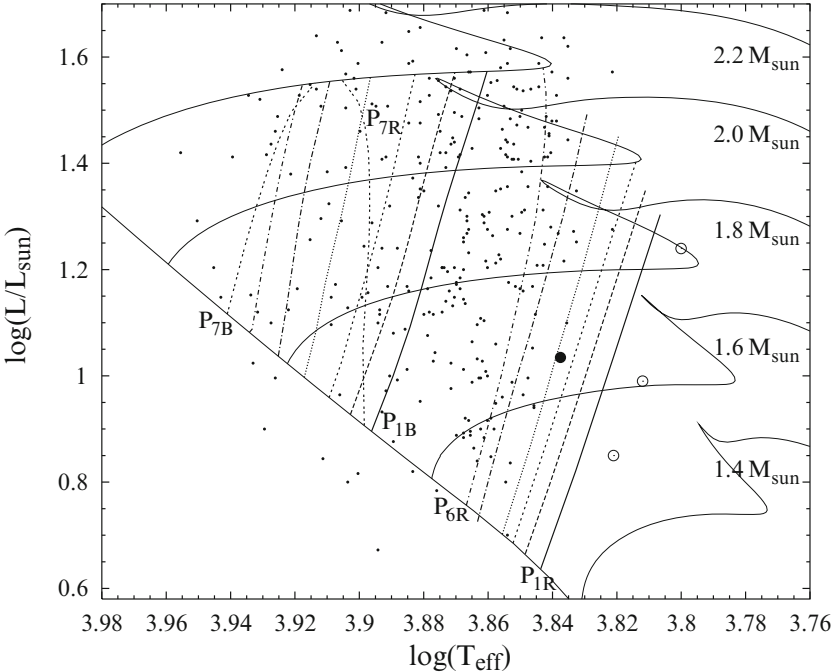


**Fig. 2.11.** Blue and red edges of the instability strip of the  $\delta$  Sct stars obtained by Dupret *et al.* (2005a). The lines are for radial modes  $p_1$  to  $p_7$  taking a mixing length parameter  $\ell_{\text{ML}} = 1.8 H_p$ . The red edge of the radial fundamental mode computed by Houdek (2000, ●) and by Xiong & Deng (2001, ○) are also indicated for comparison. The small dots correspond to all the  $\delta$  Sct stars in the catalogue of Rodríguez *et al.* (2000). The evolution tracks are for the masses indicated and were computed assuming overshoot from the convective core of  $\alpha_{\text{ov}} = 0.2 H_p$ . From Dupret *et al.* (2005a).

class of pulsators by Frolov & Irkaev (1984) and have been regarded as such ever since, even though they only differ from the  $\delta$  Sct stars in metallicity (and are hence not indicated as a separate class in Fig. 1.12). They can be recognized by their high amplitude, low metallicity and large spatial motion. Most of them are members of globular clusters, but some occur in galactic discs.

A part of the light curve of the prototype is shown in Fig. 2.12. This star exhibits variations with two distinct frequencies:  $18.19 \text{ d}^{-1}$  and  $23.39 \text{ d}^{-1}$  and their harmonics, along with sum and beat frequencies (Fig. 2.13 and Kim *et al.* 1993). The SX Phe stars indeed have a bimodal period distribution, which is interpreted in terms of the fundamental and first radial overtone modes being excited. Those pulsating only in the first overtone have nearly symmetrical light curves with peak-to-peak amplitudes less than 0.15 in  $V$ . The fundamen-

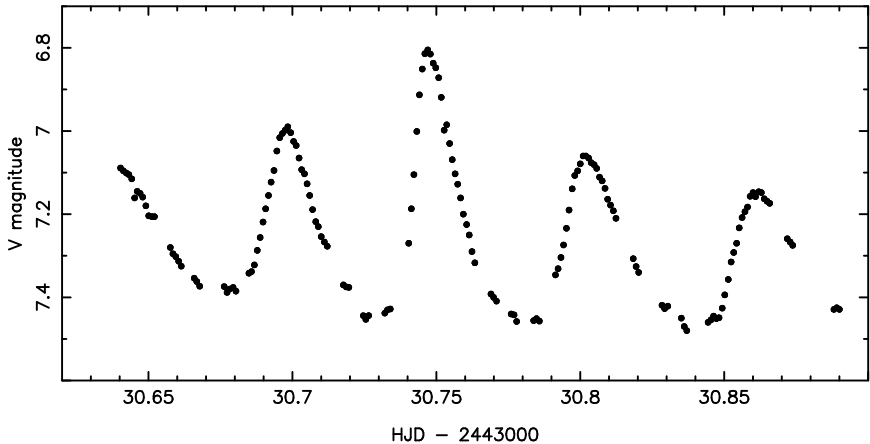


**Fig. 2.12.** Part of the Strömgren  $y$  light curve of SX Phe. Data taken from Kim *et al.* (1993).

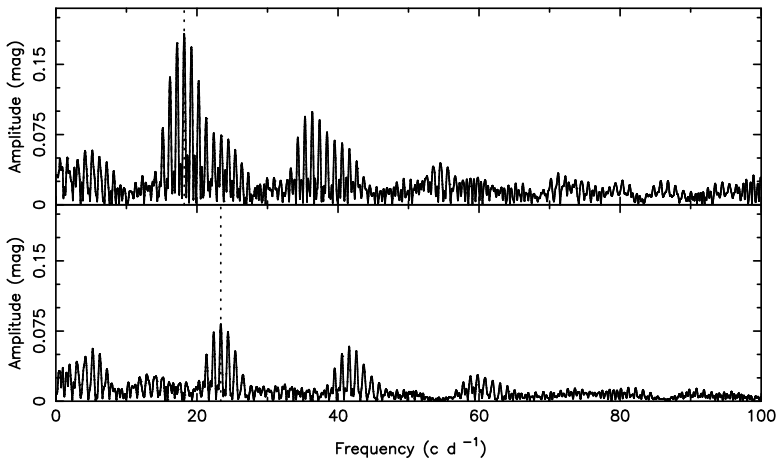


**Fig. 2.13.** Frequency spectrum of SX Phe. The dotted lines indicate the significant frequencies. The bottom panel is for the residuals after prewhitening with  $18.19 \text{ d}^{-1}$  and its two harmonics. Data taken from Kim *et al.* (1993).

tal pulsators, such as SX Phe itself (Fig. 2.12), have amplitudes above 0.15 in  $V$  and asymmetrical light curves. This period separation propagates into two distinct period-luminosity relations with an offset of 0.37 mag, in agreement with theoretical predictions (McNamara 1995).

Rodríguez & López-González (2000) presented the first catalogue of SX Phe stars containing 149 objects in 18 globular clusters of our Galaxy and in the Carina and Sagittarius dwarf galaxies. From the observational characteristics

of all these 149 members they deduced that the metal abundances and mean periods of these stars show that both parameters are correlated in the sense that the periods of the variables are longer as the metallicity is higher.

Olech *et al.* (2005) made a dedicated study of the oscillation spectra of 69 SX Phe stars with very diverse pulsational behaviour, all belonging to the globular cluster  $\omega$  Centauri. The observations are interpreted in terms of multiperiodic oscillations with at least some of the excited modes being nonradial and with the occurrence of rotationally split triplets in some cases. The stellar parameters of the radial mode pulsators are found to be consistent with standard evolutionary models for stars with  $Z$  between 0.002 and 0.0002 and in the mass range 0.9 to  $1.15 M_{\odot}$ , and the observed frequencies are in agreement with predictions for unstable modes.

A significant fraction of the SX Phe stars are believed to be blue stragglers. We come back to this issue in Section 2.8.3.

### 2.3.5 Rapidly Oscillating Ap Stars

Largely within the classical instability strip, close to the main sequence where the  $\delta$  Sct stars are situated, one also encounters the rapidly oscillating Ap (roAp) stars. These are strongly magnetic Population I stars of spectral type A or F with a peculiar (hence Ap, or sometimes Fp<sup>18</sup>) chemical surface composition caused by atomic diffusion. They were discovered by Kurtz (1982), who reported amplitudes up to about 0.01 mag peak-to-peak in blue wavelengths for five class members. The roAp stars, of which there are now about 40 known, have multiperiodic variations which correspond to high order, low degree p modes. Many of the modes show frequency multiplets interpreted as being caused by rotational amplitude modulation of modes with pulsation axes that are aligned with the magnetic fields of the star, hence are oblique to the rotation axes of the stars – the oblique pulsator model (Kurtz 1982). For extensive overviews of the photometric observations and their interpretation see Kurtz (1990) and Kurtz & Martinez (2000). In Fig. 2.14 we show part of the light curve of HD 101065, the first discovered roAp star (Kurtz 1978, 1980; Kurtz & Wegner 1979). Its frequency spectrum is shown in Fig. 2.15 and reveals a principal frequency of 1.37 mHz, corresponding to a period of 12.14 min, with an amplitude of some 6 mmag.

The rapidly oscillating Ap (roAp) stars exhibit many unusual characteristics: strong abundance anomalies – particularly of rare earth elements; strong, global magnetic fields with polar field strengths typically of several kG, but up to 24.5 kG (Hubrig *et al.* 2005; Kurtz *et al.* 2006a); non-uniform abundances – both horizontally (spots) and vertically (stratification); high radial overtone pulsation with periods in the range 5.65 – 21.2 min and amplitudes up

<sup>18</sup> The chemically peculiar stars of the upper main sequence are also classified in subgroups CP1, CP2, CP3, CP4; the roAp stars are in the CP2 subgroup. A complete discussion of the nomenclature of the chemically peculiar stars is given by Kurtz & Martinez (2000).

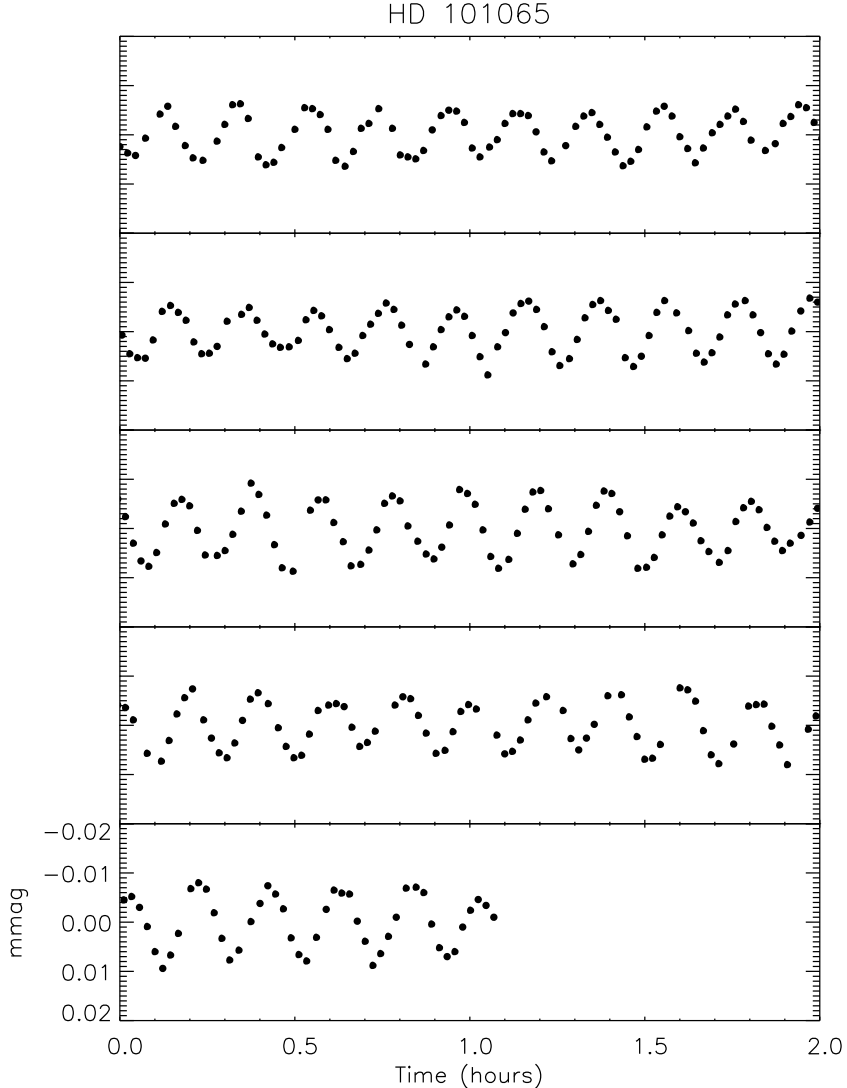


**Fig. 2.14.** Part of the Johnson  $B$  light curve of the roAp star HD 101065. Data taken from Martinez & Kurtz (1990).

to 6 mmag in broad-band photometry and up to  $5000 \text{ m s}^{-1}$  in radial velocity (see, *e.g.*, Elkin *et al.* 2005; Table 1 of Kurtz *et al.* 2006a).

Theoretical interpretation of the pulsations in roAp stars is complex. The modes appear to be more-or-less aligned with the magnetic field. They are low degree,  $\ell \leq 3$ , modes and preferentially dipole (or distorted dipole) modes where this can be determined. Both the large and small asteroseismic separa-

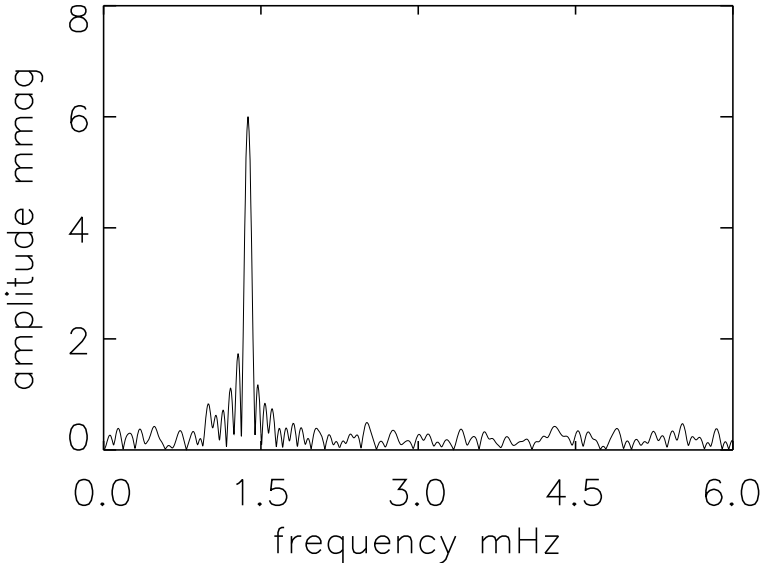


**Fig. 2.15.** Frequency spectrum of the roAp star HD 101065. Data taken from Martinez & Kurtz (1990).

tions are significantly perturbed by the magnetic field and, at least in some cases, by the rotation. The modes are magneto-acoustic – generally, magnetic pressure dominates in the observable atmosphere, although for some models with  $\sim kG$  magnetic fields the magnetic and gas pressure are comparable around  $\tau_{5000} \sim 1$ ; at higher observable levels magnetic pressure dominates in all models (Saio 2005; Sousa & Cunha 2008). Atomic diffusion not only alters the vertical and horizontal abundances, but also the atmospheric temperature structure – manifestations of the latter may be the core-wing anomaly in the hydrogen lines (Cowley *et al.* 2001; Kochukhov *et al.* 2002a) and the wing-nib anomaly in the Ca K line (Cowley *et al.* 2006). The frequencies in many roAp stars exceed the acoustic cut-off frequency of models with standard stellar atmospheres, thus also indicating abnormal atmospheric structure (see, *e.g.*, Cunha 2006; Audard *et al.* 1998). The magnetic field directly alters the eigenfrequencies and eigenfunctions, it indirectly contributes to driving the pulsations by suppression of convection, and its geometry contributes to, or defines, the mode selection. For detailed discussion of the theory of these stars see, *e.g.*, Sousa & Cunha (2008), Cunha (2005, 2006, 2007), Saio (2005), Gough (2005), Saio & Gautschy (2004), Bigot & Dziembowski (2002), Balmforth *et al.* (2001), Cunha & Gough (2000), Bigot *et al.* (2000), Gautschy *et al.* (1998), Dziembowski & Goode (1985, 1996), Takata & Shibahashi (1995), Shibahashi & Takata (1993), Dolez & Gough (1982). For more introduction to the spectroscopic observations see Kurtz *et al.* (2006b). A list of 35 roAp

stars with some photometric and spectroscopic amplitudes is given by Kurtz *et al.* (2006a).

All of these complexities make the roAp stars a challenge to understand, but the rewards for doing so are great. Here are four examples:

1. The kG-strength magnetic fields in sunspots dissipate energy in solar p-modes and shift their phases significantly, as is clearly seen in both observational and theoretical local helioseismology. While it is not possible to perform local asteroseismology in the same detail as for the Sun – for obvious reasons of angular resolution – some unique properties of the roAp stars have the potential to allow 3D mapping of their pulsation modes, magnetic fields geometries and abundance distributions within the observable layers of their atmospheres, hence allow a detailed study of the interaction of the pulsations with the strong magnetic fields, thus providing an environment significantly different to that of the Sun in which to test theories of such interactions.
2. As mentioned above, abundances of many elements and ions are non-uniformly distributed over the stellar surfaces of the roAp stars, and they are also vertically stratified. Both of these are a consequence of atomic diffusion, *i.e.*, radiative levitation and gravitational settling. In some cases overabundances can be up to five orders of magnitude greater than that of the Sun and other (relatively) chemically normal stars. The horizontal non-uniformity allows Doppler Imaging maps to be made of the surface abundance distributions and pulsation geometry (see, *e.g.*, Kochukhov *et al.* 2004a; Kochukhov 2006) and the vertical stratification provides depth information. As yet, the vertical and horizontal components of the abundances and pulsation geometries have not been disentangled, but several groups are actively working on this complex and potentially highly rewarding problem (see Kurtz *et al.* 2006b for a more extended introduction to the subject and references).
3. Fe ranges from slightly overabundant to somewhat depleted in the atmospheres of roAp stars as a consequence of atomic diffusion; lines of Fe I and Fe II typically form around continuum optical depth  $\log \tau_{5000} \sim -0.5$ . The narrow cores of the H $\alpha$  lines are a probable consequence of abnormal  $T - \tau$  that is, as yet, not successfully modelled; these H $\alpha$  line cores form between optical depths  $-4 \leq \log \tau_{5000} \leq -2$  – levels that are well into the chromosphere of the Sun. The first and second ionization states of Nd and Pr and some other rare earth elements form at, or above, optical depths  $\log \tau_{5000} \leq -4$  (see, *e.g.*, Mashonkina *et al.* 2005), as they have been radiatively levitated. Thus by studying lines of different ions, and by studying the line profile variations of individual lines, it is possible to probe the abundance distributions and pulsation behaviour as a function of atmospheric depth in some detail. This in itself has potentially great rewards, since the geometry of the pulsation modes provides new, independent constraints on the stratification of the atmospheres, hence on the

atomic diffusion that gives rise to this. Atomic diffusion is widely applicable in stellar astrophysics; it is an important process that is part of the standard solar model (at least for helium settling and the radiative levitation of a few atomic species), and has to be taken into account in any solution to the current disagreement between helioseismic sound speeds and solar abundances. It is also an important factor in our understanding of pulsational driving in subdwarf B (sdB) stars,  $\beta$  Cep stars, Slowly Pulsating B stars, in the stratification of white dwarf star atmospheres, and of globular cluster ages. In the roAp stars the pulsation amplitudes and phases allow us to specify which ions share horizontal and vertical distributions in the roAp atmospheres. Since these stars show the most extreme evidence of atomic diffusion, they provide the strongest constraints on atomic diffusion theory.

4. Theoretical models (see, *e.g.*, Sousa & Cunha 2008; Cunha 2006; Saio 2005; Saio & Gautschy 2004) indicate that the Alfvén speed and sound speed are comparable at optical depths of the order of 1 for magnetic field strengths of the order of 1 kG; higher in the atmosphere the Alfvén speed exceeds the sound speed significantly. For stronger fields the Alfvén speed exceeds the sound speed throughout the observable atmosphere. Thus the observed modes in roAp stars are magneto-acoustic. The detailed behaviour of the interaction of the pulsation modes with kG-strength magnetic fields can thus be compared with similar interactions of solar p modes and sunspots that have been studied with local helioseismology. Whereas there is a good understanding of the interaction of p modes with sunspots, with basic agreement between theoretical models and observations, the variety of behaviour for the roAp stars is still to be understood. Disentangling the complexities of the line profile variations into their horizontal, vertical, convective and pulsational mode geometry components is highly challenging.

Thus the roAp stars allow an examination of the upper atmospheres of these stars in more detail than is possible for any star but the Sun. From an observational viewpoint, the study of roAp stars has changed drastically over the past few years, with photometric studies being overtaken by the new time resolved, high spectral resolution spectroscopic studies. Clearly, further confrontation between these splendid new data and the oblique pulsator model will be undertaken in the near future. For the asteroseismic study of the global properties of roAp stars, the best frequency sets have been obtained photometrically, the outstanding example being HR 1217 which we discuss in detail in Chapter 7.

### 2.3.6 Slowly Pulsating B Stars

The term *slowly pulsating B stars* (SPB stars) was introduced by Waelkens (1991). With this term he brought attention to a group of seven young Population I variable mid-B stars with spectral type between B3 and B9, for

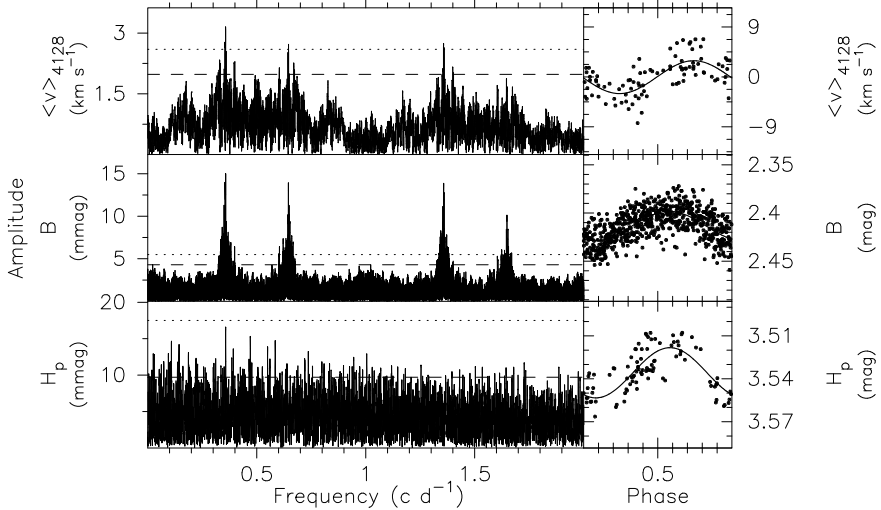


**Fig. 2.16.** The frequency spectra of Geneva  $B$ , Hipparcos, and radial velocity data derived from the Si II 4128 Å line of the single SPB star  $\alpha$ Vel (HD 74195). The horizontal dashed line indicates the 1% false alarm probability and the dotted one the 3.7 S/N ratio level (see Chapter 5). From De Cat & Aerts (2002).

which he had detected multiperiodic brightness and colour variations in photometric data spread over some 10 years. In Figs 2.16 and 2.17, the frequency spectra of the Geneva  $B$  and Hipparcos light, and radial velocity variations of the brightest among the SPB stars,  $\alpha$ Vel (HD 74195), and of a bright SB2 SPB star, HD 123515, are shown. De Cat & Aerts (2002) found respectively four and five independent frequencies for these two SPB stars after subsequent *prewhitening*. This procedure will be defined in detail in Section 5.1.2. In brief, it involves subtracting a fit with a selected frequency from the data, followed by a frequency search for additional frequencies. The intrinsic periods of SPB stars are similar to those of the  $\gamma$ Dor stars except a bit longer because the stars are bigger, *i.e.*, roughly between 0.8 and 3 d. It is therefore extremely difficult to find such variables, as long term planning is needed, just as for the  $\gamma$ Dor stars. This is readily visible in Figs 2.16 and 2.17 where the confusion between frequencies  $f$  and  $1 - f$  is prominent. Only with multisite data, or with uninterrupted data from space, can one avoid such confusion, as shown by the MOST light curve of the SPB star HD 163830 reproduced in Fig. 2.18 (Aerts *et al.* 2006b).

Line profile variable counterparts of SPB stars were known prior to the discovery of the SPB star class by Waelkens (1991). Already in the late 1970s, Myron Smith and his collaborators had done a search for line profile variability in stars surrounding the  $\beta$ Cep stars (see below for a description of this group of pulsating stars). In this way they had discovered spectroscopic variables

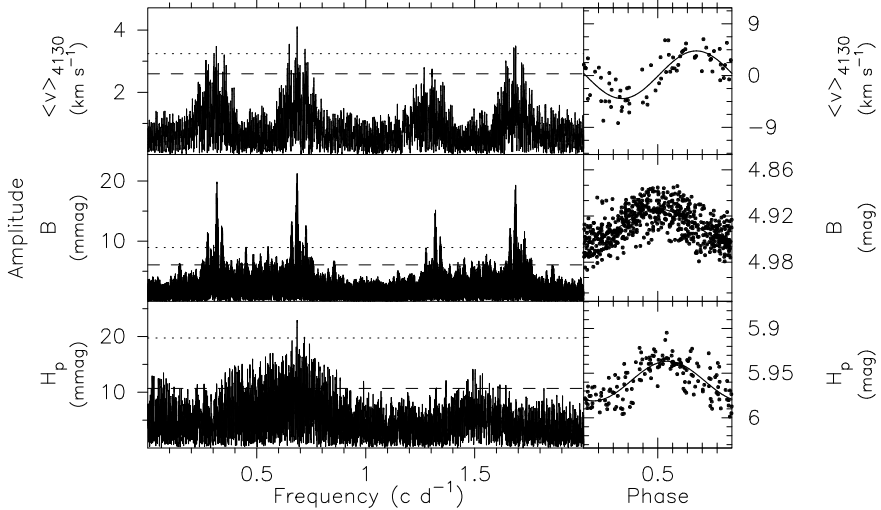


**Fig. 2.17.** The frequency spectra of Geneva  $B$ , Hipparcos, and radial velocity data derived from the Si II 4128 Å line of the SB2 SPB HD 123515. The horizontal dashed line indicates the 1% false alarm probability and the dotted one the 3.7 S/N ratio level (see Chapter 5). From De Cat & Aerts (2002).

with spectral types between O9 and B5. Smith termed them 53 Per stars after his prototypical target. It has meanwhile become clear that the coolest among Smith's variables are SPB stars, but the explanation for the hotter stars in Smith's list is different. Indeed, the hottest among the 53 Per stars have p mode oscillations like the  $\beta$  Cep stars rather than high order g modes. For this reason, the term SPB stars was finally chosen to indicate a class of stars with common pulsational properties in terms of g modes and one well-understood excitation mechanism, in contrast to the group of Smith's 53 Per stars. The masses of SPB stars range from 2 to  $7 M_{\odot}$ , whereas some of the 53 Per stars have masses as high as  $20 M_{\odot}$ .

As already emphasized, the Hipparcos mission led to a tenfold increase in the number of class members; huge long term multicolour photometric and high resolution spectroscopic follow-up campaigns were undertaken following this discovery (Aerts *et al.* 1999; Mathias *et al.* 2001). Those led to accurate frequency values and empirical mode identification for some selected targets (De Cat & Aerts 2002; De Cat *et al.* 2005) which are in excellent agreement with theoretical predictions of excited (mainly)  $l = 1$  modes (Townsend 2005a). All confirmed SPB stars are slow rotators (De Cat 2002).

As shown by Dziembowski *et al.* (1993) and Gautschy & Saio (1993), the explanation for the multiperiodic variations of SPB stars is the excitation of high order g modes by the heat mechanism, associated with an opacity enhancement due to iron-group elements, also termed the *Z bump*. These

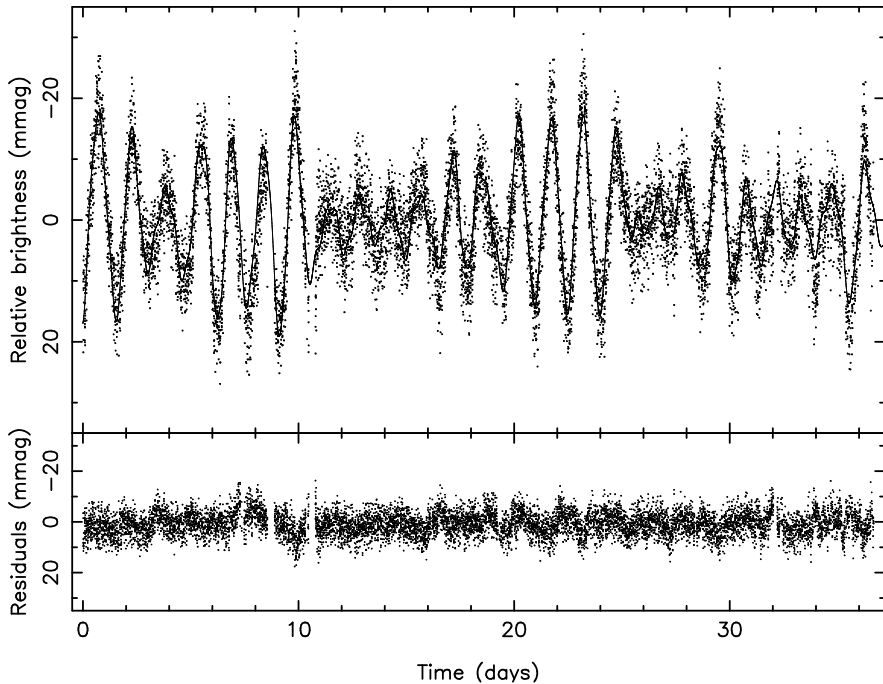


**Fig. 2.18.** The MOST light curve of the SPB HD 163830 (upper panel, dots) and the best fit based on the 21 significant frequencies (upper panel, full line). The residuals after subtraction of the fit are shown in the lower panel. From Aerts *et al.* (2006b).

features occur at a temperature near 200 000 K. This explanation for mode excitation in B stars, both for SPB stars and for  $\beta$  Cep stars (see below), had to await sufficiently accurate opacity computations of elements heavier than hydrogen and helium, such as those provided by Iglesias & Rogers (1996) in the OPAL<sup>19</sup> opacity project at Livermore, and Seaton (1996) in the Opacity Project, OP<sup>20</sup>. Accurate opacity tables for elements heavier than hydrogen and helium have only been available since the OPAL and OP projects were completed in 1992. Any previous opacity determinations for such elements were typically a factor three too low and so did not lead to mode excitation in B stars. The new opacity projects led to a natural explanation of the modes in SPB stars and in  $\beta$  Cep stars in terms of the heat mechanism at the position where the opacity bump occurs. We refer again to Pamyatnykh (1999) for a general overview of the properties of models with excited modes and their dependence on metallicity and core overshoot.

<sup>19</sup> <http://www-phys.llnl.gov/Research/OPAL/opal.html>.

<sup>20</sup> <http://vizier.u-strasbg.fr/topbase/op.html>.

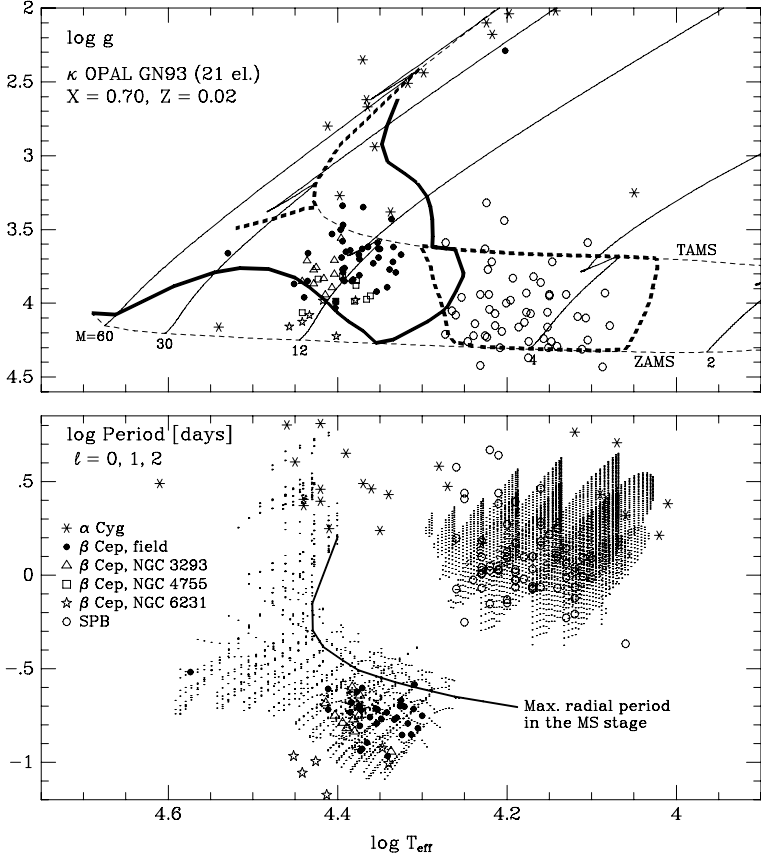


**Fig. 2.19.** The theoretical instability domains predicted by the heat mechanism for B stars of metal abundance  $Z = 0.02$  (thick lines, upper panel). The lower panel shows the oscillation periods as a function of effective temperature, pointing out the clear separation between the low order p modes in the  $\beta$  Cep stars and the high order g modes in the SPB stars. From Pamyatnykh (1999).

The agreement between theoretical predictions and observations is excellent in a statistical sense. The known SPB stars indeed lie entirely within and populate fully the computed theoretical instability strip. As parallaxes for isolated field B stars are very uncertain, one is not able to provide accurate luminosities, which is the reason why in many seismic studies the model computations are represented in a  $(\log T_{\text{eff}}, \log g)$  diagram as in Fig. 2.19.

During the last half century, there has been significant confusion and debate in the literature about the existence of a specific group of variables with spectral types between B7V–III and A2V–II and periods between 2 and 8 h, baptised *Maia stars* by Struve (1955). At the time when Struve (1955) made

his suggestion, SPB stars were still unknown. These hypothetical stars would be partly situated within the SPB instability strip, extending towards the  $\delta$  Sct strip. There are no oscillations predicted by the classical heat mechanism in this part of the HR Diagram (Pamyatnykh 1999) and indeed, despite large search campaigns (see, *e.g.*, Scholz *et al.* 1998 and references therein) unambiguous detection of short period variability was achieved for only four out of fifteen stars. Each of these four has high rotational velocity (Aerts & Kolenberg 2005). In such a situation, the effects of the Coriolis force introduce significant frequency shifts for the low frequency g modes (Townsend 2003a,b) so that shorter periods must indeed be observed in an inertial frame. Such shifts may offer the correct explanation for the relatively high observed frequencies in these four stars. Another suggestion was made independently and almost simultaneously by Savonije (2005) and Townsend (2005b), who found heat driven retrograde mixed mode instability in B stars for spectral types B4 to A0 rotating faster than half of the critical rate. Both these interpretations lead to the conclusion that the Maia stars are rapidly rotating SPB stars.

### 2.3.7 $\beta$ Cep Stars

The  $\beta$  Cep stars have been known as a group of young Population I near-main-sequence pulsating stars for more than a century. They have masses between 8 and about  $18 M_{\odot}$  and oscillate in low order p and g modes with periods between about 2 and 8 h. More than 100 members of this group are known and the class contains dwarfs up to giants. An overview of the properties of the class was provided by Stankov & Handler (2005). Most of the  $\beta$  Cep stars show multiperiodic light and line profile variations. Excluding the four stars BW Vul,  $\xi^1$  CMa, V1449 Aql, and  $\sigma$  Sco, which have exceptionally large velocity and/or light amplitudes, the phase diagrams for individual frequencies are nearly sinusoidal. The light variations clearly have larger amplitudes at blue than at red wavelengths and have a phase difference of about 0.25 with the radial velocity variations. Such a phase lag is expected for adiabatic oscillations (Dupret *et al.* 2003). As for the SPB stars, the majority of the  $\beta$  Cep stars rotate at only a small fraction of their critical velocity, two of the exceptions being 19 Mon (Balona *et al.* 2002) and SY Equ (Aerts *et al.* 2006) whose rotational velocities approach half of their critical value.

Until 2002, these stars were mainly observed during single site photometric campaigns lasting typically one or two weeks. Some stars were monitored during different seasons, most often, unfortunately, with large gaps of several years in the data. An example is the star HD 129929 that was monitored during 21 years in 3-week campaigns from La Silla with one and the same high precision photometer attached to the 0.70-m Swiss telescope (Aerts *et al.* 2003). This led to the detection of six independent oscillation modes, which was at that time the largest number of excited frequencies known in such type of star. The star 12 Lac was also known to have six oscillation modes from much earlier photometry (Jerzykiewicz 1978), and these modes turned out

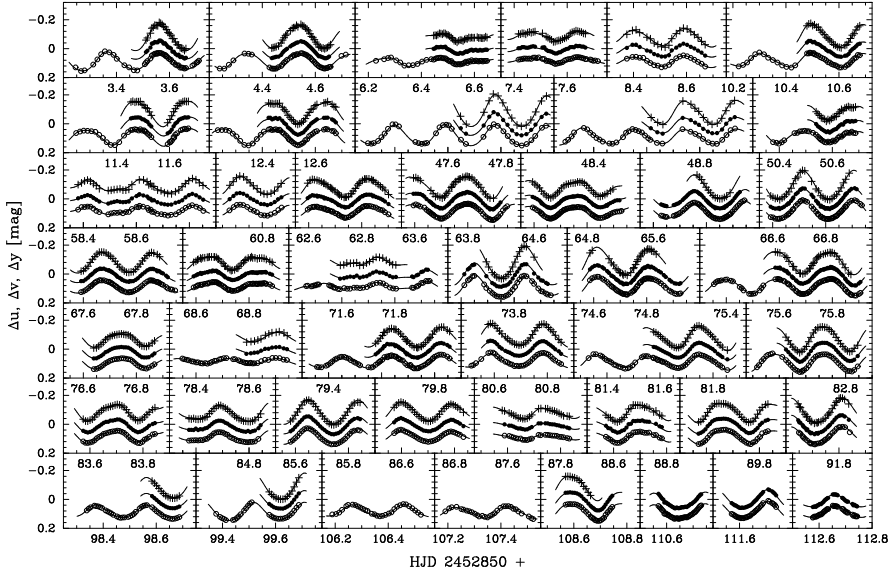


**Fig. 2.20.** Strömgren photometry of the  $\beta$  Cep star 12 Lac from a multisite campaign. From Handler *et al.* (2006).

to have very stable amplitudes during many years as they were recovered in high resolution spectroscopy more than a decade later (Mathias *et al.* 1994a). Starting from the early 1990s, the  $\beta$  Cep stars were indeed also extensively studied from high resolution spectroscopy (Aerts & De Cat 2003 and references therein).

A new era in  $\beta$  Cep star research was initiated after the international pulsation conference held at Leuven university (Aerts *et al.* 2002a), where Mike Jerzykiewicz suggested the consideration of this type of star for multisite observing campaigns similar to those performed for the  $\delta$  Sct stars. Handler & Aerts (2004) set up the largest such campaign ever performed for the star  $\nu$  Eri, including not only multi-colour photometry but also simultaneous high resolution spectroscopy during five months. This very rich dataset implied a significant step forward in the detection and interpretation of oscillation modes of a  $\beta$  Cep star. In particular, it led to the conclusion that not only low-order g modes are present in those stars, but also high-order g modes. We report on the seismic modelling of  $\nu$  Eri in Chapter 7. A subsequent campaign was carried out by Handler *et al.* (2006) on the star 12 Lac. Several additional modes, besides the six already detected by Jerzykiewicz (1978) and Mathias *et al.* (1994a), were discovered, among which a high-order g mode, just as for  $\nu$  Eri. A part of the light curve of the campaign is shown in Fig. 2.20 and the frequency spectrum in Fig. 2.21. While aliasing still occurs, this figure illustrates the gain of multisite versus single site data. A simultaneous spectroscopic multisite

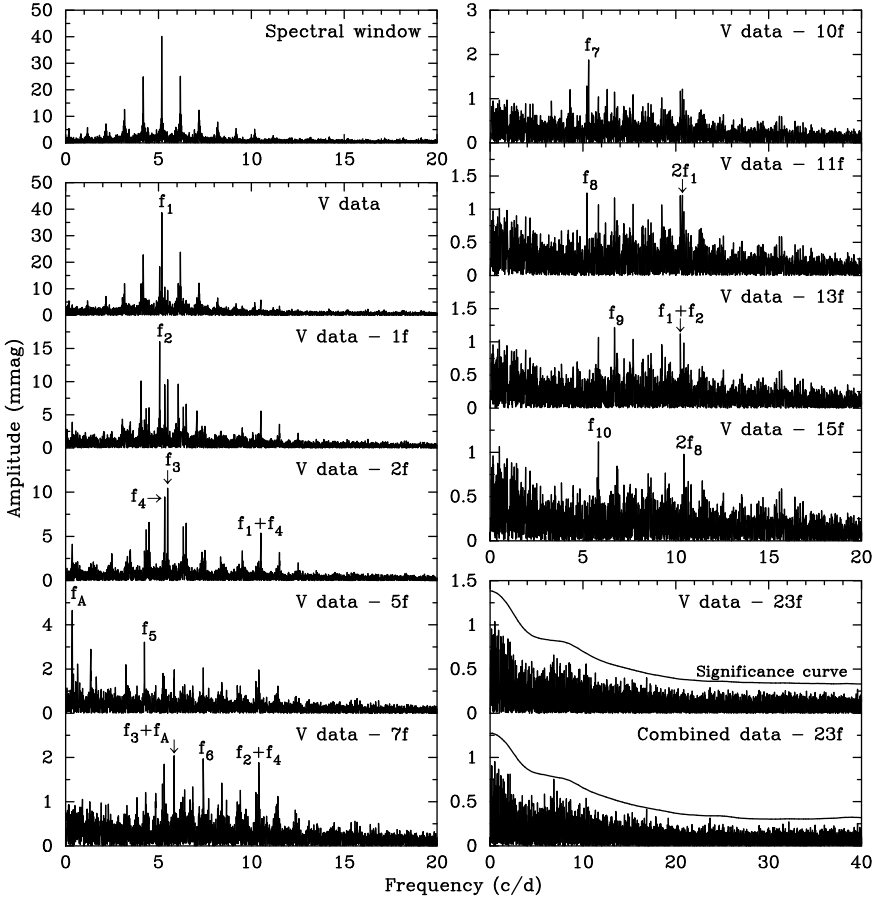


**Fig. 2.21.** Frequency spectrum of the data for 12 Lac, some of which is shown in Fig. 2.20. From Handler *et al.* (2006).

campaign led to the confirmation of ten of the independent frequencies already detected in the photometry. In particular, the SPB-like g-mode frequency of  $0.3428\text{ d}^{-1}$  was detected in the spectroscopy as well (Desmet *et al.* 2009).

The nonradial oscillations in the  $\beta$  Cep stars are caused by the heat mechanism acting through opacity features associated with elements of the iron group (Dziembowski & Pamyatnykh 1993), as discussed already for the SPB stars. The short periods of several hours are generally well explained in terms of heat driven low order p modes, but we stress that low order g modes are also simultaneously excited and observed in several class members. There is a small overlap in the theoretical instability strips of the SPB stars and  $\beta$  Cep stars but no hybrid pulsators have been found yet in that area (see Fig. 2.19). On the other hand, the presence of both high-order g modes and low-order p

modes is established for a few hotter  $\beta$  Cep stars, among which is  $\nu$  Eri (see Chapter 7). For this best studied star, the most recent seismic models still do not predict all the observed modes to be excited (Dziembowski & Pamyatnykh 2008). The extensive multisite campaign of  $\nu$  Eri thus made it clear that not all the details of the mode excitation mechanism are well understood. Bourge *et al.* (2006) have shown that atomic diffusive processes, which have been ignored so far in such hot stars, may in fact enhance significantly the amount of iron in the driving region. Their computations followed the earlier suggestions by Pamyatnykh *et al.* (2004) and by Ausseloo *et al.* (2004) that an iron abundance higher by a factor four in the driving zone, or in the star as a whole, is necessary to solve  $\nu$  Eri's excitation problem.

As can be seen in Fig. 2.19, the agreement between observed  $\beta$  Cep stars and the theoretical instability strip is very satisfactory for the class as a whole, although the blue part of the strip is not well populated. Numerous new candidate members were found from large scale surveys, in the LMC and SMC as well as in our own Galaxy (Pigulski 2005; Kołaczkowski *et al.* 2005, 2006; Narwid *et al.* 2006; Sarro *et al.* 2009). Assuming that all these faint variable stars are indeed  $\beta$  Cep this more than doubles the number of class members to over 200. The occurrence of so many  $\beta$  Cep stars in environments with very low metallicity demanded a new look at the mode excitation, which relies heavily on the iron opacity. Miglio *et al.* (2007) have shown these results at the metallicity of the LMC to be fully compatible with excitation predictions based on the OP opacities and the solar abundances by Asplund *et al.* (2005).

We describe the current status of  $\beta$  Cep star seismology by means of some case studies in Chapter 7.

### 2.3.8 Pulsating Be Stars

Be stars are Population I B stars close to the main sequence that show, or have shown in the past, Balmer line emission in their photospheric spectrum. This excess is attributed to the presence of a circumstellar equatorial disc. See the review on Be stars by Porter & Rivinius (2003) for general information on this rather inhomogeneous class of stars. Several different physical mechanisms are thought to be responsible for the disc. Numerous Be stars are members of close binary systems of very different kinds. Roche lobe overflow or mass transfer in general may cause the disc in such cases. For single Be stars, rotation close to the critical velocity (Townsend *et al.* 2004), in addition to either multimode beating of oscillation modes (Rivinius *et al.* 2003) or mass loss along magnetic field lines (Townsend & Owocki 2005) could explain the disc. However, while magnetic fields (Neiner 2007) and nonradial oscillations (Rivinius *et al.* 2003) have been detected in some Be stars, it is not at all clear if these mechanisms suffice to explain a disc for the whole class of single Be stars. Also, it is at present unclear whether the occurrence of a disc around single Be stars can be attributed to a particular evolutionary state or not. The nature and evolution

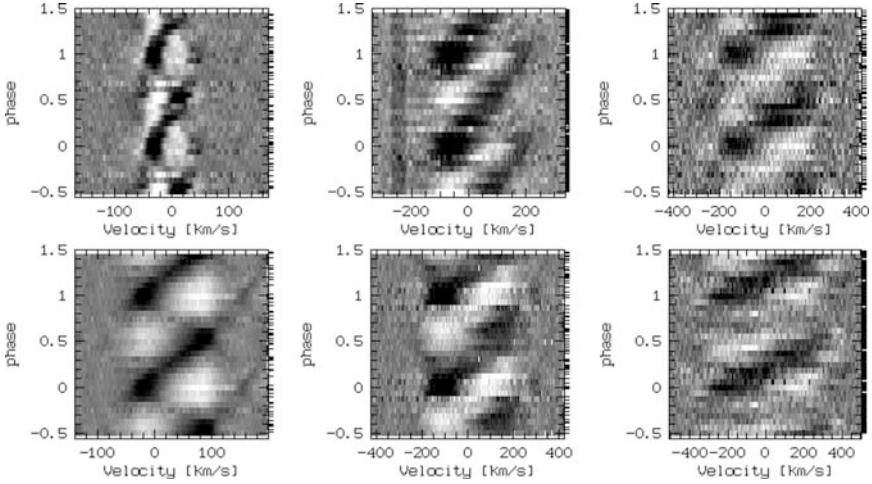


**Fig. 2.22.** Line profile variations in Be stars, with increasing  $v \sin i$  for FW CMa (top left,  $v \sin i = 40 \text{ km s}^{-1}$ ),  $\omega$  CMa (bottom left,  $v \sin i = 100 \text{ km s}^{-1}$ ),  $\mu$  Cen (top middle,  $v \sin i = 155 \text{ km s}^{-1}$ ), DX Eri (bottom middle,  $v \sin i = 180 \text{ km s}^{-1}$ ),  $\alpha$  Eri (top right,  $v \sin i = 225 \text{ km s}^{-1}$ ),  $\eta$  Cen (bottom right,  $v \sin i = 350 \text{ km s}^{-1}$ ). Data taken from Rivinius *et al.* (2003).

of discs around hot stars was summarized in the proceedings by Ignace & Gayley (2005) and by Okazaki *et al.* (2007).

Single Be stars show variability on very different time scales and with a broad range of amplitudes. Balona (1995a) studied a subclass of the Be stars which show one dominant period between 0.5 and 2 d in their photometric variability, with amplitudes of a few tens of mmag which he termed the  $\lambda$  Eri variables. He provided extensive evidence of a clear correlation between the photometric period and the rotational period of the  $\lambda$  Eri stars and interpreted that correlation in terms of rotational modulation. When observed spectroscopically, several of the  $\lambda$  Eri stars turn out to have complex line profile variations with travelling sub-features similar to those observed in the rapidly rotating  $\beta$  Cep stars, except for the much longer periods (days versus hours). This suggests oscillations as origin of this complex spectroscopic variability.

The first claim of nonradial oscillations in a Be star dates back to 1982, when Baade (1982a,b) discovered complex line profile variations for the star  $\omega$  CMa, a star listed among the  $\lambda$  Eri variables in Balona's (1995a) list. The picture became even more complicated when Balona (1995b) introduced the class of  $\zeta$  Oph variables. These are late-O type stars with clear complex multiperiodic line profile variations that he attributed to high degree nonradial oscillations. They are named after the prototypical O9.5V star  $\zeta$  Oph, whose rotation is very close to critical and whose photometric variability was firmly established by the MOST space mission. Walker *et al.* (2005a) disentangled

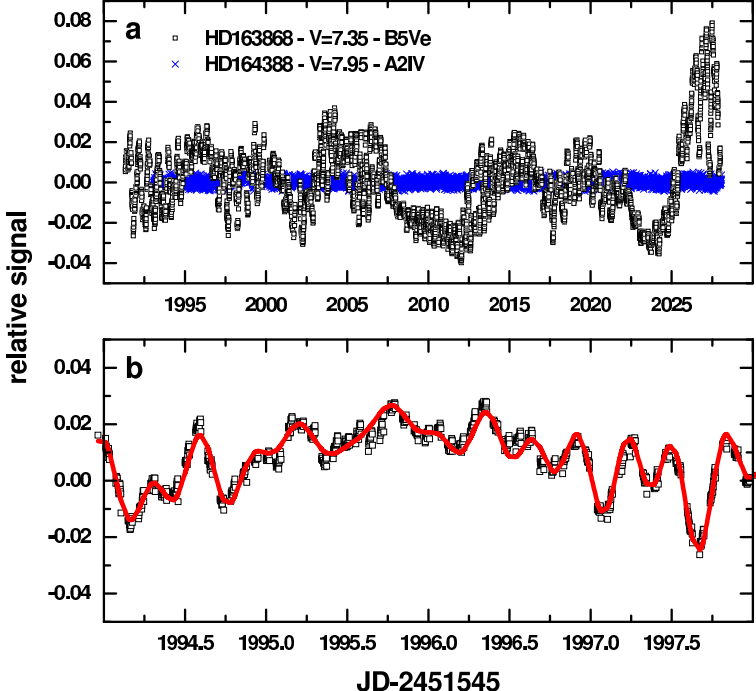


**Fig. 2.23.** Space photometric light curve of the Be star HD 163868 observed by the MOST satellite. The lower panel shows a higher time resolution look at a 5-d portion of the light curve. From Walker *et al.* (2005b).

a dozen significant oscillation frequencies in the 24-d photometric light curve assembled from space. These frequencies range from  $1$  to  $10\text{ d}^{-1}$  and clearly indicate the star's relationship to the  $\beta$  Cep stars.

An extensive summary of the detection of short period line profile variations due to oscillations in hot Be stars was provided by Rivinius *et al.* (2003). They monitored 27 early-type Be stars spectroscopically during six years and found 25 of them to be line profile variables at some level. Some of their data are shown in grey scale plots in Fig. 2.22. For several of their targets the variability was interpreted in terms of nonradial oscillations with  $l = m = +2$ . Almost all stars in the sample also show traces of outburst-like variability rather than a steady star-to-disc mass transfer. The authors interpreted the disc formation in terms of multimode beating in combination with fast rotation.

To make the picture complete, multiperiodic oscillations were reported in the rapidly rotating B5Ve star HD 163868 from a 37-d MOST light curve (see Figs 2.23 and 2.24). Walker *et al.* (2005b) derived a rich frequency spectrum, with more than 60 significant peaks, resembling that of an SPB star and

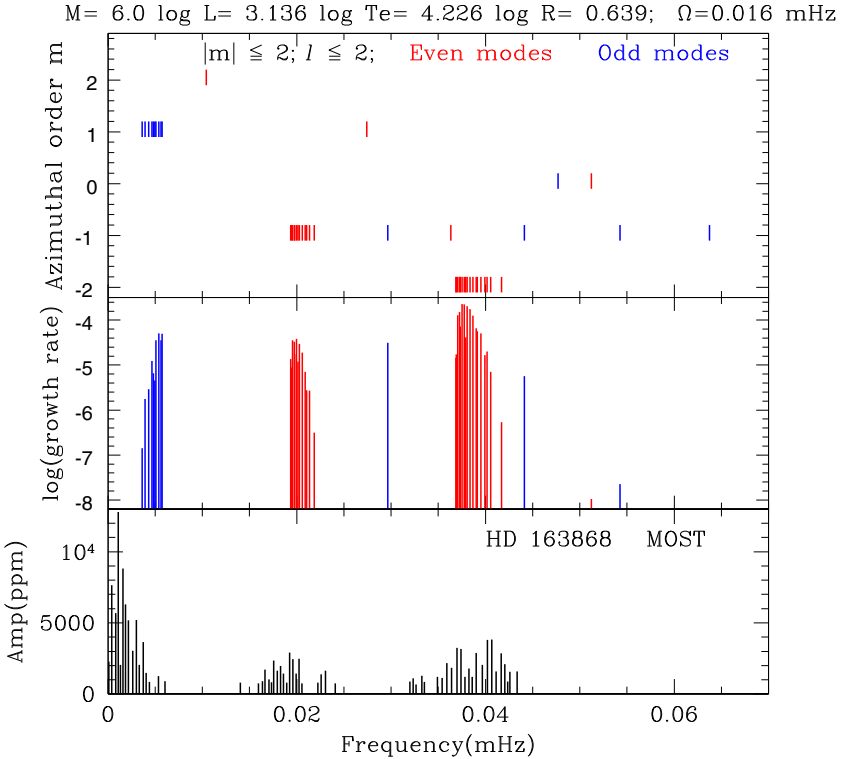


**Fig. 2.24.** Model frequency spectrum resembling the observed one for the Be star HD 163868. From Walker *et al.* (2005b).

termed the star an SPBe star in view of its Be nature. They interpreted the oscillation periods between 7 and 14 h as high order prograde sectoral g modes in the traditional approximation (which will be explained in Chapter 3) and those of several days as Rossby modes (*e.g.*, Townsend 2005b for a description of such modes). Finally, nonradial oscillations at low amplitude were also detected in the bright B8Ve star  $\beta$  CMi, again from the MOST mission (Saio *et al.* 2007).

We come to the conclusion that the oscillations detected in Be stars show a multitude of different behaviour, which is in full accordance with those of  $\beta$  Cep stars and SPB stars (which is why they have not been indicated separately on Fig. 1.12). It seems that pulsating Be stars are complicated analogues of  $\beta$  Cep stars and SPB stars rotating typically above half of the critical velocity, and with some rotating very close to critical velocity. The results from MOST and from time-resolved spectroscopy leave no doubt that many Be stars, across the entire spectral type B range, are nonradial pulsators. Be stars are among the prime targets of CoRoT and these space data will

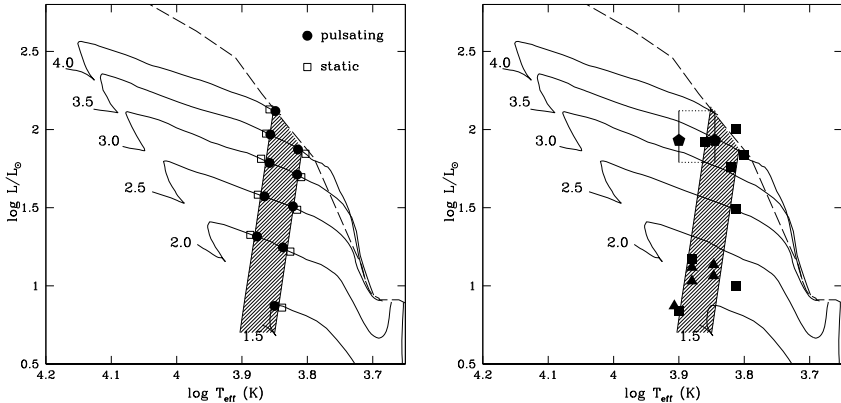


**Fig. 2.25.** Left: location of the instability strip of the pre-main-sequence stars. Right: candidate pre-main-sequence pulsators known as of 1998. Triangles: UX Ori stars from Natta *et al.* (1997), squares: Herbig Ae/Be stars from Berrilli *et al.* (1992) and van den Anker *et al.* (1998), the error box is for HD 144668 (HR 5999: Kurtz & Marang 1995). From Marconi & Palla (1998).

undoubtedly reveal details of Be star oscillations as well as shed new light on the role of oscillations in the disc formation.

## 2.4 Oscillations in Pre-Main-Sequence Stars

As newly born protostars contract towards the main sequence, either radiatively as the Herbig Ae/Be stars or convectively as the T Tauri stars, the higher mass stars enter or cross the classical instability strip. Such pre-main-sequence stars tend to be highly variable, both in photometry and spectroscopy, on time scales of minutes to years. Part of this variability is certainly due to activity and interaction with the circumstellar environment. On the other hand, part of the shorter period variability may be due to oscillations. Since the interior structure of pre-main-sequence stars is different from that of evolved stars in the instability strip, their oscillation spectra may allow us to distinguish between the two evolutionary stages for stars with the same effective temperature and luminosity.

Breger (1972) found the first two candidate pre-main-sequence  $\delta$  Sct pulsators, while monitoring the young open cluster NGC 2264 photometrically. He also found 25% of the member stars of this cluster to be short period variables and unravelled a clear correlation between the variability and shell characteristics. Some time later, Baade & Stahl (1989a,b) detected nonradial oscillations in two pre-main-sequence stars based on high resolution spectroscopy. They found line profile variability, but were unable to pinpoint clear

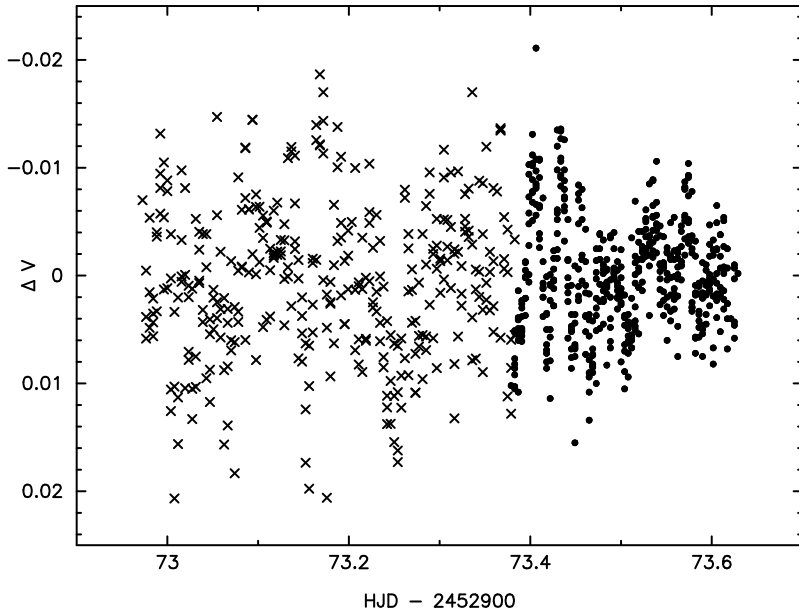


**Fig. 2.26.** Part of the multisite campaign data obtained in 2003 by Ripepi *et al.* (2006b) for the pre-main-sequence star IP Per.  $\Delta V$  stands for  $V_{\text{IP Per}} - V_{\text{comp}}$ . Crosses and dots indicate data from two different sites.

periodicities from them. Kurtz & Marang (1995) made the next step and disentangled the low amplitude (6 mmag)  $\delta$  Sct pulsation with the first clear oscillation period of about 5 h from the long term, large amplitude (0.35 mag) variations caused by variable dust obscuration in the disc of the Herbig Ae star HD 144668 (HR 5999).

Marconi & Palla (1998) investigated the pulsational properties of pre-main-sequence stars with masses in the range 1 to  $4 M_{\odot}$  by means of linear and nonlinear calculations and defined the instability strip for these stars in the HR Diagram (see Fig. 2.25). They found periods ranging from 1.5 to 7.5 h for the fundamental mode. Delta Sct type oscillations have been suggested in about thirty pre-main-sequence stars so far. The reported periods are very uncertain, and range from less than one hour to several hours, in agreement with theoretical predictions. For reviews on this topic see Catala (2003), Marconi & Palla (2004), Zwintz *et al.* (2004) and Ripepi *et al.* (2006a).

The most extensive ground-based dataset and interpretation of a pre-main-sequence  $\delta$  Sct pulsator was achieved by Ripepi *et al.* (2006b, see Figs 2.26 and 2.27). They monitored the star IP Per photometrically in a multisite campaign involving ten sites. The total time span of their data is about 500 d. IP Per is a low metallicity UX Ori type star, which is a class of precursors of the Herbig Ae/Be stars surrounded by self-shadowed discs (see Herbst & Shevchenko 1999

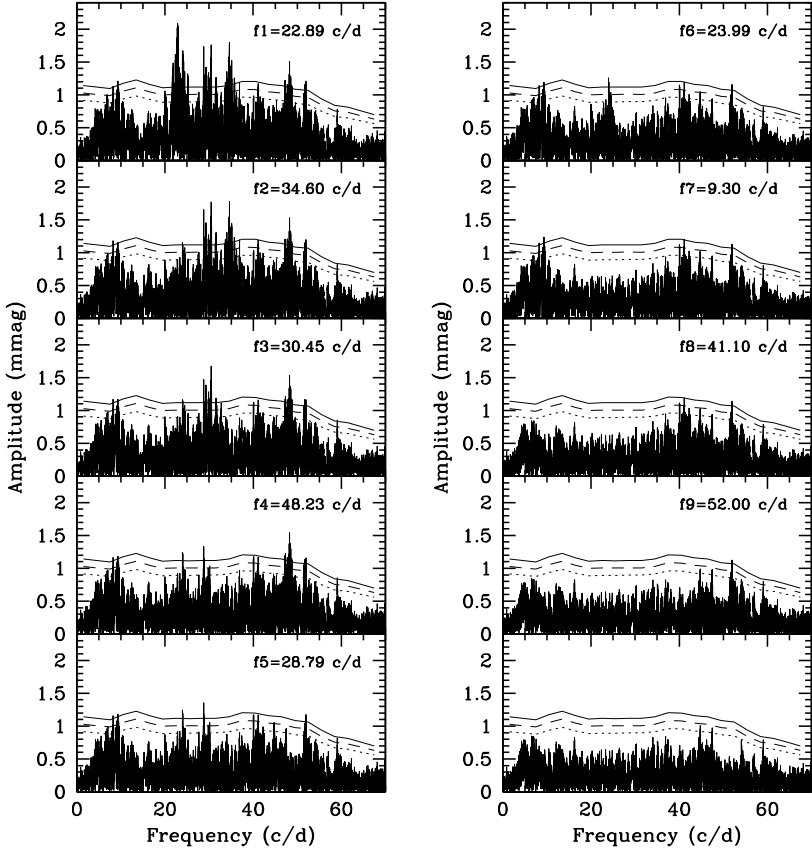


**Fig. 2.27.** Frequency spectra for the  $V$  data of IP Per of which some were shown in Fig. 2.26. The full, dashed and dotted lines indicate the 99.9%, 99% and 90% significance levels, respectively. From Ripepi *et al.* (2006b).

for a photometric catalogue and Dullemond *et al.* 2003 for a physical model). It has long term variations with an amplitude of about 0.3 mag and a duration between 10 and 50 d onto which the oscillatory variability is superposed. The authors found nine frequencies for the star, ranging from  $23$  to  $52 \text{ d}^{-1}$ , and with an amplitude range from 1.1 to 3.3 mmag (see Fig. 2.27). A fit of theoretical frequencies to the observed ones indicates that at most five of the modes can be radial; thus nonradial modes occur as well. The frequency matching of the five radial modes led to an accurate mass, luminosity and temperature estimate of the star, in agreement with previous spectroscopic derivations. Unfortunately, the frequencies alone did not allow a discrimination between a pre- and post-main sequence star.

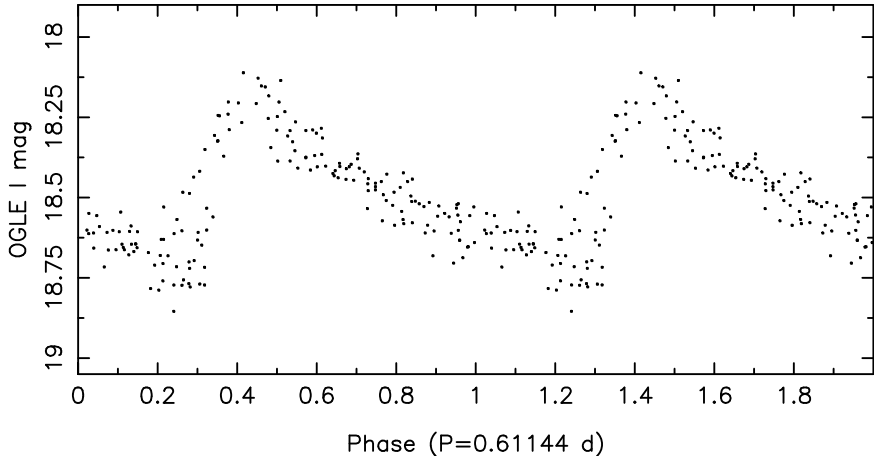


**Fig. 2.28.** Light curve of an RRab star observed by OGLE folded according to the dominant oscillation period. Data taken from Soszyński *et al.* (2003).

## 2.5 Pulsations in Evolved Stars with $M \leq 9 M_{\odot}$

By evolved low mass stars we mean objects with an initial mass below  $9 M_{\odot}$ , which have evolved off the main sequence. These stars may, at a certain phase in their life, start a burning cycle in degenerate matter in their core. This is surely the case for stars with a mass below  $2.3 M_{\odot}$ . They will undergo a helium flash at the tip of the red giant branch. The more massive among the low mass stars avoid ignition in a degenerate core. In any case, all of these stars are candidate oscillators during their post-main sequence evolution. As discussed in Section 2.3.1, solar-like oscillations are found in subgiant stars in the hydrogen shell burning phase which for stars of mass below around  $1.7 M_{\odot}$  is relatively slow. However, only more massive stars cross the instability strips for heat driven oscillations during this phase, and for such stars the phase is fast and the probability of catching a star before central helium burning is small. In the present section we therefore consider only the phases after central helium burning has started.

### 2.5.1 RR Lyrae Stars

Together with the Cepheids (see below), RR Lyrae stars are considered to be the *classical radial pulsators*. Most of them are monoperiodic stars with an oscillation period near half a day. While their monoperiodicity implies that they are not suitable for seismic studies, they are of great galactic and cosmological importance and we highlight some of their properties for this reason. See the monograph by Smith (1995) for more detailed information

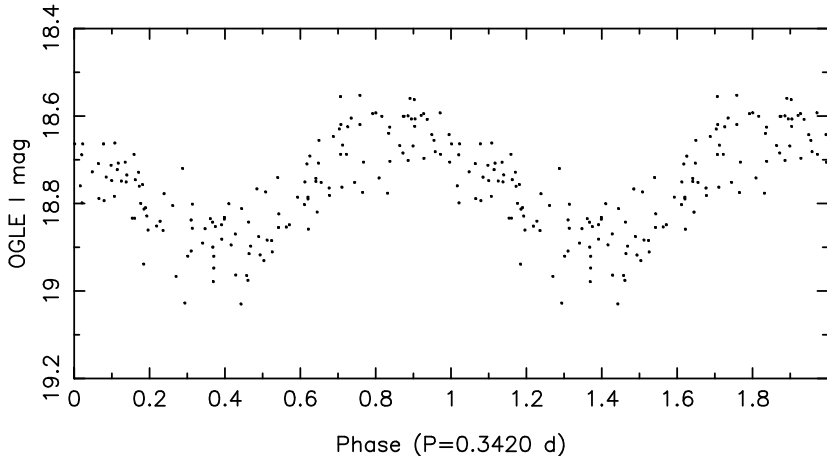


**Fig. 2.29.** Light curve of an RRc star observed by OGLE folded according to the dominant oscillation period. Data taken from Soszyński *et al.* (2003).

on their observational characteristics and to Catelan (2007) for an extensive overview of horizontal branch stars in general.

The first RR Lyrae stars were discovered in globular clusters by Bailey in 1895. Their spherical spatial distribution and kinematic properties (high velocities in all directions) imply that these stars must be extreme Population II stars. As they are low mass stars, their observed abundances are, to a good approximation, those at their birth, *i.e.*, those of the interstellar cloud from which they were born. The abundances of elements heavier than hydrogen and helium,  $Z$ , ranges from 0.0001 to 0.01. RR Lyrae stars are also used to estimate the distance and the age of the clusters they belong to. For these reasons, they are considered to be standard candles of galactic evolution.

All stars with birth masses between  $\simeq 0.5$  and  $\simeq 2.2 M_{\odot}$  start helium burning in a degenerate helium core and undergo a helium flash, after which they settle on the horizontal branch. The stars with the thickest hydrogen envelope are at the red end of the branch and those with the thinnest at the blue end. The higher the envelope mass, the more the hydrogen shell contributes to the energy production and the larger the extent of the convective zone in the envelope. Blue horizontal branch stars have thin envelopes, weak hydrogen burning shells and develop a radiative outer zone (see Prialnik 2000). As a consequence, the hydrogen envelope needs to have a particular mass to result in oscillations driven by the heat mechanism, which requires a radiative zone. It turns out that horizontal branch stars with masses between  $\simeq 0.60$  and  $0.80 M_{\odot}$  have the appropriate regions of hydrogen and helium ionization zones to become RR Lyrae stars (*e.g.*, de Santis & Cassisi 1999), the precise mass limits depending on the metallicity and on the mass lost on the giant branch. RR Lyrae stars have either settled immediately on the horizontal

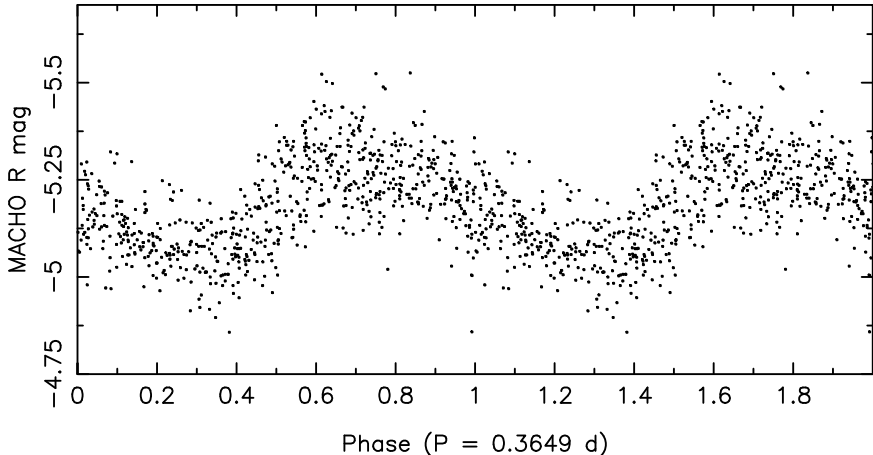


**Fig. 2.30.** Light curve of an RRd star observed by MACHO folded according to the dominant oscillation period. Data taken from Kovács (2000).

branch within the instability strip after the helium flash, or they crossed the strip while evolving on the horizontal branch. The excitation mechanism of the RR Lyrae stars is well-known as the heat mechanism acting in the partial ionization zone of He II – He III (see, *e.g.*, Stellingwerf 1984 for an instability strip). Transient phenomena, such as mode switching, are also predicted. Bono *et al.* (1995) made a thorough analysis of the different details of the mode excitation and mode transition within the instability strip.

RR Lyrae stars have been observed for more than a century, mainly in photometry. They are subdivided into three *Bailey classes*: RR<sub>a</sub>, RR<sub>b</sub> and RR<sub>c</sub> stars. This classification is based upon the amplitude and the skewness of the light curve and on the oscillation period. RR<sub>ab</sub> stars are now considered to be one class, pulsating in the radial fundamental mode and having asymmetric light curves. RR<sub>c</sub> stars, on the other hand, oscillate in the first overtone and have sinusoidal variations. Two prototypical OGLE light curves, phased according to the dominant period, are shown in Figs 2.28 and 2.29.

In the mid 1980s, a fourth class of RR Lyrae stars was introduced: the RR<sub>d</sub> stars. The amplitudes of these group members change on relatively short time scales. Such stars have periods between 0.3 and 0.5 d and their light curves have more scatter than for the RR<sub>abc</sub> stars (see Figs 2.30 and 2.31 for a prototypical case observed within the MACHO project). It turns out that the RR<sub>d</sub> stars oscillate in both the fundamental and first overtone, *i.e.*, they are *double mode* oscillators with a period ratio near 0.74 (Kovács 2001). RR<sub>d</sub> stars are found in both the Galactic plane and in globular clusters. They have the advantage that the excitation of two oscillation modes allows us to characterize the stellar parameters, such as the mass, with much higher precision than for RR<sub>abc</sub> stars (*e.g.*, Popieliski *et al.* 2000; Szabó *et al.* 2004).

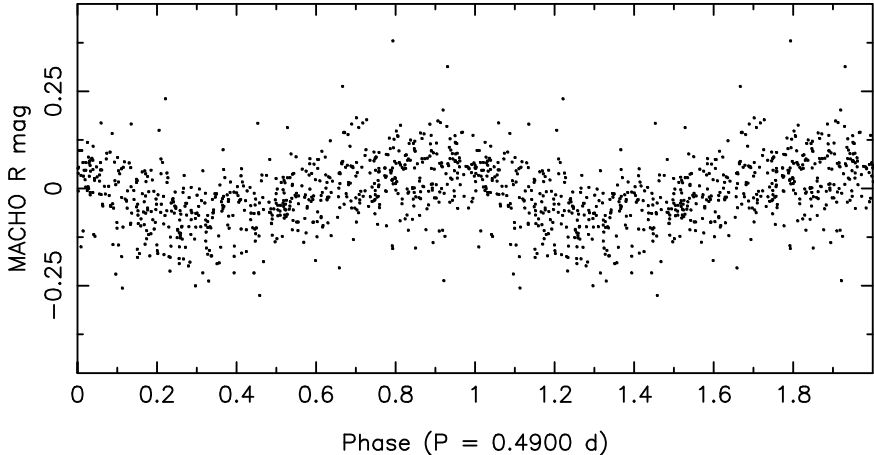


**Fig. 2.31.** Residual MACHO light curve of the RRd star shown in Fig. 2.30 after prewhitening with the dominant oscillation period and folded according to the second period. Data taken from Kovács (2000).

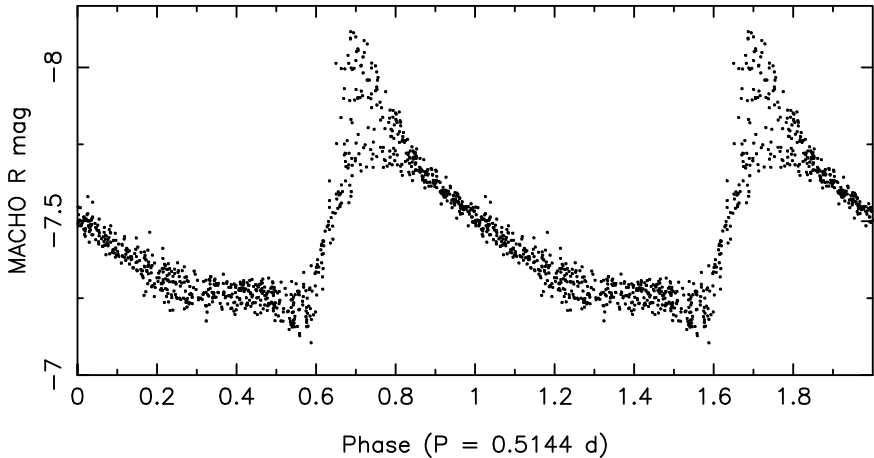


**Fig. 2.32.** Light curve of a Blazhko star observed by MACHO folded according to the dominant oscillation period. Data taken from Kurtz *et al.* (2000).

Another old classification for RR Lyrae stars concerns their host clusters. Oosterhoff (1944) pointed out that some clusters have mainly RRab stars, while others have an equal contribution in RRab and RRc stars. The former are called *Oosterhoff I* type clusters and the latter *Oosterhoff II*. The average oscillation period of the RR Lyrae stars in Oosterhoff I clusters is 0.1 d shorter

than for those in the Oosterhoff II clusters. This phenomenon is called the *Oosterhoff period dichotomy* (*e.g.*, Catelan 2007 for a discussion).

The absolute visual magnitudes of RR Lyrae stars have values roughly between 0 and 1. Although less bright than Cepheids (see further on) their large amplitude and their brightness makes them easy to recognize and hence suitable to be identified in globular clusters. Just as with Cepheids, they are used as distance indicators to these clusters. While more accurate and larger distances can be derived from the more luminous Cepheids, globular clusters do not have a population of the latter stars and so they cannot be considered for globular cluster distance determination. The RR Lyrae stars are therefore an important and good alternative.

Finally, we turn to the phenomenon called the *Blazhko effect*. For 25% of the RR Lyrae stars one observes amplitude modulation in the light curve (see Fig. 2.32 for a prototypical example from the MACHO database) on a time scale that is typically 100 times longer than the oscillation period. This modulation is observed in all three classes RRabc. It was observed for the first time by Blazhko (1907) for the star EW Dra and is named after its discoverer. RR Lyrae itself is a Blazhko star (*e.g.*, Kolenberg *et al.* 2006), with a modulation period, also termed Blazhko period, of 40.8 d. Over the Blazhko cycle the maximum brightness changes considerably, while there is hardly any change in minimum brightness (Fig. 2.32). The Blazhko effect has also been detected in line profile variations of RR Lyrae itself (Chadid *et al.* 1999). Smolec (2005) pointed out that the Blazhko effect does not correlate with metallicity.

Jurcsik *et al.* (2005) proposed a correlation between the oscillation period and the modulation period, which made them conclude that the modulation period must be equal to the rotation period. However, for some of the Blazhko stars a third, much longer modulation period is also well established, *e.g.*, seven years for RW Dra and four years for RR Lyrae. The start of a new long modulation cycle is accompanied with a phase jump of several days in the light curve. It is difficult to understand this in terms of rotation of the star.

For many years now there have been two competing theoretical explanations for the Blazhko effect:

1. It is caused by the excitation of a nonradial oscillation mode of low degree, besides the main radial mode, through nonlinear resonant mode coupling. In this model the Blazhko period is interpreted as the beat period between the radial fundamental and a nonradial mode (*e.g.*, Van Hoolst 1995; Van Hoolst *et al.* 1998; Dziembowski & Cassisi 1999).
2. It is caused by a magnetic field that influences the oscillations (similar to the oblique pulsator model for the roAp stars). In this case the Blazhko period must be interpreted as the rotation period of the star (*e.g.*, Takata & Shibahashi 1995).

There is no consensus about the correct interpretation of the Blazhko effect, particularly not in view of the variety of Blazhko light curve characteristics discovered from the MACHO database (Kurtz *et al.* 2000). The extensive

efforts to search for a magnetic field in the best studied and brightest Blazhko star, RR Lyrae itself, and the failure to detect one with modern instruments to confirm previous claims (Chadid *et al.* 2004), have not resolved the issue. Moskalik & Poretti (2003) rejected the oblique magnetic pulsator model on the basis of the properties of Blazhko stars discovered from the OGLE project.

### 2.5.2 Cepheids

After the start of central helium burning in their non-degenerate cores, stars with initial masses above  $\simeq 2.3 M_{\odot}$  decrease in luminosity while they descend the giant branch. Stars below  $3 M_{\odot}$  settle on the horizontal branch while their more massive counterparts exhibit loops in the HR diagram. For the stars with masses below  $5 M_{\odot}$  these loops are too limited to bring them into the instability strip. For more massive stars, however, the loops do extend far enough so that they become pulsationally unstable and are observed as *Cepheids*.

The importance of Cepheids is not their asteroseismic potential, except perhaps for the double- and triple-mode pulsators mentioned below, but their fundamental power for distance determinations through the well-known *period-luminosity relation*, discovered by Henrietta Leavitt from Harvard University (Leavitt & Pickering 1912)<sup>21</sup> and first calibrated by Ejnar Hertzsprung (1914). By measuring the oscillation period of a Cepheid and by using the period-luminosity relation, one can derive the absolute magnitude, hence the distance to the star. For this reason, Cepheids are also called *distance indicators*.

In principle, the relation could be calibrated by means of an accurate independent distance determination to one Cepheid. In practice, however, one tries to determine accurately the zero-point of the relation by inclusion of as many stars as possible for which accurate distance determinations are available. Given the importance of cosmological distance scales, the derivation of the zero points, including appropriate statistical error estimates, remains a matter of intense debate in the literature (see, *e.g.*, these conference proceedings: Kurtz & Pollard 2004; Walker & Bono 2006 for compilations).

#### 2.5.2.1 Population I Cepheids

The *classical Cepheids*, named after the prototype  $\delta$  Cephei, are probably the best known and most homogeneous group of pulsating stars. The variability of  $\delta$  Cephei was discovered in 1784 by John Goodricke, while Henrietta Leavitt made extensive investigations of Cepheids early in the 20<sup>th</sup> century.

---

<sup>21</sup> Although the paper is signed by Edward Pickering, its first line reads, “The following statement regarding the periods of the 25 variable stars in the Small Magellanic Cloud has been prepared by Miss Leavitt.” History and Website referencing services are fair and attribute the circular to Leavitt & Pickering.

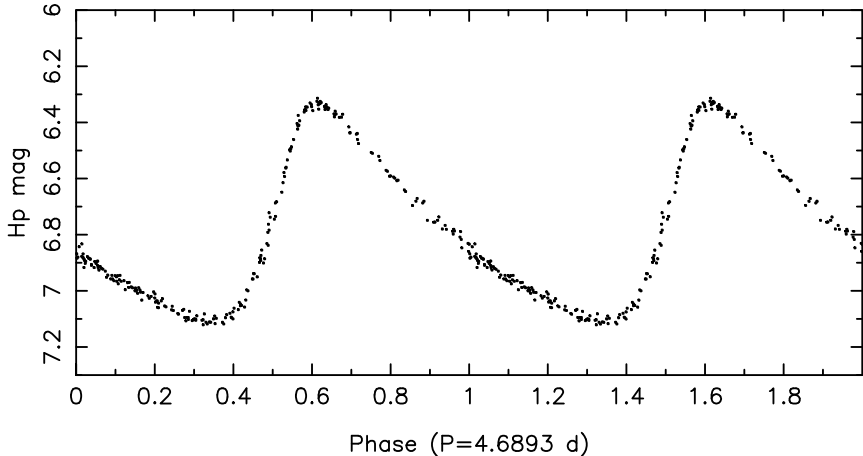


**Fig. 2.33.** Hipparcos light curve of the classical Cepheid HD 112044 folded according to the oscillation period. Data taken from Perryman (1997, ESA).

A Hipparcos light curve of a classical Cepheid is shown in Fig. 2.33. In general, the periods of the Cepheids range from 1 to 50 d and their spectral types are between F5 and G5. They are all giants or supergiants. In our Galaxy, the Cepheids are situated in the Galactic plane and they take part in the rotation of the Galaxy. Thus they are Population I objects and are therefore also called type I Cepheids. Below, we provide only a brief summary of the properties of Cepheids, referring to the extensive literature on such stars for more details.

The light curves of the Cepheids are skew and extremely periodic (see Fig. 2.33). The amplitudes are on average about one magnitude at visual wavelengths. Such brightness variations are accompanied by changes in the spectral type, colour, temperature and luminosity. For the prototype  $\delta$  Cep itself, for example, the spectral type is F5 at maximum brightness and G2 at minimum brightness, while the corresponding change in temperature amounts to some 1500 K. In general for Cepheids, the luminosity classes change roughly from III to Ib during the pulsation cycle for stars with periods below 25 d and between III and Ia for Cepheids with longer periods.

Bersier *et al.* (1994) produced an extensive radial velocity catalogue of bright Cepheids. In Fig. 2.34 we notice a so-called *stillstand* in the radial velocity curve they obtained for the star X Cyg. Such a phenomenon occurs whenever a strong shock wave propagates in the atmosphere of the star in such a way that the downfall of matter after maximum radius is stopped by rising gas due to the next shock. This shock is also markedly present at the same phase in the cycle in the Hipparcos light curve, which was taken about ten years later (Fig. 2.34).

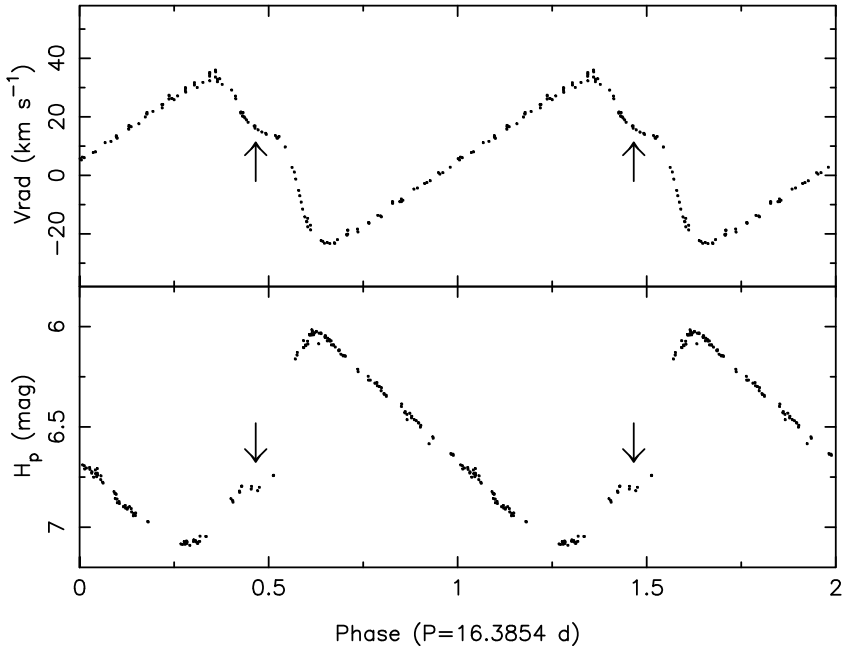


**Fig. 2.34.** The radial velocity and Hipparcos light curve of X Cyg folded according to the radial fundamental mode period of 16.38538 d. The stillstand is indicated by an arrow. Data taken from Bersier *et al.* (1994) and from Perryman (1997, ESA).

In general, maximum brightness occurs near minimal velocity. However, detailed comparison of the phased light and radial velocity curves suggests the occurrence of a small *phase lag* between the photometric and spectroscopic signatures of the oscillation. This lag typically amounts to a tenth of the period and can be spotted for X Cyg in Fig. 2.34. There also occurs a clear relation between the colour, or  $B - V$ , of the Cepheids and their oscillation period. This is called the *period-colour relation*. At a given luminosity, the stars shift to later spectral types for longer periods.

For several Cepheids a bump occurs in the light curve. Such a phenomenon occurs for Cepheids with periods between 4 and 20 d. It is due to a coincident occurrence of a 2:1 ratio between the period of the fundamental and the second overtone. The bump shifts as a function of oscillation period. This is called the *Hertzsprung progression*.

As is the case for the RR Lyrae stars, there are Cepheids in which both the fundamental mode and first overtone, or the first and second overtone, are excited. These are called *beat Cepheids* or also *double-mode Cepheids*.

Poretti & Pardo (1997) have made a thorough study of galactic double-mode Cepheids. The MACHO and OGLE projects revolutionized our knowledge of the statistical properties of Cepheids in general. In particular, numer-

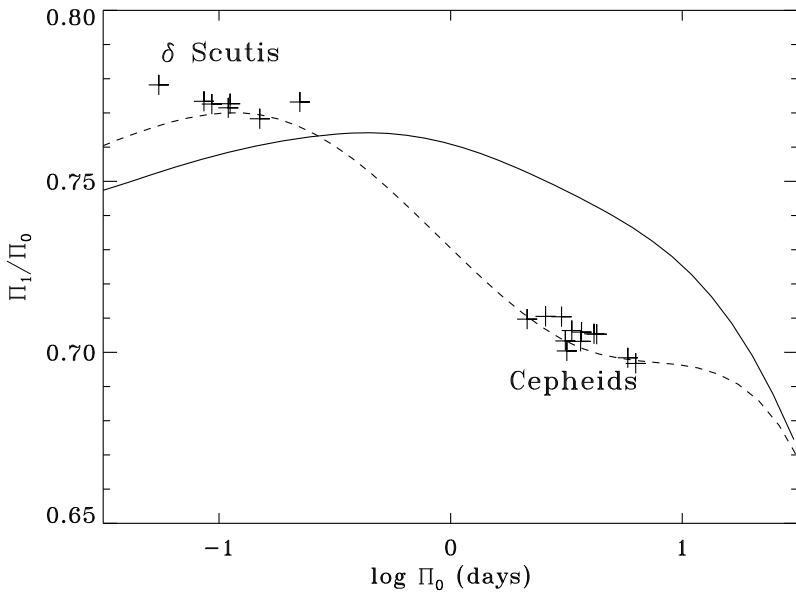


**Fig. 2.35.** Petersen diagram, plotting the ratio between the first overtone and fundamental radial period against the logarithm of the latter. The observed values are shown by crosses. The curves show the variation along the instability strip; the solid curve was based on models computed with the Cox & Tabor (1976) opacities, whereas the dashed curve used OPAL tables from Rogers & Iglesias (1992). From Christensen-Dalsgaard (1993b).

ous double-mode Cepheids were found in the LMC (Alcock *et al.* 1999), and later even more in the SMC (Udalski *et al.* 1999). These include both first overtone/second overtone and fundamental/first overtone Cepheids. Only a few first overtone/second overtone Cepheids are known in the Galaxy (*e.g.*, Beltrame & Poretti 2002).

The double-mode Cepheids may be said to constitute the first application of asteroseismology to determine stellar properties. Petersen (1973) showed that the two periods could be used to infer the mass and radius of the star. The results were in striking disagreement with the masses obtained from the position of the stars in the HR Diagram, on the basis of evolutionary calculations (for reviews of this and other “Cepheid mass problems”, see for example A. N. Cox 1980; Simon 1987), suggesting potential problems with the understanding of stellar evolution and pulsations and leading to extensive efforts to remove the discrepancy. It is common to illustrate the problem in a *Petersen diagram*, where the ratio  $\Pi_1/\Pi_0$  is plotted against  $\log \Pi_0$ , where  $\Pi_1$  is the period of the first radial overtone mode and  $\Pi_0$  is the period of

the fundamental mode. The observed location of a star in such a diagram is given with great precision. An example is illustrated in Fig. 2.35; the solid curve shows theoretical results for models along the instability strip, based on the theoretical relation between mass and luminosity and using pre-1980 opacities, compared with observations of double mode HADS and Cepheids. The discrepancy is obvious. It was suggested by Simon (1982), and demonstrated in greater detail by Andreasen & Petersen (1988), that the discrepancy could be eliminated through a substantial increase of the opacity in the range  $5.2 < \log T < 5.9$ . Remarkably, such an increase was found in the OPAL calculations (*e.g.*, Rogers & Iglesias 1992) through increased contributions from bound-bound transitions in iron group elements; it was the same effect that led to excitation of modes in, *e.g.*, SPB and  $\beta$ Cep stars (*cf.* Section 2.3.6). The effect on the period ratios is shown by the dashed curve in Fig. 2.35; obviously, with the revised opacities there is excellent agreement between the computed and observed period ratios (see also Moskalik *et al.* 1992; Kanbur & Simon 1994; Christensen-Dalsgaard & Petersen 1995).

Three stars in the Galaxy, AC And, V823 Cas and V829 Aql, are known to be triple-mode pulsators, pulsating in the fundamental, and first and second overtone modes (Jurcsik *et al.* 2006). The longest known of these is AC And which Fitch & Szeidl (1976) and Kovács & Buchler (1994) thought to be possibly similar to the  $\delta$ Sct stars. Fernie (1994) argued that this star lies intermediate between the  $\delta$ Sct stars and Cepheids. Thanks to the OGLE survey, more triple-mode Cepheids have been found. Moskalik & Dziembowski (2005) interpreted their oscillation periods as the first three radial overtones. This interpretation imposed stringent constraints on their metallicity  $Z$ , which must be in the range 0.004 to 0.007, and on their evolutionary status, indicating that the stars must be crossing the instability strip for the first time. The models also imposed an upper limit of 0.33 times the pressure scale height to the extent of overshooting from the convective core during the main sequence phase. Meanwhile the galactic triple-mode Cepheid V823 Cas, originally discovered by Antipin (1997), was subjected to a thorough photometric study. The lack of agreement between the observed periods and period ratios and those of evolutionary models led Jurcsik *et al.* (2006) to propose that this star is in a transient state during which its oscillations are probably affected by resonances.

Finally, we mention the existence of short period Cepheids with periods shorter than 7 d and sinusoidal, low amplitude light curves. They are called *s-Cepheids* or *overtone* Cepheids. They indeed pulsate in the first overtone, just as the RRc stars do. Their light curves and radial velocity curves often show a discontinuity due to a resonance between twice the first overtone and the fourth overtone radial mode frequencies. We refer to Kienzle *et al.* (1999) for a homogeneous observational study of a sample of 24 overtone Cepheids.

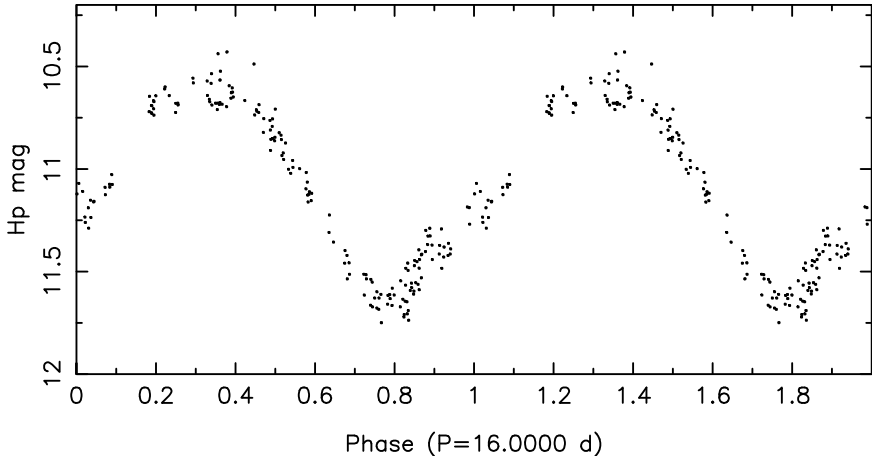


**Fig. 2.36.** Hipparcos light curve of the Population II Cepheid CO Pup folded according to the oscillation period. Data taken from Perryman (1997, ESA).

### 2.5.2.2 Population II Cepheids

After central helium burning, stars of Population II with masses higher than  $0.5 M_{\odot}$  evolve from the horizontal branch towards the AGB. During their evolution away from the horizontal branch, or during the numerous thermal pulses on the AGB, the stars may cross the instability strip and start pulsating. Such stars are called *type II Cepheids* or *Population II Cepheids*. Their periods range from 1 d for stars with luminosities similar to those of the RR Lyrae stars to about one month at higher luminosities. An example of a light curve is shown in Fig. 2.36.

The oscillations are caused by the heat mechanism active in both the partial ionization zone of He II – He III and of H I – H II. Theory predicts the excitation of either the radial fundamental mode or the first overtone (see, e.g., Bono *et al.* 1995, 1997). Despite numerous efforts, the derivation of the precise location of the instability strip of Population II Cepheids remains uncertain. As for all monoperiodic radial oscillators, the stars are not well suited for seismic studies.

The longer period Population II Cepheids were originally also discovered by Henrietta Leavitt early in the 20<sup>th</sup> century; they have been called the *W Virginis stars* for a long time. Today, the Type II Cepheids are divided in groups by period, such that the stars with periods between 1 and 5 d (BL Her class), 10 to 20 d (W Virginis class), and longer than 20 d (RV Tauri class, see below) have differing evolutionary histories (Wallerstein 2002). A period gap thus occurs for Population II Cepheids as there are no stars with periods between 5 and 10 d. It is believed that stars with periods shorter than 5 d are on their way to the AGB while stars with periods longer than 10 d move

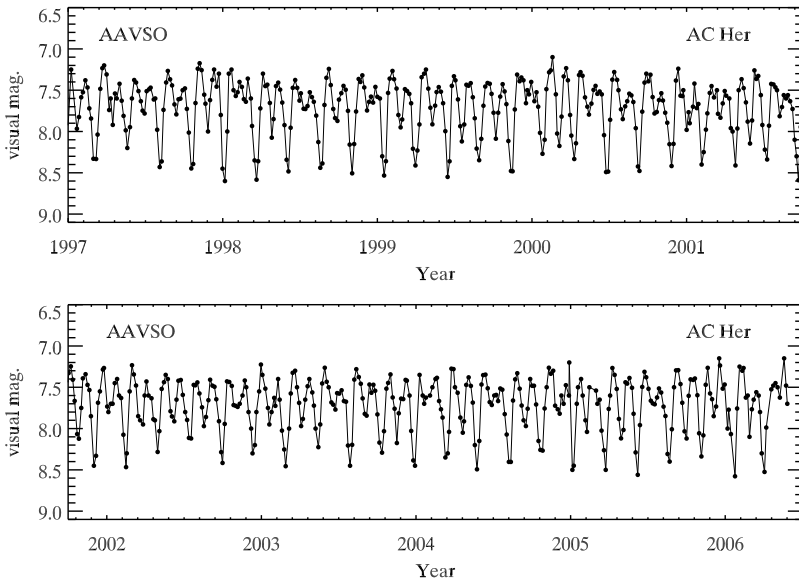


**Fig. 2.37.** The visual light curve of the RV Tauri star AC Her as observed by amateur astronomers of the American Association of Variable Star Observers (AAVSO). Figure courtesy of Matthew Templeton.

bluewards in the HR Diagram due to thermal pulses or because they are on their way to the white dwarf phase (Wallerstein 2002). For a review on Type II Cepheids we refer to Pollard & Lloyd Evans (1999).

### 2.5.3 RV Tauri Stars

The longest period W Virginis stars seem to merge continuously into yet another group of pulsators in that part of the HR Diagram, namely the *RV Tauri stars* (see Pollard *et al.* 2000 for a review). These F to K supergiant stars could also have been called the longest period W Virginis stars, but are usually considered as a separate class. For an enlightening discussion on the relation between Population II Cepheids and RV Tauri stars, and their evolutionary history, we refer to the review by Wallerstein (2002).

The oscillations of the RV Tauri stars are driven by the heat mechanism which is active in both the partial ionization zone of He I – He II and of H I – H II. A remarkable feature of RV Tauri stars is that their light curves have alternating deep and less deep minima, in a very regular way. In fact, this property is used to classify an object as an RV Tauri star. An example collected by amateur astronomers is provided in Fig. 2.37 for the star AC Her. It is evident from this figure that the light variability follows a double wave pattern. The alternations of the minima and maxima do not always repeat strictly for

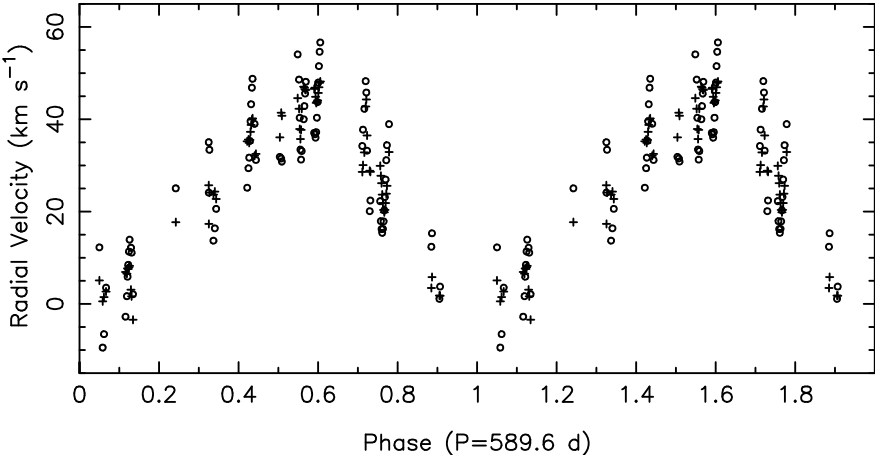


**Fig. 2.38.** The measured radial velocity variations (open circles) and those prewhitened so as to leave the dominant oscillation mode alone (crosses) of RVb star SX Cen, obtained from long term monitoring, folded according to the orbit. The variability due to the oscillations with a period of 16.4 d has an amplitude which is a large fraction of the orbital amplitude. Figure courtesy of Hans Van Winckel.

all RV Tauri stars as some of them have cycle-to-cycle changes. RV Tauri stars are further divided in RVa and RVb subclasses, the RVa stars being those without long term photometric trends and the RVb stars with such trends.

The radial velocity curves of RV Tauri stars have large amplitudes, as can be seen from Fig. 2.38. The shapes of the radial velocity curves of AC Her and R Sct were interpreted in terms of shock waves in their atmosphere by Gillet *et al.* (1990). The spectroscopic study of 11 RV Tauri stars by Pollard *et al.* (1997) indeed confirmed that the data are compatible with two shock waves propagating in the atmosphere per pulsation period, because the metallic lines show a double-peaked profile which is characteristic of an atmospheric shock as already outlined by Schwarzschild *et al.* (1948).

Infrared observations of RV Tauri stars clearly reveal the existence of circumstellar matter (Lloyd Evans 1985; Oudmaijer *et al.* 1992). This implies that the RV Tauri stars are low mass stars in the early post-AGB phase (Jura 1986). As this phase has a very short duration compared with the lifetime of the star, it is difficult to catch the objects in this stage.

A definitive interpretation for the alternating minima is not yet available. It may be that a resonant oscillation pattern is active (Fokin 1994). The oscillation periods range from 30 to 150 d, which creates an observational challenge to obtain a good inventory of the oscillatory behaviour of such stars. A further complication is that variable circumstellar absorption occurs, and is, in fact, sometimes sufficient to explain the photometric variability (Pollard *et al.* 1996). This led Van Winckel *et al.* (1999) to propose that the photometric

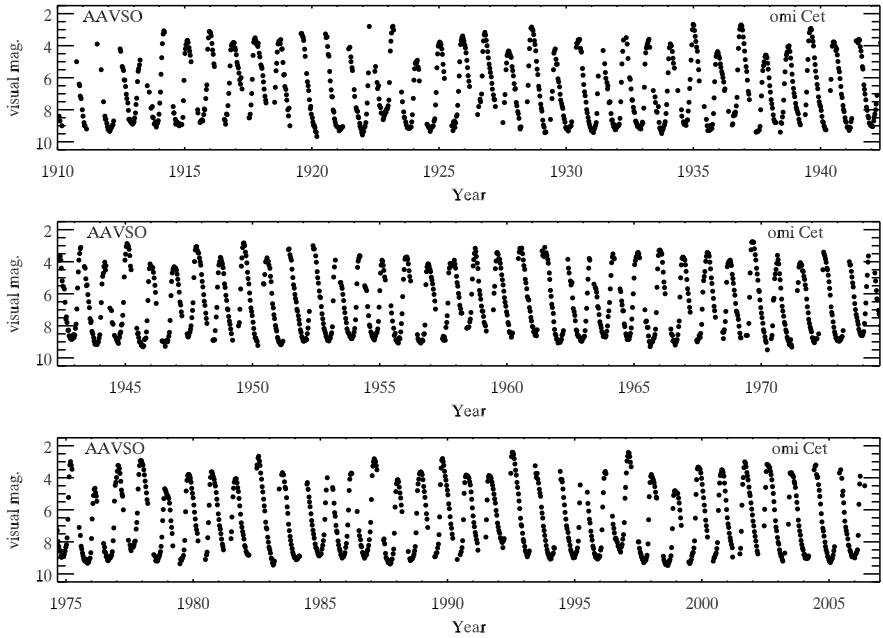


**Fig. 2.39.** The visual light curve of the Mira itself,  $\alpha$ Cet, as observed by amateur astronomers of the AAVSO. Figure courtesy of Matthew Templeton.

subclasses RVa and RVb are simply due to a geometric projection effect, and not to a physical difference.

Finally, it is found that a very high fraction of the RV Tauri stars turn out to be long period binaries (Van Winckel 2003, see Fig. 2.38). It may be that the long term variability possessed by the RVb stars is due to the binarity (*e.g.*, Maas *et al.* 2002).

#### 2.5.4 Mira and Semi-Regular Variables

Population I variable stars with long periods ( $P > 80$  d) situated at luminosities between about  $10^3 L_\odot$  and  $7 \times 10^3 L_\odot$ , and at low effective temperatures between 2500 and 3500 K, are called Mira variables (Miras) when their amplitudes are larger than 2.5 in  $V$  (see Fig. 2.39). Semi-regular (SR) variables with similar periods but smaller amplitudes are termed SRa (see Fig. 2.40). This term is highly misleading, because most of these stars have light curves as regular as Miras (compare Figs 2.39 and 2.40; see also Lebzelter & Hinkle (2002) for a discussion), but an amplitude below 2.5 in  $V$ , which implies a totally arbitrary division between the Miras and SRa stars. SRb stars, on the other hand, have lower amplitudes than the SRa stars and semi-regularity in their light curves, *i.e.*, their periodicity is poorly defined. They often show

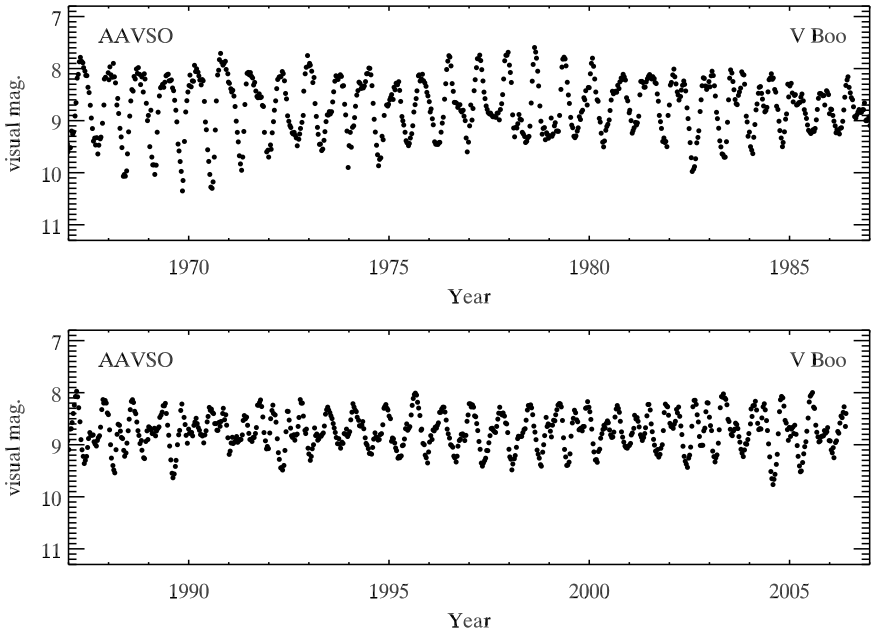


**Fig. 2.40.** The visual light curve of the SRa star V Boo as observed by amateur astronomers of the AAVSO. Figure courtesy of Matthew Templeton.

alternating intervals of periodic and slow irregular changes. The SRc stars are periodic supergiants with an amplitude below 1.0 in  $V$ . A class called the SRd stars has also been introduced. This term is again misleading, because, unlike the RRd stars, which are double-mode RR Lyrae stars, the SRd variables are not double-mode pulsators. Rather, they are weak-lined variable giants and supergiants of spectral types FGK. They are considered to be metal-poor shorter period analogues of the Miras (Lloyd Evans 1975). One of the best monitored SRd variables is  $\rho$  Cas, whose visual light curve is provided in Fig. 2.41. The Miras and SRa stars are AGB stars with large mass loss and are about to start their way to the planetary nebula phase. Some of the SRb stars are still on the RGB.

The Miras and SRs are situated to the red of the classical instability strip, at lower temperatures. They have radial oscillations which, according to modelling by Ostlie & Cox (1986), are heat driven in the partial ionization zones of H I – H II and He I – He II. Although Ostlie & Cox obtained reasonable results for the location of the instability region, they recognized that their use of the “frozen convection” approximation for the pulsations was a serious limitation. In fact, convection totally dominates the energy transport in the regions responsible for the driving. Effects of convection were considered by, e.g., Xiong *et al.* (1998), Munteanu *et al.* (2005) and Olivier & Wood (2005)

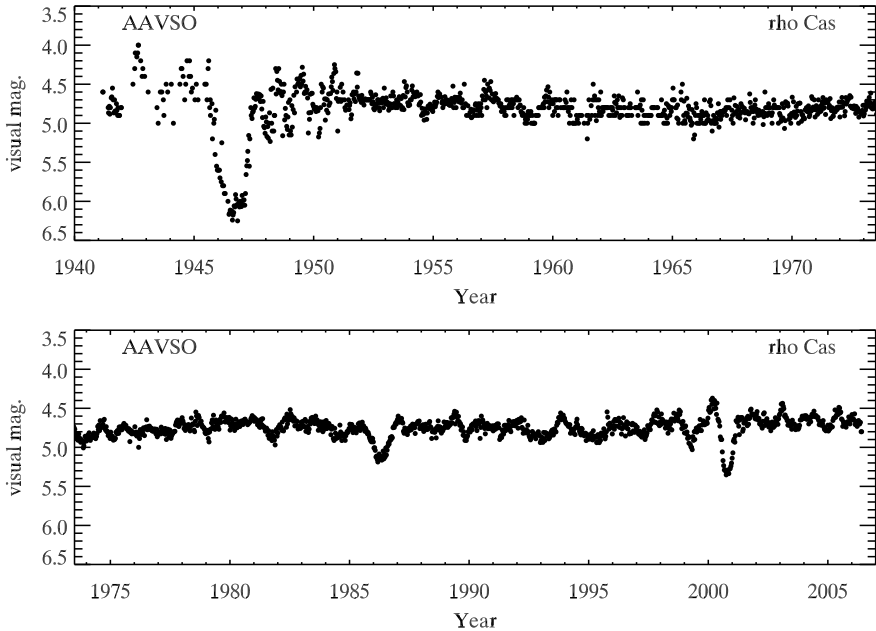


**Fig. 2.41.** The visual light curve of the SRd star  $\rho$  Cas as observed by amateur astronomers of the AAVSO. Figure courtesy of Matthew Templeton.

with somewhat conflicting results. It is evident that a full understanding of the driving of these oscillations will require a more secure treatment of the interaction between convection and pulsations.

The huge amplitudes seen in visible light in some Mira variables (*e.g.*, Fig. 2.39) do not reflect similar variations in the total luminosity. As discussed by Reid & Goldston (2002) the reduction of the visible magnitude at minimum is dominated by the cooling of the atmosphere and the conversion of the emitted radiation to the infrared by the effect of the resulting formation of metal oxides.

The MACHO and OGLE databases generated a real breakthrough in the study of long period variables. The MACHO data led to the discovery of five distinct period-luminosity (PL) sequences for the low mass giant branch, as first suggested by Cook *et al.* (1997) and worked out in detail by Wood (2000). This gave unambiguous confirmation that the Miras are radial fundamental pulsators while SR variables can pulsate in the 1st, 2nd, 3rd radial overtone, as well as in the fundamental mode. Similar results were obtained from OGLE data in a series of papers (Ita *et al.* 2004ab; Kiss & Bedding 2004; Soszyński *et al.* 2004; Groenewegen 2004). Fraser *et al.* (2005) made a careful analysis of the full 8-yr MACHO database, and disentangled six rather than five PL sequences, which they termed 1, 2, 3, 4, D and E (see Fig. 2.42). The first four

sequences are interpreted in terms of radial pulsations at rising radial order. Cioni *et al.* (2001) already showed that the large amplitude SRa stars fall on sequence 1 together with the Miras, while the low amplitude SRa stars fall on sequences 2, 3, 4. The sequences 3 and 4 contain RGB stars as well as oxygen-rich AGB stars that did not yet undergo the 3rd dredge-up, *i.e.*, less evolved stars than those in sequences 1 and 2.

The interpretation of the sequences D and E is less clear. It was suggested by Wood *et al.* (1999) that the sequence E is comprised of ellipsoidal or eclipsing red giant binaries with an invisible companion and sequence D of stars with a short primary period and a long secondary period. Later on, however, Wood *et al.* (2004) considered different physical causes for the long secondary periods of stars in sequence D and came to the conclusion that a low degree g-mode oscillation combined with large scale spots of a single red star offers the most likely interpretation. Soszyński *et al.* (2004), on the other hand, concluded that sequence D contains a mixture of AGB, RGB, Mira, SRa, SRb and small amplitude pulsators. In a follow-up study, Soszyński (2007) noted that sequence D forms a continuation of the ellipsoidal and eclipsing red giants of sequence E and therefore argued in favour of the binary hypothesis for both sequences D and E.

Given these disagreements, we must conclude that it is still unclear which physical mechanism causes red pulsators to become a Mira or an SRa/b/c/d. The latter are only rather arbitrarily defined categories introduced by observers to differentiate among the red variables from the morphology of their light curves. One suggestion for the discrimination in the physics of these different types of stars is a small difference in chemical composition, and hence in molecular grain types, resulting in a different mass loss. Another idea is that the very tenuous envelopes of these stars imply shock waves of different strength in their outer atmospheres and that these cause quasi-periodic cycles.

Christensen-Dalsgaard *et al.* (2001) suggested stochastically excited modes as an explanation for the semi-regularity. Indeed, all these stars have huge outer convection zones, so one would expect them to undergo solar-like oscillations, which, of course, have much longer periods in supergiant stars than in main sequence stars. It may therefore very well be that the differences between Miras and SRa or SRb stars simply reflect the fact that radial modes are active in the former, while there is beating with solar-like oscillations in the latter. This idea, tested on amateur astronomer data from the American Association of Variable Star Observers (AAVSO), was confirmed by OGLE data (Kiss & Bedding 2003). In fact, in a very detailed analysis of OGLE data, Soszyński *et al.* (2007) identified clear substructure in the distribution of stars in the period-luminosity diagram, in broad agreement with the predictions of stellar models. They concluded that the OGLE small-amplitude red giants most likely display solar-like oscillations and noted their potential value for the investigation of the properties of stochastic excitation. If accurate frequencies of solar-like oscillations in AGB stars can be measured, then these objects will suddenly become very interesting stars from a seismic point

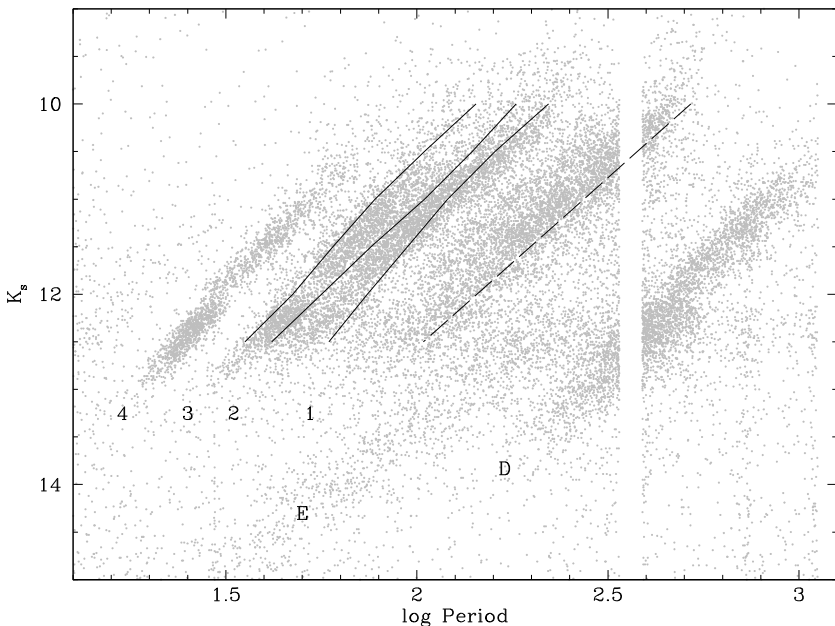


**Fig. 2.42.** Period-Luminosity diagram for MACHO data of long period variables (grey dots). The observed LMC Mira relation for the fundamental mode by Feast *et al.* (1989) is indicated as dashed line. The 3rd, 2nd and 1st overtone models of Wood & Sebo (1996) are indicated as solid lines (from left to right). Note that stars with periods near 1 yr were removed from the analysis, due to aliasing problems. From Fraser *et al.* (2005).

of view. This will indeed allow us to probe in detail the very complex stellar structure of stars that are about to end all the phases of nuclear burning they went through during their complete evolution. It is a major observational challenge to measure these frequencies for future seismic studies, given the long periods of these stars, hence the long term observational commitment needed. However, the stars have such large amplitudes that this is an area of asteroseismology where amateur astronomers can play a significant role.

### 2.5.5 Solar-Like Oscillations in Red Giants

As already mentioned in Section 2.3.1, one expects solar-like oscillations to be excited in all stars with an outer convection zone. While such oscillations are hard to establish in red supergiants with large amplitude heat driven modes,

such as the Miras or large amplitude semi-regular variables, they have become obvious in red giant stars.

The first announcements of short period variability with periods of the order of hours in a giant star were made by Smith *et al.* (1987) and Innis *et al.* (1988) for the star  $\alpha$  Boo (Arcturus, K1III), on the basis of radial velocity observations. Hatzes & Cochran (1994) found radial velocity variations, with an amplitude near  $50 \text{ m s}^{-1}$ , for the K2III star  $\beta$  Oph; no firm periodicity could be derived, although the candidate periods ranged from 0.25 up to 0.8 d. Also, using the Hubble Space Telescope, Edmonds & Gilliland (1996) found photometric variations in K giants in the globular cluster 47 Tuc which appeared to be consistent with solar-like oscillations. Merline (1999) subsequently reported solar-like oscillations from further long term radial velocity monitoring of Arcturus, with periods ranging from 1.7 to 8.3 d. This result was later confirmed by space photometry taken with the WIRE satellite, from which Retter *et al.* (2003) deduced an oscillation period of 2.3 d. The WIRE mission had been used before to claim solar-like oscillations in the K0III giant  $\alpha$  UMa (Buzasi *et al.* 2000). The longest among the ten detected periods was 6.4 d and the amplitudes ranged from 100 to  $400 \mu\text{mag}$ . Although Guenther *et al.* (2000) interpreted these frequencies to be due to low order p modes of a  $4 M_{\odot}$  giant, Dziembowski *et al.* (2001a) pointed out that the model predictions for appropriate stellar masses of  $\alpha$  UMa and with appropriate input physics disagree with the claimed modes, as far as the predicted amplitudes, frequencies and excitation are concerned.

The first firm establishment of solar-like oscillations in a giant was made for the G7III star  $\xi$  Hya (Frandsen *et al.* 2002). Nine frequencies were found in the radial velocity data of the star, spanning one full month. The strongest mode has an amplitude of about  $2 \text{ m s}^{-1}$ . An average large spacing of  $6.8 \mu\text{Hz}$  was found, in agreement with radial mode frequencies of adjacent radial order. Modelling of the pulsations by Houdek & Gough (2002), using Gough's (1977a) treatment of the interaction between convection and pulsations, yielded amplitudes in good agreement with the observed values. Stello *et al.* (2006) used the data to estimate the mode lifetime of  $\xi$  Hya and found it to be of the order of 2 d. Such a short lifetime, if confirmed for other giants, would limit the power of asteroseismology in this part of the HR Diagram. Also, interestingly, the lifetimes were far shorter than indicated by the calculations by Houdek & Gough.

A subsequent clear detection of solar-like oscillations in a giant from space-based photometry was achieved for the Hubble Space Telescope guide star GSC 09137–03505. Kallinger *et al.* (2005) found three frequencies ranging from 21 to  $71 \mu\text{Hz}$  in the 19 million data points spanning 8 d. Additional suggestions of such detections came from spectroscopy for the K4III star HD 32887 and the K3II-III star HD 81797 (Setiawan *et al.* 2006).

Recent detections of solar-like oscillations in a giant were achieved from a two-site radial velocity campaign spanning 2 full months. De Ridder *et al.* (2006) discovered an excess power near  $60 \mu\text{Hz}$  for the G9.5III star  $\varepsilon$  Oph

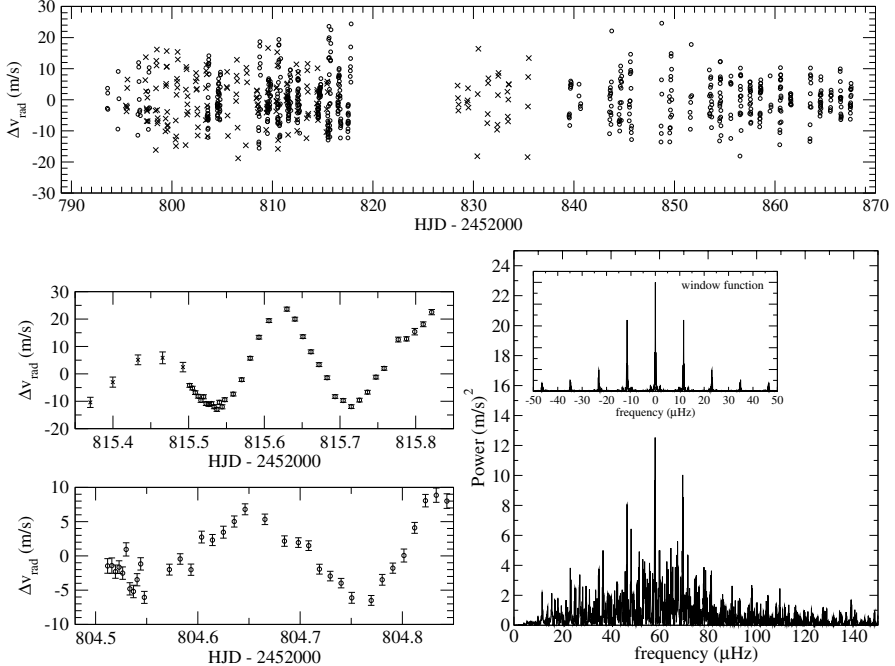


**Fig. 2.43.** Top: radial velocity data of  $\varepsilon$  Oph from a two-site campaign (dots: CORALIE data taken with the 1.2-m Swiss Euler telescope at La Silla, crosses: ELODIE data taken with the 1.9-m telescope at Haute Provence observatory). Bottom left: two enlarged parts of the dataset. Bottom right: power spectrum. From De Ridder *et al.* (2006).

(see Fig. 2.43). They derived two possible values for the large spacing (4.8 or  $6.7 \mu\text{Hz}$ ). The star was subsequently monitored from space by the MOST mission during 37 d. The MOST light curve is in full agreement with the velocity data and, having no daily aliasing problems, pointed out that  $4.8 \mu\text{Hz}$  is the correct value for the spacing (Barban *et al.* 2007). Finally, oscillations were also firmly established for the K0III star  $\eta$  Ser from the same two-site campaign (Carrier, unpublished; see also Fig. 2.3).

Red giants could potentially show a complicated mixed mode frequency structure containing much information on the interior physics of evolved stars, although the short mode lifetimes obtained by Stello *et al.* (2006) may reduce the predictive power of their observed frequency spectra. Moreover, theoretical computations by Dziembowski (1977a), Dziembowski *et al.* (2001a), and Gough & Houdek (2002) predict the nonradial modes to be damped far more strongly than the radial modes, due to the high density contrast between the core and the extended envelope (we refer to Chapter 7 for more details). This may imply that only radial modes reach observable amplitudes. This is con-

sistent with the observed frequency spacings detected so far in ground-based radial velocity data. On the other hand, Hekker *et al.* (2006) investigated the variability in the cross-correlation profiles (see Chapter 4 for a definition) of four pulsating red giants and came to the conclusion that this variability can only be understood in terms of the presence of nonradial modes. A similar conclusion was drawn from MOST data for the K2 giant star HD 20884 (Kallinger *et al.* 2008a), even though these results are controversial (as one can deduce from the editorial note added to this paper). Clearly, more observational work and theoretical work are needed to obtain a better understanding of the oscillations in red giants. The latest results are discussed in more detail in Chapter 7. Undoubtedly, observations with CoRoT will be of much value in this respect.

## 2.6 Pulsations in Evolved Stars with $M \geq 9 M_{\odot}$

In the current section we describe the variable nature of stars with initial masses above  $9 M_{\odot}$  which are evolved off the main sequence. These stars never encounter degeneracy in their core and experience different burning cycles until they have an iron core, after which they explode as supernova.

Their luminosity-to-mass ratios increase significantly as they evolve off the main sequence. Indeed, during their evolution past the TAMS towards the red supergiant phase, and then back in the direction of the ZAMS, they lose a lot of mass while keeping almost the same luminosity. Because of this,  $L/M$  increases and the stars come close to their *Eddington limit*, the upper value of  $L/M$  determined by the requirement that the inward gravitational acceleration is larger than the outward acceleration due to the strong radiation pressure. Any star close to its Eddington limit cannot be very stable. This is particularly relevant for the lifetimes of stars born with  $M > 40 M_{\odot}$ . For compilations of studies of the most massive stars we refer to, *e.g.*, Heydari-Malayeri *et al.* (2004), Humphreys & Stanek (2005), Ignace & Gayley (2005), and Bresolin *et al.* (2008). Here, we concentrate only on those variability aspects of such stars that may be related to oscillations.

The overall variability of this group of stars in the upper HR Diagram occurs at different time scales and may have very different physical causes. Sometimes the lowest amplitude variability is periodic. We term such stars PVSGs, *Periodically Variable SuperGiants*, irrespective of the cause of the periodic variability. These stars are indicated as such in the grey upper zone in Fig. 1.12. It is unfortunate that seismic modelling has not yet reached these high masses, because stellar structure and evolution models are most uncertain for such stars, due to badly understood phenomena such as rotational mixing and meridional circulation, semi-convection, strong core convective overshooting and mass loss. As further outlined below, the very first steps were made by Saio *et al.* (2006) and Godart *et al.* (2008) for the B2 Ib/II supergiant HD 163899 found to be pulsating from the MOST mission. We provide an

overview of the variable nature of such massive objects in this chapter, but will not return to them further on in the book.

### 2.6.1 Periodically Variable B and A Supergiants

#### 2.6.1.1 The A-Type Supergiants

Supergiant stars of spectral type A showing variations in photometry with amplitudes of tenths to hundredths of a magnitude were termed  $\alpha$  Cyg variables, after the A1I prototype  $\alpha$  Cygni. They have been monitored for decades by different teams, *e.g.*, Sterken (1977, 1983), Burki *et al.* (1978), van Genderen *et al.* (1989a,b,c), Lamers *et al.* (1998), van Genderen (2001), and references therein. Burki (1978) and van Leeuwen *et al.* (1998) focused on a sample of 32 and 24 late-B to G supergiants, describing the variability of these  $\alpha$  Cyg variables from ground-based Geneva and Hipparcos data, respectively. The periodicities found by these authors range from 10 to 100 d and are too long to be due to the radial fundamental mode of such objects (Lovy *et al.* 1984). It should be pointed out, however, that significant uncertainties in the theoretical oscillation calculations occur for stars of such high luminosity, as they undergo all sorts of mixing processes in their interior as well as instabilities in their atmosphere due to the large radiation pressure. These effects are usually ignored when predicting p- and g-mode frequencies.

Line profile variations in supergiant stars were discovered by Baade *et al.* (1990), who studied the O9I companion of the WR binary  $\gamma^2$  Vel. An extensive line profile study based on years of monitoring of 6 BA-type supergiants was made by Kaufer *et al.* (1997). These authors concluded that the variability patterns in the line profiles are extremely complicated and seem to point towards cyclic variations in the deduced radial velocities. Besides these cyclic changes, they concluded nonradial oscillations to be present from travelling sub-features across the line profiles whose periodicities are not compatible with the rotation of the stars.

No detailed modelling of the observed periodic variability has yet been achieved. Nonlinear radial instabilities in so-called *strange modes*, with periods between 10 and 100 d roughly, have been put forward as an explanation for the variations in stars with masses above  $40 M_{\odot}$  (Kiriakidis *et al.* 1993; Glatzel *et al.* 1999; Dziembowski & Sławińska 2005 and references therein). Such strange modes are caused by a strong enhancement in the opacity in the second partial ionization layer of helium and of the heavy elements. They are excited due to strong non-adiabatic conditions in stars with a high  $L/M$  ratio, *i.e.*, stars not too far from their Eddington limit. These strange modes are predicted to have amplitudes that are much larger than those found for the classical radial pulsators. From this, one speculates that they could perhaps be responsible for triggering the outbursts accompanying the moderate to low amplitude periodic variability of the A-type supergiants and the *Luminous Blue Variables* (see below). The occurrence of strange modes has not yet been firmly established observationally in the most massive stars.

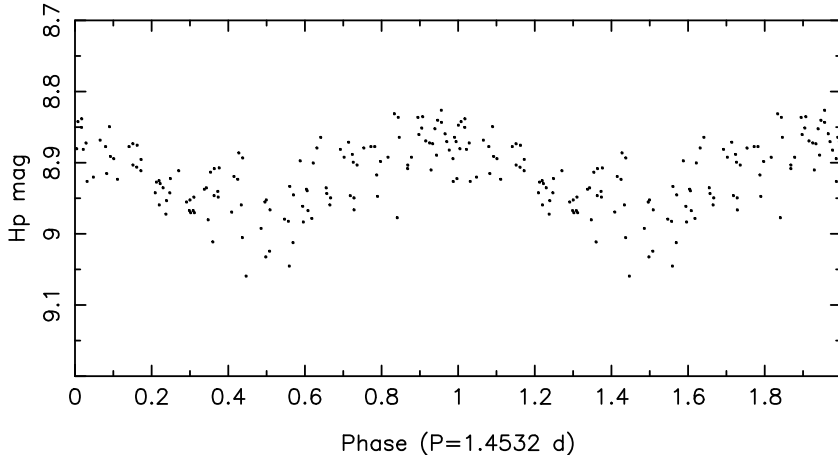


**Fig. 2.44.** Hipparcos light curve of the B2/B3Ib/II star HD 98410 folded according to the dominant period. Data taken from Perryman (1997, ESA).

### 2.6.1.2 The B-Type Supergiants

Oscillations as in  $\beta$  Cep stars have not yet been firmly established in luminous stars with  $\log L/L_{\odot} > 5$  and  $M > 20 M_{\odot}$ , although they are predicted in that part of the HR Diagram as well (Pamyatnykh 1999 and Fig. 2.19). The reason is probably that the instability strip no longer coincides with the entire main sequence, but is shifted towards more evolved stars. Pamyatnykh (1999) predicted SPB-type g modes to be unstable at such high luminosities in pre-TAMS stars (*i.e.*, stars near the end of their central hydrogen-burning stage, see Fig. 2.45). The post-TAMS evolution during the hydrogen shell burning phase of such objects is so fast that it is hard to find stars in that evolutionary state in the first place. On the other hand, the stars do not spend long in the red part of the HR Diagram, and return quickly to the position of their pre-TAMS stage (*e.g.*, Chiosi & Maeder 1986 for a thorough review). It is very difficult to unravel the evolutionary state of stars in that part of the HR Diagram from classical observations. Seismic information could help a great deal here. However, at that stage in their evolution, significant mass loss in the form of a line-driven stellar wind (*e.g.*, Kudritzki & Puls 2000 for a review) complicates the unambiguous detection of possible oscillatory motion at the stellar surface.

Waelkens *et al.* (1998) discovered a sample of B supergiants to be periodically variable with SPB-type periods from the Hipparcos mission. These stars, and additional similar ones, were subjected to detailed spectroscopic and frequency analyses by Lefever *et al.* (2007a), who found their masses to be below  $40 M_{\odot}$  and photometric periods between 1 and 25 d, *i.e.*, shorter than the periods of the periodic variations found in the more massive A-type

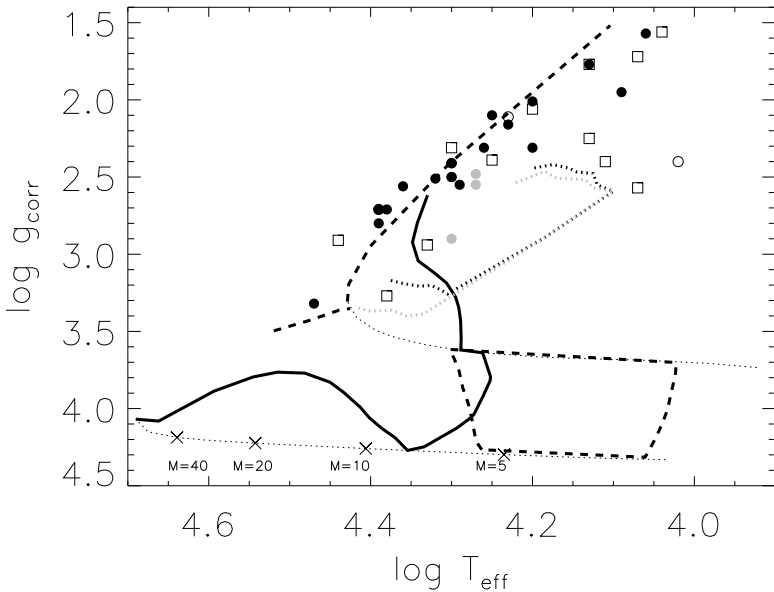


**Fig. 2.45.** The position of the sample of B supergiants discovered to be periodically variable from the Hipparcos mission is compared with Pamyatnykh's (1999) pre-TAMS instability computations for p modes (full lines) and g modes (dashed lines). The instability strips of post-TAMS g modes computed by Saio *et al.* (2006) are indicated as dotted lines (grey:  $l = 1$  modes, black:  $l = 2$  modes). From Lefever *et al.* (2007a).

supergiant variables. An example light curve is shown in Fig. 2.44. The stars in the sample perfectly fulfil the wind-momentum-luminosity relation derived for galactic A- and B-supergiants by Kudritzki *et al.* (1994). Their line-driven wind thus behaves normally. Lefever *et al.* (2007a) found the sample's periodic supergiants to be placed near the high gravity limit of Pamyatnykh's (1999) heat driven g-mode instability strip for evolved stars (see Fig. 2.45). This implies that the interpretation of their variability in terms of nonradial oscillations excited by the heat mechanism, as first suggested by Waelkens *et al.* (1998), is plausible. The authors found marginal evidence for a connection between the wind density and the photometric amplitude.

A new step ahead in the understanding of such stars was achieved by Saio *et al.* (2006), who detected both p and g modes in the B2Ib/II star HD 163899 from MOST space-based photometry. The authors deduced 48 frequencies below  $2.8 \text{ d}^{-1}$  with amplitudes below 4 mmag and constructed post-TAMS

stellar models that led to g-mode frequencies which are compatible with the observed frequency spectrum.

Further research is needed to evaluate if seismic modelling in terms of internal physics parameter tuning of individual periodically variable B-type supergiants is feasible. To achieve this, the current mode identification methods (see Chapter 6) must be adapted to the case of a dynamical atmosphere dominated by radiative forces.

### 2.6.1.3 Luminous Blue Variables

Some of the most luminous stars undergo sporadic violent outbursts, the cause of which is not yet well understood, but may be due to strange-mode instabilities. Their irregular behaviour is comparable to that of a geyser on Earth:

quiet period → moderate activity → heavy dredge-up → violent eruption → quiet period → ...

Half a century ago the existence of some very peculiar, strongly variable massive stars in our Galaxy, such as P Cyg and  $\eta$  Car, was already known. Moreover, a few such stars were also known in the Magellanic Clouds, *e.g.*, S Dor. However, it was not clear yet at that time that all of these very massive objects were undergoing the same type of instabilities. The newly discovered members were called P Cyg or SDor star, depending on their presence in our Galaxy or in the Magellanic Clouds. Moreover, similar objects began to be found in nearby galaxies, such as the so-called Hubble-Sandage variables in M31 and M33.

It wasn't until the 1970s that significant progress was made in the interpretation of these objects. Space observations in the ultraviolet (UV) made it clear that all of them are losing significant amounts of mass. Moreover, they all showed excess fluxes at infrared wavelengths. This class of stars was termed *Luminous Blue Variables* (LBVs; Conti 1984).

The outbursts of LBVs can take several decades and are of irregular nature, with long periods of quiescence in between. The stars are optically faint when they are quiet as their outer layers have temperatures of typically  $12\,000 - 30\,000\,\text{K}$  and so they mainly emit energy in the UV. During the outbursts, however, the LBVs can increase their brightness by two or three orders of magnitude because the outer layers cool significantly, typically to some  $8\,000\,\text{K}$ , so they emit much more of their energy in the visual. The stars eject about a whole solar mass of their material during such a heavy eruption. More regular and less violent eruptions also occur. In that case they only take about one year and they occur almost periodically.

At present there are several tens of confirmed LBVs and some tens of candidates known in our Galaxy and in nearby galaxies. Their luminosities are all more than a million times brighter than the Sun and remain almost constant, even during the violent eruptions.

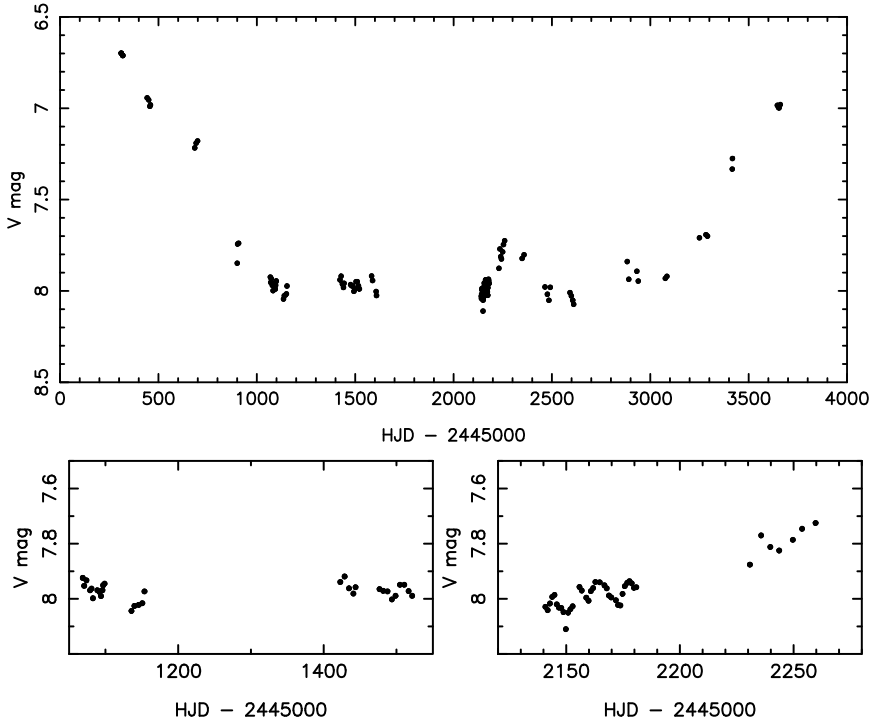


**Fig. 2.46.** Top: Light curve of the LBV AG Car obtained in the framework of the Long Term Photometric Variables programme of ESO. The bottom panels show two enlarged sections. Data taken from Sterken (1995).

Very different timescales and amplitudes are present in the light curves of LBVs. As an example we show in Fig. 2.46 the light curve of AG Car observed over almost a decade. These variations are mainly caused by changes in the temperature of the visible surface layers of the star and its radius – thus causing variations in its  $V$  magnitude – while its total luminosity remains nearly constant. We can subdivide the variations of LBVs into four different types:

1. Giant outbursts with brightness changes larger than 2 mag, which are the consequence of eruptions of large amounts of stellar matter. Examples are the eruptions of P Cygni in 1600 and of  $\eta$  Carinae in 1841 (*e.g.*, de Groot & Sterken 2001 for a compilation). During its giant eruption,  $\eta$  Carinae clearly went past its Eddington limit. The time scale of these giant eruptions is not well known for the simple reason that we have witnessed very few of them so far. For this reason one assumes that a reasonable estimate is one eruption every few hundred to thousand years.

2. Eruptions accompanied with brightness differences of one to two magnitudes. These smaller eruptions occur on time scales of 10 to 40 yr. The visual magnitude usually increases by some 2 mag during a few months and then a very slow brightness decrease occurs, which takes several years. The stars S Dor and R 127 in the Magellanic Clouds, and AG Carinae in our Galaxy experience these types of eruptions.
3. Smaller variations of about half a magnitude in brightness occur on a time scale of several months to a few years. These variations are superposed on the moderate eruptions described in 2.
4. Low amplitude (below 0.1 mag) variations occur on a time scale of several days to weeks. These variations are probably the same as those observed in the B- and A-type supergiants discussed above and may thus be due to stellar oscillations.

Since the heat mechanism is so successful in explaining the variability of many types of stars, particularly B stars on the main sequence, g modes have been proposed to be the cause of the low amplitude variations of LBVs from observations (Lamers *et al.* 1998). However, any theoretical computations needed to check the excitation of modes are very dependent on the physical parameters, which are very badly constrained for LBVs and supergiants in general. Also, one needs to combine the effect of being very close to the Eddington limit with instability calculations, which evidently leads to very uncertain predictions about the oscillations and their effect on the mass loss and outbursts (*e.g.*, Guzik *et al.* 2005). As already mentioned above, it may very well be that strange-mode instabilities with periods near 100 d are responsible for the observed variations, and perhaps even the outbursts, in stars with masses above  $40 M_{\odot}$ . The periodic variations of supergiants with masses below  $40 M_{\odot}$  having stable periods less than 20 d are due to the classical heat mechanism, as suggested by Pamyatnykh (1999), Saio *et al.* (2006) and Lefever *et al.* (2007a).

### 2.6.2 Wolf-Rayet Stars

A star is called a *Wolf-Rayet (WR) star* after it has lost a large fraction of its original massive envelope due to a radiation driven wind. The spectra of WR stars show strong emission lines caused by the rapidly expanding thick atmosphere. WR stars are situated in the HR Diagram at luminosities of  $4.5 \leq \log L / L_{\odot} \leq 6$  and temperatures  $\log T_{\text{eff}} \geq 4.6$ . They are the remnants of stars with initial masses above  $40 M_{\odot}$  which have lost so much mass that only some  $4 M_{\odot}$  is left.

The WR stars are subdivided into two groups: the carbon-rich WC stars and the nitrogen-rich WN stars. These classes are subsequently subdivided into WC5 – WC9 and WN3 – WN8 according to the presence of particular lines in the spectrum. The WN and WC stars represent different evolutionary phases. The WN stars evolve towards WC stars as more and more stellar

material gets lost through the stellar wind. For a catalogue of WR stars, see van der Hucht (2001).

The fundamental parameters of WR stars are extremely hard to determine, because of their high level of activity in terms of a strong stellar wind and due to the complex surface phenomena (*e.g.*, Crowther & Smith 1997 and references therein). The determination of their general properties constitutes a very active area of research that we will not review here. Mainly, we will focus on their variable character and even more specifically on the periodic variability.

The WR stars have quasi-periodic variability with periods ranging from a few hours to a few days. One of the earliest systematic studies of their variability was done by van Genderen *et al.* (1987), who interpreted the data in terms of temperature induced changes in the continuum emission. Numerous studies done by the same team followed this initial investigation. Marchenko *et al.* (1998a) presented an extensive study of WR stars from the Hipparcos data and found a very large diversity in the variability of these stars. The three case studies of the stars WR 6, WR 134, and WR 123, based on long strings of homogeneous photometry, did not allow a conclusion about whether their variability is due to a gradual restructuring of the stellar wind or nonradial oscillations (Marchenko & Moffat 1998). Moreover, the result of coordinated multisite photometric and spectroscopic observations of WN8 stars in 1989 and 1994-1995 by Marchenko *et al.* (1998b) still did not allow an unravelling of the cause of the high level of variability, although the authors state that it “may be supported/induced by pulsational instability”. A good example of the difficulty in interpreting the variability is in Veen *et al.* (2002a,b,c), who did not even manage to discriminate between orbital and pulsational variability for WR 46 after years of monitoring.

An important achievement was made by Lefèvre *et al.* (2005), who used MOST photometry to analyse the light variability of WR 123 with unprecedented precision from a 38 d uninterrupted time series (see Fig. 2.47). They found periodic signals with periods below 1 d, but none of them turned out to be stable for more than several days, except for a stable 9.8 h periodic signal superposed on stochastic variability throughout the whole run. In an attempt to interpret this observation, Townsend & MacDonald (2006) investigated the stability of WR stars and suggested unstable g modes of intermediate radial orders excited by a heat mechanism operating on an opacity bump at an envelope temperature near 1.8 million K. The periods they find range from 11 to 21 h for a WR model containing some surface hydrogen ( $X_{\text{surface}} = 0.12$ ), and from 3 to 12 h in a hydrogen depleted WR model. This suggests that self-excited g modes may be the source of the 9.8 h periodic variation of the star disentangled in the MOST data. Dorfi *et al.* (2006), on the other hand, explained the observed variability in terms of a strange mode oscillation due to the iron opacity bump in a hydrogen-rich ( $X = 0.35$ ) stellar model.

We must conclude that strict periodicity has not yet been found so far in WR stars except for the case of WR 123’s 9.8 h period derived from uninter-

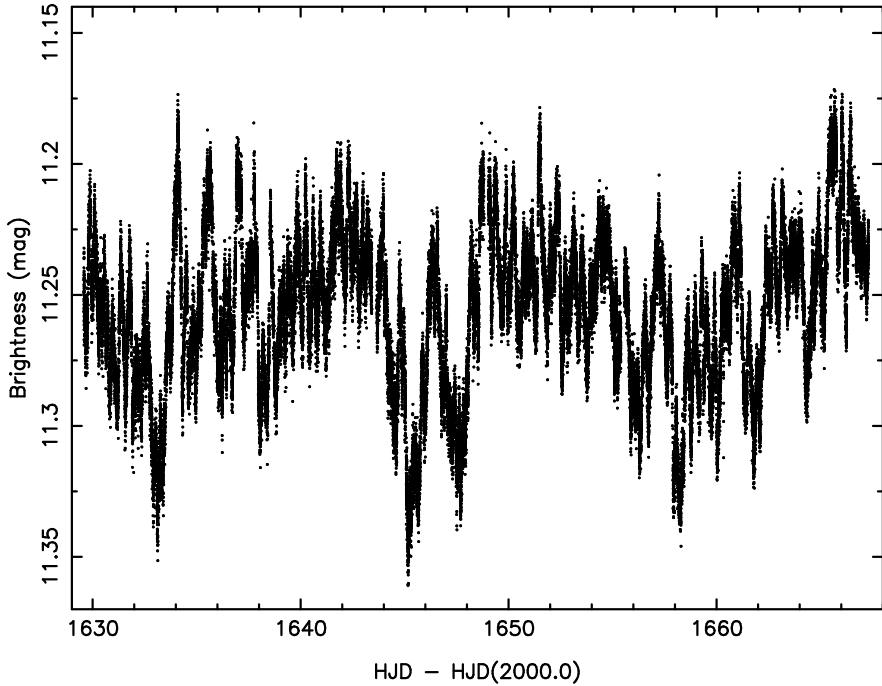


**Fig. 2.47.** The light variations of WR 123 as observed by the MOST satellite. Data taken from Lefèvre *et al.* (2005).

rupted space photometry. The physical origin of the complete observed variability remains unclear, but as far as oscillations are concerned, the promising computations pointing towards the excitation of heat driven g modes or strange modes will hopefully be continued in the near future and be confronted with more high quality data.

Some of the LBVs have exactly the same characteristics as WN9 stars during their visual minimum. For this reason, the LBVs are considered to be the immediate progenitors of WR stars and it makes sense to try to understand the LBV microvariability in terms of g modes similar to those found by Townsend & MacDonald (2006). This has so far not been done.

Once a star has reached the WR phase there is no way back: it will soon explode as a supernova, leaving a compact remnant (neutron star or black hole).

### 2.6.3 The Role of Core g Modes in Supernova Explosions

There are several observational facts that demand asymmetric supernova explosions. Many pulsars, *e.g.*, have high proper motions and a large fraction of neutron stars have such high velocities that they must have experienced a

large kick at birth. Neutrino driven convection was put forward as a viable non-spherical supernova mechanism (Burrows *et al.* 1995), although it cannot explain the highest observed velocities of neutron stars.

To solve this problem, Goldreich *et al.* (1997) proposed the  $\epsilon$  mechanism (see Chapter 3) to be the cause of the necessary asymmetry before the onset of core collapse. Murphy *et al.* (2004) have further explored the viability of g-mode oscillations excited by nuclear reactions to be at the origin of pre-collapse asymmetries by performing an eigenmode analysis. They indeed found unstable outer core g modes in all progenitor models with initial masses between 11 and  $40 M_{\odot}$ , with oscillation periods between 1 and 10 s. These modes are trapped by discontinuities between the fossil Fe core and either the O shell (lower masses) or the Si burning shell (higher masses). However promising this mechanism was, the growth time scale of the core modes ranged between 10 and 10 000 s, which is far too long for the  $\epsilon$  mechanism to become effective in the supernova progenitors. Indeed, the asymmetries must typically be achieved within one second after the onset of the collapse.

An entirely new view on core collapse supernova explosions was proposed by Burrows *et al.* (2005). They found the agent of the explosion to be the acoustic power generated by the excitation and sonic damping of core g-mode oscillations. Their 2D hydrodynamical computations for a  $13 M_{\odot}$  star show that a proto-neutron star is a self-excited oscillator in which an  $l = 1$  mode with a period of  $\sim 3$  ms (besides lower amplitude modes) grows and becomes prominent 500 ms after bounce. The source of the acoustic power is the gravitational energy of infall and the core oscillation acts like a transducer to convert this accretion energy into sound, resulting in an asymmetric ejection of the mantle. While neutrinos do not drive the explosion in this model, they do contribute to the deposition of energy in the shock. This mechanism can explain the observed morphologies and r-process properties of supernovae. Obviously, it is very hard to test this model observationally, except for the behaviour of the ejecta and the predicted neutrino fluxes.

## 2.7 Compact Oscillators

Stars at the end of the AGB phase leave the red part of the HR Diagram to become white dwarfs. This happens whenever their dust-driven and pulsation-induced wind comes to an end. During their post-AGB phase, which lasts typically only 10 000 years, they travel through the HR Diagram with constant luminosity towards higher effective temperature because their outer envelope expands quickly and the hot CO core becomes better visible. For some stars, the last thermal pulse causes a very efficient mixing with large convective overshooting, implying a drastic change in surface composition and a return towards the AGB. During this very short *born-again phase*, the star may cross the instability strip while moving redward and blueward in the HR Diagram. Examples of such fast-evolving stars are V605 Aql and Sakurai's object (*e.g.*,

Clayton *et al.* 2006). On their blueward path back from the AGB, they join the Wolf-Rayet central stars of planetary nebulae in the sense that they end up as hydrogen deficient stars whose surface layers are rich in helium, carbon and oxygen. We will soon turn to the description of the oscillations in such hot (pre-)white dwarfs. Some low mass stars, however, end up in the extreme horizontal branch and do not become AGB stars as their hydrogen envelope contains too little hydrogen to keep the hydrogen shell burning going. These objects are situated to the left of the RR Lyrae stars and have masses below  $0.5 M_{\odot}$ . They turn immediately towards the white dwarf phase once their central helium is exhausted. Some of these subdwarf B (hereafter sdB) stars turn out to have oscillations and so we describe them here as well because they are also compact stars whose oscillations have many similar characteristics to those of white dwarfs. Figure 2.48 shows a compilation of five prototypical cases of subdwarf and white dwarf pulsators. It can be seen that the time scales of the g-mode oscillations of the white dwarfs are somewhat longer than those of the p-modes of the subdwarfs (several to tens of minutes), while the g-mode subdwarf pulsators have oscillations with periods two orders of magnitudes longer (hours).

Some white dwarfs accrete matter in a binary and explode as supernovae of Type Ia. This extreme form of white dwarf variability plays a crucial role as standard light sources in cosmology (*e.g.*, Perlmutter *et al.* 1999).

Finally, the core collapse supernovae, originating from exploding massive single stars, leave behind very compact stellar remnants, such as neutron stars or black holes. We discuss the current status and prospects of asteroseismology of these most compact objects as well.

We start off with the least evolved of the compact oscillators, but not before pointing out that pulsating hydrogen-poor carbon stars and extreme helium stars will additionally be discussed in the last section of this chapter, since binarity plays a crucial role in our understanding of this diverse group of stars.

### 2.7.1 Variable Subdwarf B Stars

In 1997, a team of South African astronomers discovered a new class of pulsating stars among the sdB stars. Periodic variations with 144 s were discovered in the sdB star EC 14026 (Kilkenny *et al.* 1997, see Figs 2.49 and 2.50). The “EC” notation stands for the catalogue of the “Edinburgh-Cape Blue Object Survey”, which was the southern extension of the PG (Palomar-Green) survey.

The sdB stars are helium deficient sub-luminous B stars at relatively high galactic latitude whose spectra show broad Balmer lines and very weak He I lines. They have effective temperatures between 23 000 and 32 000 K, values of  $\log g$  between 5 and 6, and masses below  $0.5 M_{\odot}$ . They have lost almost their entire hydrogen envelope at the tip of the red giant branch such that their thin hydrogen layer does not contain enough mass to burn hydrogen. The sdB stars therefore evolve immediately from the giant branch towards

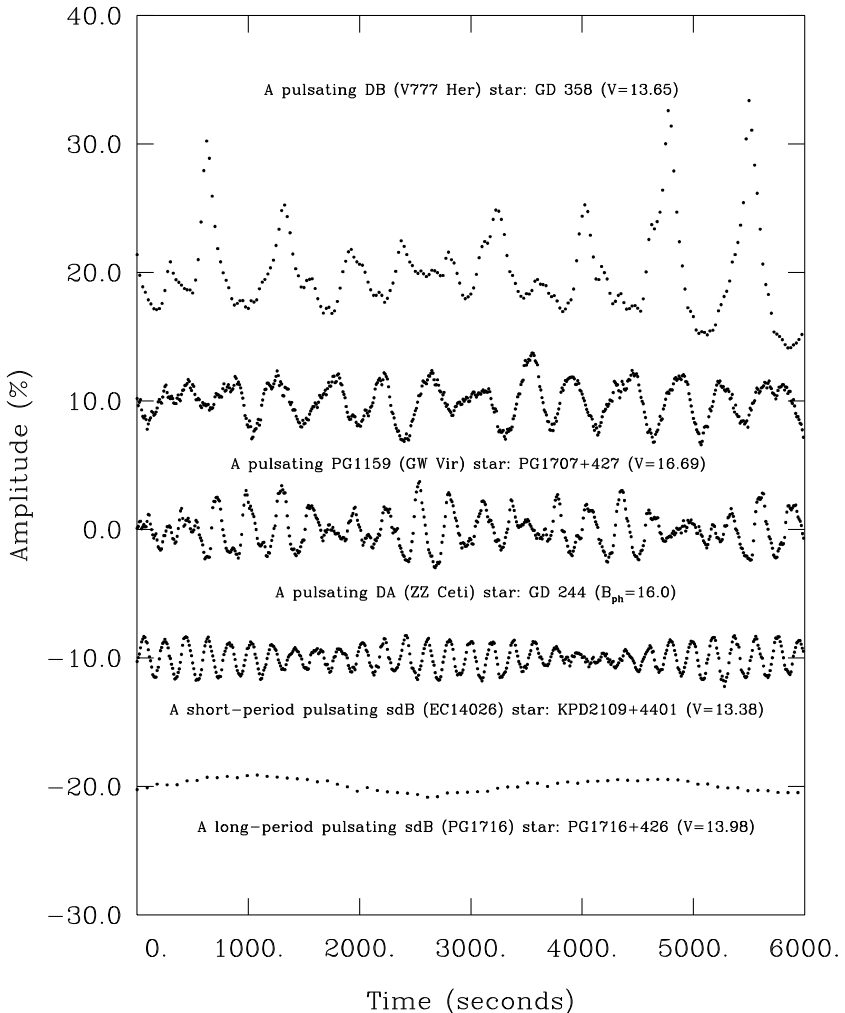


**Fig. 2.48.** The light variations for five prototypical compact pulsators taken at the Canada-France-Hawaii Telescope (CFHT) with the instrument LAPOUNE. Figure courtesy of Gilles Fontaine.

the extreme horizontal branch (EHB) and have only central helium burning. They all show a deficiency in helium and chemical anomalies of carbon and silicon, which supports the idea that they are low mass old Population I stars. They are the immediate progenitors of low mass white dwarfs.

Currently some 30 short period sdB pulsators are known among the 300 in which variability has been sought. These 30 all have multiple periods ranging from 80 to 600 s and amplitudes between 0.001 and 0.3 mag in the visible.

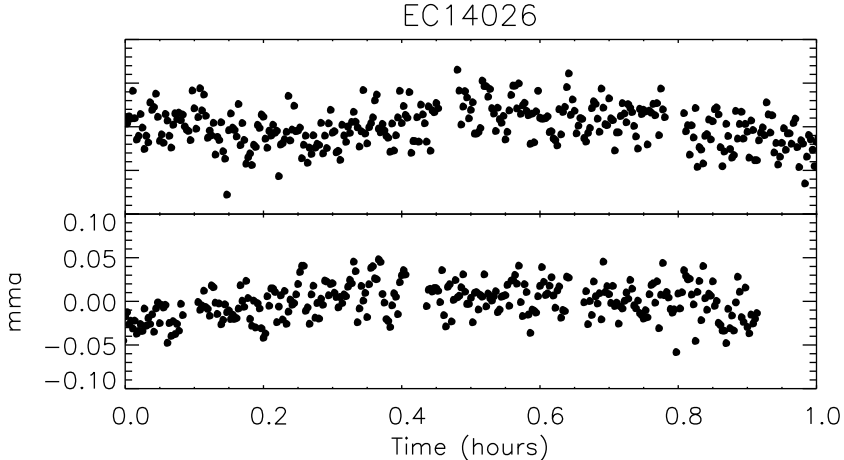


**Fig. 2.49.** The light variations in the prototype of the short period sdBV stars. The employed unit is mma, which stands for milli-modulation amplitude. This differs by a factor  $2.5 \log e = 1.08574$  from mmag. Data taken from Kilkenny *et al.* (1997).

As is expected (see Chapters 4 and 6), the amplitudes are higher at bluer wavelengths. This is nicely illustrated in Fig. 2.51 for four members of the class. We note that these objects are nowadays also termed V361 Hya stars, which is the official variable star name for the prototype. We will term these objects p-mode sdBV stars for simplicity.

The existence of pulsating sdB stars was predicted by a Canadian team (Charpinet *et al.* 1996) independently of, and simultaneously with, their observational discovery. An opacity bump associated with iron ionization turns out to be an efficient driving mechanism. The atomic diffusion processes that are at work in sdB stars, particularly radiative levitation, imply that iron becomes overabundant in the driving zone. Whenever this overabundance leads to a local  $Z$ -value above 0.04 in the partial ionization zone of iron, low order p-mode oscillations are excited (Charpinet *et al.* 1997).

During the course of an ongoing monitoring program to investigate light variations in additional sdB stars in the northern hemisphere, a group of some 20 sdB stars were discovered to have multiperiodic light variations with individual periods around one hour and very low amplitude (Green *et al.* 2003). These stars are termed *PG 1716+426 stars* after the prototype, but they have also been called “Betsy” stars as of the scientific meeting at which the discoverer announced their existence. We term them g-mode sdBV stars. Their periods are one to two orders of magnitude longer than those in the p-mode sdBV stars (see Fig. 2.52), while they are located in a similar position in the HR Diagram, at slightly cooler temperatures. This situation is very similar to those of the  $\delta$  Cep and SPB stars, and of the  $\delta$  Sct and  $\gamma$  Dor stars,

## EC 14026

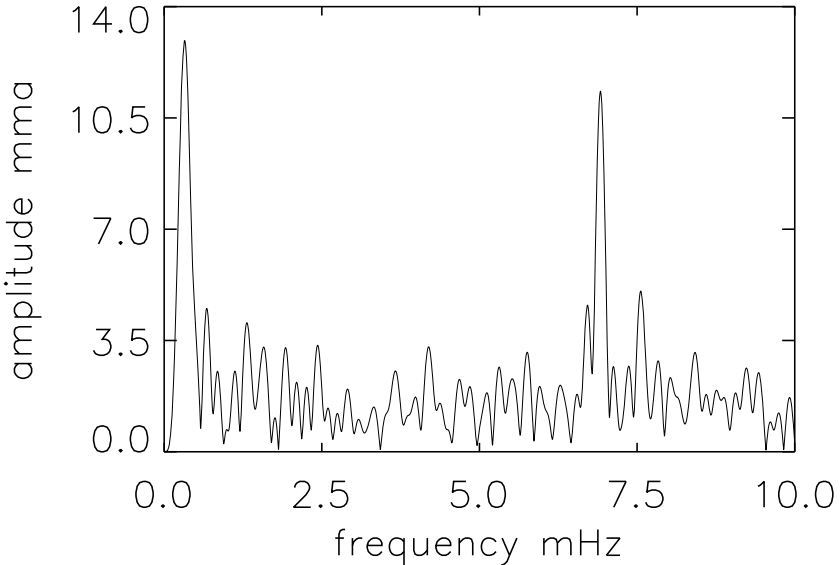


**Fig. 2.50.** The amplitude spectrum of the light curve of EC 14026 shown in Fig. 2.49. Data taken from Kilkenny *et al.* (1997).

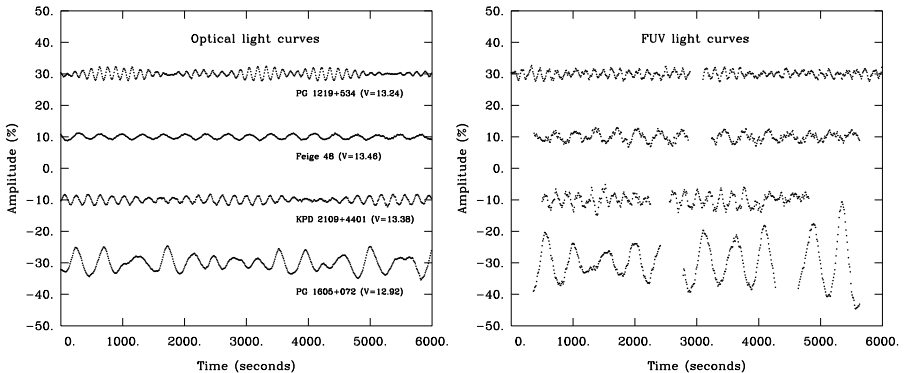


**Fig. 2.51.** The light variations in the visible (CFHT, LAPOUNCE (the Montreal 3-channel photometer); left) and in the far ultraviolet (FUSE (Far Ultraviolet Spectroscopic Explorer); right) for four prototypical p-mode sdBV stars. Figure courtesy of Gilles Fontaine.

near the main sequence. It is therefore logical to interpret these longer periods in terms of high order g modes.

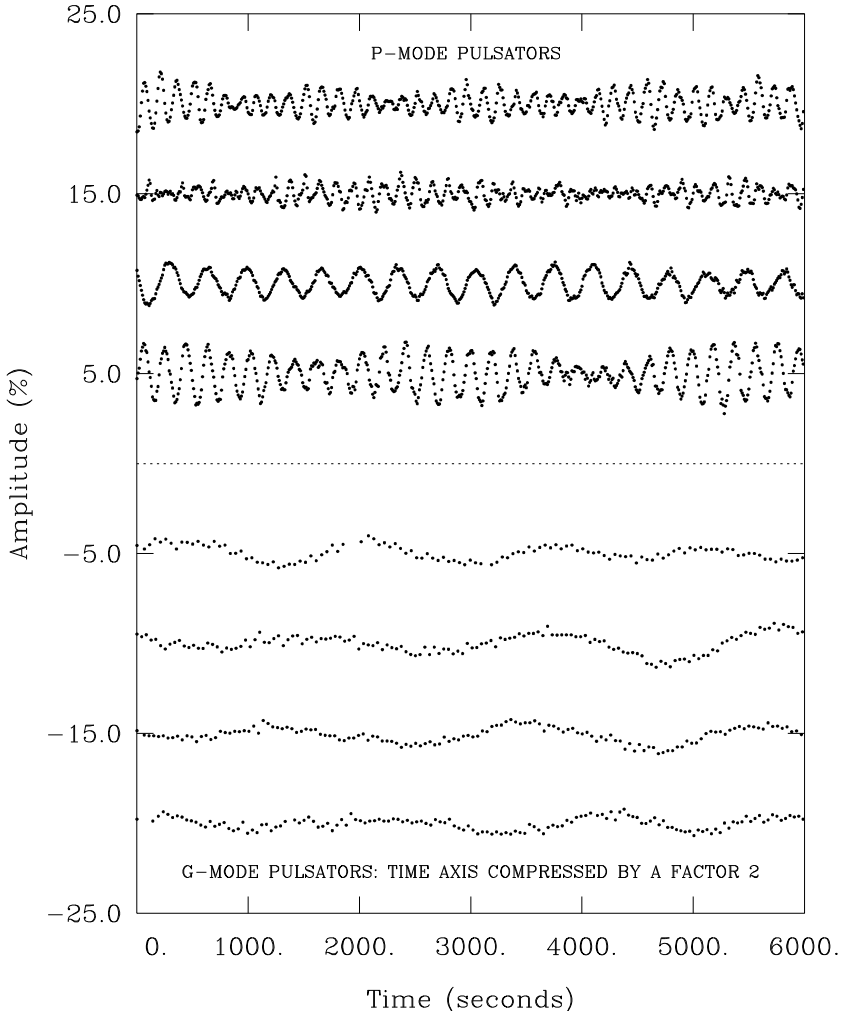


**Fig. 2.52.** Comparison between the light variations of four sdB p-mode oscillators (upper panel) and four sdB g-mode oscillators (lower panel). The time axis refers to the top half of the figure; the light curves in the bottom half have been compressed by a factor two for visual purposes. From Fontaine *et al.* (2003a).

It was indeed found that the same instability mechanism as for the p-mode oscillators predicts such modes to be unstable whenever the iron abundance in the driving region is sufficiently high (Fontaine *et al.* 2003a). Nevertheless, only modes with degree  $l = 3$  or  $4$  are found to be excited, in contrast to the results found for the p modes. This is rather unsatisfactory, since it is not evident from a physical viewpoint why only higher degree modes should be

excited. In this respect, the work by Jeffery & Saio (2006) is very promising. These authors studied mode excitation using models with envelopes having an artificial, but homogeneous, iron enhancement and found  $l = 1, 2$  g modes to be excited for appropriate temperature ranges of the observed g-mode sdBV stars. Both different approaches, *i.e.*, using a stratified composition with iron enhanced in the critical layers for excitation (Fontaine *et al.* 2003a) versus a global iron enhancement in the envelope (Jeffery & Saio 2006), are precisely the same as those used by Pamyatnykh *et al.* (2004, local iron enhancement) versus Ausseloos *et al.* (2004, global iron enhancement) to explain all the excited observed modes for the  $\beta$  Cep star  $\nu$  Eri, discussed in Section 2.3.7 earlier in this chapter and further on in Chapter 7.

A summary of sdB star research is provided in the volumes edited by Østensen (2006) and by Heber *et al.* (2008). There are at present insufficient frequencies found in any of the g-mode sdBV stars to perform in-depth seismic studies, but the observational efforts to obtain more data are ongoing. One of the best light curve, as far as the sampling is concerned, was obtained from space with MOST (Randall *et al.* 2005b). It revealed three frequencies corresponding to periods of 5227 s, 2650 s, and 7235 s, with amplitudes of 0.054%, 0.041%, and 0.038%, respectively, in fractional brightness.

Seismic applications of the p-mode sdBV stars are discussed in Chapter 7.

### 2.7.2 White Dwarf Stars

White dwarf stars are spectroscopically classified into six major subtypes with additional classifications indicating crossover spectra. In addition, there are further subtypes that specify the presence of polarization, magnetic fields and pulsation, plus there are classes for stars that do not fit any other class! For an introduction to the white dwarf alphabet zoo, see Table 1 of McCook & Sion (1999). The hottest pre-white dwarf stars that appear on the white dwarf cooling sequence in the HR Diagram (see Fig. 1.12) have effective temperatures of nearly 200 000 K, ranging down to about 80 000 K. Some of these hottest white dwarf stars are central stars of planetary nebulae, some are not; some pulsate, some do not.

For white dwarfs cooler than  $T_{\text{eff}} \leq 80\,000$  K there is a clear spectroscopic sequence into which the vast majority of known white dwarfs fit. The DO stars lie in the range  $80\,000 \geq T_{\text{eff}} \geq 45\,000$  K and show strong spectral lines of He II. It is the presence of the He II lines that gives them their “O” subclass, in analogy with the main sequence O stars, but note that there is not a direct correlation in temperature with the main sequence O stars which are generally cooler. Thus the DOs are helium atmosphere white dwarfs. Much cooler than the DOs are the DB white dwarfs with approximately  $30\,000 \geq T_{\text{eff}} \geq 12\,000$  K. These stars are also helium atmosphere white dwarfs, where in this case the DB classification indicates that generally only spectral lines of He I are seen with little or no H or metal lines. Note again that the “B” classification is in analogy with main sequence B stars that show lines of

neutral helium in their spectra, but that the temperatures do not necessarily correspond.

The vast majority of the rest of the white dwarfs are classified as DA stars because they show only lines of the Balmer series of hydrogen in their visible wavelength spectra. They are thus subclass “A” in analogy to the main sequence A stars, which by definition show the strongest Balmer lines of all main sequence stars. But even more so than for the DOs and DBs, the temperatures of the DAs do not in general correlate with main sequence A stars. While there are DAs in the main sequence A star temperature range of  $10\,000 \geq T_{\text{eff}} \geq 7400$  K, other DAs may be found with temperatures as hot as 170 000 K and as low as the coolest white dwarf stars known,  $T_{\text{eff}} \sim 4500$  K, a lower limit set by the age of the Galaxy; there has not yet been time for the first white dwarfs to cool beyond this limit.

While white dwarf stars are predicted to be the end state of evolution for main sequence stars with  $M \leq 9M_{\odot}$  and are the most common class of stars in the Galaxy, the number known is not very great as a consequence of their intrinsic faintness. Thus the study of white dwarfs is plagued by the same problem as the study of the coolest main sequence dwarfs, brown dwarfs and especially extra-solar planets: a dearth of photons.

The number of known and studied white dwarfs has increased dramatically in recent years as a consequence of the data available from the Sloan Digital Sky Survey (SDSS; York *et al.* 2000). While the SDSS is primarily an extragalactic project, its uniform, relatively deep (magnitude 23) wide-field data set is of significant use for stellar astronomy, in particular for the discovery of new white dwarf and hot subdwarf stars. McCook & Sion (1999) presented a catalogue of 2249 white dwarfs with spectroscopic classifications; their data were complete through early 1996. Kleinman *et al.* (2004) increased the number of spectroscopically classified white dwarfs by 2551 stars using the first SDSS data release, thus more than doubling the number known. A subsequent more extensive work from the SDSS data release 4 (Eisenstein *et al.* 2006a) presented a catalogue of 9316 spectroscopically confirmed white dwarf stars. Thus the majority of white dwarfs now known have been found in the SDSS. A study of these SDSS white dwarfs by Kepler *et al.* (2007) further illuminates the temperature and mass distribution for DA and DB stars roughly in the range  $40\,000 \geq T_{\text{eff}} \geq 12\,000$  K.

Eisenstein *et al.* (2006a) confirm what was earlier known from smaller samples of white dwarfs: DA white dwarfs dominate, constituting about 86% of all white dwarfs in their sample (8000 of 9316 stars). DBs are the next most numerous group comprising 8% of the sample (713 of 9316 stars). All other classes comprise the remaining 6% of the sample. Hence hydrogen atmosphere DA white dwarfs are 10 times more common than helium atmosphere DB white dwarfs.

While DAs can be found at all temperatures under 170 000 K down to the low temperature limit set by the age of the Galaxy, remarkably, few helium atmosphere white dwarfs occur in the effective temperature range between

$45\,000 \geq T_{\text{eff}} \geq 30,000$  K. The DOs and DBs are found on either side of this temperature range, but only a very few genuine helium atmosphere white dwarfs are found within it (see, *e.g.*, Eisenstein *et al.* 2006b). This exclusion is known as the “DB gap” (Liebert 1986).

The process of atomic diffusion is important in many stellar astrophysical situations, including asteroseismic applications for  $\beta$  Cep stars, SPB stars and roAp stars, as we have already mentioned in this chapter. It is a competition between gravitational settling and radiative levitation with any kind of turbulent mixing – particularly convection – potentially (usually) quenching the processes. Most importantly in the context of this section: gravitational settling stratifies the structure of white dwarf stars, and in the presence of such strong gravitational fields it does so quickly. In the absence of any mixing – particularly in the absence of convection – we would expect all white dwarf stars with sufficient residual hydrogen ( $> 10^{-15} M_{\odot}$  of H) to be DA stars. Some non-DA white dwarfs probably do not fulfil this condition, *i.e.* they lack sufficient hydrogen to be DA stars. The amount of mass loss, and in particular the amount of hydrogen loss during stellar evolution must depend on an individual star’s circumstances. The major pathway to white dwarfdom is through single star evolution with envelope loss, leaving behind as the white dwarf the previous stellar core. Two other pathways are a less common one of evolution from a hot subdwarf on the extreme horizontal branch to white dwarf, and a process with unknown frequency: binary merger. It is assumed that the vast majority of white dwarfs follow the first evolutionary path.

In that context, Fontaine & Wesemael (1987) explained the DB gap as a natural consequence of the evolution of almost all white dwarfs from planetary nebulae nuclei. They supposed that a slow rise of hydrogen to the surface, as heavier nuclei sink in the strong gravitational field, eventually makes helium-rich white dwarfs appear as DA stars at the blue edge of the DB gap at about 45 000 K. Note that hydrogen is not being radiatively levitated in this case, but rises instead as a consequence of being the lightest nucleus in an environment of gravitational settling. They then explained the red edge of the DB gap as a natural consequence of the onset of a significant convection zone at the temperature where the He I/II ionization zone coincides with the upper atmosphere, thus mixing the small amount of residual hydrogen into a deeper sea of helium, so the star then appears as a DB white dwarf. The H is essentially overwhelmed by the more abundant He and becomes observationally undetectable, or at best, difficult to detect.

Shibahashi (2005) revisited this idea and proposed a different model for the onset of the blue edge of the DB gap as white dwarfs cool: the blue edge of the DB gap occurs at the effective temperature where the He III/II ionization zone becomes deep enough that the surface convection zone of the DO stars disappears. Hence in this model the stars are always potentially DAs, but convection in the He III/II ionization zone mixes the atmosphere so the dominant helium appears in the spectrum for the DO stars, then similar mixing occurs again when the stars cool to the red edge where the He I/II

ionization zone again generates a convection zone, as in Fontaine & Wesemael's original suggestion. The difference between the two models is in the time scale for gravitational settling, hence hydrogen floating to the surface. For Fontaine & Wesemael (1987) this happens slowly during the cooling of a star from a PG 1159 pre-white dwarf stage; for Shibahashi (2005) it happens quickly as soon as the convection is turned off at 45 000 K. One possible explanation for some of the small number DB stars that do appear in the DB gap is that they are truly stars for which there is virtually no residual hydrogen to form an optically thick atmosphere. However, this is inconsistent with Eisenstein *et al.*'s (2006b) conclusion from statistical studies that some of the DB stars in the DB gap cool to be DA white dwarfs. They conclude that the DB gap is real.

There are three known classes of pulsating white dwarfs. The most common are the DAVs (DA variable white dwarfs), also known as ZZ Cet stars. These are hydrogen atmosphere white dwarfs in an exclusive instability strip that ranges between  $12\,300 \geq T_{\text{eff}} \geq 10\,850$  K with some correlation between temperature and surface gravity, in that the more massive, higher  $\log g$  are somewhat hotter. Since DAs comprise 86% of all white dwarfs, the asteroseismic study of the ZZ Cet stars is a window to understand the vast majority of white dwarfs. Until recently, there were fewer than 40 known ZZ Cet stars, but searches for new ones using the SDSS white dwarf data base and other surveys have led to this number being more than doubled, and it is still growing in ongoing programmes (Mukadam *et al.* 2004a; Mullally *et al.* 2005; Castanheira *et al.* 2006).

The hottest of the white dwarf pulsators are the pulsating PG 1159 stars, or GW Vir stars, of which there are fewer than a couple of dozen known; they have  $170\,000 \geq T_{\text{eff}} \geq 75\,000$  K. The asteroseismic record holder at the time of this writing is the prototype of this classis PG 1159–035 itself, which is discussed in detail in Chapter 7. This star has 198 pulsation modes identified from which the mass is determined to very high precision; inner stratification is constrained; the rotation period is determined to high precision; the rotational inclination is constrained; and the magnetic field strength has an upper limit less than 2 kG. The literature is large for this star with, in particular, five Whole Earth Telescope extended coverage campaigns for which the star was either the primary or a secondary target (Costa *et al.* 2008). No modes among the 198 identified for PG 1159 have a degree  $l > 2$ .

The third known type of pulsating white dwarf stars, the DBV (DB variable white dwarfs), or V777 Her stars lie between the GW Vir stars and the ZZ Cet stars in effective temperature. For his PhD thesis work Winget (1982) theoretically predicted the existence of a class of helium atmosphere white dwarf variables, then with his collaborators successfully discovered the prototype of the class, GD 358 = V777 Her (Winget *et al.* 1982). Discovering more of these stars has turned out to be difficult. They are uncommon, constituting only 8% of all white dwarfs. Also, unlike the ZZ Cet stars for which there appears to be a exclusive instability strip in which all stars pulsate, for the

DBs only some stars are V777 Her stars, while others of similar temperature and gravity do not seem to pulsate. A new survey for DBVs based on the SDSS white dwarf catalogue has nearly doubled the number known, adding 8 new V777 Her stars to the 9 known previously (Nitta *et al.* 2007). The current range in temperature of the known V777 Her stars is  $27\,800 \geq T_{\text{eff}} \geq 21\,800$  K.

All three types of pulsating white dwarfs show multiperiodic variations that are due to low degree, high order g modes, excited by the heat mechanism active in different ionization layers for the two classes DO and DB, and by convective driving for the DA class. Because of the tight mass-radius relation of white dwarfs, their oscillation periods necessarily are similar and are typically of order a few minutes. Very specific to white dwarf oscillations is the occurrence of strong mode trapping caused by the stratified envelopes, which affects the eigenfrequencies (Winget *et al.* 1981; Brassard *et al.* 1992).

Pulsating white dwarfs have the potential to allow us to examine astrophysics and high energy physics as can be done in no other laboratory. Asteroseismic study of these stars gives their total stellar masses to high precision, measures the masses of stratified layers in their atmospheres, measures or constrains rotation periods and differential rotation, magnetic field strengths, the rate of evolutionary cooling and changes in radius. For the hotter classes (DO and DB) neutrino emission through plasmon and other processes plays an important and potentially detectable role (O'Brien & Kawaler 2000; Kim *et al.* 2005). For cooler white dwarfs effects of crystallization, which play an important and uncertain role for white dwarf cooling, may be detectable (*e.g.*, Montgomery & Winget 1999; Metcalfe *et al.* 2004; Córscico *et al.* 2005a,b). White dwarfs may constrain possible axion mass, and provide a laboratory to study the  $C(\alpha, \gamma)O$  cross-section, important for the understanding of type Ia supernovae. White dwarfs constrain the age of the Galaxy and preserve an imprint of galactic history. A compilation of studies of (pulsating) white dwarfs is available in proceedings edited by Koester & Moehler (2005). For a short review of white dwarf seismology, see Kepler (2007); a longer review is available in Winget & Kepler (2008) and even more extensively in Fontaine & Brassard (2008a). Clearly, white dwarf stars are important for stellar and galactic astrophysics and as high energy physics laboratories.

We discuss below the oscillations of the three classes of white dwarfs separately. First, however, we discuss the variable central stars of planetary nebulae. These were historically treated as a separate class, called Planetary Nebula Nucleus Variables, but it has recently become clear that several of these actually behave the same as the DOV pulsators. This had led to the definition of one global class, the GW Vir pulsators, which is the terminology we adopt here.

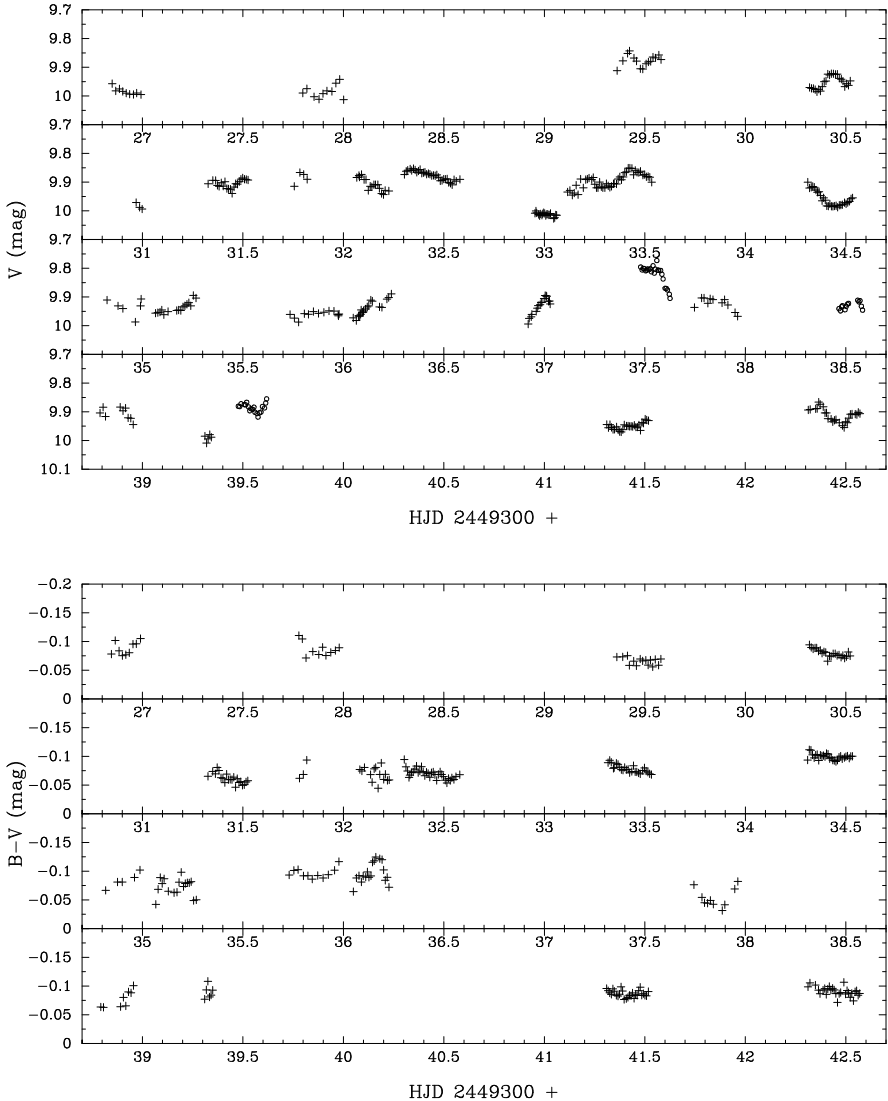


**Fig. 2.53.** Top panel:  $V$  light curve of CSPN HD 35914 from a multisite campaign. The plus signs denote photoelectric measurements and the open circles CCD data. Bottom panel:  $B - V$  variations. From Handler *et al.* (1997).

### 2.7.2.1 Variable Central Stars of Planetary Nebulae: Oscillations or Stellar Winds?

Central stars of planetary nebulae, often abbreviated as CSPN, constitute a group of stars for which some members exhibit photometric and spectro-

scopic variability with periods from several hours to days (*e.g.*, Handler 1995). This variability has been ascribed to either a variable stellar wind (Hutton & Méndez 1993; Patriarchi & Perinotto 1997) or stellar oscillations (Zalewski 1993; Gautschy 1995). The periods of order hours are much longer than those of the g modes detected in the GW Vir stars and cooler pulsating white dwarfs, as discussed below, and thus require a different interpretation.

While Méndez *et al.* (1983) reported the variability of HD 35914 (the CSPN of planetary nebula IC 418, also known as the “Spirograph Nebula” for which there is a beautiful Hubble Space Telescope picture<sup>22</sup>) and interpreted it as modulation in the outflow, Liebert *et al.* (1988) found the star VV 47 (CSPN of NGC 2474-5) to exhibit variability similar to the pulsating white dwarfs. The optical spectrum of VV 47 is also similar to those of the pulsating GW Vir stars, although somewhat broader absorption lines occurred for VV 47. The similarity to the behaviour of GW Vir led Liebert *et al.* (1988) to suggest that some CSPN have oscillations similar to the white dwarfs. Hence, they termed these objects *Planetary Nebulae Nuclei Variables* or PNNV in analogy to the naming for the variable white dwarfs at that time.

Extensive multisite observations of the best-studied variable among the CSPN, HD 35914, allowed Handler *et al.* (1997) to detect irregular light modulation with a time scale of days, as well as cyclic semi-regular variations with a time scale of 6.5 h (see Fig. 2.53). The periodicity of hours was found to be stable over more than a decade. Unfortunately, it was impossible, even from such an extensive data set, to discriminate between oscillations and wind variability for the interpretation of the data, but rotational modulation and binarity could be excluded as the dominant cause of the variability. A similar conclusion was reached for the central star of M 2-54 (Handler 1999b).

Besides “normal” CSPNs, which show absorption lines in their spectra, Wolf-Rayet stars also occur among the central stars of planetary nebulae. Their spectra are characterized by emission lines, pointing towards a strong stellar wind. They are usually denoted as [WCE] stars. Their characteristics were summarized by Górný *et al.* (1995) and Tylenda (1996), and further refined by Górný *et al.* (2004). These works point towards the presence of helium, carbon and oxygen and a deficiency of hydrogen at their surface. Their masses and luminosities are somewhat higher than those of normal CSPNs, explaining the stronger wind and the disappearance of hydrogen. Their evolutionary status is still unclear, but may involve binary evolution for some stars (De Marco *et al.* 2003). On the other hand, their characteristics are generally not different from those of normal CSPN stars (Girard *et al.* 2007). Their infrared properties even point to the presence of dust produced during a carbon-rich AGB phase before the atmospheres of these stars became hydrogen poor (Hony *et al.* 2001). Werner & Herwig (2006) found a strong evolutionary connection between the [WCE] and DO white dwarfs. The vari-

---

<sup>22</sup> <http://heritage.stsci.edu/2000/28/big.html>.

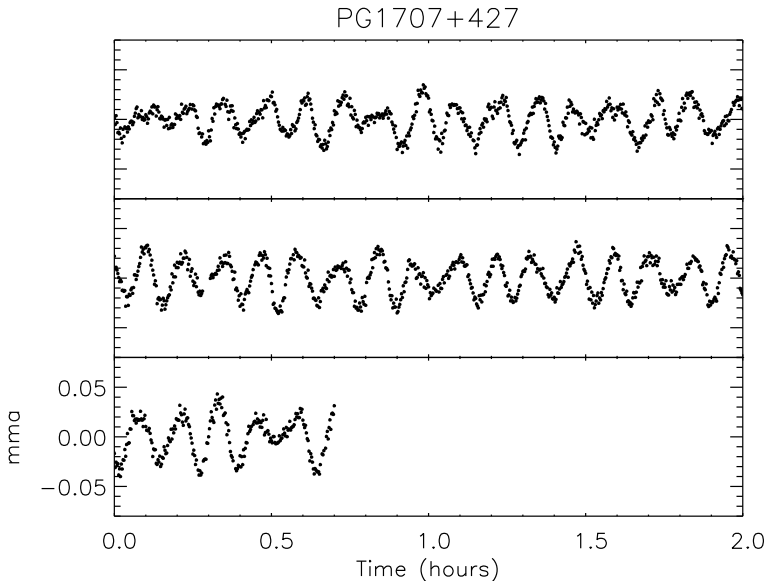


**Fig. 2.54.** Part of the light curve of the DOV white dwarf PG 1707+427 obtained during a WET campaign. Data taken from Kawaler *et al.* (2004).

ability of the [WCE] stars was interpreted in terms of oscillations by Gautschy (1995).

To make the picture even more complicated, we point out that Handler (2003a) performed a systematic study of what he termed variable Central Stars of young Planetary Nebulae, and baptized them *ZZ Lep stars* after the prototype in his sample. This group consisted of 14 members that he found to exhibit roughly sinusoidal (semi-)regular photometric and/or radial velocity variations with time scales of several hours. The sample stars' temperatures are below 50 000 K and they all show hydrogen-rich spectra. Although Handler (2003a) concluded that stellar pulsation is the most likely cause of the variability, he could not exclude variable mass loss. To our knowledge, this group of stars has not been studied further.

### 2.7.2.2 GW Vir Stars

Among the DO white dwarfs, the *PG 1159 stars* or, more recently termed the *GW Vir stars*, constitute a well-established class of 11 stars as of this writing (mid-2008). The DO white dwarfs are situated at the position in the HR Diagram where the post-AGB track stops and turns down towards the white dwarf cooling sequence. They have extremely high effective temperatures in the range 75 000 K to 170 000 K. Their spectra show a large deficiency in hydrogen and high helium, carbon and oxygen abundances due to their stellar

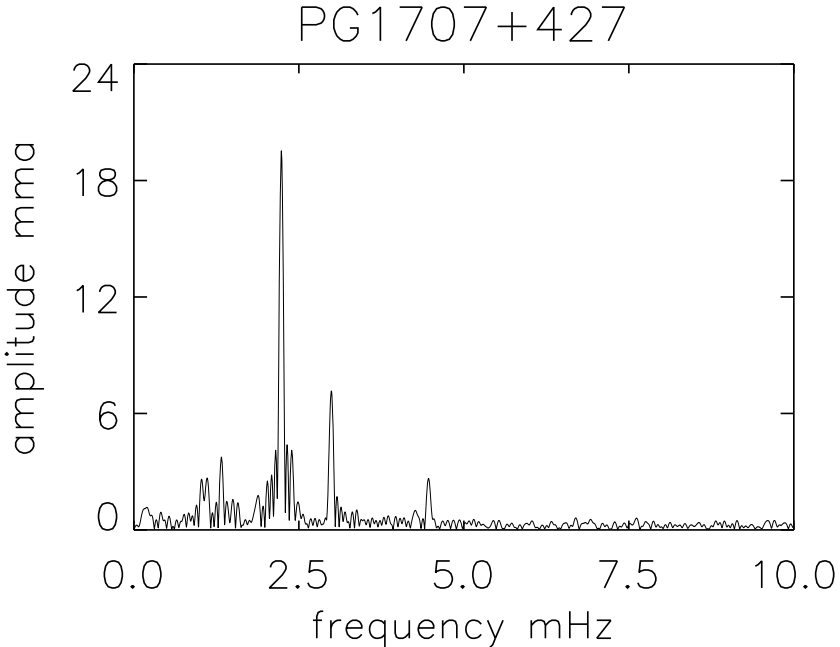


**Fig. 2.55.** The amplitude spectrum of the light curve of PG 1707+427 shown in Fig. 2.54.

wind and helium burning, respectively. The determination of the hydrogen abundance is rather difficult due to the high temperature. As outlined above, some GW Vir stars are termed PNNVs because a planetary nebula still occurs around them. DO white dwarfs are indeed the direct descendants of planetary nebulae nuclei.

The DOV (DO variable white dwarfs) pulsators are often named after their prototype, PG 1159–035 or GW Vir. This star, GW Vir itself, was discovered to be an extremely hot pulsating degenerate star by McGraw *et al.* (1979a,b). GW Vir's light variations observed by the Whole Earth Telescope<sup>23</sup> (WET, Nather *et al.* 1990) and their interpretation was a very important step for asteroseismology on which we will report in Chapter 7. Part of the DOV star PG 1707+427, and its resulting frequency spectrum, are shown in Figs 2.54 and 2.55 (Kawaler *et al.* 2004). These two plots are typical for most of the GW Vir pulsators.

Kawaler *et al.* (1985a,b) presented linear, nonradial adiabatic oscillation computations for evolutionary pre-white dwarf models, leading to predictions for the DOV star frequencies and eigenfunctions. The oscillation periods range from about 7 to 30 min. The modes are driven by the heat mechanism active

<sup>23</sup> <http://www.iastate.edu/wet>.

in the partial ionization zones of carbon and/or oxygen, as already suggested earlier by Starrfield *et al.* (1984). The exact shape of the instability domain near the kink of the evolutionary track was found to depend on the distribution of helium in the CO-rich envelope.

It is clear that the oscillation periods of several PNNVs are at least a factor of three longer than those of the DOV stars. The latter are white dwarfs that are about to start cooling, while the PNNVs are still increasing their effective temperature while keeping their luminosity essentially unchanged, *i.e.*, their radius is still decreasing drastically. This different evolutionary status is thus reflected in the oscillation period difference between the DOV stars and the PNNVs and is in agreement with the scenario of Werner & Herwig (2006).

The theoretical instability strip of both the PNNV and DOV stars was revisited by Quirion *et al.* (2004), Gautschy *et al.* (2005), C  rsico *et al.* (2006) and Quirion *et al.* (2007). From these studies, which include mass loss and diffusion, it became clear that one and the same instability mechanism, *i.e.*, the heat mechanism associated with the opacity bump due to partial ionization of the K-shell electrons in the ionization zones of carbon and oxygen, leads to an instability domain containing both the observed GW Vir stars and the [WCE] stars (see Fig. 6 of C  rsico *et al.* 2006). The instability requires the presence of carbon and oxygen in the atmosphere. This can only be achieved when the stars are subject to strong radiation pressure, causing the carbon and oxygen to remain in the envelope thanks to radiative levitation while the hydrogen is blown away in a stellar wind. As the luminosity of the star decreases, the wind becomes less strong and gravitational settling causes carbon and oxygen to sink, while helium starts floating to the surface. This diminishes the excitation of the GW Vir oscillations. This is in complete agreement with the strong evolutionary connection between the [WCE] and GW Vir stars derived by Werner & Herwig (2006). This scenario also leads to a natural explanation of the DBV pulsators whose oscillations are excited by the same heat mechanism, but this time acting on helium once it is sufficiently dominant and in the appropriate partial ionization stage in the envelope.

The seismic analysis of GW Vir presented in the seminal work by Winget *et al.* (1991) is discussed in detail in Chapter 7. This was not only a first test case for the technique of asteroseismology, but at the same time a real breakthrough in the derivation of white dwarf structure models. This study paved the road for many more seismic studies of compact stars since 1990, some of which we describe in Chapter 7. White dwarfs thus became the main targets of the WET consortium, although numerous other types of pulsators have also been studied by this group.

### 2.7.2.3 Variable DB White Dwarfs; the V777 Her Stars

Excitation of g-mode oscillations in DB white dwarfs due to the heat mechanism acting in the second partial ionization zone of helium was predicted by Winget (1982) (see also Winget *et al.* 1983a). This led to the discovery of

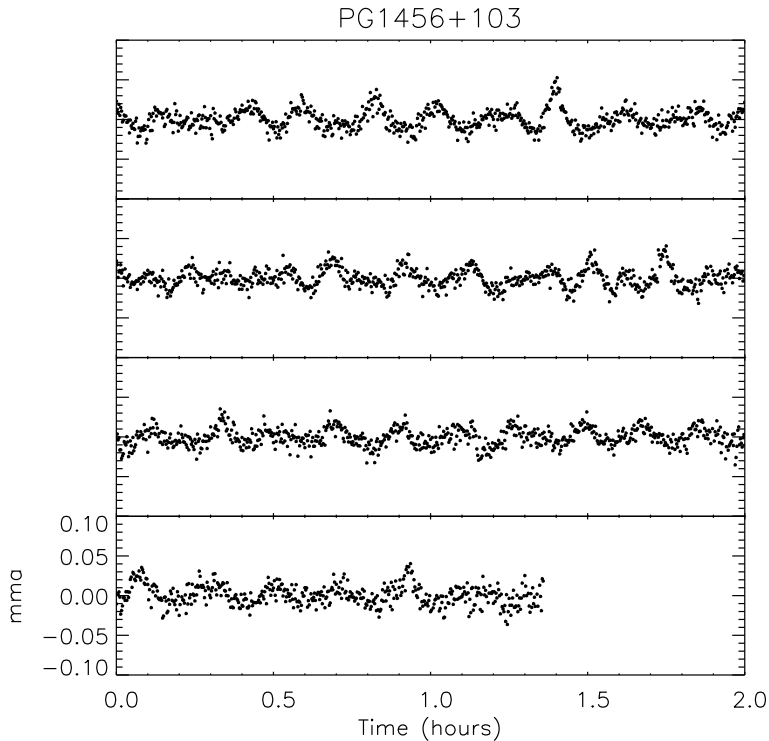


**Fig. 2.56.** Part of the light curve of the DBV white dwarf PG 1456+103 obtained with the Nordic Optical Telescope by Jan-Erik Solheim during a WET campaign (unpublished); from data provided by the WET consortium.

the first such *variable DB white dwarf*, also termed DBV star, namely GD 358 (Winget *et al.* 1982). Only 18 DBVs are known to date (Kepler 2007 and references therein; Nitta *et al.* 2007), probably due to their faintness ( $V$  near 16, except for the prototype GD 358 with a  $V = 13.6$ ). Their oscillation periods range from 4 to 16 min and their amplitudes are relatively large, from a few mmag to 0.2 mag. Bradley (1995) reviewed the properties of these stars. Their effective temperatures range from 22 000 to 28 000 K and the mass of their helium-rich envelope is estimated to be between  $10^{-6}$  and  $10^{-2}$  times their total mass. As already mentioned above, this is in full agreement with the excitation computations for hot compact stars by Quirion *et al.* (2007). It should be noted that convective driving, introduced by Brickhill (1991a) for variable DA white dwarfs, may also play an important role for the DB variables.

The light variations measured by the WET consortium of the simplest among the DBV pulsators, PG 1351+489, showed the star to have only two modes, with periods of 489 s and 333 s (Winget *et al.* 1987). The prototypical

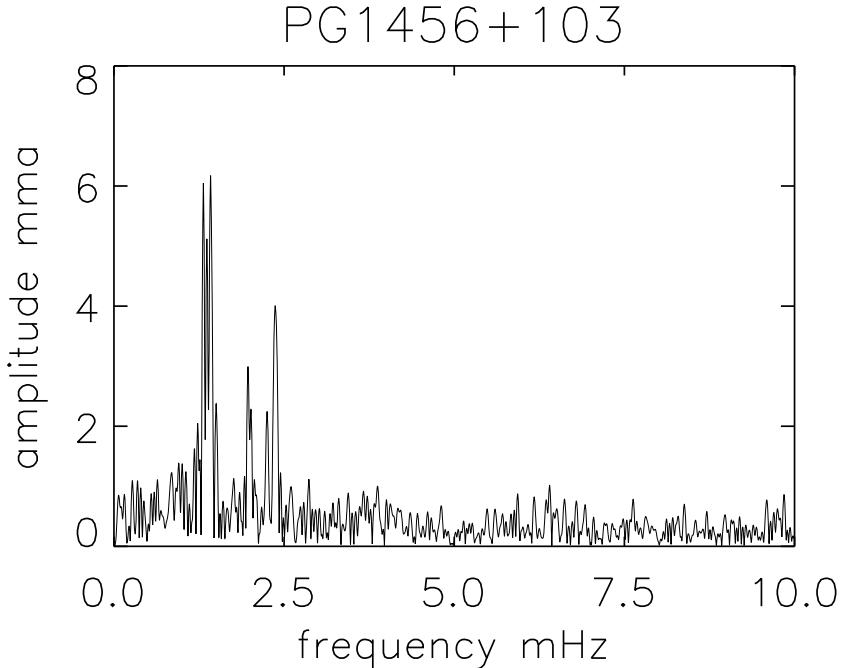


**Fig. 2.57.** The amplitude spectrum of the light curve of PG 1456+103 shown in Fig. 2.56.

DBV star GD 358, on the other hand, has a very complex frequency spectrum (Nather *et al.* 1990, see Chapter 7) with several tens of peaks. These two stars can be considered to capture the range of complexity across the DBV class. An intermediate case and its frequency spectrum are shown in Figs 2.56 and 2.57 for the star PG 1456+103 with data obtained during the WET run XCOV22 (extended coverage campaign 22, unpublished; see the WET website for more information).

Although the beating effect in GD 358 is prominent, the position of the peaks in the frequency spectrum turn out to be stable over long time scales while the amplitudes clearly vary (Kepler *et al.* 2003). Since GD 358 is by far the best studied DBV star, it was thought that the frequency spectra of all the class members were stable. Handler *et al.* (2003a), however, performed extensive monitoring of two DBV stars with the WET and found evidence for amplitude and frequency variability. They suggested nonlinear resonant mode coupling to be the cause of the complex variability in these two stars (see, *e.g.*, Buchler *et al.* 1997).

The potential of asteroseismology of DBV stars was highlighted by Bradley *et al.* (1993). Moreover, extensive seismic models and their oscillation properties for DBV and DAV stars had already been presented by Tassoul *et al.*

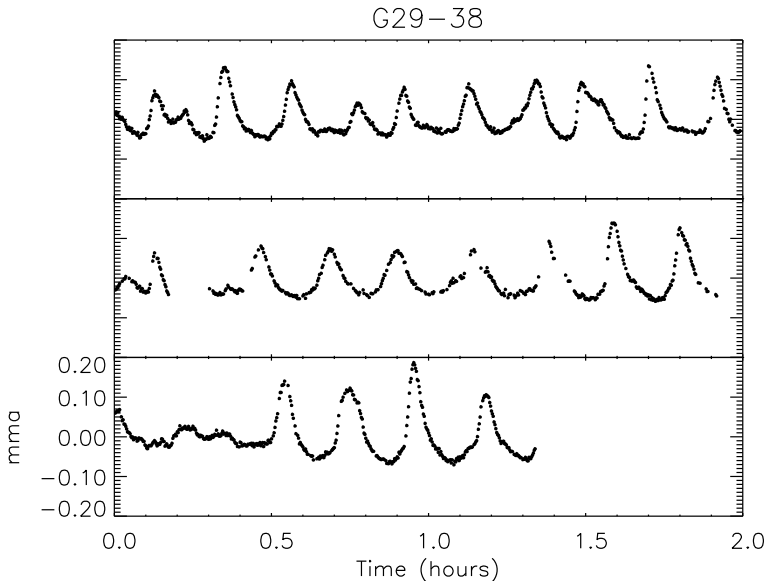


**Fig. 2.58.** Part of the light curve of the DAV white dwarf G29-38 obtained with the 0.75-m at SAAO by Retha Pretorius in the framework of a WET campaign (unpublished); data courtesy of the WET consortium.

(1990) and Bradley & Winget (1991), pointing out the maturity of this branch of asteroseismology more than a decade ahead of any other type of star, except the Sun.

#### 2.7.2.4 Variable DA White Dwarfs; the ZZ Cet Stars

Further along the white dwarf cooling track one finds the hydrogen-rich *variable DA white dwarfs*, also called DAV or ZZ Cet stars. The DAV mode excitation results from convective driving, a mechanism first proposed by Brickhill (1991a) and further developed by Goldreich & Wu (1999) and Wu & Goldreich (1999). The shape of the strip was found to be mainly determined by the effective temperature and the mass of the white dwarf, the most uncertain factor in theoretical mode prediction being the poorly known efficiency of convection. This is in very good agreement with empirical determinations of the instability strip leading to a very narrow range of less than 1 000 K in effective temperature, from 10 850 to 13 300 K (Bergeron *et al.* 2004, Mukadam *et al.* 2004b; Winget & Kepler 2008). It appears that within this narrow range of temperature all white dwarfs are ZZ Cet stars, although uncertainties in effective temperature and gravity leave this open to question.

The DAV stars vary multiperiodically with low amplitudes and fulfil a period-amplitude relation (Clemens 1994). The periods range from less than

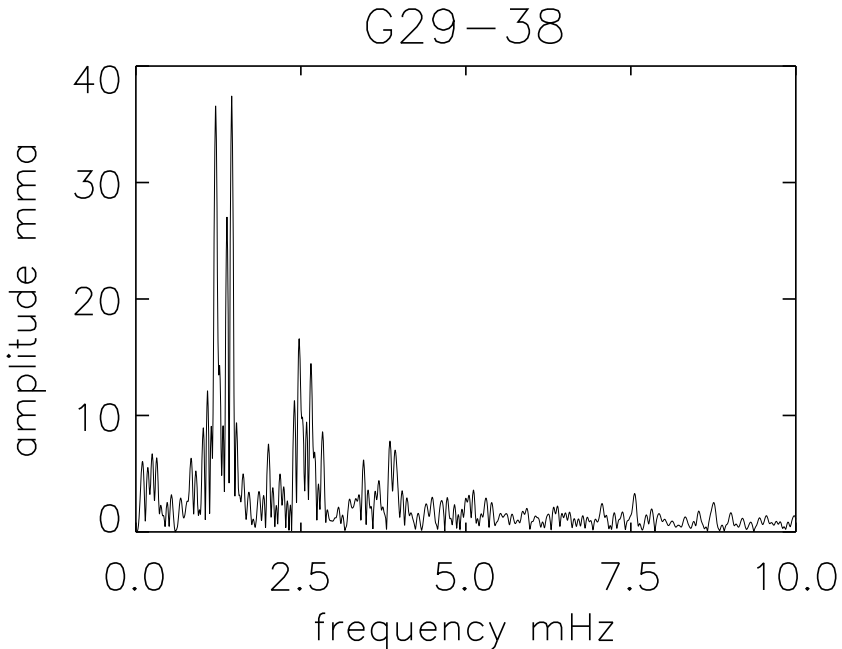


**Fig. 2.59.** The amplitude spectrum of the light curve of G29-38 shown in Fig. 2.58.

100 s to more than 1 000 s. Their frequency spectra also show multiplets and are, in general, simpler than those of the DBV and GW Vir stars. This may be an observational bias because the DAV pulsators have been less intensively monitored than the GW Vir and DBV pulsators. Indeed, the spectrum of the well-studied DAV star G29-38 appears to be very different, with numerous harmonics and beat and sum frequencies, from season to season (Vuille *et al.* 2000 and Figs 2.58 and 2.59).

While empirical mode identification in selected DAV stars is mostly achieved from multiplet structures in the frequency spectrum, or from amplitude ratios based on multicolour photometry, time resolved spectroscopy of G29-38 with the Keck telescope has allowed the identification of the modes from line profile variations as well (Clemens *et al.* 2000). All these mode identification techniques confirm the low degree nature of the oscillations. The thickness of the hydrogen envelope governs the mode selection. Typically, the mass of the hydrogen-rich envelope is estimated to be about  $10^{-4}$  times the mass of the white dwarf.

Up to 2004, 39 DAV pulsators were known (*e.g.*, Bergeron *et al.* 2004 and references therein), most of them discovered from photometry but 7 among them from spectroscopy. A remarkable step ahead in the understanding of the class was achieved by Mukadam *et al.* (2004a), who almost doubled the number of class members with their discovery of 35 new pulsating DAV stars

selected from the Sloan Digital Sky Survey and the Hamburg Quasar Survey. Mullally *et al.* (2005) subsequently found 11 new DAV stars, Kepler *et al.* (2005) another 14, and Castanheira *et al.* (2006) yet another 11, almost all again first selected from the Sloan Digital Sky Survey (the total number of members of the class is over 140 as of mid-2008). This led Mukadam *et al.* (2006) to examine changes in the pulsation properties of DAV pulsators across the instability strip. They found a well-established trend of increasing pulsation period with decreasing effective temperature. Also, they showed that the pulsation amplitude decreases just before pulsations shut down at the empirical red edge of the instability strip.

### 2.7.3 Neutron Stars

Neutron stars are the compact remnants that become gravitationally decoupled from the expanding ejecta of a supernova explosion, resulting from a core collapse of a single star with initial mass above  $9 M_{\odot}$ . The collapse results either in a compact neutron star with a mass between  $1.5$  and  $3 M_{\odot}$  and a diameter of about 12 km, or in a black hole (when the remnant mass is above about  $3 M_{\odot}$ ). The precise upper mass limit of a neutron star is not yet known, since the correct equation of state for a fully degenerate relativistic neutron gas is still much debated. Hence there is as yet no firm value for the analogue of the Chandrasekhar limit for the upper mass limit of a neutron star.

At birth, the infall causes a dramatic spin-up of the neutron star and a strengthening of its magnetic field by factors of millions, leading to a rotation period of only a few milliseconds to seconds, and likely causing the star to send out radiation along the magnetic field lines. As a result, the neutron star is observed as a *pulsar*, with regular pulses at radio, visible, X-ray or gamma-ray wavelengths, whenever the magnetic axis is inclined with respect to the rotation axis and when the geometry of the beam is such that the radiation passes in our line-of-sight during each rotation period. The radio waves originate from material above the magnetic poles, while the X- and gamma-rays are caused by the accretion of matter on the very hot magnetic poles of the neutron star.

Straight after the discovery of pulsars by Jocelyn Bell in the framework of her PhD Thesis (Hewish *et al.* 1968), nonradial oscillations were proposed as the explanation of the pulses (Ruderman 1968). Nevertheless, the pulsating model was quickly abandoned in favour of an oblique rotation model to explain the observed features of pulsars (Gold 1969). Only many years later, Strohmayer (1992) and Strohmayer *et al.* (1992) re-introduced nonradial oscillations to account for the numerous complex observed properties of pulsars, including drifting pulses and stationary sub-pulses, because the rotating models failed to explain all these details in the observed variability. The observational and theoretical progress in the understanding of pulsar beams was summarized by Graham-Smith (2003).

Clemens & Rosen (2004) presented an oblique pulsator model based on high overtone nonradial surface g-mode oscillations of very high degree ( $l$  near a few hundred and  $n$  near a few tens), aligned to, and symmetric about, the magnetic axis of the pulsar, as an explanation of the complex observed phase behaviour of the pulses and sub-pulses and of the morphology of pulsar beams. Such modes have periods near 10 s and were shown to have low energy and large surface amplitude (McDermott *et al.* 1988), in contrast to core g modes. The quasi-periodic changes in the data are explained as switching between modes of different  $l$  and  $n$ , while negative beating is held responsible for null detections occurring in the observed time series of the flux once in a while. These features of this model were claimed to be similar to mode changes observed for white dwarfs on the one hand, and to the oblique pulsator model explaining the roAp stars on the other hand. Quasi-periodic oscillations in soft gamma-ray repeaters have also been interpreted in terms of oscillation modes, causing seismic motion of the neutron star crust (Israel *et al.* 2005, Strohmayer & Watts 2006). At present, none of the pulsational models of neutron stars are sufficiently realistic to probe the interior physics to a level of precision necessary to constrain, *e.g.*, their equation of state. To reach this stage, one should make fully relativistic computations of a highly magnetized body with an elastic crust. The first steps are being undertaken (*e.g.*, Samuelsson & Andersson 2007).

A relatively new aspect of neutron star physics, in which nonradial oscillations could also play an important role, are the gravitational waves radiated during the formation process of the neutron star. After the gravitational collapse, the proto-neutron star radiates its binding energy through neutrino emission on a time scale of tens of seconds before the final neutron star is formed. This formation process is obviously very hard to study, unless we could detect the gravitational radiation associated with the birth of the hot compact remnant. Indeed, the oscillation spectrum of a forming neutron star changes drastically during the formation. This is easily understood from the argument that the frequencies are mainly dependent on the mass and radius of the object. Typically, the neutrino emission during the formation results in a mass decrease of  $0.1 M_{\odot}$  and a radius decrease from 35 km to 12 km. Such changes will have a significant effect on the mode frequency values.

Ferrari *et al.* (2003) have computed the changing frequency spectra and damping times of the oscillations of forming neutron stars. They found the oscillation spectra of p, g, and f modes of forming neutron stars to be remarkably different from those of cold old neutron stars. The frequencies of the modes cluster typically between 900 and 1500 Hz at the start of the formation process, but evolve to very distinct values for these three different types of modes about 5 s after the formation. Also, the different modes keep very different levels of the mechanical energy reservoir to send out in the form of gravitational waves after the completion of the formation. The authors ignored the effect of rotation, even though a significant amount of angular momentum is generated during the birth of the neutron star, and they ignored the bounce and

the first 200 ms after collapse, which needs to be studied hydrodynamically; even so, this pioneering study gives hopeful prospects for the near future. Ferrari *et al.* (2003) also showed that the first generation gravitational wave detectors (VIRGO<sup>24</sup>, LIGO<sup>25</sup>, EURO<sup>26</sup>) should be able to detect the gravitational signals connected to the nonradial oscillations sent out during these different stages in the life of the neutron star, within much of the Milky Way Galaxy. This would open up the field of gravitational wave asteroseismology. Similarly, the processes leading to the formation of stellar black holes may involve oscillations that can be detected through observations of gravitational waves.

## 2.8 Pulsations in Binaries

For all the classes considered above, numerous examples occur where the pulsating star resides in a binary or, more generally, in a multiple system. When this is a wide visual binary, *i.e.*, for cases where the components do not affect each other's behaviour and evolution, the binarity is of not much importance for the oscillation study, other than being an asset because it allows a more accurate determination of the fundamental parameters (such as mass, radius and age) of the pulsating component compared with a single pulsator. A notable example is the visual binary  $\alpha$  Cen A (G2V) and  $\alpha$  Cen B (K1V), whose components both show p-mode oscillations (see Chapter 7). At the upper end of the mass range, the visual binary WR 86 is worth mentioning. It is a variable WC7 Wolf-Rayet star with an initial mass of some  $40 M_{\odot}$  having a  $20 M_{\odot}$   $\beta$  Cep companion (Paardekooper *et al.* 2002). This companion pulsates in p modes with frequencies of  $6.914 \text{ d}^{-1}$  and  $7.236 \text{ d}^{-1}$ . Contrary to the  $\alpha$  Cen binary, the oscillations of this very massive binary have not yet been exploited seismically, because of lack of mode identification.

Binarity offers the same advantage of providing accurate fundamental parameters in close unevolved detached binaries for which the tidal interaction is negligible. In general, this is the case for orbital periods above some 20 d for ZAMS components and above some 100 d for TAMS components (Willems 2003). In such cases, a complication may, however, occur when both components have the same spectral type, implying a merging of their oscillatory signature in the data and hence in the Fourier spectrum. As long as the contributions of the different components can be unravelled, seismic modelling can be achieved to at least the same level as for single stars.

Another type of complication occurs when one of the components of a currently detached close binary system has already gone through one or more phases of mass loss during its evolution, usually implying that mass transfer

---

<sup>24</sup> <http://www.cascina.virgo.infn.it/>.

<sup>25</sup> <http://www.ligo.caltech.edu/>.

<sup>26</sup> <http://www.astro.cardiff.ac.uk/geo/euro/>.

between the components has taken place. In such a situation, the gainer star is polluted by material of the donor star. This may have led to different surface compositions and internal structures of both the gainer and the donor, depending on whether the outer envelope is radiative or convective. Hence, if one of them is oscillating, the mass transfer will have affected the oscillatory behaviour. In fact, asteroseismology may in this case be a good tool to reconstruct the mass transfer and angular momentum history within the binary. Unfortunately, we do not know of any example where such reconstruction of the evolutionary history from oscillations has been achieved.

Extreme cases of interaction occur when a binary system enters a *common envelope phase* where a compact component of the system effectively orbits within the envelope of a more tenuous component. This leads to rapid loss of mass and angular momentum, and hence to a drastic shrinking of the orbit.

Eclipsing binaries are of special value, because they deliver the most stringent constraints on the physical parameters of the components. For many of the classes of pulsating stars discussed above, we know of components residing in an eclipsing binary. The number of such cases is low, however, ranging from none for solar-like oscillators, roAp,  $\gamma$  Dor, RR Lyrae stars and Cepheids, to a few for B-type pulsators and compact oscillators, to a few tens for  $\delta$  Sct stars, Miras and semi-regulars (Pigulski 2006). The CoRoT and Kepler missions (see Chapter 8) will surely revolutionize the study of pulsators in eclipsing binaries. In principle, the oscillation modes can be identified from eclipse mapping in such cases. We come back to this possibility in Chapter 6.

Excellent overviews of pulsating stars in multiple systems (including clusters) were provided by Pigulski (2006) and Lampens (2006). In the following, we describe in detail some situations where the binarity is more than just a happy circumstance that delivers better fundamental parameters. In doing so, we do not consider disc oscillations as in, *e.g.*, X-ray or Be binaries; we focus entirely on cases where the oscillations can, in principle, be used to probe the stellar interiors rather than focusing on stellar disc properties.

### 2.8.1 Tidal Perturbations of Free Oscillations

An extensive compilation of studies on the tidal evolution and oscillations in binary stars is available in Claret *et al.* (2005). Free oscillation modes excited by mechanisms intrinsic to the star (see the following chapter for a detailed explanation of such excitation mechanisms) may be altered by tidal effects, in the sense that their frequencies may undergo shifts. Rigorous and detailed mathematical descriptions of tidal effects on free oscillation modes can be found in Smeyers & Denis (1971), Saio (1981), Reyniers & Smeyers (2003a,b), Willems & Claret (2005), and references in these works.

Detections of tidal effects were first suggested by Fitch (1967, 1969) in some  $\delta$  Sct and  $\beta$  Cep stars, but it became evident later on that these were premature. The first firm observational establishment of tidally affected oscillation frequencies was achieved by Fitch & Wisniewski (1979) for the  $\delta$  Sct

star 14 Aur Aa. The authors showed that the departure from equidistance in the observed frequency triplet can be explained by tidal splitting of the mode, as was confirmed by Reyniers & Smeyers (2003b). Goossens *et al.* (1984) suggested the variations of the oscillation frequency of the 33 d circular binary  $\beta$  Cep star  $\sigma$  Sco to be due to modulation by tidal action. Smith (1985a,b) subsequently made a thorough study of the line profile variability of the binary  $\beta$  Cep star Spica ( $\alpha$  Vir), with period 4.015 d and eccentricity  $e = 0.146$ , and interpreted the retrograde, toroidal-like oscillation mode he detected to be due to tidal shear exerted by the B2 companion.

There are also a number of pulsating stars in ellipsoidal variables, in which the tidally deformed components cause variability with twice the orbital frequency (*e.g.*, Aerts 2007 for a review). A noteworthy example is the star XX Pyx (Handler *et al.* 1998, 2000) which was long considered as a prototypical young  $\delta$  Sct star suitable for seismic modelling (Pamyatnykh *et al.* 1998) until Arentoft *et al.* (2001a) and Aerts *et al.* (2002b) found it to be a binary in a 1.15 d circular orbit with ellipsoidal variations in which tidal effects dominate over rotational effects. Henry *et al.* (2004) found HD 207651 to be a triple system with  $\delta$  Sct and ellipsoidal variations but no g modes triggered by tides. Lampens *et al.* (2005) also found the presence of ellipsoidal variations in the spectroscopic triple system DG Leo, which is composed of three stars of late-A spectral type. The wide component is a  $\delta$  Sct star while the inner binary consists of two Am components of which at least one is not yet rotating synchronously although the orbit is circular. Finally, De Cat *et al.* (2006, 2007) list several ellipsoidal variables among their samples of candidate  $\gamma$  Dor and pulsating B stars.

Numerous other pulsating stars reside in close binaries, but their detected frequencies, or differences among them, are not an exact multiple of the orbital frequency. Aerts & Harmanec (2004) compiled a list of close binaries with confirmed light and/or line profile variability, several of which are confirmed pulsators, so these are all good candidates to continue the search for tidally affected and/or induced oscillations. This list originated from two independent approaches, *i.e.*, the search for close binarity among confirmed pulsators and the search for oscillations in confirmed close binaries. The authors found no obvious relations among the orbital eccentricity, the orbital frequency, the rotational frequency and the intrinsic frequencies of oscillations.

### 2.8.2 Tidally Induced Oscillations

It was realized long ago that resonant excitation of free oscillation modes by the tidal action of a companion can in principle be an effective way to trigger oscillations in binary components (Cowling 1941). Tidally induced oscillations and their effect on evolution and energy dissipation within a binary have been studied theoretically, for very different types of situations, by numerous authors, *e.g.*, Kato (1974), Zahn (1975), Savonije & Papaloizou (1984), Kosovichev & Novikov (1992), Diener *et al.* (1995), Witte & Savonije (1999ab;

2001), Savonije & Witte (2002), Willems *et al.* (2003), Rathore *et al.* (2005) and references in these works. These authors show that the occurrence of suitable resonances depends not only on the properties of the oscillation modes of the stars, but mainly also on the period and the eccentricity of the orbit, as well as on the component masses and radii. The theoretical computations show that the tide generating potential within an eccentric binary implies an infinite number of partial dynamic tides with forcing angular frequencies. Whenever one of those forcing frequencies comes close to an eigenfrequency of a free oscillation mode of one of the components, it is possible that the tidal action exerted by the companion is sufficiently enhanced to excite this mode resonantly. The occurrence of such resonances between partial dynamic tides and free oscillation modes is particularly relevant for the excitation of g modes, because their frequencies are similar to those of the orbital frequencies in close binaries. Moreover, the tide generating potential is dominated by spherical harmonics of degree  $l = 2$ . Most computations for resonant excitation are therefore restricted to these modes. As discussed by, for example, Kosovichev & Novikov (1992) the excitation of modes through tidal interaction and the subsequent dissipation of the pulsation energy may play an important role in the capture of stars by massive black holes, through the loss of orbital energy by the star.

From an observational viewpoint, the detection of a tidally induced oscillation may seem simple at first sight. Indeed, whenever variations with an exact multiple of the orbital frequency are found, one may interpret these as due to a resonantly excited mode. In practice, it turns out to be extremely difficult to establish proof of tidally induced oscillations, despite numerous long term efforts to search for a relationship between the orbital frequency and variability in close binaries (*e.g.*, Aerts & Harmanec 2004; Claret *et al.* 2005, and references therein).

The detection of frequencies which are an exact multiple of the orbital frequency has, as far as we know, been established for only two stars so far: the hybrid  $\delta$  Sct/ $\gamma$  Dor star HD 209295 (Handler *et al.* 2002) and the SPB star HD 177863 (De Cat *et al.* 2000; Willems & Aerts 2002). These two stars reside in short period eccentric binaries such that the circumstances are indeed favourable for tidal resonant excitation. Seismic modelling has not yet been possible for either of these stars. For HD 209295 the modes could not be identified, while only one pulsation frequency was firmly established for HD 177863.

### 2.8.3 Are the SX Phe Stars all Blue Stragglers?

Blue straggler stars get their name from the fact that they appear close to the main sequence in stellar clusters, but substantially hotter and bluer, and hence presumably more massive, than the turn-off in the colour-magnitude diagram as defined by the bulk of the stars in the cluster. They are believed to be formed from the evolution and mass exchange of primordial binaries or from

direct stellar collisions between main sequence stars in dense globular clusters (e.g., Bailyn 1995; Hurley *et al.* 2001; Sandquist 2005; Sills *et al.* 2005, and references therein). The blue stragglers have significantly smaller projected rotational velocities, but the same chemical peculiarities, as ordinary cluster and galactic field stars of the same spectral type (Andrievsky *et al.* 2000). Ferraro *et al.* (2006) detected 300 candidate blue stragglers in the galactic globular cluster  $\omega$  Cen. They used the absence of central concentration in the blue straggler distribution across  $\omega$  Cen as an argument to rule out a collisional origin for all of the blue stragglers and suggest a non-collisional origin for some of these stars. An interesting cluster is NGC 2506, in which Arentoft *et al.* (2007) discovered several oscillating blue stragglers, along with a number of new  $\gamma$  Dor stars. Hurley *et al.* (2005) used M67 as a test bed for cluster evolution models and found different formation paths for the 28 observed blue stragglers in that cluster. In particular, a substantial population of short period primordial binaries is needed to explain the observed blue straggler population of M67. Bruntt *et al.* (2007) determined a large number of frequencies for two blue stragglers in M67. Unfortunately, mode identification is not available for these two stars, preventing seismic modelling so far.

It is a lucky circumstance that many of the SX Phe stars were found to be blue stragglers. They seem to have a relatively high mass (Rodríguez & López-González 2000). These pulsating blue stragglers are thus interpreted in terms of binary mergers leading to a globally mixed helium-enriched star and their oscillations may provide clues to the formation scenario. Gilliland *et al.* (1998) made an extensive study of six SX Phe variables in the globular cluster 47 Tuc with the Hubble Space Telescope. Two of them oscillate in the fundamental and first overtone, two others oscillate simultaneously in the fourth and fifth radial overtones and two have multiple nonradial oscillations. This allowed the authors to combine evolution and pulsation constraints, resulting in mass estimates for the four double-mode SX Phe stars ranging from  $1.3 \pm 0.1 M_{\odot}$  to  $1.6 \pm 0.2 M_{\odot}$ , and additional stellar parameters which are in excellent agreement with the cluster properties. Zhang *et al.* (2005) analysed two SX Phe stars in M67. They found these stars to have, respectively, four and five radial modes. One of them has fundamental parameters in line with an unevolved late A star. The other one is the primary of a 4.2-d eccentric spectroscopic binary and has subsynchronous rotation. This SX Phe star was probably formed through stable Roche lobe overflow.

The global enrichment of helium in blue stragglers strongly affects the temperature and luminosity of a given star, but the location of the instability strip blue edge and the slope of the period-luminosity (PL) relation are unchanged. This suggests that the PL relation is not affected by blue straggler formation provided that blue stragglers are fully mixed stellar mergers (Templeton *et al.* 2002). Nevertheless, Bono *et al.* (2002) found that the modal stability and the pulsation amplitudes are somehow affected by the He content. The detailed properties of SX Phe stars could thus supply hints on the He content and on

the formation history of these stars, but we believe it is fair to state that this stage has not yet been reached.

#### 2.8.4 Are all Dusty RV Tauri Stars Binaries?

Binaries make up a significant fraction of the post-AGB stars known to date (Van Winckel 2003). It was suggested by Lloyd Evans (1999) that IRAS (Infrared astronomical satellite) infrared colours imply that RV Tau stars are stars within the Cepheid instability strip with dusty circumstellar discs. By comparing the observational characteristics of RV Tau stars and the class of extremely iron deficient post-AGB objects, Van Winckel *et al.* (1999) concluded that binarity is indeed a widespread phenomenon among RV Tau stars.

Yudin *et al.* (2003) monitored eight RV Tauri and five R CrB stars (see below) polarimetrically, and established the presence of permanent clumpy non-spherical dust shells around them. Moreover, De Ruyter *et al.* (2006) provided compelling evidence from spectral energy distributions extending to  $850\,\mu\text{m}$  that all six well-studied dusty RV Tauri stars are binaries with a circumbinary disc originating from the AGB evolutionary stage.

The question naturally arises whether all RV Tauri stars are binaries. In any case, the large amplitude oscillations play a key role in the rapid mass loss phase on the AGB where the stars undergo a dust driven stellar wind. Mass transfer between evolving stellar components in a binary then leads to a natural explanation of a dusty circumbinary configuration and the observed infrared properties of the RV Tauri stars. This, together with the fact that their binary nature is very hard to establish on a case-by-case basis, makes it very likely that all dusty RV Tauri stars result from the evolution of a pulsating AGB binary that managed to avoid a common envelope phase. It requires very long term spectroscopic monitoring to establish firm observational proof of this, because the pulsations cause radial velocity variations that are of similar magnitude to the orbital variations (see Fig. 2.38).

#### 2.8.5 Hydrogen-Deficient Carbon Stars and Extreme Helium Stars

R Coronae Borealis (R CrB) stars are a particular subset of evolved pulsating hydrogen-deficient carbon (HdC) stars with large amplitudes. They have periods between 40 and 100 d, amplitudes of a few tenths of a magnitude in brightness (see Fig. 2.60) and a few  $\text{km s}^{-1}$  in velocity, and they have multi-periodic light curves (*e.g.*, Lawson & Kilkenny 1996). In general, the HdC stars are variables with an order of magnitude lower amplitudes than the R CrB stars. Both the R CrB stars and the HdC stars seem to be fundamental mode pulsators (Weiss 1987) with semi-regular light and radial velocity curves. In addition to pulsational variations, Feast *et al.* (1997) concluded from extensive long term infrared photometry that the R CrB and HdC stars in general show variations due to their circumstellar dust on time scales of a few hundred to a few thousand days.

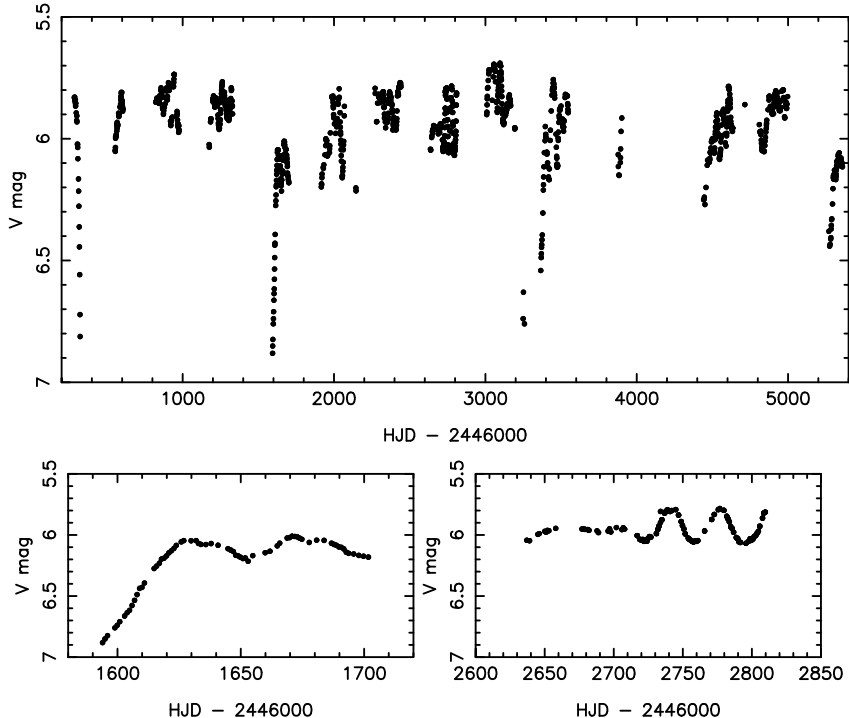


**Fig. 2.60.** Top: Light curve of the HdC pulsator R CrB. The bottom panels show two enlarged sections. Data taken from Yudin *et al.* (2002).

Extreme helium (eHe) stars, on the other hand, are highly evolved luminous stars (*e.g.*, Jeffery 1996). Their surfaces are characterized by a mixture consisting of the remnant of a H envelope, CNO-processed elements, and carbon products resulting from He burning. The eHe stars have high  $L/M$  ratios. They are expected to pulsate, either due to the heat mechanism based on the Z bump (Saio 1993, 1995; Jeffery & Saio 1999) or due to strange-mode instabilities (Saio & Jeffery 1988). The variable eHe stars are sometimes subdivided into categories according to their type of oscillation: V652 Her variables are radial and nonradial Z bump pulsators with periods near 0.1 d, PV Tel variables have radial strange modes with characteristic periods near 20 d (Kilkenny *et al.* 1999) while V2076 Oph variables seem to have nonradial strange modes with time scales between 0.5 and 8 d (Jeffery & Heber 1992; Glatzel & Gautschy 1992). The variations turn out to be very complex, with quasi-multiperiodicity only, and imply an observational challenge in view of the long periods. In fact, Wright *et al.* (2006) made a very extensive long term observational study of the hottest pulsating eHe star, V2076 Oph, and found no coherence at all in its variability. In particular, they did not manage to

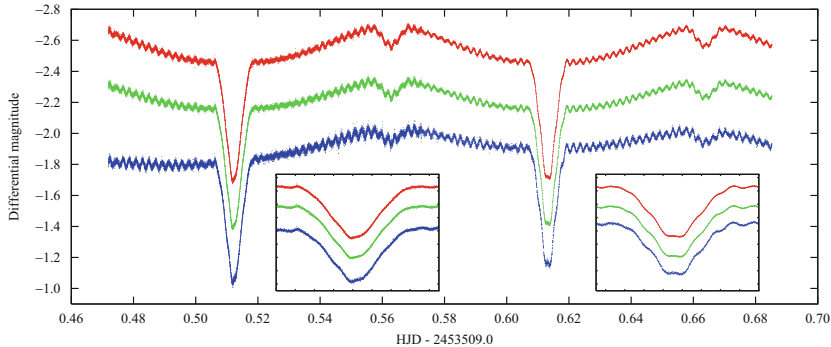


**Fig. 2.61.** The light curve for PG 1336 obtained with ULTRACAM on the Very Large telescope (VLT) on the night of 2005 May 18/19. The filters used were SDSS  $r'$  (upper curve),  $g'$  (middle curve) and  $u'$  (lower curve). The insets show the visibility of the pulsations through the primary eclipse. The ellipsoidal variability of the primary star, both primary and secondary eclipses, and the pulsations are all clearly seen. From Vučković *et al.* (2007).

recover the periods reported earlier in their photometry and spectroscopy of the star.

From an evolutionary point of view, all of the R CrB, HdC and eHe stars lie on post-AGB evolutionary tracks. Iben *et al.* (1996) originally considered three scenarios to form HdC and R CrB stars, but only two of them are commonly accepted now. A first one explains the HdC and R CrB stars as hydrogen deficient due to a late thermal pulse at the end of the post-AGB phase. The result of this born-again scenario is an HdC star with chemical surface composition in agreement with progenitors of WR stars or of hot planetary nebulae nuclei. De Marco *et al.* (2002) tested the born-again scenario on four stars but concluded that they cannot have the same evolutionary history since only two of the targets are compatible with the proposed scenario. The second scenario involves the merging of two low mass white dwarfs, one CO white dwarf and one lower mass He white dwarf, resulting in a luminous He star (Saio & Jeffery 2002). This is much more plausible as an explanation for the eHe stars, and as these show many similarities to the HdC and R CrB stars, it is probably also an important route to explain these latter objects.

## 2.8.6 Pulsating sdB Primaries

The prototypical pulsating sdB star EC 14026–2647 is a binary system, as is the case for about two thirds of the group members (Maxted *et al.* 2001; Morales-Rueda *et al.* 2003, 2005). It is very likely that the binarity is of fundamental importance for the formation of all the sdB stars. The sdB stars are believed to evolve directly to the white dwarf stage and so they are the immediate progenitors of low mass white dwarfs. Two of the members are

indeed found in a post-EHB stage (Morales-Rueda *et al.* 2003). The details of the evolutionary state of the sdB stars is still largely unknown. In order to end up on the EHB they must lose nearly all of their hydrogen at almost exactly the same phase, *i.e.*, when the helium core has attained the minimum mass required for the helium flash to occur. Moreover, many of them have short orbital periods between a few hours and a few days and several known companions are white dwarfs. These observational facts have led to the proposal of three evolutionary channels for the formation of sdB stars (see Han *et al.* 2002, 2003 and references therein):

1. common envelope ejection, leading to short period binaries with periods between 0.1 and 10 d and an sdB star with a very thin hydrogen envelope; these sdB stars have a mass distribution that peaks sharply at  $0.46 M_{\odot}$ ;
2. stable Roche lobe overflow, resulting in similar masses as in case 1, but with a rather thick hydrogen-rich envelope and longer orbital periods between 10 and 100 d;
3. double helium white dwarf mergers giving rise to single sdB stars with a wide distribution of masses.

An example of case 1 is the eclipsing binary pulsating sdBV PG1336-018 whose stunning light curve was discovered Kilkenny *et al.* (1998). This star has been intensively studied ever since, including during two WET runs (Kilkenny *et al.* 2003, see also Chapter 7). We show its  $g'$  light curve obtained with ULTRACAM<sup>27</sup> on the VLT in Fig. 2.61. The circular binary orbit has a period of 2.4 h and the companion is an M dwarf, leading to a large reflection effect. As can be seen in Fig. 2.61, the oscillations of the primary remain visible during the primary eclipse.

An important question is the possible role of the binarity in triggering the oscillations of sdB stars. This has been tackled by Fontaine *et al.* (2003b), who found that, indeed, the work done by the tidal force through the resonant excitation of a g mode becomes significant as the order of the mode increases. Thus, it seems plausible that some of the g modes observed in sdB binary pulsators may be tidally excited. It is unlikely that the p modes are tidally excited, because their frequencies are too high for that. They may, however, turn out to be affected by the binarity (see, *e.g.*, Reed *et al.* 2005).

### 2.8.7 Pulsating Cataclysmic Variables

Cataclysmic Variables (CVs) are short period interacting close binaries with a white dwarf component. The white dwarfs within such systems undergo mass accretion from their companion. The white dwarf component itself is often invisible, because the accretion process dominates the flux we receive from CVs. The accretion rates vary significantly from one CV to the other. For those systems with a low mass transfer rate, the gas of the donor settles in

---

<sup>27</sup> <http://www.shef.ac.uk/physics/people/vdhillon/ultracam/>.

a disc. This stored gas settles onto the white dwarf at semi-regular intervals, leading to a dwarf nova eruption. The white dwarf components of such systems are detectable in visible light when the systems are in a low quiet state. Such CVs are, however, intrinsically faint. Several of them have been discovered from the Sloan Digital Sky Survey (Szkody *et al.* 2004).

Several CVs turn out to have a pulsating DAV primary. The first such system discovered was GW Lib (Warner & van Zyl 1998), a dwarf nova with an orbital period of 76.8 min for which three oscillation modes with periods of 646 s, 377 s, and 236 s were established in the discovery paper. Several additional discoveries, involving systems with similar orbital periods, followed soon (Warner & Woudt 2005 and references therein). All of them turn out to have similar oscillation periods ranging from 100 s to 1 400 s. More than ten pulsating CV primaries have been discovered meanwhile (Marsh, private communication).

Townsley *et al.* (2004) managed to derive estimates of the white dwarf mass, the accreted mass and the mass transfer rate for GW Lib from seismic modelling. The rotation rate could not be derived, because the multiplet structure in its Fourier spectrum has not been resolved, despite extensive observational effort (van Zyl *et al.* 2004). It turns out that the accretion rate of the pulsating CV primaries is sufficiently low to keep the white dwarf component in the DA instability strip, even though a white dwarf of its age should be much too cool to be a DAV star. A natural question of course emerges: are the accretion rates within CVs with DO or DB primaries suitable to keep these white dwarfs in the corresponding instability strip as well?

AM CVn is the prototype of a class of ultra-short period helium-accreting cataclysmic binaries. It turns out that the AM CVn stars probably have a mass transfer rate that is too high for them to remain in the DO or DB instability strips, so it is unlikely that there will be many discoveries of pulsating primary AM CVn stars. Nevertheless, Solheim *et al.* (1998) monitored AM CVn in photometry over a 12-d time span during a WET run. While several periodic light modulations with harmonics of the basic frequency near  $950\,\mu\text{Hz}$  can be explained as a two-armed spiral structure (Savonije *et al.* 1994), the authors also found evidence for a g-mode pulsation, which indicates that the central white dwarf may in fact be a DO variable. Arras *et al.* (2006) indeed concluded from theoretical instability computations for a wide range of white dwarf masses that g-mode oscillations are predicted in a diversity of CVs.

Recently, Montgomery *et al.* (2008) discovered light variability in a hot DQ (carbon atmosphere) white dwarf star, SDSS J142625.71+575218.3, with significant amplitude at 417.7 s and 208.8 s. Their study followed the discovery of six DQ white dwarfs reported by Dufour *et al.* (2007). Montgomery *et al.* (2008) discuss the possibility that this may be the prototype of a new class of pulsating white dwarfs, but they also show that the light curve is remarkably similar to that of AM CVn, so that it may be a carbon analogue of AM CVn. Indeed, current evolutionary scenarios do not predict the existence of DQ white dwarfs and binarity may be an important factor in their

formation. Fontaine & Brassard (2008b), on the other hand, made instability computations for single white dwarfs and confirms that there exists a DQV instability region. Thus, while the precise nature of these stars and their relation to the AM CVn stars certainly needs further studies, the DQV stars may constitute an interesting new class of compact pulsators, in any case.

### 2.8.8 X-Ray Burst Oscillations

Many of the currently known neutron stars reside in close binaries, as this is a very convenient location to allow their observational detection. Besides the importance of surface oscillations in explaining the observed complex features of neutron stars discussed above, Piro & Bildsten (2006) provided evidence that nonradial surface g modes are also a good explanation for X-ray burst oscillations. Such burst oscillations are thought to be a modulation of the neutron star rotation frequency. Piro & Bildsten’s model builds further on the original ideas by Lee (2004) and Heyl (2004) that a retrograde surface mode with an observed frequency just below the rotation frequency is the cause of the burst oscillations.

## 2.9 Conclusions

This completes our introductory journey through the HR Diagram shown in Fig. 1.12. The rich diversity of pulsating stars that allow – or have the potential to allow – asteroseismic inference is impressive. New classes of pulsating stars continue to be discovered; new extreme examples that test the physical limits of known classes continue to be discovered. Most importantly, both new and established observational techniques (that we look at in Chapter 4) and vigorous new efforts are producing unprecedented data sets for asteroseismic study. We return to the details of some of the most successful studies in Chapter 7. Next, we turn to fundamental theory of asteroseismology in Chapter 3.

# 3

---

## Theory of Stellar Oscillations

To evaluate the diagnostic potential of stellar oscillations and develop effective methods to interpret the observations we need an understanding of the possible modes of oscillation and of the dependence of their frequencies on the properties of the stellar interior. This is based on numerical computations of oscillations for different stellar models, but various forms of asymptotic analysis are also highly illuminating for the understanding and form the basis for very efficient techniques to interpret the observations.

In the present Chapter we develop the theoretical foundation for the study of stellar oscillations, starting with a brief summary of the relevant aspects of hydrodynamics, and consider some examples of the behaviour of the modes, in terms of numerical calculations and asymptotic analysis. Aspects that are particularly relevant to the Sun and solar-like stars are taken up in Chapter 7.

### 3.1 General Hydrodynamics

To provide a background for the presentation of the theory of stellar oscillations, this section briefly discusses some basic principles of hydrodynamics. A slightly more detailed description, but still essentially without derivations, was given by J. P. Cox (1980). In addition, any of the many detailed books on hydrodynamics (*e.g.*, Landau & Lifshitz 1966; Batchelor 1967; Thompson 2006) can be consulted. Ledoux & Walraven (1958) give a very comprehensive introduction to hydrodynamics, with special emphasis on the application to stellar oscillations.

#### 3.1.1 Equations of Hydrodynamics

It is assumed that the gas can be treated as a continuum, so that its properties can be specified as functions of position  $\mathbf{r}$  and time  $t$ . These properties include the local density  $\rho(\mathbf{r}, t)$ , the local pressure  $p(\mathbf{r}, t)$  (and any other thermodynamic quantities that may be needed), as well as the local instantaneous

velocity  $\mathbf{v}(\mathbf{r}, t)$ . Here  $\mathbf{r}$  denotes the position vector to a given point in space, and the description therefore corresponds to what is seen by a stationary observer. This is known as the *Eulerian* description. In addition, it is often convenient to use the *Lagrangian* description, which is that of an observer who follows the motion of the gas. Here a given element of gas can be labelled, *e.g.*, by its initial position  $\mathbf{r}_0$ , and its motion is specified by giving its position  $\mathbf{r}(t, \mathbf{r}_0)$  as a function of time. Its velocity

$$\mathbf{v}(\mathbf{r}, t) = \frac{d\mathbf{r}}{dt} \quad \text{at fixed } \mathbf{r}_0 \quad (3.1)$$

is equivalent to the Eulerian velocity mentioned above.

The time derivative of a quantity  $\phi$ , observed when following the motion, is

$$\frac{d\phi}{dt} = \left( \frac{\partial \phi}{\partial t} \right)_{\mathbf{r}} + \nabla \phi \cdot \frac{d\mathbf{r}}{dt} = \frac{\partial \phi}{\partial t} + \mathbf{v} \cdot \nabla \phi . \quad (3.2)$$

The time derivative  $d/dt$  following the motion is also known as the material time derivative; in contrast  $\partial/\partial t$  is the local time derivative (*i.e.*, the time derivative at a fixed point).

The properties of the gas are expressed as scalar and vector fields. Thus we need a little vector algebra; convenient summaries can be found, *e.g.*, in books on electromagnetism (such as Jackson 1975; Reitz *et al.* 1979). In addition, we need Gauss's theorem:

$$\int_{\partial V} \mathbf{a} \cdot \mathbf{n} dA = \int_V \operatorname{div} \mathbf{a} dV , \quad (3.3)$$

where  $V$  is a volume, with surface  $\partial V$ ,  $\mathbf{n}$  is the outward directed normal to  $\partial V$ , and  $\mathbf{a}$  is any vector field. From this one also obtains

$$\int_{\partial V} \phi \mathbf{n} dA = \int_V \nabla \phi dV \quad (3.4)$$

for any scalar field  $\phi$ .

### 3.1.1.1 The Equation of Continuity

The fact that mass is conserved can be expressed as

$$\frac{\partial \rho}{\partial t} + \operatorname{div} (\rho \mathbf{v}) = 0 , \quad (3.5)$$

where  $\rho$  is density. This is a typical conservation equation, balancing the rate of change of a quantity in a volume with the flux of the quantity into the volume. Had there been any sources of mass, they would have appeared on the right-hand side. By using the relation (3.2), Eq. (3.5) may also be written

$$\frac{d\rho}{dt} + \rho \operatorname{div} \mathbf{v} = 0 , \quad (3.6)$$

giving the rate of change of density following the motion. Note that  $\rho = 1/V$ , where  $V$  is the volume of unit mass; thus an alternative formulation is

$$\frac{1}{V} \frac{dV}{dt} = \operatorname{div} \mathbf{v} . \quad (3.7)$$

Hence  $\operatorname{div} \mathbf{v}$  is the rate of expansion of a given volume of gas, when following the motion.

### 3.1.1.2 Equations of Motion

Under solar or stellar conditions one can generally ignore the internal friction (or *viscosity*) in the gas. The forces on a volume of gas therefore consist of

- i) Surface forces, *i.e.*, the pressure on the surface of the volume
- ii) Body forces.

Thus the equations of motion can be written

$$\rho \frac{d\mathbf{v}}{dt} = -\nabla p + \rho \mathbf{f} , \quad (3.8)$$

where  $\mathbf{f}$  is the body force per unit mass which has yet to be specified. The pressure  $p$  is defined such that the force on a surface element  $dA$  with outward normal  $\mathbf{n}$  is  $-p \mathbf{n} dA$ . This may be identified with the ordinary thermodynamic pressure.

By using Eq. (3.2), we may also write Eq. (3.8) as

$$\rho \frac{\partial \mathbf{v}}{\partial t} + \rho \mathbf{v} \cdot \nabla \mathbf{v} = -\nabla p + \rho \mathbf{f} . \quad (3.9)$$

Among the possible body forces we consider only gravity. Thus in particular we neglect effects of magnetic fields, which might otherwise provide a body force on the gas. The force per unit mass from gravity is the gravitational acceleration  $\mathbf{g}$ , which can be written as the gradient of the gravitational potential  $\Phi$ :

$$\mathbf{g} = -\nabla \Phi , \quad (3.10)$$

where  $\Phi$  satisfies the Poisson equation

$$\nabla^2 \Phi = 4\pi G \rho . \quad (3.11)$$

It is often convenient to use also the integral solution to the Poisson equation

$$\Phi(\mathbf{r}, t) = -G \int_V \frac{\rho(\mathbf{r}', t) dV'}{|\mathbf{r} - \mathbf{r}'|} , \quad (3.12)$$

where the integral is over the volume  $V$  of the star.

### 3.1.1.3 Energy Equation

To complete the equations we need a relation between  $p$  and  $\rho$ , which can be obtained from the thermodynamical properties and the energetics of the gas. Specifically, the system satisfies the first law of thermodynamics,

$$\frac{dq}{dt} = \frac{dE}{dt} + p \frac{dV}{dt}; \quad (3.13)$$

here  $dq/dt$  is the rate of heat loss or gain, and  $E$  the internal energy, per unit mass. As before  $V = 1/\rho$  is specific volume. Thus Eq. (3.13) expresses the fact that the heat gain goes partly into a change in the internal energy, partly into work expanding or compressing the gas. Alternative formulations of Eq. (3.13), using the equation of continuity, are

$$\frac{dq}{dt} = \frac{dE}{dt} - \frac{p}{\rho^2} \frac{d\rho}{dt} = \frac{dE}{dt} + \frac{p}{\rho} \operatorname{div} \mathbf{v}. \quad (3.14)$$

By using thermodynamical identities the energy equation can be expressed in terms of other, and more convenient, variables,

$$\frac{dq}{dt} = \frac{1}{\rho(\Gamma_3 - 1)} \left( \frac{dp}{dt} - \frac{\Gamma_1 p}{\rho} \frac{d\rho}{dt} \right) \quad (3.15)$$

$$= c_p \left( \frac{dT}{dt} - \frac{\Gamma_2 - 1}{\Gamma_2} \frac{T}{p} \frac{dp}{dt} \right) \quad (3.16)$$

$$= c_V \left[ \frac{dT}{dt} - (\Gamma_3 - 1) \frac{T}{\rho} \frac{d\rho}{dt} \right]. \quad (3.17)$$

Here  $c_p$  and  $c_V$  are the specific heat per unit mass at constant pressure and volume, and the adiabatic exponents are defined by

$$\Gamma_1 = \left( \frac{\partial \ln p}{\partial \ln \rho} \right)_{\text{ad}}, \quad \frac{\Gamma_2 - 1}{\Gamma_2} = \left( \frac{\partial \ln T}{\partial \ln p} \right)_{\text{ad}}, \quad \Gamma_3 - 1 = \left( \frac{\partial \ln T}{\partial \ln \rho} \right)_{\text{ad}}. \quad (3.18)$$

These relations are discussed in more detail in, *e.g.*, Cox & Giuli (1968; updated by Weiss *et al.* 2004).

It is evident that the relation between  $p$ ,  $\rho$  and  $T$ , as well as the  $\Gamma_i$ 's, depend on the thermodynamical state and composition of the gas. Indeed, as will be discussed in Section 7.1.7, the dependence of  $\Gamma_1$  on the properties of the gas forms the basis for using observed solar oscillation frequencies to probe the details of the statistical mechanics of partially ionized gases and to infer the helium abundance of the solar convective envelope. However, in many cases one may as a first approximation regard the gas as fully ionized and neglect effects of degeneracy and radiation pressure, as well as Coulomb interactions. Then the system behaves like an ideal gas, with the simple equation of state

$$p = \frac{k_B \rho T}{\mu m_u}, \quad (3.19)$$

where  $k_B$  is Boltzmann's constant,  $m_u$  is the atomic mass unit and  $\mu$  is the mean molecular weight which is determined solely by the composition. Also, in this case

$$\Gamma_1 = \Gamma_2 = \Gamma_3 = 5/3 . \quad (3.20)$$

We need to consider the heat gain in more detail. Specifically, it can be written as

$$\rho \frac{dq}{dt} = \rho \epsilon - \operatorname{div} \mathbf{F} ; \quad (3.21)$$

here  $\epsilon$  is the rate of energy generation per unit mass (*e.g.*, from nuclear reactions), and  $\mathbf{F}$  is the flux of energy. In most cases, radiation is the only significant contributor to the local energy flux; in particular, molecular conduction is negligible. However, very efficient electron conduction plays a major role in regions dominated by degenerate electrons, such as in the cores of highly evolved stars or in white dwarfs, making these regions nearly isothermal.

In convection zones turbulent gas motion provides a very efficient transport of energy. Ideally the entire hydrodynamical system, including convection, must be described as a whole. In this case only the radiative flux would be included in Eq. (3.21). However, under most circumstances the resulting equations are too complex to be handled analytically or numerically. Thus it is customary to separate out the convective motion, by performing averages of the equations over length scales that are large compared with the convective motion, but small compared with other scales of interest. In this case the convective flux appears as an additional contribution in Eq. (3.21). The convective flux must then be determined, from the other quantities characterizing the system, by considering the equations for the turbulent motion. A familiar example of this (which is also characteristic of the lack of sophistication in current treatments of convection) is the mixing-length theory.

The incorporation of convection in the hydrodynamical equations was discussed in some detail by Unno *et al.* (1989). However, it is fair to say that this is currently one of the principal uncertainties in stellar hydrodynamics.

The general calculation of the radiative flux is also non-trivial. In stellar atmospheres the full radiative transfer problem, as known from the theory of the structure of stellar atmospheres, must be solved in combination with the hydrodynamic equations. This is another active area of research, and the subject of a major monograph (Mihalas & Mihalas 1984). In stellar interiors the mean free path of photons is very short compared with the scale over which the structure changes; thus the radiative energy transport is a diffusive process, which can be treated in *the diffusion approximation*, where the radiative flux is given by

$$\mathbf{F} = -\frac{4\pi}{3\kappa\rho} \nabla B = -\frac{4a\tilde{c}T^3}{3\kappa\rho} \nabla T ; \quad (3.22)$$

here  $B = (a\tilde{c}/4\pi)T^4$  is the integrated Planck function,  $\kappa$  is the opacity,  $\tilde{c}$  is the speed of light<sup>1</sup> and  $a$  is the radiation density constant. Equation (3.22)

---

<sup>1</sup> We use  $\tilde{c}$  to distinguish from the extensively used  $c$  for sound speed.

provides a relation between the state of the gas and the radiative flux that is analogous to a simple conduction equation.

When the mean free path of a photon is very large, one can neglect the contribution from absorption to the heating of the gas. Then we have *Newton's law of cooling*,

$$\operatorname{div} \mathbf{F} = 4\pi\rho\kappa_a B , \quad (3.23)$$

where  $\kappa_a$  is the opacity arising from absorption. The intermediate case in principle requires a full treatment of radiative transfer. However, in simplified modelling of static stellar atmospheres one often uses the *Eddington approximation*, relating the mean intensity and the radiation pressure. As shown by Unno & Spiegel (1966), this can be generalized to the three-dimensional case, to yield

$$\operatorname{div} \mathbf{F} = -4\pi\rho\kappa_a(J - B) , \quad (3.24)$$

$$\mathbf{F} = -\frac{4\pi}{3(\kappa_a + \kappa_s)\rho} \nabla J , \quad (3.25)$$

where  $\kappa_s$  is the scattering opacity and  $J$  is the mean intensity. When  $\kappa_a\rho \rightarrow \infty$ ,  $J \simeq B$  and hence, according to Eq. (3.25), we recover the diffusion approximation, Eq. (3.25), with  $\kappa = \kappa_a + \kappa_s$ . Furthermore, the Eddington approximation has the correct limit in the optically thin case.

Here we have implicitly assumed that the scattering and absorption coefficients are independent of the frequency of radiation. In the diffusion approximation, the generalization to frequency-dependence leads to the introduction of the Rosseland mean opacity. In the optically thin case, one must in general take into account the details of the distribution of intensity with frequency; thus, in Eqs (3.23)–(3.25) the absorption and scattering coefficients must be thought of as suitable averages, whereas  $\mathbf{F}$  and  $J$  are frequency-integrated quantities.

### 3.1.2 The Adiabatic Approximation

For the purpose of calculating stellar oscillation frequencies, the complications of the energy equation can be avoided to a high degree of precision by neglecting the heating term in the energy equation. To see that this is justified, consider the energy equation in the form, using Eq. (3.22)

$$\frac{dT}{dt} - \frac{\Gamma_2 - 1}{\Gamma_2} \frac{T}{p} \frac{dp}{dt} = \frac{1}{c_p} \left[ \epsilon + \frac{1}{\rho} \operatorname{div} \left( \frac{4a\tilde{c}T^3}{3\kappa\rho} \nabla T \right) \right] . \quad (3.26)$$

Here the term in the temperature gradient can be estimated as

$$\frac{1}{\rho c_p} \operatorname{div} \left( \frac{4a\tilde{c}T^3}{3\kappa\rho} \nabla T \right) \sim \frac{4a\tilde{c}T^4}{3\kappa\rho^2 c_p \mathcal{L}^2} = \frac{T}{\tau_F} , \quad (3.27)$$

where  $\mathcal{L}$  is a characteristic length scale, and  $\tau_F$  is a characteristic time scale for radiation,

$$\tau_F = \frac{3\kappa\rho^2 c_p \mathcal{L}^2}{4a\tilde{c}T^3} \simeq 10^{12} \frac{\kappa\rho^2 \mathcal{L}^2}{T^3}, \quad \text{in cgs units.} \quad (3.28)$$

Typical values for the entire Sun are  $\kappa = 1 \text{ cm}^2 \text{ g}^{-1}$ ,  $\rho = 1 \text{ g cm}^{-3}$ ,  $T = 10^6 \text{ K}$ ,  $\mathcal{L} = 10^{10} \text{ cm}$ , and hence  $\tau_F \sim 10^7 \text{ yr}$ . This corresponds to the Kelvin-Helmholtz time for the star. For the solar convection zone the corresponding values are  $\kappa = 100 \text{ cm}^2 \text{ g}^{-1}$ ,  $\rho = 10^{-5} \text{ g cm}^{-3}$ ,  $T = 10^4 \text{ K}$ ,  $\mathcal{L} = 10^9 \text{ cm}$ , and hence  $\tau_F \sim 10^3 \text{ yr}$ . In the outer parts of the star the term in  $\epsilon$  vanishes, whereas in the core it corresponds to a characteristic time  $\tau_\epsilon \sim c_p T / \epsilon$  which is again of the order of the Kelvin-Helmholtz time.  $T/\tau_F$  or  $T/\tau_\epsilon$  must be compared with the time derivative of  $T$  in Eq. (3.26), which can be estimated as  $T/(\text{period of oscillation})$ . Typical periods are of the order of minutes to hours, and hence the heating term in Eq. (3.26) is generally very small compared with the time-derivative terms. Near the surface, on the other hand, the density, and hence the radiative time scale, is low, and the full energy equation must be taken into account.

Where the heating can be neglected, the motion occurs *adiabatically*. Then  $p$  and  $\rho$  are related by

$$\frac{dp}{dt} = \frac{\Gamma_1 p}{\rho} \frac{d\rho}{dt}. \quad (3.29)$$

This equation, together with the continuity equation (3.5), the equations of motion (3.9) and the Poisson equation (3.11), form the complete set of equations for adiabatic motion. Much of our subsequent work is based on these equations.

### 3.1.3 Equilibrium States and Perturbation Analysis

A general hydrodynamical description of a complete star, using the equations presented in the preceding section, is far too complex to handle, even numerically on the largest existing computers. Fairly realistic simulations can be made of convection in small regions near stellar surfaces (*e.g.*, Stein & Nordlund 1998; Ludwig *et al.* 2002; Stein *et al.* 2007; Trampedach 2007; Nordlund *et al.* 2009), by stretching the capabilities of existing computers to the limits; however, even computations extending over weeks only allow detailed simulations covering a few hours of stellar time. Although this is a tremendous achievement, of great value to our understanding of stellar convection and oscillations, it clearly demonstrates the impracticality of a direct numerical solution for, say, general oscillations involving an entire star. Furthermore, even to the extent that such a solution were possible, the results would in general be so complicated that a simplified analysis is needed to understand them.

Fortunately, in the case of stellar oscillations, considerable simplifications are possible. The observed solar oscillations, and solar-like oscillations of main-sequence stars, have very small amplitudes compared with the characteristic scales of the star, and so they can be treated as small perturbations around

a static equilibrium state. Even in “classical” pulsating stars, where the surface amplitudes may be large, most of the energy in the motion is in regions where the amplitudes are relatively small; thus many of the properties of these oscillations, including their periods, can be understood in terms of small-perturbation theory. In this section we discuss the general equations for such small perturbations.

### 3.1.3.1 The Equilibrium Structure

The equilibrium structure is assumed to be static, so that all time derivatives can be neglected. In addition, we assume that there are no velocities. Then the continuity equation, Eq. (3.5), is trivially satisfied. The equations of motion (3.9) reduce to the equation of hydrostatic support,

$$\nabla p_0 = \rho_0 \mathbf{g}_0 = -\rho_0 \nabla \Phi_0 , \quad (3.30)$$

where we have denoted equilibrium quantities with the subscript “0”. The Poisson equation (3.11) is unchanged,

$$\nabla^2 \Phi_0 = 4\pi G \rho_0 . \quad (3.31)$$

Finally, the energy equation (3.21) is

$$0 = \frac{dq}{dt} = \epsilon_0 - \frac{1}{\rho_0} \operatorname{div} \mathbf{F}_0 . \quad (3.32)$$

It might be noted that one often considers equilibrium structures that change on long time scales (see also Section 1.6.1). Here hydrostatic equilibrium is enforced (departures from hydrostatic equilibrium result in motion on essentially the free-fall time scale for the star, of the order of hours). However, it is not assumed that there is no heating, so that the general energy equation, Eq. (3.21), is used. Such a star is said to be in hydrostatic, but not in thermal, equilibrium. Typical examples are stars where nuclear burning does not supply the main source of energy, as during the pre-main-sequence contraction, or after hydrogen exhaustion in the core. Even during normal main-sequence evolution the heating term provides a small contribution to the energy, which is normally taken into account in calculations of stellar evolution. However, we need not consider this further here.

For the present purpose the most important example of equilibrium is clearly a spherically symmetric state, where the structure depends only on the distance  $r$  to the centre. Here  $\mathbf{g}_0 = -g_0 \mathbf{a}_r$ , where  $\mathbf{a}_r$  is a unit vector directed radially outward, and Eq. (3.30) becomes

$$\frac{dp_0}{dr} = -g_0 \rho_0 . \quad (3.33)$$

Also, the Poisson equation may be integrated once, to yield

$$g_0 = \frac{G}{r^2} \int_0^r 4\pi\rho_0 r'^2 dr' = \frac{G m_0}{r^2}, \quad (3.34)$$

where  $m_0(r)$  is the mass in the sphere interior to  $r$ . The flux is directed radially outward,  $\mathbf{F} = F_{r,0}\mathbf{a}_r$ , so that the energy equation gives

$$\rho_0\epsilon_0 = \frac{1}{r^2} \frac{d}{dr} (r^2 F_{r,0}) = \frac{1}{4\pi r^2} \frac{dL_0}{dr},$$

where  $L_0 = 4\pi r^2 F_{r,0}$  is the total flow of energy through the sphere with radius  $r$ ; hence

$$\frac{dL_0}{dr} = 4\pi r^2 \rho_0 \epsilon_0. \quad (3.35)$$

Finally, the diffusion expression (3.22) for the flux may be written

$$\frac{dT_0}{dr} = -\frac{3\kappa_0 \rho_0}{16\pi r^2 a \tilde{c} T_0^3} L_0. \quad (3.36)$$

Equations (3.33)–(3.36) are clearly the familiar equations for stellar structure (*e.g.*, Kippenhahn & Weigert 1990).

### 3.1.3.2 Perturbation Analysis

We now consider small perturbations around the equilibrium state. Thus, *e.g.*, the pressure is written as

$$p(\mathbf{r}, t) = p_0(\mathbf{r}) + p'(\mathbf{r}, t), \quad (3.37)$$

where  $p'$  is a small perturbation; this is the so-called *Eulerian* perturbation, *i.e.*, the perturbation at a given point. The equations are then linearized in the perturbations, by expanding them in the perturbations and retaining only terms that do not contain products of the perturbations.

Just as in the general case it is convenient to use also a description involving a reference frame following the motion; the perturbation in this frame is called the *Lagrangian* perturbation. If an element of gas is moved from  $\mathbf{r}_0$  to  $\mathbf{r}_0 + \boldsymbol{\delta}\mathbf{r}$  due to the perturbation, the Lagrangian perturbation to pressure may be calculated as

$$\begin{aligned} \delta p(\mathbf{r}) &= p(\mathbf{r}_0 + \boldsymbol{\delta}\mathbf{r}) - p_0(\mathbf{r}_0) = p(\mathbf{r}_0) + \boldsymbol{\delta}\mathbf{r} \cdot \nabla p_0 - p_0(\mathbf{r}_0) \\ &= p'(\mathbf{r}_0) + \boldsymbol{\delta}\mathbf{r} \cdot \nabla p_0, \end{aligned} \quad (3.38)$$

to leading order in the perturbations; thus  $\nabla p$  has been replaced by  $\nabla p_0$ . The relation (3.38) between the Eulerian and Lagrangian perturbations is completely equivalent to the relation (3.2) between the local and the material time derivative. Note also that the velocity is given by the time derivative of the displacement  $\boldsymbol{\delta}\mathbf{r}$ ,

$$\mathbf{v} = \frac{\partial \boldsymbol{\delta r}}{\partial t} . \quad (3.39)$$

Equations for the perturbations are obtained by inserting expressions like Eq. (3.37) in the full equations, subtracting equilibrium equations and neglecting quantities of order higher than one in  $p'$ ,  $\rho'$ ,  $\mathbf{v}$ , etc. For the continuity equation the result is

$$\frac{\partial \rho'}{\partial t} + \operatorname{div}(\rho_0 \mathbf{v}) = 0 , \quad (3.40)$$

or, by using Eq. (3.39) and integrating with respect to time

$$\rho' + \operatorname{div}(\rho_0 \boldsymbol{\delta r}) = 0 . \quad (3.41)$$

Note that this equation may also, by using the analogue for  $\rho$  to Eq. (3.38), be written as

$$\delta\rho + \rho_0 \operatorname{div}(\boldsymbol{\delta r}) = 0 , \quad (3.42)$$

which corresponds to Eq. (3.6).

The equations of motion become

$$\rho_0 \frac{\partial^2 \boldsymbol{\delta r}}{\partial t^2} = \rho_0 \frac{\partial \mathbf{v}}{\partial t} = -\nabla p' + \rho_0 \mathbf{g}' + \rho' \mathbf{g}_0 , \quad (3.43)$$

where, obviously,  $\mathbf{g}' = -\nabla \Phi'$ . Also, the perturbation  $\Phi'$  to the gravitational potential satisfies the perturbed Poisson equation

$$\nabla^2 \Phi' = 4\pi G \rho' , \quad (3.44)$$

with the solution, equivalent to Eq. (3.12)

$$\Phi' = -G \int_V \frac{\rho'(\mathbf{r}', t)}{|\mathbf{r} - \mathbf{r}'|} dV' . \quad (3.45)$$

The energy equation requires a little thought. We need to calculate, e.g.,

$$\frac{dp}{dt} = \frac{\partial p}{\partial t} + \mathbf{v} \cdot \nabla p = \frac{\partial p'}{\partial t} + \mathbf{v} \cdot \nabla p_0 = \frac{\partial p'}{\partial t} + \frac{\partial \boldsymbol{\delta r}}{\partial t} \cdot \nabla p_0 = \frac{\partial}{\partial t}(\delta p) , \quad (3.46)$$

to first order in the perturbations. Note that to this order there is no difference between the local and the material time derivative of the *perturbations*. Thus we have for the energy equation from, e.g., Eq. (3.15),

$$\frac{\partial \delta q}{\partial t} = \frac{1}{\rho_0(\Gamma_{3,0} - 1)} \left( \frac{\partial \delta p}{\partial t} - \frac{\Gamma_{1,0} p_0}{\rho_0} \frac{\partial \delta \rho}{\partial t} \right) . \quad (3.47)$$

This equation is most simply expressed in Lagrangian perturbations, but it may be transformed into Eulerian perturbations by using Eq. (3.38). From Eq. (3.21) the perturbation to the heating rate is given by

$$\rho_0 \frac{\partial \delta q}{\partial t} = \delta(\rho \epsilon - \operatorname{div} \mathbf{F}) = (\rho \epsilon - \operatorname{div} \mathbf{F})' , \quad (3.48)$$

if Eq. (3.32) is used. Finally, it is straightforward to obtain the perturbation to the radiative flux, in the diffusion approximation from, Eq. (3.22).

For adiabatic motion we neglect the heating term and obtain

$$\frac{\partial \delta p}{\partial t} - \frac{\Gamma_{1,0} p_0}{\rho_0} \frac{\partial \delta \rho}{\partial t} = 0 ,$$

or, by integrating over time

$$\delta p = \frac{\Gamma_{1,0} p_0}{\rho_0} \delta \rho ; \quad (3.49)$$

in Eulerian form this becomes

$$p' + \boldsymbol{\delta r} \cdot \nabla p_0 = \frac{\Gamma_{1,0} p_0}{\rho_0} (\rho' + \boldsymbol{\delta r} \cdot \nabla \rho_0) . \quad (3.50)$$

### 3.1.4 Simple Waves

It is instructive to consider simple examples of wave motion. This provides an introduction to the techniques needed to handle the perturbations. In addition, general stellar oscillations can in many cases be approximated by simple waves, which therefore give physical insight into the behaviour of the oscillations.

#### 3.1.4.1 Acoustic Waves

As the simplest possible equilibrium situation, we may consider acoustic waves in a spatially homogeneous medium. Here all derivatives of equilibrium quantities vanish. According to Eq. (3.30) gravity must then be negligible. Such a situation clearly cannot be realized exactly. However, if the equilibrium structure varies slowly compared with the oscillations, this may be a reasonable approximation. We also neglect the perturbation to the gravitational potential; for rapidly varying perturbations regions with positive and negative  $\rho'$  nearly cancel in Eq. (3.45), and hence  $\Phi'$  is small. Finally, we assume the adiabatic approximation, Eq. (3.49).

The equations of motion (3.43) give

$$\rho_0 \frac{\partial^2 \boldsymbol{\delta r}}{\partial t^2} = -\nabla p' ,$$

or, by taking the divergence

$$\rho_0 \frac{\partial^2}{\partial t^2} (\text{div } \boldsymbol{\delta r}) = -\nabla^2 p' .$$

However,  $\text{div } \boldsymbol{\delta r}$  can be eliminated by using the continuity Eq. (3.41), and  $p'$  can be expressed in terms of  $\rho'$  from the adiabatic relation. The result is

$$\frac{\partial^2 \rho'}{\partial t^2} = \frac{\Gamma_{1,0} p_0}{\rho_0} \nabla^2 \rho' = c_0^2 \nabla^2 \rho' , \quad (3.51)$$

where

$$c_0^2 \equiv \frac{\Gamma_{1,0} p_0}{\rho_0} \quad (3.52)$$

has the dimension of a squared velocity. This equation has the form of a wave equation. Thus it has solutions in the form of plane waves<sup>2</sup>

$$\rho' = a \exp[i(\mathbf{k} \cdot \mathbf{r} - \omega t)] , \quad (3.53)$$

in terms of the *wave vector*  $\mathbf{k}$  and the *angular frequency*  $\omega$ . By substituting Eq. (3.53) into Eq. (3.51) we obtain

$$-\omega^2 \rho' = c_0^2 \operatorname{div}(i\mathbf{k}\rho') = -c_0^2 |\mathbf{k}|^2 \rho' . \quad (3.54)$$

Thus this is a solution, provided  $\omega$  satisfies the *dispersion relation*

$$\omega^2 = c_0^2 |\mathbf{k}|^2 . \quad (3.55)$$

The waves are plane sound waves, and Eq. (3.55) is the dispersion relation for such waves. This identifies  $c_0$  as the speed of propagation of the waves and hence as the *adiabatic sound speed*. We note that when the ideal gas law, Eq. (3.19), is satisfied the sound speed is given by

$$c_0^2 = \frac{\Gamma_{1,0} k_B T_0}{\mu m_u} . \quad (3.56)$$

Thus  $c_0$  is essentially determined by  $T_0/\mu$ .

With a suitable choice of phases the real solution can be written as

$$\rho' = a \cos(\mathbf{k} \cdot \mathbf{r} - \omega t) , \quad (3.57)$$

$$p' = c_0^2 a \cos(\mathbf{k} \cdot \mathbf{r} - \omega t) , \quad (3.58)$$

$$\delta \mathbf{r} = \frac{c_0^2}{\rho_0 \omega^2} a \cos(\mathbf{k} \cdot \mathbf{r} - \omega t + \frac{\pi}{2}) \mathbf{k} . \quad (3.59)$$

Thus the displacement  $\delta \mathbf{r}$ , and hence the velocity  $\mathbf{v}$ , is in the direction of the wave vector  $\mathbf{k}$ .

### 3.1.4.2 Internal Gravity Waves

As a slightly more complicated case, we consider internal gravity waves in a layer of gas stratified under gravity. Thus here there is a pressure gradient,

---

<sup>2</sup> As discussed in more detail in Section C.1, it is convenient to write the solution in complex form; the physically realistic solution is obtained by taking the real part of the complex solution.

determined by Eq. (3.33). However, we assume that the equilibrium quantities vary so slowly that their gradients can be neglected compared with gradients of perturbations. Also, as before, we neglect the perturbation to the gravitational potential. Clearly one solution must be the adiabatic sound waves considered above. However, here we seek other solutions in the form of waves with much lower frequencies.

It is possible to derive an approximate wave equation under these circumstances (*cf.* Section 3.4.3). However, to simplify the analysis we assume a solution in the form of a plane wave from the outset. Thus we take all perturbation variables to vary as

$$\exp[i(\mathbf{k} \cdot \mathbf{r} - \omega t)] . \quad (3.60)$$

Because of the presence of gravity there is a preferred direction in the problem. We choose a vertical coordinate  $r$  directed upward, so that  $\mathbf{g}_0 = -g_0 \mathbf{a}_r$ , and

$$\nabla p_0 = \frac{dp_0}{dr} \mathbf{a}_r , \quad \nabla \rho_0 = \frac{d\rho_0}{dr} \mathbf{a}_r . \quad (3.61)$$

Also, we separate the displacement  $\delta\mathbf{r}$  and the wave vector  $\mathbf{k}$  into radial and horizontal components,

$$\delta\mathbf{r} = \xi_r \mathbf{a}_r + \boldsymbol{\xi}_h , \quad (3.62)$$

$$\mathbf{k} = k_r \mathbf{a}_r + \mathbf{k}_h . \quad (3.63)$$

The radial and horizontal components of Eqs (3.43) are

$$-\rho_0 \omega^2 \xi_r = -ik_r p' - \rho' g_0 , \quad (3.64)$$

$$-\rho_0 \omega^2 \boldsymbol{\xi}_h = -i \mathbf{k}_h p' , \quad (3.65)$$

and the continuity equation, Eq. (3.41), can be written

$$\rho' + \rho_0 ik_r \xi_r + \rho_0 i \mathbf{k}_h \cdot \boldsymbol{\xi}_h = 0 . \quad (3.66)$$

From Eqs (3.65) and (3.66) we find the pressure perturbation

$$p' = \frac{\omega^2}{k_h^2} (\rho' + ik_r \rho_0 \xi_r) . \quad (3.67)$$

This may be used in Eq. (3.64), to obtain

$$-\rho_0 \omega^2 \xi_r = -i \frac{k_r}{k_h^2} \omega^2 \rho' + \omega^2 \rho_0 \frac{k_r^2}{k_h^2} \xi_r - \rho' g_0 . \quad (3.68)$$

For very low frequencies the first term in  $\rho'$  can be neglected compared with the second, yielding

$$-\rho_0 \omega^2 \left(1 + \frac{k_r^2}{k_h^2}\right) \xi_r = -\rho' g_0 . \quad (3.69)$$

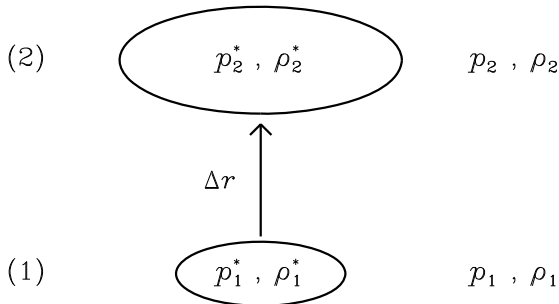


**Fig. 3.1.** Perturbations to a layer stratified under gravity, illustrated by the motion of a blob of fluid, from the lower location (1) to the upper location (2). At the lower location matter inside the blob is assumed to be in equilibrium with the surroundings, so that  $p_1^* = p_1$ ,  $\rho_1^* = \rho_1$ . At the upper location the difference, e.g.,  $\rho_2^* - \rho_2$  corresponds to the Eulerian perturbation  $\rho'$  while  $\rho_2^* - \rho_1$  corresponds to the Lagrangian perturbation  $\delta\rho$ .

This equation has a fairly simple physical meaning, which is best understood by regarding the perturbation as a blob of fluid displaced in the vertical direction, as illustrated in Fig. 3.1, with the resulting changes in pressure and density inside the blob and in the environment. Buoyancy acting on the density perturbation provides a vertical force  $-\rho'g_0$  per unit volume that drives the motion. The left-hand side gives the vertical acceleration times the mass  $\rho_0$  per unit volume; however, it is modified by the term in the wave numbers. This arises from the pressure perturbation; in order to move vertically, a blob of gas must displace matter horizontally, and this increases its effective inertia. This effect is stronger the longer the horizontal wavelength of the perturbation, and hence the smaller its horizontal wave number.

The adiabatic relation (3.50) gives

$$\rho' = c_0^{-2} p' + \rho_0 \boldsymbol{\delta r} \cdot \left( \frac{1}{p_0 \Gamma_{1,0}} \nabla p_0 - \frac{1}{\rho_0} \nabla \rho_0 \right). \quad (3.70)$$

We may estimate the importance of the term in  $p'$  by noting that, according to Eq. (3.67),

$$\frac{c_0^{-2} p'}{\rho'} \simeq \frac{\omega^2}{c_0^2 k_h^2}. \quad (3.71)$$

Here the denominator on the right-hand side is the sound-wave frequency corresponding to the horizontal wave number  $k_h$  (*cf.* Eq. (3.55)); since we are specifically interested in oscillations with frequencies far lower than the frequencies of sound waves, the term in  $p'$  can be neglected. Physically, the

neglect of the pressure perturbation essentially corresponds to assuming that the perturbation is always in hydrostatic equilibrium; in the description in Fig. 3.1 it is assumed that there is pressure balance, with  $p_2^* = p_2$ . Inserting the expression for  $\rho'$  resulting from Eq. (3.70), when  $p'$  is neglected, in Eq. (3.69) finally yields

$$\omega^2 \left( 1 + \frac{k_r^2}{k_h^2} \right) \xi_r = N^2 \xi_r , \quad (3.72)$$

where

$$N^2 = g_0 \left( \frac{1}{\Gamma_{1,0}} \frac{d \ln p_0}{dr} - \frac{d \ln \rho_0}{dr} \right) \quad (3.73)$$

is the square of the *buoyancy or Brunt-Väisälä frequency*  $N$ .

The physical significance of  $N$  is perhaps better understood by deriving this expression from the description in Fig. 3.1. The behaviour of the displaced blob depends on whether the density  $\rho_2^*$  in the displaced element is larger or smaller than the value  $\rho_2$  in its new surroundings. If the density  $\rho_2^*$  in the blob is smaller than the density in the surroundings, there is a net buoyancy accelerating the blob towards the surface; this corresponds to convective instability. In the opposite case, the blob is heavier than the surroundings and returns towards the original position; this results in an oscillation of the blob around the equilibrium position.

Assuming that the motion is sufficiently slow that pressure equilibrium is maintained, the pressure  $p_2^*$  in the element is equal to the pressure  $p_2$  outside; this obviously corresponds to the neglect above of the terms in  $p'$ , and the condition is that the speed of the motion is far below the speed of sound. Assuming also that the motion takes place adiabatically,

$$\rho_2^* - \rho_1^* \simeq \frac{1}{\Gamma_{1,0}} \frac{\rho_0}{p_0} (p_2^* - p_1^*) \simeq \frac{1}{\Gamma_{1,0}} \frac{\rho_0}{p_0} \frac{dp_0}{dr} \Delta r , \quad (3.74)$$

and hence

$$\rho' = \rho_2^* - \rho_1 - (\rho_2 - \rho_1) \simeq \rho_0 \left( \frac{1}{\Gamma_{1,0}} \frac{d \ln p_0}{dr} - \frac{d \ln \rho_0}{dr} \right) \Delta r , \quad (3.75)$$

corresponding to Eq. (3.70) above, if the term in  $p'$  is neglected. With the buoyancy force  $-g\rho'$  this leads to the equation of motion corresponding to Eq. (3.69), without the increase in the inertia, and hence to Eqs (3.72) and (3.73). When  $N^2 > 0$  the element is heavier than the displaced fluid, and buoyancy forces it back towards the original position; thus as discussed above, in this case the element executes an oscillation around the equilibrium position. On the other hand, if  $N^2 < 0$  the element is lighter than the displaced fluid and buoyancy acts to enhance the motion, forcing the element away from equilibrium; this corresponds to convective instability.

From Eq. (3.72) we obtain the dispersion relation

$$\omega^2 = \frac{N^2}{1 + k_r^2/k_h^2} . \quad (3.76)$$

In the oscillatory case, with  $N^2 > 0$ ,  $N$  is the oscillation frequency in the limit of infinite  $k_h$ , *i.e.*, for infinitely small horizontal wavelength. This corresponds to oscillations of fluid elements in the form of slender “needles”. For greater horizontal wavelength the horizontal motion increases the inertia, as discussed above, and hence decreases the frequency. These waves are known as internal *gravity waves*.<sup>3</sup>

The condition that  $N^2 > 0$  can also be written as

$$\frac{d \ln \rho_0}{d \ln p_0} > \frac{1}{\Gamma_{1,0}} ; \quad (3.77)$$

when it is not satisfied,  $\omega$  is imaginary, and the motion grows exponentially with time. This is the linear case of convective instability. Gravity waves, with positive  $\omega^2$ , cannot propagate in convective regions. We return to this when discussing the asymptotic theory of stellar oscillations.

When the stability condition is not satisfied, convection sets in. As discussed in Section 3.2.1.3, this has major consequences for stellar structure.

### 3.1.4.3 Surface Gravity Waves

In addition to the internal gravity waves described above, there is a distinct, and more familiar type of gravity waves, known, *e.g.*, from the surface of a lake. These are waves at a discontinuity in density.

We consider a liquid at constant density  $\rho_0$ , with a free surface. Thus the pressure on the surface is assumed to be constant. The layer is infinitely deep. We assume that the liquid is incompressible, so that  $\rho_0$  is constant and the density perturbation  $\rho' = 0$ . From the equation of continuity we therefore get

$$\operatorname{div} \mathbf{v} = 0 . \quad (3.78)$$

Gravity  $\mathbf{g}$  is assumed to be uniform, and directed vertically downwards. Since the density perturbation is zero, so is the perturbation to the gravitational potential.

In the interior of the liquid the equations of motion reduce to

$$\rho_0 \frac{\partial \mathbf{v}}{\partial t} = -\nabla p' . \quad (3.79)$$

The divergence of this equation gives

$$\nabla^2 p' = 0 . \quad (3.80)$$

We introduce a horizontal coordinate  $x$ , and a vertical coordinate  $z$  increasing downward, with  $z = 0$  at the free surface. We now seek a solution in the form of a wave propagating along the surface, in the  $x$ -direction. Here  $p'$  has the form

---

<sup>3</sup> not to be confused with the gravitational waves in general relativity.

$$p'(x, z, t) = f(z) \cos(k_h x - \omega t), \quad (3.81)$$

where  $f$  is a function yet to be determined. By substituting Eq. (3.81) into Eq. (3.80) we obtain

$$\frac{d^2 f}{dz^2} = k_h^2 f,$$

or

$$f(z) = a \exp(-k_h z) + b \exp(k_h z). \quad (3.82)$$

As the layer is assumed to be infinitely deep,  $b$  must be zero.

We must now consider the boundary condition at the free surface. Here the pressure is constant, and therefore the Lagrangian pressure perturbation vanishes (the pressure is constant on the perturbed surface), *i.e.*,

$$0 = \delta p = p' + \boldsymbol{\delta r} \cdot \nabla p_0 = p' + \xi_z \rho_0 g_0 \quad \text{at } z = 0, \quad (3.83)$$

where  $\xi_z$  is the  $z$ -component of the displacement. This is obtained from the vertical component of Eq. (3.79), for the solution in Eq. (3.82) with  $b = 0$ , as

$$\xi_z = -\frac{k_h}{\rho_0 \omega^2} p'. \quad (3.84)$$

Thus Eq. (3.83) reduces to

$$0 = \left(1 - \frac{g_0 k_h}{\omega^2}\right) p',$$

and hence the dispersion relation for the surface waves is

$$\omega^2 = g_0 k_h. \quad (3.85)$$

The frequencies of the surface gravity waves depend only on their wavelength and on gravity, but not on the internal structure of the layer, in particular the density. In this they resemble a pendulum, whose frequency is also independent of its constitution. Indeed, the frequency of a wave with wave number  $k_h$ , and wavelength  $\lambda$ , is the same as the frequency of a mathematical pendulum with length

$$\mathcal{L} = \frac{1}{k_h} = \frac{\lambda}{2\pi}. \quad (3.86)$$

A simple generalization of the surface gravity waves is to consider waves at a density discontinuity, between two incompressible fluids, such that the amplitude of the waves decays exponentially as one moves away from the interface. We take the density in the lower and upper layer to be  $\rho_2$  and  $\rho_1$ , respectively, with  $\rho_2 > \rho_1$ . It is straightforward to show that in this case the dispersion relation is

$$\omega^2 = \frac{\rho_2 - \rho_1}{\rho_2 + \rho_1} g_0 k_h, \quad (3.87)$$

by imposing the condition that the pressure perturbation be continuous at the interface between the two layers.

Although gravity waves at a free surface or a density discontinuity are clearly highly simplified cases, they have close analogies in asteroseismology. At high degree the Sun shows the so-called f modes with a behaviour corresponding to surface gravity waves (see Sections 3.5.1 and 7.1.4.3); also, stars with growing convective cores develop density discontinuities which give rise to g modes whose nature approximates the interfacial gravity waves (*cf.* Section 3.5.3).

## 3.2 Equilibrium Stellar Structure

The goal of asteroseismology is to understand the structure and evolution of stars. Hence a brief background on the properties of stellar interiors is useful when discussing the diagnostics that we may hope to obtain from asteroseismology. A detailed discussion of stellar structure and evolution is obviously beyond the scope of the present book. We refer to the many excellent textbooks in the field, particularly the works of Kippenhahn & Weigert (1990), Hansen *et al.* (2004) and Maeder (2009). An overview of stellar evolution was provided in Section 2.1. Here we discuss the physics of stellar interiors and some aspects of stellar evolution which will be relevant in our discussion of asteroseismic investigations.

Much of the discussion of stellar evolution is based on what may be termed the “standard” theory. This in particular neglects complicating effects such as rotation and magnetic fields, while hydrodynamical processes are either ignored or treated in a highly simplified manner. This is partly motivated by ignorance, partly by the fact that many observed properties of stars, before asteroseismology, can be understood from such simplified models. However, the effects ignored are undoubtedly important and in particular may have a drastic influence on the late evolution of stars, for example in supernova explosions. One of the hopes is that asteroseismology will clearly show the inadequacy of the simple models and point to ways in which they can be improved.

We start by discussing the simplified models and end this section with a brief discussion of the complications.

### 3.2.1 Basic Properties of Stellar Evolution

Neglecting rotation and other perturbing forces, stars are spherically symmetric; we make this assumption here.

#### 3.2.1.1 Hydrostatic Equilibrium

Stars are hydrodynamical systems and hence, at the most basic level, are described by the equations presented in Section 3.1.1. A major simplification

in most phases of stellar evolution, and certainly those that are relevant here, is the separation between the relevant time scales (see Section 1.6.1). Thus it is assumed that the stars do not change on a dynamical time scale. This requires that the star is in *hydrostatic equilibrium*, such that the time derivative on the right-hand side of Eq. (3.8) can be neglected, resulting in Eq. (3.30). On the assumption of spherical symmetry this becomes

$$\frac{\partial p}{\partial r} = -\frac{Gm\rho}{r^2}, \quad (3.88)$$

(for simplicity we drop the subscript 0 on equilibrium quantities in this section), using the gravitational acceleration given by Eq. (3.34). Here the mass  $m(r)$  inside the distance  $r$  to the centre obviously satisfies

$$\frac{\partial m}{\partial r} = 4\pi r^2 \rho. \quad (3.89)$$

### 3.2.1.2 Energy Equation and Radiative Transport

On the other hand, several evolutionary phases take place sufficiently rapidly that changes occurring on a thermal time scale are relevant. This is obviously the case in the *pre-main-sequence phase*, before hydrogen ignition, where evolution takes place on a thermal time scale. Thus we require the full energy equation, Eq. (3.21). Given the assumption of spherical symmetry it is convenient to replace the flux  $F$  by the luminosity  $L = 4\pi r^2 F$ . Then Eq. (3.21) can be written, using also Eq. (3.14), as

$$\frac{\partial L}{\partial r} = 4\pi r^2 \left( \rho\epsilon - \rho \frac{dE}{dt} + \frac{p}{\rho} \frac{dp}{dt} \right). \quad (3.90)$$

In stellar interiors, where the photon mean-free path is short compared with the typical scale of changes in structure, the energy transport by radiation can be approximated by the diffusion approximation, Eq. (3.22), which in the spherically symmetric case can be written as

$$\frac{\partial T}{\partial r} = -\frac{3\kappa\rho}{4a\tilde{c}T^3} \frac{L}{4\pi r^2}. \quad (3.91)$$

In stellar atmospheres the diffusion approximation is not valid and a more detailed treatment of radiative transfer is required. This can be included in general modelling of stellar evolution in two ways. One option is to obtain conditions at the top of the model by matching to an appropriate detailed model of the stellar atmosphere, *e.g.*, obtained from interpolation in a grid of such models. Alternatively, the atmospheric structure can be represented by the relation between temperature and the *optical depth*  $\tau$ , defined as

$$\tau = \int_r^\infty \kappa \rho dr. \quad (3.92)$$

This  $T(\tau)$  relation can be obtained from a match to detailed atmospheric models; alternatively, particularly in the case of the Sun, a match to a semi-empirical atmosphere model can be used. Given  $T(\tau)$  the pressure structure of the atmosphere can be obtained by integrating the equation of hydrostatic support, expressed in terms of  $\tau$ .

### 3.2.1.3 Convection

A more serious issue, indeed one of the major uncertainties in stellar modelling, concerns the instability implied by the discussion of internal gravity waves in Section 3.1.4.2. It follows from Eq. (3.77) that the condition for convective *instability* is that

$$\frac{1}{\Gamma} \equiv \frac{d \ln \rho}{d \ln p} < \frac{1}{\Gamma_1}. \quad (3.93)$$

In terms of the description by a displaced blob (see Fig. 3.1) it is easy to see that a rising element is hotter than the surroundings and hence carries an excess thermal energy. The simple analysis in Section 3.1.4.2 leads to exponential growth with time of the displacement of the blob; presumably nonlinear effects cause it to break up when the velocity becomes too large, leading to a release of the thermal energy to the surroundings. Thus the convective motion contributes to the energy transport and hence affects the temperature gradient, requiring that Eq. (3.91) be modified in regions with convective instability.

It is convenient to express the condition for instability in terms of the temperature gradient, which in the case of radiative transport is given by Eq. (3.91). For simplicity we use the ideal gas law, Eq. (3.19). Then Eq. (3.93) can be written as

$$\nabla \equiv \frac{d \ln T}{d \ln p} > \nabla_{ad} + \nabla_\mu, \quad (3.94)$$

where

$$\nabla_{ad} = \left( \frac{\partial \ln T}{\partial \ln p} \right)_{ad}, \quad \nabla_\mu = \frac{d \ln \mu}{d \ln p}. \quad (3.95)$$

Note that typically  $\mu$  decreases with increasing  $r$  and hence decreasing  $p$ . Hence  $\nabla_\mu$  contributes to increasing the stability: in regions of varying  $\mu$  a blob moving outwards contains matter with a higher mean molecular weight than the surroundings, contributing to making the blob heavier.

The interpretation of the instability in stellar modelling requires consideration of the temperature gradient required to transport the energy by radiation. From Eqs (3.91) and (3.88) this is obtained as

$$\nabla_{rad} = \frac{3}{16\pi a \tilde{c} G} \frac{\kappa p}{T^4} \frac{L(r)}{m(r)}. \quad (3.96)$$

Thus those regions are unstable to convection where  $\nabla_{rad}$  exceeds  $\nabla_{ad} + \nabla_\mu$ . Here part of the energy is transported by convection and hence the actual temperature gradient  $\nabla$  is smaller than  $\nabla_{rad}$ .

The equivalent conditions Eq. (3.93) and Eq. (3.94) are known as the *Ledoux criterion* of convective instability; it is obvious that they provide the correct condition for dynamical instability. However, the presence of  $\nabla_\mu$  is a complication: since convective motion mixes the stellar material the onset of convection could cause mixing which would make unstable a region that is stable according to the Ledoux criterion. Such complications motivate that models are often computed where the instability is determined according to the condition

$$\nabla_{\text{rad}} > \nabla_{\text{ad}} , \quad (3.97)$$

known as the *Schwarzschild criterion*. In fact, it may be argued by extending the blob discussion that the intermediate case,

$$\nabla_{\text{ad}} + \nabla_\mu > \nabla_{\text{rad}} > \nabla_{\text{ad}} , \quad (3.98)$$

gives rise to oscillations with growing amplitude of the blob around the equilibrium position (*e.g.*, Kippenhahn & Weigert 1990). The nonlinear development of such motion, known as *semiconvection*, might cause partial mixing of the chemical composition while it seems unlikely to have a significant effect on the temperature gradient. However, the detailed effects of this instability remain uncertain.

The expression Eq. (3.96) illustrates the circumstances under which convection instability can be expected. One important aspect is  $L/m$ , *i.e.*, the average energy-generation rate inside the point considered. If energy generation is strongly concentrated near the stellar centre, this quantity is large, clearly leading to a tendency towards instability. This is the case when  $\epsilon$  depends strongly on temperature. In the case of core hydrogen burning, this happens when the CNO cycle (see below) makes a substantial contribution to the energy generation, as is the case in stars only slightly more massive than the Sun; similarly, in later phases of central nuclear burning the energy generation rate is highly temperature sensitive. In these cases, therefore, the star has a convective core. Alternatively, convection is likely when the opacity is high. As discussed below, this happens at relatively low temperature, particularly in the ionization zones of hydrogen and helium, causing convection in the outer parts of relatively cool stars, including main-sequence stars of masses below around  $2 M_\odot$ . Red giants have very deep outer convection zones, covering much of the mass and by far the largest part of the radial extent of the star.

The calculation of the temperature gradient in convective regions remains a serious issue. However, even the simplest estimates show that in the bulk of convective regions the required difference  $\nabla - \nabla_{\text{ad}}$ , on which the efficacy of convective energy transport depends, is very small, owing to the huge heat capacity of stellar matter. Thus in most of the star an adequate approximation in convective regions is that  $\nabla \simeq \nabla_{\text{ad}}$ , or

$$\frac{\partial T}{\partial r} \simeq -\nabla_{\text{ad}} \frac{Gm\rho T}{pr^2} . \quad (3.99)$$

As a result, the bulk of a convection zone is at essentially constant specific entropy, lying on *an adiabat*, *i.e.*, a curve in parameter space where the thermodynamical quantities are related adiabatically, characterized by the specific entropy. Only near the stellar surface is the density, and hence the heat content, of matter so low that a substantial superadiabatic gradient  $\nabla - \nabla_{\text{ad}}$  is required for energy transport. This superadiabatic region of convective envelopes determines the specific entropy in the nearly adiabatic part of the envelope, and hence has a major effect on the structure of stars with extensive outer convection zones. Simple estimates also show that the typical time scales of convection is at most months or years, *i.e.*, much shorter than the nuclear time scales under all except the most extreme circumstances. This has the important consequence that convective regions can be assumed to have uniform chemical composition.

It is evident that modelling of cool stars requires at least a characterization of the upper, superadiabatic region of convective envelopes. Detailed hydrodynamical modelling of convection is possible in restricted regions in the upper parts of convective envelopes (*e.g.*, Stein & Nordlund 1998; Ludwig *et al.* 2002; for a major review of solar surface convection, including modelling, see also Nordlund *et al.* 2009). These provide remarkable good agreement with the observed properties of stellar atmospheres, including the detailed spectral line profiles, without invoking additional sources of turbulent line broadening (*e.g.*, Asplund *et al.* 2000; Allende Prieto *et al.* 2002).<sup>4</sup> However, they are far too time consuming to include in stellar evolution modelling and in any case only involve a small part of the convection zone. Also, comparably realistic modelling of deeper convective regions is not possible, owing to the huge mismatch between the relevant dynamical and thermal time scales, both of which would have to be covered in such simulations.

Thus stellar modelling typically uses a highly simplified description of convective transport, based on a rough model of the convective dynamics. A commonly used approach is to use the *mixing-length treatment* described by Böhm-Vitense (1958); a physical basis for this formulation, further developed to describe the interaction with pulsations, was presented by Gough (1977a). This is characterized by a length scale, the mixing length  $\ell_{\text{ML}}$ , determining the average scale of the convective eddies and commonly parameterized as  $\alpha_{\text{ML}} H_p$ , a constant times the pressure scale height  $H_p$ . The mixing-length parameter  $\alpha_{\text{ML}}$  is essentially a free parameter of the treatment, whose meaning furthermore depends on the value of other parameters typically introduced and differing between different implementations. In solar modelling the value of  $\alpha_{\text{ML}}$  is determined such that the model of the present Sun has the correct radius (see Section 7.1.1.1). The resulting value is often assumed to be applicable to models of other stars as well, with little justification. An interesting alternative is to calibrate  $\alpha_{\text{ML}}$  as a function of stellar parameters by matching

---

<sup>4</sup> In contrast, traditional stellar-atmosphere modelling invokes a parameterized “microturbulence” to account for the width of the spectral lines; see also Chapter 6.

mixing-length models to the results of detailed simulations (*e.g.*, Ludwig *et al.* 1999; Trampedach *et al.* 1999; Trampedach 2007). Other simplified treatments of convection have also been proposed. Canuto & Mazzitelli (1991) developed what they called the full spectrum of turbulence model, which has seen considerable use. Here, again, a parameter characterizing a convective length scale is often introduced and calibrated to obtain the correct solar radius. It should be noted that the detailed treatment of convection only affects the outermost parts of convective envelopes where the temperature gradient differs significantly from its adiabatic value. The properties of this region, together with the model of the stellar atmosphere, determines the value  $s$  of the specific entropy in the bulk of the convection zone, where the temperature stratification is essentially adiabatic and where  $s$  is therefore nearly constant.

### 3.2.1.4 Composition Changes

Stellar evolution is largely controlled by nuclear burning, fusing lighter elements into heavier; this change in composition causes changes in the structure of the star and controls the evolution of the star in the HR Diagram (*cf.* Fig. 2.1). The basic effect is simply understood: fusion increases the mean molecular weight and hence, according to the ideal-gas law, Eq. (3.19), the pressure would decrease if nothing else changed; this is incompatible with hydrostatic equilibrium and hence the core of the star contracts, increasing  $\rho$  and furthermore increasing  $T$  as a result of the release of gravitational potential energy. The increase in temperature increases both the nuclear reaction rate and the efficacy of radiative energy transport, leading to an increase in the luminosity of the star. This increase during the main-sequence phase is evident in Fig. 2.1.

Nuclear burning is not the only process changing the distribution of chemical elements in the star. As already noted, convective regions can be regarded as fully mixed. Outside convective regions, however, diffusion and settling must be taken into account. Thus the full equation for the evolution of the abundance  $X_k$  of some element can be written

$$\frac{\partial X_k}{\partial t} = \mathcal{R}_k + \frac{\partial}{\partial m} \left( \mathcal{D}_k \frac{\partial X_k}{\partial m} \right) + \frac{\partial}{\partial m} (\mathcal{V}_k X_k) . \quad (3.100)$$

Here  $X_k$  is the mass fraction of element  $k$ ,  $\mathcal{R}_k$  is the rate of change of  $X_k$  due to nuclear reactions, and  $\mathcal{D}_k$  and  $\mathcal{V}_k$  are the diffusion and settling coefficients for element  $k$ . In broad terms there is a tendency for heavier elements to settle towards the centre of the star while lighter elements rise towards the surface. Diffusion acts to oppose this effect, by reducing gradients in composition. However, the effects of settling are greatly complicated by the selective action of radiative forces on elements with spectral lines in the appropriate region of the radiative spectrum (Michaud 1970). This may cause some elements to rise towards the surface and create strong variations in the composition as well as

very unusual surface compositions in some stars. The time scales of these processes are typically far longer than the time scale of convective mixing (which can in fact be modelled as diffusion with a very large diffusion coefficient), and hence they are only relevant outside convective regions. Further complications arise from other possible mixing processes which will be discussed below.

### 3.2.1.5 Simplifications in Standard Modelling

Here we summarize the approximations made in most stellar evolution calculations which may be said to define their “standard” form:<sup>5</sup>

- The treatment of convection is generally approximated through a parametrization of the properties of the uppermost layers of the convection zone. A typical (and commonly used) example is the mixing-length formulation discussed above.
- The dynamical effect of convection (the so-called turbulent pressure) is ignored.
- It is assumed that there is no mixing outside convectively unstable regions; also element settling and diffusion are often ignored.
- Effects of rotation are ignored.
- Effects of magnetic fields are ignored.
- Effects of stellar winds are ignored.

Similarly, as discussed in Section 3.1.2, the calculations of oscillation frequencies are often done in the adiabatic approximation. Even when nonadiabatic effects are taken into account, their treatment is uncertain, since there is no definite theory for the perturbation to the convective flux induced by the oscillations. Also, the perturbations to the turbulent pressure are usually neglected.

It should also be noted that much of the uncertain macrophysics is concentrated very near the surface. In cool stars this is true of the dynamical effects of convection, since convective velocities are likely to be very small elsewhere, and of the details of convective energy transport, while in hot stars the effects of radiatively driven winds are also predominantly felt near the surface; furthermore, the effects of a visible magnetic field, such as seen in starspots, are likely only important for the structure of the near-surface layers. As discussed in Section 7.1.4.1 such near-surface problems have a very characteristic effect on the oscillation frequencies which helps in isolating their influence in asteroseismic analysis of oscillation frequencies. Apart from convective overshoot and a hypothetical strong internal magnetic field, the remaining difficulties listed are mainly concerned with the composition profile in the radiative interior of the model.

---

<sup>5</sup> This is evidently a concept that evolves with time, as more detailed and realistic calculations become feasible.

### 3.2.2 Microphysics of Stellar Interiors

As presented in the previous section, the basic equations of stellar evolution, Eqs (3.88), (3.89), (3.90), (3.91), (3.99) and (3.100), are relatively simple. These equations, together with the approximations discussed above, define what might be termed the *macrophysics* of stellar evolution. However, in addition to the complications already hinted at, these equations contain another layer of complexity in the *microphysics*, *i.e.*, the properties of stellar matter. A description of these properties is required to relate density to pressure, temperature and composition, to evaluate the opacity, the energy generation rate and the nuclear rate of change of composition and the rates of microscopic diffusion and settling. The relevant processes take place in a strongly interacting plasma of atoms, ions and electrons, and the detailed physics of these processes is still a matter of considerable uncertainty. One of the hopes of helio- and asteroseismology is to obtain substantial constraints on the microphysics of stellar matter from the observed frequencies. As discussed in Section 7.1.7 this hope has to a large extent been realized in the case of helioseismic investigations of the solar interior.

#### 3.2.2.1 Equation of State

The equation of state characterizes the thermodynamical properties of stellar matter; a review of the treatment of the equation of state, and its relation to helioseismology, was provided by Christensen-Dalsgaard & Däppen (1992). The simple approximation in Eq. (3.19) ignores a number of important effects. First of all, account must be taken of partial ionization, the degree of ionization generally increasing with increasing temperature. In the ideal-gas approximation this changes the mean molecular weight; also, the energy required to ionize the constituents of the gas changes the energetics of the gas and in particular the adiabatic exponents  $\Gamma_1$ ,  $\Gamma_2$  and  $\Gamma_3$  which are decreased below their ideal-gas value of 5/3. A simple treatment of ionization using the Saha equation leads to the unrealistic prediction that matter at the centre of, say, the Sun is far from fully ionized. This shows that other effects must contribute to the ionization; these are typically called “pressure ionization” but in reality involve various types of interaction between the constituents of the gas. The Coulomb interaction between the charged constituents of the gas makes a (negative) contribution to the pressure and furthermore affects the energetics and ionization states. Radiation makes a significant contribution to the thermodynamical properties which is relatively straightforward to include, as long as radiation can be treated in the diffusion approximation. At very high density degeneracy sets in, where electrons, and at near-nuclear densities neutrons, are pressed into higher-lying energy states as the lower quantum states in the system are filled. This gives rise to a finite pressure even in the limit of zero temperature. At sufficiently high density energies

are even reached in the degenerate matter where relativistic effects become important.

A very important aspect of dealing with these complicated effects is to ensure that the treatment, although necessarily approximate, is *thermodynamically consistent* in that it satisfies the thermodynamical identities between the different quantities. When this is not the case the results of using the treatment may depend on, for example, the choice of thermodynamic variables used to characterize the system.

One way to ensure thermodynamical consistency is to derive the equation of state from a free energy. The thermodynamical state, at given temperature, density and composition, say, is then obtained by minimizing the free energy under the relevant stoichiometric constraints, to obtain the ionization states and occupation numbers, and the relevant thermodynamic quantities can be obtained as derivatives of the free energy. This is the basis for the *chemical picture* in determining the equation of state. The various contributions to and complications of the equation of state are incorporated in the definition of the free energy. A simple, and widely used, form of such an equation of state is the EFF equation of state, developed by Eggleton *et al.* (1973); this was extended to include Coulomb effects, in the CEFF formulation, by Christensen-Dalsgaard & Däppen (1992). Perhaps the most highly developed equation of state of this form is the so-called MHD equation of state<sup>6</sup> (*e.g.*, Mihalas *et al.* 1988, 1990; Gong *et al.* 2001). It is characterized by a detailed treatment of the occupation probabilities of atomic states which eliminates, in a smooth fashion, the divergence of the partition function of an isolated atom; also, it leads naturally to full ionization at high densities.

The second way that has been used to ensure thermodynamical consistency is the *physical picture*. Here, at least in principle, the concepts of atoms and ions are dropped. Instead, the system is treated as a system of nuclei and electrons, where atoms and ions form as one of the results of the interactions in the system. In practice, the system is analysed in terms of activity expansions. A major advantage of the formalism is that the coupling to the continuum states removes the divergence of the normal partition function, which is replaced by the so-called Planck-Larkin partition function which is finite. This treatment has been developed as part of the OPAL opacity project at the Lawrence Livermore Laboratories in the ACTEX equation of state (Rogers *et al.* 1996; Rogers & Nayfonov 2002).

Interestingly, despite their fundamentally different treatments, these two formulations lead to rather similar results (*cf.* Trampedach *et al.* 2006), although the remaining differences may to a large extent reflect simplifications in the MHD treatment. On the other hand, the latter treatment has the advantage of being somewhat computationally simpler, hence allowing the calculation of equation-of-state tables of higher numerical accuracy or possibly direct calculation of the equation of state in stellar modelling, as is done routinely,

---

<sup>6</sup> named after Mihalas, Hummer and Däppen.

*e.g.*, with simple formulations. Thus an emulation of the ACTEX equation of state through an extension of the MHD formulation is an attractive option (*e.g.*, Däppen, 2007).

### 3.2.2.2 Opacity

The opacity depends on the detailed interaction between the radiation and the constituents of stellar matter; the total flux of energy obviously depends on an integral over all radiation frequencies. In stellar interiors, where the diffusion approximation is valid, the relevant average is the *Rosseland mean opacity*, obtained as a harmonic mean of the frequency-dependent opacity. This has contributions from bound-bound, bound-free and free-free interactions between radiation and electrons. Thus it depends on the detailed thermodynamical state of the gas, including the distribution of atoms on ionization and excitation states; hence the equation of state is a crucial part of the opacity calculation. The bound-free and free-free contributions approximately depend on density and temperature as  $\rho T^{-3.5}$ ; this so-called Kramers dependence, as well as a very large contribution from the ionization of hydrogen and helium, lead to the large opacity at low temperature. To these atomic contributions must be added scattering from free electrons; this obviously depends on the density of free electrons but is otherwise largely independent of density and temperature.

At sufficiently high density, where the electrons become strongly degenerate, electron conduction dominates energy transport. This is the case, in particular, for low-mass stars on the red-giant branch where the effective transport renders the stellar core essentially isothermal (*e.g.*, Cassisi *et al.* 2007).

The bound-bound transitions are a major complication in the opacity calculation since literally millions of transitions must be taken into account. This has had interesting asteroseismic consequences, in solving two major problems in the study of stellar oscillations: the instability of the  $\beta$  Cep and SPB stars and the period ratios between the fundamental and first overtone of radial pulsation in double-mode Cepheids and high-amplitude  $\delta$  Sct stars. It was pointed out by Simon (1982) that both problems could be solved by invoking a very substantial opacity increase, by a factor of 2 – 3. The opacity increase required to match the observed period ratios were determined more precisely by Andreassen & Petersen (1988). This was subsequently confirmed in the so-called OPAL opacity calculations (Iglesias *et al.* 1990, 1992), the opacity increase being caused by contributions from bound-bound transitions in predominantly iron. Very similar results were obtained by a totally independent effort in the so-called Opacity Project (OP) (Seaton *et al.* 1992; Seaton 1993). The result was that instability, through the heat-engine mechanism, could account for the occurrence of  $\beta$  Cep and slowly pulsating B stars (*e.g.*, Cox *et al.* 1992; Moskalik & Dziembowski 1992; see Sections 2.3.6 and 2.3.7). More recently, Jeffery & Saio (2006) found that the use of the OP opacities, with the inclusion

of nickel lines, improved the agreement with the observed instability region for the pulsating subdwarf B stars, and Miglio *et al.* (2007) similarly found that using the OP opacities gave rise to somewhat more extended instability regions for main-sequence B stars than did the OPAL tables. Also, period ratios in agreement with observations were found for Cepheid and  $\delta$  Sct star models with masses corresponding to the relevant evolution tracks (Moskalkic *et al.* 1992; Kanbur & Simon 1994). This is probably the first example where asteroseismic inference, in the broadest sense, has led to an update of the physics of stellar interiors. As discussed in Section 7.1.7 helioseismology has recently provided evidence that further revisions of the opacity may be required; corresponding evidence has been found from the modelling of the range of unstable modes in the  $\beta$  Cep star  $\nu$  Eri (*cf.* Section 7.3.2.4).

### 3.2.2.3 Nuclear Reactions

Apart from the very latest stages of the evolution of massive stars the relevant reactions are fusion of lighter nuclei into heavier. This requires that the nuclei approach quite closely, overcoming the very considerable Coulomb repulsion. The processes take place through quantum-mechanical tunnelling, at energies far below the Coulomb energy corresponding to the radii of the nuclei. Thus, under stellar conditions, nuclear reactions are slow processes: the average lifetime of a hydrogen nucleus at the centre of the Sun is of the order of  $5 \times 10^9$  yr. Also, in main-sequence stars the rate  $\epsilon$  of energy generation is low compared with typical energy producing devices: at the centre of the Sun  $\epsilon \simeq 17 \text{ erg g}^{-1} \text{ s}^{-1}$  or  $0.0017 \text{ W kg}^{-1}$ . Of course, the total energy generation is huge, as a result of the large mass in the star that is involved in the energy generation.

The Coulomb barrier depends of the product of the charges of the interacting nuclei. Thus nuclei with lower charges can react at lower energies, corresponding to lower temperature. Although details of nuclear properties may cause deviation from this tendency it clearly indicates that the first reactions that take place are those that lead to fusion of hydrogen into helium. A second important consequence is that reactions involving more highly charged nuclei depend more strongly on temperature. The temperature sensitivity is often characterized by using a power-law approximation to  $\epsilon$ ,

$$\epsilon \simeq \epsilon_0 \rho T^n , \quad (3.101)$$

where  $n$  determines the temperature sensitivity. An important example are the reactions involved in hydrogen fusion. The net reaction,



takes place through various series of reactions, each involving fusion of two nuclei. One chain of reactions, the *PP chain*, starts with the fusion of two hydrogen nuclei to a deuterium nucleus, continuing to the formation of a

helium nucleus. Here the reaction  ${}^1\text{H} + {}^1\text{H}$  controls the combined rate of the chain; as a result of the low charges involved the temperature sensitivity is relatively low, with  $n \simeq 4$ . The second type of reaction is a catalytic reaction, the *CNO cycle*, consisting of the successive addition of hydrogen nuclei to nuclei of carbon, nitrogen and oxygen, starting from  ${}^{12}\text{C}$  and ending with the production of a helium nucleus and a  ${}^{12}\text{C}$  or  ${}^{14}\text{N}$  nucleus. Here the reaction controlling the overall rate is  ${}^1\text{H} + {}^{14}\text{N}$ , with a higher product of charges and hence leading to a temperature dependence corresponding to  $n \simeq 20$ . It is obvious that the PP chain dominates at relatively low temperature and the CNO cycle at higher temperature. Since the central temperature increases with stellar mass along the main sequence, the PP chain tends to dominate in relatively low-mass stars and the CNO cycle in more massive stars. In practice, for stars of mass higher than around  $1.6 M_\odot$  the CNO cycle produces more than 75 per cent of the energy at the centre of main-sequence stars and more than 50 per cent of the total energy. As discussed above, a consequence of the high temperature sensitivity of the CNO cycle is that  $L/m$  in Eq. (3.96) becomes very large in the core of such stars, leading to the occurrence of a convective core.

In Eq. (3.102) charge conservation leads to the release of two positrons which are immediately annihilated by electrons and hence contribute to the energy release. In addition, lepton number conservation leads to the emission of two neutrinos. These have an extremely small probability of interacting with stellar matter and hence escape the star, carrying a fraction of the energy released in the reaction. Thus the effective energy available to the star depends on the details of the reactions. As discussed in Section 7.1.1.1 the neutrinos emitted by the Sun provide an important, if for a long time problematic, diagnostic of conditions in the solar core.

When one nuclear fuel has been exhausted in the core of a star, the core contracts and heats up until the temperature becomes sufficiently high that the next set of reactions can take place. Furthermore, outside the core the temperature is typically sufficiently high that burning of the original fuel can continue in a *shell-burning source*. Following exhaustion of hydrogen the next burning stage is the fusion of helium which takes place in the *triple-alpha process*,



accompanied by further fusion with helium to produce  ${}^{16}\text{O}$ . These are the final reactions for stars of masses below around  $8 M_\odot$ . In more massive stars nuclear fusion continues until the formation of iron-group nuclei; since these are the most strongly bound nuclei no further energy can be produced from fusion.

A substantial uncertainty in the computation of the energy generation rate and the rate of change of the abundances are the basic parameters of the nuclear reactions. These must be determined experimentally, but owing to the relatively low energies at which the reactions take place in stars the experiments are extremely difficult and significant uncertainties remain in

many important reactions, including the reaction  ${}^1\text{H} + {}^{14}\text{N}$  (Formicola *et al.* 2004). Further uncertainties come from the fact that the reactions take place in a plasma, where the other constituents may partly shield the Coulomb repulsion between the reacting nuclei. A procedure has been developed for dealing with the screening (Salpeter 1954), but doubts have been raised about the physical background of this procedure (*e.g.*, Shaviv & Shaviv 2001). Stellar models are in general relatively insensitive to modifications to the reactions rates: owing to the high temperature sensitivity a change in the reaction rate can be compensated for by a small modification to the temperature. However, the onset of convective cores is obviously sensitive to the balance between the PP chain and the CNO cycle and hence might be a useful diagnostic of the nuclear reactions, if the presence or not of convective cores in a sufficient sample of stars could be ascertained from asteroseismology.

### 3.2.2.4 Diffusion and Settling

The transport processes in stellar matter are described by the Boltzmann equation of the kinetic theory of gases, solved in a suitable approximation. The transport coefficients depend in a complex manner on the collisions and other interactions between the constituents of the gas. The long-range nature of the Coulomb interaction causes particular problems, related also to the corresponding effects in the treatment of the equation of state and the screening of nuclear reactions. A further complication is the need to deal with a mixture of atoms, ions and free electrons. A detailed discussion of the treatment of diffusion and settling was provided by Burgers (1969); this provides the basis for many of the implementations currently used (for a brief, recent review, see Thoul & Montalbán 2007). Michaud & Proffitt (1993) gave simple approximate expressions for the diffusion velocity, highlighting the contributions from the pressure and temperature gradients.

As discussed above, radiative forces caused by strong selective absorption can have a strong effect on the distribution of elements, in some cases leading to extreme accumulation of certain elements at the stellar surface. Evidently, the treatment of these radiative effects require consideration of the detailed frequency-dependent absorption coefficients of the ions involved and hence is closely related to the determination of the opacity. As a further complication, such effects may cause strong variations in the relative distribution of heavy elements with time and with the location of the star, requiring recomputation of the opacity from its individual contributions at each location in space and time. This clearly results in a major increase in the computation effort for stellar modelling. Such effects are therefore most often ignored; however, extensive and very interesting calculations of this nature have been carried out by the Montreal group (*e.g.*, Turcotte *et al.* 1998a,b, 2000, Richard *et al.* 2001, Michaud *et al.* 2007).

As discussed above, diffusion and settling are relevant outside convective regions. The speed of settling depends strongly on the interaction between the

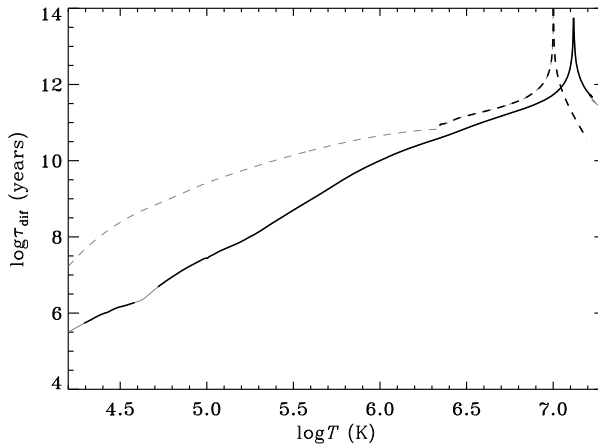


**Fig. 3.2.** Diffusion time scales (*cf.* Eq. (3.104)) for models of a ZAMS  $2 M_{\odot}$  star (continuous) and the present Sun (dashed). The thinner grey lines mark regions in convection zones, where convection ensures complete mixing.

constituents of the gas and hence on the density. Thus the characteristic time scale of settling varies greatly through the star. This is illustrated in Fig. 3.2 for a zero-age main-sequence model of a  $2 M_{\odot}$  star and a model of the present Sun. Here we show an effective settling time scale  $\tau_{\text{dif}}$ , defined as

$$\tau_{\text{dif}}^{-1} = \frac{1}{X_k} \frac{\partial}{\partial m} (\mathcal{V}_k X_k) \quad (3.104)$$

(*cf.* Eq. (3.100)) for the case of helium settling. In the solar case the settling time scale exceeds 9 Gyr in the region (indicated in the figure by the bolder curve) beneath the convective envelope; thus settling has a modest, if very significant, effect on solar models (see Section 7.1.7 and Fig. 7.29). However, in the  $2 M_{\odot}$  star the settling time scale is only 5 Myr just beneath the very thin outer convection zone; thus in this case helium very rapidly drains out of the near-surface layers, unless settling is counteracted by other processes, such as circulation or turbulence which cause mixing outside convective regions, or mass loss which drags fresh helium to the surface layers at a rate which compensates for settling (see also Vauclair *et al.* 1974).

### 3.2.3 Standard Stellar Evolution

Section 2.1 provided a general overview of stellar properties and stellar evolution. Here we concentrate on those evolutionary stages for which asteroseismic

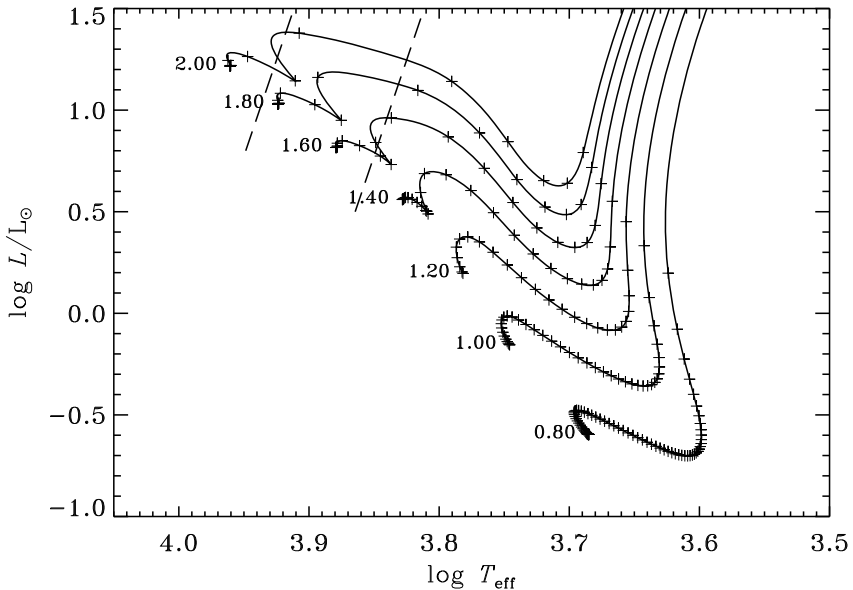


**Fig. 3.3.** Evolution tracks for pre-main-sequence evolution for a selection of masses, indicated in units of  $M_{\odot}$ . The crosses mark the age along the tracks, in steps of 1 Myr. The dashed lines sketch the location of the classical instability strip.

investigations may be relevant. Figure 3.3 shows evolution tracks for stars in the pre-main-sequence phase, before the onset of equilibrium hydrogen burning.<sup>7</sup> This phase is dominated by the contraction of the stars, with much of the stellar luminosity coming from the release of gravitational potential energy, and hence evolution takes place on the Kelvin-Helmholz time scale. As a result of the contraction the effective temperature increases and the stars move across the HR Diagram. In particular, for masses above around  $1.5 M_{\odot}$  the stars pass through the Cepheid instability strip where pulsations would be expected. In fact, as discussed in Section 2.4  $\delta$  Sct-like pulsations have been observed in a number of pre-main-sequence stars (*e.g.*, Zwintz *et al.* 2004), providing a potential for investigating these early phases of stellar evolution (see also Fig. 2.25). A particularly interesting aspect is the potential

<sup>7</sup> The evolution tracks were obtained from CESAM computations as part of the ESTA effort under the CoRoT project (*e.g.*, Monteiro *et al.* 2006; Lebreton *et al.* 2008). See <http://astrotheor3.astro.ulg.ac.be/montalban/ESTA/>. We are grateful to A. Miglio for making them available.

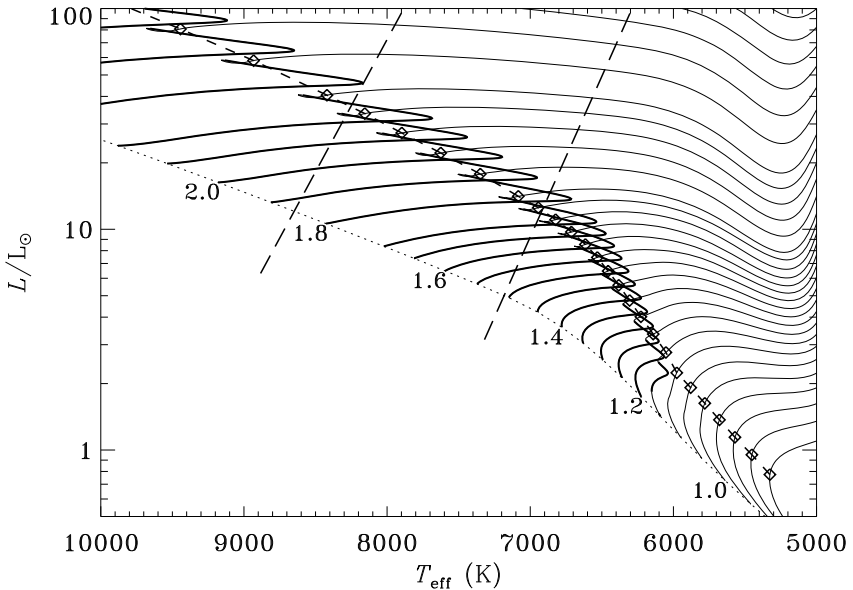


**Fig. 3.4.** Evolution tracks for main-sequence evolution for selected masses, some of which are indicated in units of  $M_{\odot}$ . The bolder parts of the curves indicate the part of the evolution where the model has a convective core. The dotted line shows the zero-age main sequence, while the dashed line shows the terminal-age main sequence (TAMS) where the central hydrogen abundance  $X_c$  has been reduced to  $10^{-5}$ ; the diamonds indicate where the TAMS crosses the evolution tracks. The dashed lines sketch the location of the classical instability strip.

to determine frequency changes resulting from the relatively rapid evolution (Breger & Pamyatnykh 1998).

Since pre-main-sequence stars have extensive outer convection zones, solar-like oscillations would be expected (*cf.* Sections 1.6.2, 2.3.1; see also Samadi *et al.* 2005). However, as noted in Section 2.1, these stars typically show other forms of activity and hence are likely to have an intrinsic noise level too high to allow the detection of solar-like oscillations, at their typical amplitudes of less than  $1 \text{ m s}^{-1}$  in velocity or a few parts per million in intensity.

Evolution after the onset of hydrogen burning was illustrated in Fig. 2.1. A more detailed representation of the evolution during and just after central hydrogen burning is provided in Fig. 3.4. This illustrates the striking distinction between stars without and with a convective core during the main-sequence evolution. For the parameters chosen here this transition takes place at a mass

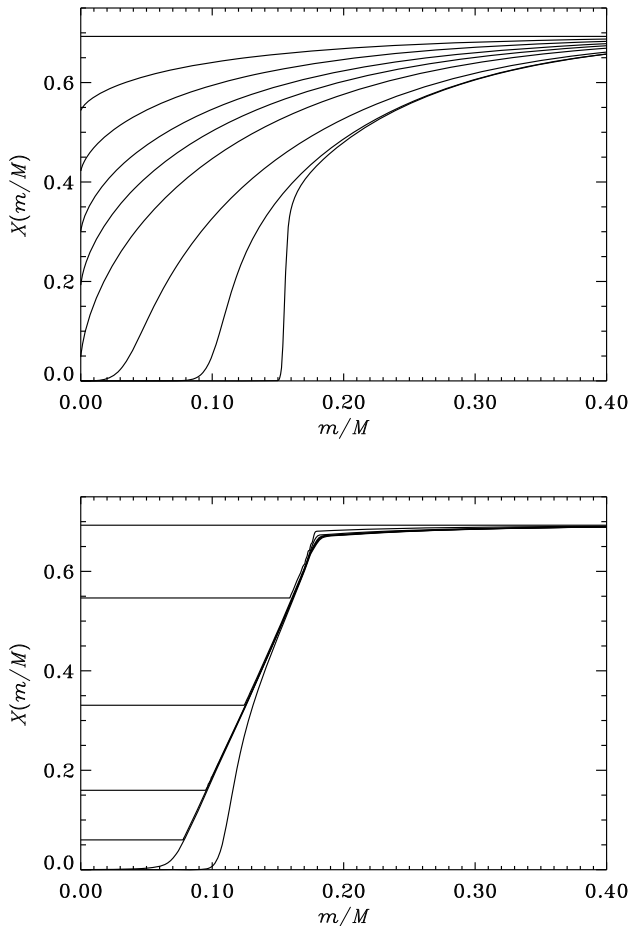


**Fig. 3.5.** The evolution of the hydrogen-abundance profile in stars with a radiative or a convective core on the main sequence. The top panel shows a  $1 M_{\odot}$  star with a radiative core, at ages 0, 2.0, 3.6, 5.0, 6.2, 7.5, 9.6, 11.0 and 11.6 Gyr. The bottom shows the case of  $2.5 M_{\odot}$ , with a convective core, at ages 0, 0.15, 0.31, 0.4, 0.44, 0.46 and 0.48 Gyr. No convective overshoot was included in the latter case.

of around  $1.15 M_{\odot}$ . The difference in the evolution can be understood from the changes in the hydrogen profile as the star evolves, shown in Fig. 3.5. In stars with a radiative core, hydrogen is depleted most rapidly at the centre where the temperature is highest. When hydrogen is exhausted at the centre, hydrogen burning continues just outside the resulting very small helium

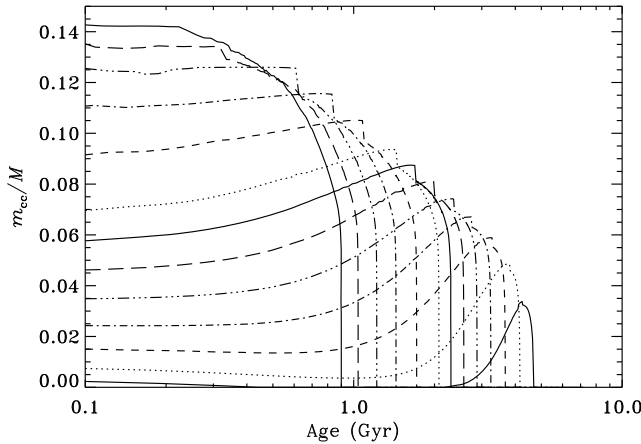


**Fig. 3.6.** The mass  $m_{cc}$  of the convective core, in units of the stellar mass, as function of stellar age, in models with no convective core overshoot. Results are shown for masses between  $1.15 M_{\odot}$  (which for this calculation marks the lowest mass with a significant convective core) to  $1.5 M_{\odot}$  in steps of  $0.05 M_{\odot}$  and thence to  $2 M_{\odot}$  in steps of  $0.1 M_{\odot}$ . Note that for  $1.15 M_{\odot}$  there is a phase where the core is radiative.

core which gradually increases in size. As a result there is a gradual transition from central hydrogen burning to hydrogen burning in a shell source. In contrast, in a star with a convective core the hydrogen abundance is reduced uniformly throughout the core which, as mentioned above, can be regarded as fully mixed on a nuclear time scale. Consequently, towards the end of central hydrogen burning hydrogen is depleted throughout much of the region of energy generation. To maintain its luminosity the star undergoes overall contraction; this increases the central temperature and hence the nuclear energy generation rate, and in addition the release of gravitational potential energy contributes to the luminosity. This brief phase of contraction is reflected in the increasing effective temperature in what is commonly known as the “hook” in the evolution tracks. Finally, when hydrogen is completely exhausted in the core, hydrogen burning is established in a shell source and the star begins to expand.

As is evident in Fig. 3.5, the extent in mass of the convective core decreases with increasing age in the  $2.5 M_{\odot}$  model. This is largely the result of the decrease in the hydrogen abundance and the resulting decrease in the opacity. The decreasing core leaves behind a steep gradient in the hydrogen abundance which, as discussed in Sections 3.4.2 and 3.5.3 has a strong effect on the pulsation properties of the star. This behaviour is typical of stars of masses

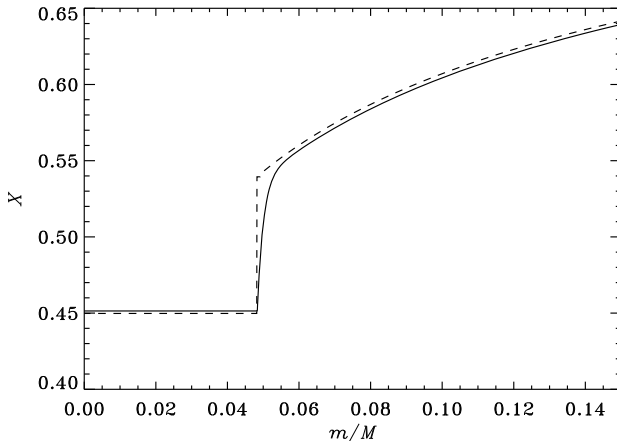


**Fig. 3.7.** The hydrogen profile in a  $1.3 M_{\odot}$  star with  $Z = 0.017$ , at age 1.47 Gyr, computed without (dashed curve) and with (continuous curve) helium diffusion.

higher than around  $2 M_{\odot}$ . In the mass range  $1.15 - 2 M_{\odot}$ , however, there is a phase of increasing size of the convective core, as illustrated in Fig. 3.6. This is caused by an increase in the importance of the CNO cycle, relative to the PP chain, caused by an increase in the  $^{14}\text{N}$  abundance through burning of  $^{16}\text{O}$  (in more massive stars the CNO cycle dominates from the outset of central hydrogen burning and this effect is not relevant to the size of the convective core). It is evident that if diffusion is not taken into account, the growing core causes a discontinuity in the composition at the edge of the core. Since pressure and temperature are continuous, this results in a density discontinuity which potentially may give rise to a new class of oscillation modes (see Section 3.5.3). The discontinuity in composition also causes a discontinuity in  $\nabla_{\text{rad}}$  which may lead to semiconvection (Popiel'ski & Dziembowski 2005). This is very similar to the behaviour found during core helium burning, which leads to substantial uncertainties in the modelling of the subsequent evolution of the star, and hence asteroseismic diagnostics on the hydrogen main sequence are potentially very valuable (see also Mazumdar *et al.* 2006a). If diffusion is included, the discontinuity is replaced by a very sharp gradient in abundance and density. This is illustrated in Fig. 3.7. However, the interaction between diffusion and settling of helium and heavy elements, combined with the evolution of the convective core, may lead to variations in composition and hence opacity which also induce semiconvection (*e.g.*, Richard *et al.* 2001; Montalbán *et al.* 2007).

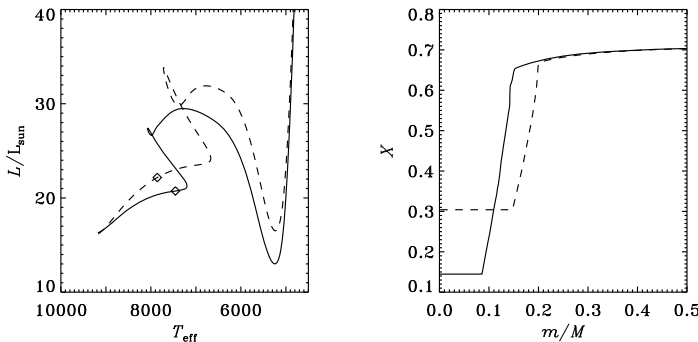


**Fig. 3.8.** Left panel: evolution tracks for models of a  $2 M_{\odot}$  star; the solid curve shows evolution without overshoot from the convective core, while the dashed curve shows a model with an overshoot of  $\alpha_{\text{ov}} = 0.2$  pressure scale heights. Right panel: hydrogen profiles at the age 0.8 Gyr for the two models, using the same line styles. The models are marked by diamonds in the left panel.

A further complication at the edge of convective cores is the likely presence of convective overshoot: matter moving towards the boundary of a convectively unstable region reaches the boundary with some velocity and hence continues the motion into the stable layer, although the distance of penetration is highly uncertain (for simplified treatments of this, see for example Maeder (1975) and Zahn (1991)). Overshoot increases the mixed region and hence the amount of hydrogen available for nuclear burning, with potentially fairly substantial effects on stellar evolution. As an example, Fig. 3.8 shows evolution tracks and selected hydrogen-abundance profiles in a  $2 M_{\odot}$  model without and with overshoot. The actual extent of overshoot is uncertain; Roxburgh (1978, 1989) derived integral constraints on the properties of convective cores, although not of a form that allows calculation of the extent of overshoot. In stellar modelling it is typically parameterized as a fraction  $\alpha_{\text{ov}}$  of the pressure scale height, in analogy with the mixing length, with  $\alpha_{\text{ov}}$  regarded as a free parameter that must be calibrated to match observed properties. Evidence for convective-core overshoot has been obtained from “classical” observations, particularly of double-lined detached eclipsing binaries (*e.g.*, Andersen *et al.* 1990; Ribas *et al.* 2000; Claret 2007) and isochrone fits to observations of stellar clusters (*e.g.*, Mermilliod & Maeder 1986; VandenBerg *et al.* 2006).

The evident uncertainties in the treatment of convective cores, in terms of overshoot and semiconvection, have very substantial effects on the later evolution of the stars, particularly in the case of massive stars that evolve into supernova explosions (*e.g.*, Woosley *et al.* 2002, Poelarends *et al.* 2008). Thus

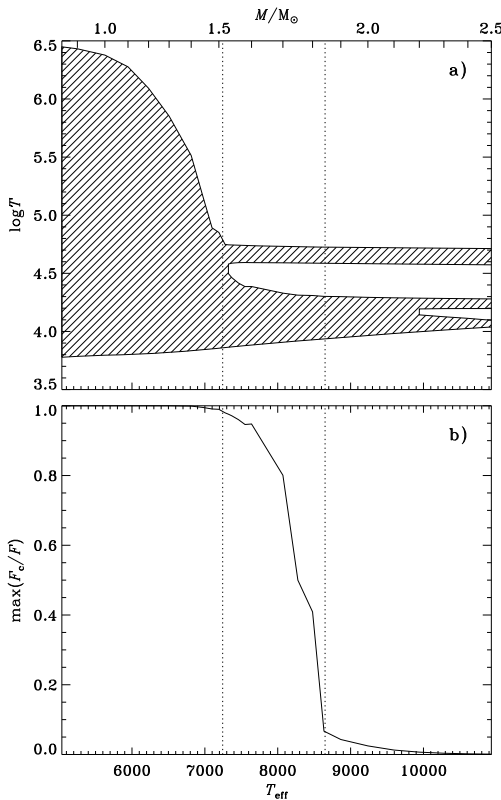


**Fig. 3.9.** Properties of convective envelopes in zero-age main-sequence stars, as functions of the effective temperature  $T_{\text{eff}}$  (lower abscissa) and stellar mass in solar units (upper abscissa). The vertical dotted lines indicate the approximate limits of the instability strip. (a) The hatched area shows the extent of the convective envelope, indicated in terms of temperature  $T$ . Note that the convective envelope shrinks rapidly as the red edge of the instability strip is approached from lower temperature. The separate convective regions are associated with ionization zones of helium and hydrogen. (b) The maximum ratio between the convective flux  $F_c$  and the total flux  $F$ . Adapted from Christensen-Dalsgaard (2000).

a major goal of asteroseismology is to obtain constraints on the properties of convective cores. As discussed in Chapter 7 this has been, and surely will become, possible for several classes of pulsating stars.

The properties of convective envelopes are very important to the behaviour of stellar oscillations, particularly their excitation. Figure 3.9 illustrates the extent of the outer convection zone, and the contribution of convection to energy

transport, along the zero-age main sequence. For  $T_{\text{eff}} \gtrsim 7500$  K the convection zone in these models splits into two components, associated respectively with the ionization of hydrogen and the first ionization of helium (at lower temperature) and the second ionization of helium (at higher temperature); for the hottest models the former separates into two components, from hydrogen and helium ionization. These models are simple mixing-length models with no overshoot. In reality it seems more likely that overshoot links the whole region, causing it to be mixed (*e.g.*, Latour *et al.* 1981; Kupka & Montgomery 2002; Trampedach 2004; Silvers & Proctor 2007). This is particularly important for the effects of diffusion on the stellar surface composition.

Heat-engine excitation (*cf.* Section 1.6.2) is in most cases determined by the energetics of the near-surface layers where convection dominates the energy transport in stars with extensive outer convection zones. Since the effect of convection in many cases appears to act to damp the oscillations (see Section 3.7.3) we would expect the modes to be damped in such stars. Figure 3.9b shows the maximum fraction of energy carried by convection, as a function of effective temperature, compared with the extent of the Cepheid instability strip. It is evident that the “red” (or cool) edge of the instability strip does, in fact, correspond to the point where convection begins to dominate. On the other hand, convective transport remains important throughout the instability strip and hence should be taken into account in the computation of stellar stability. In cool stars, including the Sun, convection apparently stochastically excites otherwise damped oscillations (see Section 1.6.2). As a first, rough, approximation the result is that the energy in a single mode of oscillation is equal to the energy in a single convective eddy with a time scale corresponding to the oscillation period (Goldreich & Keeley 1977); for masses exceeding  $\simeq 1.5 M_{\odot}$  the relevant convective energy decreases rapidly with increasing mass and so, therefore, do the expected amplitudes (*e.g.*, Christensen-Dalsgaard & Frandsen 1983a; Houdek *et al.* 1999).

As with the convective cores, overshooting is likely below the convectively unstable region in convective envelopes. The effect on stellar evolution is less significant than the effect of core overshoot; however, the resulting deepening on the convectively mixed region in stars on the red-giant branch affects the location of the so-called “bump” in the distribution of stars in the HR Diagram of stellar clusters (*e.g.*, Cassisi *et al.* 2002). Also, overshoot below the solar convective envelope is amenable to helioseismic investigations which provide significant constraints on the properties of overshoot (see Section 7.1.7). Similar investigations may become possible from observations of solar-like oscillation in distant stars, when sufficiently accurate observations become available. Such investigations will undoubtedly improve our general understanding of the processes of convective overshoot. We also note that heavy-element settling may cause semiconvection just below convective envelopes, as has been found, *e.g.*, in solar-mass stars somewhat more evolved than the Sun (*e.g.*, Bahcall *et al.* 2001; Christensen-Dalsgaard & Di Mauro 2007).

After the exhaustion of hydrogen in the central region, hydrogen burning continues in a shell around a gradually growing helium core. Owing to its increasing mass the core contracts. The response of the outer layers, outside the burning shell, follows what might be termed the shell-burning law (or the mirror principle): when a region inside a shell source contracts the layer outside the source expands; and vice versa. This behaviour is generally found in numerical modelling of stellar evolution, but, despite extensive efforts, a fully convincing rationalization of the behaviour has not been found (see Faulkner 2004 for references, and what is probably the most convincing analysis to date). For stars more massive than around  $2 M_{\odot}$  the Schönberg-Chandrasekhar instability of the core leads to core contraction and envelope expansion on a thermal time scale (Schönberg & Chandrasekhar 1942; for a simplified discussion, see, *e.g.*, Kippenhahn & Weigert 1990). The evolution in this phase is generally relatively rapid and hence the likelihood of finding a star in this phase is correspondingly small. The rapid evolution across the HR Diagram towards the red-giant branch is also reflected along the evolution tracks in Fig. 3.8, and in more detail in Fig. 3.10 where the diamonds mark steps of 5 Myr in evolution, which are clearly greatly separated in this phase. The energy used to expand the star strongly reduces the energy available for radiative output, causing the marked dip in the luminosity at  $\log T_{\text{eff}} \simeq 3.71$  in Fig. 3.10. The expansion of the envelope leads to a reduction in the effective temperature and a rapid deepening of the convective envelope until the star reaches the vicinity of the Hayashi track. It may be shown that stars with an effective temperature on the cool side of the Hayashi track are unstable; thus the continuing expansion takes the star up the Hayashi track, as illustrated in Fig. 2.1. At this point the star has a very compact core surrounded by an extensive convective envelope.

The evolution up the red-giant branch stops when the temperature in the core reaches around  $100 \times 10^6$  K, sufficient for the ignition of helium burning in the triple-alpha process. However, even after the establishment of core helium burning a substantial fraction of the energy produced in the star comes from the hydrogen shell source. Helium ignition leads to an expansion of the core and hence, in accordance with the shell burning “law”, to contraction of the outer layers of the star. This causes evolution down the red-giant branch. At masses below around  $2.3 M_{\odot}$  the core is strongly degenerate at the point of helium ignition; as a result the pressure is independent of temperature, and the helium ignition takes place as a thermal run-away, with an extremely high release of energy during a few hours. However, this energy is largely absorbed in work to expand the layers immediately outside the core and hence does not have a dramatic effect on the outer layers of the star. When the core has expanded sufficiently degeneracy is lifted and helium burning settles down into equilibrium; at this point the star is on the horizontal branch (see Section 2.1). At higher masses helium ignition takes place more gradually; the evolution into the phase of central helium burning is illustrated in Fig. 3.10. It is evident from the markers indicating time intervals of 5 Myr that the evolution between

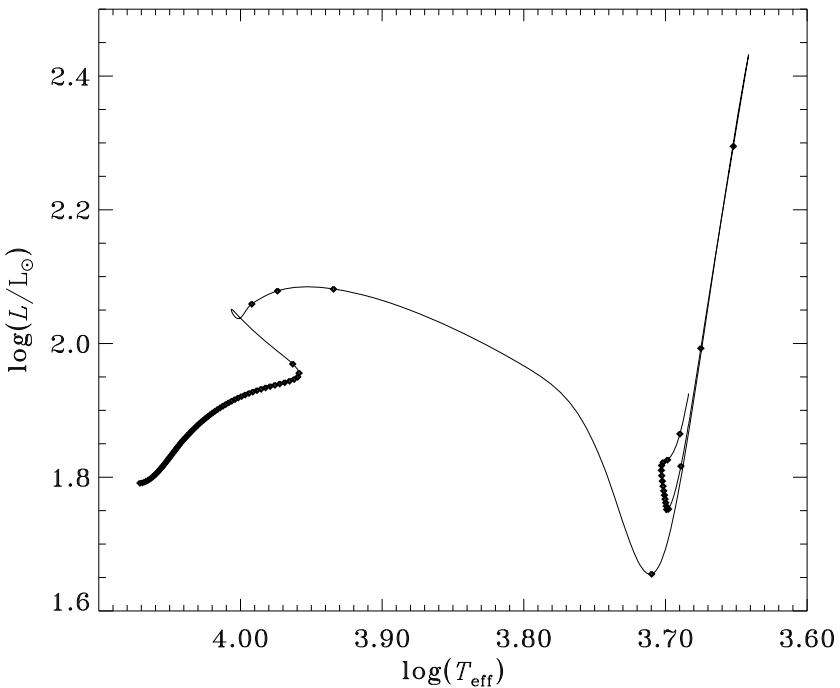


**Fig. 3.10.** Evolution of a model of  $\varepsilon$  Oph, of mass  $2.35 M_{\odot}$ . The diamonds are placed at 5 Myr intervals along the evolution sequence. (see Section 7.2.5).

the end of central hydrogen burning and the stabilization of helium burning is very fast.

After helium is exhausted in the core, the star has a helium shell source, outside the carbon-oxygen core, as well as the continuing hydrogen shell source. However, this double-shell situation develops instabilities, where the star alternates between burning in the hydrogen- and the helium-shell source. At the same time the core contracts strongly and the envelope expands, the star returning to the Hayashi track and moving up what is known as the Asymptotic Giant Branch (AGB). For stars with masses below around  $8 M_{\odot}$  nuclear burning stops with helium burning: as a result of the onset of degeneracy and strong cooling from the emission of neutrinos the temperature never gets high enough that the subsequent reactions can take place. Strong mass loss (see below) removes the outer parts of the star, leaving behind the degenerate carbon/oxygen core which cools down as a white dwarf. Following the mass loss the white dwarf consists predominantly of carbon and oxygen,

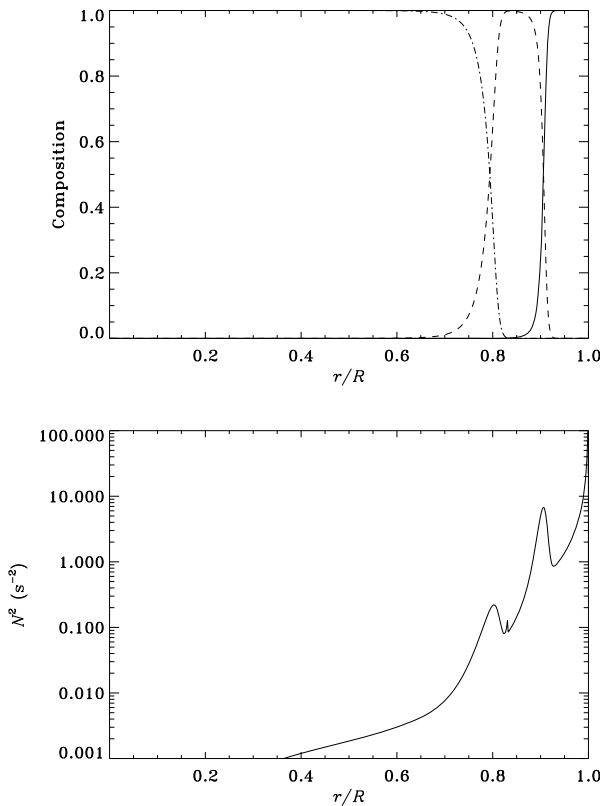


**Fig. 3.11.** Results for a model of a  $0.65 M_{\odot}$  DA white dwarf, of effective temperature 12 000 K. The top panel shows the hydrogen abundance (continuous curve), the helium abundance (dashed curve) and the combined carbon and oxygen abundance (dot-dashed curve), as a function of fractional radius. The bottom panel shows the squared buoyancy frequency. Note the bumps in  $N^2$  associated with the steep composition gradients. See Brassard & Fontaine (2006). Data courtesy of P.-O. Quirion.

resulting from the helium burning, although with small amounts of helium and possibly hydrogen; as discussed in Section 2.7.2, some white dwarfs, the DB class, appear to lack hydrogen altogether. Owing to the very strong gravity the elements separate according to weight through settling, resulting in a composition structure as illustrated in Fig. 3.11. This layered structure has a strong influence on the oscillation properties of the white dwarf and hence asteroseismology can be used to determine the masses in, in particular, the hydrogen and helium layers. Also, the relative abundance of carbon and oxygen

in the core depends strongly on the, somewhat uncertain, reaction parameters for the reaction  $^{12}\text{C} + ^4\text{He}$ . Thus an asteroseismic determination of the relative abundance of oxygen and carbon may provide a measure of the rate of this reaction (*e.g.*, Metcalfe *et al.* 2002), although obviously subject to other uncertainties in the modelling of the relevant evolutionary phases (*e.g.*, Straniero *et al.* 2003).

The cooling time scale of white dwarfs exceeds the age of the Galaxy. Thus their observed luminosity and temperature distribution reflects the star formation history of the Galactic disc, including its age, provided that the modelling of the cooling is sufficiently well understood or constrained (for a review, see Fontaine *et al.* 2001). Asteroseismic determination of the cooling rate may provide important constraints on the cooling processes.

In more massive stars the reactions continue to the formation of iron-group nuclei, after which energy generation by fusion has to stop. Instead an instability sets in which causes the central approximately  $1\,\text{M}_\odot$  of the star to collapse to nuclear density, releasing a huge amount of gravitational potential energy and causing a supernova explosion. The collapsed core is largely converted to neutrons, or possibly more exotic matter, and ends up as a *neutron star*.

### 3.2.4 Complications

The above description, complicated as it might seem, still leaves out a number of effects which are observed and which surely play an important role in stellar evolution. These are at the frontier of stellar modelling; undoubtedly the steadily improving data from asteroseismology will be a strong guide and inspiration to develop more appropriate treatments of them, and deeper understanding of their physical nature.

#### 3.2.4.1 Mass Loss

Many stars are observed to lose mass at a rate that implies significant losses during their lifetime; an introduction to the physics and properties of mass loss was given by Lamers & Cassinelli (1999). In hot main-sequence stars the mass loss is driven by radiative effects on the ions in the stellar atmosphere (*e.g.*, Kudritzki & Puls 2000). This is dominated by the interaction with elements heavier than hydrogen and helium. Thus the heavy-element abundance  $Z$  has a strong effect on the mass-loss rate and hence on the evolution of such massive stars. In stars of near-solar metallicity and masses exceeding  $\sim 30\,\text{M}_\odot$  the effect is that a large fraction of the outer hydrogen-rich layers of the stars are lost, leading to the formation of *Wolf-Rayet stars* with spectra dominated by helium and carbon or nitrogen (for a review, see Crowther 2007). This has a strong effect on the properties of the supernova explosions resulting at the end of the evolution of these stars, limiting the mass of the supernova precursor and hence also the potential for forming black holes (*e.g.*, Woosley *et al.* 2002).

On the other hand, in stars of the first generation after the Big Bang (the so-called Population III stars) the very low  $Z$  and the consequent much less efficient mass loss lead to the prediction of massive supernova precursors and hence the potential formation of black holes of considerable mass.

Main-sequence stars with effective temperatures below around 6500 K have hot coronae, heated by stellar activity, and hence expected to cause mass loss of the same nature as seen in the solar wind (*e.g.*, Parker 1958). In the case of the present Sun this leads to a mass loss of around  $2 \times 10^{-14} M_{\odot} \text{ yr}^{-1}$ . Comparable or somewhat larger mass loss has been inferred in solar-like stars by observations of Lyman  $\alpha$  absorption from the “astrospheres” surrounding the stars (Wood *et al.* 2005). Mass loss in somewhat hotter stars was invoked by Michaud *et al.* (1983) to account for certain abundance anomalies, although without suggestion of a specific mass-loss mechanism. In both cases, the assumed level of mass loss is too low to be detectable observationally, except in the case of the Sun. The total loss of mass is likely insignificant for the evolution of the stars, but the combined effect of mass loss, mixing and settling is important for the surface composition of the stars and hence for the excitation of stellar oscillations by the heat-engine mechanism. Also, as discussed in the following section, in lower-main-sequence stars the resulting loss of angular momentum has a strong effect on the evolution of stellar rotation.

Mass loss becomes important near the tip of the red giant branch and on the asymptotic giant branch (for a review, see Willson 2000). Here an important driver of mass loss is radiation acting on dust grains formed in the cool atmosphere of these stars (*e.g.*, Andersen 2007), although effects of an extended chromosphere (*e.g.*, Schröder & Cuntz 2005) and acoustic waves (Pijpers & Habing 1989) are likely also important. The amount of mass lost has important effects on the subsequent evolution, including the location of low-mass stars on the horizontal branch during the phase of core helium burning (D’Antona & Caloi 2004). The first observations in mass loss in Population II stars on the red-giant branch were recently obtained with the Spitzer infrared satellite (Origlia *et al.* 2007).

Near the tip of the asymptotic giant branch even stronger mass loss is found, eventually leading to the expulsion of the entire envelope (see, for example, Decin *et al.* 2006, 2008). A contributing factor in this dramatic mass loss are the large-amplitude radial pulsations observed in these stars, *e.g.*, in the case of Mira variables (see Section 2.5.4). The formation of dust plays an important role in this process. It was argued by Höffner & Andersen (2007) that carbon dust grains play a dominant role, even in stars with oxygen-rich atmospheres, as a result of non-equilibrium processes in the outflow. The mass loss becomes critical when the rate of mass loss matches the rate of the evolution of the star (Willson 2000). The outcome of this rapid mass loss is the formation of a planetary nebula, lasting only a few times  $10^4$  yr, and of a white dwarf, as discussed above.

### 3.2.4.2 Rotation, Mixing and Magnetic Fields

Rotation has very substantial effects on many aspects of stellar evolution, and the treatment of these effects remains a serious uncertainty in stellar modelling. Effects of rotation on stellar structure were discussed by Tassoul (2000); also, many aspects of stellar rotation, both observational and theoretical, were considered in the volume edited by Maeder & Eenens (2004). A comprehensive presentation of the effects of rotation on major parts of stellar evolution was provided by Maeder (2009).

It is evident that a rotating star loses its spherical symmetry, and hence a major simplification in stellar modelling is lost; in particular, the centrifugal force must be taken into account in the hydrostatic balance, resulting in an oblate structure. For relatively slow rotation the stellar structure can still be approximated by a spherically symmetric model, by including the spherically symmetric component of the centrifugal force in the equation of hydrostatic support, to obtain

$$\frac{\partial p}{\partial r} = -\frac{Gm\rho}{r^2} + \frac{2}{3}\rho r\Omega^2, \quad (3.105)$$

where  $\Omega$  is the angular velocity. For more rapid rotation this approximation no longer holds and fully two-dimensional model calculations are required (e.g., Deupree 1995; Roxburgh 2006; MacGregor *et al.* 2007); in the last case extremely distorted models were found in cases of very rapid rotation.

The surface distortion strongly affects conditions in the atmosphere of rapidly rotating stars. The centrifugal acceleration results in a reduced effective surface gravity  $g_{\text{eff}}$  that depends on latitude, such that it is smallest at the equator. The magnitude of this effect is measured by the ratio  $\Omega^2 \bar{R}^3 / (GM)$  between typical centrifugal and gravitational accelerations, where  $\bar{R}$  is a suitable average surface radius. An important consequence of this is the so-called *gravity darkening* (von Zeipel 1924), a reduction in the flux and hence the effective temperature resulting from the reduced gravity. This is often expressed as

$$T_{\text{eff}} = T_{\text{eff,p}} \left( \frac{g_{\text{eff}}}{g_{\text{eff,p}}} \right)^\beta, \quad (3.106)$$

where  $T_{\text{eff,p}}$  and  $g_{\text{eff,p}}$  are the effective temperature and effective gravity at the pole. For a radiative envelope, the case considered by von Zeipel,  $\beta = 1/4$ . Lucy (1967) considered convective envelopes and found  $\beta \simeq 0.08$ . It is interesting that interferometric observations of rapidly rotating stars have revealed the rotationally induced oblateness and latitude dependence of the surface temperature in a few cases (e.g., Domiciano de Souza *et al.* 2003, 2005; Monnier *et al.* 2007); the analysis of Altair in the latter two papers suggests a value of  $\beta$  close to 0.25, in accordance with von Zeipel's result. Maeder (1999) pointed out that these variations with latitude are also likely to have strong effects on mass loss in rapidly rotating stars. From a combination of gravity and opacity effects he found that the distribution of mass loss depends strongly on the temperature of the star. In very hot stars (O stars) the result

is a predominantly polar mass loss; an important consequence of this is that little angular momentum is lost from the star as a result of the mass loss. For somewhat cooler and evolved stars (B supergiants), on the other hand, the mass loss takes place predominantly in the equatorial region. A more detailed investigation of these effects, with application to  $\eta$  Carinae, was carried out by Aerts *et al.* (2004c).

In Eq. (3.105)  $\Omega$  is in general a function of position and time. This is a major complication and a large uncertainty in stellar modelling. There is little doubt that stars are generally born with rapid rotation resulting from the contraction of interstellar clouds and infalling material from a disc. The initial rotation profile  $\Omega(r, \theta)$  on the zero-age main sequence is uncertain, but it is perhaps not implausible that it is approximately uniform: at least the star has gone through a fully convective phase on the Hayashi track where convection must have led to rapid angular-momentum transport and hence strong coupling between rotation in the different parts of the star. However, there are no such obvious angular-momentum transport processes in the radiative part of the star. The evolution on and beyond the main sequence, at least until the red-giant branch, involves contraction of the core and expansion of the envelope. Thus if there is local conservation of angular momentum the angular velocity of the core increases as the radius and hence moment of inertia of the core decreases, and conversely the outer layers rotate more slowly.

Two closely related complications affect this simple picture. One is the loss of angular momentum of the star through a stellar wind. Evidently, the angular momentum of the material lost to the wind is carried away from the star. In stars with extended strong winds, such as massive stars, this can play a major role for the rotational evolution of the star. However, also in lower-main-sequence stars, with weak winds driven by hot coronae, the loss of angular momentum is very significant. Here the wind is coupled to the star through the magnetic field that threads it and hence is forced to rotate with the stellar angular velocity out to a substantial distance from the star; decoupling takes place at the *Alfvén radius*  $r_A$ , the point inside which the magnetic energy is larger than the kinetic energy of the flow. In the solar case this happens at roughly  $10 R_\odot$ . The result is a very significant angular-momentum loss in these stars, in the case of the present Sun corresponding to a typical time scale of around  $10^9$  yr. The properties of the wind depend on the strength of the magnetic activity. It is believed that the stellar magnetic field is created through a dynamo mechanism resulting from the interplay between rotation and motion in the convective envelope. This gives rise to a direct relation between the value of the angular velocity and the angular-momentum loss which can be solved to derive the evolution of the angular velocity with stellar age. From a limited set of observations Skumanich (1972) demonstrated that as a result both rotation and stellar activity decrease as  $\tau^{-1/2}$ ,  $\tau$  being the age of the star. Motivated by this Durney (1972) showed that such behaviour results from the dependence of angular-momentum loss and activity on the stellar angular velocity (see also Schrijver & Zwaan 2000). While the actual

behaviour is likely more complicated there is strong observational evidence that the angular velocity of stars in this part of the HR Diagram decreases with increasing age (*e.g.*, Soderblom *et al.* 2001; Barnes 2007). Thus we must expect that the Sun rotated much more rapidly, and consequently was more active, early in its evolution.

The angular-momentum loss takes place from the stellar surface or, in the case of magnetic winds, from the convective envelopes of these stars since this is strongly rotationally coupled. The resulting evolution of the internal rotation depends on the transport of angular momentum in the stellar interior. Were there no transport in the radiative regions, we would expect the stars to retain a rapidly rotating interior. In fact, rotation is directly responsible for such transport processes. These processes not only affect the evolution of the angular velocity but also, very importantly, have a strong influence on the chemical evolution of the star. Radial gradients in the angular velocity may give rise to a variety of instabilities, which cause transport that can be modelled as a turbulent diffusion.

Another very important effect caused by rotation is *meridional circulation*. It was noted by von Zeipel (1924) that a rotating star can be in thermal equilibrium only under very special circumstances. In general, heat transport by meridional currents is required to maintain balance between energy generation and energy transport, as pointed out by Eddington and Vogt (see Kippenhahn & Weigert 1990 for a discussion). This was analysed more quantitatively by Sweet (1950) who found that the circulation was relatively weak and hence likely of limited significance. However, Zahn (1992) noted that much more important circulation would be set up when changes of the angular velocity at the surface<sup>8</sup> cause radial gradients in the internal angular velocity. He also argued that the stable stratification, *i.e.*, the positive buoyancy frequency, in the radiative regions causes a strong anisotropy in the transport processes, with transport along surfaces of constant pressure (isobars, *i.e.*, approximately spherical surfaces in the case of slow rotation) being much easier than transport in the radial direction. As a result, he argued that rotation would be constant on isobars, in a so-called *shellular rotation*. He derived equations for the spherically averaged transport in the radial direction. In the case of element abundances the combined effects of circulation and the assumed very efficient transport along spherical surfaces lead to transport in the form of turbulent diffusion (Chaboyer & Zahn 1992); hence it simply corresponds to including an appropriate turbulent diffusion coefficient  $D_{\text{turb}}$  to  $D$  in Eq. (3.100). However, the transport of angular momentum in addition involves advection by the meridional circulation. The resulting equations, further developed by, for example, Maeder & Zahn (1998) and Mathis & Zahn (2004), have seen fairly extensive use in stellar modelling; importantly, the formulation has successfully accounted for many aspects of the evolution of massive stars, including

---

<sup>8</sup> either a decrease as a result of angular-momentum loss to a stellar wind or an increase caused by accretion.

variations in surface abundances (for a review, see Maeder & Meynet 2000). Also, rotational mixing is likely required to account for the “normal” surface abundances observed in most intermediate-mass stars with thin outer convection zones, despite the short time scale for settling near the surface of these stars (*cf.* Fig. 3.2).

Even given this formulation, the rotational evolution in lower main-sequence stars still gives rise to problems. Most striking is the fact that calculations of the evolution of solar rotation with advection and/or diffusion predict a rapidly rotating solar radiative interior, in clear contrast to the helioseismic inferences (for a review, see Thompson *et al.* 2003; see also Section 7.1.8). Additional problems arise in the understanding of the depletion of  $^7\text{Li}$  in lower main-sequence stars, including the Sun, relative to the meteoritic and assumed primordial composition, and the abundance in post-main-sequence stars.  $^7\text{Li}$  is destroyed at temperatures over  $2.5 \times 10^6 \text{ K}$  over the main-sequence lifetime of typical stars such as the Sun, and hence the depletion requires mixing well below the convective envelopes in such stars; on the other hand, the mixing must not be so efficient that lithium is totally destroyed.

The combined constraints of the lithium abundances and the solar internal rotation strongly argue that to understand the latter additional transport processes must be invoked (Charbonnel & Talon 2005). These must also explain the detailed properties of the helioseismically inferred *tachocline*, the transition in rotation between the latitudinally differential rotation in the convection zone and the largely solid-body rotation in the radiative interior (*cf.* Fig. 7.36). One set of proposals has invoked magnetic coupling. This could involve coupling through a primordial magnetic field (Charbonneau & MacGregor 1993; Gough & McIntyre 1998; MacGregor & Charbonneau 1999); however, unless such a field is entirely confined to the radiative interior the link to the differential rotation in the solar convection zone would cause differential rotation, not observed, in the radiative interior (see Garaud 2007 for a review). Such confinement was recently demonstrated in calculations imposing plausible boundary conditions at the interface between the convection zone and the radiative interior (Garaud & Garaud 2008). Alternatively, a small-scale field might be generated by dynamo action in the interior (Spruit 2002). This model has successfully reproduced the solar internal rotation profile (Eggenberger *et al.* 2005a); also, it was used by Suijs *et al.* (2008) to explain, at least partly, the low rotation rates of white dwarfs inferred from asteroseismology (for a review, see Kawaler 2004). On the other hand, more detailed simulations by Zahn *et al.* (2007) failed to find the required dynamo action under solar conditions.

Another set of proposals invokes transport by gravity waves generated within or at the base of the convective envelope and dissipating in the radiative interior, giving rise to angular-momentum transport (*e.g.*, Schatzman 1993; Kumar & Quataert 1997; Zahn *et al.* 1997). As noted by Gough & McIntyre (1998) the simple form of this process leads to an oscillatory

behaviour, similar to oscillations observed in the Earth's atmosphere. This may be avoided through the action of differential filtering of the waves in the layers just beneath the convection zone (*e.g.*, Talon & Charbonnel 2005). A detailed investigation of the properties of such gravity waves throughout the cool part of the HR Diagram was carried out by Talon & Charbonnel (2008). However, the spectrum of gravity waves remains somewhat uncertain (Rogers *et al.* 2008), and some models suggest that the resulting rotation profile may be unstable (Denissenkov *et al.* 2008). A separate problem concerns the details of rotation in the solar convection zone; detailed hydrodynamical calculations have made substantial progress towards accounting for the helioseismic results (*e.g.*, Miesch *et al.* 2006), although the models are probably still rather far from matching the true solar conditions. It may be fair to say that we still lack a fully convincing description of the origin of the solar internal rotation. Indeed, despite its apparent successes amongst massive stars, the Zahn model for rotational evolution and mixing probably also requires a more solid theoretical underpinning.

The effects of the magnetic fields discussed above generally refer to relatively weak or small-scale fields. However, global, basically dipolar fields with strengths up to 30 kG are found in the magnetic peculiar A stars (Ap stars). These stars are slowly rotating; competition between gravitational settling and radiative levitation gives rise to strong atmospheric abundance anomalies (see Section 3.2.2.4). The magnetic fields modify these processes, as well as the mass loss which also contributes to the surface composition, resulting in atmospheric abundances that vary horizontally and are stratified vertically. Important examples of magnetic Ap stars for asteroseismology are the *rapidly oscillating Ap stars*, which are discussed in depth in Sections 2.3.5 and 7.3.4.

### 3.2.4.3 Evolution of Close Binary Systems

Many stars are members of binary systems. If the components are sufficiently close, their mutual interaction can have drastic consequences for the evolution of the system. The two stars orbit around their common centre of mass; in a coordinate system rotating with the pair, the stars feel an effective potential which is composed of the gravitational potential of each component, the tidal interaction from one component on the other, and the centrifugal effect. A detailed discussion of the dynamical properties of such systems, and their relation to observed binary stars, was provided by Hilditch (2001).

In the Roche approximation, where the stars are represented by point masses and the orbit is circular, the result is the potential sketched in Fig. 3.12a; near the stars the potential is dominated by the gravitational effect of the star, but with increasing distance it becomes deformed. This leads to a point between the two stars, the *first Lagrange point* L<sub>1</sub>, where the force along the line between the stars vanishes, and similarly the *second Lagrange point*

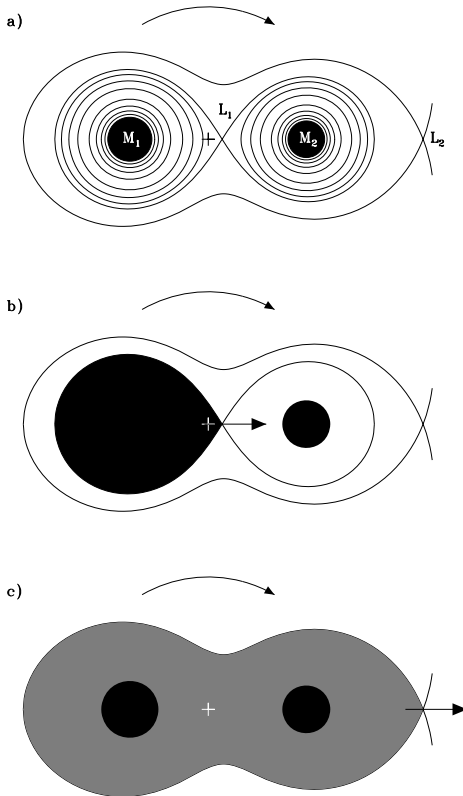


**Fig. 3.12.** Possible processes in the evolution of a close binary system. Panel a) shows contours of the combined potential in the co-rotating coordinate system for a binary system in a circular orbit, in the plane of the orbit. The mass ratio  $M_2/M_1$  is 0.8. The cross marks the centre of gravity, and  $L_1$  and  $L_2$  are at the first and second Lagrange points. In panel b) the more massive component has evolved to fill its Roche lobe and mass transfer to the less massive component has started. Panel c) sketches the situation of common envelope evolution, with loss of mass and angular momentum from the system through  $L_2$ .

$L_2$  beyond the least massive of the two components.<sup>9</sup> The potential surface passing through the  $L_1$  point defines the *Roche lobes* around the two stars.

<sup>9</sup> The Lagrange points in the Sun-Earth system play an important role in spacecraft navigation: the SOHO spacecraft is located near the  $L_1$  point, while, for example, the Planck and Herschel missions are near the  $L_2$  point.

As the stars evolve as a result of nuclear burning they generally expand. Consequently, one or the other of the two stars may fill its Roche lobe. Since the more massive of the two stars,  $M_1$ , say, evolves most rapidly, it is likely to reach this point first. Matter at the  $L_1$  point is then no longer bound to  $M_1$  but is transferred to the second star,  $M_2$ . As a result this star may become the more massive, evolve more rapidly, and start a transfer of mass back to  $M_1$ . It is evident that, depending on the initial masses and separation of the two components, a bewildering variety of evolutionary scenarios may result. An early review of these possibilities, related also to observed types of binary systems, was provided by Paczyński (1971).

The various types of mass transfer add to the complexity. The expansion of a single star takes place on a nuclear, or at most a thermal, time scale, leading to gradual mass transfer that allows the system to adjust (see Fig. 3.12b). This adjustment also includes the change in the size of the Roche lobe as a result in the changing masses. In this case, it is plausible that the transfer is conservative, with no change in the total mass and angular momentum of the system. However, it was noted by Paczyński (1965) that in stars with extensive outer convective zones the loss of mass leads to an expansion of the star. If this expansion is more rapid than a possible expansion of the Roche lobe, the mass loss takes place on a dynamical time scale, faster than the material can be accreted in equilibrium by the second star. The result is that the accreting star's Roche lobe fills up, and that subsequently the material spills out of the Roche lobes, forming a *common envelope* within which the stars orbit. As a result the envelope is heated by the friction generated by the motion of the stars through it. This contributes to overall loss of mass from the system, through the  $L_2$  point or more generally, and a consequent loss of angular momentum, causing the stars to spiral closer together. A detailed review of such common-envelope evolution was provided by Iben & Livio (1993).

The outcome of this process may be an extremely close binary system, the components of which have shed their envelopes. As discussed by Han *et al.* (2002, 2003) this may be a likely origin for at least a fraction of the subdwarf B stars (*cf.* Section 2.7.1). Hu *et al.* (2008) pointed out that asteroseismic investigations of such stars will be a powerful tool to help us understand the details of their evolution.

A special case of interaction in binary stars is likely responsible for at least some of the *blue stragglers*, *i.e.*, stars near the main sequence of stellar clusters that appear to have masses so high that they should have reached the end of their evolution before the inferred age of the cluster. These stars are believed to be formed either through collisions between stars or through mass exchange in close binary systems (*e.g.*, Bailyn & Pinsonneault 1995). As discussed in Section 2.8.3 many SX Phe stars appear to be blue stragglers; thus analysis of their oscillations offers the potential of studying the internal structure and hence get an understanding of the details of the formation process. An interesting case is the cluster NGC 2506 where Arentoft *et al.* (2007) found several oscillating blue stragglers as well as a number of  $\gamma$  Dor

stars. Also, Bruntt *et al.* (2007) determined a large number of frequencies in two blue stragglers in M67. In very old clusters, including globular clusters, blue stragglers may fall in the region where solar-like oscillations are expected, thus offering further information about their interior; however, in such cases the stars are likely too faint for their oscillations to be observed with existing facilities.

### 3.3 Equations of Linear Stellar Oscillations

In the present section the equations governing small oscillations around a spherical equilibrium state are derived. The general equations were presented in Section 3.1.3. However, here we make explicit use of the spherical symmetry. These equations describe the general, so-called *nonradial* oscillations, where spherical symmetry of the perturbations is not assumed. The case of *radial*, or spherically symmetric, oscillations, is contained as a special case.

#### 3.3.1 The Oscillation Equations

##### 3.3.1.1 Separation of Variables

We assume that the equilibrium model is non-rotating and ignore possible effects of magnetic fields. Thus the equilibrium model is spherically symmetric. Furthermore, in almost all cases it can be taken to be static, on the relevant time scale of the oscillations. Because of the independence of time, solutions of the linearized oscillation equations can be found where the time dependence is given by  $\exp(-i\omega t)$ , as already used in Section 3.1.4, where the frequency  $\omega$  must in general be assumed to be complex. Also, given the spherical symmetry, it is most natural to describe the star in spherical polar coordinates  $(r, \theta, \phi)$  (*cf.* Fig. 3.13), where  $r$  is the distance to the centre,  $\theta$  is colatitude (*i.e.*, the angle from the polar axis), and  $\phi$  is longitude. Here the equilibrium is independent of  $\theta$  and  $\phi$ , and hence the solution must be separable in these coordinates. However, the form of the separated solution depends on the physical nature of the problem, and so must be discussed in the context of the reduction of the equations.

The first step is to separate the displacement  $\delta\mathbf{r}$  into radial and horizontal components as

$$\delta\mathbf{r} = \xi_r \mathbf{a}_r + \boldsymbol{\xi}_h . \quad (3.107)$$

The horizontal component of the equations of motion, Eq. (3.43), is

$$\rho_0 \frac{\partial^2 \boldsymbol{\xi}_h}{\partial t^2} = -\nabla_h p' - \rho_0 \nabla_h \Phi' . \quad (3.108)$$

As the horizontal gradient of equilibrium quantities is zero, the horizontal divergence of Eq. (3.108) gives

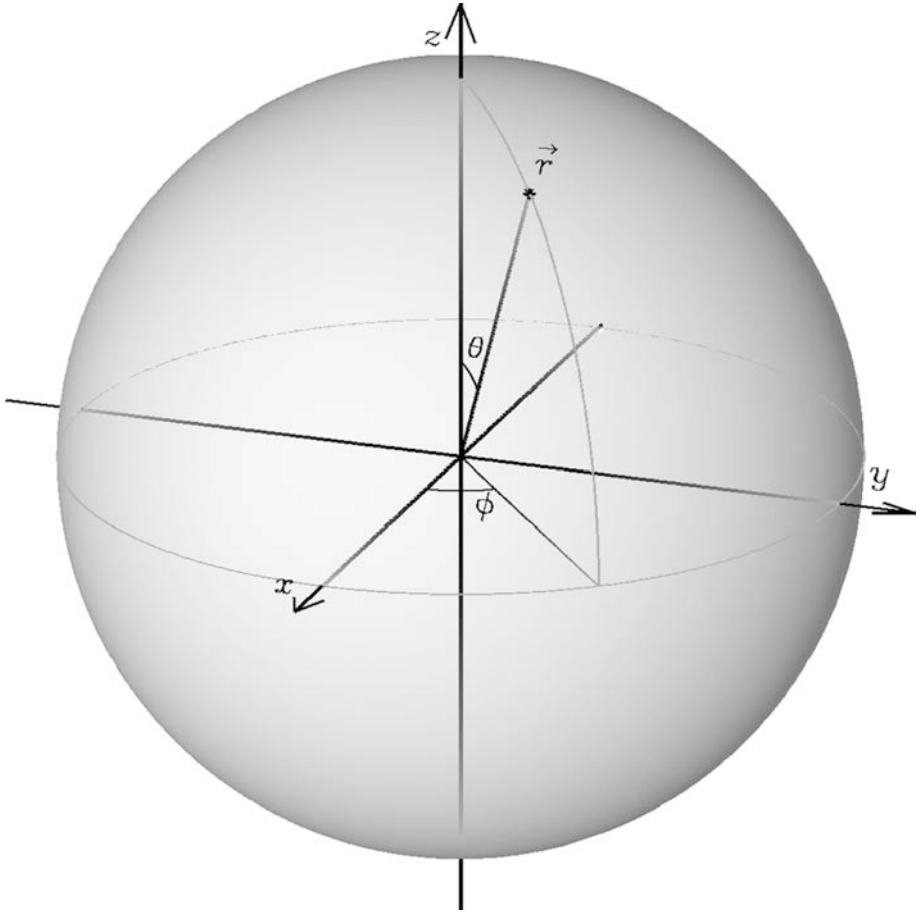


**Fig. 3.13.** The spherical polar coordinate system. Figure courtesy of Regner Trampedach.

$$\rho_0 \frac{\partial^2}{\partial t^2} \nabla_h \cdot \xi_h = -\nabla_h^2 p' - \rho_0 \nabla_h^2 \Phi'. \quad (3.109)$$

The equation of continuity, Eq. (3.41), can be written as

$$\rho' = -\frac{1}{r^2} \frac{\partial}{\partial r} (\rho_0 r^2 \xi_r) - \rho_0 \nabla_h \cdot \xi_h. \quad (3.110)$$

This can be used to eliminate  $\nabla_h \cdot \xi_h$  from Eq. (3.109), which becomes

$$-\frac{\partial^2}{\partial t^2} \left[ \rho' + \frac{1}{r^2} \frac{\partial}{\partial r} (r^2 \rho_0 \xi_r) \right] = -\nabla_h^2 p' - \rho_0 \nabla_h^2 \Phi'. \quad (3.111)$$

The radial component of Eq. (3.43) is

$$\rho_0 \frac{\partial^2 \xi_r}{\partial t^2} = -\frac{\partial p'}{\partial r} - \rho' g_0 - \rho_0 \frac{\partial \Phi'}{\partial r}. \quad (3.112)$$

Finally, the Poisson equation (3.44) may be written as

$$\frac{1}{r^2} \frac{\partial}{\partial r} \left( r^2 \frac{\partial \Phi'}{\partial r} \right) + \nabla_h^2 \Phi' = 4\pi G \rho'. \quad (3.113)$$

It should be noticed that in Eqs (3.111)–(3.113) derivatives with respect to the angular variables  $\theta$  and  $\phi$  only appear in the combination  $\nabla_h^2$ .

We now have to consider the energy equation (3.47), together with Eq. (3.48) for the heat gain. The result clearly depends on the form assumed for the flux  $\mathbf{F}$ . However, if the flux can be expressed in terms of a gradient of a scalar, as in the diffusion approximation [Eq. (3.22)], the energy equation also only contains derivatives with respect to  $\theta$  and  $\phi$  in  $\nabla_h^2$ .

We may now address the separation of the angular variables. The object is to factor out the variation of the perturbations with  $\theta$  and  $\phi$  as a function  $f(\theta, \phi)$ . From the form of the equations this is clearly possible, if  $f$  is an eigenfunction of the horizontal Laplace operator,

$$\nabla_h^2 f = -\frac{1}{r^2} \Lambda f, \quad (3.114)$$

where  $\Lambda$  is a constant. That  $1/r^2$  has to appear is obvious from Eq. (C.14); the choice of sign is motivated later. Writing it out in full, Eq. (3.114) becomes

$$\frac{1}{\sin \theta} \frac{\partial}{\partial \theta} \left( \sin \theta \frac{\partial f}{\partial \theta} \right) + \frac{1}{\sin^2 \theta} \frac{\partial^2 f}{\partial \phi^2} = -\Lambda f. \quad (3.115)$$

As the coefficients in this equation are independent of  $\phi$ , the solution can be further separated, as

$$f(\theta, \phi) = f_1(\theta) f_2(\phi). \quad (3.116)$$

It follows from Eq. (3.115) that  $f_2$  satisfies an equation of the form

$$\frac{d^2 f_2}{d\phi^2} = \alpha f_2, \quad (3.117)$$

where  $\alpha$  is another constant; this has the solution  $f_2 = \exp(\pm \alpha^{1/2} \phi)$ . However, the solution has to be continuous and hence periodic, *i.e.*,  $f_2(0) = f_2(2\pi)$ . Consequently we must demand that  $\alpha^{1/2} = im$ , where  $m$  is an integer.

When used in Eq. (3.115), this gives the following differential equation for  $f_1$ :

$$\frac{d}{dx} \left[ (1-x^2) \frac{df_1}{dx} \right] + \left( \Lambda - \frac{m^2}{1-x^2} \right) f_1 = 0, \quad (3.118)$$

where  $x = \cos \theta$ . It can be shown that this equation has a regular solution only when

$$\Lambda = l(l+1) , \quad (3.119)$$

where  $l$  is a non-negative integer, and

$$|m| \leq l . \quad (3.120)$$

The regular solution is

$$f_1(\theta) = P_l^m(\cos \theta) , \quad (3.121)$$

where  $P_l^m$  is the Legendre function. By including an appropriate scaling factor we may finally write

$$f(\theta, \phi) = (-1)^m c_{lm} P_l^m(\cos \theta) \exp(im\phi) \equiv Y_l^m(\theta, \phi) , \quad (3.122)$$

where  $Y_l^m$  is a spherical harmonic; here  $c_{lm}$  is a normalization constant, given in Eq. (1.6) in Chapter 1, such that the integral of  $|Y_l^m|^2$  over the unit sphere is 1.  $Y_l^m$  is characterized by its *degree*  $l$  and its azimuthal order  $m$ ; the properties of spherical harmonics were discussed in more detail in Chapter 1 (see also Appendix B). From Eqs (3.114) and (3.119) we also have that

$$\nabla_h^2 f = -\frac{l(l+1)}{r^2} f . \quad (3.123)$$

The dependent variables in Eqs (3.111)–(3.113) can now be written as

$$\xi_r(r, \theta, \phi, t) = \sqrt{4\pi} \tilde{\xi}_r(r) Y_l^m(\theta, \phi) \exp(-i\omega t) , \quad (3.124)$$

$$p'(r, \theta, \phi, t) = \sqrt{4\pi} \tilde{p}'(r) Y_l^m(\theta, \phi) \exp(-i\omega t) , \quad (3.125)$$

etc. Also it follows from Eq. (3.38) that if the Eulerian perturbations are in the form given in these equations, so are the Lagrangian perturbations. Then the equations contain  $Y_l^m(\theta, \phi) \exp(-i\omega t)$  as a common factor. After dividing by it, the following ordinary differential equations for the amplitude functions  $\tilde{\xi}_r, \tilde{p}', \dots$ , result:

$$\omega^2 \left[ \tilde{p}' + \frac{1}{r^2} \frac{d}{dr} (r^2 \rho_0 \tilde{\xi}_r) \right] = \frac{l(l+1)}{r^2} (\tilde{p}' + \rho_0 \tilde{\Phi}') , \quad (3.126)$$

$$-\omega^2 \rho_0 \tilde{\xi}_r = -\frac{d\tilde{p}'}{dr} - \tilde{p}' g_0 - \rho_0 \frac{d\tilde{\Phi}'}{dr} , \quad (3.127)$$

$$\frac{1}{r^2} \frac{d}{dr} \left( r^2 \frac{d\tilde{\Phi}'}{dr} \right) - \frac{l(l+1)}{r^2} \tilde{\Phi}' = 4\pi G \tilde{p}' , \quad (3.128)$$

together with the energy equation

$$\delta\tilde{p} - \frac{\Gamma_{1,0} p_0}{\rho_0} \delta\tilde{\rho} = \rho_0 (\Gamma_{3,0} - 1) \delta\tilde{q} . \quad (3.129)$$

It should be noted that Eqs (3.126)–(3.129) do not depend on the azimuthal order  $m$ . This is a consequence of the assumed spherical symmetry of

the equilibrium state, which demands that the results should be independent of the choice of polar axis for the coordinate system. Changing the polar axis would change the spherical harmonics, in such a way that a new spherical harmonic, with given  $l$  and  $m$ , would be a linear combination over  $m$  of the old spherical harmonics with the given value of  $l$  (see Appendix B). As this change of axis can have no effect on the dynamics of the oscillations, the equations must be independent of  $m$ , as found here.

From Eq. (3.108) the horizontal component of the displacement is given by

$$\boldsymbol{\xi}_h = \sqrt{4\pi} \tilde{\xi}_h(r) \left( \frac{\partial Y_l^m}{\partial \theta} \mathbf{a}_\theta + \frac{1}{\sin \theta} \frac{\partial Y_l^m}{\partial \phi} \mathbf{a}_\phi \right) \exp(-i\omega t), \quad (3.130)$$

where

$$\tilde{\xi}_h(r) = \frac{1}{r\omega^2} \left( \frac{1}{\rho_0} \tilde{p}' + \tilde{\Phi}' \right). \quad (3.131)$$

Thus the (physical) displacement vector can be written as

$$\begin{aligned} \boldsymbol{\delta r} = \sqrt{4\pi} \Re \left\{ & \left[ \tilde{\xi}_r(r) Y_l^m(\theta, \phi) \mathbf{a}_r \right. \right. \\ & \left. \left. + \tilde{\xi}_h(r) \left( \frac{\partial Y_l^m}{\partial \theta} \mathbf{a}_\theta + \frac{1}{\sin \theta} \frac{\partial Y_l^m}{\partial \phi} \mathbf{a}_\phi \right) \right] \exp(-i\omega t) \right\}. \end{aligned} \quad (3.132)$$

The frequency  $\omega$  is in general complex. This may be seen from the energy equation (3.129), if the expression (3.48) for the heating rate perturbation is used. Assuming the time dependence given in Eqs (3.124) and (3.125) for the perturbed quantities, Eq. (3.48) can be written as

$$\delta q = \frac{i}{\rho_0 \omega} \delta(\rho \epsilon - \operatorname{div} \mathbf{F}). \quad (3.133)$$

Here the perturbations on the right-hand side can be expressed in terms of the perturbations to, say, density and temperature. For instance, since  $\epsilon$  is a function  $\epsilon(\rho, T)$  of density and temperature, we obtain

$$\delta(\rho \epsilon) = \rho_0 \epsilon_0 \left\{ \left[ 1 + \left( \frac{\partial \ln \epsilon}{\partial \ln \rho} \right)_T \right] \frac{\delta \rho}{\rho_0} + \left( \frac{\partial \ln \epsilon}{\partial \ln T} \right)_\rho \frac{\delta T}{T_0} \right\}. \quad (3.134)$$

The expression for  $\delta(\operatorname{div} \mathbf{F})$  depends on the treatment of the energy transport, discussed in Section 3.1.1. Often the diffusion approximation is adequate; then  $\delta(\operatorname{div} \mathbf{F})$  may be obtained in a fashion similar to the derivation of Eq. (3.134) by perturbing Eq. (3.22), although with considerable effort. Note that this gives rise to a term in the second derivative of  $\delta T$  with respect to  $r$ ; the same is true if the Eddington approximation, Eq. (3.24), is used, whereas the use of Newton's law of cooling, Eq. (3.23), gives a direct relation between the heat loss and the local thermodynamic variables, and hence does not increase the order of the equations. However, regardless of the approximation used, substitution of the relevant relations into the energy equation, written

in terms of  $\rho$  and  $T$ , results in an equation which, because of the factor  $i/\omega$  in the expression for  $\delta q$ , has complex coefficients. Hence the oscillation equations cannot in general have a real solution.

The complex frequency can be expressed as  $\omega = \omega_r + i\omega_i$ , where  $\omega_r$  and  $\omega_i$  are real; consequently the dependence of the perturbations on  $\phi$  and  $t$  is of the form

$$\cos(m\phi - \omega_r t + \delta_0) e^{\omega_i t}, \quad (3.135)$$

where  $\delta_0$  is the initial phase. For  $m \neq 0$  this describes a wave traveling around the equator with angular phase speed  $\omega_r/m$ , whereas for  $m = 0$  the perturbation is a standing wave. The period of the perturbation is  $\Pi = 2\pi/\omega_r$ . Its amplitude grows or decays exponentially with time, depending on whether the *growth rate*  $\omega_i$  is positive or negative.

Neglecting  $\omega_i$ , we may obtain the mean square components of the displacement, when averaged over a spherical surface and time, from Eq. (3.132). For the radial component the result is

$$\begin{aligned} \delta r_{\text{rms}}^2 &= \langle |\delta \mathbf{r} \cdot \mathbf{a}_r|^2 \rangle \\ &= \frac{1}{\Pi} \int_0^\Pi dt \frac{1}{4\pi} \oint \left\{ \sqrt{4\pi} \Re \left[ \tilde{\xi}_r(r) Y_l^m(\theta, \phi) \exp(-i\omega t) \right] \right\}^2 d\Omega \\ &= \frac{1}{2} |\tilde{\xi}_r(r)|^2, \end{aligned} \quad (3.136)$$

where in this equation  $\Omega$  denotes solid angle. Similarly, the mean square length of the horizontal component of  $\delta \mathbf{r}$  is

$$\delta h_{\text{rms}}^2 = \langle |\boldsymbol{\xi}_h|^2 \rangle = 1/2 l(l+1) |\tilde{\xi}_h(r)|^2, \quad (3.137)$$

where  $\tilde{\xi}_h$  is the amplitude function introduced in Eq. (3.131).

The kinetic energy of pulsation is

$$E_{\text{kin}} = \frac{1}{2} \int_V |\mathbf{v}|^2 \rho_0 dV. \quad (3.138)$$

As in Eqs (3.136) and (3.137) it follows from Eq. (3.132) that the time-averaged energy is  $1/4 \omega^2 \mathcal{E}$ , where

$$\mathcal{E} = 4\pi \int_0^R [|\tilde{\xi}_r(r)|^2 + l(l+1) |\tilde{\xi}_h(r)|^2] \rho_0 r^2 dr \quad (3.139)$$

is the mode inertia. For  $m \neq 0$   $E_{\text{kin}}$  is independent of  $t$ , in accordance with the running-wave nature of the oscillation in this case, whereas for  $m = 0$  we have  $E_{\text{kin}} = \frac{1}{2} \omega^2 \mathcal{E} \cos^2(\omega t - \delta_0)$ . It is convenient to introduce the dimensionless measure  $E$  of  $\mathcal{E}$ , by

$$E = \frac{4\pi \int_0^R [|\tilde{\xi}_r(r)|^2 + l(l+1) |\tilde{\xi}_h(r)|^2] \rho_0 r^2 dr}{M [|\tilde{\xi}_r(R)|^2 + l(l+1) |\tilde{\xi}_h(R)|^2]} = \frac{M_{\text{mode}}}{M}, \quad (3.140)$$

where  $M$  is the total mass of the star, and  $M_{\text{mode}}$  is the so-called *modal mass*; thus  $E$  provides a measure of the normalized *inertia* of the mode. These quantities are defined such that the time-averaged kinetic energy in the oscillation is

$$\frac{1}{2}M_{\text{mode}}V_{\text{rms}}^2 = \frac{1}{2}EMV_{\text{rms}}^2, \quad (3.141)$$

where  $V_{\text{rms}}^2$  is the mean, over the stellar surface and time, of the squared total velocity of the mode.

From Eq. (3.123) it follows that for any perturbation quantity  $\psi'$ ,

$$\nabla_h^2 \psi' = -\frac{l(l+1)}{r^2} \psi'. \quad (3.142)$$

Thus if the oscillations are regarded locally as plane waves, as in Eq. (3.53), we may make the identification

$$\frac{l(l+1)}{r^2} = k_h^2, \quad (3.143)$$

where  $k_h$  is the length of the horizontal component of the wave vector, as in Eq. (3.63); note in particular that  $k_h$  depends on  $r$ .

For completeness, we note that the modes discussed so far are known as *spheroidal modes*. In addition there is a second class of modes, the *toroidal modes*, which are briefly discussed in J. P. Cox (1980), Section 17.3 and Unno *et al.* (1989), Section 13.3. In a spherically symmetric (and hence non-rotating) non-magnetic gaseous star, and hence with no internal strain, infinitely slow motion can proceed unhindered along spherical surfaces. Formally this corresponds to oscillations with zero frequency. For such motion,  $\xi_r = 0$ , and  $p'$ ,  $\rho'$  and  $\Phi'$  are zero. This case, assuming no time dependence, is evidently a solution to the basic perturbation equations, Eqs (3.42), (3.43), (3.44) and (3.50), provided that  $\nabla \cdot \boldsymbol{\xi} = 0$  or, since  $\xi_r = 0$ ,  $\nabla_h \cdot \boldsymbol{\xi}_h = 0$ . A solution satisfying this condition can be obtained as  $\boldsymbol{\xi}_h = \nabla_h \times (\psi \mathbf{a}_r)$  where  $\psi(r, \theta, \phi)$  is an arbitrary scalar function. Corresponding to the spherical-harmonic expression of the spheroidal modes it is convenient to write the toroidal modes in terms of an expansion in spherical harmonics, such that the individual modes have the form

$$\boldsymbol{\xi}_h = \nabla_h \times [\psi_{lm}(r) Y_l^m(\theta, \phi)] = r^{-1} \psi_{lm}(r) \left( \frac{1}{\sin \theta} \frac{\partial Y_l^m}{\partial \phi} \mathbf{a}_\theta - \frac{\partial Y_l^m}{\partial \theta} \mathbf{a}_\phi \right); \quad (3.144)$$

here  $\psi_{lm}(r)$  is an arbitrary function of  $r$ .

In a rotating star the toroidal modes give rise to oscillations whose frequencies are of the order of the rotation frequency. We return to this in Section 3.8.1.

### 3.3.1.2 Radial Oscillations

For *radial* oscillations, with  $l = 0$ , the perturbation to the gravitational field may be eliminated analytically. From the Poisson equation in the form

Eq. (3.128) we have, by using the equation (3.110) of continuity with no horizontal part, that

$$\frac{1}{r^2} \frac{d}{dr} \left( r^2 \frac{d\tilde{\Phi}'}{dr} \right) = -\frac{4\pi G}{r^2} \frac{d}{dr} (r^2 \rho_0 \tilde{\xi}_r) , \quad (3.145)$$

or, as the gravitational force must be finite at  $r = 0$ ,

$$\frac{d\tilde{\Phi}'}{dr} = -4\pi G \rho_0 \tilde{\xi}_r . \quad (3.146)$$

Furthermore, the term containing  $\tilde{\Phi}'$  drops out in Eq. (3.126).

With these eliminations, the oscillation equations can be reduced to a relatively simple form. We write the energy equation (3.129) as

$$\tilde{\rho}' = \frac{\rho_0}{\Gamma_{1,0} p_0} \tilde{p}' + \rho_0 \tilde{\xi}_r \left( \frac{1}{\Gamma_{1,0} p_0} \frac{dp_0}{dr} - \frac{1}{\rho_0} \frac{d\rho_0}{dr} \right) - \frac{\rho_0^2}{\Gamma_{1,0} p_0} (\Gamma_{3,0} - 1) \delta \tilde{q} . \quad (3.147)$$

Then Eq. (3.126) may be written as

$$\frac{d\tilde{\xi}_r}{dr} = -\frac{2}{r} \tilde{\xi}_r - \frac{1}{\Gamma_{1,0} p_0} \frac{dp_0}{dr} \tilde{\xi}_r - \frac{1}{\Gamma_{1,0} p_0} \tilde{p}' + \frac{\rho_0}{\Gamma_{1,0} p_0} (\Gamma_{3,0} - 1) \delta \tilde{q} , \quad (3.148)$$

or, introducing  $\zeta \equiv \tilde{\xi}_r/r$ ,

$$\tilde{p}' = -\Gamma_{1,0} p_0 r \left( \frac{d\zeta}{dr} + \frac{3}{r} \zeta + \frac{1}{\Gamma_{1,0} p_0} \frac{dp_0}{dr} \zeta \right) + \rho_0 (\Gamma_{3,0} - 1) \delta \tilde{q} . \quad (3.149)$$

By substituting Eqs (3.146), (3.147) and (3.149) into Eq. (3.127) we obtain, after a little manipulation,

$$\frac{1}{r^3} \frac{d}{dr} \left( r^4 \Gamma_{1,0} p_0 \frac{d\zeta}{dr} \right) + \frac{d}{dr} [(3\Gamma_{1,0} - 4)p_0] \zeta + \rho_0 \omega^2 r \zeta = \frac{d}{dr} [\rho_0 (\Gamma_{3,0} - 1) \delta \tilde{q}] . \quad (3.150)$$

It is important to note that the apparent simplicity of Eq. (3.150) hides a great deal of complexity in the heating term on the right-hand side. Nevertheless, this equation is convenient for discussions of the properties of radial oscillations. In these notes, however, we shall mostly consider the general equations for *nonradial* oscillations, where  $l$  can take any value.

### 3.3.2 Linear, Adiabatic Oscillations

To simplify the notation, from now on we drop the tilde on the amplitude functions, and the “0” on equilibrium quantities. This should not cause any confusion.

### 3.3.2.1 Equations

For adiabatic oscillations,  $\delta q = 0$  and Eq. (3.129) can be written

$$\rho' = \frac{\rho}{\Gamma_1 p} p' + \rho \xi_r \left( \frac{1}{\Gamma_1 p} \frac{dp}{dr} - \frac{1}{\rho} \frac{d\rho}{dr} \right). \quad (3.151)$$

This may be used to eliminate  $\rho'$  from Eqs (3.126)–(3.128). From Eq. (3.126), using that  $c^2 = \Gamma_1 p / \rho$  is the square of the adiabatic sound speed [cf. Eq. (3.52)], we obtain

$$\frac{d\xi_r}{dr} = - \left( \frac{2}{r} + \frac{1}{\Gamma_1 p} \frac{dp}{dr} \right) \xi_r + \frac{1}{\rho c^2} \left( \frac{S_l^2}{\omega^2} - 1 \right) p' + \frac{l(l+1)}{\omega^2 r^2} \Phi', \quad (3.152)$$

where we introduced the characteristic acoustic frequency  $S_l$  by

$$S_l^2 = \frac{l(l+1)c^2}{r^2} = k_{\text{h}}^2 c^2. \quad (3.153)$$

Equation (3.127) gives

$$\frac{dp'}{dr} = \rho(\omega^2 - N^2) \xi_r + \frac{1}{\Gamma_1 p} \frac{dp}{dr} p' - \rho \frac{d\Phi'}{dr}, \quad (3.154)$$

where, as in Eq. (3.73),  $N$  is the buoyancy frequency, given by

$$N^2 = g \left( \frac{1}{\Gamma_1 p} \frac{dp}{dr} - \frac{1}{\rho} \frac{d\rho}{dr} \right). \quad (3.155)$$

Finally, Eq. (3.128) becomes

$$\frac{1}{r^2} \frac{d}{dr} \left( r^2 \frac{d\Phi'}{dr} \right) = 4\pi G \left( \frac{p'}{c^2} + \frac{\rho \xi_r}{g} N^2 \right) + \frac{l(l+1)}{r^2} \Phi'. \quad (3.156)$$

Equations (3.152), (3.154) and (3.156) constitute a fourth-order system of ordinary differential equations for the four dependent variables  $\xi_r$ ,  $p'$ ,  $\Phi'$  and  $d\Phi'/dr$ . Thus it is a complete set of differential equations.

For radial oscillations Eqs (3.152) and (3.154), after elimination of the terms in  $\Phi'$  by means of Eq. (3.146), reduce to a second-order system in  $\xi_r$  and  $p'$ ; an alternative formulation of this set of equations is obtained from Eq. (3.150), by setting the right-hand side to zero. The reduction to second order is a useful simplification from a computational point of view, and it may be exploited in asymptotic analyses. However, here we shall always treat radial oscillations in the same way as the nonradial case.

It should be noticed that all coefficients in Eqs (3.152), (3.154) and (3.156) are real. Also, as discussed below, the same is true of the boundary conditions. Since the frequency only appears in the form  $\omega^2$ , we may expect that the solution is such that  $\omega^2$  is real, in which case the eigenfunctions may also

be chosen to be real. As will be demonstrated in Section 3.6.1 this is true in general. Thus the frequency is either purely real, in which case the motion is an undamped oscillator, or purely imaginary, so that the motion grows or decays exponentially. From a physical point of view this results from the adiabatic approximation, which ensures that energy cannot be fed into the motion, except from the gravitational field; thus the only possible type of instability is a dynamical instability. We shall almost always consider the oscillatory case, with  $\omega^2 > 0$ ; note, however, that the convective instability discussed briefly in Section 3.1.4.2 is an example of a dynamical instability, which clearly must be contained in the equations developed here.

### 3.3.2.2 Boundary Conditions

To supplement the four equations in the general case, we need four boundary conditions. These are discussed in considerable detail in Unno *et al.* (1989), Section 18.1, and in J. P. Cox (1980), Section 17.6. Here we give only a brief summary.

The centre,  $r = 0$  is a regular singular point of the equations. Thus, as is usual in the theory of differential equations, the equations admit both regular and divergent solutions at this point. Two of the conditions serve to select the regular solutions. By expanding the equations, it may be shown that near  $r = 0$ ,  $\xi_r$  behaves like  $r^{l-1}$ , whereas  $p'$  and  $\Phi'$  behave as  $r^l$ . In the special case of radial oscillations, however, the coefficient to the leading-order term in  $\xi_r$  vanishes, and  $\xi_r$  goes as  $r$ . Indeed it is obvious from geometrical considerations that for spherically symmetric oscillations, the displacement must vanish at the centre. From the expansions, two relations between the solution near  $r = 0$  may be obtained. In particular, it may be shown that for  $l > 0$ ,

$$\xi_r \simeq l \xi_h , \quad \text{for } r \rightarrow 0 . \quad (3.157)$$

In the radial case, one of the conditions was implicitly used to obtain Eq. (3.146), and only one central condition remains.

One surface condition is obtained by demanding continuity of  $\Phi'$  and its derivative at the surface radius  $r = R$ . Outside the star the density perturbation vanishes, and the Poisson equation may be solved analytically. The solution vanishing at infinity is

$$\Phi' = A r^{-l-1} , \quad (3.158)$$

where  $A$  is a constant. Consequently  $\Phi'$  must satisfy

$$\frac{d\Phi'}{dr} + \frac{l+1}{r} \Phi' = 0 \quad \text{at } r = R . \quad (3.159)$$

The second condition depends on the treatment of the stellar atmosphere, and may consequently be quite complicated. These complications are discussed further in Appendix D. For the moment, we note that if the star is

assigned a definite boundary at  $r = R$ , it is physically reasonable to assume that the boundary is free, so that no forces act on it. In this way the star can be considered as an isolated system. This is equivalent to requiring the pressure to be constant at the perturbed surface. Thus as the second surface boundary condition we take that the Lagrangian pressure perturbation vanish, *i.e.*,

$$\delta p = p' + \xi_r \frac{dp}{dr} = 0 \quad \text{at } r = R. \quad (3.160)$$

As shown in Appendix D, a more detailed analysis of the atmospheric behaviour of the oscillations gives a very similar result, except at high frequencies.

The equations and boundary conditions have non-trivial solutions only for specific values of the frequency  $\omega$ , which is therefore an *eigenvalue* of the problem. Each eigenfrequency corresponds to a mode of oscillation; from the solution one obtains also the *eigenfunction*, *i.e.*, the variation of the perturbations  $\xi_r$ ,  $p'$ , *etc.* with  $r$ . As the equations are homogeneous, the solution is determined only to within a constant factor. Thus the equations do not determine the amplitude of the motion. This is fixed by nonlinear effects, or by a possible external forcing that may be responsible for the oscillations. However, the eigenfunctions resulting from the calculation give the *distribution* of the amplitude with position in the star; thus they may be used, *e.g.*, to relate the observable surface amplitude to the amplitude in the interior, or to the total energy in the oscillation.

From Eq. (3.160) one can estimate the ratio between the radial and horizontal components of the displacement on the surface. The amplitude of the horizontal displacement is given by Eq. (3.131). In most cases, however, the perturbation to the gravitational potential is small. Thus we have approximately, from Eq. (3.160), that

$$\frac{\xi_h(R)}{\xi_r(R)} \simeq \frac{g_s}{R\omega^2} \equiv \sigma^{-2}, \quad (3.161)$$

where  $g_s$  is the surface gravity, and  $\sigma$  is a dimensionless frequency, defined by

$$\sigma^2 \equiv \frac{R^3}{GM} \omega^2. \quad (3.162)$$

Thus the surface value of  $\xi_h/\xi_r$ , to this approximation, depends only on frequency. The ratio of the *rms* horizontal to vertical displacement [*cf.* Eqs (3.136) and (3.137)] is

$$\frac{\delta h_{\text{rms}}}{\delta r_{\text{rms}}} = \frac{\sqrt{l(l+1)}}{\sigma^2} \quad \text{at } r = R. \quad (3.163)$$

Typical values for  $\sigma^{-2}$  are  $0.01 - 0.1$  for low-order acoustic modes, and  $10 - 100$  for high-order g modes such as found in slowly pulsating B stars or

$\gamma$  Dor stars. Thus it is generally true that p modes have predominantly vertical surface velocities and g modes have predominantly horizontal velocities; however, it is important to emphasize that these properties are solely related to the frequency and not to the overall nature of the mode. For the important case of the solar five-minute oscillations,  $\sigma^{-2} \sim 0.001$ , and so the motion is predominantly vertical, except at large  $l$ .

As discussed in Sections 6.1.2.2 and 6.2.1 the ratio  $\xi_h(R)/\xi_r(R)$ , typically denoted  $K$  in analysis of observations, is important for the characterization of the observed properties of oscillations and issues of mode identification. The approximation in Eq. (3.161) is useful but should probably be replaced by a more careful calculation of the properties of the modes in the stellar atmosphere. Given this theoretical uncertainty, in applications to mode identification a range of values of  $K$  is considered in practice to test the robustness of the result to a varying value for the true model-dependent ratio  $\xi_h(R)/\xi_r(R)$ .

### 3.3.3 The Dependence of the Frequencies on the Equilibrium Structure

#### 3.3.3.1 The Scaling with Mass and Radius

It is evident that the oscillation frequencies depend on the total mass and radius of the star. Indeed, as noted in Section 1.6.1 the dynamical time scale  $t_{\text{dyn}}$  (*cf.* Eq. (1.15)) can be regarded as a characteristic period of radial oscillation. It is interesting that a similar estimate can be obtained by regarding the oscillations as standing acoustic waves. Here we expect that the period is approximately given by the sound travel time across the star, *i.e.*,

$$\Pi \sim \frac{R}{\langle c \rangle}, \quad (3.164)$$

where  $\langle c \rangle$  is a suitable average of the sound speed. Approximating the density by the mean density and using the equation of hydrostatic support we furthermore have the estimates

$$\rho \sim \frac{M}{R^3}, \quad p \sim \frac{GM^2}{R^4} \quad (3.165)$$

(*e.g.*, Kippenhahn & Weigert 1990). Using these to estimate  $\langle c \rangle$  in Eq. (3.164) yields

$$\Pi \sim \left( \frac{R^3}{GM} \right)^{1/2} = t_{\text{dyn}}, \quad (3.166)$$

where we neglected  $\Gamma_1$ .

This scaling can be brought on a firmer footing. Motivated by the estimates in Eq. (3.165) we express  $p$  and  $\rho$  in terms of

$$\hat{p} = \frac{R^4}{GM^2} p, \quad \hat{\rho} = \frac{R^3}{M} \rho. \quad (3.167)$$

Also, we measure distance  $r$  to the centre, and the mass  $m$  inside  $r$ , in terms of

$$x = r/R, \quad q = m/M. \quad (3.168)$$

Then gravity, sound speed, characteristic acoustic frequency  $S_l$  and buoyancy frequency  $N$  may be written as

$$\begin{aligned} g &= \frac{GM}{R^2} \hat{g}, \quad c = \left( \frac{GM}{R} \right)^{1/2} \hat{c}, \\ S_l &= \left( \frac{GM}{R^3} \right)^{1/2} \hat{S}_l, \quad N = \left( \frac{GM}{R^3} \right)^{1/2} \hat{N}, \end{aligned} \quad (3.169)$$

where

$$\begin{aligned} \hat{g} &= \frac{q}{x^2}, \quad \hat{c}^2 = \frac{\Gamma_1 \hat{p}}{\hat{\rho}}, \quad \hat{S}_l^2 = \frac{l(l+1) \hat{c}^2}{x^2}, \\ \hat{N}^2 &= \hat{g} \left( \frac{1}{\Gamma_1 \hat{p}} \frac{d\hat{p}}{dx} - \frac{1}{\hat{\rho}} \frac{d\hat{\rho}}{dx} \right). \end{aligned} \quad (3.170)$$

Finally, we introduce scaled perturbations  $\hat{\xi}_r$ ,  $\hat{p}'$  and  $\hat{\Phi}'$  by

$$\xi_r = R \hat{\xi}_r, \quad p' = \frac{GM^2}{R^4} \hat{p}', \quad \Phi' = \frac{GM}{R} \hat{\Phi}'. \quad (3.171)$$

Then the adiabatic oscillation Eqs (3.152), (3.154) and (3.156), written in terms of  $\hat{\xi}_r$ ,  $\hat{p}'$  and  $\hat{\Phi}'$  as functions of  $x$ , can be expressed solely in terms of  $\hat{p}$ ,  $\hat{\rho}$ ,  $\Gamma_1$ ,  $\hat{g}$ ,  $\hat{c}$ ,  $\hat{S}_l$  and  $\hat{N}$ , if  $\omega$  is replaced by the dimensionless frequency  $\sigma$ , defined by Eq. (3.162). This evidently corresponds to measuring the period in units of the dynamical time scale.

For models that constitute a so-called *homologous series* (e.g., Kippenhahn & Weigert 1990), the functions  $q(x)$ ,  $\hat{p}(x)$  and  $\hat{\rho}(x)$  are uniquely determined. Thus the dimensionless frequencies  $\sigma$  for a given mode or, equivalently, the pulsation constants  $Q$  (cf. Eq. (1.16)) are the same for all models in such a series: in this case the periods scale precisely as  $t_{\text{dyn}}$ . A particular example is the case of polytropic models: for each polytropic index there is a unique set of dimensionless adiabatic oscillation frequencies  $\sigma$ . For more realistic stellar models the scalings are not exactly satisfied and hence  $\sigma$  (or  $Q$ ) shows some dependence on stellar parameters; however, it is still often the case that the scaling with  $t_{\text{dyn}}^{-1}$  dominates the variation of the oscillation frequencies.

### 3.3.3.2 Dependence on the Internal Structure

The coefficients in the adiabatic oscillation Eqs (3.152), (3.154) and (3.156) obviously depend on the structure of the equilibrium model. Indeed, this is the whole basis for the asteroseismic use of observed frequencies to probe

the structure of stars. A closer inspection reveals that the coefficients are determined solely by the set of equilibrium variables

$$\rho, p, \Gamma_1, g, \quad (3.172)$$

as functions of  $r$ . However, the equilibrium model satisfies the stellar structure Eqs (3.33) and (3.34); in addition we initially assume the model to have a given mass and radius, which at least in the case of the Sun are known with high precision.

If  $\rho(r)$  is given,  $g(r)$  is determined by Eq. (3.34); and, given  $g$ , the equation (3.33) of hydrostatic support may be integrated from the surface to provide  $p(r)$  (the surface pressure is known from theoretical or empirical atmospheric models). Thus of the set in Eq. (3.172) only the two functions  $\rho(r)$  and  $\Gamma_1(r)$  are independent, and the adiabatic oscillation frequencies are determined solely by these two functions. Conversely, if no other constraints are imposed, the observed frequencies give direct information only about  $\rho$  and  $\Gamma_1$ .

In the general stellar case we cannot assume the mass and radius to be known. In this case, it is reasonable to discuss the properties of the stellar interior in terms of the scaled variables introduced in Eqs (3.167)–(3.170) above. It similarly follows from the dimensionless form of the stellar-structure equations, as discussed in more detail by Christensen-Dalsgaard *et al.* (2005), that the structure is fully characterized by specifying  $\hat{\rho}$  as a function of  $x$ . Thus the adiabatic oscillation equations, and hence the dimensionless frequency  $\sigma$  defined in Eq. (3.162), are determined by  $(\hat{\rho}, \Gamma_1)$  specified as a function of  $x$ . Also, when analysing the region below the hydrogen and helium ionization zones in main-sequence stars of modest mass one can often assume that  $\Gamma_1 \simeq 5/3$ ; in this case the relevant structure is fully characterized by  $\hat{\rho}(x)$ .

The preceding discussion was made in terms of the pair  $(\rho, \Gamma_1)$ . However, any other independent pair of model variables, related directly to  $\rho$  and  $\Gamma_1$ , may be used instead. As will be discussed extensively below, observed oscillations have in many cases (including the Sun) essentially the nature of standing acoustic waves. Their frequencies are largely determined by the behaviour of sound speed  $c$ , and hence it would be natural to use  $c$  as one of the variables, combined with, *e.g.*,  $\rho$  or  $\Gamma_1$ . Also, it is evident that analysis of such oscillations may be used to determine properties of the sound speed. Indeed, the observations for the Sun are sufficiently rich that the observed frequencies may be inverted to obtain an estimate of the sound speed in most of the Sun (see Section 7.1.7). It follows from Eq. (3.56) that this provides a measure of  $T/\mu$ . However, it is important to note that measurements of adiabatic oscillation frequencies do not by themselves allow a determination of the temperature in a star. Only if the mean molecular weight can be otherwise constrained (*e.g.*, by demanding that its variation in the stellar interior results from normal stellar evolution) is it possible to estimate the stellar interior temperature. This limitation is of obvious importance for the use of

observed solar oscillation frequencies to constrain the production rate of solar neutrinos (see Section 7.1.1).

### 3.3.3.3 Dependence on the Physics of Stellar Interiors

Although asteroseismology directly only provides information about  $p$ ,  $\rho$ ,  $T_1$  and  $c$  it is obviously of major interest to use this information further to constrain the properties of stellar interiors. This requires that the oscillation frequencies are combined with other types of information. An important example is to use the fact that  $\Gamma_1$  can be determined from the equation of state if  $p$ ,  $\rho$  and the composition is known. To a fair degree of approximation the chemical composition can be specified by a single parameter, such as the abundance  $Y$  by mass of helium. In this approximation just three quantities should suffice to specify fully the thermodynamical state. In principle these three quantities could be  $\rho$ ,  $p$  and  $\Gamma_1$  which, as argued above, should be obtainable from the oscillation observations. If the equation of state were known one should be able to determine any other thermodynamic variable, including  $Y$ , from these observed quantities. Outside the ionization zones, being very nearly constant,  $\Gamma_1$  gives a poor determination of the thermodynamical state; however, it varies sufficiently in the ionization zones to allow a determination of  $Y$ , provided that the properties of the equation of state are known with sufficient accuracy. Also, a further constraint is obtained from the fact that  $Y$  can be assumed to be constant throughout the fully mixed convection zone; this may permit separately to test aspects of the equation of state and determine the helium abundance in this region (see Section 7.1.7).

In the radiative interior additional assumptions are required to constrain the properties beyond the directly determined asteroseismic variables. This could, for example, involve assuming that the microphysics (equation of state, opacity and energy generation) is known. Also, the power of asteroseismic diagnostics depends greatly on the ability to obtain independent determinations of stellar mass and radius, as well as determinations of the luminosity and surface composition of the star.

## 3.4 Asymptotic Theory of Stellar Oscillations

The general oscillation equations appear quite complicated. In particular, analytical solutions can only be obtained in certain, very restricted cases (*cf.* J. P. Cox 1980, Section 17.7). A useful example is the behaviour of oscillations in an isothermal atmosphere, discussed in Appendix D. While such results offer some insight into the behaviour of the modes, a more fruitful approach is in general to approximate the equations to a point where they can be discussed analytically; an early example is the asymptotic analysis by Ledoux (1962) of high-order radial modes. The use of such asymptotic analyses is justified by the fact that in many cases the observed modes are of high radial order.

Thus solar oscillations, solar-like oscillations in other stars and oscillations in roAp stars are generally acoustic modes of high radial order, whereas the comparatively long-period oscillations observed in, *e.g.*, white dwarfs, slowly pulsating B stars and  $\gamma$  Dor stars are high-order buoyancy-driven modes. Thus asymptotic theory is often applicable to an actually surprisingly high degree of accuracy.

### 3.4.1 The Cowling Approximation

The general equations are of fourth order. This is a difficulty in asymptotic studies which generally deal with second-order systems. Fortunately the perturbation to the gravitational potential can often be neglected. To see this we may consider the integral solution in Eq. (3.45) to the Poisson equation. This can be written on separated form as

$$\Phi'(r) = -\frac{4\pi G}{2l+1} \left[ \frac{1}{r^{l+1}} \int_0^r \rho'(r')(r')^{l+2} dr' + r^l \int_r^R \frac{\rho'(r')}{(r')^{l-1}} dr' \right]; \quad (3.173)$$

this is most easily seen by verifying that this solution satisfies the separated Poisson equation (3.128). From Eq. (3.173) it follows that  $|\Phi'|$  is small compared with  $\rho'$  under the following two circumstances:

- i) when  $l$  is large;
- ii) when the radial order  $|n|$  is large.

In the former case  $(r'/r)^{l+2}$  (which appears in the first integral) is small when  $r' < r$ , and  $(r/r')^{l-1}$  (which appears in the second integral) is small when  $r' > r$ ; in addition  $\Phi'$  is reduced by the factor  $(2l+1)^{-1}$ . In the second case  $\Phi'$  contains integrals over rapidly varying functions of  $r$  and is therefore reduced relative to the size of the integrand.

Under these circumstances it appears reasonable to neglect  $\Phi'$ . This approximation was first studied carefully by Cowling (1941), and is therefore known as the *Cowling approximation*. It reduces the order of the system of equations to two, with a corresponding reduction in the number of boundary conditions.

It must be pointed out that the neglect of  $\Phi'$  is not quite as obvious as may seem from this discussion. In fact its mathematical justification has not been fully analysed. As will be discussed in Section 3.5.2 the properties of the so-called f mode, with no radial zeros, with  $l = 1$  are drastically different in the Cowling approximation and for the full equations. Nonetheless, for high-order or high-degree modes the validity of the approximation has been confirmed computationally (*e.g.*, Robe 1968; Christensen-Dalsgaard 1991a).

### 3.4.2 Trapping of p and g Modes

The equations in the Cowling approximation can be written as

$$\frac{d\xi_r}{dr} = - \left( \frac{2}{r} - \frac{1}{\Gamma_1} H_p^{-1} \right) \xi_r + \frac{1}{\rho c^2} \left( \frac{S_l^2}{\omega^2} - 1 \right) p' , \quad (3.174)$$

$$\frac{dp'}{dr} = \rho(\omega^2 - N^2) \xi_r - \frac{1}{\Gamma_1} H_p^{-1} p' , \quad (3.175)$$

where

$$H_p^{-1} = - \frac{d \ln p}{dr} ; \quad (3.176)$$

hence  $H_p$  is the pressure scale height, *i.e.*, the distance, roughly, over which the pressure changes by a factor  $e$ . For oscillations of high radial order, the eigenfunctions vary much more rapidly than the equilibrium quantities; thus, *e.g.*, the left hand side of Eq. (3.174) is much larger than the first term on the right hand side which contains derivatives of equilibrium quantities. As a first, very rough approximation, we simply neglect these terms, reducing the equations to

$$\frac{d\xi_r}{dr} = \frac{1}{\rho c^2} \left( \frac{S_l^2}{\omega^2} - 1 \right) p' , \quad (3.177)$$

$$\frac{dp'}{dr} = \rho(\omega^2 - N^2) \xi_r . \quad (3.178)$$

These two equations can be combined into a single second-order differential equation for  $\xi_r$ ; neglecting again derivatives of equilibrium quantities, the result is

$$\frac{d^2\xi_r}{dr^2} = \frac{\omega^2}{c^2} \left( 1 - \frac{N^2}{\omega^2} \right) \left( \frac{S_l^2}{\omega^2} - 1 \right) \xi_r . \quad (3.179)$$

This equation represents the crudest possible approximation to the equations of nonradial oscillations. In fact the assumptions going into the derivations are questionable. In particular, the pressure scale height becomes small near the stellar surface,<sup>10</sup> where therefore derivatives of pressure and density cannot be neglected. We return to this question in Section 3.4.3. Similarly, the term in  $2/r$  neglected in Eq. (3.174) is large very near the centre. Nevertheless, the equation is adequate to describe the overall properties of the modes of oscillation, and in fact gives a reasonably accurate determination of their frequencies.

From Eq. (3.179) it is evident that the characteristic frequencies  $S_l$  and  $N$ , defined in Eqs (3.153) and (3.155), play a very important role in determining the behaviour of the oscillations. They are illustrated in Fig. 3.14 for a solar model; this is representative of lower-main-sequence stars.  $S_l$  tends to infinity as  $r$  tends to zero and decreases monotonically towards the surface, due to the decrease in  $c$  and the increase in  $r$ . As discussed in Section 3.1.4.2,  $N^2$  is negative in convection zones (although generally of small absolute value), and positive in convectively stable regions. The maximum in  $N$  very near the

---

<sup>10</sup> notice that  $H_p = p/(\rho g)$  is proportional to temperature.

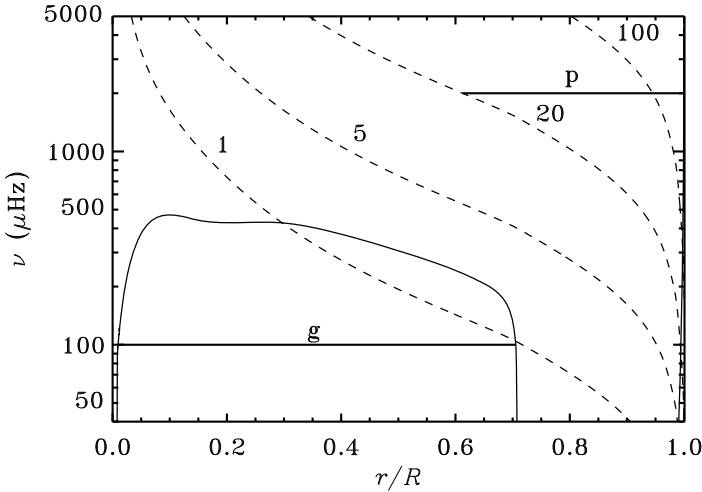


**Fig. 3.14.** Buoyancy frequency  $N$  [cf. Eq. (3.155); continuous line] and characteristic acoustic frequency  $S_l$  [cf. Eq. (3.153); dashed lines, labelled by the values of  $l$ ], shown in terms of the corresponding cyclic frequencies, against fractional radius  $r/R$  for a model of the present Sun. The heavy horizontal lines indicate the trapping regions for a  $g$  mode with frequency  $\nu = 100 \mu\text{Hz}$ , and for a  $p$  mode with degree 20 and  $\nu = 2000 \mu\text{Hz}$ .

centre is associated with the increase towards the centre in the helium abundance in the region where nuclear burning has taken place. Here, effectively, lighter material is on top of heavier material, which adds to the convective stability and hence increases  $N$ . This is most easily seen by using the ideal gas law for a fully ionized gas, Eq. (3.19) which is approximately valid in the interior of cool stars, to rewrite  $N^2$  as

$$N^2 \simeq \frac{g^2 \rho}{p} (\nabla_{\text{ad}} - \nabla + \nabla_{\mu}) , \quad (3.180)$$

corresponding to the convective instability condition written in the form given by Eq. (3.94) (see also Eq. (3.95)). In the region of nuclear burning,  $\mu$  increases with increasing depth and hence increasing pressure, and therefore the term in  $\nabla_{\mu}$  makes a positive contribution to  $N^2$ .

The behaviour of  $N$  is rather more extreme in stars with convective cores; this is illustrated in Fig. 3.15 for the case of a  $2.2 M_{\odot}$  evolution sequence. The convective core is fully mixed and here, therefore, the composition is uniform, with  $\nabla_{\mu} = 0$ . However, in stars of this and higher masses the convective core generally shrinks during the evolution, leaving behind a steep gradient in the

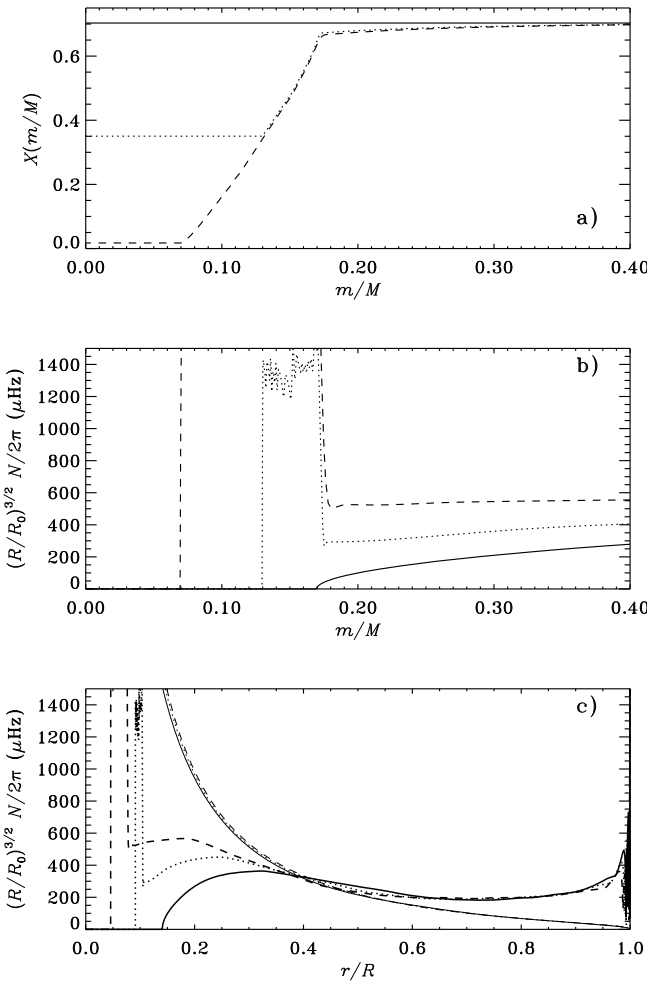


**Fig. 3.15.** (a) Hydrogen content  $X$  against mass fraction  $m/M$  for three models in a  $2.2 M_\odot$  evolution sequence. The solid line is for age 0, the dotted line for age 0.47 Gyr and the dashed line for age 0.71 Gyr. Only the inner 40 per cent in mass of the models is shown. (b) Scaled buoyancy frequency, expressed in terms of cyclic frequency, against  $m/M$  for the same three models. In the scaling factor,  $R$  and  $R_0$  are the radii of the actual and the zero-age main-sequence model, respectively. For the model of age 0.71 Gyr, the maximum value of  $(R/R_0)^{3/2} N/2\pi$  is  $2400 \mu\text{Hz}$ . (c) Scaled buoyancy frequency  $N$  (heavy lines) and characteristic acoustic frequency  $S_l$  for  $l = 2$  (thin lines), for the same three models, plotted against fractional radius  $r/R$ .

hydrogen abundance  $X$ , as shown in Fig. 3.15a. This causes a sharp peak in  $\nabla_\mu$  and hence in  $N$ . When plotted as a function of mass fraction  $m/M$ , as in panel (b) of Fig. 3.15, the location of this peak is essentially fixed although its width increases with the shrinking of the core<sup>11</sup>. However, as illustrated in Fig. 3.15c, the location shifts towards smaller radius: this is a consequence of the increase with evolution of the central density and hence the decrease in the radial extent of a region of given mass. This also causes an increase in gravity  $g$  in this region and hence in  $N$ , visible in the figure. In accordance with Eq. (3.169), the characteristic frequencies have been scaled by  $R^{3/2}$  in Fig. 3.15: it is evident that  $S_l$ , and  $N$  in the outer parts of the model, are then largely independent of evolution. Thus the stellar envelope essentially changes homologously, while this is far from the case for the core; it follows that stellar oscillations sensitive to the structure of the core might be expected to show considerable variation with evolution of the dimensionless frequency  $\sigma$  introduced in Eq. (3.162). This is confirmed by the numerical results which will be shown in Section 3.5.3.

To analyse the behaviour of the oscillations we write Eq. (3.179) as

$$\frac{d^2\xi_r}{dr^2} = -K_s(r)\xi_r , \quad (3.181)$$

where

$$K_s(r) = \frac{\omega^2}{c^2} \left( \frac{N^2}{\omega^2} - 1 \right) \left( \frac{S_l^2}{\omega^2} - 1 \right) . \quad (3.182)$$

The local behaviour of  $\xi_r$  depends on the sign of  $K_s$ . Where  $K_s$  is positive,  $\xi_r$  is locally an oscillating function of  $r$ , and where  $K_s(r)$  is negative the solution is locally an exponentially increasing or decreasing function of  $r$ . Indeed, as will be shown in more detail in Section E.2, in the former case the solution may be written approximately as

$$\xi_r \sim \cos \left( \int K_s^{1/2} dr + \phi \right) , \quad K_s > 0 , \quad (3.183)$$

( $\phi$  being a phase determined by the boundary conditions) while in the latter case

$$\xi_r \sim \exp \left( \pm \int |K_s|^{1/2} dr \right) , \quad K_s < 0 . \quad (3.184)$$

Thus according to this description the solution oscillates as a function of  $r$  when

$$\text{o1)} \quad |\omega| > |N| \quad \text{and} \quad |\omega| > S_l , \quad (3.185)$$

or

$$\text{o2)} \quad |\omega| < |N| \quad \text{and} \quad |\omega| < S_l , \quad (3.186)$$

<sup>11</sup> The erratic behaviour of  $N$  in the chemically inhomogeneous region, shown by the dotted line, is caused by small fluctuations introduced by numerical errors in  $X(m)$ .

and it is exponential when

$$\text{e1}) \quad |N| < |\omega| < S_l , \quad (3.187)$$

or

$$\text{e2}) \quad S_l < |\omega| < |N| . \quad (3.188)$$

This describes two types of oscillatory behaviour, o1) and o2), and two types of exponential behaviour, e1) and e2). The exponential behaviour is often described by saying that the mode is *evanescent* in the given region, particularly if it is decreasing exponentially as one moves away from a dominant oscillatory region.

For a given mode of oscillation there may be several regions where the solution oscillates, according to criterion o1) or o2), with intervening regions where it is exponential. However, in general one of these oscillating regions is dominant, with the solution decaying exponentially away from it. The solution is then said to be *trapped* in this region; its frequency is predominantly determined by the structure of the model in the region of trapping. The boundaries of the trapping region are generally at points where  $K_s(r) = 0$ ; such points are known as *turning points*. From Eq. (3.183) it follows that within the trapping region the mode oscillates the more rapidly as a function of  $r$ , the higher the value of  $K_s$ . Thus, if the order of the mode is roughly characterized by the number of zeros in  $\xi_r$ <sup>12</sup> the order generally increases with increasing  $K_s$ .

From the behaviour of  $S_l$  and  $N$  shown in Fig. 3.14, and the conditions for an oscillating solution, we may expect two classes of modes:

- i) Modes with high frequencies satisfying o1), labelled p modes.
- ii) Modes with low frequencies satisfying o2), labelled g modes.

These are discussed separately below.

Typical trapping regions, for a p and a g mode in a model of the present Sun, are shown in Fig. 3.14. We note also that in evolved stars with convective cores the large values of  $N$  at the edge of the core may lead to the condition o2) being satisfied even at quite high frequency. Thus here one might expect that the distinction in frequency between p and g modes becomes less clear. This results in *mixed modes* which show both a p-mode and a g-mode character. Some consequences of that are illustrated in Section 3.5.3.

We finally note that in white dwarfs the buoyancy frequency is very small in the interior which is dominated by degenerate electrons (*cf.* Fig. 3.11). Thus in this case the g modes are largely confined to the stellar envelope. Also, the modes are affected by the bumps in  $N^2$  associated with the steep composition gradients; as discussed in Section 7.4.1.3 this gives rise to a signature in the oscillation periods which provides a diagnostics of the thickness of the different layers.

---

<sup>12</sup> The concept of order is defined more precisely in Section 3.5.2.

### 3.4.2.1 p Modes

These are trapped between an inner turning point  $r = r_t$  and the surface; the trapping at the surface is in fact not contained in the analysis presented so far, but will be discussed in Section 3.4.3. The inner turning point is located where  $S_l(r_t) = \omega$ , or

$$\frac{c^2(r_t)}{r_t^2} = \frac{\omega^2}{l(l+1)}. \quad (3.189)$$

This condition determines  $r_t$  as a function of  $l$  and  $\omega$ .

For p modes, in particular those observed in the Sun or in solar-like pulsators, we typically have that  $\omega \gg N$ . Then  $K_s$  can be approximated by

$$K_s(r) \simeq \frac{1}{c^2}(\omega^2 - S_l^2). \quad (3.190)$$

In this approximation, therefore, the dynamics of the p modes is solely determined by the variation of the sound speed with  $r$ . These modes are standing acoustic waves, with the restoring force being dominated by pressure, and this motivates denoting them p modes. Indeed, Eq. (3.190) determining the radial behaviour of the modes can be obtained very simply from the dispersion relation (3.55) for a plane sound wave. We write the squared length  $|\mathbf{k}|^2$  of the wave vector as the sum of a radial and a horizontal component, *i.e.*,

$$|\mathbf{k}|^2 = k_r^2 + k_h^2. \quad (3.191)$$

Here  $k_h$  is determined from  $l$  by Eq. (3.143); thus Eq. (3.55) becomes

$$\frac{\omega^2}{c^2} = k_r^2 + \frac{l(l+1)}{r^2}, \quad (3.192)$$

or

$$k_r^2 = \frac{1}{c^2}(\omega^2 - S_l^2). \quad (3.193)$$

Here, according to Eq. (3.181),  $k_r^2$  must be identified with  $K_s$ , and Eq. (3.193) is therefore identical to Eq. (3.190).

The sequence of approximations used to derive Eq. (3.190) corresponds closely to the approximations made in the analysis of simple sound waves. Thus it is not surprising that the same dispersion relation is recovered. Nevertheless, it is gratifying to see that the full oscillation equations reduce to the correct behaviour in this limit.

The interior reflection of the p modes can be understood very simply in terms of ray theory. A mode can be regarded as a superposition of propagating sound waves. Two such waves are illustrated in Fig. 3.16. As they propagate into the star, the deeper parts of the wave fronts experience a higher sound speed and therefore travel faster. Consequently, the direction of propagation is bent away from the radial direction. This is completely analogous to the refraction experienced by light rays when traveling into a medium with a

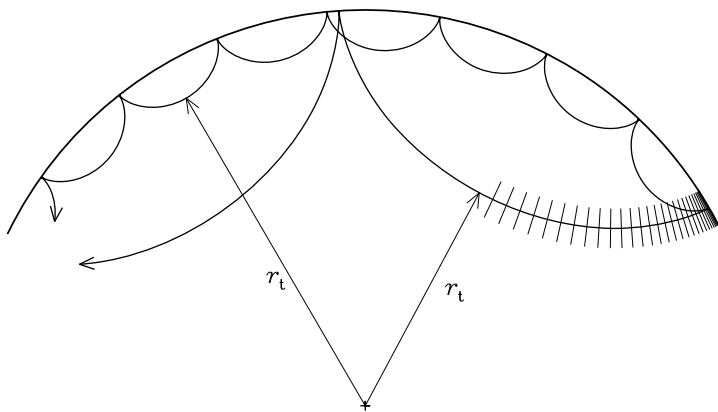


**Fig. 3.16.** Propagation of acoustic waves, corresponding to modes with  $l = 30$ ,  $\nu = 3 \text{ mHz}$  (deeply penetrating rays) and  $l = 100$ ,  $\nu = 3 \text{ mHz}$  (shallowly penetrating rays). The lines orthogonal to the former path of propagation illustrate the wave fronts.

higher speed of light, as reflected by Snell's law; the speed of light is lower in materials with higher index of refraction, leading to the change in direction of the light rays. Mathematically, the effect is expressed by the decrease in the radial component of the wave vector with increasing sound speed shown in Eq. (3.193). At the reflection point the wave travels horizontally, with  $k_r = 0$ ; the condition (3.189) then follows directly from the dispersion relation for sound waves, in the form given in Eq. (3.192). A detailed analysis of p modes in terms of ray theory has been given by Gough (1984a, 1986a).

The reflection of the waves at the surface is not contained in this simple description; it results from the decrease of the scale of variation in the equilibrium quantities, making invalid the approximations leading to Eq. (3.179). A simple analytical description of this is possible in the case of an isothermal atmosphere, discussed in Appendix D. An asymptotic treatment including the surface reflection is discussed in Section 3.4.3 below.

From Eq. (3.190) it follows that  $K_s$  increases with the frequency. This increases the number of zeros in the eigenfunction, *i.e.*, the mode order. This means, equivalently, that the frequency increases with mode order.

Equation (3.193) can be used to make plausible a very simple, yet powerful, relation for the frequencies of acoustic modes. To obtain a standing wave the change in phase of the eigenfunction in the radial direction must be an integral

multiple of  $\pi$ , apart from phase changes at the boundaries of the region; this is entirely equivalent to simple standing waves. Thus

$$\int_{r_t}^R k_r dr = \pi(n + \alpha) , \quad (3.194)$$

where  $\alpha$  accounts for the phase change at the lower turning point and in the reflection of the wave at the surface,  $r = R$ . Using Eq. (3.193) this becomes

$$\int_{r_t}^R (\omega^2 - S_l^2)^{1/2} \frac{dr}{c} = (n + \alpha)\pi , \quad (3.195)$$

or

$$F\left(\frac{\omega}{L}\right) = \frac{(n + \alpha)\pi}{\omega} , \quad (3.196)$$

where

$$F\left(\frac{\omega}{L}\right) \equiv \int_{r_t}^R \left(1 - \frac{L^2 c^2}{\omega^2 r^2}\right)^{1/2} \frac{dr}{c} , \quad (3.197)$$

with  $L^2 = l(l + 1)$ .<sup>13</sup> That solar oscillations satisfy a relation of the form given in Eq. (3.196) was first found by Duvall (1982), and thus this relation is known as *the Duvall law*. It has played a fundamental role in the analysis of solar oscillations, as discussed in Chapter 7. A more rigorous derivation is provided in Section E.3, and we discuss further properties of the relation in Section 7.1.4.4.

### 3.4.2.2 g Modes

Here the turning-point positions are determined by the condition  $N = \omega$ . As seen in Fig. 3.14, for low-frequency modes in solar-like stars this gives rise to one turning point very near the centre, and a second just below the base of the convection zone. At higher frequencies the upper turning point is deeper in the model, and for frequencies close to the maximum in  $N$ , the modes are trapped in the deep interior. In more massive main-sequence stars with a convective core and a very thin outer convection zone the inner turning point is at the edge of the core and the mode extends nearly to the surface; obviously a more complex behaviour may result in evolved stars with a large peak in the buoyancy frequency associated with regions of varying mean molecular weight (*cf.* Fig. 3.15). However, to this approximation the position of the turning points is independent of  $l$ .

For high-order g modes typically  $\omega^2 \ll S_l^2$ , and we may approximate  $K_s$  by

$$K_s(r) \simeq \frac{1}{\omega^2} (N^2 - \omega^2) \frac{l(l + 1)}{r^2} ; \quad (3.198)$$

---

<sup>13</sup> Note that  $r_t$ , as given by Eq. (3.189), is indeed determined by  $\omega/L$ .

thus in this case the dynamics is dominated by the variation of the buoyancy frequency  $N$  with  $r$ . Gravity, acting on the density perturbation, provides the dominant restoring force, and this is the reason that the modes are called g modes. The modes are trapped internal gravity waves. In fact, by arguments similar to those used above for the p modes, one obtains from the dispersion relation (3.76) for gravity waves that the radial component of the wave number is given by

$$k_r^2 = \frac{l(l+1)}{r^2} \left( \frac{N^2}{\omega^2} - 1 \right); \quad (3.199)$$

this is in accordance with the relation for  $K_s$  given in Eq. (3.198).

From Eq. (3.198) it follows that  $K_s$  increases with decreasing  $\omega$ . Thus the order of the mode increases with decreasing  $\omega$ , or, equivalently,  $\omega$  decreases with increasing order. It may also be noticed that the frequencies of g modes cannot exceed the maximum  $N_{\max}$  in the buoyancy frequency in the stellar interior. As shown below (*cf.* Fig. 3.20) one does indeed find an upper limit on numerically computed g-mode frequencies. The approach to this limit as  $l$  gets large was analysed by Christensen-Dalsgaard (1980).

### 3.4.3 Asymptotic Properties of Frequencies and Eigenfunctions

The analysis presented above is clearly inadequate as an asymptotic representation of stellar oscillations. In particular, it neglects the fact that the properties of the equilibrium model vary on a scale that may not be long compared with the radial wavelength of the modes in some regions of the star, particularly near the stellar surface. For acoustic modes the variation of the mode is characterized by the radial wave number  $k_r \simeq \omega/c$ , whereas the variation of the equilibrium structure can be characterized by, for example, the density scale height  $H$ , defined by

$$H^{-1} = \left| \frac{d \ln \rho}{dr} \right|. \quad (3.200)$$

Only when  $k_r \gg H^{-1}$ , or  $\omega \gg c/H$ , is the assumption of a slowly varying equilibrium structure satisfied. As discussed in Appendix D a more precise analysis in the simple case of an isothermal atmosphere shows that the modes oscillate as a function of  $r$  only where

$$\omega > \omega_a, \quad (3.201)$$

where

$$\omega_a = \frac{c}{2H_p} \quad (3.202)$$

is the *acoustic cut-off frequency* for an isothermal atmosphere,  $H_p$  being the pressure scale height (see Eq. (3.176))

$$H_p^{-1} = \left| \frac{d \ln p}{dr} \right| = \frac{Gm\rho}{pr^2} \quad (3.203)$$

(here we used the equation of hydrostatic support, Eqs (3.33) and (3.34)). Near the stellar surface  $\rho/p \propto T^{-1}$  (*cf.* Eq. (3.19)) becomes very large and hence Eq. (3.201) may no longer be satisfied at a given frequency.

It is possible to extend the analysis in Section 3.4.2 by including derivatives of the equilibrium quantities (see Unno *et al.* 1989). In this way the variation of the equilibrium structure can be taken into account in a more consistent way. However, the resulting equations contain singularities which make their analysis somewhat complex. Here instead we discuss the asymptotic properties in terms of a formalism developed by Gough (*e.g.*, Deubner & Gough 1984), based on an analysis by Lamb (1932). As in Section 3.4.2 it assumes the Cowling approximation; derivatives of equilibrium quantities are generally included, with the exception of the derivative of  $g$  and  $r$ . The derivation is presented in Section E.1. The result is a second-order differential equation,

$$\frac{d^2 X}{dr^2} + \frac{1}{c^2} \left[ S_l^2 \left( \frac{N^2}{\omega^2} - 1 \right) + \omega^2 - \omega_c^2 \right] X = 0 , \quad (3.204)$$

in terms of the quantity

$$X = c^2 \rho^{1/2} \chi , \quad (3.205)$$

where  $\chi = \text{div } \delta \mathbf{r}$ . Here

$$\omega_c^2 = \frac{c^2}{4H^2} \left( 1 - 2 \frac{dH}{dr} \right) \quad (3.206)$$

is a generalized acoustic cut-off frequency.<sup>14</sup>

Before analysing Eq. (3.204) in more detail we note that the analysis also shows the existence of a solution with

$$\omega^2 \simeq Lg/R , \quad (3.207)$$

and with the radial eigenfunction varying as

$$\xi_r \propto \exp(Lr/R) . \quad (3.208)$$

Comparison with Eq. (3.85), with  $k_h = L/R$ , identifies this as a surface gravity wave (see also Section 7.1.4.3).

As in the discussion of Eq. (3.181) the overall properties of the eigenfunctions are determined by the properties of

$$K \equiv \frac{1}{c^2} \left[ S_l^2 \left( \frac{N^2}{\omega^2} - 1 \right) + \omega^2 - \omega_c^2 \right] . \quad (3.209)$$

---

<sup>14</sup> Note that in an isothermal atmosphere  $H = H_p$  is constant, and consequently  $\omega_c = \omega_a$ .

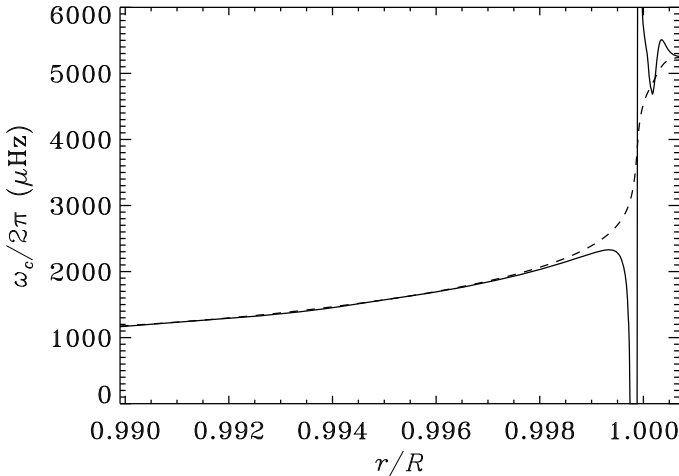


**Fig. 3.17.** The acoustic cut-off frequency  $\omega_c$  defined in Eq. (3.206) (solid line), and the approximation  $\omega_a$  appropriate to an isothermal region [cf. Eq. (3.202); dashed line] in the outermost parts of a model of the present Sun.

As in the simplified discussion in Section 3.4.2 a mode is oscillatory as a function of  $r$  where  $K > 0$  and behaves exponentially where  $K < 0$ . Near the surface  $S_l^2$  is small, and  $K$  is dominated by the last two terms; hence  $X$  is exponential when  $\omega^2 < \omega_c^2$ . This provides the trapping of the modes at the surface, which was not included in the analysis in Section 3.4.2. Figure 3.17 shows  $\omega_c$  and  $\omega_a$  in the outer parts of a solar model; they are in fact quite similar, except in a thin region very near the top of the convection zone, where the rapid variation in the superadiabatic gradient causes large excursions in  $\omega_c$ . In the interior of models of the present Sun  $\omega_c^2$  (which roughly varies as  $g^2/T$ ) is generally small, corresponding to cyclic frequencies below about 600  $\mu\text{Hz}$ .

To characterize the oscillatory properties of the solution we write Eq. (3.209) as

$$\begin{aligned} K(r) &= \frac{\omega^2}{c^2} \left[ 1 - \frac{\omega_c^2}{\omega^2} - \frac{S_l^2}{\omega^2} \left( 1 - \frac{N^2}{\omega^2} \right) \right] \\ &\equiv \frac{\omega^2}{c^2} \left( 1 - \frac{\omega_{l,+}^2}{\omega^2} \right) \left( 1 - \frac{\omega_{l,-}^2}{\omega^2} \right), \end{aligned} \quad (3.210)$$

defining the characteristic frequencies  $\omega_{l,+}$  and  $\omega_{l,-}$ . They are plotted in Fig. 3.18, in a model of the present Sun. Equation (3.210) shows that the trapping of the modes is determined by the value of the frequency, relative to

behaviour of  $\omega_{l,+}$  and  $\omega_{l,-}$ . In the interior of the star, particularly for large  $l$ ,

$$\omega_{l,+} \simeq S_l , \quad \omega_{l,-} \simeq N . \quad (3.211)$$

Thus here we recover the conditions for trapping discussed in Section 3.4.2. This was indeed to be expected, as the assumptions entering the present formulation provide a natural transition from the previously discussed simplified asymptotic treatment to the atmospheric behaviour of the oscillations. On the other hand, near the surface where  $S_l/\omega \ll 1$

$$\omega_{l,+} \simeq \omega_c , \quad (3.212)$$

while  $\omega_{l,-}$  is small. Thus the trapping near the surface is controlled by the behaviour of  $\omega_{l,+}$ . As shown in Fig. 3.18 trapping extends in frequency up to about 5.3 mHz in the solar case, although the spike in  $\omega_{l,+}$  just beneath the photosphere provides some partial reflection at even higher frequency. Also, it was noted by Balmforth & Gough (1990) that the rapid variation in temperature, and hence sound speed, at the transition between the chromosphere and the corona in stars like the Sun, can cause partial reflection. Modes with frequency  $\nu \gtrsim 2$  mHz propagate essentially to the photosphere, while modes of lower frequency are reflected at some depth in the convection zone.

As in the simplified case considered in Section 3.4.2 a given mode is typically characterized by a single region, between  $r_1$  and  $r_2$ , say, where  $K(r) > 0$  and where the mode consequently has an oscillatory behaviour, and such that the eigenfunctions decrease exponentially as one moves away from this region. As discussed in Section E.2 an approximate expression for the eigenfrequencies of such a trapped mode can be found from JWKB analysis of Eq. (3.204). The result is that the frequencies satisfy

$$\int_{r_1}^{r_2} K(r)^{1/2} dr = \left( n - \frac{1}{2} \right) \pi , \quad n = 1, 2, \dots . \quad (3.213)$$

Note that in a given frequency interval there may be two or more regions in the star where  $K > 0$ ; in this case the star may have separate but weakly interacting spectra of frequencies each associated with one of these regions. Numerical examples of this behaviour are discussed in Sections 3.5.3 and 7.2.4. From JWKB analysis asymptotic approximations to the eigenfunctions are also obtained (see Section E.4).

### 3.4.3.1 Acoustic Modes

If  $\omega^2 \gg |N|^2$  Eq. (3.213) can be approximated by

$$\omega \int_{r_1}^{r_2} \left( 1 - \frac{\omega_c^2}{\omega^2} - \frac{S_l^2}{\omega^2} \right)^{1/2} \frac{dr}{c} \simeq \pi(n - 1/2) . \quad (3.214)$$

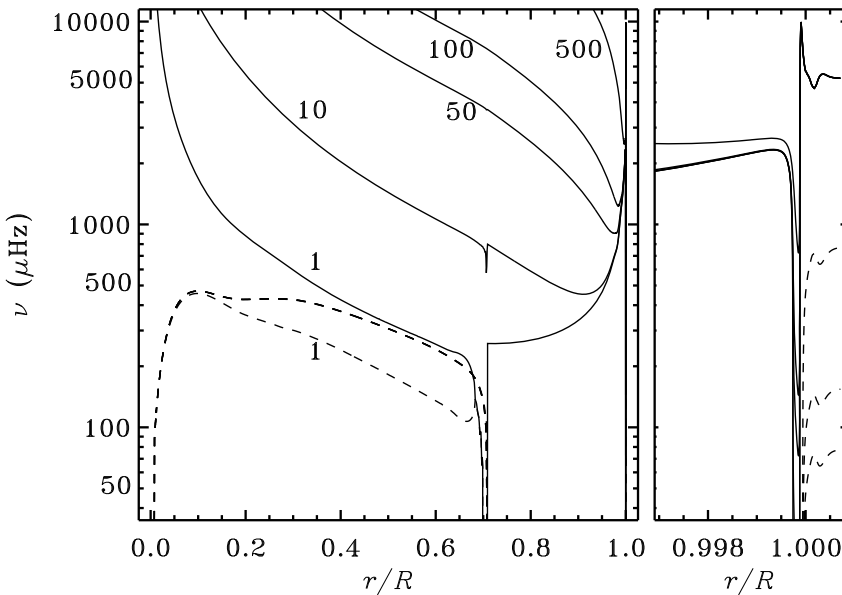


**Fig. 3.18.** Characteristic frequencies  $\omega_{l,+}/(2\pi)$  (continuous curves) and  $\omega_{l,-}/(2\pi)$  (dashed curves) for a model of the present Sun (*cf.* Eq. (3.210)). The curves are labelled with the degree  $l$ . The right-hand panel shows the outermost parts of the model on an expanded horizontal scale. The figure may be compared with the simple characteristic frequencies plotted in Fig. 3.14.

Since  $\omega_c$  is generally large only near the surface, the lower turning point is approximately at  $r_1 \simeq r_t$ , defined in Eq. (3.189), where  $\omega = S_l$ . Unless  $l$  is large the upper turning point  $r_2 \simeq R_t$ , where  $\omega = \omega_c(R_t)$ ; note in particular that  $R_t$  is independent of  $l$ . Also, in this case  $\omega_c$  can be neglected in the integrand in Eq. (3.214) except near the surface. Consequently the integral can be approximately expanded to separate the contribution from  $\omega_c$ . As discussed in Section E.3 the result is the Duvall law,

$$\int_{r_t}^R \left(1 - \frac{L^2 c^2}{\omega^2 r^2}\right)^{1/2} \frac{dr}{c} = \frac{[n + \alpha(\omega)]\pi}{\omega}, \quad (3.215)$$

corresponding to Eqs (3.196) and (3.197), with  $\alpha = \alpha(\omega)$  being a function of frequency that is determined by the properties of the near-surface region (see also Christensen-Dalsgaard & Pérez Hernández 1992).

For modes of low degree,  $r_t$  is very close to the centre. In Eq. (3.215), therefore, the second term in the bracket on the left-hand side is much smaller than unity over most of the range of integration. To leading order this results in the following simple relation for frequencies of low-degree p modes:

$$\nu_{nl} = \frac{\omega_{nl}}{2\pi} \simeq \left( n + \frac{l}{2} + \frac{1}{4} + \alpha \right) \Delta\nu , \quad (3.216)$$

where

$$\Delta\nu = \left[ 2 \int_0^R \frac{dr}{c} \right]^{-1} , \quad (3.217)$$

the so-called *large frequency separation*, is the inverse of twice the sound travel time between the centre and the surface. This equation predicts a uniform spacing  $\Delta\nu$  in  $n$  of the frequencies of low-degree modes. Also, modes with the same value of  $n + l/2$  should be almost degenerate,

$$\nu_{nl} \simeq \nu_{n-1,l+2} . \quad (3.218)$$

This frequency pattern has been observed for the solar five-minute modes of low degree (see Fig. 1.9) and may be used in the search for stellar oscillations of solar type. In fact, as shown in Fig. 3.25 below it is visible even down to very low radial order for computed frequencies of models near the zero-age main sequence.

The simple relation (3.216) is only a first approximation. There are departures from the apparent degeneracy in Eq. (3.218), of considerable diagnostic potential, characterized by the so-called *small frequency separations*  $\delta\nu_{nl} = \nu_{nl} - \nu_{n-1,l+2}$ . By carrying the asymptotic expansion further, one may show that

$$\nu_{nl} \simeq \left( n + \frac{l}{2} + \frac{1}{4} + \alpha \right) \Delta\nu - (AL^2 - \delta) \frac{\Delta\nu^2}{\nu_{nl}} \quad (3.219)$$

(Tassoul 1980, 1990; Gough 1986a), where

$$A = \frac{1}{4\pi^2 \Delta\nu} \left[ \frac{c(R)}{R} - \int_0^R \frac{dc}{dr} \frac{dr}{r} \right] . \quad (3.220)$$

Thus

$$\delta\nu_{nl} \equiv \nu_{nl} - \nu_{n-1,l+2} \simeq -(4l+6) \frac{\Delta\nu}{4\pi^2 \nu_{nl}} \int_0^R \frac{dc}{dr} \frac{dr}{r} , \quad (3.221)$$

where we neglected the term in the surface sound speed. This shows that  $\delta\nu_{nl}$  has substantial sensitivity to the sound-speed gradient in the core, which in turn is sensitive to the composition profile. Thus the small separation is a very important diagnostics of stellar evolution. Physically, this may be understood from the fact that for these modes only near the centre is  $k_h$  comparable with  $k_r$ . Elsewhere the wave vector is almost vertical, and the dynamics of the oscillations is largely independent of their horizontal structure, *i.e.*, of  $l$ ; therefore at given frequency the contributions of these layers to the frequency are nearly the same, and hence almost cancel in the difference in Eq. (3.221).

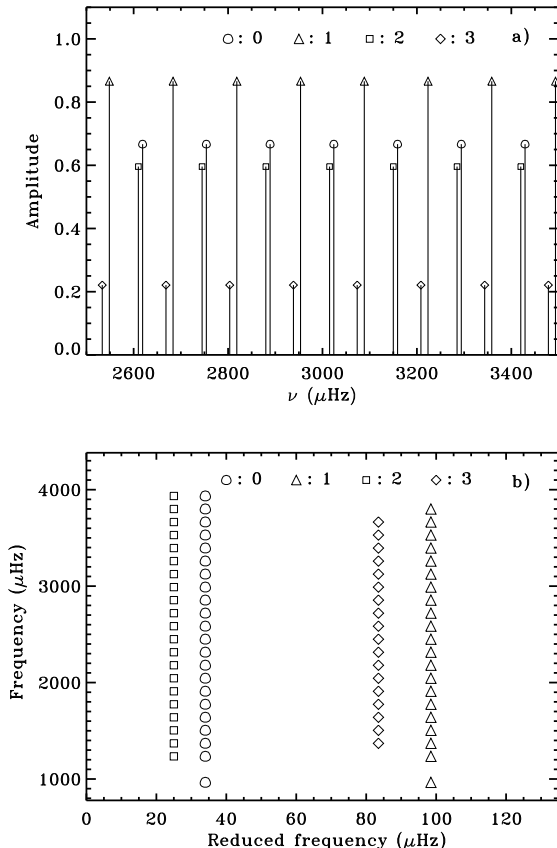


**Fig. 3.19.** Schematic oscillation spectrum (a) and échelle diagram (b), based on Eq. (3.223); the parameters,  $\Delta\nu_0 = 135 \mu\text{Hz}$ ,  $D_0 = 1.5 \mu\text{Hz}$  and  $\epsilon_0 = 1.4$ , were chosen to match approximately the solar values. In panel (a) the amplitudes were chosen as the sensitivities of Doppler-velocity observations in disc-integrated light (*cf.* Fig. 7.1).

From an observational point of view, and to illustrate its structure, it is convenient to represent the spectrum by the average quantities  $\Delta\nu_0$  and  $D_0$ , with

$$\langle \nu_{n+1l} - \nu_{nl} \rangle_{nl} = \Delta\nu_0 , \quad \delta\nu_l \equiv \langle \nu_{nl} - \nu_{n-1l+2} \rangle_n \simeq (4l + 6)D_0 \quad (3.222)$$

(e.g., Scherrer *et al.* 1983), such that

$$\nu_{nl} \simeq \Delta\nu_0 \left( n + \frac{l}{2} + \epsilon_0 \right) - l(l+1)D_0 , \quad (3.223)$$

where  $\epsilon_0 = \alpha + 1/4$ . The resulting structure is illustrated schematically in Fig. 3.19a, for frequency separations corresponding to the solar case. To illustrate in more detail the properties of the spectrum, it is convenient to use an *échelle diagram* (e.g., Grec *et al.* 1983). Here the frequencies are reduced modulo  $\Delta\nu_0$  by expressing them as

$$\nu_{nl} = \nu_0 + k\Delta\nu_0 + \tilde{\nu}_{nl}, \quad (3.224)$$

where  $\nu_0$  is a suitably chosen reference, and  $k$  is an integer such that  $\tilde{\nu}_{nl}$  is between 0 and  $\Delta\nu_0$ ; the diagram is produced by plotting  $\tilde{\nu}_{nl}$  on the abscissa and  $\nu_0 + k\Delta\nu_0$  on the ordinate. Graphically, this may be thought of as cutting the frequency axis into pieces of length  $\Delta\nu_0$  and stacking them above each other. This is illustrated in Fig. 3.19b. According to the simple asymptotic expression in Eq. (3.223) the result yields points arranged on a set of vertical lines corresponding to the different values of  $l$ , the lines being separated by the appropriate  $\delta\nu_l$ .

The eigenfunctions of p modes are discussed in Section E.4. The result is

$$\begin{aligned} \xi_r(r) &\simeq & (3.225) \\ A\rho^{-1/2}c^{-1/2}r^{-1} \left|1 - \frac{S_l^2}{\omega^2}\right|^{1/4} \cos \left[ \omega \int_r^R \left(1 - \frac{S_l^2}{\omega^2}\right)^{1/2} \frac{dr'}{c} - (1/4 + \alpha)\pi \right], \end{aligned}$$

where we have again neglected  $N^2/\omega^2$ . To simplify this expression further we note that  $S_l^2$  decreases quite rapidly with increasing  $r$ . Near  $r = r_t$ ,  $\omega^2$  and  $S_l^2$  are comparable, but at some distance from the turning point we can assume that  $S_l^2/\omega^2 \ll 1$ . Here, therefore

$$\xi_r(r) \simeq A\rho^{-1/2}c^{-1/2}r^{-1} \cos \left[ \omega \int_r^R \frac{dr'}{c} - (1/4 + \alpha)\pi \right]. \quad (3.226)$$

It is convenient to express this as

$$\rho^{1/2}c^{1/2}r\xi_r(r) \simeq A \cos [\omega\tau - (1/4 + \alpha)\pi], \quad (3.227)$$

where we introduced the *acoustic depth*

$$\tau = \int_r^R \frac{dr'}{c}. \quad (3.228)$$

Thus the scaled displacement is a simple harmonic function of  $\omega\tau$ . To this approximation the eigenfunction is independent of  $l$ . Oscillations with the same frequency but different  $l$  therefore have approximately the same eigenfunctions near the surface, if they are normalized to the same surface value.

We finally note that it follows from the analysis in Section E.4.1 that the energy integral (*cf.* Eq. (3.139)) can be written as

$$\mathcal{E} \simeq \tilde{\eta}(\omega) \xi_r(R)^2 \int_{r_t}^R \left(1 - \frac{L^2 c^2}{\omega^2 r^2}\right)^{-1/2} \frac{dr}{c} \quad (3.229)$$

(see Eq. (E.92)), where  $\tilde{\eta}(\omega)$  accounts for the behaviour of the eigenfunction near the upper turning point.

### 3.4.3.2 Asymptotic Properties of g Modes

For g modes in general  $\omega^2 \ll S_l^2$ , and we approximate  $K$  by

$$K(r) \simeq \frac{l(l+1)}{r^2} \left( \frac{N^2}{\omega^2} - 1 \right). \quad (3.230)$$

Typically a mode is trapped between two zeros  $r_1$  and  $r_2$  of  $K$ , and Eq. (E.41) shows that the frequencies are determined by

$$\int_{r_1}^{r_2} L \left( \frac{N^2}{\omega^2} - 1 \right)^{1/2} \frac{dr}{r} = (n - 1/2)\pi, \quad (3.231)$$

or

$$\int_{r_1}^{r_2} \left( \frac{N^2}{\omega^2} - 1 \right)^{1/2} \frac{dr}{r} = \frac{(n - 1/2)\pi}{L}. \quad (3.232)$$

Here the left-hand side is solely a function of  $\omega$ , so that Eq. (3.232) can be written, in analogy with Eq. (3.196), as

$$\frac{n - 1/2}{L} = G(\omega), \quad (3.233)$$

where

$$G(\omega) = \frac{1}{\pi} \int_{r_1}^{r_2} \left( \frac{N^2}{\omega^2} - 1 \right)^{1/2} \frac{dr}{r}. \quad (3.234)$$

For high-order, low-degree g modes  $\omega$  is much smaller than  $N$  over most of the interval  $[r_1, r_2]$ . This suggests that a similar approximation to the one leading to Eq. (3.216) should be possible; however, now the properties obviously depend on whether the star has a radiative or convective core. In the case of a radiative core, as in Fig. 3.14, the lower turning point is very near the centre and here the integral may be expanded, in much the same way as the integral in Eq. (3.197), by using the fact that  $N \sim r$  near  $r = 0$ ; as in the p-mode case this gives rise to a dependence on  $l$ . However, the expansion near the upper turning point can apparently not be done in a similarly simple fashion, and in any case the result does not quite have the correct dependence on  $l$ . In the case of a convective core the phase shift at the lower boundary is independent of degree. A proper asymptotic analysis (Tassoul 1980) shows that the frequencies of low-degree, high-order g modes are given by

$$\omega = \frac{L \int_{r_1}^{r_2} N \frac{dr}{r}}{\pi(n + \alpha_{l,g})}, \quad (3.235)$$

where the phase term  $\alpha_{l,g}$  depends on the details of the boundaries of the trapping region. This may also be written as

$$\Pi = \frac{\Pi_0}{L}(n + \alpha_{l,g}), \quad (3.236)$$

where

$$\Pi_0 = 2\pi^2 \left( \int_{r_1}^{r_2} N \frac{dr}{r} \right)^{-1}. \quad (3.237)$$

Thus in this case the *periods* are asymptotically equally spaced in the order of the mode, the spacing decreasing with increasing  $l$ . The analysis was carried to the next asymptotic order by Tassoul (1980). Smeyers & Moya (2007) made a detailed analysis of the asymptotic properties of g modes in stars with a convective core, considering both the case of a radiative envelope and an outer convection zone.

The phase term  $\alpha_{l,g}$  depends on whether the star has a radiative or convective core. In the case of a radiative core,  $\alpha_{l,g} = l/2 + \alpha_g$ , such that the period depends on  $n + l/2$ , as in the case of the acoustic modes (*cf.* Eq. (3.216)). With a convective core  $\alpha_{l,g} = \alpha_g$  is independent of  $l$ . In both cases  $\alpha_g$  depends on the detailed properties of the buoyancy frequency in the vicinity of turning points, which will often be associated with boundaries of convective regions. Thus Ellis (1986), Provost & Berthomieu (1986) and Gabriel (1986) considered the signature of the detailed properties of the buoyancy frequency just beneath a convective envelope, in the asymptotic behaviour of g-mode periods, as a potential diagnostic of the stratification of this region in the Sun.

The eigenfunctions in the trapping region are discussed in Section E.4. We may assume that  $\omega^2 \ll S_l^2$ , and so obtain

$$\xi_r(r) \simeq A \rho^{-1/2} r^{-3/2} \left| \frac{N^2}{\omega^2} - 1 \right|^{-1/4} \cos \left[ L \int_{r_1}^r \left( \frac{N^2}{\omega^2} - 1 \right)^{1/2} \frac{dr'}{r'} - \frac{\pi}{4} \right]. \quad (3.238)$$

Except close to the turning points  $r_1, r_2$  we may assume that  $N^2/\omega^2 \gg 1$  (note, from Fig. 3.14, that  $N$  increases very rapidly from 0 both at the centre and at the base of the convection zone). Here, therefore,

$$\xi_r(r) \simeq A \omega^{1/2} \rho^{-1/2} r^{-3/2} N^{-1/2} \cos \left[ L \int_{r_1}^r \left( \frac{N^2}{\omega^2} - 1 \right)^{1/2} \frac{dr'}{r'} - \frac{\pi}{4} \right]. \quad (3.239)$$

Hence we expect that  $\rho^{1/2} r^{3/2} N^{1/2} \xi_r$  behaves like a distorted cosine function.

The behaviour at high degree depends on the detailed properties of the buoyancy frequency. Assuming that  $N$  has a single maximum,  $N_{\max}$ , in the stellar interior it follows from Eq. (3.234) that

$$G(\omega) \rightarrow 0 \quad \text{for } \omega \rightarrow N_{\max} . \quad (3.240)$$

Consequently

$$\omega \rightarrow N_{\max} \quad \text{for } L \rightarrow \infty . \quad (3.241)$$

More complex behaviour, although mostly of theoretical interest, is found when  $N$  has several local maxima, each with an associated spectrum of g modes at high degree (*e.g.*, Christensen-Dalsgaard *et al.* 1980).

## 3.5 Computed Properties of Modes of Oscillation

To get a feeling for the basic properties of the oscillations, it is useful to consider results of calculations of eigenfrequencies and eigenfunctions. The results presented in this section are largely based on models computed with the code described by Christensen-Dalsgaard (2008a). This is similar to other “standard model” calculations (see Section 3.2.1). The oscillation properties were computed with the adiabatic code of Christensen-Dalsgaard (2008b).

### 3.5.1 Results for the Present Sun

Figure 3.20 shows computed eigenfrequencies for a model of the present Sun, as functions of the degree  $l$ . It is convenient to regard  $l$  as a continuously varying, real parameter; this is mathematically completely permissible in the separated oscillation equations, although clearly only integral  $l$  have physical meaning. Consequently, the curves are shown as continuous, which helps in identifying the modes. The curves are labelled by the radial order which is essentially given by the number of zeros in the radial direction in the eigenfunctions (see also Section 3.5.2).

It is evident that there are two distinct, but slightly overlapping, groups of modes, with very different behaviour of the frequency as a function of  $l$ , and reflecting the asymptotic behaviour discussed in Section 3.4.2. The upper set of modes corresponds to the *p modes* whose dominant restoring force is pressure. The radial order has been indicated on some of the curves; it is evident that the frequencies of these modes increase with order, as mentioned in Section 3.4.2. The modes labelled with order 0, although similar in behaviour to the p modes, are in fact physically distinct; for  $l$  greater than about 20 their frequencies are approximately given by the expression (3.207) for a surface gravity wave, as predicted by the asymptotic analysis in Section E.1. They are known as *f modes*. Finally, the lower group of modes corresponds to the *g modes*, discussed in Section 3.4.2, where the dominant restoring force is buoyancy. For these modes the frequencies decrease with increasing number of nodes (*cf.* Section 3.4.2). It is evident that buoyancy demands variation over horizontal surfaces; thus there are no g modes for spherically symmetrical oscillations, *i.e.*, for  $l = 0$ . Only the g modes of order less than 50 have been

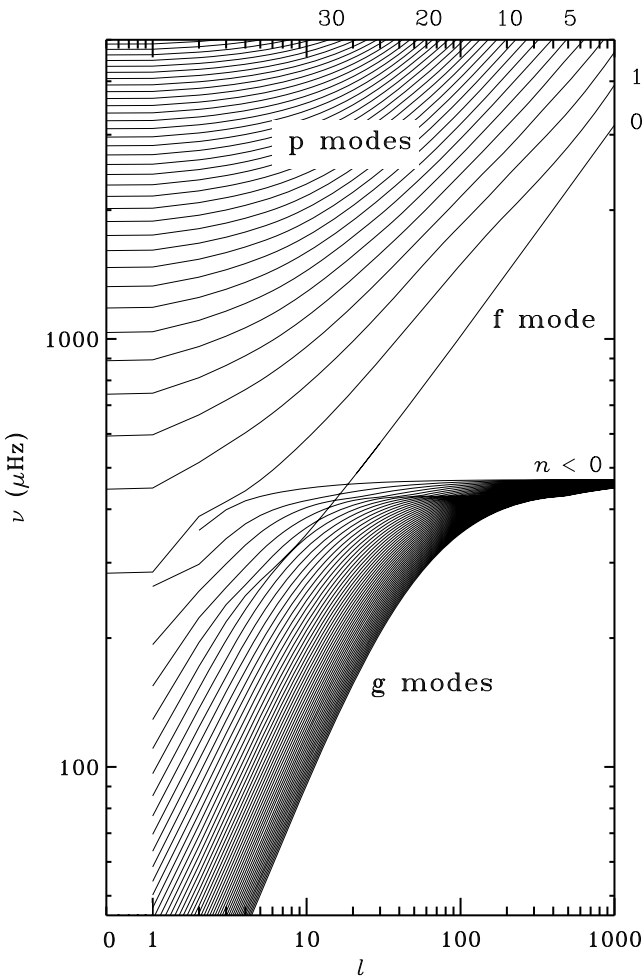


**Fig. 3.20.** Cyclic frequencies  $\nu = \omega/2\pi$ , as functions of degree  $l$ , computed for a solar model. Selected values of the radial order  $n$  have been indicated.

shown; in fact, the g-mode spectrum extends to zero frequency at all degrees, although the modes obviously become increasingly crowded with increasing degree. On the other hand the gap between the g and the f modes is real. In accordance with Eq. (3.241) the g-mode frequencies tend to the maximum in the buoyancy frequency for large  $l$ . In fact, the buoyancy frequency in this model, illustrated in Fig. 3.14, has a weak secondary maximum near  $r/R = 0.35$ , and at a frequency of about  $410 \mu\text{Hz}$ ; this is faintly reflected in the behaviour of the frequencies shown in Fig. 3.20, where there is an accumulation of modes at this frequency, for  $l > 15$ .

It might be noticed that there are apparent crossings of the frequencies, as functions of  $l$ , between the f mode and some of the g modes. A closer examination shows that instead the modes make so-called *avoided crossings* where they approach very closely without actually crossing. This phenomenon is well-known from atomic physics; a very clear discussion of the behaviour in the vicinity of an avoided crossing was given by von Neuman & Wigner (1929). Indeed, there is a deep mathematical similarity between the equations of non-radial oscillations and the Schrödinger equation (see Christensen-Dalsgaard 1980, 1981; also, Section 3.6 below).

Figures 3.21 and 3.22 illustrate typical eigenfunctions for p modes. According to Eq. (3.139) the quantity plotted, *viz.*  $r \rho^{1/2} \xi_r$ , is related to the contribution to the energy density from the radial component of velocity. This shows that for p modes the energy, at least at low degrees, is distributed throughout most of the star. In particular, the radial modes penetrate essentially to the centre. At higher degree the modes are trapped in the outer part of the model. This is in accordance with the predictions of Section 3.4.2; the arrows for the modes with  $l = 20$  and 60 show the locations of the turning points predicted by Eq. (3.189). The sensitivity of the frequency of a mode to the properties of the star is given roughly by the energy density, in a sense to be made more precise below; thus the frequencies of low-degree p modes depend on averages of stellar structure over the entire star. In contrast to the energy, the displacement is strongly peaked towards the surface; this is obvious from Fig. 3.21 if it is recalled that the density decreases by about 9 orders of magnitude from the centre to the surface of the Sun. With increasing degree the p modes become confined closer and closer to the surface. It should also be noticed that the behaviour near the surface, at a given frequency, changes little with  $l$ , in accordance with the asymptotic Eq. (3.227). This property is important for the interpretation of the observed frequencies. It may be understood physically by noting that near the surface the vertical wavelength is much shorter than the horizontal wavelength (*i.e.*,  $k_r \gg k_h$ ); the tangential behaviour of the oscillation therefore has essentially no influence on its dynamics, which consequently is independent of  $l$ . Also, as shown by the dotted lines in Fig. 3.21a, the envelope of the eigenfunction closely tracks the asymptotically expected scaling as  $c^{-1/2}$ .

Figure 3.22 shows the eigenfunctions in the outer few per cent of the radius of a solar model, for modes of degree  $l = 1$  with different frequencies. It is evident that the mode energy decreases in the atmosphere; this can be understood from the discussion in Section 3.4.2, which shows that the modes are evanescent in the atmosphere for frequencies below the acoustic cut-off frequency  $\omega_c$ ; in the present case the atmospheric value corresponds to a cyclic frequency of about 5000  $\mu$ Hz. It should be noticed that at frequencies below about 2000  $\mu$ Hz even the photospheric amplitude is substantially smaller than the amplitudes at greater depth. This is related to the reflection of the modes near the surface at the point  $r = R_t$ , of increasing depth with decreasing frequency, where the frequency is equal to  $\omega_c$  (*cf.* Fig. 3.17). For frequencies

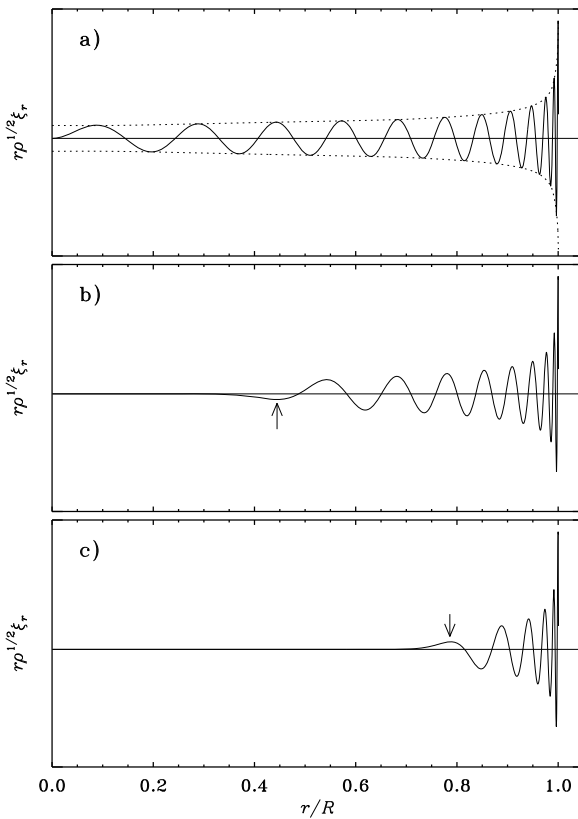


**Fig. 3.21.** Scaled radial displacement eigenfunctions, on an arbitrary scale, for selected p modes in a solar model, with a)  $l = 0$ ,  $n = 23$ ,  $\nu = 3310 \mu\text{Hz}$ ; b)  $l = 20$ ,  $n = 17$ ,  $\nu = 3375 \mu\text{Hz}$ ; c)  $l = 60$ ,  $n = 10$ ,  $\nu = 3234 \mu\text{Hz}$ . The dotted lines in panel a) show the asymptotically expected amplitude envelope, proportional to  $c^{-1/2}$  (see Eq. (3.227)). In panels b) and c) the arrows mark the asymptotic location of the turning points  $r_t$  (cf. Eq. (3.189)).

above  $2000 \mu\text{Hz}$  that figure shows that the reflection takes place essentially at the photosphere.

Figure 3.23 shows eigenfunctions for g modes. These have their largest amplitudes in the deep interior of the Sun, with maximum energy very near the centre. At a given frequency the number of radial zeros increases rapidly with  $l$ ; on the other hand there is little change in the overall distribution of the energy. That the modes extend over essentially the same region of the star is consistent with the fact, mentioned in Section 3.4.2, that for these modes

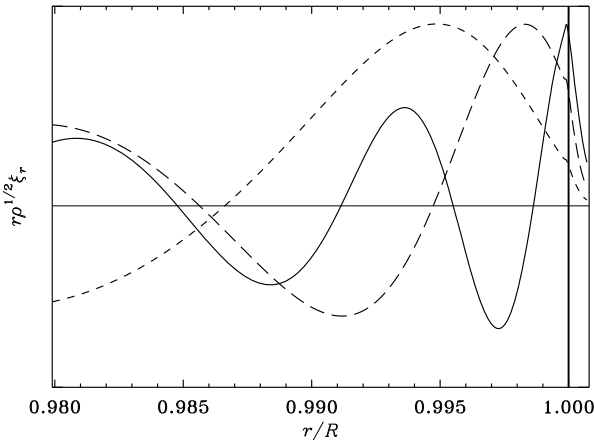


**Fig. 3.22.** Scaled radial displacement eigenfunctions of p modes with  $l = 1$ , plotted against fractional radius  $r/R$  in the outermost parts of a solar model. The cases shown are:  $\nu = 1612 \mu\text{Hz}$  (-----);  $\nu = 2293 \mu\text{Hz}$  (- - - -);  $\nu = 3650 \mu\text{Hz}$  (—).

the locations of the turning points depend on frequency but not on degree. It should be noticed in panel (d) that the surface displacement amplitudes for low degree (in this case  $l = 2$ ) remain comparable with the amplitude in much of the interior. Thus, even though the modes are formally evanescent in the convection zone, they retain a potentially observable surface response, providing of course that they are excited in a given star.

The global properties of the eigenfunctions are reflected in the inertia parameter  $E$  defined in Eq. (3.140). It is shown for p modes and low-degree g modes in Fig. 3.24, as a function of the cyclic frequency  $\nu = \omega/2\pi$ . Each curve corresponds to a given value of  $l$ , with the points for the individual modes being connected.<sup>15</sup> The p-mode results in panel (a) show an obvious marked decrease of the inertia, at fixed surface amplitude, with increasing frequency, as well as a weaker but still substantial decrease with increasing degree. The dependence on degree is a direct result of the variation of the depth of penetration: with increasing degree the lower turning point moves closer to the surface and hence the oscillation involves a smaller part of the star, thus decreasing the inertia. Similarly, the increase with decreasing fre-

<sup>15</sup> This format for displaying results on the oscillations clearly makes little physical sense, in that non-integer mode orders do not have any meaning; nevertheless, it provides a convenient illustration of the dependence of oscillation quantities on frequency and degree.

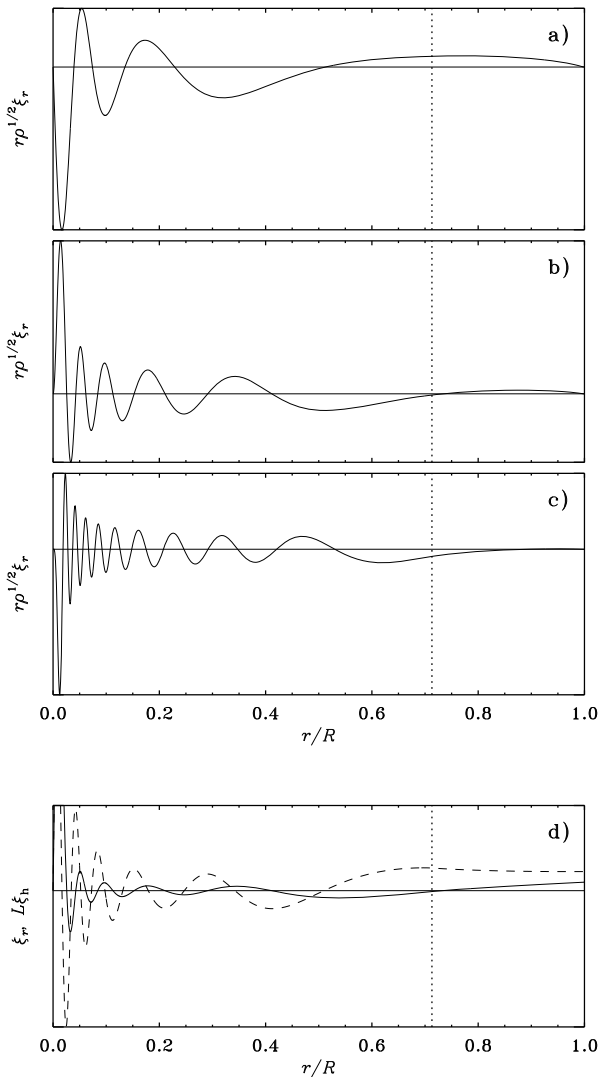


**Fig. 3.23.** Eigenfunctions, on an arbitrary scale, for selected g modes in a solar model. Panels a) to c) show scaled radial displacement eigenfunctions with a)  $l = 1, n = -5, \nu = 110 \mu\text{Hz}$ ; b)  $l = 2, n = -10, \nu = 103 \mu\text{Hz}$ ; c)  $l = 4, n = -19, \nu = 100 \mu\text{Hz}$ . In panel d) the solid and dashed curves show unscaled radial ( $\xi_r$ ) and horizontal ( $L\xi_h$ ) displacement eigenfunctions, for the  $l = 2, n = -10$  mode. For clarity, the curves have been truncated: the maximum values of  $\xi_r$  and  $L\xi_h$  are about 2.7 times higher than the largest value shown. The vertical dotted line marks the base of the convective envelope.

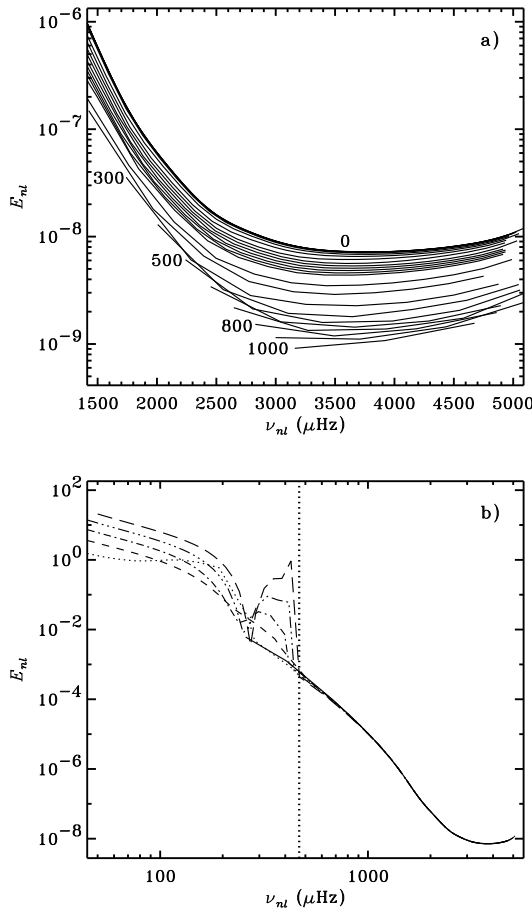


**Fig. 3.24.** The dimensionless inertia  $E$  [cf. Eq. (3.140)] for computed modes of oscillation in a solar model, plotted against frequency  $\nu$  for fixed values of the degree  $l$ . The inertia has been normalized by the norm of the total displacement at the photospheric level. (a) Results for p modes; selected values of  $l$  have been indicated. (b) Results for low-degree g and p modes, using the following line styles:  $l = 0$  (solid),  $l = 1$  (dotted),  $l = 2$  (short-dashed),  $l = 3$  (dot-dashed),  $l = 4$  (triple-dot-dashed), and  $l = 5$  (long-dashed). The heavy vertical dotted line marks the maximum in the buoyancy frequency (cf. Fig. 3.14).

quency can be understood from the reflection properties near the surface and is consistent with the eigenfunctions shown in Fig. 3.22: since the inertia measure in Eq. (3.140) is normalized with the surface displacement, the decrease

in the value of the eigenfunction at the surface, relative to the interior, leads to an increase in  $E$  at low frequency.

Panel (b) shows that at the lowest degrees there is essentially a continuous transition between the p and the g modes, the inertia continuing to rise rapidly with decreasing frequency. At slightly higher degree ( $l = 3 - 5$ ) there is a beginning tendency towards stronger g-mode trapping as the frequency approaches the maximum in  $N$  in the deep interior of the model and the evanescent region with  $\omega < S_l$  extends closer to the surface as  $l$  increases. Note also the strong local decrease in  $E$  near  $200 \mu\text{Hz}$ ; this occurs where the modes predominantly take on the character of an f mode, corresponding to the extension towards low degree of the f-mode ridge, visible in Fig. 3.20.

### 3.5.2 The Classification of Modes

The precise assignment of the radial order  $n$  is a useful tool to ensure that all modes of a given model, in a certain frequency range, have been computed, and to follow the evolution of the frequency spectrum as the star evolves. However, the definition of  $n$  presents some interesting problems. It appears that at each  $l$  it is possible to assign to each mode an integral order  $n$ , which ranges from minus to plus infinity, such that, at least for reasonably simple stellar models<sup>16</sup>  $|n|$  gives the number of zeros in  $\xi_r$ ; the possible zero at  $r = 0$  is only counted in the radial case, where  $l = 0$ . As hinted above, this is arranged such that in simple models  $n > 0$  for p modes,  $n = 0$  for the f modes and  $n < 0$  for g modes. Also, with the single exception of the dipolar f mode discussed below, the frequency is an increasing function of  $n$ ; this rule is evidently consistent with the fact, mentioned above, that the frequency increases with the number of radial nodes for p modes and decreases with the number of radial nodes for g modes. It is conventional to denote p, f and g modes of a given degree  $l_0$  as  $p_n(l = l_0)$ ,  $f(l = l_0)$  and  $g_{|n|}(l = l_0)$ . In Fig. 3.20 such radial orders have been indicated for the modes.

Eckart (1960) proposed a general, and mathematically precise, scheme for the classification of waves in a stratified medium. It was applied by Scuflaire (1974) and Osaki (1975) to the definition of the radial order  $n$  for a nonradially pulsating star, on the basis of the *phase curve*, traced by  $(\xi_r(r), p'(r))$  in the so-called phase diagram as  $r$  varies from 0 to  $R$ . Specifically, the order is determined by counting the zeros of  $\xi_r$ , assigning a positive value for zeros where the  $p'$  axis is crossed in the counter-clockwise direction in the phase diagram, and negative values when the crossing is in the clockwise direction; the former case applies where the mode behaves as a p mode and the latter to g-mode behaviour. It may be shown (e.g., Christensen-Dalsgaard 1980) that in the Cowling approximation this definition has the desirable property of

---

<sup>16</sup> The definition of a “simple” model in this context is not straightforward; examples might be zero-age main-sequence models or, e.g., polytropes of index between 1.5 and 3.

being invariant under a continuous modification of the equilibrium model or a continuous change of  $l$ . This follows from the fact that such changes correspond to a continuous change to the phase curve which furthermore cannot cross  $(0, 0)$ . As a result new zeros of  $\xi_r$  appear in pairs with no net effect on the mode order. Also, for simple models or in the limit of high-order modes this definition reduces to the simple counting of radial nodes in the eigenfunction, described above.

The power of this scheme becomes apparent in stellar models where modes may be trapped in more than one region at a given frequency. A typical example is illustrated by the characteristic frequencies illustrated for the evolved models in Fig. 3.15 (see also Osaki 1975). Here we expect mixed modes with an oscillatory behaviour in both the outer parts, where the mode physically behaves like a p mode, and in the inner part of the model, beneath the peak in the buoyancy frequency, where the mode behaves like a g mode. In the former case the nodes in  $\xi_r$  give a positive contribution to the mode order, whereas in the latter case the contribution is negative. At the same time this illustrates a weakness of the scheme: a given mode in a given stellar model may be classified as a p mode, with  $n > 0$ , yet have its largest amplitude in the inner trapping region and hence physically behave like a g mode. Examples of this behaviour are found in Fig. 3.25 below.

The Eckart scheme in this form is not generally applicable when solutions of the full equations are considered. Here the scheme fails for dipolar modes, with  $l = 1$ , in centrally condensed models; typically, the problem sets in first in acoustic modes of the lowest order and gradually spreads to higher orders with increasing central condensation. This has been observed in the case of  $1 M_\odot$  models at and beyond solar age (Christensen-Dalsgaard 1978; Guenther 1991), in evolved models of  $\delta$  Sct stars (Lee 1985), and in polytropic models of index exceeding 3.3 (Christensen-Dalsgaard & Mullan 1994). It is interesting that these difficulties appear to be restricted to  $l = 1$ , at least for realistic stellar models.

In a major breakthrough in the theory of stellar oscillations, Takata (2005, 2006a,b) has defined a classification scheme that is generally applicable to dipolar modes in the case where the Cowling approximation is not made, in the process obtaining further insight into the properties of these modes.<sup>17</sup> He demonstrated that the eigenfunctions of dipolar modes satisfy the identity

$$p' + \frac{g}{4\pi G} \left( \frac{d\Phi'}{dr} + \frac{2}{r}\Phi' \right) = \omega^2 r \left[ \rho\xi_r - \frac{1}{4\pi G} \left( \frac{d\Phi'}{dr} - \frac{\Phi'}{r} \right) \right]. \quad (3.242)$$

On this basis he was able to demonstrate that the dipolar modes are solutions to a second-order differential equation, and finally as a result showed that phase curves in terms of  $(\mathcal{Y}_1, \mathcal{Y}_2)$ , where

---

<sup>17</sup> Interestingly, Takata (2008) demonstrated that the analysis could be generalized to dipolar oscillations of stars treated in general relativity.

$$\mathcal{Y}_1 = \frac{1}{g} \left[ \frac{\delta\Phi}{r} - \delta \left( \frac{d\Phi}{dr} \right) \right], \quad \mathcal{Y}_2 = \frac{\delta p}{p}, \quad (3.243)$$

have the properties required for mode classification. It is important to emphasize that this scheme is valid only for  $l = 1$ . No corresponding identity or reduction to a second-order system has been found for other degrees.

There are a few special cases of the mode classification. For  $l = 0$  only modes with  $n > 0$  are found; this is in accordance with the fact, mentioned above, that buoyancy can only act in the presence of horizontal variation. Also, for  $l = 1$  the mode with  $n = 0$  is peculiar in that its frequency is zero; indeed a mode with  $l = 1$  and no zero in the radial direction may seem somewhat unphysical, as it displaces the centre of mass of the star. However, the mode corresponds to an infinitely slow, uniform motion of the entire star, without deformation; as noted by Lebovitz (1965) this must be a solution to the original equations which, if written as an oscillation, has zero frequency (see also Christensen-Dalsgaard 1976).

It is interesting that this f mode with  $l = 1$  behaves very differently in the Cowling approximation and for the full set of equations. In the Cowling approximation there is a mode with  $l = 1$  having no nodes in the radial displacement, intermediate in frequency between the p and the g modes, which must be identified with the f mode. From a physical point of view it can be thought of roughly as an oscillation of the whole star in the gravitational potential defined by the equilibrium model. The connection between this mode and the zero-frequency mode for the full problem can be investigated by making a continuous transition from the Cowling approximation to the full set of equations; this can be accomplished formally by introducing a factor  $\lambda$  on the right-hand side of Eq. (3.113), such that  $\lambda = 0$  corresponds to the Cowling approximation and  $\lambda = 1$  to the full equations (Christensen-Dalsgaard 1978; Christensen-Dalsgaard & Gough 2001). When  $\lambda$  is increased from 0 to 1, the transition from the  $l = 1$  f mode in the Cowling approximation to the zero-frequency “mode” in the full case takes place through a sequence of avoided crossings with the g modes, where the frequencies approach very closely without actually crossing. A similar transition occurs for solutions of the full equations, between the f mode with  $l = 2$  and the zero-frequency mode with  $l = 1$ , as  $l$  is decreased continuously from 2 to 1 (Aizenman *et al.* 1977; Christensen-Dalsgaard 1978; Christensen-Dalsgaard & Gough 2001).

### 3.5.3 Results for the Models with Convective Cores

To illustrate the effect of a convective core, particularly the maximum in the buoyancy frequency at the edge of the core, Fig. 3.25 shows the behaviour of the oscillation frequencies, as functions of stellar age, for a  $2.2 M_{\odot}$  evolution sequence. These models may represent  $\delta$  Sct stars; characteristic frequencies at a few ages in the sequence were illustrated in Fig. 3.15. As in that figure we have applied the scaling according to  $t_{\text{dyn}}^{-1}$ . As a result, the frequencies of

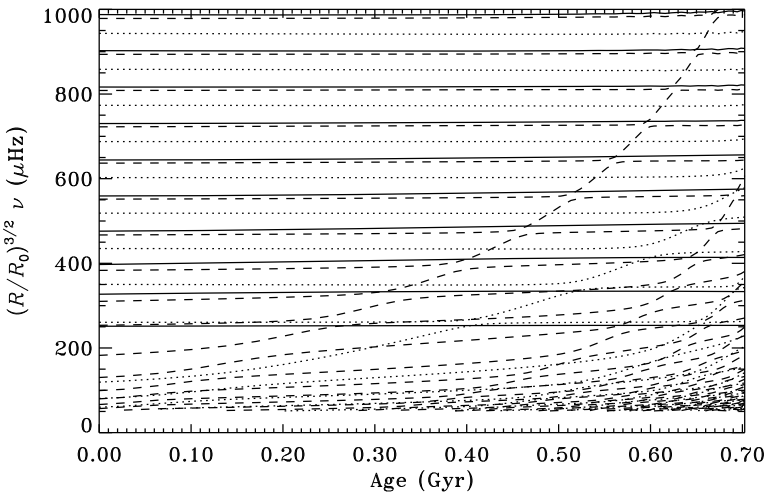


**Fig. 3.25.** Scaled oscillation frequencies, as functions of age, in a  $2.2 M_{\odot}$  evolution sequence; here  $R$  is the radius of the model and  $R_0$  is the ZAMS radius. Modes of the same radial order have been connected. The solid lines are for radial modes, of degree  $l = 0$ , the dotted lines are for  $l = 1$  and the dashed lines for  $l = 2$ .

largely acoustic modes, including the radial modes, change very little with age. It should be noticed also that, except at low order, the acoustic modes exhibit a distinct pattern, with a close pairing of the radial and  $l = 2$  modes. Such a pattern of closely-spaced peaks is familiar in solar data (see Fig. 1.9). This was predicted by the asymptotic results presented in Section 3.4.3 (see Eq. (3.219)); however, it is striking that it can be followed to quite low mode orders.

The most striking feature of the computed frequencies, however, is the interaction for  $l = 1$  and 2 between the p modes and the g modes. At zero age, there is a clear distinction between the p modes, with frequencies exceeding that of the lowest radial mode, and the g modes with frequencies below  $200 \mu\text{Hz}$ . However, with increasing age the scaled g-mode frequencies increase; this is a consequence of the increase in the scaled buoyancy frequency with age (*cf.* Fig. 3.15c) which effectively acts to “pull up” the frequencies of the g modes. As was first found by Osaki (1975), this leads to an interaction between the p and g modes which takes place through a sequence of avoided crossings. At the avoided crossing the two modes exchange nature, while still maintaining the original labelling, as defined in Section 3.5.2. Thus, for example, the  $n = 1$  mode for  $l = 2$ , which at age zero is a purely acoustic mode

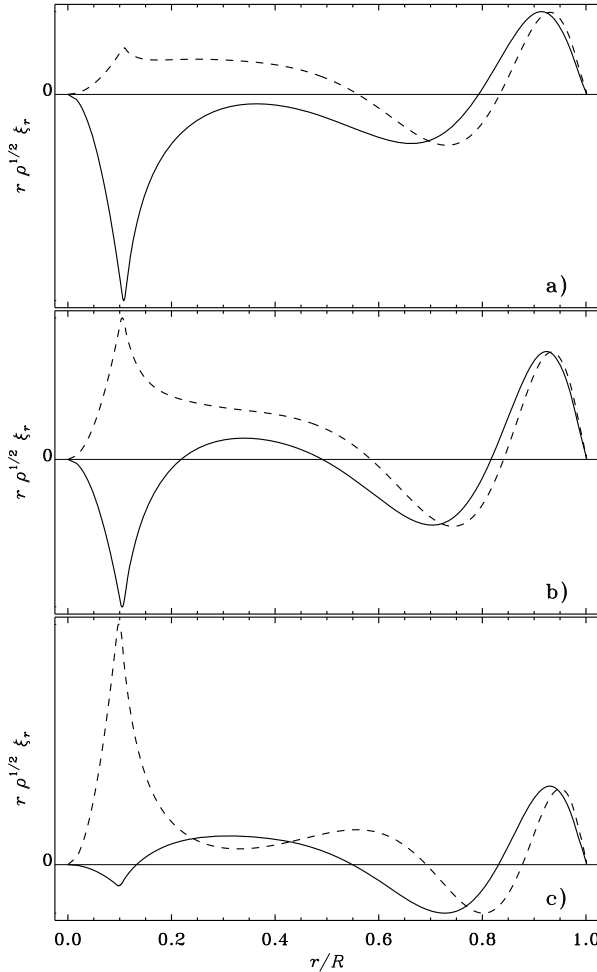


**Fig. 3.26.** Scaled eigenfunctions for the  $p_1(l = 2)$  mode (continuous line) and the  $p_2(l = 2)$  mode (dashed line) in the vicinity of the avoided crossing near age 0.4 Gyr,  $(R/R_0)^{3/2}\nu = 400 \mu\text{Hz}$  in Fig. 3.25. (a) Age 0.36 Gyr. (b) Age 0.39 Gyr. (c) Age 0.44 Gyr.

of frequency  $310 \mu\text{Hz}$  takes on the nature of a g mode trapped just outside the convective core at the age 0.32 Gyr and again at the age 0.4 Gyr changes back to being predominantly an acoustic mode. As discussed in Chapter 7 such *mixed modes*, with both p-mode and g-mode character, have a very substantial asteroseismic diagnostic potential.

This behaviour is further emphasized by considering the eigenfunctions of these modes; examples of eigenfunctions near the  $p_1 - p_2(l = 2)$  avoided crossing at age 0.4 Gyr are shown in Fig. 3.26. Before the avoided crossing, the  $p_1$  mode has a substantial amplitude near the edge of the convective core, and hence to a large extent behaves like a g mode, whereas the  $p_2$  mode is predominantly a p mode, with largest amplitude in the outer parts. At the point of closest approach of the frequencies, at an age of 0.39 Gyr, both modes have a mixed character, with substantial amplitudes in the deep interior and near the surface, whereas after the avoided crossing the  $p_2$  mode looks like a g mode, whereas the  $p_1$  mode largely behaves like a p mode. It should be noted that this behaviour illustrates the potential difference between the mathematical classification of the modes and their physical nature, already mentioned in Section 3.5.2: modes with order  $n > 0$ , which in simple models would be p modes, may take on the character of g modes.

The component of the eigenfunctions in Fig. 3.26 behaving like a g mode is trapped in the vicinity of the peak in the buoyancy frequency which corresponds to the steep gradient in composition and hence density. In fact, it may be shown that this mode approximates the interface gravity wave described by Eq. (3.87). This mode was denoted the  $g_c$  mode by Dziembowski & Pamyatnykh (1991) who pointed out that, if observed, it might provide a powerful diagnostics of the properties of the convective core, including the possible presence of overshoot.

In general, it is evident that the presence of the g-like modes in the p-mode spectrum, particularly at late evolutionary stages, may provide very useful information about the deep interior of the stars. Examples are the identification of such modes in several observations of  $\beta$  Cep stars, as already discussed in Sect. 2.3.7. We come back to this for the star  $\nu$  Eri in Chapter 7 (see Section 7.3.2.4). On the other hand it complicates the analysis of the observed frequencies. Dziembowski & Królikowska (1990) pointed out that mode selection might be affected by the larger energy of the modes that behave like g modes, thereby restricting the choice of modes in the identification. However, such arguments depend on the mechanisms responsible for exciting the modes and limiting their amplitudes, which are so far incompletely understood.

## 3.6 Variational Properties of Stellar Adiabatic Oscillations

A great deal of insight into the properties of adiabatic oscillations can be obtained by regarding the equations as an eigenvalue problem in a Hilbert space (Eisenfeld 1969; Dyson & Schutz 1979; Christensen-Dalsgaard 1981). Here we consider two different, but very closely related, formulations: one based on the unseparated oscillation equations, valid for general perturbations and a second obtained after separation of the oscillation equations in terms of spherical harmonics.

### 3.6.1 The Oscillation Equations as Linear Eigenvalue Problems in a Hilbert Space

To obtain the general form, we go back to the perturbed equations of motion, Eq. (3.43). After separation of the time dependence as  $\exp(-i\omega t)$  this can be written as

$$\omega^2 \delta r = \mathcal{F}(\delta r) , \quad (3.244)$$

where

$$\mathcal{F}(\delta r) = \frac{1}{\rho_0} \nabla p' - g' - \frac{\rho'}{\rho_0} g_0 . \quad (3.245)$$

Here the perturbation quantities denote the amplitudes, after the separation of the time dependence. As indicated,  $\mathcal{F}$  is a linear functional of  $\delta r$ . To see this, note that from the continuity equation (3.41)  $\rho'$  is a linear functional of  $\delta r$ ; so, therefore, is the gravitational potential perturbation  $\Phi'$  as given by Eq. (3.45). In the adiabatic case  $p'$  is obtained from  $\rho'$  and  $\delta r$  as in Eq. (3.50); this defines the adiabatic operator  $\mathcal{F}_a$ . The nonadiabatic case is more complicated, but here also it is possible to obtain  $p'$  as a linear functional of  $\delta r$  (see Christensen-Dalsgaard 1981).

To cast the problems in terms of functional analysis, we introduce a space  $\mathcal{H}$  of vector functions of position in the star, with suitable regularity properties, and define an inner product on  $\mathcal{H}$  by

$$\langle \xi, \eta \rangle = \int_V \rho_0 \xi^* \cdot \eta \, dV , \quad (3.246)$$

for  $\xi, \eta$  in  $\mathcal{H}$ ; here “ $*$ ” denotes the complex conjugate. We also introduce the domain  $\mathcal{D}(\mathcal{F})$  of the operator  $\mathcal{F}$  as those vectors in  $\mathcal{H}$  such that the boundary condition (3.160) is satisfied. The central result of this section is now that, as shown by Lynden-Bell & Ostriker (1967), the operator  $\mathcal{F}_a$  corresponding to Eq. (3.245) for adiabatic oscillations is symmetric, in the sense that

$$\langle \xi, \mathcal{F}_a(\eta) \rangle = \langle \mathcal{F}_a(\xi), \eta \rangle , \quad \text{for } \xi, \eta \in \mathcal{D}(\mathcal{F}) . \quad (3.247)$$

The formulation in terms of the spatially separated variables proceeds in a very similar manner. The separated oscillation Eqs (3.112) and (3.111) may be written

$$\frac{1}{\rho} \frac{dp'}{dr} + \frac{\rho'}{\rho} g + \frac{d\Phi'}{dr} = \omega^2 \xi_r , \quad (3.248)$$

$$\frac{1}{r} \left( \frac{p'}{\rho} + \Phi' \right) = \omega^2 \xi_h . \quad (3.249)$$

As before, the quantities on the left-hand side can be obtained in terms of  $\xi_r$  and  $\xi_h$ ; in particular,  $\Phi'$  is found from  $\rho'$  from the separated integral solution to the Poisson equation given in Eq. (3.173). We introduce the subspace  $\mathcal{H}_l$  of

the space of pairs of quadratically integrable functions on the interval  $[0, R]$ , with vectors

$$\xi \equiv (\xi_r, \xi_h) \in \mathcal{H}_l . \quad (3.250)$$

Then Eqs (3.248) and (3.249) can be written as

$$\mathcal{F}_l(\xi) = \omega^2 \xi , \quad (3.251)$$

defining the operator  $\mathcal{F}_l$  corresponding to the separated oscillation equations. Assuming again the adiabatic relation for  $p'$  one obtains the linear operator  $\mathcal{F}_{a,l}$  for adiabatic oscillations in  $\mathcal{H}_l$ . The boundary conditions on  $\xi_r$  and  $\xi_h$  can be imposed by restricting the part of  $\mathcal{H}_l$  where  $\mathcal{F}_{a,l}$  is defined. Thus we define the domain of  $\mathcal{F}_{a,l}$  by

$$\mathcal{D}(\mathcal{F}_{a,l}) = \{(\xi_r, \xi_h) | \xi_r - l\xi_h \rightarrow 0 \text{ for } r \rightarrow 0 \wedge \delta p(R) = 0\} ; \quad (3.252)$$

the boundary conditions on  $\Phi'$  are satisfied automatically by the integral expression (3.173). The inner product on  $\mathcal{H}_l$  is defined by

$$\langle \xi, \eta \rangle_l \equiv 4\pi \int_0^R [\xi_r^*(r)\eta_r(r) + l(l+1)\xi_h^*(r)\eta_h(r)]r^2 \rho dr , \quad (3.253)$$

for two vectors  $\xi = (\xi_r, \xi_h)$  and  $\eta = (\eta_r, \eta_h)$  in  $\mathcal{H}_l$ ; in particular,  $\|\xi\|^2 = \langle \xi, \xi \rangle = \mathcal{E}$ , where  $\mathcal{E}$  is the mode inertia defined in Eq. (3.139). Again one may show, using the explicit expression, that the operator  $\mathcal{F}_{a,l}$  is symmetric, *i.e.*,

$$\langle \mathcal{F}_{a,l}(\xi), \eta \rangle_l = \langle \xi, \mathcal{F}_{a,l}(\eta) \rangle_l \quad \text{for all } \xi, \eta \in \mathcal{D}(\mathcal{F}_{a,l}) . \quad (3.254)$$

From Eqs (3.247) and (3.254) follow immediately a number of useful properties of  $\mathcal{F}_a$  and  $\mathcal{F}_{a,l}$ . For simplicity we generally present them in terms of  $\mathcal{F}_a$ ; precisely analogous relations are obviously valid for  $\mathcal{F}_{a,l}$ . The simplest result is that the squared eigenfrequencies are real. This may be demonstrated by introducing the functional  $\Sigma$  on  $\mathcal{D}(\mathcal{F})$  by

$$\Sigma(\xi) = \frac{\langle \xi, \mathcal{F}_a(\xi) \rangle}{\langle \xi, \xi \rangle} ; \quad (3.255)$$

it follows from Eq. (3.247) that  $\Sigma(\xi)$  is real. If  $\omega_0^2$  is an eigenvalue of the problem with eigenvector  $\xi_0$ , *i.e.*,

$$\mathcal{F}_a(\xi_0) = \omega_0^2 \xi_0 , \quad (3.256)$$

then

$$\Sigma(\xi_0) = \omega_0^2 , \quad (3.257)$$

and hence  $\omega_0^2$  is real. Since the coefficients in Eqs (3.152), (3.154) and (3.156) are then real, it follows that we may also choose the eigenfunctions to be real at all  $r$ .

As is well known, a second property of a symmetric operator is that eigenvectors corresponding to different eigenvalues are orthogonal. Thus if

$$\mathcal{F}_a(\xi_1) = \omega_1^2 \xi_1; \quad \mathcal{F}_a(\xi_2) = \omega_2^2 \xi_2; \quad \omega_1^2 \neq \omega_2^2, \quad (3.258)$$

then

$$\langle \xi_1, \xi_2 \rangle = 0. \quad (3.259)$$

A very important result concerns the effect of a small perturbation to the oscillation equations. This perturbation could result from a small change to the equilibrium model, from the inclusion of nonadiabatic effects (Christensen-Dalsgaard 1981) or, as discussed in Section 3.8, from the inclusion of the effect of large-scale velocity fields in the model. We characterize the perturbation by a change  $\delta\mathcal{F}$  in the operator defining the oscillation equations. If  $\delta\mathbf{r}_0$  and  $\omega_0$  are solutions to the adiabatic oscillation equations,

$$\omega_0^2 \delta\mathbf{r}_0 = \mathcal{F}_a(\delta\mathbf{r}_0), \quad (3.260)$$

the change in  $\omega^2$  caused by the perturbation  $\delta\mathcal{F}$  can be obtained from first-order perturbation analysis (*e.g.*, Schiff 1949) as

$$\delta\omega^2 \simeq \frac{\langle \delta\mathbf{r}_0, \delta\mathcal{F}(\delta\mathbf{r}_0) \rangle}{\langle \delta\mathbf{r}_0, \delta\mathbf{r}_0 \rangle}. \quad (3.261)$$

Thus the frequency change can be computed from the unperturbed eigenvector. Similarly, if  $\delta\mathcal{F}_l$  is a perturbation to the operator  $\mathcal{F}_l$  defining the separated oscillation equations, and  $\omega_0^2$ ,  $\xi_0$  is a solution to the unperturbed problem,

$$\mathcal{F}_{a,l}(\xi_0) = \omega_0^2 \xi_0, \quad (3.262)$$

then the frequency change can be obtained from

$$\delta\omega^2 \simeq \frac{\langle \xi_0, \delta\mathcal{F}_l(\xi_0) \rangle_l}{\langle \xi_0, \xi_0 \rangle_l}. \quad (3.263)$$

Some further consequences of this relation are discussed in Section 3.6.2.

From the symmetry of the operator of adiabatic oscillations it follows that  $\omega^2$  satisfies a variational principle (*cf.* Chandrasekhar 1964). Indeed, it is easy to show from Eq. (3.247) that if  $\delta\xi \in \mathcal{H}$  is a small change to the eigenvector, then

$$\Sigma(\xi_0 + \delta\xi) = \omega_0^2 + \mathcal{O}(\|\delta\xi\|^2), \quad (3.264)$$

where  $\|\cdots\|$  is the norm corresponding to  $\langle \cdots, \cdots \rangle$ . Thus  $\Sigma$  is stationary at the eigenfrequencies. From a physical point of view this reflects Hamilton's principle for the system consisting of the pulsating star. It is conservative, because of the assumption of adiabaticity, and isolated because of the boundary condition (3.160). As noted by Christensen-Dalsgaard (1982b) this property can be used to improve the precision of computed eigenfrequencies: if computed eigenfunctions  $\xi$ , with numerical errors of order  $\epsilon$ , are used to evaluate  $\omega^2$  as  $\Sigma(\xi)$ , the resulting value should have an error of order  $\epsilon^2$ .

### 3.6.2 Effects on Frequencies of a Change in the Model

As an example of the use of Eq. (3.263), we discuss in more detail the interpretation of changes in the frequencies caused by changes in the equilibrium model. Consider a mode  $(n, l)$ , with eigenvector  $\xi_{nl} = (\xi_{r,nl}, \xi_{h,nl}) \in \mathcal{H}_l$ ; without loss of generality we may assume that  $\xi_{r,nl}(r)$  and  $\xi_{h,nl}(r)$  are real. The relative frequency change caused by the perturbation  $\delta\mathcal{F}_l$  is then, according to Eq. (3.263),

$$\frac{\delta\omega_{nl}}{\omega_{nl}} = \frac{1}{2} \frac{\delta\omega_{nl}^2}{\omega_{nl}^2} = \frac{\langle \xi_{nl}, \delta\mathcal{F}_l(\xi_{nl}) \rangle_l}{2\omega_{nl}^2 \langle \xi_{nl}, \xi_{nl} \rangle_l}. \quad (3.265)$$

Here the denominator is proportional  $\omega_{nl}^2 E_{nl}$ , where  $E_{nl}$  was defined in Eq. (3.140). Also, we represent  $\delta\mathcal{F}_l$  in component form as

$$\delta\mathcal{F}_l(\xi_{nl}) = (\phi_r[\xi_{nl}], \phi_h[\xi_{nl}]), \quad (3.266)$$

where  $\phi_r[\xi_{nl}](r)$  and  $\phi_h[\xi_{nl}](r)$  are functions of  $r$ . Then we can write Eq. (3.265) as

$$E_{nl} \frac{\delta\omega_{nl}}{\omega_{nl}} = I_{nl}, \quad (3.267)$$

where

$$I_{nl} = \frac{2\pi \int_0^R [\xi_{r,nl}(r)\phi_r[\xi_{nl}](r) + l(l+1)\xi_{h,nl}(r)\phi_h[\xi_{nl}](r)] \rho r^2 dr}{M\omega_{nl}^2 [\xi_r^2(R) + l(l+1)\xi_h^2(R)]}. \quad (3.268)$$

Thus  $I_{nl}$  gives the integrated effect of the perturbation, normalized to the total surface displacement.

Equations (3.267) and (3.268) provide a linear relation between the change in the model and the change in the frequency. These expressions are somewhat formal. However, it follows from the discussion in Section 3.3.3 that the changes in the coefficients of the oscillation equations, and hence the changes  $\phi_r[\xi_{nl}](r)$  and  $\phi_h[\xi_{nl}](r)$  in the components of  $\delta\mathcal{F}_l$ , can be expressed in terms of changes in two suitably chosen model variables, for example density and sound speed. For simplicity, we assume that the change in the model occurs without a change in its radius (this would in general be the case for models of the Sun, where the radius is known with high accuracy)<sup>18</sup> and let  $\delta_r\rho$  and  $\delta_rc^2$  denote the changes, between the equilibrium models, in  $\rho$  and  $c^2$  at fixed  $r$ .<sup>19</sup> Then, after some manipulation, Eq. (3.267) can be written as

$$\frac{\delta\omega_{nl}}{\omega_{nl}} = \int_0^R \left[ K_{c^2,\rho}^{nl}(r) \frac{\delta_r c^2}{c^2}(r) + K_{\rho,c^2}^{nl}(r) \frac{\delta_r \rho}{\rho}(r) \right] dr \quad (3.269)$$

<sup>18</sup> For stars the mass and radius cannot be assumed to be accurately known; however, here a similar expression can be obtained for the correction to the dimensionless frequency  $\sigma$  in terms of corrections to the dimensionless density and sound speed introduced in Eqs (3.167) and (3.170).

<sup>19</sup> These *model changes* should not be confused with the Lagrangian perturbations associated with the oscillations, introduced in Section 3.1.3.

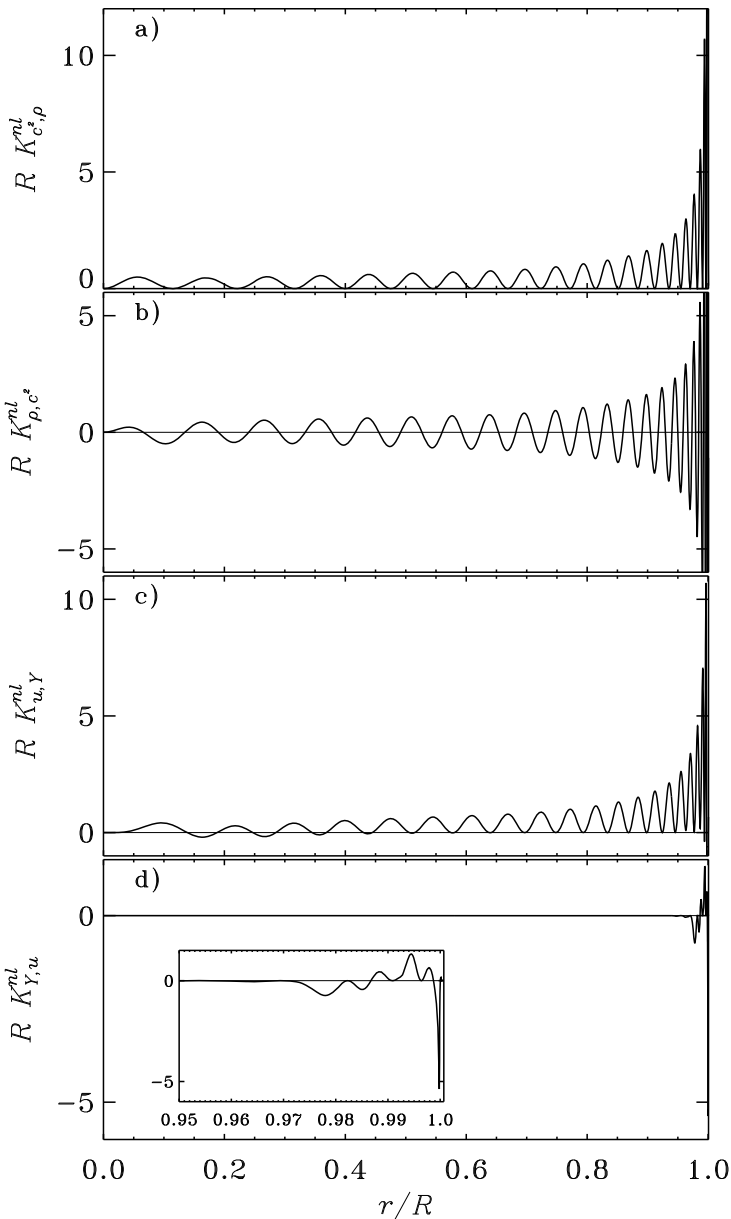


**Fig. 3.27.** Kernels for an  $l = 0$ ,  $n = 21$  mode (with frequency  $\nu = 3.04$  mHz) of a model of the present Sun. Panels (a) and (b) show  $RK_{c^*,\rho}^{nl}$  and  $RK_{\rho,c^2}^{nl}$  (the kernels are multiplied by  $R$  to correspond to integration with respect to  $r/R$ ).  $K_{c^2,\rho}^{nl}$  is positive everywhere, while the kernel  $K_{\rho,c^2}^{nl}$  takes on both positive and negative values. Panels (c) and (d) similarly show the kernels  $RK_{u,Y}^{nl}$  and  $RK_{Y,u}^{nl}$  for the same mode, where  $u = p/\rho$ ; the inset in panel (d) shows the detailed behaviour of  $RK_{Y,u}^{nl}$  in the hydrogen and helium ionization zones.

(e.g., Gough & Thompson 1991), where the kernels  $K_{c^2,\rho}^{nl}$  and  $K_{\rho,c^2}^{nl}$  are computed from the eigenfunctions. As illustrated by Eq. (3.269) kernels are weight functions, indicating the sensitivity of the frequency of a given mode to specific aspects of the stellar interior, in this case changes to the squared sound speed and density. Examples of such kernels are shown in Fig. 3.27.

As discussed in Section 3.3.3, other pairs of “mechanical” variables may be used instead of  $(c^2, \rho)$ ; the transformation between these pairs can be accomplished by means of the equation of hydrostatic support and mass, expressed in terms of the model changes, and suitable integrations by parts. If it is also assumed that the equation of state is known, further transformation is possible. An important example is provided by the relation  $c^2 = \Gamma_1 p / \rho$ , where  $\Gamma_1$  can be obtained as a function  $\Gamma_1(p, \rho, Y, Z)$  of pressure, density and chemical composition as specified by the abundances  $Y$  and  $Z$  by mass of helium and heavy elements. This yields<sup>20</sup>

$$\frac{\delta_r c^2}{c^2} = \left[ \left( \frac{\partial \ln \Gamma_1}{\partial \ln p} \right)_{\rho, Y, Z} + 1 \right] \frac{\delta_r p}{p} + \left[ \left( \frac{\partial \ln \Gamma_1}{\partial \ln \rho} \right)_{p, Y, Z} - 1 \right] \frac{\delta_r \rho}{\rho} \\ + \left( \frac{\partial \ln \Gamma_1}{\partial Y} \right)_{p, \rho, Z} \delta_r Y + \left( \frac{\partial \ln \Gamma_1}{\partial Z} \right)_{p, \rho, Y} \delta_r Z . \quad (3.270)$$

For analysis of acoustic modes it is convenient to work in terms of the squared isothermal sound speed  $u = p/\rho$ . By substituting Eq. (3.270) into Eq. (3.269), and expressing  $\delta_r p/p$  and  $\delta_r \rho/\rho$  in terms of  $\delta_r u/u$  by means of the perturbed equations of stellar structure,  $\delta\omega_{nl}/\omega_{nl}$  can be expressed in terms of  $\delta_r u/u$ ,  $\delta_r Y$  and  $\delta_r Z$ . Since the surface heavy-element abundance may be obtained from spectroscopic observations it is reasonable to assume  $Z$  to be known; neglecting therefore the term in  $\delta_r Z$ , we finally obtain

$$\frac{\delta\omega_{nl}}{\omega_{nl}} = \int_0^R \left[ K_{u,Y}^{nl}(r) \frac{\delta_r u}{u}(r) + K_{Y,u}^{nl}(r) \delta_r Y(r) \right] dr . \quad (3.271)$$

Examples of these kernels are shown in Fig. 3.27, panels (c) and (d). In particular, it should be noticed that  $K_{Y,u}^{nl}$  is significantly different from zero only in the hydrogen and helium ionization zones. As discussed in Section 7.1.6.1 this substantially facilitates the determination of  $\delta_r u/u$  through inverse analysis.

## 3.7 Driving Mechanisms

So far we have almost exclusively considered adiabatic oscillations, and therefore have been unable to investigate the stability or instability of the modes.

<sup>20</sup> As noted by Basu & Christensen-Dalsgaard (1997) one may in addition include a contribution from the intrinsic difference  $(\delta\Gamma_1)_{\text{int}}$  between the model and the true  $\Gamma_1$ , at fixed thermodynamical conditions and composition.

Such questions are of obvious interest, however. Here we consider some simple aspects of mode excitation, including properties of the nonadiabatic problem. A major goal is to get a feel for the conditions under which a mode may be *self-excited*, *i.e.*, with a positive growth rate; in this case the star functions as a heat engine, converting thermal energy directly into mechanical energy, and we refer to this driving mechanism as *the heat-engine mechanism*.<sup>21</sup> In cases where all modes are damped, they may still be driven to observable amplitudes by *stochastic forcing* from near-surface convection; this is, for example, the case for solar oscillations.

### 3.7.1 The Work Integral

The stability properties of stellar oscillations can obviously be investigated by solving the full set of nonadiabatic oscillation equations. However, to understand the conditions under which modes may become unstable it is useful to consider an integral expression for the growth rate. This is closely related to the perturbation expression in Eq. (3.261) which was derived from the oscillation equations written as a linear eigenvalue problem in Eq. (3.244). Now, however, we need to consider the departure from adiabatic oscillations of the pressure perturbation in the momentum equation. From the perturbed energy equation, Eqs (3.47) and (3.48), it follows that

$$\begin{aligned} \frac{p'}{p} &= \Gamma_1 \frac{\rho'}{\rho} + \xi_r \left( \frac{d \ln p}{dr} - \Gamma_1 \frac{d \ln \rho}{dr} \right) + \frac{i}{\omega} \frac{\Gamma_3 - 1}{p} (\rho \epsilon - \operatorname{div} \mathbf{F})' \\ &= \frac{p'_{\text{ad}}}{p} + \frac{i}{\omega} \frac{\Gamma_3 - 1}{p} (\rho \epsilon - \operatorname{div} \mathbf{F})', \end{aligned} \quad (3.272)$$

where we dropped the subscript “0” on equilibrium quantities, and assumed a time dependence as  $\exp(-i\omega t)$ . Here

$$p'_{\text{ad}} = p \Gamma_1 \frac{\rho'}{\rho} + \xi_r p \left( \frac{d \ln p}{dr} - \Gamma_1 \frac{d \ln \rho}{dr} \right) \quad (3.273)$$

is the pressure perturbation corresponding to adiabatic oscillations. It follows that the perturbed momentum equation (3.43) can be written, after separation of the time dependence, as

$$-\rho \omega^2 \delta \mathbf{r} = -\nabla p'_{\text{ad}} + \rho \mathbf{g}' + \rho' \mathbf{g} - \frac{i}{\omega} \nabla [(\Gamma_3 - 1)(\rho \epsilon - \operatorname{div} \mathbf{F})']. \quad (3.274)$$

This is of the form considered in Eq. (3.244):

$$\omega^2 \delta \mathbf{r} = \mathcal{F}_{\text{ad}}(\delta \mathbf{r}) + \delta \mathcal{F}, \quad (3.275)$$

with

---

<sup>21</sup> Since very often it is caused by the properties of the opacity it is most commonly known as the  $\kappa$  mechanism.

$$\mathcal{F}_{\text{ad}}(\boldsymbol{\delta r}) = \frac{1}{\rho} \nabla p'_{\text{ad}} - \mathbf{g}' - \frac{\rho'}{\rho} \mathbf{g} , \quad (3.276)$$

and

$$\delta \mathcal{F} = \frac{i}{\omega \rho} \nabla [(\Gamma_3 - 1)(\rho \epsilon - \text{div } \mathbf{F})'] . \quad (3.277)$$

As argued in Section 3.6.1,  $\mathcal{F}_{\text{ad}}$  is in fact a linear operator on  $\boldsymbol{\delta r}$ .

Near the surface the nonadiabatic correction to  $p'$  cannot in general be regarded as a small perturbation, and hence we cannot directly use the perturbation expression (3.261). However, by multiplying Eq. (3.275) by  $\rho \boldsymbol{\delta r}^*$  and integrating over the volume of the star we obtain

$$\omega^2 \|\boldsymbol{\delta r}\|^2 = \|\boldsymbol{\delta r}\|^2 \Sigma(\boldsymbol{\delta r}) + \int_V \boldsymbol{\delta r}^* \cdot \delta \mathcal{F} \rho dV , \quad (3.278)$$

where  $\Sigma$  is defined by Eq. (3.255). As argued in Section 3.6.1  $\Sigma(\boldsymbol{\xi})$  is real for any  $\boldsymbol{\xi}$  satisfying the boundary conditions; neglecting possible complications in the treatment of the atmosphere in the outer boundary condition this is also the case for the nonadiabatic eigenfunction  $\boldsymbol{\delta r}$ . Writing  $\omega = \omega_r + i\omega_i$  and taking the imaginary part of Eq. (3.278) we therefore obtain

$$2\omega_r \omega_i = \text{Im} \left( \int_V \boldsymbol{\delta r}^* \cdot \delta \mathcal{F} \rho dV \right) , \quad (3.279)$$

where  $\text{Im}$  denotes the imaginary part. Using Eq. (3.277) and the definition of  $\|\boldsymbol{\delta r}\|^2$  and assuming that  $|\omega_i| \ll |\omega_r|$  we obtain

$$\omega_i \simeq \frac{1}{2\omega_r} \frac{\text{Re} \left\{ \int_V \boldsymbol{\delta r}^* \cdot \nabla [(\Gamma_3 - 1)(\rho \epsilon - \text{div } \mathbf{F})'] dV \right\}}{\int_V \rho |\boldsymbol{\delta r}|^2 dV} . \quad (3.280)$$

The integral in the numerator can be rewritten as

$$\int_V \text{div} [\boldsymbol{\delta r}^* (\Gamma_3 - 1)(\rho \epsilon - \text{div } \mathbf{F})'] dV - \int_V \text{div} (\boldsymbol{\delta r}^*) (\Gamma_3 - 1)(\rho \epsilon - \text{div } \mathbf{F})' dV ; \quad (3.281)$$

the first integral can be transformed, by using Gauss's theorem Eq. (3.3), into an integral over the stellar surface which can be neglected, whereas in the second integral we use the continuity equation (3.42). The result is, finally, that the imaginary part of the frequency, resulting from nonadiabaticity, is

$$\begin{aligned} \omega_i &= \frac{1}{2\omega_r^2} \frac{\int_V \frac{\delta \rho^*}{\rho} (\Gamma_3 - 1)(\rho \epsilon - \text{div } \mathbf{F})' dV}{\int_V \rho |\boldsymbol{\delta r}|^2 dV} \\ &= \frac{1}{2\omega_r^2} \frac{\int_V \frac{\delta \rho^*}{\rho} (\Gamma_3 - 1) \delta(\rho \epsilon - \text{div } \mathbf{F}) dV}{\int_V \rho |\boldsymbol{\delta r}|^2 dV} , \end{aligned} \quad (3.282)$$

where in the second equation we also transformed to Lagrangian perturbations, using that the equilibrium model is essentially in thermal equilibrium, with  $\rho\epsilon = \text{div } \mathbf{F}$ . This is the desired expression.

The physical meaning of Eq. (3.282) is straightforward. Instability (with  $\omega_i > 0$ ) occurs if  $\delta\rho^*$  and  $\delta(\rho\epsilon - \text{div } \mathbf{F})$  are in phase. The latter expression is obviously the heating associated with the oscillation; thus the condition for instability is that heating occurs during the phase of compression of the gas. This is precisely the condition for the operation of a heat engine, and hence the background for calling this general excitation mechanism the heat-engine mechanism. An interesting mechanical analogue to the excitation of acoustic waves is provided by Rijke's tube (see Jones 1976). Here a heated gauze, appropriately placed in a vertical tube, excites acoustic modes in the tube; the driving takes place as colder air is drawn past the gauze at compression, heating the air, while warmer air passes the gauze at expansion, hence with less heating.<sup>22</sup>

### 3.7.1.1 Expressions for the Heating

The detailed properties of the excitation obviously depend on the expression for  $(\rho\epsilon - \text{div } \mathbf{F})'$ . Using that  $\epsilon = \epsilon(\rho, T)$  (we neglect a possible Eulerian perturbation to the composition) it is easy to see that

$$(\rho\epsilon)' = \rho\epsilon \left[ \epsilon_T \frac{T'}{T} + (\epsilon_\rho + 1) \frac{\rho'}{\rho} \right], \quad (3.283)$$

where

$$\epsilon_T = \left( \frac{\partial \ln \epsilon}{\partial \ln T} \right)_\rho, \quad \epsilon_\rho = \left( \frac{\partial \ln \epsilon}{\partial \ln \rho} \right)_T. \quad (3.284)$$

Similarly, the perturbation to the flux can be evaluated from the diffusion approximation, Eq. (3.22), and in particular assuming that there are no other contributions (such as convection) to the heat transport. The result is

$$\mathbf{F}' = \left[ (3 - \kappa_T) \frac{T'}{T} - (1 + \kappa_\rho) \frac{\rho'}{\rho} \right] F_r \mathbf{a}_r - \frac{4a\tilde{c}T^3}{3\kappa\rho} \nabla T', \quad (3.285)$$

where

$$\kappa_T = \left( \frac{\partial \ln \kappa}{\partial \ln T} \right)_\rho, \quad \kappa_\rho = \left( \frac{\partial \ln \kappa}{\partial \ln \rho} \right)_T, \quad (3.286)$$

and  $F_r$  is the equilibrium radiative flux (which is of course in the radial direction).

---

<sup>22</sup> A set of tuned Rijke's tubes was once used by students at a Christmas party in Aarhus for a striking rendition of Danish Christmas melodies.

### 3.7.1.2 The Quasi-Adiabatic Approximation

Equation (3.282) can be used to estimate  $\omega_i$  on the basis of *adiabatic* eigenfunctions. Regardless of the assumption of adiabaticity we may obtain  $\rho'$  from the equation of continuity as

$$\frac{\delta\rho}{\rho} = -\operatorname{div}(\boldsymbol{\delta r}), \quad \rho' = \delta\rho - \xi_r \frac{d\rho}{dr}. \quad (3.287)$$

From adiabaticity it follows that the temperature perturbation can be computed from

$$\frac{\delta T}{T} = (\Gamma_3 - 1) \frac{\delta\rho}{\rho}, \quad T' = \delta T - \xi_r \frac{dT}{dr}. \quad (3.288)$$

Hence, if  $\boldsymbol{\delta r}$  is given,  $\rho'$  and  $T'$  can be computed, and then  $(\rho\epsilon - \operatorname{div} \mathbf{F})'$  can be obtained from Eqs (3.283) and (3.285). Since this approximation to the damping rate can be obtained from the adiabatic eigenfunction, it is known as the *quasi-adiabatic* approximation. As the adiabatic eigenfunctions may be chosen to be real, the integrals in Eq. (3.282) are real, and hence  $\operatorname{Re}$  is not required. The use of the adiabatic eigenfunction essentially corresponds to regarding the nonadiabatic effects as a small perturbation and evaluating the imaginary part of the frequency from the general expression for the perturbation to  $\omega^2$ , Eq. (3.261).

It should be noted that the approximation is not without problems. The perturbation approach is based on the assumption that the perturbation is small. This is true in most of the star, but not very near the surface where nonadiabatic effects become strong. Here nonadiabaticity has a substantial effect on the eigenfunction, and hence an evaluation of the integral in Eq. (3.282) based on the adiabatic eigenfunctions is questionable. Nonetheless, we may hope that the quasi-adiabatic approximation at least gives an indication of the stability properties of the mode.

To illustrate some simple properties of Eq. (3.282) we consider the case where the nonadiabaticity is dominated by the energy generation. Here it is convenient to work purely in terms of Lagrangian perturbations. It is obvious that  $\delta(\rho\epsilon)$  can be obtained from an expression analogous to Eq. (3.283). Neglecting the term in  $\mathbf{F}$  and using Eq. (3.288) we find

$$\delta\omega = \frac{i}{2\omega^2} \frac{\int_V \left| \frac{\delta\rho}{\rho} \right|^2 (\Gamma_3 - 1)[\epsilon_\rho + 1 + (\Gamma_3 - 1)\epsilon_T]\rho\epsilon dV}{\int_V \rho |\boldsymbol{\delta r}|^2 dV}. \quad (3.289)$$

Since  $\epsilon_T$  and  $\epsilon_\rho$  are positive, and  $\Gamma_3 \simeq 5/3$ , it is obvious that the integrals in Eq. (3.289) are positive. With the assumed time dependence as  $\exp(-i\omega t)$  this corresponds to a growth in the oscillation amplitude, *i.e.*, to instability of the mode.

The physical nature of this instability, generally known as the  $\epsilon$  mechanism, is very simple and closely related to the operation of a normal heat

engine. At compression the gas is hotter than normal and this, together with the increased density, causes an increase in the release of energy; this increases the tendency of the gas to expand back towards equilibrium. At expansion the gas is cooler and less dense and hence the energy production is low, similarly increasing the tendency of collapse towards the equilibrium. Thus both effects increase the oscillation amplitude. This is obviously a heat-engine mechanism, which is closely analogous to the operation of a normal car engine where energy is also released (through the ignition of the air–fuel mixture) at the point of maximum compression.

The destabilization through nuclear reactions may play an important role for g modes in several cases; this includes the Sun which becomes unstable towards a few low-order g modes in relatively early phases of its evolution (see, for example, Christensen-Dalsgaard *et al.* 1974; Boury *et al.* 1975; Shibahashi *et al.* 1975). For acoustic modes, which have large amplitudes in the outer part of the star, the damping and excitation are normally dominated by the effects of the flux. This is more complicated and will be discussed in Section 3.7.2.

We note that high-order or high-degree modes, with rapidly varying eigenfunctions, have a tendency to be stable. Here the last term in Eq. (3.285) often dominates such that  $-\operatorname{div} \mathbf{F}'$ , as a rough approximation, can be obtained, neglecting gradients of equilibrium quantities, as

$$-\operatorname{div} \mathbf{F}' \simeq -\frac{4a\tilde{c}T^3}{3\kappa\rho} |\mathbf{k}|^2 T' , \quad (3.290)$$

where  $\mathbf{k}$  is the local wave number. Since in the quasi-adiabatic approximation  $T'$  and  $\delta\rho$  are essentially in phase this leads to cooling at compression and hence damping. Physically, this effect arises because of energy loss from hot compressed regions to nearby cool expanded regions when the mode has a short wavelength.

### 3.7.1.3 Convective Effects

The description has so far neglected convection. The flux perturbation  $\mathbf{F}'$  should obviously include a contribution from the convective flux in addition to the radiative flux evaluated in Eq. (3.285). In addition, the perturbation to the turbulent pressure makes a direct contribution to the momentum equation which should be included as an additional term in Eq. (3.272) for the pressure perturbation and hence in the expression (3.277) for  $\delta\mathcal{F}$ . A slightly simplified version of the resulting expression for  $\omega_i$  can conveniently be expressed as<sup>23</sup>

$$\eta \equiv \frac{\omega_i}{\omega_r} \simeq \eta_t + \eta_g = \frac{W_t}{J} + \frac{W_g}{J} , \quad (3.291)$$

where

---

<sup>23</sup> For a more complete expression, see Balmforth (1992a).

$$\begin{aligned}
W_t &= -\omega_r \operatorname{Im} \left[ \int_0^R \frac{\delta\rho^*}{\rho} \delta p_t r^2 dr \right], \\
W_g &= \operatorname{Re} \left[ \int_0^R \frac{\delta\rho^*}{\rho} (\Gamma_3 - 1) \delta(\rho\epsilon - \operatorname{div} \mathbf{F}) r^2 dr \right], \\
J &= 2\omega_r^3 \int_0^R \rho |\delta\mathbf{r}|^2 r^2 dr;
\end{aligned} \tag{3.292}$$

here  $\delta p_t$  is the perturbation to the turbulent pressure. Also, obviously,  $\mathbf{F} = \mathbf{F}_{\text{rad}} + \mathbf{F}_{\text{con}}$  has a radiative and a convective part,  $\mathbf{F}_{\text{rad}}$  being given by Eq. (3.285). The evaluation of the turbulent contributions remains a serious uncertainty in the computation of stellar oscillation frequencies and stability (*e.g.*, Balmforth 1992a). We return to this in Section 3.7.3. Furthermore, as discussed by Balmforth (1992b) effects of turbulent pressure, both in the equilibrium model and in the pulsations, may have a significant influence on the oscillations frequencies; this is likely a substantial part of the near-surface errors seen in analysis of observed solar frequencies (*cf.* Sections 7.1.4.1 and 7.1.7).

### 3.7.2 The Condition for Instability

The analysis of stellar instability goes back to Eddington (1926), who pointed out that the star could function as a heat engine as a result of the phasing of the heat leak and hence the opacity. The detailed understanding of the location of the Cepheid instability strip in the HR Diagram was developed in a series of papers by S. A. Zhevakin (*e.g.*, Zhevakin 1953) and J. P. Cox and C. Whitney (*e.g.*, Cox & Whitney 1958); a review of the early development of these studies was provided by Zhevakin (1963). Cox (1967, 1974) provided a clear insight into the reason why unstable stars tend to be found in well-defined regions of the HR Diagram, particularly the Cepheid instability strip; the following description is largely based on Cox's analysis.

We neglect the effect of turbulent pressure so that, according to Eq. (3.291),  $\eta \simeq W_g/J$ . Clearly the question of stability or instability depends on the sign of  $W_g$ : if  $W_g > 0$  the mode is unstable, whereas if  $W_g < 0$  the mode is stable.

We consider just the outer parts of the star, where the nuclear energy generation can be neglected and  $L$  consequently is constant. The analysis is restricted to radial oscillations; however, as we know that the behaviour of the modes is largely independent of degree near the surface the results are likely to be at least qualitatively valid for nonradial oscillations as well. Also, we neglect convection. Finally, we assume that the oscillations are either quasi-adiabatic or strongly nonadiabatic. The strongly nonadiabatic situation is discussed below. In the quasi-adiabatic region all perturbation quantities can be taken to be real, and we can approximate  $W_g$  by

$$W_g \simeq -L \int_M \frac{\delta\rho}{\rho} (\Gamma_3 - 1) \frac{d}{dm} \left( \frac{\delta L}{L} \right) dm. \tag{3.293}$$

We now assume that  $\delta\rho > 0$  everywhere in the region of interest. This would in general hold for the fundamental mode. However, even for higher-order modes the dominant excitation and damping generally take place so close to the surface that  $\delta\rho$  has constant sign in this region. It now follows from Eq. (3.293) that the contribution of a given layer to the damping or excitation depends on the rate of change of  $\delta L$ : if  $\delta L$  increases towards the surface, the layer gives a negative contribution to  $W_g$  and hence contributes to the damping, whereas if  $\delta L$  decreases towards the surface, the layer contributes to the excitation. This is entirely consistent with the simple heat-engine argument given in Section 3.7.1, if we notice that we are considering the situation at positive  $\delta\rho$ , *i.e.*, at compression: if  $\delta L$  increases outwards, more energy leaves the layer at the top than flows in at the bottom; hence there is a net energy loss from the layer at compression, which acts to damp the motion. The reverse is true, of course, if  $\delta L$  decreases towards the surface: then energy is dammed up at compression, and the motion is excited. Clearly, the behaviour of the mode depends on the global effect as determined by the integral in Eq. (3.293).

We now need to consider the behaviour of the luminosity perturbation in more detail. It is given by an expression corresponding to Eq. (3.285) for the perturbation to the flux. The radiative luminosity may be expressed as

$$L_{\text{rad}} = -\frac{4a\tilde{c}}{3\kappa} 16\pi^2 r^4 T^4 \frac{d \ln T}{dm}; \quad (3.294)$$

hence, writing the equation in terms of the Lagrangian luminosity perturbation,

$$\frac{\delta L_{\text{rad}}}{L_{\text{rad}}} = 4\frac{\delta r}{r} + (4 - \kappa_T) \frac{\delta T}{T} - \kappa_\rho \frac{\delta\rho}{\rho} - \left( \frac{d \ln T}{dm} \right)^{-1} \frac{d}{dm} \left( \frac{\delta T}{T} \right). \quad (3.295)$$

To simplify the subsequent discussion, we note that for low-order modes one can neglect the term in  $d(\delta T/T)/dm$ , as well as the term in the displacement. Thus we approximate Eq. (3.295) by

$$\frac{\delta L_{\text{rad}}}{L_{\text{rad}}} \simeq (4 - \kappa_T) \frac{\delta T}{T} - \kappa_\rho \frac{\delta\rho}{\rho}. \quad (3.296)$$

In the region where the oscillations are nearly adiabatic,  $\delta T/T \simeq (\Gamma_3 - 1)\delta\rho/\rho$ , and hence

$$\frac{\delta L_{\text{rad}}}{L_{\text{rad}}} \simeq \left( \frac{\delta L_{\text{rad}}}{L_{\text{rad}}} \right)_a = -\psi_{\text{rad}} \frac{\delta\rho}{\rho}, \quad (3.297)$$

where

$$\psi_{\text{rad}} = [(\kappa_T - 4)(\Gamma_3 - 1) + \kappa_\rho]. \quad (3.298)$$

Thus in the quasi-adiabatic region we have

$$W_g \simeq L \int_0^R (\Gamma_3 - 1) \frac{\delta\rho}{\rho} \frac{dr}{dr} \left( \psi_{\text{rad}} \frac{\delta\rho}{\rho} \right) dr, \quad (3.299)$$

assuming that the energy transport is dominated by radiation.

In most of the star,  $\kappa_\rho$  is close to unity,  $\kappa_T$  is negative (as, for example, for Kramers opacity) and  $\Gamma_3 \simeq 5/3$ . Also,  $\delta\rho/\rho$  generally increases outwards. Hence it follows from Eq. (3.297) that in most cases  $\delta L_{\text{rad}}$  increases towards the surface, so that the tendency is towards stability. This is quite reassuring: after all most stars do not show obvious variability, suggesting that special circumstances are required to excite modes to large amplitudes.

In fact, it is clear that a strong increase in  $\kappa_T$  may give rise to a decrease in  $(\delta L_{\text{rad}})_a$ ; a decrease in  $\Gamma_3$  might also contribute. Both effects are likely to occur in ionization zones of abundant elements. In particular, such regions tend to be associated with a rapid variation in the opacity and hence with “bumps” in  $\kappa_T$ : it should be noted that since what matters in Eqs (3.293) and (3.297) is effectively the second derivative of opacity, even quite minor features in the opacity can lead to substantial contributions to the excitation, provided that they are confined to a narrow temperature interval. Excitation due to the properties of the opacity is known as the  $\kappa$  mechanism; one occasionally also talks about the  $\gamma$  mechanism, resulting from the variation in  $\Gamma_3$ .

The description given so far suffers from two problems. First, it is clearly only the lower part of an increase in  $\kappa_T$  that will contribute to driving; the upper part similarly contributes to damping, and since  $\delta\rho/\rho$  is assumed to increase outwards the damping part is likely to dominate. Secondly, the argument depends on the quasi-adiabatic approximation, in that the adiabatic relation was used to derive Eq. (3.296) for  $\delta L$ . The great beauty of Cox’s analysis is that it is precisely the transition to nonadiabaticity which is decisive for the occurrence of instability of a star.

To make plausible the transition from adiabaticity to nonadiabaticity we use an argument very similar to the one presented in Section 3.1.2. We write the perturbed energy equation, neglecting the term in  $\epsilon$ , as

$$\frac{d}{dt} \left( \frac{\delta T}{T} \right) - (\Gamma_3 - 1) \frac{d}{dt} \left( \frac{\delta \rho}{\rho} \right) \simeq - \frac{L}{4\pi\rho r^2 c_V T} \frac{d}{dr} \left( \frac{\delta L}{L} \right). \quad (3.300)$$

We integrate this expression over  $r$  and approximate  $d/dt$  by  $1/\Pi$ , where  $\Pi$  is the oscillation period. The result can be written, approximately, as

$$\Delta \left( \frac{\delta L}{L} \right) \sim \Psi \left[ \frac{\delta T}{T} - (\Gamma_3 - 1) \frac{\delta \rho}{\rho} \right], \quad (3.301)$$

where

$$\Psi = \frac{\langle c_V T \rangle \Delta m}{\Pi L} \equiv \frac{\tau_{\text{th}}}{\Pi}, \quad (3.302)$$

defining the thermal time scale  $\tau_{\text{th}}$ . Here  $\Delta(\delta L/L)$  is the change in  $\delta L/L$  between the surface and the point considered,  $\Delta m$  is the mass outside this point, and  $\langle c_V T \rangle$  is a suitable average over this region. Thus  $\Psi$  has a very simple physical meaning: it is the ratio between the thermal energy stored in the layer outside the point considered and the energy radiated by the star in a pulsation period.

Now Eq. (3.301) can be understood in simple physical terms. Very near the surface  $\Psi \ll 1$ : the energy content in the stellar matter is so small that it cannot appreciably affect the luminosity perturbation; thus the luminosity perturbation is *frozen in*, *i.e.*, constant. This is clearly the strongly nonadiabatic limit. Conversely, at great depth  $\Psi \gg 1$ : the energy content is so large that the flow of energy over a pulsation period has no effect on the energy content; this corresponds to the almost adiabatic case. Thus the transition from adiabatic to nonadiabatic oscillations occurs in the *transition region*, where

$$\frac{\langle cvT \rangle_{\text{TR}} (\Delta m)_{\text{TR}}}{\pi L} \sim 1 . \quad (3.303)$$

The question of stability or instability is now decided by the relative location of the transition region and the relevant ionization zone. It has been shown by Cox that the Cepheid instability strip is controlled by the ionization of  $\text{He}^+$ ; thus in the following we consider only this zone. Also, to understand the location of the instability strip it is convenient to think in terms of varying the surface radius, and hence the effective temperature, at fixed luminosity.

Consider first a star of small radius and hence large effective temperature. Here the  $\text{He}^+$  ionization zone lies close to the surface, *i.e.*, very likely above the transition region (*cf.* Fig. 3.28a). Below the transition region  $\delta L/L$  follows the adiabatic behaviour and hence increases outwards; this contributes to the damping. Above the transition region  $\delta L$  is approximately constant, and there is no contribution to the excitation and damping. Thus the net effect is that  $W_g < 0$ , *i.e.*, the star is stable.

Now increase the radius, and hence reduce  $T_{\text{eff}}$ , sufficiently that the transition region coincides with the  $\text{He}^+$  ionization zone. As illustrated in Fig. 3.28b, at this critical radius  $R_{\text{crit}}$  the situation changes dramatically. We still get damping in the interior of the star; however, the lower part of the ionization zone now contributes strongly to the excitation, and the corresponding damping in the upper part of the ionization zone is absent because the luminosity perturbation is frozen in here. Thus in this case there is chance for instability. This is precisely what happens: the point where  $R = R_{\text{crit}}$  corresponds to the location of the instability strip.

Finally, at even larger radius and lower  $T_{\text{eff}}$  the entire ionization zone lies in the quasi-adiabatic region and hence it makes both positive and negative contributions to the excitation. As argued above, the general increase towards the surface of  $\delta\rho/\rho$  makes it plausible that the net effect is damping of the modes (*cf.* Fig. 3.28c).

In fact, computations show that it is difficult to reproduce the lower (so-called red) edge of the instability strip unless effects of perturbations to the convective flux are taken into account. We return to this in Section 3.7.3.

This argument may be more quantitative, to determine the approximate location of the instability strip. It was arguments of this kind that first led Cox & Whitney (1958) to identify the  $\text{He}^+$  ionization as being mainly responsible for the Cepheid instability.

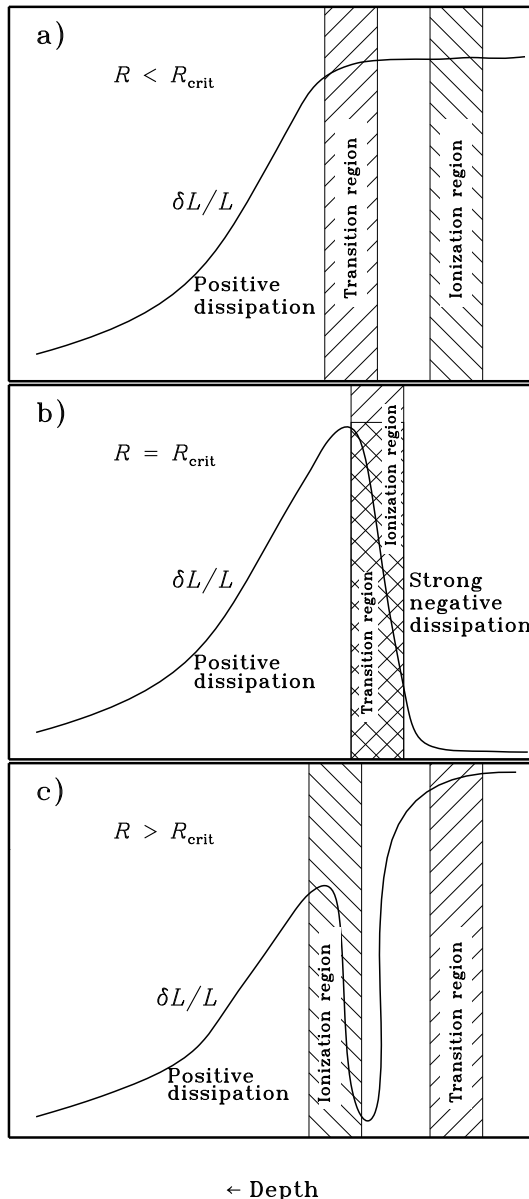


**Fig. 3.28.** Schematic illustration of  $\delta L/L$  at instant of minimum stellar radius and hence maximum compression against depth below the surface. a) For a star with  $R < R_{\text{crit}}$  (see text for explanation of symbols); b) for a star with  $R = R_{\text{crit}}$ ; c) for a star with  $R > R_{\text{crit}}$ . Only the He<sup>+</sup> ionization zone is shown. After Cox (1967).

The location of the transition region, as given in Eq. (3.303), depends on the period of oscillation. We have so far argued for the behaviour of a single mode (although the changing radius would also tend to increase the period and hence push the transition region deeper). However, it should be noticed that higher-frequency modes would tend to have transition regions closer to the surface. It follows that they should become unstable at higher effective temperatures. This is indeed confirmed by more detailed stability calculations.

The arguments as given here refer specifically to the Cepheid instability strip. However, very similar arguments can be applied to other driving mechanisms, at least in fairly hot stars where convection can be neglected. Thus any suitable feature that may cause a substantial dip in  $(\delta L/L)_a$  might be expected to give rise to an instability region. It has been found, for example, that there is a bump in the opacities near temperatures of  $2 \times 10^5$  K which accounts for the  $\beta$  Cep and other B star pulsations in this way (*e.g.*, Moskalik & Dziembowski 1992); this arises from opacity contributions from iron-group elements.<sup>24</sup> An opacity-driven heat-engine mechanism is responsible for the excitation of g modes in at least some pulsating white dwarfs (*e.g.*, Winget *et al.* 1982).

An extensive overview of the excitation of oscillations through the opacity mechanism was given by Pamyatnykh (1999). Following him, Fig. 3.29 shows the differential work integral for two modes in a model of a  $\delta$  Sct star, as well as the quantity  $\psi_{\text{rad}}$ , which determines the luminosity perturbation in terms of the density perturbation, and the thermal time scale. Evidently, regions where  $-dW_g/d\log T$  is positive contribute to the excitation of the mode. The peak in  $\psi_{\text{rad}}$  at  $\log T \simeq 4.6$  corresponds to the second ionization of helium. As expected, the rising part of this peak causes excitation for both the  $n = 1$  and  $n = 9$  modes; in the former case the transition to strongly nonadiabatic oscillations, with  $\tau_{\text{th}}/\Pi \ll 1$ , takes place sufficiently close to this region that the corresponding damping contribution is insignificant, while in the latter case there is strong damping in the outer parts of the helium peak in  $\psi_{\text{rad}}$ . The net effect is that the  $n = 1$  mode is unstable while the  $n = 9$  mode is stable. (The secondary excitation around  $\log T \simeq 4.1$  arises from the first ionization of helium and the ionization of hydrogen but makes a relatively modest contribution to the overall excitation.)

With increasing effective temperature the helium peak in  $\psi_{\text{rad}}$  moves closer to the surface, in the direction of decreasing  $\tau_{\text{th}}$ . Consequently, higher-order modes, with shorter periods, have a tendency to be excited. Thus we may expect to see excitation of higher-order modes on the blue (high-temperature) side of the instability strip. This is confirmed by the detailed calculations presented by Pamyatnykh (1999). As discussed by Pamyatnykh, a similar effect operates amongst the B stars. These are excited by an opacity feature (visible in Fig. 3.29b around  $\log T \simeq 5.2$ ) caused by contributions from iron-group

---

<sup>24</sup> This contribution was identified in opacity updates around 1990; before these improvements the origin of B-star pulsations was a major mystery.

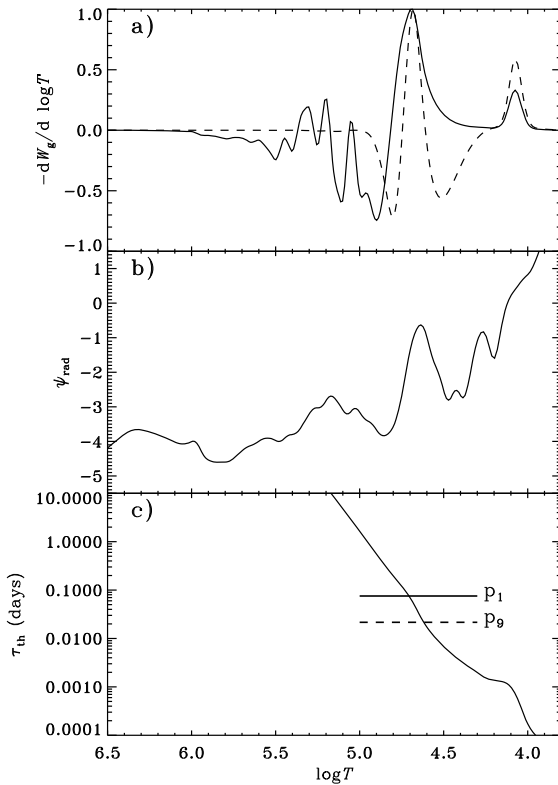


**Fig. 3.29.** a) Differential work integral  $-dW_g/d \log T$  (cf. Eq. (3.292)); the minus sign is included for consistency with that equation); b) the function  $\psi_{\text{rad}}$  (cf. Eq. (3.298)) determining the response of the opacity; c) the thermal time scale  $\tau_{\text{th}}$  (cf. Eq. (3.302)). Results are shown for a model of a  $\delta$  Sct star of mass  $1.8 M_\odot$ , age 0.8 Gyr and effective temperature 7500 K. The solid and dashed curves in panel a) and the solid and dashed heavy horizontal lines in panel c) correspond to radial modes of radial order  $n = 1$  and 9, respectively. Adapted from Pamyatnykh (1999).

elements. This causes excitation of low-order acoustic and gravity modes with periods of a few hours in the  $\beta$  Cep stars, with masses of around  $10 M_\odot$  and effective temperatures around 25 000 K. The same mechanism causes excitation of the high-order g-mode oscillations, with periods of a day or more, in the Slowly Pulsating B stars with masses around  $4 M_\odot$  and effective temperatures around 15 000 K.<sup>25</sup>

<sup>25</sup> As discussed in Section 2.3.2 the apparently analogous situation regarding the long-period oscillations in the  $\gamma$  Dor stars on the cool side of the instability strip

### 3.7.3 Effects of Convection on Stellar Stability

As already mentioned, the treatment of convective contributions to the heat flux and other convective effects is a serious problem in computations of stellar oscillations, introducing a major uncertainty in the calculation of the stability of modes in cool stars with extensive outer convection zones. As discussed in Section 3.2.1 even the treatment of convection in the equilibrium model is highly uncertain. These complications are greatly magnified for convection in the time-varying environment of a pulsating star.

Simple analyses show that convection may contribute to the excitation in the extreme cases of very long and very short convective time scales, compared with the pulsation period. In the former case it is plausible that the convective flux does not react to the pulsations, leading to a negligible convective-flux perturbation  $\delta L_{\text{con}}$ . It was noted by Cox & Giuli (1968) that this might cause excitation if the radiative flux and hence the radiative-flux perturbation become small in the convection zone: since  $\psi_{\text{rad}}$  is typically negative,  $\delta L$  is in phase with  $\delta\rho/\rho$  just beneath the convection zone; thus the change to very small  $\delta L$  in the convection zone corresponds to a negative  $d\delta L/dr$  in Eq. (3.293) and hence to a contribution to the driving. Physically this effect arises from the effective blocking by convection of the luminosity perturbation at the base of the convection zone, leading to heating in phase with compression. Thus the mechanism was dubbed “convective blocking” by Pesnel (1987). It has been shown that this may account for the driving of the long-period g modes in the  $\gamma$  Dor stars (*e.g.*, Guzik *et al.* 2000; Warner *et al.* 2003). More extensive calculations by Dupret *et al.* (2004a, 2005b), using a detailed convection formulation, essentially confirmed that convective blocking dominates the driving of these oscillations (see Fig. 2.6).

The opposite extreme, the convective time scale being much shorter than the pulsation period, is relevant to DB and DA white dwarfs, given their long-period g-mode pulsations and relatively thin convection zones. It was argued by Brickhill (1991a,b) that in this case also the convection zone may act to excite the modes; this was confirmed in a more detailed analysis by Goldreich & Wu (1999). In this case the energy input to the convection zone by the flux perturbation at its base is redistributed throughout the convection zone as a result of the short convective time scale, causing heating of the convection zone; since the radiative flux perturbation is in phase with the density perturbation at the top of the radiative region, as argued above, and the density perturbation varies little through the convection zone, heating is in phase with the density perturbation throughout the convection zone, which therefore contributes to the excitation of the mode. A more detailed investigation of convective effects on the excitation of oscillations in DB white dwarfs was carried out by Dupret *et al.* (2008a), using a time-dependent formulation of convection.

---

has a different physical origin, since the oscillations in these stars are excited through convective blocking; see below.

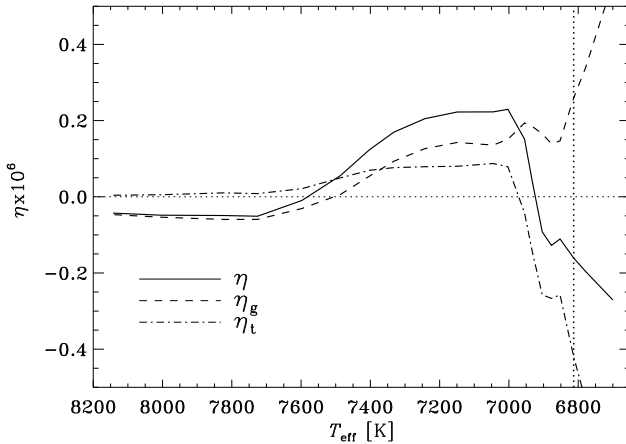


**Fig. 3.30.** Stability coefficients  $\eta = \omega_i/\omega_r$  for the fundamental radial mode as a function of effective temperature  $T_{\text{eff}}$ , for a  $1.7 M_\odot$  model of a  $\delta$  Sct star evolving during the core hydrogen-burning phase. The dashed and dot-dashed curves show the contributions from the thermal effect and the perturbation to the turbulent pressure, respectively (see Eqs (3.291) and (3.292)), and the solid curve shows their sum. The vertical dotted line marks the location of the model illustrated in Fig. 3.31. Adapted from Houdek (2000).

Various time-dependent convection formulations have been developed to deal with the convection-pulsation interactions, based on differing physical models. The formulation by Unno (1967) was further developed by Gabriel *et al.* (1974, 1975) and Gabriel (1996, 2000), as summarized by Grigahcène *et al.* (2005). Gough (1977a) developed a somewhat different formulation based on a detailed physical description of the dynamics of convective elements; this was extended to a nonlocal formulation by Balmforth (1992a). Alternative formulations were proposed by Stellingwerf (1982), further developed by, *e.g.*, Kuhfuß (1986), Gehmeyr & Winkler (1992) and Feuchtinger (1999), as well as by Xiong *et al.* (1997). A review of these different formulations was provided by Baker (1987). Smolec & Moskalik (2008) recently implemented the formulation of Kuhfuß (1986) in a nonlinear hydrodynamical code for radial oscillations and discussed some limitations in previous calculations of this nature.

Early detailed calculations of the excitation of modes in the Cepheid instability strip (*e.g.*, Baker & Kippenhahn 1962, 1965) found reasonable agreement between the upper limit in effective temperature of instability and the observed blue edge of the instability strip. However, the models remained unstable at much lower effective temperature than observed. In these calculations the interaction between convection and pulsations was ignored. An

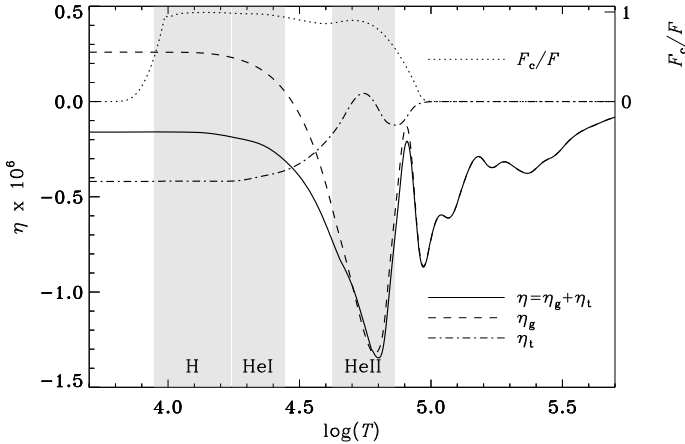


**Fig. 3.31.** Relative work integrals, as functions of the upper limit of integration expressed in terms of  $\log T$ , for the fundamental radial model in a model with  $T_{\text{eff}} = 6813$  K in the  $1.7 M_{\odot}$  sequence illustrated in Fig. 3.30. The dashed and dot-dashed curves show the contributions from the thermal effect and the perturbation to the turbulent pressure, respectively (see Eqs (3.291) and (3.292)), and the solid curve shows their sum; note that the mode is damped in this model. The shaded areas indicate the regions of hydrogen ionization (H) and first and second helium ionization (HeI and HeII, respectively). The dotted curve, using the right-hand ordinate scale, shows the contribution  $F_c/F$  of convection to the total flux in the equilibrium model. Adapted from Houdek (2000).

early demonstration that convective effects can in fact delimit the Cepheid instability strip on the cool side was obtained by Baker & Gough (1979), using the formulation by Gough (1977a), for models of RR Lyrae stars. Gonczi (1981) similarly found stability at the red edge, for Cepheid models, using the formulation of Unno (1967). Stellingwerf (1984) also delimited the RR Lyrae instability strip using the formulation by Stellingwerf (1982). Gehmeyr (1993) studied the suppression of instability by convection at the red edge of the RR Lyrae region, in a fully nonlinear calculation, while Xiong & Deng (2001) used the nonlocal time-dependent theory of Xiong *et al.* (1997) to locate the red edge of the  $\delta$  Sct instability strip. However, although these calculations generally find that convective effects can account for the stabilization of the cool models, it is striking that the physical description of the effect depends strongly on the detailed convection formulation employed.

To illustrate the effects of convection on the location of the instability strip we consider calculations carried out by Houdek (2000), using a formulation

developed by Gough (1977a) and Balmforth (1992a). Figure 3.30 shows the resulting relative growth rates, for an evolution sequence of  $1.7 M_{\odot}$  models evolving through the Cepheid instability strip during core hydrogen burning and hence corresponding to  $\delta$  Sct stars. The onset of instability, at the blue edge of the strip, takes place at  $T_{\text{eff}} \simeq 7600$  K. Interestingly, the thermal contribution  $\eta_g$  to excitation, which includes the effects of the perturbation to the convective flux, grows strongly as the model  $T_{\text{eff}}$  decreases; however, this is more than balanced by the large negative values of  $\eta_t$  arising from the perturbation to the turbulent pressure, leading to overall return to stability at a red edge of the instability strip near  $T_{\text{eff}} = 6900$  K. Further details on the contributions to excitation and damping are illustrated in Fig. 3.31, for a model just on the cool side of the instability strip. Obviously, the bulk of the HeII ionization zone contributes to the excitation of the mode, essentially as in Fig. 3.29; but the contribution from the turbulent pressure is damping in most of the convection zone, leading to overall stability.

### 3.7.4 Excitation of High-Order g Modes

As discussed in Sections 2.3.2 and 2.3.6 both the  $\gamma$  Dor and the SPB stars show preferentially high-order g modes, with periods of order days. This seems at first sight surprising: the high-order modes would be expected to suffer more strongly from radiative diffusive damping in the core, where the local wavenumber is high (*cf.* Eq. (3.290)). As discussed by Dupret *et al.* (2008b) the preferential excitation of these modes is an excellent illustration of the properties of the eigenfunctions and their dependence on the characteristic frequencies  $S_l$  and  $N$  (see Section 3.4.2).

As an example, Fig. 3.32a shows these frequencies in a typical model of a  $\gamma$  Dor star. Also indicated are the frequencies of two g modes, at periods of around 3.5 hr and 14 hr, the latter of which would be expected to be unstable. As discussed in Section 3.4.2, the modes propagate in the region where  $\omega < N, S_l$  or  $\omega > N, S_l$  and are evanescent elsewhere. Thus the  $g_6(l = 2)$  mode has a substantial evanescent region between the deep interior and the base of the convection zone, whereas the  $g_{26}(l = 2)$  is propagating in essentially the full radiative interior. This is reflected in the eigenfunctions; Fig. 3.32b shows the inertia density  $\rho|\delta\mathbf{r}|^2 r^2$ , normalized by the mode inertia (*cf.* Eq. (3.139)). It is evident that for the  $g_6(l = 2)$  the mode amplitude decreases very substantially between the deep interior and the region near the base of the convection zone where the modes are excited; thus in this case the radiative damping in the deep interior dominates over the excitation. For  $g_{26}(l = 2)$ , on the other hand, the amplitude remains substantial all the way to the driving region and the mode may be excited, despite the stronger radiative damping in the deep interior. This is indeed what is found in the computations of the instability; it is obvious that the same will be true of modes of even higher order, up to the point where the radiative damping becomes so strong as to yield overall stability.

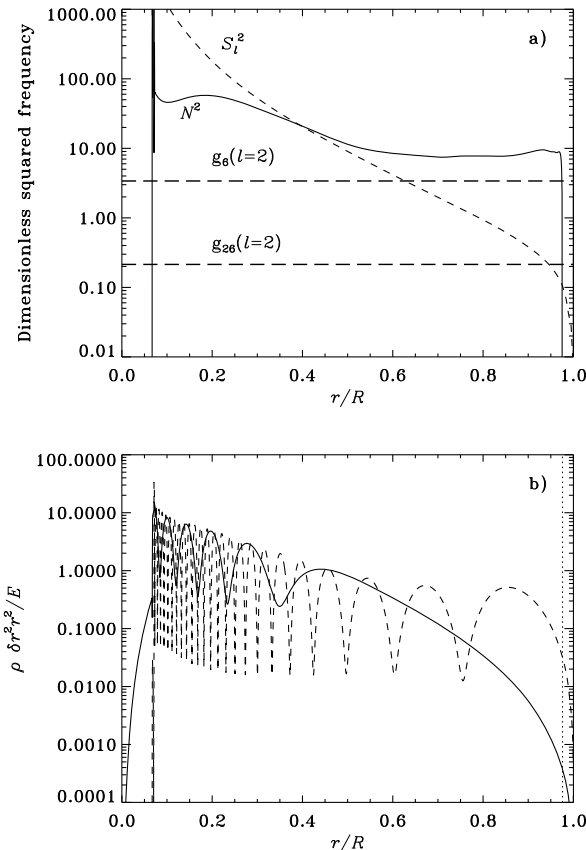


**Fig. 3.32.** Pulsation properties of a  $1.6 M_{\odot}$  star with an age of 1.3 Gyr and effective temperature  $T_{\text{eff}} = 6761$  K. a) Characteristic squared frequencies, in units of  $GM/R^3$ ; also indicated are the squared dimensionless frequencies of two g modes, the lower of which likely corresponding to an excited mode in a  $\gamma$  Dor star. b) Eigenfunctions of these two modes, illustrated in terms of the normalized differential inertia (*cf.* Eq. (3.139)). The solid curve is for the  $g_6(l = 2)$  mode and the dashed curve for the  $g_{26}(l = 2)$  mode. The vertical dotted line marks the base of the convective envelope. See Dupret *et al.* (2008b).

As noted by Dupret *et al.* (2008b) a very similar mechanism operates in the case of the SPB stars where the driving region, associated with the bump in the iron-group opacity, is again located very near the surface.

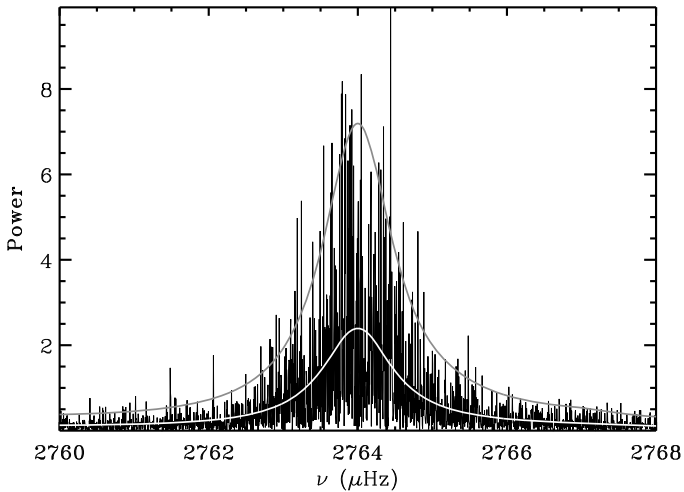


**Fig. 3.33.** Observed spectrum, from Doppler observations extending over 8 yr with the BiSON network, of a single radial mode of solar oscillations. The white curve shows the fitted Lorentzian profile, and the smooth grey curve shows the fit multiplied by three for clarity. See Chaplin *et al.* (2002a). Data courtesy of W.J. Chaplin.

### 3.7.5 Stochastic Excitation of Oscillations

The return to stability at the cool edge of the Cepheid instability strip observed in Fig. 3.30 extends to acoustic modes in stars at cooler temperature in most nonadiabatic calculations taking convection into account. In particular, this is the case for the modes observed in the Sun (*e.g.*, Balmforth 1992a). Thus the presence of oscillations in the Sun and other cool stars requires other excitation mechanisms. In these stars the convective motion near the surface likely reaches speeds close to that of sound. Such turbulent motion with near-sonic speed is an efficient source of acoustic radiation, and it is likely that this “noise” excites the normal modes of the star, to the observed amplitude. For a recent review of such stochastic excitation in solar-like stars, see Houdek (2006).

Since the excitation is caused by a very large number of convective elements, the driving is essentially random. The problem of a damped oscillator driven by random forcing was considered by Batchelor (1956). Stein (1968) estimated the flux of acoustic energy generated by the solar convection zone, and Goldreich & Keeley (1977) considered the specific problem of the excitation of solar oscillations by convection. Here we discuss a simple analysis by Duvall & Harvey (1986) and Christensen-Dalsgaard *et al.* (1989a) which

captures the essence of the problem. We consider a damped linear oscillator,  $A(t)$ , with random forcing and hence satisfying

$$\frac{d^2A}{dt^2} + 2\eta \frac{dA}{dt} + \omega_0^2 A = f(t) , \quad (3.304)$$

where  $\eta$  is the damping rate,  $\omega_0$  is the (undamped) frequency and  $f(t)$  is the random forcing function. We introduce the Fourier transforms of  $A$  and  $f$ ,

$$\tilde{A}(\omega) = \int A(t)e^{i\omega t} dt , \quad \tilde{f}(\omega) = \int f(t)e^{i\omega t} dt , \quad (3.305)$$

where we do not attempt to specify the limits of integration precisely, hence essentially ignoring initial transients in the solution. Thus Eq. (3.304) is transformed to

$$-\omega^2 \tilde{A} - 2i\eta\omega \tilde{A} + \omega_0^2 \tilde{A} = \tilde{f} , \quad (3.306)$$

with the power spectrum of the solution given by

$$P(\omega) = |\tilde{A}(\omega)|^2 = \frac{|\tilde{f}(\omega)|^2}{(\omega_0^2 - \omega^2)^2 + 4\eta^2\omega^2} . \quad (3.307)$$

Equation (3.307) describes the solution resulting from a particular realization of the forcing. It is more interesting to consider an average over several such realizations (obtained either by repeated observation of the same mode or by averaging data for several similar modes). Furthermore, since the damping rate is generally very small compared with the oscillation frequency, we are mainly interested in the behaviour close to  $\omega = \omega_0$ . Thus we finally obtain that the average power spectrum resulting for a mode of frequency  $\omega_0$ , and damping rate  $\omega_i$ , is approximately

$$\langle P(\omega) \rangle \simeq \frac{1}{4\omega_0^2} \frac{\langle P_f(\omega) \rangle}{(\omega - \omega_0)^2 + \omega_i^2} , \quad (3.308)$$

where  $\langle P_f(\omega) \rangle$  is the average power spectrum of the forcing function. If the forcing spectrum is a slowly varying function of frequency, the result is therefore a Lorentzian spectrum, with a width determined by the linear damping rate of the mode.

If a single realization, rather than the average, of the spectrum is considered, as is generally the case for observations of stellar oscillations, the result is a random function with a Lorentzian envelope, as essentially given by Eq. (3.307). An example is shown in Fig. 3.33; this is based on observations of low-degree solar oscillations with the BiSON network, comprising 6 stations with an appropriate geographical distribution to ensure nearly continuous observations (see Section 7.1.1.2). Such Lorentzian profiles are often assumed in the fits carried out to determine the frequency and other properties of the modes.

Based on a detailed description of the excitation, Chaplin *et al.* (2005) discussed the dependence of the expected amplitudes on mode properties. The result for the mean squared velocity can be written as

$$\langle V^2 \rangle \simeq \frac{1}{|\omega_i| E} \frac{\tilde{\mathcal{P}}_f(\omega)}{E}, \quad (3.309)$$

where  $E$  is the normalized mode inertia (*cf.* Eq. (3.140)), and  $\tilde{\mathcal{P}}_f(\omega)$  is a measure of the acoustic energy input which depends on the properties of the eigenfunction in the near-surface region and hence, as indicated, predominantly on frequency. It should also be noted that, according to Eq. (3.291),  $\omega_i E$  is given by  $W_t$  and  $W_g$  which again are predominantly functions of frequency. Thus at given frequency we expect that  $\langle V^2 \rangle \propto E^{-1}$  or, in other words, that the mode energy  $1/2EM\langle V^2 \rangle$  (*cf.* Eq. (3.141)), is predominantly a function of frequency.

Chaplin *et al.* (2005) stressed that some care is required in converting the root-mean-square signal to the height  $H$  of the corresponding peak in the power spectrum which provides a measure of the observational detectability of the mode. If the mode is observed for a time  $T$  much longer than the damping time, such that  $|\omega_i|T \gg 1$ , the Lorentz profile in Eq. (3.308) is fully resolved and  $H \simeq 2\langle V^2 \rangle / |\omega_i|$ . In other words, since both  $\langle V^2 \rangle$  and  $\omega_i$  are proportional to  $E^{-1}$  at fixed frequency,  $H$  is independent of  $E$ . However, if  $|\omega_i|T \ll 1$  the profile is completely unresolved; in this case  $H \simeq T\langle V^2 \rangle$  and therefore proportional to  $E^{-1}$ . As a suitable interpolation formula between these two extreme cases, Fletcher *et al.* (2006) proposed

$$H \simeq \frac{2\langle V^2 \rangle}{|\omega_i| + 2/T}. \quad (3.310)$$

As noted by Dupret *et al.* (2009) this distinction is particularly relevant in the analysis of stochastically excited mixed modes; here neighbouring modes of predominantly p- and g-mode character and hence of very different inertia may likely have very different damping times and hence visibility in realistic observations, even though the height in the power spectrum would be similar if the modes were observed for an infinitely long time.

As a result of the stochastic nature of the excitation, the observed amplitude of a mode varies over time. The statistical properties of this variation were discussed by Kumar, Franklin & Goldreich (1988) and Chang & Gough (1998). If the modes are observed over a time short compared with the damping time, the mode energy distribution is exponential,

$$p(\mathcal{E})d\mathcal{E} = \langle \mathcal{E} \rangle^{-1} \exp(-\mathcal{E}/\langle \mathcal{E} \rangle)d\mathcal{E}, \quad (3.311)$$

where  $\langle \mathcal{E} \rangle$  is the average energy, and the energy  $\mathcal{E}$  is proportional to the squared amplitude.

It is straightforward, and instructive, to simulate such stochastically excited, damped, oscillations. An example of such a simulation, for a long-period

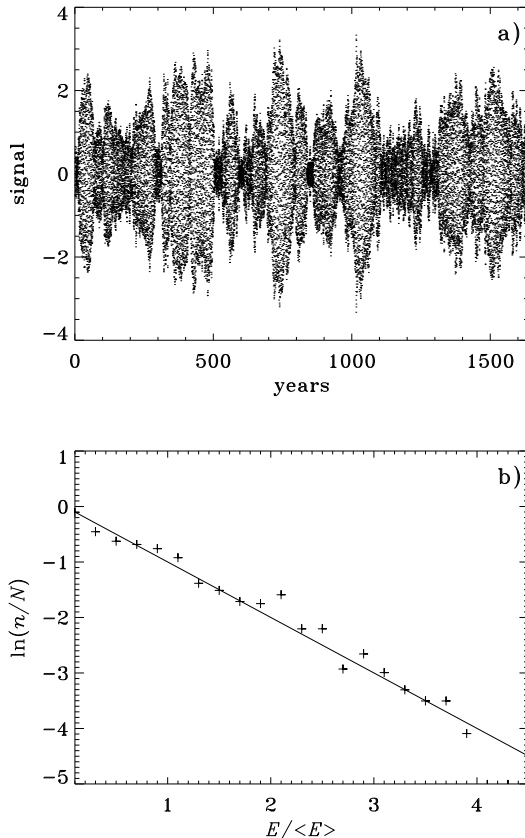


**Fig. 3.34.** Artificial time series for a stochastically excited oscillation with a period of 82 d and a damping time of 60 yr, observed at a 20-d cadence. The top panel shows the computed time series which, as indicated, covers about 1600 yr. In the bottom panel the points show the binned, normalized distribution of mode power, in units of the mean power, obtained by analysing the time series in 1-yr segments. The line corresponds to the expected exponential distribution in Eq. (3.311) (see text). From Christensen-Dalsgaard *et al.* (2001).

variable, is illustrated in Fig. 3.34. It is evident that the amplitude varies strongly and in an irregular fashion, and hence at any given time there is a significant probability that any given mode may be invisible; this must be kept in mind in the interpretation of such pulsating stars. Panel b) shows the distribution of mode energy, obtained by analysing the time series in 1-yr segments. Here  $N$  is the total number of segments, and  $n$  is a scaled binned

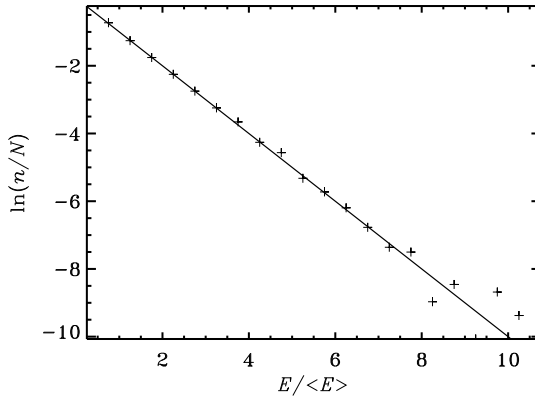


**Fig. 3.35.** Binned, normalized distribution of observed solar mode power, in units of mean power; this is based on 3368 individual samples, each containing 14 modes, of BiSON observations. The line corresponds to the expected exponential distribution in Eq. (3.311). See Chaplin *et al.* (1997). Data courtesy of Y. Elsworth.

number of realizations,

$$n = \frac{\Delta n(\mathcal{E})}{\exp(\Delta\mathcal{E}/2\langle\mathcal{E}\rangle) - \exp(-\Delta\mathcal{E}/2\langle\mathcal{E}\rangle)} , \quad (3.312)$$

where  $\Delta n(\mathcal{E})$  is the number of realizations in the interval  $[\mathcal{E} - \Delta\mathcal{E}/2, \mathcal{E} + \Delta\mathcal{E}/2]$ . It may be shown that  $n/N$  behaves like  $\exp(-\mathcal{E}/\langle\mathcal{E}\rangle)$  (*cf.* Chang & Gough 1998); as is clear from Fig. 3.34b the simulated data do indeed have this property. Very interestingly, the observed distribution of solar oscillation amplitudes satisfies this relation quite closely (*e.g.*, Chaplin *et al.* 1997). An example, based on BiSON data, is shown in Fig. 3.35.

The distribution function in Eq. (3.311) also defines the relation between the average  $\langle A \rangle$  and the standard deviation  $\sigma(A)$  of the amplitude:

$$\sigma(A) = \left( \frac{4}{\pi} - 1 \right)^{1/2} \langle A \rangle \simeq 0.52 \langle A \rangle . \quad (3.313)$$

It was noticed by Christensen-Dalsgaard, Kjeldsen & Mattei (2001) that observed amplitudes of semiregular variables on the asymptotic giant branch approximately followed this relation, suggesting that their variability may have a cause similar to the solar oscillations.

As indicated by Eq. (3.308) this excitation mechanism results in a definite prediction of the oscillation amplitude, given a model for the power in the stochastic forcing. This can be evaluated from models of convection, such as

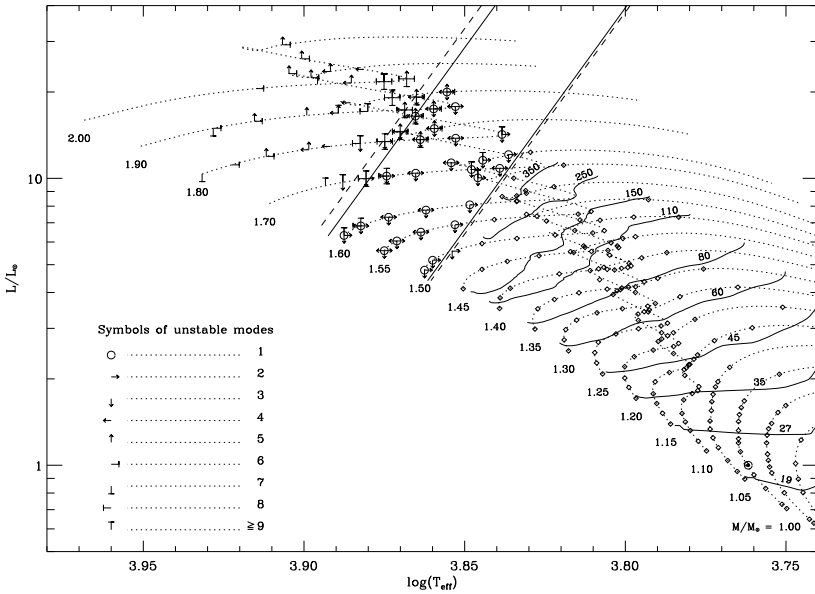


**Fig. 3.36.** Unstable modes and mean velocity amplitudes of stochastically excited modes, for radial oscillations. Evolution tracks, at the masses indicated, are shown with dotted curves, some models being marked with diamonds. Selected models with unstable modes are indicated by the symbols, as listed in the figure; note that, as argued in Section 3.7.2, the higher-order modes tend to be excited in models with higher effective temperature. The solid and dashed straight lines indicate the instability strips of the  $n = 1$  and 2 modes, respectively. The contours to the right of the instability strip show computed velocity amplitudes, averaged over frequency; the values of the amplitudes, in  $\text{cm s}^{-1}$ , are given. For the Sun, indicated by  $\odot$ , the predicted mean amplitude is  $20 \text{ cm s}^{-1}$ . From Houdek *et al.* (1999).

the mixing-length description. A rough estimate was made by Christensen-Dalsgaard & Frandsen (1983a); following Goldreich & Keeley (1977) they assumed equipartition between the energy in a single mode of oscillation and the energy of a convective eddy with a time scale corresponding to the period of the mode. The results were analysed by Kjeldsen & Bedding (1995) who found that the amplitudes scaled as  $L/M$ . A more careful calculation was carried out by Houdek *et al.* (1999), who determined the damping or excitation rates of radial modes using the nonlocal mixing-length description of Balmforth (1992a) of the interaction between convection and pulsation; for the stable modes they estimated the stochastically excited amplitudes, from the computed damping rates and a mixing-length calculation of the energy input to the modes from convection, following Balmforth (1992c). Further estimates of oscillation amplitudes for stars across the HR Diagram were made

by Samadi *et al.* (2005, 2007), who pointed out the importance of the assumed frequency dependence of the turbulent energy input, while Belkacem *et al.* (2008) considered the excitation of high-degree acoustic modes in the Sun. These predictions are increasingly being tested against observations (see Houdek 2006 for a summary); it appears that the predicted and observed amplitudes are in reasonably agreement for stars at or below the solar effective temperature, while the predictions are substantially higher than the observations for hotter stars.

The detailed hydrodynamic simulations of near-surface convection in the Sun and other stars are fully compressible and hence contain acoustic waves and oscillations, although obviously confined to the computational box by the imposed boundary conditions. Thus these simulations provide a very valuable tool for investigating the interaction between convection and pulsations, including those aspects that lead to stochastic excitation (for a review, see Nordlund *et al.* 2009). Computations by Stein & Nordlund (2001) of the energy input from convection to the oscillations, based on the simulations, have yielded results in general agreement with the observed properties of solar oscillations. Such simulations were extended by Stein *et al.* (2004) to a broader range of stars, qualitatively confirming the results from the simpler models that the energy input increases with increasing effective temperature and decreasing surface gravity.

The stochastic mechanism is expected to result in the excitation of all modes in a broad range of frequencies, with amplitudes reflecting the presumed slow frequency dependence of the forcing function and the damping rate. In more detailed calculations this in addition involves the overlap between the oscillation eigenfunctions and the dominant forcing (*e.g.*, Goldreich *et al.* 2004); the forcing at the relevant time scales tends to be concentrated quite near the surface while, as discussed in connection with Figs 3.17 and 3.22, the modes tend to be evanescent near the surface at relatively low frequency, hence decreasing the efficiency of the driving, as also reflected in the mode inertia normalized to the surface amplitude (*cf.* Fig. 3.24). This effect causes a decrease in the mode amplitudes at low frequency; at high frequency the amplitudes decrease as a result of a decrease in convective energy at the time scale of the oscillations, combined with an increase in the damping rate.

These properties of the amplitude distribution are indeed observed in the Sun and in the cases where solar-like oscillations have been observed in other stars (see Figs 1.9 and 2.3). It greatly simplifies the identification of the modes, compared with oscillations excited through the heat-engine mechanism. In the latter case the mechanisms determining the final amplitude are largely unknown (see Nowakowski 2005). As illustrated, for example, in Fig. 2.9, the result is typically a wide range of mode amplitudes, with no obvious systematics, and hence a complex selection of modes which reach an observable level, at a given sensitivity. It seems likely that in many cases only a small subset of the modes actually excited in the star are detected. This obviously com-

plicates the identification of the observed modes with modes computed for a stellar model, and hence the asteroseismic analysis of the observations.

## 3.8 Effects of Rotation

We have so far assumed that stars are spherically symmetric and that there are no velocity fields in the equilibrium model. This is manifestly false in the common case of rotating stars; in the solar case, at least, the observed surface rotation depends on latitude, thus implying the presence of velocity fields regardless of the choice of a rotating coordinate system. In addition, other large-scale velocity fields, such as those caused by convection, could have an effect on the modes. Hence we must investigate such effects. Apart from their intrinsic interest, the principal purpose of such studies is obviously to be able to probe the velocity fields from the observed properties of the oscillations.

Departures from spherical symmetry are also caused by large-scale magnetic fields. Such fields are key to the properties of the rapidly oscillating Ap stars (see Sections 2.3.5 and 7.3.4) and they are undoubtedly important in the study of the effects of the solar cycle on solar oscillations (*cf.* Section 7.1.9); however, a theoretical discussion of the effects of magnetic fields is regrettably beyond the scope of this book.

### 3.8.1 A Simplified Description of the Effect of Rotation

It is straightforward to see, from a purely geometrical argument, that rotation affects the observed frequencies. Assume the angular velocity  $\Omega$  to be uniform, and consider an oscillation with a frequency  $\omega_0$ , independent of  $m$ , in the frame rotating with the star. We introduce a coordinate system in this frame, with coordinates  $(r', \theta', \phi')$  which are related to the coordinates  $(r, \theta, \phi)$  in an inertial frame through

$$(r', \theta', \phi') = (r, \theta, \phi - \Omega t) \quad (3.314)$$

(*cf.* Fig. 3.37). It follows from Eq. (3.132) that, in the rotating frame, the perturbations depend on  $\phi'$  and  $t$  as  $\cos(m\phi' - \omega_0 t)$ ; hence, the dependence in the inertial frame is  $\cos(m\phi - \omega_m t)$ , where

$$\omega_m = \omega_0 + m\Omega . \quad (3.315)$$

Thus an observer in the inertial frame finds that the frequencies are split uniformly according to  $m$ .

This description is obviously incomplete. Even in the case of uniform rotation, the effects of the Coriolis force must be taken into account in the rotating frame, causing a contribution to the frequency splitting (Cowling & Newing 1949; Ledoux 1949, 1951). Furthermore, in general the angular velocity is a

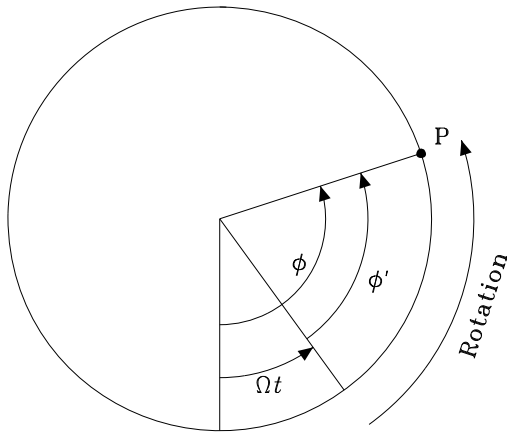


**Fig. 3.37.** Geometry of rotational splitting. The star is rotating with uniform angular velocity  $\Omega$ . The point  $P$  has longitude  $\phi'$  in the system rotating with the star and longitude  $\phi = \phi' + \Omega t$  in the inertial system.

function  $\Omega(r, \theta)$  of position. Nevertheless, as shown below, the effect of the Coriolis force is often small and Eq. (3.315) is approximately correct if  $\Omega$  is replaced by a suitable average of the position-dependent angular velocity.

To arrive at an expression valid for any rotation law it is convenient to consider first the even more general case of an arbitrary stationary velocity field in the star.

### 3.8.2 The Effect of Large-Scale Velocities on the Oscillation Frequencies

We need to reconsider the derivation of the perturbation equations, including the effects of a velocity field. We shall assume that the equilibrium structure is stationary, so that all local time derivatives vanish. Even with this assumption the determination of the equilibrium structure is a non-trivial problem, due to the distortion caused by the velocity fields (*e.g.*, due to centrifugal effects in a rotating star; see Section 3.2.4.2). However, we initially assume that the velocity  $\mathbf{v}_0$  in the equilibrium state is sufficiently slow that terms quadratic in  $\mathbf{v}_0$  can be neglected; effects of rapid rotation are discussed in Section 3.8.6. The equation of continuity (3.6) gives, because of the assumed stationarity

$$\operatorname{div}(\rho_0 \mathbf{v}_0) = 0. \quad (3.316)$$

Also, because of the neglect of terms of order  $|\mathbf{v}|^2$ , the equations of motion (3.9) reduce to

$$0 = -\nabla p_0 + \rho_0 \mathbf{g}_0 . \quad (3.317)$$

As usual we have replaced the body force per unit mass  $\mathbf{f}$  by the gravitational acceleration  $\mathbf{g}$ . Thus Eq. (3.30) of hydrostatic support is unchanged. In the solar case, the ratio between the neglected centrifugal force and surface gravity is of order  $2 \times 10^{-5}$  and so the error in Eq. (3.317) is in fact small.

The perturbation analysis also requires some care. It was treated in considerable detail by Lynden-Bell & Ostriker (1967), and is discussed in J. P. Cox (1980), Chapter 5. Here we just present a few of the main features.

The velocity at a given point in space can be written as

$$\mathbf{v} = \mathbf{v}_0 + \mathbf{v}' , \quad (3.318)$$

where  $\mathbf{v}'$  is the Eulerian velocity perturbation. The displacement  $\delta\mathbf{r}$  must be determined relative to the moving equilibrium fluid; it is related to the velocity perturbation by

$$\frac{d\delta\mathbf{r}}{dt} = \delta\mathbf{v} = \mathbf{v}' + (\delta\mathbf{r} \cdot \nabla)\mathbf{v}_0 . \quad (3.319)$$

Here  $\delta\mathbf{v}$  is the Lagrangian velocity perturbation and, as in Section 3.1.1,  $d/dt$  is the material time derivative,

$$\frac{d\delta\mathbf{r}}{dt} = \frac{\partial \delta\mathbf{r}}{\partial t} + (\mathbf{v}_0 \cdot \nabla)\delta\mathbf{r} ; \quad (3.320)$$

in contrast to the zero-velocity case, the local and the material time derivatives of perturbations are now different.

The perturbed continuity equation may be written as

$$\begin{aligned} 0 &= \frac{\partial \rho'}{\partial t} + \operatorname{div}(\rho' \mathbf{v}_0 + \rho_0 \mathbf{v}') \\ &= \frac{\partial}{\partial t}[\rho' + \operatorname{div}(\rho_0 \delta\mathbf{r})] + \operatorname{div}\{\rho' \mathbf{v}_0 + \rho_0[(\mathbf{v}_0 \cdot \nabla)\delta\mathbf{r} - (\delta\mathbf{r} \cdot \nabla)\mathbf{v}_0]\} , \end{aligned} \quad (3.321)$$

on using Eqs (3.319) and (3.320). After some manipulation, using Eq. (3.316), this may be reduced to

$$\frac{\partial A}{\partial t} + \operatorname{div}(A \mathbf{v}_0) = 0 , \quad (3.322)$$

where

$$A = \rho' + \operatorname{div}(\rho_0 \delta\mathbf{r}) . \quad (3.323)$$

This may also, by using again Eq. (3.316), be written as

$$\rho_0 \frac{d}{dt} \left( \frac{A}{\rho_0} \right) = 0 , \quad (3.324)$$

from which we conclude that  $A = 0$ , *i.e.*, that Eq. (3.41) is valid in this case also.

To obtain the perturbed momentum equation we use Eq. (3.8); from the fact that Lagrangian perturbation and material time derivative commute,

$$\frac{d}{dt}(\delta\psi) = \delta \left( \frac{d\psi}{dt} \right) \quad (3.325)$$

for any quantity  $\psi$ , we then obtain

$$\rho_0 \frac{d\delta\mathbf{v}}{dt} = \delta(-\nabla p + \rho\mathbf{g}) = -\nabla p' + \rho_0\mathbf{g}' + \rho'\mathbf{g}_0 , \quad (3.326)$$

by using Eq. (3.317). Alternatively this may be written, from Eq. (3.319), as

$$\rho_0 \frac{d^2\delta\mathbf{r}}{dt^2} = -\nabla p' + \rho_0\mathbf{g}' + \rho'\mathbf{g}_0 , \quad (3.327)$$

or, by using Eq. (3.320) and neglecting the term quadratic in  $\mathbf{v}_0$ ,

$$\rho_0 \frac{\partial^2\delta\mathbf{r}}{\partial t^2} + 2\rho_0(\mathbf{v}_0 \cdot \nabla) \left( \frac{\partial\delta\mathbf{r}}{\partial t} \right) = -\nabla p' + \rho_0\mathbf{g}' + \rho'\mathbf{g}_0 , \quad (3.328)$$

which replaces Eq. (3.43). Finally, from the commutativity in Eq. (3.325), one finds that the perturbed energy Eq. (3.46) is still valid. Thus to this level of accuracy, the only change in the perturbation equations is the inclusion of the term in the first time derivative of  $\delta\mathbf{r}$  in Eq. (3.328).

As the equilibrium structure is independent of time, we may still separate the time dependence as  $\exp(-i\omega t)$ . Using, for simplicity, the same symbols for the amplitude functions in this separation, we obtain from the equations of motion

$$-\omega^2\rho_0\delta\mathbf{r} - 2i\omega\rho_0(\mathbf{v}_0 \cdot \nabla)\delta\mathbf{r} = -\nabla p' + \rho_0\mathbf{g}' + \rho'\mathbf{g}_0 . \quad (3.329)$$

Here the term in  $\mathbf{v}_0$  is a small perturbation. Thus we can investigate its effect by means of perturbation analysis, as discussed in Section 3.6.1. Following Eqs (3.244) and (3.245) we write Eq. (3.329) as

$$\omega^2\delta\mathbf{r} = \mathcal{F}(\delta\mathbf{r}) + \delta\mathcal{F}(\delta\mathbf{r}) , \quad (3.330)$$

where

$$\delta\mathcal{F}(\delta\mathbf{r}) = -2i\omega(\mathbf{v}_0 \cdot \nabla)\delta\mathbf{r} . \quad (3.331)$$

It now follows from Eq. (3.261) and the definition of the inner product that the change in  $\omega$  caused by the velocity field is, to first order,

$$\delta\omega = -i \frac{\int_V \rho_0 \delta\mathbf{r}^* \cdot (\mathbf{v}_0 \cdot \nabla) \delta\mathbf{r} dV}{\int_V \rho_0 |\delta\mathbf{r}|^2 dV} . \quad (3.332)$$

Although our main interest is rotation, we note that Eq. (3.332) has wider applicability. Lavelly & Ritzwoller (1992, 1993) made a detailed analysis of the effects of stationary flows, such as large-scale convection, on the properties of stellar oscillations. Roth & Stix (1999) applied the formalism to simple models of giant-cell convection in the Sun, and Roth *et al.* (2002) made more extensive numerical experiments to test whether such effects might be visible in current observational data. Also, Roth & Stix (2008) investigated the effects on global solar oscillation frequencies of meridional circulations, concluding that such effects might be detectable with suitable analysis of the extensive data now available.

### 3.8.3 The Effect of Pure Rotation

Now  $\mathbf{v}_0$  is taken to correspond to a pure rotation, with angular velocity  $\Omega = \Omega(r, \theta)$  that may depend on  $r$  and  $\theta$ . We assume that the entire star is rotating around a common axis and choose this as the axis of the spherical polar coordinate system. Then

$$\mathbf{v}_0 = \Omega r \sin \theta \mathbf{a}_\phi = \boldsymbol{\Omega} \times \mathbf{r}, \quad (3.333)$$

where we have introduced the rotation vector, defined to be along the rotation axis and of magnitude given by the angular velocity, by

$$\boldsymbol{\Omega} = \Omega(\cos \theta \mathbf{a}_r - \sin \theta \mathbf{a}_\theta). \quad (3.334)$$

We must now evaluate Eq. (3.332) for a normal mode of oscillation, and hence we have to consider the derivative in the direction of  $\mathbf{v}_0$ ; the relevant relations for the vector operations in spherical polar coordinates are given in Section C.2. From Eq. (3.122) the perturbations depend on  $\phi$  as  $\exp(im\phi)$ ; thus for a scalar quantity  $a$

$$(\mathbf{v}_0 \cdot \nabla)a = \Omega r \sin \theta \frac{1}{r \sin \theta} \frac{\partial a}{\partial \phi} = im\Omega a. \quad (3.335)$$

For a vector  $\mathbf{F}$  we use Eq. (C.10), and note that the directional derivatives of the coordinates of  $\mathbf{F}$  can be found by using Eq. (3.335). The result is

$$(\mathbf{v}_0 \cdot \nabla)\mathbf{F} = im\Omega\mathbf{F} + \Omega[-F_\phi \sin \theta \mathbf{a}_r - F_\phi \cos \theta \mathbf{a}_\theta + (F_r \sin \theta + F_\theta \cos \theta) \mathbf{a}_\phi]. \quad (3.336)$$

This can also be written as

$$(\mathbf{v}_0 \cdot \nabla)\mathbf{F} = im\Omega\mathbf{F} + \boldsymbol{\Omega} \times \mathbf{F}. \quad (3.337)$$

Thus Eq. (3.329) becomes

$$-\omega^2 \rho_0 \boldsymbol{\delta r} + 2m\omega \Omega \rho_0 \boldsymbol{\delta r} - 2i\omega \rho_0 \boldsymbol{\Omega} \times \boldsymbol{\delta r} = -\nabla p' + \rho_0 \mathbf{g}' + \rho' \mathbf{g}_0. \quad (3.338)$$

In the case of a constant angular velocity  $\Omega$  this equation may be obtained much more simply. Here we may transform to a coordinate system rotating with the star, with coordinates  $(r', \theta', \phi') = (r, \theta, \phi - \Omega t)$ . In this system the dependence of the perturbations on  $\phi'$  and  $t$  is as

$$\cos(m\phi' + m\Omega t - \omega t) = \cos(m\phi' - \omega't), \quad (3.339)$$

where  $\omega' \equiv \omega - m\Omega$  (see also the simple analysis in the introduction to this section). To write down the equations of motion in the rotating system we note that in this system there is no term in the equilibrium velocity; however, we must add the term  $-2\rho_0\boldsymbol{\Omega} \times \boldsymbol{\delta v}$  from the Coriolis force on the right-hand side. Using that to the required order of precision the velocity perturbation is  $\boldsymbol{\delta v} = -i\omega\boldsymbol{\delta r}$ , the result is

$$-\omega'^2\rho_0\boldsymbol{\delta r} = -\nabla p' + \rho_0\boldsymbol{g}' + \rho'\boldsymbol{g}_0 + 2i\omega\rho_0\boldsymbol{\Omega} \times \boldsymbol{\delta r}. \quad (3.340)$$

But this agrees with Eq. (3.338), if a term in  $\Omega^2$  is neglected.

In the general case of non-uniform rotation it might be argued that this relation would hold locally at any given point in the fluid, thus resulting again in Eq. (3.338). However, it is not obvious whether this is a consistent derivation of that relation, or whether it results from fortuitous cancellation of terms coming from the variation of  $\Omega$ . In any case it allows a simple interpretation of the two terms in  $\Omega$  in Eq. (3.338): the first term comes from the coordinate rotation, or equivalently from the advection of the rotating star relative to an observer in an inertial frame, and the second term comes from the Coriolis force. Neglecting the Coriolis term it follows from this analysis that a reasonable generalization of the argument leading to Eq. (3.315) for non-uniform rotation is to replace  $\Omega$  by the average

$$\langle \Omega \rangle \simeq \frac{\int \Omega |\boldsymbol{\delta r}|^2 dV}{\int |\boldsymbol{\delta r}|^2 dV}. \quad (3.341)$$

We must now calculate the integrals in Eq. (3.332). By substituting  $\boldsymbol{\delta r}$ , given by the complex form of Eq. (3.132), for  $\boldsymbol{F}$  in Eq. (3.336) we obtain

$$(\boldsymbol{v}_0 \cdot \nabla)\boldsymbol{\delta r} = im\Omega\boldsymbol{\delta r} + \sqrt{4\pi}\Omega \left[ -\xi_h \frac{\partial Y_l^m}{\partial \phi} \boldsymbol{a}_r - \xi_h \frac{\cos \theta}{\sin \theta} \frac{\partial Y_l^m}{\partial \phi} \boldsymbol{a}_\theta \right. \\ \left. + \left( \xi_r \sin \theta Y_l^m + \xi_h \cos \theta \frac{\partial Y_l^m}{\partial \theta} \right) \boldsymbol{a}_\phi \right]. \quad (3.342)$$

Thus

$$\tilde{R} \equiv \int_V \rho_0 \boldsymbol{\delta r}^* \cdot (\boldsymbol{v}_0 \cdot \nabla) \boldsymbol{\delta r} dV = im \int_V \rho_0 \Omega |\boldsymbol{\delta r}|^2 dV \\ + 4\pi \int_V \rho_0 \Omega \left[ -\xi_r^* (Y_l^m)^* \xi_h \frac{\partial Y_l^m}{\partial \phi} - |\xi_h|^2 \left( \frac{\partial Y_l^m}{\partial \theta} \right)^* \frac{\partial Y_l^m}{\partial \phi} \frac{\cos \theta}{\sin \theta} \right. \\ \left. + \xi_h^* \xi_r \left( \frac{\partial Y_l^m}{\partial \phi} \right)^* Y_l^m + |\xi_h|^2 \left( \frac{\partial Y_l^m}{\partial \phi} \right)^* \frac{\partial Y_l^m}{\partial \theta} \frac{\cos \theta}{\sin \theta} \right] dV. \quad (3.343)$$

Here  $Y_l^m$  is always multiplied by its complex conjugate, so that the  $\phi$ -dependence cancels. Hence the integration over  $\phi$  is trivial. It should be noticed also that all terms in the second integral in Eq. (3.343) contain the  $\phi$ -derivative of  $Y_l^m$  or its complex conjugate, which is proportional to  $im$ . Thus  $\tilde{R}$  contains  $im$  as a factor, and can be written, using Eq. (3.122), as

$$\tilde{R} = im 8\pi^2 c_{lm}^2 R_{nlm}, \quad (3.344)$$

where

$$\begin{aligned} R_{nlm} = & \int_0^\pi \sin \theta d\theta \int_0^R \left\{ |\xi_r(r)|^2 P_l^m(\cos \theta)^2 \right. \\ & + |\xi_h(r)|^2 \left[ \left( \frac{dP_l^m}{d\theta} \right)^2 + \frac{m^2}{\sin^2 \theta} P_l^m(\cos \theta)^2 \right] \\ & - P_l^m(\cos \theta)^2 [\xi_r^*(r)\xi_h(r) + \xi_r(r)\xi_h^*(r)] \\ & \left. - 2P_l^m(\cos \theta) \frac{dP_l^m}{d\theta} \frac{\cos \theta}{\sin \theta} |\xi_h(r)|^2 \right\} \Omega(r, \theta) \rho_0(r) r^2 dr. \end{aligned} \quad (3.345)$$

Similarly, the denominator in Eq. (3.332) can be written as

$$\tilde{I} \equiv \int_V \rho_0 |\delta \mathbf{r}|^2 dV = 8\pi^2 c_{lm}^2 I_{nlm}, \quad (3.346)$$

where

$$\begin{aligned} I_{nlm} = & \int_0^\pi \sin \theta d\theta \int_0^R \left\{ |\xi_r(r)|^2 P_l^m(\cos \theta)^2 \right. \\ & + |\xi_h(r)|^2 \left[ \left( \frac{dP_l^m}{d\theta} \right)^2 + \frac{m^2}{\sin^2 \theta} P_l^m(\cos \theta)^2 \right] \right\} \rho_0(r) r^2 dr \\ = & \frac{2}{2l+1} \frac{(l+|m|)!}{(l-|m|)!} \int_0^R [|\xi_r|^2 + l(l+1)|\xi_h|^2] \rho_0(r) r^2 dr \end{aligned} \quad (3.347)$$

(compare with Eq. (3.139)). From Eqs (3.332), (3.344) and (3.346) we finally obtain the *rotational splitting*, i.e., the perturbation to the frequencies caused by rotation, as

$$\delta\omega_{nlm} = m \frac{R_{nlm}}{I_{nlm}}. \quad (3.348)$$

This may obviously be written in the form

$$\delta\omega_{nlm} = m \int_0^R \int_0^\pi K_{nlm}(r, \theta) \Omega(r, \theta) r dr d\theta, \quad (3.349)$$

where the *kernel*  $K_{nlm}$  is defined by Eqs (3.345) and (3.347).

From Eqs (3.345) and (3.347), as well as the symmetry property of the Legendre function with respect to  $m$  (Eq. (B.8)), it follows that  $R_{nlm}/I_{nlm}$  is an even function of  $m$  and hence that  $\delta\omega_{nlm}$  is an odd function of  $m$ ,

$$\delta\omega_{nl-m} = -\delta\omega_{nlm} . \quad (3.350)$$

Also, since  $P_l^m(x)$  is either symmetrical or antisymmetrical around  $x = 0$ , the factor multiplying  $\Omega(r, \theta)$  in Eq. (3.345) is symmetrical around the equator,  $\theta = \pi/2$ ; thus

$$K_{nlm}(r, \pi - \theta) = K_{nlm}(r, \theta) . \quad (3.351)$$

This has the important consequence that the rotational frequency splitting is sensitive only to the part of  $\Omega$  that is symmetrical around the equator.

The rotational splitting for a uniformly rotating star was first obtained by Cowling & Newing (1949) and Ledoux (1949). The general case, as presented here, was considered by Hansen, Cox & van Horn (1977) and Gough (1981).

### 3.8.4 Properties of Rotational Splitting

To proceed we must make an explicit assumption about the variation of  $\Omega$  with  $\theta$ . For simplicity we shall assume first that  $\Omega$  is independent of  $\theta$  (even though, as mentioned earlier, the solar surface rotation depends on  $\theta$ ; this may well be the case for other pulsating stars). In this case the integrals over  $\theta$  in Eq. (3.345) only involve Legendre functions and may be evaluated analytically. Two of the terms require a little care. One contains

$$\begin{aligned} \int_0^\pi P_l^m(\cos \theta) \frac{dP_l^m}{d\theta} \frac{\cos \theta}{\sin \theta} \sin \theta d\theta &= - \int_{-1}^1 P_l^m(x) \frac{dP_l^m}{dx} x dx \\ &= - \frac{1}{2} x P_l^m(x)^2 \Big|_{-1}^1 + \frac{1}{2} \int_{-1}^1 P_l^m(x)^2 dx , \end{aligned} \quad (3.352)$$

and here the integrated term vanishes, as  $P_l^m(x)$  is either symmetrical or anti-symmetrical in  $x = \cos \theta$ . The other non-trivial integral, which was already encountered in the evaluation of  $I_{nlm}$ , is

$$\begin{aligned} &\int_0^\pi \left[ \left( \frac{dP_l^m}{d\theta} \right)^2 + \frac{m^2}{\sin^2 \theta} P_l^m(\cos \theta)^2 \right] \sin \theta d\theta \\ &= - \int_0^\pi P_l^m(\cos \theta) \left[ \frac{d}{d\theta} \left( \sin \theta \frac{dP_l^m}{d\theta} \right) - \frac{m^2}{\sin \theta} P_l^m(\cos \theta) \right] d\theta \\ &= L^2 \int_{-1}^1 P_l^m(x)^2 dx , \end{aligned} \quad (3.353)$$

by using that  $P_l^m$  satisfies Eq. (3.118). As usual, we have introduced  $L^2 \equiv l(l+1)$ . For adiabatic oscillations we can take  $\xi_r$  and  $\xi_h$  to be real. Thus, from Eqs (3.345), (3.347) and (3.348), we finally obtain for the rotational splitting

$$\delta\omega_{nlm} = m \frac{\int_0^R \Omega(r) (\xi_r^2 + L^2 \xi_h^2 - 2\xi_r \xi_h - \xi_h^2) r^2 \rho dr}{\int_0^R (\xi_r^2 + L^2 \xi_h^2) r^2 \rho dr} , \quad (3.354)$$

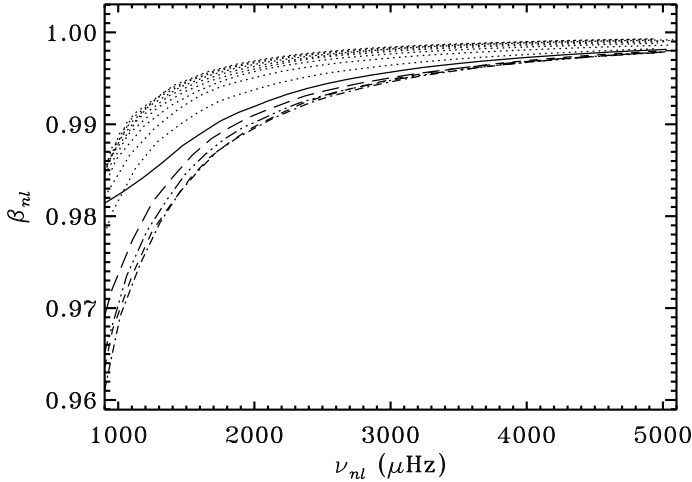


**Fig. 3.38.** Coefficients  $\beta_{nl}$  for acoustic modes in a normal solar model. Points corresponding to fixed  $l$  have been connected, according to the following line styles:  $l = 1$ : solid;  $l = 2$ : dashed;  $l = 3$ : dash-dot;  $l = 4$ : long-dash-dot;  $l = 5$ : short-dash-dot;  $l = 10, 15, \dots, 50$ : dotted (with  $\beta_{nl}$  increasing with  $l$ ).

where we have dropped the subscript “0” on  $\rho$ . It should be noticed that the integrands in Eq. (3.354) are given solely in terms of  $\xi_r$ ,  $\xi_h$  and  $l$ , and therefore are independent of  $m$ . Hence in the case of spherically symmetric rotation the rotational splitting is proportional to  $m$ .

It is convenient to write Eq. (3.354) as

$$\delta\omega_{nlm} = m\beta_{nl} \int_0^R K_{nl}(r)\Omega(r)dr , \quad (3.355)$$

where

$$K_{nl} = \frac{(\xi_r^2 + L^2\xi_h^2 - 2\xi_r\xi_h - \xi_h^2) r^2 \rho}{\int_0^R (\xi_r^2 + L^2\xi_h^2 - 2\xi_r\xi_h - \xi_h^2) r^2 \rho dr} , \quad (3.356)$$

and

$$\beta_{nl} = \frac{\int_0^R (\xi_r^2 + L^2\xi_h^2 - 2\xi_r\xi_h - \xi_h^2) r^2 \rho dr}{\int_0^R (\xi_r^2 + L^2\xi_h^2) r^2 \rho dr} . \quad (3.357)$$

By using this definition we ensure that the *rotational kernel*  $K_{nl}$  is unimodular, i.e.,

$$\int_0^R K_{nl}(r)dr = 1 . \quad (3.358)$$

For high-order or high-degree p modes the terms in  $\xi_r^2$  and  $L^2\xi_h^2$  dominate; as shown in Fig. 3.38,  $\beta_{nl}$  is then close to one. Physically, the neglected terms in Eq. (3.357) arise from the Coriolis force; thus rotational splitting for p modes is dominated by advection, and Eq. (3.355) essentially corresponds to the average angular velocity defined in Eq. (3.341). For high-order g modes, on the other hand, we can neglect the terms containing  $\xi_r$ , so that

$$\beta_{nl} \simeq 1 - \frac{1}{L^2}. \quad (3.359)$$

For uniform rotation, where  $\Omega = \Omega_s$  is constant,

$$\delta\omega_{nlm} = m\beta_{nl}\Omega_s. \quad (3.360)$$

In this case the effect of rotation is completely given by the constant  $\beta_{nl}$ . For high-order or high-degree p modes, where  $\beta_{nl} \simeq 1$ , the rotational splitting between adjacent  $m$ -values is given approximately by the rotation rate. For high-order g modes, on the other hand,  $\beta_{nl}$  is given by Eq. (3.359). In particular, the splitting of high-order g modes of degree 1 is only *half* the rotation rate.

It is common to describe the effect of uniform rotation also in terms of *the Ledoux constant*

$$C_{nl} = 1 - \beta_{nl} = \frac{\int_0^R (2\xi_r\xi_h + \xi_h^2) r^2 \rho dr}{\int_0^R (\xi_r^2 + L^2\xi_h^2) r^2 \rho dr} \quad (3.361)$$

(Ledoux 1951). It is easily seen that in the frame rotating with the star the rotational splitting is given by  $-mC_{nl}\Omega$ , resulting from the Coriolis force. It follows from the above discussion that for high-order or high-degree p modes  $C_{nl}$  is small.

Figure 3.39 shows a few kernels for the case of spherically symmetric rotation, for high-order p modes in a model of the present Sun. It is evident that the kernels increase rapidly towards the surface; it follows from the asymptotic properties of the eigenfunctions in Eq. (3.227) that the overall variation of the kernels scales as  $c^{-1}$ , reflecting also that the sensitivity of the mode to a given part of the star depends on the time spent by the mode, regarded as a superposition of sound waves, in that region (see also Eq. (7.26) below). Also, the kernels clearly get very small beneath the turning point, but are locally enhanced just above it. This effect arises from the term in  $\xi_h$  in Eq. (3.356); physically it corresponds to the fact that the waves travel approximately horizontally in this region, and hence spend a relatively long time there.

In other asteroseismically interesting cases the rotational kernels may have a rather different structure. This is the case for solar-like oscillations giving rise to mixed modes (see Fig. 7.66), or for stars with heat driven pulsations in low-order p or g modes (see Figs 7.81 and 7.88). In such cases the rotational splitting may have a substantial sensitivity to the rotation of the deep stellar interior.

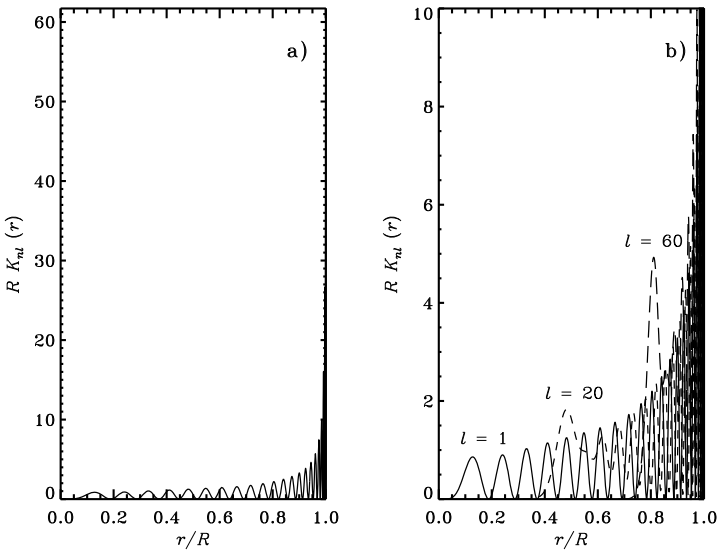


**Fig. 3.39.** Kernels  $K_{nl}$  for the frequency splitting caused by spherically symmetric rotation (*cf.* Eq. (3.356)) in a model of the present Sun (the kernels are made dimensionless by scaling with  $R$ , so as to correspond to integration with respect to the abscissa  $r/R$ ). In a) is plotted  $RK_{nl}(r)$  for a mode with  $l = 1$ ,  $n = 22$  and  $\nu = 3239\ \mu\text{Hz}$ . The maximum value of  $RK_{nl}(r)$  is 62. In b) is shown the same mode, on an expanded vertical scale, (—) together with the modes  $l = 20$ ,  $n = 17$ ,  $\nu = 3375\ \mu\text{Hz}$  (-----), and  $l = 60$ ,  $n = 10$ ,  $\nu = 3234\ \mu\text{Hz}$  (----). Notice that the kernels almost vanish inside the turning-point radius  $r_t$ , and that there is an accumulation just outside the turning point.

In the general case, where  $\Omega$  depends on both  $r$  and  $\theta$ , the rotational splitting may be computed from Eqs (3.345), (3.347) and (3.348), by evaluating the two-dimensional integral in Eq. (3.345). This integral is in general  $m$ -dependent, and so the splitting is no longer a linear function of  $m$ . Selected examples of the resulting kernels  $K_{nlm}(r, \theta)$  (*cf.* Eq. (3.349)) are illustrated in Fig. 3.40.

To illustrate the properties of the splitting, it is instructive to rewrite Eq. (3.345) for  $R_{nlm}$ , using integration by parts:

$$R_{nlm} = \int_0^\pi d\theta \int_0^R P_l^m(\cos \theta)^2 \left\{ [\xi_r^2 + (L^2 - 1)\xi_h^2 - 2\xi_r\xi_h] \sin \theta \Omega(r, \theta) + \xi_h^2 \left( \frac{3}{2} \cos \theta \frac{\partial \Omega}{\partial \theta} + \frac{1}{2} \sin \theta \frac{\partial^2 \Omega}{\partial \theta^2} \right) \right\} r^2 \rho dr \quad (3.362)$$

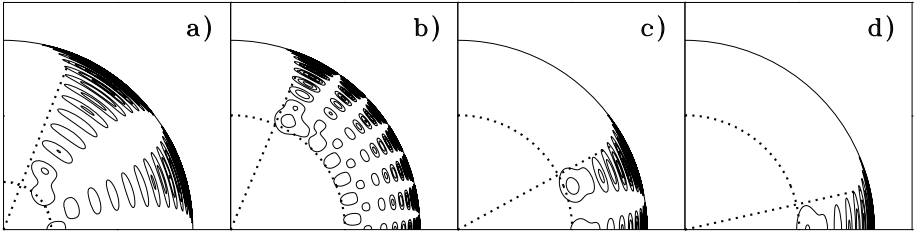


**Fig. 3.40.** Contour plots of rotational kernels  $K_{nlm}$  in a solar quadrant. The modes all have frequencies near 2 mHz; the following pairs of  $(l, m)$  are included: a)  $(5, 2)$ ; b)  $(20, 8)$ ; c)  $(20, 17)$ ; and d)  $(20, 20)$ . The dotted circles mark the locations of the lower radial turning point  $r_t$  and the dotted lines show the latitudinal turning points, at co-latitude  $\Theta$ , defined by  $\sin \Theta = m/L$  (cf. Eq. (B.16)).

(Cuypers 1980). We consider again the case of high-order p modes; here the terms in  $\xi_r^2$  and  $L^2\xi_h^2$  dominate, and consequently

$$\delta\omega_{nlm} \simeq m \frac{\int_0^\pi \sin \theta [P_l^m(\cos \theta)]^2 \int_0^R \Omega(r, \theta) [\xi_r(r)^2 + L^2\xi_h(r)^2] r^2 \rho dr d\theta}{\int_0^\pi \sin \theta [P_l^m(\cos \theta)]^2 d\theta \int_0^R [\xi_r(r)^2 + L^2\xi_h(r)^2] r^2 \rho dr}. \quad (3.363)$$

Hence, the splitting is simply an average of the angular velocity  $\Omega(r, \theta)$ , weighted by  $r^2 \rho [\xi_r(r)^2 + L^2\xi_h(r)^2] P_l^m(\cos \theta)^2$ , corresponding to the simple average in Eq. (3.341).

### 3.8.5 Effects of Rotation on Low-Frequency Modes

The simple perturbative treatment fails when  $\omega$  is of the same order of, or smaller than,  $\Omega$  since in that case the term in the Coriolis force in Eq. (3.338) cannot be regarded as a small perturbation compared with the acceleration term in  $\omega^2$ . This is relevant, for example, for SPB and  $\gamma$  Dor stars with high-order g modes. This needs a treatment beyond the simple spheroidal modes considered so far. For simplicity we only consider uniform rotation in this section and assume it to be so slow that terms quadratic in  $\Omega$  can still be neglected. Also, we impose the Cowling approximation; this is reasonable since the relevant modes, except for very rapid rotation, are high-order g modes. Finally, we consider only the case of adiabatic oscillations.

In terms of spherical harmonics the equations are still separable in  $\phi$  (since the equilibrium model is rotationally symmetric) but not in latitude. Thus motion corresponding to different degrees is coupled. Formally, the solutions to Eq. (3.338) treated in a non-perturbative manner, together with Eq. (3.41) and the adiabatic relation Eq. (3.50) cannot be expressed in terms of single

spherical harmonics. Furthermore, the full solution for the displacement includes a component corresponding to the toroidal motion (*cf.* Eq. (3.144)). As a result of the completeness of the set of angular functions the solution can be expanded on these functions. Owing to the rotational symmetry, we can still write the  $\phi$  dependence as  $\exp(im\phi)$ ; the dependence on latitude then only involves Legendre functions such that  $l \geq |m|$ . Consequently, writing the displacement as

$$\boldsymbol{\delta r} = \xi_r \mathbf{a}_r + \xi_\theta \mathbf{a}_\theta + \xi_\phi \mathbf{a}_\phi , \quad (3.364)$$

we express  $\xi_r$ ,  $\xi_\theta$  and  $\xi_\phi$  as

$$\xi_r = \sum_{l \geq |m|}^{\infty} \Xi_{lm}(r) Y_l^m(\theta, \phi) e^{-i\omega t} ,$$

$$\xi_\theta = \sum_{l \geq |m|}^{\infty} \left[ H_{lm}(r) \frac{\partial Y_l^m}{\partial \theta} + T_{lm}(r) \frac{1}{\sin \theta} \frac{\partial Y_l^m}{\partial \phi} \right] e^{-i\omega t} , \quad (3.365)$$

$$\xi_\phi = \sum_{l \geq |m|}^{\infty} \left[ H_{lm}(r) \frac{1}{\sin \theta} \frac{\partial Y_l^m}{\partial \phi} - T_{lm}(r) \frac{\partial Y_l^m}{\partial \theta} \right] e^{-i\omega t} ; \quad (3.366)$$

also, the perturbation to a scalar quantity, *e.g.*, pressure  $p$ , is written as

$$p' = \sum_{l \geq |m|}^{\infty} p'_{lm}(r) Y_l^m(\theta, \phi) e^{-i\omega t} \quad (3.367)$$

(see Zahn 1966). Substituting these expansions into the oscillation equations one obtains an infinite set of coupled differential equations for the radial expansion functions. The properties and numerical solutions of these equations, after suitable truncation, were discussed, for example, by Berthomieu *et al.* (1978), Lee & Saio (1986, 1987) and Dziembowski & Kosovichev (1987a,b,c). As noted by, for example, Lee & Saio (1987) the equations are very considerably simplified by neglecting the tangential component of the rotation vector  $\boldsymbol{\Omega}$ , *i.e.*,  $-\Omega \sin \theta \mathbf{a}_\theta$  in Eq. (3.334); this approximation, which was essentially also used by Berthomieu *et al.* (1978), is commonly used in geophysics where it is known as *the traditional approximation* (*e.g.*, Eckart 1960). It is then possible, through a transformation of the expansion in  $\theta$ , to bring the equations in a fully separated form that is very similar to the equations of pulsation in the non-rotating case (see also Unno *et al.* 1989).

A simple justification for the traditional approximation can be obtained from a local analysis of the oscillation equations, extending the analysis in Section 3.1.4.2 to include the effects of rotation (*e.g.*, Unno *et al.* 1989; Thorne & Gough, in preparation). In the appropriate limit of high-order g modes, this leads to the dispersion relation

$$\omega^2 \simeq \frac{N^2 k_h^2 + (2\boldsymbol{\Omega} \cdot \mathbf{k})^2}{k^2} . \quad (3.368)$$

The resulting waves may be characterized as gravito-rotational waves, with a restoring force resulting from a combination of buoyancy and the Coriolis force. Since  $k_r \gg k_h$  the term in  $\boldsymbol{\Omega} \cdot \mathbf{k}$  is dominated by the radial component

of  $\Omega$  and hence the tangential component can be neglected. This is the traditional approximation (see also Lee & Saio 1997). It should be noted that Eq. (3.368) was derived under the assumption that  $|N| \gg \omega$ . Thus the traditional approximation is not valid in convection zones.

The separation of variables can be derived more simply in terms of *Laplace's Tidal Equation* (Laplace 1799).<sup>26</sup> This has been used extensively in geophysics (see Eckart 1960) and was introduced to the study of stellar pulsations by Bildsten *et al.* (1996). To derive it we consider Eq. (3.338) in a frame rotating with the star, so that the term in  $2m\omega\Omega\delta r$  disappears. Expanding the result in component form we obtain

$$\begin{aligned} -\omega^2\xi_r + 2i\omega\Omega\sin\theta\xi_\phi &= -\frac{1}{\rho_0}\frac{\partial p'}{\partial r} - \frac{\rho'}{\rho_0}g_0 , \\ -\omega^2\xi_\theta + 2i\omega\Omega\cos\theta\xi_\phi &= -\frac{1}{\rho_0}\frac{\partial p'}{\partial\theta} , \\ -\omega^2\xi_\phi - 2i\omega\Omega(\sin\theta\xi_r + \cos\theta\xi_\theta) &= -\frac{1}{\rho_0}\frac{1}{\sin\theta}\frac{\partial p'}{\partial\phi} . \end{aligned} \quad (3.369)$$

The traditional approximation now consists of neglecting  $\Omega\sin\theta$  in the first and third of these equations. As a result, the last two equations can be solved for  $\xi_\theta, \xi_\phi$  in terms of the derivatives of  $p'$ . The result can be expressed as

$$\begin{aligned} \xi_\theta &= -\frac{1}{r\omega^2\rho_0}\frac{(1-\mu^2)^{1/2}}{1-s^2\mu^2}\left[\frac{\partial p'}{\partial\mu} - is\frac{\mu}{(1-\mu^2)}\frac{\partial p'}{\partial\phi}\right] , \\ \xi_\phi &= \frac{1}{r\omega^2\rho_0}\frac{(1-\mu^2)^{1/2}}{1-s^2\mu^2}\left[is\mu\frac{\partial p'}{\partial\mu} + \frac{1}{(1-\mu^2)}\frac{\partial p'}{\partial\phi}\right] , \end{aligned} \quad (3.370)$$

where  $\mu = \cos\theta$  and we introduced the *rotation parameter*

$$s = \frac{2\Omega}{\omega} . \quad (3.371)$$

Substituting Eqs (3.370) into the equation of continuity, Eq. (3.41), and assuming that  $p'$  depends on  $\phi$  as  $\exp(im\phi)$ , we obtain

$$\begin{aligned} 0 &= \rho' + \frac{1}{r^2}\frac{\partial}{\partial r}(r^2\rho_0\xi_r) \\ &\quad + \frac{1}{r^2\omega^2}\left\{\frac{\partial}{\partial\mu}\left(\frac{1-\mu^2}{1-s^2\mu^2}\frac{\partial p'}{\partial\mu}\right) + \frac{1}{1-s^2\mu^2}\left[\frac{ms(1+s^2\mu^2)}{1-s^2\mu^2} - \frac{m^2}{1-\mu^2}\right]p'\right\} . \end{aligned} \quad (3.372)$$

It follows that the dependence of  $\xi_r$  and  $p'$  on  $\theta$  and  $\phi$  can be separated in terms of a function of the form  $\Theta_s(\mu)\exp(im\phi)$ , provided that  $\Theta_s$  is a regular solution to the eigenvalue problem

$$\mathcal{L}_s\Theta_s = -\hat{L}_s^2\Theta_s , \quad (3.373)$$

---

<sup>26</sup> See Première Partie, Tome Second, Livre IV, Chapitre III, n°. 15.

where the operator  $\mathcal{L}_s$  is defined by

$$\mathcal{L}_s \equiv \frac{d}{d\mu} \left( \frac{1 - \mu^2}{1 - s^2\mu^2} \frac{d}{d\mu} \right) + \frac{1}{1 - s^2\mu^2} \left[ \frac{ms(1 + s^2\mu^2)}{1 - s^2\mu^2} - \frac{m^2}{1 - \mu^2} \right]. \quad (3.374)$$

Equation (3.373) is known as the Laplace tidal equation, and the regular solutions  $\Theta_s$  are the *Hough functions*,<sup>27</sup> extensively discussed by Longuet-Higgins (1968) (see also Bildsten *et al.* 1996; Lee & Saio 1997; Townsend 2003a; Dziembowski *et al.* 2007). Bildsten *et al.* (1996) discussed the numerical solution of this equation, particularly the treatment of the regular singularities at  $\mu = \pm s^{-1}$  when  $s > 1$ . We also note that Dzhalilov & Staude (2004) generalized the Laplace tidal equation to the case of the angular velocity varying in latitude or radius.

It is evident that  $\xi_r$  can be similarly separated in the first of Eqs (3.369), given the neglect of the term in  $\xi_\phi$ ; given  $\Theta_s$ , the remaining components of the displacement can be determined from Eqs (3.370). Also, the adiabatic condition, Eq. (3.50), can obviously be separated. Thus we obtain the following equations for the amplitude functions for adiabatic oscillations in the traditional approximation:

$$\frac{d\xi_r}{dr} = - \left( \frac{2}{r} - \frac{1}{\Gamma_1} H_p^{-1} \right) \xi_r + \frac{1}{\rho c^2} \left( \frac{\hat{L}_s^2 c^2}{r^2 \omega^2} - 1 \right) p', \quad (3.375)$$

$$\frac{dp'}{dr} = \rho(\omega^2 - N^2) \xi_r - \frac{1}{\Gamma_1} H_p^{-1} p'. \quad (3.376)$$

These are evidently identical to the equations in the non-rotating case in the Cowling approximation, Eqs (3.175),<sup>28</sup> except that  $S_l^2 = l(l+1)c^2/r^2$  has been replaced by  $\hat{L}_s^2 c^2/r^2$ . Thus the structure of the equations, and hence the insights that have been obtained by analysing them, carries over immediately to the rotating case in this approximation. It should also be noted that for  $s = 0$ , Eqs (3.373) and (3.374) reduce to Eq. (3.118) for the Legendre function, with  $\hat{L}_s^2 = \Lambda$ . Thus in the non-rotating limit we recover the separation in terms of spherical harmonics (up to the normalization), with  $\hat{L}_0^2 = L^2 = l(l+1)$ . We also note that for  $m = 0$ , a constant  $\Theta_s$  is a solution to Eq. (3.373), with  $\hat{L}_s = 0$ . Thus, regardless of the angular velocity, the radial oscillations are solutions in the traditional (and Cowling) approximation, with frequencies unaffected by the rotation. It is conventional, and convenient, to identify modes obtained in the traditional approximation by  $(l, m)$ , where  $l$  is the degree such that  $\hat{L}_s^2 \rightarrow l(l+1)$  for  $s \rightarrow 0$ .

<sup>27</sup> See Hough (1898).

<sup>28</sup> We note, following Thorne & Gough (in preparation), that the Poisson equation (3.113) cannot be similarly separated; thus this does not generalize to the full set of equations. However, as already noted the effects of the perturbation to the gravitational potential are likely small for the relevant modes and hence could be treated through a perturbation expansion.

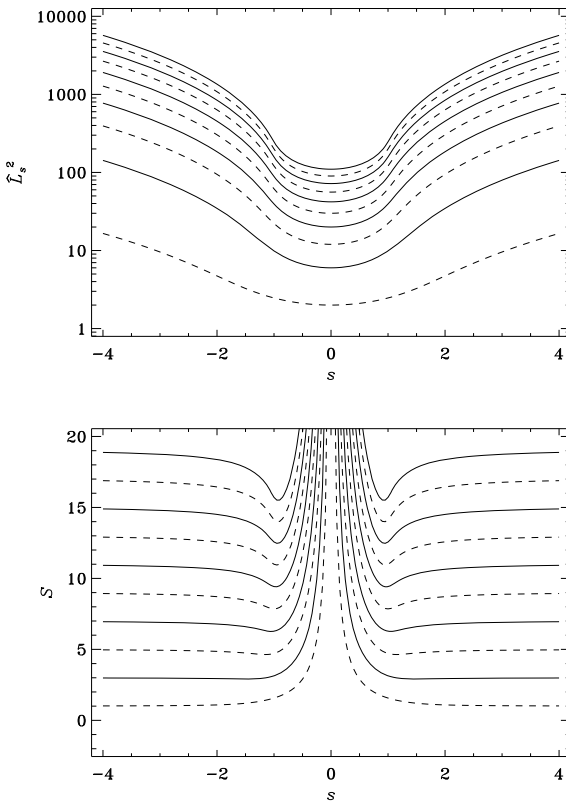


**Fig. 3.41.** The top panel shows numerically computed eigenvalues  $\hat{L}_s^2$  of Laplace's Tidal Equation as functions of the rotation parameter  $s$ , for  $m = 0$ . Modes symmetric around  $\mu = 0$  are shown as solid curves, antisymmetric modes as dashed curves. The lowest case corresponds to  $l = 1$  at  $s = 0$ . The lower panel shows the quantity  $S$  (cf. Eq. (3.377)) resulting from Townsend's (2003a) approximate analysis for the same modes.

Numerical solutions for the eigenvalue  $\hat{L}_s^2$ , for  $m = 0$  and 2, are illustrated in the top panels of Figs 3.41 and 3.42 (we return to the bottom panels below).<sup>29</sup> Here we have distinguished the modes according to their parity around  $\mu = 0$ , modes where  $\Theta_s$  is symmetric being shown with continuous curves and those with antisymmetric  $\Theta_s$  with dashed curves. As mentioned above the values at  $s = 0$  correspond to  $L^2 = l(l + 1)$  for  $l \geq m$  (the case corresponding

<sup>29</sup> We are very grateful to D. O. Gough for his assistance in computing the solutions to the Laplace Tidal Equation illustrated here.

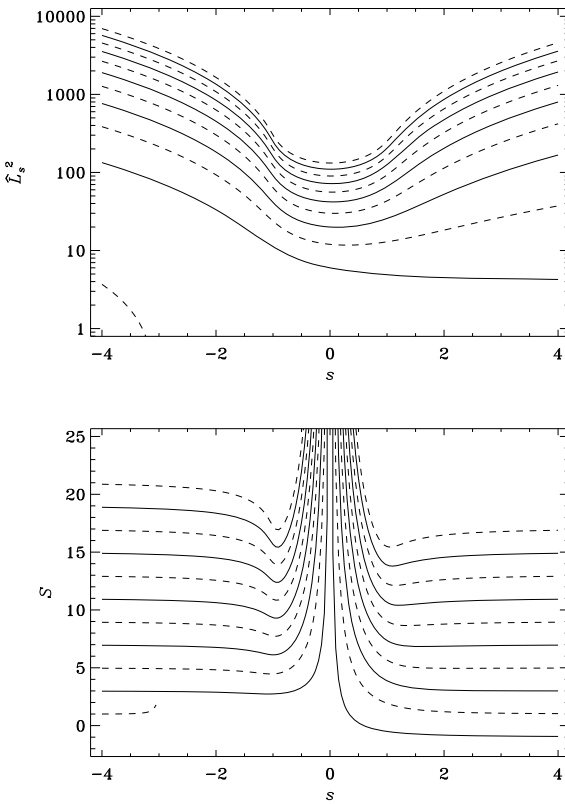


**Fig. 3.42.** Numerically computed eigenvalues  $\hat{L}_s^2$  of Laplace's Tidal Equation, for  $m = 2$ . See caption to Fig. 3.41.

to  $l = 0$  is obviously excluded in Fig. 3.41). It should also be noticed that in Fig. 3.42 a new branch of eigenvalues appears for large negative  $s$ ; these correspond to modes that have no counterpart in the non-rotating case.

$\hat{L}_s^2$  generally increases with increasing  $|s|$ . From the form of Eqs (3.375) and (3.376), and the analogy with the equations in the non-rotating case, it is natural to identify  $\hat{L}_s/r$  with a horizontal wavenumber, such that the increase in  $\hat{L}_s$  corresponds to an increase in  $k_h$  and hence a decrease in the horizontal wavelength. This in fact is in accordance with the horizontal behaviour of the computed eigenfunctions, as reflected in  $\Theta_s$ . As an example, Fig. 3.43 shows  $\Theta_s$ , normalized to  $\Theta_s = 1$  at  $\mu = 0$ , as a function of  $\mu$ , for the lowest symmetric case in Fig. 3.41 (and hence corresponding to  $l = 2$  for  $s = 0$ ). At  $s = 0$  the solution is  $\Theta_s(\mu) \propto P_2(\mu)$ ,  $P_2$  being the Legendre polynomial. However, it is

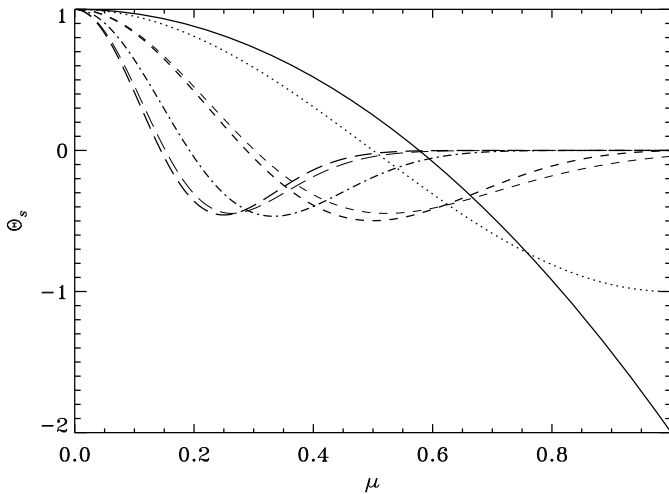


**Fig. 3.43.** Numerically computed solutions  $\Theta_s$  of Laplace's Tidal Equation, for  $m = 0$  and the mode reducing to  $l = 2$  at  $s = 0$ , as functions of  $\mu$ . The solutions have been normalized to 1 at  $\mu = 0$ . The cases shown are  $s = 0$  (solid),  $s = 1$  (dotted),  $s = 2$  (dashed),  $s = 3$  (dot-dashed) and  $s = 4$  (long dashes). The thin lines for  $s = 2$  and 4 show the approximate solution obtained by Townsend (2003a), given in Eq. (3.379).

evident that for  $s \geq 2$  the mode becomes increasingly confined to low  $\mu$ , *i.e.*, towards the equator. This effect was interpreted as confinement in a wave guide by the Coriolis force by Matsuno (1966) in a terrestrial setting; the importance for stellar pulsations was probably first recognized by Lee & Saio (1990).

Townsend (2003a) noted that this property allowed an illuminating approximation to the Laplace Tidal equation for large  $|s|$ ,<sup>30</sup> by neglecting  $\mu^2$  compared with 1 he obtained an equation with a solution in terms of Hermite polynomials. Also, the eigenvalues satisfy

$$\frac{\hat{L}_s^2 - m^2 - ms}{\hat{L}_s |s|} = S \simeq 2\zeta + 1 , \quad (3.377)$$

where  $\zeta$  is an integer. This property is illustrated in Figs 3.41 and 3.42, where the lower panels show  $S$  computed from Eq. (3.377). It is evident that this quantity does indeed approximate odd integers for large  $|s|$ . The corresponding

<sup>30</sup> A detailed asymptotic analysis in this limit was carried out by Longuet-Higgins (1968).

solution can be written in terms of the new independent variable

$$v \equiv (\hat{L}_s |s|)^{1/2} \mu \quad (3.378)$$

as

$$\Theta_s(\mu) = c_s \left[ \zeta \left( 1 - \frac{m}{\hat{L}_s} \right) H_{\zeta-1}(v) - \frac{1}{2} \left( 1 + \frac{m}{\hat{L}_s} \right) H_{\zeta+1}(v) \right] \exp(-v^2/2), \quad (3.379)$$

clearly displaying the confinement with increasing  $|s|$ ; here  $H_k$  is the Hermite polynomial of order  $k$ . The thin curves in Fig. 3.43 show this approximation for  $s = 2$  and  $4$ ; it is evident that in the latter case the agreement with the numerical solution is reasonable.

The physical nature of the solutions to Laplace's Tidal Equation, including the characterization of the modes obtained in the asymptotic limit of large  $|s|$ , has been discussed in detail by, for example, Longuet-Higgins (1968), Lee & Saio (1997) and Townsend (2003a). For  $|s| > 1$  the spectrum of solutions also include modes with negative  $\hat{L}_s^2$ , not considered here, which Lee & Saio identified as oscillatory convective modes, stabilized by rotation.<sup>31</sup> The modes with  $m = 0$  (*cf.* Fig. 3.41) can essentially be identified as rotationally modified g modes. For  $m = 2$  (Fig. 3.42) the situation is more complicated. For positive  $s$  the lowest solution tends to  $\hat{L}_s^2 = 4 = m^2$ ; as noted by Townsend (2003a) this case requires special treatment, although the result still conforms to Eq. (3.377) with  $\zeta = -1$ . This mode is identified as a *Kelvin mode*. The branch appearing at negative  $s$  can be identified with an r mode, resulting from the effect of rotation on the toroidal modes which have zero frequency in the non-rotating case (see the discussion in connection with Eq. (3.144)); these can be regarded as global Rossby waves with frequencies in the rotating frame, to lowest order, of

$$\omega = -\frac{2m\Omega}{l(l+1)} \quad (3.380)$$

(Papaloizou & Pringle 1978). With increasing  $|s|$  this mode takes on the nature of a rotationally modified g mode. A more extensive discussion of these modes, and their physical interpretation, is beyond the scope of this book. A detailed analysis of the possible waves in a rotating system, and how they relate to the global modes, was provided by Unno *et al.* (1989).

The confinement of the eigenfunctions for large  $|s|$  has important effects on the observational signature of the modes; these effects obviously also depend strongly on the orientation of the rotation axis relative to the plane of the sky. Lee & Saio (1990) considered the effect on line-profile variations, noting that prograde modes were enhanced while retrograde modes became almost invisible. Townsend (2003b) presented results for the light variations

<sup>31</sup> It is interesting to note that such modes were considered as possible sources of the  $\beta$ Cep pulsations (*e.g.*, Osaki 1974; Lee & Saio 1986) before the revision of the opacity showed that the modes were excited by the opacity mechanism.

for low-frequency modes in rotating stars. He noted that the confinement very strongly reduces the observed amplitude for stars that are not viewed from high latitudes (*i.e.*, nearly pole-on), possibly explaining the lack of observations of low-frequency photometric pulsations in rapidly rotating stars. He furthermore pointed out that amplitude ratios between observations in different wavelength bands would depend on the orientation of the star and the azimuthal order of the mode, thus greatly complicating photometric mode identification (see Section 6.1). Dziembowski *et al.* (2007) modelled a rapidly rotating Be star observed by Walker *et al.* (2005), attempting to identify the nature of the very large number of modes detected, and noting that many modes would be unobservable for geometrical reasons as a result of the confinement of the eigenfunctions.

### 3.8.6 Higher-Order Rotational Effects

In rapidly rotating stars terms quadratic and of higher order in  $\Omega$  can no longer be ignored. This also includes the distortion of the star by rotation (see Section 3.2.4.2). For moderate rotation a perturbation expansion including terms of order  $\Omega^2$  can be carried out. This was initially discussed by Simon (1969) and further developed, *e.g.*, by Chlebowski (1978), Saio (1981), Gough & Thompson (1990) and Dziembowski & Goode (1992).<sup>32</sup> The treatment was extended to third order in  $\Omega$  by Soufi *et al.* (1998; see also Karami 2008). An interesting analysis to  $\mathcal{O}(\Omega^2)$  was carried out by Sobouti (1980), considering also an expansion around the convectively neutral state. Christensen-Dalsgaard & Dziembowski (2000) summarized the main aspects of the perturbation treatment of rapid rotation; the present section draws heavily on their presentation. For simplicity we assume uniform rotation in the following.

As discussed in Section 3.2.4.2 the spherically symmetric component of the centrifugal force (*cf.* Eq. (3.105)) is included in the normal modelling of stellar evolution; thus this effect is assumed to be included in the equilibrium model used for the oscillation calculations. However, the distortion of the star must be taken into account in the analysis to obtain the rotational perturbation of the frequencies; it can be represented as an expansion in Legendre polynomials, often restricted to second order, as  $P_2(\cos \theta)$ . The pulsation equations now contain terms of order  $\Omega^2$ , neglected in Eq. (3.338). Also, in the analysis we must take into account the perturbations to  $\mathcal{O}(\Omega)$  in the eigenfunctions.<sup>33</sup> These also include toroidal components (*cf.* Eq. (3.144)); for a given mode  $(l, m)$  toroidal components  $(l', m)$  with  $l' = l \pm 1$  must be included. The result of the analysis of Gough & Thompson (1990) can be written as

---

<sup>32</sup> See also Martens & Smeyers (1982) and Smeyers & Martens (1983), who in addition included tidal effects in a binary system.

<sup>33</sup> Owing to the variational property of the equations these cause perturbations to the frequency of order  $\Omega^2$ .

$$\omega_{nlm} = \omega_{nl} + m(1 - C_{nl})\Omega + \left(\frac{\Omega^2}{\omega_{nl}}\right)(\Delta_{nl}^{(1)} + m^2\Delta_{nl}^{(2)}) + \left(\frac{\Omega^2 R^3}{GM}\right)\omega_{nl}\Delta_{nl}^{(3)}Q_{2lm} \quad (3.381)$$

(see also Kjeldsen *et al.* 1998), where

$$Q_{2lm} = \frac{\int_{-1}^1 P_2(x)P_l^m(x)^2 dx}{\int_{-1}^1 P_l^m(x)^2 dx} = \frac{l(l+1) - 3m^2}{(2l-1)(2l+3)}. \quad (3.382)$$

In Eq. (3.381)  $\omega_{nl}$  is the frequency of the spherically symmetric model (which already includes the spherically symmetric component of the effect of rotation). The second term on the right-hand side is the term linear in  $\Omega$ , already encountered above, and given by the Ledoux constant  $C_{nl}$  (*cf.* Eq. (3.361)). The remaining terms contain the various contributions quadratic in  $\Omega$ . The  $m$ -independent term in  $\Delta_{nl}^{(1)}$  arises from the toroidal component of the perturbed eigenfunction, induced by the Coriolis force. This also causes a frequency shift for radial modes, with  $\Delta_{n0}^{(1)} = 4/3$ , independent of  $n$ , while the remaining contributions are zero for  $l = 0$ ; hence<sup>34</sup>

$$\omega_{n00} = \omega_{n0} + \frac{4\Omega^2}{3\omega_{n0}}. \quad (3.383)$$

The term in  $\Delta_{nl}^{(2)}$  includes the  $\mathcal{O}(\Omega^2)$  contribution in the equations of motion, as well as from the spheroidal perturbation to the eigenfunctions from the Coriolis force. Finally, the term in  $\Delta_{nl}^{(3)}$  results from the non-spherical distortion of the equilibrium model. The explicit expressions for these coefficients can be obtained, with considerable effort, from Gough & Thompson (1990).

For high-order, low-degree acoustic modes simple approximations are obtained for  $\Delta_{nl}^{(1)}$  and  $\Delta_{nl}^{(2)}$ :

$$\Delta_{nl}^{(1)} \simeq \frac{2}{2l+1} \left[ \frac{(l+1)(l+2)}{2l+3} + \frac{l(l-1)}{(2l-1)} \right], \quad (3.384)$$

$$\Delta_{nl}^{(2)} \simeq \frac{4}{(2l-1)(2l+3)}. \quad (3.385)$$

Also,  $\Delta_{nl}^{(3)}$  can be approximated by

$$\Delta_{nl}^{(3)} \simeq \frac{4}{3} \frac{\int_0^R (r/R)^3 dr/c}{\int_0^R dr/c}. \quad (3.386)$$

---

<sup>34</sup> Note that in the corresponding Eq.(138) of Christensen-Dalsgaard & Dziembowski (2000)  $\omega$  is mistakenly missing in the denominator.

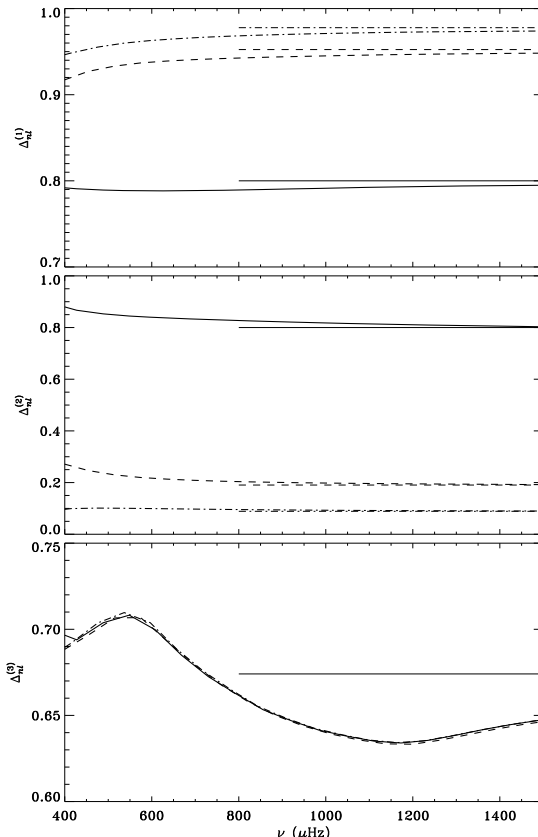


**Fig. 3.44.** Coefficients  $\Delta_{nl}^{(1)}$ ,  $\Delta_{nl}^{(2)}$  and  $\Delta_{nl}^{(3)}$  for acoustic modes in a  $2 M_\odot$  star of age  $4 \times 10^8$  yr. Continues, dashed and dot-dashed lines show results for  $l = 1$ , 2 and 3, respectively. The heavy curves are the numerical results and the thin horizontal lines are the asymptotic approximations (*cf.* Eqs (3.384)–(3.386)). Based on software developed by Burke & Thompson (in preparation).

For a centrally condensed star, and approximating the outer layers by a polytrope,  $c^2 \propto R/r - 1$  in the outer parts of the star (*cf.* Eq. (E.54)) which dominate the integrals in Eq. (3.386). Then the integrals can be evaluated analytically, to yield  $\Delta_{nl}^{(3)} \simeq 35/48$  (Burke & Thompson, in preparation).<sup>35</sup> The computed and asymptotic coefficients are compared in Fig. 3.44, for a  $2 M_\odot$

<sup>35</sup> This result was quoted as  $\Delta_{nl}^{(3)} \simeq 2/3$  by Kjeldsen *et al.* (1998) and  $\Delta_{nl}^{(3)} \simeq 3/4$  by Christensen-Dalsgaard & Dziembowski (2000).

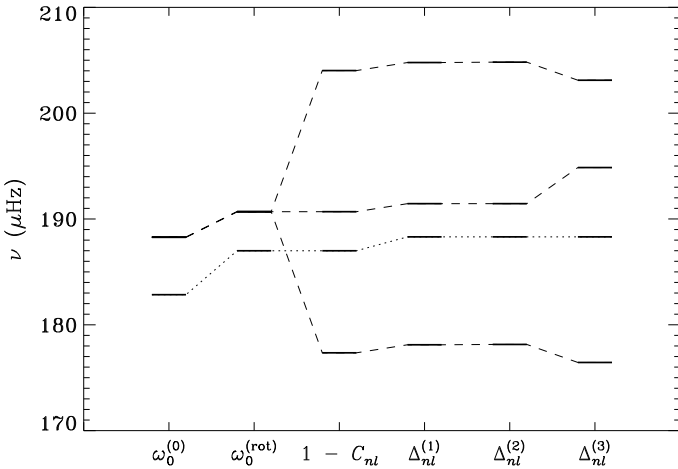


**Fig. 3.45.** Effect of rotation on the  $n = 1$ ,  $l = 0$  and 1 modes of a  $2 M_{\odot}$  star of age  $4 \times 10^8$  yr. Here  $\omega^{(0)}$  indicates the frequencies of a non-rotating star with the same mass and effective temperature;  $\omega^{(\text{rot})}$  corresponds to the unperturbed frequencies of the rotating model and the remaining bars show the effect of successively including the terms in Eq. (3.381). Note in particular the importance of the term in  $\Delta_{nl}^{(3)}$  for  $l = 1$ . Adapted from Kjeldsen *et al.* (1998).

model. It is evident that in the region corresponding to solar-like oscillations the asymptotic expressions match the computed values quite well.

In the opposite case, for high-order g modes, Chlebowski (1978) showed that

$$\omega_{nlm} \simeq \omega_{nl} + m (1 - L^{-2}) \Omega - \frac{m^2 \Omega^2}{\omega_{nl}} \frac{4L^2(2L^2 - 3) - 9}{2L^4(4L^2 - 3)} \quad (3.387)$$

(see also Dziembowski & Goode 1992), where, as before,  $L^2 = l(l+1)$  and we used  $C_{nl} \simeq L^{-2}$ , as implied by Eq. (3.359).

Figure 3.45 illustrates the frequency pattern resulting from Eq. (3.381) for a relatively rapidly rotating star, assuming uniform rotation, and comparing it with a star of the same mass, composition and effective temperature. The change in the unperturbed frequency corresponds to the reduction in luminosity relative to the non-rotating star of 0.8% and the corresponding reduction in the radius. It should be noted that the rotational perturbation now also shifts the frequencies for modes with  $m = 0$ , including radial modes, and the

pattern of splitting is no longer uniform, even for constant rotation or rotation that depends only on  $r$ .

The expansion was taken to third order in  $\Omega$  by Soufi *et al.* (1998). They also emphasized the importance of the case of near-degeneracy where the perturbation method discussed so far cannot be applied. This occurs when the difference between the frequencies of two modes, 1 and 2, say, is comparable with, or less than, the rotational splitting and the selection rules  $l_1 = l_2$  or  $l_1 = l_2 \pm 2$  are satisfied; the latter case, in particular, often arises as a result of the asymptotic properties of high-order acoustic modes, as illustrated by the small frequency separation (*cf.* Eq. (3.221)). The perturbation treatment then has to involve both modes simultaneously (*e.g.*, Goupil *et al.* 2004). This may result in a substantial shift of the frequencies of the modes involved, relative to the values obtained from Eq. (3.381). This is illustrated for  $(l_1, l_2) = (0, 2)$  in Fig. 3.46, which also shows the effect of including in addition the coupling to modes of degree 4. As noted by Goupil *et al.* this also may have a substantial effect on the average small separation, thus potentially affecting the use of the small separation as a diagnostics of conditions in the stellar core, and of the stellar age. Goupil *et al.* presented a procedure based on the detailed properties of the interaction between the modes which allows this effect to be minimized. However, it must certainly be kept in mind in analysis of data for stars with moderately fast rotation.

For sufficiently rapid rotation the expansion in terms of  $\Omega/\omega$  clearly breaks down; also, as discussed in Section 3.2.4.2, a fully two-dimensional treatment of stellar structure is required. Already Perdang (1986) noted that the distortion of the star might result in chaotic behaviour of the oscillations, analogous to quantum chaos.<sup>36</sup> Since the star is still assumed to have rotational symmetry, the dependence of the oscillations on  $\phi$  can be separated as  $\exp(im\phi)$ , as in the case of slow rotation. However, in general no such separation is possible in latitude, and the amplitude as a function of  $(r, \theta)$  satisfies a set of partial differential equations which must be solved numerically. A simplified case was considered by Papaloizou & Pringle (1980). Pulsation calculations in the fully two-dimensional case were treated by, amongst others, Dintrans & Rieutord (2000), Lignières *et al.* (2006) and Reese *et al.* (2006), for polytropic models. A very careful calculation was carried out by Reese *et al.* (2006) who developed the full numerical formalism in the case of polytropic models, and tested the results for internal consistency as well as by comparing with previous computations. They proceeded to make extensive calculations for a polytrope of index 3, as a function of  $\tilde{\Omega} = (R_{\text{eq}}^3/GM)^{1/2}\Omega$ ,  $R_{\text{eq}}$  being the equatorial radius, defined such that  $\tilde{\Omega} = 1$  represents the Keplerian limit where matter would be unbound at the equator. At low values of  $\tilde{\Omega}$  the frequency pattern discussed above, obtained from the perturbation expansion in  $\Omega$ , was recovered.

<sup>36</sup> Such behaviour might also result from other types of distortion of the star; an interesting example is the δ Sct star XX Pyx which appears to show a substantial tidal deformation (Aerts *et al.* 2002b; see also Section 2.8.1).

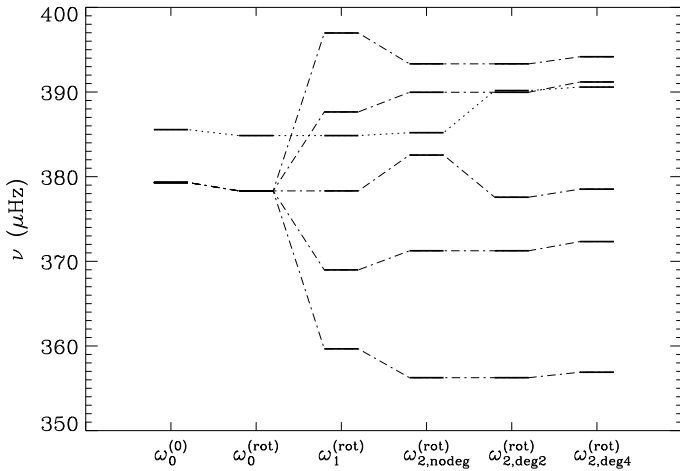


**Fig. 3.46.** Effects of rotation, as seen from an inertial frame, in a case of near-degeneracy, in a slightly evolved model of mass  $1.8 M_{\odot}$  and effective temperature 7516 K. The star is uniformly rotating with a surface velocity of  $92 \text{ km s}^{-1}$ . The dot-dashed lines show modes with degree  $l = 2$  and the dotted line is for  $l = 0$ . Going from left to right increasingly complete effects of rotation are included, starting with a non-rotating model of the same mass and effective temperature ( $\omega_0^{(0)}$ ). Next,  $\omega_0^{(\text{rot})}$  illustrates the effect of the change in the spherically symmetric equilibrium structure,  $\omega_1^{(\text{rot})}$  corresponds to the first-order rotational splitting, and  $\omega_{2,\text{nodeg}}^{(\text{rot})}$  corresponds to the full inclusion of the effects in Eq. (3.381). Finally,  $\omega_{2,\text{deg}2}^{(\text{rot})}$  shows the inclusion of the coupling between the nearly degenerate modes of degree  $l = 0$  and 2, and  $\omega_{2,\text{deg}4}^{(\text{rot})}$  in addition includes the coupling to the nearby modes with  $l = 4$ . Adapted from Christensen-Dalsgaard & Dziembowski (2000).

However, for a model roughly representing a δ Sct star the results showed that the third-order perturbation expansion fails to match the expected frequency precision of, for example, the CoRoT data of around  $0.1 \mu\text{Hz}$  at a value of  $\tilde{\Omega} \simeq 0.15$ , corresponding in the model considered to a rotational velocity of around  $50 \text{ km s}^{-1}$ .<sup>37</sup> For the acoustic modes considered, the dominant effects come from the centrifugal terms. It is evident that a non-perturbative treat-

<sup>37</sup> Somewhat similar results were obtained in preliminary calculations of Lovekin & Deupree (2008), although their conclusions were based on rather less stringent requirements on the frequency precision. Lovekin *et al.* (2009) made a more extensive analysis, considering also conservative differential rotation.

ment of rotation will be essential for many of the asteroseismically interesting cases of pulsating stars.

As already noted above the oscillation spectrum becomes increasingly complex as the angular velocity increases, making very difficult the identification of the modes. This obviously also affects the asymptotic behaviour of high-order, low-degree acoustic modes. However, Lignières *et al.* (2006) found an asymptotic behaviour of the results of calculations including only the centrifugal effects which might replace the non-rotating expression in the analysis of the observations. This was further analysed by Reese *et al.* (2008) who found an empirical formula for the frequencies which provided a good approximation to the computed frequencies for the full calculation for the polytropic model of Reese *et al.* (2006). This has the form, as seen from an inertial frame,

$$\omega_{nlm} \simeq \tilde{\Delta}_n \tilde{n} + \tilde{\Delta}_l \tilde{l} + \tilde{\Delta}_m |\tilde{m}| + m\Omega + \tilde{\alpha}, \quad (3.388)$$

where the new quantum numbers  $\tilde{n}$  and  $\tilde{l}$  are related to  $(n, l)$  in the corresponding non-rotating case by  $\tilde{n} = 2n + \iota$ ,  $\tilde{l} = (l - |m| - \iota)/2$ , where  $\iota$  is 0 or 1 for even or odd  $l + m$ , respectively. The coefficients in Eq. (3.388) can be obtained from fitting to the numerically computed frequencies and could in principle also be recovered from observed frequencies.

The eigenfunctions are also distorted by the rapid rotation. This is illustrated in Fig. 3.47. As in the case discussed above for low-frequency modes affected by slow rotation (*cf.* Fig. 3.43) the eigenfunction is concentrated towards the equator, although in the present case this is predominantly caused by centrifugal effects (Lignières *et al.* 2006). This class of modes, originating from the modes in the non-rotating case, may be termed *island modes*. However, with rapid rotation additional classes of modes develop: the so-called *whispering gallery modes* and *chaotic modes*; examples are illustrated in Fig. 3.48. A very illustrative analysis of these three classes of modes in terms of acoustic rays was presented by Lignières & Georgeot (2008, 2009). For the island modes in the axisymmetric ( $m = 0$ ) case they recovered the approximate expression, Eq. (3.388), and related the coefficients  $\tilde{\Delta}_n$  and  $\tilde{\Delta}_l$  to the structure of the star. It should be noted that the whispering gallery and chaotic modes have rapidly varying structure on the stellar surface, as do high-degree modes in the non-rotating case, and hence are unlikely to be observed in stellar observations without spatial resolution.

Preliminary results for rapidly rotating realistic models, computed by MacGregor *et al.* (2007) with the so-called self-consistent field method, were presented by Reese *et al.* (2009a,b). They are qualitatively similar to the results for the polytropic models although, interestingly, it appears that the island modes at low  $m$  disappear in a model with highly differential rotation.

### 3.8.7 Effect of Rotation on the Excitation of Oscillations

Even slow rotation affects the eigenfunctions and hence potentially the stability of the modes. Hansen *et al.* (1978) carried out a quasi-adiabatic analysis

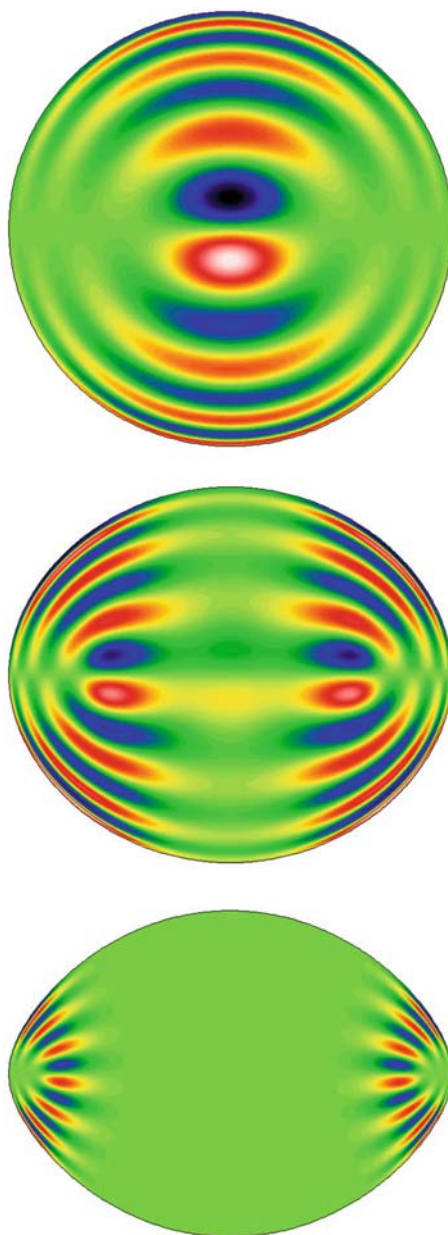


**Fig. 3.47.** So-called island modes, corresponding to a mode of degree  $l = 1$ ,  $m = 0$  in the non-rotating case in polytropic models of index 3. From top to bottom the dimensionless angular velocity is  $\tilde{\Omega} = 0.18596$ ,  $0.58946$  and  $0.83662$ . Figure courtesy of Daniel Reese; see Reese *et al.* (2009a,b).

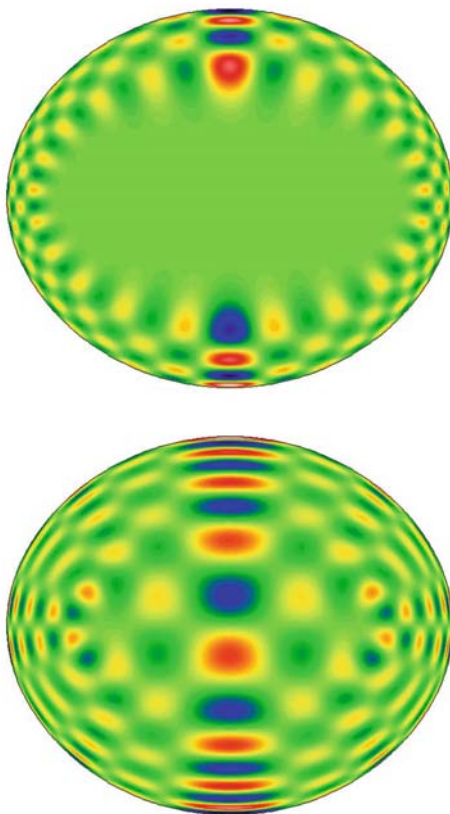


**Fig. 3.48.** So-called whispering-gallery (top) and chaotic (bottom) modes, in a polytropic model of index 3 rotating with  $\tilde{\Omega} = 0.58946$ . Figure courtesy of Daniel Reese; see Reese *et al.* (2009a,b).

for low-order, low-degree modes in a white dwarf and a massive main-sequence model and found a correction to  $\omega_i$ , proportional to  $2m\Omega/\omega$ , such that prograde modes, with  $m > 0$ , were made more unstable by rotation, with the opposite effect for retrograde modes. This tendency was essentially confirmed in fully nonadiabatic calculations by Carroll & Hansen (1982).

The formalism for treating second-order effects of rotation in nonadiabatic oscillation calculations was developed by Lee & Baraffe (1995). Lee (1998) considered the effect of rapid rotation, to  $\mathcal{O}(\Omega^2)$ , on the instability of modes

in B stars. For quasi-radial modes<sup>38</sup> the effect was small. However, for axisymmetric quasi-quadrupole modes he found stabilization of acoustic modes at large  $\tilde{\Omega}$ ; this was caused by a shift towards the surface of the transition point to strongly nonadiabatic oscillations (see Section 3.7.2) resulting from the distortion of the star in the equatorial region. Since the quasi-quadrupolar modes, unlike the quasi-radial modes, are concentrated towards the equator this led to a significant damping region outside the dominant driving region coming from the iron bump.

The effect of rotation on the instability of g modes in massive stars was investigated by Townsend (2005a). For most modes he found a shift of the instability region towards somewhat higher effective temperature with increasing angular velocity; for sectoral prograde modes the effect was small and generally in the opposite direction. He identified this as being predominantly related to the change in periods caused by rotation and hence the shift in the nonadiabatic transition region. Townsend (2005b) studied retrograde modes with properties mixed between rotationally modified g modes<sup>39</sup> and Rossby modes, considering rapidly rotating stars in the traditional approximation. In late B and early A main-sequence stars he found instability resulting from the  $\kappa$  mechanism in the iron bump. The instability properties showed little relation to the SPB or  $\beta$  Cep stars but he pointed out that this might be the mechanism responsible for the Maia stars (see also Section 2.3.6).

The detection of a dense spectrum of low-frequency modes in the rapidly rotating Be star HD 163868 by the MOST satellite (see Section 2.3.8) by Walker *et al.* (2005b) led to increased interest in the effect of rotation on the mode excitation. Using the techniques of Lee & Baraffe (1995), Walker *et al.* found instability of a large number of prograde g modes, with frequencies in the rotating frame much lower than the rotation frequency; the excitation was due to the  $\kappa$  mechanism operating in the iron-group opacity bump. As observed in the inertial frame, this corresponds to groups of excited modes, of a width corresponding to the frequency range in the co-rotating frame of the unstable modes, and separated essentially by the rotation frequency. The comparison between this predicted pattern and the observed frequencies was illustrated in Fig. 2.24. The theoretical analysis also found instability of high-order retrograde r modes, with frequency close to the rotation frequency in the corotating frame and hence at very low frequency in the inertial frames. As shown in Fig. 2.24 these can to some extent, although not fully, account for the lowest-frequency observed modes.

A somewhat different interpretation of the observations was provided by Dziembowski *et al.* (2007) who took careful account of the likely visibility of the computed modes and did not in all cases agree with Walker *et al.* (2005b) on the stability or instability of the modes; however, the general interpretation of the observations in terms of clusters of excited modes roughly separated

---

<sup>38</sup> *i.e.*, modes corresponding to radial modes in the non-rotating case.

<sup>39</sup> which he termed *Poincaré modes*.

in the inertial frame by the rotation frequency was the same. The differences in the results on mode excitation can probably be traced to the different approximations used in the pulsation calculations: Walker *et al.* (2005b) used a truncated expansion of the eigenfunctions, while Dziembowski *et al.* (2007) used the traditional approximation. Saio *et al.* (2007) carried out an analysis similar to Walker *et al.* (2005b) and obtained similar results; they also compared with a treatment using the traditional approximation and found that this tended to overestimate the instability of the modes, possibly as a result of the neglect of mode coupling, as discussed earlier by Lee (2001).

---

## Observational Techniques for Asteroseismology

The fundamental data of asteroseismology are pulsation frequencies and mode identifications (see Chapters 5, 6, and 7). There are two main observational techniques for obtaining these data: 1) photometric observations of variability in the stellar flux, and 2) spectroscopic observations of velocity variations caused by the motion of surface elements. Of course, the observations are always the sum of the effects of all of the pulsation modes simultaneously, hence the need for frequency analysis techniques (explained in detail in Chapter 5) to extract the individual frequencies of the pulsation modes. For very large amplitude pulsating stars it is becoming possible to use interferometry to study the radial cross-section changes in a few stars, but this technique is in its infancy and will not be discussed further here. The relationship between asteroseismology and interferometry – primarily using the latter to provide precise fundamental stellar data – is discussed in detail in Cunha *et al.* (2007).

We discuss the two techniques of photometry and spectroscopy separately. They require different instrumentation and observing conditions, sources of noise are different for them, and they sample the physics of the pulsation differently. For example, in the Sun – and by implication in all solar-like stars – granulation generates much higher noise in photometric measurements than in spectroscopic measurements at the frequencies of interest, as is illustrated in Fig. 4.1 with observations from the GOLF (Global Oscillations at Low Frequencies) and VIRGO (Variability of Solar Irradiance and Gravity Oscillations) instruments onboard the SOHO (Solar and Heliospheric Observatory) satellite.

Photometry is primarily sensitive to temperature variations caused by pulsation, and generally less so to the apparent stellar cross-section variations, except for very large amplitude stars such as Cepheids and Mira variables; as those tend to be singly periodic, they are, in any case, less interesting for asteroseismology. Spectroscopy is most sensitive to velocity variations with some contribution from temperature variations.

While the pulsation amplitudes contain rich information about the physics of the driving, growth, damping and decay of pulsation modes, we cannot yet

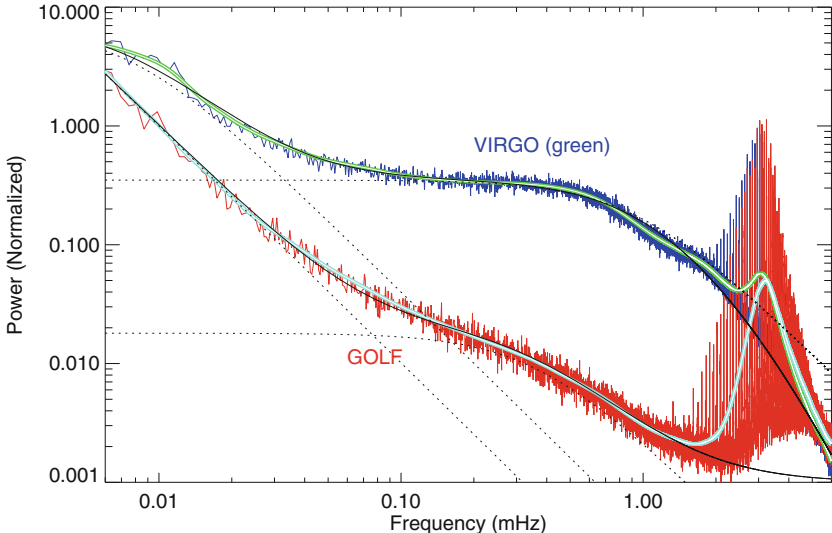


**Fig. 4.1.** Frequency spectra of the Sun derived from the VIRGO (photometry) and GOLF (spectroscopy) experiments onboard SOHO. Figure courtesy of Hans Kjeldsen.

put observed amplitudes to much use because our theoretical understanding of those processes is not yet advanced enough to take advantage of the observations. Thus for both photometry and spectroscopy we do not attempt rigorous definitions of exactly what is being measured photometrically or spectroscopically. At the precision of photometric observations from space (a few parts per million in intensity), and of ground-based high-resolution spectroscopy (as little as a few  $\text{cm s}^{-1}$  in radial velocity), the definitions of what is meant by the terms “intensity variation” and “radial velocity variation” are complex. See Lindegren & Dravins (2003), for example, for a discussion of the concept of “radial velocity” for precisions better than  $1 \text{ m s}^{-1}$  (we return to this point again in Section 4.4.4 below). For our purposes here, we will think of the observations as measuring luminosity variability and radial velocity, respectively.

There is an over-riding principle in observational astronomy, and nowhere is it more relevant than in asteroseismology. Let us call it the Tychonic principle. Tycho Brahe was driven to measure the positions of stars and planets more precisely than any who had come before him. This drive may have been based more on a “gut feeling” than on an intellectual understanding that higher precision would lead to fundamentally new understanding of the universe, but he was right. The Tychonic principle can be summarised as: If you observe anything more carefully, you may make discoveries, and if you improve your precision by orders of magnitude, then new discoveries are guaranteed.

We see this clearly in asteroseismology where in the lifetimes of the authors of this book the precision of astronomical photometry has gone from  $\sim 0.01$  mag down to a few  $\mu$ mag, and that of radial velocity determination from  $\sim 1 \text{ km s}^{-1}$  down to 10s of  $\text{cm s}^{-1}$  – improvements by 4 orders of magnitude! It follows from this that it is imperative that the observer makes every effort to minimize error, to increase precision. There is no such thing as “good enough” in observational astronomy; only the best is acceptable!

It is the need for higher and higher precision in both photometry and spectroscopy that drives instrumental development in both asteroseismology and planet-hunting. For planet-hunting, high precision in photometry is needed to detect and study transiting planets and gravitationally-lensed planets, and high precision is needed in radial velocity to constrain the orbits, hence masses, of extra-solar planets. In asteroseismology higher precision in both photometry and spectroscopy leads to larger sets of frequencies. Other criteria that we will discuss determine which method is best for particular targets or classes of targets. Asteroseismology and planet-hunting are thus intimately connected in their instrumental needs so that space missions such as MOST, CoRoT and Kepler provide data for both fields, as will planned high-duty-cycle ground-based projects, such as SONG (Stellar Oscillations Network Group) and SIAMOIS (**S**ismomètre **I**nterférentiel **A** Mesurer les **O**scillations des **I**ntérieurs **S**tellaires; see Chapter 8).

It is important here to make clear the distinction between precision and accuracy in the way we use these two terms, since we have repeatedly emphasized the need for precision. Accuracy is absolute; it refers to how well a value may be measured relative to the true value. Precision refers to how well a number can be measured relative to other measurements of the same value, irrespective of the systematic uncertainty (or bias) of the value. Thus, in photometry accurate measurements give the apparent magnitude or apparent luminosity of a star; precise measurements only give the changes in that value. In spectroscopy accurate measurements give the radial velocity of a star; precise measurements only give changes in that value. Accuracy requires the zero point and amplitude of measurements of a variation to be determined, whereas precision only requires the amplitude to be estimated. Examples we give below will illustrate this difference more concretely.

## 4.1 Duty Cycle

One of the most important criteria for observational asteroseismology is the *duty cycle*. This is a measure of the fraction of time that is spent successfully observing the variability of the target star. The combination of the day-night cycle, weather, telescope scheduling, instrumental reliability, astronomers’ work schedules, travel funding and other factors makes it extremely difficult to obtain continuous data sets for extended periods from the ground; from space it is much easier, but the costs are vastly greater. Even small

time gaps in data can cause unacceptable confusion in the determination of the pulsations frequencies, as we discuss in more detail in Chapter 5. The observational goal is 100% duty cycles. The reality is that for ground-based observing consortia – *e.g.*, such as the Whole Earth Telescope<sup>1</sup> (WET) – duty cycles of 30 – 70% are typical, and that still leaves confusion in frequency determination, although it is a great improvement on single site data which can only reach duty cycles of about 40% for short time spans under ideal conditions.

The future of asteroseismology lies in space missions – such as MOST, CoRoT and Kepler which are discussed in Chapter 8 – and in ground-based networks and polar sites capable of obtaining duty cycles greater than 70% – such as the proposed SONG<sup>2</sup> (Grundahl *et al.* 2006) and SIAMOIS (Mosser *et al.* 2007) projects, also discussed in Chapter 8. Data sets with duty cycles approaching 100% will dominate theoretical studies, relegating lower duty cycle observational studies to the roles of discovery, specialist determination of particular physical results, and support to provide additional data for the high duty cycle data sets.

## 4.2 Time

Time series are the observations that allow us to derive asteroseismic frequencies, the principal data of asteroseismology. Obviously, observations must be made with times known to high precision, and for long data sets to high accuracy. Just as radial velocity becomes difficult to define for the highest precision measurements, the definition of the measurement of time is complex. We refer the reader to McCarthy (2005) for an introduction to those complexities, as well as to the United States Naval Observatory (USNO) Website<sup>3</sup>. For asteroseismology we normally rely on Coordinated Universal Time (UTC) which depends on the Earth’s rotation. We also remove the effects of the Earth’s motion about the Sun, or about the solar system barycentre, depending on the precision desired, and we convert all times to one form or another of Julian Date, which we discuss further below.

Coordinated Universal Time is not a uniform time scale. The length of the day has an annual variation of about a millisecond, and has long term drifts caused primarily by tidal interaction of the Earth and Moon. As a consequence, to keep UTC in phase with atomic time, “leap seconds” are intercalated as needed. For many asteroseismic studies UTC is acceptable, even for studies over many years for which there have been leap seconds introduced into UTC. For the most precise studies, however, a constant time scale is needed and leap seconds must be removed from the time scale to give

---

<sup>1</sup> <http://www.physics.udel.edu/darc/wet>; <http://wet.physics.iastate.edu>.

<sup>2</sup> [astro.phys.au.dk/SONG](http://astro.phys.au.dk/SONG).

<sup>3</sup> [tycho.usno.navy.mil/systime.html](http://tycho.usno.navy.mil/systime.html).

“ephemeris time”. See the USNO website for a list of leap seconds that have been introduced into the calendar.

The best choice of time scale for asteroseismology is Barycentric Julian Ephemeris Date (BJED). This is the Julian Date corrected to the solar system barycentre to remove the effects of the Earth’s orbital motion on the times of observations (giving BJD; see Stumpff 1980), and with leap seconds removed from the time scale. Another choice that is often used in asteroseismology is Heliocentric Julian Date (HJD) where observation times are corrected to the solar centre, rather than the solar system barycentre. The major difference between HJD and BJD arises from Jupiter’s orbit which produces an oscillation in the HJD time scale with a period of 12 yr (Jupiter’s orbital period) and an amplitude of about 2 s (the distance in light seconds of the Jupiter-Sun barycentre from the solar centre). Of course, the other bodies of the solar system must be included for highest precision. For the ultimate case of pulsar timing, only BJED is good enough; for other applications, less precise scales may suffice.

The very first claim of a discovery of an exoplanet was made by Bailes *et al.* (1991) around the pulsar PSR 1829–10; the planet had a period of 6 months. That was later retracted by Lyne & Bailes (1992) who found that a small correction to the ellipticity of the Earth’s orbit needed in their calculation of BJD, combined with an imprecise position of the pulsar, resulted in a 6-month periodicity in their timings. They did discover a planet, but it was the Earth – which had already been discovered by other means. This was a subtle mistake from which we can learn two lessons: The first is the Tychonic lesson that only the best is good enough for the highest precision. The second is that a discovery of any period that is in the instrumental system should always be examined with the most critical eye; in the case of the purported pulsar planet, the instrumental system included the observational platform – the Earth. The orbital periods of the Earth and Moon, the rotational period of the Earth, orbital periods of asteroseismic satellites are all periods to be wary of if they appear in stellar data.

Although we have emphasized the need for the highest precision, it is acceptable for short data sets from single sites to use HJD, rather than BJD or BJED. But for multi-site campaigns, and for analysis of data spanning years, BJD or BJED should be used.

There are two ways to think about the effect of the Earth’s motion on asteroseismic observations: Doppler shift or light travel time. Any observed frequency is Doppler shifted by the radial velocity of the Earth in the direction of the target star, and that includes the pulsation frequencies of a star. This effect could be removed by correcting the Doppler shift of the pulsation frequencies, but this is not normally done. Instead, we correct the times of the observations to the solar system barycentre and this removes the varying times of arrival of the pulsation pulse as the Earth orbits the barycentre. This is all that needs to be done for photometric observations, but for spectroscopic observations there are two corrections to be made. The first is the removal of

the light travel time effect which removes the Doppler shift of the pulsation frequencies caused by the Earth's motion; this is done by correcting the times of the observations. The second is the correction of measured radial velocities for the Doppler shift of the Earth's motion. These corrections are not the same. The radial velocities are affected by Doppler shifts to the frequencies of the incoming electromagnetic radiation; the light travel time correction removes the Doppler shift to the pulsation frequencies. Thus for spectroscopic observations both corrections need to be applied, one correction to the times, the other to the measured radial velocities.

It is interesting to note that changes in light travel time for pulsation frequencies also occur for the target star itself when it is part of a binary system, including cases where the secondary object is a planet. That is how Wolszczan & Frail (1992) discovered the first extrasolar planets by noting the variation in the precise times of arrival of pulses from PSR 1257+12. This timing method has recently been used again by the WET consortium to discover a planet orbiting the sdBV star V391 Peg that has survived its parent star's red giant stage, giving a glimpse of the Earth's possible future in  $\sim 5$  Gyr (Silvotti *et al.* 2007).

Julian Date is defined to start at midnight UT (Universal Time). This was originally for the convenience of English astronomers working nights near longitude zero, so that the astronomical date did not change during the night. This zero point is not so convenient at other longitudes, and is irrelevant for astronomical observations that now span the globe and are obtained in space. Joseph Justus Scaliger chose to start his Julian Date scale in 4713 BCE for the arcane reason of the coincidence of the zero points of the solar 28-yr calendar cycle, the Metonic 19-yr cycle and the 15-yr cycle of the Roman induction (introduced by Emperor Constantine for tax reasons – the historical baggage we astronomers get saddled with!).

This distant zero point of the Julian Date scale obviates the need for negative times of observations, but it also means that the Julian Date is a big number nowadays. For example, 00:00:00 UT on 1 January 2008 was JD2454466.500000, where we have given 6 decimal precision to specify that time to less than 0.1 s, as is needed in asteroseismic observations. The unwieldy length of the JDs, as well as a desire by geologists and others to have a time scale starting at midnight, instead of noon as the astronomers chose, led to *Modified Julian Date* (MJD), defined as  $MJD = JD - 240\,000.5$ . Thus  $JD2454466.500000 = MJD54466.000000$ . While this conveniently shortens the numbers, it is dangerous territory. The possibility of confusion, of the loss of a day or a half-day, in the determination of JD and MJD hangs over asteroseismic time determination. Great care needs to be taken to avoid mistakes. Some pipelines work in MJD – that of the VLT UVES (Ultraviolet-Visual Echelle Spectrograph) spectrograph, for example. Almost all asteroseismology has been done in HJD, BJD and BJED. Awareness of the differences of these time scales is needed to avoid mistakes in times of observations, especially when combining data from different sources, such as in multi-site campaigns

and in data mining of public archives. This latter certainly has a big role to play in the future of asteroseismology.

While major observatories usually have reliable, accurate time sources, much asteroseismology using photometric data is still done with small telescopes where the time source may not be so reliable. Amateur astronomers now have CCDs that are capable of producing much useful data for asteroseismology, and many observatories with smaller telescopes participate in multi-site campaigns. It is imperative that clocks used to stamp times on raw data are checked before each observing run (on each night) against a reliable time standard. GPS (Global Positioning System) clocks are cheap and often used, but care still must be taken to synchronise the clock recording the times of observations. Computer clocks generally have very low accuracy and should not be used for asteroseismic observations. If there is no other choice than a computer clock, then checks against time standards should be done hourly. Mistakes in observatory clocks are common. The Whole Earth Telescope consortium has long experience with multi-site campaigns that put together extensive photometric data sets from many observatories. For their observing campaigns a headquarters runs 24 hours a day throughout the observing runs. Those staffing the headquarters telephone all observers at the start of each night's observing to discuss observational strategy, the results from the previous night's observations and any problems that may have arisen, and *to check the observatory clock*. This is done every night for every observer; experience shows that this is necessary. All asteroseismic observing runs should emulate this policy.

Beware of time traps! Mistakes are easy to make.

### 4.3 Photometry

Stellar photometry for asteroseismology has as its goal the precise measurement of stellar intensity for the purpose of determining pulsation frequencies. It also is useful in mode identification, as discussed in Chapter 6. Note the use of the word “precise” here, not “accurate”. It is still the case that the accuracy of stellar apparent magnitude determination is generally no better than a few mmag, while ground-based photometry has reached precisions of 10s of  $\mu$ mag, and space photometric missions are capable of  $\mu$ mag precision. Thus while we may only know the mean magnitude of a target star to a few mmag accuracy, we may determine the amplitudes of the pulsation variations about that mean to precisions 1000 times better. The more precisely we can determine pulsation amplitude, the more frequencies we can determine, and – as we said at the start of this chapter – they are fundamental data for asteroseismic inference of stellar structure.

Stellar photometry has used a variety of detectors over the last few centuries. At first, of course, the detector was the human eye, and there is still a place for this in asteroseismology. The American Association of Variable Star

Observers (AAVSO<sup>4</sup>) has coordinated observations by amateur astronomers since 1911. Many of these observations are now done with CCDs, but historically (and often still) they are visual observations with accuracy of about 0.05 – 0.10 mag. While this is low accuracy for many kinds of pulsating variable stars, it is sufficient for large amplitude variables such as Mira stars. The data base of the AAVSO is an important resource for many studies. An example is the measurement of phase lags between infrared light curves observed with satellite data and optical light curves from the AAVSO (Smith *et al.* 2006) which lead to conclusions about TiO absorption in the atmospheres of the stars and suggest that the Mira variables are pulsating in fundamental modes. Similar comparisons for some semi-regular variables suggest first-overtone pulsation, so here is a case where photometry using the eye as the detector is valuable for mode identification in certain pulsating stars.

More precise measurement of stellar brightness was attained from the 19<sup>th</sup> century with photographic plates as the photon detector. Then, prior to WWII photoelectric photometry began in earnest, and following the war was the dominant instrumental method of measuring stellar brightnesses until CCDs became ubiquitous in the 1990s. In the 21<sup>st</sup> century CCD photometry is and will be almost the only method of measuring stellar brightnesses in the visible part of the spectrum, so our discussion hereafter is mostly confined to CCD photometry. Photoelectric photometers do still exist and are used; Kurtz & Martinez (2000 – see their pages 341 – 345) give an extensive discussion of pitfalls and sources of error in their use and we refer the reader to that article.

### 4.3.1 Sources of Error in Photometry

The fundamental limitation in the measurement of stellar brightness is photon statistics. Photon arrival times and detection are a normally distributed process, so that the photon statistical error on a measurement goes as  $\sqrt{N}$ , where N is the number of photons detected. The *signal-to-noise (S/N) ratio* thus goes as  $N/\sqrt{N} = \sqrt{N}$ , so the longer the integration time, the lower the error from photon statistics alone. For the most accurate measurements of a star's mean magnitude, photon statistical error can be overcome by a sufficiently long integration time; in that case, other sources of error dominate.

For asteroseismology we are measuring time variability of stellar brightness, and for many kinds of asteroseismic targets – such as pulsating white dwarfs, sdB variables, solar-like oscillators and roAp stars – the integration time must be short to resolve the time variability. Particularly for the white dwarfs and sdBVs, many targets are faint enough that photon statistics do dominate the errors. Since integration times cannot be increased (because of the need to resolve variations over a short period), the solution to this problem is to use a larger telescope, if possible. However, even the largest telescopes still produce asteroseismic data that is limited by photon statistics for fainter targets of particular interest.

---

<sup>4</sup> <http://www.aavso.org>.

For brighter targets where photon statistics are not the limiting factor in the error budget, there are many other sources of error. The major ones are variations in apparent intensity of starlight caused by atmospheric effects, variations caused by instrumental effects, and variations caused by data reduction and analysis procedures. If possible, these must be controlled and minimized, and where they are beyond control they must be understood. There are many examples of discoveries of variability in photometric data where the signal was not from the star. Here is an example of how even experienced, careful observers can be trapped into misinterpretation of an observed signal in their photometric data: In February of 1987 the first naked-eye supernova since the one seen by Kepler in 1604 appeared in the southern skies. Supernova 1987A was not in the Milky Way Galaxy, but in the Large Magellanic Cloud which is close enough that at its brightest SN1987A was easily visible to the naked eye; one of us (DWK) remembers seeing it nightly for weeks following its appearance from his back garden in Cape Town, in spite of the bright city lights.

From the month following the discovery of the supernova, a team began to search for the remnant pulsar that is expected in many core-collapse supernovae. They used the CTIO 4-m telescope and were rewarded in January 1989 with the discovery of a pulsar with an unprecedented high frequency of 1968.629 Hz – a period of only 0.5 ms (Kristian *et al.* 1989). Of course, the observers were aware of the possibility of an instrumental source for the frequency, so they turned the same telescope and equipment on some brighter known pulsars and showed that only the frequencies known for those stars were detected and there was no sign of the new 1969-Hz frequency – proof that the signal was stellar in origin. Unfortunately, follow-up observations with the Las Campanas 2.5-m telescope failed to confirm the optical pulsar; the suggested explanation was that debris from the supernova had hidden it. While the observational search went on, theoreticians had an enjoyable time exploring how it could be possible for such a star to exist, and how it could have such a high rotation frequency. Woosley & Chavallier (1989), for example, argued in favour of spin-up from accretion of material falling back onto the remnant. Many other theoretical papers were published. This was a most interesting, amazing and important discovery.

Then, two years later, the first author of the observational discovery had to make a lone-author retraction (Kristian 1991). In attempts to confirm the pulsar with the same equipment used in the discovery with the CTIO 4-m telescope, it was discovered that the television guiding system used for the expected faint signal of the expected SN1987A pulsar had a frequency of 1968.629 Hz: the signal was in the equipment, not in the star. This was very disappointing for the whole astronomical community, and a bit embarrassing for the observers. What went wrong? When the control test was done on known pulsars, the television guiding system was turned off because the control stars were brighter and it was not needed. The observers failed to note that there was this difference between the discovery observations and the experimental

controls. This is a subtle observing error; it could happen to you or to us, too. The lesson that it enforces is: “You can never be too careful”. Do not trust your equipment; do not trust your observations; do not trust yourself. Always ask, “What might I have done wrong?” Always look for improvements.

Edwin Hubble famously said: “When a theoretician says something, no one believes him – except himself. When an observer says something, everyone believes him – except himself.” The first source of error in photometric measurements (or any other observations) is observer error; only you can guard against it.

#### 4.3.1.1 Atmospheric Sources of Error in Photometry: Sky Transparency Variations and Scintillation

How fortunate we are that the Earth’s atmosphere is stunningly transparent in the visible part of the electromagnetic spectrum under clear skies. All planets are not like this, as we can easily see for Venus, or for Saturn’s moon Titan. Yet there is more gas between you and the top of the atmosphere, than there is from there to the Big Bang! Would we have developed astronomy on a cloud-bound planet? This is an interesting question to which the answer may be “no”. Our experience observing at wavelengths to which the Earth’s atmosphere is opaque supports this contention. For example, we would not have discovered  $\gamma$ -ray bursts without observations from space.

*Transparency* is a technical term that we use to refer to both the amount of light transmitted from space to the ground through the atmosphere, and to the steadiness of that transmission. A night referred to as “photometric” is one where there are no clouds and no strongly variable dust or aerosols (*e.g.*, due to humidity, or from volcanoes or forest fires) that cause the transparency to vary. At some of the best observing sites the transparency is so good that it is not possible to watch a sunset without pain and possible eye damage.

The corollary to transparency is *extinction*. This is a measure of the amount of starlight removed from the light path per unit airmass, where 1 airmass is defined for observations at the zenith. For a plane-parallel approximation to the Earth’s atmosphere, the airmass for an observation is just  $\sec z$ , where  $z$  is the angular zenith distance. This is a rough, but convenient measure that is often used for planning photometric observations. For the real atmosphere with its curvature a polynomial approximation (Hardie 1964) is usually used:

$$X = \sec z - 0.0018167(\sec z - 1) - 0.002875(\sec z - 1)^2 - 0.0008083(\sec z - 1)^3. \quad (4.1)$$

This is useful up to zenith angles of  $85^\circ$  which is far closer to the horizon than photometric observations are made, except under special circumstances, such as an important time-dependent event. Often, just the first two terms of the relation are sufficient.

Typical extinction coefficients are 0.15 mag/airmass in Johnson *V* and 0.27 mag/airmass in Johnson *B* (we discuss the filter systems in Section 4.3.4).

Thus the amount of starlight removed from the light path by the atmosphere depends only on the zenith angle of the observations for a photometric night with perfectly stable transparency. In practice, there is no such night. The atmospheric extinction is always variable in time, zenith angle and azimuth, even after mean extinction has been taken into account. The extinction depends on temperature; it depends on humidity; it depends on the dust and aerosol levels; it varies with zenith angle; it varies with azimuth. And, of course, it varies with clouds, the bane of photometric observations.

In the absence of clouds on the best photometric nights sky transparency variations occur on times scales of about 15 min, and longer. They do not affect time scales shorter than this. On nights with poor conditions this is not true. Thus photometric observations of stars with pulsation periods shorter than about 15 min can be made without knowledge of the sky transparency variations. In practice, the pulsation frequencies are well-separated from the sky transparency variation frequencies in Fourier space (see Chapter 5). For pulsating stars with periods longer than about 15 min knowledge of the sky transparency variations is usually necessary.

The major source of atmospheric noise in photometric observations (after clouds!) is thus transparency variations, and that can be partially controlled by observation of non-variable comparison stars. We discuss this further and give examples below. This is described as “pink” noise, meaning that it is frequency dependent and has higher amplitude at lower frequencies.

The second major source of atmospheric noise in photometry is *scintillation* which is seen by the naked eye as “twinkling” of stars. Scintillation is caused not by variable extinction, but by variable refraction. The atmosphere is composed of cells of gas typically 10s of cm in radius with slight variations in temperature, pressure and humidity between cells, leading to slightly different refraction of a ray path entering the cell. The light path to the telescope thus passes through many individual cells, changing direction slightly at each one. As the cells move with wind conditions, the set of cells along the light path varies and the amount of light reaching the telescope (or eye) varies. This leads to the apparent twinkling seen by eye, and it leads to variable intensity in stellar photometric observations. It is a “white” noise source with no frequency dependence. Hence on a photometric night scintillation is the dominant noise source at frequencies higher than those of the sky transparency variations, *i.e.*, for periods shorter than about 15 min.

Scintillation is not the same as *atmospheric seeing* or briefly *seeing* by which we mean the size of the point spread function (PSF) of the stellar image, usually characterised by the full-width-at-half-maximum (FWHM) of the two-dimensional point spread function of the starlight on the instrumental detector. Diffraction at the aperture of the telescope is the ultimate limit to the stellar PSF; in that limit it is specified by the well-known Rayleigh resolution of  $R = \frac{1.22\lambda}{D}$ , where  $\lambda$  is the wavelength of the light, and  $D$  is the diameter of the aperture of the telescope (both in the same units, hence the resolution is in radians; multiply by 206205 to put into arcseconds). Atmospheric seeing

degrades the stellar image to make it larger than the Rayleigh limit. As an example, an 8-m telescope has a Rayleigh resolution of  $R = 0.^{\prime\prime}016$  ( $\lambda = 5000 \text{ \AA}$ ), whereas the typical FWHM seeing size of the PSF at good observatories is  $0.^{\prime\prime}5$  to  $1.^{\prime\prime}$  under good conditions. While adaptive optics (AO) is now able to overcome seeing and produce diffraction-limited images using guide stars, or artificial laser guide stars, this does not solve the independent problem of scintillation noise in astronomical photometry. Seeing and scintillation are not well correlated. For example, seeing is dramatically affected by ground-level humidity, whereas scintillation is strongly dependent on high-level wind speed.

Because the atmospheric cells that produce scintillation are relatively small – say for argument’s sake  $\sim 20 \text{ cm}$  – all but the smallest telescopes look through multiple independent cells simultaneously. This, too (as for photon statistics) is a normally distributed noise source, so the scintillation noise goes down as the square root of the number of scintillation cells in the light path. Since that goes up with telescope area, it follows that scintillation noise goes down roughly inversely with telescope aperture. Thus for bright asteroseismic target stars for which the limiting noise source is scintillation, larger telescope aperture is needed to reduce noise, even though there is no strong need for more photons. In practice, scintillation noise drops somewhat more slowly than  $1/\text{aperture}$  of the telescope; see Dravins *et al.* (1998), and previous papers in the same series, for a thorough discussion of atmospheric intensity scintillation.

There are two noticeable visual consequences of scintillation for both naked-eye observations and for viewing stars through telescope eyepieces. It is often noted that “stars twinkle; planets do not”. This is because the angular size of the stars is smaller than the angular size of scintillation cells in the atmosphere, which are of the order of  $1.^{\prime\prime}$  at a height of  $20 \text{ km}$  for a  $10\text{-cm}$  cell. Thus the starlight passes through only one cell at each height and twinkles noticeably. Planets, on the other hand, have angular sizes greater than  $1.^{\prime\prime}$ ; Jupiter, for example has an angular diameter  $\geq 16.^{\prime\prime}$ . Thus the light from planets passes through many scintillation cells at each height which averages the variability and causes the planet to shine with a steadier light than that of a star. The other noticeable effect is of the image size and stability of a star seen in a telescope. Small aperture telescopes are of similar size to scintillation cells, hence the starlight passes through few cells at each height and is not averaged much. The image then appears sharper to the eye, but moves around rapidly. For larger aperture telescopes the averaging over many cells makes the image appear steadier, but with a larger PSF. See Young (1971) for a discussion of seeing and scintillation.

The character of sky transparency noise and scintillation noise can be seen in the amplitude spectrum in Fig. 4.2 where photometric data obtained for the roAp star HR 1217 without a comparison star has clear low-frequency variations with periods longer than  $30 \text{ min}$  (frequencies below about  $0.6 \text{ mHz}$ ), and some residual sky transparency variation for periods longer than  $15 \text{ min}$  (frequencies below about  $1.1 \text{ mHz}$ ). For higher frequencies the noise is white,

i.e., flat in the amplitude spectrum, and is caused by scintillation noise for this bright star. The actual pulsation frequencies are evident near 2.6 mHz. The scintillation noise is governed by the 1-m aperture of the telescope; a larger telescope would reduce that and produce a higher S/N ratio roughly proportional to telescope aperture.

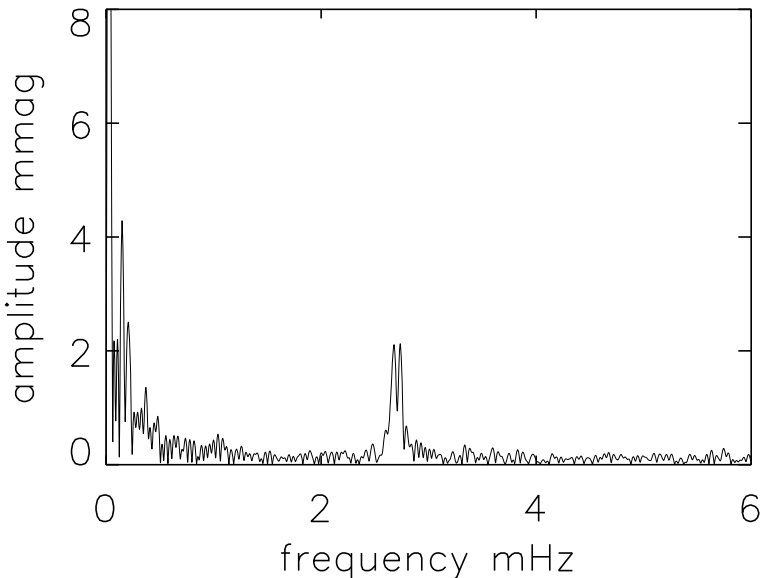


**Fig. 4.2.** An amplitude spectrum (see Chapter 5 for an explanation of amplitude spectra) for a photometric time series for the roAp star HR 1217 obtained through a Johnson *B* filter using 10-s integrations with the South African Astronomical Observatory 1-m telescope on 10/11 November 1986 (JD2446745); see Kurtz *et al.* (1989). Low-frequency sky transparency noise drops to level scintillation noise at higher frequencies. The actual pulsation frequencies in HR 1217 are evident near 2.6 mHz.

#### 4.3.1.2 Instrumental Sources of Noise: Periodic and Random

The most important source of instrumental noise in a photometer is sensitivity variation across the detector. Photometers using photomultiplier tubes always use a Fabry lens to defocus the starlight onto the detector so that these sensitivity variations are averaged out. For CCDs defocusing is sometimes used for stars that are so bright that they saturate the central pixels of the PSF; in this case higher precision is also obtained from the averaging over more pixels, although the handling of the doughnut-shaped PSF for a strongly out-of-focus image also brings problems.

High quality CCDs have sensitivity variations from pixel to pixel of about 1% – vastly higher than the noise level we strive for in asteroseismic observations. For all uses of CCDs the first level of correction for the pixel to pixel variation in the detector is the “flat field”. For this a uniform light source (often the twilight sky) is imaged. Variations in that flat field image are then known to be caused by pixel to pixel variations in the sensitivity of the CCD and a correction can be made for this. For imaging purposes and for observations that are not as demanding as the precise photometry needed for asteroseismology, this is usually a sufficient correction. For the most precise photometry, however, autoguiding which can keep a stellar image fixed at the sub-pixel scale is needed. No telescopes track to this precision – autoguiding is needed. This is true even for the usual case where the plate scale is such that the stellar PSF covers many pixels. With the star kept fixed on a particular set of pixels, pixel-to-pixel sensitivity variations do not contribute to the noise. Let the star wander on the CCD, however, and such sensitivity variations are a major contributor to the noise – even after flat-fielding.

We saw at the beginning of this section how an instrumental electronic signal appeared in the data in the search for a pulsar at the core of SN1987A and was mistaken for a real stellar signal. This story was told as a warning about the care that is needed in interpretation of observations. It is also a warning about periodic instrumental signals appearing in photometric data. Of course, the test for any periodic instrumental signal is to observe a standard star that is constant in brightness. At high photometric accuracy it can be difficult to find constant brightness stars, so it is important to test purported constant stars against each other, as we discuss further in Section 4.3.2 below.

Other sources of noise for CCDs are dark current, bias and read-out noise. These all must be dealt with in the data reduction and observing strategy planned around them. For faint sources, for example, read-out noise may dictate the binning of pixels before readout for the highest S/N. The CCD itself collects charge, and the read out of a pixel involves measuring the charge in the potential well of that pixel. The conversion of that charge to a digital number for further processing then gives measurements in *Analogue-to-Digital Units*, or ADUs. The *gain* of a CCD is the number of electrons per ADU; for photon counting this is 1. Typical 16-bit A-to-D converters can handle counts up to 65 535 ADU which is therefore the saturation level for a particular pixel. If a star saturates pixels then photometric accuracy will be compromised. The PSF is then flat for the saturated pixels and information has been lost. Of course, this must be avoided.

It is standard to de-bias and flat-field observation in the reduction procedure. An important decision to be made in the reduction of photometric data is whether to use *aperture photometry* where all light within a selected radius of the centroid of a stellar image is used to measure the brightness of the star, or *PSF photometry* where a PSF is fitted to a bright star in the field-of-view and then scaled for use in measuring the brightnesses of target stars. This

decision depends on sky background, stellar brightness and field crowding; it often has to be made by testing a particular field for the best results.

For a thorough discussion of CCDs, how they work, how data is read out and reduced, and how these affect the final S/N ratio, see the monograph “Handbook of CCD astronomy” by Howell (2006). Kurtz & Martinez (2000) give a long list of other problems that can arise in photoelectric photometry, many of which are also relevant to CCD photometry. For troubleshooting photometry that is of lower precision than expected, this is a starting point in the search for the source of the problem. For an introduction to CCD photometric data reduction three commonly used reduction packages are DOPHOT (Schechter *et al.* 1993), DAOPHOT (Stetson 1987) and, for aperture photometry, the Image Reduction and Analysis Facility (IRAF) APPHOT package<sup>5</sup> (Davis 1989).

One source of periodic instrumental signal that appears all-too-often in photometric data arises from periodic drive error in the telescope. In the absence of autoguiding any periodic error in the right ascension drive will cause the image of a star to move back and forth on the detector. Since flat fielding does not remove all sensitivity variation on a CCD, this then injects a signal into the photometric time series with the period of the telescope drive – usually 2 sidereal minutes or 4 sidereal minutes (8.36 mHz and 4.18 mHz, respectively). As these are frequencies in the range of expected pulsation frequencies in many asteroseismic targets – solar-like oscillators, sdBV stars, pulsating white dwarfs, roAp stars – the discovery of any frequency near to these should be examined carefully. Tracking rates are proportional to  $\cos \delta$ , where  $\delta$  is the declination of the observations, so tracking error signals, when they do arise, diminish with increasing declination. Where this problem does exist, as long as it is not large, frequent autoguiding can eliminate it.

### 4.3.2 Differential Photometry

Differential photometry is the standard for all photometric asteroseismic observations. It is always desirable to have constant comparison stars in the same field of view as a target star. Changes in the brightnesses of the comparison stars thus give knowledge of sky transparency changes and, for stars that have small angular separations, even some reduction in scintillation noise. Ideally, at least two – and preferably more – comparison stars brighter than the target star should be measured on each CCD frame. Two are necessary to show that they do not vary with respect to each other, since at high precision many stars are variable. In fact, at  $\mu$ mag precision there may be no constant stars; this is still to be determined. Once constancy of the comparison stars has been proved, the differential measurement consists of subtracting the comparison star magnitude from that of the target star, or dividing the target star intensity by that of the comparison star. This process, to first order (see below),

---

<sup>5</sup> [iraf.noao.edu/iraf/ftp/iraf/docs/apuser.ps.Z](http://iraf.noao.edu/iraf/ftp/iraf/docs/apuser.ps.Z).

removes sky transparency variations and can even be used to correct for extinction. The reason the comparison stars need to be brighter than the target star is to keep photon statistical noise in their measurement from increasing the noise in the final differential magnitude.

In practice, the comparison stars seldom remove all atmospheric effects. The major reason for this is differential extinction. Observations are over a limited wavelength range, either because a filter has been purposely chosen, or because of the wavelength response of the detector. If the target star and comparison star have different effective temperatures, then the convolution of the spectral energy distribution with the wavelength response of the detector plus filter results is slightly different *effective wavelengths* of the observations. This, because of the variation of atmospheric extinction with wavelength, then gives rise to slightly different extinction curves for the target star and comparison star and a residual signal in their differential magnitudes.

The comparison stars and target stars seldom have the same effective temperature, therefore do not have the same effective wavelengths and atmospheric extinction. Fig. 4.3 shows an amplitude spectrum for the differential magnitudes between two comparison stars observed with the ULTRACAM<sup>6</sup> photometer in a study of white dwarf pulsation (Kurtz *et al.* 2008). The low frequency peak is significant at the  $6.5\sigma$  level, yet is probably the result of differential extinction between the two comparison stars. The time span of the data was 1.82 hr, and the period of the peak is 2.89 hr. If a real variation in one of the stars were suspected to be present with that period, much longer data sets covering many cycles would need to be obtained, and more thorough analysis of the comparison stars would be needed to prove it. The highest *accuracy* photometric measurements – ones that remove atmospheric low frequency peaks such as this one – need detailed knowledge of the fundamental parameters of the comparison stars (especially  $T_{\text{eff}}$ ), and excellent comparison stars in the same field of view as the target star.

Good comparison stars are often a problem. For brighter stars for which photon statistics do not limit precision, there is seldom a sufficiently bright comparison star in the field of view. For many photometers the field of view may be only arcminutes, hence few stars may be present. In fact, frequently no comparison stars are present and the asteroseismic target star is the only object in the CCD image. In that case, there are two choices. For stars with periods long enough to allow it, the telescope can be moved from target star to nearby comparison stars and back in a continuous cycle over the observing run. Differential photometry is then still possible, but with loss of observing time while moving the telescope. Automated photometers can do this automatically; if the observer has to do it, then it is very hard work.

If, however, the period of the asteroseismic target star is too short – for solar-like oscillators, pulsating white dwarfs, sdBV stars, roAp stars, for example – then it is not feasible to cycle from target star to comparison stars

---

<sup>6</sup> <http://www.shef.ac.uk/physics/people/vdhillon/ultracam/>.

and back in a time shorter than the pulsation period. In that case, we use what is known as *high speed photometry*.

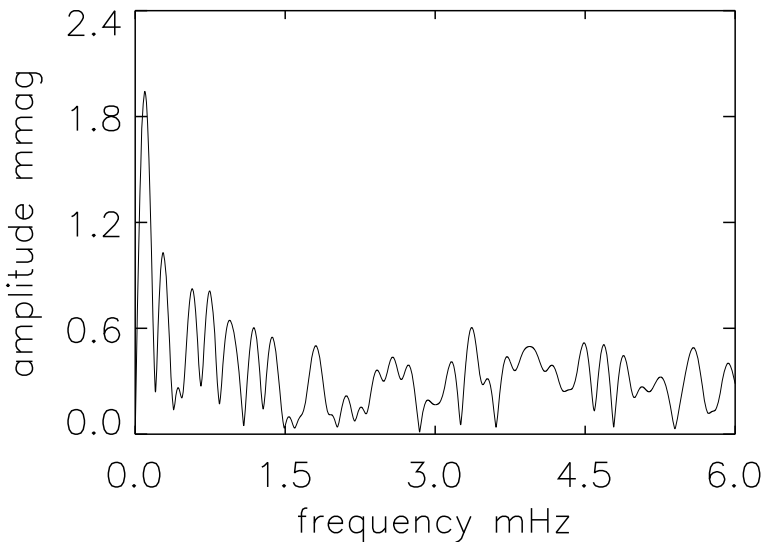


**Fig. 4.3.** An amplitude spectrum (see Chapter 5 for explanation of amplitude spectra) for a photometric time series for the differential light curve for two supposedly constant comparison stars. The low frequency peak at 0.096 mHz ( $P = 2.89$  hr) is significant at the  $6.5\sigma$  level. It is likely to be caused by differential extinction, rather than to be a real variation in one of the stars.

#### 4.3.3 High-Speed Photometry (Non-differential Photometry)

To study stellar pulsation it is necessary to use integration times that are shorter than the pulsation period. In Chapter 5 the Nyquist frequency is discussed. While two points per cycle are sufficient for frequency analysis, it is important to determine if stellar light variations are sinusoidal; if they are not, then at least two points per cycle are needed for frequencies as high as the highest frequency harmonic that is needed to describe the light curve shape. Furthermore, integration times that are a significant fraction of the pulsation period (only a few points per cycle) will smear the signal and reduce the observed amplitude. In practice, observers often opt for about 10 points per cycle, or more, where the target is bright enough to allow for this. Photometric integration times for asteroseismic targets are often selected to be 10 s, then may be averaged to longer integrations if such short integration times are not needed. For Fourier analysis it makes no difference to the noise levels whether integrations are averaged, or not, but for viewing a light curve in the time

domain, longer integration times will show lower high frequency scatter, hence make it easier to compare frequency solution fits with actual light curves.

One problem with short integration times is poor use of telescope time when the readout time of the CCD is significant compared to the integration time. In that case much of the night is wasted not collecting photons as the CCD is read out. For brighter stars this can be very wasteful of telescope time. Photoelectric photometers have no significant readout time, so are still used for bright star high speed photometry. Frame transfer CCDs also can cope with very short integration times without loss of time to readout. In this case half the CCD is used for data acquisition; the other half is masked off so no light falls upon it. The collected charge in the observing half of the CCD can be transferred to the unused half of the CCD in typically just tens of ms, then a new integration can begin while the dark half of the CCD is read out. Obviously integration times still have to be longer than the readout time of the dark half of the CCD, but there is no significant loss of observing time as long as this is the case.

It is not the length of the integration times that defines what is meant by the term *high speed*. The use of 10-s integration is very low speed in comparison with 1-ms integrations that may be used in optical studies of pulsars, for example. Therefore, “high speed” photometry does not necessarily equate to high time resolution photometry. What it does mean is that the target star varies too quickly for the observer to move between it and comparison stars, so that the telescope is trained continuously on the target star, in spite of there being no comparison stars. Thus, this could be called non-differential photometry (but it never is).

High speed photometry foregoes the use of comparison stars for better time resolution on the target star. This has a high price: there is no control over sky transparency variations. In practice, good photometric sites have sky transparency variations that are confined to low frequency, as we showed in Fig. 4.2, so that the actual pulsation frequencies – as is the case for the roAp star HR 1217 shown in that figure – are well-separated in frequency space from the low frequency noise. Information about low-frequency variability in the target star is lost, but good time resolution of the pulsation is the reward.

High speed photometry is widely used in asteroseismology, in particular for the higher frequency pulsators such as white dwarfs, sdBV stars and roAp stars. For estimating errors on frequency, amplitude and phase in the frequency solutions to the light variability of these stars, the noise level in the frequency region of the pulsations should be used. One easy way to do that is to assure that the noise in the amplitude spectrum is white across all frequencies. A variety of *high pass* filters (those that reduce the low frequency noise level) can be used for this. It is important not to reduce the noise level below that of the rest of the amplitude spectrum, if least squares estimates of errors on frequency, amplitude and phase are wanted, as those depend on the total variance in the data which should be representative of the frequency region of interest, as it is for white noise.

#### 4.3.4 Filters

Photometric observations can provide us with neither the bolometric magnitude of a star, nor with a monochromatic magnitude. Because of the wavelength dependence of the transmission of the atmosphere and the wavelength dependence of the detector, the observations of stellar brightness are always over a range of wavelengths, transmission curves and sensitivity curves. This is a very important point, since stellar pulsation amplitude and phase are not constant as a function of the observed wavelength.

A first-order reason for this is that variation in stellar brightness from pulsation depend primarily on temperature changes. Fig. 4.4 shows sections of black body curves from the blue to the near infrared for various temperature ranges, including those of many pulsators discussed in Chapter 2. It is easy to see that the monochromatic pulsation amplitude as a result of the temperature variation is much higher in the blue than in the red and infrared for all stars, including solar-like oscillators. Thus pulsation amplitude is strongly a function of the wavelength of the observations. In fact, subtler effects than the gross one illustrated in Fig. 4.4 for temperature allow differences in pulsation amplitude and phase as a function of wavelength to be used for mode identification, as is discussed in Chapter 6.

To use mode identification techniques that depend on pulsation amplitude and phase as a function of wavelength of the observations, and for multi-site campaigns that combine data from many observatories to obtain high duty cycles, it is usually necessary to use filters to define precisely the wavelength range of the observations. For some multi-site campaigns on faint targets, such as the pulsating white dwarf stars, no filter has been used (the observations are said to be in “white light”). This is only practical for hotter stars where the blue part of the spectrum dominates the light variations. In principle, differences in the effective wavelength of the observations from telescope to telescope can generate apparent (but instrumental) amplitude variations that generate additional peaks in the amplitude spectrum. When data analysis is pushed down to the noise level to try to extract the maximum number of frequencies for asteroseismic analysis, it is important to be aware of a potential problem and guard against it. For other types of pulsating stars such as the roAp stars, filters are mandatory because of strong pulsation amplitude and phase variations with observed wavelength.

The filter systems used are those that are common in astronomical photometry, are well-defined and which are in wide-spread use at most observatories so that all observers will have the same filters. Three of the most common are Johnson *UBVRI* filters, Strömgren *uvby* and Sloan Digital Sky Survey (SDSS) *u'g'r'i'z'* (Fukugita *et al.* 1996), in addition to many others such as Geneva, DDO, Vilnius, Walraven, Washington, HST, Hipparcos-Tycho and other filter systems. These filters for standard photometry, and their important transmission curves, are discussed in detail by Bessell (2005). As an example, Fig. 4.5 shows the transmission curves of the SDSS filters along with the response

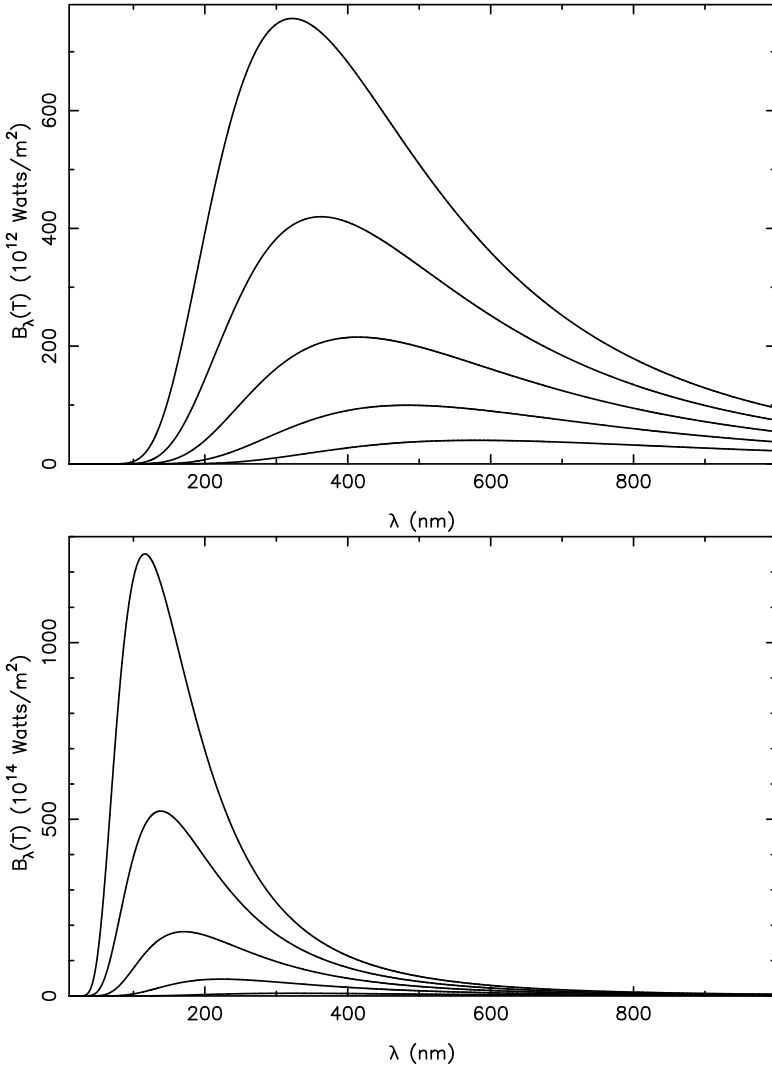


**Fig. 4.4.** Black body curves for objects of various temperatures. Top: temperatures range from 5000 K (lower line) to 9000 K (upper line) in steps of 1000 K; bottom: temperatures range from 9000 K (lower line) to 25000 K (upper line) in steps of 4000 K. The pulsation amplitudes are generally greater at shorter wavelengths for asteroseismic targets.

curve of one of the CCDs used in the SDSS. It is the convolution of those two curves with the observed (through the Earth's atmosphere) spectral energy distribution of a star that defines the effective wavelength for a particular filter. Other filter systems and detectors are analogous to this.

We can see from Fig. 4.5 that we can think of photometry through filters as a form of very low resolution spectroscopy. It is high resolution spectroscopy that provides the most information for asteroseismology, so we now turn our attention to that.

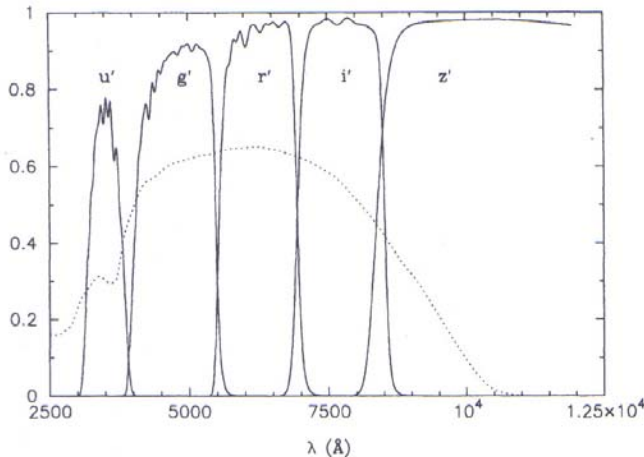


**Fig. 4.5.** The transmission curves for the SDSS filters, along with the response curve of a CCD typical of those used in the SDSS (dotted curve). From Fukugita *et al.* (1996).

## 4.4 Spectroscopy

Spectroscopy is an important observational tool for all fields of astrophysics. For stellar astronomy, it allows for spectral classification, for the derivation of the atmospheric parameters such as the effective temperature and gravity, for estimates of the abundances of the chemical elements in the stellar atmosphere, for the derivation of the amount of mass loss and circumstellar material through emission line and P Cygni line modelling, etc. It also allows the detection of binarity, or, more generally, multiplicity of the studied object whenever a time series is available. The discovery of the first exoplanet orbiting a main sequence star, 51 Peg b, in 1995 was made thanks to high-precision spectroscopy, and this has been the technique that has allowed the discovery of the vast majority of the more than 300 exoplanets known today<sup>7</sup> (*i.e.*, mid-2008; the number of exoplanet candidates is growing rapidly). In view of the

<sup>7</sup> <http://exoplanet.eu/>.

small orbital velocity of the parent star about the star-planet barycentre, the discovery of exoplanets, through the Doppler effect, requires special observing and analysis methods. These will be outlined below and compared with the methodology used in asteroseismic diagnostics for the interpretation of small oscillatory velocity perturbations.

Spectra with sufficiently high resolution for asteroseismology can at present only be obtained from ground-based telescopes. The modern spectrographs mounted on them usually consist of a collimator, a dispersive element (prism or grating) and a CCD camera (linear detector arrays are less common these days). Very complicated set-ups may occur, such as curved gratings or multiple-pass optical systems<sup>8</sup>. Some of the reflection gratings are designed in such a way as to maximise the efficiency at certain wavelengths, so that one has to take into account the so-called *blaze function* in the reduction.

Each of the instruments requires its own reduction procedure. The basic steps are, however, the same for most spectrographs, *i.e.*, the removal of dark current, offset and bias correction, sky background subtraction, flat fielding as discussed in Section 4.3 above, and wavelength calibration. To this one must add identification of the orders and correction for the blaze function in the case of échelle spectra (this is not needed for a linear array). The wavelength calibration is usually achieved by means of the measurements of a suitable calibration lamp. For asteroseismology, a high-accuracy wavelength calibration of the spectrograph throughout the oscillation cycle is essential, as well as accurate flat-fielding. It is therefore necessary to measure several calibration and white lamps between the target exposures; the stability properties of the spectrograph determine how often such calibration measurements must be done throughout the night.

For major spectrographs on large telescopes there are often pipelines for data reduction. For more flexible data reductions tools are provided by the European Southern Observatory-Munich Image Data Analysis System (ESO-MIDAS) and by the Image Reduction and Analysis Facility (IRAF). Both of these major facilities have on-line manuals and freely available software.

After the spectroscopic data have been reduced, the spectra should be shifted to the solar system barycentric reference frame. This can be achieved, *e.g.*, by application of the algorithm by Stumpff (1980), after computation of the UT of mid-exposure. This step is also included in most of the pipeline reduction software packages provided by the observatories. The times also need barycentric correction, as discussed in Section 4.2.

Fig. 4.6 gives parts of a fully reduced normalised high-resolution spectrum of the B1III  $\beta$  Cep star  $\xi^1$  CMa and of the iron-depleted F6I RV Tau star RU Cen. The S/N ratio for  $\xi^1$  CMa is more than twice that of the RU Cen spectrum. These two examples illustrate the range in S/N level we aim for to study the stellar oscillations from *line profile variations*. Fig. 4.6 demonstrates the diversity in spectral line occurrence, line depth and line shape for pulsators

---

<sup>8</sup> several examples are available from <http://www.eso.org>.

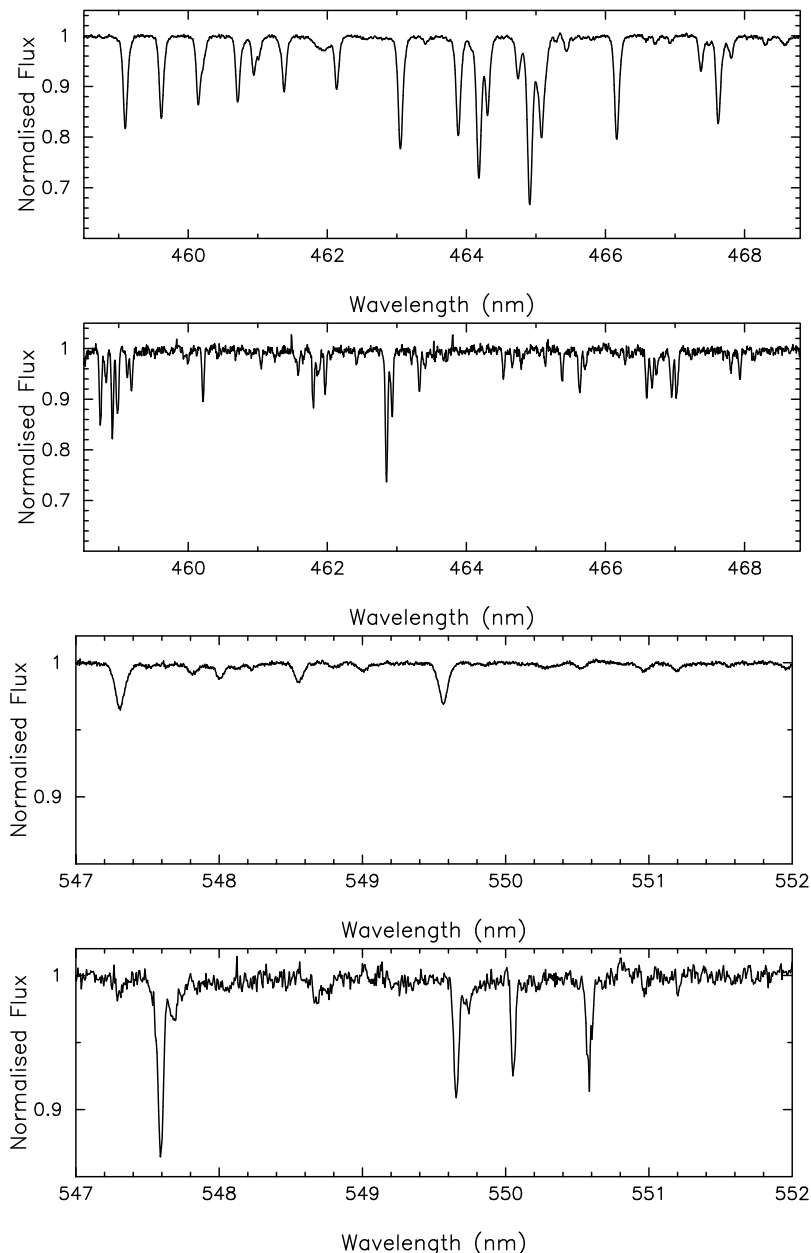


**Fig. 4.6.** Parts of the spectrum of the B1III  $\beta$  Cep star  $\xi^1$  CMa (top and 3rd panel, S/N ratio  $\sim 400$ ) and of the F6I RV Tau star RU Cen (2nd and bottom panel, S/N  $\sim 150$ ). Data taken from Saesen *et al.* (2006) and Maas *et al.* (2002).

in different areas of the HR Diagram. We will want to exploit time series of deep, well-isolated (*i.e.*, unblended) spectral lines that are little affected by pressure broadening. As is clear from Fig. 4.6, the choice of such line(s) and the region in wavelength to focus on during the observing depend entirely on the type of pulsator and its rotational broadening.

#### 4.4.1 Wavelength Stability and Low Frequency Noise in Spectroscopy

Modern high resolution spectrographs are placed in stabilised temperature and pressure environments to minimize the wavelength shifts that come with changes in those parameters. Nevertheless, for radial velocity measurements precise to the  $\text{m s}^{-1}$  level, or better, observations still show wavelength drifts during an observing night. Control of those drifts can be made by observing through a cell with iodine vapour to impress the rich spectrum of molecular  $\text{I}_2$  onto the stellar spectrum (Marcy & Butler 1992), as we discuss further in Section 4.4.6 below. That can be used to characterise the instrumental line profile, as well as control the wavelength calibration of the spectrograph on a spectrum-by-spectrum basis. It leads to the highest possible radial velocity *accuracy*, as is needed in exoplanet studies, where the periods are long – days and more. It comes at a cost, however, since the iodine spectrum must be deconvolved from the stellar spectrum for line profile studies, and the iodine reduces the intensity of the starlight by about 50%, hence reduces the S/N.

Therefore, for asteroseismology iodine wavelength calibration is not normally used. This, then, leads to low-frequency drifts in the wavelength calibration on a time scale of hours typically, hence leads to low-frequency noise in the amplitude spectra of the radial velocity variations. For asteroseismic targets with short enough periods, the frequencies of interest are well-separated in frequency space from the low frequency noise generated by the wavelength drifts. This situation is completely analogous to that discussed above for photometry, where instead of sky transparency variations causing the low-frequency noise, small changes in the wavelength calibration as the result of temperature, pressure and humidity changes in the spectrograph produce the low-frequency noise.

Fig. 4.7 shows an example for the roAp star HD 101065. The observations were obtained with UVES the on the VLT in Chile. The data span 2 hr with 65-s time resolution. The noise level is only  $\sigma = 7 \text{ m s}^{-1}$  for radial velocities measured from a single spectral line. The pulsation is clear, as is a low-frequency peak with an amplitude of  $75 \text{ m s}^{-1}$  that is the result of drift in the wavelength calibration during the 2 hr of observations. A Th-Ar reference spectrum was taken before the observations commenced, but not during the 2-hr observing run. A comparison of Fig. 4.7 with Fig. 4.2 for high-speed photometry shows that the wavelength shifts in spectrographs such as UVES are of minimal concern in asteroseismology of stars with sufficiently high pulsation frequencies.

On the other hand, of course, that low amplitude, low frequency peak seen in Fig. 4.7 would destroy any study of an exoplanet radial velocity variation or longer period pulsation on a time scale of days, or longer. As for photometry, we give up information about longer time-scale variability in the study of such data. We pay that price to obtain the highest possible S/N ratio for line profile studies.

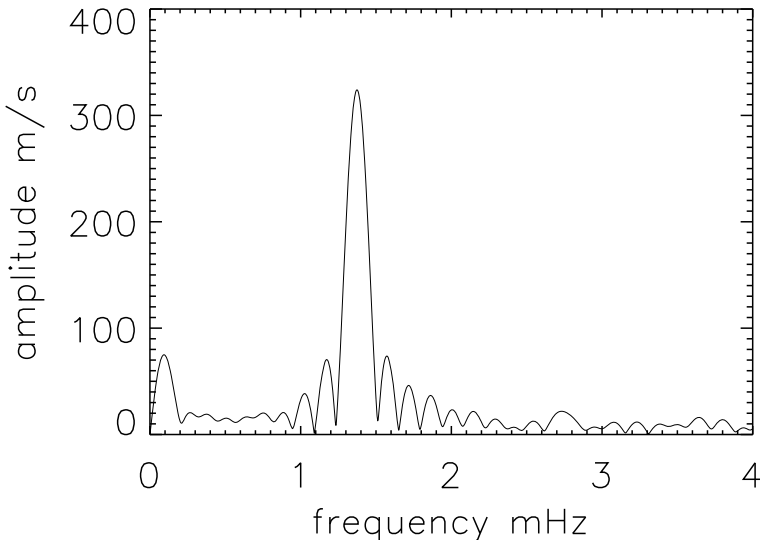


**Fig. 4.7.** An amplitude spectrum of the radial velocity variations of a single spectral line of Nd III at  $\lambda 6145 \text{ \AA}$  in the roAp star HD 101065 showing a low-frequency peak caused by wavelength drift during the 2 hr of observations with UVES on the VLT. The pulsation frequency is obvious at higher frequency. The precision of the data in amplitude is  $\sigma_{\text{amplitude}} = 7 \text{ m s}^{-1}$ . Data courtesy of D.W. Kurtz, V.G. Elkin and G. Mathys.

#### 4.4.2 High-Resolution Spectroscopy and Line Profile Variations

A *line profile* is an isolated spectral line in the spectrum of a star. Whenever the shape of such a line profile varies in time, one speaks of *line profile variations*. We restrict our discussion here to variations caused by motions at the stellar surface, not by circumstellar material due to an outflowing stellar wind nor to the presence of a disc, a hot stellar corona or a magnetic active region. With this restriction, the line profile variations are either caused by intrinsic surface velocity changes, or a non-uniform temperature, gravity or chemical element distribution across the stellar surface, or a combination thereof. Stellar

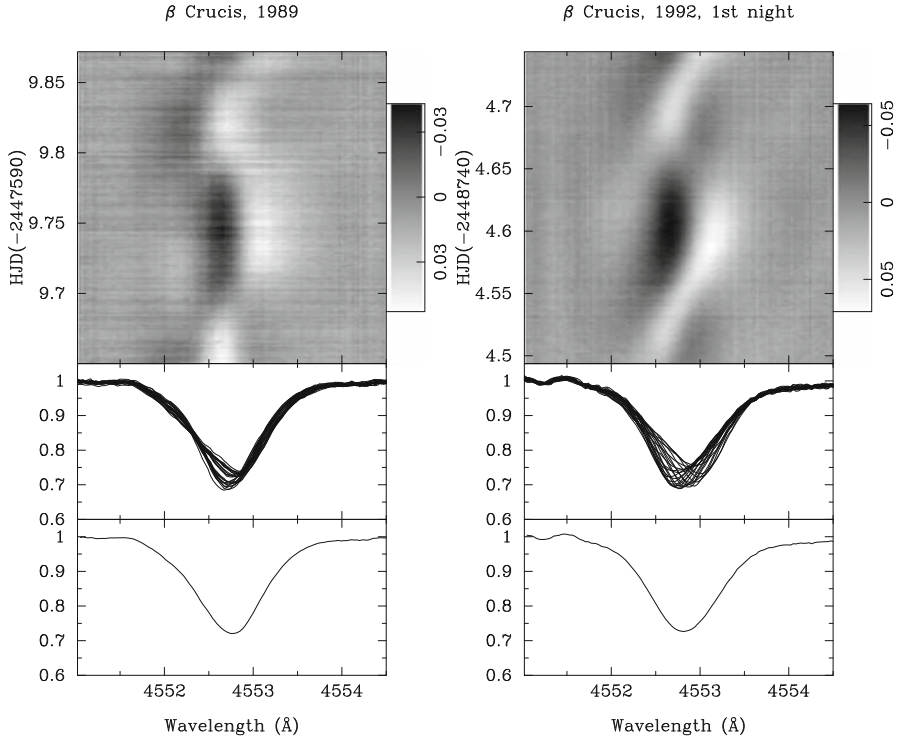


**Fig. 4.8.** Grey-scale representations (top panel) of the line profile variations (of which some are shown in the middle panel) of Si III at  $\lambda 4553 \text{ \AA}$  of the  $\beta$  Cep star  $\beta$  Cru, measured in different years. The average profile of the night is shown in the bottom panel and was subtracted from each of the measured profiles, after which the residual flux at each wavelength pixel was assigned a grey value according to the scale (in continuum units) shown on the right of each upper panel (white means less absorption than for the average profile, black means deeper absorption than the average). From Aerts *et al.* (1998a).

oscillations cause both velocity and flux (*i.e.*, temperature and gravity) perturbations. The effects of the flux perturbations are usually smaller than those caused by the velocity perturbations for nonradial oscillations of chemically normal stars, as will be explained in detail in Chapter 6.

Line profile variations can be visualised in different ways. Two of them are shown in Fig. 4.8 which displays line profile variations observed during two nights of different years of the bright  $\beta$  Cep star  $\beta$  Cru. The classical way to show the variability is to overplot the measured profiles, as in the middle panels of the figure. The upper panels present the variations in a *grey-scale* plot. This concept was introduced for pulsating stars by Gies & Kullavanijaya (1988) in their pioneering study of the line profile variations of the  $\beta$  Cep

star  $\varepsilon$  Per whose oscillations are not detected in photometric data because their degree,  $l$ , is greater than 4. A grey-scale plot makes it easy to detect line profile variations by eye. In such a representation, it is much easier to see patterns travelling across the profile in time than in simple overplots of the time series of the profiles, as in the middle panels of Fig. 4.8 and as in Fig. 2.22. One can readily see from Fig. 4.8 that the pattern of the line profile variations is different on the two different nights, while this is hard to see in the overplots of the observed profiles in the middle panels of the figure. This different behaviour on the different nights is due to the beating of several oscillation modes (Aerts *et al.* 1998a).

Periodic extrinsic motion of a star (*e.g.*, due to binarity or orbiting planets) only leads to global Doppler shifts of the line profiles and not to a variation of their shape. This important difference famously led to a debate in the pages of the journal *Nature* about the very existence of the first exoplanet discovered orbiting a main sequence star, 51 Peg (Mayor & Queloz 1995) when Gray (1997) claimed detection of line profile variations, implying a nonradial g mode was responsible for the 4.2-d period in the star, not a hot Jupiter exoplanet. Both low-amplitude radial velocity variations caused by a planet and line profile variations caused by nonradial pulsation were at the limit of observational capabilities at the time of the debate over 51 Peg. Further research showed no line profile variations, hence the case for the existence of the planet 51 Peg b is strong. At the time of the debate tempers flared in public discussions – there was fame and fortune in the discovery of exoplanets. Now that the dust has settled and exoplanet and asteroseismology work so closely together, we wistfully think it is too bad that the line profile variations were not present in 51 Peg. Had they been, it would have implied a g mode in a solar analogue – a probe of the star’s core. As of this writing there are more than 300 known exoplanets and no known g modes in a solar-like star, so, in retrospect, the discovery of a g mode would have been astrophysically more important in the long run. We fully understand, of course, the incredible importance of the discovery of 51 Peg b for exoplanet science, and, along with it, for asteroseismology.

In cases where line profile variability is caused by temperature or chemical spots rotating at the stellar surface, one detects only periodicity connected with the stellar rotation (but affected by the spectral window – see Chapter 5). In the case of rigid surface rotation, this implies the detection of only one basic frequency and its (sub)harmonics in the line profile variations, depending on the number and distribution of spots across the visible surface. In contrast to these “monoperiodic” variations, multiperiodic stellar oscillations may cause very complex variations of the line profiles.

Observed line profile variations are one of the most important diagnostics for a detailed study of the pulsational behaviour of a star, including mode identification. This will be explained in detail in Chapter 6, where we will show that an in-depth interpretation of observed line profile variations offers the possibility of a complete reconstruction of the velocity due to nonradial

oscillations at the stellar surface, provided that they are measured with a sufficiently high S/N ratio and spectral and temporal resolution, and that they cover the entire beat period. These very stringent requirements on the data are detailed in this chapter, which serves as a guide for future spectroscopic observing campaigns of nonradial pulsators. We also define the most important diagnostics derived from the spectra for asteroseismology. The methodology for the interpretation of observed line profile variations and their diagnostics is treated in Chapters 5 and 6.

#### 4.4.3 Requirements of Spectroscopy for Asteroseismology

The goal of the spectroscopic time series is to interpret small time-dependent perturbations of the spectral lines due to the oscillations. These perturbations imply that the spectral lines deviate from a constant symmetrical shape, which they would have if only time-independent thermal, pressure and rotational broadening occurred. In order to detect these relatively small deviations, it is necessary to have spectra with a sufficiently high resolving power and S/N level.

The *spectral resolution* of the measurements, defined as  $\lambda_0/\Delta\lambda$  with  $\lambda_0$  the laboratory wavelength of the spectral line under consideration, needs to reach at least 30 000 and is preferably above 50 000 given that all successful applications of asteroseismology so far concern slow rotators and were based on metal lines. The optimal value to adopt depends, of course, on the instrument capabilities in terms of the dispersive element, as well as on the brightness and rotational broadening of the target. Ideally, one would want the observed individual line profiles to be covered with some 50 wavelength points (20 is still useful for low-degree modes) and to reach a S/N level above 200. If these demands are too stringent for the available instrument and target, compromises should be made such as to have the highest possible spectral resolution. In other words, it is possible to come up with clever methods to increase the S/N ratio, as will be discussed below, but making up for insufficient resolving power is impossible.

The observed spectrum is necessarily a convolution between the “true” spectrum and the instrumental profile. The latter is caused by imperfections in the instrument and limitations due to the instrumental setup which imply an effective spectral resolution lower than the theoretically expected one. The instrumental profile can usually be approximated by a Gaussian with a specific width of typically a few  $\text{km s}^{-1}$  and can best be estimated from the narrowest emission lines in the calibration measurements. One can also estimate it from telluric lines if the observed spectrum contains such signatures from the Earth’s atmosphere, but that usually leads to a less accurate approximation. In Gray (2005) the reader finds a clear description of the method to deconvolve the instrumental spectrum from the observed one. In principle, it involves only a deconvolution. In practice, however, this deconvolution is

affected by the noise in the measured spectrum due to which additional filtering is necessary. Gray (2005) defined such an optimum additional filter, assuming white noise, in terms of a free parameter to be adopted to each data set. Given the complication, this deconvolution with the instrumental profile is usually omitted for the analysis of a time series of single instrument spectra. In this case, the intrinsic broadening of the stellar lines will simply be overestimated with a value according to the instrumental profile width. In a case where spectra of different instruments constitute one time series, one should do the deconvolution with the instrumental profile before merging the data sets, unless the differences in the widths of the instrumental profiles among the instruments are much smaller than the amplitude of the line profile variations caused by the oscillations.

It is of paramount importance to achieve an accurate wavelength calibration of the spectroscopic data for asteroseismology, since one will be interpreting tiny velocity changes caused by the oscillations. Several internal emission-line lamps are therefore usually observed in between the stellar exposures, in order to correct for small changes in the thermal conditions of the instrument. In view of its rich emission spectrum, a thorium-argon (Th-Ar) lamp is often preferred as a wavelength calibration source (*e.g.*, Kaufer *et al.* 2000). The pixel coordinates of the emission lines of the lamp are then fitted with a suitable function, *e.g.*, a polynomial or a spline. A standard deviation typically of 1 mÅ, or less, between the measured emission line positions and those of the laboratory wavelengths of the calibration source should be attempted.

A particular point of attention in the reduction of the spectroscopy for asteroseismology, is the *spectrum normalisation* according to the continuum flux. We will be dealing with the interpretation of *relative* line profile variations in time rather than variations in the absolute flux. The latter are appreciably affected by atmospheric and instrumental conditions compared to the variations induced by the oscillations, so one usually does not attempt an absolute flux calibration for each spectrum. The choice not to measure standard stars, but rather use all the available telescope time on the target itself, is also due to the decrease in the quality of such a flux calibration as the slit width decreases, because the seeing conditions and guiding quality become more and more important. Since asteroseismology involves high-resolution spectroscopy, and thus tiny slit widths, absolute flux calibration is not a priority. Nevertheless, it may be useful to measure the spectrum of a bright standard star during the night and estimate the correspondence between the measured ADUs and the real flux value. This also allows an independent check of the wavelength calibration, although the radial velocities of the standards are often not known to an accuracy required for the wavelength calibration. A standard star spectrum may also help in the normalisation of the target spectra, even though the averaged target spectrum is often a better option.

It is essential to apply one and the same normalisation procedure to the whole time series, such that the deviations from symmetry, which may be

slightly affected by the normalisation, are always affected in the same way. This imperfect treatment then cancels out in the time variations of the normalised line profiles with respect to the mean. One can normalise the spectra near absorption lines by computing a polynomial or spline function through manually selected points of the continuum flux at each wing of a line profile. When dealing with hundreds or thousands of spectra, it may be advantageous to consider an automated routine that selects these continuum points and computes the fit. Care should be taken, however, not to include atypical continuum points. This can be achieved by accepting points only when they deviate less than a specified threshold from the mean continuum value in the neighbouring wavelength pixels. It is always advisable to inspect the fit to the continuum visually, after its computation, before dividing the observed spectrum by it, even when one opts for an automated normalisation procedure. In the case of pulsators in a single or double-lined binary, or for single pulsators with high-degree modes inducing moving bumps travelling through the profiles between the line wings, we advise manual selection of the points for the continuum fit.

As asteroseismologists, we are concerned with the signature of stellar oscillations in *time-resolved spectroscopy*. As we discussed in the section above on high speed photometry, we want to have several (typically more than ten) spectroscopic measurements spread over each oscillation cycle. Ideally, this is done in such a way that many cycles are observed to have a sufficiently long time base, and that each, or at least some of the cycles are densely covered to have appropriate conditions for the derivation of a good frequency spectrum (see Chapter 5 for these requirements), *i.e.*, there are at least two points per cycle for all harmonics needed to describe the shape of the radial velocity curve. Unlike photometric CCDs where frame transfer can reduce readout times to negligible fractions of integration times, spectroscopic CCDs are not generally providing this possibility yet. Thus for studies of very bright stars – where nevertheless the largest telescopes are needed to have the required S/N ratio and temporal resolution – it can be the case that only a small fraction of the observing night is spent actually gathering photons. When the integration time is much shorter than the readout time, much of the night is wasted. As an example, in their pioneering study of the solar-like oscillation of  $\alpha$  Cen A, Butler *et al.* (2004) used integration times of only 1 – 3 s with UVES on the VLT with a 23-s readout time, hence for most of the night the VLT was idle while the CCD was being read out. Spectrographs for high precision radial velocity measurements are being designed to overcome this problem.

Besides being time-resolved in the sense of covering the cycles with sufficient data points, the spectra also must have a good *temporal resolution*, as we discussed for photometry above. This condition requires the data to have an integration time that is only a fraction of the oscillation period. Ideally, this fraction is only 1 or 2 %, such that the measurement can be considered as instantaneous. In practice, this is often not possible, particularly for faint and/or short-period oscillators, depending on the telescope size and the

properties and efficiency of the spectrograph. In that case, one must simulate the effect of smearing out the measurement over a fraction of the oscillation cycle and account for this in the interpretation of the data, especially for multi-site campaigns that combine data taken with different integration times and numbers of points per pulsation cycle.

Depending on the purpose of the data, *e.g.*, frequency analysis (Chapter 5) alone, or mode identification (Chapter 6), the observational strategy must be carefully chosen. For accurate frequency analysis, for example, we need to cover many oscillation cycles to achieve a good estimate of the frequency values, particularly when complicated beating patterns due to multiperiodic oscillations occur. Any diagnostic derived from the time series of spectra will suffice in this case. Usually, one takes the time series of the *radial velocity*, which we define below, to derive the oscillation frequencies from spectroscopic data. For mode identification, on the other hand, we need very precise, *i.e.*, high S/N ( $> 200$ ), high-resolution ( $> 50\,000$ ) spectra covering a few oscillation cycles whenever the frequency values are already known from other diagnostics, *e.g.*, from photometric time series. A rule of thumb is that one needs about 100 line profile measurements for each mode to identify, although strong beating may require more than that.

It is clear that the optimal cadence and integration times of the observations, as well as the details of the instrumental set-up, depend, for ideal atmospheric conditions, on the target's brightness, on the instrumental capabilities and of course also on the oscillation period of the star under study. The latter may be unknown for some targets, since modes of degree typically higher than 3 or 4 are invisible in ground-based photometry. As we explained in Chapter 2, the periods range from only a few minutes to several days for different types of stars. One should make a compromise between the optimal observational requirements listed in this section, according to the goal of the time series. Lower quality than the guidelines given here can, to a certain extent, be made up for by a larger number of measurements. The last parameter to compromise is the spectral resolution.

#### 4.4.4 Observational Line Diagnostics

The most widespread diagnostic value derived from a time series of stellar spectra is the *radial velocity*. As mentioned in the introduction to this chapter, Lindegren & Dravins (2003) analysed the different concepts and usages of this term with the aim of deriving a fundamental definition of radial velocity for  $\text{m s}^{-1}$  precision. They proposed the quantity derived from accurate spectroscopic measurements to be termed the *barycentric radial velocity measure*. This equals the line-of-sight velocity in the absence of relativistic effects. It is not a physical quantity, however, such as the astrometric or kinematic velocity. The definitions of those are adopted in an IAU resolution given as appendix to their paper. Lindegren & Dravins (2003) also pointed out that,

even though spectroscopy cannot deliver accuracies of order  $\text{m s}^{-1}$  for absolute stellar radial motions (the zero-point), the precisions of the *variations* of derived quantities, such as the radial velocity measure, can easily reach such level for modern equipment.

Having defined the theoretical concept or the definition of radial velocity is one thing, how to compute the radial velocity measures from data (such as those shown in Fig. 4.8) in practice is another. Different approaches are made to achieve this, the simplest one being the estimate of the displacement of the minimum of an absorption line due to the Doppler effect with respect to the laboratory wavelength. Very often, this minimum is derived from making a Gaussian fit to the profile. This procedure is, however, inappropriate in the case of spectra of a pulsating star, as its line profiles will be skew and deviate from a Gaussian during most of the oscillation phase (see Fig. 4.8 and numerous additional examples in Chapter 6). This has to be taken into account in the derivation of an accurate radial velocity measure. The best way to do so is to compute the centroid (also referred to as the *centre-of-gravity*) of the spectral lines:

$$V_{\text{rad}} \equiv \frac{\int_{v_{\text{blue}}}^{v_{\text{red}}} v [1 - F(v)] dv}{\int_{v_{\text{blue}}}^{v_{\text{red}}} [1 - F(v)] dv}, \quad (4.2)$$

with  $v$  the line-of-sight velocity,  $v_{\text{blue}}$  and  $v_{\text{red}}$  the blue and red edges of the line profile and  $F(v)$  the normalised flux at  $v$ . Whenever we speak of “radial velocity” further on, we mean the quantity defined by Eq. (4.2). The time series of  $V_{\text{rad}}$  is very suitable to search for the oscillation frequencies.

Note that this quantity we have just defined as the radial velocity is *not* the pulsation velocity of any particular part of the stellar atmosphere. For nonradial pulsation the actual velocity of motion is a function of stellar latitude, longitude and atmospheric depth. Even a single spectral line samples a range of depth in the atmosphere; for the roAp stars, for example, which have radial pulsation wavelengths that are short compared to optical depth 1, pulsation amplitude and phase vary strongly with depth in a single spectral line. Additionally, we are viewing the limb-darkened spherical surface of the visible hemisphere of the star in projection and we are integrating over that surface to produce the radial velocity. The projection factor reduces our measured velocity compared to the atmospheric pulsation velocity, even in the simplest case where a single layer radial pulsation is a good approximation to the observed pulsation mode. This is, to first order, the case for Cepheid pulsation and the projection factor, including limb-darkening, in that case is 1.3 (Parsons 1972), meaning that the pulsation velocity is 1.3 times the measured radial velocity. For the more complex case of nonradial pulsation, projection factors can easily be calculated by integrating the local pulsational velocity over the visible hemisphere, taking into account the geometry of the pulsation

and limb darkening, as will be described in Chapter 6. The radial velocities defined by Eq. (4.2) are usually, but not always, sufficient for the purpose of deriving pulsation frequencies.

The computation of the radial velocity requires the determination of the *equivalent width* of the line, whose definition is given in the denominator in Eq. (4.2). This equivalent width does not change in time if the temperature, gravity, pressure, density and chemical composition of the line-forming region in the atmosphere do not change during the oscillation cycle. The equivalent width is thus a very valuable measure to test any changes of conditions in the line-forming region.

To get an idea about the absolute radial velocity precision, one usually considers the mean values  $\bar{V}_{\text{rad}}$  for each time series, and this for the different spectral lines. Subsequently, one computes the average of those  $\bar{V}_{\text{rad}}$  and its standard deviation. The latter will depend on the quality of the data, but also, and not negligibly, on the appropriateness of the laboratory wavelengths used for the different spectral lines and the detailed understanding of line-blending. These are quite often not well known, which may lead to systematic differences of several  $\text{km s}^{-1}$  for the different  $\bar{V}_{\text{rad}}$  values. We are not bothered by this situation in our interpretation of the oscillations, as long as we will be dealing with the variability in each of the  $V_{\text{rad}}$  time series for the different lines separately, irrespective of the systematic differences in their  $\bar{V}_{\text{rad}}$ . This is a good demonstration case where the precision is high, but not necessarily the accuracy; it is the precision we need. Another thing to keep in mind is that the amplitude and phase of the oscillations may reach different values for the various spectral lines. This is the case whenever the lines are formed in regions of the atmosphere that are so far apart that the oscillation displacement vector has changed in modulus and phase between the different line-forming layers. All these effects are the reason why one often limits a line profile analysis to the best isolated unblended line that is not heavily affected by pressure broadening. We refer to Chapter 5 for guidelines on how to combine radial velocity data from different spectral lines in the frequency analysis.

Stellar oscillations cause not only periodic changes in  $V_{\text{rad}}$ , and perhaps in the equivalent width, but also in the line width and the line skewness of the profiles, as is clearly visualised for the case of  $\beta$  Cru in the middle panels of Fig. 4.8. The variations of these four quantities are readily interpretable in terms of stellar oscillation theory, *i.e.*, theoretical expressions exist for these four quantities in terms of the oscillation frequencies and their quantum numbers  $(l, m)$ , as well as the pulsation amplitudes and the inclination angle of the star. These expressions and their exploitation in terms of mode identification will be discussed extensively in Chapter 6. This is the reason why these quantities, and not others such as line bisectors and their span (*e.g.*, Brown *et al.* 1998a,b; Gray 2005), are used by asteroseismologists in the interpretation of line profile variations. It was shown independently by Dall *et al.* (2006) and by Hekker *et al.* (2006) that line bisectors (and their spans) are not suitable

as a diagnostic for solar-like oscillations. In particular, they are not a good tool for mode identification.

#### 4.4.5 Increasing the Signal-to-Noise Ratio of the Line Profile Variations

Given the requirements on the signal-to-noise ratio for a line profile analysis, it is tempting to combine the information contained in different spectral lines. Whenever the amplitude and phase of the profile variations of different spectral lines are equal within their errors, one can do this, provided that the intrinsic line broadening is similar. The latter condition implies that we must exclude H and He lines in this exercise. Moreover, we can use only unblended lines for the interpretation of the line profile variability, as this was already a condition for the analysis of a single line profile. Let us assume that the available spectrum contains a number  $N$  of lines that fulfil these requirements.

Different methods have been proposed in the literature to merge the information contained in different lines that are spread over a wavelength range. We outline some of them here. We stress that any analysis based on merged profiles must be done very cautiously, because none of these methods is fool-proof. They usually work for frequency analysis, where the time variations in line diagnostics are analysed. In that case, the manipulations done to increase the S/N ratio are safe. When it comes to mode identification, however, the precise shape variations are interpreted, and their precision can suffer from the merging. This is why one should strive to restrict the interpretation of profile variability to a single well-chosen line whenever possible, *i.e.*, merging should only be done when the S/N ratio of all single unblended lines is insufficient for the analysis.

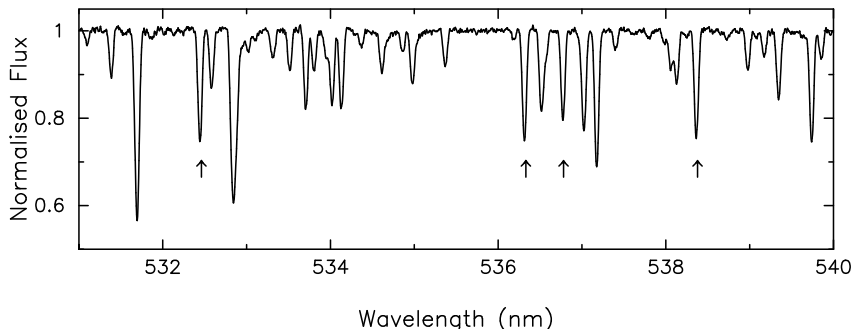


**Fig. 4.9.** Part of the spectrum of the  $\delta$  Sct star FG Vir taken by Zima *et al.* (2006). The four indicated Fe I lines were averaged for the interpretation of the line profile variability.

The simplest way to merge information in different spectral lines is to compute an average of carefully chosen line profiles of the same chemical element that have very similar depth and broadening. This method was adopted by Zima *et al.* (2006) in their mode identification of the δ Sct star FG Vir. We show part of a spectrum of that star in Fig. 4.9. The authors have averaged the four Fe lines indicated in the figure to obtain a combined line profile with higher S/N ratio and analysed its variations to derive frequencies and identify modes. As one can see from Fig. 4.9, the four selected lines do not have the same depth, nor are they broadened by exactly the same amount, although they look very similar. This means that the variations of the shape of the combined profile cannot be a perfect representation of the individual line shape variations, but come very close to it for lines with similar depth, broadening, and central wavelength (to avoid too different limb-darkening coefficients). In the case of FG Vir, the averaging of four lines allowed the authors to increase the S/N ratio by a factor  $\sim 2$  and to find frequencies and identify modes for more than ten modes, in agreement with photometric results that had been obtained before.

For photon-noise dominated signals, the S/N level within a merged profile increases roughly as  $\sqrt{N}$ , with  $N$  the number of lines used in the merging process, compared to the one of a single spectral line. It is therefore tempting to merge as many lines as possible. This same idea was originally used by planet hunters to obtain ultra-precise radial velocity measures (Mayor 1980). The quest for higher S/N ratios thus led to the consideration of *cross-correlation functions*. In order to compute these, we define a *line mask* based on the  $N$  lines selected for the merging. The simplest mask one can imagine has a boxed shape and is defined as

$$M(v) \equiv \sum_{i=1}^N w_i \delta(v - v_i), \quad (4.3)$$

where the  $v_i$  are the velocity pixels belonging to each of the  $N$  considered lines and  $w_i$  is the weight given to each line. If all lines considered in the mask are treated equally, one has  $w_i = 1/N$  within a line and  $w_i = 0$  outside of the lines. One then defines the *cross-correlation function* (CCF) of the observed spectrum  $(v, F(v))$  with the line mask at velocity  $v$  by

$$\text{CCF}(v) \equiv (F \star M)(v) = \sum_{i=1}^N w_i F(v - v_i). \quad (4.4)$$

This is a weighted mean of all the spectral lines considered in the mask. For a thorough description, we refer to Baranne *et al.* (1996). The CCF should contain the line profile variability, but with a higher S/N level, *provided that this variability is coherently present in these chosen mask lines*.

Equation (4.4) is the simplest form of a CCF. More sophisticated procedures are available in the literature. They have mainly been defined in the

context of planet hunting, but are suitable here as well. The basic idea of the improvement over Eq. (4.4) is to differentiate better between the suitability of the spectral lines by assigning weights according to the true line profile shapes and depths. One thus replaces the boxed-shaped mask by a synthetic spectrum for the fundamental stellar parameters of the star, appropriately broadened according to its rotation, and uses that as a mask  $(v, M(v))$ . This mask has an infinite S/N ratio, just as the simple boxed one. However, it still has the drawback that the “real” stellar spectrum will not be matched perfectly by the synthetic one. In particular, the chemical composition is often not known with a high precision. Also, many small blended lines will be present in the true spectrum of the star, but not in the synthetic one because the atomic data are unknown for them. To avoid these uncertainties, it is better to choose a very high S/N spectrum of the target itself as the mask  $(v, M(v))$ . In that case, the mask has noise, but it represents in the best way the true stellar spectrum.

The computation of the CCF  $(v) = (F \star M)(v)$  with  $(v, F(v))$ , the individual measurements of the spectrum within the time series, and  $(v, M(v))$ , the high S/N mask, is still by no means a guarantee for successful line profile analysis. It does result in very high S/N CCFs compared to the individual spectral lines. However, one should realise that the inclusion of small blended lines in the mask implies artificial broadening in the CCFs, particularly for moderate to rapid rotators. This artificial broadening is only averaged out well if one considers a large part of the spectrum containing many lines, because the line blending leads to incoherent contamination of the signal while the nonradial oscillation adds up coherently. It is thus not well suited for hot stars with few spectral lines. Moreover, as is well known, there are many lines in the spectra of stars cooler than, say, 10 000 K. For such stars, it is usually very difficult to achieve a safe normalisation over a large part of the spectrum. The numerous lines form a kind of pseudo-continuum, making it very difficult to derive the position of the true continuum. This introduces uncertainty in the depth and wings of the profiles from different échelle orders. This uncertainty is of different importance for different lines and it propagates into the computation of the CCF.

A slightly different type of line merging was considered by Donati *et al.* (1997) and Kennelly *et al.* (1998). Donati *et al.* (1997) developed their method in the context of spectropolarimetric signatures in the line profiles of magnetically active stars, while Kennelly *et al.* (1998) applied it for their interpretation of the line profile variability of  $\delta$  Sct stars. Their method also comes down to a convolution, just as defined above, but a slightly more sophisticated one. They make a *least-squares deconvolution* (LSD), as they termed it, of the time series of data  $(v, F(v))$  with a carefully constructed mask, but in such a way as to take into account the error of the extracted flux level measured in each of the CCD pixels as an additional factor in the weighting. In the study of non-radial oscillations, one can thus also work with the time series of  $(v, \text{LSD}(v))$  as a more sophisticated version than  $(v, \text{CCF}(v))$  provided that the flux noise

can be well estimated. The same remark about the artificial broadening and normalisation holds true here.

One is thus left with the following situation. If, and only if, it is necessary to increase the S/N ratio of the observed spectral lines for an interpretation in terms of the nonradial oscillations, then one has essentially two choices. Either one uses a very small number (a few) of carefully-chosen unblended lines, as in the example of FG Vir above, or one uses a mask consisting of hundreds to thousands of spectral lines selected from carefully-defined line-selection criteria concerning their width and depth to compute a CCF or LSD to replace each spectrum in the time series. The type of spectroscopic data available to the user should determine the best strategy.

#### **4.4.6 Increasing the Radial Velocity Precision in the Context of Exoplanet Finding and Solar-Like Oscillations**

The first exoplanets were discovered in an exotic environment orbiting a pulsar, PSR 1257+12 (Wolszczan & Frail 1992). The quest for extrasolar planets intensified dramatically following the first discovered around the solar-type star 51 Peg by Mayor & Queloz (1995). Exoplanet hunting requires radial velocity measures with a precision of the order of  $\text{m s}^{-1}$ . It was realised before the first exoplanet was discovered that such a precision is also necessary in the context of solar-like oscillations (Brown & Gilliland 1990; Gilliland *et al.* 1993; Hatzes & Cochran 1994; Kjeldsen *et al.* 1995). One can achieve the necessary precision by monitoring the atmospheric and instrumental conditions simultaneously with the target star. This can be done in essentially two ways.

A first method relies on the simultaneous measurement of the Th-Ar calibration lamp and the target star. This can be done with a spectrograph having two fibres, where one is used to measure at the same time the sky background and the Th-Ar lamp and the other one is reserved for the target. In this way, the instrumental conditions are ideally monitored. Those conditions must still be kept as stable as possible, putting stringent constraints on the environment of the spectrograph in terms of temperature, pressure and humidity stability. This method is therefore expensive. The advantage is that the needed precision is reached by applying the technique of CCF, as detailed in the last section.

For exoplanet hunting, the goal is to derive the best possible radial velocity measure from a minimal number of spectral lines. As the latter are not deformed, but merely displaced by the stellar motion about the planet-star barycentre, there is no change in line shapes. This led to the development of specific methods to acquire the highest possible accuracy in the radial velocity. These methods are based on the original one introduced by Connes (1985) and use the full spectral information. The optimum weight method by Bouchy *et al.* (2001) gives a clear description of how to optimise the computation of the weights  $w_i$  to be used for the radial velocity measure derivation. In this method, one considers the full 2-D wavelength-calibrated échelle spectrum

consisting of numerous orders to compute the CCF and the  $V_{\text{rad}}$ . In this way, one avoids having to normalise the flux level. Such a procedure is not optimal for the interpretation of line profile variations because the simultaneous recording of the Th-Ar and stellar spectrum implies contamination of the stellar lines during the reduction process, particularly at blue wavelengths. For asteroseismology of heat-driven modes with amplitudes at  $\text{km s}^{-1}$  level, one thus preferably separates the recording of the stellar and calibration spectra. For solar-like oscillations with  $\text{m s}^{-1}$  amplitude, one must do the recording simultaneously to achieve the necessary accuracy.

The second method of obtaining high-precision radial velocity measures relies on the simultaneous measurement of the stellar spectrum and the spectrum of gaseous molecular iodine,  $I_2$  (Marcy & Butler 1992). To achieve this, an iodine vapour absorption cell is placed in front of the spectrograph slit. This method is cheap and implies high flexibility. The stellar and iodine spectrum are thus simultaneously convolved with the instrumental profile and are recorded together. The iodine lines provide a direct wavelength calibration over the wavelength area where they occur (between 500 and 600 nm). The radial velocity measure is then obtained by deconvolving the measured stellar and iodine spectrum with the instrumental one and subsequently using the iodine transmission function known from laboratory measurements. We refer to the paper by Marcy & Butler (1992) for a detailed description. This method works fine for the derivation of  $V_{\text{rad}}$ , but a reconstruction of the line shape variations is far from trivial, and requires an iterative procedure to correct for small iodine features left in the stellar spectrum, as explained in detail by Brown *et al.* (1998b).

We conclude that the simultaneous measurement of the stellar spectrum with either a Th-Ar calibration lamp or an iodine absorption gas both affect the spectral lines of the reduced spectrum. It is therefore unclear how line profile variations are preserved in the merged profiles or CCFs computed from such data. Hekker *et al.* (2006) have used CCFs computed from the optimum weight method by Bouchy *et al.* (2001) to study the line profile variations induced by solar-like oscillations of red giant stars. They managed to detect the line profile variability, with frequencies in full agreement with those found in the  $V_{\text{rad}}$  variations. This seems to point out that the optimum weight method is also suitable for the interpretation of line profile variations in terms of nonradial oscillation modes. From extensive simulations of line profile variations of stochastically-excited solar-like oscillations taking into account the damping, Hekker *et al.* (2006) subsequently found the surprising result that some of the modes of three of the four red giants they studied seem to be nonradial. This result certainly deserves further attention, from both the theoretical and instrumental/observational point of view.

#### 4.4.7 Disentangling Spectra to Interpret the Oscillations of Double-Lined Binaries

The determination of radial velocity measures from line profiles of double-line spectroscopic binaries (SB2s) is not straightforward. This is illustrated in Fig. 4.10, where we show an observed Si III  $\lambda 4552.6\text{ \AA}$  line profile of the SB2  $\beta$  Cep star  $\beta$  Cen. Whenever the  $V_{\text{rad}}$  of the narrow-lined component is estimated from integration between the two vertical bars indicated on the plot, a systematic error is introduced. Such a systematic error will occur in the radial velocity measures for any spectroscopic binary in which both components contribute to the lines. This problem led to the development of methods to separate the component spectra of stars in a double-lined binary. Early developments were done by Bagnuolo & Gies (1991) and Simon & Sturm (1994). An attempt to avoid such systematic error in the study of a nonradial pulsator can be found in Tomkin *et al.* (1995) for the  $\delta$  Sct star  $\theta^2$  Tau. In that work, the authors subtracted the lines of the primary by means of spectra of reference stars with the same spectral type before computing the secondary star's  $V_{\text{rad}}$ -values. Ausseloo *et al.* (2006) provided analysis schemes based on disentangling to overcome such systematic errors in a more accurate way. The authors used the disentangling methodology KOREL developed in a series of papers by Hadrava (1995, 1997, 2001, 2004a, 2007) and applied it to the double-lined  $\beta$  Cep star  $\beta$  Cen, which does not show photometric variability but strong line profile variations due to oscillations.

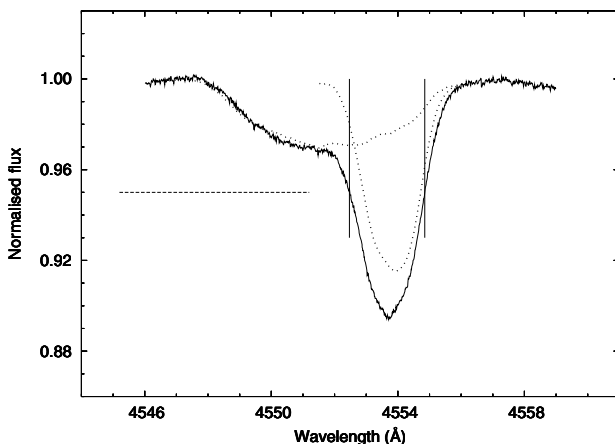


**Fig. 4.10.** Si III  $\lambda 4552.6\text{ \AA}$  line profile of the SB2  $\beta$  Cep star  $\beta$  Cen. The two vertical and the horizontal lines denote the integration limits used by Ausseloo *et al.* (2002) to calculate the  $V_{\text{rad}}$  of the component with the deep line. The two dotted lines denote the disentangled line profiles of both components.

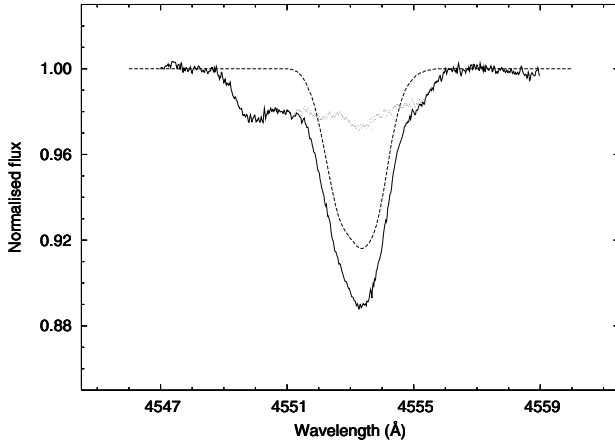


**Fig. 4.11.** A Si III  $\lambda$  4552.6 Å line (full line) and the secondary's disentangled line profile, which is shifted according to its corresponding orbital  $V_{\text{rad}}$  (dashed line). The residual spectrum obtained by subtracting the shifted disentangled line profile from the original spectrum is shown as dots.

Another disentangling method, termed FDBINARY was developed by Ilijic *et al.* (2001, 2004). The disentangling can be done in the wavelength domain or in the Fourier space. Ilijic (2004) briefly compared the performance and advantages/disadvantages of these two approaches.

For an overview of the history of the method of disentangling, and a thorough discussion of the comparison between the various methods, we refer to Hensberge *et al.* (2008). In that paper, the reader also finds a comprehensive mathematical description, as well as a discussion on the spurious effects which might occur in applications and a practical guideline to observers to plan their observing strategy according to the best performance. Present-day versions of the algorithms can handle flux variations, *e.g.*, due to the eclipsing nature of the binary or due to oscillations.

Applications of the disentangling of spectra of double-lined binaries with a pulsating component, besides those mentioned above, can be found in, *e.g.*, Harmanec *et al.* (2004), De Cat *et al.* (2004), Uytterhoeven *et al.* (2005a,b), Frémat *et al.* (2005) and Freyhammer *et al.* (2005) to which we refer for details. In these applications, the disentangling not only led to a significant improvement in the precision of the physical parameters and dynamical parallax of the components of the binaries, but it also allowed one to study the oscillations of (one of) the components. In Fig. 4.11 we show the disentangled profile of the deep-lined secondary shifted to the orbital  $V_{\text{rad}}$ . This disentangled spectrum was subsequently subtracted from the measured one and reveals at once that it is the broad-lined primary that exhibits oscillations, and not the component with the deep lines as was thought until the study by Ausseloo *et al.* (2006).

As soon as the spectra are disentangled reliably, they can be used to study line profile variability as for a single star.

As a final remark, we point out that Hrudková & Harmanec (2005) and Hadrava (2006) demonstrated that the disentangling technique can also be used to remove telluric lines from the spectrum of a single star by treating the telluric spectrum as a second star. They illustrated that the method works well and is valuable especially for the spectra of red stars which may be heavily blended with telluric lines. One can thus obtain a disentangled stellar spectrum with a higher S/N ratio than the original one by the removal of the telluric lines. Similar applications to reliably remove iodine line signatures still need to be explored.

---

## Frequency Analysis

As already discussed in Chapter 3, the three components of the Lagrangian displacement vector of an undamped oscillator contain a time-dependent factor  $\exp(-i\omega t)$ , with  $\omega = 2\pi\nu$  the angular frequency of the oscillation mode and  $\Pi = 2\pi/\omega = 1/\nu$  its period (see, *e.g.*, Eq. (3.124) where it was explained that all Eulerian and Lagrangian perturbations contain a common factor). It is therefore clear that stellar oscillations give rise to periodic variations of the physical quantities. These translate into periodic variations of observables, such as the brightness, the colours, the radial velocity and the spectral line profiles. In this Chapter we describe methodology to derive the oscillation frequencies from time series of data of pulsating stars.

*Time series analysis* is a well-developed field in statistics (*e.g.*, Bloomfield 1976; Kendall & Ord 1990). Unfortunately, the available classical theory is not appropriate to analyse data of pulsating stars because this theory almost always assumes uninterrupted measurements which are evenly spaced in time. Astronomical time series usually contain large gaps and *unevenly spaced data*. Moreover, the gaps themselves may have quasi-periodicities, *e.g.*, daily interruptions of single-site measurements by the Sun, monthly interruptions because of telescope scheduling based on the phases of the moon and annual interruptions because of the Earth's orbital motion for the large majority of stars that are not circumpolar. While techniques to treat several types of missing data (missing completely at random, missing at random, missing not at random) are also well developed in statistics (*e.g.*, Little & Rubin 2002; Molenberghs & Verbeke 2005), it is not advised to apply them to astronomical time series because

- the oscillation frequencies need to follow a well-known deterministic distribution in order to make an appropriate reconstruction to fill the gaps, which is not always a safe assumption;
- the amount of missing data is often larger than the available data, *i.e.*, one usually deals with low duty cycles implying uncertain reconstruction by interpolation as well.

The latter concern is particularly relevant for ground-based data, even those assembled from multi-site campaigns. It is less of a problem for data assembled from space with missions dedicated to oscillation studies, where duty cycles above 90% can be achieved. However, here we provide methodology that is appropriate to treat the hardest possible type of time series of pulsating stars, *i.e.*, unevenly spaced data with a low duty cycle. The methods will also work for data sets with a high-duty cycle that are (quasi-)equidistant. In such cases, additional classical methods, such as those based on Fast Fourier Transforms (*e.g.*, Press *et al.* 1992, Chapter 12; Bracewell 1999), will also be applicable and may imply faster computations.

In the present Chapter, illustrations of the theory are based on simulated data. The reader is referred to Chapters 2 and 7 for extensive applications of the methodology to real modern data.

## 5.1 Harmonic Analysis by Least Squares

With a harmonic analysis we mean the search for a certain sum of harmonic functions that best describe the data in the time domain in the least-squares sense. Least-squares fitting is a well-known statistical technique familiar to most readers, which is why we consider it here as a first easy case of a parametric method for frequency search in time series of stellar oscillations, before treating other methods. The particular case of harmonic fitting described here is equivalent to taking a Fourier transform of the time series, which will be considered in Section 5.3.

Consider measurements of a quantity  $x$  at different times  $t_i$ :  $x(t_i) \equiv x_i$  with  $i = 1, \dots, N$ . Considering the time dependence of the oscillation modes, we aim at using a model of the following form:

$$x(t_i) = \sum_{k=1}^M a_k \cos[2\pi\nu_k(t_i - \tau)] + b_k \sin[2\pi\nu_k(t_i - \tau)] + c + \epsilon_i, \quad (5.1)$$

describing the variations due to  $M$  oscillation modes with frequencies  $\nu_k$ ,  $k = 1, \dots, M$  which are excited with amplitudes above the detection threshold, with  $\tau$  an arbitrary reference epoch,  $a_k$ ,  $b_k$  and  $c$  the free fitting parameters and  $\epsilon_i$  the measurement errors. The latter are usually assumed to be independent and normally distributed with average zero and constant variance  $\sigma_N^2$ , *i.e.*, we assume to be dealing with white Gaussian noise. We come back to this assumption in Section 5.5. We have to find a way to derive each frequency  $\nu_k$ , as well as the unknowns  $a_k$ ,  $b_k$  and  $c$ , from the data.

### 5.1.1 Searching for a Single Frequency

Let us first assume that the time series is due to one single undamped oscillation mode whose frequency  $\nu_1$  we seek to find, *i.e.*,  $M = 1$  and  $a_1 = a$ ,  $b_1 = b$ .

For each test frequency  $\nu$  we determine the unknowns  $a, b, c$  by means of a least-squares algorithm. The best estimates for  $a, b, c$  are those that minimize the quadratic deviations between the observed and calculated values. We define the likelihood function  $L$  as:

$$L \equiv \sum_{i=1}^N \{x_i - a \cos[2\pi\nu(t_i - \tau)] - b \sin[2\pi\nu(t_i - \tau)] - c\}^2, \quad (5.2)$$

with  $\tau$  a fixed reference epoch. We then find  $a, b, c$  by solving the set of equations:

$$\frac{\partial L}{\partial a} = 0, \frac{\partial L}{\partial b} = 0, \frac{\partial L}{\partial c} = 0. \quad (5.3)$$

After some manipulation this results in the following values for the unknowns:

$$\left\{ \begin{array}{l} a = \frac{c_x}{c_2} - \frac{c_1}{c_2} \frac{\frac{c_x c_1}{c_2} + \frac{s_x s_1}{s_2} - x_{\text{sum}}}{\frac{c_1^2}{c_2} + \frac{s_1^2}{s_2} - N}, \\ b = \frac{s_x}{s_2} - \frac{s_1}{s_2} \frac{\frac{c_x c_1}{c_2} + \frac{s_x s_1}{s_2} - x_{\text{sum}}}{\frac{c_1^2}{c_2} + \frac{s_1^2}{s_2} - N}, \\ c = \frac{\frac{c_x}{c_2} c_1 + \frac{s_x}{s_2} s_1 - x_{\text{sum}}}{\frac{c_1^2}{c_2} + \frac{s_1^2}{s_2} - N}, \end{array} \right. \quad (5.4)$$

in which we have used the following definitions:

$$\begin{aligned} c_2 &\equiv \sum_{i=1}^N \cos^2[2\pi\nu(t_i - \tau)], \quad s_2 \equiv \sum_{i=1}^N \sin^2[2\pi\nu(t_i - \tau)], \\ c_x &\equiv \sum_{i=1}^N x_i \cos[2\pi\nu(t_i - \tau)], \quad s_x \equiv \sum_{i=1}^N x_i \sin[2\pi\nu(t_i - \tau)], \\ c_1 &\equiv \sum_{i=1}^N \cos[2\pi\nu(t_i - \tau)], \quad s_1 \equiv \sum_{i=1}^N \sin[2\pi\nu(t_i - \tau)], \\ x_{\text{sum}} &\equiv \sum_{i=1}^N x_i. \end{aligned} \quad (5.5)$$

The solutions for  $a, b, c$  allow us to compute the predicted value of  $x_i^c(\nu)$  for the test frequency  $\nu$ :

$$x_i^c(\nu) \equiv a \cos[2\pi\nu(t_i - \tau)] + b \sin[2\pi\nu(t_i - \tau)] + c. \quad (5.6)$$

The difference between the measured value  $x_i$  and the predicted value  $x_i^c(\nu)$  is called the *residual* at time  $t_i$ :

$$R_i(\nu) \equiv x_i - x_i^c(\nu). \quad (5.7)$$

Searching for the most likely frequency comes down to searching for the frequency  $\nu$  for which the sum of squares of the residuals is minimal, *i.e.*, searching for a minimum of the function

$$R^2(\nu) = \sum_{i=1}^N R_i^2(\nu) = \sum_{i=1}^N [x_i - x_i^c(\nu)]^2. \quad (5.8)$$

We note that estimating the best value of  $a, b, c$  for the test frequency  $\nu$  is equivalent to searching for the best value of  $A, \delta, c$  such that

$$x_i^c = A \cos \{2\pi[\nu(t_i - \tau) + \delta]\} + c. \quad (5.9)$$

This is perhaps a more often used harmonic model, as the *amplitude*  $A$  and the *phase*  $\delta$  of the frequency  $\nu$  are readily interpretable observables that result from the data, unlike  $a$  and  $b$  whose meaning is more complicated. It is indeed easy to show that  $A^2 = a^2 + b^2$  and  $2\pi\delta = \arctan(-b/a)$ .

After having determined the value of  $A, \delta, c$  such that the curve describes as well as possible the data with the least-squares method for each test frequency  $\nu$ , we derive the variance of the data with respect to the best average curve. Whenever this variance is small we have found a frequency that explains a large percentage of the variability in the data. This percentage is called the *variance reduction* or *fraction of the variance* ( $f_v$ ) and is defined as:

$$f_v = 1 - \frac{\sum_{i=1}^N (x_i - \{A \cos \{2\pi[\nu(t_i - \tau) + \delta]\} + c\})^2}{\sum_{i=1}^N (x_i - \bar{x})^2} = 1 - \frac{L}{\sum_{i=1}^N (x_i - \bar{x})^2}. \quad (5.10)$$

with  $\bar{x} \equiv \sum_{i=1}^N x_i / N$ . The search for a minimum of  $R^2(\nu)$  is, in fact, a search for a maximal variance reduction in the data. We thus assign to  $\nu_1$  the test frequency  $\nu$  with the largest variance reduction and our procedure at once gives us its amplitude  $A$  and phase  $\delta$ .

As the very simple example shown in Fig. 5.1 demonstrates, one can easily have equivalent solutions whenever the observed time series is limited in number of points and in time coverage. It is important to keep in mind that almost equivalent solutions occur whenever the times of measurement cover a limited number of cycles and are taken with intervals equal to the beat periods of the occurring frequencies.

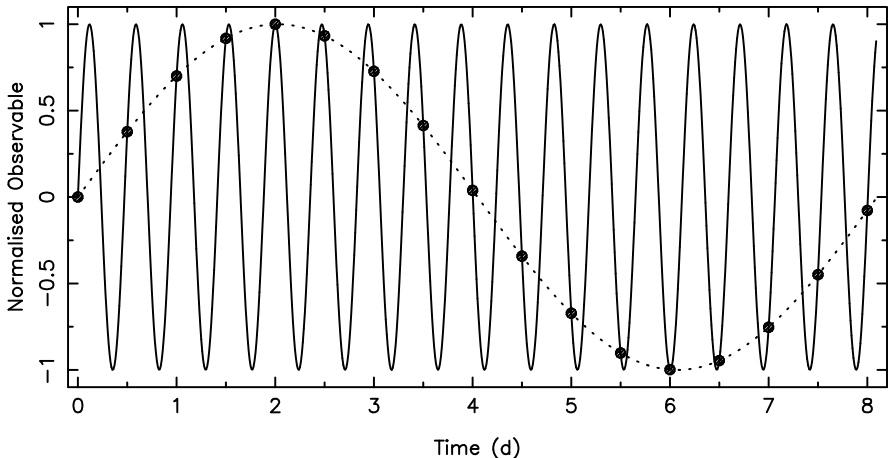


**Fig. 5.1.** Simulated data (dots) representing a periodic signal with frequency  $\nu = 0.123456789 \text{ d}^{-1}$ . The dotted line is a harmonic fit for this frequency. The full line represents a fit with the frequency  $2.123456789 \text{ d}^{-1}$ .

### 5.1.2 Searching for Multiple Frequencies

In principle, we could now repeat the previous derivation in order to find the most likely set of frequencies  $\nu_k, k = 1, \dots, M$  of the model fit in Eq. (5.1) from the data. Unfortunately, as explained in Chapter 3, we are unable to predict the amplitude of excited oscillation modes in a star. Thus, we do not know the number  $M$  of oscillations that will be excited with detectable amplitude in the observed time series. This implies that this discrete unknown  $M$  has to be estimated along with the frequency search itself.

Estimation of discrete parameters is a very poorly developed field in statistics. This is a mathematical problem with very important implications for many fields, among which is asteroseismology. Besides causing a problem here for frequency determination, a similar situation will occur in Chapter 6 on mode identification, where the discrete wavenumbers of each of the detected oscillation modes  $(l, m, n)$  have to be estimated. A consequence of this is that frequency analysis for asteroseismology is unavoidably *data-driven*. This is a huge disadvantage from a statistical viewpoint compared with the situation where we would be able to estimate simultaneously the number of frequencies present in the data and their value from a model description.

We cannot but conclude that the search for multiple oscillation frequencies necessarily must be done by means of some kind of *prewhitening* procedure by which we mean that, at each stage of the frequency search, a fit with the selected frequency is computed and subtracted from the data values before a subsequent frequency search is started. The statistical interpretation of such

a data-driven approach is much more challenging than one based on a model-driven treatment, unfortunately.

A prewhitening strategy thus has to be chosen to perform the frequency analysis. The simplest such strategy is to prewhiten the data according to Eqs (5.9) and (5.7) after the frequency  $\nu_1$  with the largest variance reduction was derived and to start a new frequency analysis to search for  $\nu_2$  in the residuals, and so on. One thus determines, at each stage of prewhitening, the values of  $\nu_k, A_k, \delta_k$ .

As pointed out by Vaníček (1971), one can improve this procedure by fitting the original data at each step with all the frequencies found up to then (he termed them “known constituents”), fixing only the frequency values and leaving their amplitudes and phases (the “unknown constituents”) free during the whole procedure. Vaníček showed that these unknown constituents determine “systematic noise” that is present in the data, besides the additional random noise, and there is in principle no need to fix them while searching for additional frequencies.

A rather evident next step is then to recompute a least-squares solution according to Eq. (5.1) at every prewhitening stage, starting each time from the original data and leaving also the frequency values  $\nu_k$  free in making the fit, using the outcome of one or several different frequency search methods described here as a good starting value. This procedure is most commonly used nowadays in asteroseismology. It works fine as a prewhitening strategy and as a method to derive the most likely values for the frequencies, amplitudes and phases, provided that good starting values for the frequencies, already very close to their true values, are known and that a sufficient number of data points is available with respect to the degrees of freedom of the fit. As a rule of thumb we advise against making such a fit for data sets with fewer points than ten times the number of degrees of freedom. Additional requirements have to be fulfilled for such a fit to be meaningful. We discuss these in Sects 5.3 and 5.4 and the reader is strongly advised to take these into account. Error estimation is treated in Section 5.5.

## 5.2 Non-parametric Frequency Analysis Methods

Non-parametric methods imply that one does not *a priori* assume a chosen model function to describe the data. This is in contrast to the search for the maximal variance reduction described above, as well as to any method based on Fourier transforms discussed further on, where harmonic model functions are assumed from the start.

### 5.2.1 String Length Methods

The *string* or *rope length methods* are also based on the principle of least squares. Lafler & Kinman (1965) initially introduced such a method with the

purpose to determine periods of RR Lyrae stars from small samples of visual data. Clarke (2002) presented a clear recent evaluation of these methods and proposed their generalization to the application for multivariate data, the so-called Rope Length Method. This methodology is very suitable to analyse time series of multicolour photometric observations or of radial velocity variations from different spectral lines. The prime disadvantage of these methods, the long computation time needed, has largely been reduced with current speed of modern computers, except for very rich data sets. Nevertheless, the string and rope length methods are much less often applied compared with those discussed in the following sections. This has to do with the multitude of false peaks compared with Fourier methods, as we will show below. On the other hand, the non-parametric methods may be preferred to search for periodicity in strongly non-sinusoidal variations. These not only occur for large-amplitude pulsators, but also for eccentric and/or eclipsing binary light curves.

Consider again measurements of a quantity  $x$  at different times  $t_i$ ,  $x(t_i)$  with  $i = 1, \dots, N$ . The phase  $\phi(t_i)$  corresponding to the frequency  $\nu$ , or to the period  $\Pi = 1/\nu$ , with respect to the reference epoch  $\tau$  is defined as follows:

$$\phi(t_i) = [\nu(t_i - \tau)] = \left[ \frac{t_i - \tau}{\Pi} \right], \quad (5.11)$$

where  $[y]$  stands for the decimal part of  $y$ , increased by one if  $y$  is negative. From this definition it follows that  $0 \leq \phi < 1$ . A plot of the observations  $x(t_i)$  as a function of  $\phi(t_i)$  is called a *phase diagram*. An example for the simulated data shown in Fig. 5.1 is provided in Fig. 5.2.

For each trial frequency  $\nu$ , taken from a grid of test frequencies, the original data  $x(t_i)$  are first assigned phases  $\phi(t_i)$ , which are then ordered in ascending value  $0 \leq \phi_1, \dots, \phi_N < 1$ . For each trial frequency, the original Lafler-Kinman statistic performs a “string length” summation of the squares of the differences between the consecutive phase-ordered values. Following Clarke (2002), we advise the use of the following modified string length statistic:

$$\Theta_{SL}(\nu) \equiv \frac{\sum_{i=1}^N [x(\phi_{i+1}) - x(\phi_i)]^2}{\sum_{i=1}^N [x(\phi_i) - \bar{x}]^2} \times \frac{N-1}{2N}, \quad (5.12)$$

where  $\bar{x}$  is the mean value of the measurements and  $x(\phi_{N+1})$  is taken to be equal to  $x(\phi_1)$ . The sum in the denominator of Eq. (5.12) is nothing but the product of the number of measurements with the variance of the data set such that  $\Theta_{SL}$  is independent of the noise in the data. Moreover, the factor 2 results in a normalized statistic with continuum level unity. If the time series contains periodicity with frequency  $\nu$ , then  $\Theta_{SL}$  will reach a minimum at  $\nu$  while fluctuations in  $\Theta_{SL}$  due to the noise will result in a level  $\Theta_{SL} \approx 1.0$ .

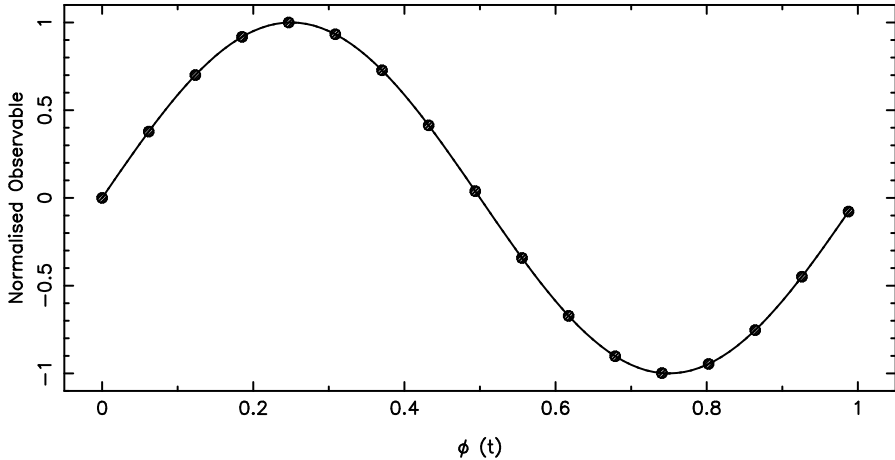


**Fig. 5.2.** Simulated data from Fig. 5.1 drawn in a phase diagram where the arbitrary reference epoch  $\tau$  was chosen such as to place the maximum of the observable at phase  $\phi = 0.25$ . The full line is the phased fit for the frequency  $0.123456789 \text{ d}^{-1}$  or for  $2.123456789 \text{ d}^{-1}$  shown as dotted and full line in Fig. 5.1.

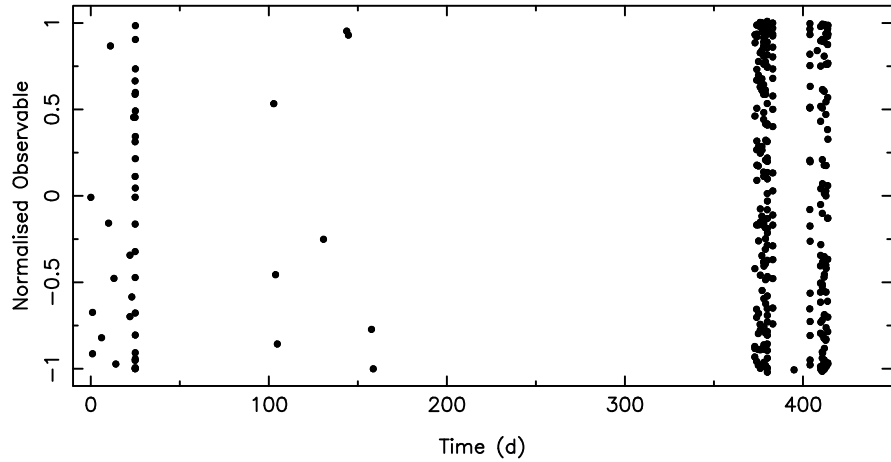


**Fig. 5.3.** Simulated gapped data representing a typical time series for a ground-based single-site campaign of a pulsating star.

A typical example of a simulated single-site time series of a star discovered as a new variable is shown in Fig. 5.3. These data represent the following situation. The discovery of the variability is made in one season. A few follow-up tests are being done some months later, confirming the variability, and a dedicated campaign is then undertaken to derive the periodicity in the next year. The simulated data have a standard deviation of 0.696 and a variance

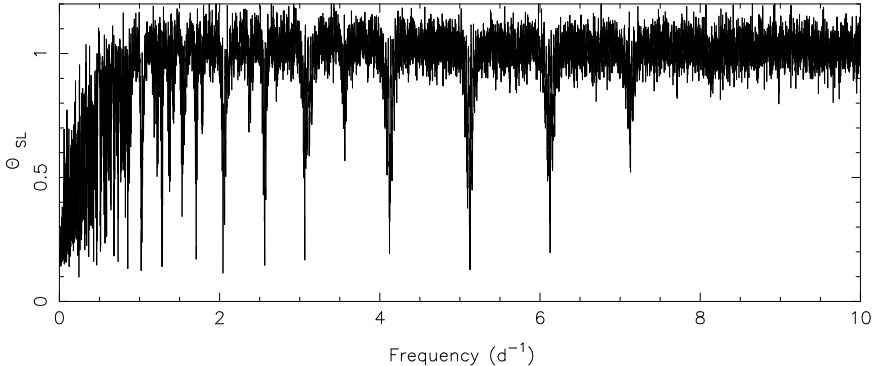


**Fig. 5.4.** Statistic  $\Theta_{SL}$  according to Eq. (5.12) of the data shown in Fig. 5.3.

of 0.485. The white noise has a standard deviation of 0.01111 and a variance of 0.00012.

The string-length statistic of this prototypical time series is shown in Fig. 5.4. One notices clear minima with a daily repetition, the minimum of  $\Theta_{SL}$  occurring at the input frequency  $5.123456789 \text{ d}^{-1}$ . A forest of peaks also occurs for frequencies below  $2 \text{ d}^{-1}$ . The occurrence of minima at subharmonics of the frequency and of their *aliases* (see Section 5.3 for a definition) is a general property of the frequency analysis methods based on phase diagrams (see, *e.g.*, Cuypers 1987 for an extensive discussion) and is considered as one of its disadvantages.

After having computed  $\Theta_{SL}$  comes the task to try and disentangle which of the minima is the real oscillation frequency. In principle, this is the one corresponding to the deepest minimum. In practice, however, the interaction between the effects of the time sampling and (non-white) noise may imply a minimum in  $\Theta_{SL}$  deeper than the one for the true oscillation frequency. It can be helpful to draw phase diagrams of the few deepest peaks in  $\Theta_{SL}$  to discriminate the true frequency from false ones, besides comparing their variance reduction  $f_v$  from a least-squares fit using the peak values of the candidate frequencies as starting values for the fit. In Fig. 5.5 six such phase diagrams are shown. These make it evident, in this prototypical example, that  $5.123 \text{ d}^{-1}$  is the true frequency. Note, however, that also its alias frequencies near  $4.121 \text{ d}^{-1}$  (middle left) and  $7.129 \text{ d}^{-1}$  (lower left) give “good” phase diagrams in the sense that the periodic variability is clearly present in them. These phase diagrams also make it clear why the string-length statistic leads to a minimum for them. One should therefore not mistakenly believe that the frequency is real as soon as clear variation is seen in its phase diagram. All apparently significant deep minima in the statistic (or high peaks in Fourier analysis, see further) will produce phase diagrams in which one can see the variability, even if the selected frequency is a noise peak. The right panels are

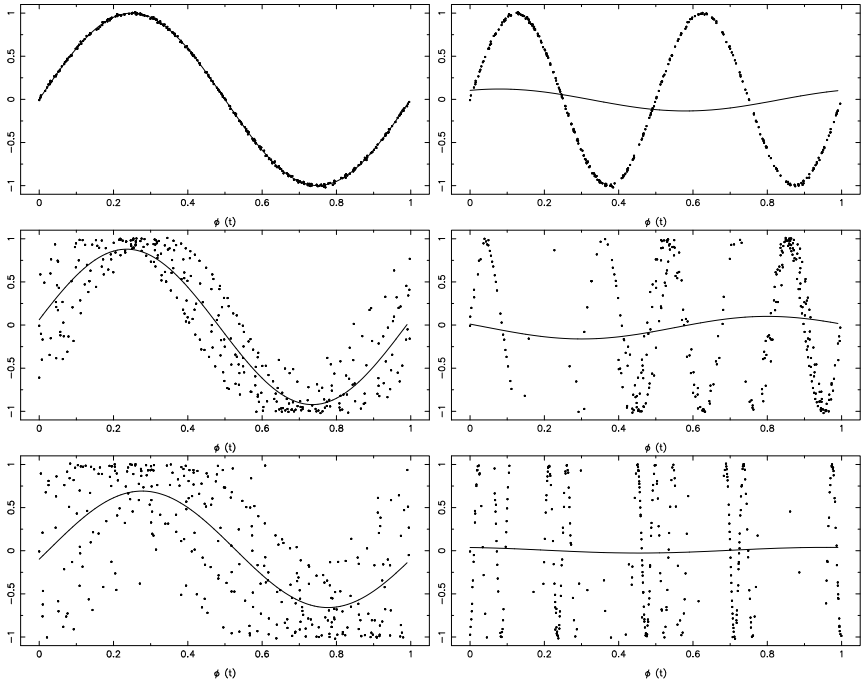


**Fig. 5.5.** Phase diagrams for six minima in  $\Theta_{\text{SL}}$  found from Fig. 5.4. The phases for the data (dots) and harmonic fit (full lines) are computed for  $5.123 \text{ d}^{-1}$  (upper left),  $4.121 \text{ d}^{-1}$  (middle left),  $7.129 \text{ d}^{-1}$  (lower left),  $2.562 \text{ d}^{-1}$  (upper right),  $1.021 \text{ d}^{-1}$  (middle right),  $0.244 \text{ d}^{-1}$  (lower right).

those for half of the true frequency, and for frequencies due to a mixture of effects due to harmonics, the noise and the sampling. From the upper right panel it is again apparent why subharmonics of the true frequency also deliver a low value of the string-length statistic. The examples for the other two spurious frequencies show that the phase diagram can be a very useful tool. The phase coverage of the data and the amplitude of the fit with respect to the peak-to-peak variation is bad for these diagrams. This would also have been clear from a least-squares fit as it would result in an insignificant amplitude and a low variance reduction  $f_v$  for these cases. If the data are not well-spread in phase for limited data sets, but cluster narrowly at particular phases and/or the variability occurs mainly at phases where there are no data points, then one is probably also dealing with a false frequency. These issues are important to check for and justify the use of phase diagrams besides computation of  $f_v$ .

The behaviour of  $\Theta_{\text{SL}}$  was studied extensively from simulations by Clarke (2002), to whom we refer for more information. He computed cumulative distribution functions for  $\Theta_{\text{SL}}$  in order to develop confidence levels for it as a function of data sampling and size. His work mainly focused on small time

series, though. This is also the case for the evaluation of earlier versions of different string length statistics as those by Lafler & Kinman (1965), Burke *et al.* (1970), Renson (1978) and Dworetsky (1983).

With the goal to perform empirical mode identifications, asteroseismologists often gather multicolour observations of their target stars. The measurements in different filters of a photometric system are usually taken as close as possible in time, or ideally simultaneously, as explained in Chapter 6. Most often, however, the frequency analysis is performed for the different colours separately. One then either accepts the frequency value derived from the filter that delivered the highest *signal-to-noise ratio* (S/N ratio), or determines a weighted average frequency based on the values obtained for the different colours. The same is true for observables derived from different spectral lines, which are of course necessarily simultaneous. Although it is in principle possible to extend most frequency analysis techniques to multivariate data (see Section 5.6), such an endeavour is usually not undertaken. Nevertheless, using a weighted statistic has significant advantages in some cases, as we will discuss below for the parametric methods. It is a major advantage of the string length methods that they allow straightforward generalisation to a multivariate treatment.

The brightness variations in different photometric bands due to oscillations are strongly correlated. Depending on whether or not there are phase differences between the colour curves of the pulsating star, the measurements plotted in a brightness-brightness diagram for two different filters lie on a straight line or an ellipse-like structure. They can hence be connected by a “rope” consisting of various connecting strings, whose squared length can be added, again after assigning a phase to each measurement and ordering the data according to increasing phase. The same reasoning can be repeated for all the  $k = 1, \dots, Z$  filters in which a photometric time series has been obtained or for the  $Z$  spectral lines from which a radial velocity has been derived. Clarke (2002) proposes the following statistic for multivariate time series:

$$\Theta_{\text{RL}}(\nu) \equiv \frac{1}{Z} \sum_{k=1}^Z \left( \frac{\sum_{i=1}^{N[k]} [x_k(\phi_{i+1}) - x_k(\phi_i)]^2}{\sum_{i=1}^{N[k]} [x_k(\phi_i) - \bar{x}_k]^2} \times \frac{N[k] - 1}{2N[k]} \right), \quad (5.13)$$

where  $x_k(\phi_i)$  is the magnitude in filter  $k$  or radial velocity from line profile  $k$  for each of the measurements taken at times  $t_1, \dots, t_N$  after re-arranging the data such that  $\phi_1, \dots, \phi_N$  increases from 0 to 1 for each of the test frequencies  $\nu$ . It is rather cumbersome, however, to interpret the outcome of this statistic for extensive multicolour asteroseismic time series due to the numerous false frequency peaks.

### 5.2.2 Phase Dispersion Minimization

The *Phase Dispersion Minimization*, or briefly PDM method, is another non-parametric approach. It was introduced as an improved method compared with string length methods. One searches for the frequency by requiring that the spread of the data around an average curve in the phase diagram reaches a minimum. The average curve is determined from average values of the data in different phase intervals. We describe here the method as developed by Stellingwerf (1978).

For each test frequency  $\nu$  one divides the phase interval  $[0, 1]$  into  $B$  equal sub-intervals, called *bins*. The bin index  $J_i = \text{INT}(B\phi_i) + 1$ , with  $\text{INT}(x) \equiv x - [x]$ , determines to which bin each observation  $x(t_i)$  belongs. Suppose that the  $j$ -th bin contains  $N_j$  measurements. The average value of the data, the sum of the quadratic deviations and the variance for this bin are

$$\bar{x}_j = \frac{1}{N_j} \sum_{i=1}^{N_j} x_{ij}, \quad (5.14)$$

$$V_j^2 = \sum_{i=1}^{N_j} (x_{ij} - \bar{x}_j)^2 = \sum_{i=1}^{N_j} x_{ij}^2 - N_j \bar{x}_j^2, \quad (5.15)$$

$$s_j^2 = \frac{V_j^2}{N_j - 1}, \quad (5.16)$$

with  $x_{ij}$  the observation  $x(t_i)$  with bin index  $J_i = j$ . The analogous quantities for all data,  $\bar{x}$ ,  $V^2$  and  $s^2$ , are defined as

$$\bar{x} = \frac{1}{N} \sum_{i=1}^N x_i, \quad (5.17)$$

$$V^2 = \sum_{i=1}^N (x_i - \bar{x})^2 = \sum_{i=1}^N x_i^2 - N \bar{x}^2, \quad (5.18)$$

$$s^2 = \frac{V^2}{N - 1}. \quad (5.19)$$

For the  $B$  bins we introduce the following quantities:

$$V_B^2 = \sum_{j=1}^B V_j^2, \quad (5.20)$$

$$V_G^2 = \sum_{j=1}^B N_j (\bar{x}_j - \bar{x})^2. \quad (5.21)$$

We hence find that

$$V^2 = V_B^2 + V_G^2. \quad (5.22)$$

The differences between the bin averages  $\bar{x}_j$  and the average of the entire data set are small whenever the test frequency is not present in the data. In that case  $V_G^2$  is small compared with  $V^2$ . In the case where the true frequency is close to the test frequency, the bin averages are very different from the overall average and  $V_G^2$  is comparable with  $V^2$ . The search for the most likely frequency in the data hence comes down to the search for a maximum of  $V_G^2$ , which is equivalent with a search for the minimum of  $V_B^2$ .

The partition of the phase diagram into  $B$  equal bins can have disadvantages. It may very well happen that some bins are almost empty if  $B$  is chosen to be large or if we have only few data points with a particular time spread. For this reason one makes use of a more complicated *bin/cover structure* ( $B, C$ ). The phase diagram is divided into  $B$  bins, each of length  $1/B$ . This partition is then applied  $C$  times, such that each partition is shifted over  $1/(B \times C)$  with respect to the previous one. The incomplete bin near phase 1 is completed with the data of the corresponding phase interval near  $\phi = 0$ . In this way one covers the phase diagram  $C$  times, and each partition contains  $B$  bins. Such a bin structure allows one to make sure that each observation belongs to at least one bin. Further on we denote the total number of bins as  $B_C \equiv B \times C$ .

We subsequently introduce the statistic  $\Theta_{\text{PDM}}$ :

$$\Theta_{\text{PDM}} \equiv \frac{\left( \sum_{j=1}^{B_C} (N_j - 1) s_j^2 \right) / \left( \sum_{j=1}^{B_C} N_j - B_C \right)}{\left( \sum_{i=1}^N (x_i - \bar{x})^2 \right) / (N - 1)}, \quad (5.23)$$

where  $s_j^2$  is defined as:

$$s_j^2 \equiv \frac{\sum_{i=1}^{N_j} (x_{ij} - \bar{x}_j)^2}{N_j - 1}. \quad (5.24)$$

With the notation introduced we can also write  $\Theta_{\text{PDM}}$  as:

$$\Theta_{\text{PDM}} = \frac{V_{B_C}^2 / \left( \sum_{j=1}^{B_C} N_j - B_C \right)}{V^2 / (N - 1)} = \frac{V_{B_C}^2 / C(N - B)}{V^2 / (N - 1)}. \quad (5.25)$$

A minimum in the  $\Theta_{\text{PDM}}$ -statistic corresponds to a minimum of  $V_{B_C}$  and so this statistic is suitable to search for frequencies in the data. For each test frequency that is not present in the data we will find  $\Theta_{\text{PDM}} \simeq 1$ .

The  $\Theta_{\text{PDM}}$ -statistic defined in (5.23) was introduced by Stellingwerf (1978) and is a generalisation of the  $\Theta$  statistic used by Jurkevich (1971)

which is only based on bins. Jurkevich's method is therefore equivalent to Stellingwerf's for  $C = 1$ .

The more covers one uses, the larger the probability of finding the true frequency, but the longer the computation time. In practice one usually takes  $B$  between 5 and 20, so that sufficient data points per bin occur in order to guarantee a well-determined bin average. Typical values for the number of covers is from 1 to 10.

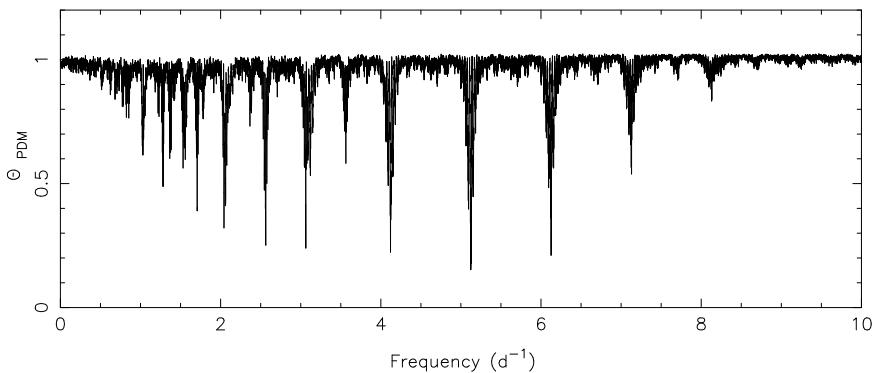


**Fig. 5.6.** Statistic  $\Theta_{\text{PDM}}$  according to Eq. (5.23) of the data shown in Fig. 5.3 using 10 bins and 2 covers.

In Fig. 5.6 we show  $\Theta_{\text{PDM}}$  for the time series shown in Fig. 5.3. Comparing this statistic with  $\Theta_{\text{SL}}$  shown in Fig. 5.4 highlights a much “cleaner” statistic. The peak structure is similar, except for the low frequency region where we see much less false peaks for the PDM version of the statistic. This is due to the far better ability of  $\Theta_{\text{PDM}}$  to judge the spread of data within the bins with respect to the average bin value, compared with  $\Theta_{\text{SL}}$ 's evaluation of the string lengths across the phase diagram as a whole. This comparison at once makes it clear why users prefer the PDM statistic among the non-parametric methods. Subharmonics still occur prominently, though.

Far more in use in asteroseismology these days are, however, the parametric methods to which we turn now.

### 5.3 Parametric Frequency Analysis Methods

All the methods described in this category are based upon Fourier analysis, *i.e.*, one fits a harmonic model function to the data. One must therefore keep in mind that these methods will do a very good job as long as the signal consists of a combination of sine (or cosine) functions. Of course, any function that has a more or less smooth behaviour can always be approximated by a Fourier

series, such that the applicability of the parametric methods discussed here is very good, particularly for frequency search. The methods are less suited to analyse time series with strong discontinuous behaviour.

In frequency analysis based on Fourier transforms one also defines a function of test frequencies in such a way that it reaches an extremum for the test frequency that is close to the true frequency present in the data, just as for the non-parametric methods. The plot of this function is usually called the *periodogram*, rather than the terminology of a statistic used in the non-parametric methods.

We first recall some useful properties of Fourier analysis and subsequently introduce different types of periodograms in use today.

### 5.3.1 The Continuous Fourier Transform of an Infinite Time Series

The *Fourier transform* of a function  $x(t)$  that fulfils the necessary conditions of continuity and finiteness is given by

$$F(\nu) \equiv \int_{-\infty}^{+\infty} x(t) \exp(2\pi i \nu t) dt. \quad (5.26)$$

Whenever we perform this transformation, we move from the time domain to the frequency domain. The Fourier transform of the constant function 1, *e.g.*, is *Dirac's delta function*:

$$\delta(\nu) \equiv \int_{-\infty}^{+\infty} \exp(2\pi i \nu t) dt, \quad (5.27)$$

which has the following properties:

$$\int_{-\infty}^{+\infty} \delta(\nu) d\nu = 1, \quad \int_{-\infty}^{+\infty} \delta(\nu - \xi) g(\nu) d\nu = g(\xi). \quad (5.28)$$

Frequency determination from Fourier analysis is based on the fact that the Fourier transform  $F(\nu)$  of a function  $x(t)$ , which can be written in terms of a sum of harmonic functions with frequencies  $\nu_1, \dots, \nu_M$  and amplitudes  $A_1, \dots, A_M$ :

$$x(t) = \sum_{k=1}^M A_k \exp(2\pi i \nu_k t), \quad (5.29)$$

is given by

$$F(\nu) = \sum_{k=1}^M A_k \delta(\nu - \nu_k). \quad (5.30)$$

Whenever  $x(t)$  is a sinusoidal function with frequency  $\nu_1$ , the Fourier transform of  $x$  is only different from zero for  $\nu = \nu_1$  and  $\nu = -\nu_1$ . The Fourier transform of a multiperiodic function  $x(t)$ , which is the sum of  $M$  harmonic functions with frequencies  $\nu_1, \dots, \nu_M$ , is a sum of  $\delta$ -functions that are different from zero for the frequencies  $\pm\nu_1, \dots, \pm\nu_M$ .

### 5.3.2 The Continuous Fourier Transform of a Finite Time Series

In practice, we never have the luxury to work with infinite continuous time series. Let us go back to the definition of the Fourier transform of a signal  $x(t)$  given in Eq. (5.26) and consider the case of a signal  $x(t) = A \cos[2\pi(\nu_1 t + \delta_1)]$  for which we have observations from  $t = 0$  until  $t = T$ . In that case, the continuous Fourier transform is

$$\begin{aligned}
 F(\nu) &= \int_0^T x(t) \exp(2\pi i \nu t) dt \\
 &= \frac{A}{2} \int_0^T \exp(2\pi i \nu t) \{ \exp[2\pi i (\nu_1 t + \delta_1)] + \exp[-2\pi i (\nu_1 t + \delta_1)] \} dt \\
 &= \frac{A}{2} \left\{ \frac{\exp(2\pi i \delta_1)}{2\pi i (\nu + \nu_1)} [\exp[2\pi i (\nu + \nu_1)T] - 1] + \right. \\
 &\quad \left. \frac{\exp(-2\pi i \delta_1)}{2\pi i (\nu - \nu_1)} [\exp[2\pi i (\nu - \nu_1)T] - 1] \right\} \\
 &= A \left\{ \exp[i T \pi (\nu + \nu_1) + 2\pi i \delta_1] \frac{\sin[\frac{T}{2} 2\pi (\nu + \nu_1)]}{2\pi (\nu + \nu_1)} + \right. \\
 &\quad \left. \exp[i T \pi (\nu - \nu_1) - 2\pi i \delta_1] \frac{\sin[\frac{T}{2} 2\pi (\nu - \nu_1)]}{2\pi (\nu - \nu_1)} \right\}.
 \end{aligned} \tag{5.31}$$

The periodograms are often displayed as power periodograms, *i.e.*,  $|F(\nu)|^2$  is plotted as a function of frequency  $\nu$ . In this case, their shape is determined by the function

$$\text{sinc}(x)^2 \equiv \left( \frac{\sin x}{x} \right)^2. \tag{5.32}$$

We strongly prefer to work with amplitude periodograms, however, in which case  $|F(\nu)|$  is displayed. This will be done throughout the book, except for some figures taken from the literature that display power. For simplicity we omit the notation of absolute values and note  $F(\nu)$  on the periodograms. The function  $\text{sinc}(x)$  and its square are graphically depicted in Fig. 5.7.

Whenever  $T \gg 1/\nu_1$ , the two frequency peaks following from Eq. (5.31) centred at  $-\nu_1$  and  $\nu_1$  are well separated such that it is justified to limit display of the transform to  $\nu_1 > 0$  as we will do throughout the book. In this simple case, the maximum of the sinc or  $\text{sinc}^2$  and its centre of gravity occur exactly at  $\nu_1$ .

As a *first rough* measure of the frequency accuracy, we could consider the width of the sinc peak, *i.e.*,  $\simeq 1/T$ . This is sometimes termed the *Rayleigh criterion*. In practice, however, any observed peak will have a much more complex

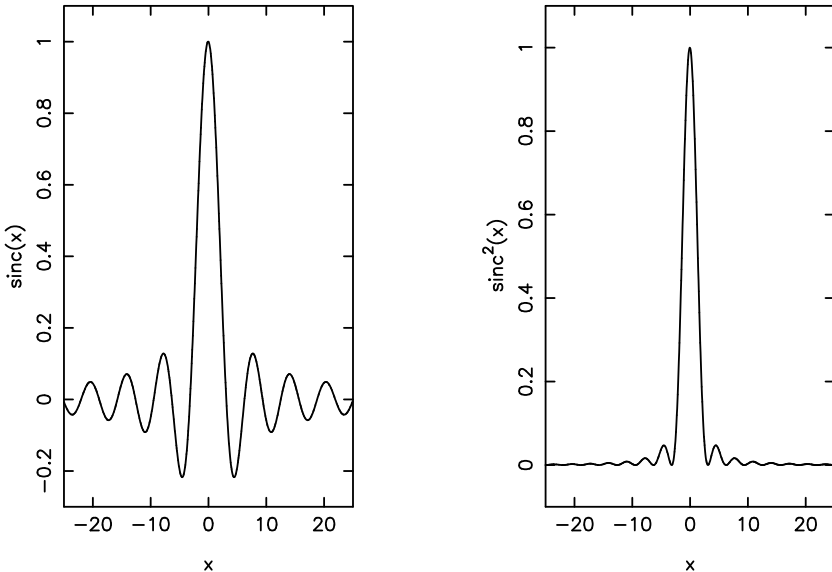


**Fig. 5.7.** The sinc function (left) and its square (right).

shape due to observational noise, to the finite number of measurements over the interval  $[0, T]$ , and to multiperiodic beating between oscillation modes resulting in frequency interference. As stressed by Schwarzenberg-Czerny (2003), the Rayleigh criterion only provides a *lower* limit to the accuracy reachable. The true accuracy is necessarily dependent on the S/N ratio. The realistic case thus requires a more sophisticated estimate of the frequency error, which will be treated in Section 5.5.

Whenever simultaneous oscillations occur,  $x(t)$  will be of a form like Eq. (5.1). In such a situation, the frequencies  $\nu_1, \dots, \nu_k$  can only be well separated provided that  $T \gg 1/|\nu_i - \nu_j|$  for all pairs  $i \neq j$ . When this condition is not fulfilled, interference occurs in the periodogram and the ability to identify the correct frequency values depends largely on the phase difference between the modes as well as on their amplitude ratios. Loumos & Deeming (1978) first studied the *resolving power* of a periodogram and derived that the frequencies  $\nu_i$  and  $\nu_j$  are separated when  $1/T < |\nu_i - \nu_j| < 1.5/T$ , but *the maxima do not occur necessarily at the real frequencies*. They also concluded that the difference between two peak frequencies in the periodogram and the real frequencies are negligible whenever  $|\nu_i - \nu_j| > 2.5/T$ , because the first sidelobe of one sinc function no longer interferes with the main peak of the other sinc function. This rule-of-thumb was further elaborated upon by Christensen-Dalsgaard & Gough (1982), who made a deeper investigation of the resolving power in a periodogram focussing on solar-like oscillations. They came up with a similar

condition for accurate frequency separation of  $|\nu_i - \nu_j| > 2/T$  covering all cases of relative phases of the modes.

Things get more complicated when the time series does not cover one time interval  $[0, T]$ , but is a concatenation of continuous data spread over several different time intervals  $[0, T_1], [T_2, T_3], [T_4, T_5], \dots$ , *i.e.*, in the case of *gapped* data.

The degradation of the Fourier transform from dream to what is not even yet reality in frequency analysis is illustrated in Fig. 5.8. In this figure, we compare the Fourier transforms for an almost infinite noiseless time series (1 000 000 data points spread over 1 000 d) with one of a finite noiseless series of 10 000 points spread over 10 d and a randomly gapped finite noiseless series of 4472 points with a total time span of 10 d, all for a simple noise-free sinusoidal signal in the approximation of continuous measurements (*i.e.*, still far too optimistic). The graph speaks for itself and makes one realize why frequency analysis of astronomical time series is so inherently difficult even if the data are close to being noise-free.

In reality, the gaps in data sets are not randomly distributed. In the simple case with one interruption during a time  $\Delta T$ , the sinc function determining the periodogram (see Fig. 5.7) will be modulated by a term  $\cos[\Delta T \pi(\nu - \nu_1)]$ . This modulation factor introduces fine structure in the periodogram peaks whose relevance depends mostly on the values of  $\Delta T$  and  $T$ . Two examples are provided in Fig. 5.9 where the time series used in the middle panel of Fig. 5.8 was interrupted for respectively two days from day 4 until day 6 and for six days from day 2 until day 8. These interruptions imply a strong rise in the height of spurious frequencies that are due to the gap compared with the situation where there is no interruption in the data (middle panel of Fig. 5.8), particularly when the gap is large. These spurious frequencies are termed *alias frequencies* and will be defined in the following section.

In real data, the value of the modulation factor will be affected by noise and may differ substantially from a simple cosine value, even if there is only one large gap.

### 5.3.3 Real Life: The Discrete Fourier Transform

For a real data set, the function  $x(t)$  is only known for a discrete number of time points  $t_i, i = 1, \dots, N$ . We are thus unable to determine its  $F(\nu)$ . Following Deeming (1975), we introduce the *discrete Fourier transform* of the function  $x(t)$ :

$$F_N(\nu) \equiv \sum_{i=1}^N x(t_i) \exp(2\pi i \nu t_i). \quad (5.33)$$

This transform can be calculated whenever the  $N$  measurements of the function  $x(t)$  are available.

It is clear that  $F_N$  differs from  $F$ , but we can associate them with each other through the *window function* defined as

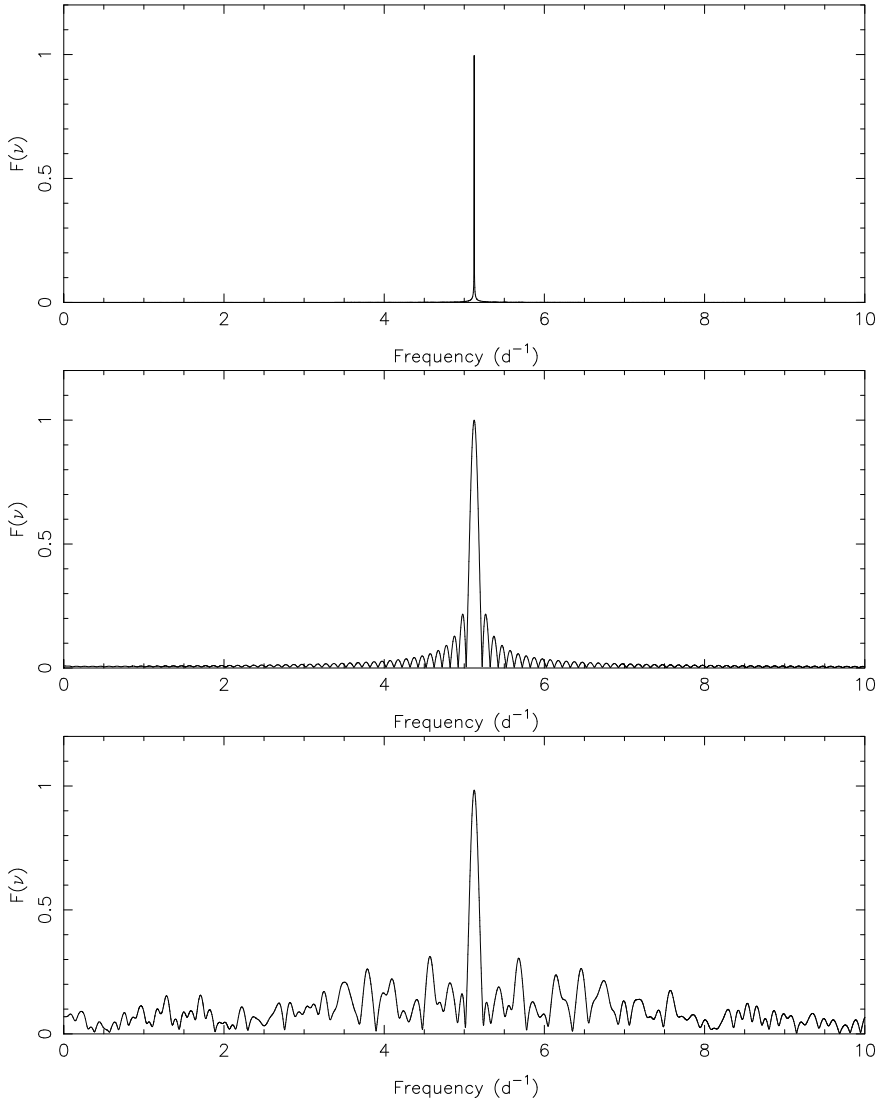


**Fig. 5.8.** Fourier transforms of an almost infinite noiseless time series with 1 000 000 points spread over 1 000 d for a harmonic signal with frequency  $\nu = 5.123456789 \text{ d}^{-1}$  (top), of a noiseless time series with ten thousand points and a finite time span of 10 d (middle) and of a gapped finite noiseless time series with 4472 points and a time span of 10 d (bottom).

$$w_N(t) \equiv \frac{1}{N} \sum_{i=1}^N \delta(t - t_i). \quad (5.34)$$

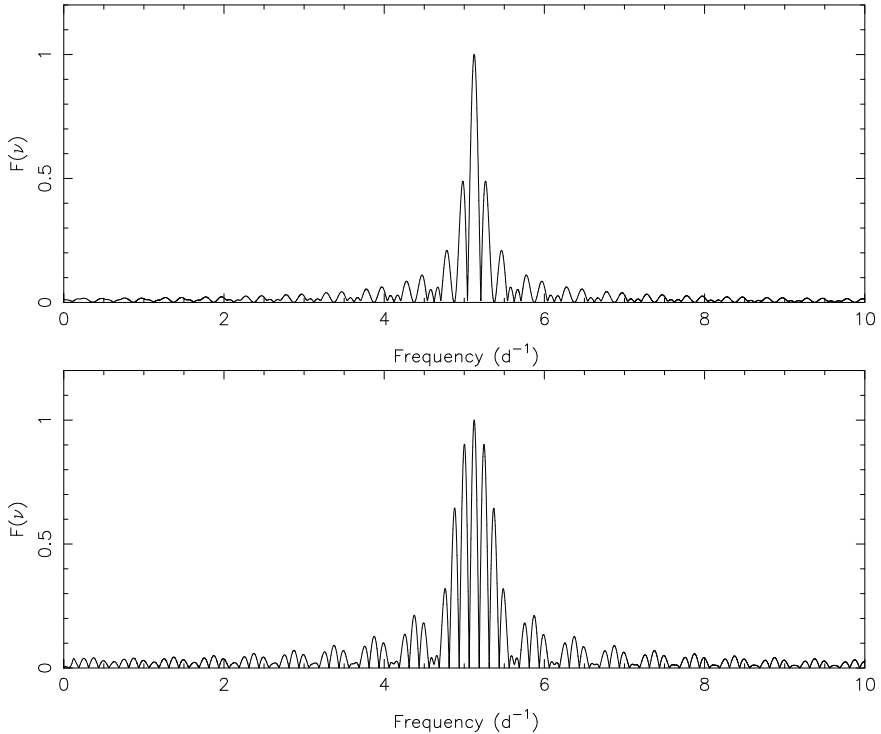


**Fig. 5.9.** Fourier transforms of a noiseless time series of a sine function with frequency  $5.123456789 \text{ d}^{-1}$  generated for a finite time span of 10 d and containing one large gap from day 4 until day 6 (top) and from day 2 until day 8 (bottom).

The window function and the properties of the Dirac function allow us to transfer  $F_N$  to an integral form:

$$\frac{F_N}{N} = \int_{-\infty}^{+\infty} x(t)w_N(t) \exp(2\pi i \nu t) dt. \quad (5.35)$$

The discrete Fourier transform of the window function is called the *spectral window*  $W_N(\nu)$ :

$$W_N(\nu) = \frac{1}{N} \sum_{i=1}^N \exp(2\pi i \nu t_i). \quad (5.36)$$

The discrete Fourier transform can be written as the convolution of the spectral window and the Fourier transform:

$$F_N(\nu)/N = (F * W_N)(\nu). \quad (5.37)$$

If  $F(\nu)$  is a  $\delta$ -function at frequency  $\nu_1$ , then  $F_N(\nu)/N$  will have the same behaviour as the spectral window  $W_N(\nu)$  at  $\nu_1$  because  $F_N(\nu)/N = W_N(\nu) *$

$\delta(\nu - \nu_1) = W_N(\nu - \nu_1)$ . Comparison of the  $W_N(\nu)$  with  $F_N(\nu)/N$  near the frequency  $\nu_1$  thus helps one to conclude if the frequency  $\nu_1$  may be real or not. Whenever  $F(\nu)$  is a sum of  $M$   $\delta$ -functions we have:

$$\begin{aligned} \frac{F_N(\nu)}{N} &= W_N(\nu) * \sum_{k=1}^M \delta(\nu - \nu_k) \\ &= \sum_{k=1}^M W_N(\nu) * \delta(\nu - \nu_k) \\ &= \sum_{k=1}^M W_N(\nu - \nu_k) \\ &= \frac{1}{N} \sum_{k=1}^M \sum_{i=1}^N \exp(2\pi i (\nu - \nu_k) t_i). \end{aligned} \quad (5.38)$$

Hence,  $F_N(\nu)/N$  is the sum of  $M$  spectral windows that are all centred around the different frequencies  $\nu_k$ . Due to the fact that  $W_N(\nu)$  can differ from zero at frequencies  $\nu$  that are not necessarily equal to  $\nu_k, k = 1, \dots, M$ , we expect the presence of interference. This will give rise to maxima in the periodogram that do not correspond to real frequencies. These maxima are due to noise and/or the times of observation, which introduce spurious frequencies in the periodogram. This phenomenon is called *aliasing* when it concerns peaks due to the times of measurement and the false frequencies are termed *alias frequencies*. The latter can be recognized as maxima in the window function at frequencies different from zero. This property of the alias frequencies occurring in the spectral window highlights one of the big advantages of Fourier analysis in frequency searches.

The question of course arises: which alias frequencies are most common? Let us assume for simplicity that we are dealing with measurements that are evenly spaced:  $t_j = \tau + j\Delta t$ . In such a case of evenly spaced data, the spectral window is given by:

$$\begin{aligned} W_N(\nu) &= \frac{1}{N} \sum_{j=1}^N \exp(2\pi i \nu \tau) \exp(2\pi i \nu j \Delta t) \\ &= \frac{1}{N} \exp(2\pi i \nu \tau) \sum_{j=1}^N \exp(2\pi i \nu j \Delta t) \\ &= \exp(2\pi i \nu \tau) \exp(\pi i \nu \Delta t (N+1)) \frac{\sin(\pi \nu N \Delta t)}{N \sin(\pi \nu \Delta t)}, \end{aligned} \quad (5.39)$$

in which we have made use of

$$\sum_{j=0}^{N-1} z^j = \frac{1 - z^N}{1 - z} \quad (5.40)$$

with  $z = \exp(2\pi i \nu \Delta t)$ . For  $\tau = -(N+1)\Delta t/2$  we obtain

$$W_N(\nu) = \frac{\sin(\pi N\nu\Delta t)}{N \sin(\pi\nu\Delta t)}. \quad (5.41)$$

The absolute value of this function is periodic with period  $1/\Delta t$  because

$$\left| W_N \left( \nu + \frac{n}{\Delta t} \right) \right| = |W_N(\nu)|. \quad (5.42)$$

The function  $F_N(\nu)$  hence reaches a maximum in an infinite number of frequencies  $\nu_j = j/\Delta t$ . Evenly spaced data therefore give rise to a strong aliasing effect.

The situation of unevenly spaced data does not allow one to derive the alias frequencies in such a straightforward analytical way. However, one can show by simulations that certain periodicities in the observation times, such as  $\Delta t = 1$  sidereal day, 1 sidereal year, etc., will also give rise to alias frequencies. We call these the *one-day aliases*, or the *daily sidelobes*, occurring with intervals of  $\pm 1, \pm 2, \dots$  when the frequency is expressed in  $\text{d}^{-1}$  or, equivalently, with intervals of multiples of  $\pm 11.5741 \mu\text{Hz}$ . These are particularly troublesome in the observation of solar-like oscillations, showing high-order acoustic modes, where frequency separations of this magnitude are common. The *one-year alias* occurs with intervals of  $0.00274 \text{ d}^{-1} = 0.0317 \mu\text{Hz}$ , etc. Thus also aliases with intervals of  $1.00274 \text{ d}^{-1} = 11.6225 \mu\text{Hz}$  occur for data sets spanning more than one year. Such an alias structure was already very clearly seen in Figs 5.4 and 5.6.

The total time span of the data, as well as particular gaps in them, will give rise to additional alias frequencies that are due to uncertainties in the number of cycles in or between the gaps. Moreover, regularity in the sampling with intervals close to (a multiple of) the intrinsic periodicities of the star will inevitably hamper the discrimination between the true frequencies and their aliases. An example of the latter situation occurred in Figs 2.16 and 2.17, where peaks at  $\nu$  and  $1 - \nu$  are almost indistinguishable in the single-site ground-based data of the slowly pulsating B stars HD 74195 and HD 123515, which exhibit periodicities near one day.

All these caveats due to aliasing should be checked carefully in any frequency analysis through a detailed study of the spectral window. We show in Fig. 5.10 the spectral window according to the definition in Eq. (5.36) of the time series shown in Fig. 5.3. Spectral windows computed according to Eq. (5.36) are symmetric with respect to zero frequency. The daily and yearly aliasing are apparent in this plot. Other examples were given in Figs 2.4 and 2.43 in Chapter 2. Nevertheless, we advise to take a different approach in practice. Indeed, for real data it is more informative to plot the discrete Fourier transform of an artificial, noise-free sinusoid at a determined frequency (or frequencies). The reason is that the negative part of the discrete Fourier transform may have an effect on the positive part of the periodogram. The latter approach therefore gives the best guidance to discriminate real from false frequencies. This approach is represented in Fig. 5.11 for the data shown in

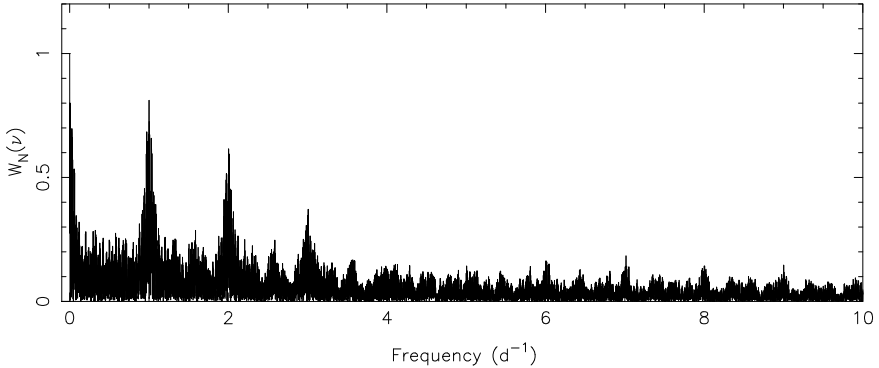


**Fig. 5.10.** Spectral window of the data shown in Fig. 5.3 computed according to Eq. (5.36).

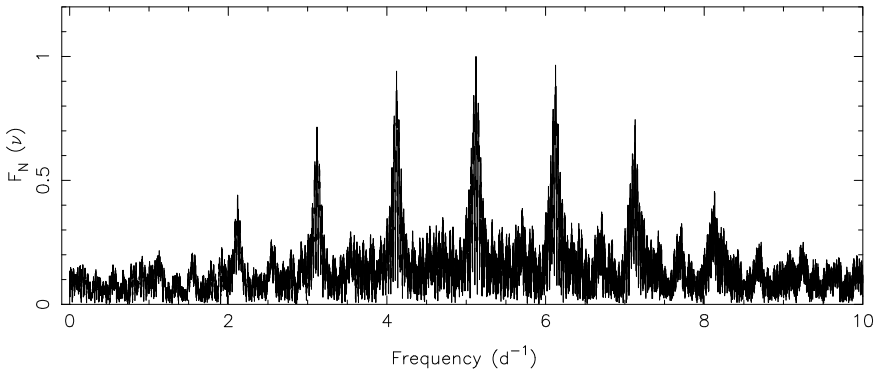


**Fig. 5.11.** Discrete Fourier transform of an noise-free sinusoid with amplitude 1 at frequency  $5.123456789 d^{-1}$  for the sampling shown in Fig. 5.3.

Fig. 5.3, in which the discrete Fourier transform of an artificial sinusoid computed at the sampling of the time series is shown. It gives us at once the complete picture of how  $F_N(\nu)$  would look like if only this one frequency is present in the data. In the current artificial example with only one periodic signal, the discrete Fourier transform of this artificial noise-free sinusoid will be almost indistinguishable from the one of the observed time series, since the latter had white noise with a low standard deviation of only 0.0111. For another example in the case of a multiperiodic pulsator we refer to Fig. 2.21 in Chapter 2.

All these examples, and numerous others in the literature as well as simulations, lead one to the following conclusions. The heights of the alias peaks and of the noise peaks in the spectral window express the lack of knowledge from the data set. One must realize that both the noise and the true sig-

nal have an amplitude and a phase and that both are convolved in complex Fourier space. The noise signal may thus add to or subtract from a real frequency peak. Noise may also add to or subtract from an alias peak. Finally noise may do nothing to real peaks. We therefore advise to study the spectral window in detail in any frequency analysis before making firm conclusions on frequencies.

So far, we have not discussed the practicalities of the interval of test frequencies one should consider. This can and should be derived from the data set. It is customary to take zero frequency as a lower limit, since the limiting case of an infinite oscillation period is then covered. The highest useful frequency to search for is the so-called *Nyquist frequency*  $\nu_{\text{Ny}}$ . One can show that  $\nu_{\text{Ny}} = 1/2\Delta t$ , with  $\Delta t$  the sampling step in the case of evenly spaced data. Some authors therefore use the same formula, taking as  $\Delta t$  the average of all the sampling intervals in the case of unevenly spaced data. In practice, however, the Nyquist frequency can be quite different from this value if numerous large gaps and/or serious undersampling or oversampling occur in the data set. In that case, it was shown by Eyer & Bartholdi (1999) that a better approach to obtain the Nyquist frequency is to take  $\nu_{\text{Ny}} = 1/2p$ , with  $p$  being the greatest common divisor of all differences between consecutive observation times. This is rather cumbersome to be used as daily approach in practice. A good and fast way to make a realistic estimate  $\nu_{\text{Ny}}$  in the case of unevenly sampled data, appropriate whenever the deviation from equidistance is not too severe, is to take the inverse of twice the median value of all the time differences between two consecutive measurements of the entire data set.

One should not blindly believe that peaks occurring above the Nyquist frequency in the periodogram cannot correspond to true frequencies. It may very well be that a particular frequency occurring as highest peak in the computed periodogram is, in fact, an alias of the true frequency that occurs above  $\nu_{\text{Ny}}$ . This would still allow the detection of the true frequency, by implication, even though it occurs above  $\nu_{\text{Ny}}$ . In any case, such a situation would call for further observations at higher sampling rate to rule out the original low-frequency aliases. If the type of star is known, one can also accept the frequency outside of the interval up to  $\nu_{\text{Ny}}$  on astrophysical arguments.

As we have shown, the irregular sampling of data usually implies a complicated response in the Fourier transform. It can alter the peak frequencies and the amplitudes of the signal, besides introducing the occurrence of very large false peaks. Several different definitions of periodograms have been devised to try and overcome impracticalities in the Fourier transform. We discuss some of them below.

### 5.3.4 The Classical Periodogram

Assume we have a time series of  $N$  measurements  $(t_i, x(t_i))$ . The *classical periodogram* was defined originally in meteorology (Schuster 1898) and is written as follows:

$$\begin{aligned} P_N(\nu) &= \frac{1}{N} |F_N(\nu)|^2 = \frac{1}{N} \left| \sum_{i=1}^N x(t_i) \exp(2\pi i \nu t_i) \right|^2 \\ &= \frac{1}{N} \left\{ \left( \sum_{i=1}^N x(t_i) \sin(2\pi \nu t_i) \right)^2 + \left( \sum_{i=1}^N x(t_i) \cos(2\pi \nu t_i) \right)^2 \right\}. \end{aligned} \quad (5.43)$$

If the signal we are searching is a pure harmonic one of the form  $x(t_i) = A \cos(2\pi\nu_1 t_i)$ , the periodogram will have the value

$$P_N(\nu_1) = \frac{1}{N} \left\{ \sum_{i=1}^N A \cos(2\pi\nu_1 t_i) \sin(2\pi\nu_1 t_i) \right\}^2 + \frac{1}{N} \left\{ \sum_{i=1}^N A \cos^2(2\pi\nu_1 t_i) \right\}^2 \quad (5.44)$$

at frequency  $\nu_1$ . For large  $N$  we have

$$\sum_{i=1}^N \cos(2\pi\nu_1 t_i) \sin(2\pi\nu_1 t_i) \approx 0, \quad \sum_{i=1}^N \cos^2(2\pi\nu_1 t_i) \approx N/2, \quad (5.45)$$

and so  $P_N(\nu_1) \approx A^2 N/4$  for  $N \rightarrow \infty$ . For  $\nu \neq \nu_1$ , positive as well as negative terms occur and these will largely compensate each other. The overall sum will thus be small for such a test frequency.

The frequency  $\nu$  for which  $P_N(\nu)$  is maximal is the most likely one present in the data. For sufficiently extensive data sets, *e.g.*, those with a couple of hundred data points (as in Fig. 5.3, *e.g.*), the approximation  $P_N(\nu_1) \approx A^2 N/4$  is reasonably good. This is why we advise to consider the *amplitude spectrum* rather than the power spectrum, *i.e.*, to plot and analyse

$$A(\nu) = \sqrt{\frac{4P_N(\nu)}{N}} \quad (5.46)$$

as a function of test frequency  $\nu$ . After all, the amplitude of a mode is what we hope to interpret in terms of the physics of the star.

### 5.3.5 The Lomb-Scargle Periodogram

The periodogram introduced by Lomb (1976) and further improved by Ferraz-Mello (1981) and Scargle (1982), is defined in a different way than the classical periodogram. We present here the formulation by Scargle (1982) and speak of the *Lomb-Scargle periodogram* as it is often done in the literature:

$$P_{LS}(\nu) = \frac{1}{2} \frac{\left\{ \sum_{i=1}^N x(t_i) \cos[2\pi\nu(t_i - \tau)] \right\}^2}{\sum_{i=1}^N \cos^2[2\pi\nu(t_i - \tau)]} + \frac{\left\{ \sum_{i=1}^N x(t_i) \sin[2\pi\nu(t_i - \tau)] \right\}^2}{\sum_{i=1}^N \sin^2[2\pi\nu(t_i - \tau)]}. \quad (5.47)$$

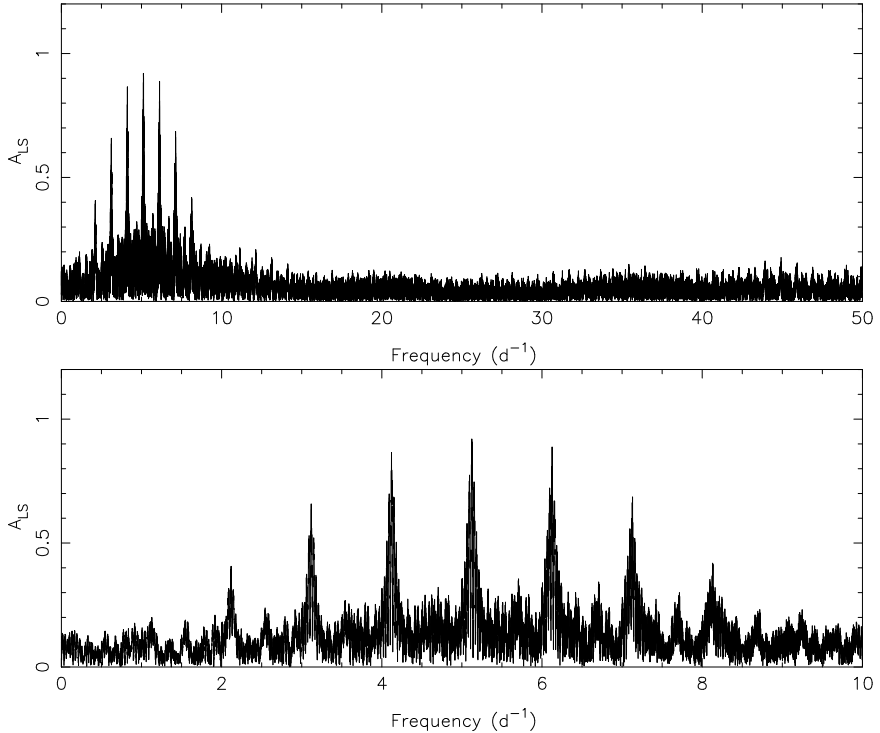


**Fig. 5.12.** Lomb-Scargle periodograms according to Eq. (5.47) for the data shown in Fig. 5.3.

In this expression, the reference epoch  $\tau$  is chosen in such a way that

$$\sum_{i=1}^N \cos[2\pi\nu(t_i - \tau)] \sin[2\pi\nu(t_i - \tau)] = 0, \quad (5.48)$$

or, equivalently

$$\tan(4\pi\nu\tau) = \frac{\sum_{i=1}^N \sin(4\pi\nu t_i)}{\sum_{i=1}^N \cos(4\pi\nu t_i)}. \quad (5.49)$$

Using the simplifications in notation introduced in Eqs (5.5), the Lomb-Scargle periodogram is written as:

$$P_{\text{LS}}(\nu) = \frac{1}{2} \left\{ \frac{c_x^2}{c_2} + \frac{s_x^2}{s_2} \right\}. \quad (5.50)$$

It takes the value  $A^2 N/4$  for a harmonic signal with frequency  $\nu_1$  and for sufficiently large  $N$ . The amplitude spectrum based on the Lomb-Scargle periodogram is therefore defined by Eq. (5.47):

$$A_{\text{LS}}(\nu) = \sqrt{\frac{4P_{\text{LS}}(\nu)}{N}}. \quad (5.51)$$

We show in Fig. 5.12  $A_{\text{LS}}(\nu)$  for the simulated data shown in Fig. 5.3. The median value of the subsequent time differences for this data set amounts to  $0.012 \text{ d}$ , such that the Nyquist frequency is estimated to be near  $42 \text{ d}^{-1}$ . The whole Lomb-Scargle periodogram up to that value is shown in the top panel, while the lower panel is an enlarged section focusing on the region  $[0, 10] \text{ d}^{-1}$  where significant amplitude occurs. It can be seen that this lower panel is indeed almost indistinguishable from Fig. 5.11 as predicted for this monoperiodic signal with white noise of low standard deviation. Compare this with the idealized situation of having a continuous Fourier transform of an almost infinite noiseless signal at one frequency with which we started this section (upper panel of Fig. 5.8)!

One of the reasons to have introduced the Lomb-Scargle periodogram is that its value does not change when all time values  $t_i$  are replaced by  $t_i + T$  because of the definition of  $\tau$ . Another reason has to do with hypothesis testing (see Section 5.4).

Horne & Baliunas (1986) and Schwarzenberg-Czerny (1997) have proved the Lomb-Scargle periodogram to be equivalent to the variance reduction  $f_v$  obtained from fitting a sinusoid at test frequencies by least squares, as explained in Section 5.1. It is thus good practice to fit harmonic series of sinusoids at test frequencies to data to search for non-sinusoidal signals as well. This proof implied that the original motivation for the use of non-parametric methods as more efficient tools to detect non-sinusoidal signals than parametric ones weakened considerably, particularly so since they require a lot more computational time and introduce a complex spectrum with subharmonics and their aliases.

## 5.4 Significance Criteria

During a frequency analysis, one of course needs to adopt a stop criterion to decide whether or not a candidate frequency is still *significant* or not. For obvious reasons, this aspect of frequency analysis has received a lot of attention. To derive the significance of a frequency one needs to know the distribution function of the employed frequency statistic. As a consequence of the data-driven approach of the frequency analysis methods outlined above, one is unable to construct appropriate distribution functions based on theoretical principles.

Stellingwerf (1978) and Cuypers (1987) derived that the significance of  $\Theta_{\text{PDM}}$  can be related to an  $F$ -test. However, Schwarzenberg-Czerny (1997)

pointed out that the sensitivity of the significance test proposed by these authors is poor and he demonstrated that  $\Theta_{\text{PDM}}$  rather follows a  $\beta$  distribution. It was shown by Scargle (1982) that the distribution function for the Lomb-Scargle periodogram belongs to the exponential family, but it has to be kept in mind that this is only true for  $N \rightarrow \infty$ . Moreover, the author could not come up with a simple treatment of the statistical properties of  $A_{\text{LS}}$ . Schwarzenberg-Czerny (1997) came to the important conclusion that all methods outlined in this chapter are mathematically equivalent for a given sampling, binning and weighting pattern.

Schwarzenberg-Czerny (1998) demonstrated that an empirically derived  $\beta$  distribution is the only valid approach to derive good significance levels and that theoretical distributions as used in *e.g.*, Scargle (1982) or Horne & Baliunas (1986, the so-called False-Alarm Probability or FAP) have to be treated with caution. It is therefore common practice these days to take a frequency peak as significant whenever its amplitude in the periodogram is above a particular empirically determined critical value, *i.e.*, to let the data speak for itself rather than relying on assumptions about the (uncertain) statistical model distributions.

Depending on the data set and authors, different so-called *S/N level significance criteria* are considered appropriate and adopted. The S/N level is computed as the average amplitude in a well sampled periodogram of the final residuals and for an appropriate interval in the frequency region where the candidate frequency is situated. We denote this level by  $\sigma_{\text{res}}$ . The S/N level of a particular frequency is then computed as the ratio between its amplitude and  $\sigma_{\text{res}}$ . Breger *et al.* (1993) derived empirically, from experience with numerous data sets resulting from  $\delta$  Sct network campaigns, that a frequency can be very safely considered to be significant whenever its amplitude, computed either in the time domain or in the frequency domain, fulfils  $A > 4\sigma_{\text{res}}$ . This result was supported from simulations based on data assembled with the Hubble Space Telescope Fine Guide Sensors and assuming photon-dominated white noise by Kuschnig *et al.* (1997). They concluded that the criterion  $A > 4\sigma_{\text{res}}$  corresponds to a 99.9% confidence level of having found an intrinsic peak rather than one due to noise. The confidence levels corresponding to  $A > 3.6\sigma_{\text{res}}$  and  $A > 3\sigma_{\text{res}}$  are respectively 95% and 80% for photon-dominated noise. Since noise peaks can reach a  $3\sigma_{\text{res}}$  level with 20% probability, we do not consider this to be a sufficiently safe significance criterion. In reality, the noise is not photon-dominated for most data sets, particularly those assembled from the ground. Moreover, the noise is usually correlated, *i.e.*, non-white. Unfortunately, the true noise profile may be very hard to compute (see also Section 5.5). This is why this step is often omitted and the abovementioned criterion of  $A > 4\sigma_{\text{res}}$  is adopted as a very safe one, at least when only one data set is at hand.

For the example of the simulated data shown in Fig. 5.3, we derive the frequency from Fig. 5.12, compute the residuals from subtracting the least-squares fit shown in the upper left panel of Fig. 5.5 from the data, recompute

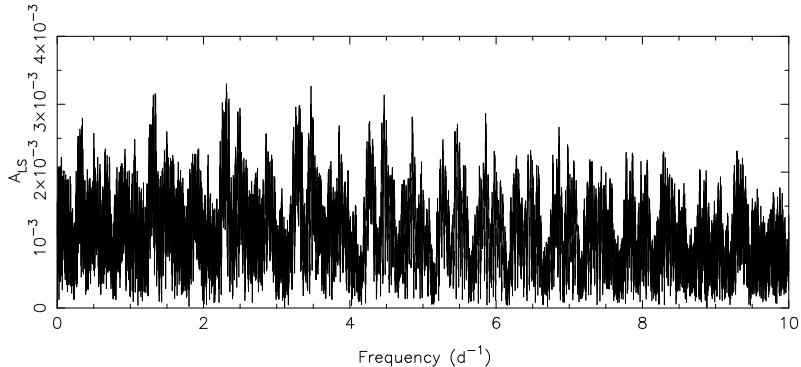


**Fig. 5.13.** Lomb-Scargle periodogram of the residuals after subtracting the fit shown as full line from the data in the upper left panel of Fig. 5.5. Note that this periodogram's  $y$ -axis is enlarged with a factor 300 compared with the one for the original data before prewhitening shown in Fig. 5.12.

the Lomb-Scargle periodogram for these residuals and derive the noise level of the residuals in the frequency domain. The periodogram of the residuals is shown in Fig. 5.13 and was computed with the same sampling as the original periodogram according to the frequency accuracy discussed in the following section. One should not undersample the periodogram for the S/N level computation (nor for the frequency derivation!). The average amplitude in Fig. 5.13 amounts to 0.0011 and is a good estimate of  $\sigma_{\text{res}}$  in the considered frequency interval of  $[0, 10] \text{ d}^{-1}$ . This implies that the frequency  $\nu = 5.123456789 \text{ d}^{-1}$  reaches a level of  $909 \sigma_{\text{res}}$  for this example. One can easily derive from Fig. 5.13 that the highest noise peaks in  $[0, 10] \text{ d}^{-1}$  reach a level of  $3 \sigma_{\text{res}}$ . The highest noise peaks in the interval  $[0, \nu_{Ny}] \text{ d}^{-1}$  reach  $3.6 \sigma_{\text{res}}$ .

Examples of significance level computations for real data were already shown graphically in Figs 2.21 and 2.27 for the multisite campaigns of the  $\beta$  Cep star 12 Lac (Handler *et al.* 2006) and of the pre-main-sequence star IP Per (Ripepi *et al.* 2006b). We refer to the original papers for the details of the adopted criteria and their means of computation of the S/N level. More examples will be treated in Chapter 7.

One can take a less conservative attitude than  $A > 4\sigma_{\text{res}}$  whenever more than one independent data set is available for analysis (see, *e.g.*, Figs 2.16 and 2.17 and De Cat & Cuypers (2003) for additional examples). One is usually also less conservative when it concerns the acceptance of combination frequencies, such as multiples or linear combinations of frequencies, which have already passed the requirement of  $A > 4\sigma_{\text{res}}$ . In both these cases, *i.e.*, for frequencies present in independent data sets or for combination frequencies searched in one data set, we advise to use  $A > 3.6\sigma_{\text{res}}$  as a safe condition of acceptance.

## 5.5 Error Estimation of the Derived Frequencies

Once the user has reached the stage to have concluded that  $M$  frequencies with determined values are present in the data, the question of final error estimation of all the unknowns needs to be settled. We limit ourselves here to the case of linear oscillations, with time dependence  $\sim \cos[2\pi(\nu t + \delta)]$ . In order to compute the errors in an appropriate way, one can consider the model described in Eq. (5.1), where  $M$  is assumed to be error-free due to our inability to treat discrete parameter estimation in the data-driven frequency analysis. The error estimation is done in the time domain here, by means of least-squares fitting, because the periodograms only give a good amplitude estimate in the limit of large  $N$ .

In general, error estimation is usually based on derivatives of a kind of likelihood function, *e.g.*, the one defined in Eq. (5.2). The goal should be to make appropriate assumptions on the character of the data, on the properties of the noise and on the inter-dependence of the model parameters that are in our case the frequencies, their amplitudes and phases, and the mean value of the observable  $x_i$ , when deriving the errors. Appropriate error propagation is a poorly developed field in astronomy in general, and its application in asteroseismology is, unfortunately, no exception to this rule. We emphasize below the shortcomings we have to live with in current analyses. The reader is advised to keep these in mind in all the seismic interpretations based on observed frequencies.

### 5.5.1 Data without Alias Problems

As a first approach to the problem of error estimation, we consider data not suffering from aliasing and oscillation modes with infinite lifetime. This implies that we assume there to be no ambiguity in selecting the true frequency values from the methods outlined above. We discuss the complication introduced by aliasing separately further on.

A first approximation usually adopted is to assume the times of measurement  $t_i$ , as well as the reference epoch  $\tau$ , to be error-free. As already emphasized in Chapter 4, the observers always should care about the accuracy of the clocks they are using during the data gathering, particularly when observing short-period oscillators. Even for data assembled with a carefully calibrated clock, the assumption of having instantaneous measurements with error-free timings is in general not valid. Indeed, the data gathering is done by adopting a certain integration time during which photons are detected by the instrument, and  $t_i$  is usually taken to be the error-free time of mid-exposure. The integration of course implies a smearing out of the oscillatory signal over a fraction of the oscillation cycle for each of the modes. Moreover, the integration time is sometimes not constant during an observing run, *e.g.*, it is continuously adapted to the atmospheric conditions for ground-based spectroscopic data.

All this implies that the timings  $t_i$  cannot be error-free. Moreover, they are not independent of each other. The assumption of instantaneous measurements with error-free timings may be a good approximation as long as the *temporal resolution* of the data, *i.e.*, the ratio of the integration times to the oscillations periods, is very small, let's say below 1%. This will in general not be the case for high-resolution spectroscopic time series or for ground-based photometric time series of compact oscillators. A remedy to this problem is achievable, but it requires a good model description of the oscillatory behaviour and it is time consuming. The user can check *a posteriori* how much the data set suffered from smearing over the oscillation cycles for each of the modes *after* the frequency derivation is finished. This allows a measure of the effect of this assumption on the frequency values and their amplitudes.

A second approximation in deriving error estimates is much more problematic than the first one: the assumption of having white uncorrelated noise with average zero and constant variance  $\sigma_N^2$  in time. The overall noise profile of the data contains, in general, contributions from the instrument performance and from the environmental conditions, such as the behaviour of the atmosphere for ground-based data and the effect of stray light, satellite jitter, proton impact, *etc.*, for space data. It is clear that the noise profile must be time dependent and that the different noise factors are by no means uncorrelated. Unfortunately, it is in general impossible to propagate all the different noise factors appropriately, due to lack of good model descriptions for each of them. The conclusion must therefore be that any error estimate ignoring the correlations among the noise factors and their time dependence cannot be but lower limits of the true errors.

A third approximation is to assume that there is no interference between the different true frequencies and the noise peaks. This is an additional condition compared with the resolution issue described in Section 5.3.2, where interference among intrinsic frequencies was considered. For similar reasons as outlined there, this approximation is valid whenever the noise peaks are well separated from those of the intrinsic frequencies, a situation seldom encountered.

The three approximations described here are followed out of necessity to avoid an ill-conditioned statistical description for the error derivation. Indeed, in the derivation of the error of one particular parameter, a significant simplification is met when assuming that all other parameters are perfectly known. This situation occurs when adopting the discussed four approximations. In this case, one ends up with the following standard error estimate for the derived amplitudes, phases and frequencies:

$$\sigma_\nu = \frac{\sqrt{6} \sigma_N}{\pi \sqrt{N} A T}, \quad \sigma_A = \sqrt{\frac{2}{N}} \sigma_N, \quad \sigma_\delta = \frac{\sigma_N}{\pi \sqrt{2N} A} \quad (5.52)$$

with  $T$  the total time span of the data and  $N$  the number of data points (Bloomfield 1976; Cuypers 1987; Montgomery & O'Donoghue 1999). In these formulae,  $\sigma_N$  stands for the average error on each of the data points. Quite

often, error estimates are not available for individual measurements, even in the simplified assumption of uncorrelated time-independent noise. It is then good practice to take the standard deviation of the residuals after removal of all accepted significant frequencies as a realistic and conservative estimate of  $\sigma_N$ . If the data are correlation, one should take this into account in the error estimation (see, e.g., Schwarzenberg-Czerny 2003).

We note that the error estimates provided in Eq. (5.52) are  $1\sigma$  errors, *i.e.*, the true values of the frequency, amplitude and phase belong with 68.3% certainty to the intervals  $[\nu - \sigma_\nu, \nu + \sigma_\nu]$ ,  $[A - \sigma_A, A + \sigma_A]$ ,  $[\delta - \sigma_\delta, \delta + \sigma_\delta]$  respectively. Much more common practice in statistics is to use the so-called  $2\sigma$  error estimates, which imply that the true values are with 95.4% certainty in the intervals  $[\nu - 2\sigma_\nu, \nu + 2\sigma_\nu]$ ,  $[A - 2\sigma_A, A + 2\sigma_A]$ ,  $[\delta - 2\sigma_\delta, \delta + 2\sigma_\delta]$ .

Schwarzenberg-Czerny (1991) has shown that the error estimate of the frequency can also be done in the frequency domain, leading to the same accuracy as the one discussed above in the time domain. Since he proved both methods to be statistically equivalent, error estimation in the frequency domain suffers from the same limitation of underestimating the variance due to the four assumptions outlined above.

For the choice of the interval of test frequencies it does not make sense to search for frequencies with a step much smaller than the value of  $\sigma_\nu$  given in Eq. (5.52). A good guideline to start the first frequency search, before an estimate of  $\sigma_\nu$  can be made, is to take a step of  $0.1/T$ . Once the first frequency is found, one can improve the frequency step by calculating  $\sigma_\nu$  and adapting the step to this value for all subsequent frequency searches.

Another issue in the derivation of the errors is to assume that the oscillation frequencies are independent. As described in Chapter 3, the oscillation spectrum of a star is determined by its stellar structure and follows a clear pattern dependent on the internal physical properties. So, even in the linear approximation, the oscillation frequencies cannot be independent because they are determined by the same stellar structure. Deviations from linearity even imply complex coupling between oscillation modes and their frequencies that are also dependent on the stellar model. This is usually ignored in the error estimation of frequency analysis. It will be discussed further for the Sun in Chapter 7.

### 5.5.2 Data suffering from Aliasing

Most data sets have gaps, quite often leading to ambiguity in the selection of the true frequency peak from its aliases when the duty cycle is limited. The situation is usually far more complex than having one simple modulation factor as in Fig. 5.9, because numerous data gaps, all with different values of  $\Delta T$ , occur. An accurate study of the spectral window, or the consideration of independent data sets of the same star if available, may help to discriminate between the true frequency peaks and their aliases. Sometimes, however, this is impossible and in such a situation one has to take the uncertainty due to

alias confusion into account in the error estimate of the frequency. As a rule-of-thumb, one can take a peak to be uncertain when the difference between its amplitude and the one of its aliases is less than the height of the highest noise peaks. Indeed, noise peaks and real peaks convolve with each other in complex space, such that they may add in amplitude, subtract in amplitude, or anything in between.

The best way to proceed when alias confusion cannot be overcome is to determine the full-width-at-half-maximum of the envelope of all alias peaks that bring confusion, and to add this value to the frequency error given in Eq. (5.52). While the full-width-at-half-maximum of the central peak depends on the total time span of the data, as shown by Eqs (5.52), the one of the envelope depends mainly on the duty cycle, as is clear from Fig. 5.9.

Finally, if the addition of a new frequency implies a modification of the derived amplitudes and phases for previously determined frequencies (say by more than  $3\sigma$ ) during the process of fitting multiple frequencies by least squares, then there is *interaction* between the spectral window patterns of the frequencies. In that case, the formal errors on amplitude and phase given in Eqs (5.52) underestimate the true uncertainties.

## 5.6 The use of Weights in Merging different Data Sets for Frequency Analysis

Very often, more than one time series is available for the analysis of a pulsator and the question arises if one should merge them or simply analyse each of them separately before making final conclusions. The goal of merging them would be to reach a lower noise level in the Fourier transform, or a higher frequency precision or a cleaner spectral window. In any case, appropriate weights cannot be but data-driven, *i.e.*, based on the noise properties and the sampling of each of the separate data sets. This is why one cannot provide one simple theoretical statistical treatment, nor perform all-encompassing simulations encapsulating each of the different circumstances. We therefore limit ourselves here to a brief discussion of some prototypical situations.

As a first example, we consider the situation of a white-light photometric multisite campaign with different instruments attached to telescopes of different apertures and data gathered in different atmospheric conditions. In this case, the data from the smaller telescopes have higher noise level, but, on the other hand, they usually imply a better duty cycle. In such a situation one wants to investigate what data to include in the final analysis, and whether weights should be used or not in the computation of the Fourier transforms. It was shown in the highly recommended seminal paper by Handler (2003b), who studied in detail the merging of such type of data from the different telescopes of the WET consortium and for different targets, that the use of appropriate weights is indeed advantageous compared with the use of unweighted merged sets. He considered three different weighting schemes and

concluded that weights proportional to the inverse local scatter in the light curves produce the best result in Fourier space. The advised procedure is as follows. After having completed the frequency analysis for the unweighted merged data set, one computes the residuals and their standard deviation  $\sigma$ . Each individual point is then weighted as follows:

$$\begin{cases} w_i = 1 & \text{if } R_i \leq K\sigma, \\ w_i = (K\sigma/R_i)^\alpha & \text{if } R_i > K\sigma, \end{cases} \quad (5.53)$$

where  $R_i$  is the residual of data point  $i$  with respect to the unweighted least-squares solution and  $K$  and  $\alpha$  are free parameters to be adapted to the merged data set. A Fourier transform of the weighted data is then computed to try and improve the result in terms of finding the frequencies with amplitudes of better S/N level and/or to find more significant frequency peaks. The best values of  $K$  and  $\alpha$  must be derived by using a few trial values and evaluating the noise level in the Fourier transform. Typical values turn out to be  $K, \alpha \in [0, 2]$ . Since this method depends on the frequency solution found from the unweighted merged data set, a scheme with a few iterations is the best approach. A similar strategy may be advantages to follow when new data are merged with archival ones of the same kind. Recent applications of the methodology evaluated by Handler (2003b) are available in Rodríguez *et al.* (2003) for a  $\delta$  Sct star and in Vučković *et al.* (2006) for an sdB star.

As a second example, we consider the case of multicolour photometric data obtained with the same instrument and having (almost) the same sampling. This is also an often encountered situation, because the identification of the degree  $l$  of the oscillation may be within reach in this circumstance. In this case, the duty cycle is not improved by merging the different sets. As we will show in the following Chapter, the amplitude of a mode is different in different wavelengths and it depends also on the geometry of the mode (*i.e.*, the number and position of the surface nodal lines  $l$  and  $m$ ) and on the direction to the line of sight (inclination angle). For a specific star, the amplitude ratios will be shown to be dependent on  $l$  only (Chapter 6). This implies that the best wavelength to detect a mode is dependent on its degree. In addition, it involves limb-darkening effects, as well as flux, gravity and temperature variations and these may be quite different for different types of oscillations in different types of stars. Pulsating B stars, *e.g.*, have their largest amplitude in the  $U$  filter, while the amplitude of pulsating A or F stars peaks at wavelengths of the  $B$  filter, irrespective of the mode geometry. For one and the same star, the  $l$ -dependence of the amplitudes implies that a particular mode may have an amplitude just above the detection threshold of  $A > 4$  S/N in one or a few of the used filters, but not in all of them. It is therefore surely necessary to analyse the time series of the different filters explicitly to decide upon the reality of all the significant oscillation frequencies, and not just look at the filter where the best S/N is reached. Indeed, the difference in detected mode amplitude for the various filters may be larger than the difference in the noise

level among the filters. Recent examples of this situation can be found in De Cat *et al.* (2007) and Cuypers *et al.* (2009). The modes that have significant amplitude in all filters will pop up better after (weighted) merging of the data sets because the noise level is proportional to the number of data points as  $\sqrt{N}$ , but those that are only significant in a subset of the filters may increase or decrease in significance.

A similar situation to the previous one occurs for radial-velocity measurements of different line profiles from échelle spectra. The amplitudes of the modes may turn out to be quite different for different spectral lines because of various reasons, such as a different intrinsic profile (Gaussian broadening due to temperature versus Stark broadening due to pressure, *e.g.*), a different line depth, a different skewness due to blending, different formation depth in the atmosphere, a different limb darkening effect, *etc.* It may therefore be worthwhile to consider merged data sets for the different spectral lines with the same sampling, in the same way as outlined for the multicolour photometry.

Finally, we consider the case of having data sets of very different nature, *i.e.*, different quantities obtained for different sampling, for one and the same star. Examples are shown in Figs. 2.16 and 2.17 where Hipparcos, Geneva and radial-velocity data of two SPBs are displayed. In this case, it is not obvious to think of an appropriate weighting scheme similar to the one in (5.53) because of the different physical units. Usually, the data are analysed separately first. In a second step, one could simply lower the threshold of accepting a peak in terms of amplitude, *e.g.*, take  $A > 3.6 \text{ S/N}$  as a necessary condition whenever it is met for all the available independent time series. Sometimes, however, oscillation frequencies are easier to detect in spectroscopy than in photometry, depending on their  $l$ -value and one would want to give different weights to the various data sets and lower the detection threshold further. This holds the danger of taking noise peaks for real. A simple test in such a case may be to standardize each of the separate Fourier transforms, *i.e.*, to rescale them to  $[0, 1]$  by dividing through the amplitude of the highest peak, and then multiply them with the idea that, if additional frequencies at S/N below 4 would be present in each of the periodograms, they would have an improved S/N in the multiplied periodogram while they would reduce in amplitude if the frequency was a spurious peak present in only one of the independent data sets. This method was employed by Aerts *et al.* (2006c) to unravel low-amplitude frequencies from MOST, Hipparcos and radial-velocity data of the  $\beta$  Cep star  $\delta$  Ceti and by Rauw *et al.* (2008) to investigate the coherence between candidate oscillation frequencies in photometry and spectroscopy of a low-amplitude O-type pulsator.

## 5.7 Damped Oscillations

The descriptions in the preceding parts were valid under the assumption that the oscillation amplitude  $A$  and phase  $\delta$  are constant in time, *i.e.*, that the modes under consideration have an infinite lifetime or a lifetime several orders of magnitudes longer than the time series and that phase coherence is preserved over the entire observing run. This assumption is not valid whenever growth and/or decay of modes occur during the obtained time series. The best known example of such a situation is, of course, the one of stochastically excited solar-like oscillations. Also modern high-precision radial-velocity measurements of roAp stars contain evidence of growing and damping of mode amplitudes.

We recall from Chapter 3 that, whenever an oscillation with frequency  $\nu_1$  is damped, one has, instead of Eq. (5.9):

$$x(t_i) = A \cos [2\pi(\nu_1 t_i + \delta)] \exp(-\eta t) + c, \quad (5.54)$$

with  $\eta$  the damping rate which is also the inverse of the mode lifetime. Suppose such a signal would be observed continuously over an infinite amount of time. In that case, it is easy to show that the power at a test frequency  $\nu$  equals

$$P(\nu) = \frac{1}{4} \frac{A^2}{4\pi^2(\nu - \nu_1)^2 + \eta^2}. \quad (5.55)$$

The power spectrum thus takes a Lorentzian profile around the frequency  $\nu_1$  with a half-width-at-half-maximum equal to  $\eta$  (see, *e.g.*, Fig. 3.33). If the signal is continuously observed during a finite time  $T$ , then the resulting peak in the power spectrum is intermediate between the  $\text{sinc}^2$  function and the Lorentzian, tending to the former for  $\eta T \ll 1$ , and towards the latter for  $\eta T \gg 1$ .

Even Eq. (5.54) is an idealization in that it implicitly assumes a sudden excitation of the mode, followed by an exponential decay. As already explained in Chapter 3, the modes are stochastically excited by random fluctuations due to the turbulent motions in the convection zone. In this case, one has

$$P(\nu) = \frac{P_f(\nu)}{16\pi^2\nu_1^2 [4\pi^2(\nu - \nu_1)^2 + \eta^2]} \quad (5.56)$$

(*cf.* Eq. (3.308)), with  $P_f(\nu)$  the average power spectrum of the forcing function. Given that the forcing function is a slowly varying function of frequency, the result is a Lorentzian spectrum with a width determined by the linear damping rate of the mode.

The uncertainty of the frequency, amplitude and linewidth of the stochastically excited modes is usually computed from maximum likelihood estimators of fits to the Lorentzian profile expected for a mode, see, *e.g.*, Libbrecht (1992), Toutain & Appourchaux (1994), and Chaplin *et al.* (2002a,b), to list just a few of the key papers in this area. These maximum likelihood estimators are based

on the assumption of dealing with independent harmonic oscillators superposed on a general background noise spectrum, such as the one measured for the Sun (*e.g.*, Duvall & Harvey 1986, Kumar & Goldreich 1989). The appropriate computation of the estimators requires the addition of a large number of independent realizations of the mode whose parameters are searched for. Libbrecht (1992) cleverly solved this problem analytically, by splitting the solar time series into a large number of sub-series, each with length longer than the lifetime of the mode under study. This allowed him to compute the standard error of the mode frequency. Toutain & Appourchaux (1994) improved this approach by comparing results based upon general maximum likelihood theory applied to appropriate estimators for a symmetric Lorentzian profile with those from Monte Carlo simulations. For a single mode, they came up with the following approximation for the error of the mode parameters:

$$\begin{aligned}\sigma_\nu^2 &= \frac{\eta}{2\pi T} \sqrt{1+\beta} \left[ \sqrt{1+\beta} + \sqrt{\beta} \right]^3, \\ \sigma_A^2 &= \frac{\eta\pi T}{2} (1+\beta)^{-3/2} \left( \sqrt{1+\beta} + \sqrt{\beta} \right)^{-1/2}, \\ \sigma_\gamma^2 &= 2\pi\eta T \left( \sqrt{1+\beta} + \sqrt{\beta} \right)^{-4},\end{aligned}\quad (5.57)$$

with  $\gamma \equiv \ln(2\eta)$  and where  $\beta$  is the inverse signal-to-noise ratio in a single frequency peak. These formulae are a good approximation of the lengthy full expressions (given in Toutain & Appourchaux 1994) and replace the results given in Eqs (5.52) for non-damped modes with an infinite lifetime.

Whenever the observed time series is a single realization of the spectrum, the resulting frequency spectrum is only a random function with a Lorentzian envelope. The observed profiles are asymmetric in this case and representing them by a Lorentzian cannot be but an approximation. Neglecting such asymmetries in the fitting of the frequency peak causes systematic errors in the inferred frequencies, such that the approximate formulae given in Eqs (5.57) provide only a lower limit. The best way to proceed in this case is, therefore, to perform simulations and fit the Fourier transforms of the observed time series with Lorentzian profiles to determine acceptable ranges for the frequency, amplitude, and the mode lifetime. Such simulations have been performed extensively for the solar oscillation spectrum. It was found that the stochastic nature of the excitation gives rise to a number of sharp frequency peaks, with a distribution around the Lorentzian envelope. It thus cannot be assumed that the maximum observed amplitude corresponds to the true frequency of the mode.

Substantial care is required in analysing data of stochastically-excited oscillators and the simulations have to be designed on a case-by-case basis. We refer to some of the case studies in Chapter 7 for more details on the technical aspects of appropriate frequency analysis and mode parameter estimation for damped oscillators.

## 5.8 Eliminating Aliases

Several methods designed to “remove” false peaks from a periodogram have been devised. The widest used one among them is the so-called CLEAN method. The original CLEAN algorithm was written by Högbom (1974) in the context of aperture synthesis. It was developed to help radio astronomers in their interpretation of interferometric data by cleaning up the *spatial* window pattern. This algorithm was later adapted by Roberts *et al.* (1987) to clean up the spectral window pattern for frequency analysis.

CLEANing implies that one first constructs the *dirty* spectrum, which is the Fourier transform of the data. Subsequently, one deconvolves this observed spectrum with the window function shifted to the highest peak of the dirty spectrum (*cf.* Figs 5.10 and 5.11). This deconvolution is done by first applying a particular scaling to the window function according to the gain factor  $g$ , with  $0 < g < 2$ . Thus, one subtracts the scaled spectral window from the dirty spectrum to produce a residual spectrum. This deconvolution process is repeated until the strongest residual peak is below a specified cutoff level or for a chosen number of iterations. At that point, the CLEAN algorithm restores the removed frequency to the spectrum by convolving it with the CLEANed residual spectrum. This process can be repeated at each prewhitening stage.

The first application of the adapted CLEAN version by Roberts *et al.* (1987) in pulsating star research was made by Gies & Kullvaniaya (1988), who used it to treat their data of line-profile variations of the B2III star  $\varepsilon$  Per, an archetypical line-profile variable without clear periodic photometric variations due to high- $l$  modes. Numerous applications have followed since.

Foster (1996ab) developed the CLEANest frequency spectrum. The naming is quite unfortunate, because CLEANest has not much to do with CLEAN. The CLEANest spectrum is the sum of a discrete amplitude spectrum and the residual spectrum. The discrete spectrum is derived from a model fit of the best  $M$  frequencies to the data according to Eq. (5.1). This is done for one frequency at a time, *i.e.*, one starts with one frequency, tests the significance of its amplitude, next one makes a fit to find the best pair of frequencies, tests their amplitudes, continues with a fit for the best triple of frequencies, *etc.* At a certain point, the fit for the best  $(M + 1)$  frequency set does no longer lead to a significant peak for the  $(M + 1)$ th frequency. At that stage, one constructs a composite graphical representation of the optimal discrete amplitude representation of the  $M$  accepted frequencies and the amplitude spectrum of the residuals after prewhitening the best fit for  $M$  frequencies. This CLEANest spectrum thus is not a true frequency spectrum, but merely a convenient graphic that captures the different stages of a least-squares fitting procedure and its resulting residual spectrum.

Following Kurtz (2002), we issue some warnings in the use of these two methods that were designed to eliminate aliases. It is in fact a crucial mistake in frequency analysis to think that methods capable of eliminating aliases exist. Alias confusion in a data set can only be overcome by additional data.

All the two methods described above do, is to *hide* the aliases for the user, seemingly easing the interpretation in terms of intrinsic frequency detection. One must keep in mind that the final result obtained by CLEANing depends crucially on the choices of highest peaks made during the deconvolution, while the CLEANest spectrum assumes that frequencies are not confused with their aliases in the least-squares fitting. So both the CLEAN and CLEANest methods are ambiguous.

The main danger of CLEANing occurs in situations where the noise in the data set under analysis has added amplitude to an alias or subtracted amplitude from the true peak. If this is the case in such a way that the alias peak has become the highest one in the periodogram, then this false peak will be selected as the true frequency by the algorithm. The subsequent iteration schemes of CLEAN will take away an amount of amplitude of the true frequency according to the gain and number of iterations.

CLEANest will consider the least-squares fit at the alias frequency if the noise has boosted its amplitude above the one of the true peak. It will then start or continue an iterative least-squares fitting scheme based on one or more alias frequencies rather than on true frequencies.

The user is thus easily fooled by these algorithms if they are used as a black boxes without making a careful analysis of the spectral window at each step of the prewhitening. We advise against their use for this reason, particularly for inexperienced frequency analysts.

## 5.9 Conclusions

We provided the most commonly used methods to treat frequency analysis of unevenly spaced data with large gaps of observables of variable stars. All methods discussed here in detail are suitable to determine the oscillation frequencies of stars whose modes have infinite lifetime. The string length methods and the phase dispersion minimization methods are of broader application than stellar oscillations because they can handle non-sinusoidal signals or signals with variable amplitude without loss of accuracy. On the other hand, the approximation of having sinusoidal signals, the basic assumption of the methods based on Fourier transforms, is usually very good in the study of stellar oscillations.

The reader has hopefully learned that frequency analysis of unevenly spaced gapped data with noise is an inherently difficult mathematical problem to solve. Methods based on Fourier analysis are best suited to apply significance criteria and to obtain frequency error estimation. One should never forget to make a detailed inspection of the spectral window before coming to final conclusions on the detected significant frequencies. One should also check if the assumption of white Gaussian noise is justified.

Frequency analysis of data resulting from stars with damped modes is much more cumbersome and requires a specific treatment, whose basic ingredi-

ents have been pointed out here but whose detailed application is case-specific and will be illustrated in Chapter 7.

---

## Mode Identification

The basic data for asteroseismology are the pulsation frequencies, and we have just shown in Chapter 5 how those are derived from the observations. But before the frequencies can be used for detailed modelling, it is imperative to know what pulsation mode gives rise to each frequency. Determining this is called *mode identification*. The reason it is so important can easily be seen in Fig. 1.7 in Chapter 1 for p modes. The frequency of pulsation is a measure of the sound travel time along the ray path for p modes, and that is determined by the variable sound speed and the length of the ray path itself. It is thus critical to know the ray path, and that is specified by the pulsation mode geometry. The situation is similar for g modes (see Fig. 1.8). Mode-identification techniques assign values to the discrete spherical harmonic quantum numbers  $(l, m)$  of each of the detected oscillation modes. The amount of astrophysical information that can be derived from the observed pulsations depends directly on the number of successfully identified modes. Therefore, great effort is put into mode identification in any seismic analysis.

For oscillations in the asymptotic frequency regime, the derivation of frequency or period spacings often suffices to identify the modes for slowly rotating pulsators. This can be achieved for the Sun, for solar-like oscillators and for white dwarfs (Chapter 7). However, when only a limited number of modes is excited to observable amplitudes, or when the modes do not follow particular frequency patterns, or whenever a very dense frequency spectrum is predicted, the frequency values alone are insufficient to derive the  $(l, m, n)$ . In this case, one cannot proceed with seismic modelling considering *all* values for  $(l, m, n)$  for any of the detected frequencies. In order to limit the computation time of such forward modelling, the values of the degree  $l$  are usually limited from arguments of partial cancellation. As we will show later on in this chapter (see Fig. 6.4), the observed photometric amplitude of modes with  $l \geq 3$  are a factor five to ten less than those of modes with  $l < 3$  having the same intrinsic amplitude, as first demonstrated by Dziembowski (1977b) and already emphasized in Chapter 1. It is then customary to consider modes with

$l \leq 2$  and to assume  $m = 0$  when no obvious evidence for rotational splitting is found in the Fourier transform of the time series.

This procedure is not very satisfactory, though, because rotation can easily result in non-equidistant splitting and imply merging of frequency multiplets in such a way that they cannot be unravelled. Moreover, quite a number of classical pulsators show evidence for modes with degree  $l \geq 3$  from spectroscopy, where the partial cancellation has a different effect than in photometry, as will become clear from comparing Figs 6.4 and 6.14 further on. In these cases, the assumption of  $l \leq 2$  or  $m = 0$  is unjustified. Within asteroseismology the quest for *empirical mode identification* has therefore become an extended topic by itself. By this term we mean the assignment of values of the spherical harmonic quantum numbers  $(l, m)$  to each of the frequencies derived from the data, without relying on the (unknown) details of the model properties of the star. To obtain a correct mode identification for each detected oscillation frequency is usually impossible. However, even only one correct  $(l, m)$  identification, *e.g.*, the one for the dominant mode, can imply a significant reduction of the free parameter space in the modelling, and is therefore worthwhile to attempt.

Empirical mode identification is a sophisticated and time-consuming task. It requires a detailed confrontation between oscillation theory applied to the outer stellar atmosphere and observational characteristics different from the frequencies, such as observed amplitudes and phases. All the methods we present in this chapter were developed for the identification of heat-driven nonradial modes whose lifetimes can be assumed infinite for their application. The reason is that it is relatively easy to establish a value for the large frequency separation of damped stochastically-excited oscillations and this usually suffices to start the process of forward modelling efficiently. Examples of mode identification from pattern recognition of solar-like oscillation frequencies will be treated in Chapter 7. The current chapter is thus restricted to mode identification of heat-driven modes. In what follows, we will speak of the *atmosphere* of the star as the regions with negative  $\log \tau$ ,  $\tau$  being the optical depth, while the parts where  $\log \tau$  is positive will be termed the *stellar envelope*.

Essentially two types of diagnostics are in use to identify the modes. One of them is based on time series of multicolour photometry, and the other relies on time series of line-profile variations detectable from high-resolution spectroscopy. The introduction of high-resolution spectrographs with sensitive detectors in the 1980s, as outlined in Chapter 4, had a large impact on the field of empirical mode identification. Spectroscopic data indeed offer a very detailed picture of the pulsation velocity field, as will be outlined below. On the other hand, it requires moderate to large telescopes equipped with sophisticated instrumentation to be available for extended observing time spans. It remains a challenge to obtain spectra covering the overall beat period of the multiperiodic oscillation, with a high resolving power and with a high signal-to-noise ratio for a good temporal resolution, *i.e.*, for a ratio of the integration

time to the oscillation periods below a few per cent. The latter condition is necessary in order to avoid smearing out the oscillations during the cycle. Also, the methodology to derive the full details of the pulsational velocity field (at least six unknowns – see Section 6.2) is complicated. For this reason, multicolour photometric observations, which can only lead to an estimate  $l$ , but which can be obtained from small telescopes, are still of utmost importance for mode identification. These kinds of data are especially more suitable to study long-period pulsations because small telescopes are available on longer time scales. The most reliable results are obtained from the exploitation of simultaneous multicolour photometry and line-profile data.

One remark we wish to repeat here was already made in Chapter 5: seeking mode identification from observables implies the estimation of the discrete numbers  $(l, m)$ . However, while doing so, one also must estimate real-valued unknowns, such as amplitudes and phases of the frequencies detected in observable quantities. This mixture of real and discrete unknowns cannot be treated simultaneously with standard statistical techniques to estimate  $(l, m)$ . Therefore, any of the discriminating functions that will be defined below will be computed for each set of  $(l, m)$  separately, and its minimal value for the best choice of the continuous parameters will subsequently be compared among the  $(l, m)$  couples to decide about the most likely one.

In the following, we describe the methods for empirical mode identification. We divided the chapter according to the observational data available to apply them. This also corresponds to the historical progression in this field of research.

## 6.1 Mode Identification from Multicolour Photometry

A pulsating star changes in temperature and in geometrical cross-section over its pulsation cycle, both of these contributing to variations in its bolometric luminosity. As we discussed in Chapter 4, photometric observations measure the intensity of the starlight reaching us – usually through various filters, and never bolometrically; no photometer can measure the entire electromagnetic spectrum! So in all observational cases we are measuring the starlight and its variations over some wavelength range. The wavelength dependence of the effect of the temperature variation on the light variability in a pulsating star was already shown in Fig. 4.4. We recall that the intensity change is much greater in the blue than it is in the red – just because of the shape of the black body curves. That effect alone means that most pulsating stars will have larger photometric variations in the blue than in the red.

In addition to this basic effect, the light variations at different wavelengths depend on the geometry of the temperature variations – hence on the spherical harmonic of the pulsation mode – and on the change in geometrical cross-section, also dependent on the pulsation mode. Both the pulsation amplitude and phase as a function of wavelength are affected by the geometry of the

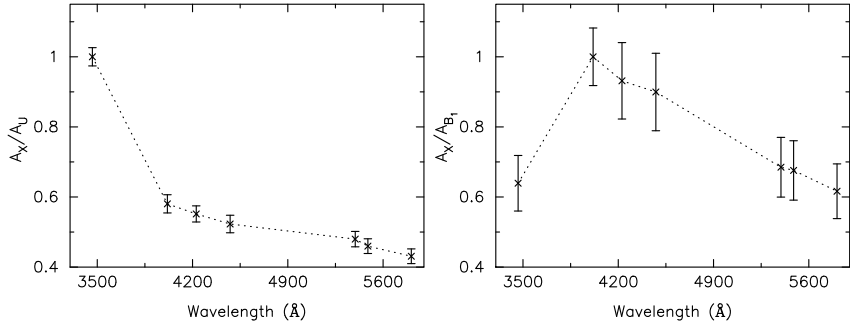


**Fig. 6.1.** Observed amplitude ratios from long-term monitoring of the  $l = 0$  mode of the B2  $\beta$ Cep star HD 71913 (left, Aerts 2000) and for the  $l = 1$  mode of the F2  $\gamma$ Dor star HD 12901 (right, Aerts *et al.* 2004a) in the Geneva 7-band photometric system with filters X =  $UB_1BB_2V_1VG$ .

temperature changes and the cross-section changes; thus observations of the pulsation amplitudes and phases in different photometric passbands can constrain mode identification. In the best cases the spherical degree  $l$  can be uniquely determined – an important step for asteroseismology.

The mode-identification method that uses photometric amplitudes and phases is based on the time variations of the stellar magnitude measured with different filters of a photometric system. One considers only the oscillation frequencies that are found in all the different filters for the mode identification; when the amplitude is too small in one or more filters of the system being used, then there is too little information for that mode. For reasons given above the amplitudes of a mode can be markedly different in the different filters. This is illustrated for two main-sequence stars in Fig. 6.1. As will be explained below, this amplitude difference depends on the kind of oscillation mode – more particularly on the degree  $l$  of the mode as illustrated in Fig. 6.2. Similarly, the difference in phase behaviour of the light curves in the different photometric bands is connected to the degree of the mode. This implies that, for a certain oscillation mode whose frequency is detected with sufficient signal-to-noise in all the filters of the photometric system, the comparison of the amplitude and phase values for the different filters allows one to derive the mode degree. This can be seen for the case of the amplitude ratios by comparing Figs 6.1 and 6.2.

### 6.1.1 General Considerations

Different versions of the photometric mode-identification method are present in the literature. It was originally proposed by Stamford & Watson (1981), relying on the work by Dziembowski (1977b), Balona & Stobie (1979) and Buta & Smith (1979). A specific treatment for the case where temperature variations dominate the light variations was provided in Robinson *et al.* (1982),

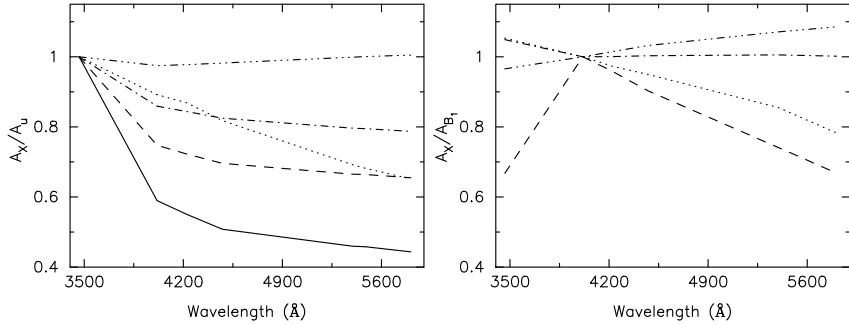


**Fig. 6.2.** Theoretically predicted amplitude ratios for various degrees  $l$  of a typical B2 star for the dominant p-mode frequency of HD 71913 (left) and of a typical F2 star for the dominant g-mode frequency of HD 12901 (right). The computations were done in the adiabatic approximation and assumed  $Z = 0.02$ . The line style coding is as follows: full for  $l = 0$  (not applicable in the right panel), dashed for  $l = 1$ , dashed-dot for  $l = 2$ , dotted for  $l = 3$  and dash-dot-dot-dotted for  $l = 4$ . Comparison of these predictions with the observations shown in Fig. 6.1 allows the identification of the mode degree  $l$ . In the current examples we find  $l = 0$  for HD 71913 and  $l = 1$  for HD 12901.

with an application to white dwarfs. Watson (1988) improved the Balona & Stobie (1979) method by bringing it into applicable form, while Garrido *et al.* (1990) and Heynderickx *et al.* (1994) included the perturbation of the limb darkening and, subsequently, of the surface normal, respectively, in a proper way. All these versions are based on adiabatic oscillation theory, and treat the non-adiabaticity of the oscillatory behaviour in the outer atmosphere by means of an ad-hoc parameter. For an extensive review of the methods in this approximation, we refer to Garrido (2000).

The theoretical expressions of the amplitude and phase of the light curve in the different filters (*i.e.*, as a function of wavelength) depend on, among other things, the geometrical configuration of the nodal lines with respect to the observer, *i.e.*, on the values of  $(l, m, i)$ , where  $i$  is the inclination angle between the symmetry axis of the oscillation and the line-of-sight, as defined in Eq. (6.1) further on and also in Appendix B. The symmetry axis of the oscillation is usually taken to be the rotation axis, except for stars with a strong magnetic field, such as the rapidly oscillating Ap stars, where the magnetic axis is probably a more natural and better choice, and possibly for some close binaries where the pulsation axis could be the tidal axis. It was already realised by Watson (1988) that the functional dependence of the amplitude and phase on the mode geometry allows one to group the terms depending on  $m$  and  $i$  into one single factor which is independent of wavelength. One can thus make this factor disappear, and with it the very disturbing and unknown inclination angle, by considering amplitude ratios and phase differences among the different filters. This is the procedure that is usually adopted. The

disadvantage is that one loses the information on the  $m$ -value and one can thus only identify the degree  $l$  of the mode.

A big step forward was achieved by the new versions of the method developed by Cugier *et al.* (1994) and Cugier & Daszyńska (2001) for  $\beta$  Cep stars, by Brassard *et al.* (1995) for ZZ Ceti stars, by Balona & Evers (1999) for  $\delta$  Sct stars, by Townsend (2002) for slowly pulsating B stars, and by Dupret *et al.* (2003) for all main-sequence oscillators. In these works, a non-adiabatic treatment of the oscillations was included, with different levels of sophistication, through which the unknown ad-hoc factor was eliminated. Dupret *et al.* (2003) included for the first time a detailed non-adiabatic treatment of the oscillations in the optically-thin atmosphere of main-sequence stars. They illustrated the applicability of their method to  $\beta$  Cep stars, slowly pulsating B stars,  $\delta$  Sct stars, and  $\gamma$  Dor stars. A non-adiabatic treatment similar to the one by Dupret *et al.* (2003) was presented by Randall *et al.* (2005b) in the context of pulsating subdwarf B stars. It does not contain an equally detailed treatment of the oscillations in the outer atmosphere, however.

In order to achieve identification of  $l$ , the theoretical expressions for amplitude ratios and phase differences must be computed, and this requires the computation of the perturbed version of the adopted limb darkening and of the perturbed stellar flux as a function of the effective temperature and the gravity, which are also affected by the oscillations. This brings us to the need for good atmosphere models and an appropriate limb-darkening description. In particular, it turns out that this identification method is rather sensitive to the adopted treatment of convection when constructing the atmosphere models for stars with outer convection zones, such as  $\delta$  Sct and  $\gamma$  Dor stars (Garrido 2000; Dupret *et al.* 2005a,b). This treatment of convection is not a problem in the application of the method to stars with a radiative envelope, but here, the results of the identification turn out to depend on the adopted metallicity (Dupret *et al.* 2003). These two dependencies must always be kept in mind when making conclusions about the  $l$ -value.

The theoretical amplitude ratios and phase differences are dependent on the stellar flux, which is determined by the metallicity, the effective temperature, and the mass and radius, or, equivalently the gravity, of the star. These parameters are often not known with high precision. Their uncertainties must be propagated into the final selection of the best value for  $l$  from the observed amplitude ratios. This was often ignored in the past, but is accounted for in modern applications of this method, following Balona & Evers (1999). Examples of such applications were provided by Handler *et al.* (2003b, 2005, 2006), De Ridder *et al.* (2004) and Shobbrook *et al.* (2006) for  $\beta$  Cep stars, by De Cat *et al.* (2005, 2007) for slowly pulsating B stars, by Dupret *et al.* (2005a,b) for  $\delta$  Sct and  $\gamma$  Dor stars, and, finally, by Jeffery *et al.* (2004, 2005) and Tremblay *et al.* (2006) for subdwarf B stars. We refer the reader to these papers for more detailed information.

### 6.1.2 Detailed Description

In the following, we provide a detailed mathematical description of the photometric mode-identification method. In doing so, we use two reference frames: a first one with Cartesian coordinates  $(x, y, z)$  and spherical coordinates  $(r, \theta, \phi)$  such that the unit vector  $\mathbf{a}_z$  coincides with the symmetry (*i.e.*, polar) axis of the star and the origin at the stellar centre; and a second one with Cartesian coordinates  $(x', y', z')$  and spherical coordinates  $(r', \theta', \phi')$ , also with origin at the centre of the star but with  $\mathbf{a}_{z'}$  pointing towards the observer. As origin for the angular coordinates  $\phi$  and  $\phi'$ , we take the meridian passing through the  $\mathbf{a}_z$  and  $\mathbf{a}_{z'}$  axes. We define the *inclination angle* of the star as the angle between  $\mathbf{a}_z$  and  $\mathbf{a}_{z'}$  such that

$$\mathbf{a}_{z'} = -\sin i \mathbf{a}_x + \cos i \mathbf{a}_z \quad (6.1)$$

and we adopt the usual definitions of  $\mu$  and  $\mu'$ :

$$\mu = \cos \theta = \mathbf{a}_r \cdot \mathbf{a}_z, \quad (6.2)$$

$$\mu' = \cos \theta' = \mathbf{a}_{r'} \cdot \mathbf{a}_{z'}. \quad (6.3)$$

#### 6.1.2.1 Treatment of the Atmosphere

The equations valid in the interior of the star, as described in Chapter 3, are no longer valid in the outer stellar atmosphere. First of all, the diffusion approximation, which connects the radiative flux to the temperature gradient, does not hold when the density is very low, *i.e.*, when the mean free path of the photons becomes a considerable fraction of the remaining distance to the surface. Secondly, the approximation that the radiation field is isotropic is no longer appropriate, implying that the momentum equation must be modified. The approximations made in Chapter 3 are fine for the computation of the oscillation frequencies, which are determined by the interior structure of the star, as well as for the instability computations, but they are not sufficient for the description of the photometric amplitudes and line-profile variations. In the following, we adopt the approach outlined in detail in Dupret (2002) and summarised in Dupret *et al.* (2002, 2003).

It is assumed that the local atmosphere characterised by the coordinates  $\theta$  and  $\phi$  remains in radiative equilibrium during the oscillation. This approximation is valid because the heat capacity in the atmosphere is very low, such that its thermal relaxation time is far shorter than any of the relevant oscillation periods. In that case, a plane-parallel atmosphere in hydrostatic equilibrium is fully described by its effective temperature  $T_{\text{eff}}$ , its gravity  $g$  and its chemical composition. For a given chemical composition, we write the temperature of the local atmosphere as

$$T = T(\tau, T_{\text{eff}}, g), \quad (6.4)$$

with  $\tau$  the Rosseland mean optical depth, and we assume that this temperature law does not change during the oscillation cycle. Hence, the temperature of the local atmosphere at position  $(\tau, \theta, \phi)$  varies according to

$$\begin{aligned} T(\tau, \theta, \phi) &= T_0 + \delta T(\theta, \phi) \\ &= T(\tau_0 + \delta\tau(\theta, \phi), T_{\text{eff},0} + \delta T_{\text{eff}}(\theta, \phi), g_0 + \delta g_e(\theta, \phi)), \end{aligned} \quad (6.5)$$

where  $\delta g_e$  is the Lagrangian perturbation of the gravity corrected for the pulsational acceleration. In the linear approximation, Eq. (6.5) can be written as

$$\frac{\delta T}{T_0} = \frac{\partial \ln T}{\partial \ln T_{\text{eff}}} \frac{\delta T_{\text{eff}}}{T_{\text{eff},0}} + \frac{\partial \ln T}{\partial \ln g_e} \frac{\delta g_e}{g_0} + \frac{\partial \ln T}{\partial \ln \tau} \frac{\delta \tau}{\tau_0}. \quad (6.6)$$

From the definition of the Rosseland mean optical depth we find

$$\frac{\partial \delta \tau}{\partial \tau_0} = \frac{\delta \kappa}{\kappa_0} + \frac{\delta \rho}{\rho_0} + \frac{\partial \xi_r}{\partial r}. \quad (6.7)$$

As in Eqs (3.124), (3.125), etc. the Lagrangian perturbations again contain a common factor  $\sqrt{4\pi}Y_l^m(\theta, \phi) \exp(-i\omega t)$ . Elimination of  $\delta\tau$  between Eqs (6.6) and (6.7), and division by this common factor leads to

$$\begin{aligned} \frac{\partial(\delta\tilde{T}/T_0)}{\partial \ln \tau_0} &= \frac{\partial \ln T}{\partial \ln \tau} \left( \frac{\delta\tilde{\kappa}}{\kappa_0} + \frac{\delta\tilde{\rho}}{\rho_0} + \frac{\partial \tilde{\xi}_r}{\partial r} \right) \\ &\quad - \left( 1 - \frac{\partial^2 \ln T / \partial \ln \tau^2}{\partial \ln T / \partial \ln \tau} \right) \left( \frac{\delta\tilde{T}}{T_0} - \frac{\partial \ln T}{\partial \ln T_{\text{eff}}} \frac{\delta\tilde{T}_{\text{eff}}}{T_{\text{eff},0}} - \frac{\partial \ln T}{\partial \ln g_e} \frac{\delta\tilde{g}_e}{g_0} \right) \\ &\quad + \frac{\partial^2 \ln T}{\partial \ln \tau \partial \ln T_{\text{eff}}} \frac{\delta\tilde{T}_{\text{eff}}}{T_{\text{eff},0}} + \frac{\partial^2 \ln T}{\partial \ln \tau \partial \ln g_e} \frac{\delta\tilde{g}_e}{\tilde{g}_0}. \end{aligned} \quad (6.8)$$

This equation, rather than Eq. (3.129) is used as energy equation in the atmosphere. The derivatives in Eq. (6.8) must be estimated numerically from a set of atmosphere models with effective temperatures and gravities surrounding those of the star.

While the temperature variation in the atmosphere can be computed locally, as just explained, the variation of the density, pressure and Lagrangian displacement must come from the solution of the mass and momentum equation considering the entire outer atmosphere. In general, the momentum equation contains a pressure gradient with a contribution from the gas pressure and one from the radiation pressure. The latter implies a radiative acceleration vector, which is, in the case of continuum radiation, given by  $\mathbf{g}_{\text{rad}} = \kappa_F \mathbf{F}/c$  with  $\kappa_F$  the flux weighted mean opacity (e.g., Lamers & Cassinelli 1999). It is in general safe to ignore the line radiation, except for the hottest main-sequence stars ( $T_{\text{eff}} > 25\,000\,\text{K}$ ) and for supergiants ( $\log g < 3.0$ ), which suffer from a line-driven stellar wind (e.g., Kudritzki & Puls 2000). In that case, one is dealing with a dynamical atmosphere and the treatment we present here is not strictly valid (but a better approximation is not available).

While solving the continuity and momentum equations one assumes that  $\delta|\mathbf{F}|$  remains constant from the base of the atmosphere to the outermost layer, that  $\mathbf{F}$  remains parallel to the temperature gradient during the oscillation cycle and that the relative variation of  $\kappa_F$  equals the relative variation of the Rosseland opacity:  $\delta\kappa_F/\kappa_F \simeq \delta\kappa/\kappa$ . The first two assumptions are again related to the short thermal relaxation time in the very thin outer layer, which allows the plane-parallel approximation. The validity of the third assumption was checked numerically by Dupret (2002). The first assumption implies, through Stefan's law, that

$$\frac{\delta|\mathbf{F}|}{\mathbf{F}_0} = \frac{\delta F_r}{F_{r,0}} = 4 \frac{\delta T_{\text{eff}}}{T_{\text{eff},0}} \quad (6.9)$$

and leads to the radial component of  $\delta\mathbf{g}_{\text{rad}}$ :

$$(\delta\mathbf{g}_{\text{rad}})_r = g_{\text{rad}} \left( \frac{\delta\kappa}{\kappa_0} + 4 \frac{\delta T_{\text{eff}}}{T_{\text{eff},0}} \right), \quad (6.10)$$

where  $g_{\text{rad}}$  is the equilibrium value of the radial component of  $\mathbf{g}_{\text{rad}}$ . This leads to the following expression for the radial component of the equation of motion:

$$\begin{aligned} \omega^2 \tilde{\xi}_r &= \frac{\partial(\delta\tilde{p}_g/\tilde{p}_g)}{\partial r} \frac{p_{g,0}}{\rho_0} \\ &+ \frac{\partial\tilde{\Phi}'}{\partial r} + \frac{\partial(g_0\tilde{\xi}_r)}{\partial r} + \left( \frac{\delta\tilde{\rho}}{\rho_0} - \frac{\delta\tilde{p}_g}{p_{g,0}} \right) (g_0 - g_{\text{rad}}) \\ &- g_{\text{rad}} \left( \frac{\delta\tilde{\kappa}}{\kappa_0} + 4 \frac{\delta\tilde{T}_{\text{eff}}}{T_{\text{eff},0}} + \frac{\partial\tilde{\xi}_r}{\partial r} \right). \end{aligned} \quad (6.11)$$

This equation is used in the atmosphere, instead of Eq. (3.127). The horizontal component of the momentum equation becomes, through the assumption that  $\mathbf{F}$  remains parallel to the temperature gradient:

$$\omega^2 \tilde{\xi}_h = \frac{1}{r} \left( \frac{\delta\tilde{p}_g}{\rho_0} + \tilde{\Phi}' + g_0\tilde{\xi}_r - g_{\text{rad}} \frac{\delta\tilde{T}}{\partial T/\partial r} \right). \quad (6.12)$$

This equation replaces Eq. (3.131). And, finally, the continuity equation Eq. (3.126) is replaced by its version valid in the outer atmosphere:

$$\omega^2 \left[ \frac{\delta\tilde{\rho}}{\rho_0} + \frac{1}{r^2} \frac{\partial}{\partial r} \left( r^2 \tilde{\xi}_r \right) \right] = \frac{l(l+1)}{r^2} \left( \frac{\delta\tilde{p}_g}{\rho_0} + \tilde{\Phi}' + g_0\tilde{\xi}_r - \frac{g_{\text{rad}}\delta\tilde{T}}{\partial T/\partial r} \right). \quad (6.13)$$

Following Dupret *et al.* (2002), appropriate boundary conditions are imposed at the outermost layer of the star. This requires a little more attention than the discussion in Chapter 3 when we derived Eqs (3.157), ..., (3.163). Contrary to several other versions of the method, it is preferable to choose a

mechanical boundary condition that is valid for application to all stars, *i.e.*, for the case where both the gas and radiation-pressure accelerations may be significant. Therefore, Dupret *et al.* (2002) considered as boundary condition the version of Eq. (6.11) in which the contribution of the gas pressure at the surface is ignored, but not the radiation pressure, thus deleting the first term of the right-hand side of Eq. (6.11). As boundary condition for the gravitational potential, we impose, as usual, continuity of  $\tilde{\Phi}'$  and its first derivative between the inner solution given by the Poisson equation and the outer solution given by the Laplace equation:

$$\frac{\partial \tilde{\Phi}'}{\partial r} + \frac{l+1}{r} \tilde{\Phi}' = -4\pi G \rho_0 \tilde{\xi}_r. \quad (6.14)$$

As boundary condition for the energy equation, Eq. (6.8), Eq. (6.6) is evaluated in the outermost layer by computing  $\lim_{\tau \rightarrow 0} \delta\tau/\tau$  from Eq. (6.7), resulting in

$$\frac{\delta \tilde{T}}{T_0} = \frac{\partial \ln T}{\partial \ln T_{\text{eff}}} \frac{\delta \tilde{T}_{\text{eff}}}{T_{\text{eff},0}} + \frac{\partial \ln T}{\partial \ln g_e} \frac{\delta \tilde{g}_e}{g_0} + \frac{\partial \ln T}{\partial \ln \tau} \left( \frac{\delta \tilde{\kappa}}{\kappa_0} + \frac{\delta \tilde{\rho}}{\rho_0} + \frac{\partial \tilde{\xi}_r}{\partial r} \right) \quad (6.15)$$

(Dupret 2002).

In order to solve for the unknown quantities  $\tilde{\xi}_r, \tilde{\xi}_h, \tilde{T}, \dots$ , we must require continuity of these variables at a so-called connecting layer, bridging the stellar interior and the outer atmosphere. As explained in Dupret (2002) and for the reasons outlined below, this connecting layer must be chosen carefully, *i.e.*, at a position where the flux is predominantly radiative. In this case, Dupret (2002) derived the following matching conditions for the connecting layer:

$$3 \frac{\delta \tilde{T}}{T_0} - \frac{\delta \tilde{\kappa}}{\kappa_0} - \frac{\delta \tilde{\rho}}{\rho_0} + \frac{d\delta T/dr}{dT/dr} - \frac{d\tilde{\xi}_r}{dr} = 4 \frac{\delta \tilde{T}_{\text{eff}}}{T_{\text{eff},0}} \quad (6.16)$$

and

$$\frac{\delta \tilde{g}_e}{g_0} = \frac{\partial \tilde{\Phi}' / \partial r}{g_0} + \frac{4\pi \rho_0 r^3}{m} \frac{\tilde{\xi}_r}{r} - \left( 2 + \frac{\omega^2 r}{g_0} \right) \frac{\tilde{\xi}_r}{r} \quad (6.17)$$

which reduces to the simpler condition

$$\frac{\delta \tilde{g}_e}{g_0} = - \left( 2 + \frac{\omega^2 r}{g_0} \right) \frac{\tilde{\xi}_r}{r} \quad (6.18)$$

in the Cowling approximation, if one ignores the surface density divided by the mean density of the star. By means of Eqs (6.16) and (6.17), Dupret (2002) showed that Eqs (6.11) and (6.13) are mathematically equivalent to Eqs (3.127) and (3.126) for the stellar interior, thus guaranteeing the continuity of the derivatives of  $\tilde{\xi}_r/R$  and  $\delta \tilde{\rho}_g/p_{g,0}$ . Following Dupret *et al.* (2002), the continuity of  $\delta \tilde{T}/T_0$  should be checked *a posteriori*. These authors achieved this condition by placing the connecting layer at  $\log \tau = 1$  for main-sequence

B stars and at  $\log \tau = 0$  for  $\delta$  Sct stars, confirming the validity of their treatment.

The theory presented here is more sophisticated than what is often used in the literature, where the Eddington approximation with temperature distribution

$$T^4(r) = \frac{3}{4} T_{\text{eff}}^4 \left( \tau + \frac{2}{3} \right) \quad (6.19)$$

is regularly adopted for the stellar atmosphere rather than the general form given by Eq. (6.4) for a non-grey atmosphere. The advantage of the treatment presented above is mainly important for hot stars as it includes the radiative acceleration due to continuum radiation. The current treatment also allows one to use any type of equilibrium atmosphere model, as long as it is static, *i.e.*, whenever the acceleration due to line-driving can be ignored. When the atmosphere is perturbed due to the oscillations, it is, in fact, no longer strictly static. Dupret *et al.* (2002) checked for the difference between the perturbed atmosphere due to an oscillation and the static one in the LTE approximation with corresponding temperature and gravity, and found relative differences less than 20% in the quantities, depending on the order of the oscillation mode. This slight inconsistency is negligible compared with the gain of using much better equilibrium atmosphere models.

We compare in Fig. 6.3 the temperature structure of an Eddington atmosphere with state-of-the-art NLTE line-blanketed atmosphere models with and without a line-driven wind, for a star with  $T_{\text{eff}} = 24\,000$  K and  $\log g = 4.5$ . It can be seen that significant deviations from the Eddington model are encountered for the atmosphere region where  $\log \tau < 0$ , even for the static plane-parallel non-grey atmosphere without mass loss (dash-dotted line). This discrepancy in  $T(\tau)$  for  $\log \tau < 0$  is a general property for all effective temperatures of relevance for mode identification. The Eddington approximation is thus only appropriate for the connecting layer, provided that it can be positioned in the regime of  $\log \tau > 0$ . We therefore advise that any user of the methodology checks for the validity of the Eddington approximation for the connecting layer and for the outer atmosphere. In any case, when computing the amplitude ratios and phase differences it can easily be replaced by the treatment provided here, based on a non-grey static plane-parallel atmosphere model.

Coming back to Fig. 6.3, the discrepancy between the grey atmosphere and more realistic models is particularly significant for hot stars and supergiants. One can see from Fig. 6.3 that even a state-of-the-art NLTE plane-parallel model (Lanz & Hubeny 2007) does not give a good description of the temperature distribution in the atmosphere where a temperature bump occurs near  $\log \tau < -2$  in the case of a unified spherical NLTE line-blanketed atmosphere with a line-driven wind. This bump is generally understood in terms of line-heating (*e.g.*, Mihalas 1978) but its exact position and height depend on the presence of particular ions in the wind (see, *e.g.*, Pauldrach *et al.* 2001; Puls *et al.* 2005 for discussions of this effect). As can be derived from Fig. 6.3,

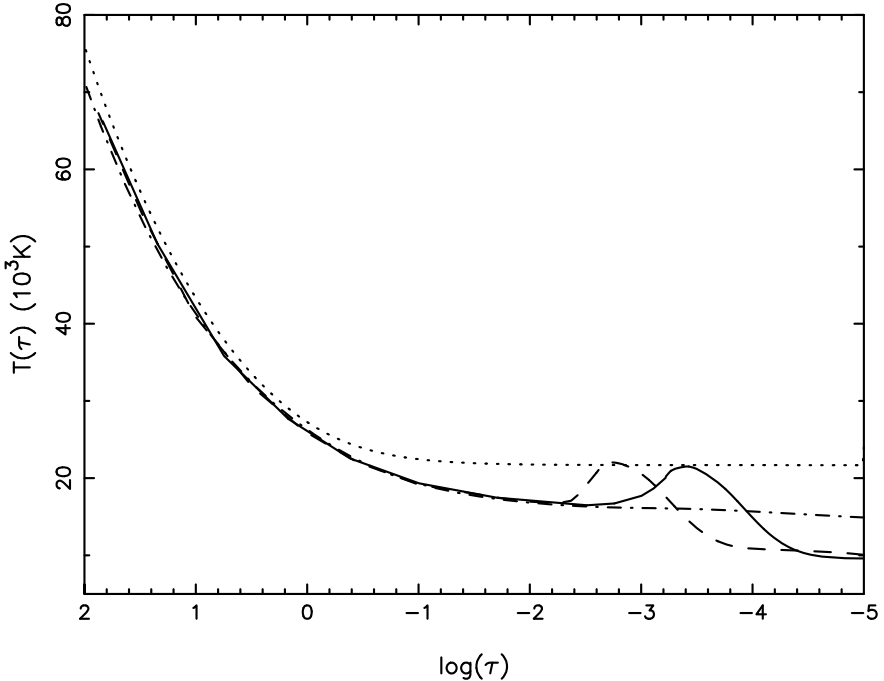


**Fig. 6.3.** Temperature distributions in the envelope and outer atmosphere of a hot star with  $T_{\text{eff}} = 24\,000$  K and  $\log g = 4.5$  for different approximations. Dotted line: grey atmosphere as in Eq. (6.19), dot-dashed line: NLTE plane-parallel line-blanketed static atmosphere model without wind (Lanz & Hubeny 2007), full/dashed line: NLTE spherical unified atmosphere model with weak/strong wind. Data from Lefever *et al.* (2007b).

the current treatment of the outer atmosphere in mode identification should be improved by also considering the line acceleration in the dynamical atmospheres of OB-type stars and supergiants, but this has not yet been done to our knowledge.

Finally, we come back to the prerequisite that the connecting layer must be situated in a part of the atmosphere where the flux is predominantly radiative. The reason is that the assumptions made about the link between the temperature structure and the flux are no longer valid when the convective flux dominates. It is therefore important to position the connecting layer in the very outer part of the envelope for stars with envelope convection zones, such as  $\delta$  Sct and  $\gamma$  Dor stars along the main sequences and any type of evolved pulsator.

### 6.1.2.2 Non-Adiabatic Observables

In what follows, we adopt the single-layer approximation as has always been done so far in photometric mode identification. This means we assume there to be a single stellar photosphere, whose distance to the stellar centre is characterised by the stellar radius  $R$  and whose temperature equals the effective temperature of the star. Moreover, it is assumed that the outward flux does not depend on the optical depth in the atmosphere. The deformation of the photosphere is thus derived from the evaluation of the displacement vector  $\xi$  at  $r = R$  in the linear approximation.

We seek to determine the monochromatic amount of energy radiated by the star as measured by a distant observer:  $E(\lambda, t)$ . In doing so, we again recall the short thermal relaxation time of the atmosphere which has led us to assume that, at each moment in the oscillation cycle, the atmosphere remains in radiative equilibrium and the temperature distribution in the atmosphere  $T(\tau)$  remains the same as in the equilibrium model. We also use the same argument now to keep a fixed prescription for the monochromatic outgoing flux of the local atmosphere  $\mathbf{F}_\lambda^+$  and limb-darkening law  $h_\lambda(\theta)$  during the oscillation cycle. Moreover, we assume that the local atmosphere's chemical composition stays constant and that  $\mathbf{F}_\lambda^+$  remains perpendicular to the local photosphere. Under these assumptions, the monochromatic flux variation in the local atmosphere is given by

$$F_{\lambda,0}^+ + \delta F_\lambda^+(\theta, \phi, t) = F_\lambda^+ [T_{\text{eff},0} + \delta T_{\text{eff}}(\theta, \phi, t), g_0 + \delta g_e(\theta, \phi, t)], \quad (6.20)$$

where we have introduced the notation  $F_\lambda^+ = |\mathbf{F}_\lambda^+|$ . In the linear approximation, this can be written as

$$\frac{\delta \tilde{F}_\lambda^+}{F_{\lambda,0}^+} = \left( \frac{\partial \ln F_\lambda^+}{\partial \ln T_{\text{eff}}} \right) \frac{\delta \tilde{T}_{\text{eff}}}{T_{\text{eff},0}} + \left( \frac{\partial \ln F_\lambda^+}{\partial \ln g_e} \right) \frac{\delta \tilde{g}_e}{g_0} \quad (6.21)$$

$$\equiv \alpha_{T,\lambda} \frac{\delta \tilde{T}_{\text{eff}}}{T_{\text{eff},0}} + \alpha_{g,\lambda} \frac{\delta \tilde{g}_e}{g_0}. \quad (6.22)$$

Similarly, the variation of the limb-darkening law  $h_\lambda(\theta)$  in the linear approximation is written as

$$\frac{\delta_r \tilde{h}_\lambda}{h_{\lambda,0}} = \left( \frac{\partial \ln h_\lambda}{\partial \ln T_{\text{eff}}} \right) \frac{\delta \tilde{T}_{\text{eff}}}{T_{\text{eff},0}} + \left( \frac{\partial \ln h_\lambda}{\partial \ln g_e} \right) \frac{\delta \tilde{g}_e}{g_0} + \left( \frac{\partial \ln h_\lambda}{\partial \mu'} \right) \delta_r (\mathbf{n} \cdot \mathbf{a}_{z'}), \quad (6.23)$$

where  $\mathbf{n}$  is the normal to the stellar photosphere and  $\delta_r$  stands for the *radial Lagrangian perturbation* defined in this Section by

$$\delta_r X = \delta X \quad (6.24)$$

for a scalar quantity  $X$ , and

$$\delta_r \mathbf{Y} = \mathbf{Y}' + \frac{dY_r}{dr} \xi_r \mathbf{a}_r \quad (6.25)$$

for a vector quantity  $\mathbf{Y}$ . With Eq. (6.23) we thus assume  $\delta_r\theta = \delta_r\phi = 0$ . It is noteworthy that Heynderickx *et al.* (1994) and De Ridder *et al.* (2002) did not make this approximation and considered the more general classical Lagrangian perturbation in their description. It was, however, shown explicitly by Dupret (2002) and by Townsend (2003b) that these treatments are mathematically equivalent in the linear approximation for the perturbations. Hence, we limit ourselves to the simpler treatment here, which comes down to the approximation that the geometrical distortion is not affected by the horizontal components of the displacement field.

As we have shown in Eq. (6.18),  $\delta g_e/g_0$  is to a very good approximation in antiphase with the radial displacement. The phase of  $\delta T_{\text{eff}}/T_{\text{eff},0}$  can in principle take any value, depending on the kind of oscillation mode and on the stellar model. Therefore, it is customary to introduce the coefficients  $f_T$ ,  $\psi_T$  and  $f_g$  defined as

$$\frac{\delta \tilde{T}_{\text{eff}}}{T_{\text{eff},0}}(R, \theta, \phi) = f_T \frac{\tilde{\xi}_r(R)}{R} \exp(-i\psi_T) \quad (6.26)$$

and

$$\frac{\delta \tilde{g}_e}{g_0}(R, \theta, \phi) = -f_g \frac{\tilde{\xi}_r(R)}{R}. \quad (6.27)$$

We recall that these amplitude functions are the true amplitudes divided by the common factor  $\sqrt{4\pi}Y_l^m(\theta, \phi) \exp(-i\omega t)$  as before. The coefficients  $f_T$ ,  $\psi_T$  and  $f_g$  are termed *non-adiabatic observables*; in particular, the coefficient  $\psi_T$  is called the *phase lag*. They follow directly from the integration of the basic equations in the stellar interior and in the atmosphere through the connecting layer, with the treatment of the atmosphere as discussed above. In models with an outer convection zone, their values depend on the treatment of convection, including the choice of mixing-length parameter and the possible inclusion of modelling of the coupling between convection and pulsations; thus, inferring them observationally provides a possibly diagnostic of the physics of convection in the outer layers (*cf.* Section 6.1.3).

For the equilibrium model, we have

$$E(\lambda) = \frac{R^2}{2\pi d^2} \int_0^1 \int_0^{2\pi} F_\lambda^+ h_\lambda(\mu') \mu' d\mu' d\phi', \quad (6.28)$$

with  $d$  the distance to the observer, so we must determine  $\delta E(\lambda, t)$ . We omit this long derivation here, as it is readily available in several extensive papers in the literature, such as Heynderickx *et al.* (1994), Brassard *et al.* (1995), Dupret (2002), Townsend (2002), Dupret *et al.* (2003), Daszyńska-Daszkiewicz *et al.* (2003), and Randall *et al.* (2005b), all of which following the original work by Dziembowski (1977b). The outcome, written in terms of the observed variation of the monochromatic visual magnitude at wavelength  $\lambda$  and for our choice of the coordinate systems as described in Section 6.1.2, can be written as

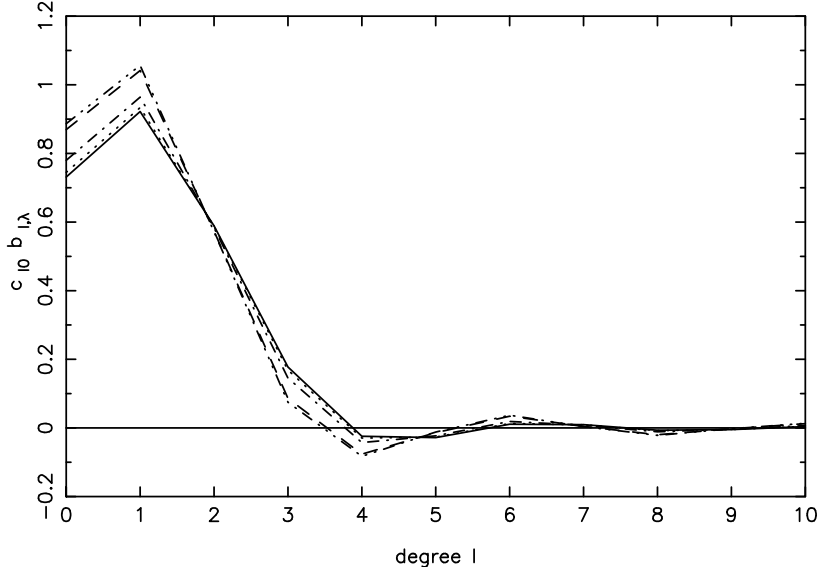


**Fig. 6.4.** The product of the normalisation constant  $c_{l0}$  and the integral  $b_{l,\lambda}$  defined in Eq. (6.30) is shown for different mode degrees  $l$  for a linear limb-darkening law taken from Claret (2000). The lower three curves are for a star of  $T_{\text{eff}} = 6000$  K and  $\log g = 4.0$  at the wavelengths of the  $U$  (full line),  $B$  (dotted line) and  $V$  (dash-dotted line) filters. The two upper curves are for a star of  $T_{\text{eff}} = 25000$  K and  $\log g = 4.0$  at  $U$  and  $B$  (indistinguishable, shown as dashed line) and  $V$  (dash-dot-dot-dotted line) wavelengths.

$$\delta m_\lambda = - \frac{2.5}{\ln 10} \sqrt{4\pi} \frac{\xi_r(R)}{R} c_{l0} P_l^m(\cos i) b_{l,\lambda} \quad (6.29)$$

$$\times [-(l-1)(l-2) \cos(\omega t)$$

$$+ f_T \cos(\psi_T + \omega t)(\alpha_{T,\lambda} + \beta_{T,\lambda})$$

$$- f_g \cos(\omega t)(\alpha_{g,\lambda} + \beta_{g,\lambda})] ,$$

with

$$b_{l,\lambda} = \int_0^1 \mu' h_\lambda(\mu') P_l d\mu', \quad \beta_{T,\lambda} = \frac{\partial \ln b_{l,\lambda}}{\partial \ln T_{\text{eff}}}, \quad \beta_{g,\lambda} = \frac{\partial \ln b_{l,\lambda}}{\partial \ln g}. \quad (6.30)$$

The terms proportional to  $(l-1)(l-2)$ ,  $f_T$  and  $f_g$  correspond to the variation of the surface, of the local effective temperature and of the gravity, respectively. We show the value of the integral  $b_{l,\lambda}$  for different  $l$  in Fig. 6.4, for two different types of stars and for the wavelengths of the U, B, V filters. It can be seen that there is a steep decrease in value as  $l$  increases from 0 to 3, and fluctuating values converging to zero as  $l$  raises above 9. While Eq. (6.29) makes it clear that the computation of the decrease in the observed amplitude of the brightness variations as a function of  $l$  is far more complex than simply

considering  $b_{l,\lambda}$ , this dependence of  $b_{l,\lambda}$  on  $l$  forms the basis of the so-called *partial cancellation effect*. We can see from Fig. 6.4 that  $b_{l,\lambda}$  is a factor  $\sim 4$  smaller for  $l = 2$  than for  $l = 0$ . The factor is even larger for  $l = 5, 6$ , while  $b_{3,\lambda} \approx 0$ . This is the reason why one often assumes  $l \leq 2$  in the modelling of the photometrically detected oscillation frequencies.

Another point of attention in Eq. (6.29) is the factor  $P_l^m(\cos i)$ . For each  $(l, m)$ , there exists at least one inclination angle  $i$  for which  $P_l^m(\cos i) = 0$ . Such angles are termed *Inclination Angles of Complete Cancellation*, abbreviated as IACC. We list them for  $l = 0, \dots, 5$  in Appendix A.

As explained in Chapter 4, observations usually do not provide us with the monochromatic magnitude, but rather magnitudes for particular filters  $j$  with transmission curves  $w_j(\lambda)$  and a wavelength range from  $\lambda_{j,\text{blue}}$  to  $\lambda_{j,\text{red}}$ . One thus computes

$$\delta m_j = \frac{\int_{\lambda_{j,\text{blue}}}^{\lambda_{j,\text{red}}} \delta m_\lambda w_j(\lambda) d\lambda}{\int_{\lambda_{j,\text{blue}}}^{\lambda_{j,\text{red}}} w_j(\lambda) d\lambda} \quad (6.31)$$

for comparisons with observations. It is readily seen from Eq. (6.29) that one eliminates the common factor  $-(2.5/\ln 10)\sqrt{4\pi}(\xi_r(R)/R)P_l^m(\cos i)$ , which is independent of wavelength, by considering amplitude ratios for different photometric bands. With it, the dependence on the inclination angle and on the position of the nodal lines on the stellar surface (by means of  $m$ ) disappears. This is an asset of the method, because the inclination angle is often not, or only very poorly, known, but it is also a disadvantage as it cannot deliver an estimate of  $m$ .

Finally, we wish to emphasize that, in the early development phase of this method, some less accurate approximations have been proposed for the computation of  $f_T$ ,  $f_g$  and  $\delta p_g$ . These were mainly based on adiabatic approximations or an ad-hoc generalization thereof, and/or the assumption that the Lagrangian perturbation of the local temperature equals that of the effective temperature. These assumptions are not appropriate for the outer stellar atmosphere. We advise against usage of the treatments published before 2000. Cugier & Daszyńska (2001) first came up with an improved computation of  $f_g$  in terms of the dimensionless frequency of a mode already defined in Eq. (3.161) in Chapter 3:

$$f_g \simeq 2 + \sigma^2 \simeq 2 + \frac{\omega^2 R^3}{GM}. \quad (6.32)$$

This result is equivalent to the one we encountered in Eq. (6.18), which was a special case of the more general Eq. (6.17) in the Cowling approximation and ignoring the surface density divided by the mean density of the star in the outer atmosphere.

We point out that the ratio  $\xi_h(R)/\xi_r(R)$ , *i.e.*, the ratio between the horizontal and radial components of the displacement evaluated at the stellar

surface, is termed *the K-value* of the mode by observers. They introduced this concept of  $K$  while interpreting data of stellar oscillations. The  $K$ -value is usually approximated by Eq. (3.161), although it is often also kept as a free parameter, when interpreting observations of stellar oscillations.

### 6.1.3 Mode Identification Schemes

Even though the oscillations always behave highly non-adiabatically in the outer atmosphere, some stars have  $\psi_T$ -values close to the adiabatic values. This is, for example, the case for main-sequence B stars and is understood in terms of their excitation by the heat mechanism acting on an opacity feature resulting from iron-like elements, near a temperature of  $\log T \simeq 5.3$ . This is rather deep in the star where the quasi-adiabatic approximation is still quite good. Therefore, the phase difference between the variation of the luminosity and the radial displacement amounts to almost the adiabatic value, *i.e.*,  $180^\circ$  for the p modes in  $\beta$  Cep stars and  $0^\circ$  for the high-order g modes in SPB stars. In such cases, it is customary to exploit only the amplitudes in the different photometric bands, and not the phase differences, when identifying the degree of the modes. The same holds true for the pulsating sdB stars. Other pulsators, such as  $\delta$  Sct stars and all other pulsators in the classical instability strip, are predominantly driven by the partial ionization zone of once ionized helium. This layer is positioned near  $\log T \simeq 4.6$ , *i.e.*, much further out where the non-adiabatic effects are stronger. Non-adiabatic theoretical computations indeed predict large phase differences in the magnitude variations for different filters for such stars. This is confirmed by the observations. In that case, it is advantageous to exploit also these phase differences in identifying  $l$ , besides the amplitude ratios. We treat these two situations below.

#### 6.1.3.1 Mode Identification Schemes using only Amplitudes

When using only the amplitudes, the following scheme is advised, after Dupret *et al.* (2003):

- i) Compute stellar models with appropriate effective temperatures and gravities. One must make sure to cover the observational error box in  $(T_{\text{eff}}, \log g)$  with models for a safe propagation of the uncertainty of these fundamental parameters on the mode identification. As  $T_{\text{eff}}$  and  $\log g$  follow readily from an interpretation of the stellar spectrum, it is best to use these as constraints to construct the models. Observational values for the luminosity (or the absolute magnitude) require additional information, such as the distance which is often poorly known, or rely on calibrations which can suffer from unknown systematic uncertainties.
- ii) Perform non-adiabatic computations to derive  $f_T, \psi_T, f_g$  for modes with frequencies close to the observed ones, for different degree  $l$ , for all the

models that pass through the observational error box computed in 1. Usually, one restricts the search to  $l = 0, \dots, 4$  by arguments of observational cancellation for higher degree modes.

- iii) For each filter  $j$  and for each degree  $l$ , compute the theoretical amplitude while omitting the common factor  $-(2.5/\ln 10)\sqrt{4\pi}(\xi_r(R)/R)c_{lm}P_l^m(\cos i)$ , *i.e.*, compute the amplitude factor:

$$A_{j,\text{th}} = \frac{\int_{\lambda_{\text{blue}}}^{\lambda_{\text{red}}} |b_{l,\lambda}| |T_1 + T_2 + T_3| w_j(\lambda) d\lambda}{\int_{\lambda_{\text{blue}}}^{\lambda_{\text{red}}} w_j(\lambda) d\lambda}, \quad (6.33)$$

with

$$T_1 \equiv (1-l)(l+2), \quad (6.34)$$

$$T_2 \equiv f_T \exp(-i\psi_T) (\alpha_{T,\lambda} + \beta_{T,\lambda}), \quad (6.35)$$

$$T_3 \equiv -f_g (\alpha_{g,\lambda} + \beta_{g,\lambda}). \quad (6.36)$$

- iv) Choose a reference filter  $A_{\text{ref},\text{th}}$  to compute the amplitude ratios. The best choice is to take the particular filter for which the relative uncertainty of the measured amplitude is smallest. Quite often, this is the filter in which the highest intrinsic amplitude is reached, but not always as this also depends on the instrumental noise.
- v) Compare the theoretical amplitude ratios  $A_{j,\text{th}}/A_{\text{ref},\text{th}}$  with the observed ones  $A_{j,\text{obs}}/A_{\text{ref},\text{obs}}$ , *for all the stellar models that pass through the error box* in  $(T_{\text{eff}}, \log g)$ . This comparison can be made by visual inspection, as is often done, as it makes it possible to see the confusion regions due to the uncertainty in  $(T_{\text{eff}}, \log g)$ . It can also be done by computing the  $\chi^2$  function defined as:

$$\chi^2(l) = \sum_{j=1}^{\# \text{filters}} \left( \frac{A_{j,\text{th}}/A_{\text{ref},\text{th}} - A_{j,\text{obs}}/A_{\text{ref},\text{obs}}}{\sigma_{j,\text{obs}}} \right)^2, \quad (6.37)$$

where  $\sigma_{j,\text{obs}}$  is the properly propagated standard error of the observed amplitude ratio for filter  $j$  and the reference filter, *i.e.*,

$$\sigma_{j,\text{obs}} = \frac{A_{j,\text{obs}}}{A_{\text{ref},\text{obs}}} \sqrt{\left( \frac{s_{A_{j,\text{obs}}}}{A_{j,\text{obs}}} \right)^2 + \left( \frac{s_{A_{\text{ref},\text{obs}}}}{A_{\text{ref},\text{obs}}} \right)^2}, \quad (6.38)$$

with  $s_{A_{j,\text{obs}}}$  the standard error of the observed amplitude in filter  $j$ . Also in this case, one must consider different stellar models across the entire observational error box.

While performing step 3, one needs to derive the coefficients  $\alpha_{T,\lambda}$  and  $\beta_{T,\lambda}$ , which are derivatives of the monochromatic flux at wavelength  $\lambda$ , from

appropriate stellar atmosphere models. Several grids of state-of-the-art models are available in the literature, well suited to particular kinds of pulsating stars, *e.g.*, the LTE plane-parallel models by Kurucz (1993) or Smalley & Kupka (1997) for main-sequence stars cooler than spectral type B and the NLTE plane-parallel line-blanketed models for B stars (Lanz & Hubeny 2007) and O stars (Lanz & Hubeny 2003) without wind. As already discussed in the context of the connecting layer and Fig. 6.3, one should in principle adapt the theory presented here to NLTE unified spherical line-blanketed models including winds, such as those computed by Lefever *et al.* (2007b), for O and B stars. For the time being, such generalization is not available, but Dufton *et al.* (2005) made a comparison between the NLTE static plane-parallel models without wind and the dynamical spherical models with wind and concluded that most of the atmospheric parameters and chemical compositions are quite similar. One may thus hope that the current description and the use of static NLTE models are sufficient to compute appropriate values for  $\alpha_{T,\lambda}$  and  $\beta_{T,\lambda}$ . Nevertheless, it would be very useful if the current treatment of the atmosphere were generalised to a dynamical spherical unified atmosphere with a line-driven wind for the identification of the oscillations of O and the hottest B stars.

One also needs good values for the limb darkening  $h_\lambda(\mu')$  to perform step 3. In a series of papers, Claret (2000, 2003, 2004) has computed several limb-darkening laws for a very broad range of effective temperatures, gravities and metallicities, and for several photometric systems. These are ideally suited to be used for mode identification. In the approaches by Ramachandran *et al.* (2004) and Randall *et al.* (2005b), on the other hand, the use of a perturbed atmosphere model is constructed in such a way that it automatically incorporates the wavelength-dependence of the limb darkening, so that approximate parameterised limb-darkening coefficients are not needed for the computation of  $\beta_{T,\lambda}$  and  $\beta_{g,\lambda}$ .

In all of the applications of the method so far, steps 1 and 2 are done for non-rotating stellar models. For each evolutionary stage of each track through the error box, one selects, for each  $l$ , the mode with frequency closest to the observed one and considers its amplitude for comparison with the observed ones. *This implicitly assumes that the observed frequency corresponds to the central peak of a multiplet.* Given that the Ledoux constant defined in Eq. (3.361) is usually substantially smaller than 1, the assumption thus becomes that  $m = 0$  or  $\Omega \simeq 0$ . This is invalid for many pulsators. For stars with rapid rotation, the first-order approximation of the rotational splitting breaks down, and even the central peaks of the multiplets are shifted (Goupil *et al.* 2000). Rotational mode coupling also occurs between modes whose degree  $l$  differs by 2 when they have the same azimuthal order  $m$  (Daszyńska-Daszkiewicz *et al.* 2002). All these effects are ignored in the mode identification. It is very important for readers to realise the limitation of assuming the measured frequency to be equal to the central peak of the excited modes. *This is, in fact, quite a weak point of the photometric mode-identification method, except when the*

star is a very slow rotator in the sense that its rotation period is far shorter than the pulsation periods in the co-rotating frame. Indeed, in many cases, we have clear spectroscopic evidence that the observed mode has  $m \neq 0$  (see Section 6.2), even for moderate rotators. This is particularly the case for the high-order g modes in SPB stars and  $\gamma$  Dor stars with their long pulsation periods, but also for some of the p modes in  $\beta$  Cep stars and  $\delta$  Sct stars. One should, therefore, not expect perfect agreement between the theoretical and observed amplitude ratios. It should also be kept in mind that deviations from linearity may occur, and that non-linear effects can also be the cause of a departure from the theoretical predictions based on the linear approximation.

While performing step 2, one can take two attitudes. Either one gives full confidence to excitation computations, and one considers only the modes that are predicted to be excited when computing the theoretical amplitude ratios. Or, a more conservative approach is taken, and one does not restrict the search by using predicted theoretical amplitudes, but rather considers all modes with frequencies close the observed ones, irrespective of their excitation predictions. As we have shown in Chapter 3, we have a good, but not perfect, view of mode excitation in main sequence stars. Thus we advise the conservative approach.

**Table 6.1.** The ten independent frequencies for the  $\beta$  Cep star  $\nu$  Eri, and their amplitude in the radial velocity derived from the Si III 455.3nm line as well as in the Strömgren  $u$  filter (from De Ridder *et al.* 2004).

ID	Frequency (d <sup>-1</sup> )	Amplitude (km s <sup>-1</sup> )	Amplitude (mmag)	Degree $l$
$\nu_1$	5.7633	22.4	73.5	0
$\nu_2$	5.6539	8.9	37.9	1
$\nu_3$	5.6201	8.1	34.6	1
$\nu_4$	5.6372	7.9	32.2	1
$\nu_5$	7.898	1.0	4.3	1
$\nu_6$	6.244	1.0	3.9	1
$\nu_7$	6.223	0.3	—	—
$\nu_8$	6.262	0.8	2.8	1
$\nu_9$	7.200	—	1.4	—
$\nu_{10}$	0.432	—	5.5	—

The most likely mode degree  $l$  is, obviously, the one with the best agreement between theory and observations. Discrimination among the  $l$ -values is achieved by comparing the results for the amplitude ratios, either by visual inspection or from comparison of the  $\chi^2(l)$ -values. These two approaches are illustrated in Figs 6.5 and 6.6 for nine of the ten independent oscillation frequencies detected for the  $\beta$  Cep star  $\nu$  Eri, the values of which are available

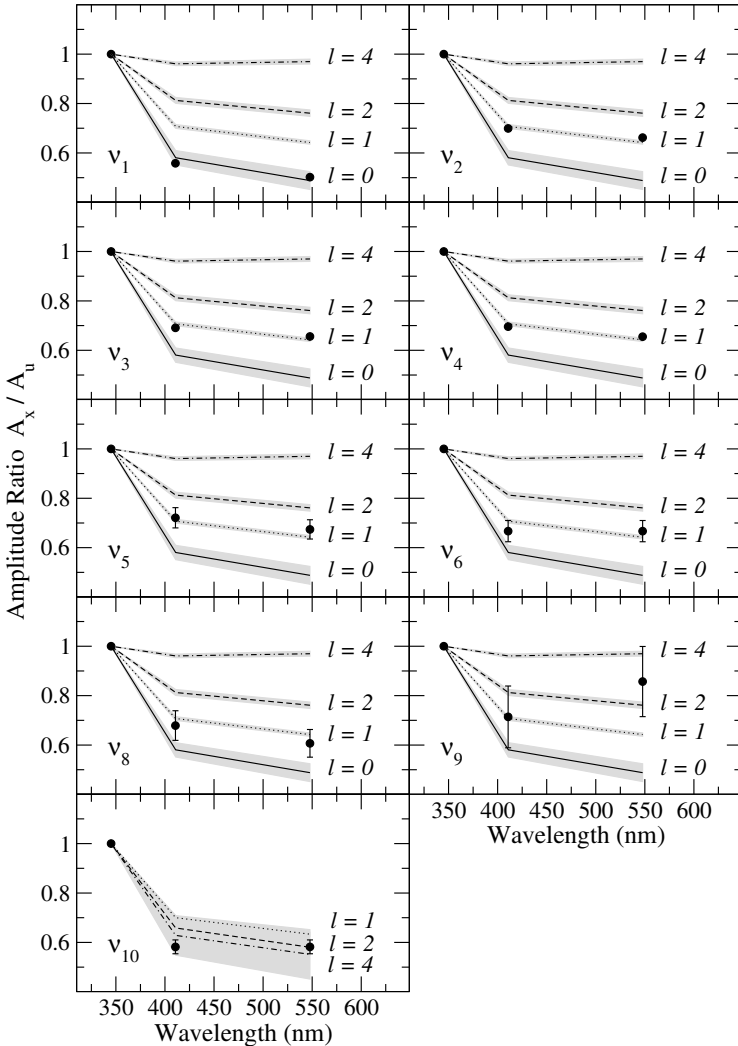


**Fig. 6.5.** Amplitude ratios with respect to the Strömgren  $u$  filter for the  $\beta$ Cep star  $\nu$ Eri, resulting from a 5-month multisite campaign. The dots are the observed values with their errors, and the full lines are the predicted values as a function of  $l$ , for a model in the centre of the observational ( $T_{\text{eff}}, \log g$ ) box. The grey zones indicate the uncertainty of the theoretical prediction due to the observational error of ( $T_{\text{eff}}, \log g$ ). All modes close in frequency to the observed ones were considered for the theoretical prediction, irrespective of their excitation. For a description of the data and the derived frequencies, we refer to Chapters 2 and 7. From De Ridder *et al.* (2004).

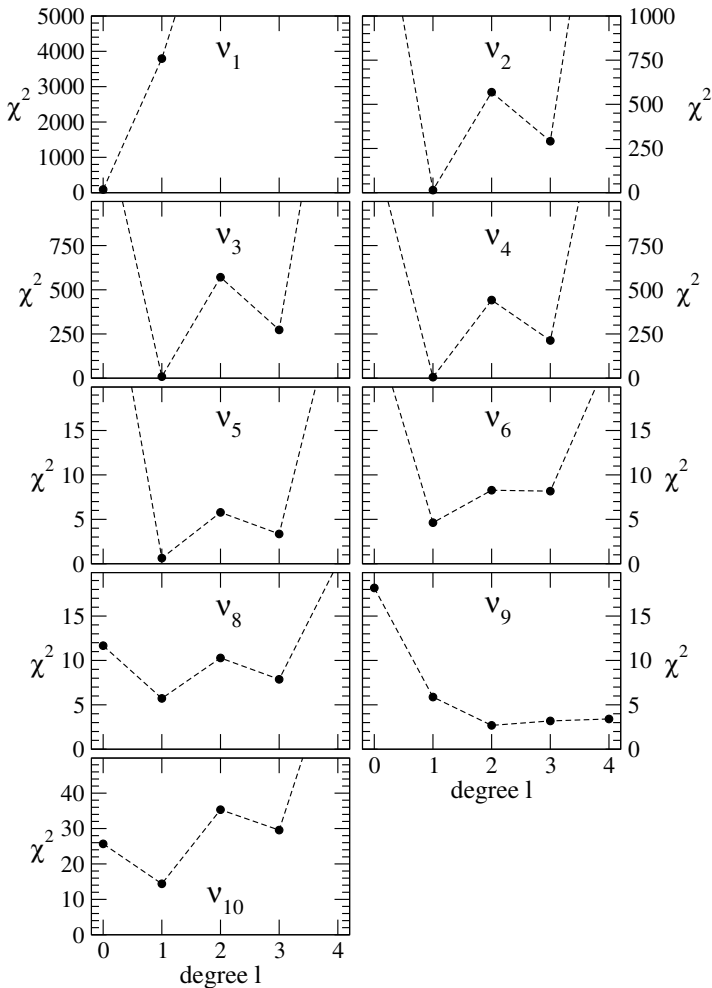


**Fig. 6.6.**  $\chi^2(l)$  as defined in Eq. (6.37) for the excited modes closest to the observed frequencies of one model in the observational error box ( $T_{\text{eff}}$ ,  $\log g$ ) of the  $\beta$  Cep star  $\nu$  Eri. Compare this figure with Fig. 6.5. From De Ridder *et al.* (2004).

from De Ridder *et al.* (2004) and are repeated here in Table 6.1. As can be seen in Table 6.1, the frequency  $\nu_7$  is only detected in the spectroscopy and could thus not be identified from the photometry. In Fig. 6.5, all the modes of numerous models within the error box with frequencies close to the observed ones are considered for the theoretical predictions of the amplitude

ratios (indicated as the grey zones). *With this way of working, one assumes that the theory is error-free, and that the uncertainty in the theoretical prediction of the amplitude ratios comes from the errors of the fundamental stellar parameters.* It can be seen that the first four dominant modes  $\nu_1, \dots, \nu_4$  are safely identified as a radial mode on the one hand and an  $l = 1$  triplet on the other hand, given the similar frequency values of  $\nu_2, \nu_3, \nu_4$ . The modes with frequencies  $\nu_5, \nu_6$  and  $\nu_8$  are also still safely identified as  $l = 1$  modes. The identification of  $\nu_9$  and  $\nu_{10}$  is impossible. For  $\nu_9$  this due to the uncertainties on the observed amplitude. For  $\nu_{10}$ , which corresponds to a high-order g mode, numerous such modes with different  $l$ - and  $n$ -values have almost similar frequency values which makes a discrimination among the possibilities impossible, as is reflected by the large grey area in the bottom panel of Fig. 6.5. The reader will have noticed that the theoretical predictions of the  $l = 3$  modes do not occur in Fig. 6.5. This is due to the authors' choice to omit them in order to keep the graphs clear, because odd modes with  $l > 1$  have a very specific wavelength dependence crossing the one of the even modes for B stars (see Fig. 6.1) which was not compatible with the observed ones. From Fig. 6.6 one would get the impression that all modes but the one with frequency  $\nu_9$  can be safely identified. We use this example to illustrate the importance of propagating the errors on  $(T_{\text{eff}}, \log g)$  into the theoretical predictions, as is done in Fig. 6.5, before making firm conclusions on the mode degree.

In principle, one could take one step further and use standard quality-of-fit measures of the  $\chi^2$  approach (*e.g.*, Press *et al.* 1992) to decide if a model is acceptable or not in an absolute sense, *i.e.*, as a deterministic tool to decide when to accept a mode identification as well as to decide which of the solutions  $\chi^2(l)$  are statistically equivalent/different. However, we refrain from using such a cut-off value for  $\chi^2$  as a decision criterion to decide if we can accept the mode identification or not, because it assumes that the complicated non-adiabatic oscillation theory, the construction of the model atmospheres, the treatment of the oscillations in the atmosphere, and the input physics of the models (including the metal mixture, the description of convection and the ignorance of rotation) are error-free, besides the assumption that the determination of the fundamental parameters of the star does not suffer from systematic uncertainties. While all of this may be true, it is rather optimistic, to say the least. In fact, a discrepancy between the theoretical and observed amplitude ratios, translating into a high value for  $\chi^2(l)$ , was exploited by Dupret *et al.* (2003), by Daszyńska-Daszkiewicz *et al.* (2003) and by Daszyńska-Daszkiewicz *et al.* (2005a) to improve the metallicity of main-sequence B stars, the treatment of convection of  $\delta$  Sct stars, and the values for the opacities of  $\beta$  Cep stars, respectively, after securely identifying the degree(s) of the mode(s). Dupret *et al.* (2003) termed this *non-adiabatic asteroseismology*. Such fine-tuning can only be applied when there is no overlap among the amplitude ratios of different  $l$ -values, after consideration of the propagated uncertainties on the ratios due to the observational error box and after making sure that the total neglect of rotation and non-linear effects in the models and oscillations is justified.

A final remark on the amplitude-ratio method concerns the slightly different treatment of the deviation parameter by Randall *et al.* (2005b). Instead of Eq. (6.37), they preferred to minimize

$$\chi^2(l) = \sum_{j=1}^{\text{#filters}} \left( \frac{\frac{f_l^* A_{\text{ref,obs}}}{A_{\text{ref,th}}} A_{j,\text{th}} - A_{j,\text{obs}}}{\sigma_{j,\text{obs}}} \right)^2 = \sum_{j=1}^{\text{#filters}} \left( \frac{f_l A_{j,\text{th}} - A_{j,\text{obs}}}{\sigma_{j,\text{obs}}} \right)^2, \quad (6.39)$$

where  $f_l^*$  and  $f_l$  are free parameters that are solved for by minimizing the  $\chi^2$ . The main difference with Eq. (6.37) is thus the introduction of the factor  $f_l$ . In this way, one still uses amplitude ratios, but one does not give preference any longer to the amplitude of one specific reference filter to compute the ratios. This is more objective in the sense that all filters are treated equally, but, on the other hand, introduces an additional free parameter that is adapted for each  $l$  separately. This is done in such a way that the shape of the amplitude-ratio distribution across the wavelength range is matched with the observed shape. This is a valid treatment within the  $\chi^2$  approach, where the number of degrees of freedom is simply increased by one. An example of this  $\chi^2$ , as an application to identify the dominant mode of the sdBV star KPD 2109+4401, is shown in Fig. 6.7. The data have a very high S/N level and were taken with ULTRACAM by Jeffery *et al.* (2004). These authors also tentatively identified this mode in the adiabatic approximation and found it to be radial, albeit that confusion among the  $l = 0, 1, 2$  solutions occurred. The results in the figure contain a non-adiabatic treatment and leave no doubt that the dominant mode is radial (Randall *et al.* 2005b), thanks to the small error bars on the observed amplitudes.

### 6.1.3.2 Mode Identification Schemes also using Phase Differences

For the case of  $\delta$  Sct oscillations, information is also encapsulated in the observed phase differences. Typical  $\psi_T$ -values for such oscillators range from  $60^\circ$  to  $200^\circ$ , depending on the mixing-length parameter, the mass and the degree of the mode. This strong dependence of  $\psi_T$  on the mode degree has led to a slightly different mode-identification method for such stars. Pioneering work in this respect was done by Garrido *et al.* (1990), who defined so-called *regions of interest* for the Strömgren system. These are areas in diagrams of, *e.g.*,  $v/y$  versus  $\delta(v) - \delta(y)$  (where  $\delta(x)$  is the phase of time series  $x$ ) as a function of the degree  $l$ . The level of non-adiabaticity and  $\psi_T$  were rather arbitrarily treated as free parameters in the ranges  $[0.25, 1]$  (where adiabatic equals 1) and  $[90^\circ, 135^\circ]$ , respectively, for the computation of these areas. Several examples of such regions are shown in Fig. 6.8, where a confrontation with the modes detected in several  $\delta$  Sct stars is also shown. It can be seen that the identification of the degree is easiest to achieve by considering the  $u$  filter in combination with one of the three other filters. For an overview of applications of this method we refer to Garrido (2000). In particular, this method was

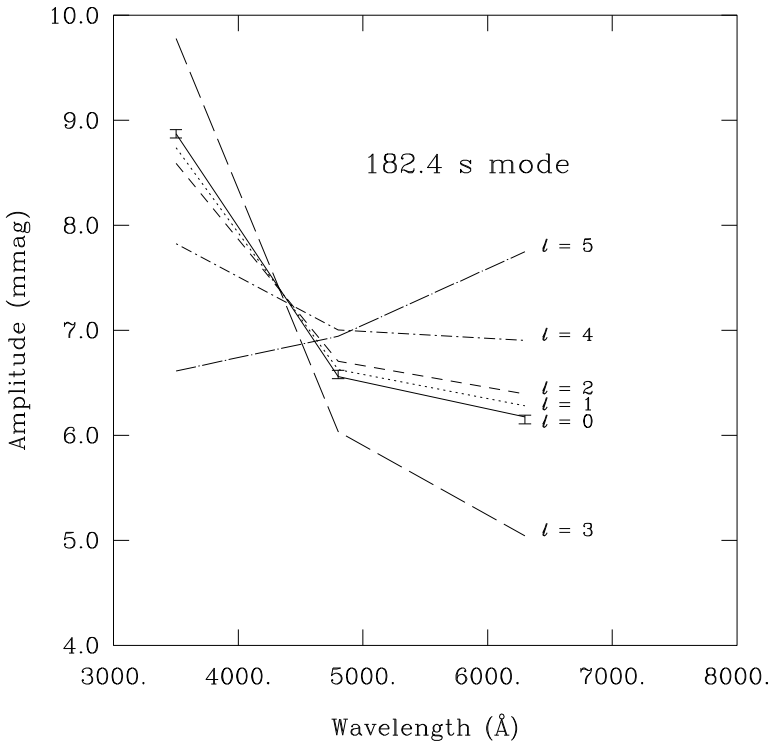


**Fig. 6.7.** Identification of the dominant mode of the sdBV star KPD 2109+4401 from ULTRACAM photometry according to Eq. (6.39). The data are taken from Jeffery *et al.* (2004) while the identification was done by Randall *et al.* (2005b).

applied by Breger *et al.* (1999b) to identify several modes of the prototypical multiperiodic  $\delta$  Sct star FG Vir.

A higher level of sophistication in  $\delta$  Sct oscillation mode identification was reached by Dupret *et al.* (2003), following the scheme outlined above, and subsequently by Daszyńska-Daszkiewicz *et al.* (2003). These authors developed a method based on non-adiabatic computations similar to those described here, but considering the amplitudes and phases themselves in the different passbands by re-arranging the equations. While doing so, they defined a different type of  $\chi^2$ , which they minimized as a function of the coefficients  $[\xi_r(R)/R] P_l^m(\cos i)$  and  $f_T [\xi_r(R)/R] P_l^m(\cos i)$ . In this way, one does not need to know a value for the unknown factor  $P_l^m(\cos i)$  because this factor is considered together with the unknown amplitude  $\xi_r(R)/R$  of the mode. In fact, seeking the best solution for the two chosen unknowns by means of

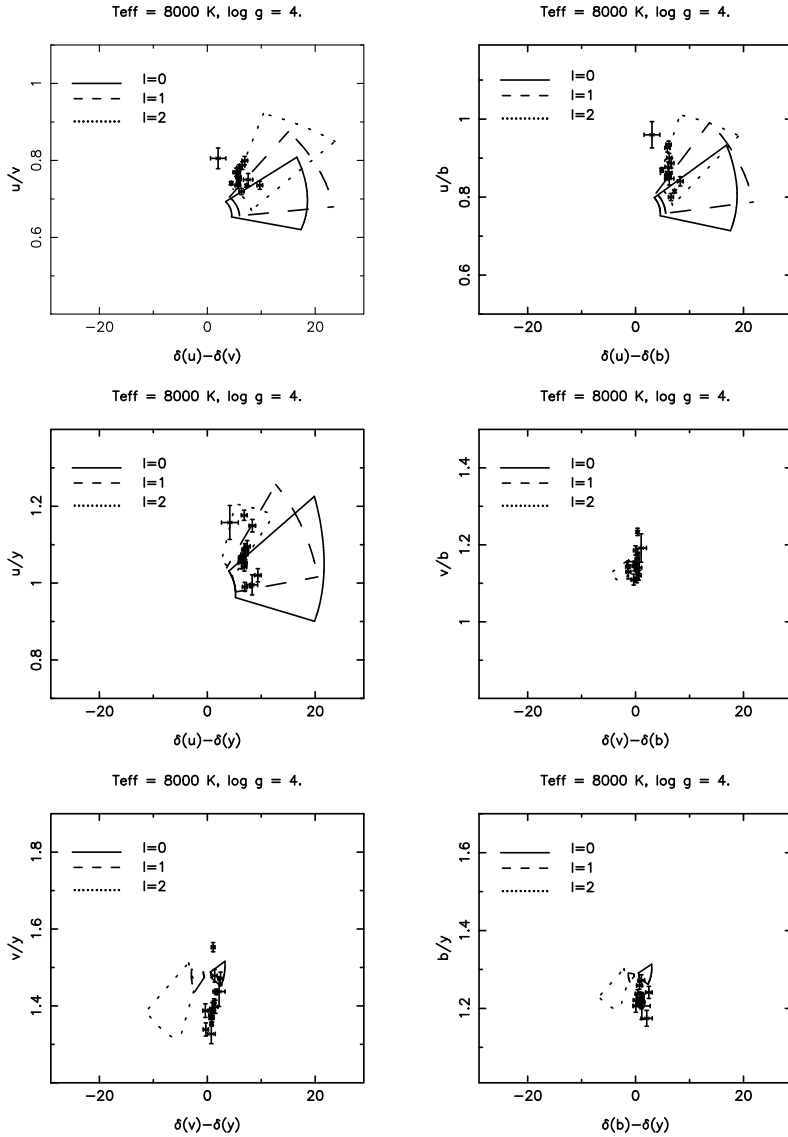


**Fig. 6.8.** Regions of interest based on amplitude ratios and phase differences for the Strömgren system in the case of modes with degree  $l = 0, 1, 2$ . The dots with error bars denote the observed values for modes detected in several  $\delta$  Sct stars. Figure kindly reproduced from Garrido *et al.* (1990) by Rafa Garrido.

a minimum in their  $\chi^2$  for models with different parameters allowed them to constrain these parameters. The identification of  $l$  then comes as a by-product, excluding the  $l$ -values whenever their  $\chi^2(l)$  turned out to be too

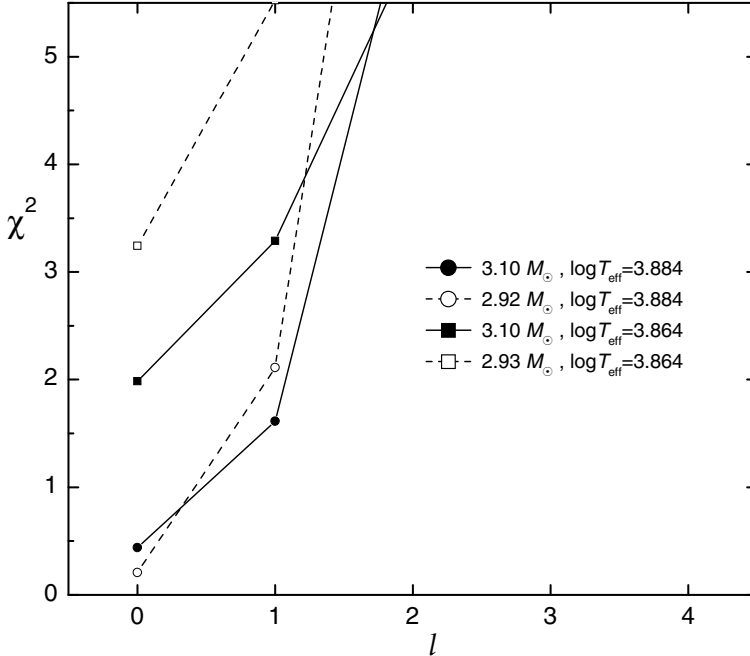


**Fig. 6.9.**  $\chi^2$  for the observed photometric data of the  $\delta$  Sct star 20 CVn for four models in the observational error box in the HR Diagram From Daszyńska-Daszkiewicz *et al.* (2003).

high and discriminating among  $l$  whenever possible. We show in Fig. 6.9 the application of their method to the low-amplitude  $\delta$  Sct star 20 CVn, which was already known to have a radial mode (see also Section 6.2 below). There is no ambiguity in the mode identification for this star, as all modes with  $l > 0$  have much higher  $\chi^2$ -values than the radial mode. The main goal of the authors was to constrain the properties of the convection treatment by comparing the value of  $f_T$  resulting from the fit with theoretically computed values. Using a simplified treatment of the convection-pulsation interaction by assuming “frozen convection” they noted a preference for very small values of the mixing-length parameter  $\alpha$ , although in all cases the agreement between the observationally inferred and computed values of  $f_T$  was rather poor; this clearly indicates inadequacies in the convection modelling.

Daszyńska-Daszkiewicz *et al.* (2005b) applied a similar method, in which the radial velocity amplitude and phase is included and which will be discussed further in Section 6.3, to the data of FG Vir; this led to the same result for the eight dominant modes as the one obtained already by Viskum *et al.* (1998) and Breger *et al.* (1999). We display these results in Fig. 6.10 and compare them with the spectroscopic mode identification in Section 6.2 by means of Table 6.4.

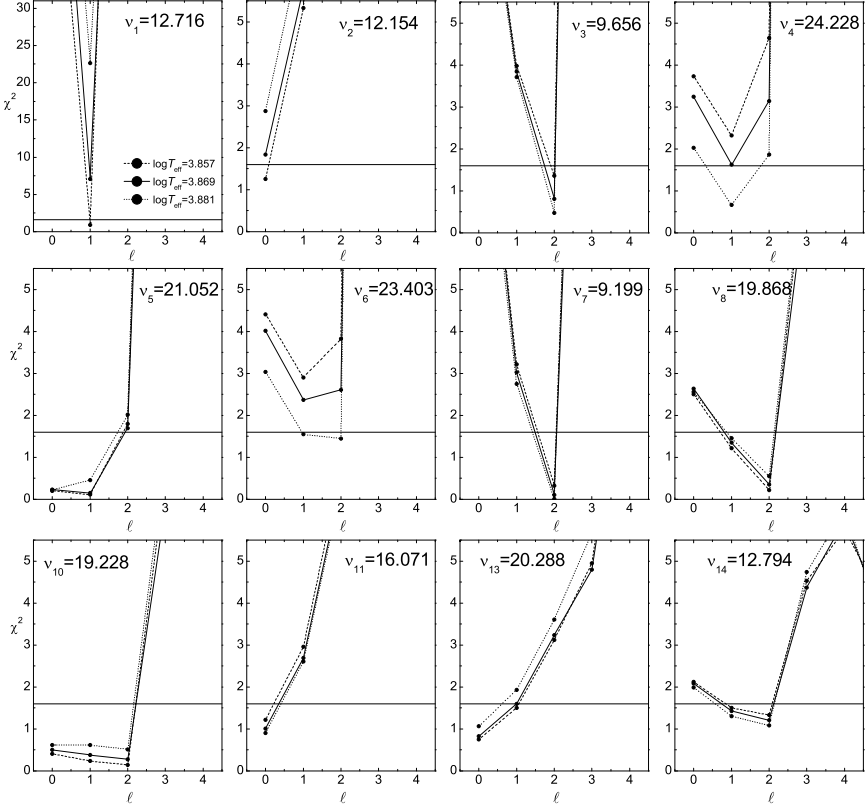


**Fig. 6.10.**  $\chi^2$  for the twelve dominant modes in the photometry of the  $\delta$  Sct star FG Vir, for three different stellar models characterised by the given effective temperature. The full horizontal line indicates a confidence level of 80%. From Daszyńska-Daszkiewicz *et al.* (2005b).

Here again a major goal was to investigate the treatment of convection. Using a time-dependent formulation of mixing-length theory originally proposed by Gough (1977a) resulted in a somewhat better agreement between inferred and computed  $f_T$  than for the frozen-convection approximation, without requiring a possibly unrealistically low value of  $\alpha$ .

Even though the method by Daszyńska-Daszkiewicz *et al.* (2003) is a significant improvement to the one by Garrido *et al.* (1990), it suffers from the same limitation as Dupret *et al.*'s (2003) amplitude-ratio scheme outlined above, *i.e.*, it uses model and oscillation computations for non-rotating stars and assumes the theory to be well enough developed so that the discriminating values of the  $\chi^2$  are mainly due to different  $l$ -values and not to limitations of the theoretical models.

The application of the above theory to the case of the high-overtone p modes of the roAp stars was used with a different goal. As explained in Chapter 2, some of these stars are known to have a dominant dipole ( $l = 1$ ) mode from frequency splitting in terms of the oblique pulsator model. This information can thus be used to derive observational information on the badly known limb darkening, and from it of the temperature structure  $T(\tau)$  of the atmosphere, from a confrontation between observed amplitudes in different filters and Eq. (6.29). This idea was put forward by Matthews *et al.* (1990, 1996) who derived such an empirical  $T(\tau)$  relation for the star HR 3831 in the approximation of a grey atmosphere as in Eq. (6.19) and assuming the steep amplitude decrease with increasing wavelength to be dominated by the limb-darkening variations. Kurtz & Medupe (1996), on the other hand, showed from an analytical derivation that the limb-darkening could not account for the observed steep decline of the amplitudes towards red wavelengths. They suggested instead that this is a consequence of a depth effect in the atmosphere, and settled the ambiguity between these two different interpretations by showing that the factor two difference between the theoretical predictions according to Eq. (6.29) and the observations cannot be due to limb-darkening variations alone. They re-affirmed the failure of the theory outlined above due to the basic assumption adopted at the start of Section 6.1.2.2, *i.e.*, the single-layer approximation. This is inappropriate for roAp stars, given that depth effects are clearly visible in the line-profile variations of such stars (*e.g.*, Mkrtchian *et al.* 2003; Elkin *et al.* 2005; Kurtz *et al.* 2007a; Ryabchikova *et al.* 2007a). The generalization of the method of photometric amplitudes to a multi-layer approach is still awaited.

To conclude this section, we stress that the photometric mode-identification methodology, in whichever of the modern formulations, has to be treated with care. It relies rather heavily on the theoretical models and assumes the input physics to be free of errors. In this sense, it is not really *empirical*. Nevertheless, it works well for the large-amplitude p-mode oscillations in  $\beta$  Cep and  $\delta$  Sct stars, provided that they are not fast rotators. The performance of the method has not yet been tested properly for the very dense frequency spectra of high-order g modes in SPB stars and  $\gamma$  Dor stars, and it needs to be modified to include better atmosphere models and depth effects for the application to roAp stars. Despite these limitations, we stress once more that even the secure identification of the  $l$ -value of only one or two of the dominant modes is a huge step forward in the seismic modelling.

## 6.2 Mode Identification from High-Resolution Spectroscopy

As already explained in Chapter 4, the velocity field caused by the nonradial oscillation(s) leads, through Doppler displacement, to periodic variations in the profiles of spectral lines. The introduction of high-resolution spectrographs

with sensitive detectors in the 1980s thus had a large impact on the field of empirical mode identification. Spectroscopic data offer a very detailed picture of the pulsational velocity field. As we will show below, its interpretation in terms of  $(l, m)$  is far less dependent on the details of the oscillation theory in the outer atmosphere than multicolour photometry. Indeed, it basically relies on the interpretation of the data in terms of the oscillation velocity vector, derived from  $\xi$ , and not so much on the Lagrangian variation of the temperature and of the flux.

From an observational point of view, it remains a challenge to obtain spectra covering the overall beat period of the multiperiodic oscillations, with a high resolving power (typically above 40 000) and with a high signal-to-noise ratio (typically above 200 and preferably much higher than that), for a good temporal resolution (typically below a few per cent) in the sense of the ratio of the integration time to the oscillation period. The latter condition is necessary in order to avoid smearing out of the oscillations during the cycle.

The methodology to derive the full details of the pulsational velocity field at the stellar surface contains at least six unknowns, as will be shown below, and therefore tends to be complicated. For this reason, multicolour photometric observations, which can only lead to an estimate of the  $l$ , but which can be obtained from small telescopes, are still of utmost importance for mode identification. These kinds of data are in particular more suitable to study long-period pulsations because small telescopes are available on longer time scales. Ideally, one combines both types of data, in ways outlined in Section 6.3. In the current section we first explain how theoretical line-profile variations can be calculated. Subsequently we describe two modern mode-identification methods based on line-profile variations.

### 6.2.1 Calculation of Theoretical Line-Profile Variations

Osaki (1971) published a pioneering paper including a scheme on how to compute theoretical line-profile variations for nonradial oscillations. This is remarkable since, at the time Osaki published his work, high-resolution spectroscopy was not yet available. His scheme could therefore not be tested on real data. We follow below the basic ingredients of a modern line-profile generation code based on Osaki's description.

In the case of one linear spheroidal mode with infinite lifetime, the surface pulsation velocity vector expressed in the coordinate system  $(r, \theta, \phi)$  is given by

$$\begin{aligned} \mathbf{v}_{\text{osc}}(R, \theta, \phi, t) &= (v_r, v_\theta, v_\phi, t) \\ &= \Re \left\{ -i\omega \xi_r(R) \left( 1, K \frac{\partial}{\partial \theta}, \frac{K}{\sin \theta} \frac{\partial}{\partial \phi} \right) Y_l^m(\theta, \phi) \exp(-i\omega t) \right\}, \end{aligned} \quad (6.40)$$

in the approximation where one can ignore the effects of the rotation in the computation of the oscillation eigenfunctions. We recall that the value of  $K$

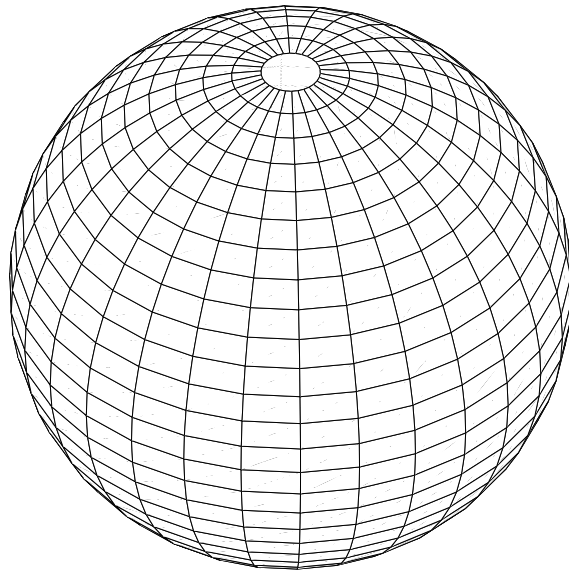


**Fig. 6.11.** The stellar surface is subdivided into a finite number of surface elements determined by a step-size in  $\theta$  and  $\phi$  for the computation of theoretical line-profile variations.

can be approximated by Eq. (3.161) but that it is advised to consider a range in  $K$  when applying mode identification, in order to test the robustness of the result against the true unknown model-dependent ratio  $\xi_h(R)/\xi_r(R)$ .

To this, we add the rotational surface velocity vector in the approximation of uniform time-independent rotation:

$$\mathbf{v}_{\text{rot}}(R, \theta, \phi, t) = \Omega R \mathbf{a}_\phi \quad (6.41)$$

to obtain the total velocity vector  $\mathbf{v}(R, \theta, \phi, t) = \mathbf{v}_{\text{osc}}(R, \theta, \phi, t) + \mathbf{v}_{\text{rot}}(R, \theta, \phi, t)$  at the stellar surface for the surface element with coordinates  $(R, \theta, \phi)$ .

In order to compute the observed line-profile shape corresponding to this velocity vector field, denoted as  $p(\lambda, t)$ , we have to determine the velocity vector component, as well as the normalised flux of a particular stellar surface element with coordinates  $(R, \theta', \phi')$ , in the line-of-sight:

$$p(\lambda, t) \equiv \frac{\int_{\theta'=0}^{\pi/2} \int_{\phi'=0}^{2\pi} (d\mathbf{A}(R, \theta', \phi', t) \cdot \mathbf{a}'_z) I_\lambda(R, \theta', \phi', t, \mathbf{a}'_z)}{\int_{\theta'=0}^{\pi/2} \int_{\phi'=0}^{2\pi} (d\mathbf{A}(R, \theta', \phi', t) \cdot \mathbf{a}'_z) I_\lambda^{\text{cont}}(R, \theta', \phi', t, \mathbf{a}'_z)}, \quad (6.42)$$

where  $d\mathbf{A}$  is the local surface normal,  $I_\lambda(R, \theta', \phi', t, \mathbf{a}'_z)$  is the intensity of the point with coordinates  $(R, \theta', \phi')$  at time  $t$  in the line-of-sight and  $I_\lambda^{\text{cont}}$  is the continuum intensity, *i.e.*, the intensity that would be observed if the spectral line were absent. In practice, one subdivides the visible stellar surface into a large number of elements with central coordinates  $(\theta'_i, \phi'_j)$ ,  $i = 1, \dots, N; j = 1, \dots, M$  for the computation of the integrals in Eq. (6.42) (see Fig. 6.11). For present-day computational power, one usually takes a step of  $1^\circ$  in the angles  $\theta'$  and  $\phi'$ , leading to  $N = 180$  and  $M = 360$ . In order to get reliable results,  $N$  and  $M$  must be at least 45 and 90, respectively.

We now consider all the ingredients necessary for the computation of  $p(\lambda, t)$  through Eq. (6.42). The velocity field due to the rotation and the pulsation leads to a Doppler shift at a point  $(R, \theta', \phi')$  on the visible equilibrium surface of the star. The local contribution of a point  $(R, \theta', \phi')$  to the line profile is proportional to the flux at that point. We assume that the intensity  $I_\lambda(\theta', \phi')$  is the same for all points of the considered surface element. The flux through the surface element surrounding the point  $(R, \theta', \phi')$  thus is the product of the intensity  $I_\lambda(\theta', \phi')$  and the projection on the line-of-sight of the surface element around the considered point:

$$I_\lambda(\theta', \phi') R^2 \sin \theta' \cos \theta' d\theta' d\phi'. \quad (6.43)$$

An important effect that changes the flux over the visible surface is the limb darkening. The flux of a surface element centred around the point  $P(R, \theta', \phi')$  of the equilibrium surface with size  $R^2 \sin \theta' d\theta' d\phi'$  is

$$F_\lambda(R, \theta', \phi') = I_0 h_\lambda(\theta') R^2 \sin \theta' \cos \theta' d\theta' d\phi', \quad (6.44)$$

where  $I_0$  is the continuum intensity at  $\theta' = 0$ . For line-profile variation calculations, a linear approximation of the limb darkening largely suffices, because the profile variations are dominated by the Doppler shifts due to the surface velocity. One therefore often encounters the limb darkening in terms of one coefficient  $u_\lambda(T_{\text{eff}}, \log g, Z)$  because this saves an order of magnitude in computation time for spectroscopic mode identification, where numerous parameter combinations must be considered.

Perturbations of the intensity and of the surface due to the oscillations change the line profile. Usually, however, these effects are far less important than the velocity effect for classical pulsators, and one often assumes  $\delta F_\lambda(\theta', \phi') = 0$  during the oscillation cycle. However, one can easily generalise any line-profile generation code to include the non-adiabatic perturbation of the intensity,  $\delta[I_0 h_\lambda(\theta')]$ , as well as the perturbed surface due to the oscillation, according to the treatment in the outer atmosphere discussed above. This has been tested for the spectroscopic identification methods we discuss below and has been found to be an unnecessary complication.

A spectral line with central wavelength  $\lambda_0$  is subject to different broadening mechanisms, which we also have to take into account in the computation of  $p(\lambda, t)$ :

- i) *Atomic broadening* results in a Lorentz profile and is caused by the finite lifetime of the energy levels of the ions responsible for the line.
- ii) Neighbouring particles disturb the energy levels of the ions, causing a small change in the wavelength of the spectral line. This *pressure broadening* results in a Lorentz profile. The higher the pressure the larger this broadening becomes.
- iii) All ions move on a microscopic scale due to thermal agitation. This *thermal broadening* leads to a Gaussian profile as the particles follow a Maxwellian velocity law with a temperature dependence  $\sim \sqrt{T}$ .
- iv) The stellar rotation causes *rotational broadening*. We assume the rotation to be uniform across the stellar disc, and time independent. The resulting line profile is then symmetrically broadened by the rotation.
- v) Stellar oscillations give rise to periodic broadening of the line profile. The shape of the line profile is completely determined by the parameters occurring in the expression of the pulsation velocity given in Eq. (6.40). In particular, it is dependent on the  $(l, m)$  of all the oscillation modes.

The first three of these are usually combined and termed the *intrinsic line broadening*. In order to take into account such intrinsic broadening effects, the local line profile is convolved with an intrinsic profile, which, in the simplest approximation of thermal broadening, is a Gaussian whose variance depends on the spectral line considered as well as on the fundamental stellar parameters. Generalisations to an intrinsic Voigt profile or a profile derived from a stellar atmosphere model are easily performed, but are not necessary for mode identification (see below) while implying much longer computation times. In principle, if the theory of model atmospheres and the time-independent broadening mechanisms were well enough understood, we would not need a free parameter to describe the intrinsic line broadening, but we could simply take the intrinsic shape of the considered spectral line. In practice, however, one is always faced with the need to introduce some unknown level of time-independent non-thermal microturbulence, of up to several  $\text{km s}^{-1}$ , when fitting observed spectral line profiles, and quite often even time-independent non-thermal macroturbulence, which may reach velocities as high as or even above the speed of sound in hot massive stars (Howarth *et al.* 1997; Morel *et al.* 2006; Lefever *et al.* 2007a; Markova & Puls 2008). Various models to describe the micro- and macroturbulence are in use (see Gray 2005, for a description of turbulence in stellar atmospheres), but there is no physical argumentation to prefer one above the other. For this reason, we may as well omit the computation of the intrinsic line profile from atmosphere models and estimate a time-independent intrinsic profile which is a convolution of all the unknown time-independent thermal and non-thermal broadening effects that occur, in addition to rotational and pulsational broadening. For the purpose of mode identification, one always works with carefully selected metal lines whose intrinsic broadening is dominated by thermal effects, which is why the intrinsic profile is assumed to be a Gaussian with an unknown time-independent

variance  $v_{\text{int}}^2$ . This assumption does not impose a restriction on the mode identification methods based on high-resolution spectroscopy, because the time-independent rotational broadening profile is sufficiently different from the intrinsic profile, while the pulsational broadening is time dependent and it is this part that will be used for the mode identification.

We have now considered all the ingredients for the computation of the observed line profile  $p(\lambda, t)$ . We represent by  $\lambda_{ij}$  the Doppler-corrected wavelength for a point on the star with coordinates  $(R, \theta'_i, \phi'_j, t)$ , *i.e.*,

$$\frac{\lambda_{ij} - \lambda_0}{\lambda_0} \equiv \frac{\lambda(R, \theta'_i, \phi'_j, t) - \lambda_0}{\lambda_0} = \frac{\Delta\lambda(R, \theta'_i, \phi'_j, t)}{\lambda_0} = \frac{v(R, \theta'_i, \phi'_j, t)}{\tilde{c}}. \quad (6.45)$$

An explicit expression for  $v(R, \theta'_i, \phi'_j, t)$  can be found in, *e.g.*, Aerts *et al.* (1992):

$$\begin{aligned} v(R, \theta'_i, \phi'_j, t) = & -v_\omega \sin \theta' \sin \phi' \\ & + v_p \sum_{k=-l}^l a_{lmk}(i) \left( \cos \theta' P_\ell^k - K \sin \theta' \frac{dP_\ell^k}{d\theta'} \right) \\ & \times \sin((\omega - m\Omega)t + k\phi'), \end{aligned} \quad (6.46)$$

where the velocity amplitude is defined as  $v_p \equiv \sqrt{4\pi} c_{lm} \tilde{\xi}_r(R) \omega$  with the normalization constant  $c_{lm}$  introduced in Chapter 3 and where we use  $v_\omega \equiv \Omega R \sin i$ , usually denoted as  $v \sin i$ , for the projected rotation velocity for convenience of shorter notation. Equation (6.46) is based on the transformation formula for spherical harmonics for two different coordinate systems whose polar axes are inclined with angle  $i$  and whose zero point for the azimuthal angles  $\phi$  and  $\phi'$  were chosen to be equal:

$$Y_l^m(\theta, \phi) = \sum_{k=-l}^l a_{lmk}(i) Y_l^k(\theta', \phi'), \quad (6.47)$$

where

$$\begin{aligned} a_{lmk}(i) \equiv & (l+m)!(l-m)! \\ & \times \sum_{r=\max\{0, -k-m\}}^{\min\{l-m, l-k\}} (-1)^{l+k+r} \frac{\sin(i/2)^{2l-2r-m-k} \cos(i/2)^{2r+m+k}}{r!(m+k+r)!(l-m-r)!(l-k-r)!} \end{aligned} \quad (6.48)$$

(Jeffreys 1965, Condon & Odabasi 1980, see also Appendix B). Note that  $a_{lm0}(i) = P_l^m(\cos i)$  as used in Eq. (6.29), but the use of the more general transformation formula as in Eqs (6.47) and (6.48) is more convenient for the computation of line profile diagnostics, such as the moments (see Section 6.2.3).

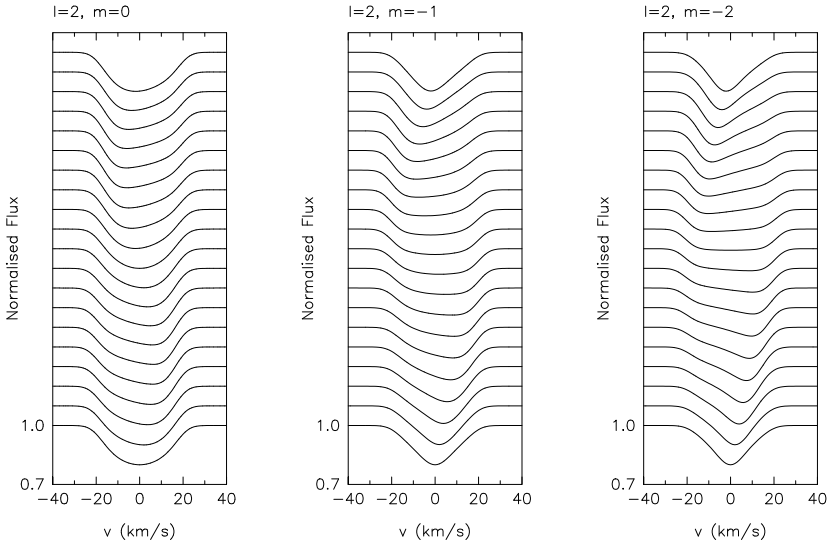


**Fig. 6.12.** Theoretically determined line-profile variations calculated by means of the basic formalism described in the text considering an  $l = 2$  mode and  $m = 0$  (left panel),  $m = -1$  (middle panel), and  $m = -2$  (right panel) respectively. The other velocity parameters are: pulsation amplitude  $v_p = 5 \text{ km/s}$ , projected rotational velocity  $v \sin i = v_\Omega = 30 \text{ km/s}$ , thermal velocity  $v_{\text{int}} = 4 \text{ km/s}$ , and inclination  $i = 55^\circ$ . The line-of-sight velocity is given on the  $x$ -axis while the normalised flux (unitless, with values between 0.7 and 1.0) is drawn on the  $y$ -axis. The profiles are stacked according to increasing oscillation phase, from 0.00 (lowest profile) to 0.95 (uppermost profile) in steps of 0.05.

The line profile is then approximated by

$$p(\lambda, t) = \frac{\sum_{i,j} \frac{I_0 h_\lambda(\theta'_i)}{\sqrt{2\pi} v_{\text{int}}} \exp\left(-\frac{(\lambda_{ij} - \lambda)^2}{2v_{\text{int}}^2}\right) R^2 \sin \theta'_i \cos \theta'_i \Delta \theta'_i \Delta \phi'_j}{\sum_{i,j} I_0 h_\lambda(\theta'_i) R^2 \sin \theta'_i \cos \theta'_i \Delta \theta'_i \Delta \phi'_j}, \quad (6.49)$$

where the sum is taken over the visible stellar surface, *i.e.*,  $\theta' \in [0^\circ, 90^\circ]$ ,  $\phi' \in [0^\circ, 360^\circ]$  and where we have assumed a constant Gaussian intrinsic profile and a non-variable surface normal for simplicity. Equation (6.49) essentially represents the line-profile computation suggested by Osaki (1971). We show in Figs 6.12 and 6.13 sets of theoretically calculated profiles for  $l = 2$  and  $l = 6$  modes computed from Eq. (6.49).

It is obvious that the pulsational broadening is easiest to unravel from the intrinsic broadening for the sharpest lines in the spectrum, provided that they are well resolved. Indeed, for sharp lines with narrow wings, the deformation of the line is detectable across the whole profile and not only in the

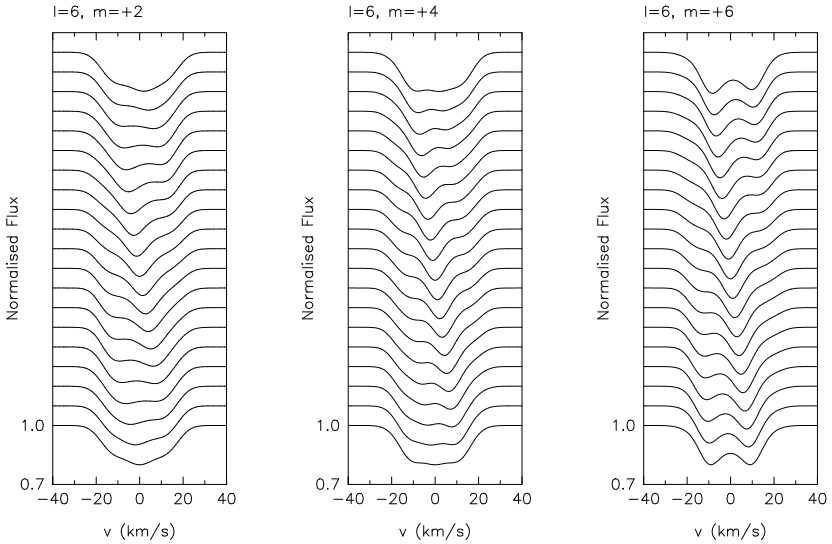


**Fig. 6.13.** Same as in Figure 6.12, but for  $l = 6$  with  $m = +2$  (left panel),  $m = +4$  (middle panel), and  $m = +6$  (right panel).

line centre. This is why we want to avoid hydrogen and helium lines for mode identification whenever possible, because the former suffer heavily from Stark broadening and both types of lines may be strongly affected by a stellar wind. Nevertheless, Viskum *et al.* (1998) used the equivalent-width variations of Balmer and metal lines in low-resolution ( $R = 4\,000$ ) spectra to identify the dominant modes of FG Vir. They discriminated among different possibilities for  $l$  from a plot of the ratio of the amplitude of the equivalent-width variation of the H $\alpha$  and an Fe I line versus the ratio of the amplitude for H $\alpha$  and an average photometric amplitude for the four Strömgren filters. In this way, they noticed “different observational regions” in their plot, similar to those used by Garrido *et al.* (1990) for multicolour photometry of  $\delta$  Sct stars. The application by Viskum *et al.* (1998) concerned a purely observational diagram. In fact, the amplitude ratios in photometry are replaced here by amplitude ratios of the equivalent-width variations of lines that are strongly affected by  $\delta T/T$ . On this basis they identified  $l$  for the eight dominant modes; this identification was later confirmed by Breger *et al.* (1999) and Daszyńska-Daszkiewicz *et al.* (2005b) (see Table 6.4 below). With the advent of high-resolution spectroscopy and the coupling between pulsation theory and observations in the quantitative methods outlined below, this Balmer-line application was not pursued for other stars.

As explained, the time dependence of the spectral line caused by the temperature eigenfunction  $\delta T$  may be important for the computation of the

intrinsic line profile for lines that are sensitive to small temperature variations. This is particularly the case for metal lines with significant equivalent-width changes because the  $\delta T/T$  is such that it brings the ion into a higher/lower ionization stage at compression/expansion compared with equilibrium. For this reason, one carefully selects the best spectral line for mode identification. It is advantageous to use an unblended, deep line which is insensitive to small temperature changes in the line-forming region in the atmosphere, so that one can avoid having to include  $\delta T/T$  in the computations. This has been thoroughly investigated by De Ridder *et al.* (2002) for pulsating B stars. The choice of the best line depends, of course, on the effective temperature and gravity of the star. For  $\beta$  Cep stars, *e.g.*, the best line is the Si III 4560Å triplet (Aerts & De Cat 2003), while for slowly pulsating B stars the Si II 4130Å doublet is ideally suited (Aerts *et al.* 1999). For very fast B-type rotators, these multiplet lines are unfortunately blended and one has little choice but to consider the isolated He I 6678Å line (*e.g.*, Balona *et al.* 1999) or other helium lines (Rivinius *et al.* 2003). Temperature effects on line-profile variations of  $\delta$  Sct and  $\gamma$  Dor stars have not been studied in the same detail as for B stars.

As discussed above, Eq. (6.49) for the computation of line-profile variations can be generalised in order to take into account the following additional time-dependent effects: a perturbed surface, a perturbed flux through non-adiabatic temperature and gravity variations, a time-dependent intrinsic profile. For fast rotators, Coriolis and centrifugal correction terms to the pulsation velocity expression should also be included. The most up-to-date line-profile generation codes take into account several of these effects, except those due to the centrifugal force. We refer the reader to Lee *et al.* (1992), Aerts & Waelkens (1993), Townsend (1997), Schrijvers *et al.* (1997), De Ridder *et al.* (2002), and Zima (2008) for a detailed description of such codes. Among these, the code presented by De Ridder *et al.* (2002) is the only one that treats the eigenfunctions appropriately in the line-forming regions of the atmosphere, where one should not rely on the diffusion approximation. The properties of the eigenfunctions in the stellar atmosphere are discussed in detail in Dupret *et al.* (2002), to which we refer the reader for additional information. De Ridder *et al.* (2002) have shown that the effects of the non-adiabatic temperature perturbations on the resulting line profiles remain modest for hot massive stars in the case that the rotation can be ignored.

The complication due to the centrifugal force is not included in spectroscopic mode-identification methods at present. It would thus be necessary to adapt the methodology presented below in the case of oscillations in rapid rotators, *i.e.*, for stars that rotate at a considerable fraction of their critical velocity (say above 50%). In such a case, the expression for the velocity field in terms of one spherical harmonic as in Eq. (6.40) is inaccurate. It is clear that the applicability of the methodology breaks down in such a situation. As already emphasized in Chapter 3, we have no good theory of stellar oscillations for fast rotators. Thus, one cannot hope to build a good mode-identification method for such cases at present.

The improved stability of spectrographs, some of which have been developed for exoplanet searches since the beginning of this century, has allowed radial-velocity measurements with a precision of order  $\text{m s}^{-1}$ . This led Hekker *et al.* (2006) to generalise the computation of line-profile variations to the case of solar-like damped oscillations. This revealed that line bisectors, as defined in Chapter 4, are not a good diagnostic to investigate such oscillations, as was also found independently by Dahl *et al.* (2006). Hekker *et al.* (2006) compared their simulations with the variations detected in the cross-correlation functions (CCF) of three red giants in which such damped oscillations were firmly established from radial-velocity measurements. This led to the surprising result that nonradial modes seem to explain the CCF far better than radial modes for some of the detected frequencies. This is at present not well understood in terms of the theory outlined briefly in Chapter 3 and more thoroughly in Chapter 7.

### 6.2.2 Line Profile Fitting

It is clear that the velocity expression based on the nonradial oscillation theory contains many free parameters, even in the simple formulation in which rotational and non-adiabatic effects are neglected. The very large number of candidate modes is especially a problem when constructing identification techniques and it often keeps the predictive power low. This is particularly the case for the methods that are based on a trial-and-error principle. Quantitative methods are better to obtain a reliable mode identification. This need for quantitative methods has become apparent since more and more detailed spectroscopic analyses have revealed that multimode pulsations are more the rule than exception. Below, we treat two such methods, but first we mention trial-and-error line-profile fitting as a mode-identification method for historical reasons.

This rather subjective method was pioneered by M. Smith and his collaborators. They obtained for the first time high-resolution spectroscopic observations for various types of pulsating stars along the main sequence and implemented Osaki's (1971) scheme to compare these data with theoretical predictions (*e.g.*, Campos & Smith 1980a,b; Smith 1983, 1985a,b,c; Smith *et al.* 1984, 1986). The idea to identify modes is the following: one generates theoretical line profiles  $(\lambda, p(\lambda))$  over the oscillation cycle from Eqs (6.45) and (6.49), or their more sophisticated version including temperature and Coriolis effects, and one compares them with the observed ones to select the best set of line-profile parameters. These are the velocity amplitude  $v_p$  of each of the modes, the projected rotation velocity  $v_\Omega$ , the inclination angle  $i$ , and the intrinsic profile width  $v_{\text{int}}$ . This selection of  $(l, m, v_p, i, v_\Omega, v_{\text{int}})$  is either done by simple visual inspection (early days) or by defining a criterion that includes the deviation of the theoretical profiles from the observed ones in each wavelength pixel. In order to do this objectively, one must construct a

fine grid of theoretical profiles for different values of  $(l, m)$  and for realistic ranges of the other line-profile parameters.

This method is relatively easy and straightforward to apply to a monoperiodic oscillator. Assume we have  $M$  observed normalised profiles of a spectral line  $(\lambda_j, p_{\text{obs}}(\lambda_j, t_k))$  with  $j = 1, \dots, N$  and  $k = 1, \dots, M$ . We can then compute theoretical line profiles  $(\lambda_j, p_{\text{theo}}(\lambda_j, t_k))$  as explained above using Eq. (6.49) for different input parameters  $v_p, i, v_\Omega$  and  $v_{\text{int}}$ . Subsequently, we derive the *line deviation parameter* based on the classical statistical technique of *standardised residuals* (e.g., McCullagh & Nelder 1989):

$$\Sigma_l^m(v_p, i, v_\Omega, v_{\text{int}}) \equiv \sqrt{\frac{1}{(M \cdot N) - 1} \sum_{k=1}^M \sum_{j=1}^N \frac{[p_{\text{obs}}(\lambda_j, t_k) - p_{\text{theo}}(\lambda_j, t_k)]^2}{p_{\text{theo}}(\lambda_j, t_k)[1 - p_{\text{theo}}(\lambda_j, t_k)]}}. \quad (6.50)$$

The optimal choice of the continuous parameters  $(v_p, i, v_\Omega, v_{\text{int}})$  leads to a minimum of  $\Sigma_l^m$  for each  $(l, m)$ . By carefully screening a four-dimensional parameter space for each  $(l, m)$ , and by subsequently comparing the  $\Sigma_l^m$ -values, one can thus identify the most likely mode.

Whenever more than one mode is present, however, the method becomes unrealistic in computation time because one cannot search a large enough parameter space. The latter has six dimensions for one mode and increases by 3 for any additional mode, in the approximation where one neglects temperature and Coriolis effects as well as mode coupling. Also, this method is sensitive to the neglect of low-amplitude modes that do affect the profiles slightly, because the time series of line profiles is used in an absolute sense. Quite often one constructs theoretical line profiles after the mode identification has been achieved with quantitative methods for direct comparison with the data. This is of course no longer line-profile fitting, but serves as an empirical goodness-of-fit test to check identifications resulting from other methods.

### 6.2.3 The Moment Method

To overcome the computational obstacle of line-profile fitting, and to make the identification more objective, quantitative mode-identification methods have been developed since the second part of the 1980s. With each of these, one replaces the observed line profiles by carefully studied diagnostics derived from the data. One such method is based on the moment variations of the spectral lines and was first introduced by Balona (1986ab, 1987) and further developed by Aerts *et al.* (1992), De Pauw *et al.* (1993), Aerts (1996), Cugier & Daszyńska (2001) and Briquet & Aerts (2003). This method essentially relies on the statistical property that a line profile is fully characterised by all of its velocity moments. Given this, one derives information about the velocity of the nonradial oscillations from the time series of the moments of the line profiles. The moment method has meanwhile been applied to many different types of heat-driven pulsators along the main sequence. It is very powerful to

identify low-degree modes ( $l \leq 4$ ) in slow rotators ( $v \sin i \leq 50 \text{ km s}^{-1}$ ). We discuss now the basic ingredients of this method and refer the reader to the papers listed above for details.

### 6.2.3.1 Definition of the Moments

As discussed above, a line profile  $p_{\text{theo}}(v) \equiv (f * g)(v)$  is the convolution of an intrinsic profile denoted here as  $g(v)$  for brevity, with the flux in the direction of the observer, denoted for convenience as  $f(v)$ , integrated over the visible stellar surface. The function  $f(v)$  corresponds to the one defined in Eq. (6.44) while the velocity  $v$  is a function of the angular coordinates  $\theta'$  and  $\phi'$  and of time  $t$ :  $v = v(R, \theta', \phi', t)$ . The function  $g(v)$  is assumed to be a Gaussian with variance  $v_{\text{int}}^2$  for reasons described above.

We define the  $j$ th moment of the line profile as follows:

$$\langle v^j \rangle_{f*g} \equiv \frac{\int_{-\infty}^{+\infty} v^j p_{\text{theo}}(v) dv}{\int_{-\infty}^{+\infty} p_{\text{theo}}(v) dv} = \frac{\int_{-\infty}^{+\infty} v^j (f * g)(v) dv}{\int_{-\infty}^{+\infty} (f * g)(v) dv} \quad (6.51)$$

with  $v$  the component of the total (pulsation + rotation) velocity field in the line-of-sight.

All the information contained in the line profile can be reconstructed from the entire series of moments of order  $j$ . In practice, we consider the first three moments, *i.e.*, those for  $j = 1, 2, 3$ . There are several reasons for that, the major one being that each of these first three moments is connected to a specific property of the line profile:

- i) the first moment  $\langle v \rangle$  is the *centroid* of the line profile in a reference frame with origin at the stellar centre;
- ii) the second moment  $\langle v^2 \rangle$  is a measure of the width of the line profile;
- iii) the third moment  $\langle v^3 \rangle$  is a measure of the skewness of the line profile.

All higher-order moments can be written in terms of the first three moments for profiles whose wings do not deviate much from a Gaussian. For the practical application to observed line-profile variations one easily shows that the noise level in the observed moments increases with increasing moment order and that the noise is higher for even moments than for odd moments. Aerts *et al.* (1992) and Aerts (1996) showed that the use of the three lowest-order moments is the optimal balance between having a clear signal and adding independent information. Thus, each measured line profile is replaced by its first three normalised moments  $\langle v \rangle$ ,  $\langle v^2 \rangle$  and  $\langle v^3 \rangle$ .

### 6.2.3.2 Theoretical Expression of the Moments for a Monoperiodic Oscillation

In Eq. (6.51) we consider *normalised* moments, *i.e.*, each moment is divided by the *moment of order zero*  $M_0$ . The latter is the equivalent width of the line

profile, already defined in Chapter 4. The division by the equivalent width is very convenient because small temperature and flux variations during the oscillation are more or less averaged out in this way, as they occur in the same way in the numerator and denominator in the definition of the moments. De Pauw *et al.* (1993) tested the robustness of the mode identification against small equivalent-width variations and found the assumption of a constant  $M_0$  to be acceptable up to equivalent-width changes of 5% in amplitude.

We subsequently make use of the property that the integral of a convolution equals the product of the integrals of the functions to be convolved. Hence it is straightforward to show that the first three moments can be written as:

$$\langle v \rangle_{f*g} = \langle v \rangle_f + \langle v \rangle_g, \quad (6.52)$$

$$\langle v^2 \rangle_{f*g} = \langle v^2 \rangle_f + 2\langle v \rangle_f \langle v \rangle_g + \langle v^2 \rangle_g, \quad (6.53)$$

$$\begin{aligned} \langle v^3 \rangle_{f*g} = 3\langle v^2 \rangle_f \langle v \rangle_g + 3\langle v \rangle_f \langle v^2 \rangle_g \\ + \langle v^3 \rangle_f + \langle v^3 \rangle_g. \end{aligned} \quad (6.54)$$

The odd moments of a Gaussian with average 0 km/s and variance  $v_{\text{int}}^2$  are zero. The second moment of the intrinsic Gaussian equals  $v_{\text{int}}^2$ . Thanks to these simple properties of a Gaussian, the convolution with the Gaussian intrinsic profile can be written as follows:

$$\langle v \rangle_{f*g} = \langle v \rangle_f, \quad (6.55)$$

$$\langle v^2 \rangle_{f*g} = \langle v^2 \rangle_f + v_{\text{int}}^2, \quad (6.56)$$

$$\langle v^3 \rangle_{f*g} = \langle v^3 \rangle_f + 3v_{\text{int}}^2 \langle v \rangle_f. \quad (6.57)$$

By considering the component of the total velocity vector  $\mathbf{v} = \mathbf{v}_{\text{puls}} + \mathbf{v}_{\text{rot}}$  and by transforming the expression for  $f(v)$  given by (6.44) to the reference frame  $(r, \theta, \phi)$  connected with the stellar rotation axis, we obtain the following expressions for the three normalised moments of a monoperiodic nonradial pulsator whose mode has infinite lifetime, after integration over the visible stellar surface:

$$\langle v \rangle_{f*g} = v_p A(l, m, i) \sin(\omega t + \delta), \quad (6.58)$$

$$\langle v^2 \rangle_{f*g} = v_p^2 C(l, m, i) \sin(2\omega t + 2\delta + 3\pi/2) \quad (6.59)$$

$$+ v_p v_\Omega D(l, m, i) \sin(\omega t + \delta + 3\pi/2)$$

$$+ v_p^2 E(l, m, i) + v_{\text{int}}^2 + b_2 v_\Omega^2$$

$$\langle v^3 \rangle_{f*g} = v_p^3 F(l, m, i) \sin(3\omega t + 3\delta) \quad (6.60)$$

$$+ v_p^2 v_\Omega G(l, m, i) \sin(2\omega t + 2\delta + 3\pi/2)$$

$$+ [v_p^3 R(l, m, i) + v_p v_\Omega^2 S(l, m, i) + v_p v_{\text{int}}^2 T(l, m, i)] \\ \times \sin(\omega t + \delta).$$

In these expressions,  $\delta$  is a phase constant depending on the chosen reference epoch and  $b_2$  is a constant that depends only on the limb-darkening law. The

functions  $A, C, D, E, F, G, R, S, T$  depend on the  $(l, m)$  of the oscillation mode and on the inclination angle. Together with the pulsation velocity amplitude  $v_p$ , these dimensionless and normalised functions contain the complete physical information connected with the theoretical expression of the nonradial oscillation mode. The derivation of the expressions for these (complicated) functions was presented by Aerts *et al.* (1992) to which we refer the reader for further information. We only consider the case of the first moment in somewhat more detail here. The function  $A(l, m, i)$  can be decomposed as

$$A(l, m, i) = a_{lm0}(i) \cdot a(l, K, h_\lambda). \quad (6.61)$$

An explicit expression for  $a(l, K, h_\lambda)$  is available in Aerts *et al.* (1992) and in De Ridder *et al.* (2002) and is omitted here. From this decomposition, we encounter in a natural way again the same IACCs as for a photometric light curve, as the angles  $i$  for which  $a_{lm0}(i) = 0$ . Moreover, we can estimate the partial cancellation effect for spectroscopy from  $a(l, K, h_\lambda)$ .

Some values are graphically depicted in Fig. 6.14 for two main-sequence stars with different spectral types (B and G) and for a typical p mode (upper panel) and g mode (lower panel). First of all, a comparison of Figs 6.4 and 6.14 shows at once that the partial cancellation effect is very different for a photometric time series compared with a spectroscopic one. While the decrease in detectability of modes with increasing  $l$  is apparent for photometry, this is not the case for spectroscopy. This explains why a larger variety of mode degrees is detected in spectroscopic data. It can be seen from Fig. 6.14 that, for p modes with the same intrinsic amplitude, those with  $l = 1$  and 4 are easiest to detect in the time series of the first moment *if we ignore the projection effect*, particularly for hot stars. Modes with  $l = 2$  and 3 have about equal probability of being detected if they have the same intrinsic amplitude and similar projection effect. This explains why such modes have been derived from spectroscopy for some stars, while  $l = 3$  modes are usually absent in photometry (see, *e.g.*, the example of the  $\beta$  Cep star  $\beta$  Cru, Aerts *et al.* 1998a). In general, the detected heat-driven p modes in individual target stars that have been studied do not follow the patterns predicted from Figs 6.4 and 6.14. This probably means that the intrinsic amplitudes of the excited p modes are clearly different, although the inclination effect may also partly be the cause of this.

The situation is somewhat different for g modes, which have, first of all, smaller  $a(l, K, h_\lambda)$  values than p modes. They are thus harder to detect in spectroscopy. In this case, the modes with  $l = 1, 2, 3, 4$  are almost equally probable of being detected and the bottom panel of Fig. 6.14 shows that it is easier to achieve this for B stars than for G stars. Modes with degree  $l > 5$  are very hard to detect in the first moment. This is fully compatible with the observations of g modes in SPBs (De Cat *et al.* 2005) and in  $\gamma$  Dor stars (Aerts *et al.* 2004a).

The detectability of modes in  $\langle v^2 \rangle$  is different than in  $\langle v \rangle$ . It would lead us too far to discuss this in detail; we refer to Aerts *et al.* (1992), De Pauw

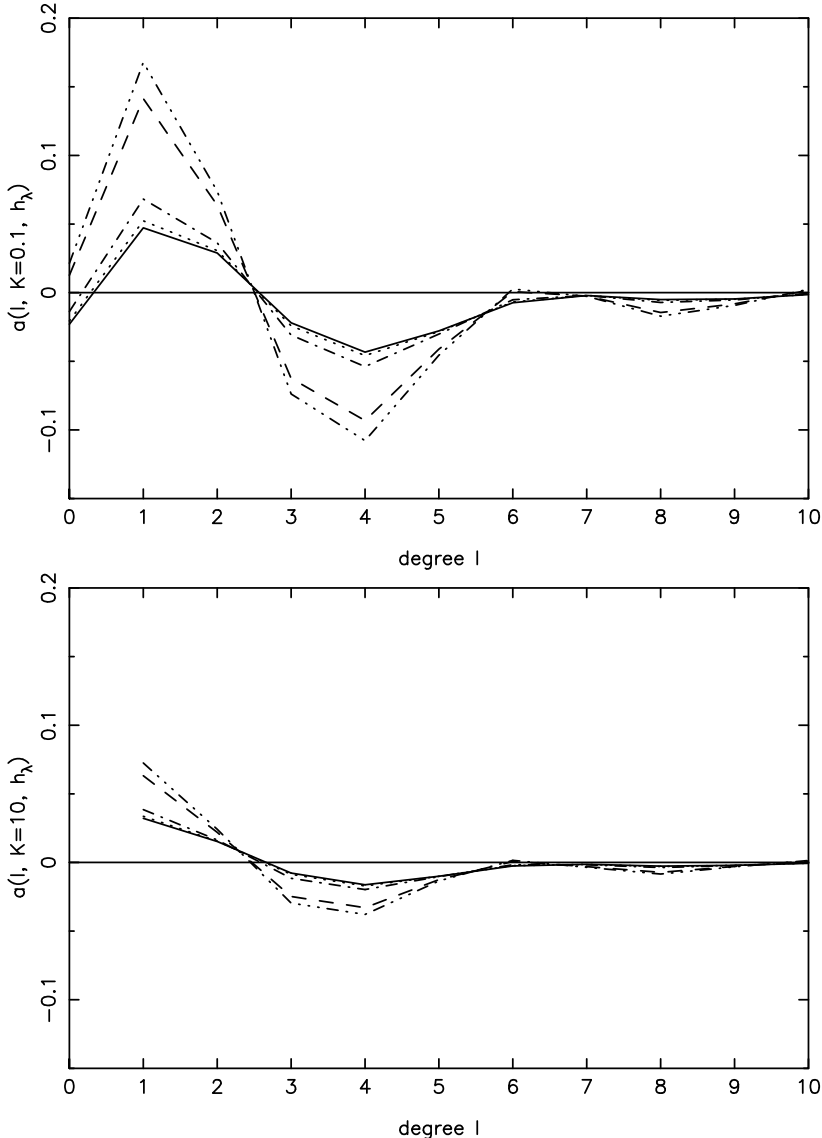


**Fig. 6.14.** The function  $a(l, K, h_\lambda)$  is shown for different mode degrees  $l$  for a linear limb-darkening law taken from Claret (2000). We considered a star of  $T_{\text{eff}} = 6000$  K and  $\log g = 4.0$  at the wavelengths of the  $U$  (full line),  $B$  (dotted line) and  $V$  (dash-dotted line) filters, as well as a star of  $T_{\text{eff}} = 25000$  K and  $\log g = 4.0$  at  $U$  and  $B$  (indistinguishable, shown as dashed line) and  $V$  (dash-dot-dot-dotted line) wavelengths. Upper panel: results for a typical p mode with  $K = 0.1$ ; lower panel: results for a g mode with  $K=10$ .

*et al.* (1993), and Aerts (1996). The important message is that photometric and spectroscopic observables not necessarily favour the same degrees to be detected in the case of equal intrinsic amplitudes.

### 6.2.3.3 Computation of the Observational Moments

In practice we have sets of numbers  $(\lambda_i, F_i)$  with  $i = 1, \dots, N$  at our disposal for each measured line profile. Here,  $F_i$  stands for the normalised flux value measured at wavelength  $\lambda_i$  for pixel  $i$ . These profiles are considered to be barycentric, *i.e.*, their observation time and wavelengths have been shifted to the barycentre of the solar system in order to take into account the motion of the Earth around the Sun. The star under consideration exhibits an (*a priori* unknown) radial velocity with respect to the Sun caused by its space motion and possibly any binary orbital motion. These space motions are not of interest to us here and are not contained in the theoretical expressions of the moments, which are valid for a reference frame connected to the stellar centre. We therefore have to correct the observed line profile  $(\lambda_i, F_i)$  for the radial velocity shift of this space motion, before we can study the intrinsic velocity due to the oscillation of the star as it occurs in the theoretical expressions (6.58), (6.59), (6.60) of the moments. This implies that we have to determine the observed moment variations in three different stages:

- i) First we determine the *small unnormalised moments* as follows:

$$m_0 = \sum_{i=1}^N (1 - F_i) \Delta x_i, \quad (6.62)$$

$$m_1 = \sum_{i=1}^N (1 - F_i) x_i \Delta x_i, \quad (6.63)$$

$$m_2 = \sum_{i=1}^N (1 - F_i) x_i^2 \Delta x_i, \quad (6.64)$$

$$m_3 = \sum_{i=1}^N (1 - F_i) x_i^3 \Delta x_i, \quad (6.65)$$

with  $\Delta x_i \equiv x_i - x_{i-1}$  where  $x_i$  is the velocity corresponding to  $\lambda_i$  with respect to the laboratory wavelength of the spectral line. One has to make a clever choice for the velocity (or wavelength) range  $[x_1, x_N]$ : not too narrow a range in order to have all the information in the line profile contained in the moment values and not too broad to limit the noise in the calculated higher-order moments.

- ii) The reduction of the small moments to average zero is achieved by correcting for the relative motion of the star with respect to the Sun. This motion is given by the average radial velocity of the star, which is the

average value of  $m_1/m_0$  (unit  $\text{km s}^{-1}$ ). We denote this average by  $x_0$ . The *large unnormalised moments* are obtained by using  $x_0$  as a reference value:

$$M_0 = \sum_{i=1}^N (1 - F_i) \Delta x_i, \quad (6.66)$$

$$M_1 = \sum_{i=1}^N (1 - F_i)(x_i - x_0) \Delta x_i, \quad (6.67)$$

$$M_2 = \sum_{i=1}^N (1 - F_i)(x_i - x_0)^2 \Delta x_i, \quad (6.68)$$

$$M_3 = \sum_{i=1}^N (1 - F_i)(x_i - x_0)^3 \Delta x_i. \quad (6.69)$$

This leads to odd moments with average zero.

- iii) Finally, we obtain the observed normalised moments  $\langle v^j \rangle$  for  $j = 1, \dots, 3$  as  $M_j/M_0$ . These moments now have velocity units ( $\text{km s}^{-1}$ ) $^j$  and can be compared with the theoretical expressions (6.58) – (6.60).

In the case of a spectroscopic binary, the spectra need to be shifted to prewhiten the orbital motion before the moments are computed.

#### 6.2.3.4 Interpretation of the Moments

The periodograms of the three moments are immediately interpretable in terms of the oscillation frequencies of the detected modes. The variations of the moments  $\langle v^j \rangle$  in time are thus a very suitable diagnostic that allows one to derive the temporal behaviour of the oscillations in full detail. It usually suffices to search the frequencies of the modes in the observed first moment variations, but some modes may show up easier in  $\langle v^2 \rangle$  because this quantity has a different partial cancellation than the first moment.

As soon as the oscillation frequencies have been derived, one is able to construct phase diagrams of the moment variations from a harmonic analysis as explained in Chapter 5. The results of such a harmonic analysis are observational values for the different amplitudes that occur in the theoretical expressions Eqs (6.58), (6.59), (6.60) of the moments. We are therefore able to derive information about the six oscillation parameters  $(l, m, i, v_p, v_\Omega, v_{\text{int}})$ . We explain how to do that, by means of an example.

In Figs 6.15 and 6.16 we show some observed profile variations and the three normalised moments of the δ Sct star ρ Puppis. The full lines in Fig. 6.16 correspond to the result of a harmonic analysis according to the Eqs (6.58), (6.59) and (6.60). The peak-to-peak value of the first moment gives an idea about the overall velocity range due to the oscillation with that particular

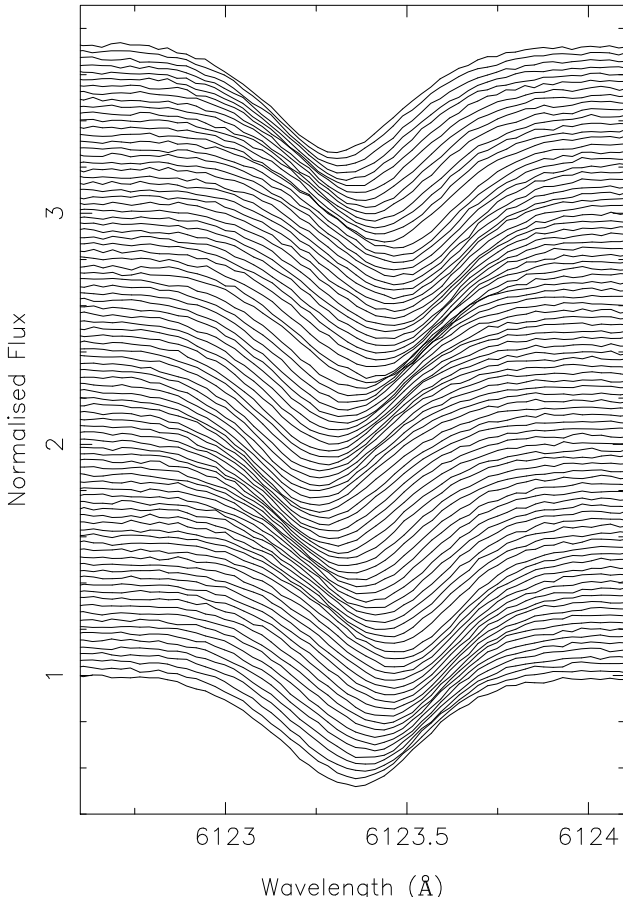


**Fig. 6.15.** Some observed line-profile variations of the  $\delta$  Sct star  $\rho$  Pup obtained in 1995 with the Coudé Auxiliary Telescope of the European Southern Observatory in Chile phased with the dominant frequency of  $7.098 \text{ d}^{-1}$ . Data taken from Mathias *et al.* (1997).

frequency, although it is an integrated quantity. For linear oscillations (an assumption we adopted for the theoretical description of the moment method) we expect this range to be well below the sound speed in the line-forming region within the stellar atmosphere. If not, shock waves occur and the description of the modes in terms of a sine function is no longer valid. For a linear oscillation, the first moment is expected to behave sinusoidally as is the case for  $\rho$  Puppis (see Figure 6.16).

The second moment turns out to be a very good diagnostic for the azimuthal number  $m$ . Indeed, as shown in Aerts *et al.* (1992), the function  $D(l, m, i)$  equals zero for  $m = 0$ . This allows us readily to distinguish between

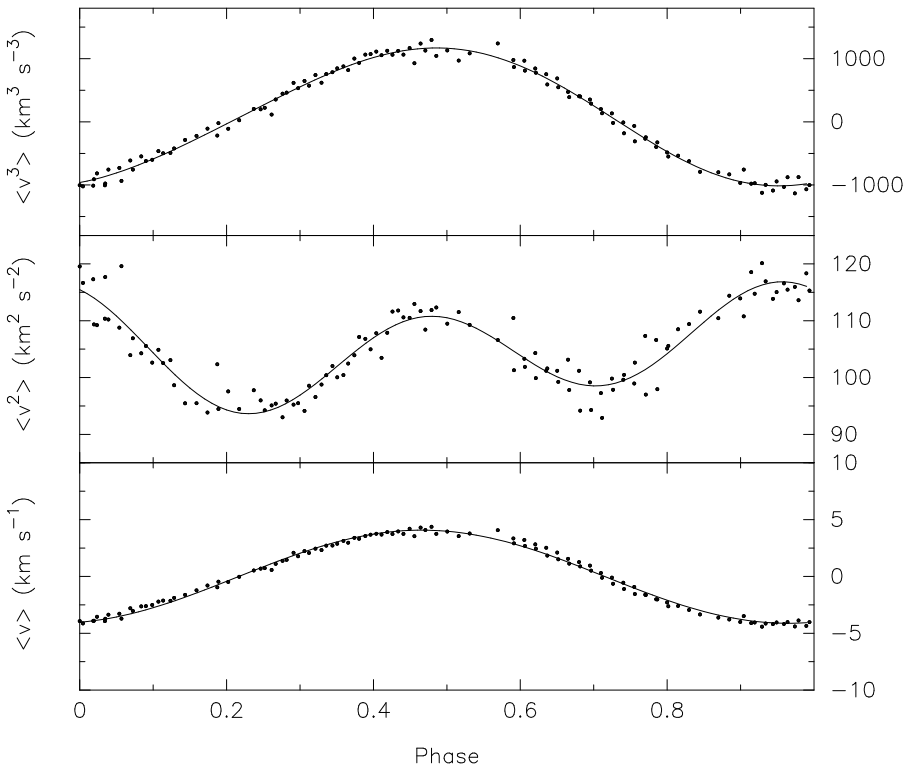


**Fig. 6.16.** Phase diagrams of the normalised moments of the  $\delta$  Sct star  $\rho$  Pup for the dominant frequency  $7.098 \text{ d}^{-1}$ . The dots are the observations and the lines are the result of harmonic analyses according to expressions (6.58), (6.59) and (6.60). Data taken from Mathias *et al.* (1997). The analysis shows that this mode is radial. Part of the scatter in the diagrams arises from the presence of other, weaker modes.

$m = 0$  and  $m \neq 0$  from a harmonic analysis of  $\langle v^2 \rangle$ . Whenever the temporal behaviour of  $\langle v^2 \rangle$  can be described by a single sine function with frequency  $2\omega$  we are sure that  $m = 0$ . The middle panel of Figure 6.16 therefore implies that it is likely that  $m = 0$  for the main mode of  $\rho$  Puppis, although there is clearly a small sinusoidal contribution with frequency  $\omega$  since the shape of  $\langle v^2 \rangle$  is not fully symmetric. On the other hand, Aerts *et al.* (1992) have shown that  $C(l, l, i) = 0$ . This implies that  $\langle v^2 \rangle$  will behave purely sinusoidally with frequency  $\omega$  in the case of a sectoral mode. Any intermediate situation, *i.e.*, a second moment in which both a term with  $\omega$  and one with  $2\omega$  occur with equal amplitudes, points towards a tesseral mode.

In order to obtain a complete identification of the mode from the three moments, one proceeds as follows. The idea is to compare the observed variations of the moments with their theoretical expectations and to select the

most likely set of parameters  $(l, m, i, v_p, v_\Omega, v_{\text{int}})$ . This comparison is done objectively by means of the calculation of the so-called *discriminant*. This is a function based on the observed amplitudes of the moments for all terms that occur in the moment variations, *i.e.*, one term in  $\langle v \rangle$ , three terms in  $\langle v^2 \rangle$  and three terms in  $\langle v^3 \rangle$ . The discriminant is defined as follows:

$$\begin{aligned} \Gamma_l^m(v_p, i, v_\Omega, v_{\text{int}}) \equiv & \left[ \left| A_{\text{obs}} - v_p |A(l, m, i)| \right|^2 f_A^2 \right. \\ & + \left( \left| C_{\text{obs}} - v_p^2 |C(l, m, i)| \right|^{1/2} f_C \right)^2 \\ & + \left( \left| D_{\text{obs}} - v_p v_\Omega |D(l, m, i)| \right|^{1/2} f_D \right)^2 \\ & + \left( \left| E_{\text{obs}} - v_p^2 |E(l, m, i)| - v_{\text{int}}^2 - b_2 v_\Omega^2 \right|^{1/2} f_E \right)^2 \\ & + \left( \left| F_{\text{obs}} - v_p^3 |F(l, m, i)| \right|^{1/3} f_F \right)^2 \\ & + \left( \left| G_{\text{obs}} - v_p^2 v_\Omega |G(l, m, i)| \right|^{1/3} f_G \right)^2 \\ & \left. + \left( \left| T_{\text{obs}} - v_p^3 |R(l, m, i)| - v_p v_\Omega^2 |S(l, m, i)| \right. \right. \right. \\ & \quad \left. \left. \left. - v_p v_{\text{int}}^2 |T(l, m, i)| \right|^{1/3} f_T \right)^2 \right]^{1/2} \end{aligned} \quad (6.70)$$

(Aerts 1996). Here  $A_{\text{obs}}, C_{\text{obs}}, \dots, T_{\text{obs}}$  are the observed values of the functions  $A(l, m, i), C(l, m, i), \dots$  etc. occurring in Eqs (6.58), (6.59) and (6.60) of the theoretical predictions of the moments. These can be found from a harmonic least-squares fit to the observed moment time series. The quantities  $f_A, \dots, f_T$  are normalised weights that take into account the quality of such a fit to the observed moments. An amplitude that has a smaller standard error will receive a larger weight in the discrimination among the candidate  $l$ -values because it is more dominant in the discriminant  $\Gamma_l^m$  compared with an amplitude with a large standard error. The discriminant is constructed in such a way that it is expressed in  $\text{km s}^{-1}$ . From its definition, it is unable to distinguish between positive and negative  $m$ . However, a greyscale representation of the observed line profiles or the phase behaviour across the line profile (see below) provides this additional information on the sign of  $m$ .

The adopted criterion for mode identification works as follows: the function  $\Gamma_l^m(v_p, i, v_\Omega, v_{\text{int}})$  is minimized for each set  $(l, m)$ :

$$\gamma_l^m \equiv \min_{v_p, i, v_\Omega, v_{\text{int}}} \Gamma_l^m(v_p, i, v_\Omega, v_{\text{int}}). \quad (6.71)$$

As “overall best solution” for  $l$  and  $m$  we retain the one with the lowest  $\gamma_l^m$ . This solution also provides us the most likely values for the continuous unknowns in the velocity expression, namely  $v_p, i, v_\Omega$  and  $v_{\text{int}}$ .

De Pauw *et al.* (1993) and Aerts (1996) each made an extensive simulation study to test the performance of the discriminant, taking into account realistic gapped time series with an appropriate noise level. In these papers, one also finds numerous examples of the behaviour of the three moments as a function of  $(l, m, i)$ , and of the radial and horizontal amplitudes  $v_p$  and  $Kv_p$ . We advise a new user of the method to study these two simulation papers carefully and we refer to the paper by Aerts (1996) for more information on the performance of the discriminant defined in Eq. (6.70). In particular we warn the user not to accept solutions with  $i$  close to an IACC. Viewing in the direction of a nodal line of a mode is an easy way to get small amplitudes for the moment terms. Thus, stars with low moment amplitudes are easily explained by any  $(l, m)$  for inclinations equal to their IACC. The predictive power of the discriminant cannot be large in such a case. This must be kept in mind whenever interpreting the minima  $\gamma_l^m$ . Such a situation occurred for the star 20 CVn and is discussed in detail further in this Section.

A robustness test was done by De Pauw *et al.* (1993) to assess the assumption of constant equivalent width despite the occurrence of  $\delta T/T$ . It turned out that the discriminant defined in Eq. (6.70) keeps performing well in identifying the correct input mode as long as the peak-to-peak variations of  $M_0$  remain below 10% (De Pauw *et al.* 1993). This good performance occurs thanks to the use of normalised moments. It would not hold if we would work with  $M_1, M_2, M_3$  without dividing them by  $M_0$ . Since most of the pulsating stars fulfil the criterion of having equivalent-width variations below 10% (see, *e.g.*, De Ridder *et al.* 2002 for B pulsators), it is indeed not necessary to include the consequences of  $\delta T/T$  in the discriminant of the moment method, as already anticipated above. This is a very comforting situation, as we are thus not dependent on the details of the non-adiabatic oscillation theory in the outer atmosphere to identify the modes. All one relies on is the velocity expression in Eq. (6.40). *This is a serious advantage over photometric mode identification.* Of course, the condition of the relative amplitude of  $M_0$  being below 10% should be tested in any application of the discriminant.

The moment method as presented here is a good identification method, particularly for low-degree modes ( $l \leq 4$ ). It is complementary to the Pixel-by-Pixel method outlined below. Modes with high degree ( $l \geq 5$ ) have very small moment amplitudes with large standard errors, which limits the application of the discriminant for such cases.

The application of the discriminant defined in Eq. (6.70) for the moments of  $\rho$ Puppis shown in Figure 6.16 is given in Table 6.2. One finds a radial main mode for this star, as was already suggested by Campos & Smith (1980a). The finding that  $m = 0$  could be anticipated from the behaviour of  $\langle v^2 \rangle$ . The latter, however, does deviate from a pure double sine (see Fig. 6.16). Such a deviation is expected whenever additional modes, besides the dominant one,

are present. Mathias *et al.* (1997) indeed found two additional candidate low-amplitude modes in  $\rho$  Pup. Due to their beating with the dominant mode,  $\langle v^2 \rangle$  is not perfectly symmetric. The same situation occurs for the line-profile variations and their  $\langle v^2 \rangle$  of the  $\beta$  Cep star  $\delta$  Ceti (Aerts *et al.* 1992), whose low-amplitude modes were revealed in MOST space photometry (Aerts *et al.* 2006c). The second moment is thus a suitable diagnostic to detect low-amplitude modes.

**Table 6.2.** The minima of the discriminant for the main mode of the  $\delta$  Sct star  $\rho$  Pup.  $\gamma_l^m$ ,  $v_p$ ,  $Kv_p$ ,  $v_\Omega$  and  $v_{\text{int}}$  are expressed in  $\text{km s}^{-1}$ .

$l$	$ m $	$\gamma_l^m$	$v_p$	$Kv_p$	$i$	$v_\Omega$	$v_{\text{int}}$
0	0	0.08	5.6	0.218	–	15.3	6.5
1	1	0.13	10.0	0.390	$38^\circ$	14.8	5.9
2	1	0.17	12.1	0.472	$64^\circ$	16.4	2.2
1	0	0.18	5.0	0.195	$7^\circ$	19.6	1.7
2	2	0.23	15.0	0.585	$53^\circ$	10.3	4.8
:	:	:	:	:	:	:	:

The largest shortcoming of the discriminant is that it lacks a statistical significance test. In other words, we have no means to decide if the mode with the lowest  $\gamma_l^m$  in the list of best candidates in Table 6.2 is truly better than the following solutions, or if it is acceptable to a certain significance level. This was elaborated upon by De Ridder *et al.* (2005), but the complexity of the theoretical expressions for the moments, and the mixture of discrete and continuous unknowns, prevented a solid goodness-of-fit test. The best procedure to adopt, as already mentioned above, is to generate theoretical line-profile variations for the top listed solutions and compare them with the data. In this way, one first eliminates a sufficient number of unlikely combinations of  $l$ ,  $m$ ,  $v_p$ ,  $i$ ,  $v_\Omega$  and  $v_{\text{int}}$  from the moment variations before starting a line-profile fitting method, fixing  $l$  and  $m$  combinations from a list like the one in Table 6.2 and allowing for slight changes in the continuous parameters to minimize the deviation between the observed and theoretically computed profiles. Even after such a test, it may still be impossible to discriminate among several  $(l, m)$  combinations and one should not do so in such a situation. In fact, confusion between different  $(l, m)$  is inherent to the mode-identification problem. A radial mode, *e.g.*, will resemble a  $(1, 1)$  mode looked upon from the equator and is indistinguishable from a  $(1, 0)$  mode viewed from the pole. There are several combinations of  $(l, m, v_p, i)$  that have closely resembling profiles, and thus moment variations. There are also cases where the profiles are not very similar, but the moment values are, because of the integration over the surface. Such cases can still be distinguished by applying the Pixel-by-Pixel

method discussed in Section 6.2.4. To unravel similar profiles resulting from different combinations of  $(l, m, v_p, i)$ , one needs a strong constraint on the inclination angle. Multiperiodicity helps in this respect, as will be shown below, but independent observational information is needed as well. This will be illustrated for the case of the  $\delta$  Sct star 20 CVn in Section 6.2.3.6.

### 6.2.3.5 Generalisation to Multiperiodic Oscillations and to a Numerical Version of the Discriminant

A generalization of the mode-identification method described above for a multiperiodic star was provided by Mathias *et al.* (1994b). Whenever more than one mode is excited to measurable amplitude, the moment variations become more complicated. The first moment will simply consist of a linear superposition of all the separate modes. However, this is no longer the case for the second and third moments, as they will contain coupling terms from taking the square and the third power of the velocity expression in the integrand of Eq. (6.51). For example, a biperiodic oscillation with frequencies  $\omega_1$  and  $\omega_2$  will give rise to six frequencies in the second moment:  $\omega_1$ ,  $2\omega_1$ ,  $\omega_2$ ,  $2\omega_2$ ,  $\omega_1 - \omega_2$  and  $\omega_1 + \omega_2$ . The third moment will in that case have to be fitted with twelve frequencies: those of  $\langle v^2 \rangle$  and in addition  $3\omega_1$ ,  $3\omega_2$ ,  $2\omega_1 + \omega_2$ ,  $2\omega_1 - \omega_2$ ,  $2\omega_2 + \omega_1$  and  $2\omega_2 - \omega_1$ . The number of frequencies occurring in the moment expressions increases very rapidly with the number of modes. *This is a disadvantage of this method.*

In order for the harmonic analysis to be accurate for a multiperiodic oscillation, *i.e.*, to lead to amplitudes with a small standard error as input for the discriminant, it is necessary to cover all the beat frequencies with line-profile observations. The sampling of the data also has to be of high temporal resolution in order to estimate the amplitudes of the sum frequencies in an accurate way. This fact implies large observational challenges. An example in which a beat phenomenon occurs in the time series of centroid velocities derived from spectra of the  $\beta$  Cep star  $\nu$  Eri, which was the target of a multisite campaign, is shown in Fig. 6.17. A beat pattern is clearly visible in this figure. It is even more apparent in the night-to-night photometric variations which will be discussed in Chapter 7. Several other time series including beating phenomena were already shown in Chapter 2, such as in Figs 2.8, 2.12, 2.18, 2.20, 2.23, 2.52. The challenges are most prominent for stars with multiperiodic g-mode oscillations, such as slowly pulsating B stars,  $\gamma$  Doradus stars, pulsating Be stars and pulsating supergiants. In all of those, the beat periods can be of the order of months to years.

Solving the mode identification for multiperiodic oscillations is, of course, more complex than for a single mode. Three unknowns  $(l, m, v_p)$  are added for each additional oscillation mode. On the other hand, having more than one mode helps significantly to discriminate among almost equivalent solutions with different inclination angles  $i$ . From the very complicated analytical expressions for  $\langle v^2 \rangle$  and  $\langle v^3 \rangle$  available in Mathias *et al.* (1994b), one sees that

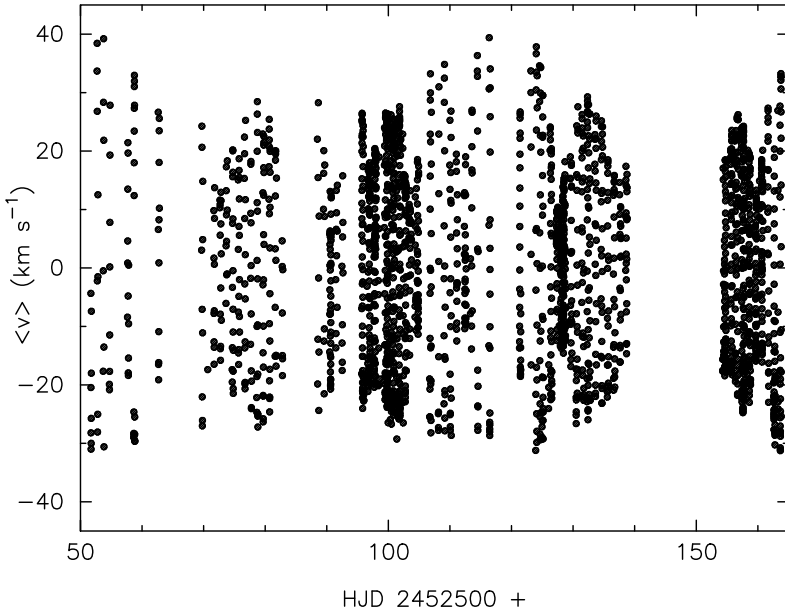


**Fig. 6.17.** Time series of the first velocity moment of the multiperiodic  $\beta$  Cep star  $\nu$  Eri derived from a five-month dedicated multisite campaign. From Aerts *et al.* (2004b).

almost all of the terms contain couplings between different frequencies. As a consequence, identification of the modes is best performed simultaneously, and not mode by mode as was originally done by Mathias *et al.* (1994b). With the advent of faster computers, the option of simultaneous identification of all detected frequencies in the moments was implemented by Briquet & Aerts (2003). With this technique, the authors did not use the analytical expressions of the moments to identify the modes as Aerts (1996) did. Instead, they computed line-profile variations for various combinations of the parameters, derived their moments numerically as in Section 6.2.3.3, and compared them with the corresponding values derived from the observations, in a similar way as in Eq. (6.70). Given that many of the factors occurring in the moments can be separated, one only needs to compute them once and stack them into huge tables. In that way, the moment method of Briquet & Aerts (2003) is more than a factor of ten faster than the version of Mathias *et al.* (1994b). Some applications will be discussed in Chapter 7.

#### 6.2.3.6 Application to Cross-Correlation or Least-Squares-Deconvolved Profiles

The requirements on the quality of the spectra to apply the moment method successfully are stringent. The same is true for the Pixel-by-Pixel method, as

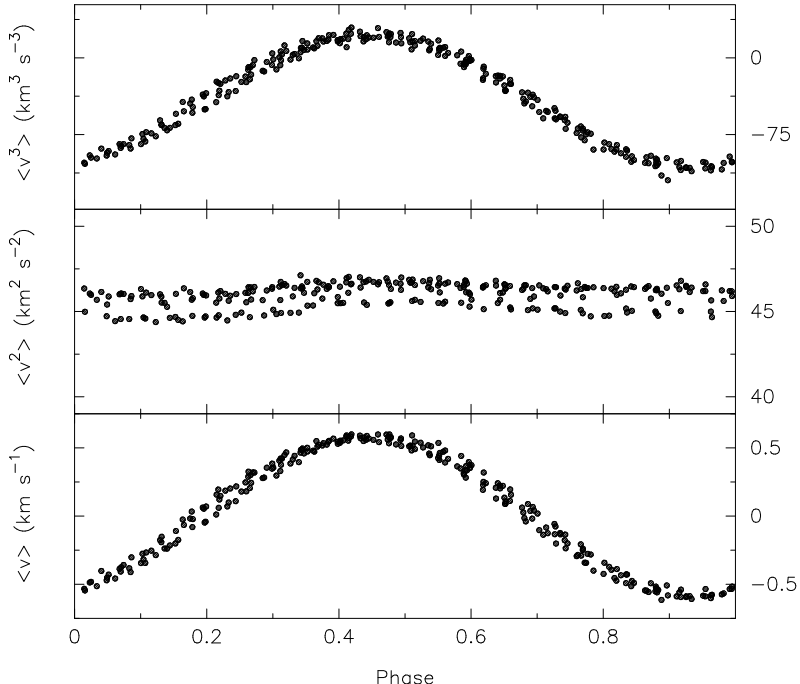


**Fig. 6.18.** Phase diagrams of the observed normalised moments derived from cross-correlation functions of the  $\delta$  Sct star 20 CVn for the frequency  $8.2168 \text{ d}^{-1}$ . From Chadid *et al.* (2001).

will be discussed below. This limits the applicability of the methods to very bright stars (typically with  $V < 6$  for telescopes with diameter below 4m) with not too short oscillation periods (typically longer than 15 min). One can overcome this obstacle, to a certain extent, by combining the information present in different spectral lines, such that fainter stars can be considered as well, or the integration times can be limited, or lower-amplitude modes can be searched for. Although of interest, one will seldom gain information on the correct  $(l, m)$  when repeating an analysis on additional different individual lines, because the best line will have been picked to start with in the first place.

While one can in principle combine the  $\langle v \rangle$  values of different lines, this is certainly not true for  $\langle v^2 \rangle$  and  $\langle v^3 \rangle$ . Indeed, each of the lines has its own thermal broadening, *i.e.*, its own value of  $v_{\text{int}}$ . This leads to a different constant term  $EE$  for  $\langle v^2 \rangle$  and different amplitudes for  $\langle v^3 \rangle$  for each of the lines, as can be seen from Eqs (6.59) and (6.60). One could still merge the second moments  $\langle v^2 \rangle$  of different lines, after shifting them to a common constant term  $EE = 0$  and by avoiding using that term in Eq. (6.70) for the mode identification. However, the amplitudes are also different for different lines, because

**Table 6.3.** The minima of the discriminant according to Eq. (6.70) (left) and of the deviation parameter from line-profile fitting following Eq. (6.50) (right) for the monoperiodic  $\delta$  Sct star 20 CVn (Chadid *et al.* 2001).

$l$	$ m $	$\gamma_l^m$	$v_p$	$Kv_p$	$i$	$v_\Omega$	$v_{\text{int}}$	$l$	$m$	$\Sigma_l^m$	$v_p$	$Kv_p$	$i$	$v_\Omega$	$v_{\text{int}}$
3	2	0.09	4.50	0.27	75°	6	5.0	2	0	0.0022	2.50	0.15	45°	4.0	5.5
0	0	0.12	0.75	—	—	5	6.0	3	0	0.0022	2.00	0.12	25°	4.0	5.7
3	0	0.12	4.00	0.24	55°	6.0	4.0	0	0	0.0023	0.85	—	—	7.0	5.0
1	1	0.13	1.00	0.06	80°	6.0	5.0	3	+1	0.0024	2.50	0.15	85°	6.0	5.5
1	0	0.15	2.00	0.12	70°	6.0	5.0	4	+4	0.0026	1.50	0.09	70°	6.0	5.5
3	1	0.15	5.00	0.30	55°	5.0	5.0	3	+2	0.0026	3.00	0.18	15°	6.0	5.5
2	0	0.17	1.50	0.09	35°	7.0	5.5	3	-2	0.0027	3.00	0.18	15°	4.0	5.5
2	1	0.17	3.50	0.21	80°	4.0	5.5	2	+1	0.0029	2.00	0.12	90°	4.0	5.5
:	:	:	:	:	:	:	:	:	:	:	:	:	:	:	:

there is always some level of blending and this is different for different lines (see, *e.g.*, Mathias *et al.* (1994b) for a thorough discussion and illustrations). *The conclusion is that a simple line-by-line treatment is not helpful, from the viewpoint of improving the mode identification.* Such an analysis is very useful, however, to detect small shock phenomena and details of wave propagation in the outer stellar atmosphere (*e.g.*, Crowe & Gillet 1989; Mathias *et al.* 1991; Mathias & Gillet 1993).

We thus must search for a different way to combine the information in different spectral line variations. Whenever the different line-forming regions do not enclose nodal surfaces and are situated not too far from each other, one expects the moments to vary perfectly in phase with each other. This can easily be tested in practice. In that case, one may combine them to increase the S/N level. This can be done by computing a cross-correlation function (CCF) of each spectrum, or by least-squares deconvolution (LSD), as outlined in Chapter 4. The reader finds numerous examples of oscillation signatures in the CCFs of  $\gamma$  Dor stars in De Cat *et al.* (2006). It is very clear from that paper that the oscillations turn up in the CCFs. How to use them for mode identification, is, however, another issue to that of detecting the modes.

While computing the CCF or LSD, the same requirement as for the individual lines should be respected, *i.e.*, the study must be restricted to unblended thermally-broadened metal lines. This usually reduces the number of spectral lines considerably compared with the case where computation of the most accurate radial-velocity value is the goal. The S/N level in the CCF or LSD will increase by a factor  $\sqrt{N}$ , with  $N$  the number of lines used for the CCF or LSD, so even using only four lines for a mask to derive the CCF or for the computation of the LSD will imply doubling the S/N level.

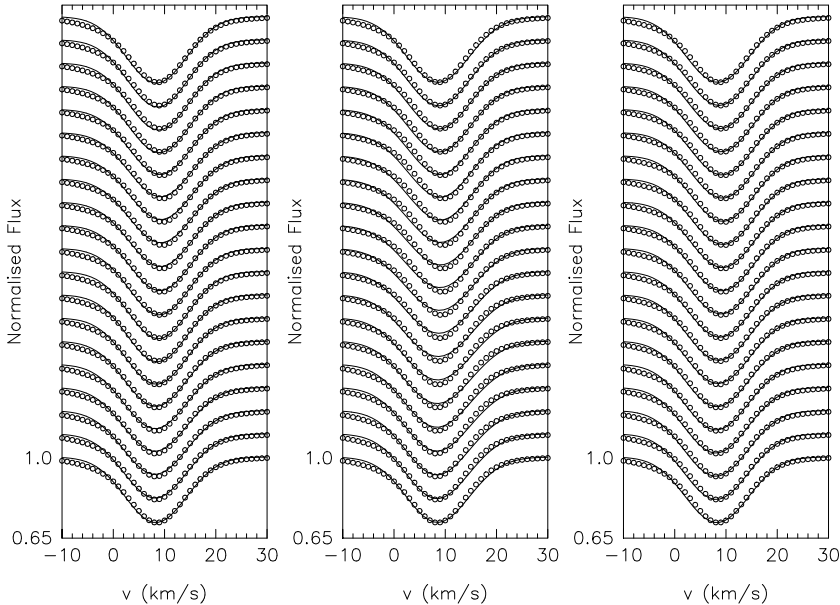


**Fig. 6.19.** Theoretically determined line-profile variations (full lines) are compared with the observed cross-correlation functions (open circles) of the  $\delta$  Sct star 20 CVn. The input modes are  $(l, m)$  equal to  $(2, 0)$  (left),  $(4, +4)$  (middle),  $(0, 0)$  (right). The continuous input parameters are listed in the right part of Table 6.3. From Chadid *et al.* (2001).

One should not be fooled by thinking that the application of the moment method to such type of variations is exactly the same as for the individual spectral lines. This is not the case, because the second moment  $\langle v^2 \rangle$  of the CCF or LSD is again affected by the merging of lines with different  $v_{\text{int}}$  and by slight differences in the line blending of the different lines. The  $EE$  value is therefore affected, and, if computed without giving this thought, also the discriminant defined in Eq. (6.70).

A thorough discussion of such a situation is presented in Chadid *et al.* (2001) for the F3III monoperiodic  $\delta$  Sct star 20 CVn. The purpose of their paper was to investigate the appropriateness of using CCF and the moment method to identify low-amplitude modes, because photometric mode-identification efforts for this star in the literature, before the one done by Daszyńska-Daszkiewicz *et al.* (2003) discussed above, led to a large discrepancy between the theoretical predictions and the observed values. We show in Fig. 6.18 the moment values derived from a CCF computed from a mask for an F-type star including some 2000 lines using the ELODIE spectrograph. The curves are phased according to the frequency  $8.2168 \text{ d}^{-1}$  known from photometric light curves. It can be seen that the second moment hardly varies,

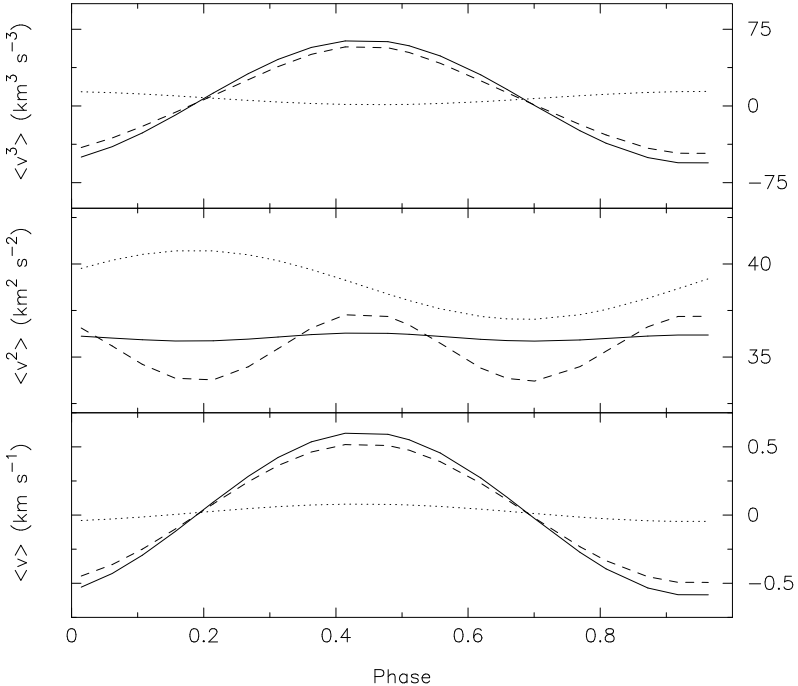


**Fig. 6.20.** Theoretically determined moment variations for  $(l, m)$  equal to  $(0, 0)$  (full line),  $(2, 0)$  (dashed line) and  $(4, +4)$  (dotted line) for the parameters listed in the right part of Table 6.3. These moments correspond to the theoretical line-profile variations shown in Fig. 6.19 and should be compared with the observed ones shown in Fig. 6.18.

while the first and third moments have clear observed variations. This means that the constant term  $EE$  dominates in  $\langle v^2 \rangle$ . This is a case where one has to be careful with the mode identification because solutions with  $i$  close to the IACC risk being favoured. The discriminant was subsequently computed, leaving out the constant terms of  $\langle v^2 \rangle$  and  $\langle v^3 \rangle$  following the careful analysis of all the terms occurring in the observed moments by Chadid *et al.* (2001). The values of this modified discriminant are provided in the left part of Table 6.3. It turns out that several solutions with  $i$  closer than  $15^\circ$  to an IACC occur (rows 1, 3, 6 and 8). These cannot be trusted. The minima  $\gamma_l^m$  are very close to each other, such that a unique solution cannot be derived without additional effort.

In order to check for the power of the modified discriminant for this monoperiodic star, the spectral deviation parameter in Eq. (6.50) through line-profile fitting was computed for all modes with  $l \leq 4$ . The results are listed in the right part of Table 6.3. It can be seen that the discriminating power of this method is lower than the one of the moment method for this star. Several

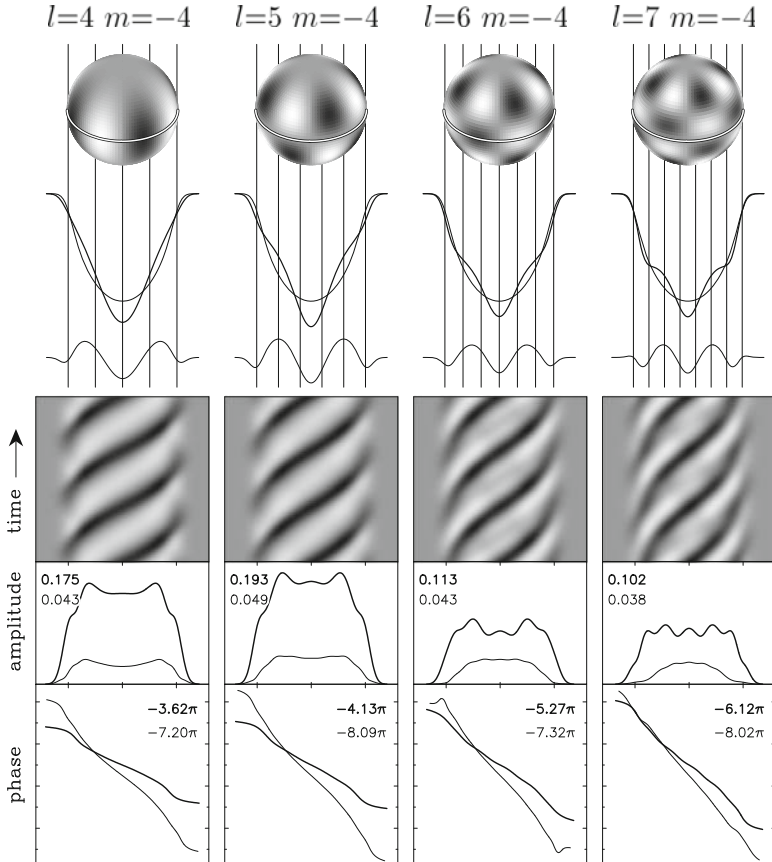


**Fig. 6.21.** Simulated line-profile variations due to nonradial oscillations of different  $(l, m)$ . From top to bottom we show: a representation of the real part of the radial component of the eigenfunction, the line profile due to the mode at a particular phase in the cycle in comparison with the profile without an oscillation, the difference between the two profiles, a grey-scale representation of the profiles with respect to the mean during three cycles, the distribution of the amplitude across the pulsation-induced line-profile variations (thick line) and its first harmonic (thin line) with the maximum values indicated, the distribution of the phase across the pulsation-induced line-profile variations (thick line) and its first harmonic (thin line) in units of  $\pi$  radians with the blue-to-red phase differences  $\Delta\psi_0$  and  $\Delta\psi_1$  used in Eqs (6.72) and (6.73) indicated. The projected equatorial rotation velocity is indicated by the outer vertical lines in the top panel. From Telting & Schrijvers (1997).

solutions of almost equal quality occur. Three of those are compared with the observed CCFs in Fig. 6.19: one with an inclination angle close to an IACC (left), one with  $i$  far from an IACC (middle) and the radial mode. This is a clear case where line-profile fitting, even when using an objective deviation

parameter, does not work, but where the addition of the moment variations allows the selection of one unique solution for  $(l, m)$ . Indeed, a choice among the solutions in Table 6.3 can be made, by considering the theoretical moments belonging to the best solutions from  $\Sigma_l^m$  and comparing them with the observed ones shown in Fig. 6.18. These are plotted in Fig. 6.20. It is clear that only one set of  $\langle v^2 \rangle$  is in agreement with the observed ones and that 20 CVn is a radial oscillator. This is the second-best solution of the modified discriminant, the first one having  $i \simeq \text{IACC}$ .

This example shows that, indeed, it is valid to work with CCFs in identifying modes, provided that one makes a very careful analysis. The moment method has not yet been tested on LSDs, but we expect similar performance. The performance of the Pixel-by-Pixel method, to which we turn next, has not yet been tested for CCFs or LSDs.

#### 6.2.4 The Pixel-by-Pixel Method

A second quantitative identification method was first introduced by Gies & Kullavanijaya (1988) and further developed by Kennelly & Walker (1996), Telting & Schrijvers (1997), Mantegazza (2000) and Zima (2006). Its use is illustrated and explained in Fig. 6.21. It is based on the properties of the amplitude and phase distribution of each oscillation frequency and its first harmonic across the entire line profile. These properties are linked to the  $(l, m)$ -value of the mode, and to the inclination angle, as can be seen from Fig. 6.21.

The computation of the amplitude and phase behaviour across the profile is particularly suited to analyse line-profile variations in moderate to rapid rotators ( $v \sin i \geq 50 \text{ km s}^{-1}$ ), because we need a high resolving power within the lines to interpret small changes in the skewness of the line, and/or moving subfeatures. The method can also be applied to slow rotators with low-degree modes, however, when combined with the moment method (see Telting *et al.* 1997 for the first such application).

A particularly promising idea related to this method was to transform the line profile variations into 2D Fourier space, where power is sought for appropriate combinations of time and spatial frequency, in analogy to what had been done for the solar oscillations. This idea was put forward by Kennelly *et al.* (1992) and was further developed by Kennelly *et al.* (1998), who applied it to the  $\delta$  Sct star  $\tau$  Peg (see Fig. 6.23). In order to obtain the amplitude of the frequency as a function of  $l$ , however, one must perform a deconvolution of the original data into a time-dependent and a time-independent broadening function, and this relies on particular assumptions. Kennelly *et al.* (1998) assumed to be dealing with p modes having  $K \simeq 0$ , with profiles having a constant intrinsic width which can be disentangled from the constant rotationally broadened profile ignoring pulsational broadening, and with spectral lines which can all be well described by one and the same linear limb darkening law. Based on these assumptions, the authors developed a deconvolution scheme

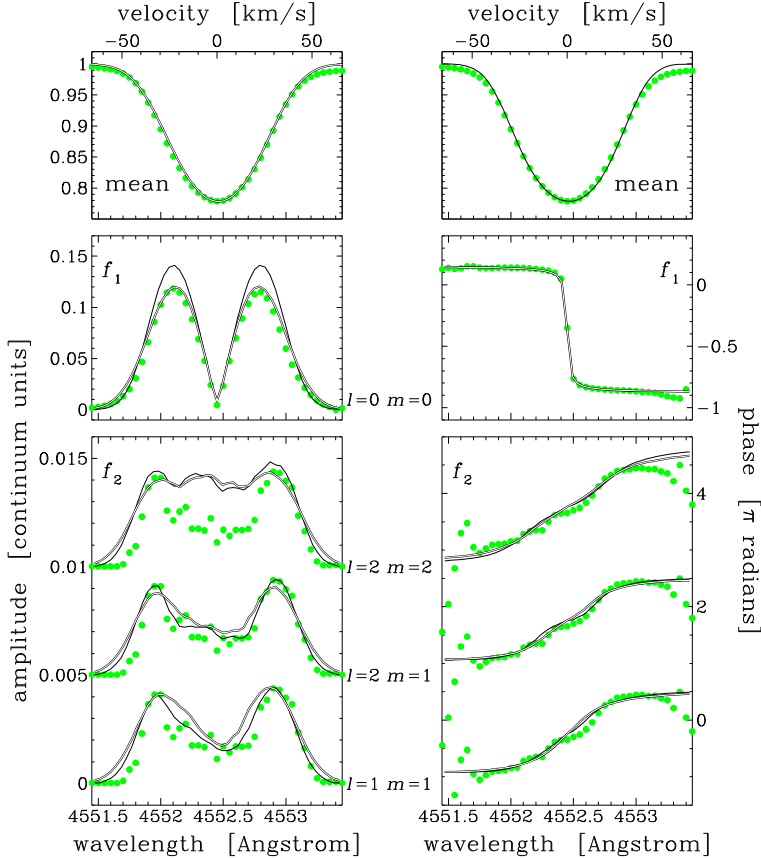


**Fig. 6.22.** Line-profile computations (full lines) for two different biperiodic models are compared with data (dots) for the star  $\beta$  Cephei. The double full line has a slightly lower rotational velocity and amplitude for the radial mode (labelled as  $f_1$ ), but a somewhat larger intrinsic width  $v_{\text{int}}$  (differences of  $2 \text{ km s}^{-1}$ ) than the single thin full line. The amplitude of the nonradial mode (labelled as  $f_2$ ) was adopted to fit the observations after having fixed the parameters of the dominant radial mode, and varies between  $1$  and  $2 \text{ km s}^{-1}$ , depending on its  $(l, m)$  assignment. The top panel shows the average profile, the middle panels the amplitude and phase across the profile for the dominant radial mode and the lower panels the amplitude and phase of the three most likely identifications of the small-amplitude nonradial mode ( $f_2$ ). Discrimination among these three possibilities is not possible. From Telting *et al.* (1997).

that connects the two-dimensional Fourier transform of the line profile with the time and spatial frequency, where the latter is assumed to be a particular measure of the mode degree  $l$  which is valid in the case of  $K = 0$ . The example shown in Fig. 6.23 shows this two-dimensional Fourier transform visually for  $\tau$  Peg. While this idea was very attractive at first sight, the many assumptions

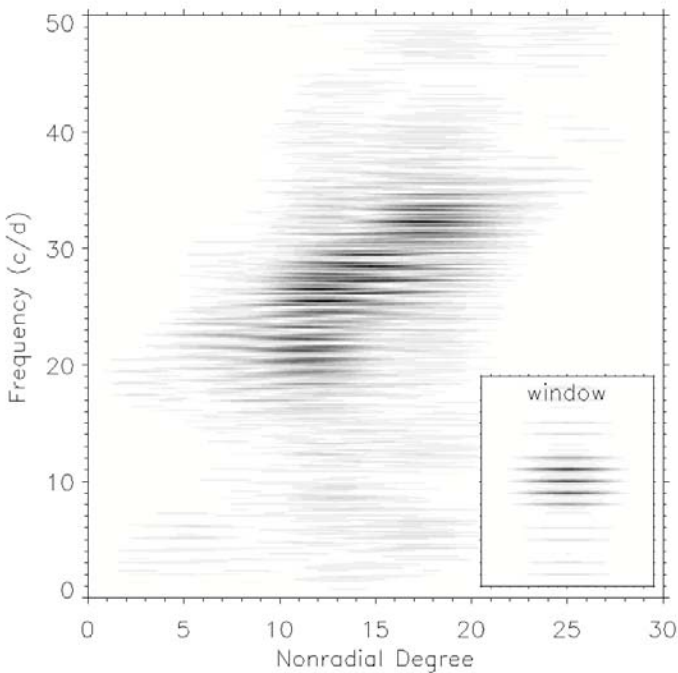


**Fig. 6.23.** The observed line profile variations of the  $\delta$  Sct star  $\tau$  Peg were Fourier transformed and displayed as a function of the degree  $l$  by relying on particular assumptions (see text). The inset is the same transform representing the pattern due to the window function and gives an idea about the uncertainty in the identification of the mode degree due to the sampling. From Kennelly *et al.* (1998).

underlying this method and the iterative manipulations of the data to end up with the result displayed in Fig. 6.23 leave a rather high level of uncertainty for the identification of the mode degree, in addition to the limitations of the predictive power introduced by the window function. This is due to the absence of a rigorous mathematical derivation of theoretical expressions for the amplitude and phase variations across the profile, as a function of  $l$  and  $m$ . Hao (1998) tried to achieve such expressions, but did not succeed. This is thus the main difference between this method and the moment method, for which such expressions are readily available in Eqs (6.58), (6.59) and (6.60).

In order to remedy this situation and to understand the behaviour of the amplitude and phase variation across the profiles, without having to rely too much on assumptions and omitting deconvolution operations, Telting & Schrijvers (1997) performed an extensive simulation study to exploit the method visualised in Fig. 6.21 in terms of mode identification. Their simulations were restricted to p modes and low-order g modes, and included the

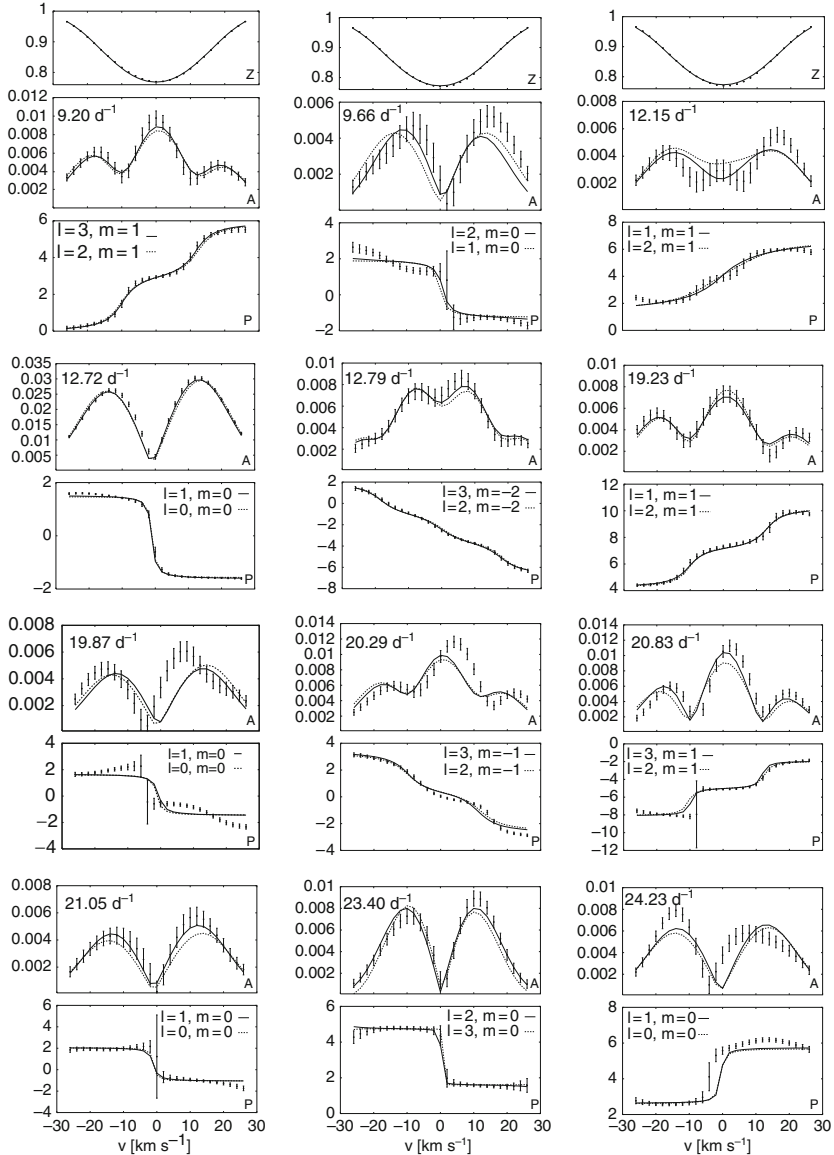


**Fig. 6.24.** Fit of the amplitude and phase across the profile for the twelve dominant oscillation modes in the spectroscopy of the  $\delta$  Sct star FG Vir. The top panels show the average, also termed zero profile (indicated as “Z”). For every single frequency, the observed amplitude (label “A”) in units of the continuum and the phase distribution (label “P”) in radians are shown together with the two best fitting models. Reproduced from Zima *et al.* (2006).

**Table 6.4.** Comparison of the results for the mode identification of the thirteen dominant modes of the multiperiodic  $\delta$  Sct star FG Vir, as available from the literature. Whenever more than one value for  $l$  or  $m$  is given in a column, discrimination among them was impossible.

Frequency $\text{d}^{-1}$	Viskum <i>et al.</i> (1998)	Breger <i>et al.</i> (1999)	Daszyńska-Daszkiewicz <i>et al.</i> (2005b)	Zima <i>et al.</i> (2006)	
9.199	$l = 2$	$l = 2$	$l = 2$	$l = 1, 2, 3$	$m = +1$
9.656	$l = 2$	$l = 1, 2$	$l = 2$	$l = 0, 1, 2$	$m = 0$
12.154	$l = 0$	$l = 0$	$l = 0$	$l = 0, 1, 2$	$m = 0, +1$
12.716	$l = 1$	$l = 1$	$l = 1$	$l = 1$	$m = 0$
12.794	–	–	$l = 2, 1$	$l = 2, 3, 4$	$m = -2$
16.071	–	–	$l = 0$	–	–
19.227	–	–	$l = 2, 1, 0$	$l = 1, 2$	$m = +1$
19.867	$l = 2$	$l = 2$	$l = 2, 1$	$l = 0, 1, 2$	$m = 0$
20.287	–	–	$l = 0, 1$	$l = 1, 2, 3$	$m = -1$
20.834	–	–	–	$l = 2, 3, 4$	$m = +1$
21.051	$l = 2$	$l = 2$	$l = 1, 0$	$l = 0, 1, 2$	$m = 0$
23.403	$l = 0$	$l = 0, 1$	$l = 2, 1$	$l = 2$	$m = 0$
24.227	$l = 1$	$l = 1, 2$	$l = 1$	$l = 0, 1$	$m = 0$

effects of the Coriolis force in the velocity eigenfunctions. They computed more than 15 000 time series of line-profile variations for different combinations of  $(l, m, v_p, i, v_\Omega, v_{\text{int}})$  considering  $l \leq 15$  and all corresponding  $m$ -values  $m \in [-l, l]$ , realistic amplitudes for the modes, with or without the effects of the Coriolis force, with or without parameterised equivalent-width variations. For each of these time series, they subsequently computed the amplitude and phase across the profile for the input frequency and its first harmonic, in the way visualised in the lower panels of Fig. 6.21. The differences in phase between the bluest and reddest point in the line profile were then derived, for the frequency ( $\Delta\psi_0$ ) and for its first harmonic ( $\Delta\psi_1$ ). The authors then compared these values for  $\Delta\psi_0$  and  $\Delta\psi_1$  with the input values for  $(l, m)$  for all these simulated time series and reached the following conclusions:

- there exists a strong correlation between the phase difference  $\Delta\psi_0$  at the blue and red edge of the profile for the oscillation frequency  $\omega$  and the degree of the mode. A good estimate of  $l$  can be derived from the empirical relation

$$l \simeq (0.10 + 1.09 |\Delta\psi_0|/\pi) \pm 1; \quad (6.72)$$

- there exists a clear, but less strong correlation between the phase difference  $\Delta\psi_1$  from blue to red for the first harmonic of the oscillation frequency  $2\omega$  and the azimuthal number of the mode. A good estimate of  $m$  can be derived from the empirical relation

$$m \simeq (-1.33 + 0.54 |\Delta\psi_1|/\pi) \pm 2. \quad (6.73)$$

The simulations of Telting & Schrijvers (1997) clearly showed that the original suggestion by Gies & Kullavanijaya (1988) to associate the phase differences  $\Delta\psi_0$  with a measure of the  $m$ -value of the mode, assuming only sectoral modes to occur, is too limited for appropriate mode identification. This was also concluded by Kennelly *et al.* (1998). In a generalisation of their work, Schrijvers & Telting (1999) took into account the effects of intrinsic profile variations and equivalent width changes as well. This resulted in very similar fitting formulae than those given in Eqs (6.72) and (6.73). A similar simulation study to the one by Telting & Schrijvers (1997), but for stars with g modes, is not available.

The fitting formulae in Eqs (6.72) and (6.73) are easy to apply once the oscillation frequencies are determined. However, they provide only a crude estimate of the degree and azimuthal order with a large uncertainty, particularly for low-degree modes. It is therefore necessary to model the amplitude and phase across the profile in full detail to achieve a reliable identification. In order to do that, one computes theoretical line-profile variations from Eqs (6.45) and (6.49), derives their amplitude and phase across the profile as in Fig. 6.21 and compares them with those derived from the observations. The earliest such application was made for the star  $\beta$  Cephei by Telting *et al.* (1997) and is depicted in Fig. 6.22 for a biperiodic model with a dominant radial mode and with the three best solutions for the identification of the second, low-amplitude mode.

Slightly different versions of the method by Telting & Schrijvers (1997) have been presented (*e.g.*, Mantegazza 2000). The most important and recent one is by Zima (2006), who introduced a statistical significance test into the method. In this way, he was able to discriminate more easily between different mode identification solutions. He tuned and applied his method, which he termed the *Pixel-by-Pixel Method* or PPM, after Mantegazza (2000), to observed line-profile variations of the  $\delta$  Sct star FG Vir (Zima *et al.* 2006). Zima *et al.* (2006) found eleven modes in the line-profile variations in common with those detected with significant amplitude in the multicolour photometry. The fits to the amplitude and phase variation across FG Vir's profile for the best two identifications of the twelve dominant modes in spectroscopy, are shown in Fig. 6.24. This shows at once the big advantage of this method over the moment method: each mode can be treated separately without having to worry about coupling between the modes, at least in the linear approximation. The drawback, however, is that its discriminating power starts to fail whenever  $v \sin i$  drops below, say typically,  $20 \text{ km s}^{-1}$ .

The spectroscopic mode identification for FG Vir is in good agreement with previous identifications. In particular, Fig. 6.24 illustrates the power to identify  $m$  from spectroscopy. In Table 6.4 we show the evolution of the ability to identify the dominant modes for this star from the literature. It can be seen that it is more difficult to find a unique  $l$ -value from the high-resolution

spectroscopy. Despite the many identified modes, a good seismic model of FG Vir is still not available. This is true in general for the class of  $\delta$  Sct stars. We thus do not return to this class in Chapter 7.

It is evident from Table 6.4 that the ideal way to proceed with mode identification of multiperiodic stars is to use multicolour photometry to find the  $l$ -values, and line-profile variations to fix  $m$ . Depending on  $v \sin i$ , a moment or PPM analysis should be preferred, but there is no reason not to do both since they are complementary. This brings us in a natural way to the following section.

### 6.3 Mode Identification from Combined Photometry and Spectroscopy

Numerous applications of the mode-identification methods outlined above are available in the literature. The successful applications mainly concern p modes in  $\beta$  Cep or  $\delta$  Sct stars, but also the dominant g modes in SPB stars (De Cat *et al.* 2005). Given the complementarity between the photometric and spectroscopic methods in terms of observational requirements and ability to derive  $l$  versus  $m$ , it is only natural to check whether consistency in the identifications is reached. This was already shown to be the case for the complex oscillations of FG Vir, besides the “simple” cases of 20 CVn and  $\rho$  Pup, all  $\delta$  Sct stars discussed above. Agreement between photometric and spectroscopic mode identifications was also achieved for the  $\beta$  Cep stars, such as for the dominant mode of  $\delta$  Ceti (Aerts *et al.* 1992; Cugier *et al.* 1994), all three modes of 16 Lac (Cugier *et al.* 1994; Aerts *et al.* 2003a), and most (but not all) of the modes of  $\nu$  Eridani (De Ridder *et al.* 2004). There are, however, also cases with differences in the mode-identification results. One example is the famous  $\beta$  Cep star  $\beta$  Cru, which was found to be a monoperiodic  $l = 2$  pulsator from photometric data (Cugier *et al.* 1994), while Aerts *et al.* (1998a) found it to have two low-amplitude modes of  $l = 3$  or 4, besides a dominant  $l = 1$  mode for the frequency detected in the photometry, from a line-profile analysis. The three modes found in the spectroscopy were later also detected in WIRE space white-light photometry (Cuypers *et al.* 2002). The misidentification from the multicolour photometry is probably due to the presence of the companion, which was ignored in that analysis but which is of similar spectral type to the oscillating component, and/or due to the neglect of the low-amplitude modes that are invisible in the ground-based photometry but clearly detected in spectroscopy. Consistency was also reached between the most likely  $l = 1$  mode identification of SPB stars as a group by Townsend (2002) and the mode identification from multicolour photometry and high-resolution spectroscopy of seven selected SPB stars by De Cat *et al.* (2005).

The case of  $\beta$  Cru brings us to the fact that several  $\beta$  Cep stars and some SPB stars have modes that are invisible in ground-based photometry, while they are clearly present in the line-profile variations. The example of  $\beta$  Cru

shows that this may occur for slow rotators, but, most frequently, such finding is obtained for moderate to rapid rotators, *e.g.*,  $\omega^1$  Sco (Telting & Schrijvers 1998),  $\lambda$  Sco (Uytterhoeven *et al.* 2004),  $\kappa$  Sco (Uytterhoeven *et al.* 2005a),  $\beta$  Cen (Ausseloo *et al.* 2006) and numerous pulsating Be stars (Rivinius *et al.* 2003), all of which have  $v \sin i$  above  $60 \text{ km s}^{-1}$ . Of course, in such cases, one cannot rely on photometry to help in the mode identification, except that one can test *a posteriori* if the solutions found from the spectroscopy are compatible with the absence of photometric variations. The many B stars found to be oscillating from WIRE (Bruntt 2007) and MOST (Walker *et al.* 2005a,b; Aerts *et al.* 2006b,c; Saio *et al.* 2006, 2007) space photometry, while being essentially constant in ground-based photometry, prove that numerous low-amplitude modes are excited by the heat mechanism.

With the occurrence of low-amplitude modes in spectroscopy, only some of which are detectable in multicolour photometry in some cases, the idea arose to obtain simultaneous observations of these kinds. This is particularly the case for  $\beta$  Cep stars, for which extensive multisite, multi-technique campaigns were initiated by G. Handler from Vienna since 2002, as already outlined in Chapter 2. Cases where the multicolour photometry allowed the derivation of  $l$ , while the spectroscopy did not, occurred for the stars  $\beta$  CMa (Handler *et al.* 2005) and  $\theta$  Oph (Shobbrook *et al.* 2006). The spectroscopists then were able to find the  $m$ -values, by fixing the photometric values for  $l$  and applying the moment method and evaluating the phase and amplitude across the profile for the best solutions as in Fig. 6.22 (Mazumdar *et al.* 2006b, Briquet *et al.* 2005). We come back to the case of  $\theta$  Oph in Chapter 7, where we discuss its seismic modelling based on the detected frequencies and the mode identification.

Whenever modes are detected in quasi-simultaneous multicolour photometry and high-resolution spectroscopy, one can do better than simply compare the mode identification results by exploiting the data simultaneously. This was first done by Daszyńska-Daszkiewicz *et al.* (2005a) for the  $\beta$  Cep stars  $\delta$  Cet and  $\nu$  Eri. These authors added the amplitude and phase of the first moment to the multicolour amplitudes and phases, and upgraded the  $\chi^2$  criterion as in Eq. (6.37) accordingly. This led them to a safer mode identification, and also an estimate of the parameter  $f_T$ , provided that the different types of data are not obtained too far apart in time to avoid different beat patterns to occur in the two types of data. From the derived  $f_T$  values for models with different opacities, the authors found a way to derive information on the most appropriate opacities to explain the modes. It is this combined method that also led to the identification of twelve modes for FG Vir discussed in the previous section and listed in Table 6.4. A natural extension of this method would be to include also the second and third moment variations to obtain an even more powerful discriminant, but this has not yet been done so far.

Finally, we point out that the empirical identification of the  $(l, m)$  values for the multiperiodic  $\gamma$  Dor stars remains difficult to achieve. There are hardly any simultaneous long-term multi-technique data sets available for such g-mode pulsators. The mode-identification results by De Cat *et al.* (2005) for

some selected SPB stars show that the modes can be successfully identified, provided that one assembles multicolour photometry and high-resolution spectroscopy with a time span of a few years. Multicolour photometry with such a time span has been assembled from multisite campaigns dedicated to specific targets such as 9 Aur (Zerbi *et al.* 1997a), HD 164615 (Zerbi *et al.* 1997b), QW Pup (Poretti *et al.* 1997), HR 8799 (Zerbi *et al.* 1999), and from single-site campaigns dedicated to samples of  $\gamma$  Dor stars (Henry *et al.* 2004; Henry & Fekel 2005; Cuypers *et al.* 2009). Long-term spectroscopic campaigns for large samples were also carried out (Mathias *et al.* 2004; De Cat *et al.* 2006). Unfortunately, these extensive data have not led to mode identification. The modes of only five  $\gamma$  Dor stars have been identified so far from multicolour photometry (Dupret *et al.* 2005b). This seems to point towards the excitation of only  $l = 1$  modes, but this conclusion must be considered as preliminary. Indeed, a huge ground-based campaign set up for the CoRoT main target  $\gamma$  Dor star HD 49434, which is a fairly rapid rotator, only revealed modes with  $l > 2$  (Uytterhoeven *et al.* 2008). Very likely, ground-breaking results for g-mode oscillators will come from the CoRoT and Kepler photometry, in combination with ground-based spectroscopy.

## 6.4 Towards Mode Identification from Combined Interferometry and Spectroscopy?

In an extensive review, Cunha *et al.* (2007) have discussed the synergies and cross-fertilisation between interferometry and asteroseismology. Interferometric measurements can help a lot in asteroseismic analyses in several different ways. Direct radius estimates with a relative precision better than a few per cent, *e.g.*, can be obtained for several hundred stars in the solar neighbourhood with VLTI/AMBER. The masses of binary stars with a pulsating component can be derived independently from asteroseismology by interferometry, with precision of only a few per cent. As far as mode identification is concerned, the combination of interferometric and spectroscopic data allows, in principle, the identification of the oscillation modes.

The PPM method described above exploits the amplitude and phase across the profile as a mode-identification diagnostic by relying, through Eqs (6.45) and (6.49), on the expression for the pulsational velocity in terms of  $l$  and  $m$ . The Doppler effect is considered to be the dominant source of information in identifying  $l$  and  $m$  from the variations through Eq. (6.49). A new interesting idea was put forward by Berdyugina *et al.* (2003a). They inverted a time series of line-profile variations, in this way turning the data into a stellar surface brightness distribution. This comes down to an image reconstruction method, also termed Doppler Imaging in the context of spotted stars. They applied this inversion without assuming any prior knowledge of the physical cause of the variations of the line profiles. After having performed the inversion,

the authors assumed that the most important cause of the line-profile variations are surface brightness variations superposed onto a time-independent broadened Doppler profile. Rather than focusing on  $v(R, \theta'_i, \phi'_j, t)$  in the interpretation through Eq. (6.49), they thus considered  $\delta[F_\lambda(\theta', \phi')]$  to be the dominant information for the mode identification. Such a situation may occur for rapidly rotating stars, whose velocity perturbation due to the oscillations is very small compared with its rotational broadening. In such a case, the pulsation-induced intensity perturbations gain importance with respect to the velocity perturbations. Berdyugina *et al.* (2003b) applied their method to the  $\beta$  Cep star  $\omega^1$  Scorpii and found it to be capable of recovering  $l$  and  $m$  of the oscillation, which had been derived before from a PPM-like application by Telting & Schrijvers (1998). This brings us to the capability of combining surface brightness variations, *e.g.*, derived from interferometry, with surface velocity variations derived from high-resolution spectroscopy.

Long before the availability of appropriate instrumentation, Vakili *et al.* (1994) had already suggested the study of surface variations due to nonradial oscillations of rapidly rotating stars from long-baseline differential interferometry (see Cunha *et al.* 2007 for the technicalities of how this can be achieved). As shown by Jankov *et al.* (2001, 2002), such a combined technique can be successful in identifying oscillation modes with  $l > 2$  in rapid rotators, providing information on the modes that can perhaps not be obtained from each of the two types of observations, interferometry and spectroscopy, separately. The flux variations due to the nonradial modes introduce a complex pattern in the so-called interferometric  $UV$  plane (Cunha *et al.* 2007). This pattern can be disentangled by comparing the photocentre displacements in this plane due to the oscillations with predicted monochromatic intensity maps of a constant star. In practice, one simulates photocentre displacements as a function of  $(l, m, i)$ . Such a simulation defines a kind of “spatial filter” for each  $(l, m, i)$ . Applying one-by-one all these spatial filters to the data allows one to identify the true nature of the mode. This is illustrated in Fig. 6.25, in which the original signal in panel (a) is compared with a map (b) recovered from spectra alone with a method similar to the one of Berdyugina *et al.* (2003a), as well as with the map based on the photocentre shifts alone displayed in panel (c), and a combination of both shown in panel (d). The limitations of panels (b) and (c) are particularly apparent in the reconstruction of the features below the equator, where a loss of contrast occurs. A significant improvement with respect to these separate reconstructions is obtained using both spectra and photocentre shifts simultaneously, as in panel (d).

Domiciano de Souza *et al.* (2002, 2003) and Jankov *et al.* (2004) showed that measurements of the displacement of the photocentre across the stellar disc allows mapping of the surface brightness, but requires a minimum of three telescopes in an interferometric array in such a way that fringes are collected for all three baselines. The simulation study by Jankov *et al.* (2004) anticipates that the interferometric measurements are sufficiently sensitive to detect a mode of low  $(l, m)$ . In general, however, numerous modes are

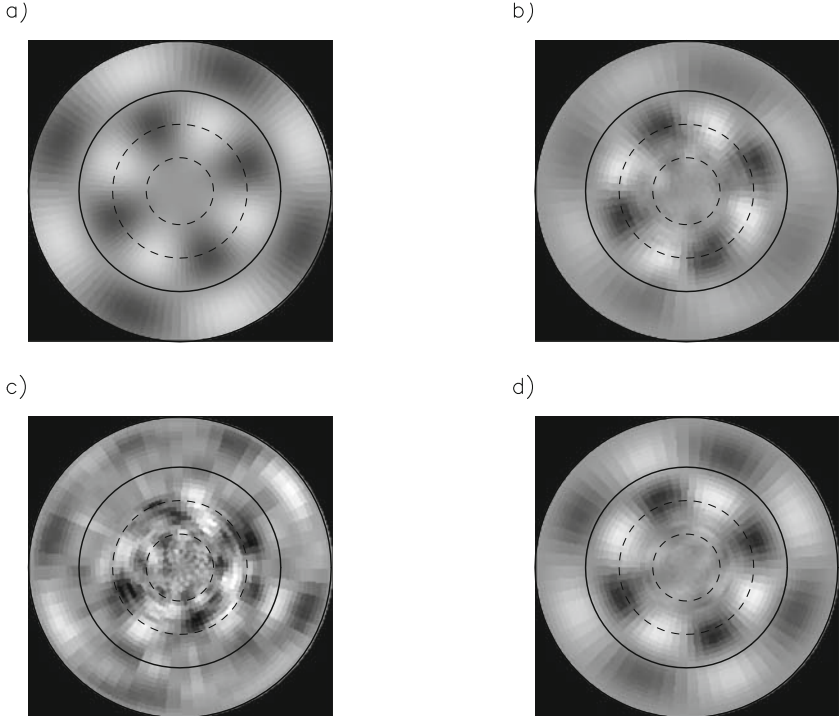


**Fig. 6.25.** (a) Simulation of the pole-on projection of the stellar surface brightness perturbations due to an  $l = 5, m = 4$  mode on a star with an inclination angle of  $i = 45^\circ$ . The equator and the latitudes  $30^\circ$  and  $60^\circ$  are presented by full and dashed circles, respectively. Reconstruction based on (b) simulated flux spectra, (c) photocentre shifts, and (d) combined flux spectra and photocentre shifts. From Jankov *et al.* (2002).

simultaneously excited. In such more realistic cases, the photocentre displacements are “washed out” by the averaging effect of the many  $(l, m)$ -values. In that case, one can still obtain identification for a fixed number of oscillation frequencies which have been derived from time series analysis of observables of any kind. When carrying out the interferometric measurements, a selected oscillation frequency is used to phase-lock the data to this frequency. In this way, all surface structures that are not associated with this frequency are assumed to be removed, greatly improving the signal strength for the frequency under consideration. Such frequency filtering can be done as a post-processing step by an appropriate weighting procedure. It is possible to design the appropriate weights for each of the measured oscillation frequencies separately, and use the same set of interferometric observations to constrain the identification of all the oscillation modes whose frequencies are known from other diagnostics.

Concrete applications of this promising mode-identification method are still awaited.

## 6.5 Towards Mode Identification from Eclipse Mapping?

Unno *et al.* (1989, p.22) pointed out the possibility to observe phase shifts due to nonradial oscillations during the eclipse of a pulsating star by a companion, and to use this as a mode-identification method. No applications of this technique existed at the time they wrote the second edition of their monograph on nonradial oscillations of stars. Unno *et al.* (1989) realised that the earlier interpretation of phase jumps of  $360^\circ$  in the nova-like binary UX UMa in terms of nonradial oscillation modes of  $l = 2$  by Nather & Robinson (1974) was premature, and that the observed phase phenomenon could be far better explained in terms of an oblique rotator model.

Current versions of the eclipse-mapping method for cataclysmic variables are based on the original development by Horne (1985). He introduced the method with the goal of mapping the surface brightness distributions in eclipsing cataclysmic variables. Eclipse mapping allows a test of accretion theory because the spatial structure of the discs can be derived from the light-curve behaviour. Moreover, the spot structure, including the hot spot originating from the collision of the stream of the donor onto the disc of the gainer, can be derived. For early applications to interacting binaries we refer to, *e.g.*, Rutten *et al.* (1993), Collier Cameron & Hilditch (1997) and Hilditch *et al.* (1998).

In the case of mode identification of a non-radially pulsating star in an eclipsing binary, one needs to reconstruct a time-dependent intensity map from the data, and subsequently infer the amplitude and phase behaviour of the pulsation mode. Nuspl & Bíró (2002) and Nuspl *et al.* (2004) modified Horne's method for mode identification from photometric data, as did Gamarova *et al.* (2003) who baptised their method the Spatial Filtration method. Unfortunately, these studies were only published in short proceedings papers and there is as yet no extensive simulation study of the methodology, highlighting its applicability to multiperiodic oscillations and an evaluation of the uniqueness of solutions.

While several  $\delta$  Sct stars in eclipsing binaries are known (Pigulski 2006), the mode identifications performed for them are almost all based on the out-of-eclipse data, *e.g.*, RZ Cas (Ohshima *et al.* 2001; Rodríguez *et al.* 2004b) and Y Cam (Kim *et al.* 2002). The next step towards application of mode identification through eclipse mapping was performed by Mkrtichian *et al.* (2004) for the Algol-type eclipsing binary star AS Eri. They did not use the eclipse-mapping method, but they excluded the odd  $l + m$  combinations of  $(l, m)$  from the fact that their disc-integrated amplitude disappears during the eclipse. Rodríguez *et al.* (2004a,b) made preliminary estimates of  $(l, m)$  for the Algol-type eclipsing binaries AB Cas and RZ Cas from Spatial Filtration.

Rodríguez *et al.* (2004a) also applied Spatial Filtration to AB Cassiopeia. Both studies provided a radial mode for the star, in agreement with the out-of-eclipse identification. This result was recently confirmed by Riazi & Abedi (2006), who considered only radial modes in their methodology. As far as we are aware, the case of AB Cas, a radial pulsator, is the only application they made so far.

By far the best documented version of mode identification from photometric data using eclipse mapping was provided by Reed *et al.* (2005). While their primary goal was to search for evidence of tidally tipped pulsation axes in close binaries, they also made simulations for the very specific case of eclipse mapping of pulsating subdwarf B star binaries, *i.e.*, assuming that the secondary has more or less the same size as the primary and does not contribute to the light. They assumed that the pulsation axis can take any value and is not necessarily aligned with the rotation or orbital axis. They investigated how the visibility of different types of modes varies between the out-of-eclipse and in-eclipse phase. In particular, they found that  $l > 2$  modes become visible during an eclipse while they are essentially absent outside of eclipse. Their tools have so far only been applied to concrete cases of KPD 1930+2752 (Reed *et al.* 2006a) and of PG 1336–018 (Reed *et al.* 2006b; see also Fig. 2.61) but without clear results.

We must conclude that, still today, more than 35 years after the original idea of Nather & Robinson (1974), eclipse mapping has hardly been evaluated critically as a mode-identification method, nor has it been applied successfully in practice for binary stars that have been subjected to seismic modelling afterwards.

We end this Chapter by directing attention to the software package **FAMIAS**<sup>1</sup> (**F**requency **A**nalysis and **M**ode **I**dentification for **A**stero**S**eismology; Zima 2008) which was developed in the framework of the FP6 Coordination Action in Helio- and asteroseismology (HELAS<sup>2</sup>). This package allows mode identification from multi-colour photometry or high-resolution spectroscopy with the methods discussed in this Chapter. Along with FAMIAS, a **D**atabase for **A**stero**S**eismology (DAS<sup>3</sup>), which contains numerous published suitable data sets to apply FAMIAS to, has been published in the framework of HELAS as well (Østensen 2008).

---

<sup>1</sup> <http://www.ster.kuleuven.be/~zima/famias/>.

<sup>2</sup> <http://www.helas-eu.org/>.

<sup>3</sup> <http://newton.ster.kuleuven.be/~roy/helas/>.

---

## Applications of Asteroseismology

This chapter is devoted to case studies of asteroseismology, starting with a section on *helioseismology*, which also discusses aspects of stellar oscillations of specific relevance to this case. We have selected stars that have been the subjects of successful seismic modelling, in the sense that quantitative measures of internal structure parameters have been derived from their oscillations or that shortcomings in the current stellar models were encountered when fitting the oscillation frequencies. We did not aim to present an overview of applications of asteroseismology, but rather to highlight some carefully chosen examples across the HR diagram that are instructive to illustrate the current status of the research field. Our choice is biased towards the interests of the authors.

### 7.1 Helioseismology

#### 7.1.1 Introduction

Quite apart from its obvious practical importance, the Sun is an ideal case for seismic investigations. Its proximity makes it the only case where oscillations of high degree (up to  $l \gtrsim 1500$ ) can be studied. As discussed in Sections 7.1.7 and 7.1.8 this provides sufficiently extensive, rich sets of data that we can infer properties as functions of position within most of the solar interior. Also, we have accurate determinations of the solar mass, radius and luminosity as well as independent determinations of the age of the solar system, from radioactive dating of meteorites, further constraining the solar models. The solar surface rotation rate can be determined directly from Doppler observations and from the apparent motion of features on the surface, showing a *differential rotation* with latitude, the equator rotating more rapidly than the poles. Finally, very detailed spectroscopic analysis has been used to determine the composition of the solar atmosphere, which in many cases can be verified through comparison with the composition of undifferentiated meteorites; however, as

discussed in Section 7.1.7, recent analyses have raised some questions about the abundances of carbon, oxygen and nitrogen in the solar atmosphere.

Here we consider mainly the study of the solar interior on the basis of observed frequencies of global modes of the Sun; such *global helioseismology* is obviously the case of most relevance to asteroseismic studies of other stars. However, we note that the high spatial resolution of solar data has also allowed the development of *local helioseismology*, based on the analysis of other aspects of the wave field on the solar surface. This has provided information about the three-dimensional time-dependent properties of the subsurface layers, flows associated with large-scale convection, meridional flows in the solar convection zone and the wave propagation speed beneath active regions. Such investigations are of major importance to the understanding of the dynamic solar interior, including the origin and properties of the solar magnetic cycle; however, they are beyond the scope of the present book. We refer instead to the major review by Gizon & Birch (2005).

General overviews of the properties of the Sun have been provided, for example, by Stix (2002) and Foukal (2004), while Schrijver & Zwaan (2000) discussed the magnetic activity of the Sun and sun-like stars. An extensive review of helioseismology was given by Christensen-Dalsgaard (2002), while Chaplin & Basu (2008) gave a recent overview of the present status and perspectives of global helioseismology. Basu & Antia (2008) presented a detailed discussion of helioseismology, emphasizing the application to solar structure and in particular the consequences of the assumed solar composition, while Howe (2009) similarly considered solar rotation, particularly from the point of view of helioseismic inferences. Here we discuss aspects of stellar oscillations which so far are specific to the solar case, including the application of inverse analyses, and present some recent results of helioseismology.

### 7.1.1.1 Solar Modelling

In many ways the Sun is a simple star. It is half-way through central hydrogen burning, it does not have a convective core and it is slowly rotating. Also, compared with other stars the conditions in the solar interior are relatively benign. On the other hand, its proximity allows us to realize the complexity of the phenomena in even simple stars. Particularly striking is the complex magnetic activity, varying in a 22-year cycle, which dominates the properties of the outer solar atmosphere. Based on our understanding of the solar magnetic activity, evidence for similar activity, in some cases much more dramatic, has been found in other stars, although the observational data are unavoidably very limited. Another important set of observations, so far only possible, amongst main-sequence stars, in the Sun is the measurement of the flux of neutrinos from the nuclear reactions in the solar core (*cf.* Section 3.2.2). As reviewed by Bahcall (1989) there was until fairly recently an apparent discrepancy between the measured flux and the flux predicted by solar models, possibly indicating deficiencies in stellar modelling. In fact, helioseismology

provided strong indications that the model predictions were essentially correct (see Section 7.1.7); this was confirmed with the detection of the conversion of the electron neutrinos generated in the nuclear reactions into other types of neutrinos, the combined number agreeing with the solar models. Recent reviews on solar neutrinos were provided by Bahcall & Peña-Garay (2004), McDonald (2004) and Haxton *et al.* (2006).

A model of the Sun must obviously be consistent with the accurately known overall properties: the solar mass, radius and luminosity,  $M_\odot$ ,  $R_\odot$  and  $L_\odot$ , at an assumed age  $\tau_\odot$  of the present Sun. In addition, the model should match the observed surface composition, often represented by the ratio  $Z_s/X_s$  between the abundance by mass of heavy elements and hydrogen. Although helium, as indicated by its name, is observed in the solar spectrum, the lines are formed under conditions that are too complex to allow a reliable determination of the abundance. Thus the individual abundances of hydrogen and heavy elements cannot be determined. Since mass loss is typically neglected in solar modelling, the models are calculated with the appropriate mass. To match the remaining observables,  $R_\odot$ ,  $L_\odot$  and  $Z_s/X_s$ , at  $\tau_\odot$  the models are calibrated by adjusting three parameters that are otherwise essentially free: a parameter, such as the mixing-length parameter  $\alpha_{\text{ML}}$ , characterizing the near-surface convection (*cf.* Section 3.2.1) and the initial abundances  $Y_0$  and  $Z_0$  of helium and heavy elements.<sup>1</sup> All models discussed in the present section are assumed to be calibrated in this manner.

The near-surface layers of solar-like stars present particular problems in the modelling of the stars and their oscillations. The use of the mixing-length formulation in the treatment of convection is an obvious limitation, in the superficial part of the convection zone where the temperature gradient is substantially superadiabatic. Also, turbulent Reynolds stresses, often described as a turbulent pressure, undoubtedly have a significant effect on the hydrostatic structure of stellar models, given that the convective Mach number approaches unity near the surface. Nonadiabaticity and other effects of mode excitation clearly affect the oscillations in this region. Although nonadiabatic calculations of stellar oscillations are entirely feasible (see Section 3.7), the treatment of the effects of the convective flux and turbulent pressure on the oscillations remains a serious uncertainty (*cf.* Section 3.7.3). As discussed in Section 7.1.7 these issues play a major role in the analysis of the observed solar oscillations.

Important goals of the helioseismic analysis of observed frequencies are evidently to test both the microphysics of the solar interior and the other assumptions underlying the model calculation. A complication is that a given region of the model in general is affected by several aspects of the microphysics, *e.g.*, both the opacity and the equation of state; under these circumstances it may evidently be difficult or impossible to isolate the cause of discrepan-

---

<sup>1</sup> As diffusion and settling are generally included in the modelling, these do not match the present surface abundances.

cies between observations and models. In the analysis of solar data a very considerable simplification results from the presence of the convection zone, despite the uncertainties in the detailed description of convection. The reason is that, regardless of these uncertainties, there is no doubt that convection in almost the entire convection zone is a very efficient means of energy transport, requiring only a minute superadiabatic gradient. Thus to a very good approximation the relation between pressure and density is determined by

$$\frac{d \ln \rho}{d \ln p} \simeq \frac{1}{\Gamma_1}, \quad (7.1)$$

such that the specific entropy  $s$  is virtually constant; accordingly, the temperature structure is essentially adiabatic and hence independent of opacity. The value of  $s$  is determined by the structure of the thin region just beneath the surface where the gradient is significantly superadiabatic, as characterized, for example, by the value of the mixing-length parameter  $\alpha_{ML}$ . It follows that the structure of the bulk of the convection zone is determined just by the value of  $s$ , by the composition (which, because of the very efficient mixing can be assumed to be uniform), and by the equation of state. Consequently modes of oscillation that are sensitive just to the structure of the convection zone are ideally suited to test the properties of the equation of state and to determine the solar composition (see also Christensen-Dalsgaard & Däppen 1992). It will be shown in Section 7.1.4 that solar five-minute oscillations of degree higher than about 40 have this property.

### 7.1.1.2 A Brief History of Helioseismology

The first detections of oscillatory motion in the solar atmosphere, with periods near five minutes, were made by Leighton (1961) and Leighton *et al.* (1962). Measurements in small regions on the solar surface (*e.g.*, Musman & Rust 1970) suggested that these might be localized oscillations, possibly excited by granular motion. However, preliminary observations by Frazier (1968) of the distribution of power with wavenumber  $k_h$  and frequency  $\nu$  led Ulrich (1970) and Leibacher & Stein (1971) to suggest that the oscillations were acoustic modes trapped in the solar interior. This was dramatically confirmed by the observations of Deubner (1975) which showed a clear modal structure in the  $(k_h, \nu)$  diagram. The analysis by Ulrich, and more detailed modelling by Ando & Osaki (1975), showed that these were modes trapped in outer parts of the convection zone. Although they therefore only provided direct information about this region, this constrains the adiabat of the bulk of the convection zone (*cf.* Section 3.2.1.3) and hence its overall structure. Thus, Gough (1977b) showed that to match the observations the depth of the convection zone had to be substantially higher than the value in the models of the time; he inferred a value close to the 200 Mm now determined from helioseismic analysis of more complete data (*cf.* Section 7.1.7).

At approximately the time when Deubner's results were published, additional data strongly indicated the presence of global solar oscillations. Hill *et al.* (1976) found a set of peaks in measurements of the apparent solar diameter, corresponding to periods between around 5 and 60 min, and preliminary calculations seemed to indicate that they were consistent with frequencies of a solar model. Also, Brookes *et al.* (1976) and Severny *et al.* (1976) detected an oscillation in the solar Doppler shift with a period very close to 160 min. The latter detection clearly suggested the presence of a high-order g mode but the lack of additional observed modes in the relatively dense predicted g-mode spectrum was peculiar; however, their presence appeared to be confirmed by further observations (Scherrer *et al.* 1979; Severny *et al.* 1979<sup>2</sup>). These detections, even more than Deubner's observations of high-degree modes trapped near the surface, immediately suggested the possibility of seismic investigations of the entire solar interior and led to a flurry of activity (*e.g.*, Scuflaire *et al.* 1975; Christensen-Dalsgaard & Gough 1976; Iben & Mahaffy 1976). It is somewhat ironic that this promise of helioseismology has since been amply fulfilled, beyond the wildest dreams of the initial investigations, while the observations of the diameter oscillations and the 160-minute oscillations have failed to be confirmed by later data.

The first true detection of global solar modes of oscillation was obtained by the Birmingham group (Claverie *et al.* 1979) who found five-minute oscillations in light integrated over the solar disc, indicating that the modes were of low degree. Evidence for power in this frequency region had previously been found by Fossat & Ricort (1975) although without resolving the modal structure. This was followed by a week-long nearly continuous observation in integrated light from the geographical South Pole by Grec *et al.* (1980), which clearly resolved the multiplet structure of the oscillations, confirming the asymptotic behaviour of high-order acoustic modes (*cf.* Section 3.4.3, in particular Eq. (3.219)) and determining the large and small frequency separations. It is interesting, as discussed in Section 2.3.1, that present observations of solar-like oscillations in other stars are now at a similar stage to these early helioseismic results. From more extensive observations of low-degree modes, particularly with the beginning BiSON network, it became clear that models of the solar core were in reasonable agreement with the observations, while this was not the case for models modified to reduce the neutrino flux to match the neutrino detections (see above). Thus Elsworth *et al.* (1990) concluded that, unlike standard solar models, models proposed to explain the low observed neutrino flux were inconsistent with the observed small separation; on this basis they argued for a solution to the neutrino discrepancy in terms of neutrino oscillations and a finite neutrino mass, as confirmed by more recent neutrino measurements.

Given just the low-degree modes, the degrees of the modes, as in the case of solar-like stars, could be determined from the structure of the frequency

---

<sup>2</sup> This appears to be the first paper where the term “helioseismology” was used.

spectrum by identifying the small separations between modes of degree 0, 2 and 1, 3. However, as in the stellar case there was no observational determination of the radial order. Christensen-Dalsgaard & Gough (1981) fitted solar models to the observed frequencies and in this way obtained a plausible mode identification. The major breakthrough came with the observations of Duvall & Harvey (1983) who covered the range of degree from the low-degree modes to the results of further observations of high-degree modes by Deubner *et al.* (1979). In the latter case, modes of the full range of radial orders, starting at the f mode, had been observed and by following the modes to lower and lower degree a full identification could be established.

On the basis of these results, including the determination of the rotational splitting between modes of azimuthal order  $m = \pm l$  (Duvall & Harvey 1984), it was possible to infer the variation of the solar internal angular velocity as a function of radius near the equatorial plane (Duvall *et al.* 1984); this, somewhat surprisingly, showed that the radiative interior rotated at or perhaps slightly below the surface equatorial rate. Also, Christensen-Dalsgaard *et al.* (1985) carried out the first asymptotic inversion for the solar internal sound speed, finding reasonable agreement with solar models although with evidence that the opacity required an increase in the region below the convection zone.

The final major breakthrough in observational global helioseismology was the detection of modes over a range in  $m$ , allowing the study of the latitude variation of solar rotation (Brown 1985; Duvall *et al.* 1986; Libbrecht 1988a). Already the early analyses of such data (*e.g.*, Brown & Morrow 1987; Christensen-Dalsgaard & Schou 1988; Kosovichev 1988; Brown *et al.* 1989; Dziembowski *et al.* 1989) established the presence of a region of strong shear, dubbed the *tachocline* by Spiegel & Zahn (1992) near the base of the convection zone; these results led to a drastic revision of the dynamo models attempting to account for the solar magnetic cycle.

The early successes of helioseismology have motivated major observational efforts. To reach the required frequency precision, observations extending over at least several weeks or months are required. A severe problem for such observations of solar (and stellar) oscillations is the gaps in data from single-site observations; as discussed in Section 5.3 these increase the noise level and greatly complicate the analysis of the data. As mentioned above, continuous data extending over several days can be obtained from Antarctica, although even there breaks in the observations may be introduced by weather. In order to ensure near continuity over longer periods it is necessary to combine data from several sites or to carry out observations from space. This led quite early to multi-site disc-integrated observations by the BiSON<sup>3</sup> group, expanded into a six-station network that has been operating since 1992 (Chaplin *et al.* 1996). Extensive disc-integrated data have also been obtained by the IRIS<sup>4</sup>.

---

<sup>3</sup> Birmingham Solar Oscillation Network, <http://bison.ph.bham.ac.uk>.

<sup>4</sup> Installation d'un Réseau International de Sismologie solaire; see <http://www-luan.unice.fr/iris/>.

network (Fossat 1991). A major ground-based effort is the GONG<sup>5</sup> project (Harvey *et al.* 1996); this has established a six-station network of observatories in operation since 1995, with an optimal global distribution to secure nearly continuous data, carrying out helioseismic observations with high spatial resolution. Observations from space have been carried out by the very successful SOHO<sup>6</sup> spacecraft (Domingo *et al.* 1995), in operation since 1996<sup>7</sup> at the first Lagrange point L<sub>1</sub> point between the Sun and the Earth.

A more detailed overview of the development of helioseismology was provided by Christensen-Dalsgaard (2004a). Very enjoyable accounts, including a general introduction to the field, were given in the books by Zirker (2003) and Chaplin (2006).

### 7.1.1.3 Observations of Solar Oscillations

The solar oscillations evidently affect many aspects of the solar atmosphere and hence may be observed with a number of different techniques. An overriding requirement is obviously to reach a sufficient signal-to-noise ratio in the face of the very small oscillation amplitudes: the velocity amplitude per mode is typically less than  $15 \text{ cm s}^{-1}$ , while the corresponding amplitude in broad-band intensity is around 4 parts per million (4 ppm) (see also Section 2.3.1). This places strong demands on the stability of the observing techniques, in terms of wavelength references for velocity observations or photometric stability for intensity observations. The solar background “noise”, resulting from phenomena other than the oscillations, must also be taken into account: as noted by Harvey (1988) this background is substantially higher, relative to the oscillations, for intensity than for velocity observations (see also Fig. 4.1). An additional important issue is the possibility of observations resolving the variation of the oscillations across the solar disc and hence allowing detection of modes of higher degree. However, as discussed below, disc-integrated observations, *i.e.*, observations in light integrated over the disc of the Sun, also provide very valuable information about low-degree modes. Finally, we note that observations of the same modes with different techniques, such as velocity and intensity, provides information about the behaviour of the oscillations in the solar atmosphere and hence in principle about mode physics or atmospheric structure.

At the very low amplitudes of solar oscillations, the effects of the Earth’s atmosphere make observations in broad-band intensity impractical from the ground (but see Nishikawa 1986). However, from space such observations are feasible. Early observations were made in irradiance by the Solar Maximum

<sup>5</sup> Global Oscillations Network Group; see <http://gong.nso.edu/>.

<sup>6</sup> SOlar and Heliospheric Observatory.

<sup>7</sup> Apart from relatively brief periods, including June – October 1998, where contact was lost with SOHO because of operational or technical problems (see *Nature*: 394, 5; 395, 313; 396, 399).

Mission (*e.g.*, Woodard & Hudson 1983), even though the instrumentation was not designed for this purpose, and interesting results were obtained from the Phobos mission to Mars (Toutain & Fröhlich 1992). In both cases disc-integrated observations were made, and hence only modes of the lowest degrees were detected (*cf.* Fig. 1.5). The SOHO spacecraft carries the VIRGO<sup>8</sup> instrument (Fröhlich *et al.* 1995, 1997) to measure irradiance variations and to carry out disc-integrated oscillation observations in three wavelength intervals, as well as intensity observations with limited spatial resolution.

Oscillation observations in line intensity, relative to the surrounding continuum, is feasible from the ground. Particularly successful have been observations in the calcium H and K lines which have been used in several productive observing campaigns from the South Pole (*e.g.*, Duvall *et al.* 1986; Jefferies *et al.* 1988), as well as in the Taiwanese Oscillation Network (TON; Chou *et al.* 1995).

In radial-velocity observations the critical issue is to secure wavelength stability, either through the design of the instrument or with a stable reference. An ingenious example of the latter possibility is to use the location of the Zeeman-split components of the lines in an alkaline vapour in a stable magnetic field. This was developed by Isaak (1961) and Fossat & Roddier (1971) and has been used very successfully for helioseismic observations. In its simplest form it is used in disc-integrated observations. Here light from the Sun is scattered resonantly on the Zeeman-split components and the intensity difference between the contributions from the two components, distinguished by their polarization, provides a very stable measure of the averaged velocity of the solar surface (for details, see Brookes *et al.* 1978). These observations led to the first detection of global solar five-minute oscillations (Claverie *et al.* 1979) and the first observations, from the South Pole, which clearly resolved the multiplet structure of these modes (Grec *et al.* 1980). Full-disc observations using a potassium vapour are used in the BiSON network (Chaplin *et al.* 1996). Also, similar observations using sodium vapour were used in the IRIS network (Fossat 1991) and are used in the GOLF<sup>9</sup> instrument for disc-integrated observations on the SOHO spacecraft (Gabriel *et al.* 1995, 1997).

Cacciani & Fofi (1978) developed a variant of the resonant cell technique where two cells are used to make a filter that alternates between the red and blue wings of the sodium lines, allowing the velocity field across the solar surface to be resolved (see also Rhodes *et al.* 1986). This has been used for extensive observations from the Mt Wilson observatory (*e.g.*, Rhodes *et al.* 1987, 1993). Furthermore, the technique provided very stable observations

---

<sup>8</sup> Variability of solar Irradiance and Gravity Oscillations.

<sup>9</sup> Global Oscillations at Low Frequency;  
see <http://golfwww.medoc-ias.u-psud.fr/>.

with the LOWL<sup>10</sup> instrument (Tomczyk *et al.* 1995), extended into the two-station ECHO network, which is currently not operating.

A very widely used technique was originally developed by Brown (1984) in the form of the so-called *Fourier Tachometer*. Here a Michelson interferometer is used as a filter to isolate four passbands across a suitable spectral line. By combining observations of the intensity in these passbands a velocity image can be constructed. This has proven a very stable and sensitive technique, allowing observations with very high spatial resolution. Fairly extensive results from the original Fourier Tachometer were presented by, for example, Brown (1985), Bachmann *et al.* (1993) and Schou & Brown (1994). A modification of this technique has been used in the two main helioseismic projects to measure oscillations in Doppler velocity with spatial resolution: the GONG project (Harvey *et al.* 1996) and the MDI<sup>11</sup> instrument (Scherrer *et al.* 1995; Rhodes *et al.* 1997) on the SOHO spacecraft.

The huge helioseismic observational efforts over the past several decades have resulted in very extensive datasets. Although many of these have contributed to our understanding of the solar interior, four sets stand out:

- The BiSON disc-integrated Doppler-velocity data that extend over three decades (see Chaplin *et al.* 2007a), with a full six-station network in operation since 1992.
- The results from the GONG six-station network on Doppler-velocity oscillations, starting in 1995 and upgraded to higher resolution in 2001 (Harvey *et al.* 1996, 1998).
- The GOLF disc-integrated observations from the SOHO spacecraft, starting in 1996 (*e.g.*, Gabriel *et al.* 1997). Although originally designed to observe Doppler velocity, the observations have for most of the mission been made in just the intensity of either the blue or red wing of the sodium D lines, owing to technical problems (see García *et al.* 2005). However, these observations are still dominated by the Doppler shift and have proved to be of very high quality.
- The MDI observations in Doppler velocity, starting in 1996 (Scherrer *et al.* 1995; Larson & Schou 2008). These have been run nearly continuously in the so-called medium- $l$  programme with a 20 arcsecond resolution, covering modes of degree  $l$  up to around 300. In addition, there have been yearly campaigns of a duration of 2–3 months, with a resolution of 4 arcseconds, in the so-called dynamics programme; this allows the study of modes with  $l$  as high as 1500.

We note in particular that by having observations over more than a sunspot 11-year cycle and, in the case of BiSON, more than three such cycles, the

---

<sup>10</sup> This is not an acronym; it refers to the design of the instrument to make it suitable for modes of low degree.

<sup>11</sup> Michelson Doppler Imager; see <http://soi.stanford.edu/>.

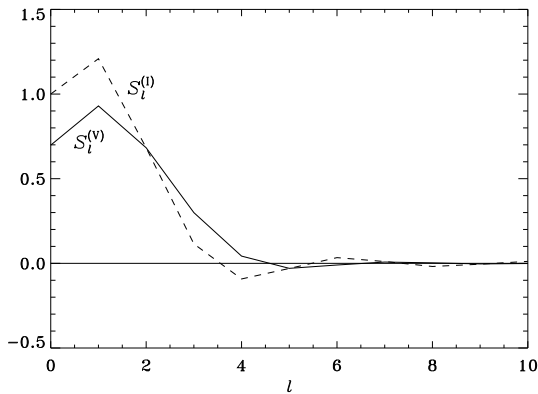


**Fig. 7.1.** Spatial response functions for intensity observations (dashed curve) and radial velocity observations, assuming a negligible horizontal component of the velocity (solid curve), computed for a typical solar limb-darkening profile. The response functions are defined such that, for example, the observed combined radial-velocity signal for all the modes for given  $n$  and  $l$ , excited to the average amplitude  $V_0$  and with random phases, is  $S_l^{(V)} V_0$ . See Christensen-Dalsgaard & Gough (1982).

data have allowed investigations of the possible variation in the solar interior associated with the sunspot cycle (*cf.* Section 7.1.9 below).

In Sections 7.1.3, 7.1.7 and 7.1.8 we present some of the results obtained from these observational projects.

### 7.1.2 Analysis of Solar-Oscillation Observations

As discussed above, disc-integrated observations of the Sun as a star are particularly suitable for the analysis of low-degree modes; also, obviously, they are relevant for observations of solar-like oscillations in other stars. In Chapters 1 and 6 we considered the resulting partial cancellation of the signal from modes of higher degree, caused by the integration over the stellar disc (see Eq. (1.7) and Fig. 1.5). As explained in Chapter 6, an accurate evaluation of this *spatial response function*, (or spatial filter) must take into account the limb darkening which reduces the contribution to the signal of the regions close to the limb. For radial-velocity observations we must include the projection of the velocity on the line of sight; a substantial simplification results from the fact that solar-like oscillations are of high frequency, such that the horizontal component of the velocity can be neglected (*cf.* Eq. (3.163)). In this case an expression similar to Eq. (1.7) is obtained, but with an additional

factor  $\cos \theta$  to account for the projection. Results of such calculations of response functions (*e.g.*, Dziembowski 1977b; Christensen-Dalsgaard & Gough 1982) are shown in Fig. 7.1 (see also Figs 6.4 and 6.14). The response for intensity ( $S_l^{(I)}$ ) is quite similar to the results shown in Fig. 1.5; however, as a result of limb darkening, the response does not vanish identically for odd degrees higher than one. For radial velocity ( $S_l^{(V)}$ ) the response is shifted to slightly higher degrees; this results from the projection which effectively reduces the area on the disc over which the signal is obtained. This has some similarity to Heisenberg's uncertainty principle: by confining the modes, at least observationally, in space they are spread out in wavenumber and hence degree.<sup>12</sup> Additional effects may arise if the observations have a non-uniform and possibly time-dependent response to the oscillations across the solar disc; an important example is the response of the resonant-scattering technique which depends on the local line-of-sight velocity between a point on the disc and the observer and hence is affected by the variation across the solar disc of the velocity associated with rotation (*e.g.*, Christensen-Dalsgaard 1989).

It is obvious, however, that a major advantage of the solar case is the ability to determine properties of frequencies over a broad range of degrees, based on observations made as functions of positions on the solar surface. The first step in the analysis of such data is to isolate, as far as possible, the modes corresponding to individual spherical harmonics. Had data been available covering the entire Sun, modes corresponding to a single pair  $(l_0, m_0)$  could in principle have been isolated by multiplying the data, after suitable scaling, with the spherical harmonic  $Y_{l_0}^{m_0}(\theta, \phi)$  and integrating over the solar surface; it follows from the orthogonality of the spherical harmonics that the result would contain only oscillations corresponding to  $(l, m) = (l_0, m_0)$ . In practice, the observations are restricted to the visible disc of the Sun, and the sensitivity to velocity oscillations is further limited close to the limb due to the projection onto the line of sight.

To illustrate the principles in the mode separation in a little more detail, we note that, according to Eqs (3.122) and (3.132) the combined observed Doppler velocity on the solar surface is of the form

$$V_D(\theta, \phi, t) = \sin \theta \cos \phi \sum_{n,l,m} A_{nlm}(t) c_{lm} P_l^m(\cos \theta) \cos[m\phi - \omega_{nlm} t - \delta_{nlm}(t)]. \quad (7.2)$$

To simplify the presentation we here neglected the horizontal component of the velocity, and assumed the axis of the coordinate system to be in the plane of the sky, measuring longitude  $\phi$  from the central meridian.<sup>13</sup> The factor  $\sin \theta \cos \phi$  results from the projection of the velocity vector onto the line of

<sup>12</sup> This effect is obviously stronger if the modes are observed through smaller apertures on the solar disc, as did Fossat & Ricort (1975); see Christensen-Dalsgaard & Gough (1982).

<sup>13</sup> Also, to simplify the notation the factor  $(-1)^m \sqrt{4\pi}$  has been included in  $A_{nlm}$ .

sight. The amplitudes  $A_{nlm}$  and phases  $\delta_{nlm}$  may vary with time, as a result of the excitation and damping of the modes.

The spatial transform to isolate modes corresponding to a given  $(l_0, m_0)$  may be thought of as an integration over the solar disc of the observations multiplied by a weight function  $W_{l_0 m_0}(\theta, \phi)$  designed to give greatest response to modes in the vicinity of  $l = l_0, m = m_0$ . The result is the filtered time string

$$\begin{aligned} V_{l_0 m_0}(t) &= \int_A V_D(\theta, \phi, t) W_{l_0 m_0}(\theta, \phi) dA \\ &= \sum_{n,l,m} S_{l_0 m_0 lm} A_{nlm} \cos[\omega_{nlm} t + \hat{\delta}_{nlm, l_0 m_0}] . \end{aligned} \quad (7.3)$$

Here, the integral is over area on the solar disc, and  $dA = \sin^2 \theta \cos \phi d\theta d\phi$ ; also, we introduced the *leakage matrix*  $S_{l_0 m_0 lm}$ , defined by

$$(S_{l_0 m_0 lm})^2 = \left( S_{l_0 m_0 lm}^{(+)} \right)^2 + \left( S_{l_0 m_0 lm}^{(-)} \right)^2 , \quad (7.4)$$

where

$$S_{l_0 m_0 lm}^{(+)} = c_{lm} \int_A W_{l_0 m_0}(\theta, \phi) P_l^m(\cos \theta) \cos(m\phi) \sin \theta \cos \phi dA , \quad (7.5)$$

and

$$S_{l_0 m_0 lm}^{(-)} = c_{lm} \int_A W_{l_0 m_0}(\theta, \phi) P_l^m(\cos \theta) \sin(m\phi) \sin \theta \cos \phi dA . \quad (7.6)$$

The new phases  $\hat{\delta}_{nlm, l_0 m_0}$  in Eq. (7.3) depend on the original phases  $\delta_{nlm}$  and on  $S_{l_0 m_0 lm}^{(+)}$  and  $S_{l_0 m_0 lm}^{(-)}$ .

It is evident that to simplify the subsequent analysis of the time string  $V_{l_0 m_0}(t)$ , it is desirable that it contain contributions from a limited number of spherical harmonics  $(l, m)$ . Thus the choice of the weight function  $W_{l_0 m_0}(\theta, \phi)$  should be such that  $S_{l_0 m_0 lm}$  is large for  $l = l_0, m = m_0$  and “small” otherwise. Indeed, it follows from the orthogonality of the spherical harmonics that if  $W_{l_0 m_0}$  is taken to be the spherical harmonic  $Y_{l_0}^{m_0}$ , if the integrals in Eqs (7.5) and (7.6) are extended to the full sphere, and if, in the integrals,  $\sin \theta \cos \phi dA$  is replaced by  $\sin \theta d\theta d\phi$ , then essentially  $S_{l_0 m_0 lm} \propto \delta_{l_0 l} \delta_{m_0 m}$ . It is obvious that, with realistic observations restricted to one hemisphere of the Sun, this optimal level of concentration cannot be achieved. However, the result suggests that suitable weights can be obtained from spherical harmonics. Weights of this nature are almost always used in the analysis. The resulting response functions are typically of order unity for  $|l - l_0| \lesssim 2$ ,  $|m - m_0| \lesssim 2$  and relatively small elsewhere (*e.g.*, Duvall & Harvey 1983; Christensen-Dalsgaard 1984a); this is roughly comparable to the mode isolation achieved in full-disc observations. Typical examples are shown in Fig. 7.2. We note that the proper calculation of the leakage matrix is a crucial part of the analysis of spatially

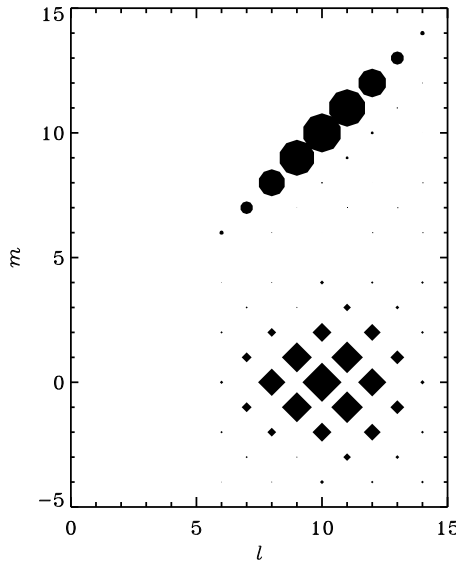


**Fig. 7.2.** Leakage matrices  $S_{l_0 m_0 l m}$  for  $(l_0, m_0) = (10, 0)$  (diamonds) and  $(l_0, m_0) = (10, 10)$  (circles), as functions of  $(l, m)$ . The size of the symbols is proportional to  $S_{l_0 m_0 l m}$ . See Christensen-Dalsgaard (2002).

resolved helioseismic data. This includes minimizing the spread (*e.g.*, Toutain & Kosovichev 2000); however, it is equally important to ensure that the inferred leakage matrix is a good representation of the actual properties of the observations, including instrumental effects and the response of the solar atmosphere, as reflected in the observations, to the oscillations (*e.g.*, Korzennik *et al.* 2004; Vorontsov & Jefferies 2005).

Given the time series in Eq. (7.3), the next step is to carry out a Fourier analysis to determine the frequencies, amplitudes and phases of the modes; procedures used in several of the major observational projects were discussed by, for example, Anderson *et al.* (1990), Schou (1992) and Hill *et al.* (1996, 1998). The fit to the Fourier transform or power spectrum must take into account the stochastic nature of the excitation, resulting in complex spectra with approximately Lorentzian envelopes (see Sections 3.7.5 and 5.7). Also, the fit obviously needs to include a background arising from instrumental effects or other phenomena, such as granulation, in the solar atmosphere (see Fig. 4.1). Thus for a single mode,  $(n, l, m)$ , the fitted function has the form (*cf.* Eq. (3.308) and Fig. 3.33)

$$P(\nu) = A_{nlm} \frac{(\Gamma_{nlm}/2)^2}{(\nu - \nu_{nlm})^2 + (\Gamma_{nlm}/2)^2} + B(\nu), \quad (7.7)$$

where  $\nu_{nlm}$ ,  $\Gamma_{nlm}$  and  $A_{nlm}$  are the frequency, full width at half maximum and amplitude of the mode and  $B(\nu)$  is a suitably parameterized representation of the background. Note in particular that the fit provides a measure of the linewidth and hence the damping rate  $\omega_i = \pi\Gamma$ . A further complication is the presence in the time series of modes corresponding to several  $(l, m)$ , as a result of the incomplete separation in the spatial analysis. This *cross-talk* between modes of different  $m$  is particularly problematic at low degree where the rotational splitting is comparable with the width of the Lorentzian profiles, corresponding to the damping rates of the modes.

At high degree the frequency separation between modes of adjacent degrees becomes comparable with, or smaller than, the width of the spectral peaks. In fact, analysis of the high-degree modes shows that, approximately,  $\nu_{nl} \propto l^{1/2}$  (see Eq. (E.61)); thus

$$\nu_{n,l+1} - \nu_{n,l} \simeq \frac{1}{2l} \nu_{n,l}. \quad (7.8)$$

With typical linewidths of several  $\mu\text{Hz}$  at relatively high degree this causes overlap between adjacent peaks at degrees of around 200. Physically, this results from the fact that the phase propagation time around the solar circumference becomes comparable to, or smaller than, the mode lifetime; as a result, the oscillations can no longer be regarded as coherent modes of the whole Sun and the description in terms of spherical harmonics becomes irrelevant. Here a local description is more appropriate, characterizing the oscillations in terms of the horizontal wavenumber  $k_h$  and describing the observations in terms of ridges in a  $(k_h, \nu)$  diagram. As discussed in Section 7.1.3, the transition between these two descriptions of the oscillations still causes substantial problems in the data analysis, limiting the usefulness of the high-degree data.

A more careful analysis shows that the observed profiles in the power spectrum have definite asymmetries and hence cannot strictly be represented by a Lorentzian envelope as in Eq. (7.7). This behaviour can be understood from the detailed properties of the excitation, in particular the fact that the dominant contributions to the forcing arise from a relatively thin region (*e.g.*, Duvall *et al.* 1993; Gabriel 1993, 2000; Roxburgh & Vorontsov 1995; Abrams & Kumar 1996; Nigam & Kosovichev 1998; Rast & Bogdan 1998; Rosenthal 1998). Neglecting this effect in the fitting causes systematic errors in the inferred frequencies; however, it appears that these are of a form similar to the effects of the near-surface errors (*cf.* Section 7.1.4) and hence have no effect on the results of structure inversion (*e.g.* Rabello-Soares *et al.* 1999a; Basu *et al.* 2000a). Observational determination of the asymmetry does, however, provide constraints on the properties of subsurface convection (Chaplin & Appourchaux 1999; Kumar & Basu 1999; Nigam & Kosovichev 1999).

Ideally, the analysis of the observations should result in determinations of the individual frequencies  $\nu_{nlm}$ . Because of observational errors and the large

amount of data resulting from such determination, it has been common to present the results in terms of coefficients in fits to the  $m$  dependence of the frequencies, either averaged over  $n$  at given  $l$  (Brown & Morrow 1987) or for individual  $n$  and  $l$  (*e.g.*, Libbrecht 1989). A convenient form of the expansion was established by Ritzwoller & Lavelle (1991); this can be expressed as

$$\nu_{nlm} = \nu_{nl0} + \sum_{j=1}^{j_{\max}} a_j(n, l) \mathcal{P}_j^{(l)}(m), \quad (7.9)$$

in terms of the so-called  $a$  coefficients  $a_j(n, l)$ . Here the  $\mathcal{P}_j^{(l)}$  are polynomials of degree  $j$  which satisfy the orthogonality relation  $\sum_m \mathcal{P}_i^{(l)}(m) \mathcal{P}_j^{(l)}(m) = 0$  for  $i \neq j$  (see also Schou *et al.* 1994). Explicit expressions for these polynomials were given by Pijpers (1997). The coefficients with odd  $j$  result from the leading-order effects of rotation (*cf.* Section 3.8.1), whereas coefficients with even  $j$  result from magnetic effects, rotational distortion of the equilibrium model and higher-order effects of rotation. The  $a$  coefficients can be determined through fits to the individual frequencies  $\nu_{nlm}$ ; however, a more stable technique may be to use the parametrization in Eq. (7.9) directly in the fits to the Fourier or power spectra.

The determination of solar oscillation frequencies is affected by systematic errors which may have significant effects on the results of the helioseismic analysis of the frequencies. These are to a large extent caused by the complex physics of the mode excitation and damping, as well as the unavoidable mixture in any given time series of modes corresponding to several  $(l, m)$ . Although in principle this provides several measures of a given frequency, in practice it is dealt with in various approximate ways, each with its own problems, as discussed by Schou (1998). The resulting systematic errors are probably now the dominant barrier for obtaining even more accurate frequencies and hence better inferences about the solar interior. Ideally, the analysis should take all modes present into account, and include suitable models for the excitation and damping processes, as well as for the solar background. A programme to approach this ideal has been outlined by Jefferies & Vorontsov (2004) and Jefferies *et al.* (2006) and is now under development. A very interesting aspect is the proposal to include the seismic structure of the Sun in the fit to the time-series data, thus bypassing the determination of the frequencies. Further results of this project are eagerly awaited.

### 7.1.3 Observational Results on Solar Oscillations

#### 7.1.3.1 Solar p and f Modes

We begin by considering observations of the Sun as a star. Figure 7.3 shows an example of an observed power spectrum of solar oscillations. This was obtained by means of Doppler velocity measurements in light integrated over the solar

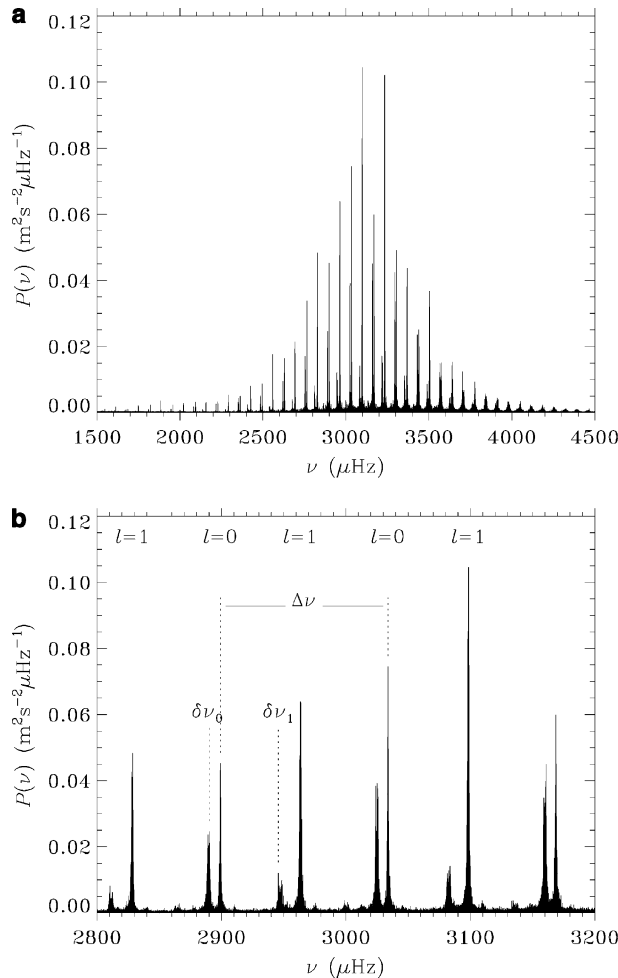


**Fig. 7.3.** Power spectrum of solar oscillations, obtained from Doppler observations in light integrated over the disc of the Sun. The ordinate is normalized to show velocity power per frequency bin. The data were obtained from the full six-station BiSON network and span approximately 15 yr. Panel (b) provides an expanded view of the central part of the frequency range. Here some modes have been labelled by their degree  $l$ , and the large and small frequency separations  $\Delta\nu$  and  $\delta\nu_l$  have been indicated. See Chaplin *et al.* (2007a).

disc, and hence, according Fig. 7.1, is dominated by modes of degrees 0 – 3. The data were obtained from the BiSON network of six stations globally distributed in longitude, to suppress the daily side-bands, and span 15 yr. Thus the intrinsic frequency resolution (see Section 5.3.1) is much smaller

than the thickness of the lines. There is a visible increase in the linewidth when going from low to high frequency. The broadening of the peaks at high frequency is probably caused by the damping and excitation processes, as discussed in Section 3.7.5; thus the observations indicate that the damping rate increases with increasing frequency, as confirmed by the more detailed analysis illustrated in Fig. 7.7 below. Finally, there is clearly a well-defined distribution of amplitudes, with a maximum around  $3000 \mu\text{Hz}$  and very small values below  $2000 \mu\text{Hz}$  and above  $4500 \mu\text{Hz}$ . The maximum power corresponds to a velocity amplitude of around  $15 \text{ cm s}^{-1}$ ; observations in broad-band intensity show amplitudes up to around 4 ppm.

The spectrum illustrated in Fig. 7.3 evidently has a highly regular frequency structure, most clearly visible in the expanded view in panel (b). This reflects the asymptotic expression in Eq. (3.223). According to the leading term in Eq. (3.223), the peaks should occur in groups corresponding to even and odd degree, such that  $n + l/2$  is the same, the groups being uniformly spaced with a separation  $\Delta\nu/2$ ; this apparent degeneracy is lifted by the second term in Eq. (3.223). Thus the spectrum is characterized by the *large frequency separation*  $\Delta\nu = \nu_{n+1l} - \nu_{nl}$  and the *small frequency separation*  $\delta\nu_l = \nu_{nl} - \nu_{n-1l+2}$ . These separations are indicated in Fig. 7.3b, where also selected peaks corresponding to  $l = 0$  and 1 have been labelled, in each case with a neighbouring peak with  $l = 2$  or 3, respectively. It should be noticed that the observed amplitudes of the  $l = 3$  peaks are much reduced relative to the  $l = 1$  peaks, as predicted by the spatial response function  $S_l^{(V)}$  shown in Fig. 7.1; on the other hand, the observed amplitudes for  $l = 0$  and 2 are roughly similar, as expected.

As illustrated schematically in Fig. 3.19b, it is convenient to show the structure of the spectrum in an échelle diagram. This is done in Fig. 7.4, based on frequencies from BiSON observations. The general behaviour is clearly as expected, although with significant departures in the details. The curvature of the lines indicates that the frequencies for each  $l$  are not exactly uniformly spaced; as discussed in Section 7.1.4.4 this results from the structure near the solar surface, including the effects on  $\Gamma_1$  of helium ionization. Also, it is fairly evident that the small separation varies with frequency.

Precise measurements of frequencies, frequency separations and rotational splittings for low-degree modes were published by, for example, Fröhlich *et al.* (1997), Lazrek *et al.* (1997), Gelly *et al.* (2002), García *et al.* (2004) and Chaplin *et al.* (2001a, 2007b); such measurements are of great diagnostic value for the study of the properties of the solar core (*cf.* Section 3.4.3).

Very extensive spatially resolved observations of solar oscillations have been made, particularly in Doppler velocity with the GONG network and the MDI instrument on the SOHO spacecraft. To illustrate the quality of current frequency determinations, Fig. 7.5 shows observed mean multiplet frequencies at low and moderate degree from observations spanning 72 d with the MDI instrument on SOHO (see Larson & Schou 2008). The error bars have been magnified by a factor 1000 over the usual  $1\sigma$  standard errors. For more than

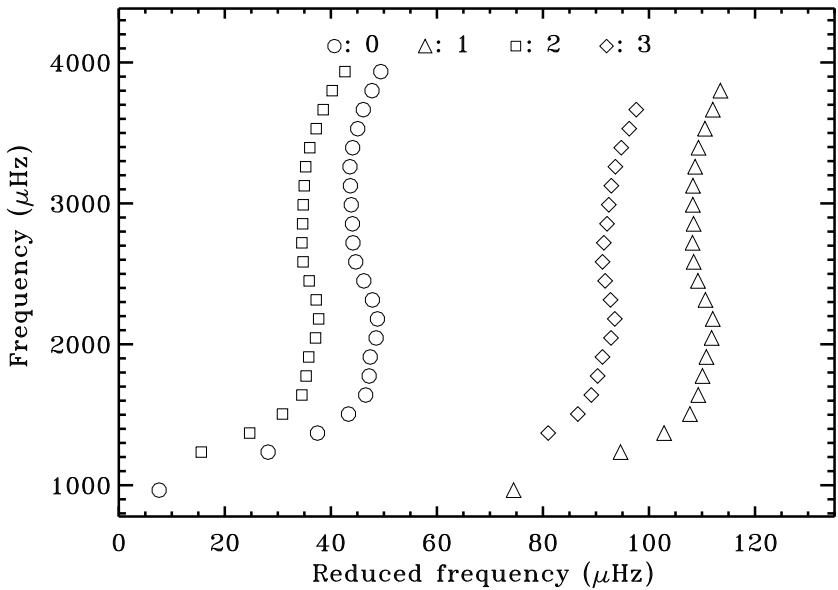


**Fig. 7.4.** Échelle diagram for observed solar frequencies obtained with the BiSON network (Chaplin *et al.* 2002a), plotted with  $\nu_0 = 830 \mu\text{Hz}$  and  $\Delta\nu = 135 \mu\text{Hz}$  (*cf.* Eq. (3.224)). Circles, triangles, squares and diamonds are used for modes of degree  $l = 0, 1, 2$  and  $3$ , respectively.

half the modes illustrated the relative standard error is well below  $10^{-5}$ , thus substantially exceeding the precision with which the solar mass is known.

As discussed in Section 7.1.2 the  $m$  dependence of the frequencies is often parameterized in terms of the so-called  $a$  coefficients (*cf.* Eq. (7.9)). To illustrate this, Fig. 7.6 shows the first three odd  $a$  coefficients from MDI observations. It may be shown that  $a_1$  is determined by the spherically symmetric component of the angular velocity  $\Omega(r, \theta)$ , while the higher-order coefficients depend on the latitude variation of  $\Omega$  (see also Section 3.8.4). In particular, as discussed in Section 7.1.8, the decrease of  $a_3$  for modes with turning point  $r_t$  in the radiative interior reflects the nearly latitude-independent rotation in this region.

As discussed in Section 7.1.2, frequencies for individual modes can be determined up to degrees around 200. For higher degree the modes merge into ridges of power, substantially complicating the analysis (for a review, see Reiter *et al.* 2004); thus, although results on high-degree mode frequencies have been published (*e.g.*, Bachmann *et al.* 1995) they have so far seen relatively

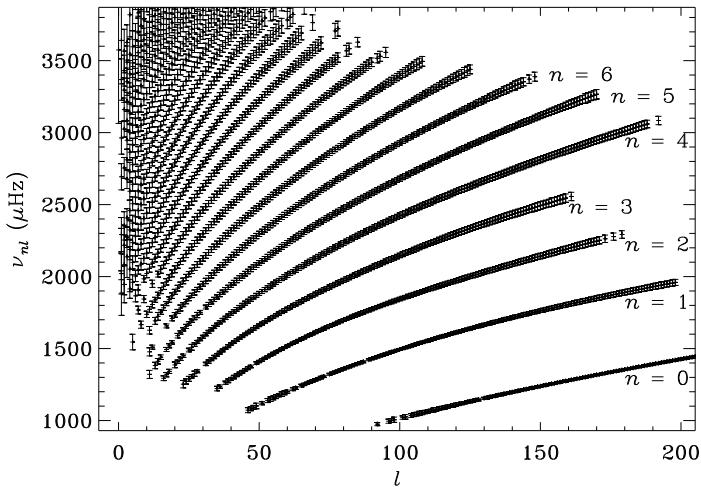


**Fig. 7.5.** Plot of observed solar p-mode multiplet frequencies, as a function of the degree  $l$ , from MDI observations spanning 72 d (Larson & Schou 2008). The vertical lines show the  $1000\sigma$  error bars. Each ridge corresponds to a given value of the radial order  $n$ , which is indicated for the lowest  $n$ ; note in particular that the lowest ridge corresponds to the f modes, with  $n = 0$ .

limited use in helioseismic analyses. Owing to the small spatial scale of the modes the analysis is very sensitive to the influence of the Earth's atmosphere in ground-based observations; these problems are avoided in the space-based observations with the MDI instrument, but here optical distortions and plate-scale errors, possibly varying with time as a result of thermal effects, add complexity (Korzennik *et al.* 2004). A recent analysis of the MDI data by Rabello-Soares *et al.* (2008) attempted to take these effects into account, but still found significant differences between the frequencies obtained from the analysis of individual modes in the MDI medium- $l$  programme and the results of the ridge fitting of the data from the dynamics programme. Since high-degree modes would be extremely valuable for helioseismic inversion (*e.g.*, Di Mauro *et al.* 2002) a resolution of these problems has high priority.

The spatially resolved observations also provide information about the dependence of the modal properties on degree and frequency. A detailed analysis of the mode lifetime and energy was carried out by Komm *et al.* (2000), based on GONG observations, for modes of degree up to 150. They found that the dependence on degree of both the linewidth  $\Gamma$  and the amplitude essentially scale inversely with the mode inertia. This is similar to the frequency changes caused by near-surface effects, discussed in Section 7.1.4.1 below, and the ef-

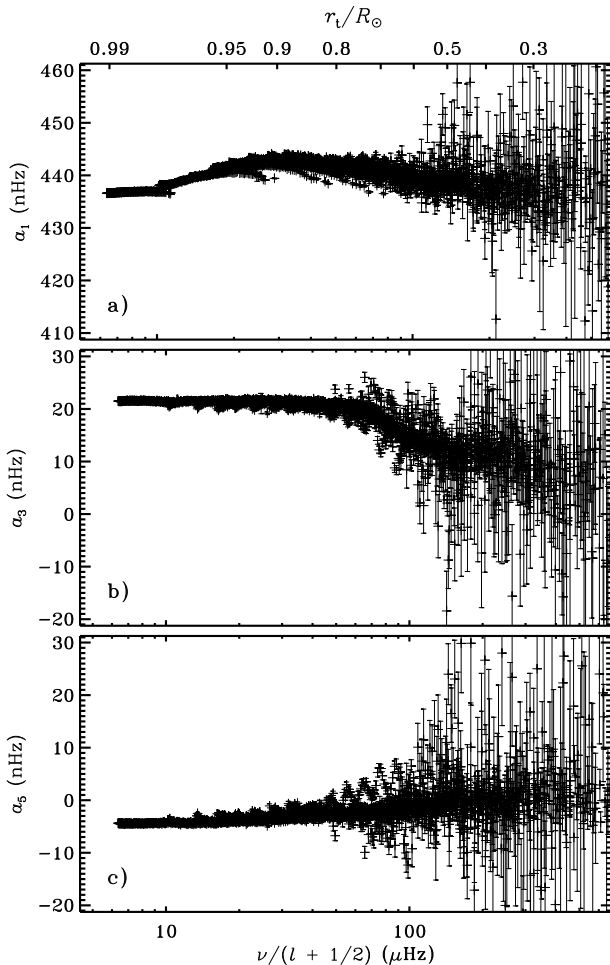


**Fig. 7.6.** Odd  $a$ -coefficients (a)  $a_1$ , (b)  $a_3$  and (c)  $a_5$  from MDI data, with one-standard-deviation error bars. The bottom axis indicates the value of  $\nu/(l + 1/2)$  of the modes, which is mapped to the location  $r_t/R$  of the lower turning point of the mode (top axis; *cf.* Eq. (3.189)). Adapted from Christensen-Dalsgaard & Thompson (2007).

fect of the inertia can similarly be suppressed by scaling with the inertia ratio  $Q_{nl}$  (*cf.* Eq. (7.10) and Fig. 7.9). Results on linewidths based on MDI observations are shown in Fig. 7.7. The linewidth shows a characteristic dependence on frequency, with a plateau, or even a slight decrease, between 2500 and

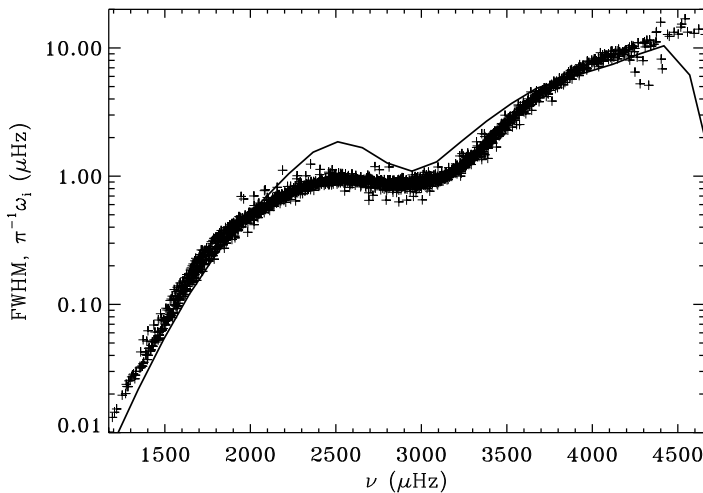


**Fig. 7.7.** The symbols show full widths at half maximum determined from 72 d of medium- $l$  MDI observations; these have been scaled by the inertia ratio  $Q_{nl}$  (*cf.* Eq. (7.10)) to correct for the degree dependence of the mode inertia. The curve is based on computed damping rates for radial modes in a solar model (Houdek 2006; see also Chaplin *et al.* 2005).

3100  $\mu$ Hz. As illustrated in the figure, this is also a feature of damping rates of solar oscillations, taking the interaction with convection into account (*e.g.*, Houdek *et al.* 1999, Houdek 2006), and appears to be a consequence of the detailed interaction between convection and the pulsations.

The distribution of mode amplitudes, resulting from the stochastic excitation (*cf.* Section 3.7.5) is clearly the result of the balance between the energy input from convection and the damping (*cf.* Eq. (3.308)). This was discussed in detail by Goldreich *et al.* (1994) and reviewed by Houdek (2006). Chaplin *et al.* (2005) carried out a careful analysis of the observed amplitudes of disc-integrated BiSON observations. According to Eq. (3.309) and the associated discussion we expect the mean square velocity  $\langle V^2 \rangle$  to be proportional to  $E^{-1}$ , where  $E$  is the surface-normalized mode inertia. This is illustrated in Fig. 7.8, based on GONG observations, where the degree dependence of the inertia has been suppressed by multiplying the mean square velocity by the inertia ratio  $Q_{nl}$ . The resulting values are essentially a function of frequency; this would be expected, for damping and excitation taking place near the surface of the Sun, where the interactions are largely independent of degree for low and moderate degree.

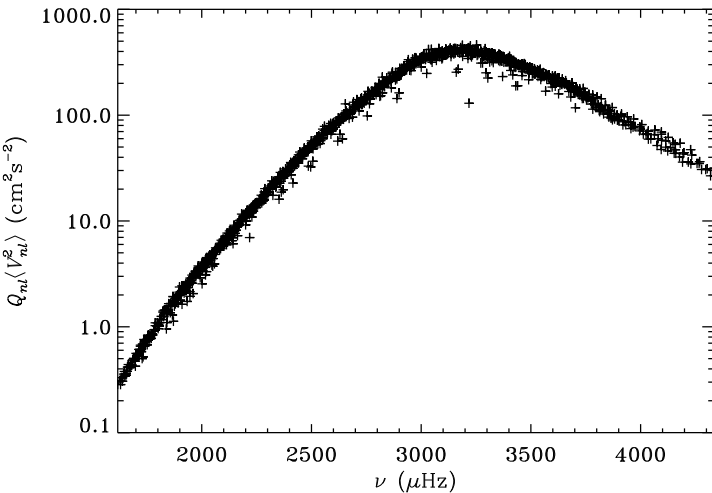


**Fig. 7.8.** Observed mean square velocities of solar oscillations of degree  $l \leq 150$ , determined from GONG observations; the results have been multiplied by the inertia ratio  $Q_{nl}$  (*cf.* Eq. (7.10)) to correct for the degree dependence of the mode inertia. Adapted from Komm *et al.* (2000).

Woodard *et al.* (2001) made a careful investigation of the dependence of the mode energy on degree and frequency of oscillation, based on observations from the SOHO spacecraft. They found a rather substantial decrease with degree, at fixed frequency, in the mode amplitudes; this appeared stronger than would be expected from the inertia scaling. They speculated that the amplitude variation might reflect additional sources of damping at higher degree.

### 7.1.3.2 Solar g Modes?

As mentioned above, one of the early claims for the detection of global solar oscillations concerned the 160-minute oscillation which was identified as a high-order g mode. In fact, observation of such modes in the Sun would be extremely interesting. As shown by Fig. 3.23 they have large amplitudes in the solar interior and hence are far more sensitive to conditions in the solar core than are the p modes (*cf.* Fig. 3.21). In particular, measurement of the rotational splitting of a few g modes would provide strong constraints on the rotation of the deep solar interior (*e.g.*, Mathur *et al.* 2008). Thus the solar g modes have been something of a holy grail of helioseismology for several decades.

Unfortunately, the quest to find them has so far met with somewhat limited success. This has been marked by a number of claims, sometimes quoting high statistical significance, that have been disproved by later observations. A major goal of two of the three helioseismic instruments on the SOHO spacecraft was to study low-frequency modes, in particular g modes. A major analysis effort, combining several different types of data, by Appourchaux *et al.* (2000a) in the so-called *Phoebus* collaboration found an upper limit on the g-mode amplitude at  $200\text{ }\mu\text{Hz}$  of  $10\text{ mm s}^{-1}$ . A slightly lower limit, based on a more extensive time series of GOLF data, was obtained by Gabriel *et al.* (2002); a further decrease will be obtained with the continued activities of the Phoebus group as more data are accumulated (Elsworth *et al.* 2006). Also, by searching for significant occurrences of multiplets Turck-Chièze *et al.* (2004a) found tentative evidence in GOLF data for a few modes between  $150$  and  $400\text{ }\mu\text{Hz}$ , with amplitudes around  $2\text{ mm s}^{-1}$ . However, the definite acceptance of these modes as real will probably require further independent confirmation.

A common technique in trying to find high-order g modes has been to use their asymptotically predicted uniform period spacing (*cf.* Eq. (3.236)). Recently García *et al.* (2007) apparently succeeded in detecting this for modes of degree  $l = 1$  in observations from the GOLF instrument on SOHO. By suitably filtering the data they furthermore obtained evidence that the solar core rotates somewhat more rapidly than the surface. This is evidently a very interesting result; however, given the complexity of the analysis and the uncertain sensitivity to the solar noise background it is probably fair to regard the evidence so far as less than compelling.

A reliable theoretical estimate of the amplitudes of the solar g modes would obviously be a great help in the search. Unfortunately, this is not available. As discussed in Section 3.7.1 a few low-order, low-degree g modes may have been unstable during earlier phases of solar evolution although it is uncertain whether the instability has been maintained until the present; see, however, Cox & Guzik (2004). Dziembowski (1983) estimated the resulting amplitude, limited by parametric resonance, to be around  $10\text{ cm s}^{-1}$ , well above present observational upper limits (see also Jordison & Gough 2000). Apart from these modes there is little doubt that the modes generally are stable and that stochastic forcing within, and perhaps below, the solar convective envelope excites them. On the other hand, the estimates of the resulting amplitudes have varied substantially; Gough (1985a) obtained amplitudes around or below  $1\text{ mm s}^{-1}$ , while Kumar *et al.* (1996) obtained values lower by an order of magnitude. Thus, in both cases the results are substantially below the observational upper limit. Recently, Belkacem *et al.* (2009) redid the analysis, assuming stochastic forcing within the convection zone, but using a different form of the temporal correlation of convection, with some basis in hydrodynamical convection simulations. This resulted in predicted amplitudes of the order of a few  $\text{mm s}^{-1}$ , very close to current observational limits. Although several aspects of the calculation, and the resulting amplitudes, remain uncertain, this is certainly encouraging. One may hope that continuing observations,

including the use of new instruments now under development for possible use in future space projects (*e.g.*, Turck-Chièze *et al.* 2008) may finally provide definite detection of g modes and determination of a sufficient number of frequencies to allow their inclusion in the helioseismic analysis.

### 7.1.4 Properties of Solar Oscillations

The availability of modes over a broad range of degrees is so far specific to the solar case and provides crucial information about the solar interior. Also, the solar data obviously serve as a model for the investigation of solar-like oscillations in other stars. Thus it is appropriate to expand the discussion of oscillation properties from Chapter 3 to cover aspects that are specifically relevant to this case.

#### 7.1.4.1 Near-Surface Effects

An important example concerns the uncertainties in the physics of the model and the oscillations in the near-surface region (*cf.* Section 7.1.1), which are generally confined to the outermost layers of the stellar interior and the atmosphere. To discuss their effects on the oscillation frequencies we use the general expression in Eqs (3.267) and (3.268). Here we assume that the perturbations to the model, characterized by  $\phi_r[\xi](r)$  and  $\phi_h[\xi](r)$ , are non-zero only in a region very near the surface, with  $r \geq r_{\text{ns}} = R(1 - \epsilon)$ , say, for some small  $\epsilon$ . For modes extending substantially more deeply than this region, with lower turning point  $r_t$  such that  $R - r_t \gg R - r_{\text{ns}}$ , the eigenfunctions are nearly independent of  $l$  at fixed frequency for  $r \geq r_{\text{ns}}$  (see also Fig. 3.21 and the associated discussion). Hence  $I_{nl}$  depends little on  $l$  at fixed  $\omega$ . To get a more convenient representation of this property, we introduce

$$Q_{nl} = \frac{E_{nl}}{\bar{E}_0(\omega_{nl})}, \quad (7.10)$$

where  $\bar{E}_0(\omega)$  is obtained by interpolating to  $\omega$  in the values of  $E_{n0}$ , *i.e.*, for radial modes. Then we expect that  $Q_{nl}\delta\omega_{nl}$  is largely independent of  $l$ , at fixed  $\omega$ , for such modes and hence can be written as a function of  $\omega$ ,  $Q_{nl}\delta\omega_{nl} \simeq \mathcal{G}(\omega)$ , say. Conversely, if  $Q_{nl}\delta\omega_{nl}$  is independent of  $l$  at fixed  $\omega$  for a given set of modes, then the cause of the frequency difference is probably largely localized well outside the most shallow inner turning point for the set of modes considered.

$Q_{nl}$  has been plotted in Fig. 7.9, for selected values of  $l$ . Its variation with  $l$  is largely determined by the change in the penetration depth. Modes with higher degree penetrate less deeply and hence have a smaller inertia at given surface displacement. As a consequence of this their frequencies are more susceptible to changes in the model.

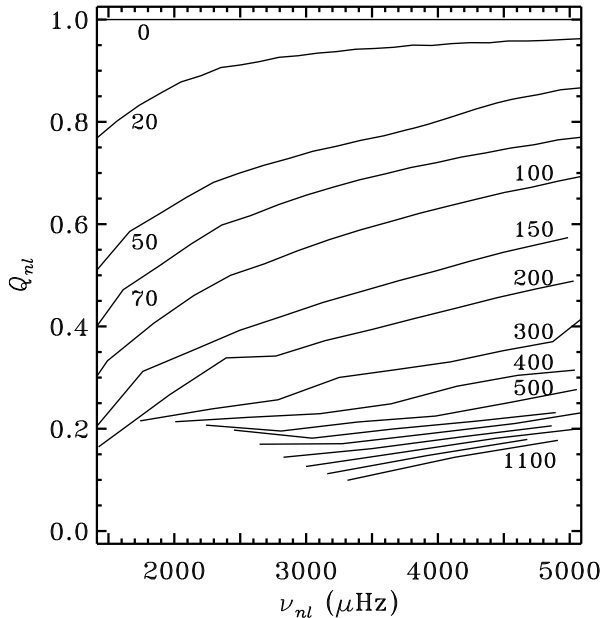


**Fig. 7.9.** The inertia ratio  $Q_{nl}$ , defined in Eq. (7.10), against frequency  $\nu$ , for f and p modes in a solar model. Each curve corresponds to a given degree  $l$ , selected values of which are indicated.

This property can be used to eliminate the effects of the uncertainties in the analysis of observed frequencies. To illustrate it, we analyse the effects of model changes localized very near the solar surface. Specifically, we consider a solar model where the opacity has been artificially increased by a factor of 2 at temperatures below about  $10^5$  K; this is compared with a normal model of the present Sun. In both models the mixing-length parameter and composition have been adjusted so as to obtain a model with solar radius and luminosity; the effect of this is that the interior of the model is virtually the same. The opacity has no effect in the bulk of the convection zone where energy transport is totally dominated by convection; hence the change in the model is largely confined to the atmosphere and the uppermost parts of the convection zone. Fig. 7.10 shows the relative sound-speed difference  $\delta_r c/c$  between the modified and the normal model.

The unscaled differences between frequencies of the two models are shown in Fig. 7.11a. It is evident that the differences show a very systematic increase in magnitude with increasing degree. As shown by Fig. 7.11b this is entirely suppressed by scaling the differences by  $Q_{nl}$ . Indeed, the differences now de-

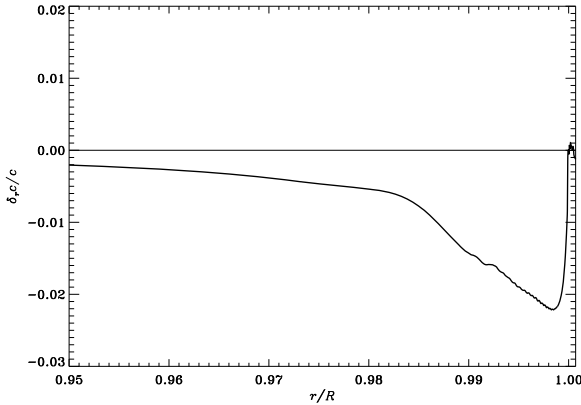


**Fig. 7.10.** Relative sound-speed difference  $\delta_r c / c$  between a model with increased surface opacity and a normal model, in the sense (modified model) – (normal model).

crease with increasing  $l$ . This is predominantly due to the fact that at the largest values of  $l$  the eigenfunctions can no longer be assumed to be independent, near the surface, of degree at fixed frequency (for an asymptotic description of this behaviour, see for example Gough & Vorontsov 1995); this results in peeling-off of the points corresponding to the lowest orders, as indicated by the symbols in Fig. 7.11b. A small additional contribution comes from the fact that the modes only penetrate partly, to a degree-dependent extent, into the region where the sound speed has been modified.

It might also be noted that the frequency differences are very small at low frequency. This is related to the fact that low-frequency modes have very small amplitudes in the surface region (*cf.* Fig. 3.22). However, a proper understanding of this feature requires a more careful analysis (see Christensen-Dalsgaard & Thompson 1997).

The probable presence of near-surface errors in the model must be taken into account when relating differences between observed and computed frequencies to the corresponding differences between the structure of the star and the model. Specifically, consider the determination of corrections  $\delta_r c^2$  and  $\delta_r \rho$  to a stellar model, from the differences  $\delta\omega_{nl} = \omega_{nl}^{(\text{obs})} - \omega_{nl}$  between observed frequencies  $\omega_{nl}^{(\text{obs})}$  and model frequencies  $\omega_{nl}$ : here we expect differences between the star and the model both in the internal structure, characterized by  $(c^2, \rho)$ , and in the near-surface layers. The analysis in Section 3.6.2 demonstrated that the effect of the differences in the internal structure can be represented by the kernels  $K_{c^2, \rho}^{nl}$  and  $K_{\rho, c^2}^{nl}$  (*cf.* Eq. (3.269)), while the analysis above leads to an effect of the near-surface errors of the form  $Q_{nl}^{-1} \mathcal{G}(\omega)$ . In

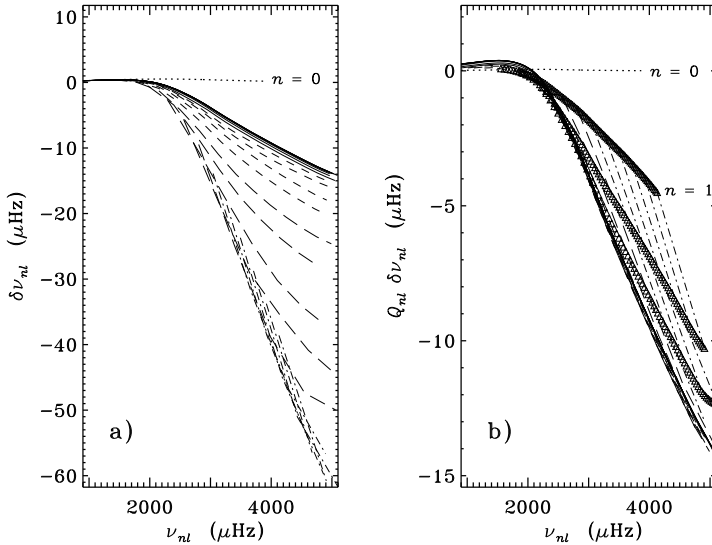


**Fig. 7.11.** Frequency differences between a model with increased surface opacity and a normal model, in the sense (modified model) – (normal model). Panel (a) shows the raw differences. In panel (b) the differences have been scaled by  $Q_{nl}$ , defined in Eq. (7.10). Points corresponding to acoustic modes of a given degree have been connected, according to the following line styles:  $l = 0, 1, 2, 3, 4, 5, 10, 20, 30$  (solid);  $l = 40, 50, 70, 100$  (short-dashed);  $l = 150, 200, 300, 400, 500$  (long-dashed);  $l = 600, 700, 800, 900, 1000, 1100$  (dot-dashed). As indicated, the dotted lines show results for f modes; the symbols in panel (b) mark modes of degree  $n = 1, 2$  and  $3$ , for every 10<sup>th</sup> value of  $l$ .

addition, the observed frequencies are unavoidably affected by errors. Thus we expect that Eq. (3.269) must be replaced by

$$\frac{\delta\omega_{nl}}{\omega_{nl}} = \int_0^R \left[ K_{c^2, \rho}^{nl}(r) \frac{\delta_r c^2}{c^2}(r) + K_{\rho, c^2}^{nl}(r) \frac{\delta_r \rho}{\rho}(r) \right] dr + Q_{nl}^{-1} \mathcal{G}(\omega_{nl}) + \epsilon_{nl}, \quad (7.11)$$

where the function  $\mathcal{G}(\omega)$  accounts for the effect of the near-surface uncertainties, and  $\epsilon_{nl}$  are the relative observational errors in the frequencies. The term in  $\mathcal{G}$  must then be determined as part of the analysis of the frequency differences, or suppressed by means of suitable filtering of the data.

### 7.1.4.2 Effects of “Acoustic Glitches”

As discussed below, asymptotic analysis is extremely powerful in assessing the diagnostic potential of solar oscillations and in analysing the observed frequencies. The analysis assumes that the equilibrium model varies on a scale long compared with the wavelength of the modes. However, the opposite situation, of features that are sharp compared with the scale of the modes, also gives rise to very interesting seismic diagnostics (*e.g.*, Thompson 1988; Vorontsov 1988; Gough 1990a). Such features were denoted “acoustic glitches” by Gough (2002a); we consider some examples of their use in Section 7.1.7 below. Here we provide a brief discussion of their properties.

A simple way to illustrate the effect of an acoustic glitch is to use the general expression in Eq. (3.269) for the effect on the frequencies of a small change to the equilibrium model. In the present case we take the reference model to be a smoothed version of the true model, containing a glitch at some location  $r = r_0$ , and the perturbation to reflect just the effects of the glitch which, for simplicity, we assume to affect only the sound speed and hence to correspond to a perturbation  $\delta_r c^2/c^2$  strongly localized near  $r_0$ . If the extent of the perturbation is small compared with the wavelength of the mode, its effects on the frequencies are simply proportional to  $K_{c^2, \rho}^{nl}(r_0)$ . The behaviour is illustrated in Fig. 7.12, for acoustic glitches near the base of the convective envelope and in the second helium ionization zone, for low-degree modes. In this case the lower turning point is well below the locations of the glitches; as discussed in Section 3.5.1 the eigenfunctions, and hence the kernels, are then essentially independent of degree and the frequency change is a function of frequency alone. The behaviour can be understood from the asymptotic behaviour of the p-mode eigenfunctions. According to Eq. (3.227)  $\xi_r \propto \cos[\omega\tau - (1/4 + \alpha)\pi]$ , in terms of the acoustic depth  $\tau$  (*cf.* Eq. (3.228)). Since the kernels are approximately proportional to the square of the eigenfunctions, we find that  $K_{c^2, \rho}^{nl}(r_0) \propto \cos(2\omega\tau_g + \phi)$ , for some suitable phase  $\phi$ , where  $\tau_g$  is the acoustic depth of the glitch. This accounts for the oscillatory behaviour found in Fig. 7.12 and shows that the “period” of the oscillation directly reflects the depth of the feature that is responsible. This provides a powerful diagnostics of sharp features in stellar interiors. More detailed analyses of these properties were provided by, *e.g.*, Monteiro *et al.* (1994) and Houdek & Gough (2007).

Figure 7.12c shows the effect of a sound-speed change in the photosphere of the model. This essentially corresponds to the effects of the near-surface changes discussed above and, in particular, confirms that these effects are very small at low frequency.

### 7.1.4.3 Properties of f Modes

The computed frequencies for solar models (*cf.* Fig. 3.20) show a mode intermediate between the p and g modes at degrees higher than above 20; at

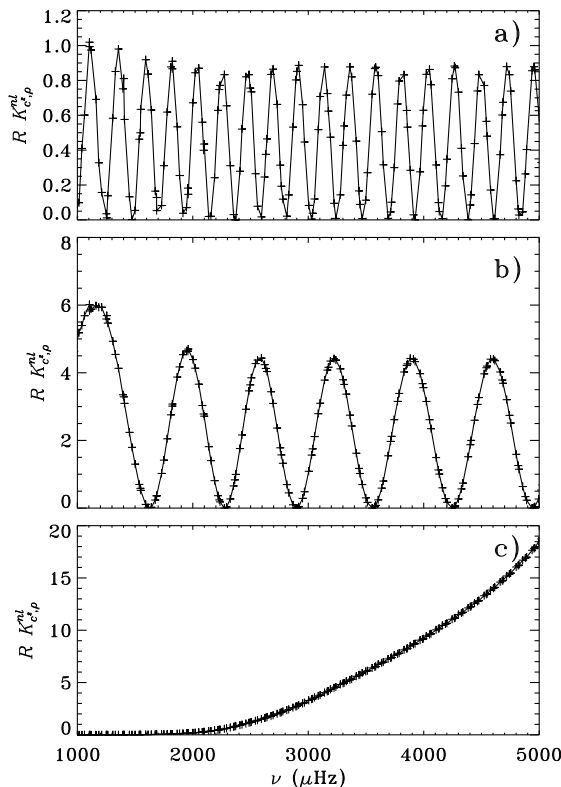


**Fig. 7.12.** Kernels  $K_{c^2, \rho}^{nl}(r_0)$  at  $r_0 = 0.72R$  (panel a)  $r_0 = 0.98R$  (panel b) and  $r_0 = R$  (panel c), for modes of degree  $l \leq 5$ , plotted against frequency. Here  $R$  is the photospheric radius. For clarity the points have been connected. Adapted from Christensen-Dalsgaard (1996).

lower degrees this can still be identified, undergoing avoided crossings with the g modes (Christensen-Dalsgaard 1980). At moderate or high degree it has the mathematical classification as the f mode, with radial order  $n = 0$ . From a physical point of view it can be identified with a surface gravity wave. Indeed, the asymptotic analysis (see Section E.1 for details) results in a mode with frequency and radial displacement given approximately by

$$\omega^2 \simeq g_s \frac{L}{R}, \quad \xi_r \propto \exp(Lr/R) \quad (7.12)$$

(*cf.* Eqs (3.207) and (3.208)), where  $g_s$  is the surface gravity; this corresponds to the solution for a simple surface gravity wave (*cf.* Section 3.1.4.3). Equation (7.12) shows that the modes are confined near the surface in a region of extent of order  $R/l$ . As shown in Fig. 7.5 these modes have in fact been observed in the Sun.

Rosenthal & Gough (1994) noted that this behaviour could not extend into the solar corona, since this would correspond to an unphysical increase in the energy with height; they proposed that the modes should be regarded as interfacial modes at the transition between the chromosphere and the corona. This model was investigated in more detail by Rosenthal & Christensen-Dalsgaard (1995) who confirmed the interfacial nature of the modes but showed that this had very modest effects on the frequencies or eigenfunctions of the modes, except at very high degree.

According to Eq. (7.12) the frequencies of the f modes are determined only by the surface gravity of the Sun and hence provide no information about the solar interior; indeed, the observed frequencies approximately satisfy this relation. However, the asymptotic analysis assumed a plane-parallel model with constant gravity. In reality sphericity must be taken into account, as well as the variation of the gravitational acceleration over the region where the modes are confined. It was shown by Gough (1993) that

$$\frac{\omega^2 R}{L g_s} = 1 - \epsilon(L), \quad (7.13)$$

where

$$\epsilon(L) = 2L^{-1} + \frac{\int_0^R (r/R - 1) \rho \exp(2Lr/R) dr}{\int_0^R \rho \exp(2Lr/R) dr}. \quad (7.14)$$

Chitre *et al.* (1998) analysed this relation in more detail and showed that it agreed very well with the computed frequencies for solar models. In principle the frequencies provide information about the density stratification of the near-surface layers of the Sun. In practice, Fig. 7.11 shows that the effect on the f-mode frequencies of even quite substantial changes to the models is very small; as will be discussed in Section 7.1.7 below, the differences between the observed f-mode frequencies and the model frequencies appear to be dominated by effects unrelated to structural differences. On the other hand, the simple structure of the eigenfunctions and hence of the kernels for rotational splitting (*cf.* Section 3.8.3) makes these modes very valuable for the determination of solar interior rotation (see Section 7.1.8).

#### 7.1.4.4 Asymptotics of Solar Oscillations

Most of the observed solar oscillations are acoustic modes of high radial order or degree, and hence a great deal of understanding of their diagnostic potential can be obtained from asymptotic analyses. As discussed in Section 3.4.2 the

acoustic modes are trapped between the surface and a lower turning point. The dependence of the turning-point position  $r_t$  on mode degree and frequency (*cf.* Eq. (3.189)) is of great importance for the interpretation of the observations of the solar 5-minute oscillations. Figure 7.13 shows  $r_t$  for a model of the present Sun, at three different frequencies, spanning the range of most observations. For small  $l$ ,  $r_t$  is very close to the centre, whereas for higher degrees the turning point moves closer to the surface. In particular, we note that for  $l \gtrsim 40$  the modes are essentially trapped in the convection zone, which has a depth of about  $0.28R$ . As discussed in Section 7.1.1 such modes are very well suited for investigations of the properties of the equation of state of stellar matter.

It was shown in Section E.3, on the basis of the asymptotic theory of p modes, that such modes satisfy the *Duvall law*: we can find a function  $\alpha(\omega)$  of frequency such that the quantity  $[n + \alpha(\omega)]/\omega$  depends principally on frequency  $\omega$  and degree  $l$  only in the combination  $w \equiv \omega/L$ ,<sup>14</sup> *i.e.*,

$$\frac{(n + \alpha)\pi}{\omega} = F\left(\frac{\omega}{L}\right). \quad (7.15)$$

Here the function  $F(\omega/L)$  is related to the adiabatic sound speed  $c(r)$  by

$$F(w) = \int_{r_t(w)}^R \left(1 - \frac{c^2}{r^2 w^2}\right)^{1/2} \frac{dr}{c} \quad (7.16)$$

Also, the function  $\alpha(\omega)$  is primarily determined by conditions near the stellar surface. As illustrated in Fig. 7.14 the observed frequencies of solar oscillation satisfy a relation of the form given in Eq. (7.15) quite accurately. This suggests that these relations are useful tools for analysing solar oscillation frequencies. It should be noted, however, that they are only approximately valid. In fact, a much more precise fit to the observed frequencies can be obtained by including additional terms (*e.g.*, Gough & Vorontsov 1995) which take into account the effect of the perturbation to the gravitational potential (significant at low degree) and the dependence of the modes on degree near the upper turning point (important at high degree).

A very powerful relation can be obtained by considering the effect on Eqs (7.15) and (7.16) of small changes to the equilibrium structure. We consider two solar models (or a model and the Sun) with the same surface radius, labelled by the superscripts <sup>(1)</sup> and <sup>(2)</sup>, and introduce the differences  $\delta\omega_{nl} = \omega_{nl}^{(2)} - \omega_{nl}^{(1)}$ ,  $\delta_r c(r) = c^{(2)}(r) - c^{(1)}(r)$  and  $\delta\alpha(\omega) = \alpha^{(2)}(\omega) - \alpha^{(1)}(\omega)$ . By substituting  $c^{(2)}(r) = c^{(1)}(r) + \delta_r c(r)$  and  $\alpha^{(2)}(\omega) = \alpha^{(1)}(\omega) + \delta\alpha(\omega)$  into Eqs (7.15) and (7.16), retaining only terms linear in  $\delta_r c$ ,  $\delta\alpha$  and  $\delta\omega$ , we obtain

$$S_{nl} \frac{\delta\omega_{nl}}{\omega_{nl}} \simeq \int_{r_t}^R \left(1 - \frac{c^2 L^2}{\omega_{nl}^2 r^2}\right)^{-1/2} \frac{\delta_r c}{c} \frac{dr}{c} + \pi \frac{\delta\alpha(\omega_{nl})}{\omega_{nl}}, \quad (7.17)$$

<sup>14</sup> as discussed after Eq. (E.52) one should here use  $L = l + 1/2$ , rather than  $L = \sqrt{l(l+1)}$  as a simple analysis would suggest; we do so in the following.

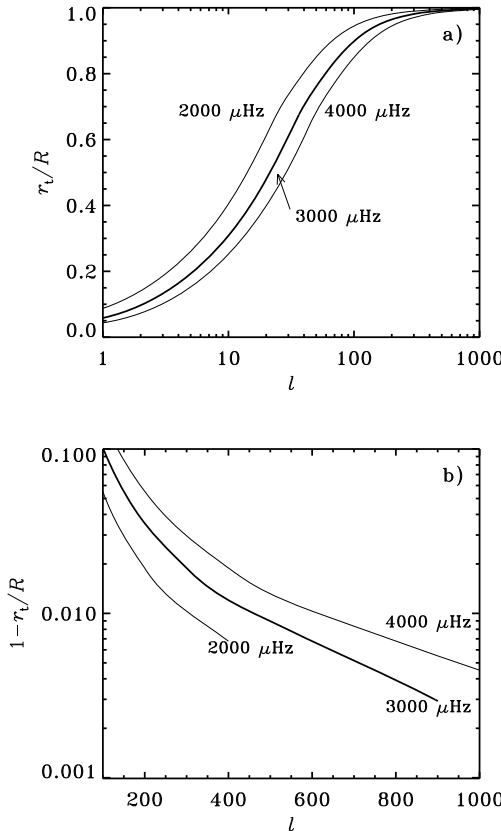


**Fig. 7.13.** The location  $r_t$  (a) of the inner turning point (cf. Eq. (3.189)), and the depth of penetration  $R - r_t$  (b), in units of the solar radius  $R$ , for p modes in a standard solar model. The results are shown as functions of degree  $l$ , for three typical frequencies of solar oscillation.

where

$$S_{nl} = \int_{r_t}^R \left(1 - \frac{L^2 c^2}{r^2 \omega_{nl}^2}\right)^{-1/2} \frac{dr}{c} - \pi \frac{d\alpha}{d\omega}, \quad (7.18)$$

and we have suppressed the superscript <sup>(1)</sup>. This relation was first obtained by Christensen-Dalsgaard *et al.* (1988a).

Equation Eq. (7.17) may be written as

$$S_{nl} \frac{\delta \omega_{nl}}{\omega_{nl}} \simeq \mathcal{H}_1 \left( \frac{\omega_{nl}}{L} \right) + \mathcal{H}_2(\omega_{nl}), \quad (7.19)$$

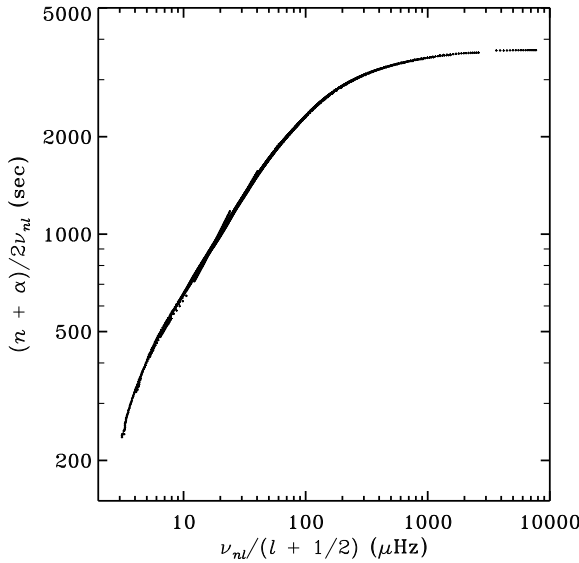


**Fig. 7.14.** Observed frequencies of solar oscillation, plotted according to Eq. (7.15). The constant value of  $\alpha$ , 1.45, was determined such as to minimize the spread in the relation Eq. (7.15). Adapted from Christensen-Dalsgaard *et al.* (1985).

where

$$\mathcal{H}_1(w) = \int_{r_t}^R \left(1 - \frac{c^2}{r^2 w^2}\right)^{-1/2} \frac{\delta_r c}{c} \frac{dr}{c}, \quad (7.20)$$

and

$$\mathcal{H}_2(\omega) = \frac{\pi}{\omega} \delta\alpha(\omega). \quad (7.21)$$

Some properties of this equation were discussed by Christensen-Dalsgaard *et al.* (1988a) and by Christensen-Dalsgaard *et al.* (1989b). As pointed out in the latter paper,  $\mathcal{H}_1(\omega/L)$  and  $\mathcal{H}_2(\omega)$  can be obtained separately, to within a constant, by means of a double-spline fit of the expression Eq. (7.19) to p-mode frequency differences. The dependence of  $\mathcal{H}_1$  on  $\omega/L$  is determined by the sound-speed difference throughout the star, whereas  $\mathcal{H}_2(\omega)$  depends on differences in the upper layers of the models.

There is a close analogy between Eq. (7.19) and the “exact” Eq. (7.11). From Eqs (3.229) and (7.18) it follows that  $S_{nl}$ , apart from the term in the derivative of  $\alpha$ , is proportional to the energy integral  $\mathcal{E}$ . Thus one finds that the scaling  $Q_{nl}$  in Eq. (7.11) is essentially asymptotically equal to  $S_{nl}/S_0$ , where  $S_0 = \lim_{w \rightarrow 0} S(w)$  (Christensen-Dalsgaard 1991b); one may show that

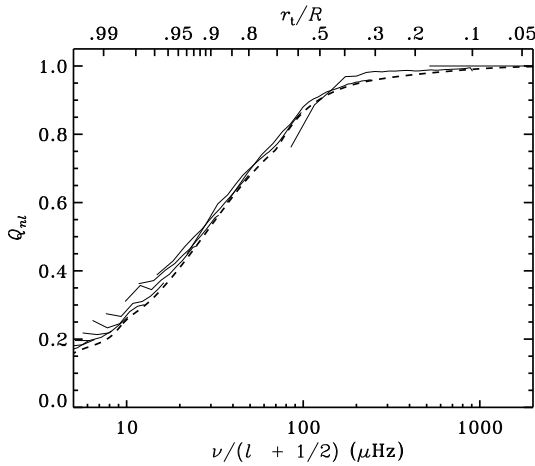


**Fig. 7.15.** The solid lines show the inertia ratio  $Q_{nl}$ , defined in Eq. (7.10), against  $\nu/(l+1/2)$  in a solar model, each curve corresponding to a given degree  $l$ . The upper abscissa shows the turning-point radius  $r_t$ , related to  $\nu/(l+1/2)$  through Eq. (3.189). The heavy dashed curve shows the asymptotic scaling  $\tilde{S}_{nl}/\tau_0$ , where  $\tilde{S}_{nl}$  is defined as in Eq. (7.18) but neglecting the term in  $d\alpha/d\omega$ .

$S_0 = \tau_0$  where

$$\tau_0 = \int_0^R \frac{dr}{c} \quad (7.22)$$

is the acoustic radius of the star. The close correspondence between  $Q_{nl}$  and  $S_{nl}/\tau_0$  is illustrated in Fig. 7.15. Furthermore, the term  $\mathcal{G}(\omega)$  in Eq. (7.11) to some extent corresponds to the term  $\mathcal{H}_2(\omega)$  in Eq. (7.19), in that both terms contain contributions from the uncertain regions very near the stellar surface.

In Eq. (7.17) the first term essentially defines a contribution to  $\delta\omega_{nl}/\omega_{nl}$  as an average of  $\delta_r c/c$ , if we neglect the term in  $d\alpha/d\omega$  in Eq. (7.18). The weight function in this average has a simple physical meaning. The waves corresponding to a given mode travel along rays, as illustrated in Fig. 3.16. It is easy to see that the distance along the ray, corresponding to a change  $dr$  in  $r$ , is given by

$$d\ell = \left( 1 - \frac{c^2 L^2}{\omega^2 r^2} \right)^{-1/2} dr . \quad (7.23)$$

Thus the weight function in the average is simply  $d\ell/c$ , i.e., the travel time of a sound wave corresponding to the distance  $dr$  in  $r$ . This shows that the change

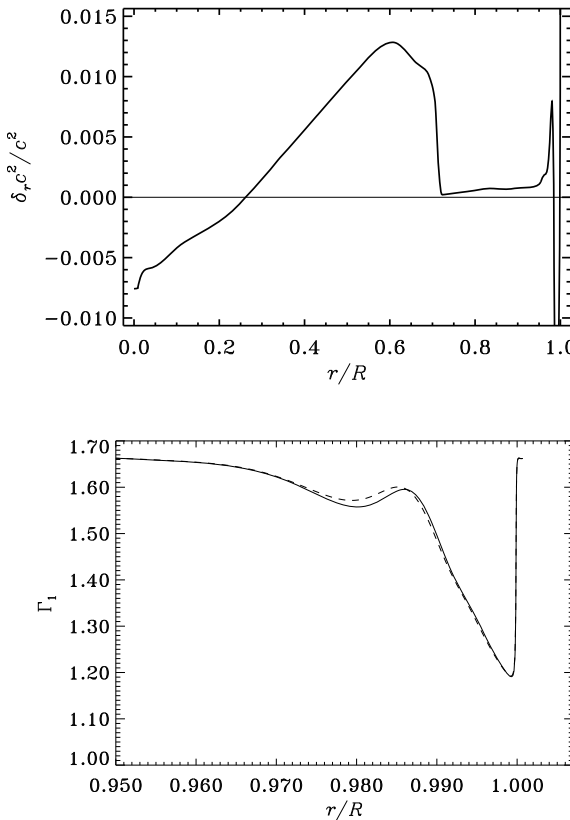


**Fig. 7.16.** The top panel shows the fractional difference in squared sound speed between a model of the present Sun with diffusion of helium and a model without diffusion, in the sense (diffusive model) – (non-diffusive model). The bottom panel shows the adiabatic exponent  $\Gamma_1$  in the model without (solid curve) and the model with (dashed curve) helium diffusion and settling. From Christensen-Dalsgaard *et al.* (1993a).

in sound speed in a region of the Sun affects the frequency with a weight determined by the time spent by the mode, regarded as a superposition of traveling waves, in that region. Thus changes near the surface, where the sound speed is low, have relatively large effects on the frequencies.

To illustrate the behaviour of the separation in Eq. (7.19) we consider differences between two models of Christensen-Dalsgaard *et al.* (1993a): a solar model with diffusion and settling of helium and a model neglecting these effects. Figure 7.16 shows the sound-speed difference between these models. It is

dominated by the fact that the convection zone is slightly deeper in the model with diffusion: since the temperature and sound-speed gradients are steeper in the convection zone than in the radiative region below, there is a region where the sound speed increases more rapidly with depth in the diffusive model, and this leads to the behaviour seen in the figure. Furthermore, due to settling of helium out of the convection zone the hydrogen abundance  $X_e$  in the convective envelope is higher by 0.030 in the model including diffusion, compared with the non-diffusive model. This causes differences in  $\Gamma_1$  (illustrated in the bottom panel of Fig. 7.16), and hence in the sound speed, in the ionization zones of hydrogen and helium.

Figure 7.17a shows scaled relative frequency differences, at selected values of  $l$ , between these two models, plotted against  $\nu/L$ .<sup>15</sup> We have normalized the scaling by  $S_0$ , such that it tends to unity at low degree; hence the scaled frequency differences correspond in magnitude to the differences for low-degree modes. The upper abscissa shows the location of the lower turning point, which is related to  $\nu/L$  through Eq. (3.189). The general behaviour of the frequency differences reflects the asymptotic expression Eq. (7.19). The dependence of  $S\delta\nu/\nu$  on  $\nu/L$  can be understood from the sound-speed difference shown in Fig. 7.16: for  $\nu/L \lesssim 100 \mu\text{Hz}$  the modes are entirely trapped in the convection zone, and the frequency difference is dominated by the term  $\mathcal{H}_2(\omega)$  arising from differences near the surface, particularly the difference in  $X_e$ . In contrast, modes with  $\nu/L > 100 \mu\text{Hz}$  sense the substantial positive  $\delta_r c$  just beneath the convection zone, and hence display a positive frequency difference; the transition occurs quite abruptly as the modes begin to penetrate beyond the convection zone.

This qualitative description suggests that the frequency differences may be analysed in detail in terms of Eq. (7.19). To do so, we have determined the functions  $\mathcal{H}_1$  and  $\mathcal{H}_2$  by means of the spline fit of Christensen-Dalsgaard *et al.* (1989b), where details about the fitting method may be found. Figure 7.17b shows the result of subtracting the function  $\mathcal{H}_2(\omega)$  so obtained from the scaled frequency differences. It is evident that what remains is in fact very nearly a function of  $\omega/L$  alone, directly reflecting the behaviour of  $\delta_r c/c$ , as discussed above. The function  $\mathcal{H}_1(\omega)$  obtained from the fit is shown in Fig. 7.17c.

In Fig. 7.18a we show the residual scaled frequency differences after subtraction of the term in  $\mathcal{H}_1(\omega/L)$ ; these are clearly predominantly functions of frequency, although with some scatter. The fitted function  $\mathcal{H}_2(\omega)$  is shown in Fig. 7.18b. The oscillatory part of  $\mathcal{H}_2$  largely arises from the modest difference in  $\Gamma_1$  illustrated in Fig. 7.16 and hence reflects the difference in the envelope helium abundance between the two models. This is an example of the effect of an ‘‘acoustic glitch’’, as discussed above. The ‘‘period’’ of the oscillation in  $\mathcal{H}_2$  corresponds to the acoustic depth of the second helium ionization zone,

---

<sup>15</sup> To facilitate the comparison with the observations, in the following we present the properties of the frequency differences in terms of the cyclic frequency  $\nu$ , rather than the angular frequency  $\omega = 2\pi\nu$ ; this should cause little confusion.

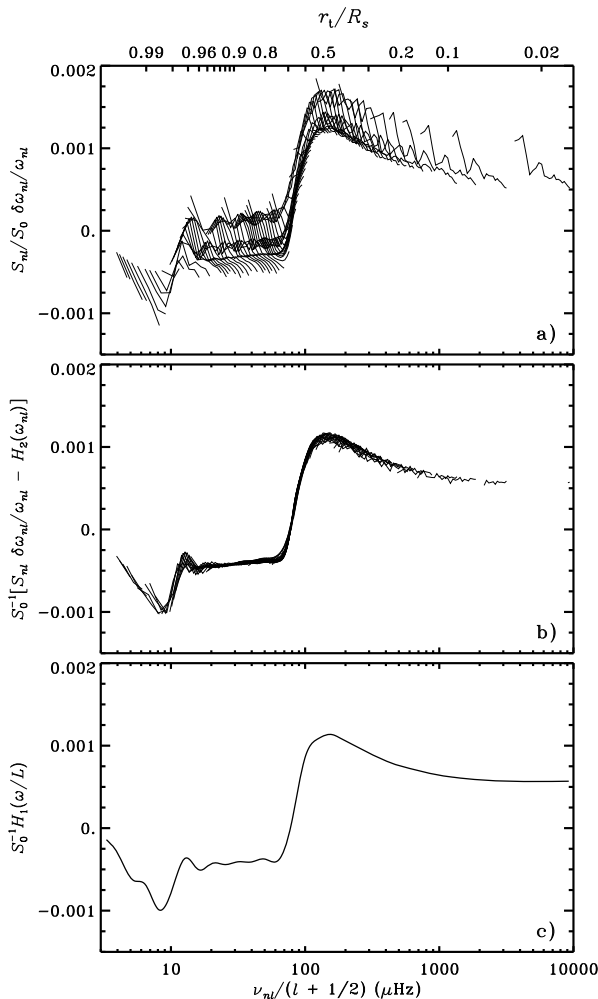


**Fig. 7.17.** Scaled frequency differences corresponding to the model differences shown in Fig. 7.16, plotted against  $\nu/(l + 1/2)$ . The upper abscissa shows the location of the lower turning point, which is related to  $\nu/(l + 1/2)$  through Eq. (3.189). In panels (a) and (b) points corresponding to fixed  $l$  have been connected. (a) Original scaled frequency differences. (b) Scaled differences, after subtraction of the function  $\mathcal{H}_2(\omega)$  obtained from the spline fit. (c) The fitted function  $\mathcal{H}_1(\omega/L)$ .

around  $r \simeq 0.98R$ . It is evident that a difference  $\Delta Y_e = -0.03$  in the envelope helium abundance results in a signal that is clearly visible in the frequencies, when analysed in this manner.

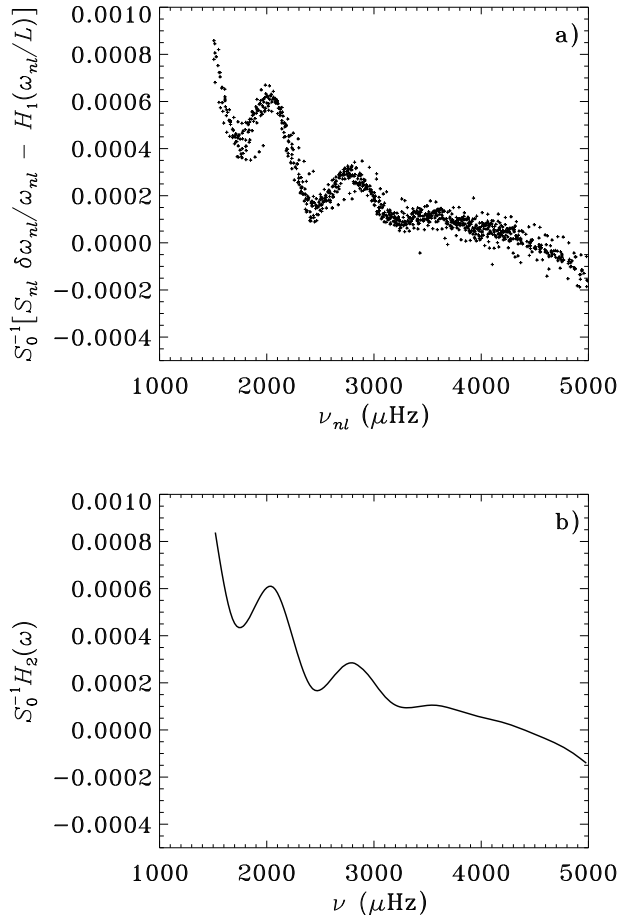


**Fig. 7.18.** The frequency-dependent part of the scaled frequency differences corresponding to the model differences shown in Fig. 7.16. (a) Scaled differences after subtraction of the function  $H_1(\omega/L)$  resulting from the spline fit. (b) The fitted function  $H_2(\omega)$ .

It was shown by Christensen-Dalsgaard & Pérez Hernández (1992) that the Duvall phase function  $\alpha(\omega)$  could be determined as a continuous function of frequency, by computing partial solutions to the oscillation equations, satisfying just the outer boundary conditions, and fitting those solutions to the asymptotic expression, Eq. (3.226), at a suitable point near the surface of the model. This provides an explicit determination of the phase change from

the near-surface reflection, as given by the structure of the outer layers of the model. The dependence of  $\alpha$  on frequency, including the variations induced by the second helium ionization zone, is reflected in the curvature in the échelle diagram shown in Fig. 7.4. Based on this analysis they demonstrated that the behaviour of  $\mathcal{H}_2$  can be understood in terms of the difference between the structure in two models, through kernels that relate  $\mathcal{H}_2$  to the change in  $c$  and the acoustic cut-off frequency  $\omega_a$  (*cf.* Eq. (3.202)).

#### 7.1.4.5 Inversion of the Duvall Law

The function  $F(w)$  in Eq. (7.15) can be determined from the observations (*cf.* Fig. 7.14). Given  $F$ , Eq. (7.16) is an integral equation of the Abel type and can be inverted analytically to obtain the sound speed implicitly, thus:

$$r = R \exp \left[ -\frac{2}{\pi} \int_{a_s}^a (w^{-2} - a^{-2})^{-1/2} \frac{dF}{dw} dw \right] \quad (7.24)$$

(Gough 1984a), where  $a = c/r$  and  $a_s = a(R)$ . This relation was used by Christensen-Dalsgaard *et al.* (1985) to infer the sound speed in the solar interior. The properties of this inversion technique were discussed in considerable detail by Gough (1986b).

The asymptotic description leading to Eq. (7.24) clearly suffers from systematic errors. It has been found, for example, that for the most deeply penetrating modes of low degree the perturbation to the gravitational potential has a substantial effect on the functions  $F(\omega/L)$  obtained by fitting the relation Eq. (7.15) to computed or observed frequencies; this may cause problems for the inversion in the solar core. Also, for modes trapped near the surface the behaviour near the upper turning point depends on the degree; this introduces what is effectively an  $l$ -dependent term in  $\alpha$ . It is possible to generalize Eq. (7.15) to take such effects into account and hence obtain a substantially more precise inversion (*e.g.*, Vorontsov & Shibahashi 1991).

Alternatively, it appears that the systematic errors cancel to some extent when differences are taken between inversions of different sets of frequencies. Christensen-Dalsgaard *et al.* (1985) made use of this by considering differences between inversions done for the solar data and for frequencies of a reference model. A more systematic approach follows from the separation of scaled frequency differences in Eq. (7.19). Here the function  $\mathcal{H}_1(\omega/L)$  is related to the sound-speed difference between the models, or between the Sun and the model, through Eq. (7.20). As shown by Christensen-Dalsgaard *et al.* (1989b), given a determination of  $\mathcal{H}_1$ , that equation is an integral equation for  $\delta_r c/c$ , with the solution

$$\frac{\delta_r c}{c} = -\frac{2a}{\pi} \frac{d}{d \ln r} \int_{a_s}^a (a^2 - w^2)^{-1/2} \mathcal{H}_1(w) dw . \quad (7.25)$$

This was first derived in the corresponding case (*cf.* Eq. (7.26) below) of the asymptotic inversion for an  $r$ -dependent angular velocity  $\Omega(r)$ , by Gough (1984a).

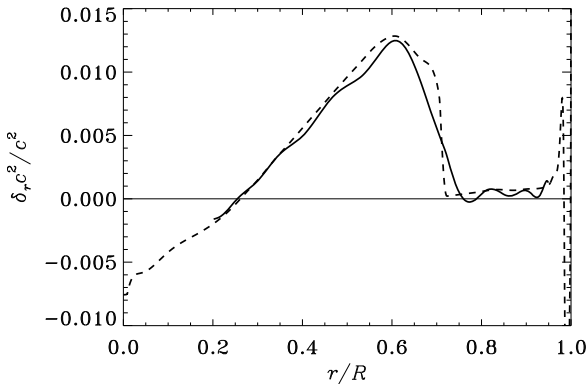


**Fig. 7.19.** The solid line shows the difference in squared sound speed  $\delta_r c^2 / c^2$  inferred by applying Eq. (7.25) to the function  $\mathcal{H}_1(\omega/L)$  shown in Fig. 7.17c. For comparison, the dashed line shows the true difference between the two models. Adapted from Christensen-Dalsgaard *et al.* (1993a).

Christensen-Dalsgaard *et al.* (1989b) carried out a careful test of the differential method, as applied to several different pairs of models. Also, Christensen-Dalsgaard *et al.* (1988b) used the method to invert differences between observed frequencies and frequencies computed for a solar model. Here we illustrate its properties by applying it to the model pair shown in Fig. 7.16.

Figure 7.19 shows the  $\delta_r c^2 / c^2$  inferred from the scaled frequency differences in Fig. 7.17 between the diffusive and the non-diffusive solar model, by applying Eq. (7.25) to the fitted function  $\mathcal{H}_1(\omega/L)$  shown in Fig. 7.17c. For comparison, the figure also shows the true sound-speed difference, previously plotted in Fig. 7.16. It is evident that the inversion reproduces the main features of the true  $\delta_r c^2 / c^2$  with considerable accuracy. One noticeable difference is that the transition at the base of the convection zone is less sharp: as discussed in Section 7.1.5 below, it is a general property of inverse analyses that they smooth the properties of the true structure. However, otherwise the inferred and the true  $\delta_r c^2 / c^2$  are quite close over the entire range,  $0.2R < r < 0.95R$ , where the solution is plotted. At smaller and larger radii the systematic errors associated with the asymptotic representation increasingly affect the results; hence here the solution has not been obtained.

It should finally be mentioned that several other techniques have been developed to invert the Duvall law, Eq. (7.15) (Brodsky & Vorontsov 1987, 1988; Shibahashi 1988; Sekii & Shibahashi 1989). Gough & Thompson (1991) have made a comparison of these different techniques. The results suggest that,

at least for the cases considered, the differential technique described here is superior. Nonasymptotic inversion of similar data sets will be discussed in Section 7.1.6.

#### 7.1.4.6 Asymptotic Properties of the Rotational Splitting

It is also instructive to consider the asymptotic description of the rotational splitting, considering first the case where  $\Omega = \Omega(r)$  depends only on  $r$ . For high-order p modes, with  $\beta_{nl} \simeq 1$ , the integral in Eq.(3.355) provides a weighted average of  $\Omega(r)$ ; using the asymptotic properties of the eigenfunctions we obtain

$$\delta\omega_{nlm} \simeq m \frac{\int_{r_t}^R \left(1 - \frac{L^2 c^2}{r^2 \omega_{nl}^2}\right)^{-1/2} \Omega(r) \frac{dr}{c}}{\int_{r_t}^R \left(1 - \frac{L^2 c^2}{r^2 \omega_{nl}^2}\right)^{-1/2} \frac{dr}{c}}. \quad (7.26)$$

Thus, as in the case of the sound-speed difference, we obtain the rotational splitting as an average of the angular velocity, weighted by the sound travel time along the ray (see the discussion in connection with Eq.(7.23)). This expression can also be obtained from ray theory (Gough 1984a). As discussed above, it can be inverted, as in Eq.(7.25), to infer  $\Omega(r)$  from  $m^{-1}\delta\omega_{nlm}$ .

In the more general case where  $\Omega = \Omega(r, \theta)$  depends also on co-latitude we obtain, using furthermore an asymptotic approximation to  $P_l^m$  (see Eqs(B.15) and (B.16)), that

$$\delta\omega_{nlm} \simeq m \frac{\int_{-\cos\Theta}^{\cos\Theta} (\cos^2\Theta - \cos^2\theta)^{-1/2} \int_{r_t}^R \left(1 - \frac{L^2 c^2}{r^2 \omega^2}\right)^{-1/2} \Omega(r, \theta) \frac{dr}{c} d(\cos\theta)}{\pi \int_{r_t}^R \left(1 - \frac{L^2 c^2}{r^2 \omega^2}\right)^{-1/2} \frac{dr}{c}}, \quad (7.27)$$

where  $\Theta = \sin^{-1}(m/L)$  (Gough & Thompson 1990, 1991). The asymptotic approximation to  $P_l^m$  shows that a given spherical harmonic is confined essentially to the latitude band between  $\pm\Theta$ ; within this region  $P_l^m$  oscillates as a function of  $\theta$ , whereas at higher latitudes it decreases exponentially. The variation of the extent of the  $P_l^m$  with  $m/L$  allows resolution of the latitudinal variation of the angular velocity, in much the same way as the variation of the depth of penetration with  $\omega/L$  allows resolution of the variation with radius. In particular, with increasing  $l$  the sectoral modes (with  $l = |m|$ ) get increasingly confined towards the equator (see also Fig.B.1). Thus, the rotational splitting of sectoral modes provides a measure of the solar equatorial angular velocity.

### 7.1.5 Principles of Inverse Analysis

The expression Eq. (3.355) for the splitting caused by spherically symmetric rotation is a particularly simple example of the relation between the observable properties of the oscillation frequencies and the properties of the solar interior which we wish to determine. The determination of  $\Omega(r)$  from the  $\delta\omega_{nlm}$  constitutes the simplest example of an *inverse problem*. In particular, there is a linear relation between the observables and the property of the solar interior. In contrast, the oscillation frequencies depend in a nonlinear fashion on the structure of the Sun, as specified by for example  $\rho(r)$  and  $c(r)$  (*cf.* Section 3.3.3). However, by assuming that the real solar structure can be obtained from the structure of a given reference model by applying small corrections, the differences in frequency between the observations and the reference model can be obtained from a linear perturbation analysis of the oscillation equations, resulting, once more, in a linear relation between the frequency differences and the corrections to the model; this was discussed in some detail in Section 3.6.2 (see Eq. (3.269)). Thus the linear inverse problem forms the basis for much of the inverse theory for solar oscillations.

Inverse problems have a vast literature, covering their application in, for example, geophysics and radiation theory (*e.g.*, Parker 1977; Craig & Brown 1986; Deepak 1977; Tarantola 1987). The application to the solar inverse problem was discussed by Gough (1985b) and Gough & Thompson (1991). Christensen-Dalsgaard *et al.* (1990) made a systematic comparison of different inversion techniques, as applied to the problem of spherically symmetric rotation; the following discussion is to a large extent based on their results.

The simplicity of the inversion for a spherically symmetric rotation rate  $\Omega(r)$ , related to the observed rotational splittings by Eq. (3.355), makes it a very useful prototype of more general inversions, and hence we discuss it in some detail. The problem may be expressed as

$$\Delta_i = \int_0^R K_i(r) \Omega(r) dr + \epsilon_i , \quad i = 1, \dots, M , \quad (7.28)$$

where, for notational simplicity, we represent the pair  $(n, l)$  by the single index  $i$ ;  $M$  is the number of modes in the data set considered.  $\Delta_i$  is the scaled rotational splitting  $m^{-1} \beta_{nl}^{-1} \delta\omega_{nlm}$ , the kernels  $K_i$  having been normalized as in Eq. (3.358), and  $\epsilon_i$  is the observational error in  $\Delta_i$ . The goal of the inversion is to determine an approximation  $\bar{\Omega}(r_0)$  to the true angular velocity, as a function of position  $r_0$  in the Sun; obviously this is only possible for those parts of the Sun about which the oscillations provide data. In most cases considered so far, the inversion is carried out through linear operations on the data. Hence  $\bar{\Omega}$  is linearly related to the data: for each  $r_0$  there exists a set of *inversion coefficients*  $c_i(r_0)$  such that

$$\bar{\Omega}(r_0) = \sum_i c_i(r_0) \Delta_i = \int_0^R \mathcal{K}(r_0, r) \Omega(r) dr + \sum_i c_i(r_0) \epsilon_i , \quad (7.29)$$

using Eq. (7.28) in the second equality; here the *averaging kernel*  $\mathcal{K}(r_0, r)$  is given by

$$\mathcal{K}(r_0, r) = \sum_i c_i(r_0) K_i(r) . \quad (7.30)$$

The inversion coefficients and averaging kernels clearly depend on the choice of the inversion method, and of possible parameters that enter into the method; indeed, the inversion may be thought of as a way to determine coefficients and averaging kernels such as to obtain as much information about the angular velocity as possible, while controlling the error in the inference. On the other hand, once the method and parameters have been chosen, the coefficients and averaging kernels are independent of the data values. Hence they can be used to make a data-independent comparison of different inversion methods; this was the approach taken by Christensen-Dalsgaard *et al.* (1990).

The averaging kernels provide an indication of the resolution of the inversion; it is clearly desirable to achieve averaging kernels that are sharply peaked around  $r = r_0$ , and with small amplitude far away from that point. As a quantitative measure of resolution it is common to use a width of  $\mathcal{K}(r_0, r)$  obtained as the distance  $r_3 - r_1$  between the first and third quartile points, defined by

$$\int_0^{r_k} \mathcal{K}(r_0, r) dr = \frac{k}{4} \int_0^R \mathcal{K}(r_0, r) dr , \quad k = 1, 2, 3 . \quad (7.31)$$

Also, from the last term in Eq. (7.29) it follows that the variance in the result of the inversion is

$$\sigma[\bar{\Omega}(r_0)]^2 = \sum_i c_i(r_0)^2 \sigma_i^2 , \quad (7.32)$$

assuming that the standard errors  $\sigma_i$  on  $\Delta_i$  are uncorrelated. In particular, if (somewhat unrealistically)  $\sigma_i = \sigma$  is assumed to be the same for all the observed modes,  $\sigma[\bar{\Omega}(r_0)] = \Lambda(r_0)\sigma$  where we introduced the *error magnification*

$$\Lambda(r_0) = \left[ \sum_i c_i(r_0)^2 \right]^{1/2} . \quad (7.33)$$

The optimization of the inversion techniques is often based on a trade-off between width of the averaging kernels and error or error magnification (*cf.* Figure 7.21 below).

A procedure which is based explicitly on the determination of the inversion coefficients is the technique of *optimally localized averages* (OLA), developed by Backus & Gilbert (1970); this has been used extensively for helioseismic inversion. The goal is to choose the coefficients  $c_i(r_0)$  such as to make  $\mathcal{K}(r_0, r)$  approximate as far as possible a delta function  $\delta(r - r_0)$  centred on  $r_0$ ; then  $\bar{\Omega}(r_0)$  provides an approximation to  $\Omega(r_0)$ . This is achieved by determining the coefficients  $c(r_0)$  such as to minimize

$$\int_0^R (r - r_0)^2 \mathcal{K}(r_0, r)^2 dr + \mu \sum_i c_i(r_0)^2 \sigma_i^2 , \quad (7.34)$$

subject to the constraint

$$\int_0^R \mathcal{K}(r_0, r) dr = 1 . \quad (7.35)$$

This is equivalent to solving the set of linear equations

$$\sum_j W_{ij} c_j = b , \quad \sum_j c_j = 1 , \quad (7.36)$$

where  $b$  is a Lagrange multiplier. Here

$$W_{ij} = S_{ij} + \mu \sigma_i^2 \delta_{ij} , \quad (7.37)$$

where

$$S_{ij} = \int_0^R (r - r_0)^2 K_i(r) K_j(r) dr . \quad (7.38)$$

Furthermore,  $\mu$  is a parameter which, as discussed below, must be adjusted to optimize the result.

The effect of the minimization is most easily understood for  $\mu = 0$ . Minimizing Eq. (7.34) subject to Eq. (7.35) ensures that  $\mathcal{K}(r_0, r)$  is large close to  $r_0$ , where the weight function  $(r - r_0)^2$  is small, and small elsewhere. This is precisely the required “delta-ness” of the combined kernel. However, with no further constraints, the optimization of the combined kernel may result in numerically large coefficients of opposite sign. Hence, the variance in  $\bar{\Omega}$ , obtained from Eq. (7.32), would be large. The effect of the second term in Eq. (7.34), when  $\mu > 0$ , is to restrict  $\sigma^2(\bar{\Omega})$ . The size of  $\mu$  determines the relative importance of the localization and the size of the variance in the result. Hence,  $\mu$  must be determined to ensure a trade-off between the localization and the error, measured by the width of  $\mathcal{K}(r_0, r)$  and  $\sigma[\bar{\Omega}(r_0)]$ , respectively;  $\mu$  is generally known as *the trade-off parameter*.

The principal difficulty of this method is computational expense: at each target radius  $r_0$  it involves the solution of a set of linear equations whose order is the number of data points. Jeffrey (1988) proposed an alternative version where the coefficients were determined by minimizing the difference between  $\mathcal{K}(r_0, r)$  and the delta function  $\delta(r - r_0)$ . This is computationally more efficient, in that only one matrix inversion is required, but results in averaging kernels with somewhat undesirable properties. Pijpers & Thompson (1992, 1994) developed this method further, by matching  $\mathcal{K}(r_0, r)$  instead to a prescribed *target function*  $T(r_0, r)$  which more closely matches the behaviour that can be achieved with the given mode set. They dubbed this the *SOLA* technique (for Subtractive Optimally Localized Averaging), to distinguish it

from the *MOLA* technique (for Multiplicative Optimally Localized Averaging) discussed above. Specifically, the coefficients  $c_i(r_0)$  are determined by minimizing

$$\int_0^R [\mathcal{K}(r_0, r) - \mathcal{T}(r_0, r)]^2 dr + \mu \sum_i \sigma_i^2 c_i(r_0)^2, \quad (7.39)$$

where again  $\mu$  is a trade-off parameter. In addition, the width of  $\mathcal{T}(r_0, r)$  functions as a parameter, in most cases depending on  $r_0$ , of the method. As before, the inclusion of the last term in Eq. (7.39) serves to limit the error in the solution. The minimization leads to the following system of linear equations for the  $c_i(r_0)$ :

$$\sum_j (K_{ij} + \mu \sigma_i^2 \delta_{ij}) c_j(r_0) = T_i(r_0); \quad (7.40)$$

here

$$K_{ij} = \int_0^R K_i(r) K_j(r) dr, \quad T_i(r_0) = \int_0^R \mathcal{T}(r_0, r) K_i(r) dr. \quad (7.41)$$

In Eq. (7.40) the coefficient matrix on the left-hand side is independent of  $r_0$ . Thus it can be inverted or, more efficiently, suitably factored, once and for all; after this the determination of the coefficients at each target point  $r_0$  is virtually free. Compared with the MOLA technique the computational effort is therefore reduced by roughly a factor given by the number of target locations. An additional advantage of the technique is the ability to choose the target function such as to tailor the averaging kernels to have specific properties. In addition to the usual trade-off parameter  $\mu$  controlling the weight given to the errors, the method obviously depends on parameters controlling the properties of the target functions  $\mathcal{T}(r_0, r)$ . These are often taken to be of Gaussian shape; it was argued by Thompson (1993) that the radial resolution, for inversion of acoustic modes, is proportional to the sound speed  $c$ , and hence the width of  $\mathcal{T}(r_0, r)$  is generally taken to be proportional to  $c(r_0)$ , the constant of proportionality serving as a parameter characterizing the targets.

A second commonly used technique is the regularized least-squares, or Tikhonov, method (the RLS method; see, for example, Craig & Brown 1986). Here the solution  $\bar{\Omega}(r)$  is parameterized, often as a piecewise constant function on a grid  $r_0 < r_1 < \dots < r_N$ , with  $\bar{\Omega}(r) = \Omega_j$  on the interval  $[r_{j-1}, r_j]$ ; the parameters  $\Omega_j$  are determined through a least-squares fit to the data. In general, this least-squares procedure needs to be regularized to obtain a smooth solution. This is achieved by including in the minimization a term which restricts the square of  $\bar{\Omega}$ , or the square of its first or second derivative. Thus, for example one may minimize

$$\sum_i \sigma_i^{-2} \left[ \int_0^R K_i(r) \bar{\Omega}(r) dr - \Delta_i \right]^2 + \mu \int_0^R \left( \frac{d^2 \bar{\Omega}}{dr^2} \right)^2 dr, \quad (7.42)$$

where in the last term a suitable discretized approximation to  $d^2\bar{\Omega}/dr^2$ , in terms of the  $\Omega_j$ , is used. The minimization of Eq. (7.42) clearly leads to a set of linear equations for  $\bar{\Omega}_j$ , defining the solution; however, it is still the case that the procedure can be formulated as in Eq. (7.29) and hence leads to the determination of inversion coefficients and averaging kernels. By restricting the second derivative, the last term in Eq. (7.42) suppresses rapid oscillations in the solution, and hence ensures that it is smooth; the weight  $\mu$  given to this term serves as a trade-off parameter, determining the balance between resolution and error for this method.

The asymptotic expression Eq. (7.26) for the frequency splitting provides the basis for a final example of an inversion method in widespread use. After multiplication by the denominator the right-hand side of that equation is a function  $\mathcal{H}(\omega/L)$  which is in principle determined by the observed splittings. Given  $\mathcal{H}(w)$ , the angular velocity can be inferred as in the determination in Eq. (7.25) of the sound-speed difference from the function  $\mathcal{H}_1(\omega/L)$ . As in that case an approximation to  $\mathcal{H}(\omega/L)$  is obtained by making a least-squares fit to the scaled splittings, *e.g.*, of a spline over a suitably chosen set of knots. The number of knots determines the resolution achieved in representing  $\mathcal{H}(w)$  and hence in the inferred solution  $\bar{\Omega}(r)$ , hence effectively serving as a trade-off parameter. Again, the processes of carrying out the spline fit to the scaled data and evaluating the integral corresponding to Eq. (7.25) are linear, and hence the method allows the evaluation of inversion coefficients and averaging kernels (see Christensen-Dalsgaard *et al.* 1990 for details).

An illustration of the use of these methods is provided by the results obtained by Christensen-Dalsgaard *et al.* (1990). They considered a set consisting of about 830 modes at selected degrees between 1 and 200, and frequencies between 2000 and 4000  $\mu$ Hz; for simplicity, the standard errors were assumed to be the same for all modes. Figure 7.20 shows examples of averaging kernels  $\mathcal{K}(r_0, r)$  for the MOLA, regularized least-squares and asymptotic methods. The trade-off parameters were chosen such that the error magnification at  $r_0 = 0.5R$  was close to 1 in all three cases. It should be realized that the kernels entering into the combination are of the form shown in Figure 3.39. Thus, a very large degree of cancellation has been achieved of the dominant contribution from near the surface. Nevertheless, it is obvious that the averaging kernels are only approximate realizations of delta functions; structure on a scale smaller than roughly  $0.05R$  is not resolved.

This limitation is inherent in any inversion method. Indeed, it is evident that from a finite set of data one can never completely resolve the function  $\Omega(r)$ . To obtain a definite solution, additional constraints must be invoked. The constraints used here essentially demand that the solution be smooth. This is ensured in the method of optimally localized kernels by representing the solution by smooth averaging kernels whose shape is determined by the minimization in Eq. (7.34). For the Tikhonov method smoothness is explicitly demanded by constraining the second derivative of the solution, whereas in the case of the asymptotic technique the constraints lie partly in using the

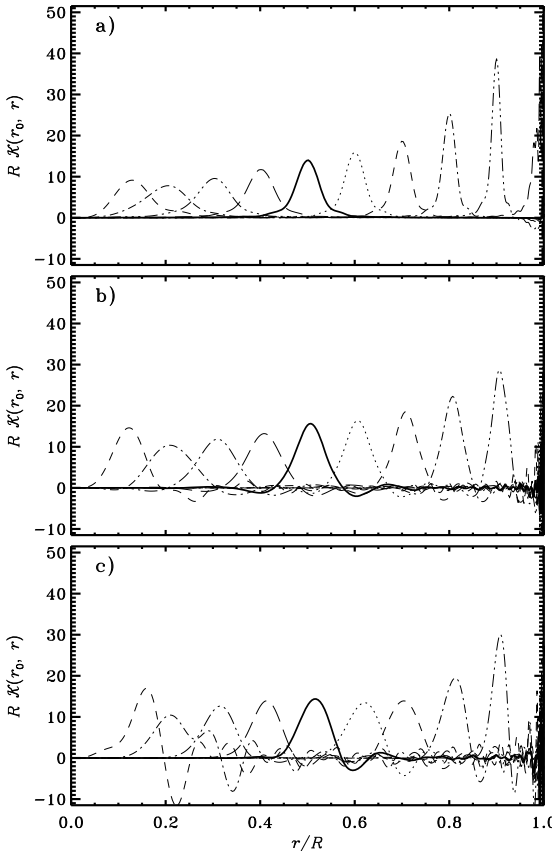


**Fig. 7.20.** Averaging kernels  $\mathcal{K}(r_0, r)$  at selected radii ( $r_0/R = 0.1, 0.2, \dots, 1.0$ ) for inversion by means of the MOLA technique (panel a), the Tikhonov inversion with second-derivative smoothing (panel b) and asymptotic inversion (panel c). The parameters in each inversion method have been chosen to obtain approximately the same error magnification for  $r_0 = 0.5R$ . In each case, the kernel at  $r_0 = 0.5R$  is shown as a bolder curve. From Christensen-Dalsgaard *et al.* (1990).

asymptotic description, which in itself assumes that the solution varies on a scale larger than the wavelength of the modes, partly in the spline fit to the scaled data.

All methods contain trade-off parameters which determine the relative weight given to the demands of resolution on the one hand, and smoothness or minimizing errors on the other. To illustrate this balance, it is common to consider trade-off diagrams, where a measure of error is plotted against a measure of the width of the averaging kernels. Examples are shown in Fig. 7.21.

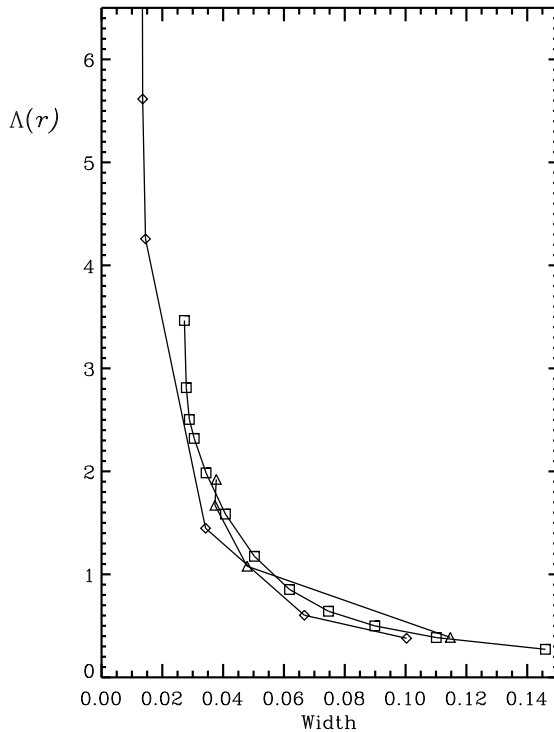


**Fig. 7.21.** The trade-off between error magnification  $\Lambda(r_0)$  (cf. Eq. (7.33)) and width (defined as distance between quartile points), for inversion at  $r_0 = 0.5R$ . Results are shown for the MOLA technique ( $\square$ ), Tikhonov inversion ( $\diamond$ ) and asymptotic inversion ( $\triangle$ ), in each case varying the relevant trade-off parameter over a wide range. From Christensen-Dalsgaard *et al.* (1990).

The similarity, in terms of such global measures, between the three conceptually rather different methods is quite striking.

It is also of interest to consider in detail the way in which the different methods utilize the data, as expressed in terms of the inversion coefficients. In the case of the asymptotic technique it may be shown that these depend on  $\omega/L$  alone; hence for the purpose of comparison it is sensible to plot the coefficients as a function of  $\omega/L$  in all cases. In Fig. 7.22 the coefficients for the optimally localized averages and the Tikhonov inversions are compared with those obtained with the asymptotic technique, for  $r_0 = 0.5R$ . It is evident that the overall behaviour of the coefficients is quite similar in all three cases; in particular, the modes dominating the inversion are those whose turning point  $r_t$  is in the vicinity of the target radius  $r_0$ . At a more subtle level, there are significant differences. In particular, unlike the Tikhonov case, inversion by

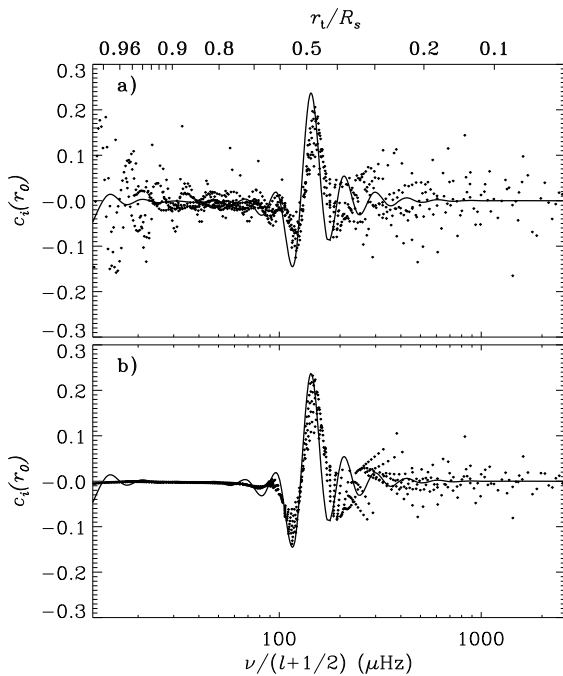


**Fig. 7.22.** Inversion coefficients  $c_i(r_0)$  for the inversions illustrated in Figure 7.20, at  $r_0 = 0.5R$ ; they have been plotted against  $\nu/(l + 1/2)$  which, according to Eq. (3.189), measures the location  $r_t$  of the lower turning point; this is indicated on the upper abscissa. The continuous line in both panels shows coefficients for the asymptotic method which are functions of  $\nu/(l + 1/2)$ . Panel (a) gives the coefficients obtained with the MOLA technique, whereas panel (b) shows coefficients for Tikhonov inversion. Adapted from Christensen-Dalsgaard *et al.* (1990).

optimally localized averages makes substantial use of modes of high degree. It may be shown that these are used essentially only to improve the averaging kernels near the surface; in fact, as can be seen in Fig. 7.20 the  $\mathcal{K}(r_0, r)$  for Tikhonov inversion have quite substantial amplitude at very short wavelength near the surface, whereas such structure is entirely suppressed by the minimization in Eq. (7.34) for the optimally localized averages.

The least-squares problem defined in Eq. (7.42) can conveniently be analysed through singular value decomposition (SVD; *e.g.*, Craig & Brown 1986). In particular, Hansen (1990) noted that the equivalent problem, but regularizing using the norm of the solution, can be solved by means of a truncated SVD expansion. Although this form of regularization is not preferred, the

expansion defines the most significant components of the data. As discussed by Christensen-Dalsgaard & Thompson (1993) this can be used to preprocess the data by extracting those components as input to the inverse analysis, thus very substantially reducing the computational effort in the inversion.<sup>16</sup> Christensen-Dalsgaard *et al.* (1993b) showed that the more general regularization, such as the second-derivative term used in Eq. (7.42), can be analysed by means of the so-called generalized singular value decomposition. This provides a natural basis for expressing the inverse problem which can then be used to study the properties of other inversion methods. In particular, Christensen-Dalsgaard *et al.* (1993b) discussed the different behaviour of the inversion coefficients for the OLA and RLS methods (see Fig. 7.22).

Graphs such as Fig. 7.21 are very useful for the choice of the trade-off parameter; however, it is evident that this choice depends critically on the particular application, including the errors in the data. The question of how to fix the trade-off parameter, or indeed even how to choose the inversion method, has given rise to a great deal of debate, occasionally of an almost philosophical (or, dare one say, religious) nature. It has been suggested that inversion methods should be chosen which aim at fitting the data; this makes the method of optimally localized averages, whose goal is instead to design the averaging kernels, less attractive. Also, a great deal of emphasis has been placed on techniques for objectively determining the trade-off parameters, based on the errors in the data and possibly the properties of the solution. In contrast, the approach taken in helioseismology has to a large extent been pragmatic: in fact, it can be argued that since no method, or choice of trade-off, can provide the exact solution given the necessarily incomplete data, the most important aspect of the inversion is to be able to interpret the result and its significance. In this respect, the averaging kernels which graphically illustrate the resolution, and the inversion coefficients which allow evaluation of effects of errors in the data, are clearly very useful. By choosing different inversion methods, and different values of the trade-off parameters, considering in each case the properties of the resulting inversion, one can hope to obtain a more complete impression of the underlying solution. In this process prior knowledge, or prejudices, about the solution clearly play a significant role; these should ideally be formulated in a well-defined statistical sense, but probably often are not.

### 7.1.5.1 Two-Dimensional Rotational Inversion

So far, we have considered inversion for a function that depends on  $r$  alone. It is evidently desirable, however, to carry out inversion for more general properties which are functions both of  $r$  and  $\theta$ . Here we concentrate on the case of determining the angular velocity  $\Omega(r, \theta)$ ; it should be noticed, however, that another interesting inverse problem concerns the departure of the structure from spherical symmetry (*cf.* Section 7.1.9).

---

<sup>16</sup> A similar analysis was carried out for structure inversion by Basu *et al.* (1997a).

As demonstrated by the asymptotic relation (7.27) the latitude dependence of rotation is reflected in the dependence of the frequencies on azimuthal order  $m$ . Thus in general individual frequencies  $\omega_{nlm}$  have to be analysed. This greatly increases the amount of data to be considered, compared with the simple 1-dimensional case discussed above, and computational efficiency becomes a crucial consideration. However, it is still generally the case that the inferred angular velocity  $\bar{\Omega}(r_0, \theta_0)$  at some location  $(r_0, \theta_0)$  is linearly related to the data; as discussed by Schou *et al.* (1992) this allows the introduction of inversion coefficients and generalized averaging kernels  $\mathcal{K}(r_0, \theta_0, r, \theta)$  defined such that  $\bar{\Omega}(r_0, \theta_0)$  is related to the true angular velocity  $\Omega(r, \theta)$  through

$$\bar{\Omega}(r_0, \theta_0) = \int_0^\pi \int_0^R \mathcal{K}(r_0, \theta_0, r, \theta) \Omega(r, \theta) r dr d\theta. \quad (7.43)$$

The form of the inverse problem evidently depends on the representation of the data. The general problem has the form

$$\omega_{nlm} - \omega_{nl0} = \delta\omega_{nlm} = m \int_0^R \int_0^\pi K_{nlm}(r, \theta) \Omega(r, \theta) r dr d\theta \quad (7.44)$$

(*cf.* Eq. (3.349)). However, it is often the case that the data do not allow determination of individual frequencies  $\omega_{nlm}$ . In that case, it is customary to make fits of the general form shown in Eq. (7.9). Since the fitting procedure is in general linear, the  $a$  coefficients  $a_j(n, l)$  are linearly related to the frequency splittings,

$$2\pi a_j(n, l) = \sum_m \gamma_j(l, m) (\omega_{nlm} - \omega_{nl0}), \quad (7.45)$$

for suitable coefficients  $\gamma_j(l, m)$ . It immediately follows from Eq. (3.349) that rotation gives rise to odd  $a$  coefficients, related to  $\Omega(r, \theta)$  by

$$2\pi a_{2j+1}(n, l) = \int_0^R \int_0^\pi K_{nlj}^{(a)}(r, \theta) \Omega(r, \theta) r dr d\theta, \quad (7.46)$$

where the kernels  $K_{nlj}^{(a)}(r, \theta)$  can be determined in a straightforward manner from the kernels  $K_{nlm}(r, \theta)$ .

A further simplification of the inverse analysis results from expanding the dependence of  $\Omega(r, \theta)$  on  $\theta$  in the form

$$\Omega(r, \theta) = \sum_{s=0}^{s_{\max}} \Omega_s(r) \psi_{2s}^{(1)}(\cos \theta), \quad (7.47)$$

where  $\psi_{2s}^{(1)}(x)$  is a polynomial in  $x^2$  of degree  $s$  (see, for example, Korzennik *et al.* 1988; Brown *et al.* 1989; Thompson 1990). Such procedures are often called 1.5-dimensional (or 1.5D) inversions. By choosing the polynomials  $\mathcal{P}_j^{(l)}$  as defined after Eq. (7.9) (Ritzwoller & Lavelle 1991; Schou *et al.* 1994), and

a suitable corresponding expansion of  $\Omega$ , each  $a_{2s+1}$  is related to a single  $\Omega_s(r)$  and the inverse problem is reduced to a series of simple one-dimensional inversions (see also Pijpers 1997).

Such 1.5-dimensional techniques very considerably reduce the computational efforts required for the inversion. However, the expansion of  $\Omega$  evidently imposes a rather special structure on the solution, unless a large number of terms is included. With current computational resources the alternative of performing direct two-dimensional inversions, based either on Eqs (7.44) or Eqs (7.46), is entirely feasible and generally used. Even given the large amount of data (as many as 200 000 individual frequencies  $\omega_{nlm}$ , or of order 50 000  $a$  coefficients  $a_j(n, l)$ ), this can be handled by means of a straightforward regularized least-squares technique (*e.g.*, Schou 1991; Sekii 1991; Schou *et al.* 1992, 1994). Here the inferred  $\bar{\Omega}(r, \theta)$  is represented on a suitable grid  $(r_p, \theta_q)$  in  $r$  and  $\theta$ ,  $p = 1, \dots, n_r$ ,  $q = 1, \dots, n_\theta$ , by expansion coefficients  $\Omega_{pq}$ . These expansion coefficients can be determined through a regularized least-squares fitting technique, analogous to the one described in Eq. (7.42). Assuming that splittings  $\delta\omega_{nlm}$  for individual modes are available, related to  $\Omega(r, \theta)$  by Eq. (7.44), the solution is determined by minimizing

$$\sum_{nlm} \left( \frac{\int_{r,\theta} K_{nlm} \bar{\Omega} r dr d\theta - \delta\omega_{nlm}}{\sigma_{nlm}} \right)^2 + \mu_r \int_{r,\theta} f_r(r, \theta) \left( \frac{\partial^2 \bar{\Omega}}{\partial r^2} \right)^2 dr d\theta + \mu_\theta \int_{r,\theta} f_\theta(r, \theta) \left( \frac{\partial^2 \bar{\Omega}}{\partial \theta^2} \right)^2 dr d\theta ; \quad (7.48)$$

here  $\sigma_{nlm}$  is the standard deviation of the observed splitting  $\delta\omega_{nlm}$ . The last two terms serve to regularize the solution, as before, and depend on the weight functions  $f_r$  and  $f_\theta$  and the trade-off parameters  $\mu_r$  and  $\mu_\theta$ . Instead of  $\delta\omega_{nlm}$ , expansion coefficients  $a_{2j+1}$  with the corresponding kernels may evidently also be used. As in the 1-dimensional case, the trade-off parameters must be determined such as to ensure a balance between resolution and error. However, here one must also balance the resolution in the radial and latitude directions, as characterized by the averaging kernels (*e.g.*, Schou *et al.* 1994).

To illustrate the resolution properties of the inversions, Fig. 7.23 shows examples of such kernels, both for an inversion using expansions of the splittings and  $\Omega$  and for a full, two-dimensional inversion. In the former case, only  $a_1$ ,  $a_3$  and  $a_5$  were included and the latitude information is consequently relatively limited; hence the kernels have a substantial extent in latitude. A particularly striking feature is the fact that the attempt to determine the angular velocity close to the pole results in what contains aspects of extrapolation from lower latitudes: indeed, it is obvious that the rotation of the region very near the pole has little effect on the frequency splittings and hence cannot be determined from the inversion. The inversion based on individual splittings provides substantially better resolution in latitude, as might have been anticipated. Within the convection zone it is possible to determine the rotation

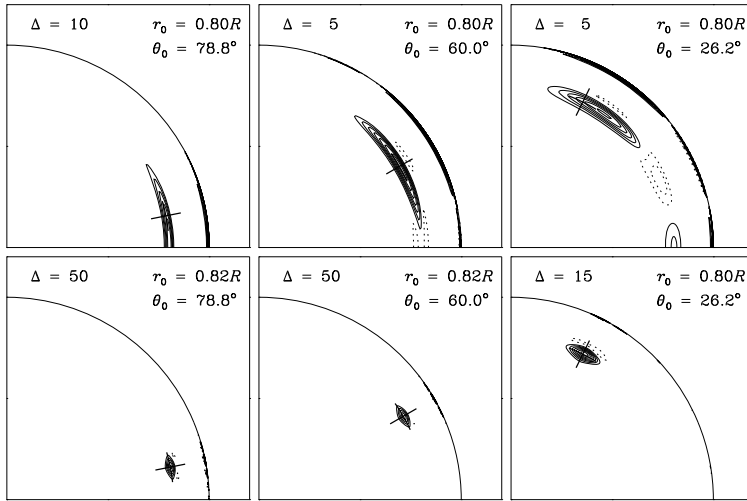


**Fig. 7.23.** Contour plots of two-dimensional averaging kernels  $R^2 \mathcal{K}(r_0, \theta_0, r, \theta)$  (cf. Eq. (7.43)). Results are shown at target radii near  $r_0 = 0.8R$  and three different target co-latitudes, as indicated. The plots are in the  $(r, \theta)$  plane, with the polar axis towards the top of the page. Positive contours are indicated by solid lines, negative contours by dashed lines;  $\Delta$  is the value of the separation between contour levels. The cross shows the target location  $(r_0, \theta_0)$ . The top row shows kernels for an inversion based on just  $a_1$ ,  $a_3$  and  $a_5$  and using a corresponding expansion of  $\Omega$ . The bottom row shows results for a full two-dimensional regularized least-squares inversion, for a mode set aiming at representing the results of 1 year of observations with high spatial resolution. Adapted from Schou *et al.* (1994).

over a region extending only a few per cent of the solar radius in both radial and latitude directions, for realistic sets of observed frequency splittings.

The MOLA and SOLA techniques (cf. Eqs (7.34) and (7.39)) can obviously also be generalized to the two-dimensional case. They offer considerable advantages in terms of the ability to control the resolution, and possibly other properties of the averaging kernels, although potentially at considerable computational expense. In fact, very substantial improvements of computational efficiency can be achieved by utilizing the special properties of the kernels (Sekii 1993; Pijpers & Thompson 1996; Pijpers 1997). Larsen & Hansen (1997) showed that the linear equations (Eqs (7.40) and (7.41)) arising in the SOLA technique can be solved efficiently by using explicitly the discretized representation of the kernels. Thus Larsen (1997) developed an iterative technique which allows two-dimensional SOLA inversion to be carried out with fairly

modest means (see also Larsen *et al.* 1998). These efficient techniques have been applied to the very extensive and accurate data obtained with the GONG and SOHO projects. We present some results of such analyses in Section 7.1.8 below.

Further details on the implementation of rotational inversion, and tests of the various techniques, were provided by Schou *et al.* (1998).

### 7.1.6 Inversion for Solar Structure

#### 7.1.6.1 Linearized Numerical Inversion

In its most general form, the dependence of the oscillation frequencies on solar structure may be expressed as

$$\omega_{nl} = \mathcal{F}_{nl}[\rho(r), c(r), \dots], \quad (7.49)$$

where, as indicated, other properties beyond the “mechanical” structure as characterized by  $\rho$  and  $c$  (see also Section 3.3.3.2) may affect the frequencies. This equation is often approximated by the corresponding equation for the adiabatic frequencies, *i.e.*,

$$\omega_{nl}^{\text{ad}} = \mathcal{F}_{nl}^{\text{ad}}[\rho(r), c(r)], \quad (7.50)$$

where the functional  $\mathcal{F}_{nl}^{\text{ad}}$  is determined through the solution of the equations of adiabatic oscillation. The inverse problem for solar structure then consists of inferring properties of the structure by “solving” Eq. (7.49) or Eq. (7.50), given a set of observed frequencies  $\{\omega_{nl}^{(\text{obs})}\}$ .

A difficulty in this process is that the frequencies depend on solar structure in a complicated, nonlinear way. As is common for nonlinear equations, the analysis proceeds through linearization around an initial reference model. Let  $(\rho_0(r), c_0(r))$  correspond to the reference model, which has adiabatic oscillation frequencies  $\omega_{nl}^{(0)}$ . We seek to determine corrections  $\delta_r \rho(r) = \rho(r) - \rho_0(r)$  and  $\delta_r c^2(r) = c^2(r) - c_0^2(r)$  to match the differences  $\omega_{nl}^{(\text{obs})} - \omega_{nl}^{(0)}$  between the observed frequencies and those of the reference model. As discussed in Sections 3.6.2 and 7.1.4.1, linearization of Eq. (7.49), assuming  $\delta_r \rho / \rho$  and  $\delta_r c^2 / c^2$  to be small, leads to

$$\frac{\delta \omega_{nl}}{\omega_{nl}} = \int_0^R \left[ K_{c^2, \rho}^{nl}(r) \frac{\delta_r c^2}{c^2}(r) + K_{\rho, c^2}^{nl}(r) \frac{\delta_r \rho}{\rho}(r) \right] dr + Q_{nl}^{-1} \mathcal{G}(\omega_{nl}) + \epsilon_{nl}, \quad (7.51)$$

where the kernels  $K_{c^2, \rho}^{nl}$  and  $K_{\rho, c^2}^{nl}$  are determined from the eigenfunctions in the reference model. In Eq. (7.51) we included a contribution from the uncertainties in the near-surface region, expressed by the term in  $\mathcal{G}$  (*cf.* Section 7.1.4.1); this may be assumed to contain the difference between the “true”

function  $\mathcal{F}_{nl}$  in Eq. (7.49) and the adiabatic approximation  $\mathcal{F}_{nl}^{\text{ad}}$  in Eq. (7.50). Furthermore, we explicitly included the observational errors  $\epsilon_{nl}$ . An additional constraint on  $\delta_r \rho$  is that the mass of the Sun and the reference model be the same, *i.e.*,

$$4\pi \int_0^R \frac{\delta_r \rho(r)}{\rho(r)} \rho(r) r^2 dr = 0. \quad (7.52)$$

In this way the original nonlinear inverse problem is reduced to a linear problem, which may be analysed by means of techniques similar to those discussed above.

Unlike the rotational case, the linearized inverse problem given by Eq. (7.51) involves three unknown functions:  $\delta_r \rho(r)$ ,  $\delta_r c^2(r)$  and  $\mathcal{G}(\omega)$ . These may, after suitable parametrization, be determined through least-squares fitting with appropriate regularization (see below). Alternatively, some form of optimally localized averages may be used, by forming a linear combination of Eqs (7.51),

$$\begin{aligned} \sum_i c_i(r_0) \frac{\delta \omega_i}{\omega_i} &= \sum_i c_i(r_0) \int_0^R K_{c^2, \rho}^i(r) \frac{\delta_r c^2}{c^2}(r) dr \\ &\quad + \sum_i c_i(r_0) \int_0^R K_{\rho, c^2}^i(r) \frac{\delta_r \rho}{\rho}(r) dr \\ &\quad + \sum_i c_i(r_0) Q_i^{-1} \mathcal{G}(\omega_i) + \sum_i c_i(r_0) \epsilon_i, \end{aligned} \quad (7.53)$$

where, as before,  $i$  labels the modes. If the goal is to determine the correction to  $c^2(r_0)$ , the coefficients  $c_i(r_0)$  must be chosen such that the first term on the right-hand side of Eq. (7.53) provides an average of  $\delta_r c^2/c^2$  localized near  $r = r_0$ , while minimizing the effect of the remaining terms.

A natural generalization of the SOLA technique is to obtain the coefficients  $c_i(r_0)$  through minimization of

$$\int_0^R [\mathcal{K}_{c^2, \rho}(r_0, r) - \mathcal{T}(r_0, r)]^2 dr + \beta \int_0^R \mathcal{C}_{\rho, c^2}(r_0, r)^2 dr + \mu \sum_i \sigma_i^2 c_i(r_0)^2, \quad (7.54)$$

where

$$\mathcal{K}_{c^2, \rho}(r_0, r) = \sum_i c_i(r_0) K_{c^2, \rho}^i(r) \quad (7.55)$$

is the averaging kernel; the *cross-term kernel*

$$\mathcal{C}_{\rho, c^2}(r_0, r) = \sum_i c_i(r_0) K_{\rho, c^2}^i(r) \quad (7.56)$$

measures the influence of the contribution from  $\delta_r \rho/\rho$  on the inferred  $\delta_r c^2/c^2$ , and  $\sigma_i$  is the standard error of  $\delta \omega_i/\omega_i$ . The constraint Eq. (7.52) is incorporated by adding a fictitious data point, with zero value and zero error, and with zero sound-speed kernel and a density kernel given by  $\rho r^2$ . The term in

$\mathcal{G}(\omega)$ , where  $\mathcal{G}$  is assumed to be a slowly varying function of frequency, may be suppressed by restricting the combinations of the data to those that are insensitive to a contribution of this form (Däppen *et al.* 1991; Kosovichev *et al.* 1992). Specifically, the coefficients may be constrained to satisfy

$$\sum_i c_i(r_0) Q_i^{-1} \psi_\lambda(\omega_i) = 0, \lambda = 0, \dots, A, \quad (7.57)$$

for a suitably chosen set of functions  $\psi_\lambda$ . It was shown by Basu *et al.* (1996a) that an equivalent, but potentially more flexible, suppression of the near-surface terms may be based on the filtering technique considered by Pérez Hernández & Christensen-Dalsgaard (1994a).

The SOLA inversion is characterized by the trade-off parameters  $\beta$  and  $\mu$  controlling the influence of the cross term and the errors, respectively, by the parameters determining the target function  $T(r_0, r)$  and by the number  $A$  of terms included in the suppression of the surface effects. The considerations involved in the choice of these parameters were discussed by Rabello-Soares *et al.* (1999b).

The form of the surface term in Eq. (7.51) assumed that the local properties of the eigenfunctions in the near-surface region are independent of degree; this is what led to the function  $\mathcal{G}$  being just dependent on frequency. From an asymptotic point of view this corresponds to assuming that the rays characterizing the modes are nearly vertical in this region. For modes of high degree this approximation no longer holds. Brodsky & Vorontsov (1993) showed how the asymptotic relation (7.15) should be modified in this case, by introducing  $l$ -dependent terms in the phase function  $\alpha$ . As discussed by Antia (1995) this has a significant effect on the inversion, at the present level of precision. The introduction of the corresponding terms in structure inversion by means of the SOLA or MOLA techniques, generalizing the constraints in Eqs (7.57), was discussed by Di Mauro *et al.* (2002); they also applied the techniques to preliminary observed frequencies of high-degree modes, obtained by Rhodes *et al.* (1998) from analysis of observations from the MDI instrument on the SOHO spacecraft.

In addition to the optimally localized techniques, the linearized Eq. (7.51) can also be analysed by means of regularized least-squares techniques (*e.g.*, Dziembowski *et al.* 1990; Antia & Basu 1994a; Basu & Thompson 1996). Here the unknowns,  $\delta_r c^2/c^2$ ,  $\delta_r \rho/\rho$  as functions of  $r$  and  $\mathcal{G}$  as a function of  $\omega$ , are defined in terms of suitable discretized representations, *e.g.*, splines, and the coefficients in these representations are determined through a least-squares fit to the observed  $\delta\omega/\omega$ , possibly with appropriate regularization. An advantage of this technique is that it provides a fit to the data and hence more effectively allows the identification and elimination of possible outliers. On the other hand, it is probably less straightforward to control the resolution and error properties of the inversion than with the OLA techniques.

Formally, the linearization leading to Eq. (7.51) can be regarded as the first step in an iterative process to infer the solar internal structure. Based

on the corrections  $\delta_r c^2$  and  $\delta_r \rho$  a new model can be constructed, imposing hydrostatic equilibrium but with no additional constraints from the theory of stellar evolution, and the inversion can be repeated using this as a reference model (*e.g.*, Antia 1996). The reconstructed model can then be considered as a “seismic solar model”, providing an inference of solar structure that depends only on the observational data (and the unavoidable limitations of resolution in the inverse analysis).

Although the inversion has been discussed in terms of the pair  $(c^2, \rho)$ , other sets of variables characterizing the equilibrium structure of the Sun may be used (see also Section 3.3.3). In particular, as discussed in Section 3.6.2, the frequency changes can be expressed in terms of changes  $\delta_r u$  and  $\delta_r Y$  in the squared isothermal sound speed  $u = p/\rho$  and helium abundance, if the equation of state and the heavy-element abundance are assumed to be known. From the point of view of inversion, these pairs have the substantial advantage that the kernels corresponding to  $\delta_r Y$  are relatively small and essentially confined to the ionization zones of hydrogen and helium (*cf.* Fig. 3.27). Thus in the minimization corresponding to Eq. (7.54), it is comparatively easy to suppress the cross term  $\mathcal{C}_{u,Y}(r_0, r)$ . Furthermore, inversion can be carried out to determine the difference  $\delta_r Y$  between the solar and model helium abundance (*e.g.*, Kosovichev *et al.* 1992).

It should be noted that differences between the solar and model equations of state may introduce systematic errors in the determination of  $Y$ . Basu & Christensen-Dalsgaard (1997) showed how the differences in equation of state might be taken explicitly into account in the analysis, by including a possible *intrinsic* relative difference  $(\delta \Gamma_1 / \Gamma_1)_{\text{int}}$  in  $\Gamma_1$  between the solar and model equations of state, *i.e.*, the difference at fixed  $p$ ,  $\rho$  and composition. The result is that Eq. (3.271) is replaced by

$$\frac{\delta \omega_i}{\omega_i} = \int_0^R \left[ K_{u,Y}^i(r) \frac{\delta_r u}{u}(r) + K_{Y,u}^i(r) \delta_r Y(r) + K_{c^2,\rho}^i \left( \frac{\delta \Gamma_1}{\Gamma_1} \right)_{\text{int}} \right] dr + Q_i^{-1} \mathcal{G}(\omega_i) + \epsilon_i , \quad (7.58)$$

where we also included the surface term and the observational error, and replaced  $nl$  by the index  $i$ . Basu & Christensen-Dalsgaard (1997) also noted that the term in  $(\delta \Gamma_1 / \Gamma_1)_{\text{int}}$  can be taken into account in the inversion, albeit at the expense of an increase in the error in the solution, and showed that the inversion might be carried out to infer  $(\delta \Gamma_1 / \Gamma_1)_{\text{int}}$ . As noted by Rabello-Soares *et al.* (2000) there is degeneracy between the effects of the intrinsic error in  $\Gamma_1$  and  $\delta_r Y$ , since they enter into Eq. (7.58) in the combination<sup>17</sup>

$$\left( \frac{\delta \Gamma_1}{\Gamma_1} \right)_{\text{int}} + \left( \frac{\partial \ln \Gamma_1}{\partial Y} \right) \delta_r Y ; \quad (7.59)$$

---

<sup>17</sup> Obviously, differences in the heavy-element abundances would have a corresponding, although likely much smaller, effect.

thus the inversion can in practice only provide information about this combination. However, Raballo-Soares *et al.* found from experiments with model pairs, assuming the availability of data for high-degree modes, that in much of the relevant region the influence of probable errors in  $Y$  on the determination of  $(\delta\Gamma_1/\Gamma_1)_{\text{int}}$  would be small. It is evident that the relation (7.59) also explicitly demonstrates the sensitivity of the determination of  $Y$  to errors in the equation of state; this is clearly not restricted to the present linearized inversion technique but would affect any analysis to infer  $Y$  from its effect on  $\Gamma_1$ . On the other hand, the effect of such errors can in part be suppressed by using the fact that  $\delta_r Y$  can be assumed to be constant in the convection zone. Further investigations of these issues are required, however.

By assuming further information about the physics of the solar interior, the hydrogen-abundance profile can be inferred also in the radiative interior. This would typically include assumed knowledge of the opacity and possibly the energy-generation rate as a function of the thermodynamic conditions.

Inversions for solar structure benefit greatly from the availability of modes over a broad range of degree and hence turning-point location, essentially resolving the structure of most of the Sun. However, it is of obvious interest to consider the potential for inversion of stellar data, where only low-degree modes will be observable in the foreseeable future. Gough & Kosovichev (1993a,b) found that, with a reasonably realistic set of modes and assumed frequency errors, it was possible to obtain relatively well-localized averaging kernels in the core of models of solar-like stars, using OLA techniques to infer differences in the squared isothermal sound speed  $u = p/\rho$  or in  $\rho$ . Similar results were obtained by Basu *et al.* (2002) who furthermore showed that substantially better localization could be obtained in inversion for  $\delta_r u$ , using  $Y$  as secondary variable, than for  $\delta_r c^2$  using  $\rho$  as secondary variable. Based on these results there is hope that we can obtain some resolution of the structure of stellar cores once data of sufficient quality are obtained.

### 7.1.6.2 Other Techniques for Structure Inversion

As discussed in Section 7.1.4.5, asymptotic inversion techniques can be used to determine the solar internal sound speed; in particular, it is possible to estimate the sound speed directly from the data, without the use of linearization. Such techniques were originally developed in geophysics (see Brodsky & Levshin 1979); their application to the helioseismic problem was first considered by Gough (1984a). As noted above, Vorontsov & Shibahashi (1991) developed the technique further by taking into account additional asymptotic terms, while Christensen-Dalsgaard *et al.* (1989b) found that the differential form of the technique suppressed some of the systematic errors in the simple Duvall law. In these techniques, the uncertainties associated with the near-surface region are contained in the function  $\alpha(\omega)$  or, for the differential technique, in the function  $\mathcal{H}_2(\omega)$  (*cf.* Eq. (7.19)).

Sophisticated techniques for structure inversion have been developed in several papers by Roxburgh and Vorontsov, starting from the so-called differential response technique presented by Vorontsov (1998) and reviewed by Roxburgh (2002, 2004) and Vorontsov (2004). This is based on the surface phase function  $\alpha(\omega)$ , defined as did Christensen-Dalsgaard & Pérez Hernández (1992) (with possible refinements to include some  $l$  dependence), and a similar internal phase function  $\delta_l(\omega)$  defined by the partial eigenfunction satisfying the central boundary conditions and a suitable condition on the perturbation to the gravitational potential in the outer parts of the model. As discussed by Roxburgh & Vorontsov (2000a) these phase functions define an equation for the eigenfrequency, in a manner similar to the JWKB matching discussed in Section E.2, although without using the JWKB approximation for the eigenfunctions. The inverse problem is now formulated in terms of the condition on the model structure that this property is satisfied for the observed frequencies, possibly obtaining the internal phase from an approximate solution using the Born approximation (Roxburgh & Vorontsov 1996). This technique was used by Marchenkov *et al.* (2000) to determine the sound-speed difference between then Sun and a solar model, with particular emphasis on the region around the bottom of the convective envelope. Also, Roxburgh & Vorontsov have tested it, using just the low-degree modes visible in distant stars, for several stellar models, with striking success in reconstructing the structure of the models (for a review, see Roxburgh 2004).

### 7.1.7 Results on Solar Structure

Here we investigate the solar internal structure through analysis of various sets of observed oscillation frequencies (*cf.* Section 7.1.3). Unless otherwise noted we use the so-called Model S of Christensen-Dalsgaard *et al.* (1996) as reference.<sup>18</sup> This model has seen extensive use as a helioseismic reference although in some aspects the model physics is not completely up to date. It used the OPAL equation of state (Rogers *et al.* 1996) and the OPAL opacities of Iglesias *et al.* (1992). Nuclear reactions were treated, in most cases, with the parameters given by Bahcall & Pinsonneault (1995), and diffusion and settling of helium and heavy elements<sup>19</sup> were included using the expressions of Michaud & Proffitt (2003).<sup>20</sup> The evolution of the model started from an assumed chemically homogeneous zero-age main-sequence model, and the age of the present Sun was taken to be 4.6 Gyr; the model was calibrated to the present observed properties of the Sun, including the ratio  $Z_s/X_s = 0.0245$  between the surface abundances of heavy elements and hydrogen (Grevesse & Noels 1993).

As a first test of a solar model, Fig. 7.24 shows differences between the observed frequencies and the frequencies of the model. The observations con-

<sup>18</sup> The model is available at [http://astro.phys.au.dk/~jcd/solar\\_models/](http://astro.phys.au.dk/~jcd/solar_models/).

<sup>19</sup> treating all heavy elements as fully ionized oxygen.

<sup>20</sup> For further details on the physics of stellar interiors, see Section 3.2.2.

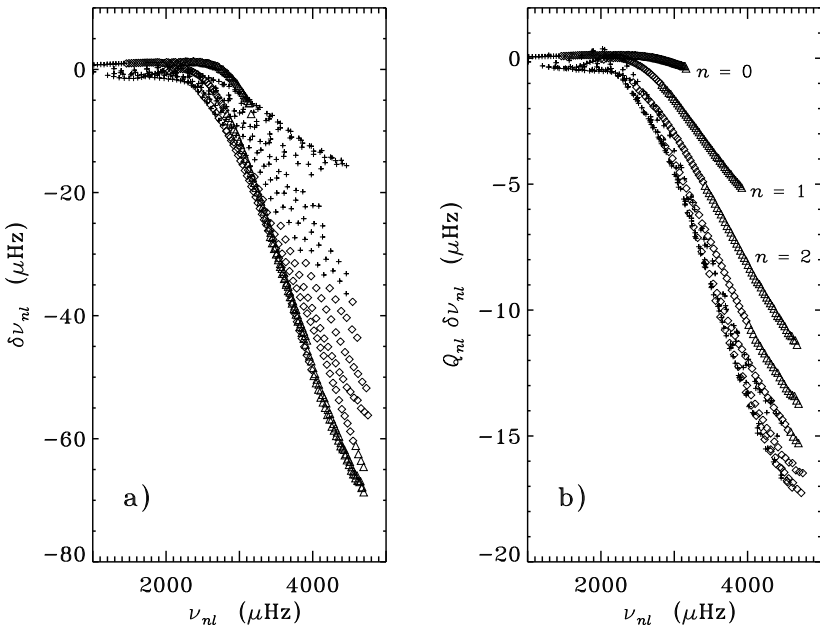


**Fig. 7.24.** Frequency differences between observed data and frequencies of a solar model, in the sense (observations) – (model). The observed frequencies were obtained by combining low-degree data from Chaplin *et al.* (2007b) with intermediate-degree (Larson & Schou 2008) and high-degree (J. Reiter, private communication) data from MDI; the model frequencies are for Model S of Christensen-Dalsgaard *et al.* (1996). Crosses indicate modes with  $l \leq 200$ , diamonds are modes with  $200 < l \leq 500$  and triangles are modes with  $500 < l$ . Panel (a) shows the raw differences. In panel (b) the differences have been scaled by  $Q_{nl}$ , defined in Eq. (7.10). Here ridges corresponding to low radial orders  $n$  are evident; the lowest values have been indicated in the figure.

sist of a suitably combined set of low-degree modes from BiSON observations (Chaplin *et al.* 2007b), as well as intermediate-degree (Larson & Schou 2008) and high-degree modes from the medium- $l$  and dynamics programmes of the MDI, respectively. The unscaled differences (panel a) show a strong dependence on  $l$ . In Section 7.1.1.1 we argued that if the dominant difference between the Sun and the model is restricted to the near-surface layers, this  $l$  dependence can be suppressed by scaling with  $Q_{nl}$ , illustrated in Fig. 7.9. In fact, as illustrated in panel b, the dependence on  $l$  is largely (but not completely) suppressed by scaling. This strongly suggests that most of the errors in the model are located very near the surface. We note that this is precisely the

region where, according to the arguments in Section 7.1.1, many of the uncertainties in the physics of the model and the oscillations are located. Thus it is not surprising that we obtain an effect on the frequencies of this nature. However, we note also in Fig. 7.24b that there is a significant dependence of the differences on degree; this must be associated with errors in the model in deeper layers. We return to the origin of these differences below.

An important part of the simplification in the modelling of the outer layers of the Sun is the use of the mixing-length treatment to characterize the structure of the outer superadiabatic part of the convection zone. As discussed in Section 3.2.1.3, this region has been modelled through hydrodynamical simulations; these extend sufficiently deeply to cover the region where the temperature gradient is significantly superadiabatic, *i.e.*, the region that is affected by the details of the mixing-length treatment. Thus the simulations can be used to determine the average structure of the region most affected by the uncertainty in the treatment of convection. Rosenthal *et al.* (1999) considered a model of the solar convective envelope, matching it to a temporally and spatially averaged simulation. Interestingly, the resulting model essentially matched the helioseismically inferred convection-zone depth (see below), without any adjustment to the parameters of the simulation. Frequencies computed for this envelope model provided a substantially better match to the observed frequencies than the frequencies of a normal solar model, such as the one illustrated in Fig. 7.24 (see also Nordlund *et al.* 2009). Similar results were obtained by Li *et al.* (2002) with a parameterized treatment of near-surface convection, determining the parameters from hydrodynamical simulations. None of these investigations, however, included the dynamical effects of convection on the frequencies; such effects likely play an important role in the remaining differences between the observed and computed frequencies.

For the highest-degree modes the figure shows a clear peeling-off into ridges for each value of the radial order  $n$ . Here the upper turning point is so close to the surface that the assumptions of nearly vertical propagation and degree-independent eigenfunctions break down. A similar behaviour was noted in Fig. 7.11 for differences between model frequencies. Also, we note that the f modes (with  $n = 0$ ) represent a special case. As discussed in Section 7.1.4.3, these essentially have the character of surface gravity waves, with frequencies given approximately by Eq. (7.12); in particular, computed frequencies of solar models are essentially independent of the details of the structure of the model, as is also illustrated by the frequency differences shown in Fig. 7.11. Thus the errors in the f-mode frequencies in Fig. 7.24b, which are much larger than the model differences in Fig. 7.11, must arise from effects other than differences between the hydrostatic structure of the Sun and the model. A likely cause are dynamical interactions between the modes and the turbulent motion in the solar convection zone (Murawski *et al.* 1998; Mędrek *et al.* 1999). However, the details of such mechanisms, and in particular their effects on the p-mode frequencies, are still rather uncertain.

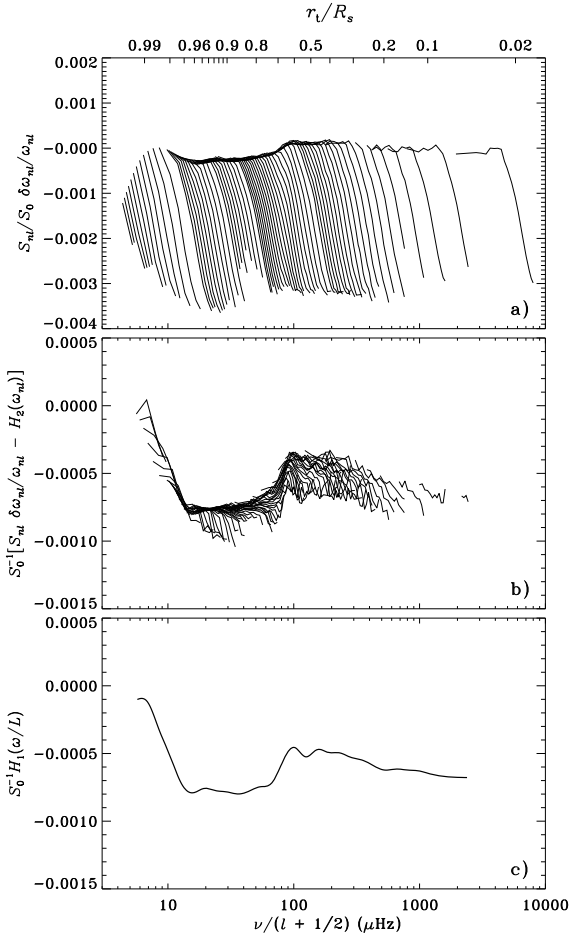


**Fig. 7.25.** Scaled differences between observed frequencies (see text) and frequencies of Model S of the present Sun, in the sense (observations) – (model), plotted against  $\nu/(l + 1/2)$ . The upper abscissa shows the location of the lower turning point, which is related to  $\nu/(l + 1/2)$  through Eq.(3.189). In panels (a) and (b) points corresponding to fixed  $l$  have been connected. (a) Original asymptotically scaled frequency differences. (b) Scaled differences, after subtraction of the function  $H_2(\omega)$  obtained from the spline fit. (c) The fitted function  $H_1(\omega/L)$ . Note the difference in scale between panel (a) and panels (b) and (c).

The different contributions to the frequency differences in Fig. 7.24 can be identified through an analysis based on the differential form, Eqs (7.19)–(7.21), of the Duvall law, as was done for model differences in Fig. 7.17. Fig-

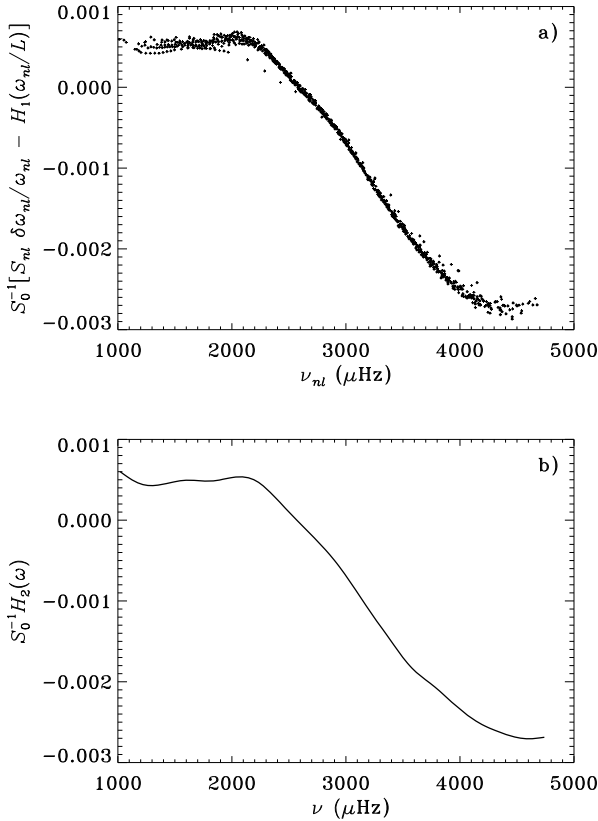


**Fig. 7.26.** The frequency-dependent part of the scaled frequency differences between observations and models. (a) Scaled differences, shown in Fig. 7.25a, after subtraction of the function  $\mathcal{H}_1(\omega/L)$  resulting from the spline fit. (b) The fitted function  $\mathcal{H}_2(\omega)$  for this data set.

ure 7.25a shows scaled differences between the observations and the model plotted against turning-point position.<sup>21</sup> It is evident already from this raw difference plot that in this case the term in  $\mathcal{H}_2$  plays the dominant role, in accordance with Fig. 7.24, as a result of the errors in the treatment of the near-surface layers. However, there is also weak evidence for a contribution from  $\mathcal{H}_1$ . This becomes clear if the spline fit is carried out and the contribution from  $\mathcal{H}_2$  is subtracted from the scaled differences. The result is shown

<sup>21</sup> Recall that the asymptotic scaling by  $S_{nl}/S_0$  used here is essentially equivalent to the scaling by  $Q_{nl}$  used in Fig. 7.24; cf. Fig. 7.15.

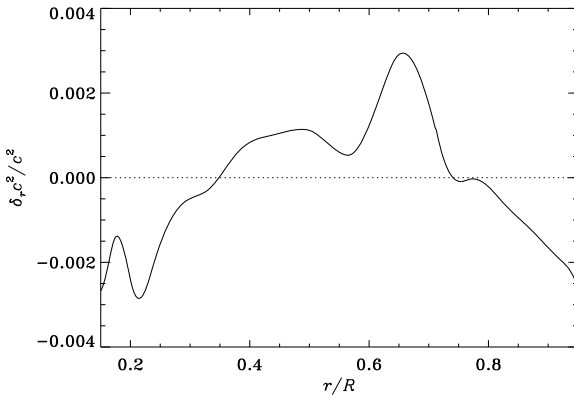


**Fig. 7.27.** Difference in squared sound speed  $\delta_r c^2 / c^2$  between the Sun and Model S (*cf.* Christensen-Dalsgaard *et al.* 1996) in the sense (Sun) – (model). This was inferred by applying Eq. (7.25) to a function  $\mathcal{H}_1(\omega/L)$  corresponding to Fig. 7.25c, but using only modes with frequencies between 1500 and 3500  $\mu\text{Hz}$ .

in Fig. 7.25b, while the fitted  $\mathcal{H}_1$  is shown in Fig. 7.25c. As in the case of the model comparison there is a sharp step corresponding in position to  $r_t \simeq 0.7R$ , *i.e.*, the base of the convection zone. This suggests that there are significant differences between the Sun and the model in this region although obviously of far smaller magnitude than between the two models considered in Fig. 7.17.

The residuals after subtraction of the fitted  $\mathcal{H}_1$  from the scaled differences, and the fitted  $\mathcal{H}_2$ , are shown in Fig. 7.26. As expected, these are predominantly a function of frequency and dominated by a slowly varying trend which reflects errors very near the surface of the model (see also Pérez Hernández & Christensen-Dalsgaard 1994a). One can perhaps discern a weak oscillatory signal showing a remaining difference between the Sun and the model in the hydrogen abundance in the convective envelope, although it is evidently substantially smaller than the corresponding difference between the two models in Fig. 7.18, indicating that the envelope hydrogen abundance is quite similar in the Sun and the model. We return to the quantitative determination of the abundance below.

It is striking that even this very simple analysis provides substantial information about the magnitude and location of the differences between the Sun and the model. A more quantitative estimate of the sound-speed error in the model can be obtained from the frequency differences illustrated in Fig. 7.25 by applying Eq. (7.25) to the resulting  $\mathcal{H}_1(\omega/L)$ . Figure 7.27 shows the resulting  $\delta_r c^2 / c^2$ . The sound-speed differences are small, corresponding to errors

in  $T/\mu$  in the models of less than 0.5 per cent. Nonetheless, the differences are clearly highly systematic. We discuss their possible physical origin after considering the results of numerical inversions below. Christensen-Dalsgaard *et al.* (1993a) used such a differential asymptotic inversion to show that a solar model without diffusion and settling was in far worse agreement with the solar sound speed than a model that included helium diffusion.

From a careful analysis of the inversion results it is possible to obtain an estimate of the convection-zone depth  $d_b$  which is largely independent of other uncertainties in the model. In this way Christensen-Dalsgaard *et al.* (1991) found that  $d_b = (0.287 \pm 0.003) R$ . From an analysis of the asymptotically fitted  $\mathcal{H}_1(\omega/L)$  Basu & Antia (1997) obtained the same value for  $d_b$  but with a substantially smaller error, and the result was further tightened by Basu (1998) who obtained  $d_b = (0.2865 \pm 0.0005) R$ .

The results in Fig. 7.27 are based on the validity of the asymptotic approximations resulting in the Duvall law, Eqs (7.15) and (7.16). Hence the analysis does not make full use of the information contained in the frequencies. This is particularly doubtful in the solar core, probed by modes of the lowest degree where departures from the asymptotic behaviour, *e.g.*, resulting from the perturbation to the gravitational potential, are likely most important. Also, it is not entirely straightforward to control the properties of the asymptotic inversion. These problems are avoided, at some computational expense, by using the numerical inversion techniques discussed in Section 7.1.6, based on linearizing the relation between structure and frequencies in terms of the appropriate kernels. Such inverse analyses have most often been carried out by means of optimally localized averages, *e.g.*, using the SOLA technique (see the discussion around Eq. (7.54)). The implementation of this was discussed in detail by Rabello-Soares *et al.* (1999b).

Typical results of the analysis are shown in Fig. 7.28. As before the reference model is Model S. Here we use the frequencies of the so-called ‘‘Best Set’’ of Basu *et al.* (1997b), obtained as a combination of data from BiSON and LOWL observations. As discussed in Section 7.1.5 the analysis provides an estimate of the standard error in the inferred sound-speed difference, as well as a measure of the resolution in terms of the distance between the first and third quartile points (*cf.* Eq. (7.31)). The inferred sound-speed difference is evidently broadly in agreement with the asymptotic results in Fig. 7.27, although it can now be determined quite close to the solar centre. Also, it is obvious that the differences are highly significant, compared with the estimated errors, which in most cases are smaller than the size of the symbols. In much of the Sun the resolution is better than  $0.04 R$ , although it deteriorates in the core where the sound speed is high and the wavelength of the eigenfunctions, and hence of the kernels, is large. It is also remarkable that the inferred differences in  $c^2$  are below 0.5% throughout the Sun. As shown in Fig. 7.28b the density differences are somewhat larger. Also, evidently the estimated errors are much larger than in the case of the sound-speed inversion.

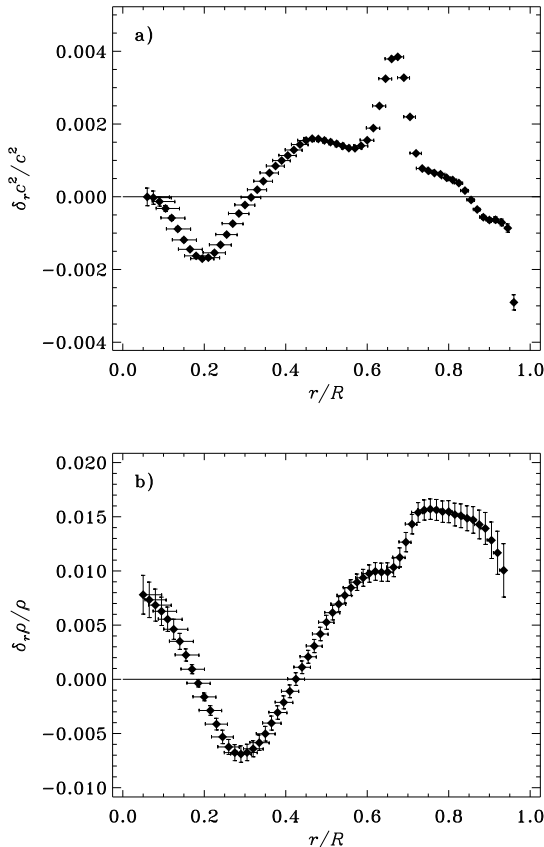


**Fig. 7.28.** Relative differences in squared sound speed  $\delta_r c^2 / c^2$  (panel a) and in density  $\delta_r \rho / \rho$  (panel b) between the Sun and Model S (*cf.* Christensen-Dalsgaard *et al.* 1996) in the sense (Sun) – (model). The differences were inferred through SOLA inversion of frequencies in the so-called “Best Set” of Basu *et al.* (1997b), a combination of BiSON and LOWL data, for modes of degree  $l \leq 99$ . The vertical bars, plotted at the target location  $r_0$ , show the estimated  $1-\sigma$  error of the inferred differences, while the horizontal bars, extending between the first and third quartile points of the averaging kernels (*cf.* Eq. (7.31)) provide a measure of the resolution of the inversion. Adapted from Christensen-Dalsgaard & Di Mauro (2007).

This is hardly surprising, given that we are analysing acoustic modes whose frequencies depend predominantly on the sound speed.

Other analyses for the solar sound speed show similar results, although with some dependence on the mode set and analysis method, particularly in the solar core (*e.g.*, Gough *et al.* 1996; Kosovichev *et al.* 1997; Turck-Chièze *et al.* 1997; Couvidat *et al.* 2003a). A detailed comparison of results based on different sets of GONG and MDI data by Basu *et al.* (2003) showed little significant dependence on the observational data for  $r \gtrsim 0.25 R$ . The inferred sound-speed differences obviously depend on the equilibrium model. However, Basu *et al.* (2000b) showed that the resulting sound speed, obtained by correcting the model sound speed with the inferred difference, depended little on the assumed reference model, within a reasonable range of “standard” solar models. Thus in this sense the analysis provides a reliable inference of the sound speed in the solar interior.

Based on the corrections to sound speed and density one can construct a new model, in terms of its hydrostatic structure, obtaining the pressure by integrating the equation of hydrostatic support. In this way a true seismic model of the Sun can be obtained. This process can in principle be iterated although this has rarely been done. As discussed, *e.g.*, by Gough (2004) additional properties of the Sun, beyond those that are directly probed by the oscillation frequencies, can be obtained by imposing further assumptions about the physics of the solar interior.

Given the high significance of the differences shown in Fig. 7.28a it is clearly of interest to consider how the model should be modified to reduce the differences. The most distinctive features are probably the relatively small differences in the outer parts of the Sun, corresponding to the convective envelope, and the peak immediately beneath this region. Concerning the former point we note that if the convection zone is assumed to be adiabatically stratified and the variations of  $\Gamma_1$  are neglected, the sound speed in the convection zone satisfies

$$c^2 \simeq (\Gamma_1 - 1) \frac{GM}{R} \left( \frac{R}{r} - 1 \right), \quad (7.60)$$

where for simplicity we assumed  $c = 0$  at  $r = R$ ; this can easily be shown from Eq. (3.99), if the ideal gas law, Eq. (3.19), is used. Thus to this approximation we expect the sound speed at fixed  $r$  to be independent of the details of the model, assuming that  $R$  is fixed. This is in fact approximately satisfied by the model differences illustrated in Fig. 7.16. The variation in  $\delta_r c^2/c^2$  seen in Fig. 7.28a is somewhat larger and could reflect inadequate suppression of the near-surface effects.

To investigate the peak in  $\delta_r c^2$  around  $r \simeq 0.65R$  it is instructive to consider the hydrogen-abundance profile in Model S, illustrated in Fig. 7.29. The dominant variation is obviously in the core, as a result of nuclear fusion. However, helium settling leads to a relatively sharp gradient in  $X$  just beneath the convection zone, in a region essentially coinciding with the peak in  $\delta_r c^2/c^2$ . It is evident that by smoothing this gradient the hydrogen abundance could be locally increased, leading to a decrease in the mean molecular weight and hence an increase in the sound speed in the model (*cf.* Eq. (3.56)). This would result

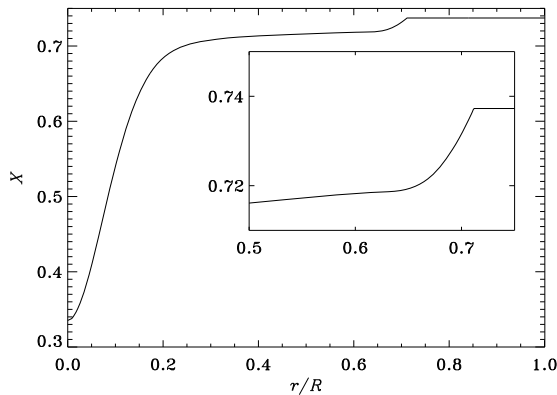


**Fig. 7.29.** The hydrogen abundance  $X$  as a function of the fractional distance to the centre, in Model S of the present Sun. The inset shows the variation near the base of the convection zone. Adapted from Christensen-Dalsgaard & Di Mauro (2007).

from mixing processes below the base of the convection zone, *e.g.*, caused by convective overshoot or possibly rotational instabilities. Modelled as a turbulent diffusion, appropriately calibrated, such mixing can essentially suppress the peak (*e.g.*, Brun *et al.* 1999; Elliott & Gough 1999; Christensen-Dalsgaard & Di Mauro 2007). Alternatively, the composition profile can be inferred by solving the equations of stellar structure, under the constraint that the solution match the helioseismically inferred structure; this similarly results in a shallower gradient in  $X$  beneath the convection zone (*e.g.*, Antia & Chitre 1998; Takata & Shibahashi 2003).

Through further modifications to the model physics it is possible to construct a solar model in close agreement with the helioseismic inferences (*e.g.*, Couvidat *et al.* 2003a). Such models are of some interest as indications of the possible errors in the model physics and as basis for investigating other aspects of the solar interiors, *e.g.*, the neutrino production rate. However, it should be kept in mind that, apart from the directly inferred variables such as sound speed, density and pressure, there may be different ways to achieve the helioseismic structure, depending on the precise manner in which the model is modified. As a trivial example, the ideal-gas approximation, Eq. (3.56), shows that a given sound speed can be obtained by adjusting either the temperature or the mean molecular weight. Thus, in particular, constraints on the solar neutrino flux require further assumptions about the physics of the solar interior.

As is clear from Fig. 7.16 the ionization of hydrogen and helium has a significant effect on  $\Gamma_1$  and hence on the sound speed, the magnitude of the effect depending on the helium abundance. The large variation nearest the surface is the combined result of the hydrogen and the first helium ionization. The effect of this on the frequencies and hence the helioseismic inferences is difficult to distinguish from other near-surface effects (*cf.* Section 7.1.4.1), making this less useful for helioseismic diagnostics. However, the smaller dip at  $r \simeq 0.98R$  is sufficiently far below the surface to be largely unaffected by the near-surface effects and hence is a potentially promising diagnostics of the envelope helium abundance. This was noted by Gough (1984b) and Däppen & Gough (1986) who pointed out that the quantity

$$W \equiv \frac{r^2}{Gm} \frac{dc^2}{dr} \quad (7.61)$$

is closely related to the thermodynamical state in the convection zone and proposed to use it in a calibration against the helium abundance.

Vorontsov *et al.* (1991) obtained a helioseismic estimate of the solar envelope helium abundance  $Y_e$  from an analysis of the Duvall phase function  $\alpha(\omega)$  and its derivatives. They noted that the effect of the second helium ionization on  $\Gamma_1$  extended over a region of size comparable to the radial wavelength and hence gives rise to an oscillatory signature in  $\alpha$ , effectively acting as an acoustic glitch (*cf.* Section 7.1.4.2). The resulting value,  $Y_e = 0.25 \pm 0.01$ , is significantly lower than the initial value required to calibrate a model of the present Sun (*cf* Section 7.1.1.1); Vorontsov *et al.* (1991) suggested that this reflects the settling of helium from the convection zone, as confirmed by more detailed inverse analyses (see above). A similar result, using also an analysis of the Duvall phase, was obtained by Christensen-Dalsgaard & Pérez Hernández (1991).

As discussed in Section 7.1.6.1 (*cf.* Eq. (7.59)) the determination of the helium abundance is sensitive to errors in the equation of state. Aspects of the equation of state were discussion in Section 3.2.2.1. The most commonly used formulations in helioseismic analyses have been the MHD and OPAL equations of state, although the simpler CEFF equation of state has also seen some use. Antia & Basu (1994b) made a careful investigation of the determination of  $Y_e$ , based on fits to the asymptotic components  $\mathcal{H}_1$  and  $\mathcal{H}_2$  of the frequency differences relative to reference models and using three different equations of state. They found  $Y_e = 0.252 \pm 0.003$ . A slightly lower value,  $Y_e = 0.242 \pm 0.003$ , was obtained by Pérez Hernández & Christensen-Dalsgaard (1994b), from analysis of  $\mathcal{H}_2$  using a filtering technique to suppress the contribution from the near-surface layers; they also found that the MHD equation of state was strongly preferred by the solar data, relative to CEFF. Later similar analyses by Basu & Antia (1995) and Basu (1998), using also  $\mathcal{H}_1$  and  $\mathcal{H}_2$ , obtained  $Y_e \simeq 0.248$  and indicated a preference for the OPAL equation of state over the MHD formulation.

Alternatively, as discussed in Section 7.1.6 the helium abundance can be inferred from a numerical inversion, *e.g.*, based on expressing the frequency differences in terms of corrections to the pair  $(u, Y)$ . An additional constraint, probably most easily incorporated in a regularized least-squares inversion, is that  $\delta_r Y$  is constant in the convection zone. Dziembowski *et al.* (1991) carried out a least-squares linearized inversion based on data from Libbrecht *et al.* (1990), using the variables  $u$  and  $Y$ , and found  $Y_e = 0.234 \pm 0.005$ , using the MHD equation of state. On the other hand, in a MOLA inversion of the same data and using also MHD, Däppen *et al.* (1991) inferred  $Y_e = 0.268 \pm 0.007$ . A careful analysis of this discrepancy was carried out by Kosovichev *et al.* (1992). They concluded that the main difference between the analyses by Dziembowski *et al.* and Däppen *et al.* was in the use of different versions of the MHD equation of state. A strong sensitivity to the equation of state was also found by Kosovichev (1997) who obtained  $Y_e = 0.232 \pm 0.006$  and  $0.254 \pm 0.006$  using the MHD and OPAL equations of state, respectively, and analysing a combination of low-degree IPHIR (InterPlanetary Helioseismology by IRradiance experiment) data (Toutain & Fröhlich 1992) and data from Libbrecht *et al.* (1990). Much more internally consistent results were obtained by Richard *et al.* (1998) from analysis of MDI data; they concluded that  $Y_e = 0.248 \pm 0.002$ . It should be noted that this value is close to the latest results of the differential asymptotic analysis discussed above.

A closely related issue is the effect of errors in the equation of state on the sound speed and hence the oscillation frequencies. This has the potential for testing the, still somewhat uncertain, modelling of the thermodynamic properties under the extreme conditions in the solar interior. In a simple comparison between observed and model frequencies, Christensen-Dalsgaard *et al.* (1988c) demonstrated that a model using the MHD equation of state was much closer to the solar properties than was a model based on EFF. This was confirmed Pamyatnykh *et al.* (1991) by considering the Duvall phase function in models of the solar envelope. Their analysis was extended in the careful investigation by Vorontsov *et al.* (1992) of the effects of various contributions to the equation of state on the phase function. Baturin *et al.* (2000) considered the quantity  $W$  (*cf.* Eq. (7.61)), determined from an asymptotic sound-speed inversion, as a diagnostics of the thermodynamical properties of matter in the solar convection zone. They demonstrated that this was sensitive to subtle details in the equation of state, including the treatment of pressure ionization, and to the relative mixture of the heavy elements. Using differential-response analysis, Vorontsov (2004) determined  $\Gamma_1$  in the convective envelope, finding a small but significant departure for  $r \lesssim 0.9R$  from the value obtained in Model S using the OPAL equation of state.

Using linearized inversion based on Eq. (7.58) Basu *et al.* (1999) determined the intrinsic error in  $\Gamma_1$  in the MHD and OPAL equations of state, concluding that the OPAL values were closer to the Sun except perhaps very near the surface. In a very interesting analysis using linearized inversion Elliott & Kosovichev (1998) showed that the  $\Gamma_1$  resulting from both the original

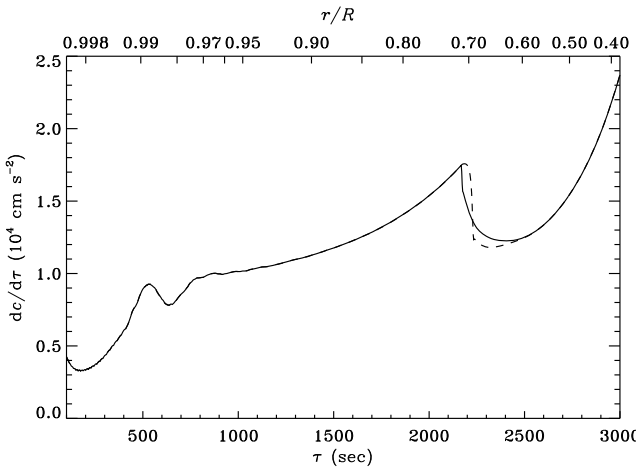


**Fig. 7.30.** Gradient of sound speed with respect to the acoustic depth  $\tau$  (*cf.* Eq. (3.228)), plotted against  $\tau$  (lower axis) and fractional radius  $r/R$  (upper axis). The solid curve shows results for Model S while the dashed curve shows the effect of including overshoot below the convective envelope. See Monteiro *et al.* (2000).

MHD and OPAL equations of state differed significantly from the inferred solar values in the core where one might naively have expected a relatively simple thermodynamical state, with full ionization, that should have been treated correctly in the calculations. They demonstrated that the difference arose because these equation of state calculations had neglected relativistic effects on electrons which become relevant, at the level of a few parts per thousand, at the temperatures near the centre of the Sun.

These examples show, as reviewed by Däppen (2004), that helioseismology is truly allowing the solar convection zone to be used as a laboratory for investigating the thermodynamical state of matter under solar conditions.

The analyses to determine the envelope helium abundance on the basis of the near-surface phase effectively makes use of the fact that this gives rise to an acoustic glitch (*cf.* Section 7.1.4.2). Such glitches are clearly seen in the sound-speed gradient, illustrated in Fig. 7.30 in models of the present Sun in terms of the acoustic depth  $\tau$  (*cf.* Eq. (3.228)). The feature at  $\tau \approx 700$  s is the result of the second helium ionization zone while the base of the convective envelope gives rise to a sharp variation at  $\tau \approx 2200$  s. As discussed in Section 7.1.4.2 an acoustic glitch at  $\tau = \tau_g$ , say, gives rise to a perturbation to the frequency with a “period” in cyclic frequency of  $(2\tau_g)^{-1}$ . Several such glitches therefore give rise to a superposition of oscillatory signals which in principle can be isolated through a Fourier analysis of a suitable

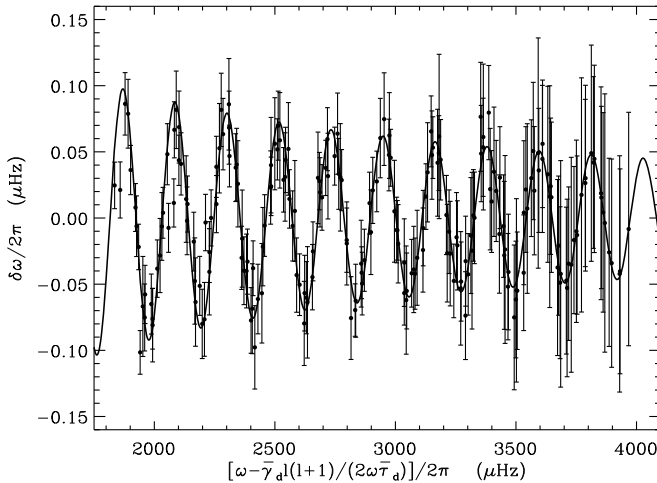


**Fig. 7.31.** Oscillatory signal extracted from observed MDI frequencies, reflecting the acoustic glitch at the base of the convection zone illustrated in Fig. 7.30; the solid curve shows the fit to the observations (Monteiro *et al.* 1994). In the abscissa  $\bar{\tau}_d$  is the inferred acoustic depth of the base of the convection zone; the term in  $\bar{\gamma}_d$  corrects for the variation in the location of the lower turning point. From Christensen-Dalsgaard & Thompson (2007).

representation of the frequencies; thus Roxburgh (2002) demonstrated how the oscillatory signals from the helium ionization zone and the base of the convective envelope could be extracted from Fourier analysis of a suitably filtered Duvall phase. Gough (1990a) pointed out that considering the second difference of the frequencies with respect to mode order  $n$ ,  $\Delta_2\nu_{nl} = \nu_{nl-1} - 2\nu_{nl} + \nu_{nl+1}$ , the leading-order variations of frequency with  $n$  are suppressed and the oscillatory signal as a function of frequency becomes evident. Fourier analysis of  $\Delta_2\nu_{nl}$  was used by Ballot *et al.* (2004) to investigate the potential for measuring the depth of convective envelopes on the basis of observations of solar-like oscillations.

The structure at the base of the convection zone is of particular interest, in analysis of acoustic glitches in the Sun. Although the depth  $d_b$  of the convective envelope can in principle be determined from the period of the oscillatory signal, the near-surface effects result in a significant unknown shift which introduces systematic errors in the inference; thus in the solar case, where modes over a broad range of degrees are observed,  $d_b$  is probably more reliably determined from analysis of  $\mathcal{H}_1$  or the inferred sound speed, as discussed above. However, the magnitude and detailed shape of the glitch is reflected in the amplitude, and its dependence on frequency, of the oscillatory signal (*e.g.*,

Monteiro *et al.* 1994). An example of such an oscillatory signal, from observed solar frequencies, is illustrated in Fig. 7.31.

A major uncertainty in the modelling of convective envelopes is the extent and properties of overshoot into the underlying stable region (see also Section 3.2.3). Zahn (1991) presented a model of overshoot that resulted in an extension of the convection zone into a slightly subadiabatic region followed by a rapid transition to the radiative gradient. The effect of a similar model on the sound-speed gradient is illustrated by the dashed curve in Fig. 7.30. This effectively increases the strength of the glitch and hence the amplitude of the oscillatory signal in the frequencies. From analysis of the observed signal, limits on the extent of this form of overshoot have been obtained as low as  $0.05H_p$ ,  $H_p$  being the pressure scale height at the base of the convection zone (Basu & Antia 1994; Monteiro *et al.* 1994; Roxburgh & Vorontsov 1994a; Christensen-Dalsgaard *et al.* 1995a; Basu 1997). It should be noted, however, that these analyses assumed spherically symmetrical and time-independent overshoot; variations with latitude, or with time over the period of a few months required to get sufficiently precise frequencies from the observations, might effectively smooth the transition and hence reduce the amplitude, as seen in the analysis. Also, other forms of overshoot (*e.g.*, Rempel 2004) give rise to a less steep transition. It remains to be seen whether such more subtle details can be probed with helioseismic investigations.

The development of reliable helioseismic diagnostic tools depends crucially on a good understanding of the dependence on the oscillation frequencies, and the quantities derived from them, on the properties of the star. This can often be obtained from asymptotic analysis; a simple but important example is the small frequency separation. Houdek & Gough (2007) carried out a careful analysis of the effects of the acoustic glitches on low-degree modes, with particular emphasis on the hydrogen and helium ionization zones. Using the asymptotic form of the eigenfunctions they obtained an expression for the signal in  $\Delta_2\nu_{nl}$ , the parameters of which are expected to be suitable for the determination of the helium abundance and the depth of the second helium ionization zone.

The results shown in Fig. 7.28 indicate that the model is in relatively good agreement with solar structure. This also applies to the depth of the convection of the model ( $d_b = 0.288$ ) and the envelope helium abundance ( $Y_e = 0.0245$ ) which are close to the helioseismically inferred values. Other “standard” solar models of the same generation agree similarly well with the helioseismic results, giving some confidence in our modelling of stellar evolution. This complacency has been shaken by recent revisions of the determination of the solar surface abundances (*e.g.*, Asplund *et al.* 2004; see Asplund 2005, 2008 for reviews). Unlike most other analyses these used time-dependent three-dimensional models of the solar atmosphere, based on hydrodynamical simulations of convection (see also Section 3.2.1.3); also, they took into account departures from local thermodynamic equilibrium, in so-called NLTE calculations of the radiative effects. This resulted in substantial

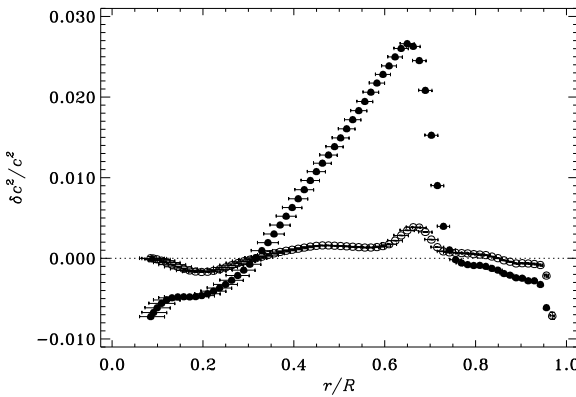


**Fig. 7.32.** The open symbols show the inferred relative difference in squared sound speed between the Sun and Model S, also illustrated in Fig. 7.28a. The closed symbols show the corresponding results for a model computed with the revised solar abundances. From Christensen-Dalsgaard *et al.* (2009).

reductions in the abundances of oxygen, carbon and nitrogen, yielding a ratio  $Z_s/X_s = 0.0165$  and, after model calibration, a present surface heavy-element abundance  $Z_s = 0.0125$ , compared with the value  $Z_s = 0.0181$  obtained in Model S. Since the opacity is approximately proportional to the heavy-element abundance this change in the composition has a strong effect on the opacity and hence a substantial effect on the structure of solar models. The consequence for the comparison of the model with the helioseismic inferences is illustrated in Fig. 7.32, which compares an inversion using as reference a model with the new composition, but otherwise corresponding to Model S, with the results for Model S previously shown (*cf.* Fig. 7.28); it is evident that the revision has led to a dramatic increase in the discrepancy between the model and the Sun. Also, the depth of the convection zone and the envelope helium abundance of the model,  $d_b = 0.271R$  and  $Y_e = 0.229$ , are inconsistent with the helioseismic inferences. Very similar results were obtained, for example, by Basu & Antia (2004), Turck-Chièze *et al.* (2004b) and Bahcall *et al.* (2005a). Furthermore, Basu *et al.* (2007) found that the very accurate measurements of the small frequency separations between low-degree modes strongly favoured the old composition. A recent comprehensive review of the issues related to the solar composition and helioseismology was provided by Basu & Antia (2008).

This discrepancy represents a potentially serious problem for solar modelling, with likely ramifications also for the modelling of other stars. Thus it is important to verify the new composition determinations. It is evident that

the use of three-dimensional atmosphere models and NLTE is preferable to the simpler treatments commonly used. Also, interestingly, the revised abundances bring the composition of the Sun closer in line with the composition of other objects in the solar neighbourhood (Turck-Chièze *et al.* 2004b; Przybilla *et al.* 2008, and references therein). An additional attractive feature is that in the new determinations consistent abundances are obtained from different spectral lines of the same element. However, they have been questioned by Ayres *et al.* (2006) who noted that the temperature profile resulting from the simulations failed to reproduce the observed continuum limb darkening. Ayres (2008) made a new determination based on a single timestep in an independent simulation, and using only one spectral line of oxygen, blended with a nickel line; this resulted in an oxygen abundance consistent with the old values, although at the expense of a perhaps questionable reduction in the inferred nickel abundance. In an analysis based on independent three-dimensional simulations Caffau *et al.* (2008, 2009) found oxygen and nitrogen abundances intermediate between the old and the revised values; for oxygen the main difference relative to the analysis of Asplund *et al.* (2004) was in the assumed strength of the oxygen lines in the solar spectrum. On this basis Caffau *et al.* (2009) recommended  $Z_s/X_s = 0.0213$ . Thus further adjustments of the abundances are certainly possible, although it is far from clear whether the old abundances will be recovered.

If we accept the abundance determinations of Asplund *et al.* we need to find ways of recovering a reasonable agreement between the solar models and the helioseismic inferences. Attempts to do so, which have met with limited success, were reviewed by Guzik (2006). Bahcall *et al.* (2005b) noted that the reduction in the oxygen abundance could be partly compensated, in the contributions to the opacity, by a substantial increase in the neon abundance, resulting in models in reasonable agreement with helioseismology; however, independent evidence for this revised neon abundance is controversial (*e.g.*, Drake & Testa 2005; Schmelz *et al.* 2005). Also, Delahaye & Pinsonneault (2006) found that models with increased neon abundance could be brought to agree with the helioseismically determined depth of the convection zone and envelope helium abundance but not with the detailed sound-speed profile in the Sun. Changes in the model physics located near the base of the convection zone, such as changes in the convective overshoot or diffusion and settling, generally fail to reproduce the sound-speed differences over the required extended region in the radiative interior. A trivial, although not *a priori* excluded, solution comes from noting that since the effect of the heavy-element abundances on solar structure is almost exclusively through the opacity, the change in composition can be counteracted by a compensating intrinsic change in the opacity (Basu & Antia 2004; Montalbán *et al.* 2004; Bahcall *et al.* 2005a). Christensen-Dalsgaard *et al.* (2009) made a detailed determination of the intrinsic opacity change, regarded as a function of temperature, which would be required to recover the structure of Model S of Christensen-Dalsgaard *et al.* (1996) with the new composition. This showed that an increase of nearly 30

per cent is required at the base of the convection zone, decreasing gradually to around 5 per cent in the core. Whether or not such an increase is physically plausible remains uncertain. However, it is perhaps relevant to recall the somewhat similar situation which led Simon (1982) to propose a large opacity increase based on serious problems with the understanding of pulsating stars (*cf.* Section 3.2.2.2).<sup>22</sup>

It is clearly highly desirable to have a determination of the heavy-element abundances that does not depend on the structure of the solar atmosphere and spectroscopy. As reviewed by Basu & Antia (2008) such a determination can in principle be based on the effect of the abundances on the thermodynamics and hence the value of  $\Gamma_1$  in the convection zone. This is similar to the methods used to determine the envelope helium abundance, as discussed above, although the effects are of course far smaller. Preliminary results by Lin *et al.* (2007) favour the original abundances; however, further investigations, including also the effect of uncertainties in the equation of state and ideally involving high-degree modes, are needed to confirm this.

### 7.1.8 Results for Solar Rotation

Unlike the structure of the solar interior, we have no solid theoretical predictions of the solar internal rotation. As discussed in Section 3.2.4.2 it is likely that the Sun, as other low-mass stars, started its evolution in a rapidly rotating state and that angular momentum has been lost through the magnetic solar wind, to lead to the present state of slow rotation of the solar surface layers. Since convection transports angular momentum effectively this spin-down is expected to be shared by the convection zone. However, angular-momentum transport in the radiative interior is far less certain and hence it might *a priori* have been expected that the Sun retained a rapidly rotating core.<sup>23</sup>

Solar surface observations also show a strong variation of the rotation rate  $\Omega$  with latitude. This is often represented as a power law in  $\cos^2 \theta$  where, as usual,  $\theta$  is co-latitude; Ulrich *et al.* (1988) obtained

$$\frac{\Omega}{2\pi} = (451.5 - 65.3 \cos^2 \theta - 66.7 \cos^4 \theta) \text{ nHz} , \quad (7.62)$$

from analysis of 21 yr of Mt Wilson data. Thus the angular velocity decreases from around 452 nHz at the equator to 365 nHz at  $60^\circ$  latitude, corresponding to an increase in the rotation period from 25.6 d to 31.7 d. This variation presumably reflects the redistribution of angular momentum by motion in the

<sup>22</sup> It is interesting to note that Magee *et al.* (1984) deemed this proposal, subsequently confirmed by new opacity calculations, to be “incompatible with atomic physics”.

<sup>23</sup> This was suggested by Demarque *et al.* (1973) as an explanation of the low observed solar neutrino flux; the resulting centrifugal force would reduce the pressure, and hence temperature, of the solar core.

convection zone. Since the stratification of the convection zone is approximately adiabatic, so that the gradients of pressure and density are parallel, one might expect from the *Taylor-Proudman theorem* (e.g., Pedlosky 1987) that the angular velocity does not change in the direction of the rotation axis within the convection zone; this is often described as *rotation on cylinders*. It would follow that the angular velocity would decrease with increasing depth in the convection zone. This was indeed found in early hydrodynamical simulations of the interaction between convection and rotation (e.g., Glatzmaier 1985; Gilman & Miller 1986).

As a rough summary, therefore, the theoretical predictions of the solar internal rotation would be that the convection zone should rotate on cylinders and the core should rotate substantially more rapidly than the surface. Strikingly, the helioseismic inferences of the internal rotation contradict both these predictions. A review of both the modelling of the solar internal rotation and the helioseismic investigations of it was given by Thompson *et al.* (2003); a recent extensive review of solar rotation was provided by Howe (2009).

As mentioned in Section 7.1.1.2 already the early measurement of the sectoral-mode splittings by Duvall & Harvey (1984) showed that the equatorial rotation rate was close to the surface rate throughout the solar interior (Duvall *et al.* 1984). This result has substantial importance beyond the study of the solar interior. From the inferred internal rotation rate, Duvall *et al.* estimated the solar gravitational quadrupole moment and found it to be consistent with the value corresponding to the surface rotation rate. This has a negligible effect on the precession of the perihelion of Mercury and hence confirms the tests of general relativity based on the observed precession; these tests might have been compromised by a rapidly rotating solar interior (Dicke 1964; Dicke & Goldenberg 1967). The determination of the quadrupole and higher moments has later been refined from more detailed determinations of the solar internal rotation (Pijpers 1998; Roxburgh 2001), confirming the conclusion of Duvall *et al.* (1984).

The observational determination of the dependence of the rotational splitting on  $m$  very soon showed that rotation in the convection zone was not constant on cylinders (e.g., Christensen-Dalsgaard & Schou 1988; Brown *et al.* 1989; Dziembowski *et al.* 1989; Rhodes *et al.* 1990; Goode *et al.* 1991). In an interesting analysis, Thompson (1990) carried out inversion for the radial gradient of the rotation rate in the convection zone, demonstrating that this was inconsistent with rotation on cylinders. The same conclusion, based on more extensive data, was reached by Schou & Brown (1994). It was found that the angular velocity, to this approximation, was independent of the distance to the centre, at fixed latitude, in what has been termed *rotation on cones*. The analyses also showed that there was a relatively sharp transition between the latitude dependence of rotation in the convection zone and a nearly latitude-independent rotation rate in the radiative interior. This region of strong rotational shear near the base of the convection zone, which Spiegel & Zahn (1992) called the *tachocline*, remains of very considerable interest in

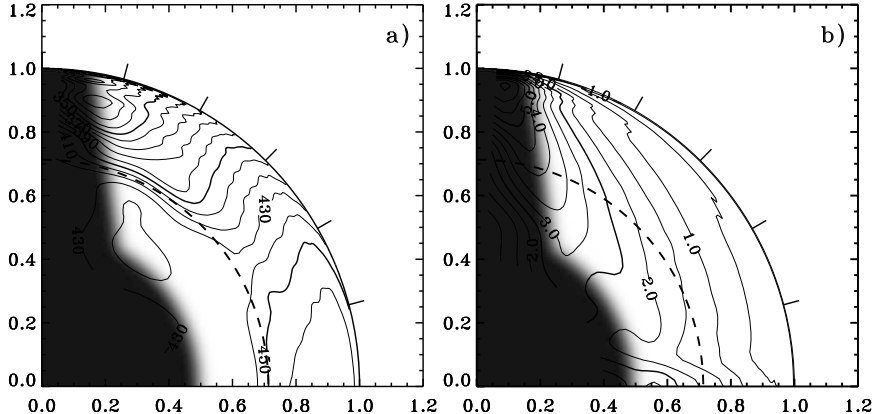


**Fig. 7.33.** Inferred rotation rate  $\Omega/2\pi$  (panel a) and the associated error (panel b) in a quadrant of the Sun, obtained by means of SOLA inversion of 144 d of MDI data. The equator is at the horizontal axis and the pole is at the vertical axis, both axes being labelled by fractional radius. Some contours are labelled in nHz, and, for clarity, selected contours are shown as bold. The dashed circle is at the base of the convection zone and the tick marks at the edge of the outer circle are at latitudes 15°, 30°, 45°, 60°, and 75°. The shaded area indicates the region in the Sun where no reliable inference can be made with the present data. Adapted from Schou *et al.* (1998).

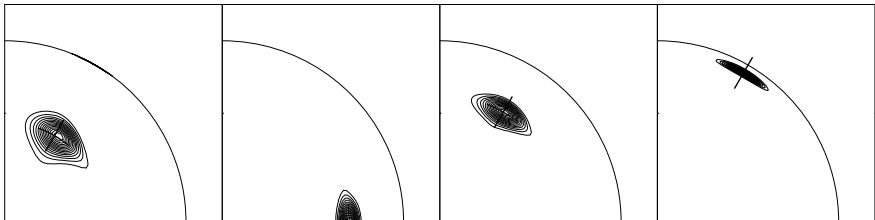


**Fig. 7.34.** Averaging kernels for the SOLA inversion shown in Fig. 7.33, targeted at the following radii and latitudes in the Sun: 0.55R, 60°; 0.7, 0°; 0.7, 60°; 0.95R, 60°. The corresponding locations are indicated with crosses. Adapted from Schou *et al.* (1998).

terms of its dynamics and its likely importance for the understanding of the generation of the solar magnetic cycle (see Tobias & Weiss 2007). Indeed, the early results on the rotation in and below the convection zone immediately led to a reconsideration of the models for such dynamo action, based at the interface between the convection zone and the radiative interior (Gilman *et al.* 1989).

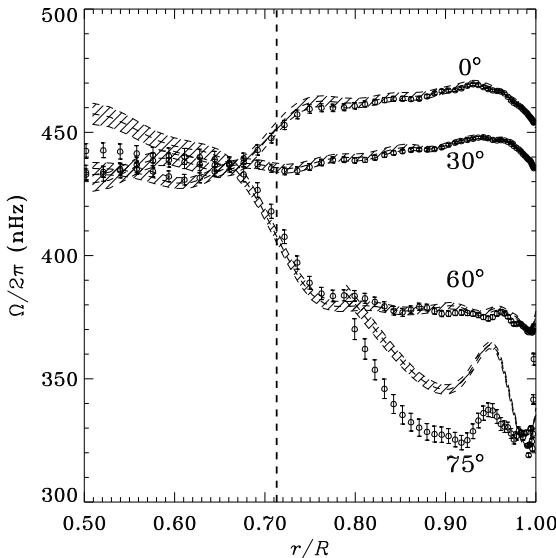


**Fig. 7.35.** Inferred rotation rate  $\Omega/2\pi$  as a function of radius at the latitudes indicated, obtained from inversion of 144 d of MDI data. The circles with  $1-\sigma$  error bars show results of a SOLA inversion, while the dashed lines with  $1-\sigma$  error band were obtained with regularized least-squares inversion. The heavy vertical dashed line marks the base of the convection zone. Adapted from Schou *et al.* (1998).

The extensive helioseismic observations allow detailed investigations of the solar internal rotation. To illustrate this, we present results obtained by Schou *et al.* (1998) from analysis of early data from the MDI instrument on the SOHO spacecraft. The inversion was carried out as a fully two-dimensional SOLA inversion of  $a$  coefficients, extending to  $a_{35}$ , to determine  $\bar{\Omega}(r_0, \theta_0)$ . The resulting  $\bar{\Omega}$  and the estimated errors are presented in Fig. 7.33, as contour plots. Strikingly, the error in a substantial part of the Sun is less than 2 nHz. To illustrate the resolution, Fig. 7.34 shows selected averaging kernels. Further details of the solution are visible in Fig. 7.35, which shows cuts at fixed latitudes, as functions of distance to the centre; here, in addition to the SOLA results, solutions obtained from a two-dimensional regularized least-squares inversion have been included.

The results clearly show the striking change in the behaviour of rotation near the base of the convection zone, at a depth of about 28 per cent of the solar radius (as inferred helioseismically; *e.g.*, Christensen-Dalsgaard *et al.* 1991); this is marked by the heavy dashed circle in Fig. 7.33 and the heavy dashed line in Fig. 7.35. Within the convection zone the variation with latitude

in the rotation rate is quite similar to the behaviour observed directly on the surface; in particular, the values at the outermost points in the solution are essentially in agreement with the surface values. (It should be noted that the inversion did not impose continuity with the surface angular velocity.) Near the base of the convection zone there is a transition in the tachocline such that the angular velocity in the radiative interior is roughly independent of position, at a value intermediate between the surface equatorial and polar values, but substantially closer to the former.

Although the overall features of rotation, as presented above, have been found using several different data sets and analysis methods, it should be mentioned that there are problems at the level of finer details, particularly at higher latitudes. These have become apparent in comparisons between results based on data from the GONG and MDI projects, in both cases analysed with the procedures used by both projects (*e.g.*, Schou *et al.*, 2002). Also, as illustrated by the comparison of the SOLA and least-squares results in Fig. 7.35, different inversion methods may give different results at high latitude. Clearly, the underlying causes for these various differences, and how to correct for them, need to be identified.

It is obviously of interest to consider the detailed properties of the inferred rotation rate. Figure 7.33a shows that rotation is in fact not strictly constant on cones. Gilman & Howe (2003) showed that the contours of constant rotation make an angle of around  $25^\circ$  with the rotation axis over a broad range of latitudes; they speculated that this might be the result of the effect on rotation of the Coriolis force arising from a meridional circulation.

A potentially important feature is the increase in the rotation rate with depth near the surface, at least at low- and mid-latitudes; evidence for this was obtained already in the analysis of high-degree Mt Wilson data by Korzennik *et al.* (1990), who related it to the observed surface rotation rate of magnetic features. A careful analysis of the subsurface gradient in angular velocity was made by Corbard & Thompson (2002), on the basis of observations of f modes with MDI; as noted in Section 7.1.4.3 the simple properties of the eigenfunctions of these modes make them particularly suited for the investigation of near-surface rotation. Corbard & Thompson showed that the logarithmic gradient  $d \ln \Omega / d \ln r$  was close to  $-1$  at latitudes below  $30^\circ$ , decreasing to near zero at a latitude of around  $50^\circ$ . As a final point concerning near-surface rotation we note that the helioseismically inferred rotation near the pole obtained from early MDI data was significantly slower than what would be inferred from fits such as that given in Eq. (7.62) (Kosovichev & Schou 1997; Birch & Kosovichev 1998; Schou *et al.* 1998). As discussed in Section 7.1.9 this feature shows striking variations with time.

The apparent width of the tachocline in Fig. 7.35 in part reflects the finite resolution of the inversion, as determined by the radial extent of the averaging kernels. This must be taken into account in estimating the true width of the tachocline. Kosovichev (1996) made an analysis of  $a_3$ , in an expansion similar to Eq. (7.9) based on data from the Big Bear Solar Observatory (Woodard &

Libbrecht 1993), to determine the location and width of the tachocline. He characterized the transition in  $\Omega$  by the function

$$\Phi(r) = \frac{1}{2}[1 + \text{erf}[(2(r - r_c)/w)]], \quad (7.63)$$

where  $\text{erf}$  is the error function and  $w$  characterizes the width, obtaining  $w = (0.09 \pm 0.04)R$ . Corbard *et al.* (1999) used a least-squares inversion with a nonlinear regularization designed to analyse sharp features in the solution, obtaining a likely smaller width, below  $0.05 R$ . A detailed analysis, employing several techniques, was carried out by Charbonneau *et al.* (1999) on LOWL data; they obtained a tachocline width, defined as in Eq. (7.63), of  $w = (0.039 \pm 0.013) R$  and a distance  $r_c = (0.693 \pm 0.002) R$  from the centre at the equator, essentially placing the transition beneath the convection zone. Interestingly, they found that the central location was significantly further from the centre at higher latitude, so that the tachocline appears to be prolate. This was also found by Antia *et al.* (1998) and Basu & Antia (2001, 2003).

The data used in the inversions presented in Figs 7.33 and 7.35 did not permit inference of the rotation rate very near the centre. This requires data on modes of the lowest degree, generally obtained from full-disc observations and hence with no observational separation between the different  $m$  components. Also, the rotational splitting is comparable to the linewidth, complicating the separation in the power-spectrum analysis. It was noted by Appourchaux *et al.* (2000b) that this tends to overestimate the determined splittings.<sup>24</sup> Analysis of low-degree splittings from the BiSON network provided a tantalizing hint that the core rotation might be *below* the general rotation rate of the radiative interior (Elsworth *et al.* 1995). On the other hand, Lazrek *et al.* (1996), from analysis of IRIS data, found no such tendency. Chaplin *et al.* (1999) carried out a more detailed analysis of a combination of LOWL and BiSON frequencies, using a version of the MOLA technique especially designed to localize the averaging kernels to the solar core. The results are shown in Fig. 7.36. They are consistent with constant rotation of the radiative interior, although with a possible suggestion of a down-turn in the core. Analysis of the averaging kernels showed that constraining the measure of rotation to the inner 20% of the solar radius was possible, as indicated by the interquartile range, but only at the expense of very substantial errors in the inferred rotation rate. Results consistent with constant rotation in the radiative interior were also obtained by Eff-Darwich *et al.* (2002), Couvidat *et al.* (2003b) and García *et al.* (2004). Eff-Darwich *et al.* (2008) made a careful combination of the existing data from the MDI, GONG and GOLF observations and similarly obtained a constant rotation in the radiative interior, although with some

<sup>24</sup> J. Schou (unpublished) has illustrated this with a plot of the published rotational splittings as a function of time, which shows a dramatic decrease up to around 1998, after which the measurements have largely stabilized. See also Howe (2009).

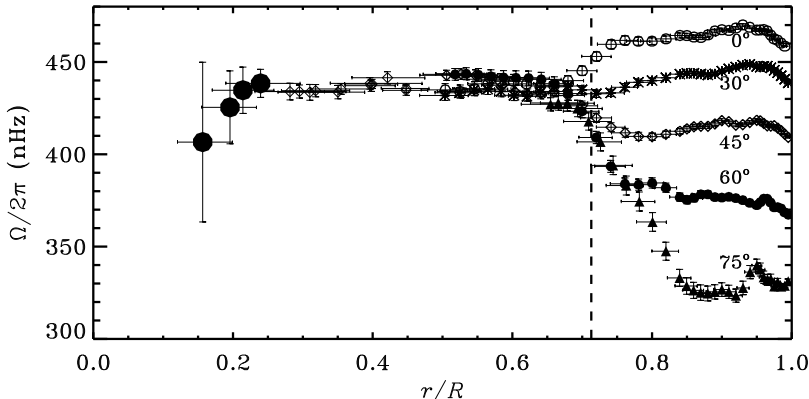


**Fig. 7.36.** The inferred rotation rate  $\Omega/2\pi$  as a function of fractional radius, at five solar latitudes: the equator,  $30^\circ$ ,  $45^\circ$ ,  $60^\circ$  and  $75^\circ$ . The vertical bars indicate  $1-\sigma$  errors, based on the quoted errors of the observations, while the horizontal bars, between the first and third quartile points (*cf.* Eq. (7.31)), provide a measure of the width of the averaging kernels and hence the resolution of the inversion. The vertical dashed line marks the helioseismically determined base of the convection zone (Christensen-Dalsgaard *et al.* 1991). The results are from OLA inversions of MDI data in the outer region,  $r > 0.45R$  (from Schou *et al.* 1998) and of combined data from the LOWL instrument and the BiSON network, in the region with  $r \leq 0.45R$  (Chaplin *et al.* 1999). The large filled circles show the result of confining the averaging kernels to the core, with no constraint in latitude. From Christensen-Dalsgaard & Thompson (2007).

evidence for a slight decrease for  $r \leq 0.2R$ . They also noted that present data provide relatively tight constraints on the latitude dependence of rotation for  $r \gtrsim 0.3R$  and concluded, in agreement with Fig. 7.36, that the rotation rate is independent of latitude in the outer parts of the radiative region.

Chaplin *et al.* (2004a) considered the requirements for a significant detection of a variation rate with  $r$  in the core and concluded, as also suggested by Fig. 7.36, that with the present data such a variation would have to be of very substantial magnitude. They also found that to constrain rotation in the deep interior, modes of relatively low frequency are most important, despite the fact that their inner turning points are further from the centre and that therefore formally they are less sensitive to the core rotation; however, this is compensated by their much longer lifetime, leading to a higher accuracy in the determination of the frequencies.

It is evident that a substantial improvement in the inferences of the core rotation, based on extending the observations of the currently detected modes, is at best a long-term process. Formally, the errors in the determination of

frequencies of stochastically excited modes decrease as the inverse square root of the observing time (see Eq. (5.57)); given that the currently used data are based on observations over more than a decade, several decades are required for a substantial improvement. The potential improvement resulting from the addition of data for just a few g modes is huge (Eff-Darwich *et al.* 2008; Mathur *et al.* 2008); however, as discussed in Section 7.1.3.2 the detection of such modes remains elusive.

### 7.1.9 Temporal Variations of the Solar Interior

The properties of the Sun change with time. On a human time scale the most important variations are associated with the magnetic activity, as reflected in the 11-year sunspot cycle (*e.g.*, Schrijver & Zwaan 2000).<sup>25</sup> The variation in the occurrence of sunspots traces the so-called butterfly diagram, with spots appearing at latitudes around  $\pm 30^\circ$  at the beginning of a cycle and the spot locations converging towards the equator as the cycle progresses. The cycle is likely the result of a complex interaction between convection, rotation, meridional flows and the magnetic field, although the details are still uncertain (see also Charbonneau 2005). This is often thought to lead to an accumulation of magnetic flux, in a toroidal equatorial belt, in the region of the tachocline. The variation in the sunspot number is accompanied by a variation of around 0.1% in the solar irradiance, with largest average irradiance at sunspot maxima (Fröhlich & Lean 2004). The possible variation in the solar radius, as determined from direct radius observations, has been much debated; in a careful analysis of an extended series of data Brown & Christensen-Dalsgaard (1998) limited any such variation to be below  $\pm 5 \times 10^{-5} R_\odot$ . As discussed by Gough (1990b, 2002b) the ratio between the radius and luminosity perturbations provides a measure of the depth of the cause of these variations, a small ratio, as observed, indicating that the variations arise predominantly in the near-surface region.

A closely related issue is the departure of solar structure from spherical symmetry. Such asphericity is evident in the distribution of magnetic fields on the solar surface, with the active regions being predominantly at low and intermediate latitude. It is plausible that large-scale, probably time-varying, asphericity is also present in the solar interior, associated with the accumulation of magnetic fields.

It is evident that our understanding of the solar cycle would be greatly improved by helioseismic determination of related changes in the solar interior. This is clearly a possibility, given the availability of helioseismic data over several sunspot cycles, and very detailed data from the GONG and MDI instruments over the last cycle (for recent overviews, see Gizon 2004; Howe 2008). In addition to studies of the variations with time in the frequencies, analysis of

---

<sup>25</sup> As the magnetic field switches polarity from one sunspot maximum to the next, the period of the magnetic cycle is 22 yr.

the even component of the dependence of the frequencies on azimuthal order  $m$  may uncover asphericities in solar structure. This is conveniently done in terms of the  $a$  coefficients of even order (*cf.* Eq. (7.9)).

Even early results based on irradiance observations from the Solar Maximum Mission showed a frequency increase in low-degree modes of  $0.42 \pm 0.14 \mu\text{Hz}$  from sunspot minimum to sunspot maximum (Woodard & Noyes 1985). Duvall *et al.* (1986) found evidence for asphericity in the lowest-order even  $a$  coefficients; their results were modelled by Gough & Thompson (1988) in terms of near-surface magnetically induced perturbations. These frequency variations were analysed in considerable detail by Libbrecht & Woodard (1990), using resolved observations from the Big Bear Solar Observatory. They showed that the dependence of the temporal frequency changes on frequency and degree corresponded to a physical cause confined very near the surface (see also Section 7.1.4.1). From analysis of the even  $a$  coefficients they furthermore demonstrated that the latitude variation of the sound speed corresponded to the activity belts where most of the sunspots were found, identified through the latitude dependence of the limb brightness, and varied with time in the same manner as activity. The close connection between the temporal variation of the surface magnetic activity and the frequency changes was further confirmed by Woodard *et al.* (1991) and Bachmann & Brown (1993), based on spatially resolved observations; they showed, by determining the frequencies in segments of roughly 1 month, that the frequency variation was strongly correlated in time with indices of solar activity. A similar correlation for low-degree modes, using full-disc BiSON observations, was found by Chaplin *et al.* (2001b). Also, using GONG and MDI observations with high latitude resolution Howe *et al.* (2002) used the  $m$  dependence of the frequency shift to localize the shift in latitude; they found a strong correlation between the frequency variations and the unsigned magnetic flux, as functions of latitude and time.

Although the correlation between the surface magnetic field and the effects on the oscillation frequencies is well established, the physical effects that mediate this correlation have still not been definitely identified. This has been reviewed, for example, by Thompson (2001) and Gough (2002b); detailed analyses of the possible mechanisms were presented by Goldreich *et al.* (1991) and Balmforth *et al.* (1996). These include the direct effect of the changing magnetic field on the propagation speed of the waves as well as the indirect effect, through the resulting change in the thermal structure of the outer layers, which also affects the propagation speed and the location of the upper turning point. Furthermore, particularly at high frequency, thermal changes in the chromosphere may be important (*e.g.*, Jain & Roberts 1993).

An interesting aspect of the analysis concerns the attempts to detect variations in the “helioseismic radius”, mostly from the analysis of f-mode frequencies which, according to Eq. (7.12), depend mainly on the radius (*e.g.*, Schou *et al.* 1997; Dziembowski *et al.* 1998; Antia *et al.* 2000; Dziembowski *et al.* 2001b; Antia 2003). Lefebvre & Kosovichev (2005) and Lefebvre *et al.* (2007)

noted that, perhaps not surprisingly, the helioseismically inferred changes in the subsurface layers did not correspond to a simple scaling with a varying surface radius. Dziembowski & Goode (2004) made a careful reconsideration of the physical effects influencing the frequencies. This was used by Dziembowski & Goode (2005) to analyse MDI observations of frequency changes; they concluded that the dominant effect on the f-mode frequencies was magnetic, while the p modes were mainly affected by the changing thermal structure which, they speculated, could be brought about by a modest change in the convective velocities in the outer layers. They also found that the resulting change of the surface radius was very small.

To understand how the solar cycle works it would clearly be very interesting to detect variations in solar structure at greater depth below the surface. Such effects have been elusive, however. From inversion of the even  $a$  coefficients Gough *et al.* (1996) inferred significant asphericity only in the near-surface layers. Gough (2002b) found some evidence for a variation with time in the wave speed roughly at the depth of the second helium ionization, visible as the result of an acoustic glitch in the frequency changes with activity. This was confirmed in a more detailed analysis of GONG and MDI data by Basu & Mandel (2004) who speculated that the effect could arise from the influence of the magnetic field on the effective equation of state and hence on  $\Gamma_1$ . Similar variations were found by Verner *et al.* (2006a) in low-degree BiSON data. At slightly greater depth Antia *et al.* (2000) and Dziembowski *et al.* (2000) found a component of asphericity located at around  $0.96 R_\odot$ . This was localized to a latitude of around  $60^\circ$  by Antia *et al.* (2003) who also found evidence that it might change with the solar cycle; they speculated that it reflected a time-varying storage of magnetic energy in this region of the convection zone.

According to the dynamo models discussed above, one might expect a visible signature of the accumulation of magnetic flux in the equatorial part of the tachocline region. Antia *et al.* (2000) put an upper limit of  $300 \text{ kG}$  on such a field, corresponding to a relative magnetic perturbation to the wave speed of around  $3 \times 10^{-5}$ . A similar upper limit was obtained by Eff-Darwich *et al.* (2002) on the variation of the wave speed in this region, associated with the solar cycle. Very interestingly, Baldner & Basu (2008) have found what seems to be a significant change in the sound speed in the tachocline region; this is illustrated in Fig. 7.37, based on their analysis of MDI data. They used principal component analysis to extract the components of the data varying with solar activity, using the  $10.7 \text{ cm}$  radio flux as a measure of activity; this analysis also serves to suppress the noise in the data as well as known artefacts. From inversion of the result they then inferred the sound-speed variation associated with activity. Interestingly, the sound speed seems to decrease with increasing activity at the base of the convection zone while it increases at slightly greater depth, essentially corresponding to the bulk of the tachocline. In a similar analysis of GONG data Baldner & Basu obtained a similar depression at the base of the convection zone but no significant increase at greater depth. It is evident that further analyses along these lines, as well

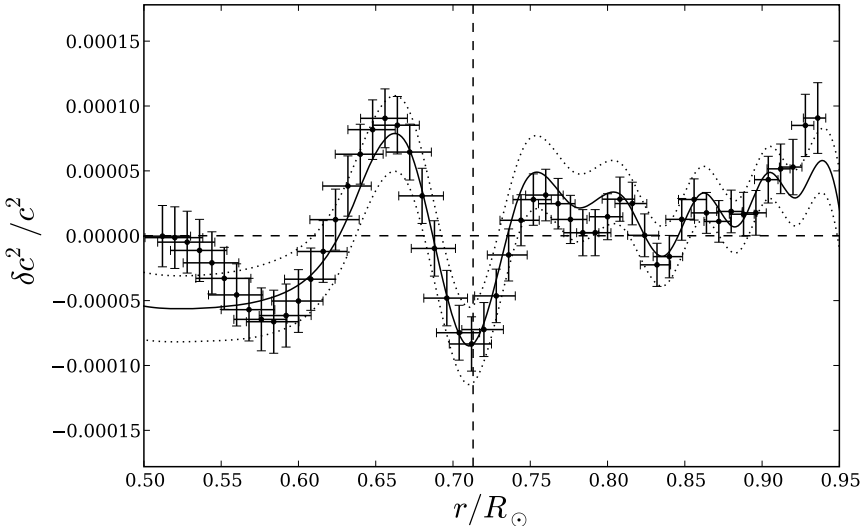


**Fig. 7.37.** Relative change in the squared sound speed associated with the solar activity cycle, in the sense (high activity) – (low activity). The symbols with bars show the results of a SOLA inversion (see also Fig. 7.28); the solid curve shows results of a regularized least-squares inversion, with  $1-\sigma$  errors indicated by the dotted lines. Adapted from Baldner & Basu (2008).

as interpretation in terms of models of the solar-cycle-related dynamics of the region around the base of the convection, are highly desirable.

Variations in the solar surface rotation with solar activity were detected by Howard & LaBonte (1980); they found bands of slightly faster and slower rotation, which they termed “torsional oscillations”, converging towards the solar equator as the sunspot cycle progresses. Similar bands were inferred in the subsurface layers in rotational inversions of MDI data from 1996 by Kosovichev & Schou (1997), Birch & Kosovichev (1998) and Schou *et al.* (1998), who in addition found that the polar regions rotated more slowly than expected from extrapolation of the lower-latitude rotation rate. In an analysis of f-mode data extending over 2.5 yr, Schou (1999) demonstrated that these bands showed the same convergence with time towards the equator as did the surface flows; interestingly, evidence for such zonal flows converging towards the equator is present already in the results of Woodard & Libbrecht (1993). Howe *et al.* (2000a) analysed more extensive sets of MDI and GONG data and demonstrated that the flows were coherent over a substantial fraction of the convection zone. Similar results were obtained by Antia & Basu (2000). A review of the variations in solar rotation associated with the solar cycle was given by Howe (2009).

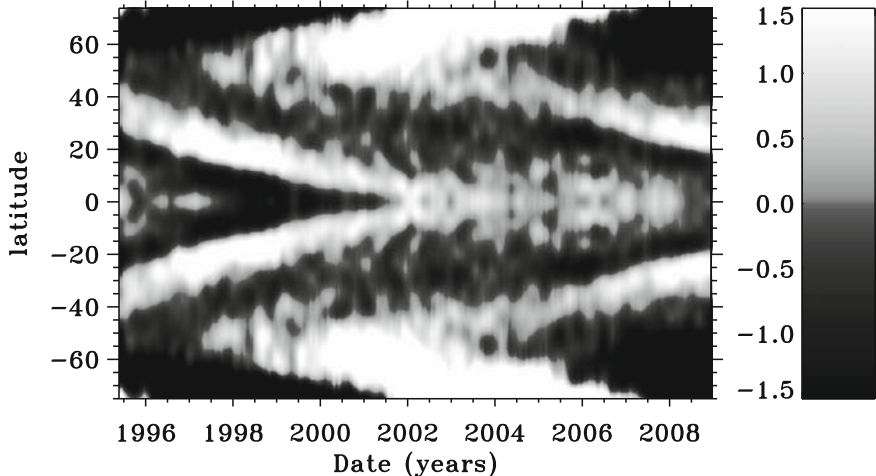


**Fig. 7.38.** Time evolution of the zonal flows at  $0.99 R_{\odot}$  inferred from regularized least-squares rotational inversion of MDI and GONG data, after subtraction of the time-averaged rotation rate. The grey scale at the right gives the residual rotation rate in nHz. The results are shown as a function of time and latitude; note that the plot is symmetrical around the equator, since global helioseismic inversions are sensitive only to the symmetrical component of the rotation rate (*cf.* Eq. (3.351)). Adapted from Howe *et al.* (2006).

Properties of the zonal flows, extending up to late 2008, are illustrated in Fig. 7.38. The low-latitude branch closely follows the evolution of the location of the sunspots, while there is clearly also a branch extending towards the pole, resulting in the slow polar rotation in 1996 noted above (see also Antia & Basu 2001). Further analysis by Vorontsov *et al.* (2002), using inversion through an adaptive regularization scheme (Strakhov & Vorontsov 2000), showed that the variation extended through most of the depth of the convection zone, the higher-latitude changes apparently reaching its base. At low latitudes it appears that the bands of faster rotation propagate outwards with time (Basu & Antia 2003; Howe *et al.* 2005), probably indicating that the zonal flows are not induced by effects near the solar surface, as had been proposed by Spruit (2003). A detailed analysis by Howe *et al.* (2006), based on artificial data created from numerical models of the solar dynamo, confirmed the sensitivity to flows near the base of the convection zone and hence supported the finding that the solar flows involve most of the convection zone.

With the availability of detailed helioseismic data for a full sunspot cycle (Antia *et al.* 2008) we are in an excellent position to use the inferred variations in rotation as constraints on models of the dynamics of the solar convection zone, including the presumed dynamo action which drives the solar cycle. In fact, zonal flows similar to the observed flows can be obtained from mean-field

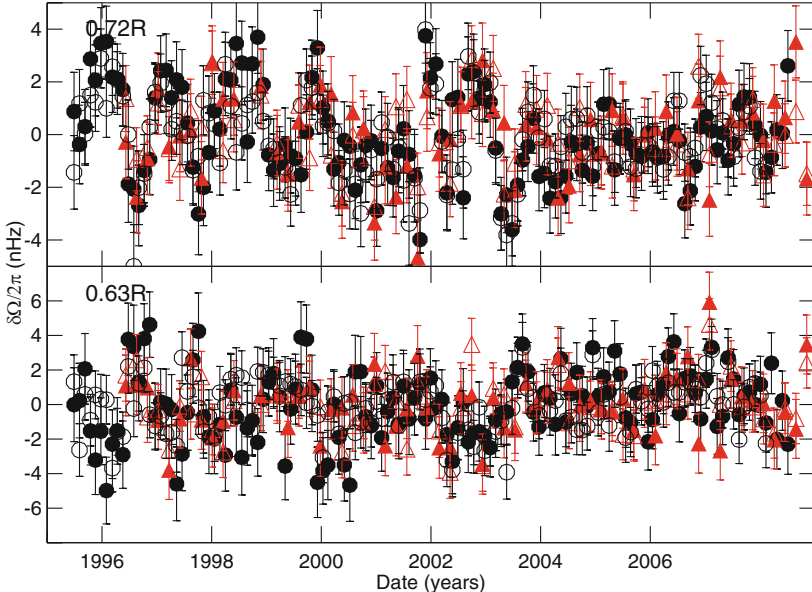


**Fig. 7.39.** Residual rotation rates, after subtraction of temporal averages; results are shown at the equator and distances from the centre of  $0.72 R_{\odot}$  (top) and  $0.63 R_{\odot}$  (bottom). Filled and open symbols were obtained from RLS and OLA inversions, respectively, of GONG data (circles) and MDI data (triangles). In the early part of the period evidence may be present for a periodic variation with a period of around 1.3 yr (Howe *et al.* 2000b). See Howe *et al.* (2007).

dynamo models (*e.g.*, Covas *et al.* 2000; Covas *et al.* 2004; Rempel 2007). Thus the observations provide interesting constraints on such models. It is evidently important to follow the further development of both the flows and the magnetic activity in the coming cycle which, at the time of writing (early 2009), promises to be rather different from the previous cycle.

While the detection of deeply penetrating zonal flows followed the surface observations of torsional oscillations, the evidence found by Howe *et al.* (2000b) for variations at the base of the convection zone was totally unexpected. On the basis of inversions of both GONG and MDI data these variations appeared as an oscillation, with a period of around 1.3 yr, in the equatorial rotation rate at a distance of  $0.72 R$  from the centre, with a weaker equatorial oscillation, with the opposite phase, around  $0.63 R$ . The variations at higher latitude were less well defined. Similar variations were visible in results obtained by Basu & Antia (2001) who, however, regarded the variation as statistically insignificant. The subsequent evolution, illustrated in Fig. 7.39,

was discussed by Howe *et al.* (2007). As is evident from the figure, the regular oscillations essentially vanished after 2001, although further potentially significant variations are found at later times. It cannot be excluded that the apparently regular oscillations are restricted to the rising phase of the solar cycle; thus it will be very interesting to follow the evolution in the period 2009 – 2012.

## 7.2 Solar-Like Pulsators

As discussed in Section 3.7.5 solar oscillations are intrinsically damped and excited stochastically by the near-surface convection. Thus similar oscillations are expected in all cool stars with vigorous outer convection zones. This has been overwhelmingly confirmed by recent observations (see Sections 2.3.1 and 2.5.5). Owing to the rich spectra of modes resulting from stochastic excitation and the relative ease of mode identification, solar-like oscillations have great promise for asteroseismology, a promise that is just beginning to be tapped.

Full use of the asteroseismic potential requires the best possible observations of “classical” observables such as effective temperature, surface composition and luminosity of the stars. Thus the compilation by Pijpers (2003) of such data for a number of relatively bright stars likely to show solar-like oscillations is very useful. We also note that Creevey *et al.* (2007) stressed the importance of interferometric determination of stellar radii, which is becoming possible for near-by solar-like stars.

### 7.2.1 Observational Aspects

Solar-like oscillations have been observed in a substantial number of stars as a result of an intensive observational effort over the past decade. This has been made possible in particular through the development of very stable spectroscopic techniques for ground-based observations, although intensity observations from space have also played an important role. Limitations in the available observing time at the large telescopes that have so far been required have restricted the duration of the spectroscopic observations to at most 1 – 2 weeks. This is further complicated by the need to organize coordinated observations to minimize the gaps in the data, an obvious difficulty when heavily oversubscribed facilities are involved. The most extensive campaign so far of this nature was organized in December 2006 and January 2007 to observe Procyon, using 11 telescopes at eight observatories, for observations spanning in total nearly one month (Arentoft *et al.* 2008). This resulted in a data set of high quality which at the time of writing is being analysed to determine the oscillation frequencies. However, it is evident that campaigns of this magnitude have to be rare; also, despite the very considerable effort invested we are still far from reaching the frequency resolution and precision available for low-degree helioseismic data.

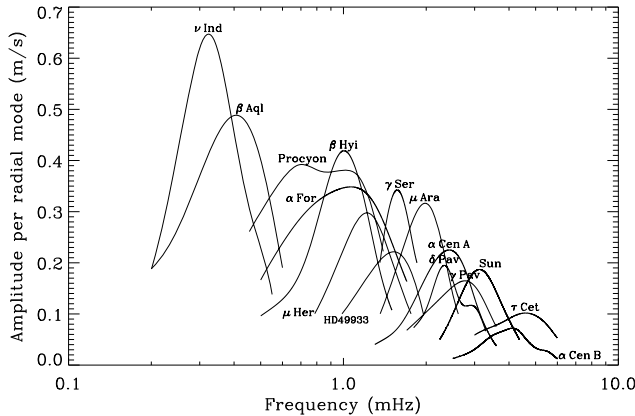


**Fig. 7.40.** Amplitudes of solar-like oscillations for a broad variety of stars, normalized to correspond to the amplitude per radial mode (see Kjeldsen *et al.* 2008a for details), as a function of frequency. The solar data, included for comparison, were obtained by observing the blue sky with a technique corresponding to the stellar observations and hence are directly comparable. From Arentoft *et al.* (2008).

An interesting result of the present observations is the distribution of mode amplitudes as a function of frequency and stellar parameters. This is illustrated in Fig. 7.40, normalized so as to correspond to the amplitude per radial mode, as described by Kjeldsen *et al.* (2008a). The location of the maximum amplitude is approximately given by  $\nu_{\max} \simeq 0.6\nu_{\text{ac}}$ , where  $\nu_{\text{ac}} = \omega/2\pi$  is the acoustic cut-off frequency in the stellar atmosphere (*cf.* Eq. (3.202)) as proposed by Brown *et al.* (1991). Thus the spectrum is shifted towards lower frequencies for more evolved stars, as already observed in Fig. 2.3. Also, the amplitude generally increases with increasing  $L/M$ , in qualitative accordance with the results discussed in Section 3.7.5. It is obvious that results such as those shown in Fig. 7.40 are very important for the understanding of the excitation of solar-like oscillations.

The power spectra of solar-like oscillations are expected to be similar to the solar spectra and hence characterized by Lorentzian mean envelopes, as in Eq. (7.7). Thus, in principle similar analysis techniques can be applied as in the solar case, fitting that equation, with a suitably parameterized background, to the power spectrum. In practice, this has proven to be somewhat difficult, probably as a result of the lower signal-to-noise level in the stellar data and observing runs extending only over a few mode lifetimes. This is illustrated by the solar power spectra shown in Fig. 7.41, for a single radial mode. With 10 d of observation the intrinsic resolution of  $1.16\,\mu\text{Hz}$  is too close to the

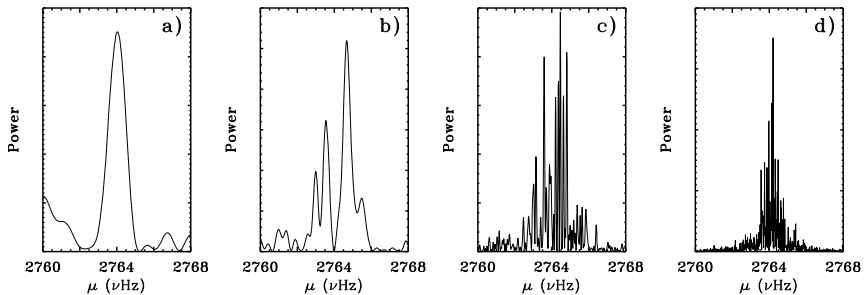


**Fig. 7.41.** Observed solar spectra for a radial mode, based on GOLF radial-velocity data from the early phase of SOHO operations (see García *et al.* 2005). The panels show analysis of time series extending over 10 d (a), 31 d (b), 151 d (c) and 805 d (d); the spectra for the shorter time series have been over-resolved by extending the data by zeros to a total length of 805 d. Note that this is the mode that was also illustrated in Fig. 3.33, based on BiSON data.

damping time of the modes of a few days to resolve the intrinsic line profile, and even after 31 d this is barely reflected in the line profile. Thus for relatively short observing runs a commonly used technique has essentially been based on prewhitening (see Section 5.1.2), successively identifying the highest peak in the power spectrum and removing the corresponding contribution from the time series. This may generate spurious frequencies, particularly at relatively low signal-to-noise ratio, and hence further, unavoidably partially subjective, analysis is needed to identify what is accepted as the true frequencies; in this, analysis of the échelle diagram is a very useful tool, at least when dealing with purely acoustic modes (see also Section 7.2.3.2 below).

In combining data from several sites, likely with rather different characteristics, it is important to assign proper weights to each site, and possibly to each segment of the data from a given site (see also Section 5.6). A simple procedure would be to base the weights on the intrinsic quality of the data. This might, however, often give substantially higher weight to one site compared with the others, and hence effectively lead to single-site observations. Thus the minimization of the daily sidelobes (see Section 5.3.3) must also be taken into account in the assignment of weights (*e.g.*, Bedding *et al.* 2004; Arentoft *et al.* 2008). The effect of this is illustrated in Fig. 7.42, based on two-site observations of α Cen A, involving the UVES spectrograph on the ESO VLT at Paranal and the UCLES (University College London Echelle Spectrograph) spectrograph at the AAT (Anglo-Australian Telescope) at Siding Spring Observatory in Australia. The former has a substantially lower noise level and hence is given higher weight, if noise in the spectrum is the only consideration; as shown in the left-hand panel this leads to very substantial daily sidelobes.

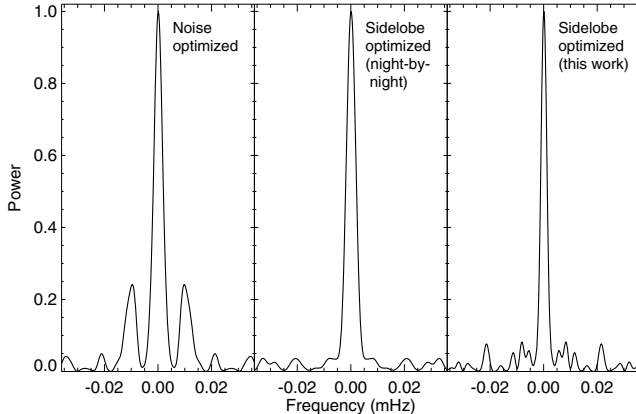


**Fig. 7.42.** Window functions for two-site observations of  $\alpha$  Cen A. In the left-hand panel data weights were chosen to minimize the noise in the power spectrum, resulting in one site being dominant and hence in strong daily sidelobes at  $\pm 0.0116$  mHz. In the remaining two panels the assignment of weights in addition aimed at suppressing these sidelobes. From Arentoft *et al.* (2009).

As illustrated by the remaining two panels these can largely be suppressed by a more appropriate weighting, although at the expense of an increase in the noise level in the amplitude spectrum of around 50% which in the present case is entirely acceptable.

For relatively short observing runs, such as those that have mostly been available so far, a fit to the Lorentzian profile in Eq. (7.7) probably does not provide a reliable measure of the mode lifetime. However, in such power spectra the lifetime is also reflected in the scatter of the inferred frequencies around the expected smooth behaviour or the scatter between the height of neighbouring peaks. Kjeldsen *et al.* (2005) used the frequency scatter, calibrating it by means of the analysis of a large number of sets of artificial data, to determine the mode lifetimes in  $\alpha$  Cen A and B; they also demonstrated that the technique recovered the lifetimes of solar modes inferred from Lorentzian fitting. Stello *et al.* (2004) used the statistics of mode amplitudes, similarly calibrated with artificial data, to infer a surprisingly short lifetime, only around 2 d, of the modes in the K giant  $\xi$  Hya, although with substantial uncertainty; this was confirmed by Stello *et al.* (2006) based on the scatter in frequencies around the expected uniformly spaced pattern. It is clear that these techniques are somewhat less direct, and hence likely less reliable, than the Lorentzian fits to properly resolved peaks; however, they have provided preliminary results for several stars covering a range of stellar parameters, of obvious interest to the understanding of the mode physics and to the planning of future observations.

It is evident that much work is required to develop optimal techniques for the analysis of asteroseismic data for solar-like stars. This is the more urgent as new projects promise large amounts of data (see Chapter 8), such that reliable and partly automatic techniques would be highly desirable. In developing and testing such techniques the use of artificial data with known properties is extremely useful. Particularly illuminating are blind tests, in the so-called ‘‘hare and hounds experiments’’, where data are produced by one participant and analysed by others without any knowledge beyond what would be available for real data. This has been organized in the solarFLAG<sup>26</sup> collaboration to test techniques for analysing disc-integrated helioseismic data (*e.g.*, Chaplin *et al.* 2006; Jiménez-Reyes *et al.* 2008) and has been extended into the asteroFLAG collaboration<sup>27</sup> dealing with the more general case of solar-like oscillations (Chaplin *et al.* 2008a). These efforts will undoubtedly be extremely important for the preparation for, and understanding of, the results of ongoing and coming asteroseismic projects.

We finally note that Chaplin *et al.* (2008b) made a detailed analysis of the expected observable properties of solar-like oscillations as a function of stellar parameters, to investigate the diagnostic potential of, in particular, the Kepler mission (see also Chapter 8). This included also the effects of rotation and possible stellar activity cycles. Such analyses are obviously important in the planning and interpretation of observations of solar-like oscillations.

## 7.2.2 Asteroseismic Diagnostics

### 7.2.2.1 Analysis of Stellar Structure

Stochastic excitation favours high-frequency oscillations, as a combined effect of the energy spectrum of convection and the properties of the eigenfunctions (see Goldreich *et al.* 1994). In unevolved stars such modes are all high-order acoustic modes; however, in evolved stars the buoyancy frequency becomes so large in the deep interior that also oscillations with g-mode character reach frequencies where efficient stochastic excitation is possible. In this case mixed modes (see Section 3.5.3) must be taken into account, further enriching the diagnostic potential of the observations. We return to such modes in Section 7.2.4.3 below and in this section consider purely acoustic modes.

Such modes approximately satisfy the asymptotic behaviour discussed in Section 3.4.3.1 (see also Tassoul 1980, 1990; Gough 1993). For the discussion of the average properties of the modes this can conveniently be approximated by

$$\nu_{nl} \simeq \Delta\nu_0 \left( n + \frac{l}{2} + \epsilon_0 \right) - l(l+1)D_0 , \quad (7.64)$$

---

<sup>26</sup> Solar Fitting at Low-Angular degree Group. See

<http://bison.ph.bham.ac.uk/~wjc/Research/FLAG.html>.

<sup>27</sup> <http://www.issi.unibe.ch/teams/Astflag/>.

(Scherrer *et al.* 1983; see Eq. (3.223)), where

$$\Delta\nu_0 \simeq \left( 2 \int_0^R \frac{dr}{c} \right)^{-1} \quad (7.65)$$

is an average large separation,

$$D_0 = -\frac{1}{4\pi^2 n_0} \int_0^R \frac{dc}{dr} \frac{dr}{r} \quad (7.66)$$

(*cf.* Eqs (3.219) and (3.220)), and  $n_0$  is a suitable reference order. Thus the average small separation is given by

$$\delta\nu_l = \langle \nu_{nl} - \nu_{n-1,l+2} \rangle_n \simeq (4l + 6)D_0 , \quad (7.67)$$

where the average is over radial order. In addition to these small separations it is also convenient to consider small separations involving adjacent degrees, such as

$$\delta^{(1)}\nu_{nl} = \frac{1}{2}(\nu_{n-1,l} + \nu_{n,l}) - \nu_{n-1,l+1} , \quad (7.68)$$

and hence

$$\delta^{(1)}\nu_l = \langle \frac{1}{2}(\nu_{n-1,l} + \nu_{n,l}) - \nu_{n-1,l+1} \rangle_n \simeq 2(l + 1)D_0 ; \quad (7.69)$$

these are particularly useful for analysing intensity observations where the range of degrees is restricted to  $0 - 2$ .

The integral in Eq. (7.66) is evidently weighted towards the stellar centre and hence provides a measure of the sound-speed gradient in the core of the star. Also, the average  $\Delta\nu_0$  of the large frequency spacing is a measure of the mean density of the star. Thus it is clear that  $\Delta\nu_0$  and  $D_0$  provide important diagnostics of stellar properties which can be determined from observations of low-degree modes.

As a star evolves, the hydrogen abundance in the core decreases and hence the mean molecular weight increases. For an approximately ideal gas, the sound speed may be obtained from

$$c^2 \simeq \frac{\Gamma_1 k_B T}{\mu m_u} ; \quad (7.70)$$

since the central temperature varies little during hydrogen burning, due to the strong temperature sensitivity of the nuclear reaction rates, the main effect on the sound speed in the core comes from the change in the mean molecular weight  $\mu$ . Consequently  $c$  decreases as the star evolves, the decrease being most rapid at the centre where hydrogen burning is fastest; this is illustrated in Fig. 7.43. As a result,  $c$  develops a local minimum at the centre, and  $dc/dr$  is positive in the core. This region gives a negative contribution to  $D_0$  (*cf.*

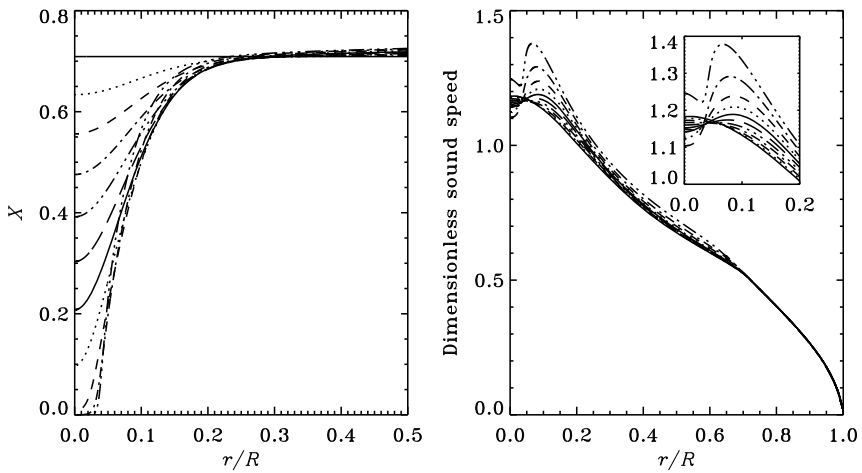


**Fig. 7.43.** Evolution of a  $1 M_{\odot}$  model during central hydrogen burning. The left panel shows the hydrogen abundance  $X$  for models of age  $1 - 10$  Gyr, in steps of 1 Gyr. The right panel shows the dimensionless sound speed (in units of  $(GM/R)^{1/2}$ ; cf. Section 3.3.3.1) in these models, with an enlargement in the inset of the behaviour in the core. Note the rapid variation in the final model, shown by the triple-dot-dashed curve. Adapted from Christensen-Dalsgaard (2009).

Eq. (3.221)), of increasing magnitude with increasing age, and hence  $D_0$  decreases with increasing age (see also Christensen-Dalsgaard 1991a). Hence  $D_0$ , which can in principle be observed, is a measure of the evolutionary state of the star. On the other hand, the overall frequency separation  $\Delta\nu_0$ , defined in Eq. (7.65), approximately scales as the inverse  $t_{\text{dyn}}^{-1}$  of the dynamical time scale which, for main-sequence stars, is largely determined by the mass.

These considerations motivate presenting the average frequency separations in a  $(\Delta\nu_0, D_0)$  diagram, as illustrated in Fig. 7.44; this is analogous to the ordinary HR Diagram. It is evident from Fig. 7.44 that on the assumption that the other parameters of the star (such as composition) are known, a measurement of  $\Delta\nu$  and  $D_0$  may allow determination of the mass and evolutionary state of the star (Christensen-Dalsgaard 1984b; Ulrich 1986; Christensen-Dalsgaard 1988). On the other hand, Gough (1987) analysed the sensitivity of this result to the other stellar parameters, and found that the uncertainty in the knowledge of the heavy element abundance, in particular, had a severe effect on the determination of the mass and age. As an example of such sensitivity, Fig. 7.44(b) shows the consequences of an increase of the hydrogen abundance by 0.03. A more extensive analysis of the sensitivity to

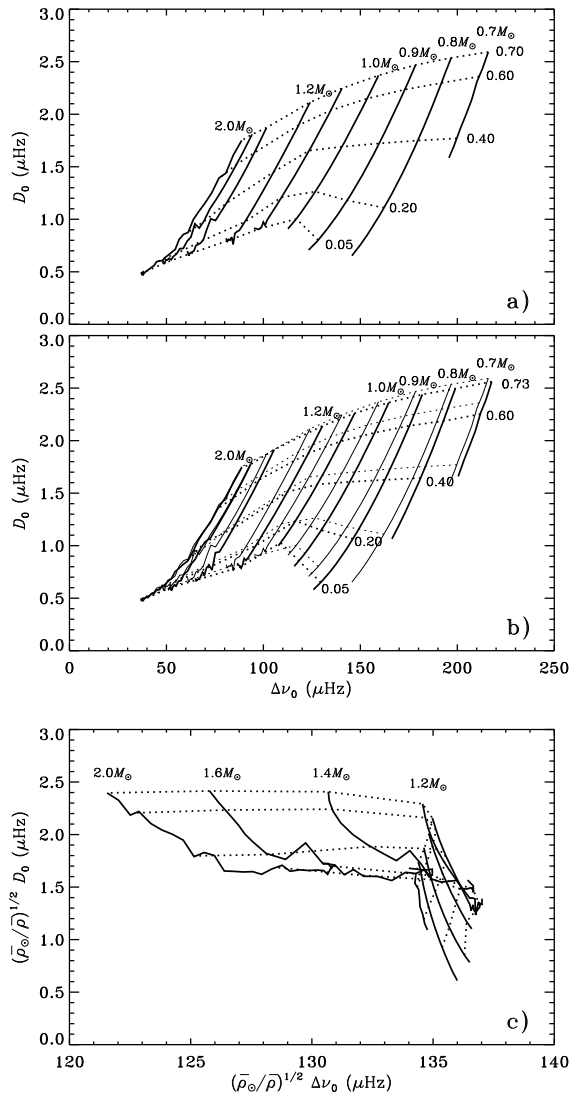


**Fig. 7.44.** Evolution tracks (——) and curves of constant central hydrogen abundance (·····) in  $(\Delta\nu_0, D_0)$  diagrams. Here  $\Delta\nu_0$  is the average separation between modes of the same degree and adjacent radial order, and  $D_0$  is related to the small separation between  $\nu_{nl}$  and  $\nu_{n-1,l+2}$  (cf. Eq.(3.221)). The stellar masses, in solar units, and the values of the central hydrogen abundance, are indicated. Panel (b) shows the effect of increasing the hydrogen abundance by 0.03 (heavy lines), relative to the case presented in panel (a) (shown here with thin lines). In panel (c), the frequency separations have been scaled by  $(\bar{\rho})^{-1/2}$ , in units of the solar value  $\bar{\rho}_\odot$  ( $\bar{\rho} \propto M/R^3$  being the mean density), to take out the variation with  $t_{\text{dyn}}^{-1}$ . Adapted from Christensen-Dalsgaard (1993a).

model parameters was presented by Monteiro *et al.* (2002). To illustrate the dependence of the separations on the global stellar parameters panel (c) (note the different scales) shows the result of scaling them by  $\bar{\rho}^{-1/2}$ ,  $\bar{\rho} \propto M/R^3$  being the mean density which is proportional to  $t_{\text{dyn}}^{-2}$  (see Section 3.3.3.1). Evidently most, but not all, of the variation in  $\Delta\nu_0$  is in fact related to  $t_{\text{dyn}}$ , such that  $\Delta\nu_0$  scales as  $M^{1/2}/R^{3/2}$ . A careful analysis of the information content in measured frequency separations, when combined with more traditional measurements of stellar properties, was given by Brown *et al.* (1994). In a similar investigation Creevey *et al.* (2007) also included interferometric measurements of the stellar radius, showing that with realistic errors this could substantially increase the precision of the determination of stellar mass and age.

The solar case, with an independent determination of the age from radioactive dating, provides an excellent test of the age calibration based on low-degree modes. The sensitivity of such determinations to other uncertainties in the model parameters, including the ratio  $Z_s/X_s$  of the surface heavy-element to hydrogen abundances, was investigated by Gough & Novotny (1990) and Gough (2001). Dziembowski *et al.* (1999) and Bonanno *et al.* (2002) made least-squares fits to the observed small frequency separations, fixing  $Z_s/X_s$  to the then current spectroscopic value and considering models calibrated to solar luminosity and radius; they obtained helioseismically inferred ages in good agreement with the meteoritic value. A similar analysis was carried out by Christensen-Dalsgaard (2009), using both the Grevesse & Noels (1993) and the Asplund *et al.* (2004) values of  $Z_s/X_s$ . In the former case the result was in accordance with the meteoritic age; however, using the Asplund *et al.* composition resulted in a helioseismic age of around 4.85 Gyr, substantially higher than the meteoritic value of 4.57 Gyr (see Wasserburg, in Bahcall & Pinsonneault 1995). This discrepancy is in accordance with the analysis by Basu *et al.* (2007) and Chaplin *et al.* (2007b) of the small frequency separations which similarly pointed towards the older determinations of the solar surface abundance (see also Section 7.1.7). It should be noticed that since these calibrations all assumed that at least the solar mass, radius and luminosity were known they are not directly representative of the results that might be expected from the less constrained general stellar case.

The accuracy of Eq. (7.66) as representing the average small separation is questionable; it appears to agree fortuitously with frequencies computed for models of the present Sun, whereas it is less successful for models of different ages or masses (Christensen-Dalsgaard 1991a). That there should be departures from this simple analysis is hardly surprising. The asymptotic analysis is based on the Cowling approximation, yet the perturbation to the gravitational potential has a significant effect on low-degree modes, which furthermore decreases rapidly with increasing degree, thus affecting the small frequency separation; a simple analysis of this effect was presented by Vorontsov (1989) (see also Christensen-Dalsgaard 1991a). Furthermore, a prerequisite for the JWKB analysis which underlies Eq. (7.64) is that the equilibrium model varies on a scale much longer than the wavelength of the modes; this is obviously

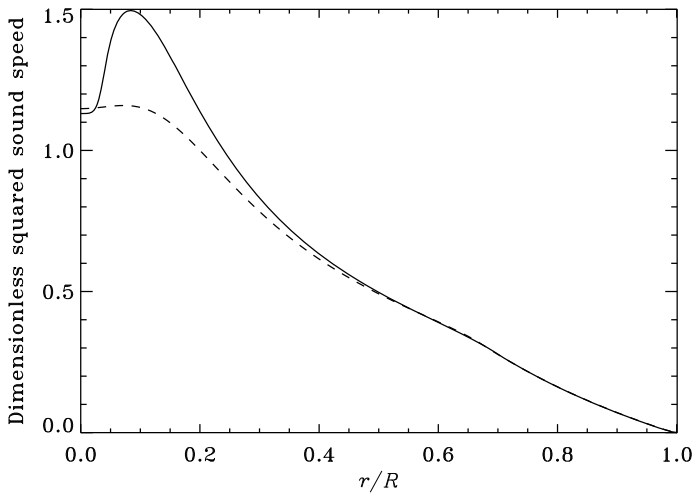


**Fig. 7.45.** Dimensionless squared sound speed, in units of  $GM/R$ , for models of  $\alpha$  Cen A (solid curve) and  $\alpha$  Cen B (dashed curve).

not satisfied by the rapid variation of the sound speed in the core of evolved models (*cf.* Fig. 7.43). Apparently, these two effects largely cancel in the solar case.

Some of these issues can be illustrated by considering the dependence of the small separation on  $l$ . From Eqs (7.67) and (7.69) we expect that  $\delta\nu_{nl}/(2l+3)$  and  $\delta^{(1)}\nu_{nl}/(l+1)$  are independent of  $l$ . To investigate the validity of these asymptotic dependencies we consider as examples the A and B components of the  $\alpha$  Cen system, discussed in Section 7.2.3 below. The dimensionless squared sound speed of models of these two stars is illustrated in Fig. 7.45. At the inferred age of the system the lower-mass B component is barely evolved whereas the more massive A component is approaching the end of the central hydrogen burning; consequently the sound speed in the latter case shows the rapid variation already noticed in Fig. 7.43. The effect on the small frequency separations is illustrated in Fig. 7.46. For the B component the scaled separations show modest scatter with degree, as expected asymptotically. On the other hand, for the A component there is substantial scatter, particularly for the  $\delta^{(1)}\nu_{nl}$ . From the point of view of asteroseismic diagnostics this clearly shows that the frequencies contain information beyond the parameters characterizing the simple asymptotic expressions. Furthermore, it should be noticed that at the highest frequencies  $\delta\nu_{n0}$  becomes slightly negative; this is contrast to Eq. (3.221) which predicts that  $\delta\nu_{nl}$  has a constant sign. This kind of be-

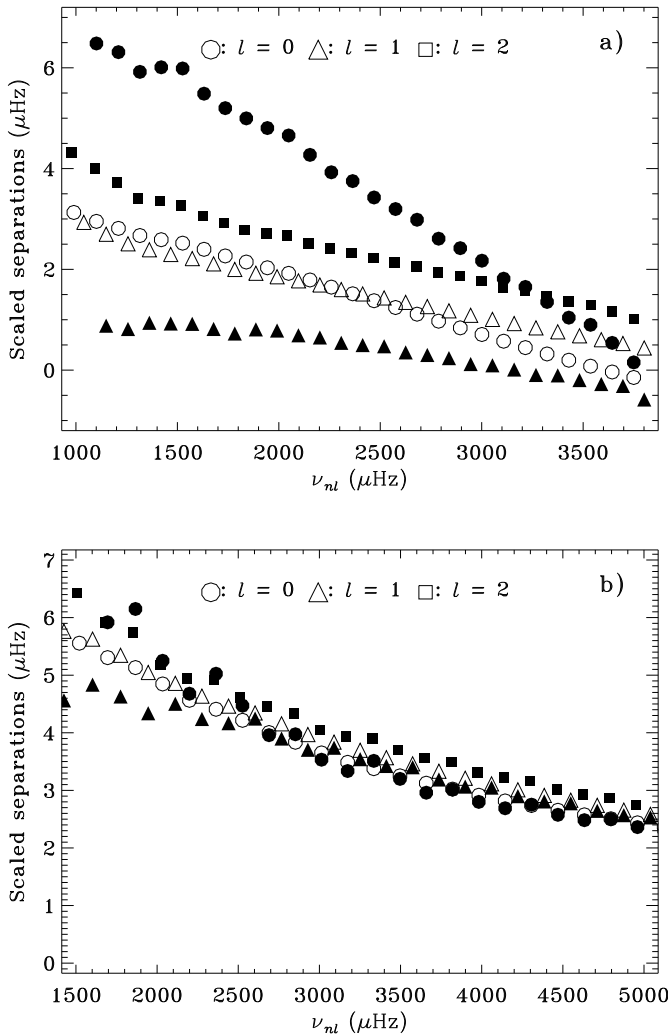


**Fig. 7.46.** Scaled frequency separations for models of  $\alpha$  Cen A (panel a) and  $\alpha$  Cen B (panel b). Open symbols show  $(\nu_{nl} - \nu_{n-1,l+2})/(2l + 3)$  and filled symbols show  $[(\nu_{n-1,l} + \nu_{nl})/2 - \nu_{n-1,l+1}]/(l + 1)$ , at the values of  $l$  indicated by the symbol type.

haviour was noted by Soriano & Vauclair (2008) who related it to the sharp variation of the sound speed in the core of evolved stars.

A more appropriate treatment of the effect of the core can be obtained by treating the interaction between the waves and the sound-speed structure in the Born approximation which does not assume that the scale of the structure variations is large compared with the wavelength. This has been developed in a series of papers by Roxburgh & Vorontsov (1994b, 1996, 2000a,b, 2001). As an interesting concept they characterize the effect of the core by a partial phase  $\delta_l$ , defined such that the asymptotic behaviour of the pressure perturbation  $p'$  satisfies

$$\frac{(\rho c)^{1/2}}{r} p' \simeq A_p \sin(\omega \tilde{\tau} - \frac{\pi}{2} l + \delta_l) . \quad (7.71)$$

Here

$$\tilde{\tau} = \int_0^r \frac{dr'}{c} = \tau_0 - \tau , \quad (7.72)$$

where  $\tilde{\tau}$  is the acoustic distance to the centre and  $\tau_0$  is the acoustic radius of the star (*cf.* Eq. (7.22)); the term  $-\pi l/2$ , corresponding to the leading-order asymptotic behaviour of the solution at the centre, was included explicitly. In the same way as the surface phase introduced, for example, by Christensen-Dalsgaard & Perez Hernández (1992) this can be defined as a continuous function of frequency from a partial solution to the oscillation equations. The full solution can then be obtained by matching the interior and exterior solutions, leading to the eigenfrequency equation

$$\omega_{nl}\tau_0 = \left( n + \frac{l}{2} \right) \pi + \tilde{\alpha}(\omega_{nl}) - \delta_l(\omega_{nl}) , \quad (7.73)$$

where  $\tilde{\alpha}$  is a similarly defined surface phase, or

$$\nu_{nl} = \frac{1}{2\tau_0} \left[ n + \frac{l}{2} + \pi^{-1}(\tilde{\alpha}(\omega_{nl}) - \delta_l(\omega_{nl})) \right] , \quad (7.74)$$

essentially corresponding to Eq. (3.219), since  $\Delta\nu_0 = (2\tau_0)^{-1}$  and the term in  $\delta_l$  contains much of the last correction term in that equation. Thus the small frequency separation is obtained as

$$\delta\nu_{nl} = \nu_{nl} - \nu_{n-1,l+2} = \frac{1}{2\pi\tau_0} [\delta_{l+2}(\omega_{n,l+2}) - \delta_l(\omega_{nl})] . \quad (7.75)$$

Roxburgh & Vorontsov (1994b) discussed the asymptotic form of  $\delta_l$ . In the simplest approximation they obtained

$$\delta_l(\omega) \simeq \delta_0(\omega) + \frac{l(l+1)}{2\omega} \left[ \frac{c(R)}{R} - \int_0^R \frac{dc}{dr} \frac{dr}{r} \right] , \quad (7.76)$$

and hence, according to Eq. (7.75),

$$\delta\nu_{nl} = (4l+6) \frac{\Delta\nu_0}{4\pi^2\nu_{nl}} \left[ \frac{c(R)}{R} - \int_0^R \frac{dc}{dr} \frac{dr}{r} \right] , \quad (7.77)$$

in accordance with the Tassoul (1980) expression (*cf.* Eqs (3.220) and (3.221)). However, it should be noted that the neglected terms include derivatives of the sound speed and buoyancy frequency which would be large in evolved models with a rapidly varying structure in the core. Thus the full diagnostic potential of the analysis by Roxburgh & Vorontsov (1994b) still remains to be explored.

Popieliski & Dziembowski (2005) recalled that the growing convective core in main-sequence stars of intermediate mass causes problems in the modelling of the convective-core boundary, including the possible occurrence of “semi-convection” (see Section 3.2.3). They made an extensive exploration of seismic diagnostics of models of this nature, including also the possibility of convective overshoot. They argued that the most sensitive measure of conditions at the core boundary is the small separation  $\delta^{(1)}\nu_{n0}$  (*cf.* Eq. (7.69)) and demonstrated a clear separation between different scenarios in a diagram plotting the mean value of  $\delta^{(1)}\nu_{n0}$  and its slope as a function of frequency.

An analysis that explicitly took the rapid variation into account was carried out by Cunha & Metcalfe (2007), in the case where a small and growing convective core leads to a discontinuity in composition and hence sound speed (*cf.* Figs 3.6 and 3.7). Through an asymptotic analysis of this specific case they found that the following combination of frequency separations,

$$\Delta_{CM} \equiv \frac{D_{n0}}{\Delta\nu_{n-11}} - \frac{D_{n1}}{\Delta\nu_{n0}}, \quad (7.78)$$

is sensitive to the properties of the sound-speed discontinuity; here  $D_{nl} = \delta\nu_{nl}/(4l + 6)$  and  $\Delta\nu_{nl} = \nu_{n+1l} - \nu_{nl}$ . In particular, they demonstrated that  $\Delta_{CM}$  provides a measure of stellar age, given observational errors that may realistically be achieved. The effect on this measure of a steep but not discontinuous change in sound speed, as would result with diffusion (*cf.* Fig. 3.7), remains to be explored. A similar diagnostic combination of small separations, averaged over radial order, was investigated by Mazumdar *et al.* (2006a), who applied it to a number of stellar models with varying parameters; they found that the size of the convective core could be determined with fairly high precision, if other parameters of the star, including its mass, were known.

As discussed in Section 7.1.4.1 the uncertainties in the modelling of the near-surface layers introduce errors in the computed frequencies which for low-degree modes are predominantly functions of frequency. Since these effects vary rapidly with frequency (see for example Fig. 7.24) they have a significant effect on the large frequency separation, to which we return below. However, even the small frequency separations are significantly affected. It was shown by Roxburgh & Vorontsov (2003) that these effects could largely be suppressed by considering separation ratios such as

$$r_{n0} = \frac{\nu_{n0} - \nu_{n-12}}{\nu_{n1} - \nu_{n-11}} \quad (7.79)$$

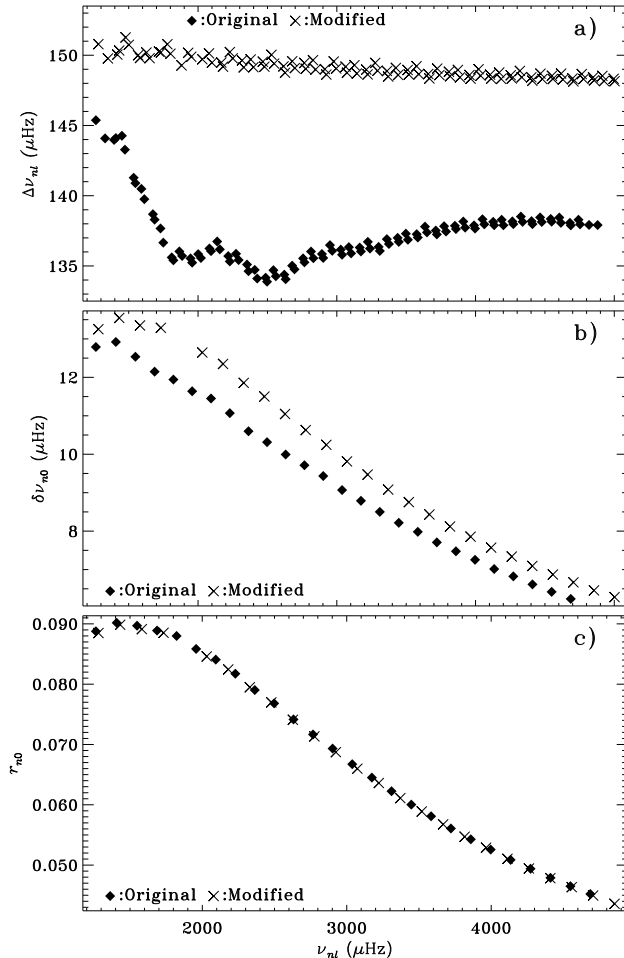


**Fig. 7.47.** Effects of a model change on frequency separations and their ratio. The original model (filled diamonds) is Model S of Christensen-Dalsgaard *et al.* (1996). In the modified model (crosses) the convection zone of Model S was replaced by a polytrope of index 3/2 and with  $\Gamma_1 = 5/3$ . Panel a) shows the large separation  $\Delta\nu_{nl} = \nu_{n-1l} - \nu_{nl}$ , for  $l = 0-3$ . Panel b) shows the small separation  $\delta\nu_{n0} = \nu_{n0} - \nu_{n-12}$  and panel c) shows the ratio  $r_{n0}$  (*cf.* Eq. (7.79)). Adapted from Otí Floranes *et al.* (2005).

between a small and large separation. They furthermore demonstrated that this is directly related to the central phase, by

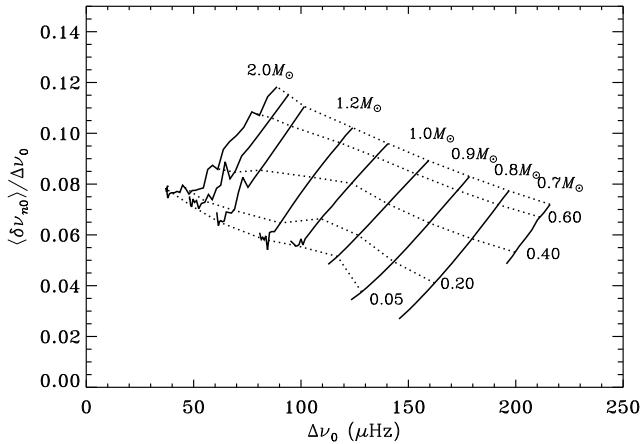


**Fig. 7.48.** Evolution tracks (continuous curves) and curves of constant central hydrogen abundance (dotted curves), in terms of the ratio between the average small and large separation. See also Fig. 7.44. Adapted from Otí Floranes *et al.* (2005).

$$r_{n0} = \frac{1}{\pi}(\delta_2 - \delta_0) , \quad (7.80)$$

even given the variation of the large separation with frequency, and illustrated the effect by means of examples of solar models differing just in the surface layers. More extensive experiments of this nature were carried out by Otí Floranes *et al.* (2005) showing the wide applicability of this scaling. As an example, Fig. 7.47 compares a standard solar model with the same model but with the convection zone replaced by a polytrope of index 3/2 and with a constant  $\Gamma_1 = 5/3$ ; thus the model does not match the radius of the original model. As shown in the figure this has a substantial effect on the large and small separations, whereas the ratio  $r_{n0}$  is unchanged by even this major model modification. Otí Floranes *et al.* also developed kernels relating changes to the model to changes in  $r_{nl}$ , demonstrating that the sensitivity of  $r_{nl}$  is indeed localized to the interior of the star, with very small sensitivity to the surface layers. Additional examples of near-surface modifications for a range of stellar models were considered by Roxburgh (2005), further demonstrating the minimal effect of the modifications on the separation ratios.

It is evidently similarly advantageous to use an average separation ratio in a two-dimensional diagram such as Fig. 7.44; as a similar plot, Fig. 7.48 uses the ratio between the averages. It is interesting that the curves of fixed mass and fixed evolutionary state are more nearly orthogonal in this diagram, indicating that it provides a more secure determination of the stellar properties.

The near-surface errors clearly affect all comparisons between the observed and model frequencies and hence must be kept in mind when analysing observations of solar-like oscillations. In the solar case, the availability of modes over a broad range of degrees allows the effect to be eliminated in, for example, inverse analyses for the solar internal structure (*cf.* Section 7.1.6.1). This is clearly not possible with just the limited set of low-degree data available from unresolved stellar observations, although the separation ratios discussed above provide powerful measures of the stellar core. To obtain a more general correction of the frequencies, additional assumptions are required. Kjeldsen *et al.* (2008b) noted that the solar surface errors are rapidly varying functions of frequency and hence assumed that they could be represented by a power law,

$$\delta^{(\text{surf})} \nu = a(\nu/\nu_0)^b , \quad (7.81)$$

where  $\nu_0$  is a suitable reference frequency and the amplitude  $a$  and exponent  $b$  can be obtained from fitting to solar frequencies.<sup>28</sup> They then assumed that the solar value of  $b$  can be applied to other stars and showed how the correction could be obtained from stellar data and a suitable reference model, on the assumption that the frequency of the reference and true model are related by a scaling by the inverse dynamical time scale (see Section 3.3.3.1). This provides a practical technique for the analysis of the observed frequencies, although under fairly strong assumptions which clearly need to be tested. Tests of the effects of near-surface model modifications, such as presented in Section 7.1.4.1, should clearly be carried out for other stellar parameters and types of modifications. Also, one may hope that the coming extensive observations of stellar oscillations (see Chapter 8) will yield data of a quality that allows a direct test and will provide further insight into the physical nature of these effects.

The above analysis, including the insensitivity of the ratio  $r_{n0}$  to the near-surface effects, assumes that these are independent of the degree of the modes and hence effectively that the star is spherically symmetric. This is probably a reasonable assumption in the case of the hydrostatic structure, for slowly rotating stars. However, as discussed in Section 7.1.9, the solar magnetic activity has a significant effect on the solar frequencies, and similar effects must be expected for solar-like stars. In the solar case the frequency changes are closely correlated with the surface magnetic field (*e.g.*, Howe *et al.* 2002) which shows a strong dependence on latitude, with a concentration at low and intermediate latitudes of the magnetically active regions; thus the effects depend on the spatial structure of the modes, including their degree. Chaplin *et al.* (2004b) and Toutain & Kosovichev (2005) did in fact find that the frequency changes associated with the solar magnetic cycle depended on the degree of the mode. It is evident that such degree-dependent effects would affect the small separations, compromising their use as diagnostics of stellar cores. In

---

<sup>28</sup> The analysis by Christensen-Dalsgaard & Gough (1980) of a specific case provides some support for this functional form.

the solar case Dziembowski & Goode (1997) argued that the effects could be suppressed by using observations of higher-degree modes. In the stellar case less direct methods, probably relying on other diagnostics of stellar activity, will be required.

The effects of the sharp variation in the sound speed in the core of evolved stars may be considered as a particular case of an *acoustic glitch*, *i.e.*, a feature in the structure of the star varying much more rapidly than the scale of the eigenfunction. As discussed in Section 7.1.4.2 these give rise to an oscillatory signature in the frequencies which can be used to characterize the location and properties of the glitch. The potential of this for the diagnostics of the solar interior, including the determination of the envelope helium abundance and the properties of the convection-zone base, was discussed in Section 7.1.7. This is obviously greatly aided by the availability of modes over a range of degrees. However, such signatures can also be extracted from just low-degree modes. Pérez Hernández & Christensen-Dalsgaard (1998) studied the diagnostics of the second helium ionization zone based on a suitably filtered version of the surface phase function  $\alpha(\omega)$  and showed that useful information can be obtained from modes of degree  $l \leq 2$ , such as are observed in unresolved intensity observations. A detailed investigation of the sensitivity of the frequencies, analysed in terms of the second difference  $\Delta_2\nu_{nl} = \nu_{n-1l} - 2\nu_{nl} + \nu_{n+1l}$  (*cf.* Section 7.1.7) was made by Basu *et al.* (2004), considering models over a range in mass and age; they concluded that the precision in the determination of the helium abundance increased with stellar mass.

Monteiro *et al.* (2000) considered the detectability of the depth of, and possible overshoot from, convective envelopes in main-sequence stars, restricting the data again to modes with  $l \leq 2$ . They found that if the error of the cyclic frequency was  $0.1\,\mu\text{Hz}$  or less a reasonably precise estimate could be obtained of the depth of the convection zone, and of the amplitude of the oscillatory signal (*cf.* Fig. 7.31) which characterizes the stratification near its base. Signatures of the edges of convective regions, both convective envelopes and convective cores, were also studied by Mazumdar & Antia (2001). They pointed out potential problems as a result of “acoustic aliasing” giving rise to indistinguishable signals from glitches at an acoustic depth  $\tau_g$ , say, and  $\tau_0 - \tau_g$ , at least if only modes of a single degree are considered;<sup>29</sup> if data from several degrees are involved this ambiguity can be avoided, however.

A detailed investigation of the diagnostic potential for determining the depth of the convection zone, as an acoustic glitch, with low-degree data was made by Ballot *et al.* (2004). They considered both realistically simulated data and low-degree solar data from GOLF and VIRGO. In addition to the second difference  $\Delta_2\nu_{nl}$  they investigated the use of lower- and higher-order differences, concluding that  $\Delta_2\nu_{nl}$  provided the best compromise between isolating the rapidly varying components of the frequencies without too strongly

---

<sup>29</sup> An illuminating discussion of such effects, with particular emphasis on g-mode diagnostics of white dwarfs, was presented by Montgomery *et al.* (2003).

increasing the error. From analysing artificial and real time series of varying length they concluded that observations over at least 150 d are required to obtain a reliable determination of the depth of the convection zone. A similar analysis was carried out by Verner *et al.* (2006b), based on solar BiSON data of degree  $l = 0\text{--}3$ , but considering the determination of both the signatures of the second helium ionization zone and the base of the convection zone. They concluded that the detection of the effect of helium ionization could be obtained with as little as 82 d of data, whereas a reliable determination of the envelope helium abundance required at least 300 d. Reasonably reliable properties of the base of the convective envelope could be found from at least 182 d of data.

To derive optimal procedures for determining, and suppressing, the effects of acoustic glitches Houdek & Gough (2007) made a careful asymptotic analysis of the effects of the helium ionization zones and the base of the convection zone on the frequencies. This resulted in an expression with a number of parameters characterizing the depth, extent and location of the glitches associated with the first and second helium ionization, the properties of the base of the convective envelope and a term corresponding to the effect of the near-surface layers on the frequencies. The analysis was carried out in terms of the second difference  $\Delta_2\nu_{nl}$ . An example is illustrated in Fig. 7.49. It is evident that just from low-degree modes it is possible to isolate the three components and hence obtain information about both the helium ionization zones and the base of the convection zone. It should also be noted that the signals are strongest at low frequency: here the wavelength of the modes is longest and hence there is least smearing of the effect of the glitches. This illustrates the importance of obtaining asteroseismic data for solar-like oscillations at the lowest possible frequencies.

As pointed out by Houdek & Gough (2008), the frequency modifications induced by the acoustic glitches also affect those properties of the frequencies which are used to determine stellar ages. Thus in an analysis of solar data to test asteroseismic age determination they applied a correction to the observed frequencies for the effects of the glitches, based on a fitted function such as the one illustrated in Fig. 7.49; the corrected frequencies were then fitted to an asymptotic expression extending Eq. (3.219) to higher asymptotic order, to determine the age and heavy-element abundance of the Sun. As in earlier attempts, the models were all assumed to have solar mass, radius and luminosity. They found that the inclusion of the glitches substantially stabilized the fit, as did the inclusion in the fit of a parameter measuring the depression in  $\Gamma_1$ , resulting from helium ionization. From this they obtained an age of 4.68 Gyr and  $Z = 0.0169$ , with some correlation between these two quantities. Although the age is not entirely consistent with the meteoritic value, and the assumption of known solar parameters has to be relaxed, these results are clearly promising for the calibration of stellar ages based on high-quality asteroseismic data.

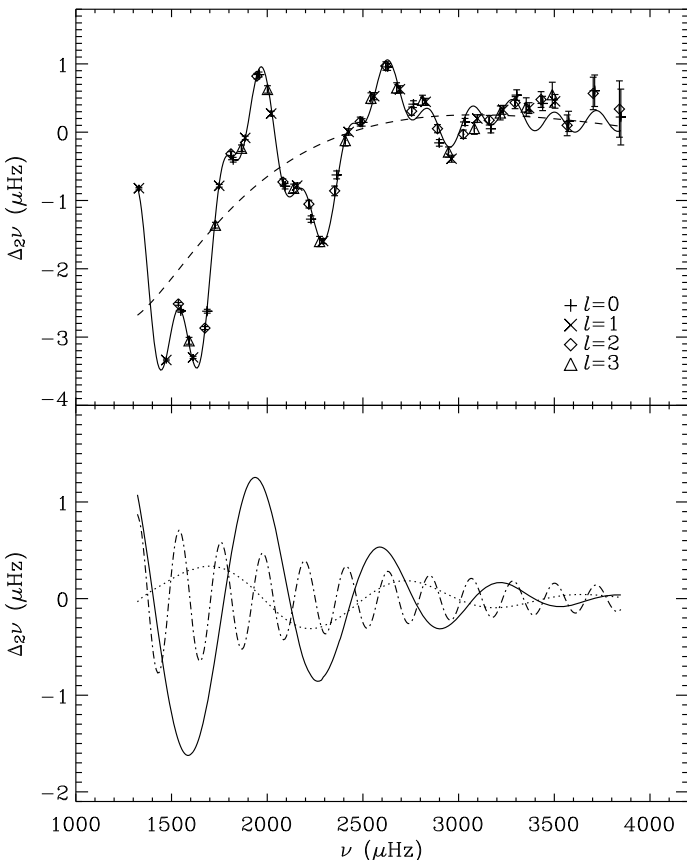


**Fig. 7.49.** Second frequency differences  $\Delta_2\nu_{nl} = \nu_{n-1l} - 2\nu_{nl} + \nu_{n+1l}$  and an asymptotic fit, based on 11 yr of BiSON data. In the top panel the symbols show  $\Delta_2\nu_{nl}$  based on the observed frequencies, for  $l = 0–3$  as indicated, and the solid curve shows the fitted function; the dashed curve is a slowly varying component of the fit arising from the near-surface behaviour of the modes. The lower panel shows the individual components of the fit, from the first (dotted curve) and second (solid curve) helium ionization zones, as well as from the base of the convection zone (dot-dashed curve). From Houdek & Gough (2007).

The sensitivity of small separations to the acoustic glitch at the base of the convection zone, particularly for those, such as  $\delta^{(1)}\nu_{nl}$ , that involve a broader range in frequency, was also noted by Roxburgh (2009). He analysed the effect for higher-order differences in terms of the inner phases  $\delta_l$  (*cf.* Eq. (7.71)) and pointed out that this can be used to define a measure of the acoustic radius at

the base of the convection zone, based just on frequencies of modes of degree  $l = 0, 1$ .

A detailed test of asteroseismic inferences was carried out by Monteiro *et al.* (2002). They combined the inference of stellar mass and evolutionary state, based on the diagram in Fig. 7.44, with an analysis of the oscillatory signal arising from the base of the convection zone. Furthermore, they noted that the determination of the appropriate measure of the large separation should be corrected for the oscillatory feature arising from the acoustic glitch associated with helium ionization. The analysis was carried out in a blind fashion, as a so-called “hare and hounds” test, where one of the participants, the hare, generated artificial data with realistic error properties, and other participants, the hounds, attempted to infer the properties of the models used to generate the data. The analysis showed the importance of combining the asteroseismic data with “classical” data such as information about effective temperature, luminosity and surface composition. In particular, this is needed to constrain other parameters of the star, as illustrated by Fig. 7.44b. These data were also provided by the hare, with realistic errors. The results of the test showed that mass and evolutionary state could be recovered reasonably successfully for the three cases considered, with indications also of differences in the assumptions used in the model calculation. In two of the three cases the signature of the base of the convection zone was also interpreted with reasonable success, including the detection of convective overshoot in one case, whereas in the third case the noise in the oscillation data led to an erroneous interpretation of the oscillatory signal.

Mazumdar (2005) also made a careful analysis of the diagnostic potential of combining frequency separations and signatures of acoustic glitches. He noted that, in addition to the diagram in Fig. 7.44, a diagram involving the large separation and the acoustic radius of the base of the convective envelope provided a useful tool for determining the mass and evolutionary state of the star. He applied these tools to the analysis of artificial data simulating a target for the CoRoT mission, succeeding remarkably well in recovering the input parameters of the underlying model.

A first step in any asteroseismic analysis is to determine the overall properties of the star. This can be formalized as the determination of a set of parameters  $\mathcal{P} = \{p_i\}, i = 1, \dots, N$  which are determined from a set of observables  $\mathcal{O} = \{o_j\}, j = 1, \dots, M$ . The observables may be “classical” observables such as photometric or spectroscopic quantities, quantities obtained from such observables such as effective temperature or surface gravity, oscillation frequencies or quantities obtained from combinations of frequencies, such as frequency separations or more complex combinations perhaps inspired by the asymptotic analysis discussed above. It is assumed that the standard error  $\sigma_j$  for each observable is known. The observables are related to the parameters through a model that allows each observable  $o_j$  to be calculated as  $o_j = o_j^{(m)}(p_i)$  as a function of the parameters. The parameters are then

typically determined in a least-squares sense by minimizing<sup>30</sup>

$$\chi^2(p_i) \equiv \sum_j \left[ \frac{o_j - o_j^{(m)}(p_i)}{\sigma_j} \right]^2. \quad (7.82)$$

In general, the dependence of the observables on the parameters is quite complicated and hence it may be difficult to find the absolute minimum. One way is to search in an extensive grid of stellar models, covering the appropriate ranges of the relevant parameters (*e.g.*, Guenther & Brown 2004); however, the number of models in such grids increases very rapidly with the number of parameters. A possibly more efficient technique is the use of nonlinear optimization techniques, such as genetic algorithms (*e.g.*, Metcalfe & Charbonneau 2003), which generally succeed remarkably well in finding the true optimum. On the other hand, near the true solution where the relation between observables and parameters can be linearized, singular-value decomposition provides a powerful tool for analysing the statistical properties of the parameters (see Brown *et al.* 1994; Creevey *et al.* 2007).

The model obtained from the  $\chi^2$  minimization forms the basis for further analysis of the observed data, in the, likely common, case where the computed observables differ significantly from the observations. This can involve further analyses of the observations, for example in terms of additional combinations of the frequencies, to inspire the required changes in the physics of the models and hence the insight that is a central goal of asteroseismology. We recall, as discussed in Section 7.1.6, that with sufficiently good data on just low-degree modes it may in particular become possible to carry out inverse analyses to infer the structure of the cores of solar-like stars.

### 7.2.2.2 Analysis of Stellar Rotation

Information about the internal rotation of solar-like stars would be of obvious interest. This can in principle be obtained from measurement of the rotational splitting of the observed frequencies (see Section 3.8). For relatively slow rotation, as is probably relevant for most solar-like stars, this can be approximated by

$$\omega_{nlm} \simeq \omega_{nl0} + m\beta_{nl}\langle\Omega\rangle_{nl}, \quad (7.83)$$

as a function of the azimuthal order  $m$ , where  $\beta_{nl}$  is close to one for high-order acoustic modes;  $\langle\Omega\rangle_{nl}$  is an average over the stellar interior, weighted by the rotational kernel, examples of which are shown in Fig. 3.39.<sup>31</sup> For low-degree acoustic modes the kernels are quite similar and all extend throughout most of the stellar interior. Thus only limited information is available about the

<sup>30</sup> Note that this is equivalent to the regularized least-squares inversion (see Section 7.1.5, particularly Eq. (7.42)), although without the regularization.

<sup>31</sup> Formally Eq. (7.83) is valid only for rotation that depends only on  $r$ ; see Section 3.8.4 for further details.

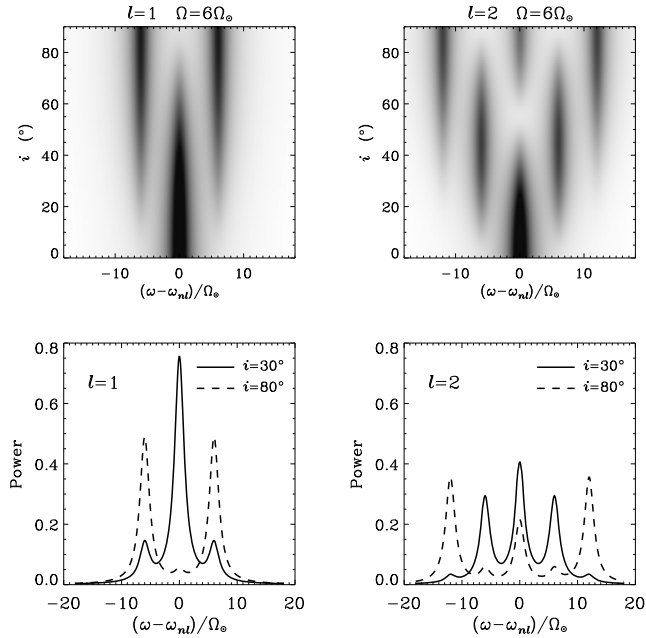


**Fig. 7.50.** Schematic illustration of the observed power spectra for modes of degree  $l = 1$  and  $2$ , assumed to be excited to the same true amplitude, as functions of the inclination angle  $i$  between the rotation axis and the line of sight. The plots assume a line width of  $1\,\mu\text{Hz}$  and an angular velocity of six times the solar value; no background noise was included. From Gizon & Solanki (2003).

variation of rotation with position in the star from such modes. In many cases the available information will probably be restricted to a general measure of the average internal angular velocity; however, if this can be combined with a measurement of the surface rotation rate, for example from observation of photometric variations associated with spots, evidence can be found for variations with position in the angular velocity, including a possible rapidly rotating interior as might be expected from stellar evolution (see Section 3.2.4.2).

More detailed information is available if the observed oscillations include mixed modes, with g-mode character and hence higher sensitivity to rotation in the deep interior (see also Section 7.2.4.3). The potential for inferring the internal rotation in this case was analysed in detail by Lochard *et al.* (2005), based on predicted mode amplitudes and their detectability with the CoRoT mission, in a  $1.5\,M_{\odot}$  model towards the end of central hydrogen burning (see also Section 7.2.4.3 below). They demonstrated that reasonable resolution of the angular velocity could be obtained in the inner  $0.3\,R$  of the star, in par-

ticular detecting the presence in the model of a rapidly rotating core, whereas only an average angular velocity could be obtained in the outer parts of the star.

Such successful analysis of course assumes that the rotational splitting can be measured for a suitable mode set. This involves several challenges and opportunities. The finite width of the stochastically excited modes is a substantial challenge; in the solar case the width is comparable to the rotational splitting, making it difficult to separate the components and introducing possible systematic errors (*e.g.*, Appourchaux *et al.* 2000b; Chaplin *et al.* 2001a). This problem would obviously be less in stars rotating more rapidly than the Sun; on the other hand, it appears that the mode lifetime is shorter in stars more massive than the Sun, which would complicate the analysis (*e.g.*, Chaplin *et al.* 2008b).

A second challenge, which hides an opportunity, is the arbitrary orientation of stellar rotation axes. In the solar case the rotation axis is close to the plane of the sky and hence disc-integrated observations are essentially sensitive only to modes with even  $l - m$ . In the stellar case, the apparent amplitude of a mode depends strongly on the inclination  $i$  of the rotation axis to the line of sight (see Section B.2). This must be kept in mind when identifying the rotationally split components of the multiplet, potentially complicating the analysis of the observations. On the other hand, for stochastically excited oscillations it is expected that the modes are excited to an average amplitude which depends slowly on frequency and is likely independent of  $m$ . Thus the observed average amplitude, as a function of  $m$ , reflects the coefficients  $a_{lm0}(i)$  defining the transformation of the spherical harmonics to the star's system of reference (see Eqs(B.19) and (B.20)). With observations of a sufficient duration to determine the average amplitude, it is therefore possible to infer the inclination of the rotation axis of the star. This was pointed out by Gizon & Solanki (2003); Fig. 7.50 illustrates the observed average power as a function of frequency and inclination, in a star rotating somewhat more rapidly than the Sun. From Monte Carlo simulations Gizon & Solanki concluded that it was possible to determine inclination angles  $i \geq 30^\circ$  from observations extending over six months, assuming solar line widths and an angular velocity  $\Omega$  of at least twice the solar value  $\Omega_\odot$ . In an extension of this analysis Gizon & Solanki (2004) concluded that some information could be obtained about the latitudinal differential rotation from observations of modes with  $l = 1$  and 2, for  $30^\circ < i < 70^\circ$  and  $\Omega \geq 4\Omega_\odot$ . More detailed investigations by Ballot *et al.* (2006, 2008) highlighted the difficulties in the fit, particularly when the rotational splitting is comparable with the mode line width. However, the authors also noted the promise of observations extending over a very long time, such as expected with the Kepler mission (see Chapter 8).

### 7.2.3 The Binary $\alpha$ Centauri A and B

The  $\alpha$  Cen system is a triple system, consisting of the A and B components in a fairly close orbit with a period of 79.9 yr, and the third component, Proxima Centauri, with a mass of around  $0.1 M_{\odot}$ , in a distant orbit. Proxima Centauri is the closest known star to the solar system, at a distance of 1.29 pc. The A and B components have masses that span the solar mass, and the age of the system is somewhat higher than the solar age, although both components are still in the core hydrogen burning phase. Also, as a result of the proximity of the system and the well-observed binary orbit, the overall parameters of the stars are known with unusually high precision. Finally, solar-like oscillations have been observed in both the A and B components. These features make the system an ideal case for asteroseismic investigations, extending the results that have been obtained for the Sun.

#### 7.2.3.1 The Stars

Here we concentrate on the A and B components, of spectral types G2V and K1V, respectively. The parallax of the system has been determined as  $747.1 \pm 1.2$  mas (Söderhjelm 1999), corresponding to a distance of 1.339 pc. From the orbital motion and the parallax the masses of the components were determined by Pourbaix *et al.* (2002) as  $M_A = 1.105 \pm 0.007 M_{\odot}$  and  $M_B = 0.934 \pm 0.006 M_{\odot}$ . Also, from interferometric measurements of the angular diameter, and the parallax, Kervella *et al.* (2003) determined the radii as  $R_A = 1.224 \pm 0.003 R_{\odot}$  and  $R_B = 0.863 \pm 0.005 R_{\odot}$ .

The spectroscopic and photometric properties of the two stars are somewhat uncertain. A recent analysis and review of earlier results was provided by Porto de Mello *et al.* (2008). They obtained  $T_{\text{eff},A} = 5824 \pm 26$  K and  $T_{\text{eff},B} = 5223 \pm 62$  K. From the composition analysis they found metallicities for the two components of  $[\text{Fe}/\text{H}]_A = 0.24 \pm 0.03$  and  $[\text{Fe}/\text{H}]_B = 0.25 \pm 0.04$ . Here the logarithmic abundance ratio, relative to the Sun, for two elements  $\mathcal{A}$  and  $\mathcal{B}$  is defined as

$$[\mathcal{A}/\mathcal{B}] = \log \left[ \frac{N_{\mathcal{A}}/N_{\mathcal{B}}}{N_{\mathcal{A},\odot}/N_{\mathcal{B},\odot}} \right], \quad (7.84)$$

where  $N_{\mathcal{A}}, N_{\mathcal{B}}$  are the abundances of  $\mathcal{A}$  and  $\mathcal{B}$  in the star,  $N_{\mathcal{A},\odot}, N_{\mathcal{B},\odot}$  are the solar abundances, and log is logarithm to base 10. If the relative composition of the heavy elements is the same as in the Sun,  $[\text{Fe}/\text{H}]$  is related to the ratio  $Z_s/X_s$  between the surface abundances by mass of heavy elements and hydrogen, by

$$\frac{Z_s}{X_s} = 10^{[\text{Fe}/\text{H}]} \left( \frac{Z_s}{X_s} \right)_{\odot}. \quad (7.85)$$

In fact, Porto de Mello *et al.* (2008) found that compared with the Sun, Na, Mg, Si, Mn and Ni are somewhat overabundant relative to iron. In stellar

modelling the composition is generally characterized by  $Z_s/X_s$ ; to determine this from Eq. (7.85) the value of  $(Z_s/X_s)_\odot$  must be known but, as discussed in Section 7.1.7, there has been some debate about this value. We return to this point in Section 7.2.3.4 below. Earlier values of the effective temperature and [Fe/H] from Neuforge-Verheecke & Magain (1997) have seen extensive use in modelling of the stars; these results are essentially consistent with the results of Porto de Mello *et al.* (2008).

The luminosity can be obtained from the apparent magnitude, the parallax, and the bolometric correction required to relate the observed magnitude to the total energy output of the stars. In this way Pijpers (2003) obtained  $L_A = 1.556 \pm 0.011 L_\odot$  and  $L_B = 0.504 \pm 0.008 L_\odot$ , whereas Eggenberger *et al.* (2004) found  $L_A = 1.522 \pm 0.030 L_\odot$  and  $L_B = 0.503 \pm 0.020 L_\odot$ . Alternatively, the luminosity can be obtained from the effective temperature and radius; using the values quoted above we obtain  $L_A = 1.547 \pm 0.029 L_\odot$  and  $L_B = 0.497 \pm 0.024 L_\odot$ , which are consistent with the photometric values.

Saar & Osten (1997) determined the rotational broadening of the lines of  $\alpha$  Cen A as  $v_\Omega \sin i = 2.7 \pm 0.7 \text{ km s}^{-1}$ ; for the B component the broadening was barely significant. Assuming that the rotation axis is orthogonal to the orbital plane, whose orientation has been accurately determined (*e.g.*, Pourbaix *et al.* 1999),  $i = 79.23^\circ$ ; using also the measured radius we obtain a rotation period  $P_{\text{rot},A} = 22.5 \pm 5.8 \text{ d}$  (Bazot *et al.* 2007).

Both components have been observed in X rays (see Ayres *et al.* 2008), probably from hot coronae; the X-ray luminosity shows variations which might be associated with stellar cycles, with possible asteroseismic signatures (Metcalfe *et al.* 2007). Boccino & Mauas (2008) found possible evidence for a stellar cycle in  $\alpha$  Cen B, from observations of Mg II h+k emission; this also showed shorter-term variations, with a period of 35.1 d, which may reflect the rotation period of the star.

### 7.2.3.2 The Data

The  $\alpha$  Cen system was an obviously attractive target for early attempts at the detection of solar-like oscillations in other stars. These early observations all concentrated on  $\alpha$  Cen A as the brighter component. Gelly *et al.* (1986) used an instrument based on sodium resonance scattering (see Section 7.1.1.3) on the ESO 3.6-m telescope and claimed detection of p modes with a large separation  $\Delta\nu$  of  $165.5 \mu\text{Hz}$ . This has not been confirmed by later observations, however. Pottasch *et al.* (1992) used a Fabry-Perot-based velocity monitor on the ESO 3.6-m telescope; they detected an apparent signal from p-mode oscillations, with  $\Delta\nu = 110 \pm 8 \mu\text{Hz}$ , and identified several possible oscillation frequencies. Edmonds & Cram (1995) used the UCLES<sup>32</sup> spectrograph on the Anglo-Australian Telescope (AAT) and detected a possible signal corresponding to  $\delta\nu = 106\text{--}110 \mu\text{Hz}$ , although with no definite identification

---

<sup>32</sup> University College London Echelle Spectrograph.

of oscillations. Kjeldsen *et al.* (1999) made two-site observations, using the ESO 3.6-m telescope and the AAT to measure the equivalent width of H $\alpha$ . They also found some indications of p-mode oscillations with two possible identifications of modes, leading to  $\Delta\nu = 107.0$  or  $100.8\,\mu\text{Hz}$ , and presented a frequencies of a few modes. Schou & Buzasi (2001) analysed 50 d of photometric data from the WIRE satellite, determining a large separation of around  $106\,\mu\text{Hz}$ , but with no definite identification of individual frequencies. In none of these cases, however, was the evidence for detection of the oscillations in  $\alpha$  Cen A compelling; in particular, there was no clear enhancement of power in the region where the solar-like oscillations were expected.

Thus the observations of  $\alpha$  Cen A by Bouchy & Carrier (2001, 2002) were a major break-through for the study of the  $\alpha$  Cen system and indeed for asteroseismology of solar-like stars. They used the CORALIE fibre-fed spectrograph on the 1.2-m Swiss Euler telescope at La Silla. Their data, obtained over 13 nights of observing, showed unambiguous evidence for solar-like oscillations. Bouchy & Carrier (2002) determined the large separation as  $\Delta\nu = 105.5 \pm 0.1\,\mu\text{Hz}$  and an average small separation  $\langle\delta\nu_{n0}\rangle = 5.6 \pm 0.7\,\mu\text{Hz}$ . They also presented frequencies of 28 modes, with amplitudes between 12 and  $44\,\text{cm s}^{-1}$  and an estimated standard error in the frequencies of  $0.46\,\mu\text{Hz}$ . It is interesting that the earlier determinations of a possible large separation, except for the results of Gelly *et al.* (1986),<sup>33</sup> are consistent with the value obtained by Bouchy & Carrier (2002).

Carrier & Bourban (2003) observed  $\alpha$  Cen B for thirteen nights with the CORALIE spectrograph. The data suffered to some extent from the rather slow 80-s cadence of the observations and the correspondingly low Nyquist frequency, but the power spectrum clearly showed the power in the p-mode region. Analysis of the spectra resulted in  $\Delta\nu = 161.1 \pm 0.1\,\mu\text{Hz}$ ,  $\langle\delta\nu_{n0}\rangle = 8.7 \pm 0.8\,\mu\text{Hz}$  and the identification of twelve modes, although the frequencies may have suffered from one-day aliases resulting from the single-site observations.

Very precise measurements of the oscillations of  $\alpha$  Cen A were obtained by Butler *et al.* (2004), from two-site observations using the UVES spectrograph on the ESO VLT and the UCLES spectrograph on the AAT; out of four allocated nights on the VLT, three produced useful data, while data were obtained from five of the six nights allocated on the AAT. The observations used iodine cells as spectrographic references (see Section 4.4.1); this yielded a noise level in the combined spectrum of  $2.0\,\text{cm s}^{-1}$  at high frequency, which at the time were the most precise velocity measurements in any star apart from the Sun. The short segment of the UVES observations shown in Fig. 7.51 clearly illustrates the low noise of the individual measurements and the presence of oscillations, with beating caused by the interference of the large number of modes involved.

---

<sup>33</sup> Although possibly not significant, it is curious that the value of large separation inferred by Gelly *et al.* (1986) is close to  $3\Delta\nu/2$  and might have arisen from mis-interpreting the separation of  $\Delta\nu/2$  between modes of even and odd degree.

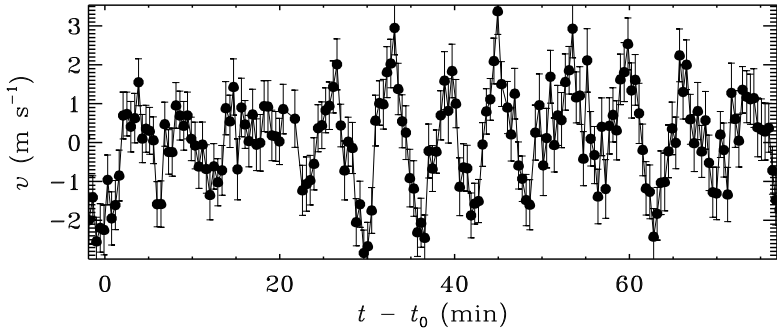


**Fig. 7.51.** A short typical stretch of Doppler-velocity observations of  $\alpha$  Cen A, with the UVES spectrograph on the VLT (Butler *et al.* 2004); the error bars show  $1-\sigma$  velocity errors on each measurement, which were taken at a typical cadence of 30 s. Data courtesy of H. Kjeldsen.

Bedding *et al.* (2004) made a careful analysis of these data. As discussed in Section 7.2.1 optimized weights were given to the individual data to optimize the sidelobes while maintaining a good signal-to-noise ratio. The result is shown in Fig. 7.52, which also illustrates the window function (see Section 5.3.3). The highest sidelobes are reduced to only 3.6% in power of the main peak, although with an increase in the noise level at high frequency from  $2.0$  to  $2.9 \text{ cm s}^{-1}$ . We discuss the detailed analysis of this spectrum in Section 7.2.3.2 below.

Similar observations, with four nights using UVES on VLT and six nights using UCLES on AAT, were made by Kjeldsen *et al.* (2005) for  $\alpha$  Cen B. The resulting power spectrum is also shown in Fig. 7.52. The fast cadence, particularly in the UVES observations, allows the spectrum to include the full region of significant power. In a noise-optimized spectrum based on these data, the noise level at high frequency is a remarkable  $1.4 \text{ cm s}^{-1}$ . The figure shows a sidelobe optimized spectrum, with sidelobes of at most 13% of the peak and a high-frequency noise level of  $2.4 \text{ cm s}^{-1}$ . As argued by Kjeldsen *et al.* (2005) this higher noise level, with the improved window function, is still preferable for the seismic analysis discussed below.

Additional high-quality data were obtained for  $\alpha$  Cen A by Bazot *et al.* (2007), in five nights' observations with the HARPS<sup>34</sup> spectrograph on ESO's 3.6-m telescope. Also, Fletcher *et al.* (2006), following Schou & Buzasi (2001), analysed 50 d of data on the A component from the WIRE satellite. Based on the frequencies known from previous observations they applied autocovariance

<sup>34</sup> High Accuracy Radial Velocity Planet Searcher.

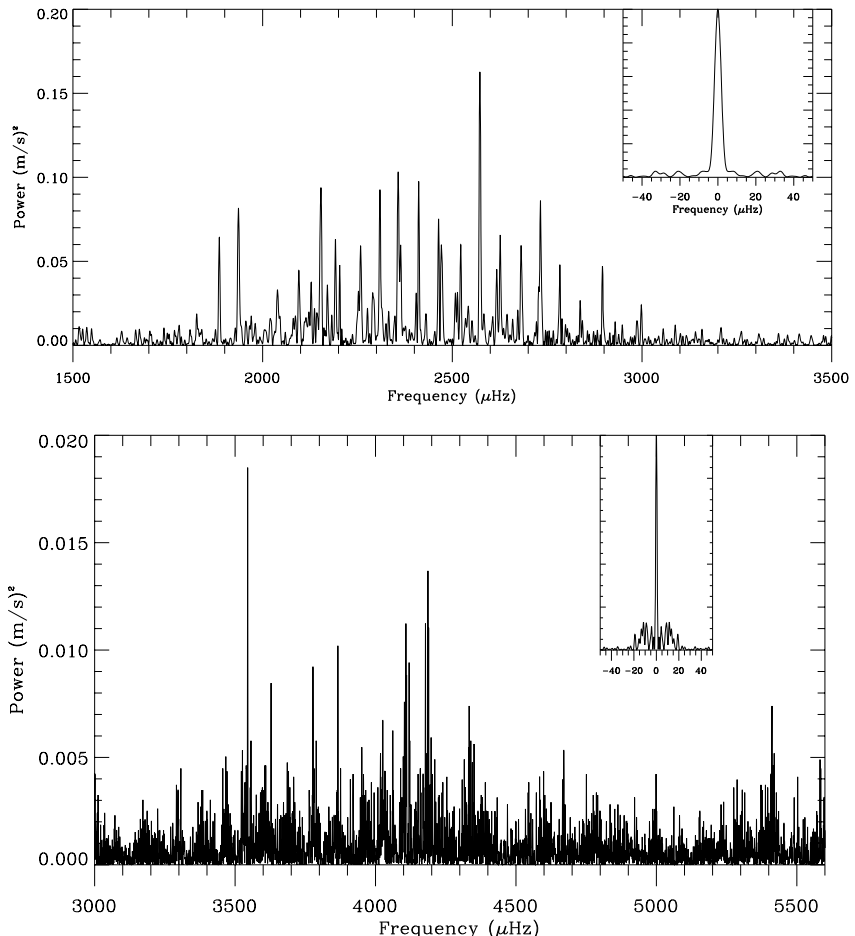


**Fig. 7.52.** Power spectra of observations of  $\alpha$  Cen A (top; Bedding *et al.* 2004) and  $\alpha$  Cen B (bottom; Kjeldsen *et al.* 2005), obtained from two-site observations at the VLT and the AAT. The data combination used weights aimed at suppressing the daily sidelobes in the window functions, which are shown in insets on an expanded frequency scale. Adapted from Bedding *et al.* (2004) and Kjeldsen *et al.* (2005).

fitting. The long time series allowed the direct fitting of the Lorentz profile (see Section 7.1.2) and hence a determination of the mode lifetime; also, they were able to measure the rotational splitting. We discuss these results in the following section.

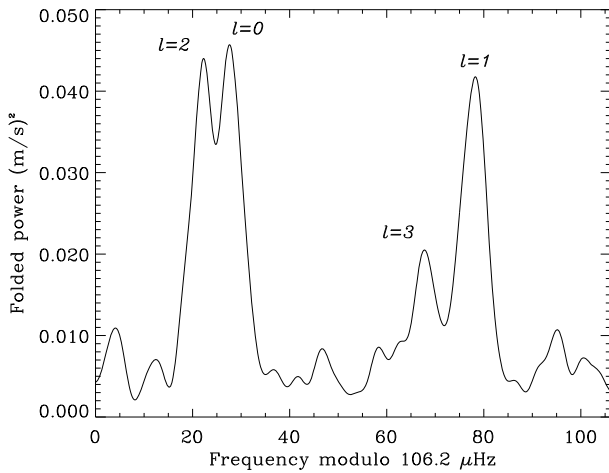


**Fig. 7.53.** Power spectrum of  $\alpha$  Cen A folded and superposed with a large separation of  $106.2 \mu\text{Hz}$ ; the peaks corresponding to  $l = 0-3$  are indicated. From Bedding *et al.* (2004).

### 7.2.3.3 Mode Identification

To illustrate aspects of the mode identification and frequency analysis we consider the analysis of the data on  $\alpha$  Cen A and B by Bedding *et al.* (2004) and Kjeldsen *et al.* (2005), respectively.

A first indication of the modes present in the data can be obtained by folding the spectrum at the average large separation which was determined as  $\Delta\nu = 106.2 \mu\text{Hz}$ ; this technique was applied to early disc-integrated helioseismic data by Grec *et al.* (1980). The result for  $\alpha$  Cen A in Fig. 7.53 clearly shows the presence in the spectrum of modes of degree  $l = 0-3$ , with approximately the expected frequency structure. Also, as expected, the average amplitude of the  $l = 3$  modes is substantially smaller than for the other modes (see also Fig. 7.1). A more detailed impression of the structure of the spectrum can be obtained by plotting the power on a grey scale, in terms of reduced frequency and frequency in an échelle format, as done in Fig. 7.54. The presence of four ridges, corresponding to the four values of  $l$ , is fairly obvious; also visible is the curvature of the ridges, corresponding to a variation of the large frequency separation with frequency, and the decrease in the small separation  $\delta\nu_{n0}$  with increasing frequency.

As discussed in Section 7.2.1 the frequencies were determined with a variant of the prewhitening technique, using sine-wave fitting successively to determine and eliminate the largest-amplitude contributions. The result is illustrated in the échelle diagram in Fig. 7.54. In some cases the procedure found two closely spaced peaks which most likely resulted from the stochastic ex-

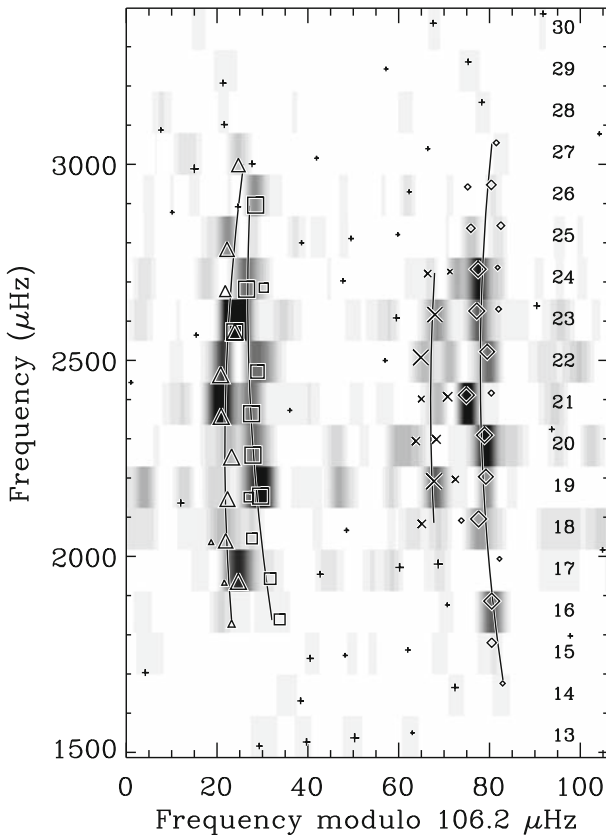


**Fig. 7.54.** The grey scale shows the observed power spectrum of  $\alpha$  Cen A in échelle format. Peaks extracted with the successive prewhitening analysis are indicated by squares ( $l = 0$ ), diamonds ( $l = 1$ ), triangles ( $l = 2$ ) and crosses ( $l = 3$ ); the plus signs indicate additional peaks whose degree could not be identified. The amplitudes of the peaks are reflected in the sizes of the symbols. The curves show fits to the frequencies (cf. Eq. (7.86)); the numbers at the right side indicate the radial orders. Adapted from Bedding *et al.* (2004).

citation of a single mode. In this case Bedding *et al.* (2004) determined the “true” frequency as a weighted mean of the two frequencies. Evidently, the analysis procedure is still far from being fully automated.

Bedding *et al.* (2004) presented detailed tables of frequencies that will not be reproduced here. However, the authors noted that the results could be

represented by polynomial fits for each  $l$  (see also Ulrich 1986), as<sup>35</sup>

$$\begin{aligned}\nu_{n0} &\simeq 2364.09 + 105.71 \tilde{n} + 0.082 \tilde{n}^2 \mu\text{Hz}, \\ \nu_{n1} &\simeq 2414.15 + 106.04 \tilde{n} + 0.082 \tilde{n}^2 \mu\text{Hz}, \\ \nu_{n2} &\simeq 2464.33 + 106.35 \tilde{n} + 0.082 \tilde{n}^2 \mu\text{Hz}, \\ \nu_{n3} &\simeq 2509.75 + 106.61 \tilde{n} + 0.082 \tilde{n}^2 \mu\text{Hz},\end{aligned}\quad (7.86)$$

where  $\tilde{n} = n - 21$ . Since the fits average over the frequency scatter resulting from the excitation they may provide a better basis for comparing with stellar models. However, they should obviously not be used to extrapolate the observed frequencies beyond the actual ranges of the observations. Bedding *et al.* (2004) also determined the average small separations

$$\begin{aligned}\langle \delta\nu_{n0} \rangle &= 5.46 \pm 0.76 \mu\text{Hz}, \quad \langle \delta\nu_{n1} \rangle = 10.99 \pm 0.77 \mu\text{Hz}, \\ \langle \delta^{(1)}\nu_{n0} \rangle &= 2.41 \pm 0.71 \mu\text{Hz}.\end{aligned}\quad (7.87)$$

A similar analysis of observations of  $\alpha$  Cen B was made by Kjeldsen *et al.* (2005). Again, the power spectrum clearly showed modes of degree  $l = 0-3$  and the frequencies of a total of 37 modes were determined. The average large separation was determined as  $\Delta\nu = 161.38 \pm 0.06 \mu\text{Hz}$  and the average small separations were

$$\begin{aligned}\langle \delta\nu_{n0} \rangle &= 10.14 \pm 0.62 \mu\text{Hz}, \quad \langle \delta\nu_{n1} \rangle = 16.73 \pm 0.65 \mu\text{Hz}, \\ \langle \delta^{(1)}\nu_{n0} \rangle &= 4.52 \pm 0.51 \mu\text{Hz}.\end{aligned}\quad (7.88)$$

As for  $\alpha$  Cen A it is convenient to represent the individual frequencies by power-law fits, as

$$\begin{aligned}\nu_{n0} &\simeq 3950.57 + 161.45 \tilde{n} + 0.101 \tilde{n}^2 \mu\text{Hz}, \\ \nu_{n1} &\simeq 4026.23 + 161.28 \tilde{n} + 0.101 \tilde{n}^2 \mu\text{Hz}, \\ \nu_{n2} &\simeq 4101.41 + 161.63 \tilde{n} + 0.101 \tilde{n}^2 \mu\text{Hz}, \\ \nu_{n3} &\simeq 4171.13 + 161.76 \tilde{n} + 0.101 \tilde{n}^2 \mu\text{Hz}.\end{aligned}\quad (7.89)$$

where now  $\tilde{n} = n - 23$ .

Kjeldsen *et al.* (2005) also determined the lifetimes of the modes in  $\alpha$  Cen A and B from analysis of the scatter of the frequencies around a smooth curve. The analysis of  $\alpha$  Cen B was calibrated on the basis of artificial data corresponding to the observations, at varying mode lifetimes and noise level. Also, the authors confirmed that application of the calibration to corresponding segments of GOLF solar data yielded lifetimes consistent with those determined from the width of Lorentzian profiles (*cf.* Section 7.1.3.1). For  $\alpha$  Cen B

<sup>35</sup> These expressions were obtained in a one-step fitting procedure, as described by Kjeldsen *et al.* (2005), and hence differ slightly from the expressions presented by Bedding *et al.* (2004).

the lifetime was determined as  $3.3^{+1.8}_{-0.9}$  d at a frequency of 3.6 mHz, whereas a similar analysis based on the  $\alpha$  Cen A observational window yielded a lifetime of modes of that star of  $2.3^{+1.0}_{-0.6}$  d at 2.1 mHz. For both stars there was a tendency towards decreasing lifetime with increasing frequency, as also observed in the solar case (see Fig. 7.7).

This analysis was repeated by Bazot *et al.* (2007), on HARPS observations of  $\alpha$  Cen A. They found that the frequency scatter increased with the degree of the modes and noted that this could be the result of rotation, with random excitation of the individual components of the multiplets. Thus the lifetime estimate obtained from the frequency scatter, averaging over all degrees, must be a lower limit to the true lifetime. The data available to Bazot *et al.* (2007) were not sufficiently extensive to allow the determination of the rotation rate or corrected lifetimes. However, the fits by Fletcher *et al.* (2006) of Lorentzian profiles to the 50 d of WIRE data yielded an average lifetime of  $3.9 \pm 1.4$  d for  $\alpha$  Cen A. Although formally consistent with the results of Kjeldsen *et al.* (2005), the somewhat longer inferred lifetime may reflect the effect of rotation on the frequency-scatter analysis of Kjeldsen *et al.* Also, the fits by Fletcher *et al.* (2006) indicated a rotational splitting of  $0.54 \pm 0.22$   $\mu$ Hz, which is consistent with the rotation period of  $22 \pm 6$  d inferred from the rotational broadening of spectral lines (see Section 7.2.3.1).

#### 7.2.3.4 Seismic Modelling

The components of a binary such as  $\alpha$  Cen A and B must be assumed to be formed at the same time and out of the same interstellar cloud. Thus models of the system assume that the two stars have the same initial abundances  $Y_i$  and  $Z_i$  by mass of helium and heavy elements, and the same age  $\tau_*$ . As discussed in Section 3.2.1.3, the models are also characterized by the mixing-length parameter  $\alpha_{\text{ML}}$  (or an equivalent parameter in other treatments of convection). Since this parameter reflects the detailed physical processes in the upper parts of the convection zone, there is no reason to expect it to be the same for the two components. However, in the same way as the solar value of  $\alpha_{\text{ML}}$  is often used for stellar modelling for the lack of a better alternative, early modelling of  $\alpha$  Cen A and B often assumed that they shared the same  $\alpha_{\text{ML}}$ , occasionally taken to be the solar value. An interesting aspect of the asteroseismic data is the possibility of relaxing this assumption, hence potentially getting precise observational information about the properties of stellar surface convection.

The results of the modelling of the system obviously also depend on the details of the physics of the calculation, such as the equation of state, opacity tables and nuclear parameters, as well as on whether or not diffusion and settling have been included.

In addition, there is some variation in the assumed “classical” observables. Thus there are significant variations in the resulting models, at least when asteroseismic constraints are not included.

Perhaps the first detailed modelling of the system was made by Flannery & Ayres (1976). From requiring that the models reached the observed luminosities at the same age they concluded, in agreement with the existing spectroscopic data, that the system was somewhat more metal-rich than the Sun; they obtained an age of around 6 Gyr. A similar conclusion was reached by Demarque *et al.* (1986) who investigated the sensitivity of the modelling to the uncertainties in the assumed parameters, including the mass. This was probably also the first investigation considering asteroseismic aspects, noting that the large separation of  $165.5 \mu\text{Hz}$  for  $\alpha$  Cen A claimed by Gelly *et al.* (1986) was inconsistent with the models.<sup>36</sup> A detailed investigation of the sensitivity of the models to the parameters of the calculation was made by Edmonds *et al.* (1992), who also allowed different values of  $\alpha_{\text{ML}}$  for the two components. In addition, they considered the effects of helium diffusion and settling, which for  $\alpha$  Cen A was found to have some effect on the inferred  $\alpha_{\text{ML}}$ , bringing it closer to the solar value. The inferred age of the system was  $4.6 \pm 0.4$  Gyr. Anticipating asteroseismic observations they presented detailed frequency results for the two components. Noels *et al.* (1991) used the observed luminosities and effective temperatures to determine  $Y_i$ ,  $Z_i$ ,  $\alpha_{\text{ML}}$  (assumed to be the same for the two components) and the age of the system. They again obtained a metal-rich composition, and the age was found to be 5–6 Gyr. Lydon *et al.* (1993) concentrated on the treatment of near-surface convection in the modelling. They compared a description based on numerical simulation of convection (Lydon *et al.* 1992) with the mixing-length treatment, in fitting the observed radii and luminosities of the stars; based on matching to these more sophisticated models they concluded that within the observational and theoretical errors the same value of  $\alpha_{\text{ML}}$  can be assumed for the Sun and  $\alpha$  Cen A and B. They also noted that the model of the A component may develop a convective core during its evolution, at sufficiently high heavy-element abundance. The inferred age of the system was around 5 Gyr. The effects of the convection treatment were also discussed by Fernandes & Neuforge (1995).

Very extensive modelling of the system was carried out by Guenther & Demarque (2000). They included diffusion and settling of helium and heavy elements, and allowed different values of  $\alpha_{\text{ML}}$  for the two components. As did Lydon *et al.* (1993) they noted the importance of the possible convective core in  $\alpha$  Cen A, including the effect on the inferred age. Their best model did include a convective core and had an age of 7.6 Gyr. They also made extensive calculations of oscillation frequencies for the two components, to investigate the potential for asteroseismic analyses. Interestingly, they noticed that their best model of the A component was sufficiently evolved to show mixed modes at frequencies below  $900 \mu\text{Hz}$  and thus the potential to obtain stronger constraints on the core of the star if such modes could be observed. Guenther & Demarque (2000) also made a detailed investigation of the sensi-

---

<sup>36</sup> This is in fact rather obvious, given the scaling of  $\Delta\nu$  as  $t_{\text{dyn}}^{-1}$  and the observational constraints on the star.

tivity of the results to the uncertainties in the global observed parameters of the system. A detailed analysis of the  $\alpha$  Cen system was also carried out by Morel *et al.* (2000). They characterized the models by the set of parameters  $\{\tau_*, Y_i, [\text{Fe}/\text{H}]_i, \alpha_{\text{ML,A}}, \alpha_{\text{ML,B}}\}$ , where  $[\text{Fe}/\text{H}]_i$  is the initial metallicity, in terms of the logarithmic ratio (*cf.* Eq. (7.84)) and assuming that  $(Z_s/X_s)_\odot = 0.0245$ . They carried out a  $\chi^2$  fit (*cf.* Eq. (7.82)) of these models to a set of observed quantities, defined as the effective temperatures, surface gravities and surface metallicities  $[\text{Fe}/\text{H}]_s$  of the two components, keeping the masses fixed, although considering two different pairs of masses, one from Pourbaix *et al.* (1999) and one that matched the models of Guenther & Demarque (2000). All models of  $\alpha$  Cen A were found to have a convective core; Morel *et al.* (2000) considered models both without and with convective core overshoot (of 0.2 pressure scale heights). Near-surface convection was treated both using the Böhm-Vitense (1958) and the Canuto & Mazzitelli (1992) treatments. The results of the fits showed a remarkable spread in the inferred age, ranging from 2.7 to 4.1 Gyr when using the Pourbaix *et al.* (1999) masses, while the age obtained using the same masses as Guenther & Demarque (2000) was 5.6 Gyr. Morel *et al.* (2000) also made an extensive analysis of the asteroseismic potential of frequency observations of the  $\alpha$  Cen system, noting the sensitivity of the second differences to the envelope helium abundance and depth of the convection zone (see Section 7.2.2.1).

With the availability of the observed frequencies for  $\alpha$  Cen A from Bouchy & Carrier (2001, 2002) a proper asteroseismic investigation of the  $\alpha$  Cen system could start. The fits to the observations have generally been made in terms of the large and small frequency separations, rather than to the individual frequencies. The argument for this is that the near-surface effects (see Section 7.1.4.1) give rise to an unknown shift between the observed and modelled frequencies, even for a model that otherwise matches the structure of the star; such a shift is often represented as a constant offset between the observed and the model frequencies, *e.g.*, when presenting the results in an échelle diagram. It should be noted, however, that this procedure ignores the strong frequency dependence of the near-surface perturbation to the frequencies, at least as seen in the Sun (*cf.* Fig. 7.24) and hence expected in solar-like stars; in particular, the perturbation also has a significant effect on the large frequency separation.

Thévenin *et al.* (2002) made a first comparison between observed frequencies determined by Bouchy & Carrier (2001) and stellar models. The modelling was an extension of the work of Morel *et al.* (2000), in this case using the Canuto & Mazzitelli (1992) convection formulation, assuming the same convective parameter for the A and B components. Thévenin *et al.* found that to obtain a good match to the observed oscillation parameters, characterized by the large and small separations, the masses should be considered as parameters constrained within the error bars of the astrometric analysis, rather than as fixed quantities. In this way they obtained models that satisfied the observational constraints, and an age of the system of  $4.85 \pm 0.50$  Gyr; the model of

	$\alpha$ Cen A		
	Eggenberger <i>et al.</i>	Miglio & Montalbán	Teixeira <i>et al.</i>
$M/M_{\odot}$	1.105	$1.105 \pm 0.007$	$1.105 \pm 0.007$
$L/L_{\odot}$	$1.522 \pm 0.030$	$1.522 \pm 0.030$	$1.556 \pm 0.011$
$T_{\text{eff}} (\text{K})$	$5810 \pm 50$	$5810 \pm 50$	$5830 \pm 30$
$R/R_{\odot}$	$1.224 \pm 0.003$	$1.224 \pm 0.003$	$1.224 \pm 0.003$
$(Z/X)_s$	$0.038 \pm 0.004$	$0.039 \pm 0.006$	$0.037 \pm 0.004$
$\bar{\nu}_{21,0} (\mu\text{Hz})$			$2364.27 \pm 0.28$
$\Delta\nu_0 (\mu\text{Hz})$	$105.5 \pm 0.1$	$105.60 \pm 0.65$	$105.78 \pm 0.10$
$\delta_{02} (\mu\text{Hz})$	$5.6 \pm 0.7$	$6.04 \pm 0.65$	$6.24 \pm 0.63$
$\delta_{13} (\mu\text{Hz})$			$10.53 \pm 0.75$
	$\alpha$ Cen B		
	Eggenberger <i>et al.</i>	Miglio & Montalbán	Teixeira <i>et al.</i>
$M/M_{\odot}$	0.934	$0.934 \pm 0.006$	$0.934 \pm 0.006$
$L/L_{\odot}$	$0.503 \pm 0.020$	$0.503 \pm 0.020$	$0.504 \pm 0.008$
$T_{\text{eff}} (\text{K})$	$5260 \pm 50$	$5260 \pm 50$	$5255 \pm 50$
$R/R_{\odot}$	$0.863 \pm 0.005$	$0.863 \pm 0.005$	$0.863 \pm 0.005$
$(Z/X)_s$	$0.040 \pm 0.005$	$0.039 \pm 0.006$	$0.037 \pm 0.004$
$\bar{\nu}_{21,0} (\mu\text{Hz})$			$3627.80 \pm 0.28$
$\Delta\nu_0 (\mu\text{Hz})$	$161.1 \pm 0.1$	$161.20 \pm 0.65$	$160.73 \pm 0.10$
$\delta_{02} (\mu\text{Hz})$	$8.7 \pm 0.8$	$8.50 \pm 0.65$	$9.99 \pm 0.97$
$\delta_{13} (\mu\text{Hz})$			$19.94 \pm 1.15$

**Table 7.1.** Observational constraints on the  $\alpha$  Cen system used in the modelling by Eggenberger *et al.* (2004), Miglio & Montalbán (2005) and Teixeira *et al.* (in preparation). The values of  $\Delta\nu_0$ ,  $\delta_{02}$  and  $\delta_{13}$  are suitable averages of the large separation and the small separations  $\delta\nu_{n0}$  and  $\delta\nu_{n1}$ , respectively. See text for details.

$\alpha$  Cen A had a small convective core. However, the individual frequencies were around  $30 \mu\text{Hz}$  higher than the observed values. Thoul *et al.* (2003) modelled the system without including diffusion and settling, fixing the masses at the values of Pourbaix *et al.* (2002). They obtained a model, at an age of 6.4 Gyr, which fitted the observational constraints; interestingly, they also found a reasonable fit between the computed and observed frequencies, with a maximum difference, around  $10 \mu\text{Hz}$ , which is similar to the differences seen in the solar case and of the same sign.

Extensive modelling of the  $\alpha$  Cen system was carried out by Eggenberger *et al.* (2004) and Miglio & Montalbán (2005), based on the observations of Bouchy & Carrier (2002) and Carrier & Bourban (2003). The (slightly different) observational constraints applied in the modelling are summarized in

Table 7.1.<sup>37</sup> The oscillation data were generally represented by frequency separations or, in some of the calculations by Miglio & Montalbán, by a ratio between the small and large separation, in the manner of Roxburgh & Vorontsov (2003) (see Section 7.2.2.1). Only modes of degree  $l = 0–2$  were included. Eggenberger *et al.* (2004) kept the masses, as determined by Pourbaix *et al.* (2002), fixed in the fit. Their models included diffusion and settling of helium and heavy elements and treated convection using the mixing-length formalism. They characterized the present surface compositions by  $[Fe/H] = 0.22 \pm 0.05$  and  $0.24 \pm 0.05$  for  $\alpha$  Cen A and B, respectively, and converted this to  $(Z/X)_s$  assuming  $(Z/X)_{s,\odot} = 0.0230$  (Grevesse & Sauval 1998). Based on a model grid the agreement between the model and the observations were characterized by a departure  $\chi^2_{\text{tot}}$  (see Eq. (7.82)) involving non-seismic observables as well as the average large and small separations. Once a preliminary solution had been obtained by minimizing  $\chi^2_{\text{tot}}$  a refined grid was computed and the final model was obtained by minimizing in addition  $\chi^2_{\text{astro}}$ , obtained from the difference between the observed and computed frequencies but subtracting a mean difference, to correct for near-surface effects. The initial application of the procedure to the observations in Table 7.1 yielded a model with a substantial discrepancy from the frequency observations. To improve the overall agreement, Eggenberger *et al.* redid the analysis increasing by a factor of two the assumed standard error of the radii for both components. The resulting models were essentially consistent with these revised observational constraints. Some properties of the solution are given in Table 7.2. The resulting frequencies were compared with the observations in échelle diagrams. These show excellent agreement between models and observations, but only if the computed frequencies were increased by  $19 \mu\text{Hz}$  for  $\alpha$  Cen A and decreased by  $0.7 \mu\text{Hz}$  for  $\alpha$  Cen B.

Miglio & Montalbán (2005) in most cases chose the same observables as did Eggenberger *et al.* (2004), although they preferred the composition given by Thoul *et al.* (2003). Also, unlike Eggenberger *et al.* they did not fix the masses but instead regarded them both as observables, as given by Pourbaix *et al.* (2002) with the associated standard error, and as parameters in the calculation. In addition to the “classical” observables they included as asteroseismic data either the average large and small separations or the ratio  $r_{no}$  (*cf.* Eq. (7.79)) which is insensitive to the near-surface problems in the model. The models in most cases included diffusion and settling of helium and heavy elements. The fit was carried out through  $\chi^2$  minimization, using the Levenberg-Marquardt method (see Bevington & Robinson 1992); this is a gradient-expansion technique which in particular guarantees rapid convergence close to the optimal solution. Thus it is far more efficient than techniques based on extensive grids, although with the risk of finding a local minimum of  $\chi^2$  that does not correspond to the true optimal solution. Miglio & Mon-

---

<sup>37</sup> We are grateful to A. Miglio for providing the frequency data used by Miglio & Montalbán (2005), shown in the table.

	Eggenberger <i>et al.</i>		Miglio & Montalbán		Teixeira <i>et al.</i>	
	A	B	A	B	A	B
$M/M_{\odot}$	1.105	0.934	1.104	0.926	1.111	0.928
$Y_i$	0.275	0.275	0.282	0.282	0.261	0.261
$(Z/X)_i$	0.0434	0.0434	0.0476	0.0476	0.0404	0.0404
$\alpha_{ML}$	1.83	1.97	1.96	2.11	2.222	2.142
Age (Gyr)	6.52	6.52	6.4	6.4	6.98	6.98
$L/L_{\odot}$	1.497	0.522	1.509	0.520	1.552	0.505
$T_{\text{eff}}$ (K)	5769	5270	5782	5259	5823	5228
$R/R_{\odot}$	1.227	0.868	1.226	0.870	1.226	0.868
$(Z/X)_s$	0.0386	0.0402	0.039	0.042	0.0342	0.0361
$\nu_{21,0}$ ( $\mu\text{Hz}$ )					2364.37	3627.84
$\Delta\nu_0$ ( $\mu\text{Hz}$ )	105.9	161.7	106.6	161.0	105.6	160.5
$\langle\delta\nu_{n0}\rangle$ ( $\mu\text{Hz}$ )	4.6	10.3	5.35	9.72	4.83	9.83
$\langle\delta\nu_{n1}\rangle$ ( $\mu\text{Hz}$ )					8.09	17.02

**Table 7.2.** Results of modelling of the  $\alpha$  Cen system by Eggenberger *et al.* (2004), Miglio & Montalbán (2005) and Teixeira *et al.* (in preparation). For Eggenberger *et al.* the case M2 is shown, where the standard errors on  $R/R_{\odot}$  were increased by a factor two. The results for Miglio & Montalbán are for their case (A2, B2), allowing variations in the masses and different  $\alpha_{ML}$  for the two stars, and representing the oscillation data by average large and small separations.

talbán considered a large number of combinations of observables, parameters and model physics; an example of their solutions is included in Table 7.2. For this model the computed frequencies agree with the observed values to within around  $10 \mu\text{Hz}$ . The inferred parameters are clearly fairly similar to those obtained by Eggenberger *et al.* (2004); as in that case the mixing-length parameter is slightly higher for  $\alpha$  Cen B than for  $\alpha$  Cen A.<sup>38</sup> Unlike the analysis by Morel *et al.* (2000) the inferred age was largely insensitive to the choice of convection treatment. Miglio & Montalbán made a detailed investigation of the effects of various modifications to the physics. In general, comparable fits although with somewhat different parameters were obtained in models without diffusion and settling, or with a different equation of state. Thus the present observational data are not sufficient to test these aspects of the physics. However, it was noted that the observed small separation  $\delta_{n0}^{(1)}$  (cf. Eq. (7.68)) favoured models without a convective core.

As a final example of a detailed fitting of the data on the  $\alpha$  Cen A system we consider the so far unpublished analysis by Teixeira *et al.* (in prepara-

<sup>38</sup> The difference in the *values* of  $\alpha_{ML}$  might reflect differences in other parameters characterizing the convection treatment.

tion).<sup>39</sup> Unlike the previous two analyses, they used the observed oscillation frequencies from Bedding *et al.* (2004) and Kjeldsen *et al.* (2005), for the A and B components, respectively. As discussed in Section 7.2.3.2 these included modes of degree  $l = 0–3$ , and the data on  $\alpha$  Cen B obtained by Kjeldsen *et al.* (2005) were also in other respects rather more extensive than those of Carrier & Bourban (2003). For the comparison with the models the frequencies were represented by fits such as those provided in Eqs (7.86) and (7.89);<sup>40</sup> oscillation quantities for the models were obtained through similar fits to precisely the mode set included in the observations, to ensure full consistency. The fitted parameters were given by

$$\bar{\nu}_{21,0} , \quad \Delta\nu_0 = \frac{1}{2}(\bar{\nu}_{22,0} - \bar{\nu}_{20,0}) , \quad \bar{r}_{21,0} = 2\frac{\bar{\nu}_{21,0} - \bar{\nu}_{20,2}}{\bar{\nu}_{22,0} - \bar{\nu}_{20,0}} , \\ \bar{r}_{21,1} = 2\frac{\bar{\nu}_{21,1} - \bar{\nu}_{20,3}}{\bar{\nu}_{22,1} - \bar{\nu}_{20,1}} , \quad (7.90)$$

where  $\bar{\nu}_{nl}$  is the frequency resulting from the fit. Masses were obtained from Pourbaix *et al.* (2002) and were regarded as observables, as did Miglio & Montalbán (2005). The remaining global properties were generally taken from Pijpers (2003). The full list of observables is included in Table 7.1; for comparison with the other analyses the separation ratios have been replaced by the corresponding small separations.

As indicated, the fit also included frequency values which are sensitive to the near-surface effects, as are the large separations. To correct for these effects Teixeira *et al.* made the assumption that they are similar to the frequency modification that has been determined in the solar case, if the frequencies are measured in terms of the acoustic cut-off frequency  $\nu_{ac}$ . Specifically, they represented the frequency change resulting from the near-surface effects as

$$\delta\nu_{\text{surf}} = \lambda_{\text{surf}} \mathcal{G}_{\odot}(\nu/\nu_{ac}) , \quad (7.91)$$

where  $\lambda_{\text{surf}}$  is a scale factor that must be determined. Here the function  $\mathcal{G}_{\odot}$  was obtained from the function  $\mathcal{H}_2(\omega)$  resulting from an asymptotic fit to the differences between observed and modelled solar frequencies (see Section 7.1.4.4, in particular Eq. (7.19)), shifted such as to be zero at low frequency. The resulting function, scaled to the case of  $\alpha$  Cen A with  $\nu_{ac} = 3827 \mu\text{Hz}$  is shown in Fig. 7.55; this was determined from MDI observations with  $l \leq 100$  and frequencies of Model S of Christensen-Dalsgaard *et al.* (1996). This correction was incorporated in the frequency calculation before deriving the quantities that were fitted to the observations.

Teixeira *et al.* used a simultaneous  $\chi^2$  fit to the observations of the A and B components, with the Levenberg-Marquardt technique similar to the fit of

<sup>39</sup> The participants in this project are T. C. Teixeira, T. R. Bedding, H. Kjeldsen, F. P. Pijpers and J. Christensen-Dalsgaard.

<sup>40</sup> The analysis by Teixeira *et al.* used earlier versions of the data and hence slightly different fitting parameters.

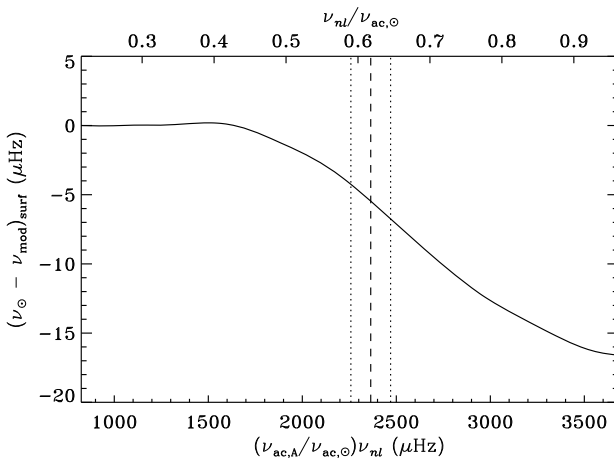


**Fig. 7.55.** Surface frequency correction  $\mathcal{G}_\odot$ ; the lower abscissa has been rescaled to correspond to  $\alpha$  Cen A, on the assumption that the correction is a function of  $\nu/\nu_{\text{ac}}$ , shown on the upper abscissa. The vertical dashed line and the vertical dotted lines indicate  $\nu_{21,0}$  and  $\nu_{21,0} \pm \Delta\nu_{21,0}$ , respectively, as observed for  $\alpha$  Cen A (*c.f.* Eq. (7.90) and Table 7.1).

Miglio & Montalbán (2005), for the parameters

$$\{M_A, M_B, Y_i, Z_i, \alpha_{\text{ML},A}, \alpha_{\text{ML},B}, \tau_*\} . \quad (7.92)$$

In principle the scaling factor  $\lambda_{\text{surf}}$  could also have been included as a parameter of the fit, probably allowing different values for the A and B components. In the present fit, however,  $\lambda_{\text{surf}}$  was fixed at the value 0.75, determined from a separate analysis. The results of the fit are presented in Table 7.2. Interestingly, a slightly higher age was obtained than in the analyses of Eggenberger *et al.* (2004) and Miglio & Montalbán (2005). Also, unlike those analyses the inferred mixing length is slightly larger for  $\alpha$  Cen A than for  $\alpha$  Cen B. Figure 7.56 shows the resulting evolution tracks, compared with the observational error boxes in  $T_{\text{eff}}$  and  $L/L_\odot$ . As is also clear from Tables 7.1 and 7.2 the fit successfully reproduced these quantities. The fit to the observed frequencies is illustrated in the échelle diagrams in Fig. 7.57. There is clearly a reasonable agreement between the computed frequencies (which include the correction for the near-surface effects) and the observations, although potentially interesting differences are visible. In particular, it appears that the small separations  $\delta\nu_{n1}$  are somewhat smaller for the models than for the observations. This certainly requires further investigations.

The best-fitting model of  $\alpha$  Cen A does not develop a convective core in this case; however, even a slight change in the parameters may lead to a model

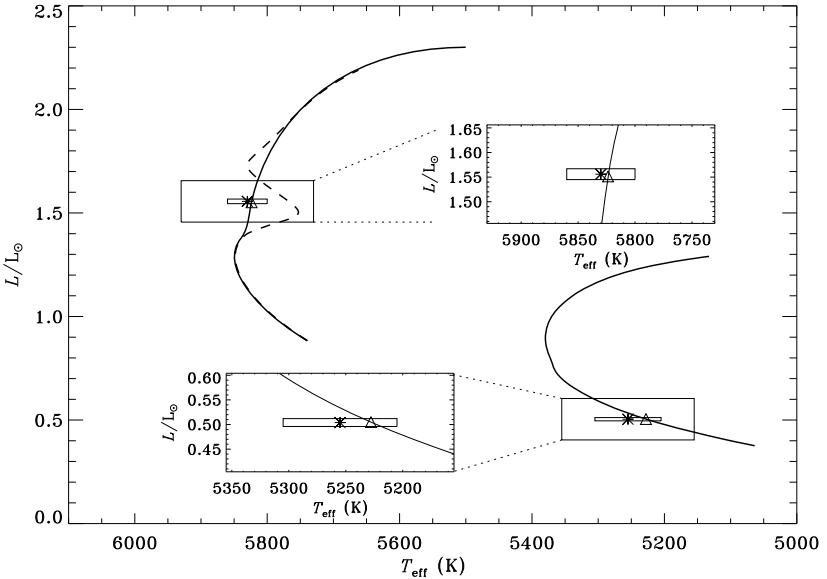


**Fig. 7.56.** The solid curves show the evolution tracks corresponding to the fit of Teixeira *et al.*, indicated in Table 7.2. The stars show the observed values of  $T_{\text{eff}}$  and  $L/L_{\odot}$ , surrounded by  $1-\sigma$  error boxes, and the best-fitting models are marked by triangles; the insets show a magnified view of the fits. The dashed curve shows a model of  $\alpha$  Cen A with slightly modified parameters which develops a convective core (see text).

with a convective core. This is illustrated by the dashed curve in Fig. 7.56 which was computed with a mass higher by 0.04% than the best-fitting model and with changes in the remaining parameters below 0.2%. In this case the model develops a convective core with a maximal mass of  $0.03 M_{\odot}$  at an age of 7.296 Gyr. As shown, this is sufficient to lead to a major deterioration in the fit. Such sensitivity to the parameters clearly complicates the fitting greatly, since the onset of the convective core corresponds to a discontinuous change in the model, so that the solution cannot be linearized in the parameters. On the other hand, it also demonstrates the potential value of the  $\alpha$  Cen system in obtaining constraints on core convection.

Additional modelling of the  $\alpha$  Cen system has been presented by Yıldız (2007, 2008). Unlike the detailed analyses presented above he found some discrepancy between the age of the system inferred from the “classical” observables compared with including the asteroseismic data. The reasons for

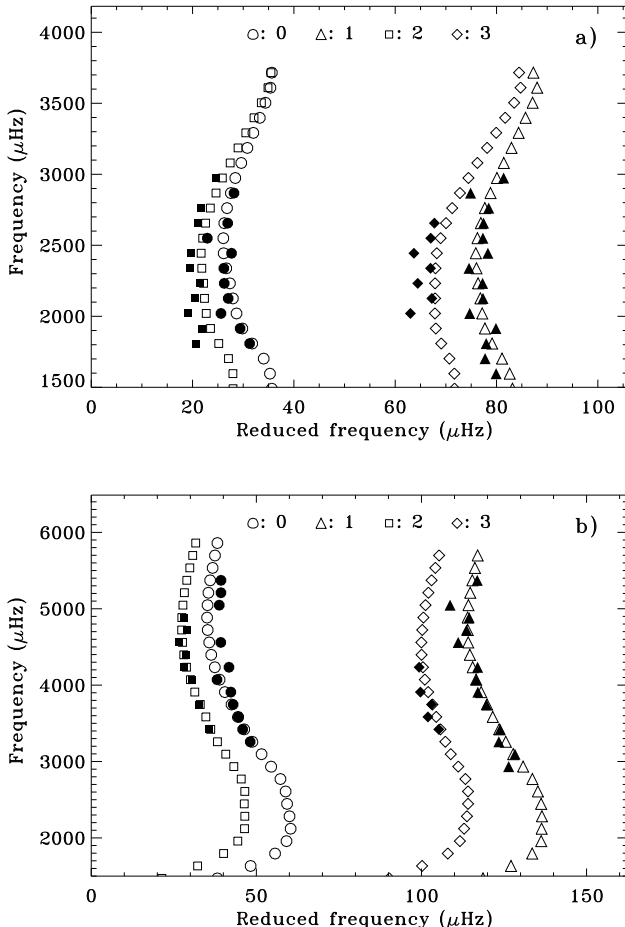


**Fig. 7.57.** Échelle diagrams for  $\alpha$  Cen A (with  $\Delta\nu = 106.0 \mu\text{Hz}$ ; panel a) and  $\alpha$  Cen B (with  $\Delta\nu = 162.6 \mu\text{Hz}$ ; panel b). The degree  $l$  is indicated by the symbol type, as shown. The filled symbols show the observed frequencies; the open symbols show the computed frequencies, based on the Teixeira *et al.* fit, corrected for near-surface effects according to Eq. (7.91) with  $\lambda_{\text{surf}} = 0.75$  (see also Fig. 7.55).

these apparently different conclusions deserve further investigation, including comparisons of the codes used for the model calculation.

The detailed data available for  $\alpha$  Cen provide interesting possibilities for investigating the physics of the models and the oscillations. Following the early

work of Lydon *et al.* (1993), Straka *et al.* (2007) computed hydrodynamical simulations of convection in the outer layers of  $\alpha$  Cen A and B and applied the results to full models of the star. As has been found in the solar case (Rosenthal *et al.* 1999; Li *et al.* 2002) the resulting change to the hydrostatic structure goes some way towards reducing the frequency differences arising from the near-surface effects (*cf.* Section 7.1.7). In an interesting analysis of the amplitudes of modes in the Sun and  $\alpha$  Cen B, Chaplin *et al.* (2009) found evidence that the computations of mode damping rates, based on the convection treatment of Balmforth (1992a), underestimated the damping rate at high frequency; this was based on assuming that the stochastic energy input rate was correctly modelled, allowing a determination of the damping rate in  $\alpha$  Cen B which was consistent with the values inferred from frequency scatter by Kjeldsen *et al.* (2005). The resulting damping rate was found to correspond in shape to the solar damping rate, if frequency was measured in units of the acoustic cut-off frequency. Further investigations along these lines, extended to other stars, will be of obvious value in the understanding of the mode physics of solar-like oscillations.

## 7.2.4 The Subgiant $\eta$ Bootis

### 7.2.4.1 The Star

$\eta$  Boo is a subgiant star of spectral type G0 IV. From the modelling discussed below it is identified to be just beyond the core hydrogen burning phase. As discussed in Section 7.2.4.3 below, the resulting compact core gives rise to mixed modes in the range of frequencies corresponding to solar-like oscillations and hence makes the star particularly interesting for asteroseismology.

The star is a member of a spectroscopic binary system with a period of 494 d (Bertiau 1957); from extensive interferometric measurements van Belle *et al.* (2007) concluded that the companion must be fainter than the primary by more than 5 magnitudes. From spectral line widths  $\eta$  Boo is found to be a moderately rapidly rotating star, with  $v_\Omega \sin i = 13 \text{ km s}^{-1}$ , recently confirmed by observations by Carrier *et al.* (2005) (see below). This somewhat reduces the sensitivity of Doppler-velocity observations to oscillations of the star. The Hipparcos parallax is  $88.17 \pm 0.75$  mas. The angular diameter was measured by Thévenin *et al.* (2005) as  $2.20 \pm 0.03$  mas, corresponding at the Hipparcos distance to  $R/R_\odot = 2.68 \pm 0.05$ ; independent measurements by van Belle *et al.* (2007) yielded very similar results, with a slightly smaller error. The star is clearly metal-rich, although the abundance determinations show considerable scatter; Taylor (2003) obtained a value of  $[\text{Fe}/\text{H}] = 0.295 \pm 0.039$ , while Carrier *et al.* (2005) preferred  $[\text{Fe}/\text{H}] = 0.23 \pm 0.07$ . Edvardsson *et al.* (1993) found substantial overabundances, relative to Fe, of Na, Mg, Al and Si, although modelling of  $\eta$  Boo has generally assumed a solar relative

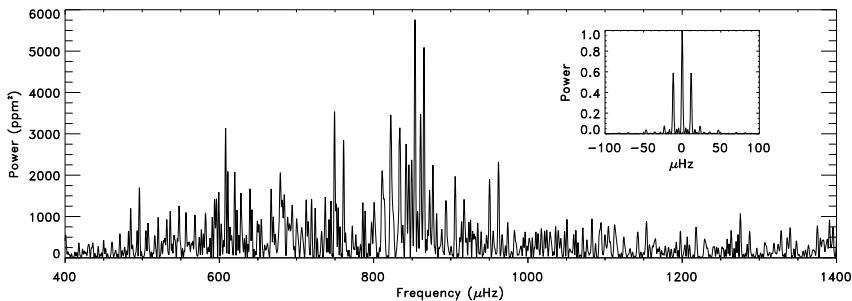


**Fig. 7.58.** Observed power spectrum of  $\eta$  Boo, based on observations of the equivalent widths of the hydrogen Balmer lines. The inset shows the window function, on an expanded frequency scale. From Kjeldsen *et al.* (1995).

composition.<sup>41</sup> The effective temperature was determined as  $6058 \pm 50$  K by Taylor (2003b) while Carrier *et al.* (2005) chose a possibly more realistic error, in setting  $T_{\text{eff}} = 6030 \pm 90$  K. From the  $V$  magnitude, parallax and bolometric correction Bedding *et al.* (1998) obtained  $L/L_{\odot} = 9.02 \pm 0.22$ , while Pijpers (2003) found  $L/L_{\odot} = 9.2 \pm 0.4$ .

#### 7.2.4.2 The Data

Solar-like oscillations were first detected in  $\eta$  Boo by Kjeldsen *et al.* (1995). This was in fact the first time that definite frequencies of such oscillations in a distant star had been identified. Kjeldsen *et al.* used a technique based on measuring the equivalent widths of the hydrogen Balmer lines, effectively reflecting the temperature variations in the stellar atmosphere (Bedding *et al.* 1996). Since the measurement is made relative to the nearby continua, effects of the Earth's atmosphere largely cancel. The observations were made over 6 nights at the Nordic Optical Telescope on La Palma. The resulting power spectrum is illustrated in Fig. 7.58; this showed a clear enhancement of power at the expected location, with peaks with a roughly uniform spacing corresponding to  $\Delta\nu \simeq 40 \mu\text{Hz}$ . The analysis led to the identification of 13 modes with  $l = 0-2$ . We discuss the detailed interpretation of these data below.

Given this remarkable detection an independent confirmation was clearly highly desirable. Thus it was cause of some concern that radial-velocity observations of  $\eta$  Boo by Brown *et al.* (1997) failed to show the oscillations. They observed the star over seven nights, with a relatively low duty cycle, using the

<sup>41</sup> In a recent analysis, Bruntt (in preparation) obtained  $[\text{Fe}/\text{H}] = 0.30 \pm 0.06$ , with relative abundances very close to solar. He also obtained  $T_{\text{eff}} = 6130 \pm 70$  K.

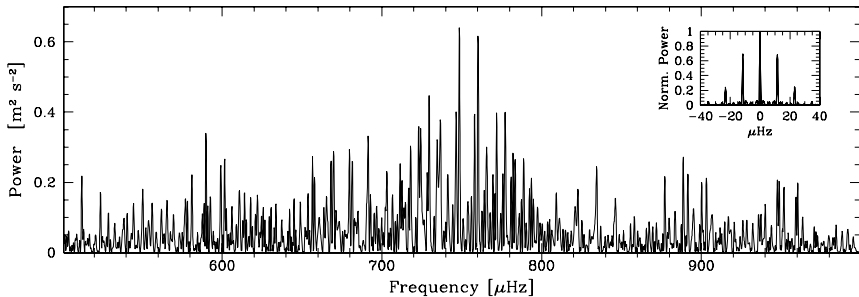


**Fig. 7.59.** Observed power spectrum of  $\eta$  Boo, based on Doppler velocity observations over 13 nights. The inset shows the window function, on an expanded frequency scale. Adapted from Carrier *et al.* (2005).

AFOE<sup>42</sup> spectrograph at the Whipple Observatory, Mount Hopkins. Their results indicated an upper limit of  $0.5 \text{ m s}^{-1}$  on any solar-like oscillations in  $\eta$  Boo; although it is not straightforward to convert the equivalent-width signal of Kjeldsen *et al.* (1995) into velocity, this limit is substantially below the expected velocity amplitude. Not surprisingly, the lack of detection by Brown *et al.* (1997) led to questioning of the original detection by Kjeldsen *et al.*

Additional observations of  $\eta$  Boo have fully confirmed the presence of solar-like oscillations and added to the identified modes. Kjeldsen *et al.* (2003) reported the results of a substantial programme to observe the star, based on six nights of measurements of the Balmer-line equivalent width with the Nordic Optical Telescope and 56 nights of Doppler-velocity observations, although with poor weather, with the Coudé Auxiliary Telescope at the Lick Observatory. The latter observations showed long-term variations which the authors identified as likely resulting from stellar activity. The two sets of data clearly showed consistent solar-like oscillations; interestingly, the amplitudes appeared to be somewhat lower than during the original observations of Kjeldsen *et al.* (1995) and consistent with the upper limit determined by Brown *et al.* (1997); while such amplitude variations are not unexpected for stochastically excited modes they clearly provide a plausible explanation for the non-detection by Brown *et al.*.

Carrier *et al.* (2005) carried out Doppler-velocity observations with the CORALIE spectrograph at the Euler telescope at La Silla and the ELODIE spectrograph at Observatoire Haute-Provence. Fourteen nights of observations were obtained with CORALIE, whereas only three nights were available on ELODIE as a result of bad weather. The resulting power spectrum is shown in Fig. 7.59. The power envelope from the stochastically excited oscillations is evident; since the ELODIE data made a modest contribution to the spectrum

<sup>42</sup> Advanced Fiber Optic Echelle.

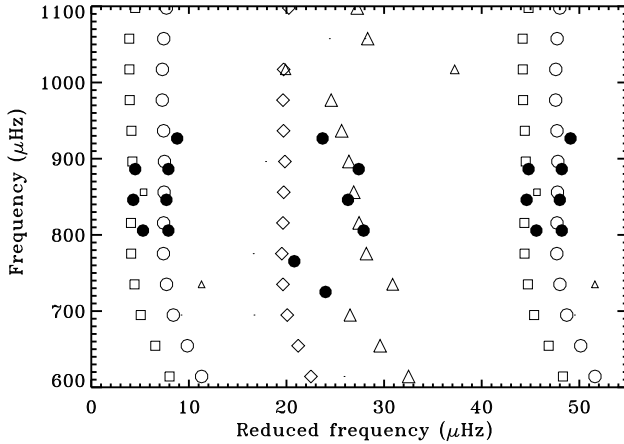


**Fig. 7.60.** Échelle diagram based on frequencies of  $\eta$  Boo, with a frequency separation of  $\Delta\nu = 40.3 \mu\text{Hz}$  (*cf.* Eq. (3.224)). The filled circles show observed frequencies from Kjeldsen *et al.* (1995), with a reference frequency of  $\nu_0^{(\text{obs})} = 846 \mu\text{Hz}$ . The open symbols show computed frequencies for a model with  $M = 1.60 M_\odot$  and  $Z = 0.03$ ; here the reference frequency was  $\nu_0^{(\text{mod})} = 856 \mu\text{Hz}$ . Circles are used for modes with  $l = 0$ , triangles for  $l = 1$ , squares for  $l = 2$  and diamonds for  $l = 3$ . Adapted from Christensen-Dalsgaard *et al.* (1995b).

the window function, illustrated in the inset, shows large daily sidelobes. From the power spectrum Carrier *et al.* identified 22 individual frequencies. The maximum amplitude was around  $80 \text{ cm s}^{-1}$ . We discuss the mode identification from this dataset and the observations of Kjeldsen *et al.* (2003) in the following section.

The MOST satellite made photometric observations of  $\eta$  Boo over 27 d, with a very high duty cycle (Guenther *et al.* 2005). The power spectrum showed little evidence for a power enhancement corresponding to solar-like oscillations; however, Guenther *et al.* identified a sequence of peaks as corresponding to radial modes, extending to very low frequency. We also discuss this identification below.

#### 7.2.4.3 Mode Identification and Seismic Modelling

From the observed power spectrum Kjeldsen *et al.* (1995) identified modes of degree  $l = 0–2$ . These are illustrated by the filled symbols in the échelle diagram in Fig. 7.60, with a large separation  $\Delta\nu = 40.3 \mu\text{Hz}$ . Christensen-Dalsgaard *et al.* (1995b) made model calculations to compare with these observations. These were based on a somewhat uncertain luminosity,  $L/L_\odot =$

$9.5 \pm 0.7$ , obtained with a parallax from Harrington *et al.* (1993); the composition was characterized by  $X = 0.7$ ,  $Z = 0.03$ . Figure 7.61 shows examples of evolution tracks in an HR Diagram, compared with the error box in effective temperature and luminosity. From comparison with the large separation a model with  $M = 1.60 M_{\odot}$ , marked by a filled circle, was identified; this is in the early phases of the hydrogen shell-burning phase with a contracting helium core. The frequencies of this model are also shown in Fig. 7.60. To match the observations the frequencies were shifted by  $10 \mu\text{Hz}$ ; this was identified as likely resulting from the near-surface effects. Given this shift there is clearly excellent agreement between the model and the observations for the modes with  $l = 0$  and 2, including the small separation, observationally determined as  $\langle \delta\nu_{n0} \rangle = 3.1 \pm 0.3 \mu\text{Hz}$ . The computed frequencies for  $l = 1$  showed an irregular behaviour which, as discussed in more detail below, is the result of the presence of mixed modes, with a partial g-mode character. Interestingly, the observed frequencies had a similar behaviour, leading the authors to speculate that mixed modes had been detected in  $\eta$  Boo and to note the potential importance for the diagnostics of the properties of the stellar core.

To assist the understanding of the behaviour of the oscillations in  $\eta$  Boo, Fig. 7.62 shows the dimensionless buoyancy frequency  $\hat{N}$  and characteristic acoustic frequencies in a model of  $\eta$  Boo, in units of  $(GM/R^3)^{1/2}$ , and compare them with the buoyancy frequency in the present Sun (*cf.* Fig. 3.14). The dominant difference between the two models is the very large peak in  $\hat{N}$  near the centre of the  $\eta$  Boo model. This is caused by two effects: during the main-sequence phase of central hydrogen burning the retreating convective core has left behind a steep gradient in the hydrogen abundance (see also Fig. 3.15 and the discussion in Section 3.4.2) leading to a highly stable stratification and hence contributing to a large value of  $N$  (*e.g.*, Dziembowski & Pamyatnykh 1991); in addition, the increasing central condensation as the core contracts after hydrogen exhaustion drives up the gravitational acceleration in the core, further increasing  $N$ . As a result, the maximum value of  $N$  exceeds the acoustic cut-off frequency in the stellar atmosphere. Thus *all* trapped acoustic modes may in principle be affected by the buoyancy frequency, taking on g-mode character in the core. The effect is similar to the behaviour discussed in Section 3.5.3, including the presence of mixed modes and avoided crossings between frequencies of modes with predominantly p- and g-mode character; but in stars such as  $\eta$  Boo and in later evolutionary phases this behaviour affects all nonradial modes. In particular, at the frequencies characteristic for the observations of  $\eta$  Boo, indicated by the horizontal line in Fig. 7.62, the modes have extended p-mode regions in the outer parts of the star and a small g-mode region near the centre. The separation between these two regions is quite small for  $l = 1$ , leading to a substantial coupling between the two types of behaviour; with increasing  $l$ , the separation increases rapidly and the coupling becomes small.

Based on the original analysis by Christensen-Dalsgaard *et al.* (1995b) the best-fitting model in Fig. 7.61 lies at the edge of the  $1-\sigma$  error box in

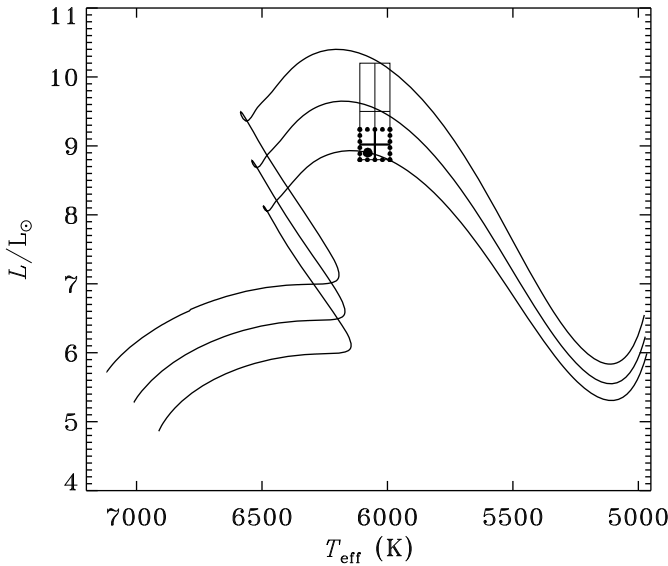


**Fig. 7.61.** Evolutionary tracks in the HR diagram, for models with  $Z = 0.03$ ,  $X = 0.7$  and a mixing-length parameter calibrated to obtain the proper solar radius. Models are shown with masses of  $1.6 M_{\odot}$ ,  $1.63 M_{\odot}$  and  $1.66 M_{\odot}$ . The thin error box indicates the original observed location of  $\eta$  Boo, while the bolder, dotted error box shows the location given the Hipparcos parallax. The filled circle shows the model identified from fits to the observed large frequency separation  $\Delta\nu$ . Adapted from Christensen-Dalsgaard *et al.* (1995b).

luminosity. However, shortly after this analysis, a determination of the parallax of  $\eta$  Boo with the Hipparcos satellite became available. As discussed by Bedding *et al.* (1998) this led to a determination of the luminosity as  $L/L_{\odot} = 9.02 \pm 0.22$ , an improvement in luminosity precision by a factor of three, and leading to the smaller error box also shown in Fig. 7.61. It was encouraging that the previously identified model was fully consistent with this new determination of the luminosity.

Guenther & Demarque (1996) made a detailed analysis of the observed frequencies of Kjeldsen *et al.* (1995), including a systematic survey of the effects of varying the relevant parameters. From this they obtained a mass of  $1.55 \pm 0.03 M_{\odot}$  and an estimate of the parallax of  $89.5 \pm 0.5$  mas, marginally consistent with the pre-Hipparcos value of  $87.0 \pm 3.4$  mas that they assumed; this was based on an assumed  $Z = 0.03$  although they argued that better agreement with the observed frequencies could have been obtained with a

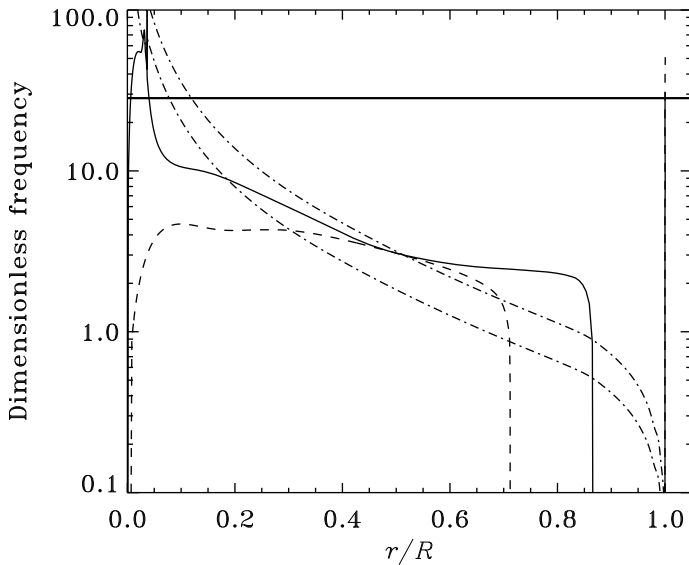


**Fig. 7.62.** Dimensionless buoyancy frequency  $\hat{N} \equiv (GM/R^3)^{-1/2}N$  plotted against fractional radius  $r/R$  for Model S of the present Sun (dashed line) and the model of  $\eta$  Boo marked in Fig. 7.63 below (solid line). The dot-dashed curves show the dimensionless characteristic acoustic frequency  $\hat{S}_l = (GM/R^3)^{-1/2}S_l$  (cf. Eq. (3.153)) in  $\eta$  Boo, for  $l = 1$  and 2. The heavy horizontal line indicates the location of a mode in  $\eta$  Boo of frequency  $850\ \mu\text{Hz}$ , typical of the observed frequencies.

higher  $Z$ . As did Christensen-Dalsgaard *et al.* (1995b) they noted the evidence for mixed modes (involved in what they termed “mode bumping”); they emphasized the resulting important asteroseismic potential, particularly for a precise determination of the stellar age.

Although obtained from two sites, the observations of Kjeldsen *et al.* (2003) did not have sufficient time coverage to suppress the daily sidelobes. Thus the interpretation of the spectrum had to take into account the fact that peaks in the power spectrum could be shifted by  $11.6\ \mu\text{Hz}$ . Based on the systematics of the frequencies, as expected from the asymptotic behaviour, Kjeldsen *et al.* identified the degrees of the modes and assigned a set of frequencies. These were modelled by Di Mauro *et al.* (2003), assuming also that  $L/L_\odot = 9.02 \pm 0.22$ ,  $T_{\text{eff}} = 6028 \pm 45\ \text{K}$  and  $[\text{Fe}/\text{H}] = 0.305 \pm 0.051$  which, with  $X = 0.7$ , led to  $Z = 0.04 \pm 0.005$ . They considered both models without and with overshoot from the convective core during the core hydrogen-burning phase, concluding that the overshooting could be at most  $0.25H_p$ ,  $H_p$  being the pressure scale

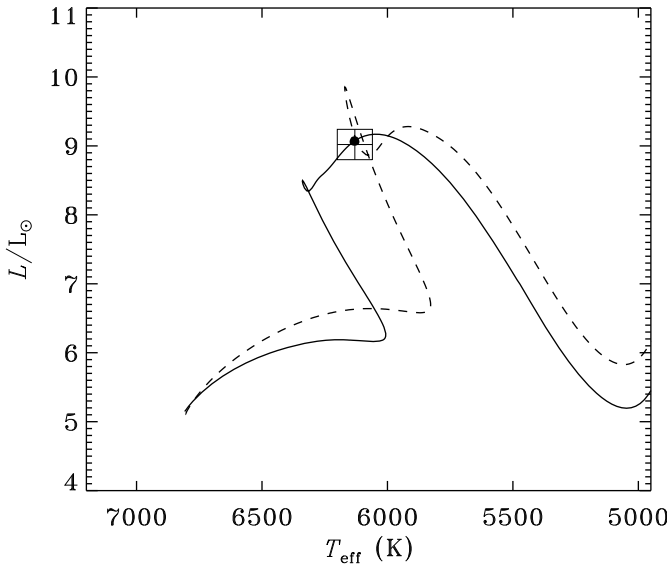


**Fig. 7.63.** Evolutionary tracks in the HR diagram, for models of mass  $1.7 M_{\odot}$ ,  $Z = 0.04$ ,  $X = 0.7$  and a mixing-length parameter calibrated to obtain the proper solar radius. The solid curve shows a model without convective core overshoot, while the dashed curve shows a model with overshoot of 0.2 pressure scale heights during the central hydrogen-burning phase. The error box indicates the observed location of  $\eta$  Boo, assuming  $L/L_{\odot} = 9.02 \pm 0.22$  (Bedding *et al.* 1998) and  $T_{\text{eff}} = 6130 \pm 70$  K (Bruntt, in preparation). The filled circle shows the model, without core overshoot, identified from fits to the observed frequencies. Adapted from Di Mauro *et al.* (2003).

height at the edge of the core, in order for the model to reproduce the observed location in the HR Diagram. Examples of two of their models are illustrated in Fig. 7.63. The model without overshoot is very similar to the best-fitting model in Fig. 7.61,<sup>43</sup> whereas the model with overshoot is immediately after the exhaustion of central hydrogen and hence has a somewhat less concentrated core. Di Mauro *et al.* (2003) made a detailed comparison of the observed and computed frequencies, obtaining a reasonable fit, particularly for the model without overshoot, although still requiring a modest constant shift of the computed frequencies. They noted that the model with overshoot of  $0.2H_p$  did not show mixed modes in the frequency range of the observed modes; thus this model could be excluded if, as it appeared, the observed  $l = 1$

<sup>43</sup> The somewhat higher value of  $Z$  is compensated by the slightly higher mass.

modes showed an irregular structure in the échelle diagram indicative of mixed modes. Additional modelling of the Kjeldsen *et al.* (2003) observations was carried out by Di Mauro *et al.* (2004) who noted that an alternative to the previous results could be a somewhat more massive model with substantial core overshoot, close to the end of central hydrogen burning. They were not able, on the basis of the existing data, to distinguish definitely between these models, although the main-sequence model clearly did not show mixed modes.

An independent analysis of the Kjeldsen *et al.* (2003) data was carried out by Guenther (2004). He used the grid-based  $\chi^2$  minimization technique of Guenther & Brown (2004), considering both  $Z = 0.03$  and  $Z = 0.04$ , but obtaining the best fits with the higher metallicity. Minimizing just the difference between the observed and model frequencies he obtained two solutions: one, on the main sequence, with a mass of around  $1.88 M_{\odot}$  and a second, on the sub-giant branch, with a mass near  $1.71 M_{\odot}$ ; none of the models included convective core overshoot. The former model was inconsistent with the luminosity and effective temperature and hence had to be excluded. The sub-giant model was essentially consistent with the model found by Di Mauro *et al.* (2003). However, somewhat surprisingly Guenther noted that his models had “a very thin convective envelope up to the model that best fits the oscillation data”. In the models of Di Mauro *et al.* the convective envelope had an extent of at least  $0.05R$  except just after the ZAMS; it is obvious that vigorous convection is required to excite the solar-like oscillations. Interestingly, Guenther (2004) found that frequency calculations including nonadiabatic effects yielded an improved agreement with the observed frequencies, presumably by correcting for part of the near-surface problems in the more usual adiabatic frequency calculations. As in previous analyses a detailed investigation was made of the evolution of the frequencies with age, noting the avoided crossings involving mixed modes and their diagnostic potential.

Given the limited contribution from the ELODIE observations, the results of Carrier *et al.* (2005) were also essentially from a single site and the power spectrum contained substantial sidelobes.<sup>44</sup> Thus, as in the case of Kjeldsen *et al.* (2003) the frequency analysis had to deal with a possible  $11.6 \mu\text{Hz}$  ambiguity in the frequency determination. Carrier *et al.* identified 22 modes with  $l = 0–2$ . A comparison with the frequencies of Kjeldsen *et al.* (2003) showed good agreement at low frequency, while at high frequency substantial disagreement was found. We return to this issue below.

Carrier *et al.* (2005) also compared the observed frequencies with models computed for  $\eta$  Boo. Unlike the other modelling efforts they took into account diffusion and settling, as well as the effects of rotation. Indeed, as noted in Section 3.2.2.4, settling in relatively massive stars with thin outer convection zones dramatically changes the surface composition on a timescale short compared with the evolution timescale (see also Fig. 3.2), unless compensated by

<sup>44</sup> A contributing factor was the declination of  $+18^\circ$  of  $\eta$  Boo, resulting in relatively short nightly observing periods from the latitude of La Silla.

mixing processes. Such mixing, resulting from rotational effects, is included in the Geneva evolution code (*e.g.*, Meynet & Maeder 2000; Eggenberger *et al.* 2005b). Thus the computation also followed the evolution of the rotational velocity, from an assumed initial velocity of around  $90 \text{ km s}^{-1}$  to the present observed velocity which was taken to be  $13 \text{ km s}^{-1}$ , assuming that  $\sin i \simeq 1$ . Carrier *et al.* (2005) assumed the same value of  $L/L_\odot$  as Di Mauro *et al.* (2003) and a similar effective temperature, although with a somewhat higher error. The metallicity was taken to be  $[\text{Fe}/\text{H}] = 0.23 \pm 0.07$ , somewhat lower than the value assumed by Di Mauro *et al.* As in the analysis of the  $\alpha$ Cen system by Eggenberger *et al.* (2004) (see Section 7.2.3.4) the fit to the observed quantities was carried out as a two-step process, first matching the observed position in the HR Diagram and subsequently making a  $\chi^2$  fit to the frequencies, allowing for a constant offset between the observed and computed frequencies to account for the near-surface effects. The best-fitting model had a mass of  $1.57 \pm 0.07 M_\odot$ , somewhat lower than the value obtained by Di Mauro *et al.* (2003), as a result of the lower metallicity. Carrier *et al.* also computed models with  $Z = 0.04$ , obtaining results very similar to those of Di Mauro *et al.* In addition, they confirmed the possibility, noted by Di Mauro *et al.* (2004), of main-sequence models with core overshoot but similarly pointed out that these models could not account for the apparent presence of mixed modes in the observed frequencies.

The extensive observations of  $\eta$  Boo with the MOST satellite by Guenther *et al.* (2005) represented a promising possibility for resolving the ambiguity of the mode identification from single-site observations and improving the frequency determination. Unfortunately, the data showed no clear evidence for solar-like oscillations. A statistical analysis to estimate the significance level in the power spectrum (Reegen 2007) isolated a number of apparently significant peaks, from which the sequence of radial modes was identified; no nonradial modes were found. At the highest frequencies considered,  $600$ – $700 \mu\text{Hz}$ , these generally coincided with the frequencies found by Kjeldsen *et al.* (2003) and Carrier *et al.* (2005); however, the sequence could be followed down to a frequency as low as  $127 \mu\text{Hz}$ , corresponding roughly to a mode of radial order  $n = 2$ . The determination of such low-order frequencies would undoubtedly be extremely valuable for the asteroseismic investigation of the star. On the other hand, their presence goes completely against the observed power distribution in other stars showing solar-like oscillations and is not consistent with our theoretical understanding of the mode excitation. Thus, until further confirmed they should probably be viewed with scepticism.

Guenther *et al.* (2005) also carried out a grid-based  $\chi^2$  fit to the inferred frequencies, obtaining a model essentially consistent with the model found by Di Mauro *et al.* (2003). In an interesting extension of this analysis Straka *et al.* (2006) used models of turbulent near-surface convection based on parameterized results from hydrodynamical simulations; a nonadiabatic frequency calculation was carried out, although neglecting the detailed interaction between convection and the oscillations. Straka *et al.* demonstrated that the

resulting frequencies were in substantially better agreement with the observations, including the data of Kjeldsen *et al.* (2003), than frequencies of models based on the usual mixing-length treatment. This is clearly an encouraging demonstration, following the earlier work on the Sun and  $\alpha$  Cen A and B (Rosenthal *et al.* 1999; Li *et al.* 2002; Straka *et al.* 2007), that some aspects of the near-surface problems can be understood from such more sophisticated models of the outer layers of the stars.

The two sets of frequencies obtained by Kjeldsen *et al.* (2003) and Carrier *et al.* (2005) represent the best data so far for the asteroseismic analysis of  $\eta$  Boo. Thus it is important to understand the discrepancies between the two sets. In a recent analysis Kjeldsen (private communication) has investigated the extent to which they can be interpreted simply in terms of different choices of daily sidelobes and, as a result, has produced a unified set of frequencies based on the two sets.<sup>45</sup> The resulting combined set of observed frequencies is illustrated in the échelle diagram in Fig. 7.64. It clearly shows the sequences of peaks corresponding to  $l = 0, 1$  and  $2$ , the sequence for  $l = 1$  having irregularities strongly suggesting the presence of mixed modes.

In Fig. 7.64 the observations are compared with computed frequencies for the model marked in Fig. 7.63 (Di Mauro *et al.* 2003). This is a  $1.7 M_{\odot}$  model with  $Z = 0.04$ , computed without convective overshoot. Panel a) shows the original computed frequencies. To give some indication of the likelihood of observing the modes the size of the symbols is proportional to the expected amplitude, under simplified assumptions concerning the mode excitation. Specifically, it follows from the discussion in Section 3.7.5 that for stochastically excited modes the energy is predominantly a function of frequency and that, consequently, the root-mean-square velocity  $\bar{V}_{nl} = \langle V_{nl}^2 \rangle^{1/2} \propto E_{nl}^{-1/2}$  where  $E_{nl}$  is the mode inertia, normalized to the surface displacement (*cf.* Eq. (3.140)). Consequently, the ratio between the amplitude  $\bar{V}_{nl}$  of a given mode and of a radial mode at the same frequency  $\nu_{nl}$  satisfies

$$\frac{\bar{V}_{nl}}{V_0(\nu_{nl})} \simeq \left[ \frac{E_{nl}}{\bar{E}_0(\nu_{nl})} \right]^{-1/2} = Q_{nl}^{-1/2}, \quad (7.93)$$

where  $V_0(\nu)$  and  $\bar{E}_0(\nu)$  are obtained by interpolating to frequency  $\nu$  in the results for radial modes. Also,  $Q_{nl}$  is the inertia ratio defined by Eq. (7.10). Thus in Fig. 7.64 the symbol size is proportional to  $Q_{nl}^{-1/2}$ , resulting in smaller symbols for mixed modes of higher inertia than the corresponding radial modes (see also Fig. 7.65 below); symbols that would otherwise be too small to be visible are shown as plusses. It should be noted that, as discussed in Section 3.7.5, the potential for observing a mode is more closely related to the peak height which has a more complex dependence on the mode inertia and the duration of the observations (*cf.* Eq. (3.310)).

---

<sup>45</sup> We are very grateful to H. Kjeldsen for providing us with these frequencies.

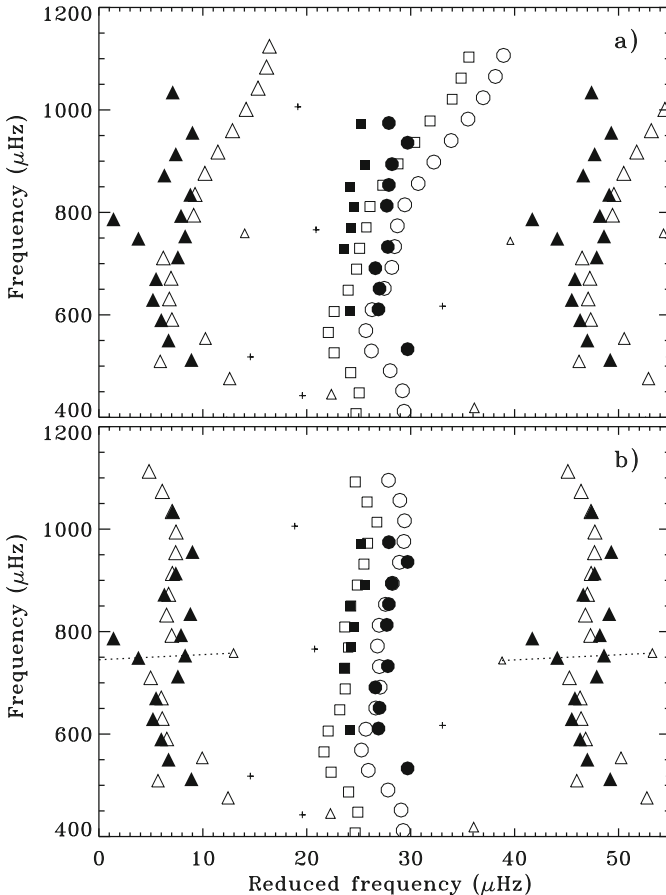


**Fig. 7.64.** Échelle diagram with a frequency separation of  $\Delta\nu = 40.3 \mu\text{Hz}$  and a reference frequency of  $\nu_0 = 866 \mu\text{Hz}$ . The filled symbols show observed frequencies combining results from Kjeldsen *et al.* (2003) and Carrier *et al.* (2005); circles are used for modes with  $l = 0$ , triangles for  $l = 1$  and squares for  $l = 2$ . The open symbols show computed frequencies for a model with  $M = 1.70 M_\odot$  and  $Z = 0.04$  (see Di Mauro *et al.* 2003). The size of the symbols indicates the expected relative amplitude of the modes (see text); symbols that would otherwise be too small have been replaced by crosses. For clarity, the  $l = 1$  sequences are repeated in the right-hand part of the diagram. Panel a): original model frequencies; panel b) model frequencies including a surface correction (Kjeldsen *et al.* 2008b; see text). In panel b) the dotted line connects the two modes undergoing an avoided crossing at the age of the present model; they are marked by triangles and squares in Fig. 7.65.

In panel b) the frequencies have been corrected using the procedure of Kjeldsen *et al.* (2008b) (see Section 7.2.2.1, in particular Eq. (7.81)), according to

$$\delta^{(\text{surf})}\nu_{nl} = Q_{nl}^{-1}a(\nu_{nl}/\nu_0)^b, \quad (7.94)$$

with  $a = -2.259 \mu\text{Hz}$ ,  $\nu_0 = 800 \mu\text{Hz}$  and  $b = 4.9$ . Also  $Q_{nl}$  takes into account the presence of mixed modes; the power-law correction is based on a fit to the radial modes and, relative to those, the effect on the nonradial modes is reduced by a factor proportional to the mode inertia (*cf.* Eq. (3.268)). For mixed modes, with a partial g-mode character and a higher inertia than for the radial modes, the near-surface effect on the frequencies is therefore smaller. It is evident that in most cases the correction successfully brings the computed frequencies into good agreement with the observations, except for  $l = 1$  modes of obvious mixed character in the model or the observations.

To gain a better understanding of the properties of the modes it is instructive to follow their evolution with the age of the star. This is done in Fig. 7.65, for a model sequence including the model analysed in Fig. 7.64; that model is marked by the vertical line. The frequencies of the radial modes, shown by dashed lines in panel (a), decrease approximately as  $t_{\text{dyn}}^{-1}$  as a result of the increasing stellar radius. The same general trend is shared by the  $l = 1$  modes when they behave like p modes. However, as in the case shown in Fig. 3.25 there is an additional g-mode branch, with frequencies increasing with age as the maximum value of  $N$  increases; as before these interact with the p-mode branches through a sequence of avoided crossings. The effect on the normalized mode inertia  $E_{nl}$ , defined in Eq. (3.140), is shown in panel (b); for clarity two modes with  $l = 1$  have been indicated in both panels by triangles and squares, respectively. Where the  $l = 1$  modes behave as p modes, their inertia is very close to that of a radial mode of similar frequency. However, the g-mode behaviour corresponds to an increase in the amplitude in the interior and hence in  $E_{nl}$ . At the avoided crossings there is an interchange of character between the two interacting modes. This is the case, for example, for the model fitting the observations; here the two modes both have a mixed character, with very similar mode inertia. These modes are connected by a dotted line in Fig. 7.64b; it is evident that their frequencies in fact lie roughly symmetrically around the expected p-mode asymptotic behaviour.

It should be noted in Fig. 7.65 that even when the  $l = 1$  modes have a predominant g-mode character, at the maxima of  $E_{nl}$ , their inertia is only larger by a moderate factor than for the neighbouring radial modes. Thus they would be expected to be excited to a comparable amplitude. This is a result of the rather narrow evanescent region between the p-mode propagation region in the envelope and the g-mode propagation region in the core for  $l = 1$  (*cf.* Fig. 7.72), giving rise to a strong coupling between the p- and g-mode behaviour, also reflected in the rather broad nature of the avoided crossings in Fig. 7.65. For  $l = 2$  and higher, on the other hand, the evanescent region is relatively broad and the coupling correspondingly weaker. As a result the avoided crossings are extremely narrow, and the inertia on the g-mode branch

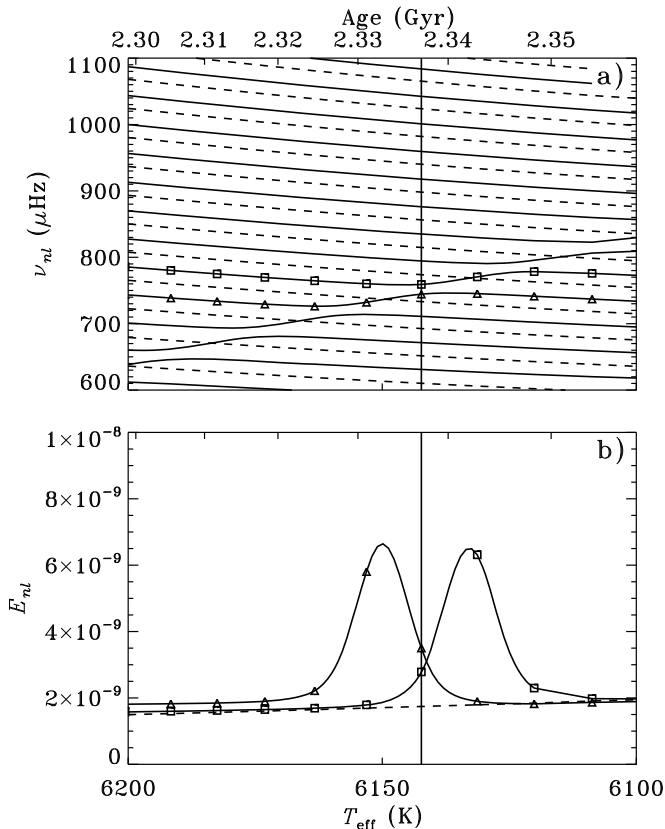


**Fig. 7.65.** (a) Evolution of adiabatic frequencies for a model of mass  $1.70 M_{\odot}$ . The lower abscissa shows the effective temperature  $T_{\text{eff}}$ , the upper abscissa the age of the model in Gyr. The dashed lines correspond to modes of degree  $l = 0$ , and the solid lines to  $l = 1$ . The vertical solid line indicates the location of the model whose frequencies are illustrated in Fig. 7.64. (b) The change with age in the normalized mode inertia (*cf.* Eq. (3.140)). The solid lines show modes with  $l = 1$ , each mode being indicated by triangles or squares as in panel (a), whereas the dashed line shows the radial mode with approximately the same frequency.

is higher, for  $l = 2$ , by around two orders of magnitude than for the radial modes. Thus it is very unlikely that such modes can be observed.

The p- and g-mode character of the modes is obviously reflected in the eigenfunctions (see also Fig. 3.26). From a diagnostic point of view a

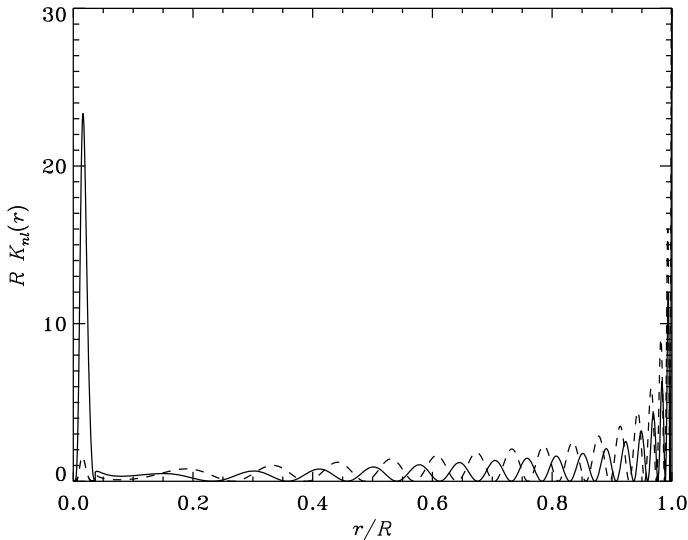


**Fig. 7.66.** Rotational kernels for spherically symmetric rotation (*cf.* Eq. (3.356)) for two modes with  $l = 1$  in the model illustrated in Fig. 7.64. The dashed line shows the mode with frequency  $711\,\mu\text{Hz}$ , with a maximum value of  $R K_{nl}$  of 54.7, very near the surface, and the solid line shows the mode with frequency  $744\,\mu\text{Hz}$ , with a maximum value 39.3.

particularly important aspect are the properties of the kernels relating the angular velocity to the rotational splitting (*cf.* Section 3.8.4). Examples of such kernels for  $l = 1$ , in the model illustrated in Fig. 7.64, are shown in Fig. 7.66. The mode with a frequency of  $711\,\mu\text{Hz}$  is predominantly an acoustic mode; as in the kernels illustrated in Fig. 3.39 the contribution to the rotational splitting comes predominantly from the outer regions of the star, with limited sensitivity to the core rotation. On the other hand, the mode at  $744\,\mu\text{Hz}$  is one of the modes undergoing an avoided crossing (*cf.* Fig. 7.65) with a mixed g- and p-mode character. Here the kernel has a substantial component in the core of the star; it contributes around 30% to the total integral of the kernel. Thus observation of the rotational splitting of such a mode, combined with data for the purely acoustic modes, would provide information about the core rotation. In fact, Lochard *et al.* (2004) considered the potential for rotational inversion based on simulated data for a similar model of  $\eta$  Boo and demonstrated that with realistic data from observations such as made with the CoRoT mission it should be possible to determine the angular velocity of the core of the star.

### 7.2.5 The Red Giant $\varepsilon$ Ophiuchi

#### 7.2.5.1 The Star

As already emphasized in Section 2.5.5 of Chapter 2, solar-like oscillations have been firmly established in only a few red giants so far. Here, we present the results for the star which has been studied most extensively in the published literature, both from an observational and modelling point of view. It is the red giant  $\varepsilon$  Oph (HD 146791), which is of spectral type G9.5III. Being a very bright star ( $V = 3.2$ ), it was included in numerous observational survey-type studies, leading to various estimates of its fundamental parameters and chemical composition, a summary of which can be found in De Ridder *et al.* (2006). This summary led to a range in effective temperature of  $4880 \pm 100$  K and in luminosity of  $59 \pm 5 L_\odot$ .

In addition to this, Richichi *et al.* (2005) provided a radius estimate of  $10.5 \pm 0.5 R_\odot$ , derived from interferometric data combined with the Hipparcos parallax. The star was again taken up more recently in a global high-resolution spectroscopy survey of numerous late G-type giants by Takeda *et al.* (2008). The stellar parameters derived by these authors are in excellent agreement with those deduced earlier and summarized by De Ridder *et al.* (2006), and as we will see below, from the seismology.

#### 7.2.5.2 The Data

Given that  $\varepsilon$  Oph is an equatorial star ( $\delta \simeq -04^\circ 41'$ ) with very narrow spectral lines due to a projected rotational velocity of only  $3.4 \pm 0.5 \text{ km s}^{-1}$  (De Ridder *et al.* 2006), it was considered to be a good prime target for a two-site high-precision spectroscopic campaign aimed at the discovery of solar-like oscillations in red giants. This campaign was set up using the CORALIE spectrograph attached to the 1.2-m Swiss Euler telescope at La Silla and the ELODIE spectrograph attached to the 1.9-m telescope at Haute Provence observatory. It led to the clear detection of solar-like oscillations in the star (De Ridder *et al.* 2006). A time series of 839 échelle spectra was gathered during 54 nights with a total time span of 75 d. The exposure time ranged from 180 s to 200 s, depending on the air mass. This led to a S/N ratio of at least 100 near 550 nm. At both telescopes and detectors, the spectrum of a thorium/argon calibration lamp was recorded simultaneously with the stellar spectrum through a second fibre, in order to guarantee a highly accurate wavelength calibration. We refer to De Ridder *et al.* (2006) for the details on the computation of the radial velocities. The finally adopted radial velocity values, as well as the power spectrum derived from them, were already shown in Fig. 2.43 of Chapter 2.

Following up on this detection, the star was taken up for a MOST run of 28 d. The adopted integration time was 7.5 s leading to a sampling time of 10 s. Due to the position of the star and the MOST satellite orbit, part of the

data was contaminated by scattered Earthshine. These points were deleted and led, in the end, to a duty cycle of 46% and gaps shorter than 87 min in the time series. For a description of the photometry data reduction, we refer to Barban *et al.* (2007) and to Kallinger *et al.* (2008b). The MOST data are shown in Fig. 7.67.

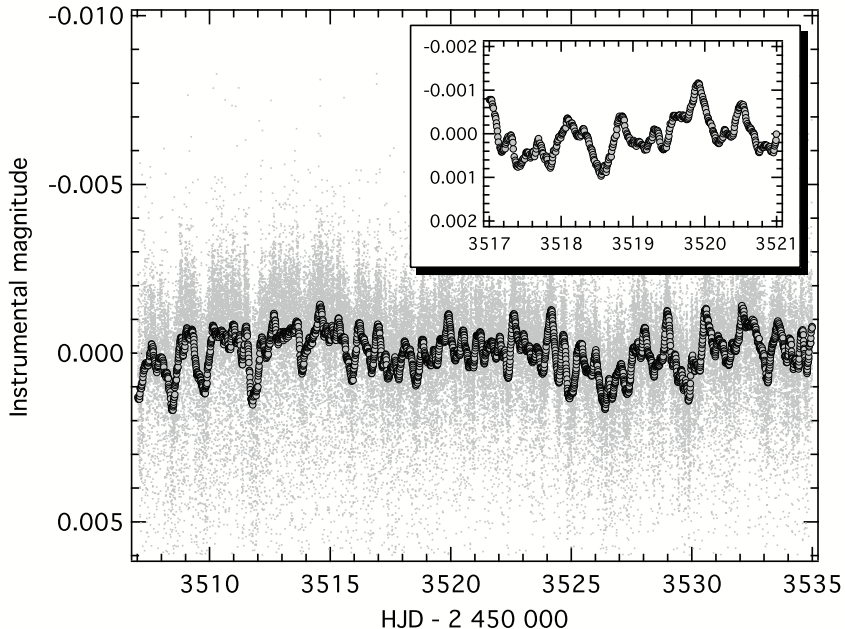


**Fig. 7.67.** MOST photometry of  $\varepsilon$  Oph (grey dots). The overplotted circles represent averages of the data over 10 min. From Kallinger *et al.* (2008b).

### 7.2.5.3 The Detected Modes

The power spectrum obtained by De Ridder *et al.* (2006, see Fig. 2.43) shows excess power between 20 and  $80\,\mu\text{Hz}$ , which is a range in agreement with expectations for solar-like p-mode oscillations for red giants. The amplitudes of the modes range from  $0.9$  to  $3.5\,\text{m s}^{-1}$ , which is compatible with the scaling law of Samadi *et al.* (2005) for the stellar parameters of  $\varepsilon$  Oph. The radial velocity power spectrum was used to compute autocorrelation functions and comb response functions. This led to two options for the large frequency separation of the star, *i.e.*  $\simeq 4.8\,\mu\text{Hz}$  or  $\simeq 6.7\,\mu\text{Hz}$  whose sum corresponds to  $\simeq 11.5\,\mu\text{Hz}$ , which represents the daily alias structure prominently present in the data despite the two-site nature of the data set.

The power spectrum of the space-based MOST data turned out to be fully compatible with the one of the ground-based radial velocity data and it is free from daily aliases (Barban *et al.* 2007). On the other hand, aliasing also occurs in that space-based data set due to gaps connected with the satellite orbit. These aliases occur at frequencies above the p-mode regime expected for the star and already found in the radial velocity data. The power spectrum of the MOST light curve is displayed in Fig. 7.68.

The autocorrelation of the power spectrum, computed from all frequency peaks between 25 and  $85\,\mu\text{Hz}$  with a power above  $3400\,\text{ppm}^2$ , is shown in Fig. 7.69. It clearly points to two features, near  $5\,\mu\text{Hz}$  and twice that value. This, along with the shape of the peaks in a smoothed power spectrum, was considered proof of the occurrence of stochastically-excited p modes. The derived large spacing amounts to  $5.3 \pm 0.1\,\mu\text{Hz}$  and is in agreement with one of the two estimates which were obtained from the ground-based radial velocities by De Ridder *et al.* (2006).

The power spectra obtained for three substrings of data indicated that some mode lifetimes must be shorter than 10 d. Power spectrum fitting led to seven secure frequencies with Lorentzian shape, with amplitudes ranging from 71 to 124 ppm and with a S/N level between 5.5 and 17.5 (Table 1 in Barban *et al.* 2007). Assuming the same mode lifetime for all detected frequencies, Barban *et al.* (2007) got a value near 2.7 d from the frequency fitting. This result is similar to the one obtained by Stello *et al.* (2004, 2006) for the pulsating red giant  $\xi$  Hya whose solar-like oscillations were established before those of  $\varepsilon$  Oph, also from CORALIE data (Frandsen *et al.* 2002) and were also interpreted in terms of radial modes. Such short mode lifetimes are typically a factor five to ten below those predicted by theory, *e.g.*, Houdek & Gough (2002), Houdek (2006, 2007).

#### 7.2.5.4 Seismic Modelling

The detected p-mode oscillations of  $\varepsilon$  Oph were modelled by three independent teams. De Ridder *et al.* (2006) used the CESAM evolution code (Morel 1997) to compute equilibrium models of stars in the shell-hydrogen burning phase that pass through the error box of the star. They adopted a metallicity of 0.012 and an initial hydrogen fraction of 0.72. For the details on the input physics, we refer to De Ridder *et al.* (2006). The authors further assumed that the observed mode frequencies correspond to radial modes following the theoretical predictions by Dziembowski *et al.* (2001a), despite the fact that Hekker *et al.* (2006) suggested from line profile variations that the dominant mode of  $\varepsilon$  Oph seems to behave as an  $l = 2$  mode rather than a radial mode. The model frequencies of the radial modes were used to compute the large separation, which was subsequently compared with the two candidate values derived from the observations. In this way, two groups of models whose radial modes fit the observed large separation were retained. Four such models, with

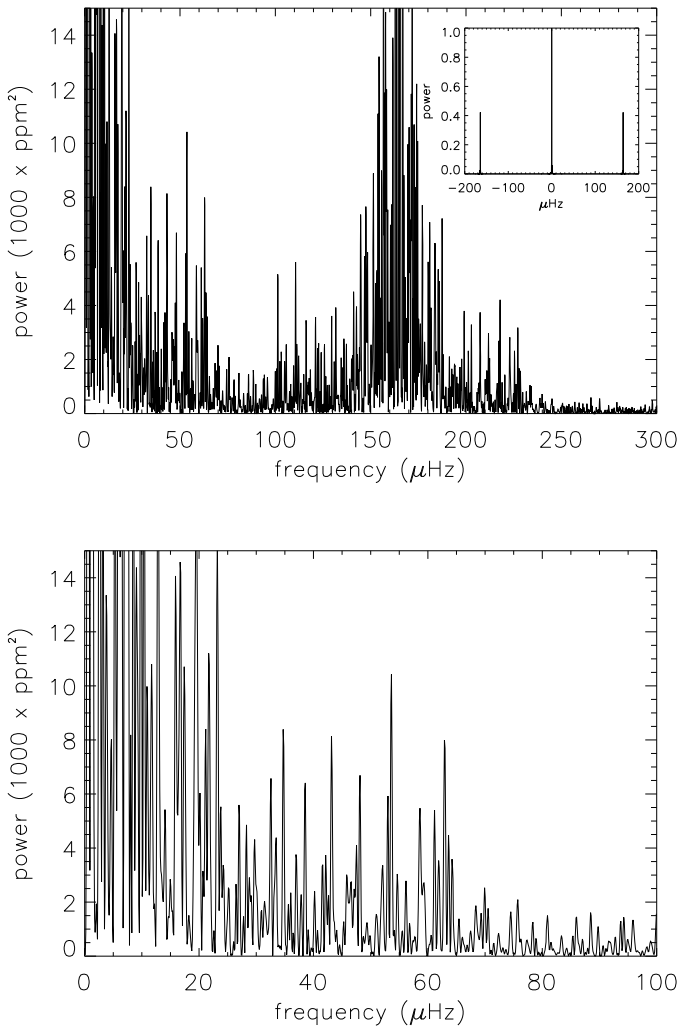


**Fig. 7.68.** Power spectrum of the MOST photometry of  $\varepsilon$  Oph. The inset in the upper panel shows the spectral window; note that in this panel the dominant power concentration around  $160\,\mu\text{Hz}$  results from aliasing of the low-frequency noise. The frequency region relevant to the expected solar-like oscillations is shown in the lower panel. From Barban *et al.* (2007).

initial masses of 1.9, 2.0, 2.7, and  $2.8\,\text{M}_\odot$ , are shown in Fig. 7.70. The lower-mass models were computed with a mixing-length parameter  $\alpha_{\text{ML}} = 1.8$  and led to a large separation near  $5\,\mu\text{Hz}$ , while the more massive models had a mixing-length parameter  $\alpha_{\text{ML}} = 1.6$  and led to a large spacing between 6 and

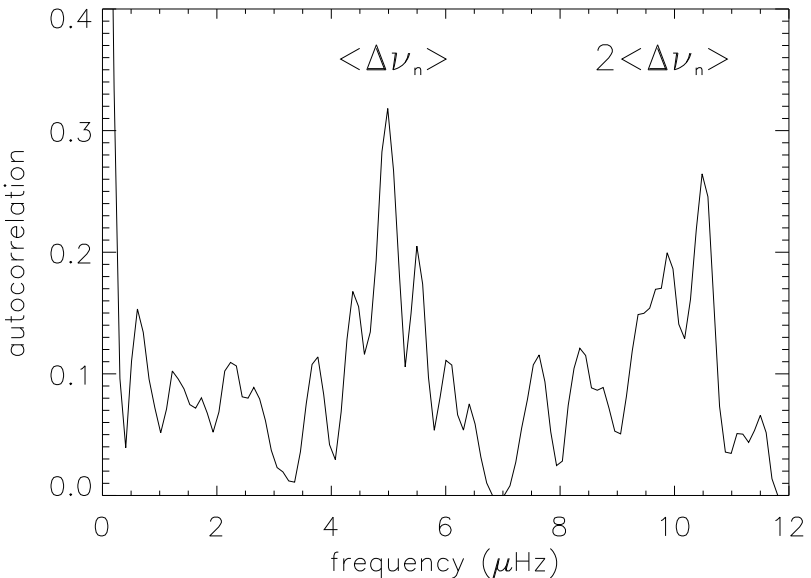


**Fig. 7.69.** Autocorrelation of the MOST power spectrum of  $\varepsilon$  Oph, computed from all frequency peaks with a S/N level above three in the interval  $[25, 85]$   $\mu$ Hz, corresponding to frequencies with power above  $3400$  ppm $^2$ . From Barban *et al.* (2007).

8  $\mu$ Hz. From the MOST data, Barban *et al.* (2007) resolved the ambiguity regarding the large separation and ruled out the more massive stellar models, resulting in a stellar mass near  $2 M_\odot$ .

An independent frequency determination and seismic analysis was performed by Kallinger *et al.* (2008b), based on both the radial velocity and MOST data. They provided a list of 59 frequencies derived from the MOST data, of which 21 were considered to be reliable enough for the modelling. Moreover, they derived 25 frequencies from the radial velocity data of De Ridder *et al.* (2006), of which 11 are in common with the MOST frequencies. Clearly, these authors were less stringent in their requirements to accept frequencies to be significant than the authors of the original data papers.

Kallinger *et al.* (2008b) further computed stellar models in the hydrogen-shell burning phase with the Yale Rotating Evolutionary Code YREC (Guenther *et al.* 1992). They adopted slightly different values for the input model parameters compared with the models by De Ridder *et al.* (2006), such as a metallicity of 0.010, an initial hydrogen fraction of 0.71 and a mixing-length parameter  $\alpha_{\text{ML}} = 1.74$ . Subsequently, an attempt was made to compute the oscillation modes of these models but this led to numerical instabilities due to strong fluctuations in the radial displacement of the modes near the dense

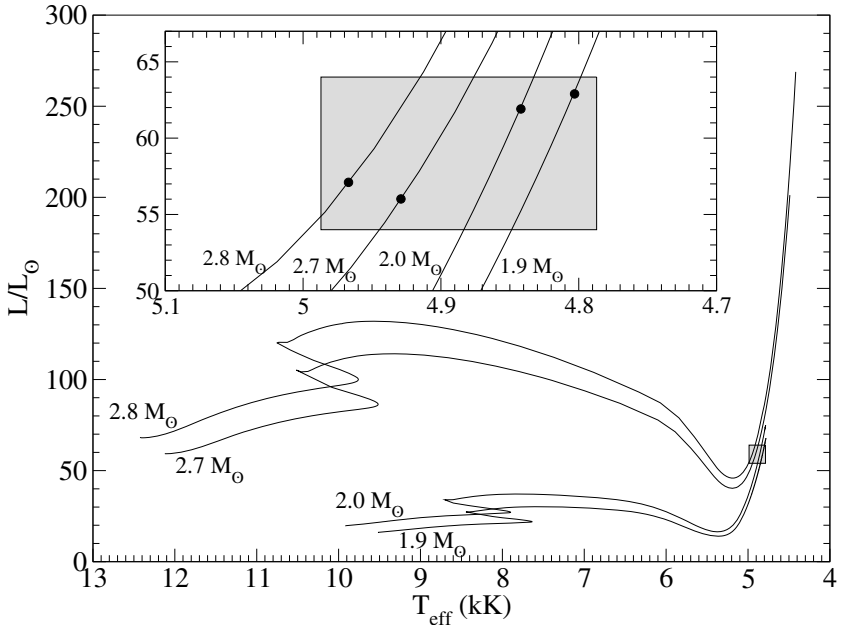


**Fig. 7.70.** The estimated position of  $\varepsilon$  Oph in the HR Diagram is indicated by the error box (enlarged version indicated in grey in the inset). Four evolutionary tracks from the ZAMS up to the ascending giant branch, computed with the CESAM code, are also indicated and labeled with their ZAMS masses. The high-mass models were computed with a low mixing-length parameter,  $\alpha_{\text{ML}} = 1.6$ , while the lower-mass models are for  $\alpha_{\text{ML}} = 1.8$ . The four dots in the inset mark the models whose measured large frequency separation of radial modes are in agreement with the two values of the large separation identified by De Ridder *et al.* (2006). Of these, the two more massive models are excluded by the MOST observations (Barban *et al.* 2007). From De Ridder *et al.* (2006).

stellar core. To solve this numerical problem, the authors artificially left out the stellar core in the models up to the inner 10% in radius and recomputed the modes and their frequencies, pointing out that this does not alter the frequency values seriously.

The most important difference with the treatments by De Ridder *et al.* (2006) and Barban *et al.* (2007), besides the treatment of the stellar core in the model computations, is that they dropped the assumption of dealing only with radial modes. Moreover, they fitted the frequency values rather than the large frequency separation, ignoring possible surface effects on the frequencies. In this way, they came up with a best seismic model which explains 18 of the 21 selected frequencies in terms of both radial and nonradial modes, with lifetimes between 10 and 20 d. Their best seismic model has a mass of  $2.02 M_{\odot}$ , an effective temperature of 4890 K, a luminosity of  $60 L_{\odot}$  and a radius of  $10.8 R_{\odot}$ . The dominant oscillation mode for this model, matching the observed

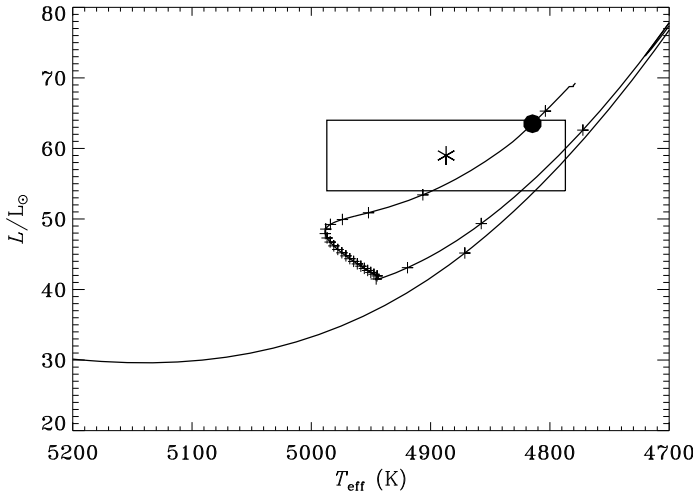


**Fig. 7.71.** Detail of the evolution track shown in Fig. 3.10, for a  $2.35 M_{\odot}$  model of  $\varepsilon$  Oph in the core helium-burning phase. Plusses are placed at 5 Myr intervals along the evolution track. The star and  $1-\sigma$  error box indicate the observed location of the star, and the filled circle marks the model identified as providing a reasonable fit to the observed large separation.

dominant frequency, is an  $l = 2$  mode which happens to be in agreement with the empirical mode identification from line profile variations (Hekker *et al.* 2006).

Liu *et al.* (2008) subsequently mixed the two previously published studies, by taking the frequencies from De Ridder *et al.* (2006) and Barban *et al.* (2007), and comparing the large frequency separation with the one of models computed with the Yale code. Their approach was somewhat different in that they studied how the variations of the input parameters of the models change the large frequency separation, again assuming radial modes. In this way, they arrived at ranges for the metallicity, mixing-length parameter, mass and age of the star which are basically in agreement with those of De Ridder *et al.* (2006).

While the seismic model of Kallinger *et al.* (2008b) seems to match all the classical observational constraints perfectly, it is based on a much more extended list of frequencies than those considered significant by De Ridder *et al.* (2006) and by Barban *et al.* (2007). Moreover, the Kallinger *et al.* (2008b) models do not have an appropriate treatment of the stellar interior, which may or may not be important in the frequency fitting. Also, it is normal that a better match between the detected and predicted oscillation frequencies is

found when all the degrees of the modes are left as a free parameter to fit the observed frequencies, compared with the case where one assumes only radial modes to fit the large frequency spacing. Exactly the same situation occurs for the seismic modelling of the pulsating subwarf B stars of which two case studies will be discussed later in this chapter. The validity of these different approaches for stellar modelling can in principle be evaluated from the application of empirical mode identification methods as described in Chapter 6, after adapting them to the case of low-amplitude stochastically excited modes with finite lifetime. The first step in this direction was made by Hekker *et al.* (2006), but it is fair to state that their methodology for spectroscopic mode identification needs to be further understood and developed before its results can be taken for granted and serve as input for seismic modelling.

The models considered above are all in the hydrogen shell-burning phase where the star is ascending the red-giant branch. In fact, it is much more likely that we are observing  $\varepsilon$  Oph in the core helium-burning stage, as this phase of evolution has a much longer time scale than the hydrogen-shell burning phase (see Fig. 3.10). The oscillation behaviour of a helium-burning model of  $\xi$  Hya was studied by Christensen-Dalsgaard (2004b). Here we consider a preliminary attempt at modelling  $\varepsilon$  Oph by such a model. Although further work is clearly required to make a complete fit to the data, the model illustrates the general properties of evolved stars with solar-like oscillations.

The models were computed with the ASTEC evolution code (Christensen-Dalsgaard 2008a). We assume the same metallicity,  $Z = 0.012$ , as De Ridder *et al.* (2006) and a hydrogen abundance  $X = 0.7$ . The mixing-length parameter was taken to be  $\alpha_{\text{ML}} = 1.6$ . The full evolution track was shown in Fig. 3.10, while Fig. 7.71 shows the last phases of evolution, including the loop associated with core helium burning. We have identified the model marked by a filled circle as generally consistent with the observed properties. The effective temperature and luminosity are within  $1\sigma$  of the observed values, as is the average large frequency separation  $\Delta\nu = 5.4\ \mu\text{Hz}$ . On the other hand, the radius,  $11.5 R_\odot$  is significantly larger than the interferometrically determined value. The model is close to the end of core helium burning, with a central helium abundance  $Y_c = 0.007$ ; consequently the evolution is relatively fast, as indicated in Fig. 7.71, although still far slower than during the ascending stage on the giant branch.

To investigate the oscillation properties of the model it is instructive to consider the characteristic acoustic and buoyancy frequencies, illustrated in Fig. 7.72. Also shown is a typical frequency for  $\varepsilon$  Oph. The most striking feature is the huge value of the buoyancy frequency in the core of the model. The convective core grows during central helium burning, leading to a discontinuity in the helium abundance and hence in the density, causing the spike in  $N$  at the edge of the convective core. Also, the very high degree of central condensation, with 15% of the mass concentrated in 0.3% of the radius, leads to a large gravitational acceleration in the core of the star and hence to a very large buoyancy frequency (*cf.* Eq. (3.180)). Thus nonradial modes at all fre-

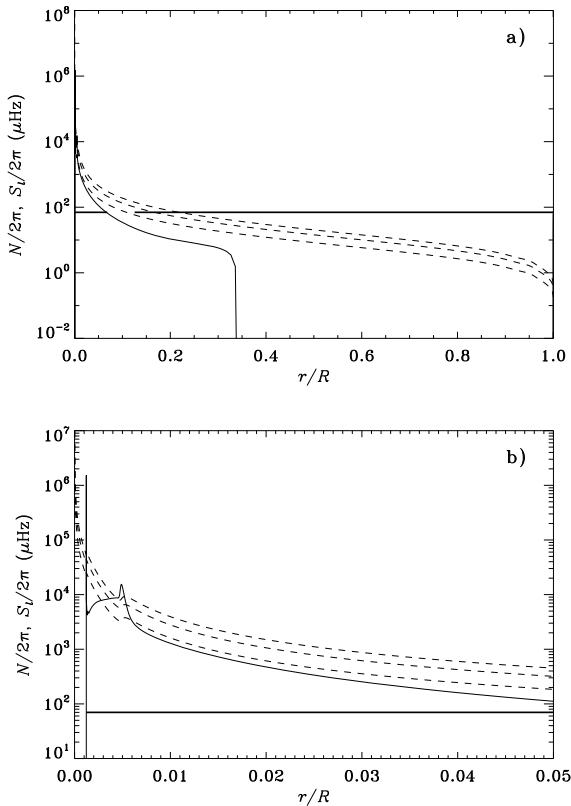


**Fig. 7.72.** Characteristic frequencies for the model, marked in Fig. 7.71, of  $\varepsilon$  Oph in the core helium-burning phase. The solid curve shows the buoyancy frequency  $N/2\pi$  and the dashed curves show the characteristic acoustic frequencies  $S_l$  (*cf.* Eq. (3.153)) for  $l = 1, 2, 3$ . The bold horizontal line indicates the trapping regions for a typical mode of  $\varepsilon$  Oph, for  $l = 1$ . Panel b) shows the core of the model; note the spike in  $N$  at the edge of the convective core, arising because of the discontinuity of the helium abundance, and the local maximum at  $r \simeq 0.05R$ , corresponding to the strong gradient in the hydrogen abundance at the outer edge of the helium core and in the hydrogen shell source.

quencies in the range of stochastically excited modes, up to the atmospheric acoustic cut-off frequency, have the character of mixed modes, with a rapidly varying g-mode behaviour of the eigenfunctions in the core. In the outer parts of the model, where the frequencies are above the acoustic frequency  $S_l$ , the modes obviously behave as acoustic modes.

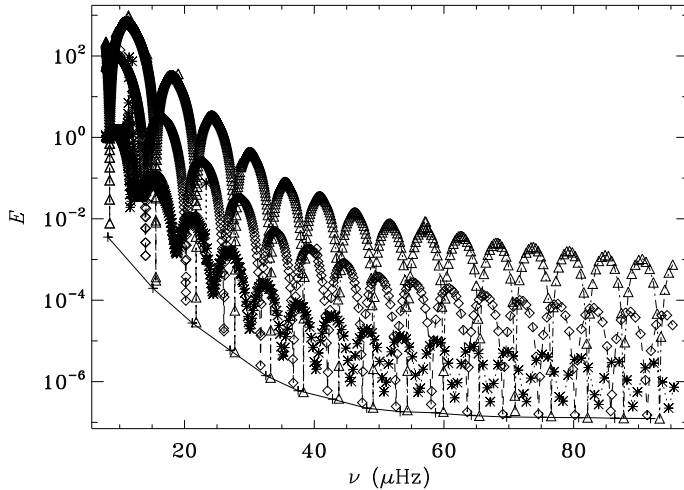


**Fig. 7.73.** Normalized mode inertia (*cf.* Eq. (3.140)) for the model of  $\varepsilon$  Oph indicated in Fig. 7.71. The modes shown are for  $l = 0$  (crosses connected by a continuous curve),  $l = 1$  (stars connected by a dotted curve),  $l = 2$  (diamonds connected by a dashed curve) and  $l = 3$  (triangles connected by a dot-dashed curve).

To illustrate these oscillation properties, we have computed full spectra of modes for  $l = 0–3$  in the model of  $\varepsilon$  Oph, using ADIPLS (Christensen-Dalsgaard 2008b). To resolve the rapid variation of the eigenfunctions, 9600 meshpoints were used in the computation, mainly located in the core but with a sufficient number of points to resolve also the acoustic behaviour in the outer parts of the model. The dense spectrum of nonradial modes and their mixed nature are reflected in the behaviour of the normalized mode inertia (*cf.* Eq. (3.140)), shown in Fig. 7.73 (see also Dziembowski *et al.* 2001a). For the radial modes the inertia decreases with increasing frequency. The nonradial modes, on the other hand, are in most cases predominantly trapped in the core, with large inertia; the inertia increases with  $l$  as a result of the increasing width of the evanescent region where the frequency is between  $N$  and  $S_l$  (see Fig. 7.72). However, at certain frequencies the mode resonates with the acoustic cavity in the outer parts of the star, such that the eigenfunction decreases with increasing depth in the evanescent region. At such frequencies the eigenfunction is small in the core and the mode inertia approaches the value for the nearby radial modes. The location of these resonances largely corresponds to the asymptotic properties of the acoustic modes, giving rise to

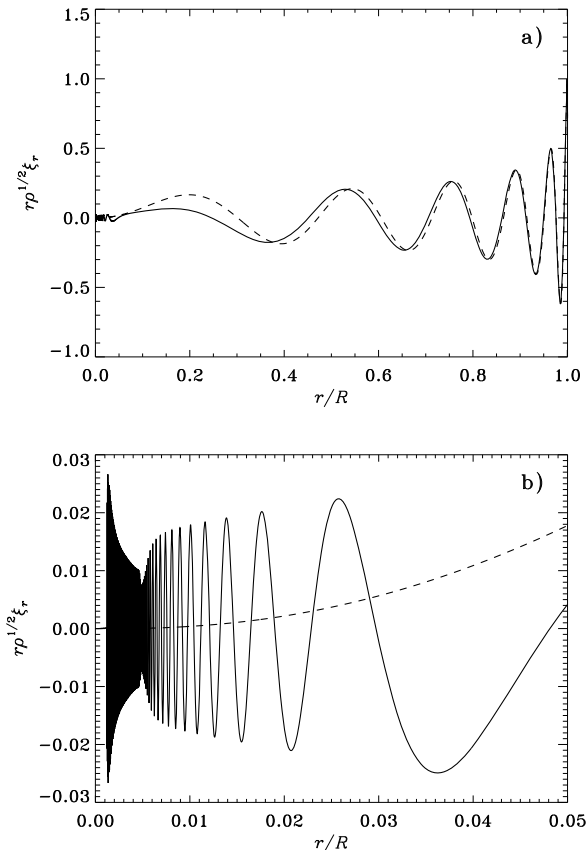


**Fig. 7.74.** Scaled radial displacement for two modes in the model of  $\varepsilon$  Oph marked in Fig. 7.71. The dashed curve shows a mode with  $l = 0$ ,  $\nu = 64.2 \mu\text{Hz}$ ,  $E = 1.48 \times 10^{-7}$  and the solid curve a mode with  $l = 2$ ,  $\nu = 63.6 \mu\text{Hz}$ ,  $E = 1.80 \times 10^{-7}$ . Panel b) shows a blow-up of the behaviour in the core.

a spectrum of low-inertia acoustic modes corresponding to the simple p-mode asymptotic expression for the frequencies, Eq. (3.216).

These properties are further illustrated in Fig. 7.74, showing eigenfunctions of two neighbouring modes with  $l = 0$  and 2, the latter resonating with the acoustic cavity outside  $S_2$  and with an only slightly higher inertia than for the radial mode. In the stellar envelope the eigenfunctions are very similar. However, as shown in panel (b), in the core the eigenfunction of the  $l = 2$  mode

is rapidly oscillating, to such an extent that the variation is not resolved in the figure.<sup>46</sup>

The effects of these properties of the oscillations on the excitation of the modes are somewhat unclear. The rapidly varying eigenfunctions in the core of the nonradial modes undoubtedly lead to strong damping, and thus the damping rates of these modes might be expected to be somewhat larger than for the radial modes at similar frequency, although the importance of this effect is not clear. It has led to the assumption that the spectrum would be dominated by radial modes; this assumption underlies both the model fit of De Ridder *et al.* (2006) and the fit presented in Fig. 7.71, since the observed large separation is taken to correspond to modes of a given degree, rather than half that value. Assuming the presence in the data of just radial modes also provided a reasonable interpretation of the observations of  $\xi$  Hya (Frandsen *et al.* 2002). On the other hand, the larger inertia leads to a lower damping rate; as discussed in Section 3.7.5, a result of this may be that the height of the peaks in the power spectrum, and hence the visibility of the modes, is independent of the mode inertia, such that a very dense spectrum of peaks might be expected. This, however, assumes that the observing time is sufficiently long to resolve the peaks; if not, the peak height is inversely proportional to the inertia (see also the interpolation formula in Eq. (3.310)). Dupret *et al.* (2009) presented a detailed discussion of these issues, which are clearly crucial for the interpretation of observations of solar-like oscillations in red giants.

We come to the conclusion that the global properties and pulsation characteristics of pulsating red giants can be explained by present day stellar structure models along the ascending giant branch or in the core helium-burning phase. However, a far better understanding of the theory of oscillations in such objects is needed before precise seismic inferences about their interior structure parameters can be derived with a high level of confidence. Moreover, the ambiguity in the derived oscillation frequencies of these stars must be resolved from far better data before real progress can be made in the asteroseismology of these evolved stars. Given that the CoRoT mission has red giant stars among its prime asteroseismology targets, we expect a serious step forward in the understanding of stellar structure models of evolved stars of low mass in the very near future.

---

<sup>46</sup> The computation did fully resolve the behaviour in this region, showing that the eigenfunction has around 160 zeros for  $r \leq 0.05R$ .

## 7.3 Heat Driven Main Sequence Stars

### 7.3.1 The $\beta$ Cep Star V836 Centauri

#### 7.3.1.1 The Star

The star V836 Cen (HD 129929) is of spectral type B3V and has  $V = 8.1$ . It is situated at intermediate galactic latitude ( $b = 20.21^\circ$ , Hill *et al.* 1974), which is unusual for such a massive object. This is the reason why Rufener (1981) included it in the Geneva database as a standard star, which led him to discover its variability. The parallax of V836 Cen measured by Hipparcos is  $\pi = 1.48 \pm 1.03$  mas which corresponds to a distance estimate of 676 pc. This value leads to a distance of 233 pc perpendicular to the Galactic plane, which is less than half the value derived earlier from multicolour photometry by Waelkens & Rufener (1983), and requires a mean vertical velocity of only some  $13 \text{ km s}^{-1}$ . The spectrum taken by Aerts *et al.* (2004d) leads to a radial velocity of  $64 \pm 1 \text{ km s}^{-1}$ , with a velocity component of  $22 \text{ km s}^{-1}$  perpendicular to the Galactic plane. This is largely sufficient to bring the star to its current position and suggests that it was kicked out of the Galactic plane, rather than having formed outside of it. It must have been kicked when it was about 10 million years old, if we assume that it has moved with constant speed ever since.

Waelkens & Rufener (1983) made the first detailed study of the variability of V836 Cen by means of Geneva photometry and found the star to vary with three frequencies:  $6.460965$ ,  $6.979940$  and  $6.449041 \text{ d}^{-1}$ . The amplitudes of these three frequencies were found to range between 10 to 18 mmag. The star was hence classified as a new  $\beta$  Cep star. Heyderickx (1992) also established three frequencies in a more extensive dataset that included the one used by Waelkens & Rufener (1983). Only two of these three are in common with those found by Waelkens & Rufener (1983) and, moreover, the values he lists are slightly different:  $6.98670$ ,  $6.45610$  and  $6.97697 \text{ d}^{-1}$ .

With such closely spaced frequencies, V836 Cen was judged to be a very interesting massive pulsating star on which to try to perform seismic modelling, once the dominant frequencies could be firmly established and the modes well identified. This goal was achieved by Aerts *et al.* (2003b) from a single-site, single-instrument photometric data set covering 21 yr. We discuss here the extensive study performed for this star and reported in the papers Aerts *et al.* (2003b, 2004d), Dupret *et al.* (2004), and Thoul *et al.* (2004). V836 Cen was the first  $\beta$  Cep star for which sufficient independent oscillation frequencies were detected to exclude stellar models without convective core overshooting. Moreover, it was the first main sequence star besides the Sun for which non-rigid internal rotation was established from two rotationally split multiplets.

### 7.3.1.2 The Data

In an effort to resolve and understand the discrepant frequency determinations by Heynderickx (1992) and Waelkens & Rufener (1983), V836 Cen was kept in the long term programme of photometric monitoring of variable B stars of the Institute of Astronomy of Leuven University. This programme was performed with the privately owned 0.7-m Swiss telescope at La Silla observatory in Chile. The telescope was equipped with the 7-passband Geneva photometer P7, which is a two-channel photometer for quasi-simultaneous band measurements. The first channel (A) is centred on the star while the second channel (B) is centred on the sky. The position angle of the sky can be changed by turning a derotator, while changing the distance between both channels needs manual interaction. The filter wheel turns at 4 Hz and a chopper directs both channels alternatively to the photomultiplier. As such, the photomultiplier measures both beams A and B through the seven filters four times each second.

The strategy for performing the observations was oriented towards obtaining high precision photometry. In order to achieve this, stars were measured within a range of 0.1 in airmass  $F_z \in [1.0; 1.1]$  for nights of good, but not superb, atmospheric conditions. For the reduction process this type of observing nights, typically two or three standard stars of different colour were observed each hour. When the atmospheric conditions were excellent, the strategy of a so-called “M&D” night (“étoile montante et étoile descendante”) was adopted (Rufener 1986). The determination of the extinction coefficients was done according to the method outlined in Burki *et al.* (1995).

Many members of the Leuven team gathered multicolour photometry of V836 Cen during numerous three-week observing runs. This led to 1493 good quality data 7-colour points with a total time base of 21.2 yr. The telescope was closed in 1997; after that, all the  $\sim 345\,000$  P7 data points of the more than 45 000 different stars underwent a global reduction for which a weight was assigned to all the measurements according to each star’s dispersion in the  $V$  band. This resulted in measurements with a typical individual point-to-point error between 2 and 5 mmag for V836 Cen.

In order to confirm the important seismic result that the star exhibits non-rigid rotation with a very low equatorial rotation velocity of some  $2\,\text{km}\,\text{s}^{-1}$  (Aerts *et al.* 2003b), a result based purely on photometry and seismic modelling, Aerts *et al.* (2004d) assembled one high resolution (wavelength step of  $0.0298\text{\AA}$ ) échelle spectrum of V836 Cen with the FEROS spectrograph attached to the ESO 2.2-m telescope. The spectrum revealed, indeed, a sharp lined star, with an upper limit of some  $17\,\text{km}\,\text{s}^{-1}$  for the overall (thermal, pulsational, and rotational) line broadening of the star. Taking into account the thermal broadening of a B3V star (some  $8\,\text{km}\,\text{s}^{-1}$ ) and the fact that considerable pulsational broadening must occur, this single spectrum provided independent *a posteriori* evidence for the slow rotation of the star, which had already been deduced seismically by Aerts *et al.* (2003b).

### 7.3.1.3 The Detected Modes

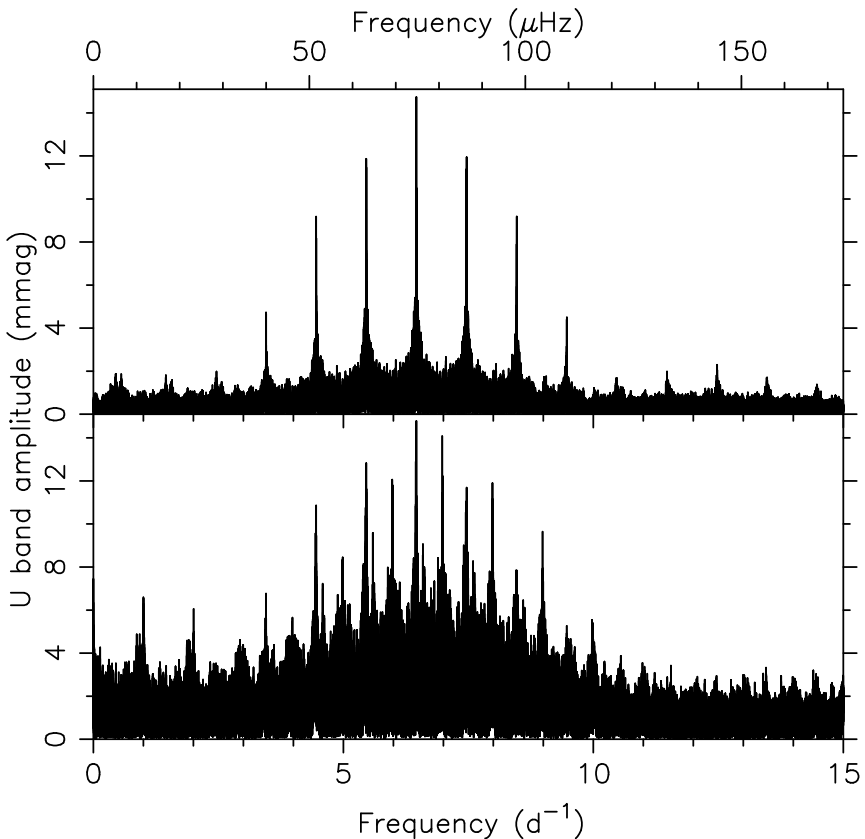


**Fig. 7.75.** Scargle periodogram (bottom) for the Geneva  $U$  data of V836 Cen published in Aerts *et al.* (2003b). The top panel is the Scargle periodogram of a noise free sinusoid with the observed dominant frequency and its amplitude, sampled at the times of the observations.

The seemingly discrepant results for the oscillation frequencies obtained by Waelkens & Rufener (1983) and Heynderickx (1992) were reconciled by Aerts *et al.* (2003b) by doubling the data set in number of measurements and in time span, which gave sufficient frequency resolution to resolve the modes. The Scargle periodogram of the data, as well as the one of a noise free sinusoid with the dominant frequency and its amplitude, are represented in Fig. 7.75. It can easily be seen that we are dealing with a multiperiodic star, even though the daily alias pattern due to the single site nature of the data is apparent. A yearly alias pattern was also readily found in the frequency analysis, as expected for data that cover so many seasons.

**Table 7.3.** Detected frequencies for V836 Cen and their significance level in the  $U$  and  $V$  bands (denoted as  $\sigma_U$  and  $\sigma_V$ ). The precision is better than  $10^{-6} \text{ d}^{-1}$  for all frequencies. The significance levels were computed over the frequency range  $[5, 10] \text{ d}^{-1}$  after prewhitening with the frequencies  $\nu_1, \dots, \nu_6$ . Table produced from Aerts *et al.* (2004d).

Oscillation Frequencies	$\sigma_U$	$\sigma_V$	Frequency Splittings
$\nu_1 = 6.461699 \text{ d}^{-1}$	14.7	16.8	
$\nu_2 = 6.978305 \text{ d}^{-1}$	14.9	14.6	
$\nu_3 = 6.449590 \text{ d}^{-1}$	11.7	12.9	
$\nu_4 = 6.990431 \text{ d}^{-1}$	11.6	10.6	$\nu_1 - \nu_3 = 0.012109 \text{ d}^{-1}$
$\nu_5 = 6.590940 \text{ d}^{-1}$	9.4	7.0	$\nu_4 - \nu_2 = 0.012126 \text{ d}^{-1}$
$\nu_6 = 6.966172 \text{ d}^{-1}$	7.6	6.8	$\nu_2 - \nu_6 = 0.012133 \text{ d}^{-1}$

In total, six oscillation frequencies were retained from the P7 photometry. These are listed in Table 7.3, together with their significance level in the  $U$  and  $V$  bands. They are shown schematically in Fig. 7.76. The frequency uncertainty  $\sigma_\nu$  computed according to Eqs (5.52) amounts to about  $10^{-6} \text{ d}^{-1}$  for  $\nu_6$  and is a factor of 10 lower for the higher amplitude modes. The significance levels  $\sigma_U$  and  $\sigma_V$  were computed from the Scargle periodogram – over the frequency interval  $[5, 10] \text{ d}^{-1}$  – of the residuals after prewhitening the light curves with the six frequencies. V836 Cen was the first pulsating B star for which *more than one multiplet* had been found. The differences in spacing in the two multiplets are also listed in Table 7.3 and will be explored below to test the rigidity of the rotation.

The full details of the frequency analysis in the seven bands are described in Aerts *et al.* (2004d) and are omitted here. We do point out that the authors were very conservative in that only frequencies with significance levels  $\sigma_U$  and  $\sigma_V$  above 6 in all 7 bands were retained. Other frequencies occurred after prewhitening with  $\nu_1, \dots, \nu_6$ , even at significance levels above 4 in the  $U$  band, but these candidate frequencies reached a level of significance only between 3 and 4 in the other wavelength bands. For safety, they were omitted in the modelling by the authors. The amplitudes of the six frequencies in the seven bands are listed in Table 7.4. The variance reductions for these fits range from 60% to 66%, indicating the likely presence of additional low amplitude modes.

### 7.3.1.4 Mode Identification and Seismic Modelling

Stars of spectral type B along the main sequence have a rather simple stellar structure, with a convective core and a radiative envelope. Their simplest standard models constitute a five dimensional parameter space: the initial hydrogen abundance  $X$ , the core convective overshooting parameter  $\alpha_{\text{ov}}$  expressed in units of the local pressure scale height  $H_p$  and usually based on the

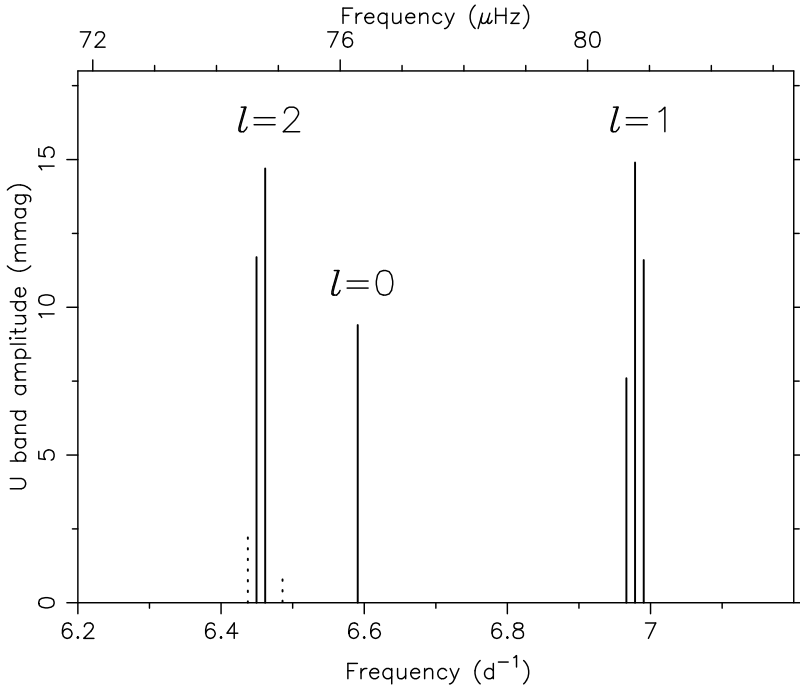


**Fig. 7.76.** Schematic amplitude spectrum for the Geneva  $U$  data of V836 Cen, reproduced from Aerts *et al.* (2004d). The two dotted lines indicate frequency components which are present in the data, but at too low of a significance level; they fit into a quintuplet structure.

time independent mixing-length theory of convection, the metallicity  $Z$ , the mass  $M$  and the central hydrogen abundance  $X_c$  which is related to the age and also to the observed  $T_{\text{eff}}$ . We point out that the mixing-length parameter  $\alpha_{\text{MLT}}$  is usually fixed to the solar value; for B stars, with their extremely thin and inefficient outer convection zones, changing  $\alpha_{\text{MLT}}$  within reasonable limits does not change the characteristics of the models.

As in the case of V836 Cen, the parallaxes of B stars are in general very uncertain, implying that the luminosity cannot be derived with appropriate precision. Moreover, estimates of  $\log g$  are relatively inaccurate with uncertainties typically as large as 0.5 dex from photometric indices and between 0.1 and 0.2 dex from high-resolution spectroscopy (*e.g.*, Morel *et al.* 2006). This is why constraints on these two fundamental parameters are sometimes ignored when modelling such stars, or the parameters are at least allowed to vary within the  $2\sigma$  estimates from photometry.

As a general strategy for the modelling of B stars, one usually fixes  $X$  in the first stage because changing  $X$  is equivalent to changing the metallicity  $Z$  for fitting the frequencies (Ausseloo *et al.* 2004). For each stellar model,

**Table 7.4.** Results of harmonic fits to the Geneva light curves of V836 Cen for the six significant frequencies.  $A_k$  stands for the amplitude of the mode with frequency  $\nu_k$ , expressed in mmag, and  $\delta_k$  for its phase, expressed in units of  $2\pi$  radians. The errors of the amplitudes and phases are given between brackets, in units of the last decimals. Table reproduced from Aerts *et al.* (2004d).

$\nu$		$U$	$B_1$	$B$	$B_2$	$V_1$	$V$	$G$
$\nu_1$	$A_1$	14.7(6)	12.2(5)	12.1(5)	11.7(5)	11.4(5)	11.8(4)	11.6(5)
	$\delta_1$	0.538(5)	0.537(4)	0.536(4)	0.534(5)	0.535(4)	0.539(4)	0.536(5)
$\nu_2$	$A_2$	14.9(8)	11.0(6)	11.0(6)	10.8(6)	10.3(6)	10.3(5)	10.2(6)
	$\delta_2$	0.755(7)	0.755(7)	0.757(7)	0.754(7)	0.748(7)	0.754(6)	0.756(7)
$\nu_3$	$A_3$	11.7(6)	10.0(5)	9.8(4)	9.8(4)	9.2(4)	9.1(4)	9.0(4)
	$\delta_3$	0.178(4)	0.180(3)	0.181(3)	0.190(4)	0.185(4)	0.182(3)	0.182(4)
$\nu_4$	$A_4$	11.6(8)	8.4(6)	8.5(6)	7.6(6)	7.6(5)	7.5(5)	7.7(6)
	$\delta_4$	0.207(6)	0.205(6)	0.211(6)	0.206(6)	0.202(6)	0.204(6)	0.207(7)
$\nu_5$	$A_5$	9.4(8)	6.0(6)	5.5(6)	5.3(6)	5.2(6)	4.9(5)	4.8(6)
	$\delta_5$	0.324(13)	0.337(16)	0.340(17)	0.345(18)	0.334(17)	0.346(17)	0.349(20)
$\nu_6$	$A_6$	7.6(6)	5.5(5)	5.5(5)	5.0(5)	4.8(4)	4.8(5)	4.8(5)
	$\delta_6$	0.254(13)	0.248(13)	0.253(13)	0.246(14)	0.249(14)	0.264(15)	0.240(14)

the theoretical frequency spectrum of low order p and g modes is calculated and compared with the observed values of identified modes. The modelling is commonly started by fixing values for the stellar parameters ( $X$ ,  $\alpha_{\text{ov}}$ ) and calculating evolutionary tracks for different masses and metallicity. For each evolutionary track, one then selects the model, thereby fixing the age, that fits the dominant oscillation mode, leading to a value for the mass and metallicity of the star, for the assumed  $X$  and  $\alpha_{\text{ov}}$ . One thus performs a mapping between the 2D ( $X$ ,  $\alpha_{\text{ov}}$ ) parameter space and the 3D ( $Z$ ,  $M$ , age) space. When fitting two frequencies, *e.g.*, one can perform a mapping between the 3D ( $X$ ,  $\alpha_{\text{ov}}$ ,  $Z$ ) parameter space and the 2D ( $M$ , age) space. This yields a mass – metallicity relation for each considered ( $X$ ,  $\alpha_{\text{ov}}$ ), *etc.* Depending on whether or not the detected frequencies probe different regions of the stellar interior, one thus sets strong constraints on the five parameters ( $X$ ,  $\alpha_{\text{ov}}$ ,  $Z$ ,  $X_c$ ,  $M$ ) from only a few securely identified modes.

The above approach was applied to V836 Cen by Aerts *et al.* (2003b) and Dupret *et al.* (2004), after the empirical mode identification of the six detected frequencies. The two frequency multiplets led the authors to suspect that the modes concerned triplets or quintuplets, but, nevertheless, an independent identification from the amplitude ratios was done. The results of this are shown in Fig. 7.77, where the observed amplitude ratios with respect to the Geneva  $U$  band are compared with those derived from the pulsational properties of evolutionary models that pass through the error box in ( $\log T_{\text{eff}}$ ,  $\log g$ ) derived

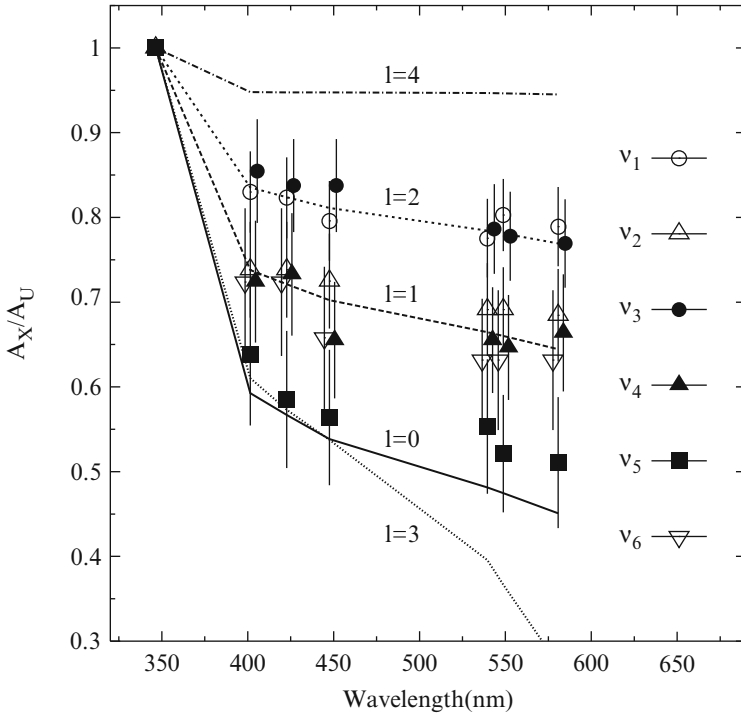


**Fig. 7.77.** The observed amplitude ratios with respect to the  $U$  band derived from the Geneva data of V836 Cen for the six detected frequencies are compared with those predicted from evolutionary models for appropriate stellar parameters. Adapted from Dupret *et al.* (2004).

from the average Geneva colours by Aerts *et al.* (2004d). The results were the same irrespective of the model chosen within the error box. It is seen that the empirical mode identification confirms the results suspected from the multiplet structure, *i.e.*, we are dealing with three independent  $m = 0$  components and three other multiplet components. In particular, the identification of the radial mode was important for the seismic modelling of the star (see Fig. 7.78).

The frequencies  $\nu_2$  and  $\nu_5$  belong to an  $l = 1, m = 0$  and a radial mode, respectively. These were used to derive the mass – metallicity relations for the star, for each  $X$  and  $\alpha_{\text{ov}}$ . The result is shown in Fig. 7.79 for the input physics adopted by Dupret *et al.* (2004).

As explained in Chapter 6, multicolour photometry does not allow the estimation of the  $m$ -value of the modes. From Fig. 7.76, we are thus left with four possibilities for the  $m$ -value of the dominant  $l = 2$  component belonging to  $\nu_1$ . The consequences of this are graphically depicted in Fig. 7.80,

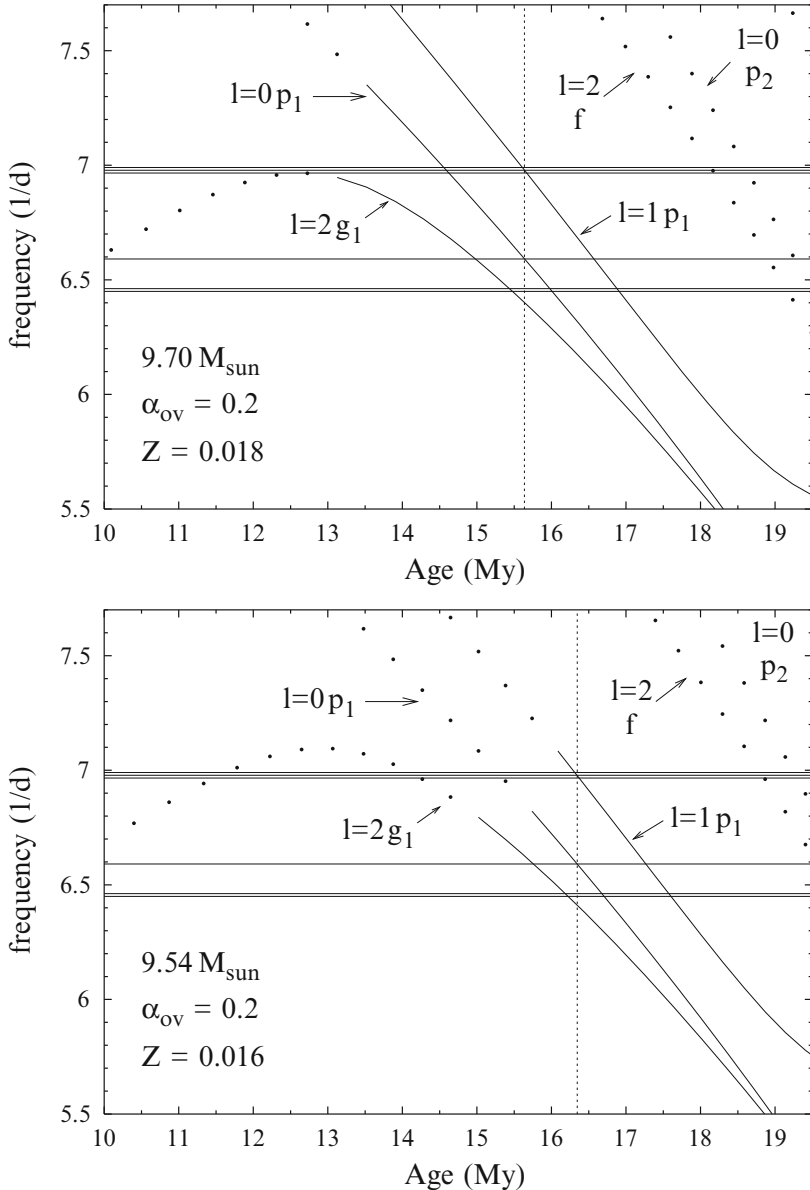


**Fig. 7.78.** Evolution of frequencies as a function of age (expressed in million years), for modes of degree  $l = 0, 1$  and  $2$ , for two evolutionary tracks with  $M = 9.54 M_{\odot}$ ,  $Z = 0.016$  and  $\alpha_{ov} = 0.2$  (bottom panel) and with  $M = 9.70 M_{\odot}$ ,  $Z = 0.018$  and  $\alpha_{ov} = 0.2$  (top panel). The horizontal lines correspond to the observed frequencies of V836 Cen. The vertical lines correspond to the models giving the best fit between the theoretical and observed frequencies of the modes ( $l = 0$ , p<sub>1</sub>), ( $l = 2$ , g<sub>1</sub>) and ( $l = 1$ , p<sub>1</sub>). The full lines correspond to the unstable modes and the dots to the stable ones. Adapted from Dupret *et al.* (2004).

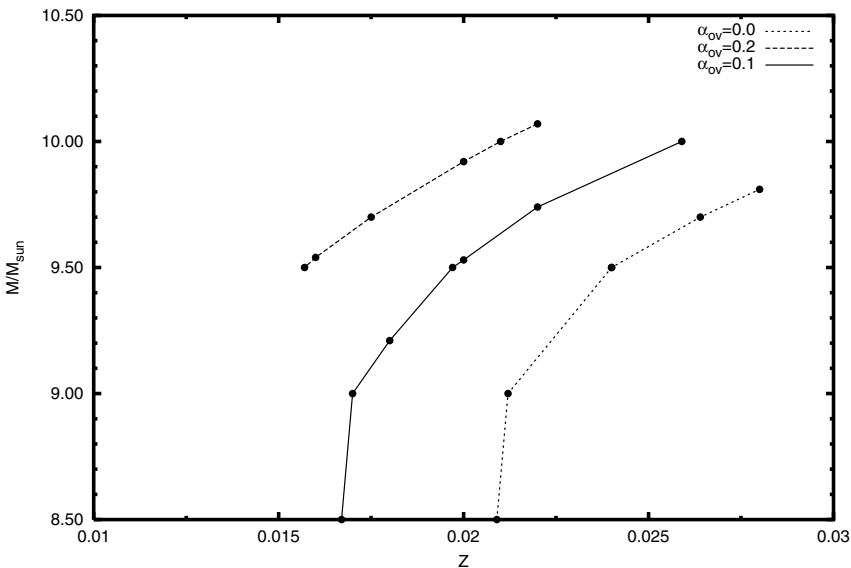


**Fig. 7.79.** Relation between the mass and the metallicity for models which fit the frequencies  $\nu_2$  and  $\nu_5$  of V836 Cen, for three families of models with different values of the core overshooting parameter:  $\alpha_{\text{ov}} = 0.0, 0.1$  and  $0.2$ . For all these models,  $X = 0.70$ . Adapted from Dupret *et al.* (2004).

for different values of the core overshooting parameter and for values of  $Z$  which are acceptable according to the observed amplitude ratios and their errors (see Dupret *et al.* (2004) for a discussion on how the observed ratios allow to derive a limitation of the  $Z$ -range). Fig. 7.80 leads to the conclusion that  $\alpha_{\text{ov}}$  cannot be 0.0 nor 0.2, irrespective of the  $m$ -value of  $\nu_1$  and  $\nu_3$ . We thus come to the conclusion that  $\alpha_{\text{ov}} = 0.10 \pm 0.05$  for V836 Cen. If we assume that  $m_1 = 0$ , as is the case if we accept the presence of the low amplitude peaks indicated as dotted lines in Fig. 7.76, then the fitting of  $\nu_1$ ,  $\nu_2$  and  $\nu_5$  leads to a narrow acceptable range in mass as shown in the right panel of Fig. 7.80, *i.e.*,  $M = 9.3 \pm 0.1 M_{\odot}$ .

The reason why we can derive the core overshooting (and also the internal rotation – see below), and provide a quantitative measure of these parameters for V836 Cen, is the different probing ability of the detected oscillation modes. As explained in Chapter 3, different types of probing kernels are used, depending on the kind of behaviour under investigation. This is illustrated in Fig. 7.81, where we show the rotational kernels  $K(x)$  as a function of the radial distance inside the star ( $x = r/R$ ) for the three modes of V836 Cen. It can be seen that the kernels of the three modes behave differently near the boundary of the core region, and thus probe that region in a different way, allowing the tuning of the core overshoot region as well as the derivation of

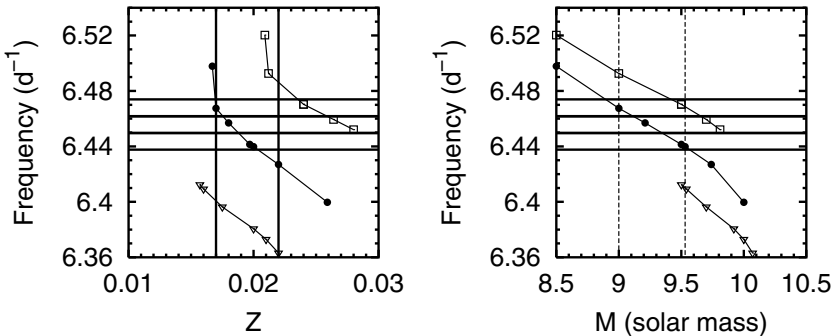


**Fig. 7.80.** Left panel: frequency of the  $l = 2$ ,  $g_1$  axisymmetric mode, as a function of metallicity. The theoretical results obtained for models fitting exactly  $\nu_2$  and  $\nu_5$  are represented by squares, circles and triangles for models with  $\alpha_{ov} = 0.0$ , 0.1 and 0.2, respectively. The four possible values for the observed frequency of this mode are given by horizontal lines. The two vertical lines represent the limits of the allowed range for the metallicity derived from the confrontation of the observed amplitude ratios and those predicted by models. Right panel: the relation for the allowed solution is exported as a mass relation, using the  $(M, Z)$ -relations shown in Fig. 7.79. Adapted from Dupret *et al.* (2004).

the rotational properties, as will be explained below. It is remarkable that the frequencies of just three well identified oscillation modes that have sufficiently different kernels allow one to derive the overshooting parameter with a precision of typically 0.05 expressed in  $H_p$ . Adding just a few better-identified modes should drastically reduce this error for specific input physics of the models.

The  $l = 1$ ,  $p_1$  triplet and the two successive frequencies of the  $l = 2$ ,  $g_1$  quintuplet were interpreted as rotational splittings by Dupret *et al.* (2004), in the way outlined in Chapter 3. In doing so, the authors ignored rotational effects higher than order one in the rotational frequency as well as the influence of a magnetic field. This approach is justified for V836 Cen, in view of its slow rotation (Aerts *et al.* 2004d), the quasi-equidistant splitting within the triplet (see Table 7.3), and the absence of a measurable magnetic field (Hubrig *et al.* 2006). Given that only two multiplets were available for V836 Cen, Dupret *et al.* (2004) assumed a linear rotation law and concluded that the rotational frequency near the stellar core is 3.6 times higher than at the surface. We repeat that it was possible to derive this because the  $g_1$  and  $p_1$  modes have different probing power near the core of the star, as already illustrated in Fig. 7.81.

Thoul *et al.* (2004) showed that the constraints on the mass and on the internal rotation for V836 Cen are robust against a change in the metal mix-

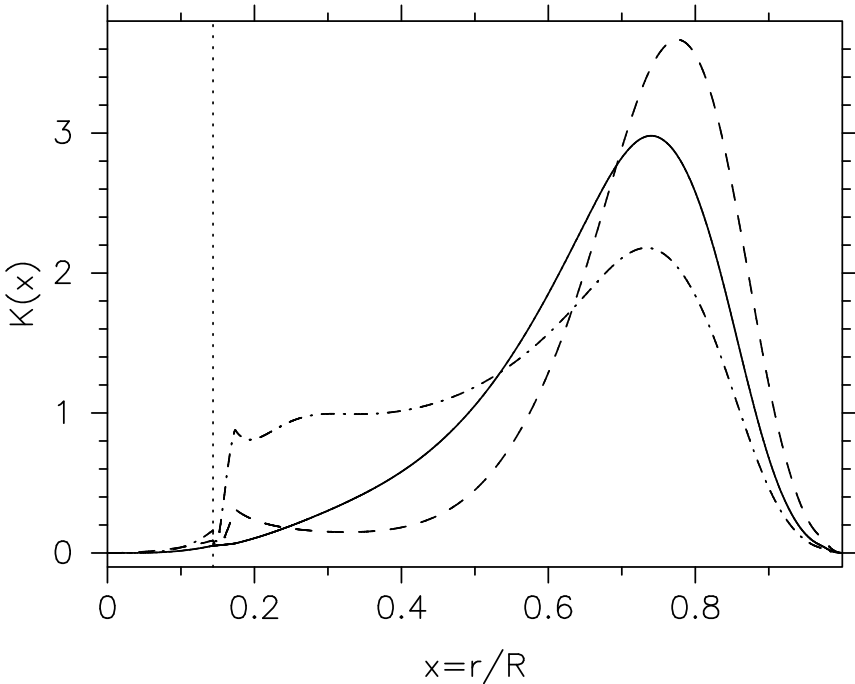


**Fig. 7.81.** The rotational kernels defined in Eq. (3.356) as a function of radial distance inside the star ( $x = r/R$ ), for the identified radial fundamental (solid line), the  $l = 1$ ,  $p_1$  mode (dashed line) and the  $l = 2$ ,  $g_1$  mode (dash-dotted line) of V836 Cen. The vertical dotted line marks the position of the boundary of the convective core, including the overshoot region. Adapted from Aerts *et al.* (2003b).

ture, which was assumed to be the standard solar one by Grevesse & Noels (1993) in all the above. The constraints on the metallicity and on the overshooting parameter, however, are dependent on the assumed metal mixture. In particular,  $\alpha_{\text{ov}}$  increases when the solar mixture by Asplund *et al.* (2004) is considered. Morel *et al.* (2006) meanwhile included V836 Cen in their high precision abundance study of  $\beta$  Cep stars for asteroseismology and derived the following fundamental parameters:  $T_{\text{eff}} = 24\,500 \pm 1\,000$  K,  $\log g = 3.95 \pm 0.20$ , and  $Z = 0.0105 \pm 0.0022$ . The abundances they derived for V836 Cen are fully consistent with those of B stars in the solar neighbourhood and also with those published for the Sun by Asplund *et al.* (2004). This implies that  $\alpha_{\text{ov}} = 0.1$  must be regarded as a lower limit for V836 Cen.

### 7.3.2 The $\beta$ Cep Star $\nu$ Eridani

#### 7.3.2.1 The Star

The bright equatorial ( $\delta \simeq -3^\circ$ ) star  $\nu$  Eri (HD 29248, HR 1463,  $V = 3.92$ , spectral type B1III,  $d = 180$  pc) was discovered to be a radial velocity variable by Frost & Adams (1903). It was extensively studied in spectroscopy during almost half a century, with conflicting results on its periodicity (Frost *et al.* 1926; Henroteau 1926, 1927; Walker 1951; McNamara 1952; Struve *et al.* 1952), until Walker (1952) started to study it in photoelectric photometry. From then until 2003, it was known to be a multiperiodic  $\beta$  Cep star, with four pulsation frequencies detected in photometric data and reconciling the seemingly conflicting results from the radial velocity studies (Lyngå 1959; Van Hoof 1959, 1961, Kubiak 1980, Cuypers & Goossens 1981, Kubiak & Seggewiss 1991).

Modern multicolour photometric and spectroscopic data pointed out that the dominant frequency belongs to a radial mode, and the triplet is consistent with a dipole mode identification (Aerts *et al.* 1994; Heynderickx *et al.* 1994, Cugier *et al.* 1994). The spacing within the triplet ( $\simeq 0.017$  d $^{-1}$ ) implies that the star has a low surface rotation, a conclusion supported by its measured  $v \sin i = 20$  km s $^{-1}$  (Abt *et al.* 2002, Levato & Grosso 2002). Dziembowski & Jerzykiewicz (2003) computed an asymmetry of order  $7 \times 10^{-4}$  d $^{-1}$  within the triplet and interpreted this in terms of possible magnetic field effects on the oscillations. This interpretation requires a field strength above 5 kG. Schnerr *et al.* (2006) monitored the star for more than one year in spectropolarimetry and rejected the hypothesis of a magnetic field above 0.3 kG in the star.

Given the exciting results for V836 Cen discussed above, and not wanting to wait another 20 yr to have acquired sufficient single site data for a second case study, Handler & Aerts (2002) decided to set up a five month multicolour photometric and high resolution spectroscopic campaign on  $\nu$  Eri from both hemispheres, with the goal to make an in-depth asteroseismic study of this bright multiperiodic  $\beta$  Cep star. In view of several intriguing results that we discuss below, an additional follow-up photometric multisite campaign was organized one year later (Jerzykiewicz *et al.* 2005). This wealth of data led to very extensive seismic studies of this star by different independent teams, the results of which we summarize here. They were distilled from the data papers by Handler *et al.* (2004), Aerts *et al.* (2004b), Jerzykiewicz *et al.* (2005), the mode identification paper by De Ridder *et al.* (2004), and the modelling papers by Pamyatnykh *et al.* (2004), Ausseloo *et al.* (2004), Daszyńska-Daszkiewicz *et al.* (2005), and Dziembowski & Pamyatnykh (2008).

It turned out that  $\nu$  Eri has the broadest range in excited mode frequencies among the  $\beta$  Cep stars so far (closely followed by 12 Lac; see Chapter 2), leading to problems in explaining them in terms of the mode excitation theory. Also, it was the third class member for which a low frequency g mode was discovered (Handler *et al.* 2004). The interpretation of this phenomenon for the

first two cases (16 Lac, Jerzykiewicz *et al.* 1993; 19 Mon, Balona *et al.* 2001) remains uncertain, but for  $\nu$  Eri it definitely concerns high order g modes. Its internal rotational behaviour is very similar to the one of V836 Cen (Pamyatnykh *et al.* 2004).

### 7.3.2.2 The Data

The photometric observations of the first multisite photometric campaign were carried out at the end of 2002 and early 2003 with eleven different telescopes and photometers at ten observatories on five different continents (Handler *et al.* 2004). At five observatories, single channel differential photometry was acquired through the Strömgren *uvby* filters. Simultaneous *uvby* photometry was obtained at one observatory and the remaining four observatories provided Johnson *V* measurements. The total time base of the assembled 600 h of photometry for this campaign was 157.9 d. The second campaign of photometric multisite observations was carried out in 2003, with five telescopes on four continents, which were also used in the first campaign (Jerzykiewicz *et al.* 2005). These data spanned 158.5 d in total. For both campaigns, the comparison stars, observing procedures, and data reduction methods were the same. They included correcting for coincidence losses, for sky background and for extinction from the computation of nightly extinction coefficients, as explained in Chapter 4. Differential magnitudes between the comparison stars were subsequently fitted with low order polynomials and represent the effects of transparency and detector sensitivity changes. These time series were binned into intervals to minimize the introduction of noise in the differential light curve of the target, and were finally subtracted from the measurements of  $\nu$  Eri. We refer to Handler *et al.* (2004) and Jerzykiewicz *et al.* (2005) for the full data description and more details on the reduction procedures.

The spectroscopic observations were assembled with eleven different spectrographs at telescopes and observatories on five continents. In nine of the eleven cases, the instrument was an échelle spectrograph and the other two instruments were linear arrays. The integration times were typically  $\sim$ 10 min, depending on the instrument and on the atmospheric conditions. This led to a temporal resolution less than 5% for the four intrinsic modes of  $\nu$  Eri which were known prior to the campaign. Some spectra were taken in advance of the intensive campaign, and some afterwards as well, to increase the total time base and achieve better frequency precision. All raw data were subjected to the usual reduction process as described in Chapter 4, *i.e.*, debiasing, flat fielding, background subtraction and wavelength calibration were performed. The latter was done by means of a ThAr or a quartz lamp. The spectra were subsequently shifted to the barycentre of the solar system and the Heliocentric Julian Dates of mid-exposure were calculated. The data analysis was based on the Si III triplet at 4552.622 Å, 4567.840 Å, and 4574.757 Å as it is well known that these triplet lines in the spectrum of B0–2 main sequence stars are the best lines for a study of the pulsational behaviour of such stars,

because they are only slightly affected by blending, they are strong lines and they are almost insensitive to temperature variations (De Ridder *et al.* 2002). (Re-)Normalization of the continuum flux near this Si triplet was done in an homogeneous way by calculating the best fitting cubic spline function through the continuum near these wavelengths and then dividing the local spectrum by this spline. In total, 2442 spectra with a S/N ratio between 100 and 700, and spread over a time base of 430 d, were gathered. The radial velocity curve of this data set exemplifies the beating between multiple heat driven oscillation modes and was already shown in Fig. 6.17. It allowed Aerts *et al.* (2004b) to exclude the possibility of  $\nu$  Eri being a spectroscopic binary with a period that would be relevant for the study of its intrinsic line profile behaviour.

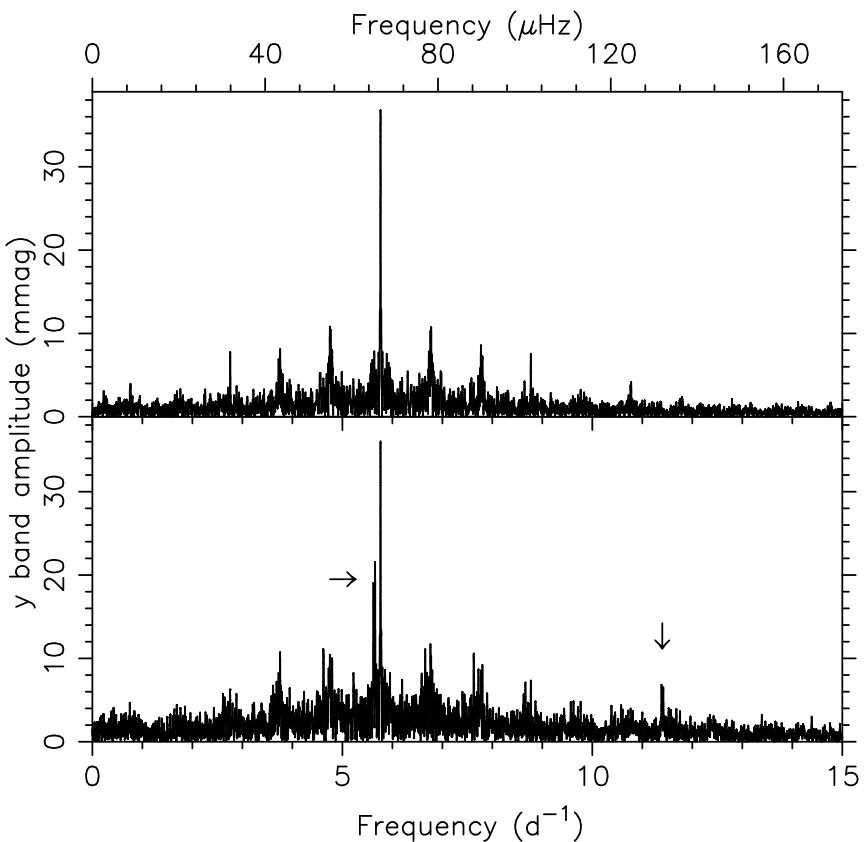


**Fig. 7.82.** Scargle periodogram (bottom) for the Strömgren  $y$  data of  $\nu$  Eri published in Handler *et al.* (2004). The horizontal arrow indicates the frequency triplet and the vertical arrow twice the dominant frequency. The top panel is the Scargle periodogram of a noise free sinusoid with the observed dominant frequency and its amplitude, sampled at the times of the observations. Data taken from Handler *et al.* (2004).

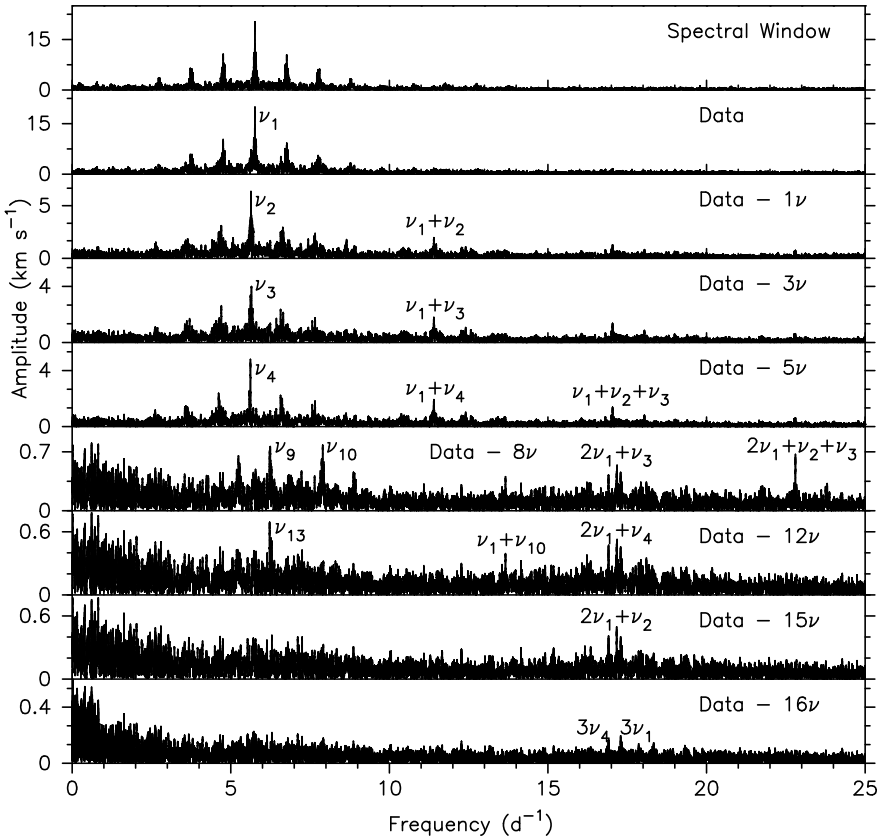


**Fig. 7.83.** Scargle periodograms of the radial velocities of  $\nu$  Eri shown in Fig. 6.17. The uppermost panel shows the Scargle periodogram of a noise free sinusoid with the observed dominant frequency and its amplitude, sampled at the times of the observations. The subsequent panels show the periodograms after different stages of prewhitening (note the different scale of the  $y$ -axes). Adapted from Aerts *et al.* (2004b).

### 7.3.2.3 The Detected Modes

A Scargle periodogram for the Strömgren  $y$  data of  $\nu$  Eri assembled by Handler *et al.* (2004) is shown in Fig. 7.82. This periodogram clearly reveals  $\nu$  Eri to have a very dominant mode with frequency  $\nu_1 = 5.763256\text{ d}^{-1}$ , in contrast to V836 Cen whose largest amplitude  $l = 2$  mode amplitude is not very dominant compared with its  $l = 1$  and radial modes (Fig. 7.75). The triplet frequencies  $\nu_2 = 5.65389\text{ d}^{-1}$ ,  $\nu_3 = 5.619979\text{ d}^{-1}$ , and  $\nu_4 = 5.637215\text{ d}^{-1}$  are apparent as well (horizontal arrow in Fig. 7.82). There is also a clear peak at  $2\nu_1$  for  $\nu$  Eri, as indicated by the vertical arrow in Fig. 7.82 and pointing towards deviations

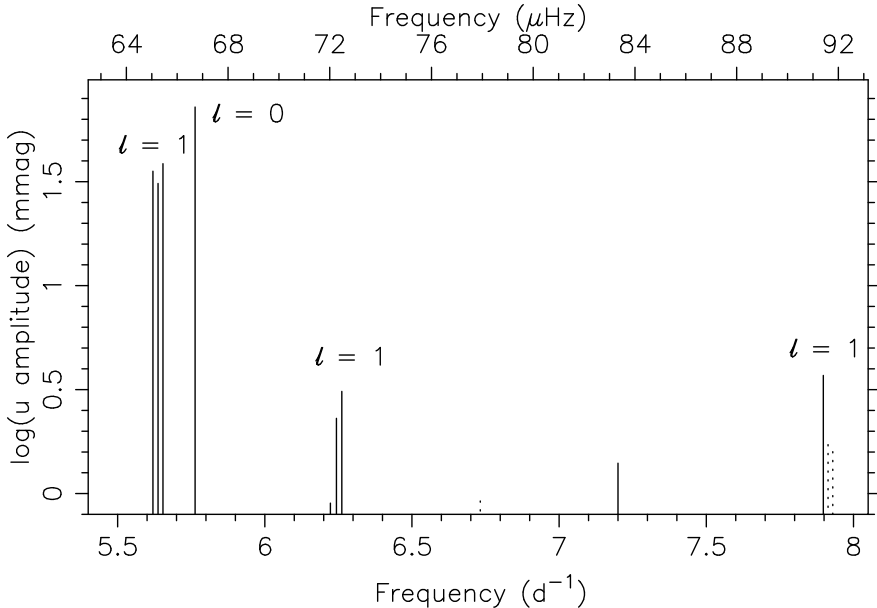


**Fig. 7.84.** Schematic amplitude spectrum for the Strömgren  $u$  data of  $\nu$  Eri reproduced from Jerzykiewicz *et al.* (2005). The full lines indicate frequencies that were detected both in photometry and in spectroscopy. The dotted lines are the frequencies that have only been found in the photometry. The mode identification derived by De Ridder *et al.* (2004) is indicated as well. The two g mode frequencies at  $0.432786 \text{ d}^{-1}$  and  $0.61440 \text{ d}^{-1}$  have been omitted to make the plot better visible. A mode identification for these two frequencies is not available.

from a linear oscillation, while such an effect is absent in V836 Cen. Comparing the spectral windows in the top panels of Figs 7.75 and 7.82 illustrates the large gain from multisite to single site data, regarding the disentangling of alias frequencies from the true ones. For a full derivation of the frequency spectrum and the adopted methodology, we refer to Handler *et al.* (2004).

Besides the four frequencies already known before the multisite campaign, the photometric data in Handler *et al.* (2004) revealed nineteen additional frequencies, among which are four new independent ones of p modes, fourteen combination frequencies and a low g mode frequency of  $0.43218 \text{ d}^{-1}$  which occurs consistently in the colours. Until the  $\nu$  Eri multisite campaign, a g mode frequency had only been suggested in two other  $\beta$  Cep stars: the slow rotator 16 Lac (Jerzykiewicz *et al.* 1993) and the rapid rotator 19 Mon (Balona *et al.* 2001), but its cause was still debated in these papers in terms of rotation or spots rather than an oscillation mode. With its firm establishment by Handler *et al.* (2004) and the impossibility to explain it from the slow rotation of the star,  $\beta$  Cep stars must be considered as hybrid pulsators with both low order p and g modes as well as low amplitude, high order g modes. Meanwhile, a

high order g mode has also been detected for 12 Lac from a multisite campaign (Handler *et al.* 2006).

The new data from the second campaign led Jerzykiewicz *et al.* (2005) to add four additional independent frequencies, among which another low one at  $0.614\text{ d}^{-1}$ . Altogether, the oscillation spectrum derived from photometry consists of twelve p mode and two g mode frequencies. Nine of the twelve p mode frequencies constitute three triplets. For improved values of these frequencies compared to those listed in Table 6.1, we refer to Table 2 in Jerzykiewicz *et al.* (2005). A schematic frequency diagram of the detected modes detected is provided in Fig. 7.84.

For the spectroscopy, frequencies were derived from the radial velocity data shown in Fig. 6.17. The results for subsequent stages of the prewhitening are graphically depicted in Fig. 7.83. The spectroscopic data suffer somewhat more from aliasing than the photometric ones. The main frequency  $\nu_1$  found in the photometry is even more dominant in the radial velocity variations (see Table 6.1). After prewhitening, the independent triplet frequencies  $\nu_2, \nu_3$ , and  $\nu_4$  are easily recovered, as well as the combination frequencies  $\nu_1 + \nu_2, \nu_1 + \nu_3, \nu_1 + \nu_4, \nu_1 + \nu_2 + \nu_3$ . The other frequencies derived from the spectroscopy are consistent with those found in the photometry and the independent ones among them were already listed with their amplitude in Table 6.1. In total, nineteen frequencies were found to have amplitudes above  $4\sigma$  (Aerts *et al.* 2004b).

### 7.3.2.4 Mode Identification and Seismic Modelling

A detailed mode identification of  $\nu$  Eri's independent frequencies was derived by De Ridder *et al.* (2004). They used the combined multisite data of Handler *et al.* (2004) and Aerts *et al.* (2004b) and applied the methodology discussed in Chapter 6, where the results for  $\nu$  Eri were already discussed extensively and used as illustrations (Figs 6.5 and 6.6 and Table 6.1). The new photometric data by Jerzykiewicz *et al.* (2005) did not reveal any new identifications. The mode identification listed in Table 6.1 is indicated in the schematic frequency diagram in Fig. 7.84.

Seismic models of  $\nu$  Eri were computed with independent evolution and pulsation codes by Pamyatnykh *et al.* (2004) and Ausseloo *et al.* (2004), both relying on the OPAL opacities (Iglesias & Rogers 1996). The radial order of the modes listed in Table 6.1 were found to be the radial fundamental ( $\nu_1$ ) and the g<sub>1</sub> ( $\nu_2, \nu_3, \nu_4$ ), p<sub>1</sub> ( $\nu_6, \nu_7, \nu_8$ ), and p<sub>2</sub> ( $\nu_5$ ) mode in both studies. The fitting of  $\nu_1$  and  $\nu_4$  led to the mass-metallicity relation shown in Fig. 7.85. The seismic modelling based on more than these two zonal modes was done differently in both the studies.

Pamyatnykh *et al.* (2004) fitted the three  $m = 0$  frequencies  $\nu_1, \nu_4$  and  $\nu_6 = 6.24384\text{ d}^{-1}$  (updated value from Jerzykiewicz *et al.* 2005) with the Warsaw-New Jersey codes. They determined the value of the metallicity  $Z$ , the mass  $M$  and the age for the two sets ( $X = 0.70, \alpha_{\text{ov}}$ ) with  $\alpha_{\text{ov}} = 0.0$  and  $0.1$  from which

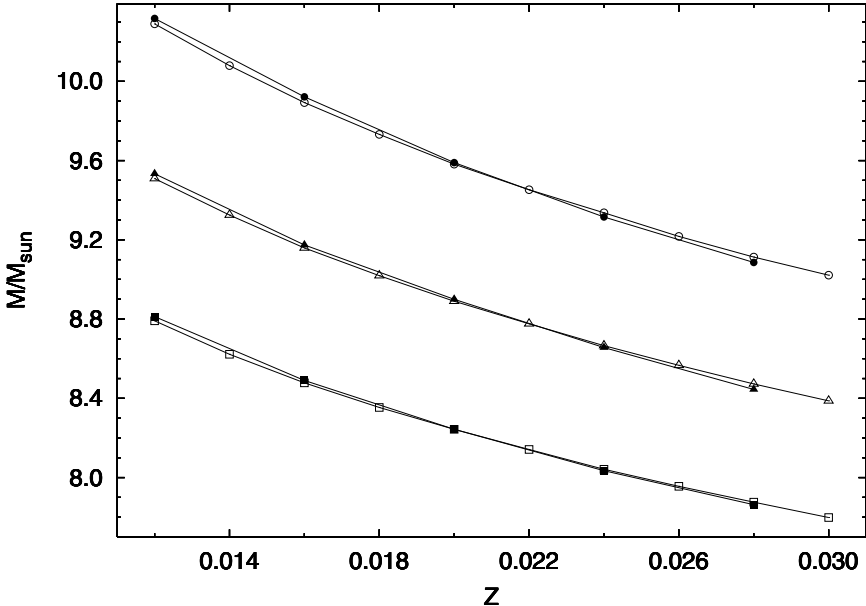


**Fig. 7.85.** The  $M$ - $Z$  relations obtained by fitting zonal mode frequencies  $\nu_1$  and  $\nu_4$  computed by Ausseloo (2005) for three different ( $X = 0.70, \alpha_{\text{ov}}$ ) sets:  $\alpha_{\text{ov}} = 0.0$  (dots), 0.1 (triangles) and 0.2 (squares). Open and filled symbols denote the results obtained by means of stellar models with, respectively, the Grevesse & Noels (1993) and the Asplund *et al.* (2004) solar mixtures. Adapted from Ausseloo (2005).

they obtained two models that fit  $\nu_1$ ,  $\nu_4$  and  $\nu_6$  with a small core convective overshooting parameter. These two models show a discrepancy between the theoretical frequency of the  $l = 1$ ,  $p_2$  mode and the observed frequency  $\nu_5 = 7.898200 \text{ d}^{-1}$  (updated value from Jerzykiewicz *et al.* 2005), which cannot be explained by rotational splitting. Moreover, the authors discovered that the mode with frequency  $\nu_5$  was not excited in either of the two models fitting the three frequencies. Pamyatnykh *et al.* (2004) “solved” this excitation problem by following the idea that the excitation of the observed modes in subdwarf B stars occurs thanks to a local iron enrichment in the driving region due to diffusion processes such as gravitational settling and radiative levitation (Charpinet *et al.* 1996, 1997). More specifically, Pamyatnykh *et al.* (2004) derived empirically that an ad hoc local enhancement of iron group elements in the driving zone, which has a log  $T_{\text{eff}}$  range [5.1, 5.5], with a factor at least four was needed to excite all the detected p mode frequencies of  $\nu_{\text{Eri}}$ . This local iron increase also caused a shift in the theoretical frequency of the  $l = 1$ ,  $p_2$  zonal mode which brought it closer to the observed frequency  $\nu_5$ . This was the reason why Pamyatnykh *et al.* (2004) did not want to use the mode with frequency  $\nu_5$  in their seismic modelling, because it seemed to be more sensitive

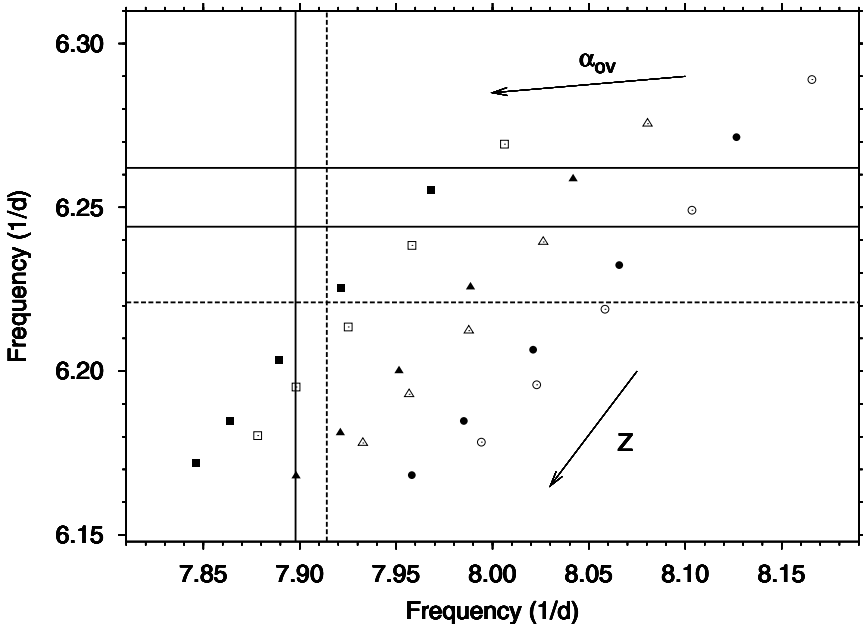


**Fig. 7.86.** Frequency -frequency diagram in which the symbols mark the frequency values of the ( $l = 1, p_2$ ) [x-axis] and ( $l = 1, p_1$ ) [y-axis] zonal mode as predicted by models that fit  $\nu_1$  and  $\nu_4$  for a given ( $X = 0.70$ ,  $\alpha_{ov}$ ,  $Z$ ) set. The sequences correspond to  $\alpha_{ov} = 0.0$  (dots), 0.1 (triangles) and 0.2 (squares). In each sequence, the metallicity of the models ranges from 0.012 to 0.028 with steps of 0.004 in the indicated direction. Open and filled symbols denote results obtained with the Grevesse & Noels (1993) and Asplund *et al.* (2004) solar mixture, respectively. The detected and suspected observed frequencies from Handler *et al.* (2004) are given by full and dashed lines. Adapted from Ausseloo (2005).

to a change in the ad hoc iron enhancement in the outer layers, including the driving zone, than the other lower frequency p modes.

The approach by Ausseloo *et al.* (2004) was to fit the four detected oscillation frequencies  $\nu_1, \nu_4, \nu_6$ , and  $\nu_5$ , irrespective of the excitation problem. The result is graphically depicted in Fig. 7.86. It can be seen that the fitting of the four frequencies requires models with a low mass and a high  $\alpha_{ov}$ . This fit is shown in Fig. 7.87, together with the results of the excitation computations. Also Ausseloo *et al.* (2004) found that the modes of this model are not excited. Subsequently, a massive data base of non-standard seismic models was computed, in which  $X$  and the iron content were allowed to deviate unlimitedly globally in the star from physically relevant values, in order to investigate what combinations of these two input parameters would solve the excitation problem and still lead to a good fit of the four frequencies. The results were that either  $X$  had to be decreased to an unrealistically low value below 0.6 or the iron content had to be increased with a factor at least four.

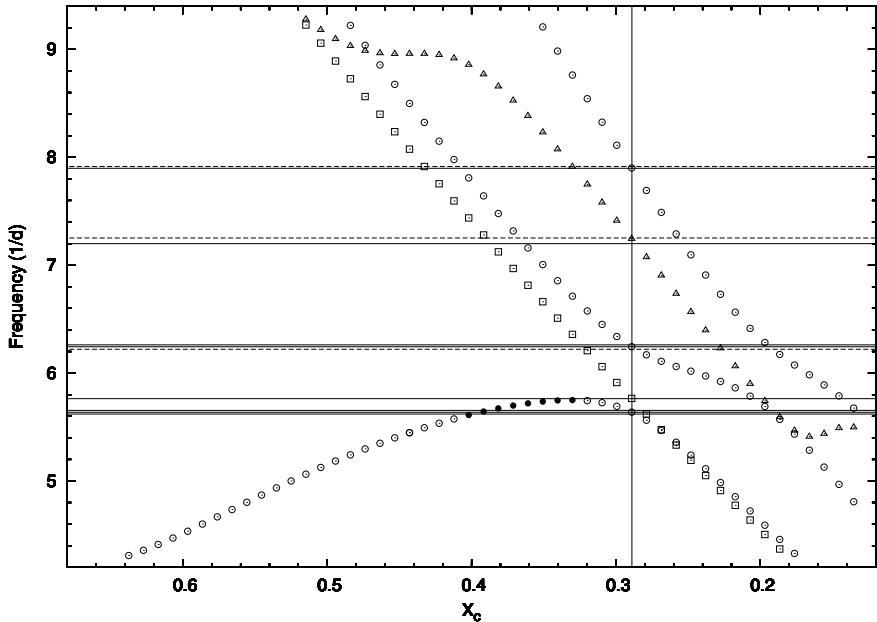


**Fig. 7.87.** Evolution of the theoretical frequencies of the observed modes for a model with  $X = 0.70$ ,  $\alpha_{ov} = 0.313$ ,  $Z = 0.0155$  and  $M/M_\odot = 7.83$  for the input physics adopted by Ausseloos *et al.* (2004). Squares, dots and triangles denote respectively  $l = 0, 1, 2$  zonal modes. Filled (open) symbols correspond to unstable (stable) modes. The full and dashed horizontal lines mark the detected and suspected observed frequencies from Handler *et al.* (2004). The vertical line denotes the model fitting the four zonal modes for  $X = 0.70$ . Adapted from Ausseloos (2005).

Another difference between the two studies was that, unlike Ausseloos *et al.* (2004), Pamyatnykh *et al.* (2004) put an upper limit on the overshooting parameter at  $\alpha_{ov} = 0.12$  because stellar models with higher  $\alpha_{ov}$  values had an effective temperature below the observational error box they used, which was based on photometric calibrations. On the other hand, an updated error box of  $\nu$  Eri's position in the HR diagram was derived by De Ridder *et al.* (2004) and by Morel *et al.* (2006) from high-resolution spectroscopy. These boxes turn out to be larger and include cooler models than the narrow box used by Pamyatnykh *et al.* (2004). This is why Ausseloos *et al.* (2004) preferred to scan the model parameter space without *a priori* confining the search. Rather, they derived a value for  $\alpha_{ov}$  by imposing an exact fit of the four  $m = 0$  frequencies and used the temperature estimate  $T_{\text{eff}} = 22\,900 \pm 1100$  K from De Ridder *et al.* (2004) to check *a posteriori* the position of the resulting models in the HR diagram. It resulted that the models that fit the four frequencies are cooler than the derived effective temperature of the star, irrespective of the adopted solar mixture (Ausseloos 2005). On the other hand, these models

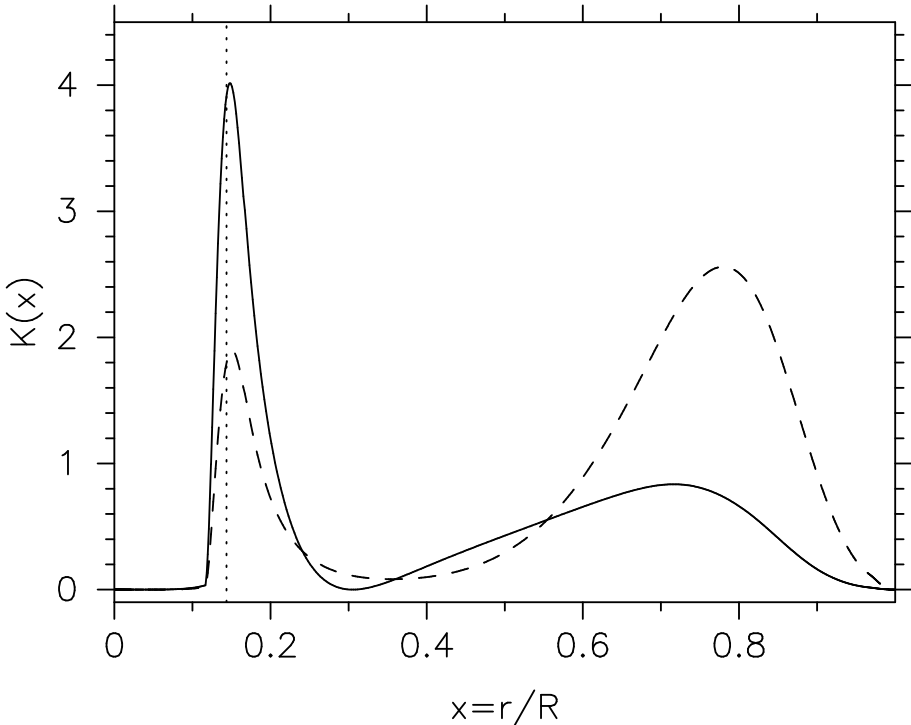


**Fig. 7.88.** The rotational splitting kernels  $K(x)$  for the  $g_1$ ,  $l = 1$  mode (full line) and the  $p_1$ ,  $l = 1$  mode (dashed line) for a model without core overshooting fitting  $\nu_1$ ,  $\nu_4$  and  $\nu_6$  of  $\nu$  Eri. The vertical dotted line marks the top of the  $\mu$ -gradient zone, *i.e.*, the position of the convective core at the ZAMS. Adapted from Pamyatnykh *et al.* (2004).

leave no doubt that the new independent frequency  $\nu_{11} = 6.73223 \text{ d}^{-1}$  found by Jerzykiewicz *et al.* (2005) (and not listed in Table 6.1) must be an  $l = 4$ ,  $g_1$  mode, while the mode with frequency  $\nu_9 = 7.20090 \text{ d}^{-1}$  (updated value from Jerzykiewicz *et al.* 2005) is the  $l = 2$ ,  $f$  mode.

The main conclusion of both approaches (uniform change of the iron abundance throughout the stellar interior versus a local iron enhancement in the driving region) was that an increase of the iron abundance by a factor of four is necessary to explain the observed pulsation modes of  $\nu$  Eri. Obviously, an overall change in the iron fraction implies a very different and unrealistic stellar model while the one with only a very local iron increase in the driving zone does not change the fundamental parameters of the model appreciably. This conclusion led to a new impetus in the computation of B star models, with efforts to include the effects of microscopic diffusion and mass loss (Bourge *et al.* (2006, 2007)). Until now, however, self-consistent evolutionary models with these effects of diffusion are not yet available.

Another route to solve the excitation problem for  $\nu$ Eri was taken by Daszyńska-Daszkiewicz *et al.* (2005). They considered, in addition to the opacity data from OPAL, also the OP (Seaton 1999, 2005) opacity computations for the Grevesse & Noels (1993) solar mixture. Significant differences in the models were found due to the higher OP opacity values compared to the OPAL values, but the excitation problem was not solved. This was further investigated by Dziembowski & Pamyatnykh (2008), who followed the results of Miglio *et al.* (2007) that many more modes are excited in  $\beta$ Cep and SPB stars when adopting the Asplund *et al.* (2004) solar mixture and the OP opacities, and re-computed new seismic models for  $\nu$ Eri. The result remained the same, *i.e.*, an increase of opacity in the driving zone is still needed to reconcile the observed and excited model frequencies. Dziembowski & Pamyatnykh (2008) confirm the mode identification by Ausseloos (2005) that  $\nu_{11}$  is an  $l = 4$ ,  $g_1$  mode, but they identified  $\nu_9$  as an  $l = 2$ ,  $p_1$  mode.

Luckily, the observed rotational splittings, which are determined by the rotational kernels of the identified modes, are not very dependent on the details of the input physics of the models, as was already shown by Thoul *et al.* (2003) for V836 Cen. The internal rotation of  $\nu$ Eri can thus be meaningfully studied without solving the excitation problem. Both Pamyatnykh *et al.* (2004) and Dziembowski & Pamyatnykh (2008) derived the internal rotational behaviour from the splittings of the  $g_1$  and  $p_1$  triplets. The probing power of these two mode kernels for a model without overshooting fitting  $\nu_1$ ,  $\nu_4$ , and  $\nu_6$  is shown in Fig. 7.88. It can be seen that these two kernels differ more from each other than the two for the multiplet frequencies of V836 Cen shown in Fig. 7.81. Again, as for V836 Cen, any inference on the internal rotation rate comes from only two multiplets and one must assume a simplified law to test for any deviation of rigid rotation. Unlike Dupret *et al.* (2004), Pamyatnykh *et al.* (2004) and Dziembowski & Pamyatnykh (2008) relied on the properties of the solar internal rotation that the rotation frequency is almost constant in a radiative zone. Thus, they allowed the rotation frequency to change only in the  $\mu$ -gradient zone surrounding the convective core rather than linearly throughout the entire envelope as was done for V836 Cen. It is well known that the convective core in  $\beta$ Cep stars shrinks when the star evolves from the ZAMS to the TAMS, due to the decrease of the hydrogen opacity. This is shown in Fig. 7.88, where the dotted vertical line indicates the original boundary of the convective core at the ZAMS. The assumed parameterized law describing the change of the internal rotation frequency in the  $\mu$ -gradient zone was treated slightly differently by Pamyatnykh *et al.* (2004) and by Dziembowski & Pamyatnykh (2008). We refer the reader to these two papers for details. The important conclusion is that the ratio of the core to envelope rotation frequency of  $\nu$ Eri is  $\sim 5.5$  and the corresponding equatorial rotational velocity of the star equals  $5.9 \text{ km s}^{-1}$  (Dziembowski & Pamyatnykh 2008). This result is very similar to the one obtained for V836 Cen.

It would be very worthwhile to repeat the seismic modelling for  $\nu$ Eri using also the observed constraints of the  $l = 2$  and  $l = 4$  modes at frequencies  $\nu_9$

and  $\nu_{11}$ , particularly since the latter mode is very sensitive to the adopted mixture and hydrogen content (Ausselooos 2005).

### 7.3.3 The $\beta$ Cep Binary $\theta$ Ophiuchi

#### 7.3.3.1 The Star

The bright ( $V = 3.27$ , spectral type B2IV)  $\beta$  Cep star  $\theta$  Oph (HD 157056, HR 6453) is situated in the Galactic plane at a distance of 173 pc. The star is a slow rotator among the early type stars, as Brown & Verschueren (1997) and Abt *et al.* (2002) essentially found the same result of  $v \sin i = 31 \pm 3 \text{ km s}^{-1}$  from high-resolution spectroscopy.

$\theta$  Oph was first reported to be a variable star with a period of 0.2862 d from radial velocity measurements (Henroteau 1922). Since that discovery, its radial velocity variability was further studied by several authors. Van Hoof *et al.* (1956) suggested a period of 0.15 d, which corresponds to about half the period found by Henroteau (1922). These authors also noticed that the mean velocity at the time of their observations was  $-8 \text{ km s}^{-1}$ , a value distinctly different from Henroteau's values from the 1920 and 1922 data, which were 0 and  $-15 \text{ km s}^{-1}$ , respectively. McNamara (1957) and Van Hoof & Blaauw (1958) confirmed the period found by Van Hoof *et al.* (1956) and refined it to 0.1404 d. From their radial velocities measurements of members of the Sco-Cen association, Levato *et al.* (1987) suspected  $\theta$  Oph to be a single-lined spectroscopic binary but they could not derive orbital elements. McAlister *et al.* (1993) and Shatsky *et al.* (2002) found  $\theta$  Oph to be a binary resolved with speckle interferometry, with a period near 100 yr, while Handler *et al.* (2005) derived this wide companion to be a B5 main sequence star.

Van Hoof (1962) and Heynderickx (1992) studied the brightness variations of  $\theta$  Oph and found the star to be multiperiodic, but their frequency analysis results only agreed for the dominant frequency of  $7.116 \text{ d}^{-1}$  and not for the other periodicities. Moreover, they did not find any evidence of the 0.14 d or 0.28 d periodicity. Heynderickx *et al.* (2004) subsequently identified the degree of the frequency  $7.116 \text{ d}^{-1}$  as  $l = 2$  from multicolour Walraven photometry.

Given its similarity with V836 Cen regarding the complexity of its variations and the seemingly contradictory reports for them in the literature, Briquet *et al.* (2005) and Handler *et al.* (2005) *independently* considered the star to be a good target for asteroseismology. The results we report here are a summary of their two observational studies, as well as of the seismic modelling performed by Briquet *et al.* (2007). As it turns out,  $\theta$  Oph is almost a twin star of V836 Cen, except that it is a multiple star while V836 Cen is a single object. In contrast to V836 Cen,  $\theta$  Oph's internal rotation was found to be rigid to a good approximation while its core overshooting parameter is much larger.

### 7.3.3.2 The Data

Spectroscopic data were obtained by Briquet *et al.* (2005) with the CORALIE échelle spectrograph attached to the 1.2-m Leonard Euler telescope in La Silla, Chile, during several 10 d runs spread over the years 2000 – 2003. Some additional spectra were also gathered with the FEROS and GIRAFFE échelle spectrographs attached to the ESO 2.2-m telescope (La Silla, Chile) and to the SAAO 1.9-m telescope (South Africa), respectively. In total, 121 spectra were assembled, with a total time spread of 1024 d. A logbook of the spectroscopy, as well as a description of the data reduction, are available in Briquet *et al.* (2005).

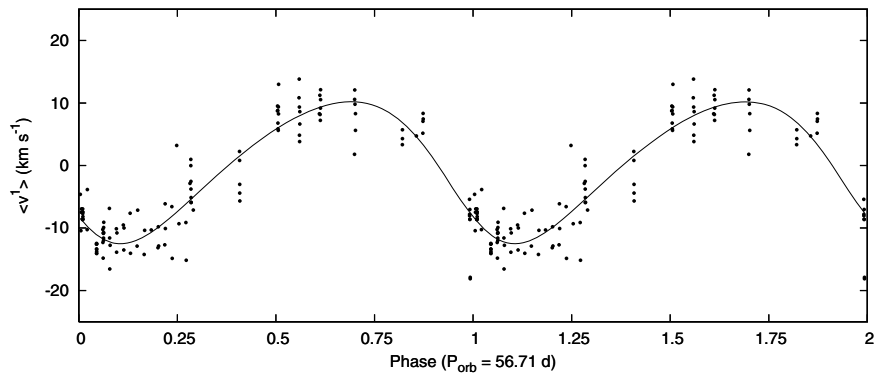


**Fig. 7.89.** The radial velocity data of the  $\beta$  Cep star  $\theta$  Oph obtained from high resolution échelle spectroscopy covering 4 yr, revealing the spectroscopic close binary nature of the star. The full line represents the best orbital solution. Adapted from Briquet *et al.* (2005).

Briquet *et al.* (2005) computed the first three velocity moments  $\langle v^1 \rangle$ ,  $\langle v^2 \rangle$  and  $\langle v^3 \rangle$  of the Si III 4553 Å line, as defined in Chapter 6. The integration boundaries for these computations were determined by visual inspection of each spectrum in order to avoid noisy continuum and to anticipate possible velocity shifts due to binarity. A frequency analysis led to the dominant frequency of  $0.0175 \text{ d}^{-1}$  in the first moment. Such a long period of some  $57/\text{d}$  does not correspond to a pulsation period for  $\beta$  Cep stars and is too long to be the rotation period of a star with  $v \sin i \simeq 30 \text{ km s}^{-1}$  and  $R \simeq 5 R_\odot$ . Consequently, Briquet *et al.* (2005) attributed this variability with a peak-to-peak amplitude of  $\simeq 25 \text{ km s}^{-1}$  to binarity. The orbital parameters were derived from the publicly available code FOTEL (Hadrava 1990), leading to an orbital period of  $P_{\text{orb}} = 56.71 \pm 0.05 \text{ d}$  and an eccentricity  $e = 0.167 \pm 0.043$ . The other orbital elements and their standard errors are given in Briquet *et al.* (2005). The phase diagram of the data and the orbital solution are shown in Fig. 7.89. From the mass function and assuming the orbital, pulsational and rotational inclination to be equal, Briquet *et al.* (2005) concluded  $\theta$  Oph

to be a triple system composed of a B2 primary, a low mass spectroscopic secondary and a physically bound Speckle B5 star.

Handler *et al.* (2005) set up a three site photometric campaign from 2003 April to August, independently of the spectroscopic single site campaign performed by Briquet *et al.* (2005) earlier on. They assembled single channel differential photoelectric Strömgren *uvw* photometry with the 0.75-m, 0.6-m, and 0.5-m telescopes at the Fairborn, Siding Spring, and South African Astronomical Observatories, respectively. Some of the acquired light curves are shown in Fig. 7.90. A total of 1303 points were gathered during 77 nights, spread over a total time base of 124 nights. The accuracy per point was 4.8 mmag in *u*, 4.3 mmag in *v* and 3.9 mmag in *y*. The authors found no sign of the binarity in the photometric measurements. This is consistent with the ephemeris for the eclipses computed for the orbital solution by Briquet *et al.* (2005), as no photometric coverage was achieved near or during the primary eclipse.

### 7.3.3.3 The Detected Modes

In the following, we shall still speak of  $\theta$  Oph as the pulsating star, even though we mean  $\theta$  Oph A.

Given the sparse sampling rate of the spectroscopy, the oscillation frequencies of  $\theta$  Oph are best derived from the photometric data. Handler *et al.* (2005) performed frequency analysis combined with simultaneous multifrequency sine wave fitting, as outlined in Chapter 5. They found the seven significant frequencies shown schematically in Fig. 7.91 and listed in Table 7.5, along with the amplitudes for the three passbands. Briquet *et al.* (2005) detected two of these frequencies ( $\nu_1$  and  $\nu_3$ ) in the velocity moments after correction for the orbital motion. The phase plots of the first moment for these two frequencies are shown in Fig. 7.92. A Scargle analysis across the entire Si III 4553Å line profile revealed, in addition, the presence of  $\nu_2$ . The amplitudes and phases across the line profile for the three oscillation modes detected in the spectra are shown in Fig. 7.93.

### 7.3.3.4 Mode Identification and Seismic Modelling

Handler *et al.* (2005) corrected the measured brightness and colours of  $\theta$  Oph for the physical B5 companion before computing the amplitude ratios with respect to the *u* passband. They did that by using the *K*-magnitude difference reported by Shatsky & Tokovinin (2002) and standard photometric relations. Their estimates of the effective temperature of the stars are  $T_{\text{eff}} = 22\,900 \pm 900$  K and  $18\,400 \pm 700$  K. Moreover, they used the estimate of  $\log g = 3.77$  (no error provided) derived from low-resolution IUE spectra, treating the star as a single object, by Niemczura & Daszyńska-Daszkiewicz (2005) to compute stellar models. These fundamental parameter estimates of the primary  $\beta$  Cep star are quite different from those obtained from the high resolution spectroscopy by Briquet *et al.* (2007), in which the contribution of

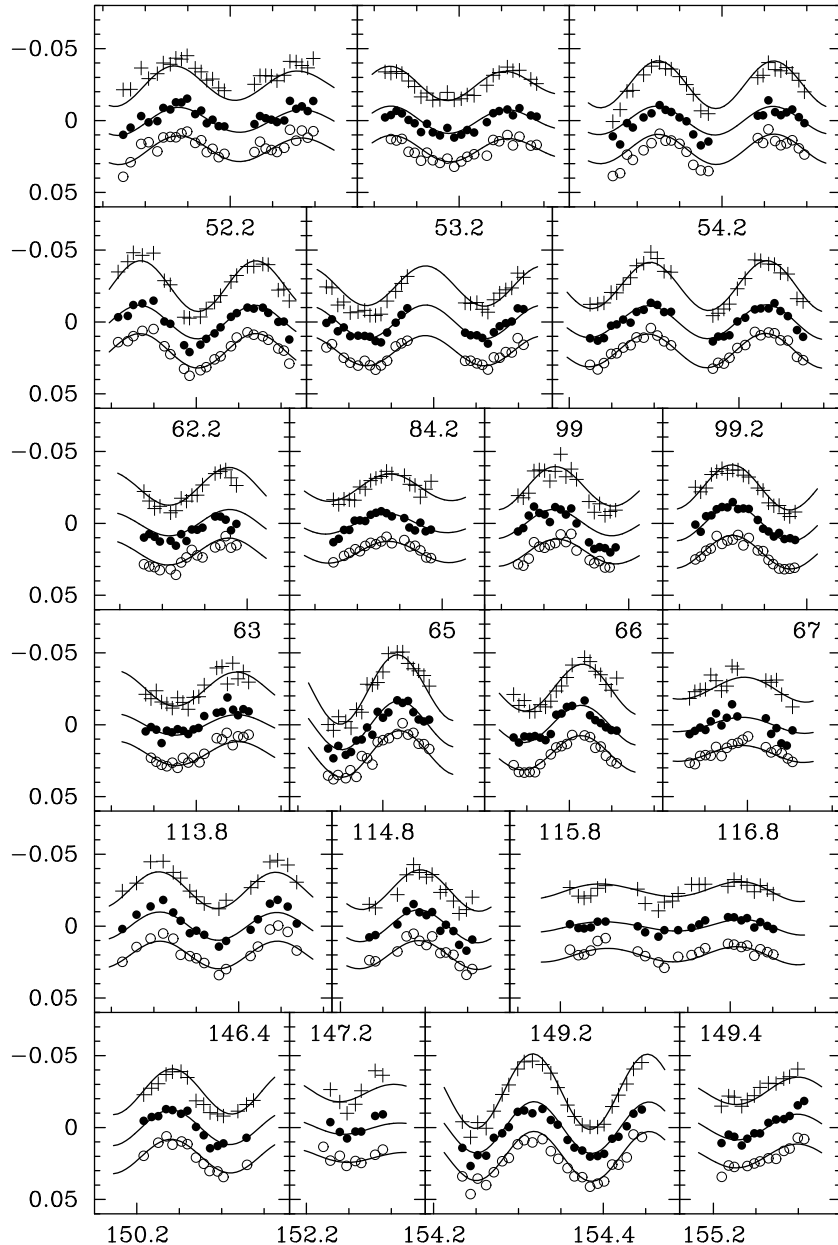


**Fig. 7.90.** Some of the light curves of  $\theta$  Oph obtained during a 5-month three site campaign. Plus signs represent the data in the  $u$  band, filled circles are the  $v$  measurements and open circles the  $y$  band data. The full line represents the fit with the seven frequencies found in the data. The zero point for the time axis is HJD 2452700. Adapted from Handler *et al.* (2005).

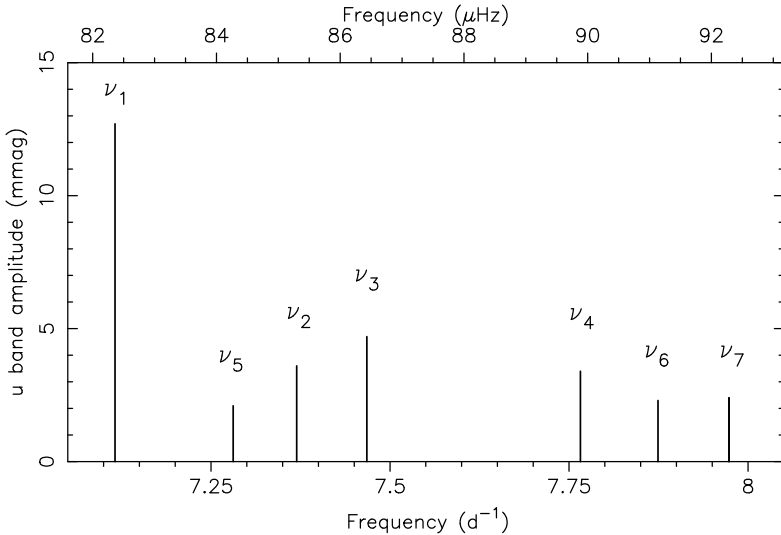


**Fig. 7.91.** The schematic frequency spectrum of the  $\beta$ Cep star  $\theta$ Oph for the Strömgren  $u$  filter as derived from a multisite photometric campaign. The measured photometric amplitude ratios led to an identification of the frequencies  $\nu_1, \nu_2, \nu_3$ , and  $\nu_4$  as, respectively,  $l = 2, 2, 0, 1$ . Adapted from Handler *et al.* (2005).

**Table 7.5.** The detected and identified pulsation modes of the  $\beta$ Cep star  $\theta$ Oph derived from multicolour photometric and high resolution spectroscopic data. The errors of the frequencies are given between brackets, in units of the last decimal. Table reproduced from Handler *et al.* (2005) and Briquet *et al.* (2005, 2007).

ID	Frequency ( $\text{d}^{-1}$ )	$u$ ampl. (mmag)	$v$ ampl. (mmag)	$y$ ampl. (mmag)	$\sigma_y$	RV ampl. ( $\text{km s}^{-1}$ )	$(l, m)$
$\nu_1$	7.11600(8)	12.7	9.2	9.4	41.4	2.54	(2, -1)
$\nu_5$	7.2881(5)	2.1	1.5	1.4	6.4	–	(2, +1)
$\nu_2$	7.3697(3)	3.6	2.9	2.4	10.8	–	(2, +2)
$\nu_3$	7.4677(3)	4.7	2.4	2.3	10.2	2.08	(0, 0)
$\nu_4$	7.7659(3)	2.3	2.1	3.4	9.7	–	(1, -1)
$\nu_6$	7.8742(5)	2.3	1.8	1.3	5.8	–	(1, 0)
$\nu_7$	7.9734(5)	2.4	1.6	1.2	5.6	–	(1, +1)

the B5 companion to the spectrum was taken into account, particularly for the gravity:  $T_{\text{eff}} = 25\,000 \pm 1000$  K and  $\log g = 4.10 \pm 0.15$ .

Handler *et al.* (2005) computed theoretical amplitude ratios for all modes with frequencies ranging from  $6.5\,\text{d}^{-1}$  to  $8.5\,\text{d}^{-1}$  and with  $l = 0, \dots, 4$ , from models with a mass range from  $8.5\,\text{M}_\odot$  to  $10\,\text{M}_\odot$ , a temperature range from 21\,800 K to 24\,000 K and for  $Z = 0.015$ , with the Warsaw-New Jersey evolution

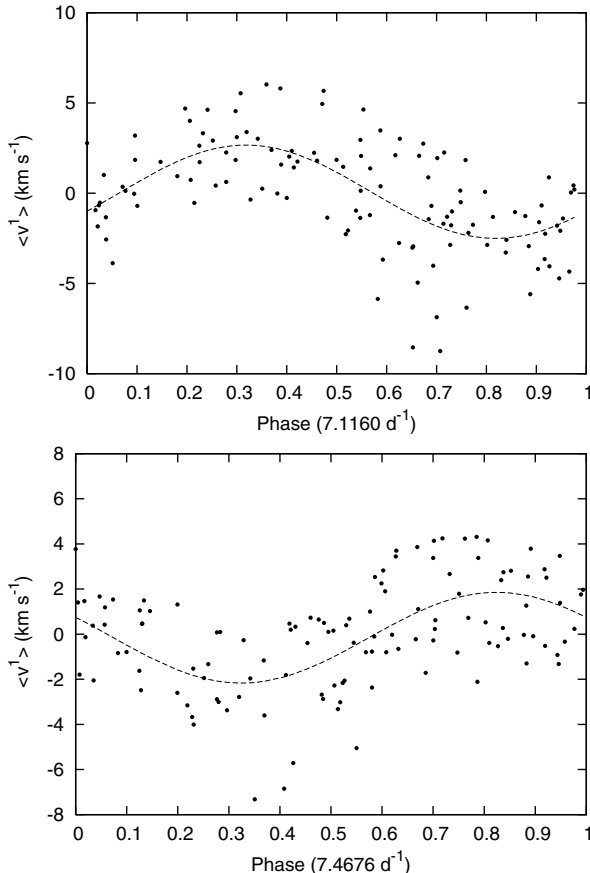


**Fig. 7.92.** Phase diagrams of the first velocity moment of the Si III 4553Å line, after subtraction of the orbital fit shown in Fig. 7.89, for the frequencies  $\nu_1$  (top panel) and for  $\nu_3$  after subsequent prewhitening with  $\nu_1$  (bottom panel). Adapted from Briquet *et al.* (2005).

and pulsation codes. These theoretical predictions were compared with the observations. For three of the seven detected modes, it led to an identification of the mode degree, as illustrated in Fig. 7.94. It was found that  $\nu_3$  is a radial mode,  $\nu_4$  a dipole mode, and  $\nu_1$  a dipole or quadrupole mode. The other modes could not be uniquely identified without further independent information, due to large uncertainties on the observed ratios. We recall that Heynderickx *et al.* (1994) identified  $\nu_1$  as an  $l = 2$  mode from Walraven photometry so that seems to be the most likely option. Moreover, the probability of dealing with an  $l = 3$  is far lower than with  $l = 1, 2$  due to the partial cancellation discussed in Chapter 6 and illustrated in Fig. 6.4. By excluding these options, Handler *et*

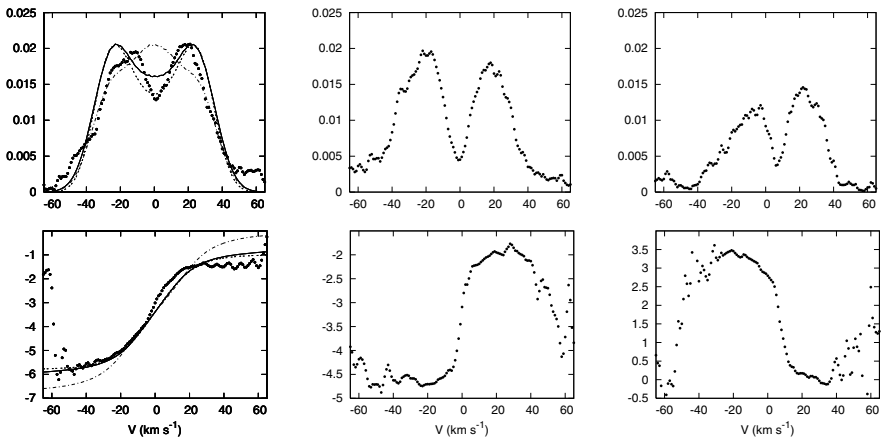


**Fig. 7.93.** The observed amplitude and phase distributions across the Si III 4553Å profile for the frequencies  $\nu_1$  (left),  $\nu_3$  (middle), and  $\nu_2$  (right) are shown as dots. The amplitudes are unitless and the phases are expressed in  $\pi$  radians. Theoretical predictions for  $(l, m) = (2, -1)$ ,  $(1, -1)$ , and  $(2, -2)$  are overplotted as full, dashed, and dash-dotted line, respectively, in the left panel. Adapted from Briquet *et al.* (2005).

*al.* (2005) came to the conclusion that  $\nu_4, \nu_6, \nu_7$  shown in Fig. 7.91 are triplet modes.

With the  $l$ -values for five of the seven modes securely identified from the photometry, it became evident that the frequency spectrum of  $\theta$  Oph shown in Fig. 7.91 is very similar to the one of V836 Cen shown in Fig. 7.76, except for larger rotational splitting and somewhat higher frequency values. It was thus concluded by Briquet *et al.* (2005) that  $\nu_1, \nu_5$ , and  $\nu_2$  must be three of five quintuplet components. This implies that the  $m$ -value of  $\nu_1$  must be  $-2$  or  $-1$ . Briquet *et al.* (2005) resolved this ambiguity from the spectroscopic time series in which both  $\nu_1$  and  $\nu_3$  were detected (see Fig. 7.92), by using both the moment method and the pixel-by-pixel method. Since  $\nu_3$  was unambiguously identified as a radial mode, Briquet *et al.* (2005) imposed this information in the application of the moment method to identify the dominant mode with frequency  $\nu_1$ . This gave three possible solutions for  $(l_1, m_1)$  from the moment variations:  $(2, -1)$ ,  $(1, -1)$  or  $(2, -2)$ , in that order of probability. Subsequently, the amplitude and phase variations of theoretical line profile variations were computed for these three solutions, and compared with the data. The outcome is shown in different line styles in the left panel of Fig. 7.93. It can be seen that the identification  $m_1 = -1$  for the dominant mode is much more likely than  $-2$ . Moreover, the drop in amplitude in the centre of the profile, as well as the phase change with a value  $\pi$  there, confirm the identification of  $\nu_3$  as a radial mode. Finally,  $\nu_1$  and  $\nu_2$  have  $m$ -values of opposite sign, since

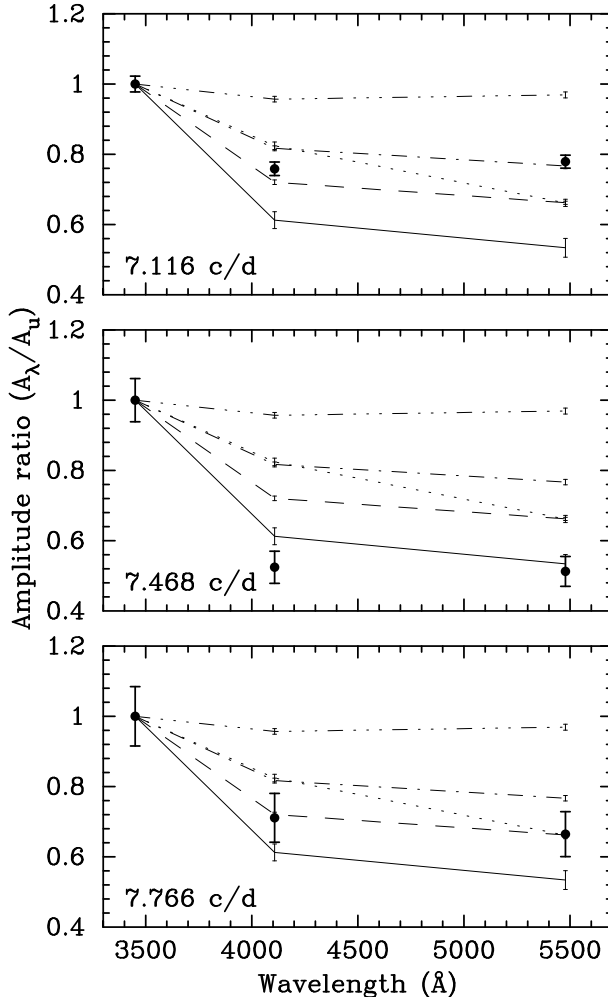


**Fig. 7.94.** Observed (dots) and theoretically computed  $uvy$  amplitude ratios for modes with  $l = 0$  (full), 1 (dashed), 2 (dash-dotted), 3 (dotted), 4 (dash-dot-dot-dotted), normalized with respect to the amplitude in the  $u$  passband, for the three frequencies that allow determination of their mode degree. The small error bars denote the uncertainty on the theoretical amplitude ratios due to the uncertainty of the  $(T_{\text{eff}}, \log g)$  values of the star. Figure reproduced from Handler *et al.* (2005).

their phase curves across the profile have opposite slopes. Briquet *et al.* (2005) therefore came to the final secure mode identification listed in Table 7.5. Their approach is a prototypical example of how multicolour photometric and high resolution spectroscopic information were appropriately intermingled to arrive at unambiguous mode identification of a star's oscillation spectrum, in the situation where the rotation frequency is too high to recognize the multiplet

structure from the frequency values. Note that this already occurs for  $\theta$  Oph, despite its low  $v \sin i$  of only  $30 \text{ km s}^{-1}$ .

As a side product, the moment method delivered the inclination angle of  $\theta$  Oph to be in the interval  $[70^\circ, 90^\circ]$ . Assuming this range to apply to the orbital inclination as well leads to a secondary component mass lower than  $1 M_\odot$  such that the neglect of this star in the interpretation of the line profiles was justified. We recall that the duty cycle of the photometric data was such that the timings of the eclipses were unfortunately not covered with observations.

Briquet *et al.* (2007) presented an extensive abundance analysis based on NLTE atmosphere models and state-of-the-art codes for all the chemical elements detectable in the average spectrum computed from the time series gathered by Briquet *et al.* (2005). We omit their results here, but report their derivation of  $Z = 0.0114 \pm 0.0028$  which is of importance for the mode excitation and the seismic modelling.

Stellar models for non-rotating stars were computed with the evolutionary code CLÉS (Code Liégeois d'Évolution Stellaire, Scuflaire *et al.* 2007), both with and without microscopic diffusion. Radiative forces and a stellar wind were ignored in the adopted diffusion formalism (Thoul *et al.* 1994), while turbulent mixing was treated according to Talon *et al.* (1997). The models with this description of diffusion reproduce the observed surface metallicity and helium abundances of  $\theta$  Oph, for models with initial composition  $X = 0.7211$ ,  $Y = 0.264$ ,  $Z = 0.01485$ . Those models turned out to be very like those obtained without diffusion and with the Asplund *et al.* (2004) solar mixture, the diffusion only affecting the very superficial layers of the star. In particular, the models calculated with and without diffusion had the same frequency spectrum.

Since the adopted description of diffusion did not affect the derived stellar parameters of the models, and may be inappropriate due to the neglect of perhaps more important effects such as radiative levitation and a radiation-driven stellar wind, Briquet *et al.* (2007) continued their seismic modelling without diffusion, while considering sufficiently safe ranges for  $X$  and  $Z$ . They computed models that fit the radial mode with frequency  $\nu_3$  together with the zonal  $l = 1$  mode with frequency  $\nu_6$ , and, subsequently, made use of the quintuplet to add additional constraints. Because the frequency spectra of  $\beta$  Cep stars are so sparse for low order p and g modes (compared with those of solar-like pulsators) one does not have many degrees of freedom to fit securely identified modes. This led to the identification of the radial order of the modes of  $\theta$  Oph as  $g_1$  for the frequency quintuplet containing  $\nu_1, \nu_5, \nu_2$ , the radial fundamental for  $\nu_3$  and  $p_1$  for the triplet  $\nu_4, \nu_6, \nu_7$ . Fitting the three independent  $m = 0$  frequencies resulted in a relation between the metallicity and the core overshooting parameter, as already explained in the case of V836 Cen. In this way, Briquet *et al.* (2007) derived  $\alpha_{\text{ov}} = 0.44 \pm 0.07$ . The accompanying other physical parameters of the models that match the observed modes, for  $X \in [0.71, 0.7211]$  and  $Z \in [0.009, 0.015]$ , are  $M = 8.2 \pm 0.3 M_\odot$ ,

$T_{\text{eff}} = 22\,260 \pm 280$  K,  $\log g = 3.950 \pm 0.006$ ,  $X_c = 0.38 \pm 0.02$ . As an *a posteriori* test, it was found that the modes of  $\theta$  Oph are well excited by the classical  $\kappa$  mechanism for a metallicity above 0.011.

Given that the detected modes of  $\theta$  Oph are exactly the same than those explored for V836 Cen to probe the internal rotation, Briquet *et al.* (2007) made a similar study. The rotational kernels for the three independent modes of  $\theta$  Oph are indeed very similar to those of V836 Cen (a figure is available in Briquet *et al.* 2007). On the other hand, the splittings within the detected multiplets are slightly asymmetric for  $\theta$  Oph. This is why Briquet *et al.* (2007) computed adiabatic frequencies with the code FILOU (Tran Minh & Léon 1995, Suárez 2002), which includes the effects of rotation up to the second order, following Soufi *et al.* (1998). The input of this code is the spherically symmetric component of the structure model. The output is the second order deformation due to rotation. In principle, the gravity must be corrected for the effect of centrifugal acceleration in the spherically symmetric component of the model. However, for  $\theta$  Oph with its slow rotation, this correction has a negligible effect on the multiplet asymmetries. Therefore, the best non-rotating model fitting the three zonal mode frequencies, whose global parameters are in the ranges listed above, was used as input model for FILOU. As a result, it was found that the asymmetry observed in the  $l = 1$  triplet can be well reproduced by taking into account the effects of rotation up to the second order. For the quintuplet, the agreement is not very good, however. Contrary to V836 Cen and  $\nu$  Eri, for which non-rigid rotation was proven, the observed rotational splittings for  $\theta$  Oph are compatible with rigid rotation, *i.e.* strong differential internal rotation is excluded.

It is evident that the seismic tuning of the internal rotation is very dependent on the frequency accuracy, as well as on the number of detected modes and the nature of their probing kernels. The frequency accuracy is of order  $10^{-6}$  d $^{-1}$  for both V836 Cen and  $\nu$  Eri, and  $10^{-4}$  d $^{-1}$  for  $\theta$  Oph. Long term monitoring is in any case required to probe the internal rotation of massive stars in far more details than possible at present.

### 7.3.4 HR 1217 among the roAp Stars

#### 7.3.4.1 The Star

HR 1217 (HD 24712; DO Eri) was the second roAp star discovered (Kurtz 1981, 1982), and it is asteroseismically the best-studied roAp star. It is a bright, single, southern-equatorial star ( $V = 5.99$ ,  $\alpha_{2000} = 03^{\circ}55\arcmin16$ ,  $\delta_{2000} = -12^{\circ}05\arcmin57$ ) accessible from observatories in both the northern and southern hemispheres, making it a excellent target for multi-site campaigns (Kurtz & Seeman 1983; Kurtz *et al.* 1989, 2005). Its spectral type is F0 in the Henry Draper Catalogue, A5p in the Bright Star Catalogue (Hoffleit 1982) and Ap SrCr(Eu) in the Michigan Spectral Catalogue (Houk & Smith-Moore 1988). Other spectral classifications place its temperature type near to F0,

making it one of the coolest known Ap stars; its H $\beta$  index,  $\beta = 2.670$  (Martinez 1993), is consistent with this. Strömgren photometry shows the typical peculiar indices of the roAp stars with a metallicity index of  $\delta m_1 = -0.023$  and a luminosity index of  $\delta c_1 = -0.074$  (Martinez 1993; see Kurtz & Martinez 2000 for a discussion of the interpretation of the Strömgren photometry).

One of the strengths of studying HR 1217 is that there is a wealth of astrophysical information known about it. Its Hipparcos parallax shows it to be in the solar neighbourhood at a mere 50 pc with a luminosity of  $L = 7.8 \pm 0.7 L_\odot$  (Matthews *et al.* 1999). As mentioned in Sect. 2.3.5, the atmospheres of the most peculiar of the roAp stars show a strong core-wing anomaly in the H lines (Cowley *et al.* 2001) and a wing-nib anomaly in the Ca II K-line (Cowley *et al.* 2006) indicating an abnormal temperature-depth structure to their atmospheres. HR 1217 has both of these anomalies. A first attempt at self-consistent atmospheric models that can account for the H core-wing anomaly was made by Kochukhov *et al.* (2002), but it is not yet possible to model the Balmer lines fully in the roAp stars, much less their entire spectra. The effective temperatures of the roAp stars are thus notoriously difficult to determine. Nevertheless, various photometric and spectroscopic studies conservatively give  $T_{\text{eff}} \approx 7300 \pm 200$  K (Ryabchikova *et al.* 1997; Lüftinger *et al.* 2008), consistent with an F0p spectral type and with the H $\beta$  index.

The magnetic field of HR 1217 has been studied extensively over the years (Preston 1972; Mathys 1991; Bagnulo *et al.* 1995; Mathys & Hubrig 1997; Leone, Cantanzaro & Catalano 2000; Wade *et al.* 2000). Bagnulo *et al.* found from broad-band linear polarimetry a polar field strength of about 3.9 kG, a rotational inclination of  $i = 137^\circ$  and a magnetic obliquity of  $\beta = 150^\circ$ , with uncertain errors on these values. This geometry of the obliquely rotating magnetic field means that we can only see one magnetic (hence also one pulsation) pole over the rotation cycle. There is some controversy about the precise rotation period with disagreement in the fourth significant figure, but all determinations are close to  $P_{\text{rot}} = 12.46$  d (see, *e.g.*, Ryabchikova *et al.* 2005; Kurtz *et al.* 2005).

HR 1217 is strongly spotted with horizontal abundance variations associated with the magnetic field (Preston 1972; Ryabchikova *et al.* 1997), making it a typical  $\alpha^2$  CVn star. Light variations with rotation associated with the horizontal abundance variations are well-known in this star (Wolff & Morrison 1973). It shows significant overabundances of rare earth elements that vary with rotation, as does Mg. Lüftinger *et al.* (2008) studied the surface abundance structures of sixteen elements and the vertical abundance stratification of Fe, as well as the magnetic field structure which they found to be well-represented by a pure dipole.

HR 1217 is of such interest that it is not only the best-studied of roAp stars, but is one of the most-studied of all types of asteroseismic targets. Multi-site campaigns in photometry have been carried out, as well as a month-long satellite photometry data set from MOST being obtained simultaneously

with an extensive spectroscopic study. This star has been the driver for much observational effort and for many of the theoretical discussions of magneto-acoustic pulsation modes (see the references in Sect. 2.3.5).

### 7.3.4.2 The Photometric Observations and Results

To obtain the frequencies that are the basic input data for asteroseismology it is thus necessary to observe roAp stars in multi-site campaigns for ground-based data, particularly to reduce or eliminate aliases in the frequency spectrum (see Chapter 5). Even from single-site observations Kurtz (1982) showed that HR 1217 has a series of frequencies with nearly equal spacing typical of alternating even and odd degree modes separated by half the large spacing,  $\Delta\nu$  (see Chapter 3), similar to the patterns seen for the Sun and for solar-like oscillators discussed earlier in this chapter. It is this asymptotic frequency pattern and its similarity to the solar-like oscillators that makes HR 1217 of such interest.

HR 1217 was investigated with an extensive global campaign in 1986 (Kurtz et al. 1989). A key result from that data set (which we refer to as the “1986 data”) was a list of six principal pulsation frequencies, five of which had alternating spacings of  $33.4\ \mu\text{Hz}$  and  $34.5\ \mu\text{Hz}$ , the sixth of which was separated by a then-inexplicable  $50\ \mu\text{Hz}$  from the fifth frequency. This was followed by the Whole Earth Telescope (WET) extended coverage campaign, Xcov20, on the roAp star HR 1217 (which we refer to as the “2000 data”). This latter data set is likely to remain the definitive ground-based photometric data set, since the MOST satellite obtained a month-long data set from space during 2004 November–December for which a complete analysis has yet to be published.

As already emphasized in Chapter 3, the large spacing,  $\Delta\nu$ , is a measure of the sound-crossing time of the star, which in turn is determined by the star’s mean density and radius. With a mass of about  $2M_\odot$  that is typical of Ap stars,  $\Delta\nu$  reflects the radius of the star, with  $\Delta\nu \propto R^{-3/2}$ . In the asymptotic limit, the number of nodes in the radial direction,  $n$ , is much larger than the spherical degree  $l$ . Assuming adiabatic pulsations in spherically symmetric stars the pulsation frequencies are,

$$\nu_{nl} = \Delta\nu(n + \frac{l}{2} + \frac{1}{4} + \alpha) + \delta\nu, \quad (7.95)$$

where  $\alpha$  is a (small) constant (Tassoul 1980, 1990; see Eqs (3.215) and (3.219) and  $\delta\nu$ , the “small spacing”, is a measure of the age of the star since it is sensitive to the central condensation, hence the core H mass fraction. Without precise identification of the degree ( $l$ ) of the pulsation modes, asymptotic theory allows the frequency spacing to be uncertain by a factor of two, depending on whether modes of alternating even and odd  $l$  are present (producing modes separated by  $\Delta\nu/2$  in frequency), or only modes of the same  $l$  with consecutive values of  $n$ .

The results of the 1986 campaign were inconclusive as to whether  $\delta\nu$  was  $68\,\mu\text{Hz}$  or  $34\,\mu\text{Hz}$ . Fortunately, the ambiguity could be resolved by a precise determination of the luminosity of the star. If  $\Delta\nu$  were  $34\,\mu\text{Hz}$ , then the radius of HR 1217 would be large enough that it would be far removed from the main sequence (i.e. more evolved) and therefore more luminous (Heller & Kawaler 1988). Matthews *et al.* (1999) used the Hipparcos parallax measurement to place HR 1217 unambiguously close to the main sequence, thus determining that  $\Delta\nu$  is indeed  $68\,\mu\text{Hz}$ . This deepened the “mystery of the sixth frequency”, lying  $\frac{3}{4}\Delta\nu$  higher than the fifth frequency. It is easy to see from the above asymptotic frequency relation that there is no clear theoretical explanation for this spacing within this relation.

That asymptotic frequency spacing is valid only for linear adiabatic pulsations in spherically symmetric stars. However, the magnetic field, the chemical inhomogeneities and rotation all contribute to breaking the spherical symmetry in roAp stars. It is therefore important to know the effects that these deviations from spherical symmetry have on the theoretical frequency spectra of roAp stars, before comparing those with the observed frequency spectra. The effects of the chemical inhomogeneities were discussed by Balmforth *et al.* (2001). The effects of the magnetic field on the oscillations of roAp stars (Dziembowski & Goode 1996; Bigot *et al.* 2000; Cunha & Gough 2000; Saio & Gautschy 2004; Saio 2005; Cunha 2006; Sousa & Cunha 2008), as well as the joint effect of rotation and magnetic field (Bigot & Dziembowski 2002), have been studied. While generally the magnetic field effect on the oscillations is expected to be small, Cunha & Gough (2000) found that at the frequencies of maximal magneto-acoustic coupling, the latter is expected to become significantly large, resulting in an abrupt drop of the separation between mode frequencies. Cunha (2006) studied this in more detail and found that sudden drops or increases in the frequency separations can occur that depend on the geometry and degrees of the modes.

The observational consequence of the results of Cunha & Gough (2000) suggested that we should see equally spaced modes in roAp stars with an occasional mode much closer to its lower frequency counterparts. Cunha (2001) suggested that the explanation of the strange separation between the last two modes observed in HR 1217 in the 1986 data could rest on the occasional abrupt decrease of the large separations predicted by Cunha & Gough (2000). For this prediction to hold, she argued that the observations of Kurtz *et al.* (1989) must have missed detecting a mode at a frequency  $34\,\mu\text{Hz}$  higher than that of the fifth mode they observed. She predicted that new, more precise measurements would find this “missing mode” if the Alfvénic losses were not large enough to stabilize it. Detailed re-examination of the 1986 data shows no peak at the key position at the  $\sim 0.1\,\text{mmag}$  level.

In the preliminary analysis of the 2000 data Kurtz *et al.* (2002) found the missing mode predicted by Cunha, giving support to her theory. Kurtz *et al.* (2005) analysed the 2000 data in far more detail and found that the new mode is in fact a pair of modes separated by  $2.6\,\mu\text{Hz}$ , a value that is potentially the

small spacing,  $\delta\nu$ . The small spacing has not been unambiguously determined for any roAp star. One of the pair of new modes fits the alternating  $33.4\,\mu\text{Hz}$ ,  $34.5\,\mu\text{Hz}$  spacing of the first five modes, and is now separated by nearly precisely  $\frac{1}{4}\delta\nu$  from the highest detected frequency. Fig. 7.95 shows a section of the frequency spectrum for the WET 2000 data and Fig. 7.96 shows schematic amplitude spectra for both the 2000 and 1986 data sets.

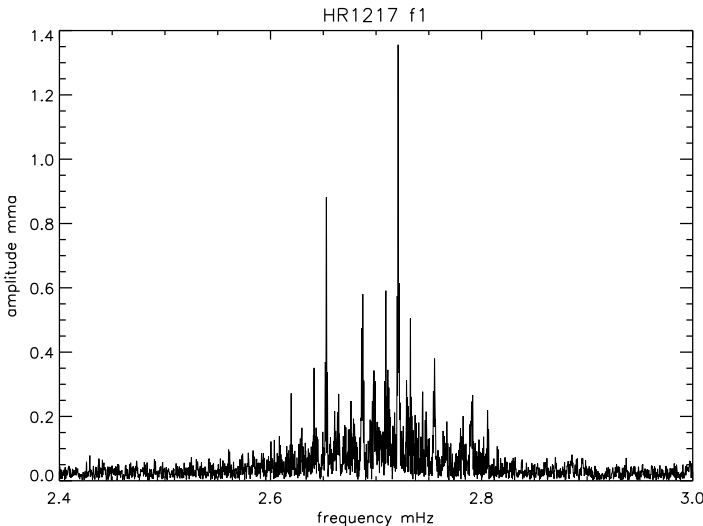


**Fig. 7.95.** The amplitude spectrum of the WET 2000 data set for HR 1217. In spite of the multi-site coverage, the aliases remain a problem, especially the  $3\,\text{d}^{-1}$  aliases which are close to half the large spacing for this star ( $34.7\,\mu\text{Hz}$  as opposed to  $34.5\,\mu\text{Hz}$  and  $33.4\,\mu\text{Hz}$  and  $34.6\,\mu\text{Hz}$ ). Figure reproduced from Kurtz *et al.* (2005).

As can be seen in Fig. 7.96, there is an alternating frequency spacing of about  $33.4\,\mu\text{Hz}$  and  $34.5\,\mu\text{Hz}$ , consistent with an interpretation of alternating even and odd  $l$  modes, although, for HR 1217 the modes cannot be pure spherical harmonic modes. The spacing of the highest two frequencies is, within the errors, exactly half of the  $33.4\text{-}\mu\text{Hz}$  spacing, and the spacing of the close doublet of the “new frequencies” is possibly the small spacing.

The rotational sidelobes seen in Fig. 7.96 are not evidence of  $m$  modes, but rather describe the rotational variation of amplitude seen as the oblique pulsation modes are viewed from different aspect angles. Within the oblique pulsator model the amplitudes of the rotational sidelobes can be used to deduce the pulsation mode, hence are a method of mode identification unique to the roAp stars, in addition to those discussed in Chapter 6 for other types of pulsating stars. Kurtz *et al.* (2005) show for HR 1217 that all of the modes are distorted from purely spherical harmonics, as is expected theoretically be-

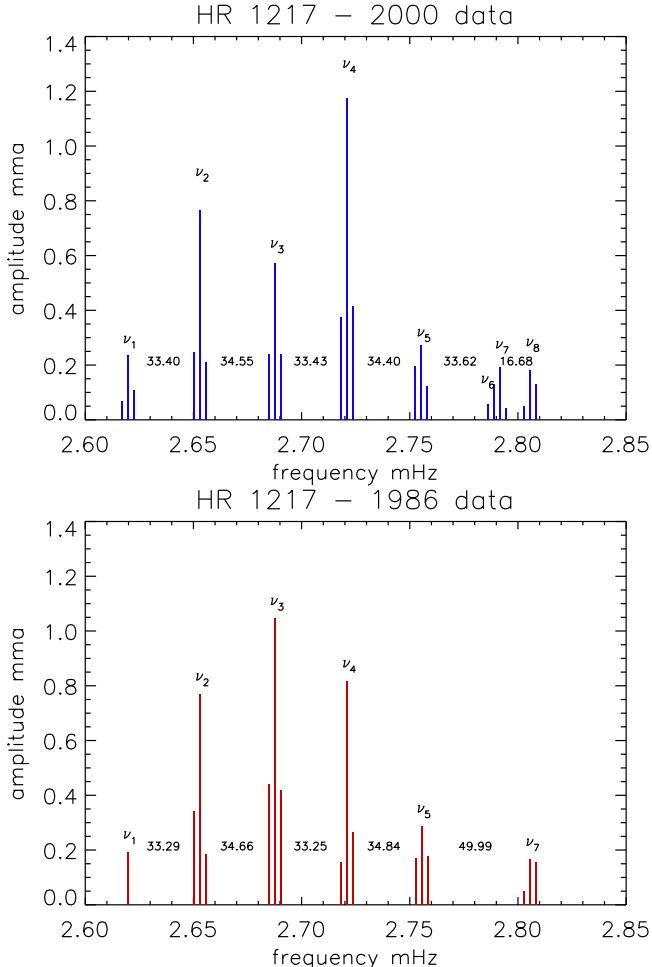


**Fig. 7.96.** Top panel: A schematic amplitude spectrum for the frequencies in the 2000 data for HR 1217. The spacing of the rotational sidelobes is exaggerated to make them easier to see. Bottom panel: The same for the 1986 data, again with exaggerated rotational sidelobe separations to make them easier to see. The frequency separations are given in  $\mu$ Hz. It is easy to see the alternating spacing of even and odd degree modes, except for the spacing of the highest frequency, discussed in detail in the text. The amplitude differences for individual mode frequencies in the two data sets are real. Figures reproduced from Kurtz *et al.* (2005).

cause of the effects of the magnetic field (see Saio 2005). They show that the modes are alternating distorted dipole modes and either distorted radial or quadrupole modes.

Thus the frequency spectrum of HR 1217 bears strong resemblance to those of the solar-like oscillators discussed earlier in this Chapter, except that the

strong magnetic field perturbs the frequencies making it more difficult to interpret them, but simultaneously promising more information about the magnetic field and its interaction with the pulsations. Further progress depends – as usual for asteroseismic targets – on better frequency sets. These are best obtained from space – as with the MOST data – or from multisite spectroscopic ground-based campaigns.

### 7.3.4.3 Spectroscopic Radial Velocity Studies of roAp Stars

While photometry has been successful for discovering roAp stars and studying their frequency spectra, it is now clear that high resolution spectroscopy is a superior tool for these purposes, and for other purposes out of the reach of photometry. In the 15 years following the announcement of the class (Kurtz 1982) only a few radial velocity studies were attempted for these stars. Libbrecht (1988b) detected low-amplitude radial velocity variations of only  $21\text{ m s}^{-1}$  in the bright roAp star  $\gamma\text{ Equ}$  ( $42\text{ m s}^{-1}$  peak-to-peak). This was done using the Palomar 5-m telescope, then one of the largest in the world, hence was pushing the limit of radial velocity precision. At about the same time Matthews *et al.* (1988) detected radial velocity variations of  $200\text{ m s}^{-1}$  in HR 1217 using the Canada-France-Hawaii telescope. While both of these detections were significant, the S/N ratios for the velocity amplitudes and phases were not high, and it did not appear that much could be extracted from such studies. In particular, the view was that a pulsating star could be characterized with one radial velocity at any given time – that is, that the whole of the observable atmosphere could be treated as a single pulsating layer. While this is a good approximation for Cepheids, RR Lyrae stars,  $\delta\text{ Sct}$  stars – in fact, for most pulsating stars – it is very much not the case for the roAp stars.

A new view of the radial velocity variations in roAp stars came quickly in studies by several groups about a decade after the above seminal studies. Kanaan & Hatzes (1998) found that different sections of the spectrum, and indeed, different individual lines, give different radial velocities – in their case with a range of  $100\text{ m s}^{-1}$  up to  $1\text{ km s}^{-1}$  in the roAp star  $\gamma\text{ Equ}$ . The errors of their amplitude determinations were as low as  $10 - 20\text{ m s}^{-1}$  for individual lines with S/N as good as 10, in some cases. They pointed out that lines of different ions form at different atmospheric depths so that studies of the radial velocities of individual lines were a powerful new tool to test independently for both surface abundance variations and, for the first time for any star other than the Sun, the *depth* distribution of ions, thus providing a new way to check the predictions of diffusion theory.

Baldry *et al.* (1998) found similar behaviour in the roAp star  $\alpha\text{ Cir}$  (HD 128898). Hatzes & Kürster (1994) had placed an upper limit of  $60\text{ m s}^{-1}$  to any radial velocity variation in  $\alpha\text{ Cir}$  using 45-Å of spectrum with an iodine cell, while Baldry *et al.* (1998) found amplitudes up to  $1\text{ km s}^{-1}$  in some 10-Å wavelength bands. They also thought that the phases suggested the presence of a radial node in the observable atmosphere of this star. In a follow-up

study Baldry *et al.* (1999) studied the line bisector for H $\alpha$  and found both amplitude and phase variations as a function of depth in the line, thus as a function of height in the atmosphere. Their observations indicated a phase reversal between the bottom and top of the line, hence supported the idea of an observed radial node.

At this same time the true picture of the radial velocity variations in roAp stars emerged from studies of  $\gamma$  Equ by Malanushenko *et al.* (1998) and Savanov *et al.* (1999) who showed that lines of the rare earth elements Pr III and Nd III have large amplitudes of up to  $400\text{ m s}^{-1}$  in  $\gamma$  Equ, while lines of Ba II and Fe II show no detectable radial velocity variations at all. These authors were able to show the radial velocity curves for individual lines with clearly visible periodic variations without having to resort to Fourier Transforms to prove the presence of the oscillations.

$\gamma$  Equ is one of the brightest roAp stars and one of the few known in the northern hemisphere, hence this star features in many studies. Following the discoveries of Malanushenko *et al.* (1998) and Savanov *et al.* (1999), Kochukhov & Ryabchikova (2001) showed the line-by-line variability in  $\gamma$  Equ spectacularly for a 26-Å section of spectrum, making it abundantly clear that the amplitudes of the pulsation in roAp stars are very strongly a function of atmospheric height. Figure 7.98 shows part of their their beautiful spectra, where the height dependence of the pulsation in  $\gamma$  Equ is abundantly evident. The 6145 Å line of Nd III forms high in the atmosphere where the pulsation amplitude is high, whereas the Ba II line forms more deeply where the amplitude is so low that no variation is seen. For the roAp stars we can resolve the pulsation behaviour as a function of optical depth over a large range,  $-5 \leq \log \tau_{5000} \leq 0$  and possibly even higher.

Figure 7.97 shows the behaviour of the pulsation amplitude and phase as a function of line depth – hence atmospheric height – for the singly-periodic roAp star HD 12932 from UVES VLT data. The amplitude increases outwardly through the hydrogen line-forming layer, then decreases in the Nd III line-forming layer. The outward increase in amplitude is partially caused by the decrease in density, requiring a larger amplitude to carry the pulsational energy, and possibly because a radial node lying below the H $\alpha$  line-forming layer. We do see such nodes directly in other roAp stars, such as HD 137949 (Mkrtychian *et al.* 2003; Kurtz *et al.* 2005). The decrease in amplitude in the Nd III line-forming layer, likewise, may be a consequence of another radial node further out in the atmosphere, or may be caused by energy losses, since at this atmospheric level the magnetic pressure is much stronger than the gas pressure and the modes are magneto-acoustic. The pulsation phases indicate that there is an outwardly travelling component to the pulsation with the time of pulsation maximum being later in the Nd III line-forming layer. See Kurtz *et al.* (2006) for the variety of behaviour in a set of 10 roAp stars and for more discussion.

While the theory and observations presented for other types of stars in this chapter concern global properties of the stars deduced from asteroseis-

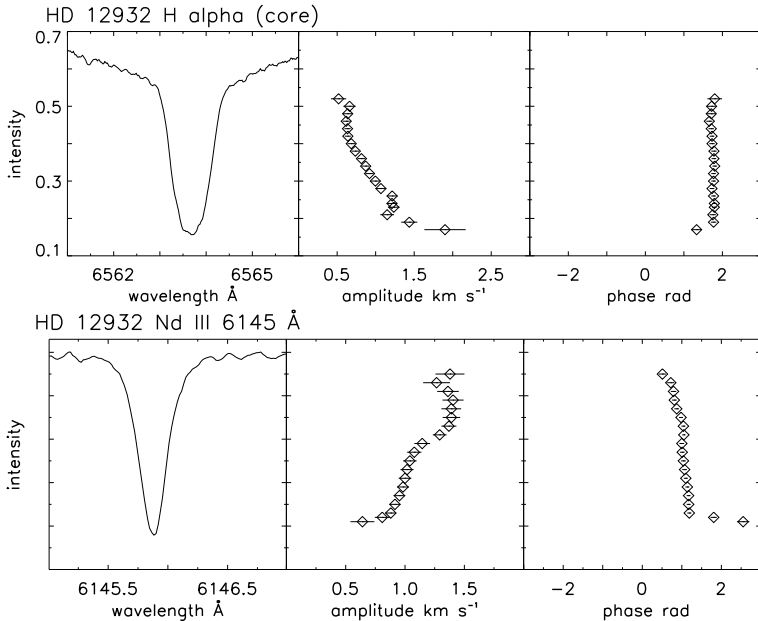


**Fig. 7.97.** The line profile of the H $\alpha$  core (top panel) and the Nd III 6145 Å line (bottom panel) on the left. Using line bisectors, the middle and right panels show the pulsation amplitude and phase as a function of line depth, hence atmospheric height. The H $\alpha$  line core forms between  $-4 \leq \log \tau_{5000} \leq -2$ , and the 6145 Å line forms even higher than that, hence these diagrams show the pulsational behaviour at atmospheric levels that would be chromospheric in the Sun. Adapted from Kurtz *et al.* (2006).

mology, the roAp stars uniquely allow detailed inference of upper atmospheric properties at levels that cannot be observed in any star but the Sun. Much of the future of roAp star studies will concentrate on this special ability, but the high precision of modern radial velocity measurements also mean that extensive frequency sets for use in global asteroseismology will also come from multi-site spectroscopic studies.

Mkrtichian *et al.* (2008) have given the first clear demonstration of this for HD 101065 where they find 15 independent mode frequencies from 4 nights of HARPS high resolution, high precision spectroscopic radial velocities. They derived a large spacing of  $64.1 \pm 0.9 \mu\text{Hz}$  for which their models, including the effects of the magnetic field, give best agreement for  $M = 1.53 \pm 0.03 M_\odot$ , an age of  $1.5 \pm 0.1 \text{ Gyr}$ ,  $T_{\text{eff}} = 6700 \pm 100 \text{ K}$  and a polar magnetic field strength of  $B_p = 8.7 \pm 0.3 \text{ kG}$ . These are exciting new results for this most peculiar of all roAp stars (and arguably the most peculiar of all stars). These results are consistent with other recent studies, with the exception of the observed magnetic field strength which is only about 2.2 kG. A  $B_p = 8.7 \text{ kG}$  field would generate clear Zeeman components in the spectra that manifestly are not

present. Here is a new puzzle to add to the many that have been encountered for this star over the decades since its discovery. Whether this is a puzzle for HD 101065 only, or a more general puzzle for the understanding of roAp stars is still to be discovered.

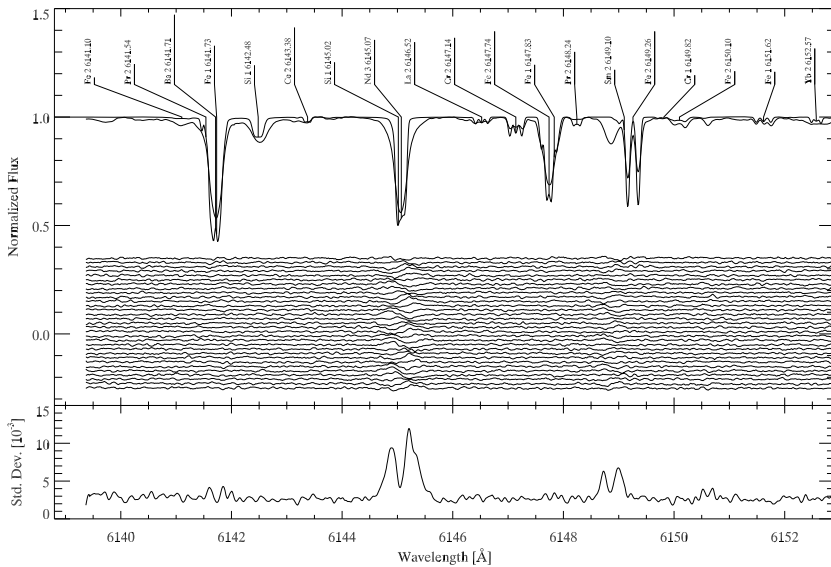


**Fig. 7.98.** A short section of the spectrum of the roAp star  $\gamma$  Equ is shown at the top, with 1-min difference spectra spanning 1 h below. The bottom curve shows the intensity standard deviation as a function of wavelength. It is clear that the Nd III 6145 Å line shows large amplitude pulsation, while the Ba II 6141 Å line shows none at all. Adapted from Kochukhov & Ryabchikova (2001).

In recent years many high-resolution spectroscopic studies of roAp stars have been made. These have succeeded in directly resolving radial nodes in the observable atmosphere, they have demonstrated the depth structure of the pulsation and of the stratified abundances of the elements, they have detected new pulsation frequencies high in the atmosphere that are not seen in photometric observations, and they have made the first steps towards full three-dimensional views of the pulsation mode geometries and abundance distributions; all of these determinations are unique to the roAp stars. Some examples of observational spectroscopic studies of the pulsation in individual stars where more detail can be found are:

- HD 24712 (HR 1217) (Balona & Zima 2002; Mkrtichian & Hatzes 2005; Ryabchikova *et al.* 2007);
- HD 83368 (HR 3831) (Baldry & Bedding 2000; Kochukhov & Ryabchikova 2001; Balona 2002; Kochukhov 2004, 2005);

- HD 99563 (Elkin, & Mathys 2005);
- HD 101065 (Mkrtichian & Hatzes 2005; Mkrtichian *et al.* 2008);
- HD 116114 (Elkin *et al.* 2005);
- HD 122970 (Gamarova *et al.* 2004);
- HD 128898 ( $\alpha$  Cir) (Baldry *et al.* 1998, 1999; Kochukhov & Ryabchikova 2001; Balona & Laney 2003);
- HD 137909 ( $\beta$  CrB) (Kurtz *et al.* 2007a);
- HD 137949 (33 Lib) (Mkrtichian *et al.* 2003; Kurtz *et al.* 2005b);
- HD 166473 (Kurtz *et al.* 2003; Mathys *et al.* 2007);
- HD 176232 (10 Aql) (Elkin *et al.* 2008);
- HD 201601 ( $\gamma$  Equ) (Malanushenko *et al.* 1998; Savanov *et al.* 1999; Kochukhov & Ryabchikova 2001; Ryabchikova *et al.* 2002; Leone & Kurtz 2003; Kochukhov *et al.* 2004a,b).

See, also, Kurtz *et al.* (2005b, 2006a,b; 2007a,b) and Ryabchikova *et al.* (2007) for more information about these ten roAp stars: HD 9289, HD 12932, HD 19918, HD 60435, HD 99563, HD 101065, HD 122970, HD 128898, HD 134214 and HD 137949, Ryabchikova *et al.* (2007). See Kurtz *et al.* (2006, 2007) for more information about the new upper-atmosphere frequencies not detected in photometric observations.

#### 7.3.4.4 Spectroscopic Radial Velocities for HR 1217

HR 1217 is difficult to study observationally for two reasons: 1) Its mode frequencies are separated by  $\sim 34\,\mu\text{Hz}$  which is close to  $3\,\text{d}^{-1}$ . This makes it mandatory that high duty cycle data sets are obtained to suppress the aliases, hence the cross-talk in the amplitude spectrum between the window patterns of the mode frequencies. 2) Its rotation period of 12.46 d requires a data set at least 50% longer than this to resolve the rotational sidelobes that describe the amplitude modulation of the obliquely pulsating modes.

To deal with these requirements the WET campaign on the star involved 8 observatories and nearly 50 astronomers for a three-week run (Kurtz *et al.* 2005a). At present the high precision needed for radial velocity studies of roAp stars requires large telescopes. This is partly because that is where the highest precision radial velocity spectrographs have been installed, but also because the need for high S/N spectra, high spectral resolution for precise radial velocity determination, and short time exposure to resolve in time the radial velocity curves of stars with periods in the 6 – 21-min range requires large aperture to gather the required photons. A three-week multi-site campaign on the appropriate telescopes, which are in high demand, has not yet been possible. Solutions to this problem lie in a dedicated network of asteroseismic telescopes measuring precise radial velocities (SONG; see Chapter 8), or a single high precision radial velocity meter in Antarctica (*e.g.*, SIAMOIS; see Chapter 8).

Until those instruments are available, Ryabchikova *et al.* (2007) have made a great effort and obtained a fine data set for HR 1217 using the GECKO (Grating EChelle speKtrOgraph) spectrograph on the Canada-France-Hawaii telescope, the SOFIN spectrograph on the Nordic Optical Telescope, on the ESO 3.6-m telescope, UVES on the Very Large Telescope and SARG (Spettrografo Alta Risoluzione Telescopio Nationale Galileo) on the TNG (Telescope Nationale Galileo). They gathered a total of 34.5 h of spectroscopic observations on 13 nights spanning 3 yr. Some of the data were taken simultaneously with the MOST month-long photometric run at the end of 2004. While alias problems precluded them from resolving completely the individual mode frequencies, they obtained detailed information about the vertical pulsation behaviour that is consistent with other results for roAp stars pulsating in single modes. In particular, they show the outwardly running component to the pulsation modes clearly in Fig. 7.99.

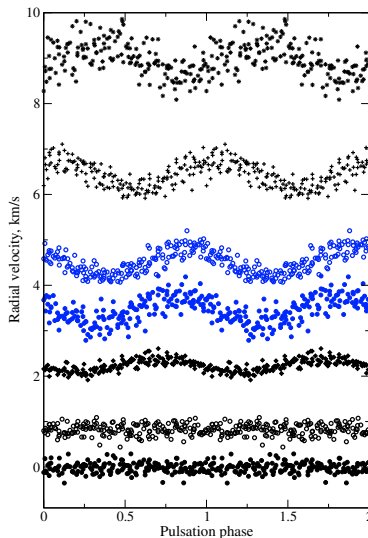


**Fig. 7.99.** The radial velocity variations of HR 1217 for particular spectral lines folded on one of the known pulsation periods. The relative amplitudes and phases are displayed with an arbitrary zero point shift to allowing ease of viewing. From the bottom upwards the ions represented are: Ca I, Fe I, Eu II, Nd II, Nd III, Pr III and Tb III. The lines are presented in the order that their line-forming layers occur in the atmosphere. Thus this figure clearly shows the increasing pulsation amplitude with height and the phase shift to later times of pulsation maximum with height, hence an outwardly running wave component to the pulsation. Adapted from Ryabchikova *et al.* (2007).

Thus HR 1217 has been studied asteroseismically both photometrically and spectroscopically in great detail, illustrating the unique information available from analysis of the pulsation modes in roAp stars. Further observational advances for the roAp stars will come from multi-site spectroscopic and photometric campaigns with higher S/N to find larger frequency sets for asteroseismic inference.

## 7.4 Compact Pulsators

### 7.4.1 The GW Vir Star PG 1159–035, GW Vir itself

#### 7.4.1.1 The Star

PG 1159–035 (PG 1159 hereafter; GW Vir;  $B = 14.9$ ) is the asteroseismic record-holder, after the Sun. It has the most pulsation frequencies detected, the most modes identified and was a seminal star in the development and expansion of the field of asteroseismology. It is the prototype of the hottest class of pulsating white dwarfs, the GW Vir stars; see Chapter 2 for an explanation of the white dwarf classification system.

PG 1159 is an equatorial pre-white dwarf star that was noted to have an ultraviolet excess by Green (1977) in a survey of white dwarfs, hot subdwarfs and quasars that show such excesses (see Green *et al.* 1986). Because Green’s PhD survey was done from Palomar Observatory, it was named the Palomar-Green Survey, hence the ultraviolet excess objects found have names beginning with “PG”. PG 1159 is one of the hottest stars known with many temperature estimates having been made since its discovery. Jahn *et al.* (2007) give  $T_{\text{eff}} = 140\,000 \pm 5\,000$  K and  $\log g = 7$  (cgs) from ultraviolet spectra obtained with the Hubble Space Telescope and the Far Ultraviolet Spectroscopic Explorer.

Two years after Green’s thesis McGraw *et al.* (1979a,b) discovered PG 1159 to be pulsating in at least two modes, using observations from the Multiple Mirror Telescope (MMT). Winget *et al.* (1985) analysed data spanning 4 yr, finding 8 pulsation modes and discussing a period change for the mode of highest amplitude. This led to the Whole Earth Telescope campaign (Xcov3) in 1989 March that is seminal for white dwarf asteroseismology and even asteroseismology in general (Winget *et al.* 1991). Other observing campaigns were carried out in 1990, 1993, 200 and 2002 with a meta-analysis of the data being carried out by Costa *et al.* (2008). The results given here are based on those and the original work of Winget *et al.* (1991).

#### 7.4.1.2 The Data

The third extended coverage campaign of the Whole Earth Telescope (Xcov3) ran for two weeks during 1989 March 1–13 with PG 1159 as its primary target; 264 h of high-speed photometric data in white light with 10-s integrations were

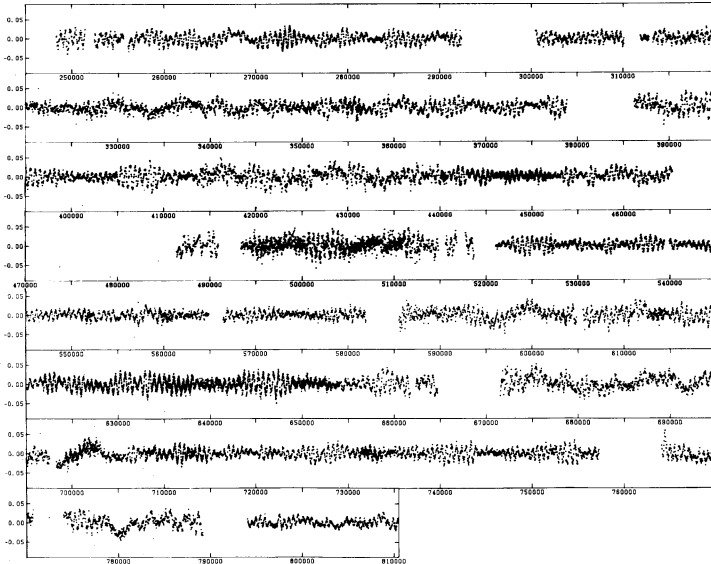


**Fig. 7.100.** This light curve shows the central 6 d of the two-week WET run in 1989 March for PG 1159. Note the very high duty cycle. There are many sections of overlap between telescopes in the network that can be seen as an apparent increase in the density of the data points. The time axis is labelled in seconds; the intensity ordinate is in units of fractional intensity. The panels read continuously like lines of print, from left-to-right, top-to-bottom. From Winget *et al.* (1991).

obtained by a consortium of 32 astronomers using telescopes at 9 observatories with a duty cycle of 65%, and a useful overlap between observing sites of 13%. Fig. 7.100 shows the light curve for 6.5 d of the run when all observatories were online; note the very high duty cycle. Fig. 7.101 shows the power spectrum of the entire data set which is a classic in asteroseismology.

A total of 125 frequencies were detected in Fig. 7.101, 101 of which were identified with individual pulsation modes. This is a record number of modes – the fundamental data for asteroseismic modelling – that has only been exceeded by the meta-analysis of this same star by Costa *et al.* (2008), including the original WET data set, for which there are now 198 identified pulsation modes. Costa *et al.*'s analysis included data from 1979, 1980, 1983, 1984, 1985, 1989, 1990, 1993, 2000 and 2002 totalling 869 h of data; see their Table 1 for further details on the many observations of this star.

#### 7.4.1.3 Mode Identification and Seismic Modelling

Figure 7.101 shows obvious triplet patterns that are the signature of dipole modes with  $(l = 1, m = -1, 0, +1)$ ; there are many of them. Less obvious at first glance, but clear upon closer inspection, are many quintuplets that

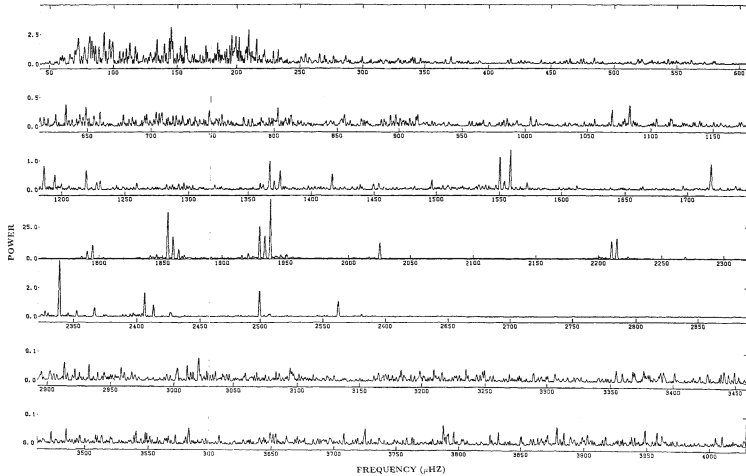


**Fig. 7.101.** The power spectrum of the entire WET Xcov3 data set for PG 1159. The panels read continuously like lines of print, from left-to-right, top-to-bottom. The abscissa shows frequency in  $\mu\text{Hz}$ ; the ordinate is labelled in units of  $10^{-6}$  in intensity power. Note the obvious dipole triplets. Careful inspection shows many quadrupole quintuplets, also. Figure reproduced from Winget *et al.* (1991).

are the signature of quadrupole modes; for some of these all members of the multiplet ( $l = 2, m = -2, -1, 0, +1, +2$ ) were detected, for others some of the multiplet components were either not excited, or had amplitudes too low to detect. Winget *et al.* (1991) averaged the triplet and quintuplet patterns to produce clear, measurable patterns for seismic inference. Figure 7.102 shows these patterns beautifully.

An important characteristic of high-overtone g modes is that the frequency spacing for dipole triplets and quadrupole quintuplets is not the same. The asymptotic relation for the period spacing is

$$\Pi = \frac{\Delta\Pi}{\sqrt{l(l+1)}}(n + \frac{l}{2} + \alpha_g) \quad (7.96)$$

(see Chapter 3, Eqs (3.236) and (3.237)). Since the multiplet spacing depends on  $l$ , it is possible to prove that the triplets are dipole triplets (not quadrupole quintuplets with two modes unexcited) and that the quintuplets are quadrupole quintuplets. Hence the identification of the degree,  $l$ , or the modes in PG 1159 is secure. From the spacings of the multiplets the rotation period of PG 1159 is precisely determined to be  $P_{\text{rot}} = 1.3935 \pm 0.0008$  d (Costa *et al.* 2008).

The period spacing for consecutive overtones of the dipole modes and separately for the quadrupole modes gives  $\Delta\Pi$  which is a sensitive measure of the mass of the star; deviations from uniform period spacing are a signature

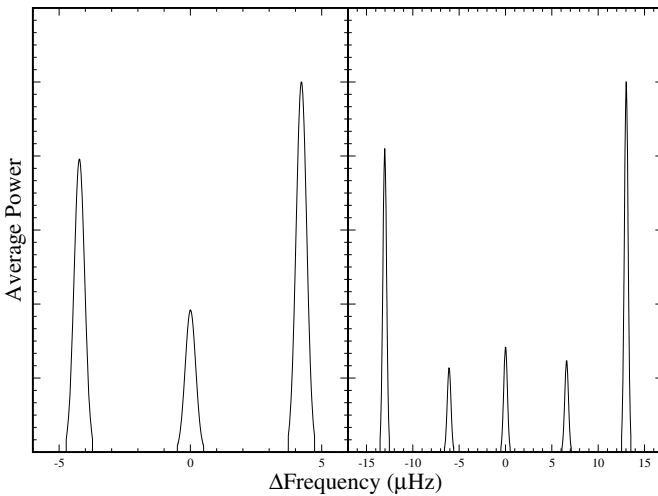


**Fig. 7.102.** Average of many frequency triplets (left) and quintuplets (right) for PG 1159. Note that the frequency spacing is different for the quintuplets than for the triplets, an important characteristic of g mode pulsation. Figure reproduced from Costa *et al.* (2008).

of mode trapping caused by strong mean molecular weight gradients at the boundary between the C/O core zone and the helium layer of the gravitationally stratified atmosphere. From all of these the mass of PG 1159 was determined to be  $M = 0.586 \pm 0.003 M_{\odot}$  (Winget *et al.* 1991), and more conservatively as  $M = 0.59 \pm 0.02 M_{\odot}$  (Costa *et al.* 2008), where the uncertainty arises from the models, rather than from the observations. The mass determination is dependent on the identification of the mode overtones, which are in the range  $14 \leq n \leq 42$  for the dipole modes and  $22 \leq n \leq 76$  for the quadrupole modes from model matching (Costa *et al.* 2008; note that the white dwarf community uses  $k$  for radial overtone, while we use the more widely used notation  $n$  throughout this book). There is some confusion in identifying some modes because the multiplet structures overlap, but many confidently identified modes remain, as is shown in Fig. 7.103, giving period spacings of  $\Delta P_1 = 21.43 \pm 0.03$  s for the axisymmetric,  $m = 0$ , dipole modes and  $\Delta P_2 = 12.38 \pm 0.01$  s for the  $m = 0$  quadrupole modes. This precision of the resulting mass determination is an astounding accomplishment of asteroseismology.

The deviations from uniform spacing lead to an estimate of the position of the transition layer between the core and the helium atmosphere to be at a fraction radius of  $0.83 \pm 0.05 R$  where  $R = 0.025 R_{\odot} = 2.73 \pm 0.16 R_{\oplus}$ . Since PG 1159 is a rapidly evolving star, it is expected that both the pulsation

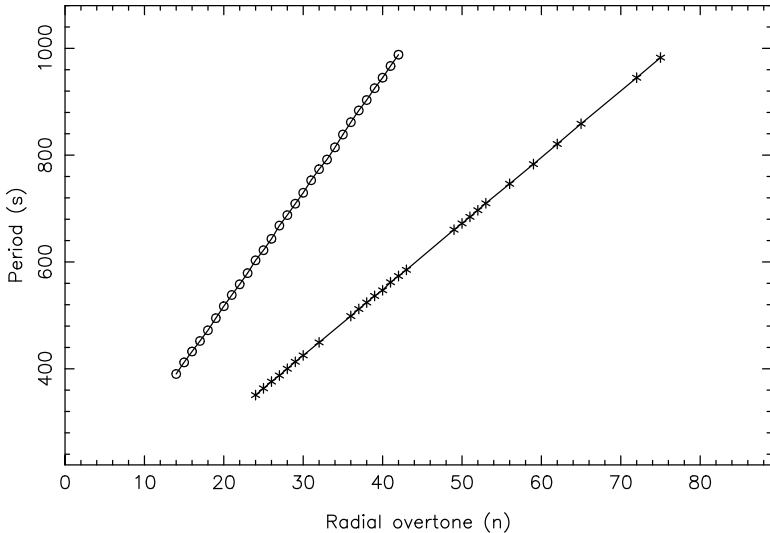


**Fig. 7.103.** The observed period sequences for confidently identified dipole (circles) and quadrupole (asterisks) axisymmetric  $m = 0$  modes for PG 1159. Some of the missing quadrupole modes are a consequence of overlap of the frequency multiplets making it difficult to identify the  $m = 0$  component with certainty. Adapted from Costa *et al.* (2008).

periods and their separations should change with time. Future studies will examine these changes.

Magnetic fields perturb the pulsation frequencies for g modes as well as p modes, as was discussed in Sect. 2.3.5 above. Because the magnetic field cannot distinguish the direction of an  $m \neq 0$  mode, magnetic perturbations to the frequencies lead to asymmetry in the spacing of the frequency multiplets. The lack of any detectable such asymmetry places an upper limit to a global magnetic field for PG 1159 of  $B \leq 2000$  G, a stringent limit given that white dwarfs can have fields of megagauss. The amplitudes of the various components of the frequency multiplets also suggest for PG 1159 that the rotation inclination is  $i \sim 70^\circ \pm 6^\circ$  (Costa *et al.* 2008).

Interestingly and importantly, no nonlinear combination frequencies have been found among the nearly 200 frequencies now detected in this star. Such combination frequencies are seen in cooler pulsating white dwarfs and are thought to arise in convection zones for these stars. Models of PG 1159 do not have a convection zone, thus give support to this hypothesis. We discuss the interaction of convection and pulsation in more detail in the next section on the DBV prototype V777 Her.

From extensive observational studies of the prototype hot pre-white dwarf star PG 1159, its mass, stratification, rotation period and rotational axis inclination have been determined, as well as a stringent limit placed on any

magnetic field that may be present. These are outstanding accomplishments of asteroseismology. We await the not-so-distant day when space observations of solar-like oscillators can surpass this success story.

### 7.4.2 The DB White Dwarf GD 358, V777 Her

#### 7.4.2.1 The Star

GD 358 (V777 Her itself;  $B = 13.5$ ) is the bright (for a white dwarf), northern hemisphere (obviously, since it is in Hercules) prototype of the DBV, V777 Her, stars. It was the first star (and its class of pulsators the first class) to be predicted to be pulsating before it was discovered to be variable (Winget 1982; Winget *et al.* 1985). It is also one of the most intensively observed of all asteroseismic targets, with many multi-site campaigns. Its asteroseismic ( $42 \pm 3$  pc; Winget *et al.* 1994), spectroscopic ( $42.7 \pm 2.5$  pc; Castanheira *et al.* 2005) and astrometric ( $36 \pm 4$  pc) distances agree well, giving confidence that asteroseismic inference for white dwarf stars is reliable.

GD 358 lies in the middle of the DBV instability strip with  $T_{\text{eff}} = 24\,900$  K and  $\log g = 7.9$  (cgs) (Beauchamp *et al.* (1999) with no atmospheric hydrogen. Castanheira *et al.* (2005) derived from HST UV spectra similar values:  $T_{\text{eff}} = 24\,100 \pm 400$  K and  $\log g = 7.9 \pm 0.3$  (cgs).

GD 358 is a spectacularly variable in its variability. That is, its pulsation amplitude spectrum varies strongly with time, as a consequence of strong non-linear mode coupling. This in itself is a consequence of the interaction of the pulsation modes with a convective layer, and that has made this star a prime target for testing and discussing the important theory of convective driving and convective interaction with pulsation (Brickhill 1983, 1990, 1991a,b, 1992a,b; Goldreich & Wu 1999; Wu 2001; Wu & Goldreich 2001; Montgomery 2005, 2008).

The GD 358 designation is often still used for this star. This nomenclature is now arcane; it comes from a survey for high proper motion objects using photographic plates taken with the Lowell Observatory 13-inch telescope (Giclas *et al.* 1965), which found many white dwarfs and white dwarf candidates. This telescope was built for the purpose of discovering a trans-Neptunian planet, and it succeeded; it was with data from the original programme that Clyde Tombaugh discovered Pluto. The normal proper motion programme used a “G” prior to the number designating the star. When lower proper motion stars (less than  $0.^{\circ}26$  per year) were included, they were differentiated with the designation “GD”; GD 358 was star number 358 of these lower proper motion stars. Giclas *et al.* elaborate no further on the choice of letters, saying only: “In designating the star number, we have employed the prefix “GD” so as to differentiate it from our regular program numbers.”

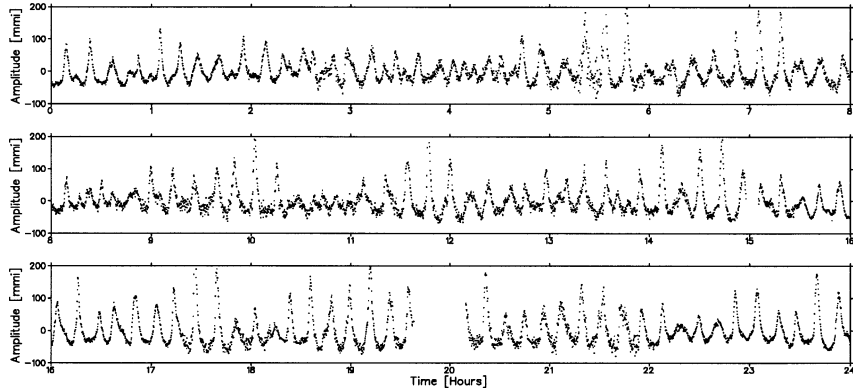


**Fig. 7.104.** A 24-h portion of the light curve for GD 358 with a duty cycle approaching 100% from the 1994 WET campaign. The ordinate is in units of  $10^{-3}$  of the intensity (milli-modulation intensity = mmi). From Vuille *et al.* (2000).

#### 7.4.2.2 The Data

GD 358 is the best-studied of the DBV stars, as we said in Sect. 2.7.2.3. Following its discovery by Winget *et al.* (1985), it has been the primary target of four WET campaigns, Xcov5 in 1990 May (Winget *et al.* 1994), Xcov10 in 1994 May, Xcov19 in 2000 June (Kepler *et al.* 2003)<sup>47</sup> and Xcov25 in 2006 June (Provencal *et al.* 2008). Observations in 1996 August and 2000 May-June were obtained simultaneously from the ground and with the HST.

The time variability of the pulsation amplitudes of GD 358 is one of its most outstanding characteristics. Fig. 7.104 shows a nearly continuous 24-h light curve of GD 358 (Vuille *et al.* 2000) where the large amplitude and multiperiodic beating are obvious. Figure 7.105 shows the amplitude spectra for GD 358 for observations obtained in four separate years where the amplitude variability is utterly clear. An expanded version of that figure covering 8 yr of data can be found in the preliminary results of WET Xcov25 (Provencal *et al.* 2008).

Kepler *et al.* (2003) even report one observing run on a single night when the amplitude spectrum consisted almost entirely of a single mode with an amplitude of 170 mma, identified as the  $n = 8, l = 1$  mode. Importantly, even though there is spectacular amplitude modulation for this star, the mode frequencies are not changing with time, hence the structure of the star is stable.

<sup>47</sup> <http://www.physics.udel.edu/darc/wet/>; <http://wet.physics.iastate.edu/>.

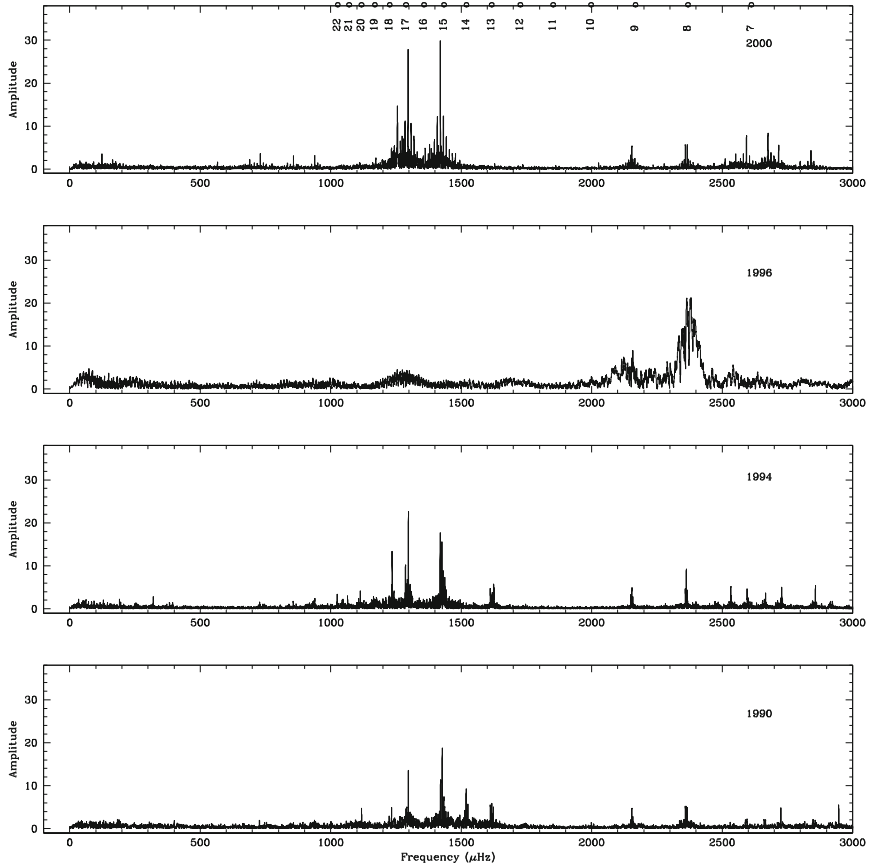


**Fig. 7.105.** Amplitude spectra for GD 358 for observations obtained in four separate years where the amplitude variability is demonstrated. The open circles along the top show the frequencies for the set of equally-spaced periods predicted from a model with numbers giving the radial overtones of the modes. This star has many nonlinear cross frequencies, *i.e.* combination peaks, in addition to the mode frequency multiplets. From Kepler *et al.* (2003).

#### 7.4.2.3 Mode Identification and Seismic Modelling

The modes of GD 358 are primarily dipole modes with triplets being detected in many cases; the radial overtones are in the range  $7 \leq n \leq 20$ . Kepler *et al.* (2003) also identified a single  $l = 2$  mode. From the period spacing of the  $l = 1, m = 0$  modes and models Winget *et al.* (1994) derived a mass for GD 358 of  $M = 0.61 \pm 0.03 M_{\odot}$  and luminosity  $L = 0.050 \pm 0.012 L_{\odot}$ . From model fitting of the *deviation* of the mode periods from equal spacing, as shown in Fig. 7.106, they found a mass for the helium envelope of  $M_{\text{He}} = 2.0 \pm 1.0 \times 10^{-6} M$ , where  $M$  is the mass of the star. As we pointed out in

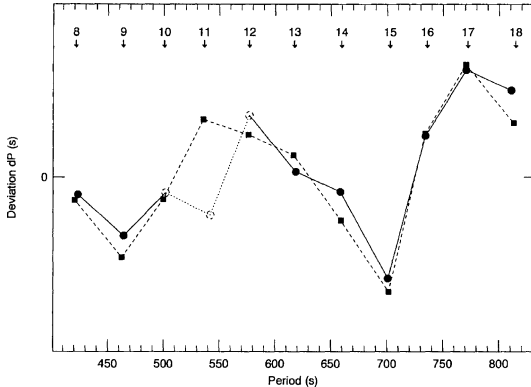


**Fig. 7.106.** The observed deviation of the dipole  $m = 0$  mode periods (open circles) from the equal spacing that would be expected for a uniform star. The squares show the best-fitting model with internal discontinuities, from which the mass fraction of the surface helium layer is derived. The numbers at the top are radial overtones for the model periods. From Winget *et al.* (1994).

Sect. 7.4.1, pulsation periods are perturbed by mean molecular weight changes at the boundary of the degenerate core, as well as by changes at the stratified layer boundaries. It is the modelling of these deviations from equal period spacing that allows the measurement of the surface layer mass.

In the last section we discussed the derivation of the rotation period for PG 1159 to high precision. That was possible because all of the multiplets for a given degree,  $l$ , for PG 1159 have the same spacing – implying uniform rotation – so it was possible to add the dipole triplets and add the quadrupole quintuplets to get higher signal-to-noise (see Fig. 7.102). For GD 358 that is not possible because the frequency triplets do *not* all have the same spacing – suggesting differential rotation. Furthermore, the individual frequency triplets themselves are not exactly equally split, as a consequence of a magnetic field of  $B = 1300 \pm 300$  G. Both  $m = \pm 1$  sectoral modes are perturbed to higher frequency by the extra tension of the magnetic field; this does not depend on the direction of the travelling wave for these modes, as the effect of the magnetic field is the same in either direction. Figure 7.107 shows the frequency splittings for the triplets.

Winget *et al.* (1994) concluded from their results shown in Fig. 7.107 and their models that the outer envelope of GD 358 rotates 1.8 times faster than the core. Kawaler *et al.* (1999) examined the possibility of inverting the frequencies for white dwarfs in general, but with the example of GD 358 examined in detail, concluding that there is a more rapidly rotating core, but without a firm derivation of a rotation curve with radius. Goupil *et al.* (1998), on the other hand, argue that the unequal spacings seen in Fig. 7.107 are not a result of differential rotation, but rather nonlinear resonant coupling. Tassoul & Tassoul (1983) also point out that only mild differential rotation is

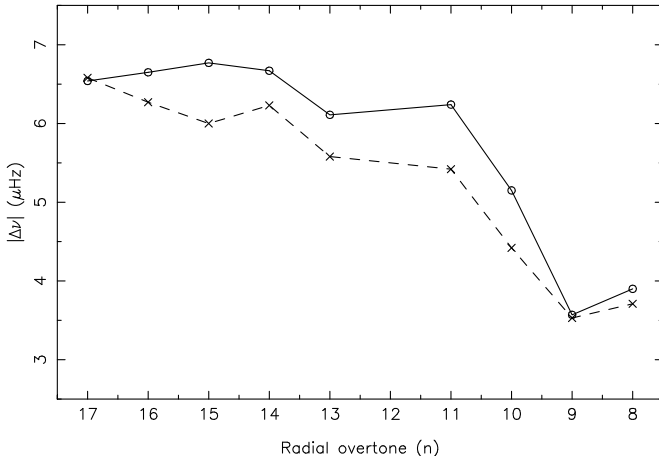


**Fig. 7.107.** This diagram shows the splittings of the prograde  $m = +1$  (circles) and retrograde  $m = -1$  (crosses) components with respect to the  $m = 0$  component for the dipole frequency triplets for GD 358. The variation with radial overtone may be a consequence of differential rotation. The inequality between the  $m = +1$  and  $m = -1$  splittings is a consequence of a magnetic field. Adapted from Winget *et al.* (1994).

expected in white dwarfs, based on examination of expected meridional circulation. Provencal *et al.* (2008) note that the triplet spacing for one multiplet was reported to be  $6.4 \mu\text{Hz}$  in 1990,  $6.7 \mu\text{Hz}$  in 1994,  $6 \mu\text{Hz}$  in 2000; in their preliminary results for WET Xcov25 it is only  $5.4 \mu\text{Hz}$ . While no errors are given for these numbers, if the changes are real, it probably points more to a nonlinear coupling origin for the different triplet spacings than towards differential rotation. We expect to hear more about this in future studies of this star.

While GD 358 has only about 15 pulsation modes detected, many of which have dipole frequency triplets, Winget *et al.* (1994) detected 180 significant peaks in the power spectrum of the light variations. Other studies also show large numbers of frequencies; which ones are present is variable with time. Most of these frequencies are combination frequencies – *i.e.* they are found at frequencies that are the sums and differences of the eigenmode frequencies. Such combination frequencies are seen in all DAV stars (Brassard *et al.* 1995) and in DBV stars as well, *i.e.* in white dwarfs with convection zones. This large number of combination frequencies is arguably the most important result of the many studies of GD 358.

Brickhill (1992a) found that nonlinear mixing of mode frequencies occurs naturally in the context of convective driving. This has been examined more extensively by Wu (2001), Wu & Goldreich (2001), and Montgomery (2005, 2008). The convective turnover time in white dwarfs is very short compared to the pulsation periods as a consequence of the high gravity and thus thin

convective layer. The convective time scale is of the order of 1 s, whereas pulsation periods are many minutes. In GD 358 the mode periods range from about 420 s to 814 s; the combination frequencies are detected from about 180 s to 976 s – all much longer than the 1-s convective turnover time. Hence the convection zone reacts “instantaneously” to the pulsation motion.

The thermal time scale of the convective zone is, *on average*, a few minutes, but, importantly, this is variable over the pulsation period. The photospheric flux is retarded and partially absorbed by its passage through the convective layer by an amount that depends on the thickness of the layer, and this thickness is itself variable with the pulsation. This variable thickness thus distorts the shape of the light curve, giving rise to the combination frequencies. Note that these frequencies describe the light curve shape; they are not associated with physical motion, *e.g.* radial velocities, of the pulsation modes. Through the combination frequencies energy is transferred between the eigenmodes so the amplitudes are time-variable, as seen in Fig. 7.105.

Brickhill (1992a) found he could reproduce amplitudes and combination frequencies for believable models. Wu (2001) and Montgomery (2005) showed that the distortion of the light curves can be used for mode identification and to determine the inclination of the mode axis (both of them assume that the pulsational flux variation at the base of the convective zone is sinusoidal). Montgomery (2005) shows excellent fits of his models to the nonlinear light curves of the DAV star G29-38 and the DBV star PG 1351+489. Fig. 7.108 shows an encouraging fit of his model for GD 358 to data obtained in the WET Xcov25 campaign, taking advantage of the fact that the modes are known to be dipolar.

The modes of GD 358 are identified with confidence by their triplet nature and the fact that quadrupole modes (or higher) are inconsistent with the all models. Other pulsating white dwarfs, however, do not have mode identifications, so the new ability to determine these from nonlinear light curve shape promises a wider selection of stars for which asteroseismic inference is possible. This technique and its application are likely to develop significantly. It also promises direct information about the structure and depth of the convection layer. This will then test the theory of convective driving for the DAV and DBV stars.

### 7.4.3 The Subdwarf B Star PG 0014+067

#### 7.4.3.1 The Star

The EHB pulsators were introduced in Sect. 2.7.1: the sdBV stars include the p-mode pulsators, the EC 14026 stars, also known as V361 Hya variables, and the g-mode pulsators, the PG 1716 stars. The latter do not yet have enough detected and identified frequencies for asteroseismic analyses. The former do, and the star for which the first such analysis was done is PG 0014+067 (EK Psc;  $B = 15.3$ ; PG 0014 hereafter), an equatorial star (of course, it is in

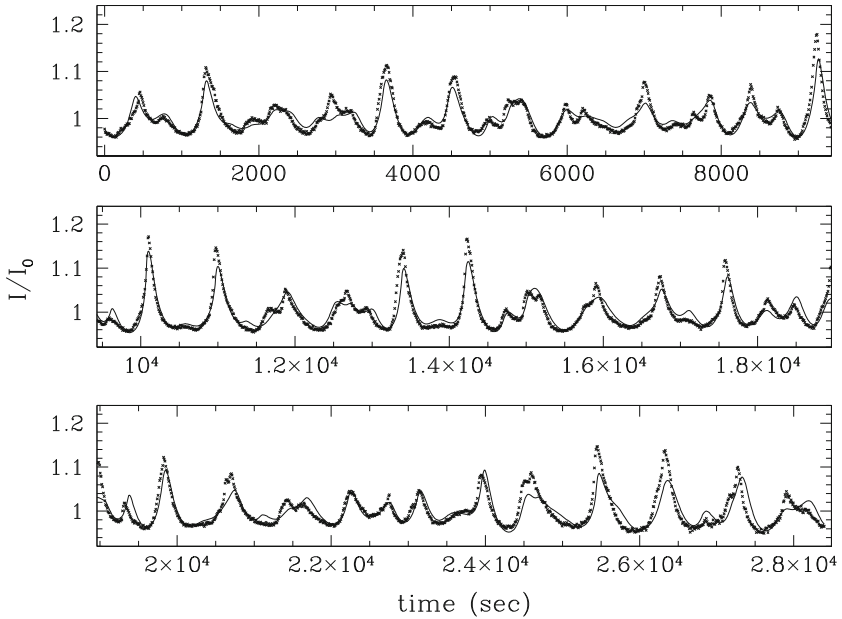


**Fig. 7.108.** Model fit of the nonlinear light curve of GD 358 to the high signal-to-noise data taken with the 2.7-m NOT during the WET Xcov25 campaign. The quality of the fit will no doubt be improved with better models, but shows that the theory is successful in reproducing, hence understanding, the nonlinearities that arise from the convective zone delays and distortions of the radiative transfer. Figure reproduced from Montgomery (2008).

Pisces) accessible to observations from both hemispheres, hence a good target for multi-site campaigns.

PG 0014 was discovered to be an sdBV star by Brassard *et al.* (2001) who also made a model atmosphere analysis using a time-average spectrum to determine  $T_{\text{eff}} = 33\,550 \pm 190\,\text{K}$ ,  $\log g = 5.77 \pm 0.05$  (cgs) and  $N(\text{He})/N(\text{H}) = 0.021 \pm 0.002$ , suggesting that twice the formal  $1\sigma$  errors quoted here on  $T_{\text{eff}}$  and  $\log g$  would be more realistic. This places PG 0014 in the middle of the instability region for the EC 14026 stars in the  $\log g - T_{\text{eff}}$  plane.

The low helium abundance is typical of the hydrogen-rich envelopes of these helium-core-burning EHB stars. These stars have masses near to  $0.5\,\text{M}_{\odot}$ , so have lost significant mass prior to arriving on the EHB, but the mechanism of the mass loss is still to be determined. The mass loss could have occurred during the red giant stage and/or during the helium flash in a single star, or it could have occurred during a common envelope stage, or during Roche lobe overflow in a binary system. The EC 14026 stars are also thought to be the direct progenitors of low-mass white dwarfs without an intervening

asymptotic giant branch stage. Asteroseismic investigation of the interiors of these EC 14026 stars promise to inform the many theoretical discussions of their fascinating evolutionary history and future.

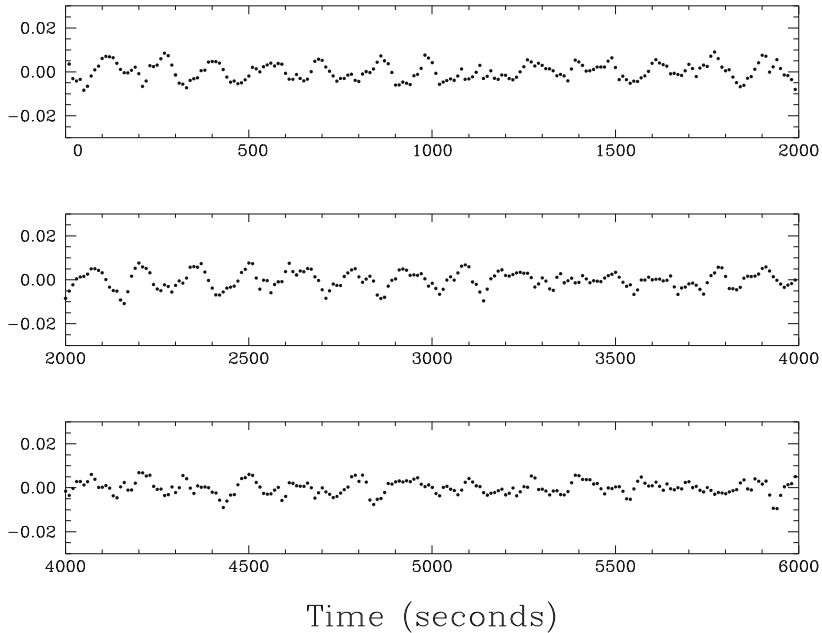
#### 7.4.3.2 The Data, Mode Identification and Seismic Modelling

Figure 7.109 shows a light curve typical of the discovery observations with the CFHT by Brassard *et al.* (2001), who identified 13 pulsation frequencies with periods in the range 80 – 170 s. Importantly, they identified three closely spaced frequency doublets that they tentatively attributed to rotationally split modes. From two grids, 1470 course and 1350 fine, of theoretical models they matched the observed frequencies best with the following deduced parameters for PG 0014:  $T_{\text{eff}} = 34\,500 \pm 2700$  K and  $\log g = 5.78 \pm 0.01$  (cgs) – both in good agreement with the spectroscopically determined values; a mass of the star of  $M = 0.49 \pm 0.02 M_{\odot}$ ; and a hydrogen envelope mass of  $\log M_{\text{env}} = -4.3 \pm 0.2$ ; a radius of  $R = 0.149 \pm 0.004 R_{\odot}$ . From the determined  $T_{\text{eff}}$  and stellar radius, the inferred luminosity is  $L = 29 \pm 10 L_{\odot}$  and that leads to a distance of  $2000 \pm 300$  pc. At its galactic latitude of  $-54^{\circ}$  that places PG 0014 1600 pc from the galactic plane.

All of the model modes of Brassard *et al.* were consecutive radial overtones with degrees of  $l = 0, 1, 2, 3$ . The higher degree modes suggested imply larger intrinsic amplitudes because of the partial cancellation effects discussed in Chapters 1 and 6, but the observed amplitudes are only of the order of 1 mmag for those modes, so the degrees are not unreasonable on grounds of observed amplitude. From the assumption that the frequency doublets are rotationally split, a rotation period of 29 h (1.2 d) was inferred. Thus the asteroseismic analysis of Brassard *et al.* fulfils two of the prime goals of asteroseismology for the sdBV stars: that of measuring the mass of the star and the mass of the hydrogen-rich envelope. The goal of measuring the chemical stratification that is predicted to be present (Charpinet *et al.* 1996) to explain driving by the heat mechanism operating on diffusion-enhanced Fe in the envelope was not attained. More frequencies and mode identifications are needed for that.

To address the question of mode identification in PG 0014, Jeffery *et al.* (2005) obtained multi-colour photometry with ULTRACAM on the 4.2-m William Herschel Telescope (WHT), supplemented with observations from the 2-m Faulkes telescope to help suppress aliases. The faintness of PG 0014 made the mode identification using the amplitude ratio method (see Chapter 6) indeterminate, except for being able to rule out any degree greater than 2 for the two highest amplitude modes. This is consistent with the analysis of Brassard *et al.* (2001). Jeffery *et al.* also confirmed the close doublets, but suggested a rotational period close to 4 d, rather than the 1.2-d period of Brassard *et al.*, admitting, however, that the interpretation was confounded by possible aliasing. They looked forward to a WET campaign on this star.

That came with WET Xcov24 which had PG 0014 as its prime target for two weeks during 2004 October 5 – 20 (Vučković *et al.* 2006). Because of the



**Fig. 7.109.** A light curve of PG 0014 in white light obtained with the CFHT. The basic time scale of the variability obvious to the eye is around 150 s with beating among the many pulsation frequencies. The ordinate is in units of fractional intensity. From Brassard *et al.* (2001).

relative faintness of PG 0014 telecopes with apertures larger than 2 m were particularly sought for this campaign. While time was assigned on telescopes of this size, the weather conditions were not good for them, so that much of the Xcov24 data comes from smaller telescopes. Figure 7.110 shows an amplitude spectrum demonstrating that the pulsation frequencies for this star lie in a narrow range around  $7000 \mu\text{Hz}$ . A search up to the Nyquist frequency shows that there are no other significant peaks in other ranges. There are only a few “high amplitude” (by sdBV standards) peaks with amplitudes of 1 – 3 mma. Other, lower amplitude frequencies were extracted from the data with sequential prewhitening with good agreement with the previous studies of this star on the CFHT by Brassard *et al.* (2001) and on the WHT by Jeffery *et al.* (2005). The star does have a set of widely spaced frequencies, some of which are close doublets, as originally discovered by Brassard *et al.*

While Vučković *et al.* found nothing that they could clearly attribute to rotational splitting in the close doublets, they discovered a phenomenological relationship in the frequency spacings which seem to be linear multiples of two small spacings they called  $\delta = 90.37 \mu\text{Hz}$  and  $\Delta = 101.22 \text{mHz}$ . Along with a zero-point frequency of  $f_0 = 5923.24 \mu\text{Hz}$ , they were able to fit the

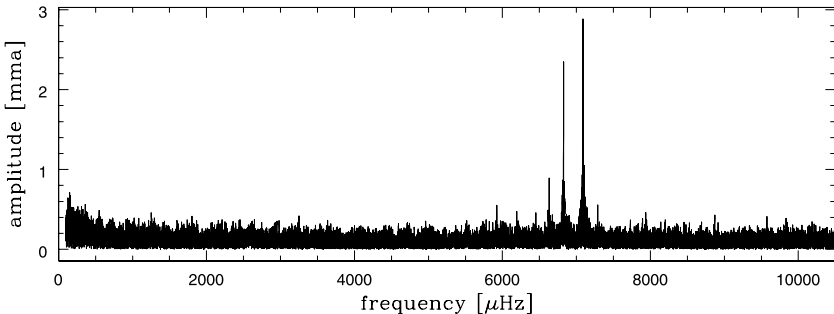


**Fig. 7.110.** Amplitude spectrum of the WET Xcov24 data for PG 0014. The pulsation frequencies can be seen to lie in a narrow range around  $7000\ \mu\text{Hz}$ . The ordinate scale is in mma (milli-modulation amplitude, meaning amplitude in units of  $10^{-3}$  in intensity). From Vučković *et al.* (2006).

entire set of observed frequencies with the relation  $f(i,j) = f_0 + i\delta + j\Delta$  to much better precision than Brassard *et al.* could fit their asteroseismic stellar model frequencies to the observed frequencies. Vučković *et al.* stated that examination of other sdBV stars showed similar empirical relationships among the frequencies, and they intriguingly concluded that asteroseismic secrets might be revealed by these apparent spacings, even though there is no known physics associated with them at the moment.

Fontaine *et al.* (2007) took a hard look at the empirical relation of Vučković *et al.* for the PG 0014 frequencies and concluded that no physical meaning can be, or is likely to be, associated with it. They show that the frequency spacings  $\delta$  and  $\Delta$  given above are so small compared to the frequency separations in PG 0014 that the fit is simply a “least-common-denominator” (loosely speaking) of the observed frequency separations. They show that an equally good fit can be obtained for the period spacings, as a demonstration that the relationship is numeric, rather than physical.

Thus, the asteroseismology of PG 0014 by Brassard *et al.* (2001) is a strong result for PG 0014, but the explanation of the closely spaced frequency doublets eludes us, or at least is still unproven to be rotational, if that hypothesis eventually turns out to be correct. It is clear that more frequencies and a better duty cycle are needed; for this higher S/N is needed, hence larger aperture telescopes. The sdBV stars are in a fascinating state of evolution; asteroseismology may have much to say about their current structure with inference possible about their progenitor structures and their future pathways to white dwarfdom. The answers may come from renewed observational efforts on PG 0014, or they may come with the discovery of other sdBV stars with rich frequency spectra, perhaps with higher amplitudes for better S/N.

## 7.4.4 The Subdwarf B Eclipsing Binary PG 1336–018, NY Vir

### 7.4.4.1 The Star

PG 1336–018 (NY Vir; hereafter PG 1336) is one of the most exciting of all asteroseismic target stars. This  $B = 13.6$  equatorial sdBV star has the second largest number of detected pulsation frequencies of any of the  $\sim 30$  known EC 14026 stars, and additionally is in a short-period eclipsing binary system. It is one of only 4 known HW Vir stars – short period eclipsing binary stars with a subdwarf B primary and an M main sequence secondary – and the only one of the four to have a pulsating primary star. Thus for PG 1336 fundamental stellar parameters can be determined spectroscopically, from orbital solutions to the eclipsing light curve and radial velocity curve, and from asteroseismology using the pulsation frequencies. As these methods are partially or fully independent (depending on the parameter being determined), this unique system can be used to test the validity of the various solutions for stellar parameters, and – particularly in the context here – to test asteroseismic modelling techniques.

More specifically, for the EHB stars, asteroseismology of PG 1336 can give precise values for the thin hydrogen surface layer, independent precise determination of the mass and deduction of the radius. As discussed in Sect. 2.7.1 and in the previous section on PG 0014, the EHB stars have masses of about  $M = 0.5 M_{\odot}$  with helium-burning cores and thin hydrogen-rich atmospheres. Several different models for the formation of these stars have been proposed which differ in the mass range expected for the sdB star and the mass of the remnant hydrogen envelope, hence precise determination of values for those two parameters may provide stringent constraints on the evolutionary history for sdB stars. For further references on HW Vir stars, theoretical models of EHB (sdB) stars and more background on PG 1336 itself, see the introductions of Hu *et al.* (2007) and Vučković *et al.* (2007), and the references therein.

PG 1336 pulsates with over 20 identified frequencies – none of which are combination frequencies – hence with over 20 identified modes, many of which appear to be components of rotationally split multiplets. The frequencies are concentrated in the range 5000 – 6000  $\mu$ Hz, thus the periods are in the range 170 – 200 s. The orbital period is accurately known to be  $P_{\text{orb}} = 0.10101599 \pm 0.00000002$  d, or 2 h 25 min 27.7815  $\pm 0.0002$  s (Kilkenny *et al.* 2000). The primary eclipse lasts for about 800 s, so encompasses 4 – 5 pulsation cycles.

An extensive study of the orbital characteristics of PG 1336 was made by Vučković *et al.* (2007) using ULTRACAM on UT3 of the VLT on one night in 2005 May for photometry in three colours, and with the high resolution spectrograph UVES on UT2 of the VLT on one night in 2005 April. Figure 2.61 already showed the beautiful  $r'$ ,  $g'$  and  $u'$  light curves from Vučković *et al.* (2007) while Fig. 7.111 shows their radial velocity curve. The light curve is a higher precision version of the stunning discovery light curve presented by Kilkenny *et al.* (1998) that brought so much deserved attention to this star.

While Vučković *et al.* (2007) were unable to discriminate among three possible orbital solutions for PG 1336, Charpinet *et al.* (2008) found only one of those to be consistent with their best asteroseismic model. This orbital solution of Vučković *et al.* gives a mass for the primary component of PG 1336 of  $M = 0.466 \pm 0.006 M_{\odot}$  and a radius of  $R = 0.15 \pm 0.01 R_{\odot}$ . Importantly, for all three binary models the inclination is  $i = 81^\circ$ . Their atmospheric analysis of the average UVES spectrum yielded  $T_{\text{eff}} = 31\,300 \pm 250$  K,  $\log g = 5.60 \pm 0.05$  (cgs) and an atmospheric helium to hydrogen abundance of  $\log(N_{\text{He}}/N_{\text{H}}) = -2.929 \pm 0.009$ . The preferred asteroseismic model of Charpinet *et al.* (2008) is in outstanding agreement with this, giving  $T_{\text{eff}} = 32\,740 \pm 400$  K,  $\log g = 5.739 \pm 0.002$  (cgs),  $M = 0.459 \pm 0.005 M_{\odot}$ ,  $R = 0.151 \pm 0.001 R_{\odot}$  and  $\log(M_{\text{env}}/M) = -4.54 \pm 0.07$  (where the quoted errors for the asteroseismic model are internal precision, not external accuracy). Of course, the last of these – the mass fraction of the thin hydrogen-rich envelope that is so important to know for modelling progenitor mass loss – can only be measured by asteroseismic means.

All three of Vučković *et al.*'s three possible orbital solutions give a mass and radius for the secondary of about  $0.12 M_{\odot}$  and  $0.16 R_{\odot}$ , respectively. The orbital separation is  $0.764 \pm 0.005 R_{\odot}$  in the model that matches the preferred asteroseismic model, so the picture is one of a hot subdwarf B star and a cool main sequence M star – both with radii of  $0.15 R_{\odot}$  – separated by only  $0.75 R_{\odot}$ .

Thus far there is no conclusive evidence of tidal influence on the pulsation modes of PG 1336, but there remains the possibility, making the system interesting for this additional reason. Being an eclipsing binary pulsating in nonradial modes, there is also the possibility to use changes in the pulsation amplitudes and phases during primary eclipse for mode identification. Again, this has not yet been realized, but remains a possibility with even more extensive observational data. The pulsation periods are so short that about 5 cycles occur over the primary eclipse; the problem is to get sufficient data in this short time to resolve the many mode frequencies.

Finally, since PG 1336 does not have enough residual hydrogen to ignite for a return to the asymptotic giant branch, it is expected to evolve directly to be a white dwarf. It is thus a direct progenitor of a cataclysmic variable and is of yet further interest for that reason.

#### 7.4.4.2 The Data

PG 1336 was discovered to be an sdBV star by Kilkenny *et al.* (1998) who obtained a total of 24.2 h of high speed photometry of the star in various filters in 1996 May – June. As mentioned in the last section, Fig. 2.61 is similar to Kilkenny *et al.*'s discovery light curve. The beauty of that light curve and the importance of the star led to it being the prime target of WET Xcov17 in 1999 April (Kilkenny *et al.* 2003) and WET Xcov21 in 2001 April<sup>48</sup>. We only

<sup>48</sup> [www.physics.udel.edu/darc/wet/XCov21/index.html](http://www.physics.udel.edu/darc/wet/XCov21/index.html).

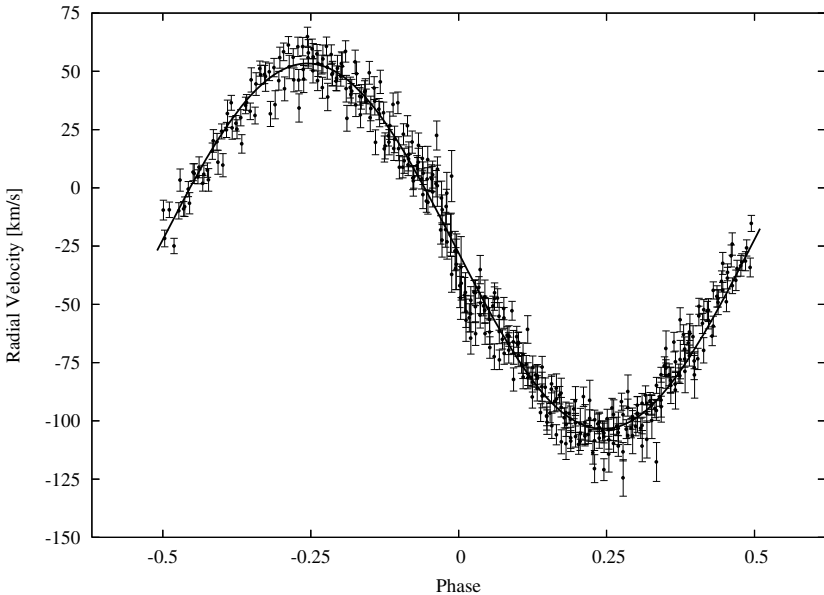


**Fig. 7.111.** The radial velocity curve for PG 1336 determined from an average of the radial velocities of the H $\beta$ , H $\gamma$ , H $\delta$  and He lines. The solid line is a best fitting orbital solution. Note the occurrence of the Rossiter-McLaughlin effect at phase zero. From Vučković *et al.* (2007).

discuss the Xcov17 results here, as the Xcov21 analysis is not published as of this writing.

The main part of the Xcov17 multisite campaign collected 172 h of high speed photometry from 14 observatories in both hemispheres. For higher time resolution 5-s integration were used at most sites, rather than the 10 s that is standard for WET campaigns. A commendable duty cycle of 47% was attained over the central 14-d time span; 206 h of data were obtained over the more extended run with a 43% duty cycle. Additional data were gathered in 1999 March and May at three of the sites. In all, 49 astronomers were involved in the Xcov17 campaign.

Figure 7.112 shows the amplitude spectrum of the central data set. These data were divided into two independent data sets. There are various methods to estimate the significance of peaks in a periodogram (see Chapter 5), but for confidence that a peak is real, nothing beats independent detection of it in separate data sets. This reproducibility is particularly important because of the need for more frequencies for modelling; there is a strong temptation to use frequencies that are not well determined. Figure 7.113 shows sections of the amplitude spectra for the two independent data sets in the range of most of the pulsation frequencies of PG 1336.

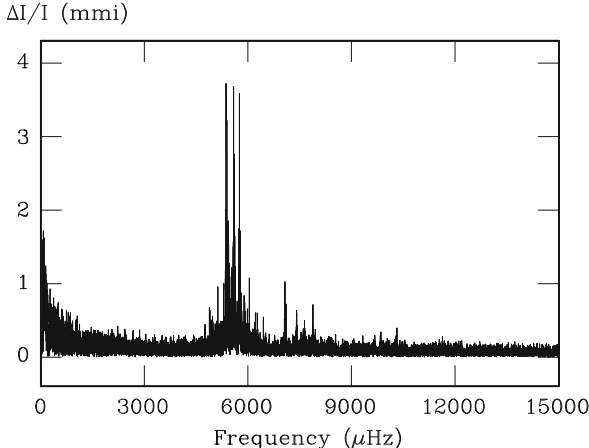


**Fig. 7.112.** An amplitude spectrum of the WET Xcov21 data for PG 1336 showing the concentration of the pulsation frequencies in the  $5000 - 6000 \mu\text{Hz}$  range, with some higher frequencies. The ordinate is amplitude in milli-fractional intensity units. From Kilkenny *et al.* (2003).

The two independent data sets produced 14 frequencies that agreed very well, *i.e.*, within  $0.4 \mu\text{Hz}$  of each other where the nominal resolution of the data sets is about  $1/T = 2 \mu\text{Hz}$  for their  $T \sim 6$ -d time spans. Those 14 frequencies were fitted to the data and prewhitened, giving another 5 frequencies that could be identified with some confidence. Prewhitening of the 19 frequencies left significant amplitude in the two separate amplitude spectra from which more frequencies were derived with less confidence. The agreement between the frequencies extracted from the two data sets was in all cases within  $0.4 \mu\text{Hz}$  – much less than the width of the peaks of  $2 \mu\text{Hz}$ . Finally, the entire data set was analysed, the same frequencies extracted and a few more peaks identified.

PG 1336 suffers from an additional aliasing problem that other asteroseismic targets do not have. The light curve is modulated with the rotation frequency, and, in particular, the amplitudes of the pulsation modes decrease through the eclipse as the primary star is partially covered by the secondary. Of course, this is a great advantage that should lead to mode identification by eclipse mapping eventually, but it also means aliases in the spectral window are generated at the rotational frequency, whether the eclipses are cut out of the light curve, or not. Only high precision orbital models of the light curve can partially alleviate this. Aliases at the rotational frequency are a particular problem in this case where, as we shall see below, there are (apparently) many rotationally split multiplets. Kilkenny *et al.* (2003) give a full list of the 24 frequencies they identified in both data sets (their table 3) and 28 frequencies they found for the whole data set (their Table 4) with good confidence in the

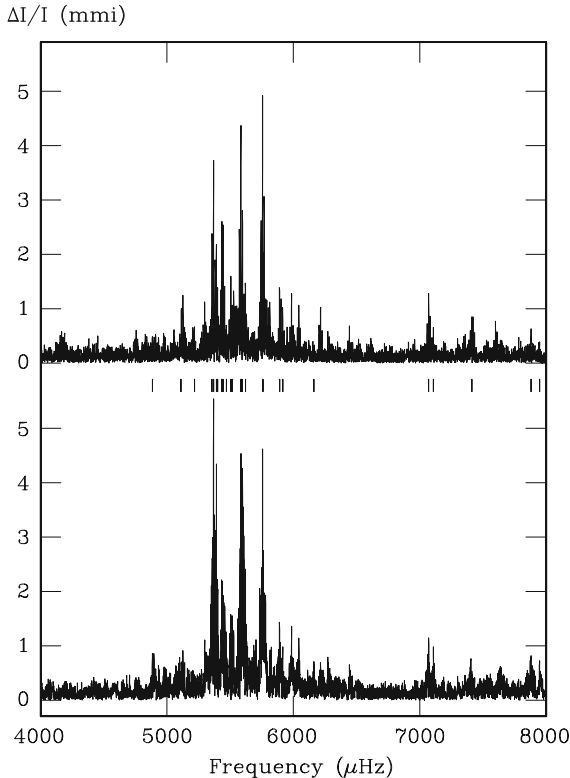


**Fig. 7.113.** Amplitude spectra for two independent data subsets of the WET Xcov21 data for PG 1336 in the frequency range of the main pulsation modes. The vertical lines in the lower panel indicate 27 frequencies identified from the whole data set. A total of 24 frequencies were found in both data sets. The ordinate is amplitude in milli-fractional intensity units. From Kilkenny *et al.* (2003).

first 20 of these. The full frequency range is  $4885 - 10315 \mu\text{Hz}$ , or period range  $97 - 205 \text{s}$ .

#### 7.4.4.3 Mode Identification and Seismic Modelling

Kilkenny *et al.* (2003) explored some models of PG 1336 and found rough agreement with low overtone ( $0 \leq n \leq 3$ ) modes with degrees  $0 \leq l \leq 2$ . The closely spaced frequencies required  $l$  up to 2, even though higher degrees suffer cancellation in photometry that necessarily samples the entire visible hemisphere of the star. With this effect and under the assumption that the pulsation axis is inclined by the same angle as the orbital axis,  $i = 81^\circ$ , Kilkenny *et al.* admitted that their mode identifications were not all plausible. They noted the need for extensive search of model parameter space and

looked forward to an application of the Montréal parameter search method to PG 1336. That has now been done.

Charpinet *et al.* (2008) searched a large 4-dimensional parameter space (the number of models searched was not specified) for sdB models that matched 25 of the frequencies determined by Kilkenny *et al.* (2003). Some closely spaced frequencies that may not have been fully resolved in the WET data set were not included. The forward modelling technique used was that of Charpinet *et al.* (2006) that incorporates a genetic algorithm for optimizing the search in the large parameter space:  $30\,000 \leq T_{\text{eff}} \leq 36\,000\,\text{K}$ ;  $5.6 \leq \log g \leq 5.9$ ;  $0.3 \leq M \leq 0.7\,\text{M}_{\odot}$ ; and an appropriately selected range in mass fraction,  $M(r)/M$ . Given their new spectroscopic determination of  $T_{\text{eff}} = 32\,780 \pm 200\,\text{K}$  and  $\log g = 5.76 \pm 0.03$  (cgs), this parameter space encompassed a reasonable range of possible models of PG 1336.

Further restrictions were made on the model searches. Following Fig. 1.5, only modes of degree  $l = 0, 1, 2, 4$  were included while modes of  $l = 3$  were considered to be of lower visibility in photometry, as are, of course, modes of higher degree  $l \geq 5$ . The closely spaced frequencies of PG 1336 could not be matched by any models without the inclusion of  $l = 4$ , even though modes of such high degree have a low amplitude averaged over the visible hemisphere (typically only 12% of the radial modes – see Fig. 1.5). The rotational inclination was assumed to be equal to the orbital inclination,  $i = 81^\circ$ , and the rotational period was taken to be the orbital period under the reasonable assumption that the rotation is synchronized.

Within these assumptions and parameter space, several models were found with good matches to the 25 observed frequencies from the WET data set. An additional requirement that the average observed amplitude should drop with increasing degree  $l$  then left only one best match. For that model the theoretical frequencies and the observed frequencies all match within 0.5%. Remarkably, the model parameters and the observed parameters are in excellent agreement with one of the orbital models of Vučković *et al.* (2007). This is a significant achievement for asteroseismology from which Charpinet *et al.* (2008) conclude that it is strong evidence in favour of both the model, and more generally the technique of forward modelling in asteroseismology.

Lots of interesting research remains to be done for this star, however, given its unique nature. Firstly, Kilkenny *et al.* (2003) were less confident of some of the frequencies Charpinet *et al.* used. Should those turn out to be aliases, then the best fitting model may change, although the very good fit to the orbital model would suggest that any such change will be small. The validity of those lowest amplitude frequencies should be tested by the WET Xcov21 frequencies when they are published.

Secondly, Charpinet *et al.* find *on average* that the higher the degree  $l$ , the lower the observed amplitudes, as is expected from visibility considerations (see Fig. 1.5). It is interesting to note, however, that three of the highest amplitude modes observed in PG 1336 are matched with model modes of ( $n = 0, l = 4, m = -1$ ), ( $n = 0, l = 4, m = -3$ ) and ( $n = 1, l = 4, m = +3$ ) while

these are expected to have an observed amplitude of only 12% that of the radial modes and 10% of the dipole modes for the same intrinsic amplitude. In addition, the mode with the highest observed amplitude is modelled with ( $n = 1, l = 2, m = -2$ ) while these are expected to reach about half of the intrinsic amplitude of radial and dipole modes. It would therefore be very interesting to model the frequency spectrum of PG 1336 with independent evolution and oscillation codes to see if that leads to the same result. In general, code comparison has been done in much detail for stars on the main sequence, in the framework of the CoRoT mission (Lebreton *et al.* 2008; Moya *et al.* 2008). Similar exercises have unfortunately not yet been done for evolved stars. PG 1336 would be an ideal test case to do so. Indeed, if confirmed, the high amplitudes for PG 1336's relatively high degree modes must be telling us something about the mode excitation physics. It would also be important to make similar tests for other sdBV pulsators.

Thirdly, while the model frequencies and observed frequencies match to within 0.5%, the rotational splittings do not, since the rotational frequency is so much lower than the pulsational frequencies. For example, the observed rotational splitting for the two multiplets identified as dipole triplets have deviations of 10% and 20% of the rotational frequency compared to their expected frequencies (for first-order rotational splitting). Charpinet *et al.* have a strong discussion of this and look at models including higher order rotational frequency splitting, which does alter the equal spacing of first-order multiplets. Their conclusion is that the splittings suggest synchronous rotation with solid body rotation half way to the core. This is the first and so far only direct seismic probe of the internal rotation profile of an sdBV pulsator. Whether this is typical of the whole sdBV class is questionable, given that PG 1336 is a member of a close binary.

Charpinet *et al.* (2008) conclude that the amplitudes of the dipole triplets – which show high amplitude for the  $m = \pm 1$  sectoral modes, and very low amplitude for the axisymmetric  $m = 0$  modes, prove that the pulsation axis is aligned with the orbital axis. While this may be the case, it is premature to rule out the possibility that the pulsation axis might be the tidal axis as discussed by Reed *et al.* (2006) in the context of another sdBV star, KPD 1930+2752. If the pulsation axis is indeed the tidal axis, then with  $i = 81^\circ$  dipole triplets with amplitudes as observed are just what is expected. Moreover, if the modes have pulsation axes that are along the tidal axis, and they are tidally distorted, then they cannot be modelled with single spherical harmonics. The distortion of the modes means that a spherical harmonic series is needed to describe them, so that lower degree modes may have frequency multiplets with far more components than expected for a simple normal mode. This is what is observed in roAp stars where the magnetic field distorts the modes from simple spherical harmonics (see, *e.g.*, Kurtz 1992; Kochukhov 2006), and it could also be expected for tidally distorted modes. In that case, high degree modes may not be needed for PG 1336 and the mode visibility issue would have to be placed into another perspective.

Whether the mode axis is the tidal axis with mode distortion, or not, is an important question of general interest in the context of close binary evolution. It can be distinguished observationally from the seismic model by Charpinet *et al.* (2008) by more precise determination of the mode frequencies. The model with the pulsation axis equal to the tidal axis, and with mode distortion, demands that the frequency multiplets be split by exactly the rotation frequency, and that all components of the multiplet be equally split; the high degree ( $l = 0, 1, 2, 4$ ) model will have multiplets split by  $(1 - C_{nl})$  times the rotation frequency to first order, and will not be equally split at all to second order (or higher), as for the model of Charpinet *et al.* Frequencies need to be determined precisely enough, therefore, to see whether the splittings are equal, or not, and if they are equal to see whether the separations are equal to the rotation frequency, or  $(1 - C_{nl})$  times the rotation frequency. This is seriously challenging, but possible.

Eclipse mapping for mode identification as described in Chapter 6 is also still a promising line of study for PG 1336. Kilkenny *et al.* (2003) showed some progress with 40% of the primary eclipses covered during Xcov17; they suggested that coverage of 80% could lead to progress. We look forward to that being successfully carried out one day when PG 1336 will then again be a good test case in this context. Already observers and theoreticians have had great success in finding a plausible asteroseismic model of this star, in its important and still partially enigmatic evolutionary stage.

The big advances to come for PG 1336 and for asteroseismology in general will be from global networks and space missions that can produce continuous data sets of months, and even years – long enough for frequency sets of unprecedented precision and with unprecedented (except for the Sun) numbers of frequencies. In the last chapter of this book, we look to that future.

---

## The Future

Global helioseismology is a mature field of research. Some models of the Sun agree with the helioseismic observations of the sound speed to within a fraction of a percent over 90% of the solar radius – a stunning achievement. Eddington’s longed-for “appliance” to pierce the outer layers of a star and see within has been discovered; with helioseismology we *see* the interior of the Sun. In addition, we understand solar nuclear fusion reactions so well that we reproduce them both explosively and non-explosively here on Earth, and we even believe that we now understand solar neutrinos, with cosmic implications. Thus the standard solar model can be elevated to “understood physics” – physics that will undergo small modifications in the future, but for which a revolutionary paradigm is unlikely.

Where do we go from here? It is important to remind ourselves that the Sun is but one star. Our model of it is exceedingly good, based on the bedrock of laboratory atomic and nuclear physics, mechanics and electromagnetism. We have a self-consistent model of one “experiment”: the Sun. As with all physics experiments, we need to alter the initial conditions and run the experiment again and again, searching parameter space, probing for weaknesses in the model, probing for new physical understanding, searching for unimagined discoveries.

These experiments are being run, and that has been the subject of this book: the stars. Within reach of our telescopes now are hundreds of stars on which we can make asteroseismic investigations. In the near future the numbers of asteroseismic targets will increase to thousands. Following global helioseismology the future is asteroseismology. The great variety of physical conditions of stars allows us to study physics far beyond that of the Sun, as we have shown throughout this book. New theoretical understanding will come from asteroseismology: *e.g.* for pulsation in the presence of strong magnetic fields, rapid rotation, convection, tidal distortion. Fundamental physics will be probed by asteroseismology under conditions not possible on Earth: in stellar cores, white dwarfs, hot subdwarf stars, and perhaps even neutron stars.

Understanding thus gained will be fed back into helioseismology where, in spite of the maturity of the field, there is much to do. Internally, the rotation of the Sun is still to be understood, as are the physics of the magnetic field, solar cycle, convection, circulation currents and the interactions amongst them. In the visible atmosphere of the Sun local helioseismology is at the forefront of studies of solar weather and its direct impact on Earth and life on our planet. Helioseismology in the future is as important and fundamental as atmospheric science and geoseismology here on Earth.

Again then, where do we go from here? We need data. In asteroseismology we have been listening to the *Music of the Spheres* with earplugs; we have been listening with distracting noise; we have been leaving the concert at regular intervals and missing some of the finest melodies. We need to hear the full symphony without interruption, without background noise, with clarity and purity never achieved before. We need observations from space, and we need *continuous* observations from the ground. As shown by the success of helioseismology, we need these observations for months and for years.

This is a demand for a Tychonic revolution in asteroseismic observation, a demand that will be met. Space missions are providing photometric observations 1 – 2 orders of magnitude more precise than those obtained from the ground, with continuity for months and years. Ground-based networks promise continuous spectroscopic data – for which intrinsic stellar noise levels are lower than for photometry for solar-like oscillators – with a precision similar to that of helioseismology only 20 years ago –  $\text{cm s}^{-1}$  in radial velocity. These new data sets will define asteroseismology; theoretical studies will expand our understanding of stellar physics from them. Ground-based, single-site asteroseismology will continue in exploratory studies and niche studies, but the future is in space and in world-wide networks, as is the case already for helioseismology.

## 8.1 Space Missions

NASA’s WIRE mission<sup>1</sup>, thanks to the clever and motivated suggestion of D. Buzasi after the failure of its main purpose (Buzasi 2000), performed excellently as an unplanned pioneer in the field of space asteroseismology. It tested for the first time the technique of high-precision continuous space photometry on very bright stars of different nature and evolutionary stage (Buzasi 2004) and led to several interesting new results and discoveries (*e.g.*, Bruntt 2007; Bruntt & Southworth 2007). Quite a few of the asteroseismology results based on the other – but this time well-planned – pioneer, the Canadian MOST mission<sup>2</sup>, have been discussed throughout this book. While WIRE has been shut down meanwhile, MOST will continue to monitor relatively bright

---

<sup>1</sup> <http://www.ipac.caltech.edu/wire/>.

<sup>2</sup> <http://www.astro.ubc.ca/MOST/>.

stars for asteroseismology in the coming years, producing light curves with time spans of the order of a few weeks.

To end this book, we turn our attention to future space missions and other projects, after giving a brief status report on the CoRoT mission which is presently fully operational. Asteroseismic results from CoRoT are eagerly awaited and will become available in the refereed literature the coming months and years.

### 8.1.1 CoRoT

The CoRoT<sup>3</sup> (**C**onvection, **R**otation & planetary **T**ransits) mission was launched on 27 December 2006 and began scientific operations on 2 February 2007. It carries a 27-cm telescope with a 4 CCD camera that can measure stellar brightnesses to  $\mu\text{mag}$  precision. It is in a polar circular orbit at an altitude of 896 km, from which it can observe an equatorial field-of-view away from the solar direction for up to 150 d. The satellite is then rotated to look in at an intermediate field for a few weeks, then is pointed again in the anti-solar direction for another 150-d observing run.

The primary science goals of CoRoT are the detection of planets by the transit method and asteroseismology. It is easy to see from a rough calculation that a planet the size of the Earth – which has a radius about  $10^{-2} R_\odot$  – will cover a relative area  $10^{-4}$  of a star the size of the Sun, thus causing a dip in the light curve of about  $100 \mu\text{mag}$ . The duration of such a transit is just the time it takes the planet to move a solar diameter in its orbit, which for the Earth at  $29.5 \text{ km s}^{-1}$  is about 7 hr. For the purpose of planetary transits data are collected on two CCDs with initial integration times of 512 s (known as the observing *cadence*) for 12 000 targets stars in the magnitude range 11 – 16; when a transit is detected the cadence is shortened to 32 s for that star. Although these data are being collected to find planets, they are a rich new source for asteroseismology for longer-period pulsators:  $\beta$  Cep stars, SPB stars,  $\delta$  Sct stars,  $\gamma$  Dor stars, Be stars, pulsating red giants, etc. They are also a rich source of new eclipsing binary stars for mass determinations across the HR Diagram. For primary asteroseismic targets CoRoT uses the other two CCDs to study 10 bright stars between magnitudes 6 – 9 with a cadence of 2 s. These 150-d light curves at  $\mu\text{mag}$  precision represent spectacular data sets for theoretical modelling.

At the time of writing, the reduced data of the first year of CoRoT observations have been sent to the co-investigators of the mission who have one-year proprietary data rights. Impressive preliminary results based on the analysis of these data, already covering large parts of the HR Diagram and proving the performance of the mission is as expected, have been presented at several conferences in the summer of 2008 (see Michel *et al.* 2008 for an overview of the first results). The data of the seismology and exoplanet programmes have

---

<sup>3</sup> <http://corot.oamp.fr/>.

already given rise to the discovery and investigation of hundreds of pulsators, with tens to hundreds of oscillation frequencies each. It is already clear now from the preliminary results that present theoretical models will have difficulty explaining the detected frequencies, *i.e.*, we have just reached the desired stage for the method of asteroseismology to become meaningful: we are obtaining data of such quality and quantity that we are forced to improve the stellar structure models to comply with what is being observed.

### 8.1.2 The Kepler Mission

Are we alone? The question of life in the Universe is one of the most fundamental that can be asked. An important component of answering that question is to find planets similar to Earth, *i.e.* planets with masses in the range  $0.5 - 2 M_{\oplus}$ , in the habitable zone around their stars where liquid water exists. The Kepler mission<sup>4</sup> is a NASA project that intends to find these planets and to characterize them, their orbits and the parent stars that they orbit.

The Kepler mission was launched successfully on 7 March 2009 and commissioning is ongoing at the time of this writing. Its telescope has an aperture of 0.95-m and 42 CCDs covering a field-of-view of 105 square degrees in the Cygnus-Lyra region. It is thus a significant advance technologically on the CoRoT mission. Kepler expects to find dozens of Earth-sized planets by the transit method with  $\mu$ mag-precision photometry of 170 000 stars in the magnitude range 9 – 16 for at least 3.5 yr, and possibly as much as 6 yr. The satellite is drifting slowly away from Earth in a solar orbit where it can observe continuously (with occasional short gaps in the observations for data downloading to Earth and repositioning of the solar panels every three months); there is no obscuring of the sky by the Earth, no scattered Earth-light, and no passage through the South Atlantic Anomaly with the increased noise from radiation that CoRoT has to contend with. The high precision of the white-light photometry for this mission, the continuity of the observations, and the duration of the mission will allow planets the size of Earth to be detected in transit, then confirmed with repeated transits over the years of the mission giving the orbital periods of the planets. The cadence of the observations is 30 min.

Although Kepler will primarily target solar-like stars for planet finding, other stars from all over the HR Diagram will be observed, providing a unique data set for asteroseismology for stars with pulsation periods significantly longer than 30 min. In addition, a small subset of stars will be observed with a cadence of 1 min. These will primarily be solar-like oscillators for which the Kepler data will become the definitive data resource for asteroseismology. Some other types of pulsating stars that lie within the field-of-view will also be observed with 1-min cadence, again producing unique data sets. Some stars may be observed for the entire mission with the 1-min cadence, but there is the option to change some targets at 90-d intervals.

---

<sup>4</sup> <http://www.kepler.arc.nasa.gov/>.

The primary reason for pursuing asteroseismology with the Kepler mission is to infer the radii, masses and ages of the planet-hosting stars, important for determining those very parameters for the planets themselves. The secondary reason is to expand the scientific returns of the mission. To manage the asteroseismic part of this mission the Kepler Asteroseismic Science Consortium (KASC) with more than 250 collaborators has been set up and is managed by Aarhus University in Denmark<sup>5</sup>.

We look forward to the data from this mission, which will complement and is expected to go beyond the CoRoT data in terms of time base for asteroseismology across the entire HR Diagram.

### 8.1.3 BRITE

With the success of the MOST satellite, for which examples are given in Chapter 2, the idea of small, relatively inexpensive satellites (also called *nanosatellites*, where this use of nano is figurative, rather than literal) has led to the **BRIght Target Explorer** mission (BRITE)<sup>6</sup>, an Austrian-Canadian space mission. BRITE will be composed of two satellites, each a cube only 20-cm on a side with a 3-cm aperture telescope, an 11-megapixel CCD and a field-of-view of  $25 \times 25$  square degrees in 800-km-high polar sun-synchronous orbits. A launch in 2009 and a mission duration of 2 yr are planned.

In our quest in astronomy for ever larger telescopes on the ground and in space to capture more photons – hence more information – we usually give up the possibility of studying the brightest stars in the sky. Our telescopes are too big for such stars; our instruments are either saturated, or even destroyed if the stars we know by their individual names are put into the field-of-view. Because of its small size, BRITE overcomes this limitation and will be able to observe stars brighter than magnitude 4 (434 stars in total) with 15-min integrations taken once per orbit (100 min) for time spans up to 100 d. At this brightness  $\mu\text{mag}$  precision will be obtainable, giving extended data sets for the study of longer-period bright pulsating stars:  $\beta$  Cep stars, SPB stars,  $\delta$  Sct stars,  $\gamma$  Dor stars, spotted and active cooler stars. Thus BRITE fills a niche that the larger missions, CoRoT and Kepler cannot: asteroseismic data for the brightest stars in the sky. A great advantage of this is that the fundamental data for these stars –  $T_{\text{eff}}$ ,  $\log g$ , distance, radius, and in some cases mass – are among the best known.

### 8.1.4 PLATO

Looking even farther to the future a European Space Agency “Cosmic Vision 2015–2025” proposal called PLATO (**PLAnetary Transits and Oscillations of**

---

<sup>5</sup> <http://astro.phys.au.dk/KASC/>.

<sup>6</sup> <http://www.brite-constellation.at/>.

stars)<sup>7</sup> has been funded for a design study. PLATO's goal is to study  $\sim 400\,000$  stars at precisions of 10s of  $\mu$ mag over a very wide field of  $\sim 1800$  square degrees for 3 yr, with a second field observed for 2 yr. The final sixth year of the mission can be spent on several other fields (including those with detected Earth analogues, stellar clusters, etc.) for several months in its so-called step-and-stare phase. PLATO is being designed, not only to extend the observations of CoRoT and Kepler to find more Earth-like planets, but to characterize the parent stars with exoplanets through asteroseismology. It is noteworthy that this is a different strategy to the one chosen for CoRoT and Kepler, whose asteroseismology and planet hunting programmes are performed on very different stellar samples: PLATO will do these two science cases simultaneously on *one and the same large sample of 20,000 bright stars* with  $V$  magnitude below 11.5. This is the only way to achieve a homogeneous seismic description of stars *and* their planetary systems, but is at the same time a technological challenge. Moreover, PLATO will additionally perform asteroseismic investigations of huge numbers of stars across the HR Diagram in its step-and-stare year. Should PLATO be funded following its present design study, the launch will be around 2018; it will be the next step in the progression in space asteroseismic and planet-finding missions from WIRE and MOST to CoRoT to Kepler.

### 8.1.5 Solar Missions

The SOHO mission has been in almost continuous operation since 1996 and has been of immense value to helioseismology. To continue the successes of SOHO, NASA is planning to launch the SDO mission (**Solar Dynamics Observatory**)<sup>8</sup> towards the end of 2009. This includes the HMI instrument (**Helioseismic and Magnetic Imager**)<sup>9</sup> which is essentially an updated version of the MDI instrument on SOHO. For helioseismology the main improvement is the much higher spatial resolution which will yield data superior to the dynamics programme of MDI throughout the mission. A major goal of this project is to carry out local helioseismology to study solar variability and the properties of solar magnetic activity. However, it will also produce data of great value for global helioseismology, particularly concerning high-degree modes and hence the properties of the regions near the solar surface. Important scientific issues concern the thermodynamics of the hydrogen and helium ionization zones and the dynamics of rotation in the convection zone. SOHO will be kept operational for a sufficient period to ensure good overlap and cross-calibration between the two missions.

Further into the future, ESA may launch the Solar Orbiter mission.<sup>10</sup> The mission will be in an orbit approaching the Sun to within 0.23 AU (48 R<sub>⊕</sub>)

<sup>7</sup> <http://lesia.obspm.fr/cosmicvision/plato/>.

<sup>8</sup> See <http://sdo.gsfc.nasa.gov/>.

<sup>9</sup> See <http://hmi.stanford.edu/>.

<sup>10</sup> <http://sci.esa.int/science-e/www/area/index.cfm?fareaid=45>.

for high-resolution observations of the solar surface and *in situ* measurements of the solar wind. Equally important, the inclination of the orbit relative to the ecliptic will gradually be increased to more than  $30^\circ$ , hence for the first time allowing detailed observations of the solar poles. The planned instrument package includes an instrument to carry out high-resolution velocity measurements, aiming in particular at local helioseismology. This will provide information about the flows near the solar poles which may play an important role in the operation of the dynamo that is likely responsible for the solar magnetic activity. If finally selected by ESA, Solar Orbiter will be launched around 2018.

## 8.2 Ground-Based Networks and Antarctica

While space mission observations are set to dominate asteroseismic studies in the near future, there is still significant scope for ground-based studies. For single-site observations and occasional multi-site campaigns these will probably concentrate on types of stars that CoRoT and Kepler are not able to observe in large numbers, or at all, because of their rarity or faintness: pulsating white dwarfs, sdBV stars and roAp stars are examples. In addition, there is a need for a ground-based network of telescopes similar to the networks that have become the major source of ground-based data for global helioseismology. This is particularly true for spectroscopic radial velocity measurements for which, as is shown in Fig. 4.1, noise levels are far lower than for photometric measurements. Finally, there is an promising possibility for single-site, high duty cycle asteroseismic observations for time spans of months from new observing sites in Antarctica that are being characterized and developed at the time of this writing.

### 8.2.1 SONG: A Ground-Based Radial Velocity Network

The Stellar Observations Network Group (SONG)<sup>11</sup> project intends to establish a network of 8 observing sites with a geographical distribution that will ensure nearly continuous coverage over the entire sky. It follows in the footsteps of the highly successful BiSON and GONG network projects in helioseismology. The network will be optimized for two scientific goals: asteroseismic observations using radial velocity measurements and a search for extra-solar planets with the gravitational microlensing technique. Since radial velocity observations of solar-like oscillations are far less affected by the stellar background noise than are photometric observations, SONG observations of a few carefully selected stars will allow in-depth investigations of these stars, complementing the investigations to be carried out by the CoRoT and Kepler missions of large numbers of stars, but with less precision. The radial

---

<sup>11</sup> <http://astro.phys.au.dk/SONG/>.

velocity measurements will also allow the detection of low-mass planets in very close orbits around their stars. Each site in the SONG network will be equipped with a 1-m telescope with a high-resolution ( $R \sim 100\,000$ ) spectrograph incorporating an iodine cell for velocity reference. As of this writing one prototype telescope to be installed on Tenerife is funded and is expected to be operational in 2011.

### 8.2.2 Antarctic Asteroseismology

During the first decade of the 21<sup>st</sup> century it has become apparent that the highest plateaus of the Antarctic continent are potentially some of the finest astronomical observing sites on Earth. Studies at Dome C by French and Italian astronomers and their collaborators show that cloud cover is low with up to 80% photometric weather; wind speeds at all atmospheric levels are exceptionally low so that scintillation noise is below that of other outstanding observing sites elsewhere on the planet; seeing during the day (summer) averages 0.5 arcsec and for part of the time drops to less than 0.1 arcsec; similar seeing is obtained at night, but only for heights of about 30 m and more above ground level because of a very steep temperature gradient; water vapour is very low. See Epcstein (2007) and other papers in the same conference proceedings volume; see also the ARENA (Antarctic Research, a European Network for Astrophysics<sup>12</sup>) website. In addition, Dome A – the highest point in Antarctica – is being tested as an astronomical site by Chinese astronomers and their collaborators<sup>13</sup>.

Neither Dome C nor Dome A is at the pole: Dome A is at latitude  $-80^\circ$  and Dome C is at  $-75^\circ$ . Even in midwinter at Dome C there is some “midday” twilight, since the Sun is  $\leq 8^\circ$  below the horizon at that time. Nevertheless, for asteroseismic research the site has the potential for data with duty cycles of  $\sim 70\%$  for time spans of 3 months (and even up to 88% duty cycle for stars bright enough to be observed through the noon twilight) for selected targets using only a single telescope. Even with the extreme environment, it appears to be cost effective for specialized studies of individual asteroseismic targets to use a small telescope at Dome C, rather than organize large numbers of astronomers and obtain telescope time at many observatories simultaneously around the world. Projects for asteroseismology have been proposed for Dome C, *e.g.*, the SIAMOIS Fourier Transform Spectrometer proposal by Mosser *et al.* (2007) that could produce a radial velocity data set for the solar-like oscillators  $\alpha$  Cen AB that would be superior for asteroseismic modelling to any photometric data set obtainable from space.

---

<sup>12</sup> <http://arena.unice.fr/>.

<sup>13</sup> <http://mcba11.phys.unsw.edu.au/~plato/>.



Technological progress in the fields of asteroseismology and planet hunting has been immense the past decade. We have moved from millimagnitude to micro-magnitude precision in photometric data and from several  $\text{m s}^{-1}$  to  $\text{cm s}^{-1}$  in velocity measurements – a factor 1000 gain! Moreover, we have evolved from the monitoring of a handful of selected asteroseismic targets to thousands of them – yet again a factor thousand improvement. It is to be expected that this impressive observational progress will lead to an order-of-magnitude improvement in the physical quantities describing the stellar interior. Asteroseismology is at the onset of a golden future. It will revolutionize stellar evolution theory across the entire HR Diagram, and all topics in astrophysics that build on it.

# A

---

## Summary of the Different Classes of Stellar Pulsators

A summary of all the classes of pulsating stars and their main properties as described in Chapter 2 is given in the tables below. This list originated from a combination of observational discoveries, measured stellar properties, and theoretical developments. Observers who found a new type of pulsator either named it after the prototype or gave the class a name according to the observed characteristics of the oscillations. Several pulsators, or even groups of pulsators, were afterwards found to originate from the same physical mechanism and were thus merged into one and the same class. We sort this out here in Tables A.1 and A.2 in order to avoid further confusion on pulsating star nomenclature.

The effective temperature and luminosity indicated in Tables A.1 and A.2 should be taken as rough indications only of the borders of instability strips. Often the theory is not sufficiently refined to consider these boundaries as final. Moreover, there is overlap between various classes where so-called *hybrid* pulsators, whose oscillations are excited in two different layers and/or by two different mechanisms, occur. Finally, new discoveries are being made frequently, which then drive new theoretical developments possibly leading to new instability regions. The results from the future observing facilities as described in Chapter 8 will surely lead to new classes and/or subclasses with lower amplitudes compared to what is presently achievable.

In the tables below, F stands for fundamental radial mode, FO for first radial overtone and S for strange mode oscillations. Several classes undergo (quasi-)periodicities with different time scales due to outbursts, cyclic variability, rotational modulation, differential rotation, activity, binarity, *etc.*, besides oscillations. We list here only the period and amplitude ranges for the oscillatory behaviour. Exceptions to the listed ranges are possible. The various names for each class as they occur in the literature are listed; the left column was the authors' choice, dominantly based on papers in the literature which discuss the physical cause of the oscillations. For a full description of the variability characteristics, we refer to Chapter 2 and the numerous references listed there.

**Table A.1.** The names and basic properties of main sequence, giant and compact pulsators.

Class name adopted here	Other names in the literature	Mode Type	Period Ranges	Amplitudes (brightness)	Amplitudes (velocity)	$\log T_{\text{eff}}$ (K) approx. range	$\log L/L_{\odot}$ approx. range
Solar-like pulsator	main sequence red giants	p p	3 to 10 min few hours	< 50 cm s <sup>-1</sup> few ms <sup>-1</sup>	[3.70, 3.82] [3.65, 3.70]	[-0.5, 1.0] [-0.5, 2.0]	
$\gamma$ Dor	slowly pulsating F	g	8 h to 5 d	< 50 mmag	< 5 km s <sup>-1</sup>	[3.83, 3.90]	[0.7, 1.1]
$\delta$ Sct	SXPhe (Pop. II)	p	15 min to 8 h	< 0.3 mag	< 10 km s <sup>-1</sup>	[3.82, 3.95]	[0.6, 2.0]
roAp	—	p	5 to 22 min	< 10mmag	< 10 km s <sup>-1</sup>	[3.82, 3.93]	[0.8, 1.5]
SPB	53 Per	g	0.5 to 5 d	< 50 mmag	< 15 km s <sup>-1</sup>	[4.05, 4.35]	[2.0, 4.0]
$\beta$ Cep	$\beta$ CMa, $\zeta$ Oph (SpT O) 53 Per	p&g p&g	1 to 12 h (p) few days (g)	< 0.1 mag < 0.01 mag	< 20 km s <sup>-1</sup> < 10 km s <sup>-1</sup>	[4.25, 4.50]	[3.2, 5.0]
pulsating Be	$\lambda$ Eri, SPBe	p&g	0.1 to 5 d	< 20 mmag	< 20 km s <sup>-1</sup>	[4.05, 4.50]	[2.0, 5.0]
pre-MS pulsator	pulsating T Tauri pulsating Herbig Ae/Be	p p	1 to 8 h 1 to 8 h	< 5 mmag < 5 mmag			
	pulsating T Tauri	g	8 h to 5 d	< 5 mmag			
p-mode sdBV	EC14026, V361 Hya	p	80 to 800 s	< 0.1 mag		[4.20, 4.50]	[1.2, 2.2]
g-mode sdBV	PG1716+426, Betsy star, lpscBV	g	0.5 to 3 h	< 0.01 mag		[4.40, 4.60]	[1.2, 2.6]
PNNV	ZZ Lep, [WCE]	g	5 h to 5 d	< 0.3 mag			
GW Vir	DOV, PG1159	g	5 to 80 min	< 0.2 mag		[4.80, 5.10]	[1.5, 3.5]
DBV	V777 Her	g	2 to 16 min	< 0.2 mag		[4.40, 4.60]	[-1.0, 0.7]
DAV	ZZ Ceti	g	0.5 to 25 min	< 0.2 mag		[3.95, 4.15]	[-2.6, -2.2]

**Table A.2.** The names and basic properties of supergiant pulsators.

Class name adopted here	Other names in literature	Mode Type	Period Ranges	Amplitudes (brightness)	Amplitudes (velocity)	approx. range	$\log T_{\text{eff}}$ (K)	$\log L/L_{\odot}$ approx. range
RR Lyr	RRab	F	~0.5 d	< 1.5 mag	< 30 km s <sup>-1</sup>	[3.78, 3.88]	[1.4, 1.7]	
	RRc	FO	~0.3 d	< 0.5 mag	< 10 km s <sup>-1</sup>			
	RRd	F+FO	0.3 to 0.5 d	< 0.2 mag	< 10 km s <sup>-1</sup>			
Type II Cepheid	W Vir	F	10 to 30 d	< 1 mag	< 30 km s <sup>-1</sup>	[3.70, 3.90]	[2.0, 4.0]	
	BL Her	F	1 to 5 d	< 1 mag	< 30 km s <sup>-1</sup>			
RV Tauri	RVa, RVb	F?	30 to 150 d	< 3 mag	< 30 km s <sup>-1</sup>	[3.60, 3.90]	[3.2, 4.2]	
Type I Cepheid	—	F	1 to 50 d	< 1 mag	< 30 km s <sup>-1</sup>	[3.55, 3.85]	[2.0, 5.5]	
	s-Cepheid	FO	< 20 d	< 0.1 mag	< 10 km s <sup>-1</sup>			
Mira	SRa, SRb	$l = 0$	> 80 d	< 8 mag		[3.45, 3.75]	[2.5, 4.0]	
	SRc	$l = 0$	> 80 d	< 1 mag				
	SRd	$l = 0$	< 80 d	< 1 mag				
PVSG (SpT A)	$\alpha$ Cyg	g,S?	10 to 100 d	< 0.3 mag	< 20 km s <sup>-1</sup>	[3.45, 4.00]	[2.5, 4.5]	
PVSG (SpT B)	SPBsg	g	1 to 10 d	< 0.3 mag	< 20 km s <sup>-1</sup>	[4.00, 4.50]	[4.3, 5.8]	
LBV	S Dor	g,S	2 to 40 d	< 0.1 mag		[3.80, 4.20]	[5.5, 6.5]	
WR	WC, WN	g,S	1h to 5 d	< 0.2 mag		[4.40, 4.70]	[4.5, 6.0]	
HdC eHe	R CrB	g?	40 to 100 d	< 0.05 mag	< 10 km s <sup>-1</sup>	[3.50, 4.20]	[3.5, 4.5]	
	PV Tel	S	~20 d					
	V652 Her	g,S?	~0.1 d					
	V2076 Oph	g,S?	0.5 to 8 d					

# B

---

## Properties of Legendre Functions and Spherical Harmonics

### B.1 Properties of Legendre Functions

We provide here some basic properties of the Legendre functions, which are essential to the understanding of nonradial oscillations. The following expressions are mainly taken from Abramowitz & Stegun (1964) and Whittaker & Watson (1927).

The Legendre function are solutions of the differential equation:

$$(1-x^2) \frac{d^2 P_l^m}{dx^2} - 2x \frac{dP_l^m}{dx} + \left[ l(l+1) - \frac{m^2}{1-x^2} \right] P_l^m = 0 , \quad (\text{B.1})$$

or, equivalently,

$$\frac{d}{dx} \left[ (1-x^2) \frac{dP_l^m}{dx} \right] + \left[ l(l+1) - \frac{m^2}{1-x^2} \right] P_l^m = 0 . \quad (\text{B.2})$$

In the special case of  $m = 0$ , we are dealing with the Legendre polynomials:  $P_l(x) = P_l^0(x)$ .

Explicit expressions for the first few cases are:

$$\begin{aligned} P_0(x) &= 1 , \\ P_1(x) &= x , \\ P_1^1(x) &= -(1-x^2)^{1/2} , \\ P_2(x) &= 1/2(3x^2 - 1) , \\ P_2^1(x) &= -3(1-x^2)^{1/2} , \\ P_2^2(x) &= 3(1-x^2) . \end{aligned} \quad (\text{B.3})$$

General expressions, valid for  $m > 0$ , are:

$$P_l(x) = \frac{1}{2^l l!} \frac{d^l (x^2 - 1)^l}{dx^l} , \quad (\text{B.4})$$

$$P_l^m(x) = (-1)^m (1-x^2)^{m/2} \frac{d^m P_l(x)}{dx^m}, \quad (\text{B.5})$$

$$P_m^m(x) = (-1)^m \frac{(2m)! 2^{-m}}{m!} (1-x^2)^{m/2}. \quad (\text{B.6})$$

Note that Eq. (B.4) shows that  $P_l(x)$  is a polynomial of degree  $l$ . Also, Eq. (B.6) shows that

$$P_m^m(\cos \theta) = (-1)^m \frac{(2m)! 2^{-m}}{m!} \sin^m \theta \quad (\text{B.7})$$

The Legendre function for negative azimuthal order is obtained from the one for positive  $m$  as

$$P_l^{-m}(\cos \theta) = \frac{(l-m)!}{(l+m)!} P_l^m(\cos \theta). \quad (\text{B.8})$$

The Legendre functions are easily computed from the following recursion relations:

$$(l-m+1)P_{l+1}^m(x) = (2l+1)xP_l^m(x) - (l+m)P_{l-1}^m(x), \quad (\text{B.9})$$

$$\begin{aligned} P_l^{m+1}(x) &= \\ &(1-x^2)^{-1/2} [(l-m)xP_l^m(x) - (l+m)P_{l-1}^m(x)], \end{aligned} \quad (\text{B.10})$$

$$(1-x^2) \frac{dP_l^m}{dx} = lxP_l^m(x) - (l+m)P_{l-1}^m(x), \quad (\text{B.11})$$

$$x \frac{dP_l}{dx} - \frac{dP_{l-1}}{dx} = lP_l(x). \quad (\text{B.12})$$

The following integral expression defines the orthogonality and normalization of the Legendre functions:

$$\int_{-1}^1 P_l^m(x) P_{l'}^m(x) dx = \delta_{ll'} \frac{(n+m)!}{(l+1/2)(l-m)!}. \quad (\text{B.13})$$

The Legendre functions have the following asymptotic expansion, for fixed  $m \geq 0$  and large  $l$ :

$$\begin{aligned} P_l^m(\cos \theta) &= \frac{\Gamma(l+m+1)}{\Gamma(l+3/2)} \left(\frac{\pi}{2} \sin \theta\right)^{-1/2} \cos \left[ \left(l + \frac{1}{2}\right) \theta - \frac{\pi}{4} + \frac{m\pi}{2} \right] \\ &+ \mathcal{O}(l^{-1}) \end{aligned} \quad (\text{B.14})$$

For arbitrary, large  $l, m$  an approximate asymptotic representation of  $P_l^m$  is

$$\begin{aligned} P_l^m(\cos \theta) &\simeq A_{lm} (\cos^2 \Theta_{lm} - \cos^2 \theta)^{-1/4} \cos[\Psi_{lm}(\theta)], \\ \cos \theta &\in [-\cos \Theta_{lm}, \cos \Theta_{lm}], \end{aligned} \quad (\text{B.15})$$

for a suitable amplitude  $A_{lm}$  and a rapidly varying phase function  $\Psi_{lm}$ ; here

$$\Theta_{lm} = \sin^{-1}[m/\sqrt{l(l+1)}] \quad (\text{B.16})$$

(e.g. Gough & Thompson 1990).<sup>1</sup> Thus the Legendre function is confined between turning-point latitudes  $\pm(\pi/2 - \Theta_{lm})$ ; in particular, as also illustrated in Fig. B.1, modes with  $m \simeq \pm l$  are confined very near the equator.

## B.2 Properties of Spherical Harmonics

The spherical harmonics are defined as

$$Y_l^m(\theta, \phi) \equiv (-1)^m c_{lm} P_l^m(\cos \theta) \exp(im\phi), \quad (\text{B.17})$$

where  $c_{lm}$  is a normalization constant, given by

$$c_{lm}^2 = \frac{(2l+1)(l-m)!}{4\pi(l+m)!}, \quad (\text{B.18})$$

such that the integral of  $|Y_l^m|^2$  over the unit sphere is unity (*cf.* Eq. (B.13)). Examples of spherical harmonics for various degrees and azimuthal orders are illustrated in Fig. B.1. Note in particular the increasing concentration towards the equator of the sectoral modes, with  $m = l$  (see also Eq. (B.16)).

The transformation formula for spherical harmonics for two different coordinate systems  $(r, \theta, \phi)$  and  $(r', \theta', \phi')$  whose polar axes are inclined with angle  $i$  and whose zero points for the azimuthal angles  $\phi$  and  $\phi'$  are the same, is given by:

$$Y_l^m(\theta, \phi) = \sum_{k=-l}^l a_{lmk}(i) Y_l^k(\theta', \phi'), \quad (\text{B.19})$$

where

$$a_{lmk}(i) \equiv (l+m)!(l-m)! \times \sum_{r=\max\{0, -k-m\}}^{\min\{l-m, l-k\}} (-1)^{l+k+r} \frac{\sin(i/2)^{2l-2r-m-k} \cos(i/2)^{2r+m+k}}{r!(m+k+r)!(l-m-r)!(l-k-r)!} \quad (\text{B.20})$$

(Edmonds 1960, Jeffreys 1965, Condon & Odabasi 1980).

Let us now consider the specific case where the polar axis of the coordinate system  $(r, \theta, \phi)$  coincides with the rotation axis of the star, which is further assumed to coincide with the symmetry axis of the spherical harmonics, while the polar axis of the system  $(r', \theta', \phi')$  points towards the observer. In practice, the inclination angle  $i$  can then take any value between  $0^\circ$  and  $180^\circ$ . From Eqs (6.58) and (B.20), one derives that the centroid velocity (first moment) as detected by the observer, or, equivalently, the radial velocity variation, is

---

<sup>1</sup> It is straightforward to demonstrate this by applying the JWKB technique, discussed below in Section E.2, to Eq. (B.1).

proportional to  $a_{lm0}(i)$  (Aerts *et al.* 1992). This leads us, in a natural way, to define the so-called *Inclination Angles of Complete Cancellation*, IACC, as the angles  $i$  for which  $a_{lm0}(i) = P_l^m(\cos i) = 0$  with  $P_l^m(\cos i)$  the factor occurring in the variation of the monochromatic visual magnitude defined in Eq. (6.29). Note that this cancellation is defined for linear quantities, such as the radial velocity or the brightness variation, but not for, *e.g.*, the second or third moments. One can thus end up with a complete cancelling in the photometric data while still detecting variations in the second or third moment of line profiles.

The cases of complete cancellation of the brightness variations or of the first moment occur whenever we look upon the star in such a way that the individual contributions of all the points on the visible stellar disc to these two quantities add up to zero. The definitions of  $P_l^m(\cos i)$  and of  $a_{lm0}(i)$  lead us to derive the following properties:

- $180^\circ - i$  is an IACC if  $i$  is an IACC;
- the mode with wavenumbers  $(l, m)$  has the same IACCs as the mode with wavenumbers  $(l, -m)$ ;
- $i = 0^\circ$  is an IACC for each mode with  $m \neq 0$ ;
- $i = 90^\circ$  is an IACC for  $\ell - m$  odd

(Chadid *et al.* 2001). The IACCs lower than  $90^\circ$  for modes with  $l \leq 5$  and  $m \geq 0$  are listed in Table B.1.

For sectoral modes with  $l > 3$ ,  $P_l^m(\cos i)$  and  $a_{lm0}(i) \simeq 0$  for quite a broad range of  $i$  near the IACC, so we have an interval of inclination angles of almost complete cancellation for near pole-on views. For a multiperiodic star, we may observe incomplete multiplets due to complete cancellation of the central peak with  $m = 0$ , or of couples of side peaks  $(l, \pm m)$ .

In analogy with IACCs, we define the *Inclination Angle of Least Cancellation* (abbreviated IALC) as the inclination angle  $i$  for which  $P_l^m(\cos i)$  and  $a_{lm0}(i)$  attain their maximum value. That is, the IALC is that inclination angle  $i$  under which the star is viewed by the observer so as to maximize the amplitude of the surface-integrated brightness variation and the radial velocity variation for the mode  $(l, m)$  under consideration, for a given intrinsic mode amplitude. It was first introduced by Buta & Smith (1979) and further elaborated on by Chadid *et al.* (2001).

Similarly as for the IACCs, we have the following properties:

- $180^\circ - i$  is an IALC if  $i$  is an IALC;
- the mode with wavenumbers  $(l, m)$  has the same IALCs as the mode with wavenumbers  $(l, -m)$ ;
- $i = 0^\circ$  is an IALC for a zonal mode;
- $i = 90^\circ$  is an IALC for a sectoral mode

(Chadid *et al.* 2001). Each nonradial mode has exactly one IALC  $\leq 90^\circ$ . These are listed in Table B.1 for  $l \leq 5$  and  $m \geq 0$ .

$(l, m)$	IACC			IALC
(1, 0)			90°	0°
(2, 0)		54.7°		0°
(3, 0)	39.2°		90°	0°
(4, 0)	30.6°		70.1°	0°
(5, 0)	25.0°	57.4°	90°	0°
(1, 1)	0°			90°
(2, 2)	0°			90°
(3, 3)	0°			90°
(4, 4)	0°			90°
(5, 5)	0°			90°
(2, 1)	0°		90°	45.0°
(3, 1)	0°	63.4°		31.1°
(3, 2)	0°		90°	54.7°
(4, 1)	0°	49.1°	90°	23.9°
(4, 2)	0°	67.8°		40.9°
(4, 3)	0°		90°	60.0°
(5, 1)	0°	40.1°	73.4°	19.4°
(5, 2)	0°	54.7°	90°	32.9°
(5, 3)	0°		70.5°	46.9°
(5, 4)	0°		90°	63.4°

**Table B.1.** A list of inclination angles of complete (IACC) and of least (IALC) cancellation for modes with  $l \leq 5$  and  $m \geq 0$ .

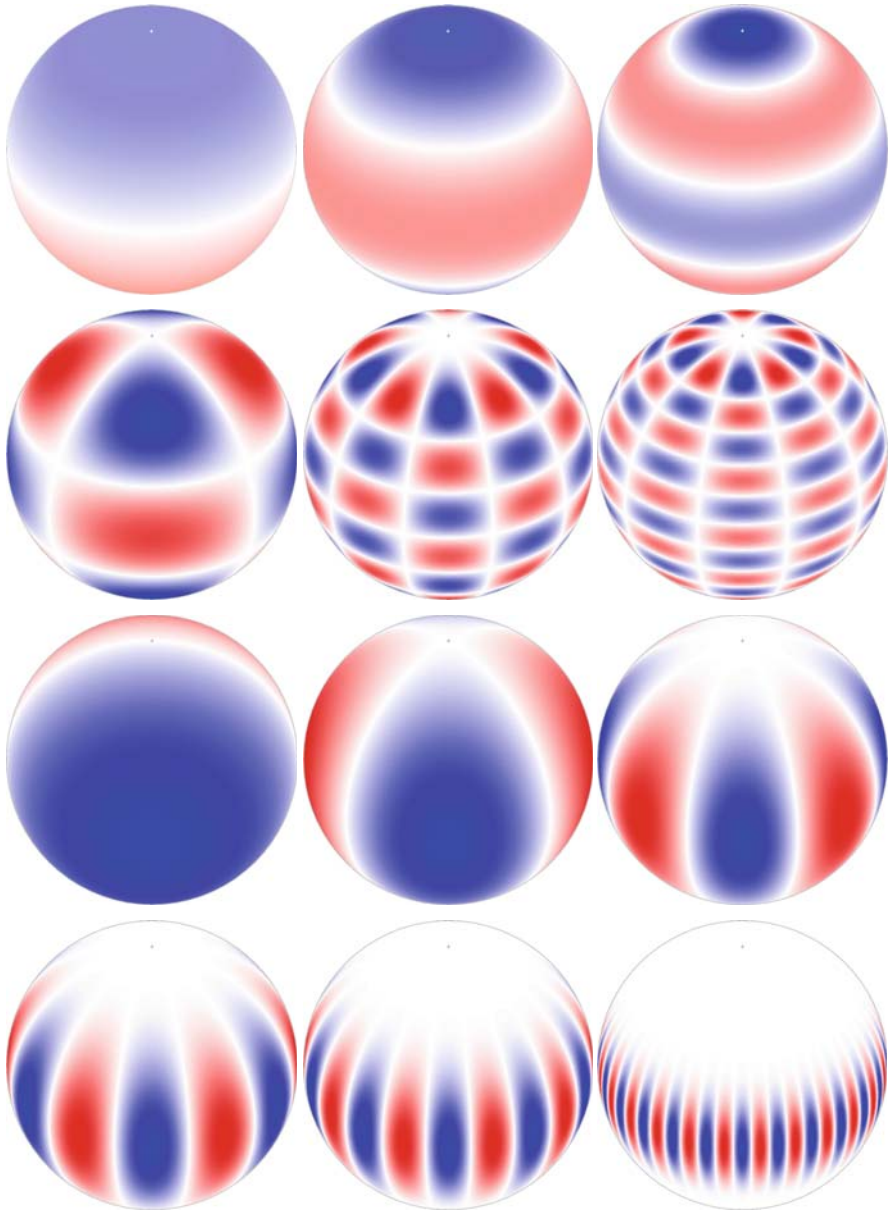


**Fig. B.1.** Snapshot of the radial component of various modes as seen by an observer under an inclination angle of  $55^\circ$ . The white bands represent the positions of the surface nodes; red and blue represent sections of the star that are moving in (out) at any given time, then vice versa. Top row: axisymmetric modes with, from left to right,  $l = 1, 2, 4$ ; 2nd row: tesseral modes with, from left to right,  $(l, m) = (4, 2), (10, 5), (15, 5)$ ; 3rd and 4th row: sectoral modes with, from left to right,  $l = 1, 2, 4$  (3rd row) and  $l = 6, 10, 25$  (bottom row). The higher the degree of sectoral modes, the more they become confined to the equator of the star.

# C

---

## Mathematical Preliminaries

### C.1 Formulation of Oscillation Equations in Complex Form

In the analysis of the equations for perturbations around an equilibrium state it is convenient to write the solution in complex form; the physically realistic solution is obtained as the real part of the complex solution. To see that this is possible, notice that the general equations can be written as

$$\mathbf{A} \frac{\partial \mathbf{y}}{\partial t} = \mathcal{B}(\mathbf{y}), \quad (\text{C.1})$$

where the vector  $\mathbf{y}$  consists of the perturbation variables  $(\delta \mathbf{r}, p', \rho', \dots)$ ,  $\mathbf{A}$  is a matrix with real coefficients, and  $\mathcal{B}$  is a linear matrix operator involving spatial gradients, *etc.*, with real coefficients. Neither  $\mathbf{A}$  nor  $\mathcal{B}$  depends on time. If  $\mathbf{y}$  is a complex solution to Eq. (C.1) then the complex conjugate  $\mathbf{y}^*$  is also a solution, since

$$\mathbf{A} \frac{\partial \mathbf{y}^*}{\partial t} = \left( \mathbf{A} \frac{\partial \mathbf{y}}{\partial t} \right)^* = [\mathcal{B}(\mathbf{y})]^* = \mathcal{B}(\mathbf{y}^*), \quad (\text{C.2})$$

and hence, as the system is linear and homogeneous, the real part  $\Re(\mathbf{y}) = 1/2(\mathbf{y} + \mathbf{y}^*)$  is a solution.

Because of the independence of time of the coefficients in Eq. (C.1), solutions can be found of the form

$$\mathbf{y}(\mathbf{r}, t) = \hat{\mathbf{y}}(\mathbf{r}) \exp(-i\omega t). \quad (\text{C.3})$$

This is a solution if the *amplitude function*  $\hat{\mathbf{y}}$  satisfies the eigenvalue equation

$$-i\omega \mathbf{A} \cdot \hat{\mathbf{y}} = \mathcal{B}(\hat{\mathbf{y}}). \quad (\text{C.4})$$

Equations of this form were considered in Section 3.1.4 for simple waves. Note that in Eqs (C.3) and (C.4) the frequency  $\omega$  must in general be assumed to be complex.

Equation (C.3) is an example of the *separability* of the solution to a system of linear partial differential equations, when the equations do not depend on one of the coordinates. As the equilibrium state is spherically symmetric, the equations are similarly separable in  $\theta$  and  $\phi$  when described in spherical polar coordinates  $(r, \theta, \phi)$  (see Section 3.1.4.2).

## C.2 Vector Operators in Spherical Polar Coordinates

We consider stars with at most modest deviations from spherical symmetry and hence the description is most naturally made in spherical polar coordinates (*cf.* Fig. 3.13). Here we present some relations for this case that are needed in the study of the properties of the pulsations [see also Appendix 2 of Batchelor (1967)]. Let  $\mathbf{a}_r$ ,  $\mathbf{a}_\theta$  and  $\mathbf{a}_\phi$  be unit vectors in the  $r$ ,  $\theta$  and  $\phi$  directions, let  $V$  be a general scalar field, and let

$$\mathbf{F} = F_r \mathbf{a}_r + F_\theta \mathbf{a}_\theta + F_\phi \mathbf{a}_\phi \quad (\text{C.5})$$

be a vector field. Then the gradient of  $V$  is

$$\nabla V = \frac{\partial V}{\partial r} \mathbf{a}_r + \frac{1}{r} \frac{\partial V}{\partial \theta} \mathbf{a}_\theta + \frac{1}{r \sin \theta} \frac{\partial V}{\partial \phi} \mathbf{a}_\phi , \quad (\text{C.6})$$

the divergence of  $\mathbf{F}$  is

$$\operatorname{div} \mathbf{F} = \frac{1}{r^2} \frac{\partial}{\partial r} (r^2 F_r) + \frac{1}{r \sin \theta} \frac{\partial}{\partial \theta} (\sin \theta F_\theta) + \frac{1}{r \sin \theta} \frac{\partial F_\phi}{\partial \phi} , \quad (\text{C.7})$$

and consequently the Laplacian of  $V$  is

$$\begin{aligned} \nabla^2 V &= \operatorname{div} (\nabla V) \\ &= \frac{1}{r^2} \frac{\partial}{\partial r} \left( r^2 \frac{\partial V}{\partial r} \right) + \frac{1}{r^2 \sin \theta} \frac{\partial}{\partial \theta} \left( \sin \theta \frac{\partial V}{\partial \theta} \right) + \frac{1}{r^2 \sin^2 \theta} \frac{\partial^2 V}{\partial \phi^2} . \end{aligned} \quad (\text{C.8})$$

Finally, we need the directional derivatives, in the direction, say, of the vector

$$\mathbf{n} = n_r \mathbf{a}_r + n_\theta \mathbf{a}_\theta + n_\phi \mathbf{a}_\phi . \quad (\text{C.9})$$

The directional derivative  $\mathbf{n} \cdot \nabla V$  of a scalar is obtained, as would be naively expected, as the scalar product of  $\mathbf{n}$  with the gradient in equation Eq. (C.6). However, in the directional derivatives  $\mathbf{n} \cdot \nabla \mathbf{F}$  of a vector field, the change in the unit vectors  $\mathbf{a}_r$ ,  $\mathbf{a}_\theta$  and  $\mathbf{a}_\phi$  must be taken into account. The result is

$$\begin{aligned} \mathbf{n} \cdot \nabla \mathbf{F} &= \left( \mathbf{n} \cdot \nabla F_r - \frac{n_\theta F_\theta}{r} - \frac{n_\phi F_\phi}{r} \right) \mathbf{a}_r \\ &\quad + \left( \mathbf{n} \cdot \nabla F_\theta - \frac{n_\phi F_\phi}{r} \cot \theta + \frac{n_\theta F_r}{r} \right) \mathbf{a}_\theta \\ &\quad + \left( \mathbf{n} \cdot \nabla F_\phi + \frac{n_\phi F_r}{r} + \frac{n_\phi F_\theta}{r} \cot \theta \right) \mathbf{a}_\phi , \end{aligned} \quad (\text{C.10})$$

where the directional derivatives of  $F_r$ ,  $F_\theta$  and  $F_\phi$  are the same as for a scalar field.

As the radial direction has a special status, it is convenient to introduce the horizontal (or, properly speaking, tangential) component of the vector  $\mathbf{F}$ :

$$\mathbf{F}_h = F_\theta \mathbf{a}_\theta + F_\phi \mathbf{a}_\phi , \quad (\text{C.11})$$

and similarly the horizontal components of the gradient, divergence and Laplacian as

$$\nabla_h V = \frac{1}{r} \frac{\partial V}{\partial \theta} \mathbf{a}_\theta + \frac{1}{r \sin \theta} \frac{\partial V}{\partial \phi} \mathbf{a}_\phi , \quad (\text{C.12})$$

$$\nabla_h \cdot \mathbf{F} = \frac{1}{r \sin \theta} \frac{\partial}{\partial \theta} (\sin \theta F_\theta) + \frac{1}{r \sin \theta} \frac{\partial F_\phi}{\partial \phi} , \quad (\text{C.13})$$

and

$$\nabla_h^2 V = \frac{1}{r^2 \sin \theta} \frac{\partial}{\partial \theta} \left( \sin \theta \frac{\partial V}{\partial \theta} \right) + \frac{1}{r^2 \sin^2 \theta} \frac{\partial^2 V}{\partial \phi^2} . \quad (\text{C.14})$$

# D

---

## Adiabatic Oscillations in an Isothermal Atmosphere

As a simple illustration of the properties of oscillations in stellar atmospheres it is convenient to consider an isothermal atmosphere. This has the significant advantage of allowing an analytical solution of the oscillation equations. Furthermore, it is a reasonable approximation to a realistic stellar atmosphere where the temperature variation is substantially slower than the variations in pressure and density. An early treatment of this problem was given by Biermann (1947); for a slightly more recent review, see Schatzman & Souffrin (1967).

### D.1 Equilibrium Structure

We neglect effects of ionization and treat the gas in the atmosphere as ideal, so that the equation of state is given by Eq. (3.19), where the mean molecular weight  $\mu$  is taken to be constant. Then Eq. (3.33) of hydrostatic support gives

$$\frac{dp}{dr} = -g\rho = -\frac{p}{H_p}, \quad (\text{D.1})$$

where the pressure and density scale heights  $H_p$  and  $H$  (which are evidently the same in this case) are given by

$$H_p = H = \frac{k_B T}{g\mu m_u}. \quad (\text{D.2})$$

As the extent of the atmosphere of at least main-sequence stars is much smaller than the stellar radius,  $g$  can be taken to be constant. Then  $H$  is constant, and the solution to Eq. (D.1) is

$$p = p_s \exp\left(-\frac{h}{H}\right). \quad (\text{D.3})$$

Thus, from Eq. (3.19),

$$\rho = \rho_s \exp\left(-\frac{h}{H}\right). \quad (\text{D.4})$$

Here we have introduced the altitude  $h = r - R$ , where  $R$  is the photospheric radius (corresponding to the visible surface of the star, *e.g.* defined as the point where the temperature equals the effective temperature), and  $p_s$  and  $\rho_s$  are the values of  $p$  and  $\rho$  at  $h = 0$ .

## D.2 Oscillation Properties

We now consider the oscillations. As argued in Section 3.1.2, the motion becomes strongly nonadiabatic near the stellar surface. Nonetheless, for simplicity, we shall here use the adiabatic approximation in the atmosphere. This preserves the most important features of the atmospheric behaviour of the oscillations, at least qualitatively. The study of atmospheric waves and oscillations, with full consideration of effects of radiative transfer, is a very complex and still incompletely developed area (*e.g.* Christensen-Dalsgaard & Frandsen 1983b; Medupe 2002; Medupe *et al.* 2002; Phorah 2008). It might be noticed that the waves are in fact approximately adiabatic in the upper part of the atmosphere. Here the diffusion approximation (upon which the argument in Section 3.1.2 was based) is totally inadequate, as the gas is optically thin; indeed the density is so low that the gas radiates, and hence loses energy, very inefficiently, and the motion is nearly adiabatic.

We use the Cowling approximation, Eqs (3.174) and (3.175). Due to the small extent of the atmosphere we neglect the term in  $2/r$  (this is consistent with assuming  $g$  to be constant, and corresponds to regarding the atmosphere as plane-parallel). Then the equations may be written as

$$\frac{d\xi_r}{dh} = \frac{1}{\Gamma_1 H} \xi_r - \frac{1}{\Gamma_1 p_s} \left(1 - \frac{k_h^2 c_s^2}{\omega^2}\right) \exp\left(\frac{h}{H}\right) p', \quad (\text{D.5})$$

and

$$\frac{dp'}{dh} = -\rho_s \exp\left(-\frac{h}{H}\right) (N_s^2 - \omega^2) \xi_r - \frac{1}{\Gamma_1 H} p'. \quad (\text{D.6})$$

Here the squared sound speed

$$c_s^2 = \frac{\Gamma_1 p_s}{\rho_s} \quad (\text{D.7})$$

and the squared buoyancy frequency

$$N_s^2 = \frac{g}{H} \left(1 - \frac{1}{\Gamma_1}\right) \quad (\text{D.8})$$

are constant. In accordance with the plane-parallel approximation we have introduced the horizontal wavenumber  $k_h$  instead of the degree  $l$ , using

Eq. (3.143). These equations may be combined into a single, second-order equation for  $\xi_r$ :

$$\frac{d^2\xi_r}{dh^2} - \frac{1}{H} \frac{d\xi_r}{dh} + \frac{1}{H^2} \left[ \frac{1}{4} \frac{\omega^2}{\omega_a^2} + \frac{k_h^2 g H}{\omega^2} \left( 1 - \frac{1}{\Gamma_1} \right) - k_h^2 H^2 \right] \xi_r = 0. \quad (\text{D.9})$$

Here

$$\omega_a = \frac{c_s}{2H} \quad (\text{D.10})$$

is a characteristic frequency for the atmosphere. In the solar atmosphere  $H$  is approximately equal to 120 km, and  $\omega_a$  is about  $0.03 \text{ s}^{-1}$ , corresponding to a cyclic frequency of about 5 mHz, or a period of about 3 min.

Equation (D.9) has constant coefficients, and so the solution can be written down immediately as

$$\xi_r(h) = a_+ \exp \left( \lambda_+ \frac{h}{H} \right) + a_- \exp \left( \lambda_- \frac{h}{H} \right), \quad (\text{D.11})$$

where

$$\lambda_{\pm} = \frac{1}{2} \pm \frac{1}{2} \left\{ 1 - \frac{\omega^2}{\omega_a^2} + 4k_h^2 H^2 \left[ 1 - 4 \frac{\omega_a^2}{\omega^2} \frac{1}{\Gamma_1} \left( 1 - \frac{1}{\Gamma_1} \right) \right] \right\}^{1/2}. \quad (\text{D.12})$$

These equations have been the subject of extensive studies in connection with early attempts to interpret observations of solar 5-minute oscillations of high degree (see *e.g.* Stein & Leibacher 1974). From the expression for  $\lambda_{\pm}$  one may qualitatively expect two regimes: one where the frequency is relatively large,  $k_h$  is relatively small and the first two terms in  $\{\dots\}$  dominate; the second where the frequency is small,  $k_h$  is large and the last term in  $\{\dots\}$  dominates. These correspond to atmospheric acoustic waves and gravity waves, respectively. From the point of view of global stellar oscillations interest centres on those waves which have a wavelength much larger than the scale height of the atmosphere.<sup>1</sup> Thus we neglect the last term, reducing Eq. (D.12) to

$$\lambda_{\pm} = \frac{1}{2} \pm \frac{1}{2} \left( 1 - \frac{\omega^2}{\omega_a^2} \right)^{1/2}. \quad (\text{D.13})$$

This is clearly the relation for purely vertical waves.

Equation (D.13) shows the physical meaning of  $\omega_a$ . When  $\omega < \omega_a$ ,  $\lambda_{\pm}$  are real, and the motion behaves exponentially in the atmosphere. When  $\omega > \omega_a$ ,  $\lambda_{\pm}$  are complex, and the motion corresponds to a wave propagating through the atmosphere. Thus  $\omega_a$  is the minimum frequency of a propagating wave, and is consequently known as *the acoustic cut-off frequency* (Lamb 1909). The exponential behaviour in the former case provides the upper reflection of p modes. As discussed in Section 3.4.3, and in more detail in Section E.1 below, this can be generalized to the case of a general stellar envelope.

---

<sup>1</sup> A detailed analysis of internal gravity waves in the solar atmosphere was presented by Mihalas & Toomre (1981, 1982).

### D.3 Boundary Conditions in a Stellar Atmosphere

To study these properties in more detail, we consider the boundary conditions for an atmosphere of infinite extent, assuming that  $\omega < \omega_a$ . Here the energy density in the motion must be bounded as  $h$  tends to infinity. The energy density is proportional to  $\rho\xi_r^2$ , which for the two solutions behaves as

$$\rho\xi_r^2 \sim \exp\left(-\frac{h}{H}\right) \exp\left(2\lambda_{\pm}\frac{h}{H}\right) = \exp\left[\pm\left(1 - \frac{\omega^2}{\omega_a^2}\right)^{1/2} \frac{h}{H}\right]. \quad (\text{D.14})$$

Therefore only the  $\lambda_-$  solution is acceptable, and here the energy density decreases exponentially. This gives rise to the atmospheric reflection. It should be noticed that  $\lambda_- > 0$ , so that the displacement *increases* with altitude in the atmosphere. This increase can in fact be observed by comparing oscillation amplitudes obtained in spectral lines formed at different levels in the atmosphere. If  $\omega > \omega_a$  we can write Eq. (D.13) as  $\lambda_{\pm} = 1/2 \pm ik_r$ , where

$$k_r = \left(\frac{\omega^2}{\omega_a^2} - 1\right)^{1/2}, \quad (\text{D.15})$$

and the corresponding full solution for the displacement, in complex form, is

$$\delta r(h) = \delta r_0 \exp(1/2 h) \exp[i(\pm k_r h - \omega t)], \quad (\text{D.16})$$

where  $\delta r_0$  is the displacement at  $h = 0$ . This corresponds to waves propagating through the atmosphere; the physically realistic case<sup>2</sup> is clearly for the waves to propagate towards increasing  $h$ , *i.e.*, to choose the solution with  $+k_r$  in Eq. (D.16). These waves transport energy away from the star, and hence oscillations at such frequencies would lose energy (such waves, generated in the convection zone, may contribute to the heating of stellar chromospheres). Thus only modes with frequencies below  $\omega_a$  are trapped in the stellar interior. In fact, the observed spectrum of solar oscillations stops at frequencies of around 5 mHz, corresponding to  $\omega_a$  in the solar case.

From this solution we may obtain a more realistic boundary condition, to replace the condition (3.160) discussed earlier. The condition of adiabaticity (3.151) and the continuity equation (3.41) give

$$\frac{\delta p}{p} = \Gamma_1 \frac{\delta \rho}{\rho} = -\Gamma_1 \operatorname{div} \boldsymbol{\delta r} \simeq -\Gamma_1 \frac{d\xi_r}{dh} = -\Gamma_1 \frac{\lambda_-}{H} \xi_r, \quad (\text{D.17})$$

or

$$p' = \delta p - \xi_r \frac{dp}{dh} = \frac{1}{H} p (1 - \Gamma_1 \lambda_-) \xi_r, \quad (\text{D.18})$$

where, for simplicity, we neglected the horizontal part of the divergence of  $\boldsymbol{\delta r}$  (this could, quite simply, be included). This provides a boundary condition

---

<sup>2</sup> assuming that there is no source of waves outside the star.

that may be used in numerical computations, in place of Eq. (3.160). Typically it is applied at a suitable point, such as the temperature minimum, in the atmosphere of the stellar model.

When  $\omega$  is small compared with  $\omega_a$ , we can approximate  $\lambda_-$  by

$$\lambda_- \simeq \frac{1}{2} \left[ 1 - \left( 1 - \frac{1}{2} \frac{\omega^2}{\omega_a^2} \right) \right] = \frac{1}{4} \frac{\omega^2}{\omega_a^2}. \quad (\text{D.19})$$

Then  $\Gamma_1 \lambda_-$  can be neglected in Eq. (D.18), compared with 1, and we recover the boundary condition in (3.160). In this limit the displacement is almost constant throughout the atmosphere. Also, it follows from Eq. (D.17) that the Lagrangian perturbations to pressure and density, and consequently also to temperature, are small. Physically, this means that the atmosphere is just lifted passively up and down by the oscillation, without changing its structure. Only when the frequency is quite close to the acoustic cut-off frequency does the oscillation have a dynamical effect on the atmosphere.

For completeness, we note that a boundary condition can also be obtained for  $\omega > \omega_a$ , by choosing the appropriate outward travelling wave in Eq. (D.16) and obtaining the corresponding relation for the pressure perturbation. In this case the energy lost in the wave causes damping, even for adiabatic oscillations, and hence the eigenfrequency and eigenfunctions are complex.

# E

---

## Asymptotic Theory of Stellar Oscillations

### E.1 A General Asymptotic Expression

An approximate asymptotic description of the oscillations has been derived by Gough (see Deubner & Gough 1984), on the basis of earlier work by Lamb (1932). This does not assume that the pressure and density scale heights are much larger than the wavelength; but it assumes that the oscillations vary much more rapidly than  $r$  and  $g$ , so that the problem is locally one of oscillations of a plane-parallel layer under constant gravity. Also, as usual, the perturbation to the gravitational potential is neglected. Then the governing equations are Eqs (3.174) and (3.175), but without the term in  $2/r$  in the former. When manipulating the equations, we neglect derivatives of  $r$  and  $g$ , but keep derivatives of the thermodynamic quantities. We note that Gough (1993) generalized this treatment to include also sphericity and varying gravity, although at the expense of obtaining considerably more complicated expressions.

The trick of the analysis is to write the equations in terms of

$$\chi = \operatorname{div} \delta \mathbf{r} . \quad (\text{E.1})$$

By using the equation of continuity and the condition of adiabaticity we may also write  $\chi$  as

$$\chi = -\frac{1}{\Gamma_1} \left( \frac{p'}{p} - \frac{\rho g}{p} \xi_r \right) . \quad (\text{E.2})$$

The oscillation equations can be written as

$$\frac{d\xi_r}{dr} = \chi + \frac{1}{\rho} \frac{k_h^2}{\omega^2} p' , \quad (\text{E.3})$$

and

$$\frac{dp'}{dr} = \rho \left( \omega^2 + g \frac{d \ln \rho}{dr} \right) \xi_r + g \rho \chi . \quad (\text{E.4})$$

In keeping with the plane-parallel approximation we have expressed  $l$  by  $k_h$ , given by Eq. (3.143), and we assume  $k_h$  to be constant.

By multiplying Eq. (E.2) by  $\Gamma_1 p$  and differentiating we obtain, on using Eqs (E.3) and (E.4)

$$\frac{d\Gamma_1}{dr} p\chi - \Gamma_1 g\rho\chi + \Gamma_1 p \frac{d\chi}{dr} = -\rho\omega^2\xi_r + \frac{gk_h^2}{\omega^2} p' . \quad (\text{E.5})$$

This equation, together with Eq. (E.2), can be used to express  $\xi_r$  in terms of  $\chi$  and its first derivative. The result is

$$\rho \left( g - \frac{\omega^4}{gk_h^2} \right) \xi_r = \Gamma_1 \left[ p\chi + \frac{\omega^2}{gk_h^2} \left( p \frac{d\chi}{dr} - g\rho\chi + p \frac{d\ln\Gamma_1}{dr} \chi \right) \right] . \quad (\text{E.6})$$

Finally, by differentiating Eq. (E.5) and using Eqs (E.3), (E.4) and (E.6) to eliminate  $\xi_r$ ,  $p'$  and their derivatives, we obtain the following second-order differential equation for  $\chi$ :

$$\begin{aligned} & \frac{d^2\chi}{dr^2} + \left( \frac{2}{c^2} \frac{dc^2}{dr} + \frac{1}{\rho} \frac{d\rho}{dr} \right) \frac{d\chi}{dr} \\ & + \left[ \frac{1}{\Gamma_1} \frac{d^2\Gamma_1}{dr^2} - \frac{2}{\Gamma_1} \frac{d\Gamma_1}{dr} \frac{g\rho}{p} + k_h^2 \left( \frac{N^2}{\omega^2} - 1 \right) - \frac{1}{\rho} \frac{d\rho}{dr} \frac{1}{\Gamma_1} \frac{d\Gamma_1}{dr} + \frac{\rho\omega^2}{\Gamma_1 p} \right] \chi = 0 . \end{aligned} \quad (\text{E.7})$$

Here we have introduced the adiabatic sound speed  $c$  from Eq. (3.52) and the buoyancy frequency  $N$  from Eq. (3.73).

The differential equation for  $\chi$  contains no interior singular points. However, it is clear from Eq. (E.6) that the case where the coefficient of  $\xi_r$  vanishes is in some sense singular. This occurs when

$$\omega^2 = gk_h . \quad (\text{E.8})$$

It is easy to show that then the solution for  $\chi$  to Eq. (E.6) grows exponentially towards the interior; as this is clearly unacceptable,  $\chi$  must be zero. Then Eq. (E.2) gives

$$p' = g\rho\xi_r , \quad (\text{E.9})$$

and Eq. (E.3) has the solution

$$\xi_r = a \exp(k_h r) , \quad (\text{E.10})$$

where  $a$  is an arbitrary constant. It is easy to show that the resulting  $p'$  satisfies Eq. (E.4). Thus this is one possible solution to the plane-parallel oscillation equations. It should be noticed that Eq. (E.8) agrees with Eq. (3.85) for the frequency of a surface gravity wave. Thus the mode we have found must be identified with a surface gravity wave; and we have shown that its frequency is independent of the structure of the model below the surface, if sphericity is neglected. This result was first obtained by Gough. Note that in accordance

with the assumption of a plane-parallel structure  $k_h$  must be taken to be constant in Eq. (E.10),  $k_h = \sqrt{l(l+1)}/R$ , where  $R$  is the surface radius. It is obvious from Fig. 3.20 that the mode can be followed to degrees well below 10, although here the correction to the frequency given by Eq. (E.8) becomes significant (see also Section 7.1.4.3).

To analyse Eq. (E.7) it is convenient to eliminate the term in  $d\chi/dr$ . Thus we introduce  $X$  by

$$X = c^2 \rho^{1/2} \chi. \quad (\text{E.11})$$

After considerable manipulation one then finds that  $X$  satisfies the differential equation

$$\frac{d^2 X}{dr^2} + \left[ k_h^2 \left( \frac{N^2}{\omega^2} - 1 \right) + \frac{\omega^2}{c^2} - \frac{1}{2} \frac{d}{dr}(H^{-1}) - \frac{1}{4} H^{-2} \right] X = 0, \quad (\text{E.12})$$

where we have introduced the density scale height  $H$  by

$$H^{-1} = -\frac{d \ln \rho}{dr}. \quad (\text{E.13})$$

Finally, we define a characteristic frequency  $\omega_c$  by

$$\omega_c^2 = \frac{c^2}{4H^2} \left( 1 - 2 \frac{dH}{dr} \right), \quad (\text{E.14})$$

and use Eq. (3.153) for the acoustic frequency  $S_l$ , to obtain

$$\frac{d^2 X}{dr^2} + \frac{1}{c^2} \left[ S_l^2 \left( \frac{N^2}{\omega^2} - 1 \right) + \omega^2 - \omega_c^2 \right] X = 0. \quad (\text{E.15})$$

This is the final second-order differential equation. Considering that the only approximations made in deriving it are the constancy of  $g$  and the neglect of the derivatives of  $r$ , it is remarkably simple.

It might be noticed that Eq. (E.15) can also be derived from a careful analysis of the propagation of waves in stellar interiors. This has been carried out by Gough (1986a).

## E.2 JWKB Analysis

To analyse Eq. (E.15) asymptotically we use the JWKB method (for Jeffreys, Wentzel, Kramers and Brillouin; in fact the method seems to have been first used by Liouville). It is widely used in quantum mechanics (see *e.g.* Schiff 1949, Section 34), and is also described in Unno *et al.* (1989), Chapter 16. An excellent description of the technique was provided by Gough (2007). It is possible to provide a firm mathematical foundation for the method; knowing that this is so, it is enough here to sketch how it works, without worrying too much about its convergence properties.

We write the equation as

$$\frac{d^2 X}{dr^2} + K(r)X = 0 , \quad (\text{E.16})$$

with

$$K(r) = \frac{1}{c^2} \left[ S_l^2 \left( \frac{N^2}{\omega^2} - 1 \right) + \omega^2 - \omega_c^2 \right] . \quad (\text{E.17})$$

The assumption is that the solution varies rapidly compared with equilibrium quantities, *i.e.*, compared with  $K(r)$ . Thus we write the solution as

$$X(r) = a(r) \exp[i\Psi(r)] , \quad (\text{E.18})$$

where  $\Psi$  is rapidly varying, so that the local radial wavenumber

$$k_r = \frac{d\Psi}{dr} \quad (\text{E.19})$$

has large magnitude;  $a(r)$  is a slowly varying amplitude function. Formally, it is always possible to write the solution in this form. Substituting Eq. (E.18) into Eq. (E.16) one obtains

$$\left( \frac{d^2 a}{dr^2} + 2ik_r \frac{da}{dr} + ia \frac{dk_r}{dr} - k_r^2 a \right) \exp(i\Psi) = -K(r)a(r) \exp(i\Psi) . \quad (\text{E.20})$$

On the left-hand side the dominant term is the one containing  $k_r^2$ ; to ensure that this term cancels with the right-hand side,  $k_r$  is chosen as

$$k_r(r) = K(r)^{1/2} . \quad (\text{E.21})$$

The next-order terms are those in  $k_r$  which must cancel. Thus

$$\frac{1}{a} \frac{da}{dr} = -\frac{1}{2} \frac{1}{k_r} \frac{dk_r}{dr} , \quad (\text{E.22})$$

or, apart from a constant factor,

$$a(r) = |k_r|^{-1/2} = |K(r)|^{-1/4} . \quad (\text{E.23})$$

This leaves in Eq. (E.20) only a term in the second derivative of  $a$ . The asymptotic approximation consists of neglecting this term, which by the assumption is small compared with  $k_r^2 a$ . Then the approximate solution is completely specified by Eqs (E.21) and (E.23). Since the solution may be chosen to be real, it can be written as

$$X(r) = A |K(r)|^{-1/4} \cos \left( \int_{r_0}^r K(r')^{1/2} dr' + \phi \right) , \quad \text{for } K(r) > 0 , \quad (\text{E.24})$$

or

$$X(r) = |K(r)|^{-1/4} \left[ A_+ \exp \left( \int_{r_0}^r |K(r')|^{1/2} dr' \right) + A_- \exp \left( - \int_{r_0}^r |K(r')|^{1/2} dr' \right) \right] \quad \text{for } K(r) < 0 , \quad (\text{E.25})$$

for some suitable  $r_0$ . Here  $A$  and  $\phi$ , or  $A_+$  and  $A_-$ , are real constants which must be determined from the boundary conditions.

Notice that this solution has the property of being locally exponential where  $K < 0$ . Thus it is in accordance with the discussion in Section 3.4.2. On the other hand, it breaks down at the zeros of  $K$ ; formally this may be seen from the fact that there  $a$ , as obtained in Eq. (E.21), is singular, and its second derivative cannot be neglected in Eq. (E.20). Thus we need to make a special analysis of the *turning points* where  $K = 0$ . In particular, this is required to connect the solution in the exponential and oscillatory regions, and hence apply the boundary conditions.

We now consider an interval  $[r_1, r_2]$  where  $K(r) > 0$ , and such that  $K(r) < 0$  for  $r < r_1$  and  $r > r_2$ ; we wish to find a solution that is trapped in this interval. If  $r_1$  is a simple zero for  $K$ , close to  $r_1$  we have approximately that

$$K(r) \simeq K_1(r - r_1) , \quad (\text{E.26})$$

where  $K_1 > 0$  is a constant. We introduce the new independent variable  $x$  by

$$x = K_1^{1/3}(r - r_1) ; \quad (\text{E.27})$$

then the equation for  $X$  can be approximated by

$$\frac{d^2 X}{dx^2} = -x X , \quad (\text{E.28})$$

with the solution

$$X(r) = C_1 \text{Ai}(-x) + C_2 \text{Bi}(-x) , \quad (\text{E.29})$$

where  $C_1$  and  $C_2$  are constants, and  $\text{Ai}$  and  $\text{Bi}$  are the Airy functions (e.g. Abramowitz & Stegun 1964).

To be definite, we consider a solution that is trapped in the oscillatory region outside  $r_1$ , and hence we need to choose the constants  $C_1$  and  $C_2$  such as to select the solution that decreases exponentially as  $r$  decreases beneath  $r_1$ . When  $x < 0$ , and  $|x|$  is large,  $\text{Ai}(-x)$  and  $\text{Bi}(-x)$  have the following asymptotic behaviour:

$$\begin{aligned} \text{Ai}(-x) &\simeq \frac{1}{2\sqrt{\pi}} |x|^{-1/4} \exp \left( -\frac{2}{3}|x|^{3/2} \right) , \\ \text{Bi}(-x) &\simeq \frac{1}{\sqrt{\pi}} |x|^{-1/4} \exp \left( \frac{2}{3}|x|^{3/2} \right) . \end{aligned} \quad (\text{E.30})$$

Thus we must require that  $C_2 = 0$ , and the solution satisfying the boundary condition for  $r < r_1$  is therefore

$$X(r) = C_1 \text{Ai}(-x) . \quad (\text{E.31})$$

We can use this solution to determine the phase  $\phi$  in Eq. (E.24). For large positive  $x$  the asymptotic expansion of  $\text{Ai}(-x)$  is

$$\text{Ai}(-x) \simeq \frac{1}{\sqrt{\pi}} |x|^{-1/4} \cos \left( \frac{2}{3} x^{3/2} - \frac{\pi}{4} \right) . \quad (\text{E.32})$$

This must agree with what is obtained from Eq. (E.24), assuming that there is a region where both this equation and the approximation in Eq. (E.32) are valid. From the expansion of  $K$  in Eq. (E.26) we obtain

$$\Psi = \int_{r_1}^r K(r')^{1/2} dr' + \phi = \frac{2}{3} x^{3/2} + \phi , \quad (\text{E.33})$$

so that Eq. (E.24) gives

$$X \simeq A K_1^{-1/6} x^{-1/4} \cos \left( \frac{2}{3} x^{3/2} + \phi \right) . \quad (\text{E.34})$$

This agrees with Eq. (E.32) if  $\phi = -\pi/4$ . Sufficiently far from the turning point  $r_1$  the JWKB solution satisfying the boundary conditions at  $r = r_1$  is thus

$$X(r) = A_1 |K(r)|^{-1/4} \cos \left( \int_{r_1}^r K(r')^{1/2} dr' - \frac{\pi}{4} \right) . \quad (\text{E.35})$$

Similarly, if there is an outer turning point at  $r = r_2$ , so that  $K(r) > 0$  for  $r < r_2$  and  $K(r) < 0$  for  $r > r_2$ , one finds that the asymptotic solution that is exponentially decaying for  $r > r_2$  is

$$X(r) = A_2 |K(r)|^{-1/4} \cos \left( \int_r^{r_2} K(r')^{1/2} dr' - \frac{\pi}{4} \right) . \quad (\text{E.36})$$

To obtain the full solution we must match the two separate solutions smoothly at a suitable point between  $r_1$  and  $r_2$ ,  $r = r_f$ , say. We define

$$\begin{aligned} \Psi_1 &\equiv \Psi_1(r_f) = \int_{r_1}^{r_f} K(r)^{1/2} dr - \frac{\pi}{4} , \\ \Psi_2 &\equiv \Psi_2(r_f) = \int_{r_f}^{r_2} K(r)^{1/2} dr - \frac{\pi}{4} . \end{aligned} \quad (\text{E.37})$$

Then the conditions that both  $X$  and its first derivative be continuous at  $r = r_f$  give

$$\begin{aligned} A_1 K(r_f)^{-1/4} \cos \Psi_1 &= A_2 K(r_f)^{-1/4} \cos \Psi_2 , \\ -A_1 K(r_f)^{-1/4} \sin \Psi_1 &= A_2 K(r_f)^{-1/4} \sin \Psi_2 . \end{aligned} \quad (\text{E.38})$$

Notice that in the derivative we have neglected terms coming from the differentiation of  $K$ ; these are small compared with the term included. These linear

equations for  $A_1$ ,  $A_2$  only have a non-trivial solution if their determinant vanishes. This leads to

$$\sin \Psi_1 \cos \Psi_2 + \cos \Psi_1 \sin \Psi_2 = \sin(\Psi_1 + \Psi_2) = 0 , \quad (\text{E.39})$$

or

$$\Psi_1 + \Psi_2 = (n - 1)\pi , \quad (\text{E.40})$$

where  $n$  is an integer. Thus

$$\int_{r_1}^{r_2} K(r)^{1/2} dr = \left( n - \frac{1}{2} \right) \pi , \quad n = 1, 2, \dots . \quad (\text{E.41})$$

Here  $K$  depends on the frequency  $\omega$ ; thus Eq. (E.41) implicitly determines the frequencies of the modes trapped between  $r_1$  and  $r_2$ . In addition, we find that  $A_1 = A_2$ .

The asymptotic behaviour of  $X(r)$  in the region where a mode is trapped, and some distance from the turning points, is given by Eq. (E.35). Asymptotic eigenfunctions in terms of the displacement for p and g modes are discussed in more detail in Section E.4.

### E.3 The Duvall Law for p-Mode Frequencies

Writing the asymptotic expression (E.41) for the frequency out in full, using Eq. (E.17) for  $K(r)$ , we obtain

$$\omega \int_{r_1}^{r_2} \left[ 1 - \frac{\omega_c^2}{\omega^2} - \frac{S_l^2}{\omega^2} \left( 1 - \frac{N^2}{\omega^2} \right) \right]^{1/2} \frac{dr}{c} \simeq \pi(n - 1/2) , \quad (\text{E.42})$$

where  $r_1$  and  $r_2$  are adjacent zeros of  $K$  such that  $K > 0$  between them.

Equation (E.42) may be used to justify the approximate relation Eq. (3.196) for the frequencies of acoustic modes, with  $\alpha = \alpha(\omega)$  being a function of frequency (see also Deubner & Gough 1984). Here we present an argument derived by Christensen-Dalsgaard & Pérez Hernández (1992). Assuming that the term in  $N^2$  can be neglected, we write Eq. (E.42) as

$$\frac{\pi(n - 1/2)}{\omega} \simeq F\left(\frac{\omega}{L}\right) - \frac{1}{\omega}(I_1 + I_2 + I_3) , \quad (\text{E.43})$$

where

$$F(w) = \int_{r_t}^R \left( 1 - \frac{c^2}{w^2 r^2} \right)^{1/2} \frac{dr}{c} , \quad (\text{E.44})$$

and the dimensionless integrals  $I_1$ ,  $I_2$  and  $I_3$  are defined by

$$I_1 = \omega \int_{r_2}^R \left(1 - \frac{S_l^2}{\omega^2}\right)^{1/2} \frac{dr}{c}, \quad (\text{E.45})$$

$$I_2 = \omega \int_{r_1}^{r_2} \left[ \left(1 - \frac{S_l^2}{\omega^2}\right)^{1/2} - \left(1 - \frac{\omega_c^2}{\omega^2} - \frac{S_l^2}{\omega^2}\right)^{1/2} \right] \frac{dr}{c}, \quad (\text{E.46})$$

$$I_3 = \omega \int_{r_t}^{r_1} \left(1 - \frac{S_l^2}{\omega^2}\right)^{1/2} \frac{dr}{c}. \quad (\text{E.47})$$

We assume that  $\omega_c^2 > 0$  in the vicinity of the lower turning point, so that  $r_t < r_1$  [where  $r_t$  is given by Eq.(3.189)]; also we have assumed that  $R > r_2$  for all modes of interest.

To show that Eq.(3.196) is approximately valid, with  $\alpha$  being a function of  $\omega$ , we must show that  $I_1 + I_2 + I_3$  is predominantly a function of frequency. In so doing we make the assumptions:

- $S_l^2/\omega^2 \ll 1$  at the upper turning point.
- $\omega_c^2/\omega^2 \ll 1$  at the lower turning point.

Near the upper turning point we may then neglect the term in  $S_l^2/\omega^2$ , and hence the position of the turning point is approximately given by  $r_2 \simeq R_t$ , where  $R_t$  is defined by  $\omega = \omega_c(R_t)$ . Thus  $r_2$  is a function of frequency alone; the same is therefore obviously true for  $I_1$ .  $I_3$  is small; in fact, by expanding  $S_l^2$  in the vicinity of  $r_t$ , neglecting the variation in  $\omega_c$  and  $c$ , it is straightforward to show that

$$I_3 \simeq \frac{1}{3} \left(\frac{\omega_{c,t}}{\omega}\right)^3 \omega \frac{H_{c,t}}{c_t} \sim \left(\frac{\omega_{c,t}}{\omega}\right)^2, \quad (\text{E.48})$$

where  $\omega_{c,t}$ ,  $c_t$  and  $H_{c,t}$  are the values of  $\omega_c$ ,  $c$  and the sound-speed scale height at  $r_t$ . Thus, although  $I_3$  depends on  $r_t$  and hence on  $\omega/L$ , the term is  $\mathcal{O}((\omega_c/\omega)^2)$  and hence negligible.

This leaves  $I_2$  to be dealt with. To investigate its dependence on  $l$  and  $\omega$  we rewrite it as

$$I_2 = \frac{1}{\omega} \int_{r_1}^{r_2} \frac{\omega_c^2}{\left(1 - \frac{S_l^2}{\omega^2}\right)^{1/2} + \left(1 - \frac{\omega_c^2}{\omega^2} - \frac{S_l^2}{\omega^2}\right)^{1/2}} \frac{dr}{c}. \quad (\text{E.49})$$

Since  $\omega_c^2/c$  decreases quite rapidly with increasing depth (*cf.* Fig.3.17), this integral is dominated by the region near the upper turning point  $r_2$ . It is true that the integrand is nearly singular, with an integrable singularity, at  $r = r_1$ ; but the contribution from that is essentially  $\mathcal{O}(\omega_{c,t}^2/\omega^2)$  and is therefore small. Near  $r_2$ ,  $S_l^2/\omega^2$  is negligible; thus we can approximate  $I_2$  as

$$I_2 \simeq \frac{1}{\omega} \int_{r_1}^{r_2} \frac{\omega_c^2}{1 + \left(1 - \frac{\omega_c^2}{\omega^2}\right)^{1/2}} \frac{dr}{c}, \quad (\text{E.50})$$

which is obviously a function of frequency alone.

It follows that Eq. (E.43) may finally be written as

$$\int_{r_t}^R \left(1 - \frac{L^2 c^2}{\omega^2 r^2}\right)^{1/2} \frac{dr}{c} = \frac{[n + \alpha(\omega)]\pi}{\omega}, \quad (\text{E.51})$$

with

$$\alpha \simeq \alpha(\omega) = \frac{1}{\pi}(I_1 + I_2) - 1/2. \quad (\text{E.52})$$

This argument is evidently valid in general for stellar models where  $\omega_c^2/c$  decreases sufficiently rapidly with increasing depth.

A minor point in these relations concerns the definition of  $L$  (which also enters into  $S_l = cL/r$ ). In the analysis we have so far taken  $L = \sqrt{l(l+1)}$ . In fact, it may be shown from a more careful analysis of the asymptotic behaviour of the oscillation equations near the centre that a more appropriate choice would have been  $L_0 = l + 1/2$  (note, however, that  $L = L_0 + \mathcal{O}(l^{-1})$  and that even for  $l = 1$  they are very similar). In the rest of this appendix we shall replace  $L$  by  $L_0$  and, for convenience, suppress the subscript “0”.

### E.3.1 Frequencies in Polytropic Envelopes

It is instructive to consider a special case of these relations, which is furthermore a reasonable approximation to stars with extensive outer convection zones, such as the Sun. The convection zone is approximately adiabatically stratified, so that

$$\frac{d \ln p}{dr} = \Gamma_1 \frac{d \ln \rho}{dr}; \quad (\text{E.53})$$

here we assume  $\Gamma_1$  to be constant (this is evidently not true in the ionization zones of H and He, but they only occupy the outer few per cent of the star). We may also assume that  $g$  is constant. Finally we take as boundary conditions on the equilibrium structure that  $p = \rho = 0$  at  $r = R$ . With these assumptions the sound speed is given by

$$c^2 = \frac{g}{\mu_p} (R - r), \quad (\text{E.54})$$

where  $\mu_p = 1/(\Gamma_1 - 1)$  is an effective polytropic index of the region considered.<sup>1</sup> Furthermore,

$$\omega_c^2 = \frac{g\mu_p}{4(R - r)} \left(1 + \frac{2}{\mu_p}\right), \quad (\text{E.55})$$

and  $N$  is zero. We also treat the layer as plane parallel, so that  $r$  can be replaced by  $R$  in the definition of  $S_l$ .

---

<sup>1</sup> This can be easily demonstrated from Eq. (3.99) if the ideal gas law, Eq. (3.19), is used.

To carry out the analysis leading to the Duvall law in this case we note from Eq. (E.55) that  $\omega_c$  is small except near the surface, and so it is reasonable to neglect it in most of the region where the p mode is trapped.<sup>2</sup> To approximate Eq. (E.42) we use a trick similar to that employed to derive Eq. (E.51). Thus we write Eq. (E.42) as

$$\frac{\pi(n - 1/2)}{\omega} = \int_{r_1}^R \left(1 - \frac{S_l^2}{\omega^2}\right)^{1/2} \frac{dr}{c} - \int_{r_2}^R \left(1 - \frac{S_l^2}{\omega^2}\right)^{1/2} \frac{dr}{c} \\ - \int_{r_1}^{r_2} \left[ \left(1 - \frac{S_l^2}{\omega^2}\right)^{1/2} - \left(1 - \frac{\omega_c^2}{\omega^2} - \frac{S_l^2}{\omega^2}\right)^{1/2} \right] \frac{dr}{c}. \quad (\text{E.56})$$

Here, approximately,  $r_2$  is given by  $\omega_c(r_2) = \omega$ , and is therefore close to the surface. Furthermore, the dominant contribution to the third integral in question Eq. (E.56) comes from the region near  $r_2$ . In the last two integrals we therefore use the approximations Eq. (E.54) and Eq. (E.55) for  $c$  and  $\omega_c$ . These integrals may then, with a little effort, be evaluated analytically. Finally, we neglect  $\omega_c$  near  $r = r_1$ . The result is

$$\frac{\pi(n - 1/2)}{\omega} = \int_{r_1}^R \left(1 - \frac{S_l^2}{\omega^2}\right)^{1/2} \frac{dr}{c} - \frac{1}{2} [\mu_p(\mu_p + 2)]^{1/2} \frac{\pi}{\omega}. \quad (\text{E.57})$$

This may also be written as Eq. (E.51), with

$$\alpha = 1/2[\mu_p(\mu_p + 2)]^{1/2} - 1/2. \quad (\text{E.58})$$

Thus in this case  $\alpha$  is a constant which is related to the effective polytropic index of the surface layers. The integral  $F(\omega/L)$  on the right hand side of Eq. (E.51) may easily be evaluated in this case, to yield

$$F(\omega) = \frac{\pi}{2} w \frac{\mu_p R}{g}. \quad (\text{E.59})$$

Thus the Eq. (E.51) gives

$$\omega^2 = \frac{2}{\mu_p} \frac{g}{R} (n + \alpha) L. \quad (\text{E.60})$$

In particular,  $\omega$  is proportional to  $L^{1/2}$ . This property is approximately satisfied by the computed (and observed) frequencies at high degree (*cf.* Fig. 3.20). Indeed, Eq. (E.60) might be expected to be approximately valid for modes whose degree is so high that they are entirely trapped within the convection zone.

If the entire layer is polytropic, with Eqs (E.54) and (E.55) everywhere valid, Eq. (E.15) may be solved analytically (*e.g.* Christensen-Dalsgaard 1980).

---

<sup>2</sup> Notice, however, that this becomes questionable for high  $l$ , where the trapping region is confined very close to the surface.

The condition that the solution decreases exponentially at great depths determines the eigenfrequencies as

$$\omega^2 = \frac{2}{\mu_p} \left( n + \frac{\mu_p}{2} \right) L \frac{g}{R}. \quad (\text{E.61})$$

This is in accordance with Eq. (E.60) obtained asymptotically, but with a different  $\alpha$ ,

$$\alpha = \frac{\mu_p}{2}. \quad (\text{E.62})$$

It is easy to show that the difference between this exact  $\alpha$  and the asymptotic approximation in Eq. (E.58) is small; it tends to zero for large  $\mu_p$ .

### E.3.2 Frequencies of Low-Degree Modes

For low-degree modes  $r_t$  is small and the second term in the bracket in Eq. (E.51) is much smaller than unity except near the centre. This allows us again to expand the integral, to obtain a very simple relation for the frequencies. Specifically, we consider the difference

$$\begin{aligned} I &= \int_0^R \frac{dr}{c} - \int_{r_t}^R \left( 1 - \frac{c^2}{w^2 r^2} \right)^{1/2} \frac{dr}{c} \\ &= \int_0^{r_t} \frac{dr}{c} + \int_{r_t}^R \left[ 1 - \left( 1 - \frac{c^2}{w^2 r^2} \right)^{1/2} \right] \frac{dr}{c} \\ &\equiv I_1 + I_2, \end{aligned} \quad (\text{E.63})$$

where  $w = \omega/L$ . Notice that  $c$  is almost constant near the centre (it may be shown that the first derivative of  $c$  is zero at  $r = 0$ ). Thus we take  $c$  to be constant in the first integral, and obtain

$$I_1 = \frac{r_t}{c(0)} \simeq \frac{L}{\omega} = \frac{1}{w}, \quad (\text{E.64})$$

by using Eq. (3.189). In the second integral the integrand is only substantially different from zero for  $r$  close to  $r_t$ , which was assumed to be small. Thus here we also approximate  $c$  by its value at  $r = 0$ . Furthermore, the upper limit of integration may be replaced by  $\infty$ . Then we obtain, with the substitution  $u = c/(wr)$ ,

$$I_2 = \frac{1}{w} \int_0^1 \left[ 1 - (1 - u^2)^{1/2} \right] \frac{du}{u^2} = \frac{1}{w} \left( \frac{\pi}{2} - 1 \right). \quad (\text{E.65})$$

Thus, finally,  $I = w^{-1}\pi/2$ , and Eq. (E.51) may be approximated by

$$\int_0^R \frac{dr}{c} - \frac{L\pi}{\omega} = \frac{(n + \alpha)\pi}{\omega}, \quad (\text{E.66})$$

or

$$\omega = \frac{(n + L/2 + \alpha)\pi}{\int_0^R \frac{dr}{c}}. \quad (\text{E.67})$$

The derivation of Eq. (E.67) clearly lacks rigour. However, it may be shown from a more careful asymptotic analysis of the central region (*e.g.* Vandakurov 1967; Tassoul 1980) that the result is correct to leading order, assuming that  $L$ , as discussed above, is taken to be  $l + 1/2$ . Equation (E.67) may also be written as

$$\nu_{nl} = \frac{\omega_{nl}}{2\pi} \simeq (n + \frac{l}{2} + \frac{1}{4} + \alpha)\Delta\nu, \quad (\text{E.68})$$

where

$$\Delta\nu = \left[ 2 \int_0^R \frac{dr}{c} \right]^{-1} \quad (\text{E.69})$$

is the inverse of twice the sound travel time between the centre and the surface.

The *deviations* from the simple relation Eq. (E.68) have considerable diagnostic potential. The expansion of Eq. (3.215), leading to Eq. (E.67), can be extended to take into account the variation of  $c$  in the core (Gough 1986a); alternatively it is possible to take the JWKB analysis of the oscillation equations to higher order (Tassoul 1980). The result may be written as

$$\nu_{nl} \simeq \left( n + \frac{l}{2} + \frac{1}{4} + \alpha \right) \Delta\nu - (AL^2 - \delta) \frac{\Delta\nu^2}{\nu_{nl}}, \quad (\text{E.70})$$

where

$$A = \frac{1}{4\pi^2 \Delta\nu} \left[ \frac{c(R)}{R} - \int_0^R \frac{dc}{dr} \frac{dr}{r} \right]. \quad (\text{E.71})$$

As discussed in detail in Section 7.2.2 the strong sensitivity of this expression to conditions in stellar cores provides an important diagnostic of stellar properties.

## E.4 Asymptotic Properties of Eigenfunctions

The analysis in Section E.2 yielded the asymptotic expressions (E.24) and (E.25) for the eigenfunction, expressed in terms of  $X(r)$  defined in Eq. (E.11). This was based on the formulation in Section E.1, however, which was derived under the assumption that derivatives of  $r$  and  $g$  could be neglected. Thus, as is indeed found from numerical applications, these asymptotic expressions lead to amplitude functions deviating from the correct variation by low powers of  $r$  or  $g$ .

As already mentioned a more complete asymptotic description which does not suffer from this approximation was developed by Gough (1993). In a

formal sense it is quite similar to the formulation presented here, although with considerably more complicated expressions for the characteristic frequencies and eigenfunction scalings. It is likely that an asymptotic analysis based on these equations would yield the correct behaviour; however, such an analysis has apparently not been published, and will not be attempted here.

Instead we shall apply a pragmatic, although certainly not rigorous, approach. As in Section 3.4.2 we base the analysis on the two equations (3.174) and (3.175) in the Cowling approximation. By differentiating Eq. (3.174), eliminating  $dp'/dr$  using Eq. (3.175) and expressing  $p'$  in terms of  $\xi_r$  and its derivative by means of Eq. (3.174) we obtain

$$\begin{aligned} \frac{d^2\xi_r}{dr^2} = & -\left(\frac{2}{r}-\frac{1}{F_1}H_p^{-1}\right)\frac{d\xi_r}{dr}+\left[-\frac{1}{F_1}H_p^{-1}+\frac{d}{dr}\ln\left|\frac{1}{\rho c^2}\left(\frac{S_l^2}{\omega^2}-1\right)\right|\right]\frac{d\xi_r}{dr} \\ & +[-K_s(r)+\tilde{h}(r)]\xi_r, \end{aligned} \quad (\text{E.72})$$

where  $K_s$  is still given by Eq. (3.182). All other terms in  $\xi_r$  are lumped together in  $\tilde{h}$ ; these contain derivatives of equilibrium quantities, and so may be assumed to be negligible compared with  $K_s$  (except, as usual, near the surface). Equation (E.72) may also be written as

$$\frac{d^2\xi_r}{dr^2}-\frac{d\ln f}{dr}\frac{d\xi_r}{dr}+[K_s(r)-\tilde{h}(r)]\xi_r=0, \quad (\text{E.73})$$

where

$$f(r)=\frac{1}{\rho r^2 c^2}\left|\frac{S_l^2}{\omega^2}-1\right|. \quad (\text{E.74})$$

It should be noticed that the principal difference between Eq. (E.73) and Eq. (3.181) derived previously is the presence of a term in  $d\xi_r/dr$ . This occurs because we have now not neglected the term in  $\xi_r$  on the right-hand side of Eq. (3.174), and the corresponding term in  $p'$  in Eq. (3.175). These terms cannot be neglected if  $\xi_r$  and  $p'$  are rapidly varying, as assumed.

To apply JWKB analysis we rewrite this equation in a form without a first derivative, by introducing  $\hat{\xi}_r$  by

$$\xi_r(r)=f(r)^{1/2}\hat{\xi}_r(r); \quad (\text{E.75})$$

$\hat{\xi}_r$  satisfies

$$\frac{d^2\hat{\xi}_r}{dr^2}+[K_s(r)-h(r)]\hat{\xi}_r=0, \quad (\text{E.76})$$

where

$$h(r)=\tilde{h}(r)-\frac{1}{2}\frac{d^2\ln f}{dr^2}+\frac{1}{4}\left(\frac{d\ln f}{dr}\right)^2. \quad (\text{E.77})$$

Here  $h$ , like  $\tilde{h}$ , is generally small compared with  $K_s$ .

It is obvious that the derivation of Eq. (E.76) fails near points where  $\omega^2=S_l^2$ , and where consequently  $f$  has a singular logarithmic derivative.

These are the turning points of p modes. This problem can be avoided by deriving instead a second-order differential equation for  $p'$  (see Unno *et al.* 1989, Chapter 16); but, hardly surprisingly, this equation has problems at the turning points for the g modes. Also,  $h(r)$  cannot be neglected near the surface and hence Eq. (E.76) cannot be used for a general asymptotic description of the oscillations. However, except near the singular points it may still be used to provide the asymptotic form of the eigenfunctions. By applying JWKB analysis to Eq. (E.76) we obtain, in mode-trapping regions where  $K_s(r) > 0$ , that

$$\begin{aligned}\xi_r(r) &= \tilde{A}\rho^{-1/2}r^{-1}c^{-1}\left|\frac{S_l^2}{\omega^2}-1\right|^{1/2}|K_s(r)|^{-1/4}\cos\left(\int_{r_1}^r K_s(r')^{1/2}dr' - \frac{\pi}{4}\right) \\ &= A\rho^{-1/2}r^{-1}c^{-1/2}\left|\frac{S_l^2/\omega^2-1}{N^2/\omega^2-1}\right|^{1/4}\cos\left(\int_{r_1}^r K_s(r')^{1/2}dr' - \frac{\pi}{4}\right),\end{aligned}\quad (\text{E.78})$$

where  $A$  is an arbitrary amplitude factor, and  $r_1$  is a turning point, such that  $K_s(r_1) = 0$ . This expression is clearly valid only at some distance from the turning points, where the asymptotic approximation, Eq. (E.32), can be used. Thus the apparently singular behaviour in  $|\dots|$  causes no problems. Although the oscillatory part of Eq. (E.78), particularly its phase, may be problematic owing to the singularities and the near-surface behaviour, we expect that it gives the asymptotically correct variation of the amplitude function, including its dependence on  $g$  and  $r$ . We shall assume that this is the case and obtain the relevant powers of  $r$  and/or  $g$  in the analysis of Eq. (E.15) such that the final p- and g-mode expressions have the correct behaviour (the dependence with  $c$  and  $\rho$  is included fully in the derivation of Eq. (E.15) and is therefore correctly represented). What is gained by using Eq. (E.15) is therefore principally the correct treatment of the phases at the turning points.

For later reference, we note that in the p-mode case, with  $\omega \gg S_l$  and  $\omega \gg |N|$ , the amplitude function  $\mathcal{A}(r)$  multiplying the cosine in Eq. (E.78) is

$$\mathcal{A}(r) \simeq \mathcal{A}_p(r) = \rho^{-1/2}r^{-1}c^{-1/2}. \quad (\text{E.79})$$

In the opposite case for g modes, with  $\omega \ll S_l$  and  $\omega \ll N$ , we obtain

$$\mathcal{A}(r) \simeq \mathcal{A}_g(r) = \rho^{-1/2}r^{-3/2}N^{-1/2}. \quad (\text{E.80})$$

#### E.4.1 Asymptotic Properties of the p-Mode Eigenfunctions

We neglect the term in  $N^2$  in Eq. (E.15), and assume that there is a region outside  $r_t$  where  $\omega_c^2$  can be neglected. In that region, except near  $r_t$ , JWKB analysis of Eq. (E.15) leads to the following approximate solution for  $X$ :

$$X(r) \simeq A_X c^{1/2} r^{-1} \left(1 - \frac{L^2 c^2}{\omega^2 r^2}\right)^{-1/4} \cos \left[ \omega \int_{r_t}^r \left(1 - \frac{L^2 c^2}{\omega^2 r'^2}\right)^{1/2} \frac{dr'}{c} - \frac{\pi}{4} \right], \quad (\text{E.81})$$

where the constant  $A_X$  is determined by the normalization; the factor  $r^{-1}$  does not follow from the analysis but was, as discussed above, introduced to obtain the correct final amplitude function, given by Eq. (E.79). An expression for  $\xi_r$  can be derived from the general Eq. (E.6). We neglect the derivative of  $\Gamma_1$  and write the equation as

$$\rho g \left(1 - \frac{\omega^4}{\omega_f^4}\right) \xi_r \simeq \Gamma_1 p \left[ \chi + \frac{\omega^2}{gk_h^2} \left( \frac{d\chi}{dr} - \frac{\Gamma_1 g}{c^2} \chi \right) \right], \quad (\text{E.82})$$

where  $\omega_f^2 = gk_h$  is the squared f-mode frequency. For high-order p modes we can assume that  $\omega \gg \omega_f$ . On the right-hand side we need to estimate the term in  $d\chi/dr$ , compared with the terms in  $\chi$ . To do so, when differentiating here and in the following we assume that the eigenfunction varies on a scale short compared with scale heights of equilibrium quantities and only differentiate through the argument of  $\cos$  in Eq. (E.81). It follows that the amplitude of  $d\chi/dr$  is, to leading order,  $\omega/c$  times the amplitude of  $\chi$ . Consequently, the magnitudes of the coefficients to  $\chi$  in the three terms in the square bracket on the right-hand side of Eq. (E.82) are

$$1, \quad \frac{\omega^3}{gk_h^2}, \quad \frac{\omega^2}{k_h^2} \frac{\Gamma_1}{c^2}. \quad (\text{E.83})$$

To estimate the magnitude of the second component we write it as

$$\frac{\omega^2}{c^2 k_h^2} \frac{\omega c}{g} = \frac{\omega^2 \omega c}{S_l^2 g}. \quad (\text{E.84})$$

In the first factor  $\omega > S_l$  in regions of p-mode trapping. The second factor may be estimated from Eq. (3.180), neglecting  $\nabla_\mu$ , by writing it as

$$N^2 \simeq \frac{\Gamma_1 g^2}{c^2} (\nabla_{\text{ad}} - \nabla); \quad (\text{E.85})$$

thus  $\omega c/g \sim (\nabla_{\text{ad}} - \nabla)^{1/2} \omega / N \gg 1$  for typical p modes, at least in radiative regions where  $\nabla_{\text{ad}} - \nabla$  is of order unity. (Near the surface, in convective regions where this estimate is not valid, it is typically the case that  $\omega^2 \gg S_l^2$ .) It follows that the second component in the set Eq. (E.83) is typically much greater than unity. The ratio between the third and second components is

$$\frac{\Gamma_1 g}{\omega c} \simeq \frac{\Gamma_1^{1/2} N}{(\nabla_{\text{ad}} - \nabla)^{1/2} \omega}, \quad (\text{E.86})$$

which by a similar argument is typically much smaller than unity.

Using these estimates, it follows from Eqs (E.82) and (E.81) that

$$\begin{aligned} \xi_r &\simeq -\frac{c^2}{\omega^2} \frac{d\chi}{dr} \simeq -\rho^{-1/2} \omega^{-2} \frac{dX}{dr} \\ &\simeq -A_X \omega^{-1} (\rho c)^{-1/2} r^{-1} \left(1 - \frac{L^2 c^2}{\omega^2 r^2}\right)^{1/4} \cos \left[ \omega \int_{r_t}^r \left(1 - \frac{L^2 c^2}{\omega^2 r'^2}\right)^{1/2} \frac{dr'}{c} + \frac{\pi}{4} \right]. \end{aligned} \quad (\text{E.87})$$

By using Eq. (E.51) this equation may be written as

$$\xi_r(r) \simeq A(\rho c)^{-1/2} r^{-1} \left(1 - \frac{L^2 c^2}{\omega^2 r^2}\right)^{1/4} \cos \left[ \omega \int_r^R \left(1 - \frac{L^2 c^2}{\omega^2 r'^2}\right)^{1/2} \frac{dr'}{c} - (\alpha + 1/4)\pi \right], \quad (\text{E.88})$$

where  $A$  is a new constant.

To find the horizontal displacement we note that in Eq. (3.174) the first term on the right-hand side can be neglected compared with the left-hand side, so that

$$\frac{d\xi_r}{dr} \simeq \frac{1}{\rho c^2} \left( \frac{S_l^2}{\omega^2} - 1 \right) p' \simeq -\frac{r\omega^2}{c^2} \left(1 - \frac{S_l^2}{\omega^2}\right) \xi_h, \quad (\text{E.89})$$

using Eq. (3.131). Thus

$$\begin{aligned} \xi_h(r) &\simeq -\frac{c^2}{r\omega^2} \left(1 - \frac{S_l^2}{\omega^2}\right)^{-1} \frac{d\xi_r}{dr} \simeq -A \rho^{-1/2} c^{1/2} r^{-2} \omega^{-1} \left(1 - \frac{L^2 c^2}{\omega^2 r^2}\right)^{-1/4} \times \\ &\quad \times \sin \left[ \omega \int_r^R \left(1 - \frac{L^2 c^2}{\omega^2 r'^2}\right)^{1/2} \frac{dr'}{c} - (\alpha + 1/4)\pi \right]. \end{aligned} \quad (\text{E.90})$$

It may be noted that the ratio between the amplitudes of the root-mean-square lengths of the horizontal and vertical components of the displacement is

$$\left| \frac{L\xi_h}{\xi_r} \right| \sim \frac{Lc}{r\omega} \left(1 - \frac{L^2 c^2}{\omega^2 r^2}\right)^{-1/2} = \frac{S_l}{\omega} \left(1 - \frac{S_l^2}{\omega^2}\right)^{-1/2} \quad (\text{E.91})$$

(cf. Eq. 3.137); thus well above the lower turning point, where  $\omega \gg S_l$ , the oscillation is predominantly vertical.

From these expressions, we can finally find the asymptotic form of the energy integral  $\mathcal{E}$  (cf. Eq. 3.139), replacing  $\sin^2$  and  $\cos^2$  by the average value 1/2:

$$\begin{aligned} \mathcal{E} &\simeq 2\pi A^2 \int_{r_t}^R \left[ c^{-1} \left(1 - \frac{L^2 c^2}{\omega^2 r^2}\right)^{1/2} + \frac{L^2 c}{\omega^2 r^2} \left(1 - \frac{L^2 c^2}{\omega^2 r^2}\right)^{-1/2} \right] dr \\ &\simeq 2\pi A^2 \int_{r_t}^R \left(1 - \frac{L^2 c^2}{\omega^2 r^2}\right)^{-1/2} \frac{dr}{c}. \end{aligned} \quad (\text{E.92})$$

It should be noted, however, that Eqs (E.88) and (E.90) are not valid near and above the upper turning point of the mode; although this region makes a negligible contribution to  $\mathcal{E}$ , it has to be taken into account when relating  $\mathcal{E}$  to the photospheric amplitude of the mode, as done, for example, in the normalized inertia  $E$  (cf. Eq. (3.140)). This effect is predominantly a function of frequency, except for high-degree modes.

### E.4.2 Asymptotic Properties of the g-Mode Eigenfunctions

We consider the region where a g mode is trapped, and assume that  $\omega^2 \ll S_l^2, N^2$ . Then

$$K \simeq k_h^2 \left( \frac{N^2}{\omega^2} - 1 \right). \quad (\text{E.93})$$

In the corresponding JWKB expression for the eigenfunction, comparison with Eq. (E.80) will show that the extra factor  $gr^{-3/2}$  must be included. Thus we obtain

$$X(r) \simeq A g r^{-3/2} \left( \frac{N^2}{\omega^2} - 1 \right)^{-1/4} \cos \left[ \int_{r_1}^r k_h \left( \frac{N^2}{\omega^2} - 1 \right)^{1/2} dr' - \frac{\pi}{4} \right], \quad (\text{E.94})$$

where  $k_h^{-1/2}$  was assumed to be constant and was absorbed in the amplitude  $A$ . To determine  $\xi_r$  we use again Eq. (E.82). On the left-hand side we can assume that  $\omega \ll \omega_f$ . On the right-hand side, according to Eq. (E.94) the amplitude of  $d\chi/dr$  is now, to leading order,  $k_h N / \omega$  times the amplitude of  $\chi$ . Thus the magnitudes of the three terms on the right-hand side of Eq. (E.82) scale as

$$1, \quad \frac{\omega N}{gk_h}, \quad \frac{\omega^2 \Gamma_1}{k_h^2 c^2}. \quad (\text{E.95})$$

Here, using Eq. (E.85), the second component is

$$\frac{\omega N}{gk_h} \simeq \frac{\omega}{ck_h} (\nabla_{\text{ad}} - \nabla)^{1/2} \simeq \frac{\omega}{S_l} (\nabla_{\text{ad}} - \nabla)^{1/2} \ll 1, \quad (\text{E.96})$$

and the third component is

$$\frac{\omega^2 \Gamma_1}{k_h^2 c^2} = \Gamma_1 \frac{\omega^2}{S_l^2} \ll 1. \quad (\text{E.97})$$

Thus the dominant term is the first. The result finally is

$$\xi_r \simeq \frac{c^2}{g} \chi = \rho^{-1/2} g^{-1} X \quad (\text{E.98})$$

$$\simeq A \rho^{-1/2} r^{-3/2} \left( \frac{N^2}{\omega^2} - 1 \right)^{-1/4} \cos \left[ \int_{r_1}^r \frac{L}{r} \left( \frac{N^2}{\omega^2} - 1 \right)^{1/2} dr' - \frac{\pi}{4} \right].$$

To find the horizontal displacement we again use Eq. (E.89), now approximated by

$$\frac{d\xi_r}{dr} \simeq \frac{L^2}{r} \xi_h. \quad (\text{E.99})$$

Thus we obtain

$$\begin{aligned}\xi_h &\simeq \frac{r}{L^2} \frac{d\xi_r}{dr} \\ &\simeq -A\rho^{-1/2} L^{-1} r^{-3/2} \left( \frac{N^2}{\omega^2} - 1 \right)^{1/4} \sin \left[ \int_{r_1}^r \frac{L}{r} \left( \frac{N^2}{\omega^2} - 1 \right)^{1/2} dr' - \frac{\pi}{4} \right].\end{aligned}\quad (\text{E.100})$$

Here the ratio between the amplitudes of the root-mean-square lengths of the horizontal and vertical components of the displacement is therefore

$$\left| \frac{L\xi_h}{\xi_r} \right| \sim \left( \frac{N^2}{\omega^2} - 1 \right)^{1/2}, \quad (\text{E.101})$$

demonstrating that the oscillation is predominantly in the horizontal direction. It should be noted that this applies to the region where the mode is trapped; as discussed in Section 3.3.2.2 the surface ratio between the horizontal and vertical displacement is predominantly determined by the frequency of the mode.

---

## Bibliography

We have chosen to give the full information at our disposal for each of the papers cited in this book, *i.e.*, to list all the authors and the title. This is not common within the astronomy and astrophysics literature, but we felt that the addition of the titles of the papers is valuable information for the reader and will allow easier decision if the paper is worth retracing for further reading. For the same reason, begin and end pages are listed whenever this information was easily available to us. Numerous proceedings papers only have a begin page in the list below because it would have taken us too long to go back to the original hardcopies in the books, but we believe that, with the title included, even those papers will be easily retrievable by the interested reader. Listing all the authors of cited papers gives credits to *all* those involved in the studies and was considered important. We hope that the current list of references is a valuable resource for the broad research fields of stellar pulsation and variable stars.

- Abramowitz M., Stegun I.A., 1965, *Handbook of Mathematical Functions*, Dover Publications Inc., New York
- Abrams D., Kumar P., 1996, “Asymmetries of solar  $p$ -mode line profiles”, *Astrophysical Journal*, **472**, 882 – 890
- Abt H. A., Levato H., Grosso M., 2002, “Rotational Velocities of B Stars”, *Astrophysical Journal*, **573**, 359 – 365
- Aerts C., 1996, “Mode identification of pulsating stars from line-profile variations with the moment method: a more accurate discriminant”, *Astronomy and Astrophysics*, **314**, 115 – 122
- Aerts C., 2000, “Follow-up photometry of six new  $\beta$  Cephei stars discovered from the HIPPARCOS mission”, *Astronomy and Astrophysics*, **361**, 245 – 257

- Aerts C., 2007, "Astroseismology of Close Binary Stars", In *Proc. IAU Symposium: Binary Stars as Critical Tools & Tests in Contemporary Astrophysics*, Eds W.I. Hartkopf, E.F. Guinan, P. Harmanec, Cambridge University Press, **240**, 432 – 441
- Aerts C., De Cat P., 2003, " $\beta$  Cep stars from a spectroscopic point of view", *Space Science Reviews*, **105**, 453 – 492
- Aerts C., Harmanec P., 2004, "Pulsating components in close binaries", In *Spectroscopically and Spatially Resolving the Components of the Close Binary Stars*, Eds R. W. Hilditch, H. Hensberge, K. Pavlovski, Publications of the Astronomical Society of the Pacific Conference Series, San Francisco, **318**, 325 – 333
- Aerts C., Kolenberg K., 2005, "HD 121190: A cool multiperiodic slowly pulsating B star with moderate rotation", *Astronomy and Astrophysics*, **431**, 615 – 622
- Aerts C., Waelkens C., 1993, "Line Profile Variations of Rotating Pulsating Stars", *Astronomy and Astrophysics*, **273**, 135 – 146 (Erratum: *Astronomy and Astrophysics*, **293**, 978, 1995)
- Aerts C., De Pauw M., Waelkens C., 1992, "Mode identification of pulsating stars from line profile variations with the moment method. an example - The Beta Cephei star Delta Ceti", *Astronomy and Astrophysics*, **266**, 294 – 306
- Aerts C., Mathias P., Gillet D., Waelkens C., 1994a, "Multiperiodicity and pulsation characteristics of  $\beta$  Cephei", *Astronomy and Astrophysics*, **286**, 109 – 120
- Aerts C., Waelkens C., De Pauw M., 1994b, "Mode identification with the moment method in four multiperiodic  $\beta$  Cephei stars: KK Velorum,  $\nu$  Eri,  $\beta$  CMa, and V348 Normae", *Astronomy and Astrophysics*, **286**, 136 – 148
- Aerts C., Mathias P., Van Hoolst T., De Mey K., Sterken C., Gillet D., 1995, "Mode identification of the  $\beta$  Cephei star BW Vulpeculae", *Astronomy and Astrophysics*, **301**, 781 – 787
- Aerts C., De Cat P., Cuypers J., Becker S. R., Mathias P., De Mey K., Gillet D., Waelkens C., 1998a, "Evidence for binarity and multiperiodicity in the  $\beta$  Cephei star  $\beta$  Crucis", *Astronomy and Astrophysics*, **329**, 137 – 146
- Aerts C., Eyer L., Kestens E., 1998b, "The discovery of new gamma Doradus stars from the HIPPARCOS mission", *Astronomy and Astrophysics*, **337**, 790 – 796
- Aerts C., De Cat P., Peeters E., Decin L., De Ridder J., Kolenberg K., Meeus G., Van Winckel H., Cuypers J., Waelkens C., 1999, "Selection of a sample of bright southern Slowly Pulsating B Stars for long-term photometric and spectroscopic monitoring", *Astronomy and Astrophysics*, **343**, 872 – 882
- Aerts C., Bedding T. R., Christensen-Dalsgaard J. (Eds), 2002a, *Radial and Nonradial Pulsations as Probes of Stellar Physics*, Publications of the Astronomical Society of the Pacific Conference Series, San Francisco, **259**

- Aerts C., Handler G., Arentoft T., Vandenbussche B., Medupe R., Sterken C., 2002b, "The  $\delta$  Scuti star XX Pyx is an ellipsoidal variable", *Monthly Notices of the Royal Astronomical Society*, **333**, L35 – L39
- Aerts C., Lehmann H., Briquet M., Scuflaire R., Dupret M. A., De Ridder J., Thoul A., 2003a, Spectroscopic mode identification for the beta Cephei star EN (16) Lacertae, *Astronomy and Astrophysics*, **399**, 639 – 645
- Aerts C., Thoul A., Daszyńska J., Scuflaire R., Waelkens C., Dupret M. A., Niemczura E., Noels A., 2003b, "Asteroseismology of HD 129929: Core Overshooting and Nonrigid Rotation", *Science*, **300**, 1926 – 1928
- Aerts C., Cuypers J., De Cat P., Dupret M. A., De Ridder J., Eyer L., Scuflaire R., Waelkens C., 2004a, "Long-term multicolour photometry and high-resolution spectroscopy of the two  $\gamma$  Doradus stars HD 12901 and HD 48501", *Astronomy and Astrophysics*, **415**, 1079 – 1088
- Aerts C., De Cat P., Handler G., Heiter U., Balona L. A., Krzesinski J., Mathias P., Lehmann H., Ilyin I., De Ridder J., Dreizler S., Bruch A., Traulsen I., Hoffmann A., James D., Romero-Colmenero E., Maas T., Groenewegen M. A. T., Telting J. H., Uytterhoeven K., Koen C., Cottrell P. L., Bentley J., Wright D. J., Cuypers J., 2004b, "Asteroseismology of the  $\beta$  Cephei star  $\nu$  Eridani - II. Spectroscopic observations and pulsational frequency analysis", *Monthly Notices of the Royal Astronomical Society*, **347**, 463 – 470
- Aerts C., Lamers H. J. G. L. M., Molenberghs G., 2004c, "Maximum mass-loss rates of line-driven winds of massive stars: the effect of rotation and an application to  $\eta$  Carinae", *Astronomy and Astrophysics*, **418**, 639 – 648
- Aerts C., Waelkens C., Daszyńska-Daszkiewicz J., Dupret M.-A., Thoul A., Scuflaire R., Uytterhoeven K., Niemczura E., Noels A., 2004d, "Asteroseismology of the  $\beta$  Cep star HD 129929. I. Observations, oscillation frequencies and stellar parameters", *Astronomy and Astrophysics*, **415**, 241 – 249
- Aerts C., De Cat P., De Ridder J., Van Winckel H., Raskin G., Davignon G., Uytterhoeven K., 2006a, "Multiperiodicity in the large-amplitude rapidly-rotating  $\beta$  Cephei star HD 203664", *Astronomy and Astrophysics*, **449**, 305 – 311
- Aerts C., De Cat P., Kuschnig R., Matthews J. M., Guenther D. B., Moffat A. F. J., Rucinski S. M., Sasselov D., Walker G. A. H., Weiss W. W., 2006b, "Discovery of the New Slowly Pulsating B Star HD 163830 (B5 II/III) from MOST Space-based Photometry", *Astrophysical Journal*, **642**, L165 – L168
- Aerts C., Marchenko S. V., Matthews J. M., Kuschnig R., Guenther D. B., Moffat A. F. J., Rucinski S. M., Sasselov D., Walker G. A. H., Weiss W. W., 2006c, " $\delta$  Ceti Is Not Monoperiodic: Seismic Modeling of a  $\beta$  Cephei Star from MOST Space-based Photometry", *Astrophysical Journal*, **642**, 470 – 477
- Aizenman M., Smeyers P., Weigert A., 1977, "Avoided crossing of modes of non-radial stellar oscillations", *Astronomy and Astrophysics*, **58**, 41 – 46

- Alcock C., Allsman R. A., Alves D., Axelrod T. S., Becker A. C., Bennett D. P., Cook K. H., Freeman K. C., Griest K., Lehner M. J., Marshall S. L., Minniti D., Peterson B. A., Pratt M. R., Quinn P. J., Rodgers A. W., Rorabeck A., Sutherland W., Tomaney A., Vandehei T., Welch D. L., The MACHO Collaboration, 1999, "The MACHO Project LMC Variable Star Inventory. VI. The Second Overtone Mode of Cepheid Pulsation from First/Second Overtone Beat Cepheids", *Astrophysical Journal*, **511**, 185 – 192
- Allende Prieto C., Asplund M., García López R. J., Lambert D. L., 2002, "Signatures of convection in the spectrum of Procyon: fundamental parameters and iron abundance", *Astrophysical Journal*, **567**, 544 – 565
- Anders E., Grevesse N., 1989, "Abundances of the elements: meteoritic and solar", *Geochim. Cosmochim. Acta*, **53**, 197 – 214
- Andersen A. C., 2007, "Dust from AGB stars", In *Why galaxies care about AGB stars: their importance as actors and probes*, Eds F. Kerschbaum, C. Charbonnel, R. F. Wing, Publications of the Astronomical Society of the Pacific Conference Series, **378**, 170 – 180
- Andersen J., Nordström B., Clausen J. V., 1990, "New strong evidence for the importance of convective overshooting in intermediate-mass stars", *Astrophysical Journal*, **363**, L33 – L36
- Anderson E. R., Duvall T. L., Jefferies S. M., 1990, "Modeling of solar oscillation power spectra", *Astrophysical Journal*, **364**, 699 – 705
- Ando H., Osaki Y., 1975, "Nonadiabatic nonradial oscillations: An application to the five-minute oscillation of the sun", *Publications of the Astronomical Society of Japan*, **27**, 581 – 603
- Andreasen G. K., Petersen J. O., 1988, "Double mode pulsating stars and opacity changes", *Astronomy and Astrophysics*, **192**, L4 – L6
- Andrievsky S. M., Schönberner D., Drilling J. S., 2000, "Blue stragglers in open clusters. Part II", *Astronomy and Astrophysics*, **356**, 517 – 528
- Antia H. M., 1995, "Effects of surface layers on helioseismic inversion", *Monthly Notices of the Royal Astronomical Society*, **274**, 499 – 503
- Antia H. M., 1996, "Nonasymptotic helioseismic inversion: iterated seismic solar model", *Astronomy and Astrophysics*, **307**, 609 – 623
- Antia H. M., 2003, "Does the Sun shrink with increasing magnetic activity?", *Astrophysical Journal*, **590**, 567 – 572
- Antia H. M., Basu S., 1994a, "Nonasymptotic helioseismic inversion for solar structure", *Astronomy and Astrophysics Supplement Series*, **107**, 421 – 444
- Antia H. M., Basu S., 1994b, "Measuring the helium abundance in the solar envelope: the role of the equation of state", *Astrophysical Journal*, **426**, 801 – 811
- Antia H. M., Basu S., 2000, "Temporal variations of the rotation rate in the solar interior", *Astrophysical Journal*, **541**, 442 – 448
- Antia H. M., Basu S., 2001, "Temporal variations of the solar rotation rate at high latitudes", *Astrophysical Journal*, **559**, L67 – L70

- Antia H. M., Chitre S. M., 1998, "Determination of temperature and chemical composition profiles in the solar interior from seismic models", *Astronomy and Astrophysics*, **339**, 239 – 251
- Antia H. M., Basu S., Chitre S. M., 1998, "Solar internal rotation rate and the latitudinal variation of the tachocline", *Monthly Notices of the Royal Astronomical Society*, **298**, 543 – 556
- Antia H. M., Chitre S. M., Thompson M. J., 2000, "The Sun's acoustic asphericity and magnetic fields in the solar convection zone", *Astronomy and Astrophysics*, **360**, 335 – 344
- Antia H. M., Chitre S. M., Thompson M. J., 2003, "On the variation of the latitudinal structure of the solar convection zone", *Astronomy and Astrophysics*, **399**, 329 – 336
- Antia H. M., Basu S., Chitre S. M., 2008, "Solar rotation rate and its gradients during cycle 23", *Astrophysical Journal*, **681**, 680 – 692
- Antipin S., 1997, "On the new triple-mode pulsating variable star GSC 4018.1807.", *Astronomy and Astrophysics*, **326**, L1 – L4
- Appourchaux T., Fröhlich C., Andersen B., Berthomieu G., Chaplin W. J., Elsworth Y., Finsterle W., Gough D. O., Isaak G. R., Kosovichev A. G., Provost J., Scherrer P. H., Sekii T., Toutain T., 2000a, "Observational upper limits to low-degree solar *g*-modes", *Astrophysical Journal*, **538**, 401 – 414
- Appourchaux T., Chang H.-Y., Gough D. O., Sekii T., 2000b, "On measuring low-degree p-mode frequency splitting with full-disc integrated data", *Monthly Notices of the Royal Astronomical Society*, **319**, 365 – 376
- Arentoft T., Sterken C., Handler G., 2001a, "Low-frequency variability and binarity of the δ Scuti star XX Pyx", *Monthly Notices of the Royal Astronomical Society*, **326**, 192 – 202
- Arentoft T., Sterken C., Knudsen M. R., Handler G., Niarchos P., Gazeas K., Manimanis V., Moalusi M. B., Vuthela F. F., Van Cauteren P., 2001b, "Irregular amplitude variations and another abrupt period change in the δ Scuti star V 1162 Ori", *Astronomy and Astrophysics*, **378**, L33 – L36
- Arentoft T., De Ridder J., Grundahl F., Glowienka L., Waelkens C., Dupret M.-A., Grigahcène A., Lefever K., Jensen H. R., Reyniers M., Frandsen S., Kjeldsen H., 2007, "Oscillating blue stragglers, γ Doradus stars and eclipsing binaries in the open cluster NGC 2506", *Astronomy and Astrophysics*, **465**, 965 – 979
- Arentoft T., Kjeldsen H., Bedding T. R., Bazot M., Christensen-Dalsgaard J., Dall T. H., Karoff C., Carrier F., Eggenberger P., Sosnowska D., Wittenmyer R. A., Endl M., Metcalfe T. S., Hekker S., Reffert S., Butler R. P., Bruntt H., Kiss L. L., O'Toole S. J., Kambe E., Ando H., Izumiura H., Sato B., Hartmann M., Hatzes A., Bouchy F., Mosser B., Appourchaux T., Barban C., Berthomieu G., Garcia R. A., Michel E., Provost J., Turck-Chièze S., Martić M., Lebrun J.-C., Schmitt J., Bertaux J.-L., Bonanno A., Bennati S., Claudi R. U., Cosentino R., Leccia S., Frandsen S., Brogaard K., Glowienka L., Grundahl F., Stempels E., 2008, "A multisite campaign to

- measure solar-like oscillations in Procyon. I. Observations, data reduction and slow variations”, *Astrophysical Journal*, **687**, 1180 – 1190
- Arentoft T., Kjeldsen H., Bedding T. R., 2009, “Optimizing weights for the detection of stellar oscillations: application to  $\alpha$  Centauri A and B, and  $\beta$  Hydri”, In *Proc. SOHO XXI/GONG 2008: Solar-stellar dynamos as revealed by helio- and asteroseismology*, Eds M. Dikpati, T. Arentoft, I. González Hernández, F. Hill, C. Lindsey, Publications of the Astronomical Society of the Pacific Conference Series, San Francisco, in press [[arXiv:0901.3632v1 \[astro-ph.SR\]](https://arxiv.org/abs/0901.3632v1)]
- Arras P., Townsley D. M., Bildsten L., 2006, “Pulsational Instabilities in Accreting White Dwarfs”, *Astrophysical Journal*, **643**, L119 – L122
- Asplund M., 2005, “New light on stellar abundance analysis: departures from LTE and homogeneity”, *Annual Review of Astronomy and Astrophysics*, **43**, 481 – 540
- Asplund M., 2008, “Does the Sun have subsolar metallicity?”, In *Proc. IAU Symp. 252: The Art of Modelling Stars in the 21<sup>st</sup> Century*, Eds L. Deng, K. L. Chan, IAU and Cambridge University Press, 13 – 26
- Asplund M., Nordlund Å., Trampedach R., Allende Prieto C., Stein R. F., 2000, “Line formation in solar granulation. I. Fe line shapes, shifts and asymmetries”, *Astronomy and Astrophysics*, **359**, 729 – 742
- Asplund M., Grevesse N., Sauval A. J., Allende Prieto C., Kiselman D., 2004, “Line formation in solar granulation. IV. [O I], O I and OH lines and the photospheric O abundance”, *Astronomy and Astrophysics*, **417**, 751 – 768 (Erratum: *Astronomy and Astrophysics* **435**, 339 – 340)
- Audard N., Kupka F., Morel P., Provost J., Weiss W. W., 1998, “The acoustic cut-off frequency of roAp stars”, *Astronomy and Astrophysics*, **335**, 954 – 958
- Ausseloo M., 2005, *Seismic Studies of selected Beta Cephei stars: Beta Centauri, Nu Eridani and 12 Lacertae*, PhD Dissertation, Katholieke Universiteit Leuven, Belgium
- Ausseloo M., Aerts C., Uytterhoeven K., Schrijvers C., Waelkens C., Cuypers J., 2002, “beta Centauri: An eccentric binary with two  $\beta$  Cep-type components”, *Astronomy and Astrophysics*, **384**, 209 – 214
- Ausseloo M., Scuflaire R., Thoul A., Aerts C., 2004, “Asteroseismology of the  $\beta$  Cephei star  $\nu$  Eridani: massive exploration of standard and non-standard stellar models to fit the oscillation data”, *Monthly Notices of the Royal Astronomical Society*, **355**, 352 – 358
- Ausseloo M., Aerts C., Lefever K., Davis J., Harmanec P., 2006, “High-precision elements of double-lined spectroscopic binaries from combined interferometry and spectroscopy. Application to the  $\beta$  Cephei star  $\beta$  Centauri”, *Astronomy and Astrophysics*, **455**, 259 – 269
- Ayres T. R., 2008, “Solar forbidden oxygen, revisited”, *Astrophysical Journal*, **686**, 731 – 740

- Ayres T. R., Plymate C., Keller C. U., 2006, "Solar carbon monoxide, thermal profiling and the abundances of C, O, and their isotopes", *Astrophysical Journal Supplement Series*, **165**, 618 – 651
- Ayres T. R., Judge P. G., Saar S. H., Schmitt J. H. M. M., 2008, "The fainting of  $\alpha$  Centauri A, resolved", *Astrophysical Journal*, **678**, L121 – L124
- Baade D., 1982a, "Does 28 CMa have a photometric period differing from its spectroscopic period", *Astronomy and Astrophysics*, **110**, L15 – L17
- Baade D., 1982b, "An unusually short stable period of absorption line asymmetries and V/R variations in the spectrum of the Be star 28 CMa", *Astronomy and Astrophysics*, **105**, 65 – 75
- Baade D., Schmutz W., van Kerkwijk M., 1990, "Short-term activity in the Gamma(2) Velorum system - The O-type supergiant is a nonradially pulsating star", *Astronomy and Astrophysics*, **240**, 105 – 115
- Baade D., Stahl O., 1989a, "Rapid line profile-variability of the A-type shell- and possible pre-main sequence star HD 163296", *Astronomy and Astrophysics*, **209**, 268 – 278
- Baade D., Stahl O., 1989b, "New aspects of the variability of the probable pre-main sequence star HR 5999", *Astronomy and Astrophysics*, **209**, 255 – 267
- Bachmann K. T., Brown T. M., 1993, "p-mode frequency variation in relation to global solar activity", *Astrophysical Journal*, **411**, L45 – L48
- Bachmann K. T., Schou J., Brown T. M., 1993, "Observations of intermediate degree solar oscillations: 1989 April–June", *Astrophysical Journal*, **412**, 870 – 879
- Bachmann K. T., Duvall T. L., Harvey J. W., Hill F., 1995, "Measurement of high-degree solar oscillation frequencies", *Astrophysical Journal*, **443**, 837 – 842
- Backus G., Gilbert F., 1970, "Uniqueness in the inversion of inaccurate gross Earth data", *Phil. Trans. R. Soc. London, Ser. A*, **266**, 123 – 192
- Bagnulo S., Landi Degl'Innocenti E., Landolfi M., Leroy J. L., 1995, "Linear polarimetry of Ap stars. 3: A diagnostic method for the magnetic structure of rotating stars", *Astronomy and Astrophysics*, **295**, 459 – 470
- Bagnulo W. G., Jr., Gies D. R., 1991, "Tomographic separation of composite spectra - The components of the O-star spectroscopic binary AO Cassiopeiae", *Astrophysical Journal*, **376**, 266 – 271
- Bahcall J. N., 1989, *Neutrino astrophysics*, Cambridge University Press, Cambridge
- Bahcall J. N., Peña-Garay C., 2004, "Solar models and solar neutrino oscillations", *New Journal of Physics*, **6**-63, 1 – 19
- Bahcall J. N., Pinsonneault M. H., 1995, (With an appendix by G. J. Wasserburg), "Solar models with helium and heavy-element diffusion", *Reviews of Modern Physics*, **67**, 781 – 808
- Bahcall J. N., Pinsonneault M. H., Basu S., 2001, "Solar models: current epoch and time dependences, neutrinos, and helioseismological properties", *Astrophysical Journal*, **555**, 990 – 1012

- Bahcall J. N., Basu S., Pinsonneault M., Serenelli A. M., 2005a, "Helioseismological implications of recent solar abundance determinations", *Astrophysical Journal*, **618**, 1049 – 1056
- Bahcall J. N., Basu S., Serenelli A. M., 2005b, "What is the neon abundance of the Sun?", *Astrophysical Journal*, **631**, 1281 – 1285
- Bailes M., Lyne A. G., Shemar S. L., 1991, "A planet orbiting the neutron star PSR1829 - 10", *Nature*, **352**, 311 – 313
- Bailyn C. D., 1995, "Blue Stragglers and Other Stellar Anomalies:Implications for the Dynamics of Globular Clusters", *Annual Review of Astronomy and Astrophysics*, **33**, 133 – 162
- Bailyn C. D., Pinsonneault M. H., 1995, "On the luminosity function, lifetimes and origin of blue stragglers in globular clusters", *Astrophysical Journal*, **439**, 705 – 714
- Baker N. H., 1987, "Time dependent convection in stars – a review of the theories", In *Physical Processes in Comets, Stars and Active Galaxies*, Eds W. Hillebrandt, E. Meyer-Hofmeister, H.-C. Thomas, Springer, Berlin, p. 105 – 124
- Baker N. H., Gough D. O., 1979, "Pulsations of model RR Lyrae stars", *Astrophysical Journal*, **234**, 232 – 244
- Baker N., Kippenhahn R., 1962, "The pulsations of models of  $\delta$  Cephei stars", *Zeitung für Astrophysik*, **54**, 115 – 151
- Baker N., Kippenhahn R., 1965, "The pulsations of models of delta Cephei stars. II", *Astrophysical Journal*, **142**, 868 – 889
- Baldner C. S., Basu S., 2008, "Solar cycle related changes at the base of the convection zone", *Astrophysical Journal*, **686**, 1349 – 1361
- Baldry I. K., Bedding T. R., Viskum M., Kjeldsen H., Frandsen S., 1998, "Spectroscopy of the roAp star  $\alpha$  Cir. I - Velocities of H-alpha and metal lines", *Monthly Notices of the Royal Astronomical Society*, **295**, 33 – 42
- Baldry I. K., Viskum M., Bedding T. R., Kjeldsen H., Frandsen S., 1999, "Spectroscopy of the roAp star  $\alpha$  Cir – II. The bisector and equivalent width of the H $\alpha$  line", *Monthly Notices of the Royal Astronomical Society*, **302**, 381 – 390
- Baldry I. K., Bedding T. R., 2000, "Time-series spectroscopy of the rapidly oscillating Ap star HR 3831", *Monthly Notices of the Royal Astronomical Society*, **318**, 341 – 353
- Ballot J., Turck-Chièze S., García R. A., 2004, "Seismic extraction of the convective extent in solar-like stars. The observational point of view", *Astronomy and Astrophysics*, **423**, 1051 – 1061
- Ballot J., García R. A., Lambert P., 2006, "Rotation speed and stellar axis inclination from modes: how *CoRoT* would see other suns", *Monthly Notices of the Royal Astronomical Society*, **369**, 1281 – 1286
- Ballot J., Appourchaux T., Toutain T., Guillet M., 2008, "On deriving  $p$ -mode parameters for inclined solar-like stars", *Astronomy and Astrophysics*, **486**, 867 – 875

- Balmforth N. J., 1992a, "Solar pulsational stability. I: Pulsation-mode thermodynamics", *Monthly Notices of the Royal Astronomical Society*, **255**, 603 – 631
- Balmforth N. J., 1992b, "Solar pulsational stability. II: Pulsation frequencies", *Monthly Notices of the Royal Astronomical Society*, **255**, 632 – 638
- Balmforth N. J., 1992c, "Solar pulsational stability. III: Acoustical excitation by turbulent convection", *Monthly Notices of the Royal Astronomical Society*, **255**, 639 – 649
- Balmforth N. J., Cunha M. S., Dolez N., Gough D. O., Vauclair S., 2001, "On the excitation mechanism in roAp stars", *Monthly Notices of the Royal Astronomical Society*, **323**, 362 – 372
- Balmforth N. J., Gough D. O., 1990, "Effluent stellar pulsation", *Astrophysical Journal*, **362**, 256 – 266
- Balmforth N. J., Gough D. O., Merryfield W. J., 1996, "Structural changes to the Sun through the solar cycle", *Monthly Notices of the Royal Astronomical Society*, **278**, 437 – 448
- Balona L. A., 1986a, "Mode identification from line profile variations", *Monthly Notices of the Royal Astronomical Society*, **219**, 111 – 129
- Balona L. A., 1986b, "Mode identification from line profile variations. II - A quantitative least-squares algorithm", *Monthly Notices of the Royal Astronomical Society*, **220**, 647 – 656
- Balona L. A., 1987, "Mode identification from line profile variations. III - Temperature variation and toroidal modes", *Monthly Notices of the Royal Astronomical Society*, **224**, 41 – 52
- Balona L. A., 1994, "Effective Temperature Bolometric Correction and Mass Calibration of O-F", *Monthly Notices of the Royal Astronomical Society*, **268**, 119 – 127
- Balona L. A., 1995a, "Tests of the Pulsation and Starspot Models for the Periodic Be-Stars", *Monthly Notices of the Royal Astronomical Society*, **277**, 1547 – 1554
- Balona L. A., 1995b, "The Early-Type Variables", *Astrophysics and Space Science*, **230**, 17 – 28
- Balona L. A., 2002, "Radial velocity study of the roAp star HR 3831", *Monthly Notices of the Royal Astronomical Society*, **337**, 1059 – 1067
- Balona L. A., Dziembowski W. A., 1999, "Excitation and visibility of high-degree modes in stars", *Monthly Notices of the Royal Astronomical Society*, **309**, 221 – 232
- Balona L. A., Evers E. A., 1999, "Mode identification and asteroseismology of delta Scuti stars", *Monthly Notices of the Royal Astronomical Society*, **302**, 349 – 361
- Balona L. A., Laney C. D., 2003, "Radial velocity study of the roAp star  $\alpha$  Circinus ", *Monthly Notices of the Royal Astronomical Society*, **344**, 242 – 246

- Balona L. A., Stobie R. S., 1979, "The effect of radial and non-radial stellar oscillations on the light, colour and velocity variations", *Monthly Notices of the Royal Astronomical Society*, **189**, 649 – 658
- Balona L. A., Zima W., 2002, "Radial velocity study of the roAp star HR 1217", *Monthly Notices of the Royal Astronomical Society*, **336**, 873 – 878
- Balona L. A., Böhm T., Foing B. H., Ghosh K. K., Janot-Pacheco E., Krisciunas K., Lagrange A.-M., Lawson W. A., James S. D., Baudrand J., Catala C., Dreux M., Felenbok P., Hearnshaw J. B., 1996, "Line profile variations in  $\gamma$  Doradus", *Monthly Notices of the Royal Astronomical Society*, **281**, 1315 – 1325
- Balona L. A., Dziembowski W. A., Pamyatnykh A., 1997, "The structure of the instability strip and mode identification for  $\beta$  Cep stars in three young open clusters", *Monthly Notices of the Royal Astronomical Society*, **289**, 25 – 36
- Balona L. A., Aerts C., Štefl S., 1999, "Simultaneous photometry and spectroscopy of the Be star 28( $\omega$ ) CMa - II. Line profile modelling", *Monthly Notices of the Royal Astronomical Society*, **305**, 519 – 526
- Balona L. A., James D. J., Motoasele P., Nombexenza B., Ramnath A., van Dyk J., 2002, "Short-period line profile and light variations in the Beta Cephei star 19 Monocerotis", *Monthly Notices of the Royal Astronomical Society*, **333**, 952 – 960
- Baranne A., Queloz D., Mayor M., Adrianzyk G., Knispel G., Kohler D., Lacroix D., Meunier J.-P., Rimbaud G., Vin A., 1996, "ELODIE: A spectrograph for accurate radial velocity measurements", *Astronomy and Astrophysics Supplement Series*, **119**, 373 – 390
- Barban C., Matthews J. M., De Ridder J., Baudin F., Kuschnig R., Mazumdar A., Samadi R., Guenther D. B., Moffat A. F. J., Rucinski S. M., Sasselov D., Walker G. A. H., Weiss W. W., 2007, "Detection of solar-like oscillations in the red giant star  $\epsilon$  Ophiuchi by MOST spacebased photometry", *Astronomy and Astrophysics*, **468**, 1033 – 1038
- Barnes S. A., 2007, "Ages for illustrative field stars using gyrochronology: validity, limitations, and errors", *Astrophysical Journal*, **669**, 1167 – 1189
- Basu S., 1997, "Seismology of the base of the solar convection zone", *Monthly Notices of the Royal Astronomical Society*, **288**, 572 – 584
- Basu S., 1998, "Effects of errors in the solar radius on helioseismic inferences", *Monthly Notices of the Royal Astronomical Society*, **298**, 719 – 728
- Basu S., Antia H. M., 1994, "Effects of diffusion on the extent of overshoot below the solar convection zone", *Monthly Notices of the Royal Astronomical Society*, **269**, 1137 – 1144
- Basu S., Antia H. M., 1995, "Helium abundance in the solar envelope", *Monthly Notices of the Royal Astronomical Society*, **276**, 1402 – 1408
- Basu S., Antia H. M., 1997, "Seismic measurement of the depth of the solar convection zone", *Monthly Notices of the Royal Astronomical Society*, **287**, 189 – 198

- Basu S., Antia H. M., 2001, "A study of possible temporal and latitudinal variations in the properties of the solar tachocline", *Monthly Notices of the Royal Astronomical Society*, **324**, 498 – 508
- Basu S., Antia H. M., 2003, "Changes in solar dynamics from 1995 to 2002", *Astrophysical Journal*, **585**, 553 – 565
- Basu S., Antia H. M., 2004, "Constraining solar abundances using helioseismology", *Astrophysical Journal*, **606**, L85 – L88
- Basu S., Antia H. M., 2008, "Helioseismology and solar abundances", *Phys. Rep.*, **457**, 217 – 283
- Basu S., Christensen-Dalsgaard J., 1997, "Equation of state and helioseismic inversions", *Astronomy and Astrophysics*, **322**, L5 – L8
- Basu S., Mandel A., 2004, "Does solar structure vary with solar magnetic activity?" *Astrophysical Journal*, **617**, L155 – L158
- Basu S., Thompson M. J., 1996, "On constructing seismic models of the Sun", *Astronomy and Astrophysics*, **305**, 631 – 642
- Basu S., Christensen-Dalsgaard J., Pérez Hernández F., Thompson M. J., 1996, "Filtering out near-surface uncertainties from helioseismic inversions", *Monthly Notices of the Royal Astronomical Society*, **280**, 651 – 660
- Basu S., Christensen-Dalsgaard J., Thompson M. J., 1997a, "SVD pre-processing of helioseismic data for solar structure inversion", *Astronomy and Astrophysics*, **321**, 634 – 642
- Basu S., Chaplin W. J., Christensen-Dalsgaard J., Elsworth Y., Isaak G. R., New R., Schou J., Thompson M. J., Tomczyk S., 1997b, "Solar internal sound speed as inferred from combined BiSON and LOWL oscillation frequencies", *Monthly Notices of the Royal Astronomical Society*, **292**, 243 – 251
- Basu S., Däppen W., Nayfonov A., 1999, "Helioseismic analysis of the hydrogen partition function in the solar interior", *Astrophysical Journal*, **518**, 985 – 993
- Basu S., Turck-Chièze S., Berthomieu G., Brun A. S., Corbard T., Gonczi G., Christensen-Dalsgaard J., Provost J., Thiery S., Gabriel A. H., Boumier P., 2000a, "Structure of the solar core: Effect of asymmetry of peak profiles", *Astrophysical Journal*, **535**, 1078 – 1084
- Basu S., Pinsonneault M. H., Bahcall J. N., 2000b, "How much do helioseismological inferences depend on the assumed reference model?", *Astrophysical Journal*, **529**, 1084 – 1100
- Basu S., Christensen-Dalsgaard J., Thompson M. J., 2002, "SOLA inversions for the core structure of solar-type stars", In *Proc. 1st Eddington Workshop, 'Stellar Structure and Habitable Planet Finding'*, Eds F. Favata, I. W. Roxburgh and D. Galadí-Enríquez, ESA SP-485, ESA Publications Division, Noordwijk, The Netherlands, 249 – 252
- Basu S., Christensen-Dalsgaard J., Howe R., Schou J., Thompson M. J., Hill F., Komm R., 2003, "A comparison of solar p-mode parameters from MDI

- and GONG: mode frequencies and structure inversions”, *Astrophysical Journal*, **591**, 432 – 445
- Basu S., Mazumdar A., Antia H. M., Demarque P., 2004, “Asteroseismic determination of helium abundance in stellar envelopes”, *Monthly Notices of the Royal Astronomical Society*, **350**, 277 – 286
- Basu S., Chaplin W. J., Elsworth Y., New R., Serenelli A. M., Verner G. A., 2007, “Solar abundances and helioseismology: fine-structure spacings and separation ratios of low-degree  $p$ -modes”, *Astrophysical Journal*, **655**, 660 – 671
- Batchelor G. K., 1956, *The theory of homogeneous turbulence*, Cambridge University Press
- Batchelor G. K., 1967, *An introduction to fluid dynamics*, Cambridge University Press
- Baturin V. A., Däppen W., Gough D. O., Vorontsov S. V., 2000, “Seismology of the solar envelope: sound-speed gradient in the convection zone and its diagnosis of the equation of state”, *Monthly Notices of the Royal Astronomical Society*, **316**, 71 – 83
- Bazot M., Bouchy F., Kjeldsen H., Charpinet S., Laymand M., Vauclair S., 2007, “Asteroseismology of  $\alpha$  Centauri A. Evidence of rotational splitting”, *Astronomy and Astrophysics*, **470**, 295 – 302
- Beauchamp A., Wesemael F., Bergeron P., Fontaine G., Saffer R. A., Liebert J., Brassard P., 1999, “Spectroscopic Studies of DB White Dwarfs: The Instability Strip of the Pulsating DB (V777 Herculis) Stars”, *Astrophysical Journal*, **516**, 887 – 891
- Bedding T. R., 2003, “Solar-like Oscillations in Semiregular Variables”, *Astrophysics and Space Science*, **284**, 61 – 64
- Bedding T. R., Kjeldsen H., 2003, “Solar-like Oscillations”, *Publications of the Astronomical Society of Australia*, **20**, 203 – 212
- Bedding T. R., Kjeldsen H., 2007, “Observations of solar-like oscillations”, *Communications in Asteroseismology*, **150**, 106 – 114
- Bedding T. R., Kjeldsen H., Reetz J., Barbuy B., 1996, “Measuring stellar oscillations using equivalent widths of absorption lines”, *Monthly Notices of the Royal Astronomical Society*, **280**, 1155 – 1161
- Bedding, T. R., Kjeldsen, H., Christensen-Dalsgaard, J., 1998, “HIPPARCOS Parallaxes for  $\eta$  Boo and  $\kappa^2$  Boo: Two successes for asteroseismology”, In *Proc. Tenth Cambridge Workshop on Cool Stars, Stellar Systems and the Sun*, Eds Donahue, R. A., Bookbinder, J. A., Astronomical Society of the Pacific Conference Series, San Francisco, **154**, 741 – 744
- Bedding T. R., Butler R. P., Kjeldsen H., Baldry I. K., O’Toole S. J., Tinney C. G., Marcy G. W., Kienzle F., Carrier F., 2001, “Evidence for Solar-like Oscillations in  $\beta$  Hydri”, *Astrophysical Journal*, **549**, L105 – L108
- Bedding T. R., Kjeldsen H., Butler R. P., McCarthy C., Marcy G. W., O’Toole S. J., Tinney C. G., Wright J. T., 2004, “Oscillation Frequencies and Mode Lifetimes in  $\alpha$  Centauri A”, *Astrophysical Journal*, **614**, 380 – 385

- Bedding T. R., Kiss L. L., Kjeldsen H., Brewer B. J., Dind Z. E., Kawaler S. D., Zijlstra A. A., 2005, "The light curve of the semiregular variable L<sub>2</sub> Puppis - II. Evidence for solar-like excitation of the oscillations", *Monthly Notices of the Royal Astronomical Society*, **361**, 1375 – 1381
- Bedding T. R., Kjeldsen H., Bouchy F., Bruntt H., Butler R. P., Buzasi D. L., Christensen-Dalsgaard J., Frandsen S., Lebrun J.-C., Martić M., Schou J., 2005, "The non-detection of oscillations in Procyon by MOST: Is it really a surprise?", *Astronomy and Astrophysics*, **432**, L43 – L48
- Bedding T. R., Kjeldsen H., Arentoft T., Bouchy F., Brandbyge J., Brewer B. J., Butler R. P., Christensen-Dalsgaard J., Dall T., Frandsen S., Karoff C., Kiss L. L., Monteiro M. J. P. F. G., Pijpers F. P., Teixeira T. C., Tinney C. G., Baldry I. K., Carrier F., O'Toole S. J., 2007, "Solar-like Oscillations in the G2 Subgiant  $\beta$  Hydri from Dual-Site Observations", *Astrophysical Journal*, **663**, 1315 – 1324
- Beichman C. A., Chester T. J., Skrutskie M., Low F. J., Gillett F., 1998, "Characteristics of the 2MASS Prototype Survey", *Publications of the Astronomical Society of the Pacific*, **110**, 480 – 489
- Belkacem K., Samadi R., Goupil M. J., Dupret M.-A., 2008, "Stochastic excitation of non-radial modes. I. High-angular-degree  $p$  modes", *Astronomy and Astrophysics*, **478**, 163 – 174
- Belkacem K., Samadi R., Goupil M. J., Dupret M. A., Brun A. S., Baudin F., 2009, "Stochastic excitation of nonradial modes. II. Are solar asymptotic gravity modes detectable?" *Astronomy and Astrophysics*, **494**, 191 – 204
- Beltrame M., Poretti E., 2002, "HD 304373, the second case of 1O/2O double-mode Cepheid in the Galaxy", *Astronomy and Astrophysics*, **386**, L9 – L12
- Berdyugina S. V., Telting J. H., Korhonen H., 2003a, "Surface imaging of stellar non-radial pulsations. I. Inversions of simulated data", *Astronomy and Astrophysics*, **406**, 273 – 280
- Berdyugina S. V., Telting J. H., Korhonen H., Schrijvers C., 2003b, "Surface imaging of stellar non-radial pulsations. II. The  $\beta$  Cephei star  $\omega^1$  Sco", *Astronomy and Astrophysics*, **406**, 281 – 285
- Bergeron P., Fontaine G., Billères M., Boudreault S., Green E. M., 2004, "On the Purity of the ZZ Ceti Instability Strip: Discovery of More Pulsating DA White Dwarfs on the Basis of Optical Spectroscopy", *Astrophysical Journal*, **600**, 404 – 408
- Berrilli F., Corciulo G., Ingrosso G., Lorenzetti D., Nisini B., Strafella F., 1992, "Infrared emission from dust structures surrounding Herbig Ae/Be stars", *Astrophysical Journal*, **398**, 254 – 272
- Bersier D., Burki G., Mayor M., Duquennoy A., 1994, "Fundamental parameters of Cepheids. II. Radial velocity data", *Astronomy and Astrophysics Supplement Series*, **108**, 25 – 39
- Berthomieu G., Gonczi G., Graff Ph., Provost J., Rocca A., 1978, "Low-frequency gravity modes of a rotating star", *Astronomy and Astrophysics*, **70**, 597 – 606

- Bertiau F. C., 1957, "The orbits of the spectroscopic binaries rho Orionis, eta Bootis, and 32 Virginis", *Astrophysical Journal*, **125**, 696 – 706
- Bevington P. R., Robinson D. K., 1992, *Data Reduction and Error Analysis for the Physical Sciences, 2nd edition*, McGraw-Hill, New York
- Bessell M. S., 2005, "Standard Photometric Systems", *Annual Review of Astronomy and Astrophysics*, **43**, 293 – 336
- Biermann L., 1947, "Über die Ursache der chromosphärischen Turbulenz und des UV-Exzesses der Sonnenstrahlung", *Zeitung für Astrophysik*, **25**, 161 – 177
- Bigot L., Dziembowski W. A., 2002, "The oblique pulsator model revisited", *Astronomy and Astrophysics*, **391**, 235 – 245
- Bigot L., Provost J., Berthomieu G., Dziembowski W. A., Goode P. R., 2000, "Non-axisymmetric oscillations of roAp stars", *Astronomy and Astrophysics*, **356**, 218 – 233
- Bildsten L., Ushomirsky G., Cutler C., 1996, "Ocean *g*-modes on rotating neutron stars", *Astrophysical Journal*, **460**, 827 – 831
- Birch A. C., Kosovichev A. G., 1998, "Latitudinal variation of solar subsurface rotation inferred from *p*-mode frequency splittings measured with SOI-MDI and GONG", *Astrophysical Journal*, **503**, L187 – L190
- Blažko S., 1907, "Mitteilung über veränderliche Sterne", *Astronomische Nachrichten*, **175**, 325 – 326
- Bloomfield P., 1976, *Fourier analysis of time series: an introduction*, Wiley Series in Probability and Mathematical Statistics, New York: Wiley
- Böhm-Vitense E., 1958, "Über die Wasserstoffkonvektionszone in Sternen verschiedener Effektivtemperaturen und Leuchtkräfte", *Zeitung für Astrophysik*, **46**, 108 – 143
- Bonanno A., Schlattl H., Paternò L., 2002, "The age of the Sun and the relativistic corrections in the EOS", *Astronomy and Astrophysics*, **390**, 1115 – 1118
- Bono G., Caputo F., Marconi M., 1995, "The Topology of the RR Lyrae Instability Strip and the Oosterhoff Dichotomy", *Astronomical Journal*, **110**, 2365 – 2368
- Bono G., Caputo F., Santolamazza P., 1997, "Evolutionary scenario for metal-poor pulsating stars. I. Type II Cepheids", *Astronomy and Astrophysics*, **317**, 171 – 177
- Bono G., Caputo F., Marconi M., Santolamazza P., 2002, "Oscillating Blue Stragglers in Galactic globular clusters", In *Observational Aspects of Pulsating B- and A Stars*, Eds C. Sterken, D. W. Kurtz, Publications of the Astronomical Society of the Pacific Conference Series, San Francisco, **256**, 249
- Bouchy F., Carrier F., 2001, "P-mode observations on  $\alpha$  Cen A", *Astronomy and Astrophysics*, **374**, L5 – L8
- Bouchy F., Carrier F., 2002, "The acoustic spectrum of alpha Cen A", *Astronomy and Astrophysics*, **390**, 205 – 212

- Bouchy F., Pepe F., Queloz D., 2001, "Fundamental photon noise limit to radial velocity measurements", *Astronomy and Astrophysics*, **374**, 733 – 739
- Bourge P.-O., Alecian G., Thoul A., Scuflaire R., Theado S., 2006, "Radiative forces and pulsation in  $\beta$  Cephei stars", *Communications in Asteroseismology*, **147**, 105 – 108
- Bourge P.-O., Théado S., Thoul A., 2007, "Effects of diffusion in  $\beta$  Cephei stars", *Communications in Asteroseismology*, **150**, 203 – 204
- Boury A., Gabriel M., Noels A., Scuflaire R., Ledoux P., 1975, "Vibrational instability of a  $1 M_{\odot}$  star towards non-radial oscillations", *Astronomy and Astrophysics*, **41**, 279 – 285
- Bracewell R., 1999, *The Fourier Transform and Its Applications*, McGraw-Hill Science Engineering
- Bradley P. A., 1995, "The DBV Stars: Progress and Problems", *Baltic Astronomy*, **4**, 311 – 320
- Bradley P. A., Winget D. E., 1991, "Asteroseismology of white dwarf stars. I - Adiabatic results", *Astrophysical Journal Supplement Series*, **75**, 463 – 497
- Bradley P. A., Winget D. E., Wood M. A., 1993, "The potential for asteroseismology of DB white dwarf stars", *Astrophysical Journal*, **406**, 661 – 673
- Brassard P., Fontaine G., 2006, "Effects of diffusion of chemical elements on the period structure: an experiment with the pulsating DA white dwarf GD 165", *Memorie della Societa Astronomica Italiana* **77**, 439 – 440
- Brassard P., Fontaine G., Wesemael F., Hansen C. J., 1992, "Adiabatic properties of pulsating DA white dwarfs. II - Mode trapping in compositionally stratified models", *Astrophysical Journal Supplement Series*, **80**, 369 – 401
- Brassard P., Fontaine G., Wesemael F., 1995, "The modeling of energy distributions and light curves of ZZ Ceti stars. 1: Basic theory and semianalytic expressions for the emergent flux", *Astrophysical Journal Supplement Series*, **96**, 545 – 580
- Brassard P., Fontaine G., Billères M., Charpinet S., Liebert J., Saffer R. A., 2001, "Discovery and Asteroseismological Analysis of the Pulsating sdB Star PG 0014+067", *Astrophysical Journal*, **563**, 1013 – 1030
- Breger M., 1972, "Pre-Main Sequence Stars. I. Light Variability, Shells, and Pulsation in NGC 2264", *Astrophysical Journal*, **171**, 539 – 548
- Breger M., 2000, "The multiperiodic  $\delta$  Scuti star 4 Canum Venaticorum: amplitude variability", *Monthly Notices of the Royal Astronomical Society*, **313**, 129 – 135
- Breger M., Montgomery M. (Eds), 2000, *Delta Scuti and Related Stars*, Astronomical Society of the Pacific Conference Series, San Francisco, **210**
- Breger M., Pamyatnykh A. A., 1998, "Period changes of  $\delta$  Scuti stars and stellar evolution", *Astronomy and Astrophysics*, **332**, 958 – 968

- Breger M., Pamyatnykh A. A., 2006, "Amplitude variability or close frequencies in pulsating stars - the  $\delta$  Scuti star FG Vir", *Monthly Notices of the Royal Astronomical Society*, **368**, 571 – 578
- Breger M., Stich J., Garrido R., Martin B., Jiang S. Y., Li Z. P., Hube D. P., Ostermann W., Paparo M., Scheck M., 1993, "Nonradial Pulsation of the Delta-Scuti Star Bu-Cancri in the Praesepe Cluster", *Astronomy and Astrophysics*, **271**, 482 – 486
- Breger M., Handler G., Garrido R., Audard N., Zima W., Paparó M., Beichbuchner F., Zhi-Ping L., Shi-Yang J., Zong-Li L., Ai-Ying Z., Pikall H., Stankov A., Guzik J. A., Sperl M., Krzesinski J., Ogloza W., Pajdosz G., Zola S., Thomassen T., Solheim J.-E., Serkowitsch E., Reegen P., Rumpf T., Schmalwieser A., Montgomery M. H., 1999a, "30+ frequencies for the delta Scuti variable 4 Canum Venaticorum: results of the 1996 multisite campaign", *Astronomy and Astrophysics*, **349**, 225 – 235
- Breger M., Pamyatnykh A. A., Pikall H., Garrido R., 1999b, "The delta Scuti star FG Virginis. IV. Mode identifications and pulsation modelling", *Astronomy and Astrophysics*, **341**, 151 – 162
- Breger M., Pamyatnykh A. A., Zima W., Garrido R., Handler G., Reegen P., 2002, "Pulsation of the  $\delta$  Scuti star  $\theta^2$  Tau: new multisite photometry and modelling of instability", *Monthly Notices of the Royal Astronomical Society*, **336**, 249 – 258
- Breger M., Lenz P., Antoci V., Guggenberger E., Shobbrook R. R., Handler G., Ngwato B., Rodler F., Rodriguez E., López De Coca P., Rolland A., Costa V., 2005, "Detection of 75+ pulsation frequencies in the  $\delta$  Scuti star FG Virginis", *Astronomy and Astrophysics*, **435**, 955 – 965
- Bresolin F., Crowther P., Puls J. (Eds), 2008, *Proc. IAU Symposium 250: Massive Stars as Cosmic Engines*, Cambridge University Press
- Brewer E. C., 1894, *Dictionary of Phrase and Fable*
- Brickhill A. J., 1983, "The pulsations of ZZ Ceti stars", *Monthly Notices of the Royal Astronomical Society*, **204**, 537 – 556
- Brickhill A. J., 1990, "The Pulsations of ZZ-Ceti Stars - Part Two - Turbulent Convection and the Maximum Period", *Monthly Notices of the Royal Astronomical Society*, **246**, 510 – 517
- Brickhill A. J., 1991a, "The pulsations of ZZ Ceti stars. III - The driving mechanism", *Monthly Notices of the Royal Astronomical Society*, **251**, 673 – 680
- Brickhill A. J., 1991b, "The pulsations of ZZ Ceti stars. IV - The instability strip", *Monthly Notices of the Royal Astronomical Society*, **252**, 334 – 341
- Brickhill A. J., 1992a, "The pulsations of ZZ Ceti stars. V - The light curves. VI - The amplitude spectra", *Monthly Notices of the Royal Astronomical Society*, **259**, 519 – 528
- Brickhill A. J., 1992b, "The Pulsations of ZZ Ceti Stars - VI. The Amplitude Spectra", *Monthly Notices of the Royal Astronomical Society*, **259**, 529 – 535

- Briquet M., Aerts C., 2003, "A new version of the moment method, optimized for mode identification in multiperiodic stars", *Astronomy and Astrophysics*, **398**, 687 – 696
- Briquet M., Aerts C., Lüftinger T., De Cat P., Piskunov N. E., Scuflaire R., 2004, "He and Si surface inhomogeneities of four Bp variable stars", *Astronomy and Astrophysics*, **413**, 273 – 283
- Briquet M., Lefever K., Uytterhoeven K., Aerts C., 2005, "An asteroseismic study of the  $\beta$  Cephei star  $\theta$  Ophiuchi: spectroscopic results", *Monthly Notices of the Royal Astronomical Society*, **362**, 619 – 625
- Briquet M., Morel T., Thoul A., Scuflaire R., Miglio A., Montalbán J., Dupret M.-A., Aerts C., 2007, "An asteroseismic study of the  $\beta$  Cephei star  $\theta$  Ophiuchi: constraints on global stellar parameters and core overshooting", *Monthly Notices of the Royal Astronomical Society*, **381**, 1482 – 1488
- Brodskii M. A., Levshin A., 1977, "Asimptoticheskiy metod opredeleniya skorostnogo razreza Zemli po chasotam yeye sobstvennykh kolebanii", *Dodl. Akad. Nauk. SSSR*, **233**, 312 – 315 (English translation: "Asymptotic method of determining the velocity profile of the Earth from its natural oscillation frequencies")
- Brodsky M. A., Vorontsov S. V., 1987, "An asymptotic technique for solving the inverse problem of helioseismology", *Pis'ma Astron. Zh.*, **13**, 438 – 443 (English translation: *Sov. Astron. Lett.*, **13**, 179 – 181)
- Brodsky M. A., Vorontsov S. V., 1988, "On the technique of the inversion of helioseismological data", *Proc. IAU Symposium No 123, Advances in helio- and asteroseismology*, Eds J. Christensen-Dalsgaard, S. Frandsen, Reidel, Dordrecht, 137 – 140
- Brodsky M. A., Vorontsov S. V., 1993, "Asymptotic theory of intermediate- and high-degree solar acoustic oscillations", *Astrophysical Journal*, **409**, 455 – 464
- Brookes J. R., Isaak G. R., van der Raay H. B., 1976, "Observation of free oscillations of the Sun", *Nature*, **259**, 92 – 95
- Brookes J. R., Isaak G. R., van der Raay H. B., 1978, "A resonant-scattering solar spectrometer", *Monthly Notices of the Royal Astronomical Society*, **185**, 1 – 17
- Brown A. G. A., Verschueren W., 1997, "High S/N Echelle spectroscopy in young stellar groups. II. Rotational velocities of early-type stars in SCO OB2", *Astronomy and Astrophysics*, **319**, 811 – 838
- Brown T. M., 1984, "The Fourier tachometer II – An instrument for measuring global solar velocity fields", In *Proc. Conf. on Solar Seismology from Space*, Eds R. K. Ulrich, J. Harvey, E. J. Rhodes, J. Toomre, NASA, JPL Publications **84**, 157 – 163
- Brown T. M., 1985, "Solar rotation as a function of depth and latitude", *Nature*, **317**, 591 – 594
- Brown T. M., Christensen-Dalsgaard J., 1998, "Accurate determination of the solar photospheric radius", *Astrophysical Journal*, **500**, L195 – L198

- Brown T. M., Gilliland R. L., 1990, "A search for solar-like oscillations in Alpha Centauri A", *Astrophysical Journal*, **350**, 839 – 845
- Brown T. M., Gilliland R. L., 1994, "Asteroseismology", *Annual Review of Astronomy and Astrophysics*, **32**, 37 – 82
- Brown T. M., Morrow C. A. 1987, "Depth and latitude dependence of solar rotation", *Astrophysical Journal*, **314**, L21 – L26
- Brown T. M., Christensen-Dalsgaard J., Dziembowski W. A., Goode P., Gough D. O., Morrow C. A., 1989, "Inferring the Sun's internal angular velocity from observed p-mode frequency splittings", *Astrophysical Journal*, **343**, 526 – 546
- Brown T. M., Gilliland R. L., Noyes R. W., Ramsey L. W., 1991, "Detection of possible p-mode oscillations on Procyon", *Astrophysical Journal*, **368**, 599 – 609
- Brown T. M., Christensen-Dalsgaard J., Mihalas B., Gilliland R. L., 1994, "The effectiveness of oscillation frequencies in constraining stellar model parameters", *Astrophysical Journal*, **427**, 1013 – 1034
- Brown T. M., Kennelly E. J., Korzennik S. G., Nisenson P., Noyes R. W., Horner S. D., 1997, "A Radial Velocity Search for p-Mode Pulsations in eta Bootis", *Astrophysical Journal*, **475**, 322 – 327
- Brown T. M., Kotak R., Horner S. D., Kennelly E. J., Korzennik S., Nisenson P., Noyes R. W., 1998a, "A Search for Line Shape and Depth Variations in 51 Pegasi and  $\tau$  Bootis", *Astrophysical Journal*, **494**, L85 – L89
- Brown T. M., Kotak R., Horner S. D., Kennelly E. J., Korzennik S., Nisenson P., Noyes R. W., 1998b, "Exoplanets or Dynamic Atmospheres? The Radial Velocity and Line Shape Variations of 51 Pegasi and  $\tau$  Bootis", *Astrophysical Journal Supplement Series*, **117**, 563 – 585
- Brun A. S., Turck-Chièze S., Zahn J. P., 1999, "Standard solar models in the light of new helioseismic constraints. II. Mixing below the convection zone", *Astrophysical Journal*, **525**, 1032 – 1041 (Erratum: *Astrophysical Journal*, **536**, 1005)
- Bruntt H., 2007, "Asteroseismology with the WIRE satellite", *Communications in Asteroseismology*, **150**, 326 – 332
- Bruntt H., Southworth J., 2007, "Eclipsing Binary Stars from Space", In *Proc. IAU Symposium 240: Binary Stars as Critical Tools & Tests in Contemporary Astrophysics*, Eds W.I. Hartkopf, E.F. Guinan, P. Harmanec, Cambridge University Press, **240**, 624 – 627
- Bruntt H., Frandsen S., Gilliland R. L., Christensen-Dalsgaard J., Petersen J. O., Guhathakurta P., Edmonds P. D., Bono G., 2001, "SX Phoenicis stars in the core of 47 Tucanae", *Astronomy and Astrophysics*, **371**, 614 – 625
- Bruntt H., Kjeldsen H., Buzasi D. L., Bedding T. R., 2005, "Evidence for Granulation and Oscillations in Procyon from Photometry with the WIRE Satellite", *Astrophysical Journal*, **633**, 440 – 446
- Bruntt H., Stello D., Suárez J. C., Arentoft T., Bedding T. R., Bouzid M. Y., Csubry Z., Dall T. H., Dind Z. E., Frandsen S., Gilliland R. L., Jacob

- A. P., Jensen H. R., Kang Y. B., Kim S.-L., Kiss L. L., Kjeldsen H., Koo J.-R., Lee J.-A., Lee C.-U., Nuspl J., Sterken C., Szabó R., 2007, “Multisite campaign on the open cluster M67 - III.  $\delta$  Scuti pulsations in the blue stragglers”, *Monthly Notices of the Royal Astronomical Society*, **378**, 1371 – 1384
- Bruntt H., De Cat P., Aerts C., 2008, “A spectroscopic study of southern (candidate)  $\gamma$  Doradus stars. II. Detailed abundance analysis and fundamental parameters”, *Astronomy and Astrophysics*, **478**, 487 – 496
- Buccino A. P., Mauas P. J. D., 2008, “Mg II emission lines as stellar activity indicators of main sequence F-K stars”, *Astronomy and Astrophysics*, **483**, 903 – 910
- Buchler J. R., Goupil M.-J., Hansen C. J., 1997, “On the role of resonances in nonradial pulsators”, *Astronomy and Astrophysics*, **321**, 159 – 176
- Burgers J. M., 1969, *Flow equations for composite gases*, Academic Press, New York
- Burke E. W., Jr., Rolland W. W., Boy W. R., 1970, “A Photoelectric Study of Magnetic Variable Stars”, *Journal of the Royal Astronomical Society of Canada*, **64**, 353 – 369
- Burki G., 1978, “The semi-period-luminosity-color relation for supergiant stars”, *Astronomy and Astrophysics*, **65**, 357 – 362
- Burki G., Maeder A., Rufener F., 1978, “Variable stars of small amplitude. III - Semi-period of variation for seven B2 to G0 supergiant stars”, *Astronomy and Astrophysics*, **65**, 363 – 367
- Burki G., Barblan F., Carrier F., 2005, “Physical parameters of the Algol system VW Hydriæ from simultaneous analysis of GENEVA seven-colour light curves”, *New Astronomy*, **11**, 197 – 206
- Burrows A., Hayes J., Fryxell B. A., 1995, “On the Nature of Core-Collapse Supernova Explosions”, *Astrophysical Journal*, **450**, 830 – 864
- Burrows A., Walder R., Ott C. D., Livne E., 2005, “Rotating Core Collapse and Bipolar Supernova Explosions”, In *The Fate of the Most Massive Stars*, Eds R. Humphreys, K. Stanek, Astronomical Society of the Pacific Conference Series, San Francisco, **332**, 358
- Buta R. J., Smith M. A., 1979, “The light variations of nonradial pulsators - Theory and application to the line profile variable 53 Persei”, *Astrophysical Journal*, **232**, 213 – 235
- Butler R. P., Bedding T. R., Kjeldsen H., McCarthy C., O’Toole S. J., Tinney C. G., Marcy G. W., Wright J. T., 2004, “Ultra-High-Precision Velocity Measurements of Oscillations in  $\alpha$  Centauri A”, *Astrophysical Journal*, **600**, L75 – L78
- Buzasi D., 2000, “Platforms of opportunity: asteroseismology by Piggyback”, In *Stellar Clusters and Associations: Convection, Rotation, and Dynamos*, Eds R. Pallavicini, G. Micela, S. Sciortino, Publications of the Astronomical Society of the Pacific Conference Series, San Francisco, **198**, 557 – 560

- Buzasi D. L., 2004, "The performance of a high-precision photometry mission in space", In *Stellar Structure and Habitable Planet Finding*, Eds F. Favata, S. Aigrain and A. Wilson, Noordwijk: ESA Publications Division, **538**, 205 – 213
- Buzasi D., Catanzarite J., Laher R., Conrow T., Shupe D., Gautier T. N., III, Kreidl T., Everett D., 2000, "The Detection of Multimodal Oscillations on  $\alpha$  Ursae Majoris", *Astrophysical Journal*, **532**, L133 – L136
- Buzasi D. L., Bruntt H., Bedding T. R., Retter A., Kjeldsen H., Preston H. L., Mandeville W. J., Suarez J. C., Catanzarite J., Conrow T., Laher R., 2005, "Altair: The Brightest  $\delta$  Scuti Star", *Astrophysical Journal*, **619**, 1072 – 1076
- Cacciani A., Fofi M., 1978, "The magneto-optical filter. II. Velocity field measurements", *Solar Physics*, **59**, 179 – 189
- Caffau E., Ludwig H.-G., Steffen M., Ayres T. R., Bonifacio P., Cayrel R., Freytag B., Plez B., 2008, "The photospheric solar oxygen project. I. Abundance analysis of atomic lines and influence of atmospheric models", *Astronomy and Astrophysics*, **488**, 1031 – 1046
- Caffau E., Maiorca E., Bonifacio P., Faraggiana R., Steffen M., Ludwig H.-G., Kamp I., Busso M., 2009, "The solar photospheric nitrogen abundance. Analysis of atomic transitions with 3D and 1D model atmospheres", *Astronomy and Astrophysics*, **498**, 877 – 884
- Campos A. J., Smith M. A., 1980a, "Pulsational mode-typing in line profile variables. II - rho Puppis and delta Scuti", *Astrophysical Journal*, **238**, 667 – 673
- Campos A. J., Smith M. A., 1980b, "Pulsational mode-typing in line profile variables. I - Four Beta Cephei stars", *Astrophysical Journal*, **238**, 250 – 265
- Canuto V. M., Mazzitelli I., 1991, "Stellar turbulent convection: a new model and applications", *Astrophysical Journal*, **370**, 295 – 311
- Canuto V. M., Mazzitelli I., 1992, "Further improvements of a new model for turbulent convection in stars", *Astrophysical Journal*, **389**, 724 – 730
- Carrier F., Bourban G., 2003, "Solar-like oscillations in the K1 dwarf star alpha Cen B", *Astronomy and Astrophysics*, **406**, L23 – L26
- Carrier F., Eggenberger P., 2006, "Astroseismology of the visual binary 70 Ophiuchi", *Astronomy and Astrophysics*, **450**, 695 – 699
- Carrier F., Bouchy F., Kienzle F., Bedding T. R., Kjeldsen H., Butler R. P., Baldry I. K., O'Toole S. J., Tinney C. G., Marcy G. W., 2001, "Solar-like oscillations in  $\beta$  Hydri: Confirmation of a stellar origin for the excess power", *Astronomy and Astrophysics*, **378**, 142 – 145
- Carrier F., Eggenberger P., Bouchy F., 2005, "New seismological results on the G0 IV  $\eta$  Bootis", *Astronomy and Astrophysics*, **434**, 1085 – 1095
- Carrier F., Eggenberger P., Leyder J.-C., Debernardi Y., Royer F., 2007, "A search for solar-like oscillations in the Am star HD 209625", *Astronomy and Astrophysics*, **470**, 1009 – 1012

- Carrier F., Kjeldsen H., Bedding T. R., Brewer B. J., Butler R. P., Eggenberger P., Grundahl F., McCarthy C., Retter A., Tinney C. G., 2007, “Solar-like oscillations in the metal-poor subgiant  $\nu$  Indi. II. Acoustic spectrum and mode lifetime”, *Astronomy and Astrophysics*, **470**, 1059 – 1063
- Carroll B. W., Hansen C. J., 1982, “The nonadiabatic analysis of nonradial modes of stellar oscillation in the presence of slow rotation”, *Astrophysical Journal*, **263**, 352 – 365
- Cassisi S., Salaris M., Bono G., 2002, “The shape of the red giant branch bump as a diagnostic of partial mixing processes in low-mass stars”, *Astrophysical Journal*, **565**, 1231 – 1238
- Cassisi S., Potekhin A. Y., Pietrinferni A., Catelan M., Salaris M., 2007, “Updated electron-conduction opacities: the impact on low-mass stellar models”, *Astrophysical Journal*, **661**, 1094 – 1104
- Castanheira B. G., Nitta A., Kepler S. O., Winget D. E., Koester D., 2005, “HST observations of the pulsating white dwarf GD 358”, *Astronomy and Astrophysics*, **432**, 175 – 179
- Castanheira B. G., Kepler S. O., Mullally F., Winget D. E., Koester D., Voss B., Kleinman S. J., Nitta A., Eisenstein D. J., Napiwotzki R., Reimers D., 2006, “Discovery of eleven new ZZ Ceti stars”, *Astronomy and Astrophysics*, **450**, 227 – 231
- Catala C., 2003, “ $\delta$  Scuti Pulsations in Pre-main Sequence Stars”, *Astrophysics and Space Science*, **284**, 53 – 60
- Catelan M., 2007, “Structure and Evolution of Low-Mass Stars: An Overview and Some Open Problems”, *Graduate School in Astronomy: XI Special Courses at the National Observatory of Rio de Janeiro (XI CCE)*, **930**, 39 – 90
- Chaboyer B., Zahn J.-P., 1992, “Effect of horizontal turbulent diffusion on transport by meridional circulation”, *Astronomy and Astrophysics*, **253**, 173 – 177
- Chadid M., Kolenberg K., Aerts C., Gillet D., 1999, “First detection of a frequency multiplet in the line-profile variations of RR Lyrae: towards an understanding of the Blazhko effect”, *Astronomy and Astrophysics*, **352**, 201 – 210
- Chadid M., De Ridder J., Aerts C., Mathias P., 2001, “20 CVn: A monoperiodic radially pulsating delta Scuti star”, *Astronomy and Astrophysics*, **375**, 113 – 121
- Chadid M., Wade G. A., Shorlin S. L. S., Landstreet J. D., 2004, “No evidence of a strong magnetic field in the Blazhko star RR Lyrae”, *Astronomy and Astrophysics*, **413**, 1087 – 1093
- Chandrasekhar S., 1964, “A general Variational Principle Governing the Radial and the Non-radial Oscillations of Gaseous Masses”, *Astrophysical Journal*, **139**, 664 – 674
- Chang H.-Y., Gough D. O., 1998, “On the power distribution of solar p modes”, *Solar Physics*, **181**, 251 – 263

- Chaplin W. J., 2006, *Music of the Sun. The story of helioseismology*, Oneworld Publications, Oxford
- Chaplin W. J., Appourchaux T., 1999, “Depth of excitation and reversal of asymmetry of low- $\ell$  solar p modes: a complementary analysis of BiSON and VIRGO/SPM data”, *Monthly Notices of the Royal Astronomical Society*, **309**, 761 – 768
- Chaplin W. J., Basu S., 2008, “Perspectives in global helioseismology, and the road ahead”, *Solar Physics*, **251**, 53 – 75
- Chaplin W. J., Elsworth Y., Howe R., Isaak G. R., McLeod C. P., Miller B. A., van der Raay H. B., Wheeler S. J., New R., 1996, “BiSON performance”, *Solar Physics*, **168**, 1 – 18
- Chaplin W. J., Elsworth Y., Howe R., Isaak G. R., McLeod C. P., Miller B. A., New R., 1997, “The observation and simulation of stochastically excited solar p modes”, *Monthly Notices of the Royal Astronomical Society*, **287**, 51 – 56
- Chaplin W. J., Christensen-Dalsgaard J., Elsworth Y., Howe R., Isaak G. R., Larsen R. M., New R., Schou J., Thompson M. J., Tomczyk S., 1999, “Rotation of the solar core from BiSON and LOWL frequency observations”, *Monthly Notices of the Royal Astronomical Society*, **308**, 405 – 414
- Chaplin W. J., Elsworth Y., Isaak G. R., Marchenkov K. I., Miller B. A., New R., 2001a, “Rigid rotation of the solar core? On the reliable extraction of low- $\ell$  rotational p-mode splittings from full-disc observations of the Sun”, *Monthly Notices of the Royal Astronomical Society*, **327**, 1127 – 1136
- Chaplin W. J., Elsworth Y., Isaak G. R., Marchenkov K. I., Miller B. A., New R., 2001b, “Changes to low- $\ell$  solar p-mode frequencies over the solar cycle: correlations on different time-scales”, *Monthly Notices of the Royal Astronomical Society*, **322**, 22 – 30
- Chaplin W. J., Elsworth Y., Isaak G. R., Marchenkov K. I., Miller B. A., New R., Pinter B., Appourchaux T., 2002a, “Peak finding at low signal-to-noise: low- $\ell$  solar acoustic eigenmodes at  $n \leq 9$  from the analysis of BiSON data”, *Monthly Notices of the Royal Astronomical Society*, **336**, 979 – 991
- Chaplin W. J., Elsworth Y., Isaak G. R., Miller B. A., New R., 2002b, “On the measurement precision of solar p-mode eigenfrequencies”, *Monthly Notices of the Royal Astronomical Society*, **330**, 731 – 736
- Chaplin W. J., Sekii T., Elsworth Y., Gough D. O., 2004a, “On the detectability of a rotation-rate gradient in the solar core”, *Monthly Notices of the Royal Astronomical Society*, **355**, 535 – 542
- Chaplin W. J., Elsworth Y., Isaak G. R., Miller B. A., New R., 2004b, “The solar cycle as seen by low- $\ell$  p-mode frequencies: comparison with global and decomposed activity proxies”, *Monthly Notices of the Royal Astronomical Society*, **352**, 1102 – 1108
- Chaplin W. J., Houdek G., Elsworth Y., Gough D. O., Isaak G. R., New R., 2005, “On model predictions of the power spectral density of radial solar

- p modes”, *Monthly Notices of the Royal Astronomical Society*, **360**, 859 – 868
- Chaplin W. J., Appourchaux T., Baudin F., Boumier P., Elsworth Y., Fletcher S. T., Fossat E., García R. A., Isaak G. R., Jiménez A., Jiménez-Reyes S. J., Lazrek M., Leibacher J. W., Lochard J., New R., Pallé P., Régulo C., Salabert D., Seghouani N., Toutain T., Wachter R., 2006, “Solar FLAG hare and hounds: on the extraction of rotational p-mode splittings from seismic, Sun-as-a-star data”, *Monthly Notices of the Royal Astronomical Society*, **369**, 985 – 996
- Chaplin W. J., Elsworth Y., Miller B. A., Verner G. A., 2007a, “Solar *p*-mode frequencies over three solar cycles”, *Astrophysical Journal*, **659**, 1749 – 1760
- Chaplin W. J., Serenelli A. M., Basu S., Elsworth Y., New R., Verner G. A., 2007b, “Solar heavy-element abundance: constraints from frequency separation ratios of low-degree *p*-modes”, *Astrophysical Journal*, **670**, 872 – 884
- Chaplin W. J., Appourchaux T., Arentoft T., Ballot J., Christensen-Dalsgaard J., Creevey O. L., Elsworth Y., Fletcher S. T., García R. A., Houdek G., Jiménez-Reyes S. J., Kjeldsen H., New R., Régulo C., Salabert D., Sekii T., Sousa S. G., Toutain T., and the rest of the asteroFLAG group, 2008a, “AsteroFLAG: First results from hare-and-hound Exercise #1”, *Astron. Nach.*, **329**, 549 – 557
- Chaplin W. J., Houdek G., Appourchaux T., Elsworth Y., New R., Toutain T., 2008b, “Challenges for asteroseismic analysis of Sun-like stars”, *Astronomy and Astrophysics*, **485**, 813 – 822
- Chaplin W. J., Houdek G., Elsworth Y., New R., Bedding T. R., Kjeldsen H., 2009, “Excitation and damping of *p*-mode oscillations of α Cen B”, *Astrophysical Journal*, **692**, 531 – 537
- Charbonneau P., 2005, “Dynamo models of the solar cycle”, *Living Reviews in Solar Physics*, **2**, 2. URL (cited on 17/6/05): <http://www.livingreviews.org/lrsp-2005-2>
- Charbonneau P., MacGregor K. B., 1993, “Angular momentum transport in magnetized stellar radiative zones. II. The solar spin-down”, *Astrophysical Journal*, **417**, 762 – 780
- Charbonneau P., Christensen-Dalsgaard J., Henning R., Larsen R. M., Schou J., Thompson M. J., Tomczyk S., 1999, “Helioseismic constraints on the structure of the solar tachocline”, *Astrophysical Journal*, **527**, 445 – 460
- Charbonnel C., Talon S., 2005, “Influence of gravity waves on the internal rotation and Li abundance of solar-type stars”, *Science*, **309**, 2189 – 2191
- Charpinet S., Fontaine G., Brassard P., Dorman B., 1996, “The Potential of Asteroseismology for Hot, Subdwarf B Stars: A New Class of Pulsating Stars?”, *Astrophysical Journal*, **471**, L103 – L107
- Charpinet S., Fontaine G., Brassard P., Chayer P., Rogers F. J., Iglesias C. A., Dorman B., 1997, “A Driving Mechanism for the Newly Discovered Class of Pulsating Subdwarf B Stars”, *Astrophysical Journal*, **483**, L123 – L127

- Charpinet S., Silvotti R., Bonanno A., Fontaine G., Brassard P., Chayer P., Green E. M., Bergeron P., Bernabei S., Leccia S., Kjeldsen H., Janulis R., Frasca A., Østensen R., Kim S.-L., Park B.-G., Jiang X., Reed M. D., Patterson R. S., Gietzen K. M., Clark P. J., Wolf G. W., Lipkin Y., Formiggini L., Leibowitz E., Oswalt T. D., Rudkin M., Johnston K., 2006, “The rapidly pulsating subdwarf B star PG 1325+101. II. Structural parameters from asteroseismology”, *Astronomy and Astrophysics*, **459**, 565 – 576
- Charpinet S., Van Grootel V., Reese D., Fontaine G., Green, E., Brassard P., Chayer P., 2008, “Testing the forward modelling approach in asteroseismology. II. Structure and internal dynamics of the hot B subdwarf component in the close eclipsing binary system PG 1336-018”, *Astronomy and Astrophysics*, **489**, 377 – 394
- Chiosi C., Maeder A., 1986, “The evolution of massive stars with mass loss”, *Annual Review of Astronomy and Astrophysics*, **24**, 329 – 375
- Chitre S. M., Christensen-Dalsgaard J., Thompson M. J., 1998, “Diagnostic potential of the solar f modes”, In *Structure and dynamics of the interior of the Sun and Sun-like stars; Proc. SOHO 6/GONG 98 Workshop*, Eds S. G. Korzennik, A. Wilson, ESA SP-418, ESA Publications Division, Noordwijk, The Netherlands, 141 – 145
- Chlebowski T., 1978, “Nonradial oscillations of slowly rotating white dwarfs”, *Acta Astronomica*, **28**, 441 – 463
- Chou D.-Y., Sun M.-T., Huang T.-Y., Jiménez A., Lai S.-P., Chi P.-J., Ou K.-T., Wang C.-C., Lu J.-Y., Chu A.-L., Niu C.-S., Mu T.-M., Chen K.-R., Chou Y.-P., Chao H., Rabello-Soares M. C., Ai G., Wang G.-P., Zirin H., Marquette W., Nenow J., 1995, “Taiwan Oscillation Network”, *Solar Physics*, **160**, 237 – 243
- Christensen-Dalsgaard J., 1976, “On isolated stars in non-radial oscillation”, *Monthly Notices of the Royal Astronomical Society*, **174**, 87 – 90
- Christensen-Dalsgaard J., 1978, *Solar oscillations*, PhD Dissertation, University of Cambridge, UK
- Christensen-Dalsgaard J., 1980, “On adiabatic non-radial oscillations with moderate or large  $l$ ”, *Monthly Notices of the Royal Astronomical Society*, **190**, 765 – 791
- Christensen-Dalsgaard J., 1981, “The effect of non-adiabaticity on avoided crossings of non-radial stellar oscillations”, *Monthly Notices of the Royal Astronomical Society*, **194**, 229 – 250
- Christensen-Dalsgaard J., 1982a, “Seismological studies of the sun and other stars”, *Advances in Space Research*, **2**, 11 – 19
- Christensen-Dalsgaard J., 1982b, “On solar models and their periods of oscillation”, *Monthly Notices of the Royal Astronomical Society*, **199**, 735 – 761
- Christensen-Dalsgaard J., 1984a, “Optimized response functions for two-dimensional observations of solar oscillations”, *Proceedings of Conference*

- on Solar Seismology from Space*, Eds R. K. Ulrich, J. Harvey, E. J. Rhodes, J. Toomre, NASA, JPL Publications **84**, 219 – 253
- Christensen-Dalsgaard J., 1984b, “What will asteroseismology teach us?”, *Space Research Prospects in Stellar Activity and Variability*, Eds A. Mangeney, F. Praderie, Paris Observatory Press, 11 – 45
- Christensen-Dalsgaard J., 1988, “A Hertzsprung-Russell diagram for stellar oscillations”, *Proc. IAU Symposium No 123, Advances in helio- and asteroseismology*, Eds Christensen-Dalsgaard, J., Frandsen, S., Reidel, Dordrecht, 295 – 298
- Christensen-Dalsgaard J., 1989, “The effect of rotation on whole-disc Doppler observations of solar oscillations”, *Monthly Notices of the Royal Astronomical Society*, **239**, 977 – 994
- Christensen-Dalsgaard J., 1991a, “Some aspects of the theory of solar oscillations”, *Geophys. Astrophys. Fluid Dynamics*, **62**, 123 – 152
- Christensen-Dalsgaard J., 1991b, “Solar oscillations and the physics of the solar interior”, In *Challenges to theories of the structure of moderate-mass stars, Lecture Notes in Physics*, vol. **388**, Eds D. O. Gough, J. Toomre, Springer, Heidelberg, 11 – 36
- Christensen-Dalsgaard J., 1993a, “On the Asteroseismic HR Diagram”, In *GONG 1992. Seismic Investigation of the Sun and Stars*, Astronomical Society of the Pacific Conference Series, San Francisco, **42**, 347 – 350
- Christensen-Dalsgaard J., 1993b, “Pulsation theory and stellar structure”, In *Proc. IAU Colloquium 137: Inside the stars*, Eds A. Baglin, W. W. Weiss, Astronomical Society of the Pacific Conference Series, San Francisco, **40**, 483 – 496
- Christensen-Dalsgaard J., 1996, “Testing a solar model: the forward problem”, In *Proc. VI IAC Winter School “The structure of the Sun”*, Eds T. Roca Cortés, F. Sánchez, Cambridge University Press, 47 – 139
- Christensen-Dalsgaard J., 2000, “An introduction to the theory of  $\delta$  Scuti stars”, In *Delta Scuti and related stars*, Eds M. Breger, M. H. Montgomery, Astronomical Society of the Pacific Conference Series, San Francisco, **210**, 187 – 214
- Christensen-Dalsgaard J., 2002, “Helioseismology”, *Reviews of Modern Physics*, **74**, 1073 – 1129
- Christensen-Dalsgaard J., 2004a, “An overview of helio- and asteroseismology”, In *Proc. SOHO 14 - GONG 2004: Helio- and Asteroseismology: Towards a golden future*, Ed. D. Danesy, ESA SP-559, ESA Publication Division, Noordwijk, The Netherlands, 1 – 33
- Christensen-Dalsgaard J., 2004b, “Physics of solar-like oscillations”, *Solar Physics*, **220**, 137 – 168
- Christensen-Dalsgaard J., 2008a, “ASTEC – the Aarhus STellar Evolution Code”, *Astrophysics and Space Science*, **316**, 13 – 24
- Christensen-Dalsgaard J., 2008b, “ADIPLS – the Aarhus adiabatic pulsation package”, *Astrophysics and Space Science*, **316**, 113 – 120

- Christensen-Dalsgaard J., 2009, "The Sun as a fundamental calibrator of stellar evolution", In *Proc. IAU Symp. 258, The Ages of Stars*, Eds E. E. Mamajek, D. R. Soderblom, R. F. G. Wyse, IAU and Cambridge University Press, in press  
[\[arXiv:0904.0358v1 \[astro-ph.SR\]\]](https://arxiv.org/abs/0904.0358v1)
- Christensen-Dalsgaard J., Däppen W., 1992, "Solar oscillations and the equation of state", *Astronomy and Astrophysics Review*, **4**, 267 – 361
- Christensen-Dalsgaard J., Di Mauro M. P., 2007, "Diffusion and helioseismology", In *Stellar Evolution and Seismic Tools for Asteroseismology: Diffusive Processes in Stars and Seismic Analysis*, Eds C. W. Straka, Y. Lebreton, M. J. P. F. G. Monteiro, European Astronomical Society Publication Series, EDP Sciences, Les Ulis, France, **26**, 3 – 16
- Christensen-Dalsgaard J., Dziembowski W. A., 2000, "Basic aspects of stellar structure and pulsation", In *Variable Stars as Essential Astrophysical Tools*, Ed. C. İbanoğlu, Kluwer Academic Publishers, 1 – 57
- Christensen-Dalsgaard J., Frandsen S., 1983a, "Stellar 5 min oscillations", *Solar Physics*, **82**, 469 – 486
- Christensen-Dalsgaard J., Frandsen S., 1983b, "Radiative transfer and solar oscillations", *Solar Physics*, **82**, 165 – 204
- Christensen-Dalsgaard J., Gough D. O., 1976, "Towards a helioseological inverse problem", *Nature*, **259**, 89 – 92
- Christensen-Dalsgaard J., Gough D. O., 1980, "Is the Sun helium-deficient?", *Nature*, **288**, 544 – 547
- Christensen-Dalsgaard J., Gough D. O., 1981, "Comparison of observed solar whole-disk oscillation frequencies with the predictions of a sequence of solar models", *Astronomy and Astrophysics*, **104**, 173 – 176
- Christensen-Dalsgaard J., Gough D. O., 1982, "On the interpretation of five-minute oscillations in solar spectrum line shifts", *Monthly Notices of the Royal Astronomical Society*, **198**, 141 – 171
- Christensen-Dalsgaard J., Gough D. O., 2001, "On the dipolar f mode of stellar oscillation", *Monthly Notices of the Royal Astronomical Society*, **326**, 1115 – 1121
- Christensen-Dalsgaard J., Mullan D. J., 1994, "Accurate frequencies of polytropic models", *Monthly Notices of the Royal Astronomical Society*, **270**, 921 – 935
- Christensen-Dalsgaard J., Pérez Hernández F., 1991, "Influence of the upper layers of the Sun on the p-mode frequencies", In *Challenges to theories of the structure of moderate-mass stars, Lecture Notes in Physics*, vol. **388**, 43 – 50, Eds D. O. Gough, J. Toomre, Springer, Heidelberg
- Christensen-Dalsgaard J., Pérez Hernández F., 1992, "Phase-function differences for stellar acoustic oscillations – I. Theory", *Monthly Notices of the Royal Astronomical Society*, **257**, 62 – 88
- Christensen-Dalsgaard J., Petersen J. O., 1995, "Pulsation models of the double-mode Cepheids in the Large Magellanic Cloud", *Astronomy and Astrophysics*, **299**, L17 – 21

- Christensen-Dalsgaard J., Schou J., 1988, "Differential rotation in the solar interior", *Seismology of the Sun, Sun-like Stars*, 149 – 153, Eds V. Domingo, E. J. Rolfe, ESA SP-286, ESA Publications Division, Noordwijk, The Netherlands
- Christensen-Dalsgaard J., Thompson M. J., 1993, "A preprocessing strategy for helioseismic inversions", *Astronomy and Astrophysics*, **272**, L1 – L4
- Christensen-Dalsgaard J., Thompson M. J., 1997, "On solar p-mode frequency shifts caused by near-surface model changes", *Monthly Notices of the Royal Astronomical Society*, **284**, 527 – 540
- Christensen-Dalsgaard J., Thompson M. J., 2007, "Observational results and issues concerning the tachocline", In *The solar tachocline*, Eds D. W. Hughes, R. Rosner, N. O. Weiss, Cambridge University Press, 53 – 85
- Christensen-Dalsgaard J., Dilke F. W. W., Gough D. O., 1974, "The stability of a solar model to non-radial oscillations", *Monthly Notices of the Royal Astronomical Society*, **169**, 429 – 445
- Christensen-Dalsgaard J., Dziembowski W., Gough D. O., 1980, "How deep is the solar convection zone?", *Lecture Notes in Physics*, **125**, Eds W. Dziembowski, H. A. Hill, Springer, Heidelberg, 313 – 341
- Christensen-Dalsgaard J., Duvall T. L., Gough D. O., Harvey J. W., Rhodes Jr E. J., 1985, "Speed of sound in the solar interior", *Nature*, **315**, 378 – 382
- Christensen-Dalsgaard J., Gough D. O., Pérez Hernández F., 1988a, "Stellar disharmony", *Monthly Notices of the Royal Astronomical Society*, **235**, 875 – 880
- Christensen-Dalsgaard J., Gough D. O., Thompson M. J., 1988b, "Determination of the solar internal sound speed by means of a differential asymptotic inversion" *Seismology of the Sun, Sun-like Stars*, Eds V. Domingo, E. J. Rolfe, ESA SP-286, ESA Publications Division, Noordwijk, The Netherlands, 493 – 497
- Christensen-Dalsgaard J., Däppen W., Lebreton Y., 1988c, "Solar oscillation frequencies and the equation of state", *Nature*, **336**, 634 – 638
- Christensen-Dalsgaard J., Gough D. O., Libbrecht K. G., 1989a, "Seismology of solar oscillation line widths", *Astrophysical Journal*, **341**, L103 – L106
- Christensen-Dalsgaard J., Gough D. O., Thompson M. J., 1989b, "Differential asymptotic sound-speed inversions", *Monthly Notices of the Royal Astronomical Society*, **238**, 481 – 502
- Christensen-Dalsgaard J., Schou J., Thompson M. J., 1990, "A comparison of methods for inverting helioseismic data", *Monthly Notices of the Royal Astronomical Society*, **242**, 353 – 369
- Christensen-Dalsgaard J., Gough D. O., Thompson M. J., 1991, "The depth of the solar convection zone", *Astrophysical Journal*, **378**, 413 – 437
- Christensen-Dalsgaard J., Proffitt C. R., Thompson M. J., 1993a, "Effects of diffusion on solar models and their oscillation frequencies", *Astrophysical Journal*, **403**, L75 – L78

- Christensen-Dalsgaard J., Hansen P. C., Thompson M. J., 1993b, "Generalized singular value decomposition analysis of helioseismic inversions", *Monthly Notices of the Royal Astronomical Society*, **264**, 541 – 564
- Christensen-Dalsgaard J., Monteiro M. J. P. F. G., Thompson M. J., 1995a, "Helioseismic estimation of convective overshoot in the Sun", *Monthly Notices of the Royal Astronomical Society*, **276**, 283 – 292
- Christensen-Dalsgaard, J., Bedding, T. R., Kjeldsen, H., 1995b, "Modelling solar-like oscillations in  $\eta$  Bootis", *Astrophysical Journal*, **443**, L29 – L32
- Christensen-Dalsgaard J., Däppen W., Ajukov S. V., Anderson E. R., Antia H. M., Basu S., Baturin V. A., Berthomieu G., Chaboyer B., Chitre S. M., Cox A. N., Demarque P., Donatowicz J., Dziembowski W. A., Gabriel M., Gough D. O., Guenther D. B., Guzik J. A., Harvey J. W., Hill F., Houdek G., Iglesias C. A., Kosovichev A. G., Leibacher J. W., Morel P., Proffitt C. R., Provost J., Reiter J., Rhodes Jr. E. J., Rogers F. J., Roxburgh I. W., Thompson M. J., Ulrich R. K., 1996, "The current state of solar modeling", *Science*, **272**, 1286 – 1292
- Christensen-Dalsgaard J., Kjeldsen H., Mattei J. A., 2001, "Solar-like oscillations of semiregular variables", *Astrophysical Journal*, **562**, L141 – L144
- Christensen-Dalsgaard J., Di Mauro M. P., Schlattl H., Weiss A., 2005, "On helioseismic tests of basic physics", *Monthly Notices of the Royal Astronomical Society*, **356**, 587 – 595
- Christensen-Dalsgaard J., Di Mauro M. P., Houdek G., Pijpers F., 2009, "On the opacity change required to compensate for the revised solar composition", *Astronomy and Astrophysics*, **494**, 205 – 208
- Cioni M.-R. L., Marquette J.-B., Loup C., Azzopardi M., Habing H. J., Lasserre T., Lesquoy E., 2001, "Variability and spectral classification of LMC giants: Results from DENIS and EROS", *Astronomy and Astrophysics*, **377**, 945 – 954
- Claret A., 2000, "A new non-linear limb-darkening law for LTE stellar atmosphere models. Calculations for  $-5.0 \leq \log[M/H] \leq +1$ ,  $2000\text{K} \leq T_{\text{eff}} \leq 50000\text{K}$  at several surface gravities", *Astronomy and Astrophysics*, **363**, 1081 – 1190
- Claret A., 2003, "A new non-linear limb-darkening law for LTE stellar atmosphere models II K at several surface gravities. Geneva and Walraven systems: Calculations for  $-5.0 \leq \log[M/H] \leq +1$ ,  $2000\text{K} \leq T_{\text{eff}} \leq 50,000\text{K}$  at several surface gravities", *Astronomy and Astrophysics*, **401**, 657 – 660
- Claret A., 2004, "A new non-linear limb-darkening law for LTE stellar atmosphere models III. Sloan filters: Calculations for  $-5.0 \leq \log[M/H] \leq +1$ ,  $2000\text{K} \leq T_{\text{eff}} \leq 50000\text{K}$  at several surface gravities", *Astronomy and Astrophysics*, **428**, 1001 – 1005
- Claret A., 2007, "Does convective core overshooting depend on stellar mass? Tests using double-lined eclipsing binaries", *Astronomy and Astrophysics*, **475**, 1019 – 1025

- Claret A., Giménez A., Zahn J.-P. (Eds), 2005, *Tidal Evolution and Oscillations in Binary Stars*, Publications of the Astronomical Society of the Pacific Conference Series, San Francisco
- Clarke D., 2002, "String/Rope length methods using the Lafler-Kinman statistic", *Astronomy and Astrophysics*, **386**, 763 – 774
- Claverie A., Isaak G. R., McLeod C. P., van der Raay H. B., Roca Cortes T., 1979, "Solar structure from global studies of the 5-minute oscillation", *Nature*, **282**, 591 – 594
- Clayton G. C., Kerber F., Pirzkal N., De Marco O., Crowther P. A., Fedrow J. M., 2006, "V605 Aquilae: The Older Twin of Sakurai's Object", *Astrophysical Journal*, **646**, L69 – L72
- Clemens J. C., 1994, *The origin and evolution of the white dwarf stars*, PhD Dissertation, The University of Texas, Austin, USA
- Clemens J. C., Rosen R., 2004, "Observations of Nonradial Pulsations in Radio Pulsars", *Astrophysical Journal*, **609**, 340 – 353
- Clemens J. C., Rosen R., 2008, "A Pulsational Model for the Orthogonal Polarization Modes in Radio Pulsars", *Astrophysical Journal*, **680**, 664 – 670
- Clemens J. C., van Kerkwijk M. H., Wu Y., 2000, "Mode identification from time-resolved spectroscopy of the pulsating white dwarf G29-38", *Monthly Notices of the Royal Astronomical Society*, **314**, 220 – 228
- Collier Cameron A., Hilditch R. W., 1997, "Eclipse mapping of starspots on XY UMa in 1992 and 1995", *Monthly Notices of the Royal Astronomical Society*, **287**, 567 – 574
- Condon E. U., Odabasi H., 1980, *Atomic structure*, Cambridge University Press
- Connes P., 1985, "Absolute astronomical accelerometry", *Astrophysics and Space Science*, **110**, 211 – 255
- Conti P. S., 1984, "Basic Observational Constraints on the Evolution of Massive Stars", In *IAU Symposium 105: Observational Tests of the Stellar Evolution Theory*, Eds A. Maeder, A. Renzini, D. Reidel Publishing Company, Dordrecht, The Netherlands, **105**, 233
- Cook K., The MACHO Collaboration, 1997, "New Results from the MACHO Project: Variable Stars in the LMC, SMC and Bulge", In *Pulsating Stars - Recent Developments in Theory and Observation, 23rd meeting of the IAU, Joint Discussion 24, Kyoto, Japan*, **24** (abstract)
- Corbard T., Thompson M. J., 2002, "The subsurface radial gradient of solar angular velocity from MDI *f*-mode observations", *Solar Physics*, **205**, 211 – 229
- Corbard T., Blanc-Féraud L., Berthomieu G., Provost J., 1999, "Non linear regularization for helioseismic inversions. Application for the study of the solar tachocline", *Astronomy and Astrophysics*, **344**, 696 – 708
- Córsico A. H., Althaus L. G., Montgomery M. H., García-Berro E., 2005a, "The Effects of Crystallization on the Pulsational Properties of Massive ZZ Ceti Stars", In *14th European Workshop on White Dwarfs*, Eds D.

- Koester, S. Moehler, Astronomical Society of the Pacific Conference Series, San Francisco, **334**, 537
- Córsico A. H., Althaus L. G., Montgomery M. H., García-Berro E., Isern J., 2005b, “New evolutionary models for massive ZZ Ceti stars. II. The effects of crystallization on their pulsational properties”, *Astronomy and Astrophysics*, **429**, 277 – 290
- Córsico A. H., Althaus L. G., Miller Bertolami M. M., 2006, “New nonadiabatic pulsation computations on full PG 1159 evolutionary models: the theoretical GW Virginis instability strip revisited”, *Astronomy and Astrophysics*, **458**, 259 – 267
- Costa J. E. S., Kepler S. O., Winget D. E., O’Brien M. S., Kawaler S. D., Costa A. F. M., Giovannini O., Kanaan A., Mukadam A. S., Mullally F., Nitta A., Provençal J. L., Shipman H., Wood M. A., Ahrens T. J., Grauer A., Kilic M., Bradley P. A., Sekiguchi K., Crowe R., Jiang X. J., Sullivan D., Sullivan T., Rosen R., Clemens J. C., Janulis R., O’Donoghue D., Ogleza W., Baran A., Silvotti R., Marinoni S., Vauclair G., Dolez N., Chevreton M., Dreizler S., Schuh S., Deetjen J., Nagel T., Solheim J.-E., Gonzalez Perez J. M., Ulla A., Barstow M., Burleigh M., Good S., Metcalfe T. S., Kim S.-L., Lee H., Sergeev A., Akan M. C., Çakırlı Ö., Paparo M., Viraghalmay G., Ashoka B. N., Handler G., Hürkal Ö., Johannessen F., Kleinman S. J., Kalytis R., Krzesinski J., Klumpe E., Larrison J., Lawrence T., Meištas E., Martinez P., Nather R. E., Fu J.-N., Pakštienė E., Rosen R., Romero-Colmenero E., Riddle R., Seetha S., Silvestri N. M., Vučković M., Warner B., Zola S., Althaus L. G., Córsico A. H., Montgomery M. H., 2008, “The pulsation modes of the pre-white dwarf PG 1159-035”, *Astronomy and Astrophysics*, **477**, 627 – 640
- Cousins A. W. J., 1992, “Gamma Doradus”, *The Observatory*, **112**, 53 – 56
- Cousins A. W. J., Caldwell J. A. R., Menzies J. W., 1989, “The Period of gamma Doradus”, *Information Bulletin on Variable Stars*, **3412**, 1 – 1
- Couvidat S., Turck-Chièze S., Kosovichev A. G., 2003a, “Solar seismic models and the neutrino predictions”, *Astrophysical Journal*, **599**, 1434 – 1448
- Couvidat S., García R. A., Turck-Chièze S., Corbard T., Henney C. J., Jiménez-Reyes S., 2003b, “The rotation of the deep solar layers”, *Astrophysical Journal*, **597**, L77 – L79
- Covas E., Tavakol R., Moss D., Tworkowski A., 2000, “Torsional oscillations in the solar convection zone”, *Astronomy and Astrophysics*, **360**, L21 – L24
- Covas E., Moss D., Tavakol R., 2004, “The influence of density stratification and multiple nonlinearities on solar torsional oscillations”, *Astronomy and Astrophysics*, **416**, 775 – 782
- Cowley C. R., Hubrig S., Ryabchikova T. A., Mathys G., Piskunov N., Mittemayer P., 2001, “The core-wing anomaly of cool Ap stars. Abnormal Balmer Profiles”, *Astronomy and Astrophysics*, **367**, 939 – 942

- Cowley C. R., Hubrig S., Kamp I., 2006, "An Atlas of K-Line Spectra for Cool Magnetic CP Stars: The Wing-Nib Anomaly (WNA)", *Astrophysical Journal Supplement Series*, **163**, 393 – 400
- Cowling T. G., 1941, "The non-radial oscillations of polytropic stars", *Monthly Notices of the Royal Astronomical Society*, **101**, 367 – 375
- Cowling T. G., Newing R. A., 1949, "The oscillations of a rotating star", *Astrophysical Journal*, **109**, 149 – 158
- Cox A. N., 1980, "The masses of Cepheids", *Annual Review of Astronomy and Astrophysics*, **18**, 15 – 41
- Cox A. N., Tabor J. E., 1976, "Radiative opacity tables for 40 stellar mixtures", *Astrophysical Journal Supplement Series*, **31**, 271 – 312
- Cox A. N., Guzik J. A., 2004, "Theoretical prediction of an observed solar *g*-mode", *Astrophysical Journal*, **613**, L169 – L171
- Cox A. N., Morgan S. M., Rogers F. J., Iglesias C. A., 1992, "An opacity mechanism for the pulsations of OB stars", *Astrophysical Journal*, **393**, 272 – 277
- Cox J. P., 1967, "The linear theory: Initiation of pulsational instability in stars. Summary-introduction", In *IAU Symposium 28: Fifth Symposium on Cosmical Gas Dynamics. Aerodynamic phenomena in stellar atmospheres*, Ed. R. N. Thomas, Academic Press, London, 3 – 72
- Cox J. P., 1974, "Pulsating stars", *Reports on Progress in Physics*, **37**, 563 – 698
- Cox J. P., 1980, *Theory of Stellar Pulsation*, Princeton University Press
- Cox J. P., Giuli R. T., 1968, *Principles of Stellar Structure*, Gordon and Breach, New York
- Cox J. P., Whitney C., 1958, "Stellar pulsation. IV. A semitheoretical period-luminosity relation for classical Cepheids", *Astrophysical Journal*, **127**, 561 – 572
- Craig I. J. D., Brown J. C., 1986, *Inverse problems in astronomy: a guide to inversion strategies for remotely sensed data*, Adam Hilger, Bristol
- Creevey O. L., Monteiro M. J. P. F. G., Metcalfe T. S., Brown T. M., Jiménez-Reyes S. J., Belmonte J. A., 2007, "The complementary roles of interferometry and asteroseismology in determining the mass of solar-type stars", *Astrophysical Journal*, **659**, 616 – 625
- Crowe R., Gillet D., 1989, "Shock phenomena in Beta Cephei stars", *Astronomy and Astrophysics*, **211**, 365 – 382
- Crowther P. A., 2007, "Physical properties of Wolf-Rayet stars", *Annual Review of Astronomy and Astrophysics*, **45**, 177 – 219
- Crowther P. A., Smith L. J., 1997, "Fundamental parameters of Wolf-Rayet stars. VI. Large Magellanic Cloud WNL stars", *Astronomy and Astrophysics*, **320**, 500 – 524
- Cugier H., Daszyńska J., 2001, "Spectroscopic nonadiabatic observables in  $\beta$  Cephei models", *Astronomy and Astrophysics*, **377**, 113 – 122

- Cugier H., Dziembowski W. A., Pamyatnykh A. A., 1994, "Nonadiabatic observables in beta Cephei models", *Astronomy and Astrophysics*, **291**, 143 – 154
- Cunha M. S., 2001, "The sixth frequency of roAp star HR 1217", *Monthly Notices of the Royal Astronomical Society*, **325**, 373 – 378
- Cunha M. S., 2005, "Asteroseismic Theory of Rapidly Oscillating Ap Stars", *Journal of Astrophysics and Astronomy*, **26**, 213
- Cunha M. S., 2006, "Improved pulsating models of magnetic Ap stars - I. Exploring different magnetic field configurations", *Monthly Notices of the Royal Astronomical Society*, **365**, 153 – 164
- Cunha M. S., 2007, "Theory of rapidly oscillating Ap stars", *Communications in Asteroseismology*, **150**, 48 – 54
- Cunha M. S., Gough D., 2000, "Magnetic perturbations to the acoustic modes of roAp stars", *Monthly Notices of the Royal Astronomical Society*, **319**, 1020 – 1038
- Cunha M. S., Metcalfe T. S., 2007, "Asteroseismic signatures of small convective cores", *Astrophysical Journal*, **666**, 413 – 422
- Cunha M. S., Aerts C., Christensen-Dalsgaard J., Baglin A., Bigot L., Brown T. M., Catala C., Creevey O. L., Domiciano de Souza A., Eggenberger P., Garcia P. J. V., Grundahl F., Kervella P., Kurtz D. W., Mathias P., Miglio A., Monteiro M. J. P. F. G., Perrin G., Pijpers F. P., Pourbaix D., Quirrenbach A., Rousselet-Perraut K., Teixeira T. C., Thévenin F., Thompson M. J., 2007, "Asteroseismology and interferometry", *Astronomy and Astrophysics Review*, **14**, 217 – 360
- Cuypers J., 1980, "On the calculation of the frequency splitting of adiabatic nonradial stellar oscillations by slow differential rotation", *Astronomy and Astrophysics*, **89**, 207 – 208
- Cuypers J., 1987, "The Period Analysis of Variable Stars" Academiae Analecta, Royal Academy of Sciences , Belgium, **49**, No. 3
- Cuypers J., Goossens M., 1981, "Frequency Analysis of Photometric Observations of the Beta-Cephei Star Nu-Eridani", *Astronomy and Astrophysics Supplement Series*, **45**, 487 – 497
- Cuypers J., Aerts C., Buzasi D., Catanzarite J., Conrow T., Laher R., 2002, "Multiperiodicity in the light variations of the beta Cephei star beta Crucis", *Astronomy and Astrophysics*, **392**, 599 – 603
- Cuypers J., Aerts C., De Cat P., De Ridder J., Goossens K., Schoenaers C., Uytterhoeven K., Acke B., Davignon G., Debosscher J., Decin L., De Meester W., Deroo P., Drummond R., Kolenberg K., Lefever K., Raskin G., Reyniers M., Saesen S., Vandenbussche B., Van Malderen R., Verhoelst T., Van Winckel H., Waelkens C., 2009, "Long-term photometric monitoring with the Mercator telescope. Frequencies and multicolour amplitudes of  $\gamma$  Doradus stars", *Astronomy and Astrophysics*, **499**, 967 – 982
- Dall T. H., Santos N. C., Arentoft T., Bedding T. R., Kjeldsen H., 2006, "Bisectors of the cross-correlation function applied to stellar spectra. Dis-

- criminating stellar activity, oscillations and planets”, *Astronomy and Astrophysics*, **454**, 341 – 348
- D’Antona F., Caloi V., 2004, “The early evolution of globular clusters: the case of NGC 2808”, *Astrophysical Journal*, **611**, 871 – 880
- Däppen W., 2004, “Equations of state for solar and stellar modelling”, In *Equation-of-State and Phase-Transition Issues in Models of Ordinary Astrophysical Matter*, Eds V. Čelebonović, W. Däppen, D. Gough, AIP Conf. Proc. vol. 731, AIP, Melville, New York, 3 – 17
- Däppen W., 2007, “Helioseismology and Plasma Physics”, In *Solar and Stellar Physics Through Eclipses*, Eds O. Demircan, S. O. Selam, B. Albayrak, Astronomical Society of the Pacific Conference Series, San Francisco, **370**, 3 – 12
- Däppen W., Gough D. O., 1986, “Progress report on helium abundance determination”, In *Seismology of the Sun and the distant Stars*, Ed. D. O. Gough, Reidel, Dordrecht, 275 – 280
- Däppen W., Gough D. O., Kosovichev A. G., Thompson M. J., 1991, “A new inversion for the hydrostatic stratification of the Sun”, In *Challenges to theories of the structure of moderate-mass stars, Lecture Notes in Physics*, vol. **388**, 111 – 120, Eds D. O. Gough, J. Toomre, Springer, Heidelberg
- Daszyńska-Daszkiewicz J., Dziembowski W. A., Pamyatnykh A. A., Goupil M.-J., 2002, “Photometric amplitudes and phases of nonradial oscillation in rotating stars”, *Astronomy and Astrophysics*, **392**, 151 – 159
- Daszyńska-Daszkiewicz J., Dziembowski W. A., Pamyatnykh A. A., 2003, “Constraints on stellar convection from multi-colour photometry of delta Scuti stars”, *Astronomy and Astrophysics*, **407**, 999 – 1006
- Daszyńska-Daszkiewicz J., Dziembowski W. A., Pamyatnykh A. A., 2005a, “Constraints on parameters of B-type pulsators from combined multicolour photometry and radial velocity data. I.  $\beta$  Cephei stars”, *Astronomy and Astrophysics*, **441**, 641 – 651
- Daszyńska-Daszkiewicz J., Dziembowski W. A., Pamyatnykh A. A., Breger M., Zima W., Houdek G., 2005b, “Inferences from pulsational amplitudes and phases for multimode  $\delta$  Sct star FG Vir”, *Astronomy and Astrophysics*, **438**, 653 – 660
- Davis, L.E., 1989, *A reference guide to the IRAF/APPHOT package*, NOAO, Tucson, Arizona, USA
- Debosscher J., Sarro L. M., Aerts C., Cuypers J., Vandenbussche B., Garrido R., Solano E., 2007, “Automated supervised classification of variable stars. I. Methodology”, *Astronomy and Astrophysics*, **475**, 1159 – 1183
- De Cat P., 2002, *An observational study of bright southern slowly pulsating B stars*, PhD Dissertation, Katholieke Universiteit Leuven, Belgium
- De Cat P., Aerts C., 2002, “A study of bright southern slowly pulsating B stars. II. The intrinsic frequencies”, *Astronomy and Astrophysics*, **393**, 965 – 981
- De Cat P., Cuypers J., 2003, “Period search zoo: observational questions”, *Interplay of Periodic, Cyclic and Stochastic Variability in Selected Areas*

- of the H-R Diagram*, Ed. C. Sterken, Publications of the Astronomical Society of the Pacific Conference Series, San Francisco, **292**, 377 – 382
- De Cat P., Aerts C., De Ridder J., Kolenberg K., Meeus G., Decin L., 2000, “A study of bright southern slowly pulsating B stars. I. Determination of the orbital parameters and of the main frequency of the spectroscopic binaries”, *Astronomy and Astrophysics*, **355**, 1015 – 1030
- De Cat P., de Ridder J., Hensberge H., Ilijic S., 2004, “Spectroscopic study of the double-lined slowly pulsating B star HD 140873 and HD 123515”, In *Spectroscopically and Spatially Resolving the Components of the Close Binary Stars*, Eds R. W. Hilditch, H. Hensberge, K. Pavlovski, Publications of the Astronomical Society of the Pacific Conference Series, San Francisco, **318**, 338 – 341
- De Cat P., Briquet M., Daszyńska-Daszkiewicz J., Dupret M. A., De Ridder J., Scuflaire R., Aerts C., 2005, “A study of bright southern slowly pulsating B stars. III. Mode identification for singly-periodic targets in spectroscopy”, *Astronomy and Astrophysics*, **432**, 1013 – 1024
- De Cat P., Eyer L., Cuypers J., Aerts C., Vandenbussche B., Uytterhoeven K., Reyniers K., Kolenberg K., Groenewegen M., Raskin G., Maas T., Jankov S., 2006, “A spectroscopic study of southern (candidate)  $\gamma$  Doradus stars. I. Time series analysis”, *Astronomy and Astrophysics*, **449**, 281 – 292
- De Cat P., Briquet M., Aerts C., Goossens K., Saesen S., Cuypers J., Yakut K., Scuflaire R., Dupret M.-A., Uytterhoeven K., Van Winckel H., Raskin G., Davignon G., Le Guillou L., van Malderen R., Reyniers M., Acke B., De Meester W., Vanautgaerden J., Vandenbussche B., Verhoelst T., Waelkens C., Deroo P., Reyniers K., Ausseloos M., Broeders E., Daszyńska-Daskiewicz J., Debosscher J., De Ruyter S., Lefever K., Decin G., Kolenberg K., Mazumdar A., van Kerckhoven C., De Ridder J., Drummond R., Barban C., Vanhollebeke E., Maas T., Decin L., 2007, “Long term photometric monitoring with the Mercator telescope. Frequencies and mode identification of variable O-B stars”, *Astronomy and Astrophysics*, **463**, 243 – 249
- Decin L., Hony S., de Koter A., Justtanont K., Tielens A. G. G. M., Waters L. B. F. M., 2006, “Probing the mass-loss history of AGB and red supergiant stars from CO rotational line profiles. I. Theoretical models – mass-loss history unravelled in VY CMa”, *Astronomy and Astrophysics*, **456**, 549 – 563
- Decin L., Hony S., de Koter A., Justtanont K., Tielens A. G. G. M., Waters L. B. F. M., 2008, “Probing the mass-loss history of VY CMa”, In *Mass Loss from Stars and the Evolution of Stellar Clusters*, eds A. de Koter, L. Smith, R. Waters, ASP Conf. Ser. **388**, 159 – 160
- Deepak A., 1977, *Inversion Methods in Atmospheric Remote Sounding*, Academic, New York
- de Groot M., Sterken C. (Eds), 2001, *P Cygni 2000 - Four hundred years of progress*, Publications of the Astronomical Society of the Pacific Conference Series, San Francisco, **233**

- Delahaye F., Pinsonneault M., 2006, "The solar heavy-element abundances. I. Constraints from stellar interiors", *Astrophysical Journal*, **649**, 529 – 540
- De Marco O., Clayton G. C., Herwig F., Pollacco D. L., Clark J. S., Kilkenny D., 2002, "What Are the Hot R Coronae Borealis Stars?", *Astronomical Journal*, **123**, 3387 – 3408
- De Marco O., Sandquist E. L., Mac Low M.-M., Herwig F., Taam R. E., 2003, "Of Wolf-Rayet Central Stars and Common Envelopes", *Revista Mexicana de Astronomia y Astrofisica Conference Series*, **15**, 34 – 37
- Demarque P., Mengel J. G., Sweigart A. V., 1973, "Rotating solar models with low neutrino flux", *Astrophysical Journal*, **183**, 997 – 1004 (Erratum: *Nature*, **252**, 368; 1974)
- Demarque P., Guenther D. B., van Altena W. F., 1986, "The case of  $\alpha$  Centauri: mass, age and  $p$ -mode oscillation spectrum", *Astrophysical Journal*, **300**, 773 – 778
- Denissenkov P. A., Pinsonneault M., MacGregor K. B., 2008, "What prevents internal gravity waves from disturbing the solar uniform rotation?", *Astrophysical Journal*, **684**, 757 – 769
- De Pauw M., Aerts C., Waelkens C., 1993, "Mode identification of pulsating stars from line profile variations with the moment method. A theoretical study of the accuracy of the method", *Astronomy and Astrophysics*, **280**, 493 – 507
- De Ridder J., Dupret M.-A., Neuforge C., Aerts C., 2002, "Influence of non-adiabatic temperature variations on line profile variations of slowly rotating beta Cephei stars and SPBs. II. Simulations of line profile time series", *Astronomy and Astrophysics*, **385**, 572 – 584
- De Ridder J., Telting J. H., Balona L. A., Handler G., Briquet M., Daszyńska-Daszkiewicz J., Lefever K., Korn A. J., Heiter U., Aerts C., 2004, "Asteroseismology of the  $\beta$  Cephei star  $\nu$  Eridani - III. Extended frequency analysis and mode identification", *Monthly Notices of the Royal Astronomical Society*, **351**, 324 – 332
- De Ridder J., Molenberghs G., Aerts C., 2005, "Estimating stellar oscillation-related parameters and their uncertainties with the moment method", *Applied Statistics*, **65**, 1 – 16
- De Ridder J., Barban C., Carrier F., Mazumdar A., Eggenberger P., Aerts C., Deruyter S., Vanautgaerden J., 2006, "Discovery of solar-like oscillations in the red giant  $\epsilon$  Ophiuchi", *Astronomy and Astrophysics*, **448**, 689 – 695
- De Ruyter S., Van Winckel H., Maas T., Lloyd Evans T., Waters L. B. F. M., De Jonghe H., 2006, "Keplerian discs around post-AGB stars: a common phenomenon?", *Astronomy and Astrophysics*, **448**, 641 – 653
- de Santis R., Cassisi S., 1999, "A pulsational approach to the luminosity of horizontal branch stellar structures", *Monthly Notices of the Royal Astronomical Society*, **308**, 97 – 110
- Desmet M., Briquet M., Thoul A., Zima W., De Cat P., Handler G., Ilyin I., Kambe E., Krzesinski J., Lehmann H., Masuda S., Mathias P., Mkrtichian

- D. E., Telting J., Uytterhoeven K., Yang S. L. S., Aerts C., 2009, “An asteroseismic study of the beta Cephei star 12 Lacertae: multisite spectroscopic observations, mode identification and seismic modelling”, *Monthly Notices of the Royal Astronomical Society*, **396**, 1460 – 1472
- Deubner F.-L., 1975, “Observations of low wavenumber nonradial eigenmodes of the Sun”, *Astronomy and Astrophysics*, **44**, 371 – 375
- Deubner F.-L., Gough D., 1984, “Helioseismology: Oscillations as a Diagnostic of the Solar Interior”, *Annual Review of Astronomy and Astrophysics*, **22**, 593 – 619
- Deubner F.-L., Ulrich R. K., Rhodes E. J., 1979, “Solar *p*-mode oscillations as a tracer of radial differential rotation”, *Astronomy and Astrophysics*, **72**, 177 – 185
- Deupree R. G., 1995, “Stellar evolution with arbitrary rotation laws. II. Massive star evolution to core hydrogen exhaustion”, *Astrophysical Journal*, **439**, 357 – 364
- Dicke R. H., 1964, “The Sun’s rotation and relativity”, *Nature*, **202**, 432 – 435
- Dicke R. H., Goldenberg H. M., 1967, “Solar oblateness and general relativity”, *Physical Review Letters*, **18**, 313 – 316
- Diener P., Kosovichev A. G., Kotok E. V., Novikov I. D., Pethick C. J., 1995, “Non-linear effects at tidal capture of stars by a massive black hole – II. Compressible affine models and tidal interaction after capture”, *Monthly Notices of the Royal Astronomical Society*, **275**, 498 – 506
- Di Mauro M. P., Christensen-Dalsgaard J., Rabello-Soares M. C., Basu S., 2002, “Inferences on the solar envelope with high-degree modes”, *Astronomy and Astrophysics*, **384**, 666 – 677
- Di Mauro, M. P., Christensen-Dalsgaard, J., Kjeldsen, H., Bedding, T. R., Paternò, L., 2003, “Convective overshooting in the evolution and seismology of  $\eta$  Bootis”, *Astronomy and Astrophysics*, **404**, 341 – 353
- Di Mauro, M. P., Christensen-Dalsgaard, J., Paternó, L., D’Antona, F., 2004, “Interpretation of the solar-like pulsational behaviour of  $\eta$  Bootis”, *Solar Physics*, **220**, 185 – 198
- Dintrans B., Rieutord M., 2000, “Oscillations of a rotating star: a non-perturbative theory”, *Astronomy and Astrophysics*, **354**, 86 – 98
- Dolez N., Gough D. O., 1982, “On the Problem of Interpreting Rapidly Oscillating Ap-Stars”, In *Pulsations in Classical and Cataclysmic Variable Stars*, 248
- Domiciano de Souza A., Vakili F., Jankov S., Janot-Pacheco E., Abe L., 2002, “Modelling rapid rotators for stellar interferometry”, *Astronomy and Astrophysics*, **393**, 345 – 357
- Domiciano de Souza, A., Kervella, P., Jankov, S., Abe, L., Vakili, F., di Folco, E., Paresce, F., 2003, “The spinning-top Be star Achernar from VLTI-VINCI”, *Astronomy and Astrophysics*, **407**, L47 – L50

- Domiciano de Souza, A., Kervella, P., Jankov, S., Vakili, F., Ohishi, N., Nordgren, T. E., Abe, L., 2005, "Gravitation-darkening of Altair from interferometry", *Astronomy and Astrophysics*, **442**, 567 – 578
- Domingo V., Fleck B., Poland A. I., 1995, "The SOHO mission: an overview", *Solar Physics*, **162**, 1 – 37
- Donati J.-F., Semel M., Carter B. D., Rees D. E., Collier Cameron A., 1997, "Spectropolarimetric observations of active stars", *Monthly Notices of the Royal Astronomical Society*, **291**, 658 – 682
- Dorfi E. A., Gautschy A., Saio H., 2006, "A MOST probable explanation of the pulsation of WR 123", *Astronomy and Astrophysics*, **453**, L35 – L37
- Drake J. J., Testa P., 2005, "The solar model problem solved by the abundance of neon in stars of the local cosmos", *Nature*, **436**, 525 – 528
- Dravins D., Lindegren L., Mezey E., Young A. T., 1998, "Atmospheric Intensity Scintillation of Stars. III. Effects for Different Telescope Apertures", *Publications of the Astronomical Society of the Pacific*, **110**, 610 – 633
- Dufour P., Liebert J., Fontaine G., Behara N., 2007, "White dwarf stars with carbon atmospheres", *Nature*, **450**, 522 – 524
- Dufton P. L., Ryans R. S. I., Trundle C., Lennon D. J., Hubeny I., Lanz T., Allende Prieto C., 2005, "B-type supergiants in the SMC: Chemical compositions and comparison of static and unified models", *Astronomy and Astrophysics*, **434**, 1125 – 1137
- Dullemond C. P., van den Ancker M. E., Acke B., van Boekel R., 2003, "Explaining UX Orionis Star Variability with Self-shadowed Disks", *Astrophysical Journal*, **594**, L47 – L50
- Dupret M. A., 2001, "Nonradial nonadiabatic stellar pulsations: A numerical method and its application to a beta Cephei model", *Astronomy and Astrophysics*, **366**, 166 – 173
- Dupret, M. A., 2002, *Non-radial non-adiabatic oscillations of near main sequence variable stars*, PhD Dissertation, Université de Liège, Belgium
- Dupret M.-A., De Ridder J., Neuforge C., Aerts C., Scuflaire R., 2002, "Influence of non-adiabatic temperature variations on line profile variations of slowly rotating beta Cep stars and SPBs. I. Non-adiabatic eigenfunctions in the atmosphere of a pulsating star", *Astronomy and Astrophysics*, **385**, 563 – 571
- Dupret M.-A., De Ridder J., De Cat P., Aerts C., Scuflaire R., Noels A., Thoul A., 2003, "A photometric mode identification method, including an improved non-adiabatic treatment of the atmosphere", *Astronomy and Astrophysics*, **398**, 677 – 685
- Dupret M.-A., Grigahcène A., Garrido R., Gabriel M., Scuflaire R., 2004a, "Theoretical instability strips for  $\delta$  Scuti and  $\gamma$  Doradus stars", *Astronomy and Astrophysics*, **414**, L17 – L20
- Dupret M.-A., Thoul A., Scuflaire R., Daszyńska-Daszkiewicz J., Aerts C., Bourge P.-O., Waelkens C., Noels A., 2004b, "Astroseismology of the  $\beta$  Cep star HD 129929. II. Seismic constraints on core overshooting, inter-

- nal rotation and stellar parameters”, *Astronomy and Astrophysics*, **415**, 251 – 257
- Dupret M.-A., Grigahcène A., Garrido R., Gabriel M., Scuflaire R., 2005a, “Convection-pulsation coupling. II. Excitation and stabilization mechanisms in  $\delta$  Sct and  $\gamma$  Dor stars”, *Astronomy and Astrophysics*, **435**, 927 – 939
- Dupret M.-A., Grigahcène A., Garrido R., De Ridder J., Scuflaire R., Gabriel M., 2005b, “Time-dependent convection seismic study of five  $\gamma$  Doradus stars”, *Monthly Notices of the Royal Astronomical Society*, **360**, 1143 – 1152
- Dupret M. A., Quirion P. O., Fontaine G., Brassard P., Grigahcène A., 2008a, “Time-dependent convection study of the driving mechanism in the DBV white dwarfs”, *Journal of Physics, Conference Series*, **118**, 012051(1 – 6)
- Dupret M.-A., Miglio A., Montalban J., Grigahcène A., Noels A., 2008b, “Driving and damping mechanisms in hybrid pressure-gravity modes pulsators”, In *Proc. HELAS II International Conference: Helioseismology, Asteroseismology and the MHD Connections*, Eds L. Gizon, M. Roth, *Journal of Physics Conference Series*, **118**, 012020(1 – 7)
- Dupret M.-A., Belkacem K., Samadi R., Montalban J., Moreira O., Miglio A., Godart M., Ventura P., Ludwig H.-G., Grigahcène A., Goupil M.-J., Noels A., Caffau E., 2009, “Theoretical amplitudes and lifetimes of non-radial solar-like oscillations in red giants”, *Astronomy and Astrophysics*, **506**, 57 – 67
- Durney B. R., 1972, “Evidence for changes in the angular velocity of the surface regions of the sun and stars. Comments”, In *Solar Wind*, Eds C. P. Sonett, P. J. Coleman, J. M. Wilcox, Washington, Scientific and Technical Information Office, National Aeronautics and Space Administration, 282 – 285
- Duvall T. L., 1982, “A dispersion law for solar oscillations”, *Nature*, **300**, 242 – 243
- Duvall T. L., Harvey J. W., 1983, “Observations of solar oscillations of low and intermediate degree”, *Nature*, **302**, 24 – 27
- Duvall T. L., Harvey J. W., 1984, “Rotational frequency splitting of solar oscillations”, *Nature*, **310**, 19 – 22
- Duvall T. L., Jr., Harvey J. W., 1986, “Solar Doppler shifts - Sources of continuous spectra”, *Proceedings of the NATO Advanced Research Workshop 169: Seismology of the Sun and the Distant Stars*, Ed. D. O. Gough, Dordrecht, D. Reidel Publishing Co., 105 – 116
- Duvall T. L., Dziembowski W. A., Goode P. R., Gough D. O., Harvey J. W., Leibacher J. W., 1984, “The internal rotation of the Sun”, *Nature*, **310**, 22 – 25
- Duvall T. L., Harvey J. W., Pomerantz M. A., 1986, “Latitude and depth variation of solar rotation”, *Nature*, **321**, 500 – 501

- Duvall T. L., Jefferies S. M., Harvey J. W., Osaki Y., Pomerantz, M. A., 1993, "Asymmetries of solar oscillation line profiles", *Astrophysical Journal*, **410**, 829 – 836
- Dworetsky M. M., 1983, "A period-finding method for sparse randomly spaced observations of 'How long is a piece of string?", *Monthly Notices of the Royal Astronomical Society*, **203**, 917 – 924
- Dyson J., Schutz B. F., 1979, "Perturbations and stability of rotating stars. I. Completeness of normal modes", *Proc. Roy. Soc. London*, **A368**, 389 – 410
- Dzhalilov N. S., Staude J., 2004, "Eigenoscillations of the differentially rotating Sun. II. Generalization of the Laplace tidal equation", *Astronomy and Astrophysics*, **421**, 305 – 322
- Dziembowski W., 1977a, "Oscillations of giants and supergiants", *Acta Astronomica*, **27**, 95 – 126
- Dziembowski W., 1977b, "Light and radial velocity variations in a nonradially oscillating star", *Acta Astronomica*, **27**, 203 – 211
- Dziembowski W., 1983, "Resonant coupling between solar gravity modes", *Solar Physics*, **82**, 259 – 266
- Dziembowski W. A., Cassisi S., 1999, "Nonradial Modes in RR Lyr Stars", *Acta Astronomica*, **49**, 371 – 382
- Dziembowski W., Goode P. R., 1985, "Frequency splitting in Ap stars", *Astrophysical Journal*, **296**, L27 – L30
- Dziembowski W. A., Goode P. R., 1992, "Effects of differential rotation on stellar oscillations: a second-order theory", *Astrophysical Journal*, **394**, 670 – 687
- Dziembowski W. A., Goode P. R., 1996, "Magnetic Effects on Oscillations in roAp Stars", *Astrophysical Journal*, **458**, 338 – 346
- Dziembowski W. A., Goode P. R., 1997, "Seismic sounding of the solar core: purging the corruption from the Sun's magnetic field", *Astronomy and Astrophysics*, **317**, 919 – 924
- Dziembowski W. A., Goode P. R., 2004, "Helioseismic probing of solar variability: the formalism and simple assessments", *Astrophysical Journal*, **600**, 464 – 479
- Dziembowski W. A., Goode P. R., 2005, "Sources of oscillation frequency increase with rising solar activity", *Astrophysical Journal*, **625**, 548 – 555
- Dziembowski W. A., Fiorentini G., Ricci B., Sienkiewicz R., 1999, "Helioseismology and the solar age", *Astronomy and Astrophysics*, **343**, 990 – 996
- Dziembowski W. A., Jerzykiewicz M., 2003, " $\nu$  Eridani: a Very Slowly Rotating and Possibly Magnetic  $\beta$  Cephei Star", In *Magnetic Fields in O, B and A Stars: Origin and Connection to Pulsation, Rotation and Mass Loss*, Eds L. A. Balona, H. F. Henrichs, R. Medupe, Publications of the Astronomical Society of the Pacific Conference Series, San Francisco, **305**, 319 – 327

- Dziembowski W., Kosovichev A., 1987a, "Low frequency oscillations in slowly rotating stars. I. General properties", *Acta Astronomica*, **37**, 313 – 330
- Dziembowski W., Kosovichev A., 1987b, "Low frequency oscillations in slowly rotating stars. II. Inertial modes in the solar convective envelope", *Acta Astronomica*, **37**, 331 – 339
- Dziembowski W., Kosovichev A., 1987c, "Low frequency oscillations in slowly rotating stars. III. Kelvin-Helmholtz instability", *Acta Astronomica*, **37**, 341 – 348
- Dziembowski W., Królikowska M., 1990, "On the mechanism of mode selection in  $\delta$  Scuti stars", *Acta Astronomica*, **40**, 19 – 26
- Dziembowski, W. A., Pamyatnykh, A. A., 1991, "A potential asteroseismological test for convective overshooting theories", *Astronomy and Astrophysics*, **248**, L11 – L14
- Dziembowski W. A., Pamyatnykh A. A., 1993, "The opacity mechanism in B-type stars. I - Unstable modes in Beta Cephei star models", *Monthly Notices of the Royal Astronomical Society*, **262**, 204 – 212
- Dziembowski W. A., Pamyatnykh A. A., 2008, "The two hybrid B-type pulsators:  $\nu$  Eridani and 12 Lacertae", *Monthly Notices of the Royal Astronomical Society*, **385**, 2061 – 2068
- Dziembowski W. A., Slawinska J., 2005, "On the Nature of Regular Pulsation in Two LBV Stars of NGC 300", *Acta Astronomica*, **55**, 195 – 204
- Dziembowski W. A., Goode P. R., Libbrecht K. G., 1989, "The radial gradient in the Sun's rotation", *Astrophysical Journal*, **337**, L53 – L57
- Dziembowski W. A., Pamyatnykh A. A., Sienkiewicz R., 1990, "Solar model from helioseismology and the neutrino flux problem", *Monthly Notices of the Royal Astronomical Society*, **244**, 542 – 550
- Dziembowski W. A., Pamyatnykh A. A., Sienkiewicz R., 1991, "Helium content in the solar convective envelope from helioseismology", *Monthly Notices of the Royal Astronomical Society*, **249**, 602 – 605
- Dziembowski W. A., Moskalik P., Pamyatnykh A. A., 1993, "The Opacity Mechanism in B-Type Stars - Part Two - Excitation of High-Order G-Modes in Main Sequence Stars", *Monthly Notices of the Royal Astronomical Society*, **265**, 588 – 600
- Dziembowski W. A., Goode P. R., Di Mauro M. P., Kosovichev A. G., Schou J., 1998, "Solar cycle onset seen in SOHO Michelson Doppler Imager seismic data", *Astrophysical Journal*, **509**, 456 – 460
- Dziembowski W. A., Goode P. R., Kosovichev A. G., Schou J., 2000, "Signatures of the rise of cycle 23", *Astrophysical Journal*, **537**, 1026 – 1038
- Dziembowski W. A., Gough D. O., Houdek G., Sienkiewicz R., 2001a, "Oscillations of  $\alpha$  UMa and other red giants", *Monthly Notices of the Royal Astronomical Society*, **328**, 601 – 610
- Dziembowski W. A., Goode P. R., Schou J., 2001b, "Does the Sun shrink with increasing magnetic activity?" *Astrophysical Journal*, **553**, 897 – 904

- Dziembowski W. A., Daszyńska-Daskiewicz J., Pamyatnykh A. A., 2007, "Excitation and visibility of slow modes in rotating B-type stars", *Monthly Notices of the Royal Astronomical Society*, **374**, 248 – 255
- Eckart C., 1960, *Hydrodynamics of Oceans and Atmospheres*, Pergamon Press, Oxford
- Eddington A. S., 1926, *The internal constitution of the stars*, Cambridge University Press, Cambridge
- Edmonds A. R., 1960, *Angular Momentum in Quantum Mechanics*, Princeton: Princeton University Press
- Edmonds P. D., Cram L. E., 1995, "A search for global acoustic oscillations on  $\alpha^1$  Cen and  $\beta$  Hyi", *Monthly Notices of the Royal Astronomical Society*, **276**, 1295 – 1302
- Edmonds P. D., Gilliland R. L., 1996, "K giants in 47 Tucanae: detection of a new class of variable stars", *Astrophysical Journal*, **464**, L157 – L160
- Edmonds P., Cram L., Demarque P., Guenther D. B., Pinsonneault M. H., 1992, "Evolutionary models and the  $p$ -mode oscillation spectrum of  $\alpha$  Centauri A and B", *Astrophysical Journal*, **394**, 313 – 319
- Edvardsson B., Andersen J., Gustafsson B., Lambert D. L., Nissen P. E., Tomkin J., 1993, "The chemical evolution of the galactic disk. I. Analysis and results", *Astronomy and Astrophysics*, **275**, 101 – 152
- Eff-Darwich A., Korzennik S. G., Jiménez-Reyes S. J., Pérez Hernández F., 2002, "An upper limit on the temporal variations of the solar interior stratification", *Astrophysical Journal*, **580**, 574 – 578
- Eff-Darwich A., Korzennik S. G., Jiménez-Reyes S. J., García R. A., 2008, "Analysis of the sensitivity of solar rotation to helioseismic data from GONG, GOLF, and MDI observations", *Astrophysical Journal*, **679**, 1636 – 1643
- Eggenberger P., Charbonnel C., Talon S., Meynet G., Maeder A., Carrier F., Bourban G., 2004, "Analysis of  $\alpha$  Centauri AB including seismic constraints", *Astronomy and Astrophysics*, **417**, 235 – 246
- Eggenberger P., Maeder A., Meynet G., 2005a, "Stellar evolution with rotation and magnetic fields. IV. The solar rotation profile", *Astronomy and Astrophysics*, **440**, L9 – L12
- Eggenberger, P., Carrier, F., Bouchy, F., 2005b, "Models of Procyon A including seismic constraints", *New Astronomy*, **10**, 195 – 208
- Eggleton P. P., Faulkner J., Flannery B. P., 1973, "An approximate equation of state for stellar material", *Astronomy and Astrophysics*, **23**, 325 – 330
- Eisenfeld J., 1969, "A completeness theorem for an integro-differential operator", *J. Math. Anal. Applic.*, **26**, 357 – 375
- Eisenstein D. J., Liebert J., Harris H. C., Kleinman S. J., Nitta A., Silvestri N., Anderson S. A., Barentine J. C., Brewington H. J., Brinkmann J., Harvanek M., Krzesiński J., Neilsen E. H., Jr., Long D., Schneider D. P., Snedden S. A., 2006a, "A Catalog of Spectroscopically Confirmed White Dwarfs from the Sloan Digital Sky Survey Data Release 4", *Astrophysical Journal Supplement Series*, **167**, 40 – 58

- Eisenstein D. J., Liebert J., Koester D., Kleinmann S. J., Nitta A., Smith P. S., Barentine J. C., Brewington H. J., Brinkmann J., Harvanek M., Krzesiński J., Neilsen E. H., Jr., Long D., Schneider D. P., Snedden S. A., 2006b, "Hot DB White Dwarfs from the Sloan Digital Sky Survey", *Astronomical Journal*, **132**, 676 – 691
- Elkin V. G., Kurtz D. W., Mathys G., 2005, "The discovery of remarkable  $5 \text{ km s}^{-1}$  pulsational radial velocity variations in the roAp star HD99563", *Monthly Notices of the Royal Astronomical Society*, **364**, 864 – 872
- Elliott J. R., Gough D. O., 1999, "Calibration of the thickness of the solar tachocline", *Astrophysical Journal*, **516**, 475 – 481
- Elliott J. R., Kosovichev A. G., 1998, "The adiabatic exponent in the solar core", *Astrophysical Journal*, **500**, L199 – L202
- Ellis A. N., 1986, "An improved asymptotic formula for solar gravity-mode periods", *Seismology of the Sun and the distant Stars*, Ed. D. O. Gough, Reidel, Dordrecht, 173 – 175
- Elsworth Y., Howe R., Isaak G. R., McLeod C. P., New R., 1990, "Evidence from solar seismology against non-standard solar-core models", *Nature*, **347**, 536 – 539
- Elsworth Y., Howe R., Isaak G. R., McLeod C. P., Miller B. A., New R., Wheeler S. J., Gough D. O., 1995, "Slow rotation of the Sun's interior", *Nature*, **376**, 669 – 672
- Elsworth Y. P., Baudin F., Chaplin W., Andersen B., Appourchaux T., Boumier P., Broomhall A.-M., Corbard T., Finsterle W., Fröhlich C., Gabriel A., García R. A., Gough D. O., Grec G., Jiménez A., Kosovichev A., Provost J., Sekii T., Toutain T., Turck-Chieze S., 2006, "The internal structure of the Sun inferred from g modes and low-frequency p modes", In *Proc. SOHO 18 / GONG 2006 / HELAS I Conf. Beyond the spherical Sun*, Ed. K. Fletcher, ESA SP-624, ESA Publications Division, Noordwijk, The Netherlands
- Epcitein N., 2007, "ARENA: Toward a European Astronomical Facility at Dome C CONCORDIA", *EAS Publications Series*, **25**, 1 – 4
- Eyer L., Aerts C., 2000, "A search for new gamma Doradus stars in the Geneva photometric database", *Astronomy and Astrophysics*, **361**, 201 – 206
- Eyer L., Bartholdi P., 1999, "Variable stars: Which Nyquist frequency?", *Astronomy and Astrophysics Supplement Series*, **135**, 1 – 3
- Eyer L., Mowlavi N., 2008, "Variable stars across the observational HR diagram", in Proc. Helioseismology, Asteroseismology and MHD Connections, Eds L. Gizon, M. Roth, *Journal of Physics, Conference Series*, **118**, 012010(1 – 21)
- Faulkner J., 2004, "Red giants: then and now", In *The Scientific Legacy of Fred Hoyle*, Ed. D. Gough, Cambridge University Press, 149 – 226
- Feast M. W., Glass I. S., Whitelock P. A., Catchpole R. M., 1989, "A period-luminosity-colour relation for Mira variables", *Monthly Notices of the Royal Astronomical Society*, **241**, 375 – 392

- Feast M. W., Carter B. S., Roberts G., Marang F., Catchpole R. M., 1997, “The R Coronae Borealis stars - I. Infrared photometry and long-term variations”, *Monthly Notices of the Royal Astronomical Society*, **285**, 317 – 338
- Fernandes J., Neuforge C., 1995, “ $\alpha$  Centauri and convection theories”, *Astronomy and Astrophysics*, **295**, 678 – 684
- Fernie J. D., 1994, “AC Andromedae: the missing link between  $\delta$  Scuti stars and classical Cepheids?”, *Monthly Notices of the Royal Astronomical Society*, **271**, L19 – L20
- Ferrari V., Miniutti G., Pons J. A., 2003, “Gravitational waves from newly born, hot neutron stars”, *Monthly Notices of the Royal Astronomical Society*, **342**, 629 – 638
- Ferraro F. R., Sabbi E., Gratton R., Piotto G., Lanzoni B., Carretta E., Rood R. T., Sills A., Fusi Pecci F., Moehler S., Beccari G., Lucatello S., Compagni N., 2006, “Discovery of Carbon/Oxygen-depleted Blue Straggler Stars in 47 Tucanae: The Chemical Signature of a Mass Transfer Formation Process”, *Astrophysical Journal*, **647**, L53 – L56
- Ferraz-Mello S., 1981, “Estimation of Periods from Unequally Spaced Observations”, *Astronomical Journal*, **86**, 619 – 625
- Feuchtinger M. U., 1999, “A nonlinear convective model for radial stellar pulsations. I. The physical description”, *Astronomy and Astrophysics Supplement Series*, **136**, 217 – 226
- Fitch W. S., 1967, “Evidence of Tidal Effects in Some Pulsating Stars. I. CC Andromedae and Sigma Scorpii”, *Astrophysical Journal*, **148**, 481 – 496
- Fitch W. S., 1969, “Evidence of Tidal Effects in Some Pulsating Stars. II. 16 Lacertae and  $\beta$  Cephei”, *Astrophysical Journal*, **158**, 269 – 280
- Fitch W. S., Szeidl B., 1976, “The three radial modes and evolutionary state of AC Andromedae”, *Astrophysical Journal*, **203**, 616 – 624
- Fitch W. S., Wisniewski W. Z., 1979, “Tidal effects in pulsating stars. III -  $l = 1$  p<sub>5</sub> modes in the ellipsoidal variable 14 Aurigae A”, *Astrophysical Journal*, **231**, 808 – 825
- Flannery B. P., Ayres T. R., 1978, “Evolution of the  $\alpha$  Centauri system”, *Astrophysical Journal*, **221**, 175 – 185
- Fletcher S. T., Chaplin W. J., Elsworth Y., Schou J., Buzasi D., 2006, “Frequency, splitting, linewidth and amplitude estimates of low- $\ell$  p modes of  $\alpha$  Cen A: analysis of Wide-Field Infrared Explorer photometry”, *Monthly Notices of the Royal Astronomical Society*, **371**, 935 – 944
- Fokin A. B., 1994, “Nonlinear pulsations of the RV Tauri stars”, *Astronomy and Astrophysics*, **292**, 133 – 151
- Fontaine G., Brassard P., 2008a, “The Pulsating White Dwarf Stars”, *Publications of the Astronomical Society of the Pacific*, **120**, 1043 – 1096
- Fontaine G., Brassard P., 2008b, “The degenerate pulsators”, *Communications in Asteroseismology*, **157**, 177 – 184

- Fontaine G., Wesemael F., 1987, "Recent advances in the theory of white dwarf spectral evolution", *IAU Colloq. 95: Second Conference on Faint Blue Stars*, L. Davis Press, Inc., New York, 319 – 326
- Fontaine G., Brassard P., Bergeron P., 2001, "The potential of white dwarf cosmochronology", *Publications of the Astronomical Society of the Pacific*, **113**, 409 – 435
- Fontaine G., Brassard P., Charpinet S., Green E. M., Chayer P., Billères M., Randall S. K., 2003a, "A Driving Mechanism for the Newly Discovered Long-Period Pulsating Subdwarf B Stars", *Astrophysical Journal*, **597**, 518 – 534
- Fontaine G., Brassard P., Charpinet S., Green E. M., Willems B., 2003b, "On the Potential of Tidal Excitation of Gravity Modes in Hot B Subdwarfs", In *Asteroseismology Across the HR Diagram*, Eds M.J. Thompson, M.S. Cunha, M.J.P.F.G. Monteiro, *Astrophysics and Space Science*, **284**, 517 – 520
- Fontaine G., Brassard P., Charpinet S., 2007, "On the Origin of the Small-Frequency Spacings Found in the Pulsation Spectra of Hot B Subdwarf Stars", *Astrophysical Journal*, **654**, 1087 – 1094
- Formicola A., Imbriani G., Costantini H., Angulo C., Bemmerer D., Bonetti R., Broggini C., Corvisiero P., Cruz J., Descouvement P., Fülöp Z., Gervino G., Guglielmetti A., Gustavino C., Gyürky G., Jesus A. P., Junker M., Lemut A., Menegazzo R., Prati P., Roca V., Rolfs C., Romano M., Rossi Alvarez C., Schümann F., Somorjai E., Straniero O., Strieder F., Terras F., Trautvetter H. P., Vomiero A., Zavatarelli S., 2004, "Astrophysical X-factor of  $^{14}\text{N}(p, \gamma)^{15}\text{O}$ ", *Physical Letters B*, **591**, 61 – 68
- Fossat E., 1991, "The IRIS network for full disk helioseismology: Present status of the programme", *Solar Physics*, **133**, 1 – 12
- Fossat E., Ricort G., 1975, "Photospheric oscillations. I. Large scale observations by optical resonance method", *Astronomy and Astrophysics*, **43**, 243 – 252
- Fossat E., Roddier F., 1971, "A sodium experiment for photospheric velocity field observations", *Solar Physics*, **18**, 204 – 210
- Foster G., 1996a, "Time Series Analysis by Projection. I. Statistical Properties of Fourier Analysis", *Astronomical Journal*, **111**, 541 – 554
- Foster G., 1996b, "Time Series Analysis by Projection. II. Tensor Methods for Time Series Analysis", *Astronomical Journal*, **111**, 555 – 566
- Foukal P. V., 2004, *Solar Astrophysics, 2nd edition*, Wiley-VCH, Weinheim
- Frandsen S., Carrier F., Aerts C., Stello D., Maas T., Burnet M., Bruntt H., Teixeira T. C., De Medeiros J. R., Bouchy F., Kjeldsen H., Pijpers F., Christensen-Dalsgaard J., 2002, "Detection of Solar-like oscillations in the G7 giant star xi Hya", *Astronomy and Astrophysics*, **394**, L5 – L8
- Fraser O. J., Hawley S. L., Cook K. H., Keller S. C., 2005, "Long-period variables in the Large Magellanic Cloud: results from MACHO and 2MASS", *Astronomical Journal*, **129**, 768 – 775

- Frazier E. N., 1968, "A spatio-temporal analysis of the velocity fields in the solar photosphere", *Zeitung für Astrophysik*, **68**, 345 – 356
- Frémat Y., Lampens P., Hensberge H., 2005, "Spectral disentangling of the triple system DG Leo: orbits and chemical composition", *Monthly Notices of the Royal Astronomical Society*, **356**, 545 – 556
- Freyhammer L. M., Hensberge H., Sterken C., Pavlovski K., Smette A., Iljić S., 2005, "The  $\beta$  Cephei variable in the eclipsing binary HD 92024. I. Determination of the orbit", *Astronomy and Astrophysics*, **429**, 631 – 643
- Fröhlich C., Lean J., 2004, "Solar radiative output and its variability: evidence and mechanisms", *Astronomy and Astrophysics Review*, **12**, 273 – 320
- Fröhlich C., Romero J., Roth H., Wehrli C., Andersen B. N., Appourchaux T., Domingo V., Telljohann U., Berthomieu G., Delache P., Provost J., Toutain T., Crommelynck D. A., Chevalier A., Fichot A., Däppen W., Gough D., Hoeksema T., Jiménez A., Gómez M. F., Herreros J. M., Roca Cortés T., Jones A. R., Pap J. M., Willson R. C., 1995, "VIRGO: Experiment for helioseismology and solar irradiance monitoring", *Solar Physics*, **162**, 101 – 128
- Fröhlich C., Crommelynck D. A., Wehrli C., Anklin M., Dewitte S., Fichot A., Finsterle W., Jiménez A., Chevalier A., Roth H., 1997, "In-flight performance of the VIRGO solar irradiance instrument on SOHO", *Solar Physics*, **175**, 267 – 286
- Frolov M. S., Irkaev B. N., 1984, "On the SX Phe-Type Stars", *Information Bulletin on Variable Stars*, **2462**, 1 – 2
- Frost E. B., Adams W. S., 1903, "Five stars whose radial velocities vary", *Astrophysical Journal*, **17**, 150 – 153
- Frost E. B., Barrett S. B., Struve O., 1926, "Radial velocities of 368 helium stars", *Astrophysical Journal*, **64**, 1 – 77
- Fukugita M., Ichikawa T., Gunn J. E., Doi M., Shimasaku K., Schneider D. P., 1996, "The Sloan Digital Sky Survey Photometric System", *Astronomical Journal*, **111**, 1748 – 1756
- Gabriel A. H., Grec G., Charra J., Robillot J.-M., Roca Cortés T., Turck-Chièze S., Bocchia R., Boumier P., Cantin M., Cespédes E., Cougrand B., Crétolle J., Damé L., Decaudin M., Delache P., Denis N., Duc R., Dzitko H., Fossat E., Fourmond J.-J., García R. A., Gough D., Grivel C., Herreros J. M., Lagardère H., Moalic J.-P., Pallé P. L., Pétrou N., Sanchez M., Ulrich R., van der Raay H. B., 1995, "Global oscillations at low frequency from the SOHO mission (GOLF)", *Solar Physics*, **162**, 61 – 99
- Gabriel A. H., Charra J., Grec G., Robillot J.-M., Roca Cortés T., Turck-Chièze S., Ulrich R., Basu S., Baudin F., Bertello L., Boumier P., Charra M., Christensen-Dalsgaard J., Decaudin M., Dzitko H., Foglizzo T., Fossat E., García R. A., Herreros J. M., Lazrek M., Pallé P. L., Pétrou N., Renaud C., Régulo C., 1997, "Performance and early results from the GOLF instrument flown on the SOHO mission", *Solar Physics*, **175**, 207 – 226

- Gabriel A. H., Baudin F., Boumier P., García R. A., Turck-Chièze S., Appourchaux T., Bertello L., Berthomieu G., Charra J., Gough D. O., Pallé P. L., Provost J., Renaud C., Robillot J.-M., Roca Cortés T., Thiery S., Ulrich R. K., 2002, “A search for solar  $g$  modes in the GOLF data”, *Astronomy and Astrophysics*, **390**, 1119 – 1131
- Gabriel M., 1986, “Solar  $g$  modes: a method to find the depth of the convection zone”, *Seismology of the Sun and the distant Stars*, Ed. D. O. Gough, Reidel, Dordrecht, 177 – 186
- Gabriel M., 1993, “On the location of the excitation of solar p-modes”, *Astronomy and Astrophysics*, **274**, 935 – 939
- Gabriel M., 1996, “Solar oscillations: theory”, *Bulletin of the Astronomical Society of India*, **24**, 233 – 243
- Gabriel M., 2000, “Linear interaction between pulsations and convection, scattering and line profiles of solar p-modes”, *Astronomy and Astrophysics*, **353**, 399 – 408
- Gabriel M., Scuflaire R., Noels A., Boury A., 1974, “Influence de la convection sur la stabilité des oscillations non radiales des étoiles”, *Bulletin de l'Académie Royal de Belgique, Classe des Sciences, 5ième Série*, **60**, 866 – 887
- Gabriel M., Scuflaire R., Noels A., Boury A., 1975, “Influence of convection on the vibrational stability of stars towards non-radial oscillations”, *Astronomy and Astrophysics*, **40**, 33 – 39
- Gamarova A. Y., Mkrtichian D. E., Rodriguez E., Costa V., Lopez-Gonzalez M. J., 2003, “Application of the Spatial Filtration Method to RZ Cas”, In *Interplay of Periodic, Cyclic and Stochastic Variability in Selected Areas of the H-R Diagram*, Ed. C. Sterken, Publications of the Astronomical Society of the Pacific Conference Series, San Francisco, **292**, 369
- Gamarova A., Hatzes A. P., Mkrtichian D. E., 2004, “Radial Velocity variations of the roAp-star HD 122970: new results”, *Communications in Asteroseismology*, **145**, 80
- Garaud P., 2007, “Magnetic confinement of the solar tachocline”, In *The solar tachocline*, Eds D. W. Hughes, R. Rosner, N. O. Weiss, Cambridge University Press, 147 – 181
- Garaud P., Garaud J.-D., 2008, “Dynamics of the solar tachocline – II: the stratified case”, *Monthly Notices of the Royal Astronomical Society*, **391**, 1239 – 1258
- García R. A., Corbard T., Chaplin W. J., Couvidat S., Eff-Darwich A., Jiménez-Reyes S. J., Korzennik S. G., Ballot J., Boumier P., Fossat E., Henney C. J., Howe R., Lazrek M., Lochard J., Pallé P. L., Turck-Chièze S., 2004, “About the rotation of the solar radiative interior”, *Solar Physics*, **220**, 269 – 285
- García R. A., Turck-Chièze S., Boumier P., Robillot J. M., Bertello L., Charra J., Dzitko H., Gabriel A. H., Jiménez-Reyes S. J., Pallé P., Renaud C., Roca Cortés T., Ulrich R. K., 2005, “Global solar Doppler velocity determi-

- nation with the GOLF/SoHO instrument”, *Astronomy and Astrophysics*, **442**, 385 – 395
- García R. A., Turck-Chièze S., Jiménez-Reyes S. J., Ballot J., Pallé P., Eff-Darwich A., Mathur S., Provost J., 2007, “Tracking solar gravity modes: the dynamics of the solar core”, *Science*, **316**, 1591 – 1593
- Garrido R., 2000, “Photometric Modal Discrimination in  $\delta$  Scuti and  $\gamma$  Doradus Stars”, In *Delta Scuti and Related Stars*, Eds M. Breger, M. Montgomery, Publications of the Astronomical Society of the Pacific Conference Series, San Francisco, **210**, 67 – 89
- Garrido R., Garcia-Lobo E., Rodriguez E., 1990, “Modal discrimination of pulsating stars by using Stromgren photometry”, *Astronomy and Astrophysics*, **234**, 262 – 268
- Gautschy A., 1995, “Wolf-Rayet-type central stars of planetary nebulae: Are there pulsations involved?”, *Astronomy and Astrophysics*, **302**, 401 – 406
- Gautschy A., Saio H., 1993, “On non-radial oscillations of B-type stars”, *Monthly Notices of the Royal Astronomical Society*, **262**, 213 – 219
- Gautschy A., Saio H., 1996, “Stellar Pulsations Across the HR Diagram: Part 2”, *Annual Review of Astronomy and Astrophysics*, **34**, 551 – 606
- Gautschy A., Saio H., Harzenmoser H., 1998, “How to drive roAp stars”, *Monthly Notices of the Royal Astronomical Society*, **301**, 31 – 41
- Gautschy A., Althaus L. G., Saio H., 2005, “On the excitation of PG 1159-type pulsations”, *Astronomy and Astrophysics*, **438**, 1013 – 1020
- Gehmeyr M., 1993, “On nonlinear radial oscillations in convective RR Lyrae stars. III. A full-amplitude investigation of the red edge”, *Astrophysical Journal*, **412**, 341 – 350
- Gehmeyr M., Winkler K.-H. A., 1992, “On a new one-dimensional, time-dependent model for turbulence and convection. I. A basic discussion of the mathematical model”, *Astronomy and Astrophysics*, **253**, 92 – 100
- Gelly B., Grec G., Fossat E., 1986, “Evidence for global pressure oscillations in Procyon and  $\alpha$  Centauri”, *Astronomy and Astrophysics*, **164**, 383 – 394
- Gelly B., Lazrek M., Grec G., Ayad A., Schmider F. X., Renaud C., Salabert C., Fossat E., 2002, “Solar  $p$ -modes from 1979 days of the GOLF experiment”, *Astronomy and Astrophysics*, **394**, 285 – 297
- Giclas H. L., Burnham R., Thomas N. G., 1965, “A list of white dwarf suspects I : special objects of small proper motion from the Lowell survey”, *Lowell Observatory Bulletin*, **6**, 155 – 164
- Gies D. R., Kullavanijaya A., 1988, “The line profile variations of Epsilon Persei. I - Evidence for multimode nonradial pulsations”, *Astrophysical Journal*, **326**, 813 – 831
- Gilman P. A., Howe R., 2003, “Meridional motion and the slope of isorotation contours”, In *Proc. SOHO 12 / GONG+ 2002. Local and Global Helioseismology: The Present and Future*, Ed. A. Wilson, ESA SP-517, ESA Publications Division, Noordwijk, The Netherlands, 283 – 285

- Gilman P. A., Miller J. 1986, "Nonlinear convection of a compressible fluid in a rotating spherical shell", *Astrophysical Journal Supplement Series*, **61**, 585 – 608
- Gilman P. A., Morrow C. A., DeLuca E. E., 1989, "Angular momentum transport and dynamo action in the Sun: implications of recent oscillation measurements", *Astrophysical Journal*, **338**, 528 – 537
- Gillet D., Burki G., Duquennoy A., 1990, "The pulsation of the photosphere of the RV Tauri stars - AC Herculis and R Scuti", *Astronomy and Astrophysics*, **237**, 159 – 168
- Gilliland R. L., Brown T. M., Kjeldsen H., McCarthy J. K., Peri M. L., Belmonte J. A., Vidal I., Cram L. E., Palmer J., Frandsen S., Parthasarathy M., Petro L., Schneider H., Stetson P. B., Weiss W. W., 1993, "A search for solar-like oscillations in the stars of M67 with CCD ensemble photometry on a network of 4 M telescopes", *Astronomical Journal*, **106**, 2441 – 2476
- Gilliland R. L., Bono G., Edmonds P. D., Caputo F., Cassisi S., Petro L. D., Saha A., Shara M. M., 1998, "Oscillating Blue Stragglers in the Core of 47 Tucanae", *Astrophysical Journal*, **507**, 818 – 845
- Girard P., Köppen J., Acker A., 2007, "Chemical compositions and plasma parameters of planetary nebulae with Wolf-Rayet and wels type central stars", *Astronomy and Astrophysics*, **463**, 265 – 274
- Gizon L., 2004, "Helioseismology of time-varying flows through the solar cycle", *Solar Physics*, **224**, 217 – 228
- Gizon L., Birch A. C., 2005, "Local helioseismology", *Living Reviews in Solar Physics*, **2**, 6. URL (cited on 14/10/06):  
<http://www.livingreviews.org/lrsp-2005-6>
- Gizon L., Solanki S., 2003, "Determining the inclination of the rotation axis of a Sun-like star", *Astrophysical Journal*, **589**, 1009 – 1019
- Gizon L., Solanki S., 2004, "Measuring stellar differential rotation with asteroseismology", *Solar Physics*, **220**, 169 – 184
- Glatzel W., Gautschy A., 1992, "The treatment of highly non-adiabatic, non-radial pulsations by application of the Riccati method to the example of hydrogen-deficient carbon stars", *Monthly Notices of the Royal Astronomical Society*, **256**, 209 – 218
- Glatzel W., Kiriakidis M., Chernigovskij S., Fricke K. J., 1999, "The non-linear evolution of strange-mode instabilities", *Monthly Notices of the Royal Astronomical Society*, **303**, 116 – 124
- Glatzmaier G., 1985, "Numerical simulations of stellar convective dynamos. II. Field propagation in the convection zone", *Astrophysical Journal*, **291**, 300 – 307
- Godart M., Dupret M.-A., Noels A., 2008, "Is HD 163899 really a supergiant star?", *Communications in Asteroseismology*, **157**, 311 – 312
- Gold T., 1969, "Rotating Neutron Stars and the Nature of Pulsars", *Nature*, **221**, 25 – 27

- Goldreich P., Keeley D. A., 1977, "Solar seismology. II. The stochastic excitation of the solar  $p$ -modes by turbulent convection", *Astrophysical Journal*, **212**, 243 – 251
- Goldreich P., Wu Y., 1999, "Gravity modes in ZZ Ceti stars. I. Quasi-adiabatic analysis of overstability", *Astrophysical Journal*, **511**, 904 – 915
- Goldreich P., Murray N., Willette G., Kumar P., 1991, "Implications of solar  $p$ -mode frequency shifts", *Astrophysical Journal*, **370**, 752 – 762
- Goldreich P., Murray N., Kumar P., 1994, "Excitation of solar  $p$ -modes", *Astrophysical Journal*, **424**, 466 – 479
- Goldreich P., Lai D., Sahrling M., 1997, "Globally asymmetric supernova", *Unsolved Problems in Astrophysics*, 269 – 280
- Gonczi G., 1981, "On local theories of time dependent convection in the stellar pulsation problem", *Astronomy and Astrophysics*, **96**, 138 – 141
- Gong Z., Däppen W., Zejda L., 2001, "MHD equation of state with relativistic electrons", *Astrophysical Journal*, **546**, 1178 – 1182
- Goode P. R., Dziembowski W. A., Korzennik S. G., Rhodes E. J., 1991, "What we know about the Sun's internal rotation from solar oscillations", *Astrophysical Journal*, **367**, 649 – 657
- Goosens M., Lampens P., de Maerschalck D., Schrooten M., 1984, "Light variability of Sigma Scorpii", *Astronomy and Astrophysics*, **140**, 223 – 229
- Górny S. K., Acker A., Stasińska G., Stenholm B., Tylenda R., 1995, "[Wolf-Rayet]-type central stars of planetary nebulae", In *Proc. IAU Symposium 163: Wolf-Rayet Stars: Binaries; Colliding Winds; Evolution*, Eds K. A. van der Hucht, P. M. Williams, Kluwer Academic Publishers, Dordrecht, **163**, 85
- Górny S. K., Stasińska G., Escudero A. V., Costa R. D. D., 2004, "The populations of planetary nebulae in the direction of the Galactic bulge. Chemical abundances and Wolf-Rayet central stars", *Astronomy and Astrophysics*, **427**, 231 – 244
- Gough D. O., 1977a, "Mixing-length theory for pulsating stars", *Astrophysical Journal*, **214**, 196 – 213
- Gough D. O., 1977b, "Random remarks on solar hydrodynamics", *Proc. IAU Colloq. No. 36: The energy balance and hydrodynamics of the solar chromosphere and corona*, Eds R. M. Bonnet, P. Delache, G. de Bussac, Clairmont-Ferrand, 3 – 36
- Gough D. O., 1981, "A new measure of the solar rotation", *Monthly Notices of the Royal Astronomical Society*, **196**, 731 – 745
- Gough D. O., 1984a, "On the rotation of the Sun", *Phil. Trans. R. Soc. London, Ser. A*, **313**, 27 – 38
- Gough D. O., 1984b, "Towards a solar model", *Memorie della Società Astronomica Italiana*, **55**, 13 – 35
- Gough D. O., 1985a, "Theory of solar oscillations", *Future missions in solar, heliospheric and space plasma physics*, Eds E. Rolfe, B. Battrick, ESA SP-235, ESTEC, Noordwijk, 183 – 197

- Gough D. O., 1985b, "Inverting helioseismic data", *Solar Physics*, **100**, 65 – 99
- Gough D. O., 1986a, "EBK quantization of stellar waves", In *Hydrodynamic and magnetohydrodynamic problems in the Sun and stars*, Ed. Y. Osaki, University of Tokyo Press, 117 – 143
- Gough D. O., 1986b, "Asymptotic sound-speed inversions", In *Seismology of the Sun and the distant Stars*, Ed. D. O. Gough, Reidel, Dordrecht, 125 – 140
- Gough D. O., 1987, "Seismological measurement of stellar ages", *Nature*, **326**, 257 – 259
- Gough D. O., 1990a, "Comments on helioseismic inference", *Progress of seismology of the sun and stars*, In *Lecture Notes in Physics*, vol. **367**, 283 – 318, Eds Y. Osaki, H. Shibahashi, Springer, Berlin
- Gough D. O., 1990b, "On possible origins of relatively short-term variations in solar structure", *Phil. Trans. R. Soc. London, Ser. A*, **330**, 627 – 640
- Gough D. O., 1993, "Course 7. Linear adiabatic stellar pulsation", In *Astrophysical fluid dynamics, Les Houches Session XLVII*, Eds J.-P. Zahn, J. Zinn-Justin, Elsevier, Amsterdam, 399 – 560
- Gough D. O., 2001, "Lessons learned from solar oscillations", In *Astrophysical Ages and Time Scales*, Eds von Hippel, T., Simpson, C., Manset, N., Astronomical Society of the Pacific Conference Series, **245**, San Francisco, 31 – 43
- Gough D. O., 2002a, "Helioseismology: some current issues concerning model calibration", In Proc. 1st Eddington Workshop: 'Stellar structure and habitable planet finding', Eds Favata, F., Roxburgh, I. W., Galadí-Enríquez, D., ESA SP-485, ESA Publications Division, Noordwijk, The Netherlands, 65 – 73
- Gough D. O., 2002b, "How is solar activity influencing the structure of the Sun?", In Proc. SOHO 11 Symposium, 'From solar Min to Max: half a solar cycle with SOHO', ESA SP-508, ESA Publications Division, Noordwijk, The Netherlands, 577 – 591
- Gough D., 2004, "The power of helioseismology to address issues of fundamental physics", In *Equation-of-State and Phase-Transition Issues in Models of Ordinary Astrophysical Matter*, Eds V. Čelebonović, W. Däppen, D. Gough, AIP Conf. Proc. Vol. 731, AIP, Melville, New York, 119 – 138
- Gough D. O., 2005, in *The Roger Taylor Memorial Lectures*, A&G, special issue, Royal Astronomical Society (London), 16 – 25
- Gough D. O., 2007, "An elementary introduction to the JWKB theory", *Astronomische Nachrichten*, **328**, 273 – 285
- Gough D. O., Kosovichev A. G., 1993a, "Initial asteroseismic inversions", In *Proc. IAU Colloq. 137: Inside the stars*, Eds A. Baglin, W. W. Weiss, Astronomical Society of the Pacific Conference Series, San Francisco, **40**, 541 – 543
- Gough D. O., Kosovichev A. G., 1993b, "Seismic analysis of stellar p-mode spectra", In *Proc. GONG 1992: Seismic investigation of the Sun and stars*,

- Ed. T. M. Brown, Astronomical Society of the Pacific Conference Series, San Francisco, **42**, 351 – 354
- Gough D. O., McIntyre M. E., 1998, “Inevitability of a magnetic field in the Sun’s radiative interior”, *Nature*, **394**, 755 – 757
- Gough D. O., Novotny E., 1990, “Sensitivity of solar eigenfrequencies to the age of the Sun”, *Solar Physics*, **128**, 143 – 160
- Gough D. O., Thompson M. J., 1988, “On the implications of the symmetric component of the frequency splitting reported by Duvall, Harvey and Pomerantz”, *Proc. IAU Symposium No 123, Advances in helio- and asteroseismology*, Eds J. Christensen-Dalsgaard, S. Frandsen, Reidel, Dordrecht, 175 – 180
- Gough D. O., Thompson M. J., 1990, “The effect of rotation and a buried magnetic field on stellar oscillations”, *Monthly Notices of the Royal Astronomical Society*, **242**, 25 – 55
- Gough D. O., Thompson M. J., 1991, “The inversion problem”, In *Solar interior and atmosphere*, Eds A. N. Cox, W. C. Livingston, M. Matthews, Space Science Series, University of Arizona Press, 519 – 561
- Gough D. O., Vorontsov S. V., 1995, “Seismology of the solar envelope: measuring the acoustic phase shift generated in the outer layers”, *Monthly Notices of the Royal Astronomical Society*, **273**, 573 – 582
- Gough D. O., Kosovichev A. G., Toomre J., Anderson E. R., Antia H. M., Basu S., Chaboyer B., Chitre S. M., Christensen-Dalsgaard J., Dziembowski W. A., Eff-Darwich A., Elliott J. R., Giles P. M., Goode P. R., Guzik J. A., Harvey J. W., Hill F., Leibacher J. W., Monteiro M. J. P. F. G., Richard O., Sekii T., Shibahashi H., Takata M., Thompson M. J., Vauclair S., Vorontsov S. V., 1996, “The seismic structure of the Sun”, *Science*, **272**, 1296 – 1300
- Goupil M. J., Dziembowski W. A., Fontaine G., 1998, “On Some Observational Consequences of Nonlinearities in Stellar Pulsations”, *Baltic Astronomy*, **7**, 21 – 41
- Goupil M.-J., Dziembowski W. A., Pamyatnykh A. A., Talon S., 2000, “Rotational Splitting of  $\delta$  Scuti Stars”, In *Delta Scuti and Related Stars*, Eds M. Breger, M. Montgomery, Publications of the Astronomical Society of the Pacific Conference Series, San Francisco, **210**, 267 – 285
- Goupil M. J., Samadi R., Lochard J., Dziembowski, W. A., Pamyatnykh A., 2004, “Inferring information about rotation from stellar oscillations”, In *Proc. 2nd Eddington workshop, “Stellar structure and habitable planet finding”*, ESA SP-538, Eds F. Favata, S. Aigrain, ESA Publications Division, Noordwijk, The Netherlands, 133 – 140
- Graham-Smith F., 2003, “The radio emission from pulsars”, *Reports of Progress in Physics*, **66**, 173 – 238
- Gray D. F., 1997, “Absence of a planetary signature in the spectra of the star 51 Pegasi”, *Nature*, **385**, 795 – 796
- Gray D. F., 2005, *The Observation and Analysis of Stellar Photospheres, 3rd Edition*, Cambridge University Press

- Grec G., Fossat E., Pomerantz M., 1980, "Solar oscillations: full disk observations from the geographic South Pole", *Nature*, **288**, 541 – 544
- Grec G., Fossat E., Pomerantz M., 1983, "Full-disk observations of solar oscillations from the geographic South Pole: latest results", *Solar Physics*, **82**, 55 – 66
- Green R. F., 1977, *A complete sample of white dwarfs, hot subdwarfs, and quasars*, PhD Dissertation, California Institute of Technology, Pasadena, USA
- Green E. M., Fontaine G., Reed M. D., Callerame K., Seitenzahl I. R., White B. A., Hyde E. A., Østensen R., Cordes O., Brassard P., Falter S., Jeffery E. J., Dreizler S., Schuh S. L., Giovanni M., Edelmann H., Rigby J., Bronowska A., 2003, "Discovery of A New Class of Pulsating Stars: Gravity-Mode Pulsators among Subdwarf B Stars", *Astrophysical Journal*, **583**, L31 – L34
- Grevesse N., Noels A., 1993, "Cosmic abundances of the elements", In *Origin and Evolution of the Elements*, Eds N. Prantzos, E. Vangioni-Flam, M. Casse, Cambridge University Press, 15 – 25
- Grevesse N., Sauval A. J., 1998, "Standard solar composition", *Proc. ISSI Workshop on Solar Composition and its Evolution – from Core to Corona*, Eds C. Fröhlich, M. C. E. Huber, S. Solanki, R. von Steiger, *Space Science Reviews*, **85**, 161 – 174, Kluwer, Dordrecht
- Grigahcène A., Dupret M.-A., Gabriel M., Garrido R., Scuflaire R., 2005, "Convection-pulsation coupling. I. A mixing-length perturbative theory", *Astronomy and Astrophysics*, **434**, 1055 – 1062
- Groenewegen M. A. T., 2004, "Long Period Variables in the Magellanic Clouds: OGLE + 2 MASS + DENIS", *Astronomy and Astrophysics*, **425**, 595 – 613
- Grundahl F., Kjeldsen H., Frandsen S., Andersen M., Bedding T., Arentoft T., Christensen-Dalsgaard J., 2006, "SONG: Stellar Oscillations Network Group. A global network of small telescopes for asteroseismology and planet searches", *Memorie della Società Astronomica Italiana*, **77**, 458
- Guenther D. B., 1991, "The  $p$ -mode oscillation spectra of an evolving  $1M_{\odot}$  sun-like star", *Astrophysical Journal*, **375**, 352 – 365
- Guenther, D. B., 2004, "Quantitative analysis of the oscillation spectrum of  $\eta$  Bootis", *Astrophysical Journal*, **612**, 454 – 462
- Guenther, D. B., Brown, K. I. T., 2004, "Matching stellar models to oscillation data", *Astrophysical Journal*, **600**, 419 – 434
- Guenther, D. B., Demarque, P., 1996, "Seismology of  $\eta$  Bootis", *Astrophysical Journal*, **456**, 798 – 810
- Guenther D. B., Demarque P., 2000, " $\alpha$  Centauri AB", *Astrophysical Journal*, **531**, 503 – 520
- Guenther, D. B., Demarque, P., Kim, Y.-C., Pinsonneault, M. H., 1992, "Standard solar model", *Astrophysical Journal*, **387**, 372 – 393
- Guenther D. B., Demarque P., Buzasi D., Catanzarite J., Laher R., Conrow T., Kreidl T., 2000, "Evolutionary Model and Oscillation Frequencies for  $\alpha$

- Ursae Majoris: A Comparison with Observations”, *Astrophysical Journal*, **530**, L45 – L48
- Guenther, D. B., Kallinger, T., Reegen, P., Weiss, W. W., Matthews, J. M., Kuschnig, R., Marchenko, S., Moffat, A. F. J., Rucinski, S. M., Sasselov, D., Walker, G. A. H., 2005, “Stellar model analysis of the oscillation spectrum of  $\eta$  Bootis obtained from *MOST*”, *Astrophysical Journal*, **635**, 547 – 559
- Guzik J. A., 2006, “Reconciling the revised solar abundances with helioseismic constraints”, In *Proc. SOHO 18 / GONG 2006 / HELAS I Conf.: Beyond the spherical Sun*, Ed. K. Fletcher, ESA SP-624, ESA Publications Division, Noordwijk, The Netherlands
- Guzik J. A., Kaye A. B., Bradley P. A., Cox A. N., Neuforge C., 2000, “Driving the gravity-mode pulsations in  $\gamma$  Doradus variables”, *Astrophysical Journal*, **542**, L57 – L60
- Guzik J. A., Cox A. N., Despain K. M., 2005, “Pulsation-Driven Mass Loss in Luminous Blue Variables”, In *The Fate of the Most Massive Stars*, Eds R. Humphreys, K. Stanek, Publications of the Astronomical Society of the Pacific Conference Series, San Francisco, **332**, 263
- Hadrava P., 1995, “Orbital elements of multiple spectroscopic stars”, *Astronomy and Astrophysics Supplement Series*, **114**, 393 – 396
- Hadrava P., 1997, “Relative line photometry of eclipsing binaries”, *Astronomy and Astrophysics Supplement Series*, **122**, 581 – 584
- Hadrava P., 2001, “The Method of Spectra Disentangling and Its Links to Doppler Tomography”, In *Astrotomography, Indirect Imaging Methods in Observational Astronomy*, Eds H.M.J. Boffin, D. Steeghs, J. Cuypers, Lecture Notes in Physics, **573**, 261
- Hadrava P., 2004a, “Disentangling of spectra of multiple stars”, In *Spectroscopically and Spatially Resolving the Components of the Close Binary Stars*, Eds R. W. Hilditch, H. Hensberge, K. Pavlovski, Publications of the Astronomical Society of the Pacific Conference Series, San Francisco, **318**, 86 – 94
- Hadrava P., 2004b, “FOTEL 4 - User’s guide”, *Publications of the Astronomical Institute of the Czechoslovak Academy of Sciences*, **92**, 1 – 14
- Hadrava P., 2007, “New Trends in Disentangling the Spectra of Multiple Stars”, In *Proc. IAU Symposium: Binary Stars as Critical Tools & Tests in Contemporary Astrophysics*, Eds W.I. Hartkopf, E.F. Guinan, P. Harmanec, Cambridge University Press, **240**, 503 – 508
- Hadrava P., 2006, “Disentangling telluric lines in stellar spectra”, *Astronomy and Astrophysics*, **448**, 1149 – 1152
- Han Z., Podsiadlowski Ph., Maxted P. F. L., Marsh T. R., Ivanova N., 2002, “The origin of subdwarf B stars – I. The formation channels”, *Monthly Notices of the Royal Astronomical Society*, **336**, 449 – 466
- Han Z., Podsiadlowski Ph., Maxted P. F. L., Marsh T. R., 2003, “The origin of subdwarf B stars – II”, *Monthly Notices of the Royal Astronomical Society*, **341**, 669 – 691

- Handler G., 1995, "Variable "COOL" Central Stars of Planetary Nebulae", *Baltic Astronomy*, **4**, 357 – 359
- Handler G., 1999a, "The domain of  $\gamma$  Doradus variables in the Hertzsprung-Russell diagram", *Monthly Notices of the Royal Astronomical Society*, **309**, L19 – L23
- Handler G., 1999b, "Variable central stars of young Planetary Nebulae. A photometric study of the central star of M 2-54", *Astronomy and Astrophysics Supplement Series*, **135**, 493 – 498
- Handler G., 2003a, "The ZZ Leporis stars: variable central stars of young planetary nebulae", In *Interplay of Periodic, Cyclic and Stochastic Variability in Selected Areas of the H-R Diagram*, Ed. C. Sterken, Publications of the Astronomical Society of the Pacific Conference Series, San Francisco, **292**, 183
- Handler G., 2003b, "Merging Data from Large and Small Telescopes – Good or Bad? And: How Useful is the Application of Statistical Weights to Time-Series Photometric Measurements?", *Baltic Astronomy*, **12**, 253 – 270
- Handler G., Shobbrook R. R., 2002, "On the relationship between the  $\delta$  Scuti and  $\gamma$  Doradus pulsators", *Monthly Notices of the Royal Astronomical Society*, **333**, 251 – 262
- Handler G., Mendez R. H., Medupe R., Costero R., Birch P. V., Alvarez M., Sullivan D. J., Kurtz D. W., Herrero A., Guerrero M. A., Ciardullo R., Breger M., 1997, "Variable central stars of young planetary nebulae. I. Photometric multisite observations of IC 418", *Astronomy and Astrophysics*, **320**, 125 – 135
- Handler G., Pamyatnykh A. A., Zima W., Sullivan D. J., Audard N., Nitta A., 1998, "On the frequency and amplitude variations of the delta Scuti star CD-24 7599 (=XX Pyx)", *Monthly Notices of the Royal Astronomical Society*, **295**, 377 – 385
- Handler G., Arentoft T., Shobbrook R. R., Wood M. A., Crause L. A., Crake P., Podmore F., Habanyama A., Oswalt T., Birch P. V., Lowe G., Sterken C., Meintjes P., Brink J., Claver C. F., Medupe R., Guzik J. A., Beach T. E., Martinez P., Leibowitz E. M., Ibbetson P. A., Smith T., Ashoka B. N., Raj N. E., Kurtz D. W., Balona L. A., O'Donoghue D., Costa J. E. S., Breger M., 2000, "Delta Scuti Network observations of XX Pyx: detection of 22 pulsation modes and of short-term amplitude and frequency variations", *Monthly Notices of the Royal Astronomical Society*, **318**, 511 – 525
- Handler G., Balona L. A., Shobbrook R. R., Koen C., Bruch A., Romero-Colmenero E., Pamyatnykh A. A., Willems B., Eyer L., James D. J., Maas T., 2002, "Discovery and analysis of p-mode and g-mode oscillations in the A-type primary of the eccentric binary HD 209295", *Monthly Notices of the Royal Astronomical Society*, **333**, 262 – 279
- Handler G., O'Donoghue D., Müller M., Solheim J.-E., Gonzalez-Perez J. M., Johannessen F., Paparo M., Szeidl B., Viraghalmay G., Silvotti R., Vau-

- clair G., Dolez N., Pallier E., Chevreton M., Kurtz D. W., Bromage G. E., Cunha M. S., Østensen R., Fraga L., Kanaan A., Amorim A., Giovannini O., Kepler S. O., da Costa A. F. M., Anderson R. F., Wood M. A., Silvestri N., Klumpe E. W., Carlton R. F., Miller R. H., McFarland J. P., Grauer A. D., Kawaler S. D., Riddle R. L., Reed M. D., Nather R. E., Winget D. E., Hill J. A., Metcalfe T. S., Mukadam A. S., Kilic M., Watson T. K., Kleinman S. J., Nitta A., Guzik J. A., Bradley P. A., Sekiguchi K., Sullivan D. J., Sullivan T., Shobbrook R. R., Jiang X., Birch P. V., Ashoka B. N., Seetha S., Girish V., Joshi S., Dorokhova T. N., Dorokhov N. I., Akan M. C., Meištas E. G., Janulis R., Kalytis R., Ališauskas D., Anguma S. K., Kalebwe P. C., Moskalik P., Ogloza W., Stachowski G., Pajdosz G., Zola S., 2003a, "Amplitude and frequency variability of the pulsating DB white dwarf stars KUV 05134+2605 and PG 1654+160 observed with the Whole Earth Telescope", *Monthly Notices of the Royal Astronomical Society*, **340**, 1031 – 1038
- Handler G., Shobbrook R. R., Vuthela F. F., Balona L. A., Rodler F., Tshenyne T., 2003b, "Asteroseismological studies of three  $\beta$  Cephei stars: IL Vel, V433 Car and KZ Mus", *Monthly Notices of the Royal Astronomical Society*, **341**, 1005 – 1019
- Handler G., Aerts C., and an International Team of 50 Astronomers, 2004, "Asteroseismology of the  $\beta$  Cep star  $\nu$  Eri: initial results", In *IAU Colloquium 193: Variable Stars in the Local Group*, Eds D. W. Kurtz, K. R. Pollard, Astronomical Society of the Pacific Conference Series, San Francisco, **310**, 221 – 224
- Handler G., Shobbrook R. R., Mokgwetsi T., 2005, "An asteroseismic study of the  $\beta$  Cephei star  $\theta$  Ophiuchi: photometric results", *Monthly Notices of the Royal Astronomical Society*, **362**, 612 – 618
- Handler G., Jerzykiewicz M., Rodríguez E., Uytterhoeven K., Amado P. J., Dorokhova T. N., Dorokhov N. I., Poretti E., Sareyan J.-P., Parrao L., Lorenz D., Zsuffa D., Drummond R., Daszyńska-Daszkiewicz J., Verhoelst T., De Ridder J., Acke B., Bourge P.-O., Movchan A. I., Garrido R., Paparó M., Sahin T., Antoci V., Udovichenko S. N., Csorba K., Crowe R., Berkey B., Stewart S., Terry D., Mkrtichian D. E., Aerts C., 2006, "Asteroseismology of the  $\beta$  Cephei star 12 (DD) Lacertae: photometric observations, pulsational frequency analysis and mode identification", *Monthly Notices of the Royal Astronomical Society*, **365**, 327 – 338
- Hansen C. J., Cox J. P., van Horn H. M., 1977, "The effects of differential rotation on the splitting of nonradial modes of stellar oscillation", *Astrophysical Journal*, **217**, 151 – 159
- Hansen C. J., Cox J. P., Carroll B. W., 1978, "The quasi-adiabatic analysis of nonradial modes of stellar oscillation in the presence of slow rotation", *Astrophysical Journal*, **226**, 210 – 221
- Hansen C. J., Kawaler S. D., Trimble V., 2004, *Stellar interiors. Physical principles, structure, and evolution, second edition*, Springer, New York

- Hansen P. C., 1990, "Truncated singular value decomposition solutions to discrete ill-posed problems with ill-determined numerical rank", *SIAM J. Sci. Stat. Comp.*, **11**, 503 – 518
- Hao J., 1998, "Line Profile Analysis of Nonradial Pulsation Modes Based on Doppler Imaging", *Astrophysical Journal*, **500**, 440 – 448
- Hardie, R. H., 1964, "Photoelectric Reductions", In *Astronomical Techniques*, Ed. W. A. Hiltner, University of Chicago Press, **184**, 178
- Harmanec P., Uytterhoeven K., Aerts C., 2004, "Disentangling component spectra of  $\kappa$  Sco, a spectroscopic binary with a pulsating primary. I. Improved physical elements and analysis of periodic rapid variations of scalar quantities", *Astronomy and Astrophysics*, **422**, 1013 – 1021
- Harrington, R. S., Dahn, C. C., Kallarakal, V. V., Guetter, H. H., Riepe, B. Y., Walker, R. L., Pier, J. R., Vrba, F. J., Luginbuhl, C. B., Harris, H. C., Ables, H. D., 1993, "U. S. Naval Observatory photographic parallaxes. List IX", *Astronomical Journal*, **105**, 1571 – 1580
- Harris H. C., Liebert J., Kleinman S. J., Nitta A., Anderson S. F., Knapp G. R., Krzesiński J., Schmidt G., Strauss M. A., Vanden Berk D., Eisenstein D., Hawley S., Margon B., Munn J. A., Silvestri N. M., Smith J. A., Szkody P., Collinge M. J., Dahn C. C., Fan X., Hall P. B., Schneider D. P., Brinkmann J., Burles S., Gunn J. E., Hennessy G. S., Hindsley R., Ivezić Z., Kent S., Lamb D. Q., Lupton R. H., Nichol R. C., Pier J. R., Schlegel D. J., SubbaRao M., Uomoto A., Yanny B., York D. G., 2003, "An Initial Survey of White Dwarfs in the Sloan Digital Sky Survey", *Astronomical Journal*, **126**, 1023 – 1040
- Harvey J. W., 1988, "Techniques for observing stellar oscillations", In *Proc. IAU Symposium No 123, Advances in helio- and asteroseismology*, 497 – 511, Eds J. Christensen-Dalsgaard, S. Frandsen, Reidel, Dordrecht
- Harvey J. W., Hill F., Hubbard R. P., Kennedy J. R., Leibacher J. W., Pinatar J. A., Gilman P. A., Noyes R. W., Title A. M., Toomre J., Ulrich R. K., Bhatnagar A., Kennewell J. A., Marquette W., Partrón J., Saá O., Yasukawa E., 1996, "The Global Oscillation Network Group (GONG) project", *Science*, **272**, 1284 – 1286
- Harvey, J., Tucker, R., Britanik, L., 1998, "High resolution upgrade of the GONG instruments", In *Structure and dynamics of the interior of the Sun and Sun-like stars; Proc. SOHO 6/GONG 98 Workshop*, Eds S. G. Korzennik, A. Wilson, ESA SP-418, ESA Publications Division, Noordwijk, The Netherlands, 209 – 211
- Hatzes A. P., Cochran W. D., 1994, "The radial velocity variability of the K giant Beta Ophiuchi. 1: The detection of low-amplitude, short-period pulsations", *Astrophysical Journal*, **432**, 763 – 769
- Hatzes A. P., Kuerster M., 1994, "A search for rapid radial velocity variations in  $\alpha$  Circini", *Astronomy and Astrophysics*, **285**, 454 – 458
- Hatzes A. P., Mkrtichian D. E., 2004, "Radial velocity variations in pulsating Ap stars - III. The discovery of 16.21-min oscillations in  $\beta$  CrB", *Monthly Notices of the Royal Astronomical Society*, **351**, 663 – 666

- Hatzes A. P., Mkrtichian D. E., 2005, "Radial velocity variations in pulsating Ap stars. V. 10 Aquilae", *Astronomy and Astrophysics*, **430**, 279 – 286
- Hawley S. L., Covey K. R., Knapp G. R., Golimowski D. A., Fan X., Anderson S. F., Gunn J. E., Harris H. C., Ivezić Ž., Long G. M., Lupton R. H., McGehee P. M., Narayanan V., Peng E., Schlegel D., Schneider D. P., Spaßn E. Y., Strauss M. A., Székely P., Tsvetanov Z., Walkowicz L. M., Brinkmann J., Harvanek M., Hennessy G. S., Kleinman S. J., Krzesinski J., Long D., Neilsen E. H., Newman P. R., Nitta A., Snedden S. A., York D. G., 2002, "Characterization of M, L, and T Dwarfs in the Sloan Digital Sky Survey", *Astronomical Journal*, **123**, 3409 – 3427
- Haxton W. C., Parker P. D., Rolfs C. E., 2006, "Solar hydrogen burning and neutrinos", *Nuclear Physics A*, **777**, 226 – 253
- Heber, U., Jeffery, C. S., Napiwotski, R. (Eds), 2008, *Hot Subdwarf Stars and Related Objects*, Astronomical Society of the Pacific Conference Series, San Francisco, **392**
- Hekker S., Aerts C., De Ridder J., Carrier F., 2006, "Pulsations detected in the line profile variations of red giants. Modelling of line moments, line bisector and line shape", *Astronomy and Astrophysics*, **458**, 931 – 940
- Heller C. H., Kawaler S. D., 1988, "Evolutionary period changes in the rapidly oscillating Ap stars", *Astrophysical Journal*, **329**, L43 – L46
- Henroteau F., 1922, "The spectroscopic system theta Ophiuchi", *Publications of the Dominion Observatory Ottawa*, **8**, 1 – 10
- Henroteau F., 1926, "An international co-operation for the photographic study of Cepheid variables", *Popular Astronomy*, **34**, 493 – 500
- Henroteau F., 1927, "The spectroscopic system nu Eridani", *Publications of the Dominion Observatory Ottawa*, **9**, 117 – 126
- Henry G. W., Fekel F. C., 2005, "HD 8801: A Unique Single Am Star with  $\gamma$  Doradus and  $\delta$  Scuti Pulsations", *Astronomical Journal*, **129**, 2026 – 2033
- Henry G. W., Fekel F. C., Henry S. M., 2004, "HD 207651: A Triple System with  $\delta$  Scuti and Ellipsoidal Variations But No  $\gamma$  Doradus Pulsations", *Astronomical Journal*, **127**, 1720 – 1726
- Henry G. W., Fekel F. C., Henry S. M., 2005, "Eleven New  $\gamma$  Doradus Stars", *Astronomical Journal*, **129**, 2815 – 2830
- Hensberge H., Ilijic S., Torres K. B. V., 2008, "On the separation of component spectra in binary and higher-multiplicity stellar systems: bias progression and spurious patterns", *Astronomy and Astrophysics*, **482**, 1031 – 1051
- Herbst W., Shevchenko V. S., 1999, "A Photometric Catalog of Herbig Ae/Be Stars and Discussion of the Nature and Cause of the Variations of UX Orionis Stars", *Astronomical Journal*, **118**, 1043 – 1060
- Hertzsprung E., 1914, "Über die räumliche Verteilung der Veränderlichen vom  $\delta$  Cephei-Typus", *Astronomische Nachrichten*, **196**, 201 – 205
- Hewish A., Bell S. J., Pilkington J. D., Scott P. F., Collins R. A., 1968, "Observation of a Rapidly Pulsating Radio Source", *Nature*, **217**, 709 – 711

- Heydari-Malayeri M., Stee P., Zahn J.-P. (Eds), 2004, *Evolution of Massive Stars, Mass Loss and Winds*, European Astronomical Society Publications Series, **13**
- Heynderickx D., 1992, “A photometric study of Beta Cephei stars. I - Frequency analyses”, *Astronomy and Astrophysics Supplement Series*, **96**, 207 – 254
- Heynderickx D., Waelkens C., Smeeyers P., 1994, “A photometric study of  $\beta$  Cephei stars. II. Determination of the degrees L of pulsation modes”, *Astronomy and Astrophysics Supplement Series*, **105**, 447 – 480
- Heyl J. S., 2004, “r-Modes on Rapidly Rotating, Relativistic Stars. I. Do Type I Bursts Excite Modes in the Neutron Star Ocean?”, *Astrophysical Journal*, **600**, 939 – 945
- Hilditch R. W., 2001, *An Introduction to Close Binary Stars*, Cambridge University Press
- Hilditch R. W., Bell S. A., Hill G., Harries T. J., 1998, “Light-curve analysis and eclipse mapping of the contact binaries KQ GEM and V412 HER”, *Monthly Notices of the Royal Astronomical Society*, **296**, 100 – 108
- Hill F., Stark P. B., Stebbins R. T., Anderson E. R., Antia H. M., Brown T. M., Duvall T. L., Haber D. A., Harvey J. W., Hathaway D. H., Howe R., Hubbard R. P., Jones H. P., Kennedy J. R., Korzennik S. G., Kosovichev A. G., Leibacher J. W., Libbrecht K. G., Pintar J. A., Rhodes E. J., Schou J., Thompson M. J., Tomczyk S., Toner C. G., Toussaint R., Williams W. E., 1996, “The solar acoustic spectrum and eigenmode parameters”, *Science*, **272**, 1292 – 1295
- Hill F., Anderson E., Howe R., Jefferies S. M., Komm R. W., Toner C. G., 1998, “Estimated mode parameters from the fitting of GONG spectra”, In *Structure and dynamics of the interior of the Sun and Sun-like stars; Proc. SOHO 6/GONG 98 Workshop*, Eds S. G. Korzennik, A. Wilson, ESA SP-418, ESA Publications Division, Noordwijk, The Netherlands, 231 – 236
- Hill H. A., Stebbins R. T., Brown T. M., 1976, “Recent oblateness observations: Data, interpretation and significance for earlier work”, In *Atomic Masses and Fundamental Constants*, **5** Ed. J. H. Sanders, A. H. Wapstra, Plenum Press, 622 – 628
- Hill P. W., Kilkenny D., van Breda I. G., 1974, “UBV photometry of southern early-type stars”, *Monthly Notices of the Royal Astronomical Society*, **168**, 451 – 462
- Hoffleit D., Jaschek C., 1982, *The Bright Star Catalogue, 4th Edition*, New Haven: Yale University Observatory
- Höffner S., Andersen A. C., 2007, “Winds of M- and S-type AGB stars: an unorthodox suggestion for the driving mechanism”, *Astronomy and Astrophysics*, **465**, L39 – L42
- Höggbom J. A., 1974, “Aperture Synthesis with a Non-Regular Distribution of Interferometer Baselines”, *Astronomy and Astrophysics Supplement Series*, **15**, 417 – 426

- Hony S., Waters L. B. F. M., Tielens A. G. G. M., 2001, “The discovery of the “21”  $\mu\text{m}$  and “30”  $\mu\text{m}$  emission features in Planetary Nebulae with Wolf-Rayet central stars”, *Astronomy and Astrophysics*, **378**, L41 – L44
- Horne J. H., Baliunas S. L., 1986, “A prescription for period analysis of unevenly sampled time series”, *Astrophysical Journal*, **302**, 757 – 763
- Horne K., 1985, “Images of accretion discs. I - The eclipse mapping method”, *Monthly Notices of the Royal Astronomical Society*, **213**, 129 – 141
- Houdek G., 2000, “Convective effects on p-mode stability in Delta Scuti stars”, In *Delta Scuti and related stars*, Eds M. Breger, M. H. Montgomery, Astronomical Society of the Pacific Conference Series, San Francisco, **210**, 454 – 463
- Houdek G., 2006, “Stochastic excitation and damping of solar-type oscillations”, In *Proc. SOHO 18 / GONG 2006 / HELAS I Conf.: Beyond the spherical Sun*, Ed. K. Fletcher, ESA SP-624, ESA Publications Division, Noordwijk, The Netherlands
- Houdek, G., 2007, “Theoretical asteroseismology of solar-like oscillations”, In *Proc. Vienna Workshop on the Future of Asteroseismology*, eds G. Handler, G. Houdek, *Comm. in Asteroseismology*, **150**, 122 – 130
- Houdek G., Gough D. O., 2002, “Modelling pulsation amplitudes of  $\xi$  Hydreae”, *Monthly Notices of the Royal Astronomical Society*, **336**, L65 – L69
- Houdek G., Gough D. O., 2007, “An asteroseismic signature of helium ionization”, *Monthly Notices of the Royal Astronomical Society*, **375**, 861 – 880
- Houdek G., Gough D. O., 2008, “Progress report on solar age calibration”, In *Proc. IAU Symp. 252: The Art of Modelling Stars in the 21<sup>st</sup> Century*, Eds L. Deng, K. L. Chan, IAU and Cambridge University Press, 149 – 156
- Houdek G., Balmforth N. J., Christensen-Dalsgaard J., Gough D. O., 1999, “Amplitudes of stochastically excited oscillations in main-sequence stars”, *Astronomy and Astrophysics*, **351**, 582 – 596
- Hough S. S., 1898, “On the application of harmonic analysis to the dynamical theory of tides. Part II: On the general integration of Laplace’s dynamical equations”, *Phil. Trans. R. Soc., Ser. A*, **191**, 139 – 185
- Howard R., LaBonte B. J., 1980, “The Sun is observed to be a torsional oscillator with a period of 11 years”, *Astrophysical Journal*, **239**, L33 – L36
- Howarth I. D., Siebert K. W., Hussain G. A. J., Prinja R. K., 1997, “Cross-correlation characteristics of OB stars from IUE spectroscopy”, *Monthly Notices of the Royal Astronomical Society*, **284**, 265 – 285
- Howe R., 2008, “Helioseismology and the solar cycle”, *Advances in Space Research*, **41**, 846 – 854
- Howe R., 2009, “Solar interior rotation and its variation”, *Living Reviews of Solar Physics*, **6**, 1. URL (cited on 16/4/09): <http://www.livingreviews.org/lrsp-2009-1>
- Howe R., Christensen-Dalsgaard J., Hill F., Komm R. W., Larsen R. M., Schou J., Thompson M. J., Toomre J., 2000a, “Deeply penetrating banded zonal

- flows in the solar convection zone”, *Astrophysical Journal*, **533**, L163 – L166
- Howe R., Christensen-Dalsgaard J., Hill F., Komm R. W., Larsen R. M., Schou J., Thompson M. J., Toomre J., 2000b, “Dynamic variations at the base of the solar convection zone”, *Science*, **287**, 2456 – 2460
- Howe R., Komm R. W., Hill F., 2002, “Localizing the solar cycle frequency shifts in global  $p$ -modes”, *Astrophysical Journal*, **580**, 1172 – 1187
- Howe R., Christensen-Dalsgaard J., Komm R., Schou J., Thompson M. J., 2005, “Solar convection-zone dynamics, 1995–2004”, *Astrophysical Journal*, **634**, 1405 – 1415
- Howe R., Rempel M., Christensen-Dalsgaard J., Hill F., Komm R., Larsen R. M., Schou J., Thompson M. J., 2006, “Solar Convection Zone Dynamics: How sensitive are inversions to subtle dynamo features?”, *Astrophysical Journal*, **649**, 1155 – 1168
- Howe R., Christensen-Dalsgaard J., Hill F., Komm R., Schou J., Thompson M. J., Toomre J., 2007, “Temporal variations in solar rotation at the bottom of the convection zone: the current status”, In *Proc. of the Second International Symposium on Space Climate*, Eds G. Maris, K. Mursula, I. Usoskin, *Advances in Space Research*, **40**, 915 – 918
- Howell S. B., 2006, *Handbook of CCD astronomy, 2nd edition*, Cambridge observing handbooks for research astronomers, **5**, Cambridge University Press
- Hrudková M., Harmanec P., 2005, “Reliable elimination of telluric lines from stellar spectra”, *Astronomy and Astrophysics*, **437**, 765 – 768
- Hu H., Nelemans G., Østensen R., Aerts C., Vučković M., Groot P. J., 2007, “An evolutionary study of the pulsating subdwarf B eclipsing binary PG 1336–018 (NY Virginis)”, *Astronomy and Astrophysics*, **473**, 569 – 577
- Hu H., Dupret M.-A., Aerts C., Nelemans G., Kawaler S. D., Miglio A., Montalban J., Scuflaire R., 2008, “A seismic approach to testing different formation channels of subdwarf B stars”, *Astronomy and Astrophysics*, **490**, 243 – 252
- Hubrig S., Nesvacil N., Schöller M., North P., Mathys G., Kurtz D. W., Wolff B., Szeifert T., Cunha M. S., Elkin V. G., 2005, “Detection of an extraordinarily large magnetic field in the unique ultra-cool Ap star HD 154708”, *Astronomy and Astrophysics*, **440**, L37 – L40
- Hubrig S., Briquet M., Schöller M., De Cat P., Mathys G., Aerts C., 2006, “Discovery of magnetic fields in the  $\beta$  Cephei star  $\xi^1$  CMa and in several slowly pulsating B stars”, *Monthly Notices of the Royal Astronomical Society*, **369**, L61 – L65
- Humphreys R., Stanek K. (Eds), 2005, *The Fate of the Most Massive Stars*, Astronomical Society of the Pacific Conference Series, San Francisco, **332**
- Hurley J. R., Tout C. A., Aarseth S. J., Pols O. R., 2001, “Direct N-body modelling of stellar populations: blue stragglers in M67”, *Monthly Notices of the Royal Astronomical Society*, **323**, 630 – 650

- Hurley J. R., Pols O. R., Aarseth S. J., Tout C. A., 2005, "A complete N-body model of the old open cluster M67", *Monthly Notices of the Royal Astronomical Society*, **363**, 293 – 314
- Hutton R. G., Mendez R. H., 1993, "The central stars of He 2-131 and He 2-138 - Photometric variations", *Astronomy and Astrophysics*, **267**, L8 – L10
- Iben I., Livio M., 1993, "Common envelopes in binary star evolution", *Publications of the Astronomical Society of the Pacific*, **105**, 1373 – 1406
- Iben I., Mahaffy J., 1976, "On the sun's acoustical spectrum", *Astrophysical Journal*, **209**, L39 – L43
- Iben I. J., Tutukov A. V., Yungelson L. R., 1996, "On the Origin of Hydrogen-deficient Supergiants and Their Relation to R Coronae Borealis Stars and Non-DA White Dwarfs", *Astrophysical Journal*, **456**, 750 – 765
- Iglesias C. A., Rogers F. J., 1996, "Updated Opal Opacities", *Astrophysical Journal*, **464**, 943 – 953
- Iglesias C. A., Rogers F. J., Wilson B. G., 1990, "Opacities for classical Cepheid models", *Astrophysical Journal*, **360**, 221 – 226
- Iglesias C. A., Rogers F. J., Wilson B. G., 1992, "Spin-orbit interaction effects on the Rosseland mean opacity", *Astrophysical Journal*, **397**, 717 – 728
- Ignace R., Gayley K. G. (Eds), 2005, *The Nature and Evolution of Disks Around Hot Stars*, Publications of the Astronomical Society of the Pacific Conference Series, San Francisco, **337**
- Ilijic S., 2004, "Thoughts about disentangling in wavelength and in Fourier-space", In *Spectroscopically and Spatially Resolving the Components of the Close Binary Stars*, Eds R. W. Hilditch, H. Hensberge, K. Pavlovski, Publications of the Astronomical Society of the Pacific Conference Series, San Francisco, **318**, 107 – 110
- Ilijic S., Hensberge H., Pavlovski K., 2001, "Fourier Disentangling of Composite Spectra", In *Astrotomography, Indirect Imaging Methods in Observational Astronomy*, Eds H.M.J. Boffin, D. Steeghs, J. Cuypers, Lecture Notes in Physics, **573**, 269
- Ilijic S., Hensberge H., Pavlovski K., Freyhammer L. M., 2004, "Obtaining normalised component spectra with FDBinary", In *Spectroscopically and Spatially Resolving the Components of the Close Binary Stars*, Eds R. W. Hilditch, H. Hensberge, K. Pavlovski, Publications of the Astronomical Society of the Pacific Conference Series, San Francisco, **318**, 111 – 113
- Innis J. L., Isaak G. R., Brazier R. I., Belmonte J. A., Palle P. L., Roca Cortes T., Jones A. R., 1988, "High precision velocity observations of Arcturus using the 7699 Å line of potassium", In *Seismology of the Sun, Sun-like Stars*, Eds V. Domingo, E. J. Rolfe, ESA SP-286, ESA Publications Division, Noordwijk, The Netherlands, 569 – 573
- Isaak G. R., 1961, "An atomic beam spectrophotometer", *Nature*, **189**, 373 – 374
- Israel G. L., Belloni T., Stella L., Rephaeli Y., Gruber D. E., Casella P., Dall'Osso S., Rea N., Persic M., Rothschild R. E., 2005, "The Discovery

- of Rapid X-Ray Oscillations in the Tail of the SGR 1806-20 Hyperflare”, *Astrophysical Journal*, **628**, L53 – L56
- Ita Y., Tanabé T., Matsunaga N., Nakajima Y., Nagashima C., Nagayama T., Kato D., Kurita M., Nagata T., Sato S., Tamura M., Nakaya H., Nakada Y., 2004a, “Variable stars in the Magellanic Clouds - II. The data and infrared properties”, *Monthly Notices of the Royal Astronomical Society*, **353**, 705 – 712
- Ita Y., Tanabé T., Matsunaga N., Nakajima Y., Nagashima C., Nagayama T., Kato D., Kurita M., Nagata T., Sato S., Tamura M., Nakaya H., Nakada Y., 2004b, “Variable stars in the Magellanic Clouds: results from OGLE and SIRIUS”, *Monthly Notices of the Royal Astronomical Society*, **347**, 720 – 728
- Jackson J. D., 1975, *Classical Electrodynamics*, 2nd edition, Wiley, New York
- Jahn D., Rauch T., Reiff E., Werner K., Kruk J. W., Herwig F., 2007, “High-resolution ultraviolet spectroscopy of PG 1159-035 with HST and FUSE”, *Astronomy and Astrophysics*, **462**, 281 – 292
- Jain R., Roberts B., 1993, “Do  $p$ -mode frequency shifts suggest a hotter chromosphere at solar maximum?”, *Astrophysical Journal*, **414**, 898 – 907
- Jankov S., Vakili F., Domiciano de Souza A., Jr., Janot-Pacheco E., 2001, “Interferometric-Doppler imaging of stellar surface structure”, *Astronomy and Astrophysics*, **377**, 721 – 734
- Jankov S., Vakili F., Domiciano de Souza A., Jr., Janot-Pacheco E., 2002, Interferometric-Doppler Imaging of Nonradial Stellar Pulsations, In *Radial and Nonradial Pulsations as Probes of Stellar Physics*, Publications of the Astronomical Society of the Pacific Conference Series, San Francisco, **259**, 172 – 173
- Jankov S., Mathias P., Domiciano de Souza A., Jr., Uytterhoeven K., Aerts C., 2004, “Latitude distribution of nonradial pulsations in rapidly rotating B stars”, In *IAU Colloquim 193: Variable Stars in the Local Group*, Eds D. W. Kurtz, K. Pollard, Publications of the Astronomical Society of the Pacific Conference Series, San Francisco, **310**, 204
- Jefferies S. M., Vorontsov S. V., 2004, “A new way to model the solar oscillation  $\ell - \nu$  power spectrum”, *Solar Physics*, **220**, 347 – 359
- Jefferies S. M., Pomerantz M. A., Duvall T. L., Harvey J. W., Jaksha D. B., 1988, “Helioseismology from the South Pole: comparison of 1987 and 1981 results”, In *Seismology of the Sun, Sun-like Stars*, Eds V. Domingo, E. J. Rolfe, ESA SP-286, ESA Publications Division, Noordwijk, The Netherlands, 279 – 284
- Jefferies S. M., Vorontsov S. V., Giebink C., 2006, “Toward improving the seismic visibility of the solar tachocline”, In *Proc. SOHO 18 / GONG 2006 / HELAS I Conf.: Beyond the spherical Sun*, Ed. K. Fletcher, ESA SP-624, ESA Publications Division, Noordwijk, The Netherlands
- Jeffery C. S., 1996, “Surface properties of extreme helium stars”, In *Hydrogen Deficient Stars*, Eds C. S. Jeffery, U. Heber, Astronomical Society of the Pacific Conference Series, **96**, 152

- Jeffery C. S., Heber U., 1992, "The extreme helium star BD-9 deg 4395", *Astronomy and Astrophysics*, **260**, 133 – 150
- Jeffery C. S., Saio H., 1999, "Non-adiabatic linear pulsation models for low-mass helium stars", *Monthly Notices of the Royal Astronomical Society*, **308**, 221 – 227
- Jeffery C. S., Saio H., 2006, "Gravity-mode pulsation in subdwarf B stars: a critical test of stellar opacity", *Monthly Notices of the Royal Astronomical Society*, **372**, L48 – L52
- Jeffery C. S., Dhillon V. S., Marsh T. R., Ramachandran B., 2004, "Multi-colour high-speed photometry of pulsating subdwarf B stars with ULTRACAM", *Monthly Notices of the Royal Astronomical Society*, **352**, 699 – 707
- Jeffery C. S., Aerts C., Dhillon V. S., Marsh T. R., Gänsicke B. T., 2005, "Multicolour high-speed photometry of the subdwarf B star PG 0014+067 with ULTRACAM", *Monthly Notices of the Royal Astronomical Society*, **362**, 66 – 78
- Jeffrey W., 1988, "Inversion of helioseismic data", *Astrophysical Journal*, **327**, 987 – 992
- Jeffreys B., 1965, "Transformation of Tesselal Harmonics under Rotation" *Geophysical Journal International*, **10**, 141 – 145
- Jerzykiewicz M., 1978, "Nonradial oscillations of the Beta Cephei star 12 Lacertae", *Acta Astronomica*, **28**, 465 – 496
- Jerzykiewicz M., 1993, "UBV photometry of the Beta Cephei type variable stars. V - 16 (EN) Lacertae", *Acta Astronomica*, **43**, 13 – 26
- Jerzykiewicz M., Handler G., Shobbrook R. R., Pigulski A., Medupe R., Mokgwetsi T., Thlagwane P., Rodríguez E., 2005, "Asteroseismology of the  $\beta$  Cephei star  $\nu$  Eridani - IV. The 2003-2004 multisite photometric campaign and the combined 2002-2004 data", *Monthly Notices of the Royal Astronomical Society*, **360**, 619 – 630
- Jiménez-Reyes S. J., Chaplin W. J., García R. A., Appourchaux T., Baudin F., Boumier P., Elsworth Y., Fletcher S. T., Lazrek M., Leibacher J. W., Lochard J., New R., Régulo C., Salabert D., Toutain T., Verner G. A., Wachter R., 2008, "solarFLAG hare and hounds: estimation of p-mode frequencies from Sun-as-star helioseismic data", *Monthly Notices of the Royal Astronomical Society*, **389**, 1780 – 1790
- Jones C. A., 1976, "Acoustic overstability in a polytropic atmosphere", *Monthly Notices of the Royal Astronomical Society*, **176**, 145 – 159
- Jordinson C., Gough D. O., 2000, "The effect of the solar cycle on the resonant coupling of g modes", In *Proc. IAU Colloq. 176: The impact of large-scale surveys on pulsating star research*, Eds L. Szabados, D. W. Kurtz, Publications of the Astronomical Society of the Pacific Conference Series, San Francisco, **203**, 390
- Jura M., 1986, "RV Tauri stars as post-asymptotic giant branch objects", *Astrophysical Journal*, **309**, 732 – 736

- Jurcsik J., Szeidl B., Nagy A., Sodor A., 2005, "On the Distribution of the Modulation Frequencies of RR Lyrae Stars", *Acta Astronomica*, **55**, 303 – 314
- Jurcsik J., Szeidl B., Váradi M., Henden A., Hurtá Z., Lakatos B., Posztobányi K., Klagyivik P., Sódor Á., 2006, "The triple-mode pulsating variable V823 Cassiopeiae", *Astronomy and Astrophysics*, **445**, 617 – 625
- Jurkevich I., 1971, "A Method of Computing Periods of Cyclic Phenomena", *Astrophysics and Space Science*, **13**, 154 – 167
- Kallinger T., Zwintz K., Pamyatnykh A. A., Guenther D. B., Weiss W. W., 2005, "Pulsation of the K 2.5 giant star GSC 09137-03505?", *Astronomy and Astrophysics*, **433**, 267 – 273
- Kallinger T., Guenther D. B., Weiss W. W., Hareter M., Matthews J. M., Kuschnig R., Reegen P., Walker G. A. H., Rucinski S. M., Moffat A. F. J., Sasselov D., 2008a, "MOST found evidence for solar-type oscillations in the K2 giant star HD 20884", *Communications in Asteroseismology*, **153**, 84 – 103
- Kallinger T., Guenther D. B., Matthews J. M., Weiss W. W., Huber D., Kuschnig R., Moffat A. F. J., Rucinski S. M., Sasselov D., 2008b, "Nonradial p-modes in the G9.5 giant  $\epsilon$  Ophiuchi? Pulsation model fits to MOST photometry", *Astronomy and Astrophysics*, **478**, 497 – 505
- Kanaan A., Hatzes A. P., 1998, "Pulsations and Radial Velocity Variations in Pulsating AP Stars. I. Analysis of gamma Equulei", *Astrophysical Journal*, **503**, 848 – 857
- Kanbur S. M., Simon N. R., 1994, "Comparative pulsation calculations with OP and OPAL opacities", *Astrophysical Journal*, **420**, 880 – 883
- Karami K., 2008, "Third order effect of rotation on stellar oscillations of a B star", *Chinese Journal of Astronomy and Astrophysics*, **8**, 285 – 308
- Kato S., 1974, "Resonant interaction between non-radial oscillations and tide and double periodicity of beta Cephei stars", *Publications of the Astronomical Society of Japan*, **26**, 341 – 353
- Kaufer A., Stahl O., Wolf B., Fullerton A. W., Gaeng T., Gummersbach C. A., Jankovics I., Kovács J., Mandel H., Peitz J., Rivinius T., Szeifert T., 1997, "Long-term spectroscopic monitoring of BA-type supergiants. III. Variability of photospheric lines", *Astronomy and Astrophysics*, **320**, 273 – 286
- Kaufer A., Stahl O., Tubbesing S., Norregaard P., Avila G., Francois P., Pasquini L., Pizzella A., 2000, "Performance report on FEROS, the new fiber-linked echelle spectrograph at the ESO 1.52-m telescope", In *Proc. SPIE: Optical and IR Telescope Instrumentation and Detectors*, Eds M. Iye, A. F. Moorwood, **4008**, 459 – 466
- Kawaler S. D., 2004, "White dwarf rotation: observation and theory", In *Proc. IAU Symposium No 215: Stellar Rotation*, eds A. Maeder, P. Eenens, Astronomical Society of the Pacific, San Francisco, 561 – 570

- Kawaler S. D., Winget D. E., Hansen C. J., 1985a, "Evolutionary period changes in rotating hot pre-white dwarf stars", *Astrophysical Journal*, **298**, 752 – 755
- Kawaler S. D., Winget D. E., Hansen C. J., 1985b, "Evolution of the pulsation properties of hot pre-white dwarf stars", *Astrophysical Journal*, **295**, 547 – 560
- Kawaler S. D., Sekii T., Gough D., 1999, "Prospects for Measuring Differential Rotation in White Dwarfs through Asteroseismology", *Astrophysical Journal*, **516**, 349 – 365
- Kawaler S. D., Potter E. M., Vučković M., Dind Z. E., O'Toole S., Clemens J. C., O'Brien M. S., Grauer A. D., Nather R. E., Moskalik P. A., Claver C. F., Fontaine G., Wesemael F., Bergeron P., Vauclair G., Dolez N., Chevreton M., Kleinman S. J., Watson T. K., Barstow M. A., Sansom A. E., Winget D. E., Kepler S. O., Kanaan A., Bradley P. A., Dixson J., Provencal J., Bedding T. R., 2004, "Whole Earth Telescope observations of the pulsating hot white dwarf PG 1707+427", *Astronomy and Astrophysics*, **428**, 969 – 981
- Kaye A. B., Handler G., Krisciunas K., Poretti E., Zerbi F. M., 1999, "Gamma Doradus Stars: Defining a New Class of Pulsating Variables", *Publications of the Astronomical Society of the Pacific*, **111**, 840 – 844
- Kendall M., Ord J. K., 1990, *Time series, 3rd edition*, London: Hodder Arnold
- Kennelly E. J., Walker G. A. H., Merryfield W. J., 1992, "Tau Pegasi - A Fourier representation of line-profile variations", *Astrophysical Journal*, **400**, L71 – L74
- Kennelly E. J., Walker G. A. H., 1996, "The Line-Profile Variations of  $\theta^2$  Tauri", *Publications of the Astronomical Society of the Pacific*, **108**, 327 – 331
- Kennelly E. J., Brown T. M., Kotak R., Sigut T. A. A., Horner S. D., Korzennik S. G., Nisenson P., Noyes R. W., Walker A., Yang S., 1998, "The Oscillations of Tau Pegasi", *Astrophysical Journal*, **495**, 440 – 457
- Kepler S. O., 2007, "Observational white dwarf seismology", *Communications in Asteroseismology*, **150**, 221 – 226
- Kepler S. O., Nather R. E., Winget D. E., Nitta A., Kleinman S. J., Metcalfe T., Sekiguchi K., Xiaojun J., Sullivan D., Sullivan T., Janulis R., Meistas E., Kalytis R., Krzesinski J., Ogoza W., Zola S., O'Donoghue D., Romero-Colmenero E., Martinez P., Dreizler S., Deetjen J., Nagel T., Schuh S. L., Vauclair G., Ning F. J., Chevreton M., Solheim J.-E., Gonzalez Perez J. M., Johannessen F., Kanaan A., Costa J. E., Murillo Costa A. F., Wood M. A., Silvestri N., Ahrens T. J., Jones A. K., Collins A. E., Boyer M., Shaw J. S., Mukadam A., Klumpe E. W., Larrison J., Kawaler S., Riddle R., Ulla A., Bradley P., 2003, "The everchanging pulsating white dwarf GD358", *Astronomy and Astrophysics*, **401**, 639 – 654
- Kepler S. O., Castanheira B. G., Saraiva M. F. O., Nitta A., Kleinman S. J., Mullally F., Winget D. E., Eisenstein D. J., 2005, "Discovery of fourteen new ZZ Cetis with SOAR", *Astronomy and Astrophysics*, **442**, 629 – 634

- Kepler S. O., Kleinman S. J., Nitta A., Koester D., Castanheira B. G., Giovannini O., Costa A. F. M., Althaus L., 2007, "White dwarf mass distribution in the SDSS", *Monthly Notices of the Royal Astronomical Society*, **375**, 1315 – 1324
- Kervella P., Thévenin F., Ségransan D., Berthomieu G., Lopez B., Morel P., Provost J., 2003, "The diameters of  $\alpha$  Centauri A and B. A comparison of the asteroseismic and VINCI/VLTI views", *Astronomy and Astrophysics*, **404**, 1087 – 1097
- Kienzle F., Moskalik P., Bersier D., Pont F., 1999, "Structural properties of s-Cepheid velocity curves. Constraining the location of the  $\omega_4 = 2\omega_1$  resonance", *Astronomy and Astrophysics*, **341**, 818 – 826
- Kilkenny D., Koen C., O'Donoghue D., Stobie R. S., 1997, "A new class of rapidly pulsating star - I. EC 14026-2647, the class prototype", *Monthly Notices of the Royal Astronomical Society*, **285**, 640 – 644
- Kilkenny D., O'Donoghue D., Koen C., Lynas-Gray A. E., van Wyk F., 1998, "The EC 14026 stars - VIII. PG 1336-018: a pulsating sdB star in an HWVir-type eclipsing binary", *Monthly Notices of the Royal Astronomical Society*, **296**, 329 – 338
- Kilkenny D., Lawson W. A., Marang F., Roberts G., van Wyk F., 1999, "A photometric study of the hydrogen-deficient stars BD+1°4381 (FQ Aqr) and BD-1°3438 (NO Ser)", *Monthly Notices of the Royal Astronomical Society*, **305**, 103 – 108
- Kilkenny D., Reed M. D., O'Donoghue D., Kawaler S. D., Mukadam A., Kleinman S. J., Nitta A., Metcalfe T. S., Provencal J. L., Watson T. K., Sullivan D. J., Sullivan T., Shobbrook R., Jiang X. J., Joshi S., Ashoka B. N., Seetha S., Leibowitz E., Ibbetson P., Mendelson H., Meištas E., Kalytis R., Ališauskas D., Martinez P., van Wyk F., Stobie R. S., Marang F., Zola S., Krzesinski J., Ogłozna W., Moskalik P., Silvotti R., Piccioni A., Vauclair G., Dolez N., Chevreton M., Dreizler S., Schuh S. L., Deetjen J. L., Solheim J.-E., Gonzalez Perez J. M., Ulla A., Østensen R., Manteiga M., Suarez O., Burleigh M., Kepler S. O., Kanaan A., Giovannini O., 2003, "A Whole Earth Telescope campaign on the pulsating subdwarf B binary system PG 1336-018 (NY Vir)", *Monthly Notices of the Royal Astronomical Society*, **345**, 834 – 846
- Kim A., Winget D. E., Montgomery M. H., Sullivan D. J., 2005, "Exploring Uncharted Territory in Particle Physics Using Pulsating White Dwarfs: Prospects", In *14th European Workshop on White Dwarfs*, Eds D. Koester, S. Moehler, Astronomical Society of the Pacific, San Francisco, **334**, 489
- Kim C., McNamara D. H., Christensen C. G., 1993, "A photometric and spectrographic study of SX Phoenicis", *Astronomical Journal*, **106**, 2493 – 2501
- Kim S.-L., Lee J. W., Youn J.-H., Kwon S.-G., Kim C., 2002, "Photometric study of a pulsating component in the eclipsing binary Y Cam", *Astronomy and Astrophysics*, **391**, 213 – 218

- Kippenhahn R., Weigert A., 1990, *Stellar structure and evolution*, Springer-Verlag, Berlin
- Kiriakidis M., Fricke K. J., Glatzel W., 1993, "The Stability of Massive Stars and its Dependence on Metallicity and Opacity", *Monthly Notices of the Royal Astronomical Society*, **264**, 50 – 62
- Kiss L. L., Bedding T. R., 2003, "Red variables in the OGLE-II data base - I. Pulsations and period-luminosity relations below the tip of the red giant branch of the Large Magellanic Cloud", *Monthly Notices of the Royal Astronomical Society*, **343**, L79 – L83
- Kiss L. L., Bedding T. R., 2004, "Red variables in the OGLE-II data base - II. Comparison of the Large and Small Magellanic Clouds", *Monthly Notices of the Royal Astronomical Society*, **347**, L83 – L87
- Kjeldsen H., Bedding T. R., 1995, "Amplitudes of stellar oscillations: the implications for asteroseismology", *Astronomy and Astrophysics*, **293**, 87 – 106
- Kjeldsen H., Bedding T. R., Viskum M., Frandsen S., 1995, "Solar-like oscillations in  $\eta$  Boo", *Astronomical Journal*, **109**, 1313 – 1319
- Kjeldsen H., Arentoft T., Bedding T. R., Christensen-Dalsgaard J., Frandsen S., Thompson M. J., 1998, "Asteroseismology and stellar rotation", In *Structure and dynamics of the interior of the Sun and Sun-like stars; Proc. SOHO 6/GONG 98 Workshop*, eds S. G. Korzennik, A. Wilson, ESA SP-418, ESA Publications Division, Noordwijk, The Netherlands, 385 – 390
- Kjeldsen H., Bedding T. R., Frandsen S., Dall T. H., 1999, "A search for solar-like oscillations and granulation in  $\alpha$  Cen A", *Monthly Notices of the Royal Astronomical Society*, **303**, 579 – 587
- Kjeldsen H., Bedding T. R., Baldry I. K., Bruntt H., Butler R. P., Fischer D. A., Frandsen S., Gates E. L., Grundahl F., Lang K., Marcy G. W., Misch A., Vogt S. S., 2003, "Confirmation of solar-like oscillations in  $\eta$  Bootis", *Astronomical Journal*, **126**, 1483 – 1488
- Kjeldsen H., Bedding T. R., Butler R. P., Christensen-Dalsgaard J., Kiss L. L., McCarthy C., Marcy G. W., Tinney C. G., Wright J. T., 2005, "Solar-like oscillations in  $\alpha$  Centauri B", *Astrophysical Journal*, **635**, 1281 – 1290
- Kjeldsen H., Bedding T. R., Arentoft T., Butler R. P., Dall T. H., Karoff C., Kiss L. L., Tinney C. G., Chaplin W. J., 2008a, "The amplitude of solar oscillations using stellar techniques", *Astrophysical Journal*, **682**, 1370 – 1375
- Kjeldsen H., Bedding T. R., Christensen-Dalsgaard J., 2008b, "Correcting stellar oscillation frequencies for near-surface effects", *Astrophysical Journal*, **683**, L175 – L178
- Kleinman S. J., Harris H. C., Eisenstein D. J., Liebert J., Nitta A., Krzesiński J., Munn J. A., Dahn C. C., Hawley S. L., Pier J. R., Schmidt G., Silvestri N. M., Smith J. A., Szkody P., Strauss M. A., Knapp G. R., Collinge M. J., Mukadam A. S., Koester D., Uomoto A., Schlegel D. J., Anderson S. F., Brinkmann J., Lamb D. Q., Schneider D. P., York D. G., 2004, "A Catalog

- of Spectroscopically Identified White Dwarf Stars in the First Data Release of the Sloan Digital Sky Survey”, *Astrophysical Journal*, **607**, 426 – 444
- Kochukhov O., 2004, “Indirect Imaging of Nonradial Pulsations in a Rapidly Oscillating Ap Star”, *Astrophysical Journal*, **615**, L149 – L152
- Kochukhov O., 2005, “Variation of the line profile moments for stars pulsating in distorted oblique non-radial modes”, *Astronomy and Astrophysics*, **438**, 219 – 226
- Kochukhov O., 2006, “Pulsational line profile variation of the roAp star HR 3831”, *Astronomy and Astrophysics*, **446**, 1051 – 1070
- Kochukhov O., Ryabchikova T., 2001a, “Time-resolved spectroscopy of the roAp star  $\gamma$  Equ”, *Astronomy and Astrophysics*, **374**, 615 – 628
- Kochukhov O., Ryabchikova T., 2001b, “Pulsational and rotational line profile variations of the roAp stars  $\alpha$  Cir, and HR 3831”, *Astronomy and Astrophysics*, **377**, L22 – L2
- Kochukhov O., Bagnulo S., Barklem P. S., 2002a, “Interpretation of the Core-Wing Anomaly of Balmer Line Profiles of Cool Ap Stars”, *Astrophysical Journal*, **578**, L75 – L78
- Kochukhov O., Landstreet J. D., Ryabchikova T., Weiss W. W., Kupka F., 2002b, “Discovery of rapid radial velocity variations in the roAp star 10 Aql and possible pulsations of  $\beta$  CrB”, *Monthly Notices of the Royal Astronomical Society*, **337**, L1 – L5
- Kochukhov O., Drake N. A., Piskunov N., de la Reza R., 2004a, “Multi-element abundance Doppler imaging of the rapidly oscillating Ap star HR 3831”, *Astronomy and Astrophysics*, **424**, 935 – 950
- Kochukhov O., Ryabchikova T., Landstreet J. D., Weiss W. W., 2004b, “The null result of a search for pulsational variations of the surface magnetic field in the roAp star  $\gamma$  Equulei”, *Monthly Notices of the Royal Astronomical Society*, **351**, L34 – L38
- Kochukhov O., Ryabchikova T., Piskunov N., 2004c, “No magnetic field variation with pulsation phase in the roAp star  $\gamma$  Equulei”, *Astronomy and Astrophysics*, **415**, L13 – L16
- Koester D., Moehler S. (Eds), 2005, *14th European Workshop on White Dwarfs*, Astronomical Society of the Pacific Conference Series, San Francisco, **334**
- Koestler, A., 1959, *The Sleepwalkers*, the Macmillan Company, New York
- Kołaczkowski Z., Pigulski A., Soszyński I., Udalski A., Szymański M., Kubiak M., Źebruń K., Pietrzyński G., Woźniak P. R., Szewczyk O., Wyrzykowski L., 2005, “Beta Cephei stars in the LMC”, *Be Star Newsletter*, **37**, 19
- Kołaczkowski Z., Pigulski A., Soszyński I., Udalski A., Kubiak M., Szymański M., Źebruń K., Pietrzyński G., Woźniak P. R., Szewczyk O., Wyrzykowski L., 2006, “Hot pulsators in the Magellanic Clouds”, *Memorie della Societa Astronomica Italiana*, **77**, 336
- Kolenberg K., Smith H. A., Gazeas K. D., Elmasli A., Breger M., Guggenberger E., van Cauteren P., Lampens P., Reegen P., Niarchos P. G., Al-

- bayrak B., Selam S. O., Özavci I., Aksu O., 2006, "The Blazhko effect of RR Lyrae in 2003-2004", *Astronomy and Astrophysics*, **459**, 577 – 588
- Komm R. W., Howe R., Hill F., 2000, "Width and energy of solar  $p$ -modes observed by Global Oscillation Network Group", *Astrophysical Journal*, **543**, 472 – 485
- Korzennik S. G., Cacciani A., Rhodes E. J., Tomczyk S., Ulrich R. K., 1988, "Inversion of the solar rotation rate versus depth and latitude", *Seismology of the Sun, Sun-like Stars*, 117 – 124, Eds V. Domingo, E. J. Rolfe, ESA SP-286, ESA Publications Division, Noordwijk, The Netherlands
- Korzennik S. G., Cacciani A., Rhodes E. J., Ulrich R. K., 1990, "Contribution of high degree frequency splittings to the inversion of the solar rotation rate", In *Progress of seismology of the sun and stars*, Lecture Notes in Physics, **367**, 341 – 347, Eds Y. Osaki, H. Shibahashi, Springer, Berlin
- Korzennik S. G., Rabello-Soares M. C., Schou J., 2004, "On the determination of Michelson Doppler Imager high-degree mode frequencies", *Astrophysical Journal*, **602**, 481 – 515
- Kosovichev A. G., 1988, "The internal rotation of the Sun from helioseismological data", *Pis'ma Astron. Zh.*, **14**, 344 – 352 (English translation: *Sov. Astron. Lett.*, **14**, 145 – 149)
- Kosovichev A. G., 1996, "Helioseismic constraints on the gradient of angular velocity at the base of the solar convection zone", *Astrophysical Journal*, **469**, L61 – L64
- Kosovichev A. G., 1997, "Inferences of element abundances from helioseismic data", In *Robotic Exploration Close to the Sun: Scientific Basis*, Ed. S.R. Habbal, AIP Conf. Proc. 385, Amer. Inst. Phys., Woodbury, NY, 159 – 168
- Kosovichev A. G., Novikov I. D., 1992, "Non-linear effects at tidal capture of stars by a massive black hole – I. Incompressible affine model", *Monthly Notices of the Royal Astronomical Society*, **258**, 715 – 724
- Kosovichev A. G., Schou J., 1997, "Detection of zonal shear flows beneath the Sun's surface from  $f$ -mode frequency splitting", *Astrophysical Journal*, **482**, L207 – L210
- Kosovichev A. G., Christensen-Dalsgaard J., Däppen W., Dziembowski W. A., Gough D. O., Thompson M. J., 1992, "Sources of uncertainty in direct seismological measurements of the solar helium abundance", *Monthly Notices of the Royal Astronomical Society*, **259**, 536 – 558
- Kosovichev A. G., Schou J., Scherrer P. H., Bogart R. S., Bush R. I., Hoeksema J. T., Aloise J., Bacon L., Burnette A., de Forest C., Giles P. M., Leibrand K., Nigam R., Rubin M., Scott K., Williams S. D., Basu S., Christensen-Dalsgaard J., Däppen W., Rhodes Jr E. J., Duvall Jr T. L., Howe R., Thompson M. J., Gough D. O., Sekii T., Toomre J., Tarbell T. D., Title A. M., Mathur D., Morrison M., Saba J. L. R., Wolfson C. J., Zayer I., Milford P. N., 1997, "Structure and rotation of the solar interior: initial results from the MDI medium-l program", *Solar Physics*, **170**, 43 – 61

- Kovács G., 2000, "The distance modulus of the Large Magellanic Cloud based on double-mode RR Lyrae stars", *Astronomy and Astrophysics*, **363**, L1 – L4
- Kovács G., 2001, "On the double-mode RR Lyrae variables of the Sculptor dwarf galaxy", *Astronomy and Astrophysics*, **375**, 469 – 475
- Kovács G., Buchler J. R., 1994, "The triple-mode variable AC Andromedae", *Astronomy and Astrophysics*, **281**, 749 – 755
- Krisciunas K., Aspin C., Geballe T. R., Akazawa H., Claver C. F., Guinan E. F., Landis H. J., Luedeke K. D., Ohkura N., Ohshima O., Skillman D. R., 1993, "The 9-AURIGAE System", *Monthly Notices of the Royal Astronomical Society*, **263**, 781 – 788
- Kristian J., 1991, "No Pulsar in Supernova 1987A", *Nature*, **349**, 747 – 749
- Kristian J., Pennypacker C. R., Morris D. E., Muller R. A., Middleditch J., Hamuy M. A., Kunkel W. E., Imamura J. N., Lucinio R., Steiman-Cameron T. Y., 1989, "Submillisecond optical pulsar in supernova 1987A", *Nature*, **338**, 234 – 236
- Kubiak M., 1980, "Beta Cephei stars as non-radial oscillators. II - Multiperiodic variables Sigma SCO and Nu ERI", *Acta Astronomica*, **30**, 219 – 235
- Kubiak M., Seggewiss W., 1991, "Simultaneous spectroscopic and photoelectric observations of Beta Cephei stars. V - Nu Eridani", *Acta Astronomica*, **41**, 127 – 148
- Kudritzki R.-P., Puls J., 2000, "Winds from hot stars", *Annual Review of Astronomy and Astrophysics*, **38**, 613 – 666
- Kudritzki R. P., Lennon D. J., Puls J., 1994, "The wind momentum-luminosity relation of early type supergiants", *Astronomische Gesellschaft Abstract Series*, **10**, 42
- Kuhfuß R., 1986, "A model of time-dependent turbulent convection", *Astronomy and Astrophysics*, **160**, 116 – 120
- Kumar P., Basu S., 1999, "Line asymmetry of solar p-modes: Properties of acoustic sources", *Astrophysical Journal*, **519**, 396 – 399
- Kumar P., Goldreich P., 1989, "Nonlinear interactions among solar acoustic modes", *Astrophysical Journal*, **342**, 558 – 575
- Kumar P., Quataert E. J., 1997, "Angular momentum transport by gravity waves and its effect on the rotation of the solar interior", *Astrophysical Journal*, **475**, L143 – L146
- Kumar P., Franklin J., Goldreich P., 1988, "Distribution function for the time-averaged energies of stochastically excited solar *p*-modes", *Astrophysical Journal*, **328**, 879 – 887
- Kumar P., Quataert E. J., Bahcall J. N., 1996, "Observational searches for solar *g*-modes: some theoretical considerations", *Astrophysical Journal*, **458**, L83 – L85
- Kupka F., Montgomery M. H., 2002, "A-star envelopes: a test of local and non-local models of convection", *Monthly Notices of the Royal Astronomical Society*, **330**, L6 – L10

- Kurtz D. W., 1978, "12.15 Minute Light Variations in Przybylski's Star, HD 101065", *Information Bulletin on Variable Stars*, **1436**, 1 – 2
- Kurtz D. W., 1980, "Frequency analysis of the light variability of HD 101065, Przybylski's star", *Monthly Notices of the Royal Astronomical Society*, **191**, 115 – 122
- Kurtz D. W., 1981, "Discovery of 6.15 Minute Oscillations in the Cool Magnetic Ap Star HD 24712", *Information Bulletin on Variable Stars*, **1915**, 1 – 4
- Kurtz D. W., 1982, "Rapidly oscillating Ap stars", *Monthly Notices of the Royal Astronomical Society*, **200**, 807 – 859
- Kurtz D. W., 1990, "Rapidly oscillating Ap stars", *Annual Review of Astronomy and Astrophysics*, **28**, 607 – 655
- Kurtz D. W., 1992, "Axisymmetric spherical harmonic decomposition of the pulsation modes in rapidly oscillating Ap stars", *Monthly Notices of the Royal Astronomical Society*, **259**, 701 – 708
- Kurtz D. W., 2002, "Meeting Summary and Outlook for the Future" In *IAU Colloq. 185: Radial and Nonradial Pulsations as Probes of Stellar Physics*, Eds C. Aerts, T. R. Bedding, J. Christensen-Dalsgaard, Publications of the Astronomical Society of the Pacific Conference Series, San Francisco, **259**, 639 – 667
- Kurtz D. W., 2005, "Asteroseismology: Past, Present and Future", *Journal of Astrophysics and Astronomy*, **26**, 123 – 138
- Kurtz D. W., Leone F., 2006, "On the roAp star status of  $\beta$  Coronae Borealis", *Astronomy and Astrophysics*, **458**, 915 – 919
- Kurtz D. W., Marang F., 1995, "The discovery of delta Scuti pulsational variability in the pre-main-sequence Herbig AE star, HR 5999, and the discovery of rotational light variability in the remarkable He-weak BP star, HR 6000", *Monthly Notices of the Royal Astronomical Society*, **276**, 191 – 198
- Kurtz D. W., Martinez P., 2000, "Observing roAp Stars with WET: A Primer", *Baltic Astronomy*, **9**, 253 – 353
- Kurtz D. W., Medupe R., 1996, "Pulsation amplitude as a function of wavelength in roAp stars - a derivation of  $\Delta T/T$  versus atmospheric depth", *Bulletin of the Astronomical Society of India*, **24**, 291 – 300
- Kurtz D. W., Pollard K. R. (Eds), 2004, *Variable Stars in the Local Group*, Publications of the Astronomical Society of the Pacific Conference Series, San Francisco, **310**
- Kurtz D. W., Seeman J., 1983, "Frequency analysis of the rapidly oscillating Ap star HR 1217 (HD 24712)", *Monthly Notices of the Royal Astronomical Society*, **205**, 11 – 22
- Kurtz D., Wegner G., 1979, "The nature of Przybylski's star - an Ap star model inferred from the light variations and temperature", *Astrophysical Journal*, **232**, 510 – 519
- Kurtz D. W., Matthews J. M., Martinez P., Seeman J., Cropper M., Clemens J. C., Kreidl T. J., Sterken C., Schneider H., Weiss W. W., Kawaler S. D.,

- Kepler S. O., 1989, "The high-overtone p-mode spectrum of the rapidly oscillating Ap star HR 1217 (HD 24712) - Results of a frequency analysis of 324 HR of multi-site photometric observations obtained during a 46-d time-span in 1986", *Monthly Notices of the Royal Astronomical Society*, **240**, 881 – 915
- Kurtz D. W., Garrison R. F., Koen C., Hofmann G. F., Viranna N. B., 1995, "Metallicism and pulsation: the discovery of large-amplitude delta Scuti pulsation in a high-metallicity rho Puppis star, HD 40765", *Monthly Notices of the Royal Astronomical Society*, **276**, 199 – 205
- Kurtz D. W., Alcock C., Allsman R. A., Alves D., Axelrod T. S., Becker A. C., Bennett D. P., Cook K. H., Freeman K. C., Griest K., Lehner M. J., Marshall S. L., Minniti D., Peterson B. A., Pratt M. R., Quinn P. J., Rodgers A. W., Stubbs C. W., Sutherland W., Tomaney A., Welch D. L., The MACHO Collaboration, 2000, "A New Look at the Blazhko Effect in RR Lyrae Stars with High-Quality Data from the MACHO Project", In *IAU Colloquium 176: The Impact of Large-Scale Surveys on Pulsating Star Research*, Eds L. Szabados, D. W. Kurtz, Astronomical Society of the Pacific Conference Series, San Francisco, **203**, 291 – 298
- Kurtz D. W., Kawaler S. D., Riddle R. L., Reed M. D., Cunha M. S., Wood M., Silvestri N., Watson T. K., Dolez N., Moskalik P., Zola S., Pallier E., Guzik J. A., Metcalfe T. S., Mukadam A. S., Nather R. E., Winget D. E., Sullivan D. J., Sullivan T., Sekiguchi K., Jiang X., Shobbrook R., Ashoka B. N., Seetha S., Joshi S., O'Donoghue D., Handler G., Mueller M., Gonzalez Perez J. M., Solheim J.-E., Johannessen F., Ulla A., Kepler S. O., Kanaan A., da Costa A., Fraga L., Giovannini O., Matthews J. M., 2002, "Discovery of the 'missing' mode in HR 1217 by the Whole Earth Telescope", *Monthly Notices of the Royal Astronomical Society*, **330**, L57 – L61
- Kurtz D. W., Elkin V. G., Mathys G., 2003, New heights in asteroseismology: VLT spectroscopy of the roAp star HD 166473, *Monthly Notices of the Royal Astronomical Society*, **343**, L5 – L9
- Kurtz D. W., Cameron C., Cunha M. S., Dolez N., Vauclair G., Pallier E., Ulla A., Kepler S. O., da Costa A., Kanaan A., Fraga L., Giovannini O., Wood M. A., Silvestri N., Kawaler S. D., Riddle R. L., Reed M. D., Watson T. K., Metcalfe T. S., Mukadam A., Nather R. E., Winget D. E., Nitta A., Kleinman S. J., Guzik J. A., Bradley P. A., Matthews J. M., Sekiguchi K., Sullivan D. J., Sullivan T., Shobbrook R., Jiang X., Birch P. V., Ashoka B. N., Seetha S., Girish V., Joshi S., Moskalik P., Zola S., O'Donoghue D., Handler G., Mueller M., Perez J. M. G., Solheim J.-E., Johannessen F., Bigot L., 2005a, "Pushing the ground-based limit: 14- $\mu$ mag photometric precision with the definitive Whole Earth Telescope asteroseismic data set for the rapidly oscillating Ap star HR1217", *Monthly Notices of the Royal Astronomical Society*, **358**, 651 – 664

- Kurtz D. W., Elkin V. G., Mathys G., 2005b, "Probing the magnetoacoustic boundary layer in the peculiar magnetic star 33 Lib (HD 137949)", *Monthly Notices of the Royal Astronomical Society*, **358**, L6 – L10
- Kurtz D. W., Elkin V. G., Cunha M. S., Mathys G., Hubrig S., Wolff B., Savanov I., 2006a, "The discovery of 8.0-min radial velocity variations in the strongly magnetic cool Ap star HD154708, a new roAp star", *Monthly Notices of the Royal Astronomical Society*, **372**, 286 – 292
- Kurtz D. W., Elkin V. G., Mathys G., 2006b, "The discovery of a new type of upper atmospheric variability in the rapidly oscillating Ap stars with VLT high-resolution spectroscopy", *Monthly Notices of the Royal Astronomical Society*, **370**, 1274 – 1294
- Kurtz D. W., Elkin V. G., Mathys G., 2007a, "The detection of the very low amplitude 16.2-min pulsation in individual lines of first ionization stage of rare earth elements in the roAp star  $\beta$  CrB", *Monthly Notices of the Royal Astronomical Society*, **380**, 741 – 748
- Kurtz D. W., Elkin V. G., Mathys G., van Wyk F., 2007b, "On the nature of the upper atmospheric variability in the rapidly oscillating Ap star HD 134214", *Monthly Notices of the Royal Astronomical Society*, **381**, 1301 – 1312
- Kurtz D. W., Shibahashi, H., Dhillon, V.S., March, T.R., Littlefair, S.P., 2008, "A search for a new class of pulsating DA white dwarfs in the DB gap", *Monthly Notices of the Royal Astronomical Society*, , **389**, 1771 – 1779
- Kurucz R. L., 1993, *SYNTHE spectrum synthesis programs and line data*, Kurucz CD-ROMs, Cambridge, MA: Smithsonian Astrophysical Observatory
- Kuschnig R., Weiss W. W., Gruber R., Bely P. Y., Jenkner H., 1997, "Microvariability survey with the Hubble Space Telescope Fine Guidance Sensors. Exploring the instrumental properties", *Astronomy and Astrophysics*, **328**, 544 – 550
- Lafler J., Kinman T. D., 1965, "An RR Lyrae Star Survey with the Lick 20-INCH Astrograph II. The Calculation of RR Lyrae Periods by Electronic Computer", *Astrophysical Journal Supplement Series*, **11**, 216 – 222
- Lamb H., 1909, "On the Theory of Waves Propagated Vertically in the Atmosphere", *Proceedings of the London Mathematical Society*, **7**, 122 – 141
- Lamb H., 1932, *Hydrodynamics*, 6th edition, Cambridge University Press, Cambridge
- Lamers H. J. G. L. M., Bastiaanse M. V., Aerts C., Spoon H. W. W., 1998, "Periods, period changes and the nature of the microvariations of Luminous Blue Variables", *Astronomy and Astrophysics*, **335**, 605 – 621
- Lamers H. J. G. L. M., Cassinelli J. P., 1999, *Introduction to Stellar Winds*, Cambridge University Press, Cambridge
- Lampens, P., 2006, "Intrinsic Variability in Multiple Systems and Clusters: Open Questions" In *Astrophysics of Variable Stars*, Eds C. Sterken, C. Aerts, Publications of the Astronomical Society of the Pacific Conference Series, San Francisco, **349**, 153

- Lampens P., Frémat Y., Garrido R., Peña J. H., Parrao L., van Cauteren P., Cuypers J., de Cat P., Uytterhoeven K., Arentoft T., Hobart M., 2005, "A photometric study of the light variations of the triple system DG Leo", *Astronomy and Astrophysics*, **438**, 201 – 209
- Landau L. D., Lifshitz E. M., 1966, *Fluid mechanics*. Pergamon Press, Oxford
- Lanz T., Hubeny I., 2003, "A Grid of Non-LTE Line-blanketed Model Atmospheres of O-Type Stars", *Astrophysical Journal Supplement Series*, **146**, 417 – 441 (Erratum: *Astrophysical Journal Supplement Series*, **147**, 225)
- Lanz T., Hubeny I., 2007, "A Grid of NLTE Line-blanketed Model Atmospheres of Early B-Type Stars", *Astrophysical Journal Supplement Series*, **169**, 83 – 104
- Laplace P. S., 1799, *Traité de Mécanique Céleste*, Imprimerie de Crapelet, Paris
- Larsen R. M., 1997, "Iterative algorithms for two-dimensional helioseismic inversion", In *Proc. Interdisciplinary Inversion Workshop*, Ed. B.H. Jacobsen, **5**, Aarhus University, 123 – 137
- Larsen R. M., Hansen P. C., 1997, "Efficient implementation of the SOLA mollifier method", *Astronomy and Astrophysics Supplement Series*, **121**, 587 – 598
- Larsen R. M., Christensen-Dalsgaard J., Kosovichev A. G., Schou J., 1998, "Improved SOLA inversions of MDI data", In *Structure and dynamics of the interior of the Sun and Sun-like stars; Proc. SOHO 6/GONG 98 Workshop*, Eds S. G. Korzennik, A. Wilson, ESA SP-418, ESA Publications Division, Noordwijk, The Netherlands, 813 – 818
- Larson T. P., Schou J., 2008, "Improvements in global mode analysis", In *Proc. HELAS II International Conference: Helioseismology, Asteroseismology and the MHD Connections, Göttingen, August 2007*, Eds L. Gizon, M. Roth, *Journal of Physics, Conference Series*, **118**, 012083(1 – 7)
- Latour J., Toomre J., Zahn J.-P., 1981, "Stellar convection theory. III. Dynamical coupling of the two convection zones in A-type stars by penetrative motion", *Astrophysical Journal*, **248**, 1081 – 1098
- Lavely E. M., Ritzwoller M. H., 1992, "The effect of global-scale, steady-state convection and elastic-gravitational asphericities on helioseismic oscillations", *Phil. Trans. R. Soc. London, Ser. A*, **339**, 431 – 496
- Lavely E. M., Ritzwoller M. H., 1993, "Average effects of large-scale convection on helioseismic line widths and frequencies", *Astrophysical Journal*, **403**, 810 – 832
- Lawson W. A., Kilkenny D., 1996, "The observational characterization of hydrogen-deficient carbon stars as pulsating stars", In *Hydrogen Deficient Stars*, Eds C. S. Jeffery, U. Heber, Astronomical Society of the Pacific Conference Series, San Francisco, **96**, 349
- Lazrek M., Pantel A., Fossat E., Gelly B., Schmider F. X., Fierry-Fraillon D., Grec G., Loudagh S., Ehgamberdiev S., Khamitov I., Hoeksema J. T., Pallé P. L., Régulo C., 1996, "Is the solar core rotating faster or slower than the envelope?" *Solar Physics*, **166**, 1 – 16

- Lazrek M., Baudin F., Bertello L., Boumier P., Charra J., Fierry-Fraillon D., Fossat E., Gabriel A. H., García R. A., Gelly B., Gouiffes C., Grec G., Pallé P. L., Pérez Hernández F., Régulo C., Renaud C., Robillot J.-M., Roca-Cortés T., Turck-Chièze S., Ulrich R. K., 1997, "First results on  $p$  modes from GOLF experiment", *Solar Physics*, **175**, 227 – 246
- Leavitt H. S., Pickering E. C., 1912, "Periods of 25 Variable Stars in the Small Magellanic Cloud", *Harvard College Observatory Circular*, **173**, 1 – 3
- Lebovitz N. R., 1965, "On Schwarzschild's criterion for the stability of gaseous masses", *Astrophysical Journal*, **142**, 229 – 242
- Lebreton Y., Monteiro M. J. P. F. G., Montalbán J., Moya A., Baglin A., Christensen-Dalsgaard J., Goupil M.-J., Michel E., Provost J., Roxburgh I. W., Scuflaire R., ESTA Team, 2008, "The CoRoT evolution and seismic tools activity", *Astrophysics and Space Science*, **316**, 1 – 12
- Lebzelter T., Hinkle K. H., 2002, "Velocity variability of semiregular and irregular variables", *Astronomy and Astrophysics*, **393**, 563 – 571
- Ledoux P., 1949, "Contributions à l'Étude de la Structure Interne des Étoiles et de leur Stabilité", *Mem. Soc. R. Sci. Liège, 4ième série*, **9**, 3 – 294 ("Chapitre V: Stabilité dynamique et pulsations d'étoiles gazeuses animées d'un mouvement de rotation uniforme", 263 – 294)
- Ledoux P., 1951, "The nonradial oscillations of gaseous stars and the problem of beta Canis Majoris", *Astrophysical Journal*, **114**, 373 – 384
- Ledoux P., 1962, "Sur la forme asymptotique des pulsations radiales adiabatiques d'une étoile. I.", *Bulletin de l'Académie Royale de Belgique, Classe des sciences, 5ième série*, **48**, 240 – 254
- Ledoux P., Walraven T., 1958, "Variable stars", In *Handbuch der Physik*, **51**, chapter IV, 353 – 604, Springer-Verlag
- Lee U., 1985, "Stability of the Delta Scuti stars against nonradial oscillations with low degrees L", *Publications of the Astronomical Society of Japan*, **37**, 279 – 291
- Lee U., 1998, "Pulsational stability of rotating main-sequence B stars", *Astrophysical Journal*, **497**, 912 – 920
- Lee U., 2001, "Pulsational stability of  $g$ -modes in slowly pulsating B stars", *Astrophysical Journal*, **557**, 311 – 319
- Lee U., 2004, "Surface r-Modes and Burst Oscillations of Neutron Stars", *Astrophysical Journal*, **600**, 914 – 926
- Lee U., Baraffe I., 1995, "Pulsational stability of rotating main sequence stars: the second order effects of rotation on the nonadiabatic oscillations", *Astronomy and Astrophysics*, **301**, 419 – 432
- Lee U., Saio, H., 1986, "Overstable convective modes in uniformly rotating massive main-sequence stars", *Monthly Notices of the Royal Astronomical Society*, **221**, 365 – 376
- Lee U., Saio H., 1987, "Low-frequency oscillations of uniformly rotating stars", *Monthly Notices of the Royal Astronomical Society*, **224**, 513 – 526

- Lee U., Saio H., 1990, "Line profile variations caused by low-frequency nonradial pulsations of rapidly rotating stars", *Astrophysical Journal*, **349**, 570 – 579
- Lee U., Saio H., 1997, "Low-frequency nonradial oscillations in rotating stars. I. Angular dependence", *Astrophysical Journal*, **491**, 839 – 845
- Lee U., Jeffery C. S., Saio H., 1992, "Line profile variations caused by low-frequency non-radial pulsations of rapidly rotating stars. II", *Monthly Notices of the Royal Astronomical Society*, **254**, 185 – 191
- Lefebvre S., Kosovichev A. G., 2005, "Changes in the subsurface stratification of the Sun with the 11-year activity cycle", *Astrophysical Journal*, **633**, L149 – L152
- Lefebvre S., Kosovichev A. G., Rozelot J. P., 2007, "Helioseismic test of non-homologous solar radius changes with the 11 year activity cycle", *Astrophysical Journal*, **658**, L135 – L138
- Lefever K., Puls J., Aerts C., 2007a, "Statistical properties of a sample of periodically variable B-type supergiants. Evidence for opacity-driven gravity-mode oscillations", *Astronomy and Astrophysics*, **463**, 1093 – 1109
- Lefever K., Puls J., Aerts C., 2007b, "A Grid of FASTWIND NLTE Model Atmospheres of Massive Stars", In *The Future of Photometric, Spectrophotometric and Polarimetric Standardization*, Ed. C. Sterken, Publications of the Astronomical Society of the Pacific Conference Series, San Francisco, **364**, 545 – 550
- Lefèvre L., Marchenko S. V., Moffat A. F. J., Chené A. N., Smith S. R., St-Louis N., Matthews J. M., Kuschnig R., Guenther D. B., Poteet C. A., Rucinski S. M., Sasselov D., Walker G. A. H., Weiss W. W., 2005, "Oscillations in the Massive Wolf-Rayet Star WR 123 with the MOST Satellite", *Astrophysical Journal*, **634**, L109 – L112
- Leibacher J., Stein R. F., 1971, "A new description of the solar five-minute oscillation", *Astrophys. Lett.*, **7**, 191 – 192
- Leighton R. B., 1961, "(Untitled comment)", *IAU Symp. No. 12, Fourth Symposium on Cosmical Gas Dynamics: Aerodynamical Phenomena in Stellar Atmospheres*, Ed. R. N. Thomas, *Nuovo Cimento Suppl.*, **22**, 321 – 325
- Leighton R. B., Noyes R. W., Simon G. W., 1962, "Velocity fields in the solar atmosphere I. Preliminary report", *Astrophysical Journal*, **135**, 474 – 499
- Leone F., Catanzaro G., Catalano S., 2000, "Spectropolarimetric measurements of the mean longitudinal magnetic field of chemically peculiar stars. On the light, spectral and magnetic variability", *Astronomy and Astrophysics*, **355**, 315 – 326
- Leone F., Kurtz D. W., 2003, "Discovery of magnetic field variations with the 12.1-minute pulsation period of the roAp star  $\gamma$  Equulei", *Astronomy and Astrophysics*, **407**, L67 – L71
- Levato H., Malaroda S., Morrell N., Solivella G., 1987, "Stellar multiplicity in the Scorpius-Centaurus association", *Astrophysical Journal Supplement Series*, **64**, 487 – 503

- Li, L. H., Robinson, F. J., Demarque, P., Sofia, S., 2002, "Inclusion of turbulence in solar modeling", *Astrophysical Journal*, **567**, 1192 – 1201
- Libbrecht K. G., 1988a, "Solar p-mode frequency splittings", *Seismology of the Sun, Sun-like Stars*, 131 – 136, Eds V. Domingo, E. J. Rolfe, ESA SP-286, ESA Publications Division, Noordwijk, The Netherlands
- Libbrecht K. G., 1988b, "Radial velocity observations reveal multimode oscillations in Gamma Equulei", *Astrophysical Journal*, **330**, L51 – L53
- Libbrecht K. G., 1989, "Solar p-mode frequency splittings", *Astrophysical Journal*, **336**, 1092 – 1097
- Libbrecht K. G., 1992, "On the ultimate accuracy of solar oscillation frequency measurements", *Astrophysical Journal*, **387**, 712 – 714
- Libbrecht K. G., Woodard M. F., 1990, "Solar-cycle effects on solar oscillation frequencies", *Nature*, **345**, 779 – 782
- Libbrecht K. G., Woodard M. F., Kaufman J. M., 1990, "Frequencies of solar oscillation", *Astrophysical Journal Supplement Series*, **74**, 1129 – 1149
- Liebert J., 1986, "The origin and evolution of helium-rich white dwarfs", In *IAU Colloquium 87: Hydrogen Deficient Stars and Related Objects*, Dordrecht, D. Reidel Publishing Co., **128**, 367 – 381
- Liebert J., Fleming T. A., Green R. F., Grauer A. D., 1988, "The nucleus of the planetary nebula VV 47 - Similarities with the pulsating PG1159-035/K1-16 variables", *Publications of the Astronomical Society of the Pacific*, **100**, 187 – 191
- Lignières F., Georgeot B., 2008, "Wave chaos in rapidly rotating stars", *Phys. Rev. E*, **78**, 016215-(1–4)
- Lignières F., Georgeot B., 2009, "Asymptotic analysis of high-frequency acoustic modes in rapidly rotating stars", *Astronomy and Astrophysics*, **500**, 1173 – 1192
- Lignières F., Rieutord M., Reese D., 2006, "Acoustic oscillations in rapidly rotating polytropic stars. I. Effects of the centrifugal distortion", *Astronomy and Astrophysics*, **455**, 607 – 620
- Lin C.-H., Antia H. M., Basu S., 2007, "Seismic study of the chemical composition of the solar convection zone", *Astrophysical Journal*, **668**, 603 – 610
- Lindegren L., Dravins D., 2003, "The fundamental definition of "radial velocity", *Astronomy and Astrophysics*, **401**, 1185 – 1201
- Little R. J. A., Rubin D. B., 2002, *Statistical Analysis with Missing Data, 2nd Edition*, Wiley Series in Probability and Statistics
- Liu Z.-E., Tang Y.-K., Gai N., 2008, "Solar-like Oscillations of the Red Giant  $\epsilon$  Ophiuchi", *Chinese Astronomy and Astrophysics*, **32**, 380 – 387
- Lloyd Evans T., 1975, "Near-infrared photometry of globular clusters - IV. The metal poor cluster NGC 6656 (M22)", *Monthly Notices of the Royal Astronomical Society*, **171**, 647 – 657
- Lloyd Evans T. L., 1985, "Circumstellar material and the light variations of RV Tauri stars", *Monthly Notices of the Royal Astronomical Society*, **217**, 493 – 506

- Lloyd Evans T., 1999, "The nature of RV Tauri stars", In *IAU Symposium 191: Asymptotic Giant Branch Stars*, Eds T. Lebertre, A. Lèbre, C. Waelkens, Publications of the Astronomical Society of the Pacific Conference Series, San Francisco, **191**, 453 – 457
- Lochard, J., Samadi, R., Goupil, M.-J., 2004, " $\eta$ Boo inversion of simulated rotational profile", *Solar Physics*, **220**, 199 – 205
- Lochard J., Samadi R., Goupil M. J., 2005, "Rotation profile inversion in solar-like stars. In the COROT framework", *Astronomy and Astrophysics*, **438**, 939 – 948
- Löffler W., 2000, "g Modes in F stars – A Non-adiabatic Investigation of the Stability of g Modes in Gamma Doradus Stars", In *IAU Colloquium 176: The Impact of Large-Scale Surveys on Pulsating Star Research*, Eds L. Szabados, D. W. Kurtz, Astronomical Society of the Pacific Conference Series, San Francisco, **203**, 447 – 448
- Lomb N. R., 1976, "Least-squares frequency analysis of unequally spaced data", *Astrophysics and Space Science*, **39**, 447 – 462
- Longuet-Higgins M. S., 1968, "The eigenfunctions of Laplace's tidal equations over a sphere", *Phil. Trans. R. Soc. London, Series A*, **262**, 511 – 607
- Loumos G. L., Deeming T. J., 1978, "Spurious results from Fourier analysis of data with closely spaced frequencies", *Astrophysics and Space Science*, **56**, 285 – 291
- Lovekin C. C., Deupree R. G., 2008, "Radial and nonradial oscillation modes in rapidly rotating stars", *Astrophysical Journal*, **679**, 1499 – 1508
- Lovekin C. C., Deupree R. G., Clement M. J., 2009, "Effects of uniform and differential rotation on stellar pulsations", *Astrophysical Journal*, **693**, 677 – 690
- Lovy D., Maeder A., Noels A., Gabriel M., 1984, "Supergiant variability - Theoretical pulsation periods and comparison with observations", *Astronomy and Astrophysics*, **133**, 307 – 312
- Lucy L. B., 1967, "Gravity-darkening for stars with convective envelopes", *Zeitschrift für Astrophysik*, **65**, 89 – 92
- Ludwig H.-G., Freytag B., Steffen M., 1999, "A calibration of the mixing-length for solar-type stars based on hydrodynamical simulations. I. Methodological aspects and results for solar metallicity", *Astronomy and Astrophysics*, **346**, 111 – 124
- Ludwig H.-G., Allard F., Hauschildt P. H., 2002, "Numerical simulations of surface convection in a late M-dwarf", *Astronomy and Astrophysics*, **395**, 99 – 115
- Lüftinger T., Kochukhov O., Ryabchikova T., Piskunov N., Weiss W. W., Ilyin I., 2008, "3D atmospheric structure of the prototypical roAp star HD 24712 (HR 1217)", *Contributions of the Astronomical Observatory Skalnate Pleso*, **38**, 335 – 340
- Lydon T. J., Fox P. A., Sofia S., 1992, "A formulation of convection for stellar structure and evolution calculations without the mixing-length theory

- approximations. I. Application to the Sun”, *Astrophysical Journal*, **397**, 701 – 716
- Lydon T. J., Fox P. A., Sofia S., 1993, “A formulation of convection for stellar structure and evolution calculations without the mixing-length theory approximations. II. Application to  $\alpha$  Centauri A and B”, *Astrophysical Journal*, **413**, 390 – 400
- Lynds C. R., 1959, “The Light-Variability of Early B Giants”, *Astrophysical Journal*, **130**, 577 – 598
- Lynden-Bell D., Ostriker J. P., 1967, “On the stability of differentially rotating bodies”, *Monthly Notices of the Royal Astronomical Society*, **136**, 293 – 310
- Lyne A. G., Bailes M., 1992, “No Planet Orbiting PSR:1829-10”, *Nature*, **355**, 213 – 215
- Maas T., Van Winckel H., Waelkens C., 2002, “RU Cen and SX Cen: Two strongly depleted RV Tauri stars in binary systems. The RV Tauri photometric b phenomenon and binarity”, *Astronomy and Astrophysics*, **386**, 504 – 516
- MacGregor K. B., Charbonneau P., 1999, “Angular momentum transport in magnetized stellar radiative zones. IV. Ferraro’s theorem and the solar tachocline”, *Astrophysical Journal*, **519**, 911 – 917
- MacGregor K. B., Jackson S., Skumanich A., Metcalfe T. S., 2007, “On the structure and properties of differentially rotating, main-sequence stars in the  $1 - 2M_{\odot}$  range”, *Astrophysical Journal*, **663**, 560 – 572
- Maeder A., 1975, “Stellar evolution III: the overshooting from convective cores”, *Astronomy and Astrophysics*, **40**, 303 – 310
- Maeder A., 1999, “Stellar evolution with rotation IV: von Zeipel’s theorem and anisotropic losses of mass and angular momentum”, *Astronomy and Astrophysics*, **347**, 185 – 193
- Maeder A., 2009, *Physics, formation and evolution of rotating stars*, Springer, Berlin
- Maeder A., Eenens P. (Eds), 2004, *Proc. IAU Symposium No 215: Stellar Rotation*, Astronomical Society of the Pacific, San Francisco
- Maeder A., Meynet G., 2000, “The evolution of rotating stars”, *Annual Review of Astronomy and Astrophysics*, **38**, 143 – 190
- Maeder A., Zahn J.-P., 1998, “Stellar evolution with rotation. III. Meridional circulation with  $\mu$ -gradients and non-stationarity”, *Astronomy and Astrophysics*, **334**, 1000 – 1006
- Magee N. H., Merts A. L., Huebner W. F., 1984, “Is the metal contribution to the astrophysical opacity incorrect?”, *Astrophysical Journal*, **283**, 264 – 272
- Malanushenko V., Savanov I., Ryabchikova T., 1998, “Rapid radial velocity variations in roAp star  $\gamma$  Equ from lines of Nd III and Pr III ”, *Information Bulletin on Variable Stars*, **4650**, 1 – 4

- Mantegazza L., 2000, "Mode Detection from Line-Profile Variations", In *Delta Scuti and Related Stars*, Eds M. Breger, M. H. Montgomery, Astronomical Society of the Pacific Conference Series, San Francisco, **210**, 138 – 169
- Marchenko S. V., Moffat A. F. J., 1998, "Time-Frequency Analysis of Three Strongly Variable Wolf-Rayet Stars: WR 6, WR 134, and WR 123", *Astrophysical Journal*, **499**, L195 – L199
- Marchenko S. V., Moffat A. F. J., van der Hucht K. A., Seggewiss W., Schrijver H., Stenholm B., Lundstrom I., Setia Gunawan D. Y. A., Sutantyo W., van den Heuvel E. P. J., de Cuyper J.-P., Gomez A. E., 1998a, "Wolf-Rayet stars and O-star runaways with HIPPARCOS. II. Photometry", *Astronomy and Astrophysics*, **331**, 1022 – 1036
- Marchenko S. V., Moffat A. F. J., Eversberg T., Morel T., Hill G. M., Tovmassian G. H., Seggewiss W., 1998b, "A comprehensive variability study of the enigmatic WN8 stars - Final results", *Monthly Notices of the Royal Astronomical Society*, **294**, 642 – 656
- Marchenko K., Roxburgh I., Vorontsov S., 2000, "Non-linear inversion for the hydrostatic structure of the solar interior", *Monthly Notices of the Royal Astronomical Society*, **312**, 39 – 50
- Marconi M., Palla F., 1998, "The Instability Strip for Pre-main-sequence Stars", *Astrophysical Journal*, **507**, L141 – L144
- Marconi M., Palla F., 2004, "Pre-Main-Sequence A-type stars", In *Proc. IAU Symposium 224: The A-Star Puzzle*, Eds J. Zverko, J. Zižňovský, S.J. Adelman, W.W. Weiss, Cambridge University Press, **224**, 69 – 79
- Marcy G. W., Butler R. P., 1992, "Precision radial velocities with an iodine absorption cell", *Publications of the Astronomical Society of the Pacific*, **104**, 270 – 277
- Markova N., Puls J., 2008, "Bright OB stars in the Galaxy. IV. Stellar and wind parameters of early to late B supergiants", *Astronomy and Astrophysics*, **478**, 823 – 842
- Martens L., Smeyers P., 1982, "On the linear adiabatic oscillations of a uniformly and synchronously rotating component of a binary", *Astronomy and Astrophysics*, **106**, 317 – 326
- Martić M., Schmitt J., Lebrun J.-C., Barban C., Connes P., Bouchy F., Michel E., Baglin A., Appourchaux T., Bertaux J.-L., 1999, "Evidence for global pressure oscillations on Procyon", *Astronomy and Astrophysics*, **351**, 993 – 1002
- Martinez P., 1993, *The Cape Oscillating Ap Star Survey*, PhD Dissertation, University of Cape Town, South Africa
- Martinez P., Kurtz D. W., 1990, "New observations and a frequency analysis of the extremely peculiar rapidly oscillating Ap star HD 101065", *Monthly Notices of the Royal Astronomical Society*, **242**, 636 – 652
- Mashonkina L., Ryabchikova T., Ryabtsev A., 2005, "NLTE ionization equilibrium of Nd II and Nd III in cool A and Ap stars", *Astronomy and Astrophysics*, **441**, 309 – 318

- Mathias P., Gillet D., 1993, "A new tool to study wave propagation: The Van Hoof effect", *Astronomy and Astrophysics*, **278**, 511 – 519
- Mathias P., Gillet D., Crowe R., 1991, "A double shock wave atmospheric model for the Beta Cephei star Sigma Scorpii?", *Astronomy and Astrophysics*, **252**, 245 – 254
- Mathias P., Aerts C., Gillet D., Waelkens C., 1994a, "A spectroscopic analysis of the beta Cephei star 12 Lacertae", *Astronomy and Astrophysics*, **289**, 875 – 884
- Mathias P., Aerts C., De Pauw M., Gillet D., Waelkens C., 1994b, "A Spectroscopic Analysis of the Beta-Cephei Star Alpha-Lupi", *Astronomy and Astrophysics*, **283**, 813 – 826
- Mathias P., Gillet D., Aerts C., Breitfellner M. G., 1997, "A spectroscopic study of the delta Scuti star rho Puppis", *Astronomy and Astrophysics*, **327**, 1077 – 1086
- Mathias P., Aerts C., Briquet M., De Cat P., Cuypers J., Van Winckel H., Le Contel J. M., 2001, "Spectroscopic monitoring of 10 new northern slowly pulsating B star candidates discovered from the HIPPARCOS mission", *Astronomy and Astrophysics*, **379**, 905 – 916
- Mathias P., Le Contel J.-M., Chapellier E., Jankov S., Sareyan J.-P., Poretti E., Garrido R., Rodríguez E., Arellano Ferro A., Alvarez M., Parrao L., Peña J., Eyer L., Aerts C., De Cat P., Weiss W. W., Zhou A., 2004, "Multi-site, multi-technique survey of  $\gamma$  Doradus candidates. I. Spectroscopic results for 59 stars", *Astronomy and Astrophysics*, **417**, 189 – 199
- Mathis S., Zahn J.-P., 2004, "Transport and mixing in the radiation zones of rotating stars. I. Hydrodynamical processes", *Astronomy and Astrophysics*, **425**, 229 – 242 (Erratum: *Astronomy and Astrophysics*, **462**, 1063 – 1064; 2007)
- Mathur S., Eff-Darwich A., García R. A., Turck-Chièze S., 2008, "Sensitivity of helioseismic gravity modes to the dynamics of the solar core", *Astronomy and Astrophysics*, **484**, 517 – 522
- Mathys G., 1991, "Spectropolarimetry of magnetic stars. II - The mean longitudinal magnetic field", *Astronomy and Astrophysics Supplement Series*, **89**, 121 – 157
- Mathys G., Hubrig S., 1997, "Spectropolarimetry of magnetic stars. VI. Longitudinal field, crossover and quadratic field: New measurements", *Astronomy and Astrophysics Supplement Series*, **124**, 475 – 497
- Mathys G., Kurtz D. W., Elkin V. G., 2007, "Pulsation in the presence of a strong magnetic field: the roAp star HD 166473", *Monthly Notices of the Royal Astronomical Society*, **380**, 181 – 198
- Matthews J. M., Wehlau W. H., Walker G. A. H., Yang S., 1988, "Detection of radial velocity variations in the rapidly oscillating Ap star HR 1217", *Astrophysical Journal*, **324**, 1099 – 1105

- Matthews J. M., Walker G. A. H., Wehlau W. H., 1990, "Rapid infrared photometry of pulsating Ap stars - A measurement of stellar limb darkening", *Astrophysical Journal*, **365**, L81 – L84
- Matthews J. M., Wehlau W. H., Rice J., Walker G. A. H., 1996, "Opening a New Window on Ap Star Atmospheres: A T- $\tau$  Relation for HR 3831 from Its Limb-darkened Pulsation Amplitudes", *Astrophysical Journal*, **459**, 278 – 287
- Matthews J. M., Kurtz D. W., Martinez P., 1999, "Parallaxes versus p-Modes: Comparing HIPPARCOS and Asteroseismic Results for Pulsating Ap Stars", *Astrophysical Journal*, **511**, 422 – 428
- Matsuno T., 1966, "Quasi-geostrophic motions in the equatorial area", *Journal of the Meteorological Society of Japan*, **44**, 25 – 43
- Maxted P. F. L., Heber U., Marsh T. R., North R. C., 2001, "The binary fraction of extreme horizontal branch stars", *Monthly Notices of the Royal Astronomical Society*, **326**, 1391 – 1402
- Mayor M., 1980, "Metal abundances of F and G dwarfs determined by the radial velocity scanner CORAVEL", *Astronomy and Astrophysics*, **87**, L1 – L2
- Mayor M., Queloz D., 1995, "A Jupiter-Mass Companion to a Solar-Type Star", *Nature*, **378**, 355 – 357
- Mazumdar A., 2005, "Asteroseismic diagrams for solar-type stars", *Astronomy and Astrophysics*, **441**, 1079 – 1086
- Mazumdar A., Antia H. M., 2001, "Seismic study of stellar convective cores", *Astronomy and Astrophysics*, **377**, 192 – 205
- Mazumdar A., Basu S., Collier B. L., Demarque P., 2006a, "Asteroseismic diagnostics of stellar convective cores", *Monthly Notices of the Royal Astronomical Society*, **372**, 949 – 958
- Mazumdar A., Briquet M., Desmet M., Aerts C., 2006b, "An asteroseismic study of the  $\beta$  Cephei star  $\beta$  Canis Majoris", *Astronomy and Astrophysics*, **459**, 589 – 596
- McAlister H. A., Mason B. D., Hartkopf W. I., Shara M. M., 1993, "ICCD speckle observations of binary stars. X - A further survey for duplicity among the bright stars", *Astronomical Journal*, **106**, 1639 – 1655
- McCarthy D. D., 2005, "Precision time and the rotation of the Earth", *IAU Colloq. 196: Transits of Venus: New Views of the Solar System and Galaxy*, 180 – 197
- McCook G. P., Sion E. M., 1999, "A Catalog of Spectroscopically Identified White Dwarfs", *Astrophysical Journal Supplement Series*, **121**, 1 – 130
- McCullagh P., Nelder J. A., 1989, *Generalized linear models*, 2nd Edition, Chapman and Hall, New York
- McDonald A. B., 2004, "Solar neutrinos", *New Journal of Physics*, **6**-121, 1 – 17
- McDermott P. N., van Horn H. M., Hansen C. J., 1988, "Nonradial oscillations of neutron stars", *Astrophysical Journal*, **325**, 725 – 748

- McGraw J. T., Liebert J., Starrfield S. G., Green R., 1979a, "PG1159-035: A new, hot, non-DA pulsating degenerate", In *Proc. IAU Colloquium 53: White Dwarfs and Variable Degenerate Stars*, University of Rochester, 377 – 381
- McGraw J. T., Starrfield S. G., Angel J. R. P., Carleton N. P., 1979b, "PG1159-035: an MMT discovery of a new short-period variable star.", In *The MMT and the future of ground-based astronomy* Ed. T. C. Weekes, SAO Special Report **385**, 125 – 130
- McNamara D. H., 1952, "The Spectrum and Velocity-Curve of  $\nu$  Eridani", *Publications of the Astronomical Society of the Pacific*, **64**, 76 – 76
- McNamara D. H., 1957, "The Radial Velocity of  $\theta$  Ophiuchi", *Publications of the Astronomical Society of the Pacific*, **69**, 570 – 572
- McNamara D. H., 1995, "Period-luminosity relations of SX Phoenicis stars", *Astronomical Journal*, **109**, 1751 – 1756
- Mędrek M., Murawski K., Roberts B., 1999, "Damping and frequency reduction of the  $f$ -mode due to turbulent motion in the solar convection zone", *Astronomy and Astrophysics*, **349**, 312 – 316
- Medupe R., 2002, *Studies of non-adiabatic pulsations in the atmospheres of the roAp stars*, PhD Dissertation, University of Cape Town, South Africa
- Medupe R., Christensen-Dalsgaard J., Kurtz D. W., 2002, "Applications of non-adiabatic radial pulsation equations to roAp stars", In *IAU Colloq. 185: Radial and Nonradial Pulsations as Probes of Stellar Physics*, Eds C. Aerts, T. R. Bedding, J. Christensen-Dalsgaard, Publications of the Astronomical Society of the Pacific Conference Series, San Francisco, **259**, 296 – 299
- Méndez R. H., Verga A. D., Kriner A., 1983, "The Photometric and Radial Velocity Variations of the Central Star of the Planetary Nebula IC4187", *Revista Mexicana de Astronomía y Astrofísica*, **8**, 175
- Merline W. J., 1999, "Precise Velocity Observation of K-Giants: Evidence for Solar-Like Oscillations in Arcturus", In *IAU Colloquium 170: Precise Stellar Radial Velocities*, Eds J. B. Hearnshaw, C. D. Scarfe, Astronomical Society of the Pacific Conference Series, San Francisco, **185**, 187 – 192
- Mermilliod J.-C., Maeder A., 1986, "Evolution of massive stars: comparison of cluster sequences and models with mass loss", *Astronomy and Astrophysics*, **158**, 45 – 59
- Metcalf T. S., Charbonneau P., 2003, "Stellar structure modeling using a parallel genetic algorithm for objective global optimization", *Journal of Computational Physics*, **185**, 176 – 193
- Metcalf T. S., Salaris M., Winget D. E., 2002, "Measuring  $^{12}\text{C}(\alpha, \gamma)^{16}\text{O}$  from white dwarf asteroseismology", *Astrophysical Journal*, **573**, 803 – 811
- Metcalf T. S., Montgomery M. H., Kanaan A., 2004, "Testing white dwarf crystallization theory with asteroseismology of the massive pulsating DA star BPM 37093", *Astrophysical Journal*, **605**, L133 – L136

- Metcalfe T. S., Dziembowski W. A., Judge P. G., Snow M., 2007, "Asteroseismic signatures of stellar magnetic activity cycles", *Monthly Notices of the Royal Astronomical Society*, **379**, L16 – L20
- Meynet, G., Maeder, A., 2000, "Stellar evolution with rotation. V. Changes in all the outputs of massive star models", *Astronomy and Astrophysics*, **361**, 101 – 120
- Michaud G., 1970, "Diffusion processes in peculiar A stars", *Astrophysical Journal*, **160**, 641 – 658
- Michaud G., Proffitt C. R., 1993, "Particle transport processes", In *Proc. IAU Colloq. 137: Inside the stars*, Eds A. Baglin, W. W. Weiss, Astronomical Society of the Pacific Conference Series, San Francisco, **40**, 246 – 259
- Michaud G., Tarasick D., Charland Y., Pelletier C., 1983, "Diffusion, meridional circulation, and mass loss in Fm-Am stars", *Astrophysical Journal*, **269**, 239 – 249
- Michaud G., Richer J., Richard O., 2007, "Horizontal branch evolution and atomic diffusion", *Astrophysical Journal*, **670**, 1178 – 1187
- Michel E., Baglin A., Weiss W. W., Auvergne M., Catala C., Aerts C., Apourchaux T., Barban C., Baudin F., Briquet M., Carrier F., Degroote P., De Ridder J., Garcia R. A., Garrido R., Gutierrez-Soto J., Kallinger T., Lefevre L., Neiner C., Poretti E., Samadi R., Sarro L., Alecian G., Andrade L., Ballot J., Benomar O., Berthomieu G., Boumier P., Charpinet S., de Batz B., Deheuvels S., Dupret M.-A., Emilio M., Fabregat J., Facanha W., Floquet M., Frémat Y., Fridlund M., Goupil M.-J., Grottsch-Noels A., Handler G., Huat A.-L., Hubert A.-M., Janot-Pacheco E., Kjeldsen H., Lebreton Y., Leroy B., Martayan C., Mathias P., Miglio A., Montalban J., Monteiro M. J. P. G., Mosser B., Provost J., Regulo C., Renan de Medeiros J., Ribas I., Roca Cortés T., Roxburgh I., Suso J., Thoul A., Toutain T., Tipene D., Turck-Chieze S., Vauclair S., Vauclair G., Zwintz K., 2008, "First asteroseismic results from CoRoT", *Communications in Asteroseismology*, **156**, 73 – 87
- Miesch M. S., Brun A. S., Toomre J., 2006, "Solar differential rotation influenced by latitudinal entropy variations in the tachocline", *Astrophysical Journal*, **641**, 618 – 625
- Miglio A., Montalbán J., 2005, "Constraining fundamental stellar parameters using seismology. Application to  $\alpha$  Centauri AB", *Astronomy and Astrophysics*, **441**, 615 – 629
- Miglio A., Montalbán J., Dupret M.-A., 2007, "Instability strips of slowly pulsating B stars and  $\beta$  Cephei stars: the effect of the updated OP opacities and of the metal mixture", *Monthly Notices of the Royal Astronomical Society*, **375**, L21 – L25
- Miglio A., Montalbán J., Noels A., Eggenberger P., 2008, "Probing the properties of convective cores through g modes: high-order g modes in SPB and  $\gamma$  Doradus stars", *Monthly Notices of the Royal Astronomical Society*, **386**, 1487 – 1502

- Mihalas B. W., Toomre J., 1981, "Internal gravity waves in the solar atmosphere. I. Adiabatic waves in the chromosphere", *Astrophysical Journal*, **249**, 349 – 371
- Mihalas B. W., Toomre J., 1982, "Internal gravity waves in the solar atmosphere. II. Effects of radiative damping", *Astrophysical Journal*, **263**, 386 – 408
- Mihalas D., 1978, *Stellar atmospheres, 2nd edition*, San Francisco, W. H. Freeman and Co.
- Mihalas D., Mihalas B. W., 1984, *Foundations of Radiation Hydrodynamics*, Oxford University Press
- Mihalas D., Däppen W., Hummer D. G., 1988, "The equation of state for stellar envelopes. II. Algorithm and selected results", *Astrophysical Journal*, **331**, 815 – 825
- Mihalas D., Hummer D. G., Mihalas B. W., Däppen W., 1990, "The equation of state for stellar envelopes. IV. Thermodynamic quantities and selected ionization fractions for six elemental mixes", *Astrophysical Journal*, **350**, 300 – 308
- Mkrtichian D. E., Hatzes A. P., 2005, "HD 101065, the Most Peculiar Star: First Results from Precise Radial Velocity Study", *Journal of Astrophysics and Astronomy*, **26**, 185 – 191
- Mkrtichian D. E., Hatzes A. P., Kanaan A., 2003, "Radial velocity variations in pulsating Ap stars - II. 33 Librae", *Monthly Notices of the Royal Astronomical Society*, **345**, 781 – 794
- Mkrtichian D. E., Kusakin A. V., Rodriguez E., Gamarova A. Y., Kim C., Kim S.-L., Lee J. W., Youn J.-H., Kang Y. W., Olson E. C., Grankin K., 2004, "Frequency spectrum of the rapidly-oscillating mass-accreting component of the Algol-type system AS Eri", *Astronomy and Astrophysics*, **419**, 1015 – 1024
- Mkrtichian D. E., Hatzes A. P., Saio H., Shobbrook, R.R., 2008, "The detection of the rich p-mode spectrum and asteroseismology of Przbylski's star", *Astronomy and Astrophysics*, **490**, 1109 – 1120
- Molenberghs G., Verbeke G., 2005, *Models for Discrete Longitudinal Data*, Springer Series in Statistics
- Monnier J. D., Zhao M., Pedretti E., Thureau N., Ireland M., Muirhead P., Berger J.-P., Millan-Gabet R., Van Belle G., ten Brummelaar T., McAlister H., Ridgeway S., Turner N., Sturmann L., Sturmann J., Berger D., 2007, "Imaging the surface of Altair", *Science*, **317**, 342 – 345
- Montalbán J., Miglio A., Noels A., Grevesse N., Di Mauro M. P., 2004, "Solar model with CNO revised abundances", In *Proc. SOHO 14 - GONG 2004: Helio- and Asteroseismology: Towards a golden future*; Yale, July 12 – 16 2004, Ed. D. Danesy, ESA SP-559, ESA Publication Division, Noordwijk, The Netherlands, 574 – 576
- Montalbán J., Théado S., Lebreton Y., 2007, "Comparisons for ESTA-TASK3: CLES and CESAM", In *Stellar Evolution and Seismic Tools for Asteroseismology: Diffusive Processes in Stars and Seismic Analysis*, Eds C. W.

- Straka, Y. Lebreton, M. J. P. F. G. Monteiro, European Astronomical Society Publication Series, **26**, EDP Sciences, Les Ulis, France, 167 – 176
- Monteiro M. J. P. F. G., Christensen-Dalsgaard J., Thompson M. J., 1994, “Seismic study of overshoot at the base of the solar convective envelope”, *Astronomy and Astrophysics*, **283**, 247 – 262
- Monteiro M. J. P. F. G., Christensen-Dalsgaard J., Thompson M. J., 2000, “Seismic study of stellar convective regions: the base of convective envelopes in low-mass stars”, *Monthly Notices of the Royal Astronomical Society*, **316**, 165 – 172
- Monteiro M. J. P. F. G., Christensen-Dalsgaard J., Thompson M. J., 2002, “Asteroseismic Inference for Solar-Type Stars”, In *Proc. 1st Eddington Workshop, ‘Stellar Structure and Habitable Planet Finding’*, Eds F. Favata, I. W. Roxburgh and D. Galadí-Enríquez, ESA SP-485, ESA Publications Division, Noordwijk, The Netherlands, 291 – 298
- Monteiro M. J. P. F. G., Lebreton Y., Montalbán J., Christensen-Dalsgaard J., Castro M., Degl’Innocenti S., Moya A., Roxburgh I. W., Scuflaire R., Baglin A., Cunha M. S., Eggenberger P., Fernandes J., Goupil M. J., Hui-Bon-Hoa A., Marconi M., Marques J. P., Michel E., Miglio A., Morel P., Pichon B., Prada P. G., Provost J., Ruoppo A., Suárez J.-C., Suran M., Teixeira T. C., 2006, “Report on the CoRoT evolution and seismic tools activity”, In *The CoRoT Mission. Pre-launch Status. Stellar Seismology and Planet Finding*, eds M. Fridlund, A. Baglin, J. Lochard, L. Conroy, ESA SP-1306, ESA Publications Division, Noordwijk, The Netherlands, 363 – 371
- Montgomery M. H., 2005, “A New Technique for Probing Convection in Pulsating White Dwarf Stars”, *Astrophysical Journal*, **633**, 1142 – 1149
- Montgomery M. H., 2008, “What We Can Learn from the Light Curves of GD 358 and PG 1351+489”, *Communications in Asteroseismology*, **154**, 38 – 48
- Montgomery M. H., Breger M. (Eds), 2000, *Delta Scuti and Related Stars*, Astronomical Society of the Pacific Conference Series, San Francisco, **210**
- Montgomery M. H., O’Donoghue D., 1999, “A derivation of the errors for least squares fitting to time series data”, *Delta Scuti Star Newsletter*, **13**, 28 – 31
- Montgomery M. H., Winget D. E., 1999, “The Effect of Crystallization on the Pulsations of White Dwarf Stars”, *Astrophysical Journal*, **526**, 976 – 990
- Montgomery M. H., Metcalfe T. S., Winget D. E., 2003, “The core/envelope symmetry in pulsating stars”, *Monthly Notices of the Royal Astronomical Society*, **344**, 657 – 664
- Montgomery M. H., Williams K. A., Winget D. E., Dufour P., DeGennaro S., Liebert J., 2008, “SDSS J142625.71+575218.3: A Prototype for a New Class of Variable White Dwarf”, *Astrophysical Journal*, **678**, L51 – L54
- Moon T. T., Dworetsky M. M., 1985, “Grids for the determination of effective temperature and surface gravity of B, A and F stars using uvby-beta

- photometry”, *Monthly Notices of the Royal Astronomical Society*, **217**, 305 – 315
- Morales-Rueda L., Maxted P. F. L., Marsh T. R., North R. C., Heber U., 2003, “Orbital periods of 22 subdwarf B stars”, *Monthly Notices of the Royal Astronomical Society*, **338**, 752 – 764
- Morales-Rueda L., Marsh T. R., Maxted P. F. L., Nelemans G., Karl C., Napiwotzki R., Moran C. K. J., 2005, “Six detached white-dwarf close binaries”, *Monthly Notices of the Royal Astronomical Society*, **359**, 648 – 662
- Morel P., 1997, “CESAM: a code for stellar evolution calculations”, *Astronomy and Astrophysics Supplement Series*, **124**, 597 – 614
- Morel P., Provost J., Lebreton Y., Thévenin F., Berthomieu G., 2000, “Calibrations of  $\alpha$  Cen A, B”, *Astronomy and Astrophysics*, **363**, 675 – 691
- Morel T., Butler K., Aerts C., Neiner C., Briquet M., 2006, “Abundance analysis of prime B-type targets for asteroseismology. I. Nitrogen excess in slowly-rotating  $\beta$  Cephei stars”, *Astronomy and Astrophysics*, **457**, 651 – 663
- Moskalik P., Dziembowski W. A., 1992, “New opacities and the origin of the  $\beta$  Cephei pulsation”, *Astronomy and Astrophysics*, **256**, L5 – L8
- Moskalik P., Dziembowski W. A., 2005, “Seismology of triple-mode classical Cepheids of the Large Magellanic Cloud”, *Astronomy and Astrophysics*, **434**, 1077 – 1084
- Moskalik P., Poretti E., 2003, “Fourier decomposition and frequency analysis of the pulsating stars with  $P < 1$  d in the OGLE database. II. Multiperiodic RR Lyrae variables in the Galactic Bulge”, *Astronomy and Astrophysics*, **398**, 213 – 222
- Moskalik P., Buchler J. R., Marom A., 1992, “Toward a resolution of the bump and beat Cepheid mass discrepancies”, *Astrophysical Journal*, **385**, 685 – 693
- Mosser B., and the Siamois Team, 2007, “A Fourier Tachometer at Dome C in Antarctica”, *Communications in Asteroseismology*, **150**, 309 – 310
- Moya A., Christensen-Dalsgaard J., Charpinet S., Lebreton Y., Miglio A., Montalbán J., Monteiro M. J. P. F. G., Provost J., Roxburgh I. W., Scuflaire R., Suárez J. C., Suran M., 2008, “Inter-comparison of the g-, f- and p-modes calculated using different oscillation codes for a given stellar model”, *Astrophysics and Space Science*, **316**, 231 – 249
- Mukadam A. S., Mullally F., Nather R. E., Winget D. E., von Hippel T., Kleinman S. J., Nitta A., Krzesiński J., Kepler S. O., Kanaan A., Koester D., Sullivan D. J., Homeier D., Thompson S. E., Reaves D., Cotter C., Slaughter D., Brinkmann J., 2004a, “Thirty-Five New Pulsating DA White Dwarf Stars”, *Astrophysical Journal*, **607**, 982 – 998
- Mukadam A. S., Winget D. E., von Hippel T., Montgomery M. H., Kepler S. O., Costa A. F. M., 2004b, “Redefining the Empirical ZZ Ceti Instability Strip”, *Astrophysical Journal*, **612**, 1052 – 1059

- Mukadam A. S., Montgomery M. H., Winget D. E., Kepler S. O., Clemens J. C., 2006, “Ensemble characteristics of the ZZ Ceti stars”, *Astrophysical Journal*, **640**, 956 – 965
- Mullally F., Thompson S. E., Castanheira B. G., Winget D. E., Kepler S. O., Eisenstein D. J., Kleinman S. J., Nitta A., 2005, “Eleven New DA White Dwarf Variable Stars from the Sloan Digital Sky Survey”, *Astrophysical Journal*, **625**, 966 – 972
- Munteanu A., Bono G., José J., García-Berro E., Stellingwerf R. F., 2005, “Limit-cycle behaviour in one-zone convective models”, *Astrophysical Journal*, **627**, 454 – 463
- Murawski K., Duvall T. L., Kosovichev A. G., 1998, “Damping and frequency shift of the solar f-mode due to the interaction with turbulent convection”, In *Structure and dynamics of the interior of the Sun and Sun-like stars; Proc. SOHO 6/GONG 98 Workshop*, Eds S. G. Korzennik, A. Wilson, ESA SP-418, ESA Publications Division, Noordwijk, The Netherlands, 825 – 828
- Murphy J. W., Burrows A., Heger A., 2004, “Pulsational Analysis of the Cores of Massive Stars and Its Relevance to Pulsar Kicks”, *Astrophysical Journal*, **615**, 460 – 474
- Musman S., Rust D. M., 1970, “Vertical velocities and horizontal wave propagation in the solar photosphere”, *Solar Physics*, **13**, 261 – 286
- Narwid A., Kołaczkowski Z., Pigulski A., Ramza T., 2006, “ $\beta$  Cephei stars in the inner part of the Galaxy”, *Memorie della Societa Astronomica Italiana*, **77**, 342 – 343
- Nather R. E., Robinson E. L., 1974, “Coherent oscillations in UX Ursae Majoris”, *Astrophysical Journal*, **190**, 637 – 651
- Nather R. E., Winget D. E., Clemens J. C., Hansen C. J., Hine B. P., 1990, “The whole earth telescope - A new astronomical instrument”, *Astrophysical Journal*, **361**, 309 – 317
- Natta A., Grinin V. P., Mannings V., Ungerechts H., 1997, “The Evolutionary Status of UX Orionis-Type Stars”, *Astrophysical Journal*, **491**, 885 – 890
- Neiner C., 2007, “Magnetic Field Measurements in OB Stars”, In *Active OB Stars: Laboratories for Stellare and Circumstellar Physics*, Eds S. Stefl, S. P. Owocki, A. T. Okazaki, Publications of the Astronomical Society of the Pacific Conference Series, San Francisco, **361**, 91
- Neuforge-Verheecke C., Magain P., 1997, “Spectroscopic analysis of the Alpha Centauri system”, *Astronomy and Astrophysics*, **328**, 261 – 268
- Niemczura E., Daszyńska-Daszkiewicz J., 2005, “Metallicities of the  $\beta$  Cephei stars from low-resolution ultraviolet spectra”, *Astronomy and Astrophysics*, **433**, 659 – 669
- Nigam R., Kosovichev A. G., 1998, “Measuring the Sun’s eigenfrequencies from velocity and intensity helioseismic spectra: asymmetrical line profile-fitting formula”, *Astrophysical Journal*, **505**, L51 – L54
- Nigam R., Kosovichev A. G., 1999, “Source of solar acoustic modes”, *Astrophysical Journal*, **514**, L53 – L56

- Nishikawa J., 1986, "Detection of solar five-minute oscillations through white-light intensity", *Solar Physics*, **38**, 277 – 283
- Nitta A., Kleinman S. J., Krzesinski J., Metcalfe T. S., Mukadam A., Mullally F., Nather R. E., Sullivan D. J., Thompson S. E., Winget D. E., Wood M. A., 2007, "Doubling the number of DBVs and a closer look at their Instability Strip", *Communications in Asteroseismology*, **150**, 249 – 250
- Noels A., Grevesse N., Magain P., Neuforge C., Baglin A., Lebreton Y., 1991, "Calibration of the  $\alpha$  Centauri system: metallicity and age", *Astronomy and Astrophysics*, **247**, 91 – 94
- Nordlund, Å., Stein, R. F., Asplund, M., 2009, "Solar surface convection", *Living Reviews in Solar Physics*, **6**, 2. URL (cited on 5/5/09): <http://www.livingreviews.org/lrsp-2009-2>
- Nowakowski R. M., 2005, "Multimode resonant coupling in pulsating stars", *Acta Astronomica*, **55**, 1 – 41
- Nuspl J., Bíró I. B., 2002, "Eclipse Mapping of Non-Radial Pulsation in Binary Stars", In *IAU Colloquium 185: Radial and Nonradial Pulsations as Probes of Stellar Physics*, Eds C. Aerts, T. R. Bedding, J. Christensen-Dalsgaard, Publications of the Astronomical Society of the Pacific Conference Series, San Francisco, **259**, 100 – 101
- Nuspl J., Biro B. I., Hegedus T., 2004, "Reconstruction of dynamical features in eclipsing binaries", In *Spectroscopically and Spatially Resolving the Components of the Close Binary Stars*, Eds R. W. Hilditch, H. Hensberge, K. Pavlovski, Publications of the Astronomical Society of the Pacific Conference Series, San Francisco, **318**, 350 – 352
- O'Brien M. S., Kawaler S. D., 2000, "The Predicted Signature of Neutrino Emission in Observations of Pulsating Pre-White Dwarf Stars", *Astrophysical Journal*, **539**, 372 – 378
- Ohshima O., Narusawa S.-y., Akazawa H., Arai K., Fujii M., Kawabata T., Morikawa K., Ohkura N., Takeuti M., 2001, "Short-Period Light Variation of an Eclipsing Binary System: RZ Cassiopeiae", *Astronomical Journal*, **122**, 418 – 424
- Okazaki A. T., Owocki S. P., Stefl S. (Eds), 2007, *Active OB-Stars: Laboratories for Stellare and Circumstellar Physics*, Astronomical Society of the Pacific Conference Series, **361**
- Olech A., Dziembowski W. A., Pamyatnykh A. A., Kaluzny J., Pych W., Schwarzenberg-Czerny A., Thompson I. B., 2005, "Cluster Ages Experiment (CASE): SX Phe stars from the globular cluster  $\omega$  Centauri", *Monthly Notices of the Royal Astronomical Society*, **363**, 40 – 48
- Olivier E. A., Wood P. R., 2005, "Non-linear pulsation models of red giants", *Monthly Notices of the Royal Astronomical Society*, **362**, 1396 – 1412
- Oosterhoff P. T., 1944, "Discussion of photographic magnitudes of bright northern stars, together with new mean values in King's photographic system", *Bulletin of the Astronomical Institutes of the Netherlands*, **10**, 45 – 55

- Origlia L., Rood R. T., Fabbri S., Ferraro F. R., Fusi Pecci F., Rich R. M., 2007, "The first empirical mass-loss law for population II giants", *Astrophysical Journal*, **667**, L85 – L88
- Osaki Y., 1971, "Non-Radial Oscillations and the Beta Canis Majoris Phenomenon", *Publications of the Astronomical Society of Japan*, **23**, 485 – 502
- Osaki Y., 1974, "An excitation mechanism for pulsations in beta Cephei stars", *Astrophysical Journal*, **189**, 469 – 477
- Osaki Y., 1975, "Nonradial oscillations of a 10 solar mass star in the main-sequence stage", *Publications of the Astronomical Society of Japan*, **27**, 237 – 258
- Østensen R. H. (Ed.), 2006, *The 2nd Meeting on Hot Subdwarf Stars and Related Objects, Baltic Astronomy*, **15**
- Østensen R., 2008, "DAS User Manual", *Communications in Asteroseismology*, **155**, 7 – 16
- Ostlie D. A., Cox A. N., 1986, "A linear survey of the Mira variable star instability region of the Hertzsprung-Russell diagram", *Astrophysical Journal*, **311**, 864 – 872
- Otí Floranes H., Christensen-Dalsgaard J., Thompson M. J., 2005, "The use of frequency-separation ratios for asteroseismology", *Monthly Notices of the Royal Astronomical Society*, **356**, 671 – 679
- Oudmaijer R. D., van der Veen W. E. C. J., Waters L. B. F. M., Trams N. R., Waelkens C., Engelsman E., 1992, "SAO stars with infrared excess in the IRAS Point Source Catalog", *Astronomy and Astrophysics Supplement Series*, **96**, 625 – 643
- Paardekooper S. J., Veen P. M., van Genderen A. M., van der Hucht K. A., 2002, "On the variability of the visual binary WR86. WC7 with a  $\beta$ -Cephei companion", *Astronomy and Astrophysics*, **384**, 1012 – 1022
- Paczynski B., 1965, "Cataclysmic variables among binary stars. I. U Geminorum stars", *Acta Astronomica*, **15**, 89 – 102
- Paczynski B., 1971, "Evolution processes in close binary systems", *Annual Review of Astronomy and Astrophysics*, **9**, 183 – 208
- Paczynski B., 1986, "Gravitational microlensing by the galactic halo", *Astrophysical Journal*, **304**, 1 – 5
- Pamyatnykh A. A., 1999, "Pulsational instability domains in the upper main sequence", *Acta Astronomica*, **49**, 119 – 148
- Pamyatnykh A. A., Vorontsov S. V., Däppen W., 1991, "A calibration of solar envelope models using the frequencies of intermediate-degree solar acoustic oscillations", *Astronomy and Astrophysics*, **248**, 263 – 269
- Pamyatnykh A. A., Dziembowski W. A., Handler G., Pikall H., 1998, "Towards a seismic model of the delta Scuti star XX Pyxidis", *Astronomy and Astrophysics*, **333**, 141 – 150
- Pamyatnykh A. A., Handler G., Dziembowski W. A., 2004, "Asteroseismology of the  $\beta$  Cephei star  $\nu$  Eridani: interpretation and applications of the

- oscillation spectrum”, *Monthly Notices of the Royal Astronomical Society*, **350**, 1022 – 1028
- Papaloizou J., Pringle J. E., 1978, “Non-radial oscillations of rotating stars and their relevance to the short-period oscillations of cataclysmic variables”, *Monthly Notices of the Royal Astronomical Society*, **182**, 423 – 442
- Parker E. N., 1958, “Dynamics of the interplanetary gas and magnetic fields”, *Astrophysical Journal*, **128**, 664 – 676
- Parker R. L., 1977, “Understanding inverse theory”, *Annual Review of Earth Planetary Science*, **5**, 35 – 64
- Parsons S. B., 1972, “The Conversion Factor from Radial to Pulsational Velocity and the Radii of Classical Cepheids”, *Astrophysical Journal*, **174**, 57 – 68
- Patriarchi P., Perinotto M., 1997, “Wind variability in central stars of planetary nebulae. II”, *Astronomy and Astrophysics Supplement Series*, **126**, 385 – 391
- Pauldrach A. W. A., Hoffmann T. L., Lennon M., 2001, “Radiation-driven winds of hot luminous stars. XIII. A description of NLTE line blocking and blanketing towards realistic models for expanding atmospheres”, *Astronomy and Astrophysics*, **375**, 161 – 195
- Pedlosky J., 1987, *Geophysical Fluid Dynamics*, 2nd Edition, Springer-Verlag, New York
- Pekeris C. L., 1938, “Nonradial Oscillations of Stars”, *Astrophysical Journal*, **88**, 189 – 199
- Perdang J., 1986, “Asymptotics and quantum chaos in stellar oscillations”, In *Seismology of the Sun and the distant Stars*, 141 – 171, Ed. D. O. Gough, Reidel, Dordrecht
- Pérez Hernández F., Christensen-Dalsgaard J., 1994a, “The phase function for stellar acoustic oscillations. II. Effects of filtering”, *Monthly Notices of the Royal Astronomical Society*, **267**, 111 – 124
- Pérez Hernández F., Christensen-Dalsgaard J., 1994b, “The phase function for stellar acoustic oscillations – III. The solar case”, *Monthly Notices of the Royal Astronomical Society*, **269**, 475 – 492
- Pérez Hernández F., Christensen-Dalsgaard J., 1998, “The phase function for stellar acoustic oscillations - IV. Solar-like stars”, *Monthly Notices of the Royal Astronomical Society*, **295**, 344 – 352
- Perlmutter S., Turner M. S., White M., 1999, “Constraining dark energy with Type Ia supernovae and large-scale structure”, *Physical Review Letters*, **83**, 670 – 673
- Perryman M. A. C., ESA, 1997, *The HIPPARCOS and TYCHO catalogues. Astrometric and photometric star catalogues derived from the ESA HIPPARCOS Space Astrometry Mission*, ESA Special Publication, **1200**
- Pesnell W. D., 1987, “A new driving mechanism for stellar pulsations”, *Astrophysical Journal*, **314**, 598 – 604

- Petersen J. O., 1973, "Masses of double mode Cepheid variables determined by analysis of period ratios", *Astronomy and Astrophysics*, **27**, 89 – 93
- Phorah M. W., 2008, *The effects of radiation and convection on stellar oscillations*, PhD Dissertation, University of Cape Town, South Africa
- Pigulski A., 2005, "Pulsating Stars in the ASAS-3 Database. I. beta Cephei Stars", *Acta Astronomica*, **55**, 219 – 236
- Pigulski A., 2006, "Intrinsic Variability in Multiple Systems and Clusters: an Overview", In *Astrophysics of Variable Stars*, Eds C. Sterken, C. Aerts, Publications of the Astronomical Society of the Pacific Conference Series, San Francisco, **349**, 137 – 152
- Pigulski A., Kołaczkowski Z., 2002, "Early-type variables in the Magellanic Clouds. I. beta Cephei stars in the LMC bar", *Astronomy and Astrophysics*, **388**, 88 – 99
- Pigulski A., Kołaczkowski Z., Kopacki G., 2003, "Reanalysis of the OGLE-I Observations with the Image Subtraction Method. I. Galactic Bar Fields MM1-A, MM1-B, MM7-A, and MM7-B", *Acta Astronomica*, **53**, 27 – 50
- Pigulski A., Kołaczkowski Z., Ramza T., Narwid A., 2006, "High-amplitude delta Scuti stars in the Galactic Bulge from the OGLE-II and MACHO data", *Memorie della Societa Astronomica Italiana*, **77**, 223 – 226
- Pijpers F. P., 1997, "Solar rotation inversions and the relationship between  $a$ -coefficients and mode splittings", *Astronomy and Astrophysics*, **326**, 1235 – 1240
- Pijpers F. P., 1998, "Helioseismic determination of the solar gravitational quadrupole moment", *Monthly Notices of the Royal Astronomical Society*, **297**, L76 – L80
- Pijpers F. P., 2003, "Selection criteria for targets of asteroseismic campaigns", *Astronomy and Astrophysics*, **400**, 241 – 248
- Pijpers F. P., Habing H. J., 1989, "Driving the stellar wind of AGB stars by acoustic waves; exploration of a simple model", *Astronomy and Astrophysics*, **215**, 334 – 346
- Pijpers F. P., Thompson M. J., 1992, "Faster formulations of the optimally localized averages method for helioseismic inversion", *Astronomy and Astrophysics*, **262**, L33 – L36
- Pijpers F. P., Thompson M. J., 1994, "The SOLA method for helioseismic inversion", *Astronomy and Astrophysics*, **281**, 231 – 240
- Pijpers F. P., Thompson M. J., 1996, "A modified  $\mathbb{R}^1 \otimes \mathbb{R}^1$  method for helioseismic inversions", *Monthly Notices of the Royal Astronomical Society*, **279**, 498 – 510
- Piro A. L., Bildsten L., 2006, "The Energy Dependence of Neutron Star Surface Modes and X-Ray Burst Oscillations", *Astrophysical Journal*, **638**, 968 – 937
- Poelarends A. J. T., Herwig F., Langer N., Heger A., 2008, "The supernova channel of super-AGB stars", *Astrophysical Journal*, **675**, 614 – 625
- Pojmański G., 1997, "The All Sky Automated Survey", *Acta Astronomica*, **47**, 467 – 481

- Pojmański G., Maciejewski G., 2004, "The All Sky Automated Survey. Catalog of Variable Stars. III. 12h–18h Quarter of the Southern Hemisphere", *Acta Astronomica*, **54**, 153 – 179
- Pojmański G., Maciejewski G., 2005, "The All Sky Automated Survey. Catalog of Variable Stars. IV. 18h–24h Quarter of the Southern Hemisphere", *Acta Astronomica*, **55**, 97 – 122
- Pollard K. R., Lloyd Evans T., 1999, "RV Tauri stars and Type II Cepheids in the LMC", In *Asymptotic Giant Branch Stars*, Eds T. Le Bertre, A. Lebre, C. Waelkens, Astronomical Society of the Pacific Conference Series, San Francisco, **191**, 459
- Pollard K. R., Cottrell P. L., Kilmartin P. M., Gilmore A. C., 1996, "RV Tauri stars. I. A long-term photometric survey", *Monthly Notices of the Royal Astronomical Society*, **279**, 949 – 977
- Pollard K. R., Cottrell P. L., Lawson W. A., Albrow M. D., Tobin W., 1997, "RV Tauri stars - II. A spectroscopic study", *Monthly Notices of the Royal Astronomical Society*, **286**, 1 – 22
- Pollard K. R., Alcock C., Allsman R. A., Alves D., Axelrod T. S., Becker A. C., Bennett D. P., Cook K. H., Freeman K. C., Griest K., Lehner M. J., Marshall S. L., Peterson B. A., Pratt M. R., Quinn P. J., Sutherland W., Tomaney A., Welch D. L., The MACHO Collaboration, 2000, "RV Tauri Stars and Type II Cepheids in the Magellanic Clouds – Results from the MACHO Database", In *IAU Colloq. 176: The Impact of Large-Scale Surveys on Pulsating Star Research*, Eds L. Szabados, D. W. Kurtz, Publications of the Astronomical Society of the Pacific Conference Series, San Francisco, **203**, 89 – 95
- Popieliski B. L., Dziembowski W. A., 2005, "Seismic diagnostics of mixing beyond the convective core in intermediate mass main-sequence stars", *Acta Astronomica*, **55**, 177 – 193
- Popieliski B. L., Dziembowski W. A., Cassisi S., 2000, "Petersen Diagram for RRd Stars in the Magellanic Clouds", *Acta Astronomica*, **50**, 491 – 507
- Poretti E., 2003, "Asteroseismology of HADS stars: V974 Oph, a radial pulsator flavoured by nonradial components", *Astronomy and Astrophysics*, **409**, 1031 – 1035
- Poretti E., Pardo I., 1997, "The galactic double-mode Cepheids. II. Properties of the generalized phase differences", *Astronomy and Astrophysics*, **324**, 133 – 136
- Poretti E., Koen C., Martinez P., Breuer F., Haupt H., de Alwis D., 1997, "Discovery and analysis of Gamma Doradus type pulsations in the F0IV star HR 2740=QWPUP", *Monthly Notices of the Royal Astronomical Society*, **292**, 621 – 630
- Poretti E., Buzasi D., Laher R., Catanzarite J., Conrow T., 2002a, "Asteroseismology from space: The delta Scuti star  $\theta^2$  Tauri monitored by the WIRE satellite", *Astronomy and Astrophysics*, **382**, 157 – 163
- Poretti E., Koen C., Bossi M., Rodríguez E., Martín S., Krisciunas K., Akan M. C., Crowe R., Wilcox M., Ibanoglu C., Evren S., 2002b, "The multi-

- periodicity of the gamma Doradus stars HD 224945 and HD 224638 as detected from a multisite campaign”, *Astronomy and Astrophysics*, **384**, 513 – 520
- Porter J. M., Rivinius T., 2003, “Classical Be Stars”, *Publications of the Astronomical Society of the Pacific*, **115**, 1153 – 1170
- Porto de Mello G. F., Lyra W., Keller G. R., 2008, “The Alpha Centauri binary system. Atmospheric parameters and element abundances”, *Astronomy and Astrophysics*, **488**, 653 – 666
- Pottasch E. M., Butcher H. R., van Hoesel F. H. J., 1992, “Solar-like oscillations on  $\alpha$  Centauri A”, *Astronomy and Astrophysics*, **264**, 138 – 146
- Pourbaix D., Neuforge-Verheecke C., Noels A., 1999, “Revised masses of  $\alpha$  Centauri”, *Astronomy and Astrophysics*, **344**, 172 – 176
- Pourbaix D., Nidever D., McCarthy C., Butler R. P., Tinney C. G., Marcy G. W., Jones H. R. A., Penny A. J., Carter B. D., Bouchy F., Pepe F., Hearnshaw J. B., Skuljan J., Ramm D., Kent D., 2002, “Constraining the difference in convective blueshift between the components of  $\alpha$  Centauri with precise radial velocities”, *Astronomy and Astrophysics*, **386**, 280 – 285
- Pourbaix D., Knapp G. R., Szkody P., Ivezić Ž., Kleinman S. J., Long D., Snedden S. A., Nitta A., Harvanek M., Krzesinski J., Brewington H. J., Barentine J. C., Neilsen E. H., Brinkmann J., 2005, “Candidate spectroscopic binaries in the Sloan Digital Sky Survey”, *Astronomy and Astrophysics*, **444**, 643 – 649
- Preston G. W., 1972, “The Unique Magnetic and Spectrum Variations of HD 24712”, *Astrophysical Journal*, **175**, 465 – 472
- Prialnik D., 2000, *An Introduction to the Theory of Stellar Structure and Evolution*, Cambridge University Press
- Press W. H., Teukolsky S. A., Vetterling W. T., Flannery B. P., 1992, *Numerical Recipes in C: the art of scientific computing, Second Edition*, Cambridge University Press
- Provencal J. L., Shipman H. L., The Wet Team, 2008, “An Update on XCOV25: GD358”, *Communications in Asteroseismology*, **154**, 25 – 36
- Provost J., Berthomieu G., 1986, “Asymptotic properties of low degree solar gravity modes”, *Astronomy and Astrophysics*, **165**, 218 – 226
- Przybilla N., Nieva M.-F., Butler K., 2008, “A cosmic abundance standard: chemical homogeneity of the solar neighborhood and the ISM dust-phase composition”, *Astrophysical Journal*, **688**, L103 – L106
- Puls J., Urbaneja M. A., Venero R., Repolust T., Springmann U., Jokuthy A., Mokiem M. R., 2005, “Atmospheric NLTE-models for the spectroscopic analysis of blue stars with winds. II. Line-blanketed models”, *Astronomy and Astrophysics*, **435**, 669 – 698
- Quirion P.-O., Fontaine G., Brassard P., 2004, “On the Driving Mechanism and the Coexistence of Variable and Nonvariable Stars in the Domain of the Pulsating PG 1159 Stars”, *Astrophysical Journal*, **610**, 436 – 442

- Quirion P.-O., Fontaine G., Brassard P., 2006, "Modeling the red edge of the GW Vir (PG 1159) instability strip : evolutionary calculations taking into account diffusion and mass loss ", *Memorie della Societa Astronomica Italiana*, **77**, 53 – 54
- Quirion P.-O., Fontaine G., Brassard P., 2007, "Mapping the Instability Domains of GW Vir Stars in the Effective Temperature-Surface Gravity Diagram", *Astrophysical Journal Supplement Series*, **171**, 219 – 248
- Rabello-Soares M. C., Christensen-Dalsgaard J., Rosenthal C. S., Thompson M. J., 1999a, "Effects of line asymmetries on the determination of solar internal structure", *Astronomy and Astrophysics*, **350**, 672 – 679
- Rabello-Soares M. C., Basu S., Christensen-Dalsgaard J., 1999b, "On the choice of parameters in solar structure inversion", *Monthly Notices of the Royal Astronomical Society*, **309**, 35 – 47
- Rabello-Soares M. C., Basu S., Christensen-Dalsgaard J., Di Mauro, M. P., 2000, "The potential of solar high-degree modes for structure inversion", *Solar Physics*, **193**, 345 – 356
- Rabello-Soares M. C., Korzennik S. G., Schou J., 2008, "Analysis of MDI high-degree mode frequencies and their rotational splittings", *Solar Physics*, **251**, 197 – 224
- Ramachandran B., Jeffery C. S., Townsend R. H. D., 2004, "Synthetic photometry for non-radial pulsations in subdwarf B stars", *Astronomy and Astrophysics*, **428**, 209 – 214
- Randall S. K., Fontaine G., Brassard P., Bergeron P., 2005a, "The Potential of Multicolor Photometry for Pulsating Subdwarf B Stars", *Astrophysical Journal Supplement Series*, **161**, 456 – 479
- Randall S. K., Matthews J. M., Fontaine G., Rowe J., Kuschnig R., Green E. M., Brassard P., Chayer P., Guenther D. B., Moffat A. F. J., Rucinski S., Sasselov D., Walker G. A. H., Weiss W. W., 2005b, "Detection of Long-Period Variations in the Subdwarf B Star PG 0101+039 on the Basis of Photometry from the MOST Satellite", *Astrophysical Journal*, **633**, 460 – 464
- Rast M. P., Bogdan T. J., 1998, "On the asymmetry of solar acoustic line profiles", *Astrophysical Journal*, **496**, 527 – 537
- Rathore Y., Blandford R. D., Broderick A. E., 2005, "Resonant excitation of white dwarf oscillations in compact object binaries - I. The no back reaction approximation", *Monthly Notices of the Royal Astronomical Society*, **357**, 834 – 846
- Rauw G., De Becker M., Van Winckel H., Aerts C., Eenens P., Lefever K., Vandenbussche B., Linder N., Nazé Y., Gosset E., 2008, "Spectroscopic and photometric variability of the O9.5 Vp star HD 93521", *Astronomy and Astrophysics*, **487**, 659 – 670
- Reed M. D., Brondel B. J., Kawaler S. D., 2005, "Pulsating Stars in Close Binaries. I. Investigations of Eclipse Mapping and Oblique Pulsations", *Astrophysical Journal*, **634**, 602 – 615

- Reed M. D., and the Whole Earth Telescope Xcov 21 and 23 Collaborations, 2006a, "The observational search for tidally tipped pulsation axes in sub-dwarf B stars", *Memorie della Societa Astronomica Italiana*, **77**, 417
- Reed M. D., and the Whole Earth Telescope XCov21 and 23 collaborations, 2006b, "Searching for Observational Evidence of Tidally Inclined Pulsations", *Baltic Astronomy*, **15**, 269 – 274
- Reegen P., 2007, SigSpec. I. Frequency- and phase-resolved significance in Fourier space, *Astronomy and Astrophysics*, **467**, 1353 – 1371
- Reese D., Lignières F., Rieutord M., 2006, "Acoustic oscillations of rapidly rotating polytropic stars. II. Effects of the Coriolis and centrifugal accelerations", *Astronomy and Astrophysics*, **455**, 621 – 637
- Reese D., Lignières F., Rieutord M., 2008, "Regular patterns in the acoustic spectrum of rapidly rotating stars", *Astronomy and Astrophysics*, **481**, 449 – 452
- Reese D., MacGregor K. B., Jackson S., Skumanich A., Metcalfe T. S., 2009a, "Comparison of pulsation modes in rapidly rotating polytropic and SCF models", In *Proc. 38<sup>th</sup> Liège International Astrophysical Colloquium: Evolution and Pulsation of Massive Stars on the Main Sequence and Close to it, Communications in Asteroseismology*, **157**, 264
- Reese D., MacGregor K. B., Jackson S., Skumanich A., Metcalfe T. S., 2009b, "Pulsation modes in stellar models based on the Self-Consistent Field method", *Astronomy and Astrophysics*, in press [[arXiv:0903.4854v1 \[astro-ph.SR\]](https://arxiv.org/abs/0903.4854v1)]
- Reid M. J., Goldston J. E., 2002, "How Mira variables change visual light by a thousandfold", *Astrophysical Journal*, **568**, 931 – 938 (Erratum: *Astrophysical Journal*, **572**, 694)
- Reiter J., Rhodes E. J., Kosovichev A. G., Schou J., 2004, "The current status of analyzing high-degree modes", In *Proc. SOHO 14 - GONG 2004: "Helio- and Asteroseismology: Towards a golden future"; Yale, July 12 – 16 2004*, Ed. D. Danesy, ESA SP-559, ESA Publication Division, Noordwijk, The Netherlands, 61 – 72
- Reitz J. R., Milford F. J., Christy R. W. 1979, *Foundations of Electromagnetic Theory, 3rd edition*, Addison-Wesley, Reading, Massachusetts
- Rempel M., 2004, "Overshoot at the base of the solar convection zone: a semianalytical approach", *Astrophysical Journal*, **607**, 1046 – 1064
- Rempel M., 2007, "Origin of solar torsional oscillations", *Astrophysical Journal*, **655**, 651 – 659
- Renson P., 1978, "A method for finding the periods of variable stars", *Astronomy and Astrophysics*, **63**, 125 – 129
- Retter A., Bedding T. R., Buzasi D. L., Kjeldsen H., Kiss L. L., 2003, "Oscillations in Arcturus from WIRE Photometry", *Astrophysical Journal*, **591**, L151 – L154 (Erratum: *Astrophysical Journal*, **596**, L125)
- Reyniers K., Smeyers P., 2003a, "Tidal perturbations of linear, isentropic oscillations in components of circular-orbit close binaries. I. Synchronously rotating components", *Astronomy and Astrophysics*, **404**, 1051 – 1065

- Reyniers K., Smeyers P., 2003b, "Tidal perturbations of linear, isentropic oscillations in components of circular-orbit close binaries . II. Validity of the perturbation method applied to equilibrium tides", *Astronomy and Astrophysics*, **409**, 677 – 688
- Rhodes E. J., Cacciani A., Tomczyk S., Ulrich R. K., 1986, "The 1984 solar oscillation program of the Mt. Wilson 60-foot tower", In *Seismology of the Sun and the distant stars*, Ed. D. O. Gough, Reidel, Dordrecht, 309 – 332
- Rhodes E. J., Cacciani A., Woodard M., Tomczyk S., Korzennik S., Ulrich R. K., 1987, "Estimates of the solar internal angular velocity obtained with the Mt. Wilson 60-foot solar tower", In *The internal solar angular velocity*, Eds B. R. Durney, S. Sofia, Reidel, Dordrecht, 75 – 82
- Rhodes E. J., Cacciani A., Korzennik S. G., Tomczyk S., Ulrich R. K., Woodard M. F., 1990, "Depth and latitude dependence of the solar internal angular velocity", *Astrophysical Journal*, **351**, 687 – 700
- Rhodes E. J., Cacciani A., Korzennik S. G., Ulrich R. K., 1993, "Confirmation of solar cycle-dependent intermediate-degree  $p$ -mode frequency shifts", *Astrophysical Journal*, **406**, 714 – 722
- Rhodes E. J., Kosovichev A. G., Schou J., Scherrer P. H., Reiter J., 1997, "Measurements of frequencies of solar oscillations from the MDI medium- $l$  program", *Solar Physics*, **175**, 287 – 310
- Rhodes Jr E. J., Reiter J., Kosovichev A. G., Schou, J., Scherrer P. H., 1998, "Initial SOI/MDI high-degree frequencies and frequency splittings", In *Structure and dynamics of the interior of the Sun and Sun-like stars; Proc. SOHO 6/GONG 98 Workshop*, Eds S. G. Korzennik, A. Wilson, ESA SP-418, ESA Publications Division, Noordwijk, The Netherlands, 73 – 82
- Riazi N., Abedi A., 2006, "Modelling eclipsing binaries with pulsating components: Phase dependence of observed pulsation amplitudes", *New Astronomy*, **11**, 514 – 519
- Ribas I., Jordi C., Giménez Á., 2000, "The mass dependence of the overshooting parameter determined from eclipsing binary data", *Monthly Notices of the Royal Astronomical Society*, **318**, L55 – L59
- Richard O., Dziembowski W. A., Sienkiewicz R., Goode P. R., 1998, "On the accuracy of helioseismic determination of solar helium abundance", *Astronomy and Astrophysics*, **338**, 756 – 760
- Richard O., Michaud G., Richer J., 2001, "Iron convection zones in B, A and F stars", *Astrophysical Journal*, **558**, 377 – 391
- Richichi, A., Percheron, I., Khristoforova, M., 2005, "CHARM2: An updated catalog of high angular resolution measurements", *Astronomy and Astrophysics*, **431**, 773 – 777
- Ripepi V., Marconi M., Palla F., Bernabei S., Ruoppo A., Cusano F., Alcalá J. M., 2006a, "Recent results on Pre-main sequence delta Scuti stars.", *Memorie della Società Astronomica Italiana*, **77**, 317 – 321
- Ripepi V., Bernabei S., Marconi M., Palla F., Arellano Ferro A., Bonanno A., Ferrara P., Frasca A., Jiang X. J., Kim S.-L., Marinoni S., Mignemi G., Monteiro M. J. P. F. G., Oswalt T. D., Reegen P., Janulis R., Rodriguez

- E., Rolland A., Ruoppo A., Terranegra L., Zwintz K., 2006b, “A multi-site photometric campaign on the pre-main-sequence  $\delta$  Scuti pulsator IP Persei”, *Astronomy and Astrophysics*, **449**, 335 – 343
- Ritzwoller M. H., Lavelle E. M., 1991, “A unified approach to the helioseismic forward and inverse problems of differential rotation”, *Astrophysical Journal*, **369**, 557 – 566
- Rivinius T., Baade D., Štefl S., 2003, “Non-radially pulsating Be stars”, *Astronomy and Astrophysics*, **411**, 229 – 247
- Robe H., 1968, “Les oscillations non radiales des polytropes”, *Annales d'Astrophysique*, **31**, 475 – 482
- Roberts D. H., Lehar J., Dreher J. W., 1987, “Time Series Analysis with Clean - Part One - Derivation of a Spectrum”, *Astronomical Journal*, **93**, 968 – 989
- Robinson E. L., Kepler S. O., Nather R. E., 1982, “Multicolor variations of the ZZ Ceti stars”, *Astrophysical Journal*, **259**, 219 – 231
- Rodríguez E., Breger M., 2001, “Delta Scuti and related stars: Analysis of the R00 Catalogue”, *Astronomy and Astrophysics*, **366**, 178 – 196
- Rodríguez E., López-González M. J., 2000, “SX Phe stars in globular clusters”, *Astronomy and Astrophysics*, **359**, 597 – 600
- Rodríguez E., López-González M. J., López de Coca P., 2000, “A revised catalogue of delta Sct stars”, *Astronomy and Astrophysics Supplement Series*, **144**, 469 – 474
- Rodríguez E., Costa V., Handler G., García J. M., 2003, “Simultaneous uvby photometry of the new delta Sct-type variable HD 205”, *Astronomy and Astrophysics*, **399**, 253 – 262
- Rodríguez E., García J. M., Gamarova A. Y., Costa V., Daszyńska-Daszkiewicz J., López-González M. J., Mkrtchian D. E., Rolland A., 2004a, “ $\delta$  Sct-type pulsations in eclipsing binary systems: AB Cas”, *Monthly Notices of the Royal Astronomical Society*, **353**, 310 – 318
- Rodríguez E., García J. M., Mkrtchian D. E., Costa V., Kim S.-L., López-González M. J., Hintz E., Kusakin A. V., Gamarova A. Y., Lee J. W., Youn J.-H., Janiashvili E. B., Garrido R., Moya A., Kang Y. W., 2004b, “ $\delta$  Sct-type pulsations in eclipsing binary systems: RZ Cas”, *Monthly Notices of the Royal Astronomical Society*, **347**, 1317 – 1326
- Rogers F. J., Iglesias C. A., 1992, “Radiative atomic Rosseland mean opacity tables”, *Astrophysical Journal Supplement Series*, **79**, 507 – 568
- Rogers F. J., Nayfonov A., 2002, “Updated and expanded OPAL equation-of-state tables: implications for helioseismology”, *Astrophysical Journal*, **576**, 1064 – 1074
- Rogers F. J., Swenson F. J., Iglesias C. A., 1996, “OPAL Equation-of-State Tables for Astrophysical Applications”, *Astrophysical Journal*, **456**, 902 – 908
- Rogers T. M., MacGregor K. B., Glatzmaier G. A., 2008, “Non-linear dynamics of gravity wave driven flows in the solar radiative interior”, *Monthly Notices of the Royal Astronomical Society*, **387**, 616 – 630

- Rosenthal C. S., 1998, “Peaks and throughs in helioseismology: the power spectrum of solar oscillations”, *Astrophysical Journal*, **508**, 864 – 875
- Rosenthal C. S., Christensen-Dalsgaard J., 1995, “The interfacial f mode in a spherical solar model”, *Monthly Notices of the Royal Astronomical Society*, **276**, 1003 – 1008
- Rosenthal C. S., Gough D. O., 1994, “The solar f-mode as an interfacial mode at the chromosphere-corona transition”, *Astrophysical Journal*, **423**, 488 – 495
- Rosenthal C. S., Christensen-Dalsgaard J., Nordlund Å., Stein R. F., Trampedach R., 1999, “Convective contributions to the frequencies of solar oscillations”, *Astronomy and Astrophysics*, **351**, 689 – 700
- Roth M., Stix M., 1999, “Coupling of solar p modes: quasi-degenerate perturbation theory”, *Astronomy and Astrophysics*, **351**, 1133 – 1138
- Roth M., Stix M., 2008, “Meridional circulation and global solar oscillations”, *Solar Physics*, **251**, 77 – 89
- Roxburgh I. W., 1978, “Convection and stellar structure”, *Astronomy and Astrophysics*, **65**, 281 – 285
- Roxburgh I. W., 1989, “Integral constraints on convective cores”, *Astronomy and Astrophysics*, **211**, 361 – 364
- Roxburgh I. W., 2001, “Gravitational multipole moments of the Sun determined from helioseismic estimates of the internal structure and rotation”, *Astronomy and Astrophysics*, **377**, 688 – 690
- Roxburgh I. W., 2002, “The tools of asteroseismology”, In Proc. 1st Eddington Workshop: ‘Stellar structure and habitable planet finding’, ESA SP-485, Eds F. Favata, I. W. Roxburgh, D. Galadí-Enríquez, ESA Publications Division, Noordwijk, The Netherlands, 75 – 85
- Roxburgh I. W., 2004, “EDDINGTON and the internal constitution of the stars”, In Proc. 2nd Eddington workshop, “Stellar structure and habitable planet finding”, ESA SP-538, Eds F. Favata, S. Aigrain, ESA Publications Division, Noordwijk, The Netherlands, 23 – 36
- Roxburgh I. W., 2005, “The ratio of small to large separations of stellar p-modes”, *Astronomy and Astrophysics*, **434**, 665 – 669
- Roxburgh I. W., 2006, “2-dimensional models of rapidly rotating stars. II. Hydrostatic and acoustic models with  $\Omega = \Omega(r, \theta)$ ”, *Astronomy and Astrophysics*, **454**, 883 – 888
- Roxburgh I. W., 2009, “Small separations and phase shift differences of  $\ell = 0, 1$  p-modes”, *Astronomy and Astrophysics*, **493**, 185 – 191
- Roxburgh I. W., Vorontsov S. V., 1994a, “Seismology of the solar envelope: the base of the convection zone as seen in the phase shift of acoustic waves”, *Monthly Notices of the Royal Astronomical Society*, **268**, 880 – 888
- Roxburgh I. W., Vorontsov S. V., 1994b, “The seismology of stellar cores: a simple theoretical description of the ‘small frequency separations’”, *Monthly Notices of the Royal Astronomical Society*, **267**, 297 – 302

- Roxburgh I. W., Vorontsov S. V., 1995, "An asymptotic description of solar acoustic oscillations with an elementary excitation source", *Monthly Notices of the Royal Astronomical Society*, **272**, 850 – 858
- Roxburgh I. W., Vorontsov S. V., 1996, "An asymptotic description of solar acoustic oscillations of low and intermediate degree", *Monthly Notices of the Royal Astronomical Society*, **278**, 940 – 946
- Roxburgh I. W., Vorontsov S. V., 2000a, "Semiclassical approximation for low-degree stellar p modes – I. The classical eigenfrequency equation", *Monthly Notices of the Royal Astronomical Society*, **317**, 141 – 150
- Roxburgh I. W., Vorontsov S. V., 2000b, "Semiclassical approximation for low-degree stellar p modes – II. Classical ray tracing", *Monthly Notices of the Royal Astronomical Society*, **317**, 151 – 157
- Roxburgh I. W., Vorontsov S. V., 2001, "Semiclassical approximation for low-degree stellar p modes – III. Acoustic resonances and diagnostic properties of the oscillation frequencies", *Monthly Notices of the Royal Astronomical Society*, **322**, 85 – 96
- Roxburgh I. W., Vorontsov S. V., 2003, "The ratio of small to large separations of acoustic oscillations as a diagnostic of the interior of solar-like stars", *Astronomy and Astrophysics*, **411**, 215 – 220
- Ruderman M. A., 1968, "Crystallization and Torsional Oscillations of Super-dense Stars", *Nature*, **218**, 1128 – 1130
- Rufener F., 1981, "Third catalogue of stars measured in the Geneva Observatory photometric system", *Astronomy and Astrophysics Supplement Series*, **45**, 207 – 366
- Rufener F., 1986, "The evolution of atmospheric extinction at La Silla", *Astronomy and Astrophysics*, **165**, 275 – 286
- Rutten R. G. M., Dhillon V. S., Horne K., Kuulkers E., van Paradijs J., 1993, "Spectrally resolved eclipse maps of the accretion disk in UX Ursae Majoris", *Nature*, **362**, 518 – 520
- Ryabchikova T. A., Landstreet J. D., Gelbmann M. J., Bolgova G. T., Tsymbal V. V., Weiss W. W., 1997, "Abundance analysis of roAp stars. IV. HD 24712", *Astronomy and Astrophysics*, **327**, 1137 – 1146
- Ryabchikova T., Piskunov N., Kochukhov O., Tsymbal V., Mittermayer P., Weiss W. W., 2002, "Abundance stratification and pulsation in the atmosphere of the roAp star boldmath gamma Equulei", *Astronomy and Astrophysics*, **384**, 545 – 553
- Ryabchikova T., Sachkov M., Kochukhov O., Lyashko D., 2007a, "Pulsation tomography of rapidly oscillating Ap stars. Resolving the third dimension in peculiar pulsating stellar atmospheres", *Astronomy and Astrophysics*, **473**, 907 – 922
- Ryabchikova T., Sachkov M., Weiss W. W., Kallinger T., Kochukhov O., Baglin S., Ilyin I., Landstreet J. D., Leone F., Lo Curto G., Lüftinger T., Lyashko D., Magazzù A., 2007b, "Pulsation in the atmosphere of the roAp star HD 24712. I. Spectroscopic observations and radial velocity measurements", *Astronomy and Astrophysics*, **462**, 1103 – 1112

- Saar S. H., Osten R. A., 1997, "Rotation, turbulence and evidence for magnetic fields in southern dwarfs", *Monthly Notices of the Royal Astronomical Society*, **284**, 803 – 810
- Sachkov M., Kochukhov O., Ryabchikova T., Huber D., Leone F., Bagnulo S., Weiss W. W., 2008, "Pulsations in the atmosphere of the rapidly oscillating Ap star 10 Aquilae", *Monthly Notices of the Royal Astronomical Society*, **389**, 903 – 918
- Saesen S., Briquet M., Aerts C., 2006, "A line-profile analysis of the large-amplitude beta Cephei star xi1 Canis Majoris", *Communications in Asteroseismology*, **147**, 109 – 112
- Saio H., 1981, "Rotational and tidal perturbations of nonradial oscillations in a polytropic star", *Astrophysical Journal*, **244**, 299 – 315
- Saio H., 1993, "Excitation of the pulsation in the helium star V 652 Her", *Monthly Notices of the Royal Astronomical Society*, **260**, 465 – 467
- Saio H., 1995, "A linear analysis of the radial pulsations of H-deficient stars", *Monthly Notices of the Royal Astronomical Society*, **277**, 1393 – 1398
- Saio H., 2005, "A non-adiabatic analysis for axisymmetric pulsations of magnetic stars", *Monthly Notices of the Royal Astronomical Society*, **360**, 1022 – 1032
- Saio H., Gautschy A., 2004, "Axisymmetric p-mode pulsations of stars with dipole magnetic fields", *Monthly Notices of the Royal Astronomical Society*, **350**, 485 – 505
- Saio H., Jeffery C. S., 1988, "Radial pulsation in luminous hot helium stars", *Astrophysical Journal*, **328**, 714 – 725
- Saio H., Jeffery C. S., 2002, "Merged binary white dwarf evolution: rapidly accreting carbon-oxygen white dwarfs and the progeny of extreme helium stars", *Monthly Notices of the Royal Astronomical Society*, **333**, 121 – 132
- Saio H., Kuschnig R., Gautschy A., Cameron C., Walker G. A. H., Matthews J. M., Guenther D. B., Moffat A. F. J., Rucinski S. M., Sasselov D., Weiss W. W., 2006, "MOST Detects g- and p-Modes in the B Supergiant HD 163899 (B2 Ib/II)", *Astrophysical Journal*, **650**, 1111 – 1118
- Saio H., Cameron C., Kuschnig R., Walker G. A. H., Matthews J. M., Rowe J. F., Lee U., Huber D., Weiss W. W., Guenther D. B., Moffat A. F. J., Rucinski S. M., Sasselov D., 2007, "MOST Detects g-Modes in the Late-Type Be Star  $\beta$  Canis Minoris (B8 Ve)", *Astrophysical Journal*, **654**, 544 – 550
- Salpeter E. E., 1954, "Electron screening and thermonuclear reactions", *Austrian Journal of Physics*, **7**, 373 – 388
- Samadi R., Goupil M.-J., Houdek G., 2002, "Solar-like oscillations in  $\delta$  Scuti stars", *Astronomy and Astrophysics*, **395**, 563 – 571
- Samadi R., Goupil M.-J., Alecian E., Baudin F., Georgobiani D., Trampedach R., Stein R., Nordlund Å., 2005, "Excitation of Solar-like Oscillations: From PMS to MS Stellar Models", *Journal of Astrophysics and Astronomy*, **26**, 171 – 184

- Samadi R., Georgobiani D., Trampedach R., Goupil M. J., Stein R. F., Nordlund Å., 2007, "Excitation of solar-like oscillations across the HR diagram", *Astronomy and Astrophysics*, **463**, 297 – 308
- Samuelsson L., Andersson N., 2007, "Neutron star asteroseismology. Axial crust oscillations in the Cowling approximation", *Monthly Notices of the Royal Astronomical Society*, **374**, 256 – 268
- Sandquist E. L., 2005, "Blue Stragglers in Low-Luminosity Star Clusters", *Astrophysical Journal*, **635**, L73 – L76
- Sarro L. M., Debosscher J., Lopez M., Aerts C., 2009, "Automated supervised classification of variable stars II. Application to the OGLE database", *Astronomy and Astrophysics*, **494**, 739 – 768
- Savanov I. S., Malanushenko V. P., Ryabchikova T. A., 1999, "Radial- velocity variations in pulsating Ap stars: Pr III and Nd III lines in the spectrum of  $\gamma$  Equ", *Astronomy Letters*, **25**, 802 – 808
- Savonije G. J., 2005, "Unstable quasi g-modes in rotating main-sequence stars", *Astronomy and Astrophysics*, **443**, 557 – 570
- Savonije G. J., Papaloizou J. C. B., 1984, "On the tidal evolution of massive X-ray binaries - The spin-up and circularization rates for systems with evolved stars and the effects of resonances", *Monthly Notices of the Royal Astronomical Society*, **207**, 685 – 704
- Savonije G. J., Witte M. G., 2002, "Tidal interaction of a rotating  $1 M_{\odot}$  star with a binary companion", *Astronomy and Astrophysics*, **386**, 211 – 221
- Savonije G. J., Papaloizou J. C. B., Lin D. N. C., 1994, "On Tidally Induced Shocks in Accretion Discs in Close Binary Systems", *Monthly Notices of the Royal Astronomical Society*, **268**, 13 – 28
- Scargle J. D., 1982, "Studies in astronomical time series analysis. II - Statistical aspects of spectral analysis of unevenly spaced data", *Astrophysical Journal*, **263**, 835 – 853
- Schaller G., Schaerer D., Meynet G., Maeder A., 1992, "New grids of stellar models from 0.8 to 120 solar masses at  $Z = 0.020$  and  $Z = 0.001$ ", *Astronomy and Astrophysics Supplement Series*, **96**, 269 – 331
- Schatzman E., 1993, "Transport of angular momentum and diffusion by the action of internal waves", *Astronomy and Astrophysics*, **279**, 431 – 446
- Schatzman E., Souffrin P., 1967, "Waves in the solar atmosphere", *Annual Review of Astronomy and Astrophysics*, **5**, 67 – 84
- Schechter P. L., Mateo M., Saha A., 1993, "DOPHOT, a CCD photometry program: Description and tests", *Publications of the Astronomical Society of the Pacific*, **105**, 1342 – 1353
- Scherrer P. H., Wilcox J. M., Kotov V. A., Severny A. B., Tsap T. T., 1979, "Observations of solar oscillations with periods of 160 minutes", *Nature*, **277**, 635 – 637
- Scherrer P. H., Wilcox J. M., Christensen-Dalsgaard J., Gough D. O., 1983, "Detection of solar five-minute oscillations of low degree", *Solar Physics*, **82**, 75 – 87

- Scherrer P. H., Bogart R. S., Bush R. I., Hoeksema J. T., Kosovichev A. G., Schou J., Rosenberg W., Springer L., Tarbell T. D., Title A., Wolfson C. J., Zayer I., and the MDI engineering team, 1995, "The Solar Oscillation Investigation – Michelson Doppler Imager", *Solar Physics*, **162**, 129 – 188
- Schiff L.I., 1949, *Quantum mechanics*, New York, McGraw-Hill
- Schmelz J. T., Nasraoui K., Roames J. K., Lippner L. A., Garst J. W., 2005, "Neon lights up a controversy: the solar Ne/O abundance", *Astrophysical Journal*, **634**, L197 – L200
- Schnerr R. S., Henrichs H. F., Oudmaijer R. D., Telting J. H., 2006, "On the  $\text{H}\alpha$  emission from the  $\beta$  Cephei system", *Astronomy and Astrophysics*, **459**, L21 – L24
- Scholz G., Lehmann H., Hildebrandt G., Panov K., Iliev L., 1998, "Spectroscopic and photometric investigations of MAIA candidate stars", *Astronomy and Astrophysics*, **337**, 447 – 459
- Schönberg M., Chandrasekhar S., 1942, "On the evolution of the main-sequence stars", *Astrophysical Journal*, **96**, 161 – 172
- Schou J., 1991, "On the 2-dimensional rotational inversion problem", In *Challenges to theories of the structure of moderate-mass stars, Lecture Notes in Physics*, **388**, 93 – 100, Eds D. O. Gough, J. Toomre, Springer, Heidelberg
- Schou J., 1992, *On the analysis of helioseismic data*, PhD Dissertation, Aarhus University, Denmark
- Schou J., 1998, "Observations of medium- and high-degree modes: methods and sand-traps", In *Structure and dynamics of the interior of the Sun and Sun-like stars; Proc. SOHO 6/GONG 98 Workshop*, Eds S. G. Korzennik, A. Wilson, ESA SP-418, ESA Publications Division, Noordwijk, The Netherlands, 47 – 52
- Schou J., 1999, "Migration of zonal flows detected using Michelson Doppler Imager  $f$ -mode frequency splittings", *Astrophysical Journal*, **523**, L181 – L184
- Schou J., Brown T. M., 1994, "On the rotation rate in the solar convection zone", *Astrophysical Journal*, **434**, 378 – 383
- Schou J., Buzasi D. L., 2001, "Observations of p-modes in  $\alpha$  Cen", In *Helio- and Asteroseismology at the Dawn of the Millennium: Proc. SOHO 10 / GONG 2000 Workshop*, ESA SP-464, ESA Publications Division, Noordwijk, The Netherlands, 391 – 394
- Schou J., Christensen-Dalsgaard J., Thompson M. J., 1992, "The resolving power of current helioseismic inversions for the Sun's internal rotation", *Astrophysical Journal*, **385**, L59 – L62
- Schou J., Christensen-Dalsgaard J., Thompson M. J., 1994, "On comparing helioseismic two-dimensional inversion methods", *Astrophysical Journal*, **433**, 389 – 416
- Schou J., Kosovichev A. G., Goode P. R., Dziembowski W. A., 1997, "Determination of the Sun's seismic radius from the SOHO Michelson Doppler Imager", *Astrophysical Journal*, **489**, L197 – L200

- Schou J., Antia H. M., Basu S., Bogart R. S., Bush R. I., Chitre S. M., Christensen-Dalsgaard J., Di Mauro M. P., Dziembowski W. A., Eff-Darwich A., Gough D. O., Haber D. A., Hoeksema J. T., Howe R., Korzennik S. G., Kosovichev A. G., Larsen R. M., Pijpers F. P., Scherrer P. H., Sekii T., Tarbell T. D., Title A. M., Thompson M. J., Toomre J., 1998, "Helioseismic studies of differential rotation in the solar envelope by the Solar Oscillations Investigation using the Michelson Doppler Imager", *Astrophysical Journal*, **505**, 390 – 417
- Schou J., Howe R., Basu S., Christensen-Dalsgaard J., Corbard T., Hill F., Larsen R. M., Raballo-Soares M. C., Thompson M. J., 2002, "A comparison of solar  $p$ -mode parameters from the Michelson Doppler Imager and the Global Oscillation Network Group: splitting coefficients and rotation inversions", *Astrophysical Journal*, **567**, 1234 – 1249
- Schröder K.-P., Cuntz M., 2005, "A new version of Reimer's law of mass loss based on a physical approach", *Astrophysical Journal*, **630**, L73 – L76
- Schrijver C. J., Zwaan C., 2000, *Solar and stellar magnetic activity*, Cambridge University Press, Cambridge
- Schrijvers C., Telting J. H., Aerts C., Ruymakers E., Henrichs H. F., 1997, "Line-profile variations due to adiabatic non-radial pulsations in rotating stars. I. Observable characteristics of spheroidal modes", *Astronomy and Astrophysics Supplement Series*, **121**, 343 – 368
- Schrijvers C., Telting J. H., 1999, "Line-profile variations due to adiabatic non-radial pulsations in rotating stars. IV. The effects of intrinsic profile variations on the IPS diagnostics", *Astronomy and Astrophysics*, **342**, 453 – 463
- Schuster A., 1898, "On the investigation of hidden periodicities with application to a supposed 26 day period of meteorological phenomena", *Terrestrial Magnetism and Atmospheric Electricity*, **3**, 13 – 41
- Schwarzenberg-Czerny A., 1991, "Accuracy of period determination", *Monthly Notices of the Royal Astronomical Society*, **253**, 198 – 206
- Schwarzenberg-Czerny A., 1997, "The Correct Probability Distribution for the Phase Dispersion Minimization Periodogram", *Astrophysical Journal*, **489**, 941 – 945
- Schwarzenberg-Czerny A., 1998, "The distribution of empirical periodograms: Lomb-Scargle and PDM spectra", *Monthly Notices of the Royal Astronomical Society*, **301**, 831 – 840
- Schwarzenberg-Czerny A., 2003, "An astronomer's guide to period searching", In *Interplay of Periodic, Cyclic and Stochastic Variability in Selected Areas of the H-R Diagram*, Ed. C. Sterken, Publications of the Astronomical Society of the Pacific Conference Series, San Francisco, **292**, 383 – 390
- Schwarzschild M., Schwarzschild B., Adams W. S., 1948, "On the Pulsation in the Atmosphere of  $\eta$  Aquilae", *Astrophysical Journal*, **108**, 207 – 233
- Scuflaire R., 1974, "The non radial oscillations of condensed polytropes", *Astronomy and Astrophysics*, **36**, 107 – 111

- Scuflaire R., Gabriel M., Noels, A., Boury A., 1975, "Oscillatory periods in the Sun and theoretical models with or without mixing", *Astronomy and Astrophysics*, **45**, 15 – 18
- Scuflaire R., Théado S., Montalbán J., Miglio A., Bourge P.-O., Godart M., Thoul A., Noels A., 2007, "CLÉS, Code Liégeois d'Évolution Stellaire", *Astrophysics and Space Science*, **316**, 83 – 91
- Seaton M. J., 1993, "Radiative opacities", In *Proc. IAU Colloquium 137: Inside the stars*, Eds A. Baglin, W. W. Weiss, Publications of the Astronomical Society of the Pacific Conference Series, San Francisco, **40**, 222 – 235
- Seaton M. J., 1996, "Interpolations of Rosseland-mean opacities for variable X and Z", *Monthly Notices of the Royal Astronomical Society*, **279**, 95 – 100
- Seaton M. J., 1999, "Diffusion of iron-group elements in the envelopes of HgMn stars", *Monthly Notices of the Royal Astronomical Society*, **307**, 1008 – 1022
- Seaton M. J., 2005, "Opacity Project data on CD for mean opacities and radiative accelerations", *Monthly Notices of the Royal Astronomical Society*, **362**, L1 – L3
- Seaton M. J., Zeippen C. J., Tully J. A., Pradhan A. K., Mendoza C., Hibbert A., Berrington K. A., 1992, *Revista Mexicana de Astronomía y Astrofísica*, **23**, 19 – 43
- Sekii T., 1991, "Two-dimensional inversion for solar internal rotation", *Publications of the Astronomical Society of Japan*, **43**, 381 – 411
- Sekii T., 1993, "A new strategy for 2D inversion for solar rotation", *Monthly Notices of the Royal Astronomical Society*, **264**, 1018 – 1024
- Sekii T., Shibahashi H., 1989, "An asymptotic inversion method of inferring the sound velocity in the Sun from the spectrum of p-mode oscillations", *Publications of the Astronomical Society of Japan*, **41**, 311 – 331
- Setiawan J., Roth M., Weise P., Dölinger M. P., 2006, "Multi-periodic oscillations of HD 32887 and HD 81797", *Memorie della Società Astronomica Italiana*, **77**, 510 – 514
- Severny A. B., Kotov V. A., Tsap T. T., 1976, "Observations of solar pulsations", *Nature*, **259**, 87 – 89
- Severny A. B., Kotov V. A., Tsap T. T., 1979, "Solar oscillations and the problem of the internal structure of the sun", *Astron. Zh.*, **56**, 1137 – 1148 (English translation: *Sov. Astron.*, **23**, 641 – 647)
- Shatsky N., Tokovinin A., 2002, "The mass ratio distribution of B-type visual binaries in the Sco OB2 association", *Astronomy and Astrophysics*, **382**, 92 – 103
- Shaviv N. J., Shaviv G., 2001, "The electrostatic screening of nuclear reactions in the Sun", *Astrophysical Journal*, **558**, 925 – 942
- Shibahashi H., 1988, "Inverse problem: acoustical potential vs acoustic length", *Proc. IAU Symposium No 123, Advances in helio- and asteroseismology*, Eds J. Christensen-Dalsgaard, S. Frandsen, Reidel, Dordrecht, 133 – 136

- Shibahashi H., 2005, "The DB gap and pulsations of white dwarfs", *European Astronomical Society Publications Series*, **17**, 143 – 148
- Shibahashi H., Takata M., 1993, "Theory for the distorted dipole modes of the rapidly oscillating Ap stars: A refinement of the oblique pulsator model", *Publications of the Astronomical Society of Japan*, **45**, 617 – 641
- Shibahashi H., Osaki Y., Unno W., 1975, "Nonradial  $g$ -mode oscillations and the stability of the Sun", *Publications of the Astronomical Society of Japan*, **27**, 401 – 410
- Shobbrook R. R., Handler G., Lorenz D., Mogorosi D., 2006, "Photometric studies of three multiperiodic  $\beta$  Cephei stars:  $\beta$  CMa, 15 CMa and KZ Mus", *Monthly Notices of the Royal Astronomical Society*, **369**, 171 – 181
- Sills A., Adams T., Davies M. B., 2005, "Blue stragglers as stellar collision products: the angular momentum question", *Monthly Notices of the Royal Astronomical Society*, **358**, 716 – 725
- Silvers L. J., Proctor M. R. E., 2007, "The interaction of multiple convection zones in A-type stars", *Monthly Notices of the Royal Astronomical Society*, **380**, 44 – 50
- Silvotti R., Schuh S., Janulis R., Solheim J.-E., Bernabei S., Østensen R., Oswalt T. D., Bruni I., Gualandi R., Bonanno A., Vauclair G., Reed M., Chen C.-W., Leibowitz E., Paparo M., Baran A., Charpinet S., Dolez N., Kawaler S., Kurtz D., Moskalik P., Riddle R., Zola S., 2007, "A giant planet orbiting the 'extreme horizontal branch' star V391 Pegasi", *Nature*, **449**, 189 – 191
- Simon K. P., Sturm E., 1994, "Disentangling of composite spectra", *Astronomy and Astrophysics*, **281**, 286 – 291
- Simon N. R., 1982, "A plea for reexamining heavy element opacities", *Astrophysical Journal*, **260**, L87 – L90
- Simon N. R., 1987, "Cepheids: problems and possibilities", In *Stellar pulsation*, Eds A. N. Cox, W. M. Sparks, G. Starrfield, Lecture Notes in Physics, Springer, Berlin, **274**, 148 – 158
- Simon R., 1969, "Rotational perturbation of a radial oscillation in a gaseous star", *Astronomy and Astrophysics*, **2**, 390 – 397
- Skumanich A., 1972, "Time scales for Ca II emission decay, rotational braking, and lithium depletion", *Astrophysical Journal*, **171**, 565 – 567
- Smalley B., Kupka F., 1997, "The role of convection on the UVBY colours of A, F, and G stars", *Astronomy and Astrophysics*, **328**, 349 – 360
- Smeyers P., 1966, "Les Oscillations Linéaires et Adiabatiques de la Sphère Homogène", *Bulletin de l'Académie Royale de Belgique, Classe des sciences* **52**, 1126 – 1142
- Smeyers P., Denis J., 1971, "Second Order Rotational Perturbation of Non-Radial Oscillations of a Star", *Astronomy and Astrophysics*, **14**, 311 – 318

- Smeysters P., Martens L., 1983, "The equations that govern rotational and tidal perturbations of stellar oscillations", *Astronomy and Astrophysics*, **125**, 193 – 199
- Smeysters P., Moya A., 2007, "The asymptotic representation of higher-order  $g^+$ -modes in stars with a convective core", *Astronomy and Astrophysics*, **465**, 509 – 524
- Smith B. J., Price S. D., Moffett A. J., 2006, "Phase Lags in the Optical-Infrared Light Curves of Asymptotic Giant Branch Stars", *Astronomical Journal*, **131**, 612 – 620
- Smith H. A., 1995, *RR Lyrae stars*, Cambridge Astrophysics Series, Cambridge University Press, **27**
- Smith M. A., 1983, "Pulsational mode-typing in line profile variables. V - Multimodes and 'moving shells' in Nu Eridani and other Beta Cephei stars", *Astrophysical Journal*, **265**, 338 – 353
- Smith M. A., 1985a, "The nonradial oscillations of Spica. I – Two commensurable modes", *Astrophysical Journal*, **297**, 206 – 223
- Smith M. A., 1985b, "The Nonradial Oscillations of Spica. II – A Quasi-Toroidal Mode", *Astrophysical Journal*, **297**, 224 – 232
- Smith M. A., 1985c, "Pulsational mode typing in line-profile variables. VI Nonradial modes in the remarkable B star Epsilon Persei", *Astrophysical Journal*, **288**, 266 – 274
- Smith M. A., Fitch W. S., Africano J. L., Goodrich B. D., Halbedel W., Palmer L. H., Henry G. W., 1984, "Stable nonradial pulsations in 53 Persei from 1977 to 1983", *Astrophysical Journal*, **282**, 226 – 235
- Smith M., 1986, "Pulsation mode typing in line-profile variables. VII - Commensurable modes and nonuniform period behavior in Delta Scorpii", *Astrophysical Journal*, **304**, 728 – 738
- Smith P. H., McMillan R. S., Merline W. J., 1987, "Evidence for periodic radial velocity variations in Arcturus", *Astrophysical Journal*, **317**, L79 – L84
- Smolec R., 2005, "Metallicity Dependence of the Blazhko Effect", *Acta Astronomica*, **55**, 59 – 84
- Smolec R., Moskalik P., 2008, "Convective hydrocodes for radial stellar pulsation. Physical and numerical formulation", *Acta Astronomica* **58**, 193 – 232
- Sobouti Y., 1980, "Normal modes of rotating fluids", *Astronomy and Astrophysics*, **89**, 314 – 335
- Soderblom D. R., Jones B. F., Fischer D., 2001, "Rotational studies of late-type stars. VII. M34 (NGC 1039) and the evolution of angular momentum and activity in young solar-type stars", *Astrophysical Journal*, **563**, 334 – 340
- Söderhjelm S., 1999, "Visual binary orbits and masses post Hipparcos", *Astronomy and Astrophysics*, **341**, 121 – 140
- Söderhjelm S., 2000, "Binary statistics from Hipparcos data - a progress report", *Astronomische Nachrichten*, **321**, 165 – 170

- Solheim J.-E., Provencal J. L., Bradley P. A., Vauclair G., Barstow M. A., Kepler S. O., Fontaine G., Grauer A. D., Winget D. E., Marar T. M. K., Leibowitz E. M., Emanuelson P.-I., Chevreton M., Dolez N., Kanaan A., Bergeron P., Claver C. F., Clemens J. C., Kleinman S. J., Hine B. P., Seetha S., Ashoka B. N., Mazeh T., Sansom A. E., Tweedy R. W., Meistas E. G., Bruvold A., Massacand C. M., 1998, "Whole Earth Telescope observations of AM Canum Venaticorum - discoseismology at last", *Astronomy and Astrophysics*, **332**, 939 – 957
- Soriano M., Vauclair S., 2008, "Asteroseismology of solar-type stars: signatures of convective and/or helium cores", *Astronomy and Astrophysics*, **488**, 975 – 985
- Soszyński I., 2007, "Long Secondary Periods and Binarity in Red Giant Stars", *Astrophysical Journal*, **660**, 1486 – 1491
- Soszyński I., Udalski A., Szymanski M., Kubiak M., Pietrzynski G., Woźniak P., Zebrun K., Szewczyk O., Wyrzykowski L., 2003, "The Optical Gravitational Lensing Experiment. Catalog of RR Lyr Stars in the Large Magellanic Cloud", *Acta Astronomica*, **53**, 93 – 116
- Soszyński I., Udalski A., Kubiak M., Szymanski M., Pietrzynski G., Zebrun K., Szewczyk O., Wyrzykowski L., 2004, "The Optical Gravitational Lensing Experiment. Small Amplitude Variable Red Giants in the Magellanic Clouds", *Acta Astronomica*, **54**, 129 – 152
- Soszyński I., Dziembowski W. A., Udalski A., Kubiak M., Szymański M. K., Pietrzynski G., Wyrzykowski L., Szewczyk O., Ulaczyk K., 2007, "The Optical Gravitational Lensing Experiment. Period-Luminosity relations of variable red giant stars", *Acta Astronomica*, **57**, 201 – 225
- Soufi F., Goupil M. J., Dziembowski W. A., 1998, "Effects of moderate rotation on stellar pulsation. I. Third order perturbation formalism", *Astronomy and Astrophysics*, **334**, 911 – 924
- Sousa S. G., Cunha M. S., 2008, "On mode conversion and wave reflection in magnetic Ap stars", *Monthly Notices of the Royal Astronomical Society*, **386**, 531 – 542
- Spiegel E. A., Zahn J.-P., 1992, "The solar tachocline", *Astronomy and Astrophysics*, **265**, 106 – 114
- Spruit H. C., 2002, "Dynamo action by differential rotation in a stably stratified stellar interior", *Astronomy and Astrophysics*, **381**, 923 – 932
- Spruit H. C., 2003, "Origin of the torsional oscillation pattern of solar rotation", *Solar Physics*, **213**, 1 – 21
- Stamford P. A., Watson R. D., 1981, "Baade-Wesselink and related techniques for mode discrimination in nonradial stellar pulsations", *Astrophysics and Space Science*, **77**, 131 – 158
- Stankov A., Handler G., 2005, "Catalog of Galactic  $\beta$  Cephei Stars", *Astrophysical Journal Supplement Series*, **158**, 193 – 216
- Starrfield S., Cox A. N., Kidman R. B., Pesnell W. D., 1984, "Nonradial instability strips based on carbon and oxygen partial ionization in hot, evolved stars", *Astrophysical Journal*, **281**, 800 – 810

- Stein R. F., 1968, "Waves in the solar atmosphere. I. The acoustic energy flux", *Astrophysical Journal*, **154**, 297 – 306
- Stein R. F., Leibacher J., 1974, "Waves in the solar atmosphere", *Annual Review of Astronomy and Astrophysics*, **12**, 407 – 435
- Stein R. F., Nordlund Å., 1998, "Simulations of solar granulation. I. General properties", *Astrophysical Journal*, **499**, 914 – 933
- Stein R. F., Nordlund Å., 2001, "Solar oscillations and convection: II. Excitation of radial oscillations", *Astrophysical Journal*, **546**, 585 – 603
- Stein R., Georgobiani D., Trampedach R., Ludwig H.-G., Nordlund, Å., 2004, "Excitation of radial p-modes in the Sun and stars", *Solar Physics*, **220**, 229 – 242
- Stein R. F., Benson D., Georgobiani D., Nordlund Å., Schaffenberger W., 2007, "Surface convection", In *AIP Conf. Proc.: Unsolved Problems in Stellar Physics*, Eds R. J. Stancliffe, J. Dewi, G. Houdek, R. G. Martin, C. A. Tout, American Institute of Physics, Melville, 111 – 115
- Stellingwerf R. F., 1978, "Period determination using phase dispersion minimization", *Astrophysical Journal*, **224**, 953 – 960
- Stellingwerf R. F., 1982, "Convection in pulsating stars. I. Nonlinear hydrodynamics", *Astrophysical Journal*, **262**, 330 – 338
- Stellingwerf R. F., 1984, "Convection in pulsating stars. III. The RR Lyrae instability strip", *Astrophysical Journal*, **277**, 322 – 326
- Stello D., Kjeldsen H., Bedding T. R., De Ridder J., Aerts C., Carrier F., Frandsen S., 2004, "Simulating stochastically excited oscillations. The mode lifetime of  $\xi$  Hya", *Solar Physics*, **220**, 207 – 228
- Stello D., Kjeldsen H., Bedding T. R., Buzasi D., 2006, "Oscillation mode lifetimes in  $\xi$  Hydrea: will strong mode damping limit asteroseismology of red giant stars?", *Astronomy and Astrophysics*, **448**, 709 – 715
- Sterken C., 1977, "Light variations of extreme galactic B- and A supergiants", *Astronomy and Astrophysics*, **57**, 361 – 371
- Sterken C., 1983, "Longterm Photometry of Variables at La-Silla", *The Messenger*, **33**, 10
- Sterken C., 1995, *Catalogue of stars measured in the Long-term Photometry of Variables Project (1992-1994) : 4 : 1995*, ESO Scientific Report, Garching: European Southern Observatory
- Stetson P. B., 1987, "DAOPHOT - A computer program for crowded-field stellar photometry", *Publications of the Astronomical Society of the Pacific*, **99**, 191 – 222
- Stix M., 2002, *The Sun. An introduction*, 2nd edition, Springer, Berlin
- Stoughton C., Lupton R. H., Bernardi M., Blanton M. R., Burles S., Castander F. J., Connolly A. J., Eisenstein D. J., Frieman J. A., Hennessy G. S., Hindsley R. B., Ivezić Ž., Kent S., Kunszt P. Z., Lee B. C., Meiksin A., Munn J. A., Newberg H. J., Nichol R. C., Nicinski T., Pier J. R., Richards G. T., Richmond M. W., Schlegel D. J., Smith J. A., Strauss M. A., SubbaRao M., Szalay A. S., Thakar A. R., Tucker D. L., Vanden Berk D. E., Yanny B., Adelman J. K., Anderson J. E., Jr., Anderson S. F.,

- Annis J., Bahcall N. A., Bakken J. A., Bartelmann M., Bastian S., Bauer A., Berman E., Böhringer H., Boroski W. N., Bracker S., Briegel C., Briggs J. W., Brinkmann J., Brunner R., Carey L., Carr M. A., Chen B., Christian D., Colestock P. L., Crocker J. H., Csabai I., Czarapata P. C., Dalcanton J., Davidsen A. F., Davis J. E., Dehnen W., Dodelson S., Doi M., Dombeck T., Donahue M., Ellman N., Elms B. R., Evans M. L., Eyer L., Fan X., Federwitz G. R., Friedman S., Fukugita M., Gal R., Gillespie B., Glazebrook K., Gray J., Grebel E. K., Greenawalt B., Greene G., Gunn J. E., de Haas E., Haiman Z., Haldeman M., Hall P. B., Hamabe M., Hansen B., Harris F. H., Harris H., Harvanek M., Hawley S. L., Hayes J. J. E., Heckman T. M., Helmi A., Henden A., Hogan C. J., Hogg D. W., Holmgren D. J., Holtzman J., Huang C.-H., Hull C., Ichikawa S.-I., Ichikawa T., Johnston D. E., Kauffmann G., Kim R. S. J., Kimball T., Kinney E., Klaene M., Kleinman S. J., Klypin A., Knapp G. R., Korienek J., Krolik J., Kron R. G., Krzesiński J., Lamb D. Q., Leger R. F., Limmongkol S., Lindenmeyer C., Long D. C., Loomis C., Loveday J., MacKinnon B., Mannery E. J., Mantsch P. M., Margon B., McGehee P., McKay T. A., McLean B., Menou K., Merelli A., Mo H. J., Monet D. G., Nakamura O., Narayanan V. K., Nash T., Neilsen E. H., Jr., Newman P. R., Nitta A., Odenkirchen M., Okada N., Okamura S., Ostriker J. P., Owen R., Pauls A. G., Peoples J., Peterson R. S., Petravick D., Pope A., Pordes R., Postman M., Prosaio A., Quinn T. R., Rechenmacher R., Rivetta C. H., Rix H.-W., Rockosi C. M., Rosner R., Ruthmansdorfer K., Sandford D., Schneider D. P., Scranton R., Sekiguchi M., Sergey G., Sheth R., Shimasaku K., Smee S., Snedden S. A., Stebbins A., Stubbs C., Szapudi I., Szkody P., Szokoly G. P., Tabachnik S., Tsvetanov Z., Uomoto A., Vogeley M. S., Voges W., Waddell P., Walterbos R., Wang S.-i., Watanabe M., Weinberg D. H., White R. L., White S. D. M., Wilhite B., Wolfe D., Yasuda N., York D. G., Zehavi I., Zheng W., 2002, "Sloan Digital Sky Survey: Early Data Release", *Astronomical Journal*, **123**, 485 – 548 (Erratum: *Astronomical Journal*, **123**, 3487)
- Strakhov V. N., Vorontsov S. V., 2000, "Adaptive regularization technique in linear inverse problems", In *Helio- and Asteroseismology at the Dawn of the Millennium: Proc. SOHO 10 / GONG 2000 Workshop* ESA SP-464, ESA Publications Division, Noordwijk, The Netherlands, 539 – 542
- Straka, C. W., Demarque, P., Guenther, D. B., Li, L., Robinson, F. J., 2006, "Space- and ground-based pulsation data of  $\eta$  Bootis explained with stellar models including turbulence", *Astrophysical Journal*, **636**, 1078 – 1086
- Straka C. W., Demarque P., Robinson F. J., 2007, "Probing turbulence with seismic observations of  $\alpha$  Centauri", In *Convection in Astrophysics. Proc. IAU Symposium No 239*, Eds F. Kupka, I. W. Roxburgh, K. L. Chan, International Astronomical Union and Cambridge University Press, 388 – 390

- Straniero O., Domínguez I., Imbriani G., Piersanti L., 2003, "The chemical composition of white dwarfs as a test of convective efficiency during core helium burning", *Astrophysical Journal*, **583**, 878 – 884
- Strohmayer T. E., 1992, "Light curves of rotating, oscillating neutron stars", *Astrophysical Journal*, **388**, 138 – 147
- Strohmayer T. E., Cordes J. M., van Horn H. M., 1992, "Determining the coherence of micropulses", *Astrophysical Journal*, **389**, 685 – 694
- Strohmayer T. E., Watts A. L., 2006, "The 2004 Hyperflare from SGR 1806-20: Further Evidence for Global Torsional Vibrations", *Astrophysical Journal*, **653**, 593 – 601
- Struve O., 1955, "Some Unusual Short-period Variables", *Sky and Telescope*, **14**, 461
- Struve O., McNamara D. H., Kung S. M., Kraft R. P., Williams A. D., 1952, "The Radial Velocity of nu Eridani", *Astrophysical Journal*, **116**, 398 – 409
- Stumpff P., 1980, "Two Self-Consistent FORTRAN Subroutines for the Computation of the Earth's Motion", *Astronomy and Astrophysics Supplement Series*, **41**, 1 – 8
- Suárez, J.-C., 2002, *Seismology of rotating stars. Application to delta Scuti stars*, PhD Dissertation, Observatoire de Paris, France
- Suijs M. P. L., Langer N., Poelarends A.-J., Yoon S.-C., Heger A., Herwig F., 2008, "White dwarf spins from low-mass stellar evolution models", *Astronomy and Astrophysics*, **481**, L87 – L90
- Sweet P. A., 1950, "The importance of rotation in stellar evolution", *Monthly Notices of the Royal Astronomical Society*, **110**, 548 – 558
- Szabados L., Kurtz D. (Eds), 2000, *The Impact of Large-Scale Surveys on Pulsating Star Research*, Astronomical Society of the Pacific Conference Series, San Francisco, **203**
- Szabó R., Kolláth Z., Buchler J. R., 2004, "Automated nonlinear stellar pulsation calculations: Applications to RR Lyrae stars. The slope of the fundamental blue edge and the first RRd model survey", *Astronomy and Astrophysics*, **425**, 627 – 639
- Szkody P., Henden A., Fraser O., Silvestri N., Bochanski J., Wolfe M. A., Agüeros M., Warner B., Woudt P., Trampesch J., Homer L., Schmidt G., Knapp G. R., Anderson S. F., Covey K., Harris H., Hawley S., Schneider D. P., Voges W., Brinkmann J., 2004, "Cataclysmic Variables from the Sloan Digital Sky Survey. III. The Third Year", *Astronomical Journal*, **128**, 1882 – 1893
- Taff L. G., Van Horn H., 1974, "Radial pulsations of finite isothermal gas spheres", *Monthly Notices of the Royal Astronomical Society*, **167**, 427 – 432
- Takata M., 2005, "Momentum conservation and model classification of the dipolar oscillations in stars", *Publications of the Astronomical Society of Japan*, **57**, 375 – 389

- Takata M., 2006a, "Analysis of adiabatic dipolar oscillations of stars", *Publications of the Astronomical Society of Japan*, **58**, 893 – 908
- Takata M., 2006b, "Rigorous analysis of dipolar oscillations of stars", In *Proc. SOHO 18 / GONG 2006 / HELAS I Conf.: Beyond the spherical Sun*, Ed. K. Fletcher, ESA SP-624, ESA Publications Division, Noordwijk, The Netherlands, 26
- Takata M., 2008, "Dipolar oscillations of stars in general relativity", *Publications of the Astronomical Society of Japan*, **60**, 245 – 258
- Takata M., Shibahashi H., 1995, "Effects of the Quadrupole Component of Magnetic Fields on the Rapid Oscillations of Ap Stars", *Publications of the Astronomical Society of Japan*, **47**, 219 – 231
- Takata M., Shibahashi H., 2003, "Hydrogen abundance in the tachocline layer of the Sun", *Publications of the Astronomical Society of Japan*, **55**, 1015 – 1023
- Takeda Y., Sato B., Murata D., 2008, "Stellar Parameters and Elemental Abundances of Late-G Giants", *Publications of the Astronomical Society of Japan*, **60**, 781 – 802
- Talon S., Charbonnel C., 2005, "Hydrodynamical stellar models including rotation, internal gravity waves, and atomic diffusion. I. Formalism and tests on Pop I dwarfs", *Astronomy and Astrophysics*, **440**, 981 – 994
- Talon S., Charbonnel C., 2008, "Angular momentum transport by internal gravity waves. IV - Wave generation by surface convection zone, from the pre-main sequence to the early-AGB in intermediate mass stars", *Astronomy and Astrophysics*, **482**, 597 – 605
- Talon S., Zahn J.-P., Maeder A., Meynet G., 1997, "Rotational mixing in early-type stars: the main-sequence evolution of a  $9M_{\odot}$  star", *Astronomy and Astrophysics*, **322**, 209 – 217
- Tarantola A., 1987, *Inverse Problem Theory*, Elsevier, Amsterdam
- Tassoul J.-L., 2000, *Stellar Rotation*, Cambridge University Press
- Tassoul M., 1980, "Asymptotic approximations for stellar nonradial pulsations", *Astrophysical Journal Supplement Series*, **43**, 469 – 490
- Tassoul M., 1990, "Second-order asymptotic approximations for stellar non-radial acoustic modes", *Astrophysical Journal*, **358**, 313 – 327
- Tassoul M., Tassoul J.-L., 1983, "Meridional circulation in rotating stars. V - Cooling white dwarfs", *Astrophysical Journal*, **267**, 334 – 339
- Tassoul M., Fontaine G., Winget D. E., 1990, "Evolutionary models for pulsation studies of white dwarfs", *Astrophysical Journal Supplement Series*, **72**, 335 – 386
- Taylor B. J., 2003a, "Statistical cataloging of archival data for luminosity class IV–V stars. II. The epoch 2001 "Fe/H] catalog", *Astronomy and Astrophysics*, **398**, 731 – 738
- Taylor B. J., 2003b, "Statistical cataloging of archival data for luminosity class IV–V stars. I. The epoch 2001 temperature catalog", *Astronomy and Astrophysics*, **398**, 721 – 729

- Telting J. H., Schrijvers C., 1997, "Line-profile variations of non-radial adiabatic pulsations of rotating stars. II. The diagnostic value of amplitude and phase diagrams derived from time series of spectra", *Astronomy and Astrophysics*, **317**, 723 – 741
- Telting J. H., Schrijvers C., 1998, "A new bright beta Cephei star: line-profile variability in  $\omega^1$  Sco", *Astronomy and Astrophysics*, **339**, 150 – 158
- Telting J. H., Aerts C., Mathias P., 1997, "A period analysis of the optical line variability of  $\beta$  Cephei: evidence for multi-mode pulsation and rotational modulation", *Astronomy and Astrophysics*, **322**, 493 – 506
- Templeton M., Basu S., Demarque P., 2002, "High-Amplitude  $\delta$  Scuti and SX Phoenicis Stars: The Effects of Chemical Composition on Pulsations and the Period-Luminosity Relation", *Astrophysical Journal*, **576**, 963 – 975
- Thévenin F., Provost J., Morel P., Berthomieu G., Bouchy F., Carrier F., 2002, "Asteroseismology and calibration of  $\alpha$  Cen binary system", *Astronomy and Astrophysics*, **392**, L9 – L12
- Thévenin F., Kervella P., Pichon B., Morel P., Di Folco E., Lebreton Y., 2005, "VLTI/VINCI diameter constraints on the evolutionary status of  $\delta$  Eri,  $\xi$  Hya,  $\eta$  Boo", *Astronomy and Astrophysics*, **436**, 253 – 262
- Thompson M. J., 1988, "Evidence for a thin perturbative layer near the base of the solar convection zone", *Seismology of the Sun, Sun-like Stars*, Eds V. Domingo, E. J. Rolfe, ESA SP-286, ESA Publications Division, Noordwijk, The Netherlands, 321 – 324
- Thompson M. J., 1990, "A new inversion of solar rotational splitting data", *Solar Physics*, **125**, 1 – 12
- Thompson M. J., 1993, "Seismic investigation of the Sun's internal structure and rotation", In *Proc. GONG 1992: Seismic investigation of the Sun and stars*, Ed. T. M. Brown, Astronomical Society of the Pacific Conference Series, San Francisco, **42**, 141 – 154
- Thompson M. J., 2001, "Temporal variations of the Sun's internal structure and dynamics: a theoretical perspective", In *Helio- and Asteroseismology at the Dawn of the Millennium: Proc. SOHO 10 / GONG 2000 Workshop* ESA SP-464, ESA Publications Division, Noordwijk, The Netherlands, 39 – 44
- Thompson M. J., 2006, *An introduction to astrophysical fluid dynamics*, Imperial College Press, London
- Thompson M. J., Christensen-Dalsgaard J., Miesch M. S., Toomre J., 2003, "The internal rotation of the Sun", *Annual Review of Astronomy and Astrophysics*, **41**, 599 – 643
- Thoul A., Montalbán J., 2007, "Microscopic diffusion in stellar plasmas", In *Stellar Evolution and Seismic Tools for Asteroseismology: Diffusive Processes in Stars and Seismic Analysis*, Eds C. W. Straka, Y. Lebreton, M. J. P. F. G. Monteiro, European Astronomical Society Publication Series, **26**, EDP Sciences, 25 – 36
- Thoul A. A., Bahcall J. N., Loeb A., 1994, "Element diffusion in the solar interior", *Astrophysical Journal*, **421**, 828 – 842

- Thoul A., Scuflaire R., Noels A., Vatovez B., Briquet M., Dupret M.-A., Montalbán J., 2003, "A new seismic analysis of Alpha Centauri", *Astronomy and Astrophysics*, **402**, 293 – 297
- Thoul A., Scuflaire R., Ausselos M., Aerts C., Noels A., 2004, "Astroseismology of the Beta Cephei star HD 129929. Effects of a change in the metal mixture", *Communications in Asteroseismology*, **144**, 35 – 40
- Tobias S., Weiss N., 2007, "The solar dynamo and the tachocline", In *The solar tachocline*, Eds D. W. Hughes, R. Rosner, N. O. Weiss, Cambridge University Press, 319 – 350
- Tomczyk S., Streander K., Card G., Elmore D., Hull H., Cacciani A., 1995, "An instrument to observe low-degree solar oscillations", *Solar Physics*, **159**, 1 – 21
- Tomkin J., Pan X., McCarthy J. K., 1995, "Spectroscopic detection of the secondaries of the Hyades interferometric spectroscopic binary  $\theta^2$  Tauri and of the interferometric spectroscopic binary alpha Andromedae", *Astronomical Journal*, **109**, 780 – 790
- Toutain T., Appourchaux T., 1994, "Maximum likelihood estimators: An application to the estimation of the precision of helioseismic measurements", *Astronomy and Astrophysics*, **289**, 649 – 658
- Toutain T., Fröhlich C., 1992, "Characteristics of solar p-modes: Results from the IPHIR experiment", *Astronomy and Astrophysics*, **257**, 287 – 297
- Toutain T., Kosovichev A. G., 2000, "Optimal masks for low-degree solar acoustic modes", *Astrophysical Journal*, **534**, L211 – L214
- Toutain T., Kosovichev A. G., 2005, "Study of the solar cycle dependence of low-degree p-modes with Michelson Doppler Imager and VIRGO", *Astrophysical Journal*, **622**, 1314 – 1319
- Townsend R. H. D., 1997, "Spectroscopic modelling of non-radial pulsation in rotating early-type stars", *Monthly Notices of the Royal Astronomical Society*, **284**, 839 – 858
- Townsend R. H. D., 2002, "Photometric modelling of slowly pulsating B stars", *Monthly Notices of the Royal Astronomical Society*, **330**, 855 – 875
- Townsend R. H. D., 2003a, "Asymptotic expressions for the angular dependence of low-frequency pulsation modes in rotating stars", *Monthly Notices of the Royal Astronomical Society*, **340**, 1020 – 1030
- Townsend R. H. D., 2003b, "A semi-analytical formula for the light variations due to low-frequency g modes in rotating stars", *Monthly Notices of the Royal Astronomical Society*, **343**, 125 – 136
- Townsend R. H. D., 2005a, "Influence of the Coriolis force on the instability of slowly pulsating B stars", *Monthly Notices of the Royal Astronomical Society*, **360**, 465 – 476
- Townsend R. H. D., 2005b, "Kappa-mechanism excitation of retrograde mixed modes in rotating B-type stars", *Monthly Notices of the Royal Astronomical Society*, **364**, 573 – 582

- Townsend R. H. D., MacDonald J., 2006, "Excitation of g modes in Wolf-Rayet stars by a deep opacity bump", *Monthly Notices of the Royal Astronomical Society*, **368**, L57 – L61
- Townsend R. H. D., Owocki S. P., 2005, "A rigidly rotating magnetosphere model for circumstellar emission from magnetic OB stars", *Monthly Notices of the Royal Astronomical Society*, **357**, 251 – 264
- Townsend R. H. D., Owocki S. P., Howarth I. D., 2004, "Be-star rotation: how close to critical?", *Monthly Notices of the Royal Astronomical Society*, **350**, 189 – 195
- Townsley D. M., Arras P., Bildsten L., 2004, "Seismology of the Accreting White Dwarf in GW Librae", *Astrophysical Journal*, **608**, L105 – L108
- Trampedach R., 2004, "3D-simulation of the outer convection-zone of an A-star", In *Proc. IAU Symposium 224: The A star puzzle*, Eds J. Zverko, J. Zižňovský, S. J. Adelman, W. W. Weiss, Cambridge University Press, 155 – 160
- Trampedach R., 2007, "A new stellar atmosphere grid - in 3D", In *AIP Conf. Proc.: Unsolved Problems in Stellar Physics*, Eds R. J. Stancliffe, J. Dewi, G. Houdek, R. G. Martin, C. A. Tout, American Institute of Physics, Melville, 141 – 148
- Trampedach R., Stein R. F., Christensen-Dalsgaard J., Nordlund Å., 1999, "Stellar evolution with a variable mixing-length parameter", In *Theory and Tests of Convection in Stellar Structure*, Eds A. Giménez, E. F. Guinan, B. Montesinos, Astronomical Society of the Pacific Conference Series, San Francisco, **173**, 233 – 236
- Trampedach R., Däppen, W., Baturin, V. A., 2006, "A synoptic comparison of the Mihalas-Hummer-Däppen and OPAL equations of state", *Astrophysical Journal*, **646**, 560 – 578
- Tran Minh F., Léon L., 1995, "Numerical solution of stellar nonradial oscillations: the Galerkin and B-splines method.", *Physical Processes in Astrophysics*, 219 – 221
- Tremblay P.-E., Fontaine G., Brassard P., Bergeron P., Randall S. K., 2006, "A Quantitative Analysis of the Available Multicolor Photometry for Rapidly Pulsating Hot B Subdwarfs", *Astrophysical Journal Supplement Series*, **165**, 551 – 567
- Turck-Chièze S., Basu S., Brun A. S., Christensen-Dalsgaard J., Eff-Darwich A., Lopes I., Pérez Hernández F., Berthomieu G., Provost J., Ulrich R. K., Baudin F., Boumier P., Charra J., Gabriel A. H., Garcia R. A., Grec G., Renaud C., Robillot J. M., Roca Cortés T., 1997, "First view of the solar core from GOLF acoustic modes", *Solar Physics*, **175**, 247 – 265
- Turck-Chièze S., García R. A., Couvidat S., Ulrich R. K., Bertello L., Varadi F., Kosovichev A. G., Gabriel A. H., Gerthomieu G., Brun A. S., Lopes I., Pallé P., Provost J., Robillot J. M., Roca Cortés T., 2004a, "Looking for gravity-mode multiplets with the GOLF experiment aboard *SOHO*", *Astrophysical Journal*, **604**, 455 – 468 [Erratum: *Astrophysical Journal*, **608**, 610]

- Turck-Chièze S., Couvidat S., Piau L., Ferguson J., Lambert P., Ballot J., García R. A., Nghiem P., 2004b, "Surprising Sun: a new step towards a complete picture?" *Phys. Rev. Lett.*, **93**, 211102-(1–4)
- Turck-Chièze S., Mathur S., Ballot J., García R. A., Carton P.-H., Barrière J.-C., Daniel-Thomas P., Delbart A., Desforges D., Granelli R., Nunio F., Piret Y., Pallé P. L., Jiménez A. J., Jiménez-Reyes S. J., Simonello R., 2008, "The GOLF-NG prototype and the solar European perspective for Cosmic Vision 2015-2025", In *Proc. HELAS II International Conference: Helioseismology, Asteroseismology and the MHD Connections, Göttingen, August 2007*, Eds L. Gizon, M. Roth, *Journal of Physics, Conference Series*, **118**, 012044(1 – 8)
- Turcotte S., Richer J., Michaud G., 1998a, "Consistent evolution of F stars: diffusion, radiative accelerations, and abundance anomalies", *Astrophysical Journal*, **504**, 559 – 572
- Turcotte S., Richer J., Michaud G., Iglesias C. A., Rogers F. J., 1998b, "Consistent solar evolution model including diffusion and radiative acceleration effects", *Astrophysical Journal*, **504**, 539 – 558
- Turcotte S., Richer J., Michaud G., Christensen-Dalsgaard J., 2000, "The effect of diffusion on pulsations of stars on the upper main sequence.  $\delta$  Scuti and metallic A stars", *Astronomy and Astrophysics*, **360**, 603 – 616
- Tylenda R., 1996, "Wolf-Rayet central stars of planetary nebulae", In *Hydrogen Deficient Stars*, Eds C. S. Jeffery, U. Heber, Astronomical Society of the Pacific Conference Series, **96**, 101
- Udalski A., Soszyński I., Szymanski M., Kubiak M., Pietrzynski G., Wozniak P., Zebrun K., 1999, "The Optical Gravitational Lensing Experiment. Cepheids in the Magellanic Clouds. V. Catalog of Cepheids from the Small Magellanic Cloud", *Acta Astronomica*, **49**, 437 – 520
- Ulrich R. K., 1970, "The five-minute oscillations on the solar surface", *Astrophysical Journal*, **162**, 993 – 1001
- Ulrich R. K., 1986, "Determination of stellar ages from asteroseismology", *Astrophysical Journal*, **306**, L37 – L40
- Ulrich R. K., Boyden J. E., Webster L., Snodgrass H. B., Padilla S. P., Gilman P., Shieber T., 1988, "Solar rotation measurements at Mount Wilson. V. Reanalysis of 21 years of data", *Solar Physics*, **117**, 291 – 328
- Unno W., 1967, "The stellar radial pulsation coupled with the convection", *Publications of the Astronomical Society of Japan*, **19**, 140 – 153
- Unno W., Spiegel E. A., 1966, "The Eddington approximation in the radiative heat equation", *Publications of the Astronomical Society of Japan*, **18**, 85 – 95
- Unno W., Osaki Y., Ando H., Saio H., Shibahashi H., 1989, *Nonradial oscillations of stars, 2nd edition*, Tokyo: University of Tokyo Press
- Uytterhoeven K., Telting J. H., Aerts C., Willems B., 2004, "Interpretation of the variability of the  $\beta$  Cephei star  $\lambda$  Scorpii. II. The line-profile diagnostics", *Astronomy and Astrophysics*, **427**, 593 – 605

- Uytterhoeven K., Briquet M., Aerts C., Telting J. H., Harmanec P., Lefever K., Cuypers J., 2005a, "Disentangling component spectra of  $\kappa$  Scorpii, a spectroscopic binary with a pulsating primary. II. Interpretation of the line-profile variability", *Astronomy and Astrophysics*, **432**, 955 – 967
- Uytterhoeven K., Harmanec P., Telting J. H., Aerts C., 2005b, "The orbit of the close spectroscopic binary  $\varepsilon$  Lup and the intrinsic variability of its early B-type components", *Astronomy and Astrophysics*, **440**, 249 – 260
- Uytterhoeven K., Mathias P., Poretti E., Rainer M., Martín-Ruiz S., Rodríguez E., Amado P. J., Le Contel D., Jankov S., Niemczura E., Pollard K. R., Brunsden E., Paparó M., Costa V., Valtier J.-C., Garrido R., Suárez J. C., Kilmartin P. M., Chapellier E., Rodríguez-López C., Marin A. J., Aceituno F. J., Casanova V., Rolland A., Olivares I., 2008, "The  $\gamma$  Doradus CoRoT target HD 49434. I. Results from the ground-based campaign", *Astronomy and Astrophysics*, **489**, 1213 – 1224
- Vakili F., Mourard D., Stee P., 1994, "Optical Resolution of Be Star Envelopes", In *Pulsation, Rotation, and Mass Loss in Early-Type Stars*, Eds L. A. Balona, H. F. Henrichs, J.-M. LeContel, Kluwer Academic Publishers, Dordrecht, **162**, 435 – 447
- van Belle G. T., Ciardi D. R., Boden A. F., 2007, "Measurement of the surface gravity of  $\eta$  Bootis", *Astrophysical Journal*, **657**, 1058 – 1063
- Vandakurov Y. V., 1967, "On the Resonance Instability in a Radially Pulsating Star", *Astrophysical Journal*, **149**, 435 – 439
- van den Ancker M. E., de Winter D., Tjin A Djie H. R. E., 1998, "HIPPARCOS photometry of Herbig Ae/Be stars", *Astronomy and Astrophysics*, **330**, 145 – 154
- VandenBerg D. A., Bergbusch P. A., Dowler P. D., 2006, "The Victoria-Regina stellar models: evolutionary tracks and isochrones for a wide range in mass and metallicity that allow for empirically constrained amounts of convective core overshoot", *Astrophysical Journal Supplement Series*, **162**, 375 – 387
- van der Hucht K. A., 2001, "The VIIth catalogue of galactic Wolf-Rayet stars", *New Astronomy Review*, **45**, 135 – 232
- van Genderen A. M., 2001, "S Doradus variables in the Galaxy and the Magellanic Clouds", *Astronomy and Astrophysics*, **366**, 508 – 531
- van Genderen A. M., Bovenschen H., Engelsman E. C., Goudfrooy P., van Haarlem M. P., Hartmann D., Latour H. J., Ng Y. K., Prein J. J., van Roermund F. H. P. M., Roogering H. J. A., Steeman F. W. M., Tijdhof W., 1989a, "Light variations of massive stars (Alpha Cygni variables). IX", *Astronomy and Astrophysics Supplement Series*, **79**, 263 – 282
- van Genderen A. M., Steemers W. J. G., van der Hucht K. A., 1987, "A high precision photometric investigation of the micro-variations of Wolf-Rayet stars", *Astronomy and Astrophysics*, **185**, 131 – 146
- van Genderen A. M., Breukers R. J. L. H., Houtekamer P., van Roermund F. H. P. M., Rottgering H. J. A., Steeman F. W. M., 1989b, "An investigation of the micro variations of highly luminous OBA-type stars

- (Alpha Cygni variables). VIII - A study of the periodicities in the radial velocity and light variations of the nitrogen-rich supergiant HD105056 (ON9.7Iae)", *Astronomy and Astrophysics*, **213**, 161 – 166
- van Genderen A. M., Hadiyanto Nitihardjo G., 1989c, "Light variations of massive stars (Alpha Cygni variables). X - The F type supergiants G266 = HDE271182 = R92 and G322 = HDE269612 in the LMC", *Astronomy and Astrophysics Supplement Series*, **79**, 401 – 406
- van Hoof A., 1957, "A Request for Photometric Observations of  $\theta$  Ophiuchi", *Publications of the Astronomical Society of the Pacific*, **69**, 179 – 179
- van Hoof A., 1959, "The Multiple Periodicity of  $\nu$  Eridani", *Publications of the Astronomical Society of the Pacific*, **71**, 455 – 460
- van Hoof A., 1961a, "The Light Variation of Nu Eridani", *Zeitschrift fur Astrophysik*, **53**, 106 – 123
- van Hoof A., 1961b, "The Velocity Changes of Nu Eridani", *Zeitschrift fur Astrophysik*, **53**, 124 – 129
- van Hoof A., 1962, "The Brightness Variation of Theta Ophiuchi", *Zeitschrift fur Astrophysik*, **54**, 255 – 259
- van Hoof A., Blaauw A., 1958, "The Behavior of Theta Ophiuchi during Four Cycles in April, 1956", *Astrophysical Journal*, **128**, 273 – 286
- van Hoof A., Bertiau F., Deurinck R., 1956, "The Radial-Velocity Variation of Theta Ophiuchi", *Astrophysical Journal*, **124**, 168 – 172
- Van Hoolst T., 1995, "Resonances between two stellar oscillation modes with nearly equal frequencies", *Astronomy and Astrophysics*, **295**, 371 – 392
- Van Hoolst T., Dziembowski W. A., Kawaler S. D., 1998, "Unstable non-radial modes in radial pulsators: theory and an example", *Monthly Notices of the Royal Astronomical Society*, **297**, 536 – 544
- Vaníček P., 1971, "Further Development and Properties of the Spectral Analysis by Least-Squares", *Astrophysics and Space Science*, **12**, 10 – 33
- van Leeuwen F., van Genderen A. M., Zegelaar I., 1998, "HIPPARCOS photometry of 24 variable massive stars (alpha Cygni variables)", *Astronomy and Astrophysics Supplement Series*, **128**, 117 – 129
- Van Winckel H., 2003, "Post-AGB Stars", *Annual Review of Astronomy and Astrophysics*, **41**, 391 – 427
- Van Winckel H., Waelkens C., Fernie J. D., Waters L. B. F. M., 1999, "The RV Tauri phenomenon and binarity", *Astronomy and Astrophysics*, **343**, 202 – 212
- van Zyl L., Warner B., O'Donoghue D., Hellier C., Woudt P., Sullivan D., Pritchard J., Kemp J., Patterson J., Welsh W., Casares J., Shahbaz T., van der Hooft F., Vennes S., 2004, "The non-radially pulsating primary of the cataclysmic variable GW Librae", *Monthly Notices of the Royal Astronomical Society*, **350**, 307 – 316
- Vauclair, G., Vauclair, S., Pamjatnikh, A., 1974, "Diffusion processes in the envelopes of main-sequence A stars: model variations due to helium depletion", *Astronomy and Astrophysics*, **31**, 63 – 70

- Veen P. M., van Genderen A. M., van der Hucht K. A., Allen W. H., Arentoft T., Sterken C., 2002a, "The enigmatic WR46: A binary or a pulsator in disguise. I. The photometry", *Astronomy and Astrophysics*, **385**, 585 – 599
- Veen P. M., van Genderen A. M., Crowther P. A., van der Hucht K. A., 2002b, "The enigmatic WR46: A binary or a pulsator in disguise. II. The spectroscopy", *Astronomy and Astrophysics*, **385**, 600 – 618
- Veen P. M., van Genderen A. M., van der Hucht K. A., 2002c, "The enigmatic WR46: A binary or a pulsator in disguise. III. Interpretation", *Astronomy and Astrophysics*, **385**, 619 – 631
- Verner G. A., Chaplin W. J., Elsworth Y., 2006a, "BiSON data show change in solar structure with magnetic activity", *Astrophysical Journal*, **640**, L95 – L98
- Verner G. A., Chaplin W. J., Elsworth Y., 2006b, "The detectability of signatures of rapid variation in low-degree stellar  $p$ -mode oscillation frequencies", *Astrophysical Journal*, **638**, 440 – 445
- Viskum M., Kjeldsen H., Bedding T. R., Dall T. H., Baldry I. K., Bruntt H., Frandsen S., 1998, "Oscillation mode identifications and models for the delta Scuti star FG Virginis", *Astronomy and Astrophysics*, **335**, 549 – 560
- von Neuman J., Wigner E., 1929, "Über merkwürdige diskrete Eigenwerte. Über das Verhalten von Eigenwerten bei adiabatischen Prozessen", *Phys. Z.*, **30**, 467 – 470
- von Zeipel H. 1924, "The radiative equilibrium of a rotating system of gaseous masses", *Monthly Notices of the Royal Astronomical Society*, **84**, 665 – 683
- Vorontsov S. V., 1988, "A search of the effects of magnetic field in the solar five-minute oscillations", *Proc. IAU Symposium No 123, Advances in helio- and asteroseismology*, Eds J. Christensen-Dalsgaard, S. Frandsen, Reidel, Dordrecht, 151 – 154
- Vorontsov S. V., 1989, "The inverse problem of helioseismology: the speed of sound in the solar interior", *Pis'ma Astron. Zh.*, **15**, 48 – 60 (English translation: *Sov. Astron. Lett.*, **15**, 21 – 26)
- Vorontsov S. V., 1998, "Seismic sounding of the solar interior: differential response technique", In *Poster Volume; Proc. IAU Symposium No 181: Sounding Solar and Stellar Interiors*, Eds J. Provost, F.-X. Schmider, Université de Nice, 135 – 136
- Vorontsov S. V., 2004, "Helioseismic inversions and the equation of state", In *Equation-of-State and Phase-Transition Issues in Models of Ordinary Astrophysical Matter*, Eds V. Ćelebonović, W. Däppen, D. Gough, AIP Conference Proceedings, **731**, AIP, Melville, New York, 47 – 63
- Vorontsov S. V., Jefferies S. M., 2005, "Modeling solar oscillation power spectra. I. Adaptive response function for Doppler velocity measurements", *Astrophysical Journal*, **623**, 1202 – 1214

- Vorontsov S. V., Shibahashi H., 1991, "Asymptotic inversion of the solar oscillation frequencies: sound speed in the solar interior", *Publications of the Astronomical Society of Japan*, **43**, 739 – 753
- Vorontsov S. V., Baturin V. A., Pamyatnykh A. A., 1991, "Seismological measurement of solar helium abundance", *Nature*, **349**, 49 – 51
- Vorontsov S. V., Baturin V. A., Pamyatnykh A. A., 1992, "Seismology of the solar envelope: towards the calibration of the equation of state", *Monthly Notices of the Royal Astronomical Society*, **257**, 32 – 46
- Vorontsov S. V., Christensen-Dalsgaard J., Schou J., Strakhov V. N., Thompson M. J., 2002, "Helioseismic measurement of solar torsional oscillations", *Science*, **296**, 101 – 103
- Vučković M., Kawaler S. D., O'Toole S., Csubry Z., Baran A., Zola S., Moskalik P., Klumpe E. W., Riddle R., O'Brien M. S., Mullally F., Wood M. A., Wilkat V., Zhou A.-Y., Reed M. D., Terndrup D. M., Sullivan D. J., Kim S.- L., Chen W. P., Chen C.-W., Hsiao W.-S., Sanchawala K., Lee H.- T., Jiang X. J., Janulis R., Siwak M., Ogloza W., Paparó M., Bognár Z., Sódor Á., Handler G., Lorenz D., Steininger B., Silvotti R., Vauclair G., Oreiro R., Østensen R., Bronowska A., Castanheira B. G., Kepler S. O., Fraga L., Shipman H. L., Provencal J. L., Childers D., 2006, "Whole Earth Telescope Observations of the Pulsating Subdwarf B Star PG 0014+067", *Astrophysical Journal*, **646**, 1230 – 1240
- Vučković M., Aerts C., Østensen R., Nelemans G., Hu H., Jeffery C. S., Dhillon V. S., Marsh T. R., 2007, "The binary properties of the pulsating subdwarf B eclipsing binary PG 1336-018 (NY Virginis)", *Astronomy and Astrophysics*, **471**, 605 – 615
- Vuille F., O'Donoghue D., Buckley D. A. H., Massacand C.-M., Solheim J. E., Bard S., Vauclair G., Giovannini O., Kepler S. O., Kanaan A., Provencale J. L., Wood M. A., Clemens J. C., Kleinman S. J., O'Brien M. S., Nather R. E., Winget D. E., Nitta A., Klumpe E. W., Montgomery M. H., Watson T. K., Bradley P. A., Sullivan D. J., Wu K., Marar T. M. K., Seetha S., Ashoka B. N., Mahra H. S., Bhat B. C., Babu V. C., Leibowitz E. M., Hemar S., Ibbetson P., Mashals E., Meištas E., Moskalik P., Zoła S., Krzesiński J., Pajdosz G., 2000, "Normal modes and discovery of high-order cross-frequencies in the DBV white dwarf GD 358", *Monthly Notices of the Royal Astronomical Society*, **314**, 689 – 701
- Wade G. A., Donati J.-F., Landstreet J. D., Shorlin S. L. S., 2000, "Spectropolarimetric measurements of magnetic Ap and Bp stars in all four Stokes parameters", *Monthly Notices of the Royal Astronomical Society*, **313**, 823 – 850
- Waelkens C., 1991, "Slowly pulsating B stars", *Astronomy and Astrophysics*, **246**, 453 – 468
- Waelkens C., Rufener F., 1983, "HD 129929 - A multiperiodic pulsating early-type star at intermediate galactic latitude", *Astronomy and Astrophysics*, **119**, 279 – 284

- Waelkens C., Aerts C., Kestens E., Grenon M., Eyer L., 1998, "Study of an unbiased sample of B stars observed with Hipparcos: the discovery of a large amount of new slowly pulsating B stars", *Astronomy and Astrophysics*, **330**, 215 – 221
- Walker A., Bono G. (Eds), 2006, *Stellar Pulsation and Evolution, Memorie della Societa Astronomica Italiana*, **77**
- Walker G. A. H., Kuschnig R., Matthews J. M., Reegen P., Kallinger T., Kambe E., Saio H., Harmanec P., Guenther D. B., Moffat A. F. J., Rucinski S. M., Sasselov D., Weiss W. W., Bohlander D. A., Božić H., Hashimoto O., Koubský P., Mann R., Ruždjak D., Škoda P., Šlechta M., Sudar D., Wolf M., Yang S., 2005a, "Pulsations of the Oe Star  $\zeta$  Ophiuchi from MOST Satellite Photometry and Ground-based Spectroscopy", *Astrophysical Journal*, **623**, L145 – L148
- Walker G. A. H., Kuschnig R., Matthews J. M., Cameron C., Saio H., Lee U., Kambe E., Masuda S., Guenther D. B., Moffat A. F. J., Rucinski S. M., Sasselov D., Weiss W. W., 2005b, "MOST detects  $g$ -modes in the Be star HD 163868", *Astrophysical Journal*, **635**, L77 – L80
- Walker M. F., 1951, "Variability of  $\nu$  Eridani", *Publications of the Astronomical Society of the Pacific*, **63**, 176 – 178
- Walker M. F., 1952, "A search for stars of the beta Canis Majoris type", *Astronomical Journal*, **57**, 227 – 231
- Wallerstein G., 2002, "The Cepheids of Population II and Related Stars", *Publications of the Astronomical Society of the Pacific*, **114**, 689 – 699
- Warner B., van Zyl L., 1998, "Discovery of non-radial pulsations in the white dwarf primary of a cataclysmic variable star", In *Proc. IAU Symposium 185: New Eyes to See Inside the Sun and Stars*, Eds F.-L. Deubner, J. Christensen-Dalsgaard, D. Kurtz, **185**, 321 – 322
- Warner B., Woudt P. A., 2005, "Non-Radial Oscillations in CV Primaries", In *14th European Workshop on White Dwarfs*, Eds D. Koester, S. Moehler, Publications of the Astronomical Society of the Pacific Conference Series, San Francisco, **334**, 453 – 458
- Warner P. B., Kaye A. B., Guzik J. A., 2003, "A theoretical  $\gamma$  Doradus instability strip", *Astrophysical Journal*, **593**, 1049 – 1055
- Watson R. D., 1988, "Contributing factors to flux changes in nonradial stellar pulsations", *Astrophysics and Space Science*, **140**, 255 – 290
- Weiss A., 1987, "Linear nonadiabatic pulsations of R CrB models", *Astronomy and Astrophysics*, **185**, 178 – 188
- Weiss A., Hillebrandt W., Thomas H.-C., Ritter H., 2004, *Cox and Giuli's Principles of Stellar Structure*, UK: Princeton Publishing Associates Ltd
- Werner K., Herwig F., 2006, "The Elemental Abundances in Bare Planetary Nebula Central Stars and the Shell Burning in AGB Stars", *Publications of the Astronomical Society of the Pacific*, **118**, 183 – 204
- Whittaker E. T., Watson G. N., 1927, *A Course of Modern Analysis*, 4th Edition, Cambridge University Press

- Willems B., 2003, "Excitation of oscillation modes by tides in close binaries: constraints on stellar and orbital parameters", *Monthly Notices of the Royal Astronomical Society*, **346**, 968 – 976
- Willems B., Aerts C., 2002, "Tidally induced radial-velocity variations in close binaries", *Astronomy and Astrophysics*, **384**, 441 – 451
- Willems B., Claret A., 2005, "Dynamic Tides and the Evolution of Stars in Close Binaries", In *Tidal Evolution and Oscillations in Binary Stars*, Eds A. Claret, A. Giménez, J.-P. Zahn, Publications of the Astronomical Society of the Pacific Conference Series, San Francisco, **333**, 52
- Willems B., Van Hoolst T., Smeyers P., 2003, "Nonadiabatic resonant dynamic tides and orbital evolution in close binaries", *Astronomy and Astrophysics*, **397**, 973 – 985
- Willson L. A., 2000, "Mass loss from cool stars: impact on the evolution of stars and stellar populations", *Annual Review of Astronomy and Astrophysics*, **38**, 573 – 611
- Winget D. E., 1982, *Gravity Mode Instabilities in DA White Dwarfs*, PhD Dissertation, University of Rochester, USA
- Winget D. E., Kepler, S. O., 2008, "Pulsating White Dwarf Stars and Precision Asteroseismology", *Annual Review of Astronomy and Astrophysics*, **46**, 157 – 199
- Winget D. E., van Horn H. M., Hansen C. J., 1981, "The nature of the ZZ Ceti oscillations - Trapped modes in compositionally stratified white dwarfs", *Astrophysical Journal*, **245**, L33 – L36
- Winget D. E., Robinson E. L., Nather R. D., Fontaine G., 1982, "Photometric observations of GD 358 - DB white dwarfs do pulsate", *Astrophysical Journal*, **262**, L11 – L15
- Winget D. E., van Horn H. M., Tassoul M., Hansen C. J., Fontaine G., 1983a, "The pulsation properties of DB white dwarfs - A preliminary analysis", *Astrophysical Journal*, **268**, L33 – L36
- Winget D. E., Hansen C. J., van Horn H. M., 1983b, "Do pulsating PG1159-035 stars put constraints on stellar evolution?", *Nature*, **303**, 781 – 782
- Winget D. E., Robinson E. L., Nather R. E., Kepler S. O., O'Donoghue D., 1985, "A measurement of secular evolution in the pre-white dwarf star", *Astrophysical Journal*, **292**, 606 – 613
- Winget D. E., Nather R. E., Hill J. A., 1987, "Two extreme examples of compact pulsators - PG 1115+1158 and PG 1351+489", *Astrophysical Journal*, **316**, 305 – 310
- Winget D. E., Nather R. E., Clemens J. C., Provencal J., Kleinman S. J., Bradley P. A., Wood M. A., Claver C. F., Frueh M. L., Grauer A. D., Hine B. P., Hansen C. J., Fontaine G., Achilleos N., Wickramasinghe D. T., Marar T. M. K., Seetha S., Ashoka B. N., O'Donoghue D., Warner B., Kurtz D. W., Buckley D. A., Brickhill J., Vauclair G., Dolez N., Chevreton M., Barstow M. A., Solheim J. E., Kanaan A., Kepler S. O., Henry G. W., Kawaler S. D., 1991, "Asteroseismology of the DOV star PG 1159 - 035 with the Whole Earth Telescope", *Astrophysical Journal*, **378**, 326 – 346

- Winget D. E., Nather R. E., Clemens J. C., Provencal J. L., Kleinman S. J., Bradley P. A., Claver C. F., Dixson J. S., Montgomery M. H., Hansen C. J., Hine B. P., Birch P., Candy M., Marar T. M. K., Seetha S., Ashoka B. N., Leibowitz E. M., O'Donoghue D., Warner B., Buckley D. A. H., Tripe P., Vauclair G., Dolez N., Chevreton M., Serre T., Garrido R., Kepler S. O., Kanaan A., Augusteijn T., Wood M. A., Bergeron P., Grauer A. D., 1994, "Whole earth telescope observations of the DBV white dwarf GD 358", *Astrophysical Journal*, **430**, 839 – 849
- Witham A. R., Knigge C., Drew J. E., Greimel R., Steeghs D., Gänsicke B. T., Groot P. J., Mampaso A., 2008, "The IPHAS catalogue of H $\alpha$  emission-line sources in the northern Galactic plane", *Monthly Notices of the Royal Astronomical Society*, **384**, 1277 – 1288
- Witte M. G., Savonije G. J., 1999a, "The dynamical tide in a rotating 10 M $_{\odot}$  main sequence star. A study of g- and r-mode resonances", *Astronomy and Astrophysics*, **341**, 842 – 852
- Witte M. G., Savonije G. J., 1999b, "Tidal evolution of eccentric orbits in massive binary systems. A study of resonance locking", *Astronomy and Astrophysics*, **350**, 129 – 147
- Witte M. G., Savonije G. J., 2001, "Tidal evolution of eccentric orbits in massive binary systems. II. Coupled resonance locking for two rotating main sequence stars", *Astronomy and Astrophysics*, **366**, 840 – 857
- Wolszczan A., Frail D. A., 1992, "A planetary system around the millisecond pulsar PSR1257 + 12", *Nature*, **355**, 145 – 147
- Wood B. E., Müller H.-R., Zank G. P., Linsky J. L., Redfield S., 2005, "New mass-loss measurements from astrospheric Ly $\alpha$  absorption", *Astrophysical Journal*, **628**, L143 – L146
- Wood P. R., 2000, "Variable red giants in the LMC: Pulsating stars and binaries?", *Publications of the Astronomical Society of Australia*, **17**, 18 – 21
- Wood P. R., Sebo K. M., 1996, "On the pulsation mode of Mira variables: evidence from the Large Magellanic Cloud", *Monthly Notices of the Royal Astronomical Society*, **282**, 958 – 964
- Wood P. R., Alcock C., Allsman R. A., Alves D., Axelrod T. S., Becker A. C., Bennett D. P., Cook K. H., Drake A. J., Freeman K. C., Griest K., King L. J., Lehner M. J., Marshall S. L., Minniti D., Peterson B. A., Pratt M. R., Quinn P. J., Stubbs C. W., Sutherland W., Tomaney A., Vandehei T., Welch D. L., 1999, "MACHO observations of LMC red giants: Mira and semi-regular pulsators, and contact and semi-detached binaries", In *Asymptotic Giant Branch Stars*, Eds T. Lebertre, A. Lèbre, C. Waelkens, Astronomical Society of the Pacific Conference Series, San Francisco, **191**, 151
- Wood P. R., Olivier E. A., Kawaler S. D., 2004, "Long Secondary Periods in Pulsating Asymptotic Giant Branch Stars: An Investigation of their Origin", *Astrophysical Journal*, **604**, 800 – 816

- Woodard M., Hudson H. S., 1983, "Frequencies, amplitudes and linewidths of solar oscillations from total irradiance observations", *Nature*, **305**, 589 – 593
- Woodard M. F., Libbrecht K. G., 1993, "Observations of time variation in the Sun's rotation", *Science*, **260**, 1778 – 1781
- Woodard M. F., Noyes R. W., 1985, "Change of solar oscillation eigenfrequencies with the solar cycle", *Nature*, **318**, 449 – 450
- Woodard M. F., Kuhn J. R., Murray N., Libbrecht K. G., 1991, "Short-term changes in solar oscillation frequencies and solar activity", *Astrophysical Journal*, **373**, L81 – L84
- Woodard M. F., Korzennik S. G., Rabello-Soares M. C., Kumar P., Tarbell T. D., Acton S., 2001, "Energy distribution of solar oscillation modes inferred from space-based measurements", *Astrophysical Journal*, **548**, L103 – L106
- Woosley S. E., Chevalier R. A., 1989, "Was the millisecond pulsar in SN1987A spun up or born spinning fast?", *Nature*, **338**, 321 – 323
- Woosley S. E., Heger A., Weaver T. A., 2002, "The evolution and explosion of massive stars", *Reviews of Modern Physics*, **74**, 1015 – 1071
- Wright D. J., Lynas-Gray A. E., Kilkenny D., Cottrell P. L., Shobbrook R. R., Koen C., van Wyk F. W., Kilmartin P. M., Martinez P., Gilmore A. C., 2006, "A photometric and spectroscopic study of the hottest pulsating extreme helium star, V2076 Oph (HD 160641)", *Monthly Notices of the Royal Astronomical Society*, **369**, 2049 – 2058
- Wu Y., 2001, "Combination frequencies in the Fourier spectra of white dwarfs", *Monthly Notices of the Royal Astronomical Society*, **323**, 248 – 256
- Wu Y., Goldreich P., 1999, "Gravity-modes in ZZ Ceti stars. II. Eigenvalues and eigenfunctions", *Astrophysical Journal*, **519**, 783 – 792
- Wu Y., Goldreich P., 2001, "Gravity Modes in ZZ Ceti Stars. IV. Amplitude Saturation by Parametric Instability", *Astrophysical Journal*, **546**, 469 – 483
- Xiong D. R., Deng L., 2001, "Turbulent convection and pulsational stability of variable stars. – IV. The red edge of the  $\delta$  Scuti instability strip", *Monthly Notices of the Royal Astronomical Society*, **324**, 243 – 248
- Xiong D. R., Chen Q. L., Deng L., 1997, "Nonlocal time-dependent convection theory", *Astrophysical Journal Supplement Series*, **108**, 529 – 544
- Xiong D. R., Deng L., Cheng Q. L., 1998, "Turbulent convection and pulsational stability of variable stars. I. Oscillations of long-period variables", *Astrophysical Journal*, **499**, 355 – 366
- Yıldız M., 2007, "Models of  $\alpha$  Centauri A and B with and without seismic constraints: time dependence of the mixing-length parameter", *Monthly Notices of the Royal Astronomical Society*, **374**, 1264 – 1270
- Yıldız M., 2008, "On the structure of the Sun and  $\alpha$  Centauri A and B in the light of seismic and non-seismic constraints", *Monthly Notices of the Royal Astronomical Society*, **388**, 1143 – 1151

- York D. G., Adelman J., Anderson J. E., Jr., Anderson S. F., Annis J., Bahcall N. A., Bakken J. A., Barkhouser R., Bastian S., Berman E., Boroski W. N., Bracker S., Briegel C., Briggs J. W., Brinkmann J., Brunner R., Burles S., Carey L., Carr M. A., Castander F. J., Chen B., Colestock P. L., Connolly A. J., Crocker J. H., Csabai I., Czarapata P. C., Davis J. E., Doi M., Dombeck T., Eisenstein D., Ellman N., Elms B. R., Evans M. L., Fan X., Federwitz G. R., Fiscelli L., Friedman S., Frieman J. A., Fukugita M., Gillespie B., Gunn J. E., Gurbani V. K., de Haas E., Haldeman M., Harris F. H., Hayes J., Heckman T. M., Hennessy G. S., Hindsley R. B., Holm S., Holmgren D. J., Huang C.-h., Hull C., Husby D., Ichikawa S.-I., Ichikawa T., Ivezić Ž., Kent S., Kim R. S. J., Kinney E., Klaene M., Kleinman A. N., Kleinman S., Knapp G. R., Korienek J., Kron R. G., Kunszt P. Z., Lamb D. Q., Lee B., Leger R. F., Limmongkol S., Lindenmeyer C., Long D. C., Loomis C., Loveday J., Lucinio R., Lupton R. H., MacKinnon B., Mannery E. J., Mantsch P. M., Margon B., McGehee P., McKay T. A., Meiksin A., Merelli A., Monet D. G., Munn J. A., Narayanan V. K., Nash T., Neilsen E., Neswold R., Newberg H. J., Nichol R. C., Nicinski T., Nonino M., Okada N., Okamura S., Ostriker J. P., Owen R., Pauls A. G., Peoples J., Peterson R. L., Petravick D., Pier J. R., Pope A., Pordes R., Prosapio A., Rechenmacher R., Quinn T. R., Richards G. T., Richmond M. W., Rivetta C. H., Rockosi C. M., Ruthmansdorfer K., Sandford D., Schlegel D. J., Schneider D. P., Sekiguchi M., Sergey G., Shimasaku K., Siegmund W. A., Smee S., Smith J. A., Snedden S., Stone R., Stoughton C., Strauss M. A., Stubbs C., SubbaRao M., Szalay A. S., Szapudi I., Szokoly G. P., Thakar A. R., Tremonti C., Tucker D. L., Uomoto A., Vanden Berk D., Vogeley M. S., Waddell P., Wang S.-i., Watanabe M., Weinberg D. H., Yanny B., Yasuda N., 2000, “The Sloan Digital Sky Survey: Technical Summary”, *Astronomical Journal*, **120**, 1579 – 1587
- Young A. T., 1971, “Seeing and Scintillation”, *Sky and Telescope*, **42**, 139
- Yudin B. F., Fernie J. D., Ikhsanov N. R., Shenavrin V. I., Weigelt G., 2002, “UBVJHKLM photometry and modeling of R Coronae Borealis”, *Astronomy and Astrophysics*, **394**, 617 – 624
- Yudin R. V., Evans A., Barrett P., Albinson J. S., Davies J. K., Hutchinson M. G., 2003, “Polarimetry of evolved stars. III. RV Tau and R CrB stars”, *Astronomy and Astrophysics*, **412**, 405 – 416
- Zahn J.-P., 1966, “Les oscillation libres d’une étoile en rotation”, *C. R. Acad. Sci. Paris, Ser. B*, **263**, 1077 – 1081
- Zahn J.-P., 1975, “The dynamical tide in close binaries”, *Astronomy and Astrophysics*, **41**, 329 – 344
- Zahn J.-P., 1991, “Convective penetration in stellar interiors”, *Astronomy and Astrophysics*, **252**, 179 – 188
- Zahn J.-P., 1992, “Circulation and turbulence in rotating stars”, *Astronomy and Astrophysics*, **265**, 115 – 132

- Zahn J.-P., Talon S., Matias J., 1997, "Angular momentum transport by internal waves in the solar interior", *Astronomy and Astrophysics*, **322**, 320 – 328
- Zahn J.-P., Brun A. S., Mathis S., 2007, "On magnetic instabilities and dynamo action in stellar radiation zones", *Astronomy and Astrophysics*, **474**, 145 – 154
- Zalewski J., 1993, "Pulsational properties of post-AGB stars", *Acta Astronomica*, **43**, 431 – 440
- Zerbi F. M., Garrido R., Rodriguez E., Krisciunas K., Crowe R. A., Roberts M., Guinan E. F., McCook G. P., Sperauskas J., Griffin R. F., Luedke K. D., 1997a, "The gamma Doradus-type variable 9 Aurigae: results from a multi-site campaign", *Monthly Notices of the Royal Astronomical Society*, **290**, 401 – 410
- Zerbi F. M., Rodríguez E., Garrido R., Martín S., Akan K., Luedke K., Keskin V., Ibanoglu C., Evren S., Tunca Z., Pekunlu R., Paparo M., Nuspl J., Krisciunas K., Jiang S. Y., 1997b, "The Gamma Dor variable HD 164615 - Results from a multisite photometric campaign", *Monthly Notices of the Royal Astronomical Society*, **292**, 43 – 51
- Zerbi F. M., Rodríguez E., Garrido R., Martín S., Ferro A. A., Sareyan J. P., Krisciunas K., Akan M. C., Evren S., Ibañoglu C., Keskin V., Pekunlu R., Tunca Z., Luedke K., Paparo M., Nuspl J., Guerrero G., 1999, "The gamma DOR variable HR 8799: results from a multisite campaign", *Monthly Notices of the Royal Astronomical Society*, **303**, 275 – 283
- Zhang X.-B., Zhang R.-X., Li Z.-P., 2005, "S1280 and S1284: Two Oscillating Blue Stragglers in the Open Cluster M67", *Chinese Journal of Astronomy and Astrophysics*, **5**, 579 – 586
- Zhevakin S. A., 1953, "K Teorii Cefeid. I (On the theory of Cepheids. I)] (in Russian), *Astron. Zh.*, **30**, 161 – 179
- Zhevakin S. A., 1963, "Physical basis of the pulsation theory of variable stars", *Annual Review of Astronomy and Astrophysics*, **1**, 367 – 400
- Zima W., 2006, "A new method for the spectroscopic identification of stellar non-radial pulsation modes. I. The method and numerical tests", *Astronomy and Astrophysics*, **455**, 227 – 234 (Erratum: *Astronomy and Astrophysics*, **497**, 827, 2009)
- Zima W., 2008, "FAMIAS User Manual", *Communications in Asteroseismology*, **155**, 17 – 121
- Zima W., Wright D., Bentley J., Cottrell P. L., Heiter U., Mathias P., Poretti E., Lehmann H., Montemayor T. J., Breger M., 2006, "A new method for the spectroscopic identification of stellar non-radial pulsation modes. II. Mode identification of the δ Scuti star FG Virginis", *Astronomy and Astrophysics*, **455**, 235 – 246
- Zirker J. B., 2003, *Sunquakes. Probing the interior of the Sun*, The Johns Hopkins University Press

- Zverko J., Zižňovský J., Adelman S. J., Weiss W. W. (Eds), 2004, *Proc. IAU Symposium 224: The A-Star Puzzle*, Cambridge University Press, **224**
- Zwintz K., Marconi M., Kallinger T., Weiss W. W., 2004, “Pulsating pre-Main Sequence stars in young open clusters”, In *Proc. IAU Symposium 224: The A star puzzle*, Eds J. Zverko, J. Zižňovský, S. J. Adelman, W. W. Weiss, Cambridge University Press, 353 – 358
- Zwitter T., Siebert A., Munari U., Freeman K. C., Siviero A., Watson F. G., Fulbright J. P., Wyse R. F. G., Campbell R., Seabroke G. M., Williams M., Steinmetz M., Bienaymé O., Gilmore G., Grebel E. K., Helmi A., Navarro J. F., Anguiano B., Boeche C., Burton D., Cass P., Dawe J., Fiegert K., Hartley M., Russell K., Veltz L., Bailin J., Binney J., Bland-Hawthorn J., Brown A., Dehnen W., Evans N. W., Re Fiorentin P., Fiorucci M., Gerhard O., Gibson B., Kelz A., Kujken K., Matijević G., Minchev I., Parker Q. A., Peñarrubia J., Quillen A., Read M. A., Reid W., Roeser S., Ruchti G., Scholz R.-D., Smith M. C., Sordo R., Tolstoi E., Tomasella L., Vidrih S., Wylie-de Boer E., 2008, “The Radial Velocity Experiment (RAVE): Second Data Release”, *Astronomical Journal*, **136**, 421 – 451

# Subject Index

- $\alpha$  Cyg variables, 96  
 $\beta$  Cep stars, 16, 23, 65  
     $\alpha$  Vir, 128  
     $\beta$  Cru, 440  
     $\delta$  Cet, 441  
     $\nu$  Eri, 66, 398, 427, 441  
        case study, 614  
     $\sigma$  Sco, 128  
     $\theta$  Oph  
        case study, 625  
     $\xi^1$  CMa, 65  
    12 Lac, 65  
    19 Mon, 65  
    atomic diffusion, 68  
    BW Vul, 65  
    HD 129929, 65  
        case study, 603  
    HD 157056 =  $\theta$  Oph  
        case study, 625  
    HD 71913, 380  
    HR 6453 =  $\theta$  Oph  
        case study, 625  
    opacity bump, 251  
    Spica, 128  
    SY Equ, 65  
    V1449 Aql, 65  
    V836 Cen = HD 129929, 603  
 $\tilde{c}$  = speed of light, 141  
 $\delta$  Del stars, 50  
 $\delta$  Sct stars, 12, 23, 49  
     $\rho$  Pup, 49, 421  
     $\tau$  Peg, 434  
     $\theta^2$  Tau, 50  
    14 Aur Aa, 128  
    20 CVn, 401, 429  
    4 CVn, 50  
    Altair, 50  
    catalogue, 50  
    core overshoot, 53  
    DG Leo, 128  
    excitation, 52  
FG Vir, 50, 401, 434  
HD 207651, 128  
HD 209295, 129  
HD 263551, 50  
instability strip, 50  
    blue edge, 52, 256  
    red edge, 52, 255, 256  
stochastic excitation, 53  
time dependent convection, 52  
work integral, 251  
XX Pyx, 50  
 $\gamma$  Dor stars, 23, 45  
     $\gamma$  Doradus, 45  
convective blocking, 253  
convective flux blocking, 47  
excitation of high order  
    g modes, 252, 256  
HD 12901, 46, 380  
HD 164515, 45  
HD 209295, 47, 129  
HD 96008, 45  
hybrid  
    HD 209295, 47  
NGC 2506, 130  
rotational splitting, 276  
 $\lambda$  Boo stars, 50  
 $\lambda$  Eri stars, *see* Pulsating Be stars  
 $\rho$  Pup stars, 50  
 $\zeta$  Oph variables, 69  
[WCE] stars, 116  
1-D oscillations, 7  
2-D oscillations, 8  
3-D oscillations, 10  
53 Per stars, 62  
AAVSO, 86, 88–90, 302  
accuracy  
    definition, 297  
acoustic aliasing, 551  
acoustic cavity, 17  
acoustic cut-off frequency, 212, 214  
isothermal atmosphere, 695

- acoustic depth, 219  
 acoustic glitch, 474, 482, 515, 517–519, 531, 551–554  
 acoustic radius, 480, 546  
 acoustic waves, 147  
     propagation, 209  
     reflection, 210  
     refraction, 209  
 adiabat, 158  
 adiabatic approximation, 142  
 adiabatic exponents, 140  
 adiabatic oscillations  
     linear, 195  
 Alfvén radius, 182  
 alias  
     definition, 357  
 amateur astronomers, 301, 302  
 angular frequency, 10  
 angular velocity, 16  
     rotation frequency, 16  
 asteroseismic HR Diagram, 22, 541, 547  
 asymptotic properties of solar oscillations, 476  
     rotational splitting, 487  
 asymptotic properties of stellar oscillations  
     g modes, 220, 715  
     p modes, 217, 710, 712  
 asymptotic relations, 20, 217, 220, 710, 712, 715  
 asymptotic theory of stellar oscillations, 202, 699  
     properties of frequencies and eigenfunctions, 212  
 atomic diffusion, 159, 166  
      $\alpha$  Cen A, 567, 570  
      $\alpha$  Cen A and B, 566  
      $\beta$  Cep stars, 68  
      $\nu$  Eri, 620  
      $\theta$  Oph, 633  
     roAp stars, 56, 58, 640  
     sdBV stars, 107, 658  
 Sun, 449, 481, 482, 505, 511, 547  
     white dwarf stars, 112  
 avoided crossings, 224, 232  
 axions, 114  
 axisymmetric mode, 13  
 B supergiants, 97  
 Barycentric Julian Date, 299  
 Barycentric Julian Ephemeris Date, 299  
 beat Cepheids, 82  
 Betsy stars, 107  
 binary stars  
      $\alpha$  Cen A, 126  
      $\alpha$  Cen B, 126  
      $\alpha$  Vir, 128  
      $\sigma$  Sco, 128  
     14 Aur Aa, 128  
     Common envelope phase, 127  
     EC 14026–2647, 133  
     eclipsing, 127  
         PG 1336–018, 661  
     ellipsoidal variables, 128  
         DG Leo, 128  
         HD 207651, 128  
         XX Pyx, 128  
     mass transfer, 127  
     post-AGB stars, 131  
     pulsation, 126  
     resonant excitation, 128  
     RV Tau stars, 131  
     sdB stars, 133  
     Spica, 128  
     tidal perturbations, 127  
     tidally induced oscillations, 128  
         HD 177863, 129  
         HD 209295, 129  
     triple stars  
          $\alpha$  Cen, 558  
         DG Leo, 128  
         HD 207651, 128  
     WR 86, 126

- BiSON, 22, 451, 452, 454–456, 462–464, 467, 506, 511, 512, 527, 528, 530, 531, 537, 552, 553  
 echelle diagram, 463  
 observed solar power spectrum, 258, 462
- Blazhko effect, 79  
 mode coupling, 79  
 oblique pulsation, 79
- blue stragglers, 129, 187  
 47 Tuc, 130  
 M67, 130  
 NGC 2506, 130  
 PL relation, 130  
 SX Phe stars, 130
- Brahe, Tycho, 296  
 Tychonic principle, 296, 299
- BRITE mission, 673
- brown dwarfs, 35
- Brunt-Väisälä frequency, 21, 151
- buoyancy frequency, 151
- butterfly diagram, 529
- cadence, 671
- cancellation factor, 13
- cataclysmic variables, 134  
 AM CVn stars, 135  
 pulsation, 134  
 GW Lib, 135
- CCD  
 data reduction, 309  
 frame transfer, 312  
 photometry, 309
- central stars of planetary nebulae, 115
- Cepheids, 11, 80  
 $\delta$  Cephei, 80  
 beat Cepheids, 82  
 Cepheid mass problem, 83  
 distance indicators, 80  
 double mode, 82, 83  
 HD 112044, 80  
 Hertzsprung progression, 82
- instability strip  
 blue edge, 254  
 red edge, 255
- period-colour relation, 82
- period-luminosity relation, 80
- Petersen diagram, 83
- phase lag, 82
- s-Cepheids/overtone Cepheids, 84
- stillstand, 81
- triple mode  
 AC And, 84  
 V823 Cas, 84  
 V829 Aql, 84  
 X Cyg, 81  
 shock wave, 81
- chaotic modes, 290
- classes of stellar pulsators  
 summary, 679
- classical radial pulsators, 75
- clusters  
 pulsating stars, 127
- co-latitude  
 definition, 10
- compact oscillators, 104
- composition changes, 159
- computed oscillation properties, 222  
 results for the Sun, 222
- condition for instability, 246
- convection, 156  
 condition for instability, 156  
 effect on stability, 253  
 frequency effects, 507, 576, 586  
 hydrodynamical simulations, 143, 158, 264
- Ledoux criterion for instability, 157
- mixing-length treatment, 141, 158
- Schwarzschild criterion for instability, 157
- semiconvection, 157
- treatment of, 141

- uniform chemical composition
  - of convection zones, 158
- convection zone
  - extent as a function of
    - effective temperature, 174
- convective blocking, 47, 253
- convective cores
  - effects on pulsation, 231
- convective overshoot, 173
- Coriolis force, 16
- CoRoT, 49, 53, 95, 297, 298, 667, 671–675
- Cowling approximation, 203
  - f mode, 203
- cross-talk
  - HR 1217, 644
  - solar oscillations, 460
- cross-term kernel, 501
- crystallization, 114
- CSPN
  - HD 35914, 116
  - VV 47 (NGC 2474-5), 116
  - Wolf-Rayet stars [WCE], 116
  - ZZ Lep stars, 117
- cyclic frequency, 10
- daily sidelobes, 358
- damped oscillations, 372
- DAV stars, *see ZZ Cet stars*
- DB gap, 112
- DBV stars, *see V777 Her stars*, 119
  - excitation, 119
  - excitation mechanism, 119
  - GD 358
    - case study, 651
  - GD 358 = V777 Her, 651
  - V777 Her
    - case study, 651
- Delta Scuti Network, 50
- density scale height
  - definition, 212
- differential rotation
  - Sun, 447
- diffusion approximation, 141
- dipole mode
  - definition, 12
  - distorted, 57
  - interesting characteristics, 230
- discrete Fourier transform, 354
- double-mode Cepheids, 82
- DOV stars, *see GW Vir stars*, 119
  - GW Vir
    - case study, 646
  - PG 1159
    - case study, 646
- DQV stars, 136
- driving mechanism, 27, 240
  - $\beta$  Cep stars, 27
  - $\epsilon$  mechanism, 28, 244
  - $\gamma$  mechanism, 248
  - $\kappa$  mechanism, 27, 241
  - adiabatic exponent, 27
  - convective blocking, 253
  - convective effects, 245, 253
  - effect of rotation, 290
  - heat-engine mechanism, 27, 241
  - opacity bump, 248, 251
    - $\beta$  Cep stars, 251
    - iron-group elements, 251
    - SPB stars, 252
  - sdBV stars, 27
  - stochastic driving, 28
  - stochastic excitation, 258
    - amplitude distribution, 264
  - stochastic forcing, 241
  - transition region, 249
  - work integral, 241
- duty cycle, 338
  - definition, 297
- Duvall law, 211, 216, 477, 705
  - inversion, 485
- dwarf nova
  - GW Lib, 135
- dynamical time scale, 25
- EC 14026 stars
  - KPD 2109+4401, 105
  - Sakurai's object, 105
  - V605 Aql, 105

- echelle diagram, 219
- $\alpha$  Cen A, 563, 574
- $\alpha$  Cen B, 574
- $\eta$  Boo, 579, 588
- Sun, 463
- echolocation, 5
- eclipse mapping, 445
- Eddington approximation, 142
- Eddington limit
  - luminous blue variables, 101
- Eddington, Sir Arthur Stanley, 2
- eHe stars, 131
  - binary merger, 133
  - excitation, 132
  - PV Tel stars, 132
  - strange modes, 132
  - V2076 Oph, 132
  - V2076 Oph stars, 132
  - V652 Her stars, 132
  - Z bump, 132
- energy equation, 140, 155
  - pre-main-sequence phase, 155
- ephemeris time, 299
- equation of continuity, 138
- equation of state, 161
  - ACTEX, 162
  - CEFF, 162, 515
  - EFF, 162, 516
  - MHD, 162, 515
- equations for adiabatic motion
  - complete set, 143
- equations of hydrodynamics, 137
- equations of motion, 139
  - solutions, 11
- equations of stellar structure, 145
- equilibrium states, 143
- equilibrium structure, 144
  - frequency dependence, 199
- estimation of discrete parameters, 341
- Eulerian
  - description, 138
  - perturbation, 145
- evanescent mode, 208
- exoplanets, 40, 315, 321, 331, 672
- extinction
  - definition, 304
- Fabricius, 27
- fast Fourier transforms, 338
- filters, 313
  - Geneva, 380
  - Hipparcos, 38
  - Johnson *UBVRI*, 313
  - other, 313
  - SDSS  $u'g'r'i'z'$ , 313
  - SDSS transmission curves, 315
  - Strömgren *uvby*, 313
  - white light, 313
- flat field, 308
- Fourier Tachometer, 455
- frequency
  - angular, 10
  - cyclic, 10
- frequency analysis, 337
  - alias, 357, 366
    - heights of peaks, 359
    - one day, 358
    - unequally spaced data, 358
  - alias ambiguity, 368
  - amplitude periodogram, 352
  - choice of frequency step, 368
  - classical periodogram, 360
  - CLEAN, 374
    - warnings, 374
  - continuous Fourier transform, 351
  - correlated noise, 367
  - damped oscillations, 372
    - frequency error, 373
    - Lorentzian profile, 372
  - discrete Fourier transform, 354
  - eliminating aliases, 374
  - Fourier analysis, 350
  - frequency error, 353, 366
  - gapped data, 354
  - Lomb-Scargle periodogram, 361
  - multiple frequencies, 341
  - non-parametric methods, 342
    - string length methods, 342
  - Nyquist frequency, 360
  - parametric methods, 350

- periodogram
  - definition, 351
  - resolving power, 353
- phase dispersion
  - minimization, 348
- power periodogram, 352
- significance criteria, 363
- sinc function, 352
- single frequency, 338
- spectral window, 356
- temporal resolution, 367
- timing error, 366
- unevenly spaced data, 337
- weighting data, 369
- white noise, 367
- frequency dependence
  - internal structure, 200
  - mass and radius, 199
  - physics of stellar interiors, 202
- f modes
  - classification, 229
  - Sun, 222, 461
- global helioseismology, 448
- GOLF, 454, 455, 469, 527, 537, 551, 565
- GONG, 453, 455, 463, 465, 468, 500, 513, 526, 527, 529–534
- Goodricke, John, 80
- GPS clocks, 301
- gravitational settling, 159, 166
- gravitational wave
  - asteroseismology, 126
- gravitational waves
  - neutron stars, 125
- gravito-rotational waves, 277
- gravity darkening, 181
- gravity waves (internal), 148, 152
- gravity waves (surface), 152, 213
- grey-scale plot, 321
- ground-based surveys, 39
- GW Vir stars, 113, 117
  - [WCE] stars, 119
  - excitation, 119
- GW Vir
  - case study, 646
  - PG 1707+427, 105, 118
- g modes, 7, 17, 208, 211
  - asymptotic equal period spacing, 221
  - asymptotic properties, 220
  - classification, 229
  - excitation of high order modes, 252, 256
- Sun, 222, 468
  - Phoebeus collaboration, 469
- hare-and-hounds, 539, 554
- Hayashi track, 33, 176
- HdC stars
  - late thermal pulse, 133
  - heating expressions, 243
- Heliocentric Julian Date, 299
- Helioseismic and Magnetic Imager, 674
- helioseismic radius
  - variations, 530
- helioseismology, 447
  - global, 448
  - history, 450
  - local, 448
  - helium flash, 36, 75–77, 134, 657
  - Heney track, 34
  - Herbig Ae/Be stars, 35, 72
  - HD 144668 = HR 5999, 73
- high pass filter, 312
- Hipparchus of Nicea, 38
- Hipparcos, 38, 371
  - Catalogue of Periodic Variables, 38
  - Catalogue of Unsolved Variables, 38
- HMI, 674
- homologous models, 200
- Hough functions, 279
- Hubble, Edwin, 304
- Hubble-Sandage variables, 99
- hydrodynamics
  - equations, 137

- hydrogen fusion
  - CNO cycle, 35, 165
  - PP chain, 35, 164
- hydrogen-deficient carbon stars, 131
- hydrostatic equilibrium, 144, 154
  - centrifugal force, 181
- ideal gas, 140
- instability strip
  - $\beta$  Cep stars, 67, 68
  - $\delta$  Sct stars, 49, 50
    - blue edge, 52, 256
    - red edge, 52, 255, 256
  - $\gamma$  Dor stars, 48
  - B supergiants, 97
  - blue stragglers, 130
  - Cepheids, 80
    - blue edge, 254
    - red edge, 255
  - classical, 32
  - compact objects, 104
  - condition for instability, 246
  - DAV stars, 113, 122
  - DBV stars, 114
  - DOV stars, 119
  - DQV stars, 136
  - first crossing, 84
  - helium opacity bump, 52
  - Maia stars, 64
  - Miras, 89
  - pre-main-sequence stars, 72
  - roAp stars, 56
  - RR Lyrae stars, 77
    - red edge, 255
  - RV Tau stars, 131
  - semi-regular variables, 89
  - SPB stars, 64
  - type II Cepheids, 85
  - ZZ Cet stars, 113, 122
- inverse analysis, 488
- inversion
  - 1.5-dimensional, 497
  - MOLA technique, 491–495, 502, 527
    - two-dimensional case, 499
- OLA, 534
- RLS, 534
- SOLA technique, 490, 499, 501, 502, 511, 512, 525, 526
  - two-dimensional case, 499
- solar structure, 500
- Tikhonov, 493–495
- two-dimensional rotational, 496
- inversion coefficients, 488
- IRIS, 453, 454, 527
- island modes, 290
- isothermal atmosphere
  - acoustic cut-off frequency, 695
  - adiabatic oscillations, 693
- isothermal sphere, 12
- Jeans criterion, 33
- Julian Date, 300
  - zero point, 300
- JWKB analysis, 701
  - turning points, 703
- Kelvin mode, 283
- Kelvin-Helmholtz time, 26, 143
- Kepler mission, 39, 297, 298, 442, 672–675
- Kepler, Johannes, 2, 303
- kernels
  - definition, 240
  - rotation, 274, 275
  - solar model, 239
- Lagrange points, 186
  - $L_1$ , 185, 186
  - $L_2$ , 186
- Lagrangian
  - description, 138
  - perturbation, 145
- Laplace Tidal Equation, 278–283
- large scale surveys, 38
- large separation, 217, 463
  - definition, 20
  - Sun, 463
- late thermal pulse, 37, 133
- HdC stars, 133

- leakage matrix, 458, 459
- leap second, 299
- least squares, 338
- Leavitt, Henrietta, 80, 85
- Legendre functions
  - properties, 683
  - solutions to linear stellar oscillation equations, 191
- Legendre polynomials, 11
  - properties, 683
- light travel time, 299
- line diagnostics, 325
  - equivalent width, 327
  - line width, 327
  - radial velocity, 326
  - skewness, 327
- line mask
  - definition, 329
- line profile variations
  - definition, 319
  - supergiant stars, 96
- line width, 467
- linear adiabatic oscillations, 195
- linear stellar oscillations
  - boundary conditions, 197
  - equations, 188
- lithium depletion, 184
- local helioseismology, 448
- Lomb-Scargle periodogram, 361
- Lorentzian profile, 372
- LOWL, 455, 511, 512, 527, 528
- luminous blue variables, 99
  - AG Car, 99
  - Eddington limit, 101
  - eruption, 101
  - giant outburst, 100
  - P Cyg, 99
  - R 127, 101
  - S Dor, 99
  - stellar oscillations, 101
  - strange modes, 99, 101
  - temperature, 99
- MACHO, 77–79, 82, 90, 92
- Maia stars, 64, 293
- MDI, 455, 463–467, 502, 506, 513, 516, 518, 524–534, 572
- meridional circulation, 183
- Mira variables, 88
  - $\alpha$  Ceti = Mira, 88
- missing data, 337
- mixed modes, 208, 233, 567, 580, 586, 588, 599
- mixing length, 158
  - solar radius, 158
- modal mass, 194
- mode
  - evanescent, 208
- mode bumping
  - $\eta$  Boo, 582
- mode classification, 229
- mode identification, 377
  - $\alpha$  Cen A, 563
  - $\beta$  CMa, 441
  - $\beta$  Cru, 440
  - $\delta$  Cet, 441
  - $\eta$  Boo, 579
  - $\gamma$  Dor stars, 442
  - $\nu$  Eri, 398, 427, 441, 619
  - $\rho$  Pup, 421
  - $\tau$  Peg, 434
  - $\theta$  Oph, 441, 627
  - $\varepsilon$  Oph, 597, 598
  - 20 CVn, 401, 429
  - 9 Aur, 442
  - discriminant, 424
  - eclipse mapping, 445
  - FG Vir, 401, 434
  - GD 358, 653
  - HD 12901, 380
  - HD 164615, 442
  - HD 71913, 380
  - high-resolution spectroscopy, 405
  - HR 1217, 638
  - HR 8799, 442
  - interferometry, 442
  - KPD 2109+4401, 400
  - line-profile variations, 406

- calculation of theoretical line-profile variations, 406
- computation of the observational moments, 420
- moment method, 415
- computation of the observational moments, 420
- interpretation of the moments, 421
- monoperiodic oscillation, 416
- multicolour photometry, 379
- $\beta$  Cep stars, 382
- $\delta$  Sct stars, 382
- $\gamma$  Dor stars, 382
- roAp stars, 405
- SPB stars, 382
- using amplitudes, 393
- using phase differences, 400
- ZZ Cet stars, 382
- non-adiabatic observables, 389
- PG 0014+067, 658
- PG 1159, 647
- PG 1336–018, 665
- QW Pup, 442
- solar-like pulsators, 535
- V836 Cen, 606
- mode inertia, 194
- mode selection, 28
  - dynamical time scale, 25
  - Kelvin-Helmholtz time scale, 26
  - nuclear time scale, 24
  - thermal time scale, 26
- mode switching, 77, 125
- mode trapping, 203
  - turning points, 208
- Model S, 505, 506, 508, 510–514, 516, 517, 520, 521, 548, 572
- Modified Julian Date
  - definition, 300
- MOLA inversion, 516
- MOLA technique, 491–495, 502, 527
  - two-dimensional case, 499
- moment method
  - definition of the moments, 416
- MOST, 61, 63, 69–71, 94, 95, 98, 102, 103, 110, 297, 298, 371, 441, 585, 591, 635, 636, 640, 645, 670, 673, 674
- multiplet
  - definition, 16
- Music of the Spheres
  - definition, 1
- nanosatellite, 673
- neutron stars, 124
  - gravitational waves, 125
  - oblique pulsator model, 125
  - quasi-periodic oscillations, 125
  - x-ray burst oscillations, 136
- Newton's law of cooling, 142
- nonradial modes, 12
- nonradial oscillations, 188
  - crudest approximation to the equations, 204
- nuclear reactions, 164
- nuclear time scale, 24
- Nyquist frequency, 311
  - definition, 360
- oblique pulsator model
  - Blazhko stars, 79
  - neutron stars, 125
  - roAp stars, 56
- observational techniques, 295
- octupole modes, 14
  - definition, 13
- OGLE, 75–77, 80, 82, 84, 90, 91
- OP, 163, 164
- OPAL, 84, 162–164, 505
- optimally localized averages, 489
- oscillations
  - organ pipe, 8
- overtone
  - definition, 7
- partial cancellation, 13, 15, 392, 456
- period ratio
  - $\delta$  Sct star, 12

- Cepheid, 12
  - organ pipe, 12
- period-luminosity relation
  - blue stragglers, 130
  - Cepheids, 80
- period-luminosity sequences, 91
- periodogram
  - amplitude, 352
  - definition, 351
  - power, 352
- perturbation analysis, 143, 145
- Petersen diagram, 83
- PG 1159 stars, 113, 117
  - GW Vir
    - case study, 646
- PG 1716 stars
  - PG 1716+426, 105
- PG 1716+426 stars, 107
- Phobos mission to Mars, 454
- Phoebus collaboration, 469
- photometric conditions
  - definition, 304
- photometry, 301
  - differential, 309
  - high speed, 311
  - sources of error, 302
    - instrumental, 307
    - other, 303
    - periodic drive error, 309
    - photon statistics, 302
    - scintillation, 305
    - sensitivity variations, 308
    - sky transparency, 304
- Planck function, 313
- planet hunting, 297
- plasmon neutrinos, 114
- Plato (Greek philosopher), 2
- PLATO mission, 673
- PNNV
  - HD 35914, 116
- PNNV stars, 119
- Poisson equation, 139, 143, 190
- Population II Cepheids
  - type II Cepheids, 85
  - W Virginis stars, 85
- pre-main sequence pulsators
  - HD 144668 = HR 5999, 73
    - IP Per, 73
- pre-main-sequence phase, 33
- pre-main-sequence stars
  - oscillations, 72
- precision
  - definition, 297
- prewhiten
  - definition, 341
- prograde modes
  - definition, 15
- protostars, 33
- Pulsating Be stars
  - $\beta$  CMi, 71
  - $\omega$  CMa, 69
    - HD 163868, 70
- pulsating Be stars, 68
- pulsation axis, 11
- pulsation HR Diagram, 23
- PV Tel stars, 132
- PVSG
  - $\gamma^2$  Vel, 96
  - HD 163899, 98
  - HD 98410, 97
- Pythagoras of Samos, 1
- p modes, 7, 17, 208, 209
  - asymptotic properties, 217
  - classification, 229
  - ray theory, 210
  - Sun, 222, 461
- quadrupole modes
  - definition, 13
- quasi-adiabatic approximation, 244
- quasi-periodic oscillations
  - neutron stars, 125
- R CrB stars, 131
  - late thermal pulse, 133
- radial modes, 11
- radial oscillations, 188, 194
- radial velocity
  - definition, 296
- radiation time scale, 142

- radiative flux
  - equation, 141
- radiative transport, 155
- rapidly oscillating Ap stars, 56
- ray paths, 18
- red clump, 37
- resolution
  - Rayleigh, 305
  - spectral
    - definition, 322
- resonant cell technique, 454
- resonant excitation, 128
- retrograde modes
  - definition, 15
- Rijke's tube, 243
- roAp stars, 12, 56, 634
  - $\alpha$  Cir, 640
  - $\gamma$  Equ, 640, 641
  - Alfvén speed, 60
  - core-wing anomaly, 58
  - distorted dipole modes, 57
  - DO Eri = HR 1217
    - case study, 634
  - Doppler imaging, 59
  - element stratification, 59
  - HD 101065, 56, 642
  - HD 128898 =  $\alpha$  Cir, 640
  - HD 12932, 641
  - HD 137949, 641
  - HD 24712 = HR 1217
    - case study, 634
  - HR 5463 =  $\alpha$  Cir, 640
  - magneto-acoustic modes, 57
  - oblique pulsator model, 56
  - spectroscopic radial velocity
    - studies, 640
  - spectroscopic studies
    - HD 101065, 644
    - HD 116114, 644
    - HD 122970, 644
    - HD 128898, 644
    - HD 137949, 644
    - HD 166473, 644
    - HD 176232, 644
    - HD 201601, 644
- HD 24712, 643
- HD 83368, 643
- HD 99563, 644
- HR 3831 = HD 83368, 643
- wing-nib anomaly, 58
- Roche lobe, 186
- Roche lobe overflow, 134
- Roseland mean opacity, 142, 163
- rotation effects, 265
- rotation on cones, 523
- rotation on cylinders, 523
- rotational splitting, 265, 271
  - chaotic modes, 290
  - co-rotating reference frame, 16
- dispersion relation for
  - high-order g modes, 277
  - effects on low-frequency modes, 276
- gravito-rotational waves, 277
- higher-order effects, 284
- island modes, 290
- Laplace Tidal Equation, 278
- Ledoux constant, 274
- Ledoux relation, 16
- observer's reference frame, 16
- properties, 272
- uniform rotation, 274
- whispering gallery modes, 290
- RR Lyrae stars, 11, 75
  - Bailey classes (RRa, RRb, RRc), 77
  - Blazhko effect, 79
  - double mode (RRd), 77
  - instability strip
    - red edge, 255
  - Oosterhoff I clusters, 78
  - Oosterhoff II clusters, 78
- RV Tauri stars, 86, 131
  - AC Her, 86, 87
  - alternating minima, 87
  - dusty discs, 131
  - excitation, 86
  - long period binaries, 88
  - R Sct, 87
  - shock waves, 87
  - SX Cen, 87

- Scaliger, Joseph Justus, 300  
 scaling relations, 199  
 Schönberg-Chandrasekhar instability, 176  
 Schrödinger equation, 224  
 sdB stars  
     binary stars, 133  
     temperature range, 105  
 sdBV stars  
     EC 14026–2647, 105, 133  
     excitation, 110  
     Fe enhancement, 110  
     KPD 1930+2752  
         eclipse mapping, 446  
     KPD 2109+4401, 400  
     PG 0014+067  
         case study, 656  
     PG 1336–018, 134  
         case study, 661  
         eclipse mapping, 446  
 SDO, 674  
 SDSS, 313  
     ZZ Cet stars, 124  
 sectoral mode  
     definition, 14  
 seeing  
     definition, 305  
 seeing with sound, 2  
 seismic solar model, 503  
 self-excited mode, 241  
 semi-regular variables, 88  
      $\rho$  Cas, 88  
     V Boo, 88  
 semiconvection, 157  
 separation of variables, 188  
 Shakespeare, William, 2  
 shell-burning source, 165  
 shellular rotation, 183  
 SIAMOIS, 298  
 slowly pulsating B stars, 60  
 small separation, 217, 463  
     definition, 20  
     Sun, 463  
 SOHO, 453–455, 463, 468, 469, 500,  
     502, 525, 537, 674  
 SOLA inversion, 524, 525, 532  
 SOLA technique, 490, 499, 501,  
     502, 511, 512, 525, 526  
     two-dimensional case, 499  
 Solar Dynamics Observatory, 674  
 solar interior  
     temporal variations, 529  
 Solar Maximum Mission, 454, 530  
 solar modelling, 448  
 solar neutrinos, 448  
 Solar Orbiter, 674  
 solar oscillations  
     analysis, 456  
     cross-talk, 460  
     line width, 467  
     observations, 453  
         resonant cell technique, 454  
 properties, 470  
     acoustic glitch, 474  
     f modes, 474  
     near-surface effects, 470  
     velocities, 468  
 solar rotation, 522  
     torsional oscillations, 532  
 solar structure  
     helioseismic results, 505  
     inversion, 500  
     linearized numerical inversion,  
         500  
 solar-like oscillators, 42  
      $\alpha$  CMi, 43  
      $\alpha$  Cen A, 44  
      $\beta$  Hyi, 44  
      $\eta$  Boo, 43  
      $\tau$  PsA, 43  
     171 Pup, 43  
     HD 139211, 43  
     HD 49933, 43  
     red giants, 92  
          $\alpha$  Boo (Arcturus), 93  
          $\alpha$  UMa, 93  
          $\beta$  Oph, 93  
          $\eta$  Ser, 94  
          $\varepsilon$  Oph, 93  
          $\xi$  Hya, 93

- 47 Tuc, 93
- GSC 09137–03505, 93
- HD 20884, 95
- HD 32887, 93
- HD 81797, 93
- solar-like pulsators, 535
  - asteroseismic diagnostics, 539
- SONG, 298, 675
- sound speed
  - in air, 4
  - in helium, 4
- sound wave, 3
- spatial filter, 443, 456
- Spatial Filtration method, 445
- spatial response function, 443, 456
- SPB stars, 23
  - o* Vel, 61
  - excitation, 62
  - excitation of high order g modes, 252, 256
  - g modes, 62
  - HD 123515, 61
  - HD 163830, 61
  - HD 177863, 129
  - line profile variability, 61
  - masses, 62
  - opacity bump, 252
  - rotational splitting, 276
  - Z bump, 62
- specific heat, 140
- specific volume, 140
- spectral disentangling, 333
  - FDBINARY, 334
  - KOREL, 333
- spectral window
  - definition, 356
- spectroscopy, 315
  - double-lined binaries, 333
  - exoplanets, 331
  - instrumental profile, 322
  - iodine, 318
  - line diagnostics, 325
    - equivalent width, 327
  - line bisectors, 328
  - line width, 327
- radial velocity, 326
- skewness, 327
- line profile merging, 328
- radial velocity precision
  - iodine, 331
  - Th-Ar, 331
- spectral disentangling, 333
- spectrum normalisation, 323
- Th-Ar, 323
  - time-resolved, 324
- UVES wavelength stability, 318
- wavelength calibration, 323
- speed of light =  $\tilde{c}$ , 141
- spherical harmonics, 11
  - inclination angles of complete cancellation, 686
  - properties, 685
  - solutions to linear stellar oscillation equations, 191
- spheroidal modes, 194
- standard models
  - simplifications, 160
- stellar evolution, 33, 167
  - close binary systems, 185
    - blue stragglers, 187
    - common envelope, 187
    - Roche lobe, 186
    - subdwarf B stars, 187
  - complications, 179
  - magnetic fields, 181
  - mass loss, 179
  - mixing, 181
  - rotation, 181
- stellar interiors
  - microphysics, 161
- Stellar Music No 1, 7
- stellar oscillations
  - asymptotic theory, 202
- stellar rotation, 555
- stellar structure
  - equilibrium, 154
- stochastic excitation, 258, 467
  - amplitude distribution, 264
- strange modes, 96, 99, 101, 102, 132
  - eHe stars, 132
- Wolf-Rayet stars, 102

- subdwarf B variables  
   EC 14026 stars, 23  
   PG 1716+426 stars, 23
- Sun  
    $l - \nu$  plot, 222  
   160-minute oscillation, 451, 468  
   differential rotation, 447  
   g mode eigenfunctions, 227  
   internal rotation, 17  
   large separation, 463  
   modelling, 448  
   radial displacement  
     eigenfunctions, 225  
     small separation, 463
- superadiabatic gradient, 158
- supernova  
    $\epsilon$  mechanism, 104  
   g mode, 103  
   type Ia, 105
- surface gravity waves, 152, 213
- SX Phe stars, 53  
   47 Tuc, 130  
   blue stragglers, 56, 130  
   SX Phe itself, 54
- T Tauri stars, 35, 72
- tachocline, 184, 523
- TAMS, 169
- tesseral mode  
   definition, 14
- thermal pulse, 37
- thermal time scale, 26
- tidally induced oscillations, 128
- Tikhonov inversion, 493–495
- time, 298  
   accuracy, 301
- time scale  
   Kelvin-Helmholtz, 143  
   radiation, 142  
   solar convection zone, 143
- time series analysis, 337
- timing error, 366
- toroidal modes, 194
- torsional oscillations, 532
- trade-off parameter, 490
- traditional approximation, 278
- transition region, 249
- transparency  
   definition, 304
- trapped mode, 208
- triple-alpha process, 165
- turbulent pressure, 160
- turning point  
   g modes, 211  
   p modes, 209
- twinkling of starlight, 305, 306
- ULTRACAM, 133, 134, 310, 400, 658, 661
- unevenly spaced data, 337
- uniform chemical composition of convection zones, 158
- UVES, 318, 319, 324, 641, 645, 661, 662
- UX Ori stars, 72
- UX Ori stars  
   IP Per, 73
- V2076 Oph stars, 132
- V361 Hya stars, 107
- V652 Her stars, 132
- V777 Her stars, 119  
   excitation mechanism, 119  
   GD 358, 105  
     case study, 651  
   GD 358 = V777 Her, 651  
   V777 Her  
     case study, 651
- variable subdwarf B stars  
   sdBV stars, 105
- variational principal, 237
- variational properties of stellar  
   adiabatic oscillations, 234
- vector operators, 690
- VIRGO, 454, 551
- VLT, 300, 318, 319, 324, 641, 661
- W Virginis stars, 86  
   Population II Cepheids, 85
- WET, 117–122, 134, 135, 298, 300, 369, 636, 638, 644, 647, 648, 652, 655–658, 660, 662–666

- whispering gallery modes, 290
- white dwarf mergers, 134
- white dwarf stars, 110
  - atomic diffusion, 112
  - axions, 114
  - case studies, 646
  - convective driving, 120, 122
  - crystallization, 114
  - DA stars, 111
  - DAV stars, 122
    - G29-38, 122
  - DB stars, 110
  - DBV stars, 113, 119
    - GD 358, 121
    - PG 1351+489, 120
    - PG 1456+103, 119
  - DO stars, 110
  - DQ stars
    - SDSS J142625.71+575218.3, 135
    - G29-38, 123
    - GD 358, 113
    - GW Vir, 113
    - GW Vir stars, 113, 117
    - mode trapping, 114
    - PG 1707+427, 117
    - PG 1159 stars, 113, 117
    - PG 1159–035, 113
  - PG 1707+427, 118
  - plasmon neutrinos, 114
  - V777 Her, 113
  - V777 Her stars, 113, 119
    - PG 1456+103, 119
  - ZZ Cet stars, 113, 122
    - convective driving, 122
    - G29-38, 122
  - white dwarfs
    - convective driving, 253
  - WIRE, 93, 440, 441, 670, 674
  - Wolf-Rayet stars, 101, 179
    - quasi-periodic variability, 102
    - strange modes, 102
    - WC stars, 101
    - WN stars, 101
    - WR 123, 102
    - WR 134, 102
    - WR 46, 102
    - WR 6, 102
  - work integral, 241
  - zenith distance, 304
  - ZZ Cet stars, 113, *see* white dwarfs
    - GD 244, 105
  - ZZ Lep stars, 117
  - Z bump
    - eHe stars, 132

# Object Index

- $\alpha$  Boo, 93
- $\alpha$  CMi, 43
- $\alpha$  Cen A, 44, 126, 537
  - case study, 558
- $\alpha$  Cen B, 126
  - case study, 558
- $\alpha$  Cir, 640
- $\alpha$  Cyg, 96
- $\alpha$  UMa, 93
- $\alpha$  Vir, 128
- $\beta$  Cen, 333
- $\beta$  Cru, 320
- $\beta$  CMa, 16, 441
- $\beta$  CMi, 71
- $\beta$  Cen, 441
- $\beta$  Cru, 327, 440, 441
- $\beta$  Hyi, 44
- $\beta$  Oph, 93
- $\delta$  Cephei, 80
- $\delta$  Cet, 441
- $\eta$  Boo, 43
- $\eta$  Ser, 94
- $\eta$  Boo
  - case study, 576
- $\gamma$  Doradus, 45
- $\gamma$  Equ, 640, 641
- $\gamma$  Equ = HD 201601, 644
- $\gamma^2$  Vel, 96
- $\kappa$  Sco, 441
- $\lambda$  Sco, 441
- $\nu$  Eri, 66, 398, 427, 441
  - case study, 614
- $\omega$  CMa, 69
- $\omega$  Cen, 130
- $\omega^1$  Sco, 441
- $\rho$  Cas, 88
- $\rho$  Pup, 49, 421
- $\sigma$  Sco, 128
- $\tau$  Peg, 434
- $\tau$  PsA = HD 210302, 43
- $\theta$  Oph, 441
  - case study, 625
- $\theta^2$  Tau, 50
- $\varepsilon$  Per, 321
- $\varepsilon$  Oph, 93
  - case study, 591
- $\xi$  Hya, 93
- $\xi^1$  CMa, 65, 316
- $o$  Ceti, 27, 88
- $o$  Vel, 61
- 10 Aql = HD 176232, 644
- 12 Lac, 65
- 14 Aur Aa, 128
- 171 Pup, 43
- 19 Mon, 65
- 20 CVn, 401, 429
- 33 Lib = HD 137949, 644
- 47 Tuc, 93, 130
- 4 CVn, 50
- 51 Peg, 321, 331
- 9 Aur, 442
- AB Cas, 445
- AC And, 84
- AC Her, 86, 87
- AG Car, 99
- Altair, 50
- AM CVn, 135
- Arcturus, 93
- AS Eri, 445
- binary stars
  - $\alpha$  Cen A, 558
  - $\alpha$  Cen B, 558
  - $\eta$  Boo
    - case study, 576
  - BW Vul, 65
  - DG Leo, 128
  - DO Eri = HR 1217
    - case study, 634
  - EC 14026–2647, 133
  - EK Psc = PG 0014+067, 656

- exoplanet  
 51 Peg b, 315, 321  
 PSR 1257+12, 300, 331  
 PSR 1829–10, 299  
 V391 Peg b, 300
- FG Vir, 50, 329, 401, 434
- G29-38, 122, 123  
 GD 244, 105  
 GD 358, 105, 113, 121  
     case study, 651  
 GD 358 = V777 Her, 651  
 GSC 09137–03505, 93  
 GW Lib, 135  
 GW Vir, 113, 118  
     case study, 646
- HD 101065, 56, 318, 642, 644  
 HD 112044, 80  
 HD 116114, 644  
 HD 122970, 644  
 HD 123515, 61, 358  
 HD 128898, 644  
 HD 128898 =  $\alpha$  Cir, 640  
 HD 12901, 46, 380  
 HD 12932, 641  
 HD 129929, 65, 603  
 HD 137949, 641, 644  
 HD 139211 = HR 5803, 43  
 HD 146791 =  $\varepsilon$  Oph, 591  
 HD 157056 =  $\theta$  Oph  
     case study, 625
- HD 163830, 61  
 HD 163868, 70, 293  
 HD 163899, 98  
 HD 164515, 45  
 HD 164615, 442  
 HD 166473, 644  
 HD 176232, 644  
 HD 177863, 129  
 HD 201601, 644  
 HD 207651, 128  
 HD 20884, 95  
 HD 209295, 47, 129
- HD 210302 =  $\tau$  PsA, 43  
 HD 24712, 643  
 HD 24712 = HR 1217  
     case study, 634  
 HD 263551, 50  
 HD 32887, 93  
 HD 35914, 116  
 HD 49933 = HR 2530, 43  
 HD 71913, 380  
 HD 74195, 358  
 HD 74195 =  $o$  Vel, 61  
 HD 81797, 93  
 HD 83368, 643  
 HD 96008, 45  
 HD 98410, 97  
 HD 99563, 644  
 HR 1217  
     case study, 634  
 HR 2530 = HD 49933, 43  
 HR 3831 = HD 83368, 643  
 HR 5463 =  $\alpha$  Cir, 640  
 HR 5803 = HD 139211, 43  
 HR 5999, 73  
 HR 6453 =  $\theta$  Oph  
     case study, 625  
 HR 8799, 442
- IC 418, 116  
 IP Per, 73
- KPD 1930+2752, 446  
 KPD 2109+4401, 105, 400
- M31, 99  
 M33, 99  
 M67, 130  
 M 2-54, 116  
 Mira, 88
- NGC 2264, 72  
 NGC 2474-5, 116  
 NGC 2506, 130  
 NY Vir = PG 1336–018, 661
- PCyg, 99  
 PG 1336–018, 133

- PG 1707+427, 117
- PG 0014+067
  - case study, 656
- PG 1159
  - case study, 646
- PG 1159–035, 113, 118
- PG 1159–035 = GW Vir, 646
- PG 1336–018, 134, 446
  - case study, 661
- PG 1336–018 = NY Vir, 661
- PG 1351+489, 120
- PG 1456+103, 119
- PG 1707+427, 105, 118
- PG 1716+426, 105
- Proxima Centauri, 558
- Przybylski's star = HD 101065, 644
- QW Pup, 442
- R 127, 101
- R Sct, 87
- RU Cen, 316
- RZ Cas, 445
- S Dor, 99
- Sakurai's object, 105
- SDSS J142625.71+575218.3, 135
- SN1987A, 303
- solar-like oscillators
  - $\alpha$  Cen A
    - case study, 558
  - $\alpha$  Cen B
    - case study, 558
- $\eta$  Boo
  - case study, 576
- $\varepsilon$  Oph, 591
  - case study, 591
  - red giants
  - $\varepsilon$  Oph, 591
- Spica, 128
- spirograph nebula, 116
- SX Cen, 87
- SX Phe, 54
- V2076 Oph, 132
- V391 Peg, 300
- V605 Aql, 105
- V777 Her, 113
  - case study, 651
- V777 Her = GD 358, 651
- V823 Cas, 84
- V829 Aql, 84
- V836 Cen = HD 129929
  - case study, 603
- V Boo, 88
- VV 47, 116
- WR 123, 102
- WR 134, 102
- WR 46, 102
- WR 6, 102
- WR 86, 126
- X Cyg, 81
- XX Pyx, 50, 128
- Y Cam, 445

# Acronym Definition Index

[WCE], 38	HADS, 49
2MASS, 41	HARPS, 561
AAT, 537	HdC, 131
AAVSO, 91	HELAS, 446
ADU, 308	Hipparcos, 38
AFOE, 578	HJD, 299
AGB, 37	HMI, 674
ARENA, 676	HR Diagram, 31
ASAS, 41	IACC, 686
astroFLAG, <i>see</i> solarFLAG	IALC, 687
BiSON, 21, 452	IPHAS, 41
BJD, 299	IPHIR, 516
BJED, 299	IRAF, 309, 316
CCD, 301	IRAS, 131
CCF, 329	IRIS, 453
CEFF, 162	JD, 298
CFHT, 106	JWKB, 701
CoRoT, 39	KASC, 673
CSPN, 115	LBV, 99
CV, 134	LOWL, 455
DAS, 446	LSD, 330
DAV, 113	MACHO, 39
DBV, 113	mas, 38
DOV, 118	MDI, 455
DSN, 50	MHD, 162
EC, 105	MIDAS, 316
EHB, 106	MJD, 300
eHe, 132	mma, 107
EROS, 40	mmi, 652
ESO, 316	MOA, 40
FAMIAS, 446	MOLA, 491
FUSE, 108	MOST, 50
FWHM, 305	OGLE, 40
GECKO, 645	OLA, 489
GOLF, 21, 295, 454	OP, 63
GONG, 453	OPAL, 63
GPS, 301	

PDM,	348	SR,	88
PG,	105	SVD,	495
PL,	90, 130	TAMS,	35
PNNV,	116	TNG,	645
PSF,	305	TON,	454
PVSG,	95	UCLES,	537, 559
RAVE,	41	USNO,	298
RLS,	491	UT,	300
roAp,	56	UTC,	298
S/N,	302	UV,	99
SARG,	645	UVES,	300
sdBV,	105	VIRGO,	295, 454
SDO,	674	VLT,	133
SDSS,	41, 111	WET,	118
SIAMOIS,	297	WIRE,	50
SOHO,	21, 295, 453	WR,	101
SOLA,	490	YREC,	595
solarFLAG,	539	ZAMS,	35
SONG,	297, 675		
SPB stars,	60		